

Handbook on the Physics and Chemistry of Rare Earths, volume 34

Elsevier, 2004

Edited by: K. A. Gschneidner, Jr., J.-C. G. Bünzli, and V. K. Pecharsky
ISBN: 978-0-444-51587-2

PREFACE

Karl A. GSCHNEIDNER Jr., Jean-Claude G. BÜNZLI, and Vitalij K. PECHARSKY

These elements perplex us in our rearches [sic], baffle us in our speculations, and haunt us in our very dreams. They stretch like an unknown sea before us – mocking, mystifying, and murmuring strange revelations and possibilities.

Sir William Crookes (February 16, 1887)

This volume of the *Handbook on the Physics and Chemistry of Rare Earths* adds five new chapters to the science of rare earths, compiled by researchers renowned in their respective fields. Volume 34 opens with an overview of ternary intermetallic systems containing rare earths, transition metals and indium (Chapter 218) followed by an assessment of up-to-date understanding of the interplay between order, magnetism and superconductivity of intermetallic compounds formed by rare earth and actinide metals (Chapter 219). Switching from metals to complex compounds of rare earths, Chapter 220 is dedicated to molecular structural studies using circularly polarized luminescence spectroscopy of lanthanide systems, while Chapter 221 examines rare-earth metal-organic frameworks, also known as coordination polymers, which are expected to have many practical applications in the future. A review discussing remarkable catalytic activity of rare earths in site-selective hydrolysis of deoxyribonucleic acid (DNA) and ribonucleic acid, or RNA (Chapter 222) completes this book.

A new feature to the *Handbook* series has been included in this volume. An abbreviated subject index to the contents of the 222 chapters published to date. This index appears right after the **Contents of Volumes 1–33**. We kept its size to a minimum by including only the most general terms and plan to update the index with every new volume.

Chapter 218. Rare Earth-Transition Metal-Indides

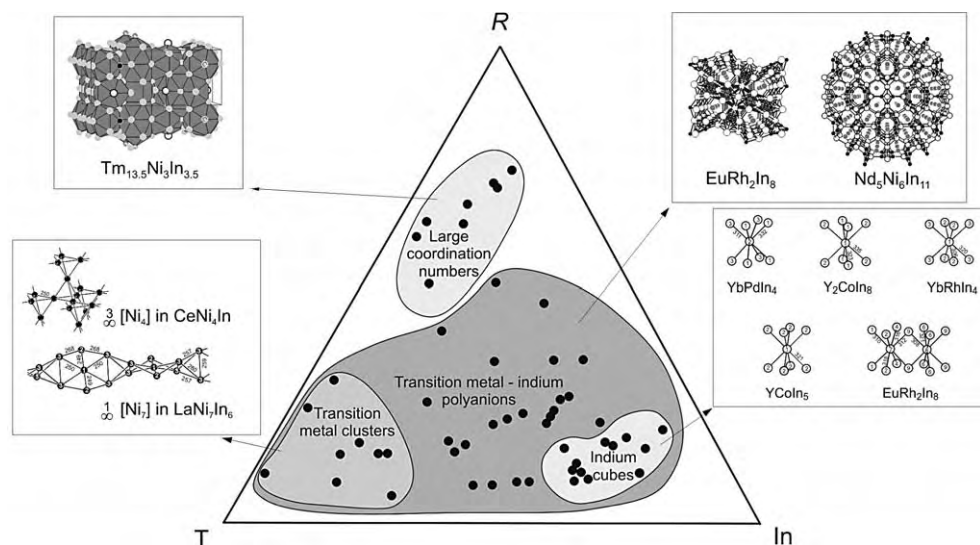
by Yaroslav Kalychak, Vasyly' Zaremba

Ivan Franko National University, Lviv, Ukraine

Rainer Pöttgen, Mar'yana Lukachuk, and Rolf-Dieter Hoffmann

Westfälische Wilhelms-Universität, Münster, Germany

The opening chapter of the *Handbook* reviews synthesis conditions, isothermal sections of phase diagrams, crystallography and basic physical properties of ternary intermetallic compounds consisting of rare-earth metals, transition metals and indium. Some of these intermetallic compounds – indides (so named because indium is usually the most electronegative



component in these ternary systems) – have been known for nearly forty years, others recently emerged as hot subjects for condensed matter physics research, especially with the discovery of heavy fermion superconductivity in a few cerium-based indium-rich intermetallics. Today, the rare earth-transition metal indides have been transformed into a playground for solid state chemists and condensed matter physicists because chemical bonding and crystallography, and therefore, physical properties of these compounds can be controlled by small changes of stoichiometry. Many systems are known to form in excess of ten individual chemical compounds. Although for the most part dominated by metallic bonding, indium-rich alloys often form well-defined clusters of indium atoms, and also a variety of low-dimensional transition metal-indium networks and chains, which just about ensures future discoveries of unusual physics, especially with respect to electronic transport and magnetic behaviors. In addition to a critical review of the up-to-date literature on the subject, Kalychak and co-authors offer the reader a challenging but very interesting subject of structure-property relationships.

Chapter 219. Unconventional Superconductivity and Magnetism in Lanthanide and Actinide Intermetallic Compounds

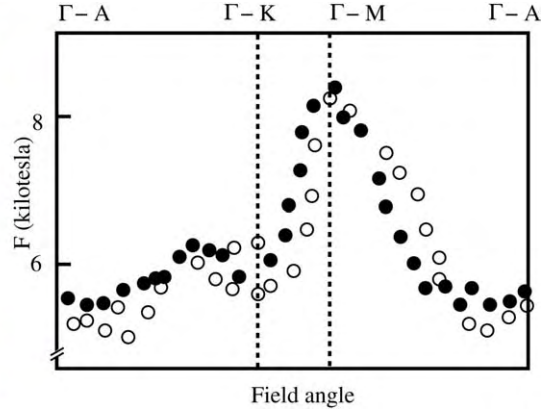
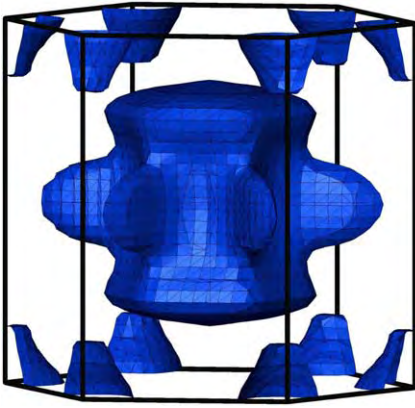
by Peter Thalmeier

Max-Planck-Institute für Chemische Physik fester Stoffe, Dresden, Germany

Gertrud Zwirnagl

Technische Universität, Braunschweig, Germany

The f-elements in general and rare earth metals in particular are celebrated for the non-conventional superconductivity, and thus this chapter of the *Handbook* revisits the last decade



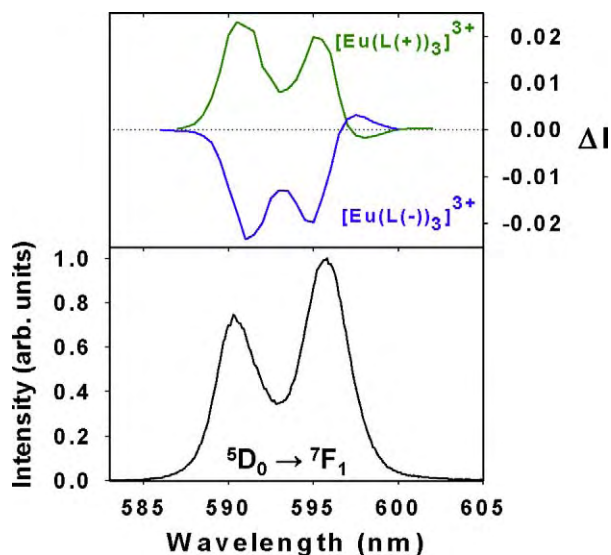
of research uncovering some of the mysteries of the superconducting state, especially those related to heavy fermion superconductivity and co-existence of the superconducting and exotic magnetically ordered states. Thalmeier and Zwicknagl first introduce the reader to the basics by reviewing the nature of heavy quasiparticles, Kondo lattice, Fermi liquid, and spin fluctuation theory, followed by the consideration of order parameters in strongly correlated electron systems and experimental techniques most effective in detecting relevant order parameters. Justifiably, the majority of this chapter is dedicated to both the well-known unconventional superconductors, such as CeCu_2Si_2 , UPt_3 , UBe_{13} , and others, as well as to the newly discovered CeCoIn_5 (hence complementing Chapter 218 in this volume), holmium- and erbium-nickel borocarbides, and skutteridites. The latter is a great addition to Chapter 212 that was written by Brian Sales and appeared last year in volume 33 of the *Handbook*.

Chapter 220. Circularly Polarized Luminescence Spectroscopy from Lanthanide Systems

by James P. Riehl and Gilles Muller

University of Minnesota, Duluth, Minnesota, USA

The phenomenon of circularly polarized luminescence, i.e., emission of partially polarized light during f - f transitions of the rare-earth ions in optically active, chiral molecules (molecules existing in two different modifications whose structures cannot be superimposed over one another), is reviewed by Riehl and Muller. They begin with the general theory, thus giving the reader a background needed to better understand experimental techniques that are used today to study the effect, followed by a critical assessment of the important structural information that has been and can be deduced while using the technique. The authors pay special attention to details and also provide their views on the future of the method as a reliable tool for probing molecular stereochemistry of lanthanide complexes both in pure forms and in mixtures.

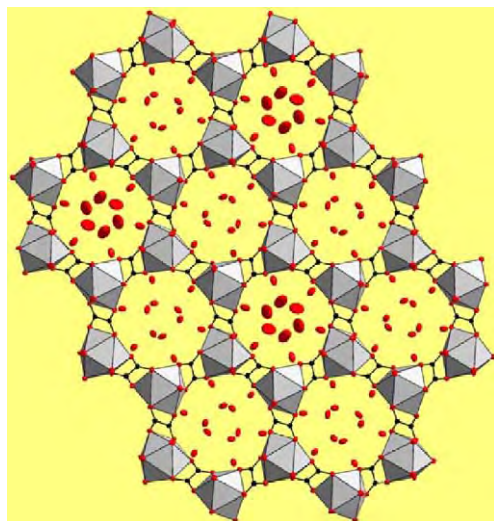


Chapter 221. Lanthanide-Containing Coordination Polymers

by Olivier Guillou and Carole Daiguebonne

Institut National des Sciences Appliquées Rennes, France

Metal-organic frameworks, also known as coordination polymers, hold a great potential as working bodies for opto-electronic and magnetic devices, microporous materials for a variety



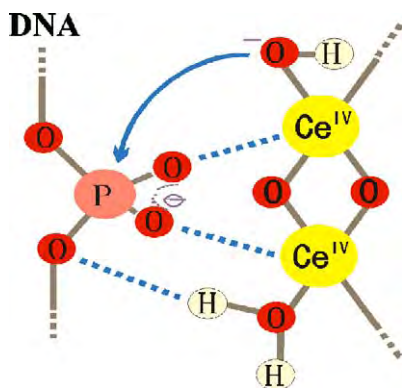
of uses, such as size- and shape-selective separations and catalyst support, and more recently, as hydrogen storage materials. A variety of physical properties that are largely defined by the 4-f electrons of lanthanide ions combined with a similarity of their chemical properties offer an unprecedented flexibility in designing coordination polymers that are chemically similar but functionally different. The subject of this chapter is truly one of the emerging fields in rare-earth science. Guillou and Daiguebonne begin with a brief introduction to transition metal-based frameworks and then quickly move to the core by reviewing various rare earth-containing coordination polymers based on different ligands, paying special attention to those compounds that were

synthesized with a practical application in mind. Polymeric complexes based on benzene-poly-carboxylates are described in the greatest detail.

Chapter 222. Cutting DNA and RNA

by Makoto Komiyama

University of Tokyo, Tokyo, Japan



Likely the best known application of rare earths, which is related to living organisms, are the remarkably effective contrast agents in magnetic resonance imaging, yet this chapter shows that site-selective cutting (scission or hydrolysis) of deoxyribonucleic acid (DNA) and ribonucleic acid (RNA) may be the next big use for lanthanides in genetic engineering. Both DNA and RNA are biological polymers that store genetic information and pass it on via synthesis of protein molecules. According to Komiyama, future biotechnology may well rely on the use of rare-earth ions as unique catalysts that can slice DNA and RNA in order to allow their reprogramming, and thus lead

to more effective bioengineered processes. The author begins with a historical overview of how the catalytic effect of Ce⁴⁺ in the hydrolysis of DNA was discovered, and then gives the current state-of-the-art in understanding of the hydrolysis mechanism. Similarly, he describes catalytic effect of lanthanide ions in hydrolysis of RNA, followed by a review of various strategies that can be employed to improve site-selectivity in the hydrolysis of both DNA and RNA.

CONTENTS

Preface v

Contents xi

Contents of Volumes 1–33 xiii

Index of Contents of Volumes 1–34 xxiii

218. Yaroslav M. Kalychak, Vasył' I. Zaremba, Rainer Pöttgen, Mar'yana Lukachuk and Rolf-Dieter Hoffman

Rare earth–transition metal–indides 1

219. P. Thalmeier and G. Zwicknagl

Unconventional superconductivity and magnetism in lanthanide and actinide intermetallic compounds 135

220. James P. Riehl and Gilles Muller

Circularly polarized luminescence spectroscopy from lanthanide systems 289

221. Oliver Guillou and Carole Daiguebonne

Lanthanide-containing coordination polymers 359

222. Makoto Komiyama

Cutting DNA and RNA 405

Author index 455

Subject index 493

CONTENTS OF VOLUMES 1–33

VOLUME 1: Metals

1978, 1st repr. 1982, 2nd repr. 1991; ISBN 0-444-85020-1

1. Z.B. Goldschmidt, *Atomic properties (free atom)* 1
 2. B.J. Beaudry and K.A. Gschneidner Jr, *Preparation and basic properties of the rare earth metals* 173
 3. S.H. Liu, *Electronic structure of rare earth metals* 233
 4. D.C. Koskenmaki and K.A. Gschneidner Jr, *Cerium* 337
 5. L.J. Sundström, *Low temperature heat capacity of the rare earth metals* 379
 6. K.A. McEwen, *Magnetic and transport properties of the rare earths* 411
 7. S.K. Sinha, *Magnetic structures and inelastic neutron scattering: metals, alloys and compounds* 489
 8. T.E. Scott, *Elastic and mechanical properties* 591
 9. A. Jayaraman, *High pressure studies: metals, alloys and compounds* 707
 10. C. Probst and J. Wittig, *Superconductivity: metals, alloys and compounds* 749
 11. M.B. Maple, L.E. DeLong and B.C. Sales, *Kondo effect: alloys and compounds* 797
 12. M.P. Dariel, *Diffusion in rare earth metals* 847
- Subject index 877

VOLUME 2: Alloys and intermetallics

1979, 1st repr. 1982, 2nd repr. 1991; ISBN 0-444-85021-X

13. A. Iandelli and A. Palenzona, *Crystal chemistry of intermetallic compounds* 1
 14. H.R. Kirchmayr and C.A. Poldy, *Magnetic properties of intermetallic compounds of rare earth metals* 55
 15. A.E. Clark, *Magnetostrictive RFe₂ intermetallic compounds* 231
 16. J.J. Rhyne, *Amorphous magnetic rare earth alloys* 259
 17. P. Fulde, *Crystal fields* 295
 18. R.G. Barnes, *NMR, EPR and Mössbauer effect: metals, alloys and compounds* 387
 19. P. Wachter, *Europium chalcogenides: EuO, EuS, EuSe and EuTe* 507
 20. A. Jayaraman, *Valence changes in compounds* 575
- Subject index 613

VOLUME 3: Non-metallic compounds – I

1979, 1st repr. 1984; ISBN 0-444-85215-8

21. L.A. Haskin and T.P. Paster, *Geochemistry and mineralogy of the rare earths* 1
 22. J.E. Powell, *Separation chemistry* 81
 23. C.K. Jørgensen, *Theoretical chemistry of rare earths* 111
 24. W.T. Carnall, *The absorption and fluorescence spectra of rare earth ions in solution* 171
 25. L.C. Thompson, *Complexes* 209
 26. G.G. Libowitz and A.J. Maeland, *Hydrides* 299
 27. L. Eyring, *The binary rare earth oxides* 337
 28. D.J.M. Sevan and E. Summerville, *Mixed rare earth oxides* 401
 29. C.P. Khattak and F.F.Y. Wang, *Perovskites and garnets* 525
 30. L.H. Brixner, J.R. Barkley and W. Jeitschko, *Rare earth molybdates (VI)* 609
- Subject index 655

VOLUME 4: Non-metallic compounds – II

1979, 1st repr. 1984; ISBN 0-444-85216-6

31. J. Flahaut, *Sulfides, selenides and tellurides* 1
32. J.M. Haschke, *Halides* 89
33. F. Hulliger, *Rare earth pnictides* 153
34. G. Blasse, *Chemistry and physics of R-activated phosphors* 237
35. M.J. Weber, *Rare earth lasers* 275
36. F.K. Fong, *Nonradiative processes of rare-earth ions in crystals* 317
- 37A. J.W. O’Laughlin, *Chemical spectrophotometric and polarographic methods* 341
- 37B. S.R. Taylor, *Trace element analysis of rare earth elements by spark source mass spectroscopy* 359
- 37C. R.J. Conzemius, *Analysis of rare earth matrices by spark source mass spectrometry* 377
- 37D. E.L. DeKalb and V.A. Fassel, *Optical atomic emission and absorption methods* 405
- 37E. A.P. D’Silva and V.A. Fassel, *X-ray excited optical luminescence of the rare earths* 441
- 37F. F.W.V. Boynton, *Neutron activation analysis* 457
- 37G. S. Schuhmann and J.A. Philpotts, *Mass-spectrometric stable-isotope dilution analysis for lanthanides in geochemical materials* 471
38. J. Reuben and G.A. Elgavish, *Shift reagents and NMR of paramagnetic lanthanide complexes* 483
39. J. Reuben, *Bioinorganic chemistry: lanthanides as probes in systems of biological interest* 515
40. T.J. Haley, *Toxicity* 553
- Subject index 587

VOLUME 5

1982, 1st repr. 1984; ISBN 0-444-86375-3

41. M. Gasgnier, *Rare earth alloys and compounds as thin films* 1
42. E. Gratz and M.J. Zuckermann, *Transport properties (electrical resistivity, thermoelectric power thermal conductivity) of rare earth intermetallic compounds* 117
43. F.P. Netzer and E. Bertel, *Adsorption and catalysis on rare earth surfaces* 217
44. C. Boulesteix, *Defects and phase transformation near room temperature in rare earth sesquioxides* 321
45. O. Greis and J.M. Haschke, *Rare earth fluorides* 387
46. C.A. Morrison and R.P. Leavitt, *Spectroscopic properties of triply ionized lanthanides in transparent host crystals* 461
- Subject index 693

VOLUME 6

1984; ISBN 0-444-86592-6

47. K.H.J. Buschow, *Hydrogen absorption in intermetallic compounds* 1
48. E. Parthé and B. Chabot, *Crystal structures and crystal chemistry of ternary rare earth–transition metal borides, silicides and homologues* 113
49. P. Rogl, *Phase equilibria in ternary and higher order systems with rare earth elements and boron* 335
50. H.B. Kagan and J.L. Namy, *Preparation of divalent ytterbium and samarium derivatives and their use in organic chemistry* 525
- Subject index 567

VOLUME 7

1984; ISBN 0-444-86851-8

51. P. Rogl, *Phase equilibria in ternary and higher order systems with rare earth elements and silicon* 1
52. K.H.J. Buschow, *Amorphous alloys* 265
53. H. Schumann and W. Genthe, *Organometallic compounds of the rare earths* 446
- Subject index 573

VOLUME 8

1986; ISBN 0-444-86971-9

54. K.A. Gschneidner Jr and F.W. Calderwood, *Intra rare earth binary alloys: phase relationships, lattice parameters and systematics* 1
55. X. Gao, *Polarographic analysis of the rare earths* 163
56. M. Leskelä and L. Niinistö, *Inorganic complex compounds I* 203
57. J.R. Long, *Implications in organic synthesis* 335
- Errata 375
- Subject index 379

VOLUME 9

1987; ISBN 0-444-87045-8

58. R. Reisfeld and C.K. Jørgensen, *Excited state phenomena in vitreous materials* 1
59. L. Niinistö and M. Leskelä, *Inorganic complex compounds II* 91
60. J.-C.G. Bünzli, *Complexes with synthetic ionophores* 321
61. Zhiquan Shen and Jun Ouyang, *Rare earth coordination catalysis in stereospecific polymerization* 395
- Errata 429
- Subject index 431

VOLUME 10: High energy spectroscopy

1988; ISBN 0-444-87063-6

62. Y. Baer and W.-D. Schneider, *High-energy spectroscopy of lanthanide materials – An overview* 1
63. M. Campagna and F.U. Hillebrecht, *f-electron hybridization and dynamical screening of core holes in intermetallic compounds* 75
64. O. Gunnarsson and K. Schönhammer, *Many-body formulation of spectra of mixed valence systems* 103
65. A.J. Freeman, B.I. Min and M.R. Norman, *Local density supercell theory of photoemission and inverse photoemission spectra* 165
66. D.W. Lynch and J.H. Weaver, *Photoemission of Ce and its compounds* 231
67. S. Hüfner, *Photoemission in chalcogenides* 301
68. J.F. Herbst and J.W. Wilkins, *Calculation of 4f excitation energies in the metals and relevance to mixed valence systems* 321
69. B. Johansson and N. Mårtensson, *Thermodynamic aspects of 4f levels in metals and compounds* 361
70. F.U. Hillebrecht and M. Campagna, *Bremsstrahlung isochromat spectroscopy of alloys and mixed valent compounds* 425
71. J. Röhrler, *X-ray absorption and emission spectra* 453
72. F.P. Netzer and J.A.D. Matthew, *Inelastic electron scattering measurements* 547
- Subject index 601

VOLUME 11: Two-hundred-year impact of rare earths on science

1988; ISBN 0-444-87080-6

- H.J. Svec, *Prologue* 1
73. F. Szabadváry, *The history of the discovery and separation of the rare earths* 33
74. B.R. Judd, *Atomic theory and optical spectroscopy* 81
75. C.K. Jørgensen, *Influence of rare earths on chemical understanding and classification* 197
76. J.J. Rhyne, *Highlights from the exotic phenomena of lanthanide magnetism* 293
77. B. Bleaney, *Magnetic resonance spectroscopy and hyperfine interactions* 323
78. K.A. Gschneidner Jr and A.H. Daane, *Physical metallurgy* 409
79. S.R. Taylor and S.M. McLennan, *The significance of the rare earths in geochemistry and cosmochemistry* 485
- Errata 579
- Subject index 581

VOLUME 12

1989; ISBN 0-444-87105-5

80. J.S. Abell, *Preparation and crystal growth of rare earth elements and intermetallic compounds* 1
 81. Z. Fisk and J.P. Remeika, *Growth of single crystals from molten metal fluxes* 53
 82. E. Burzo and H.R. Kirchmayr, *Physical properties of $R_2Fe_{14}B$ -based alloys* 71
 83. A. Szytuła and J. Leciejewicz, *Magnetic properties of ternary intermetallic compounds of the RT_2X_2 type* 133
 84. H. Maletta and W. Zinn, *Spin glasses* 213
 85. J. van Zytveld, *Liquid metals and alloys* 357
 86. M.S. Chandrasekharaiah and K.A. Gingerich, *Thermodynamic properties of gaseous species* 409
 87. W.M. Yen, *Laser spectroscopy* 433
 Subject index 479

VOLUME 13

1990; ISBN 0-444-88547-1

88. E.I. Gladyshevsky, O.I. Bodak and V.K. Pecharsky, *Phase equilibria and crystal chemistry in ternary rare earth systems with metallic elements* 1
 89. A.A. Eliseev and G.M. Kuzmichyeva, *Phase equilibrium and crystal chemistry in ternary rare earth systems with chalcogenide elements* 191
 90. N. Kimizuka, E. Takayama-Muromachi and K. Siratori, *The systems R_2O_3 – M_2O_3 – $M'O$* 283
 91. R.S. Houk, *Elemental analysis by atomic emission and mass spectrometry with inductively coupled plasmas* 385
 92. P.H. Brown, A.H. Rathjen, R.D. Graham and D.E. Tribe, *Rare earth elements in biological systems* 423
 Errata 453
 Subject index 455

VOLUME 14

1991; ISBN 0-444-88743-1

93. R. Osborn, S.W. Lovesey, A.D. Taylor and E. Balcar, *Intermultiplet transitions using neutron spectroscopy* 1
 94. E. Dormann, *NMR in intermetallic compounds* 63
 95. E. Zirngiebl and G. Güntherodt, *Light scattering in intermetallic compounds* 163
 96. P. Thalmeier and B. Lüthi, *The electron–phonon interaction in intermetallic compounds* 225
 97. N. Grewe and F. Steglich, *Heavy fermions* 343
 Subject index 475

VOLUME 15

1991; ISBN 0-444-88966-3

98. J.G. Sereni, *Low-temperature behaviour of cerium compounds* 1
 99. G.-y. Adachi, N. Imanaka and Zhang Fuzhong, *Rare earth carbides* 61
 100. A. Simon, Hj. Mattausch, G.J. Miller, W. Bauhofer and R.K. Kremer, *Metal-rich halides* 191
 101. R.M. Almeida, *Fluoride glasses* 287
 102. K.L. Nash and J.C. Sullivan, *Kinetics of complexation and redox reactions of the lanthanides in aqueous solutions* 347
 103. E.N. Rizkalla and G.R. Choppin, *Hydration and hydrolysis of lanthanides* 393
 104. L.M. Vallarino, *Macrocyclic complexes of the lanthanide(III) yttrium(III) and dioxouranium(VI) ions from metal-templated syntheses* 443
 Errata 513
 Subject index 515

MASTER INDEX, Vols. 1–15

1993; ISBN 0-444-89965-0

VOLUME 16

1993; ISBN 0-444-89782-8

105. M. Loewenhaupt and K.H. Fischer, *Valence-fluctuation and heavy-fermion 4f systems* 1
 106. I.A. Smirnov and V.S. Oskotski, *Thermal conductivity of rare earth compounds* 107
 107. M.A. Subramanian and A.W. Sleight, *Rare earths pyrochlores* 225
 108. R. Miyawaki and I. Nakai, *Crystal structures of rare earth minerals* 249
 109. D.R. Chopra, *Appearance potential spectroscopy of lanthanides and their intermetallics* 519
 Author index 547
 Subject index 579

VOLUME 17: Lanthanides/Actinides: Physics – I

1993; ISBN 0-444-81502-3

110. M.R. Norman and D.D. Koelling, *Electronic structure, Fermi surfaces, and superconductivity in f electron metals* 1
 111. S.H. Liu, *Phenomenological approach to heavy-fermion systems* 87
 112. B. Johansson and M.S.S. Brooks, *Theory of cohesion in rare earths and actinides* 149
 113. U. Benedict and W.B. Holzapfel, *High-pressure studies – Structural aspects* 245
 114. O. Vogt and K. Mattenberger, *Magnetic measurements on rare earth and actinide mononictides and monochalcogenides* 301
 115. J.M. Fournier and E. Gratz, *Transport properties of rare earth and actinide intermetallics* 409
 116. W. Potzel, G.M. Kalvius and J. Gal, *Mössbauer studies on electronic structure of intermetallic compounds* 539
 117. G.H. Lander, *Neutron elastic scattering from actinides and anomalous lanthanides* 635
 Author index 711
 Subject index 753

VOLUME 18: Lanthanides/Actinides: Chemistry

1994; ISBN 0-444-81724-7

118. G.T. Seaborg, *Origin of the actinide concept* 1
 119. K. Balasubramanian, *Relativistic effects and electronic structure of lanthanide and actinide molecules* 29
 120. J.V. Beitz, *Similarities and differences in trivalent lanthanide- and actinide-ion solution absorption spectra and luminescence studies* 159
 121. K.L. Nash, *Separation chemistry for lanthanides and trivalent actinides* 197
 122. L.R. Morss, *Comparative thermochemical and oxidation – reduction properties of lanthanides and actinides* 239
 123. J.W. Ward and J.M. Haschke, *Comparison of 4f and 5f element hydride properties* 293
 124. H.A. Eick, *Lanthanide and actinide halides* 365
 125. R.G. Haire and L. Eyring, *Comparisons of the binary oxides* 413
 126. S.A. Kinkead, K.D. Abney and T.A. O'Donnell, *f-element speciation in strongly acidic media: lanthanide and mid-actinide metals, oxides, fluorides and oxide fluorides in superacids* 507
 127. E.N. Rizkalla and G.R. Choppin, *Lanthanides and actinides hydration and hydrolysis* 529
 128. G.R. Choppin and E.N. Rizkalla, *Solution chemistry of actinides and lanthanides* 559
 129. J.R. Duffield, D.M. Taylor and D.R. Williams, *The biochemistry of the f-elements* 591
 Author index 623
 Subject index 659

VOLUME 19: Lanthanides/Actinides: Physics – II

1994; ISBN 0-444-82015-9

130. E. Holland-Moritz and G.H. Lander, *Neutron inelastic scattering from actinides and anomalous lanthanides* 1
131. G. Aeppli and C. Broholm, *Magnetic correlations in heavy-fermion systems: neutron scattering from single crystals* 123
132. P. Wachter, *Intermediate valence and heavy fermions* 177
133. J.D. Thompson and J.M. Lawrence, *High pressure studies – Physical properties of anomalous Ce, Yb and U compounds* 383
134. C. Colinet and A. Pasturel, *Thermodynamic properties of metallic systems* 479
Author index 649
Subject index 693

VOLUME 20

1995; ISBN 0-444-82014-0

135. Y. Ōnuki and A. Hasegawa, *Fermi surfaces of intermetallic compounds* 1
136. M. Gasgnier, *The intricate world of rare earth thin films: metals, alloys, intermetallics, chemical compounds, ...* 105
137. P. Vajda, *Hydrogen in rare-earth metals, including RH_{2+x} phases* 207
138. D. Gignoux and D. Schmitt, *Magnetic properties of intermetallic compounds* 293
Author index 425
Subject index 457

VOLUME 21

1995; ISBN 0-444-82178-3

139. R.G. Bautista, *Separation chemistry* 1
140. B.W. Hinton, *Corrosion prevention and control* 29
141. N.E. Ryan, *High-temperature corrosion protection* 93
142. T. Sakai, M. Matsuoka and C. Iwakura, *Rare earth intermetallics for metal–hydrogen batteries* 133
143. G.-y. Adachi and N. Imanaka, *Chemical sensors* 179
144. D. Garcia and M. Faucher, *Crystal field in non-metallic (rare earth) compounds* 263
145. J.-C.G. Bünzli and A. Milicic-Tang, *Solvation and anion interaction in organic solvents* 305
146. V. Bhagavathy, T. Prasada Rao and A.D. Damodaran, *Trace determination of lanthanides in high-purity rare-earth oxides* 367
Author index 385
Subject index 411

VOLUME 22

1996; ISBN 0-444-82288-7

147. C.P. Flynn and M.B. Salamon, *Synthesis and properties of single-crystal nanostructures* 1
148. Z.S. Shan and D.J. Sellmyer, *Nanoscale rare earth–transition metal multilayers: magnetic structure and properties* 81
149. W. Suski, *The $ThMn_{12}$ -type compounds of rare earths and actinides: structure, magnetic and related properties* 143
150. L.K. Aminov, B.Z. Malkin and M.A. Teplov, *Magnetic properties of nonmetallic lanthanide compounds* 295
151. F. Auzel, *Coherent emission in rare-earth materials* 507
152. M. Dolg and H. Stoll, *Electronic structure calculations for molecules containing lanthanide atoms* 607
Author index 731
Subject index 777

VOLUME 23

1996; ISBN 0-444-82507-X

153. J.H. Forsberg, *NMR studies of paramagnetic lanthanide complexes and shift reagents* 1
 154. N. Sabbatini, M. Guardigli and I. Manet, *Antenna effect in encapsulation complexes of lanthanide ions* 69
 155. C. Görller-Walrand and K. Binnemans, *Rationalization of crystal-field parametrization* 121
 156. Yu. Kuz'ma and S. Chykhrij, *Phosphides* 285
 157. S. Boghosian and G.N. Papatheodorou, *Halide vapors and vapor complexes* 435
 158. R.H. Byrne and E.R. Sholkovitz, *Marine chemistry and geochemistry of the lanthanides* 497
 Author index 595
 Subject index 631

VOLUME 24

1997; ISBN 0-444-82607-6

159. P.A. Dowben, D.N. McLroy and Dongqi Li, *Surface magnetism of the lanthanides* 1
 160. P.G. McCormick, *Mechanical alloying and mechanically induced chemical reactions* 47
 161. A. Inoue, *Amorphous, quasicrystalline and nanocrystalline alloys in Al- and Mg-based systems* 83
 162. B. Elschner and A. Loidl, *Electron-spin resonance on localized magnetic moments in metals* 221
 163. N.H. Duc, *Intersublattice exchange coupling in the lanthanide–transition metal intermetallics* 339
 164. R.V. Skolozdra, *Stannides of rare-earth and transition metals* 399
 Author index 519
 Subject index 559

VOLUME 25

1998; ISBN 0-444-82871-0

165. H. Nagai, *Rare earths in steels* 1
 166. R. Marchand, *Ternary and higher order nitride materials* 51
 167. C. Görller-Walrand and K. Binnemans, *Spectral intensities of f - f transitions* 101
 168. G. Bombieri and G. Paolucci, *Organometallic π complexes of the f -elements* 265
 Author index 415
 Subject index 459

VOLUME 26

1999; ISBN 0-444-50815-1

169. D.F. McMorro, D. Gibbs and J. Bohr, *X-ray scattering studies of lanthanide magnetism* 1
 170. A.M. Tishin, Yu.I. Spichkin and J. Bohr, *Static and dynamic stresses* 87
 171. N.H. Duc and T. Goto, *Itinerant electron metamagnetism of Co sublattice in the lanthanide–cobalt intermetallics* 177
 172. A.J. Arko, P.S. Riseborough, A.B. Andrews, J.J. Joyce, A.N. Tahvildar-Zadeh and M. Jarrell, *Photoelectron spectroscopy in heavy fermion systems: Emphasis on single crystals* 265
 Author index 383
 Subject index 405

VOLUME 27

1999; ISBN 0-444-50342-0

173. P.S. Salamakha, O.L. Sologub and O.I. Bodak, *Ternary rare-earth–germanium systems* 1
 174. P.S. Salamakha, *Crystal structures and crystal chemistry of ternary rare-earth germanides* 225
 175. B. Ya. Kotur and E. Gratz, *Scandium alloy systems and intermetallics* 339
 Author index 535
 Subject index 553

VOLUME 28

2000; ISBN 0-444-50346-3

176. J.-P. Connerade and R.C. Karnatak, *Electronic excitation in atomic species* 1
 177. G. Meyer and M.S. Wickleder, *Simple and complex halides* 53
 178. R.V. Kumar and H. Iwahara, *Solid electrolytes* 131
 179. A. Halperin, *Activated thermoluminescence (TL) dosimeters and related radiation detectors* 187
 180. K.L. Nash and M.P. Jensen, *Analytical separations of the lanthanides: basic chemistry and methods* 311
 Author index 373
 Subject index 401

VOLUME 29: The role of rare earths in catalysis

2000; ISBN 0-444-50472-9

- P. Maestro, *Foreword* 1
 181. V. Paul-Boncour, L. Hilaire and A. Percheron-Guégan, *The metals and alloys in catalysis* 5
 182. H. Imamura, *The metals and alloys (prepared utilizing liquid ammonia solutions) in catalysis II* 45
 183. M.A. Ulla and E.A. Lombardo, *The mixed oxides* 75
 184. J. Kašpar, M. Graziani and P. Fornasiero, *Ceria-containing three-way catalysts* 159
 185. A. Corma and J.M. López Nieto, *The use of rare-earth-containing zeolite catalysts* 269
 186. S. Kobayashi, *Triflates* 315
 Author index 377
 Subject index 409

VOLUME 30: High-Temperature Superconductors – I

2000; ISBN 0-444-50528-8

187. M.B. Maple, *High-temperature superconductivity in layered cuprates: overview* 1
 188. B. Raveau, C. Michel and M. Hervieu, *Crystal chemistry of superconducting rare-earth cuprates* 31
 189. Y. Shiohara and E.A. Goodilin, *Single-crystal growth for science and technology* 67
 190. P. Karen and A. Kjekshus, *Phase diagrams and thermodynamic properties* 229
 191. B. Elschner and A. Loidl, *Electron paramagnetic resonance in cuprate superconductors and in parent compounds* 375
 192. A.A. Manuel, *Positron annihilation in high-temperature superconductors* 417
 193. W.E. Pickett and I.I. Mazin, *$RBa_2Cu_3O_7$ compounds: electronic theory and physical properties* 453
 194. U. Staub and L. Soderholm, *Electronic 4f state splittings in cuprates* 491
 Author index 547
 Subject index 621

VOLUME 31: High-Temperature Superconductors – II

2001; ISBN 0-444-50719-1

195. E. Kaldis, *Oxygen nonstoichiometry and lattice effects in $YBa_2Cu_3O_x$. Phase transitions, structural distortions and phase separation* 1
 196. H.W. Weber, *Flux pinning* 187
 197. C.C. Almasan and M.B. Maple, *Magnetoresistance and Hall effect* 251
 198. T.E. Mason, *Neutron scattering studies of spin fluctuations in high-temperature superconductors* 281
 199. J.W. Lynn and S. Skanthakumar, *Neutron scattering studies of lanthanide magnetic ordering* 315
 200. P.M. Allenspach and M.B. Maple, *Heat capacity* 351
 201. M. Schabel and Z.-X. Shen, *Angle-resolved photoemission studies of untwinned yttrium barium copper oxide* 391
 202. D.N. Basov and T. Timusk, *Infrared properties of high- T_c superconductors: an experimental overview* 437
 203. S.L. Cooper, *Electronic and magnetic Raman scattering studies of the high- T_c cuprates* 509

204. H. Sugawara, T. Hasegawa and K. Kitazawa, *Characterization of cuprate superconductors using tunneling spectra and scanning tunneling microscopy* 563
Author index 609
Subject index 677

VOLUME 32

2001; ISBN 0-444-50762-0

205. N.H. Duc, *Giant magnetostriction in lanthanide–transition metal thin films* 1
206. G.M. Kalvius, D.R. Noakes and O. Hartmann, *μ SR studies of rare-earth and actinide magnetic materials* 55
207. Rainer Pöttgen, Dirk Johrendt and Dirk Kußmann, *Structure–property relations of ternary equiatomic YbTX intermetallics* 453
208. Kurima Kobayashi and Satoshi Hirotsawa, *Permanent magnets* 515
209. I.G. Vasilyeva, *Polysulfides* 567
210. Dennis K.P. Ng, Jianzhuang Jiang, Kuninobu Kasuga and Kenichi Machida, *Half-sandwich tetrapyrrole complexes of rare earths and actinides* 611
Author index 655
Subject index 733

VOLUME 33

2003; ISBN 0-444-51323-X

211. Brian C. Sales, *Filled skutterudites* 1
212. Oksana L. Sologub and Petro S. Salamakha, *Rare earth – antimony systems* 35
213. R.J.M. Konings and A. Kovács, *Thermodynamic properties of the lanthanide(III) halides* 147
214. John B. Goodenough, *Rare earth – manganese perovskites* 249
215. Claude Piquet and Carlos F.G.C. Geraldes, *Paramagnetic NMR lanthanide induced shifts for extracting solution structures* 353
216. Isabelle Billard, *Lanthanide and actinide solution chemistry as studied by time-resolved emission spectroscopy* 465
217. Thomas Tröster, *Optical studies of non-metallic compounds under pressure* 515
Author index 591
Subject index 637

INDEX OF CONTENTS OF VOLUMES 1–34

- 4*f* levels, thermodynamic aspects **10**, ch. 69, p. 361
4*f* state splittings in cuprates **30**, ch. 194, p. 491
- absorption spectra of ions in solution **3**, ch. 24,
p. 171; **18**, ch. 120, p. 150
- actinide concept, origin of **18**, ch. 118, p. 1
- activated phosphors **4**, ch. 34, p. 237
- activated thermoluminescence **28**, ch. 179, p. 187
- amorphous alloys **7**, ch. 52, p. 265
- Al- and Mg-based **24**, ch. 161, p. 83
 - magnetic **2**, ch. 16, p. 259
- anion interaction in organic solvents **21**, ch. 145,
p. 305
- antimony alloy systems **33**, ch. 212, p. 35
- atomic properties (free atom) **1**, ch. 1, p. 1
- atomic theory **11**, ch. 74, p. 81
- biochemistry **18**, ch. 129, p. 591
- bioinorganic chemistry **4**, ch. 39, p. 515
- biological systems **13**, ch. 92, p. 423
- carbides **15**, ch. 99, p. 61
- catalysis **29**, foreword, p. 1
- ceria-containing three-way **29**, ch. 184, p. 159
 - metals and alloys **29**, ch. 181, p. 5
 - metals and alloys in liquid ammonia solutions **29**,
ch. 182, p. 45
 - mixed oxides **29**, ch. 183, p. 75
 - zeolites **29**, ch. 185, p. 269
- cerium **1**, ch. 4, p. 337
- cerium compounds, low-temperature behavior **15**,
ch. 98, p. 1
- chalcogenides, magnetic measurements on mono-
17, ch. 114, p. 301
- chemical analysis by
- atomic emission with inductively coupled plasmas
13, ch. 91, p. 385
 - mass spectrometry, *see* spectroscopy, mass
 - neutron activation **4**, ch. 37E, p. 457
 - optical absorption **4**, ch. 37D, p. 405
 - optical atomic emission **4**, ch. 37D, p. 405
 - polarography **4**, ch. 37A, p. 341; **8**, ch. 55, p. 163
 - spectrophotometry **4**, ch. 37A, p. 341
 - trace determination in high-purity oxides **21**,
ch. 146, p. 367
 - X-ray excited optical luminescence **4**, ch. 37E,
p. 441
- chemical sensors **21**, ch. 143, p. 179
- chemical understanding and classification **11**,
ch. 75, p. 197
- coherent emission **22**, ch. 151, p. 507
- cohesion, theory of **17**, ch. 112, p. 149
- complexes **3**, ch. 25, p. 209
- antenna effect **23**, ch. 154, p. 69
 - half-sandwich tetrapyrrole **32**, ch. 210, p. 611
 - macrocycles **15**, ch. 104, p. 443
 - organometallic π type **25**, ch. 168, p. 265
 - with synthetic ionophores **9**, ch. 60, p. 321
- coordination catalysis in stereospecific
polymerization **9**, ch. 61, p. 395
- coordination in organic solvents **21**, ch. 145, p. 305
- coordination polymers **34**, ch. 221, p. 359
- corrosion prevention and control **21**, ch. 140, p. 29
- corrosion protection **21**, ch. 141, p. 93
- cosmochemistry **11**, ch. 79, p. 485
- crystal chemistry
- of intermetallic compounds **2**, ch. 13, p. 1
 - of ternary germanides **27**, ch. 174, p. 225
 - of ternary systems with chalcogenides **13** ch. 89,
p. 191
 - of ternary systems with metallic elements **13**
ch. 88, p. 1
 - of ternary transition metal borides **6**, ch. 48, p. 113
 - of ternary transition metal silicides **6**, ch. 48,
p. 113
 - of ThMn₁₂-type compounds **22**, ch. 149, p. 143
- crystal field **2**, ch. 17, p. 295
- in non-metallic compounds **21**, ch. 144, p. 263
- crystal field parametrization, rationalization of **23**,
ch. 155, p. 121
- crystal structures, *see* crystal chemistry

- diffusion in metals **1**, ch. 12, p. 847
- divalent samarium in organic chemistry **6**, ch. 50, p. 525
- divalent ytterbium derivatives in organic chemistry **6**, ch. 50, p. 525
- DNA, cutting of **34**, ch. 222, p. 405
- dynamical screening of core holes in intermetallic compounds **10**, ch. 63, p. 75
- elastic and mechanical properties of metals **1**, ch. 8, p. 591
- electron paramagnetic resonance in cuprate superconductors **30**, ch. 191, p. 375
- electronic excitation in atomic species **28**, ch. 176, p. 1
- electronic structure
- calculations for molecules **22**, ch. 152, p. 607
 - of metals **1**, ch. 3, p. 233; **17**, ch. 110, p. 1
- electronic theory of cuprates **30**, ch. 193, p. 453
- electron–phonon interaction in intermetallic compounds **14**, ch. 96, p. 225
- electron–spin resonance, *see* EPR
- emission spectra **10**, ch. 71, p. 453
- EPR **2**, ch. 18, p. 387; **24**, ch. 162, p. 221
- europium chalcogenides **2**, ch. 19, p. 507
- exchange coupling in transition metal intermetallics **24**, ch. 163, p. 339
- excited state phenomena in vitreous materials **9**, ch. 58, p. 1
- f*-electron hybridization in intermetallic compounds **10**, ch. 63, p. 75
- f*-element speciation in strongly acidic media (superacids) **18**, ch. 126, p. 507
- Fermi surfaces
- of intermetallic compounds **20**, ch. 135, p. 1
 - of metals **17**, ch. 110, p. 1
- fluorescence spectra of ions in solution **3**, ch. 24, p. 171
- fluoride glasses **15**, ch. 101, p. 287
- fluorides **5**, ch. 45, p. 387
- flux pinning in cuprates **31**, ch. 196, p. 187
- garnets **3**, ch. 29, p. 525
- geochemistry **3**, ch. 21, p. 1; **11**, ch. 79, p. 485; **23**, ch. 158, p. 497
- germanium, ternary systems **27**, ch. 173, p. 1
- halides **4**, ch. 32, p. 89; **18**, ch. 124, p. 365
- metal-rich **15**, ch. 100, p. 191
 - simple and complex **28**, ch. 177, p. 53
 - thermodynamic properties **33**, ch. 213 p. 147
 - vapors and vapor complexes **23**, ch. 157, p. 435
- Hall effect in cuprates **31**, ch. 197, p. 251
- heat capacity
- of cuprates **31**, ch. 200, p. 351
 - of metals **1**, ch. 5, p. 379
- heavy fermions **14**, ch. 97, p. 343; **16**, ch. 105, p. 1; **19**, ch. 132, p. 177
- phenomenological approach **17**, ch. 111, p. 87
 - photoelectron spectroscopy **26**, ch. 172, p. 265
- high pressure studies **1**, ch. 9, p. 707
- anomalous Ce, Yb and U compounds **19**, ch. 133, p. 383
 - optical studies of non-metallic compounds **33**, ch. 217, p. 515
 - structural aspects **17**, ch. 113, p. 245
- history of the discovery and separation **11**, ch. 73, p. 33
- Hund, F. **14**, dedication, p. ix
- hydration **15**, ch. 103, p. 393; **18**, ch. 127, p. 529
- hydrides **3**, ch. 26, p. 299; **18**, ch. 123, p. 293
- hydrogen absorption in intermetallic compounds **6**, ch. 47, p. 1
- hydrogen in metals, including RH_{2+x} phases **20**, ch. 137, p. 207
- hydrolysis **15**, ch. 103, p. 393; **18**, ch. 127, p. 529
- hyperfine interactions **11**, ch. 77, p. 323
- inelastic electron scattering **10**, ch. 72, p. 547
- infrared properties of cuprates **31**, ch. 202, p. 437
- inorganic complex compounds **8**, ch. 56 p. 203; **9**, ch. 59, p. 91
- intermediate valence **19**, ch. 132, p. 177
- itinerant electron metamagnetism in cobalt intermetallics **26**, ch. 171, p. 177
- kinetics of complexation in aqueous solutions **15**, ch. 102, p. 347
- Kondo effect **1**, ch. 11, p. 797
- lanthanide-induced shifts **4**, ch. 38, p. 483; **23**, ch. 153, p. 1; **33**, ch. 215, p. 353
- laser spectroscopy **12**, ch. 87, p. 433
- lasers **4**, ch. 35, p. 275
- light scattering in intermetallic compounds **14**, ch. 95, p. 163
- liquid metals and alloys **12**, ch. 85, p. 357
- LIS, *see* lanthanide-induced shifts
- luminescence studies of ions **18**, ch. 120, p. 150
- luminescence spectra of ions in solution **3**, ch. 24, p. 171

- μ SR studies of magnetic materials **32**, ch. 206, p. 55
magnetic and transport properties of metals **1** ch. 6, p. 411
magnetic correlations in heavy-fermion systems **19**, ch. 131, p. 123
magnetic properties
– of intermetallic compounds **2**, ch. 14, p. 55; **20**, ch. 138, p. 293
– of nonmetallic compounds **22**, ch. 150, p. 295
– of ternary RT_2X_2 type intermetallic compounds **12**, ch. 83, p. 133
– of $ThMn_{12}$ -type compounds **22**, ch. 149, p. 143
magnetic structures **1**, ch. 7, p. 489
magnetism **34**, ch. 219, p. 135
– exotic phenomena **11**, ch. 76, p. 293
– surface **24**, ch. 159, p. 1
magneto-resistance in cuprates **31**, ch. 197, p. 251
magnetostriction
– RFe_2 **2**, ch. 15, p. 231
– transition metal thin films **32**, ch. 205, p. 1
marine chemistry **23**, ch. 158, p. 497
mechanical alloying **24**, ch. 160, p. 47
mechanically induced chemical reactions **24**, ch. 160, p. 47
metal–hydrogen batteries **21**, ch. 142, p. 133
mineralogy **3**, ch. 21, p. 1
minerals, crystal structures **16**, ch. 108, p. 249
mixed valence systems
– bremsstrahlung isochromat spectroscopy **10**, ch. 70, p. 425
– calculation of $4f$ excitation energies **10**, ch. 68, p. 321
– many-body formulation of spectra **10**, ch. 64, p. 103
molybdates (VI) **3**, ch. 30, p. 609
Mössbauer effect **2**, ch. 18, p. 387
– of intermetallic compounds **17**, ch. 116, p. 539
nanostructures
– Al- and Mg-based systems **24**, ch. 161, p. 83
– properties **22**, ch. 147, p. 1
– synthesis **22**, ch. 147, p. 1
– transition metal multilayers **22**, ch. 148, p. 81
neutron scattering
– elastic **17**, ch. 117, p. 635
– inelastic **1**, ch. 7, p. 489
– – intermultiple transitions **14**, ch. 93, p. 1
– inelastic of anomalous lanthanides **19**, ch. 130, p. 1
– in heavy-fermion systems **19**, ch. 131, p. 123
– of magnetic ordering in cuprates **31**, ch. 199, p. 315
– of spin fluctuations in cuprates **31**, ch. 198, p. 281
nitride materials, ternary and higher order **24**, ch. 166, p. 51
NMR **2**, ch. 18, p. 387
– in intermetallic compounds **14**, ch. 94, p. 63
– lanthanide induced shifts for extracting solution structures **33**, ch. 215, p. 353
– of complexes **23**, ch. 153, p. 1
– of paramagnetic complexes **4**, ch. 38, p. 483
– solution structure by paramagnetic NMR analysis **33**, ch. 215, p. 353
nonradiative processes in crystals **4**, ch. 36, p. 317
nuclear magnetic resonance, *see* NMR
organic synthesis **8**, ch. 57, p. 335
organometallic compounds **7**, ch. 53, p. 446
oxidation – reduction properties **18**, ch. 122, p. 239
oxides
– binary **3**, ch. 27, p. 337; **18**, ch. 125, p. 413
– mixed **3**, ch. 28, p. 401
– sesqui, defects in **5**, ch. 44, p. 321
– sesqui, phase transformation in **5**, ch. 44, p. 321
– ternary systems, R_2O_3 – M_2O_3 – $M'O$ **13**, ch. 90, p. 283
oxygen nonstoichiometry and lattice effect in $YBa_2Cu_3O_x$ **31**, ch. 195, p. 1
permanent magnets **32**, ch. 208, p. 515
perovskites **3**, ch. 29, p. 525
– manganese **33**, ch. 214, p. 249
phase equilibria
– in cuprates **30**, ch. 190, p. 229
– in ternary systems with boron **6**, ch. 49, p. 335
– in ternary systems with chalcogenides **13** ch. 89, p. 191
– in ternary systems with metallic elements **13** ch. 88, p. 1
– in ternary systems with silicon **7**, ch. 51, p. 1
– intra rare earth binary alloys **8**, ch. 54, p. 1
phase transitions, structural distortions and phase separation in $YBa_2Cu_3O_x$ **31**, ch. 195, p. 1
phosphides **23**, ch. 156, p. 285
photoemission
– angle-resolved studies of untwinned $YBa_2Cu_3O_x$ **31**, ch. 201, p. 391
– in chalcogenides **10**, ch. 67, p. 301
– inverse spectra, local density supercell theory **10**, ch. 65, p. 165
– of Ce and its compounds **10**, ch. 66, p. 231
– spectra, local density supercell theory **10**, ch. 65, p. 165
physical metallurgy **11**, ch. 78, p. 409

- physical properties
- of cuprates **30**, ch. 193, p. 453
 - of metals **1**, ch. 2, p. 173
 - of $R_2Fe_{14}B$ -based alloys **12**, ch. 82, p. 71
- pnictides **4**, ch. 33, p. 153
- magnetic measurements on mono- **17**, ch. 114, p. 301
- positron annihilation in high-temperature superconductors **30**, ch. 192, p. 417
- preparation and purification of metals **1**, ch. 2, p. 173
- pyrochlores **16**, ch. 107, p. 225
- quasicrystalline, Al- and Mg-based systems **24**, ch. 161, p. 83
- Raman scattering of cuprates **31**, ch. 203, p. 509
- redox reactions in aqueous solutions **15**, ch. 102, p. 347
- relativistic effects and electronic structure **18**, ch. 119, p. 29
- RNA, cutting of **34**, ch. 222, p. 405
- scandium alloy systems and intermetallics **27**, ch. 175, p. 339
- scanning tunneling microscopy of cuprates **31**, ch. 204, p. 563
- selenides **4**, ch. 31, p. 1
- separation chemistry **3**, ch. 22, p. 81; **18**, ch. 121, p. 197; **21**, ch. 139, p. 1
- analytical, basic chemistry and methods **28**, ch. 180, p. 311
- shift reagents **4**, ch. 38, p. 483; **23**, ch. 153, p. 1; **33**, ch. 215, p. 353
- single crystals
- growth from molten metal fluxes **12**, ch. 81, p. 53
 - growth of cuprates **30**, ch. 189, p. 67
 - growth of metals and intermetallic compounds **12**, ch. 80, p. 1
- skutterudites, filled **33**, ch. 211, p. 1
- solid electrolytes **28**, ch. 178, p. 131
- solution chemistry **15**, ch. 103, p. 393; **18**, ch. 127, p. 529; **18**, ch. 128, p. 559; **21**, ch. 145, 305;
- solvation in organic solvents **21**, ch. 145, p. 305
- spectral intensities of ff transitions **24**, ch. 167, p. 101
- spectroscopic properties in transparent crystals **5**, ch. 46, p. 461
- spectroscopy
- appearance potential **16**, ch. 109, p. 519
 - bremsstrahlung isochromat **10**, ch. 70, p. 425
 - circularly polarized luminescence **34**, ch. 220, p. 289
 - high-energy **10**, ch. 62, p. 1
 - magnetic resonance **11**, ch. 77, p. 323
 - mass
 - spark source matrices **4**, ch. 37C, p. 377
 - spark source trace element analysis **4**, ch. 37B, p. 359
 - stable-isotope dilution analysis **4**, ch. 37G, p. 471
 - with inductively coupled plasmas analysis **13**, ch. 91, p. 385
 - optical **11**, ch. 74, p. 81
 - photoelectron in heavy fermion systems **26**, ch. 172, p. 265
 - time-resolved emission in solution chemistry **33**, ch. 216, p. 465
- Spedding, F. H., **11**, prologue, p. 1
- spin glasses **12**, ch. 84, p. 213
- stannides, transition metal ternary systems **24**, ch. 164, p. 399
- steels **25**, ch. 165, p. 1
- stresses, static and dynamic **26**, ch. 170, p. 87
- sulfides **4**, ch. 31, p. 1
- poly **32**, ch. 209, 567
- superconductivity **1**, ch. 10, p. 749; **34**, ch. 219, p. 135
- crystal chemistry of cuprates **30**, ch. 188, p. 31
 - in metals **17**, ch. 110, p. 1
 - high-temperature layered cuprates: overview **30**, ch. 187, p. 1
- surfaces
- adsorption on **5**, ch. 43, p. 217
 - catalysis on **5**, ch. 43, p. 217
- systematics, intra rare earth binary alloys **8**, ch. 54, p. 1
- tellurides **4**, ch. 31, p. 1
- ternary equiatomic YbTX intermetallics **32**, ch. 207, p. 453
- theoretical chemistry **3**, ch. 23, p. 111
- thermal conductivity of compounds **16**, ch. 106, p. 107
- thermochemical properties **18**, ch. 122, p. 239
- of cuprates **30**, ch. 190, p. 229
 - of gaseous species **12**, ch. 86, p. 409
 - of metallic systems **19**, ch. 134, p. 479
- thin films **5**, ch. 41, p. 1; **20**, ch. 136, p. 105
- toxicity **4**, ch. 40, p. 553
- transition metal indides **34**, ch. 218, p. 1
- transport properties of intermetallics **5**, ch. 42, p. 117; **17**, ch. 115, p. 409

triflates **29**, ch. 186, p. 315

tunneling spectra of cuprates **31**, ch. 204, p. 563

unconventional superconductivity and magnetism
34, ch. 219, p. 135

valence fluctuations **2**, ch. 20, p. 575; **16**, ch. 105,
p. 1

X-ray absorption spectra **10**, ch. 71, p. 453

X-ray scattering **26**, ch. 169, p. 1

Chapter 218

RARE EARTH–TRANSITION METAL–INDIDES

Yaroslav M. KALYCHAK and Vasyly I. ZAREMBA

Inorganic Chemistry Department, Ivan Franko National University, Kyryla and Mepodiya Street 6, 79005 Lviv, Ukraine

E-mail: kalychak@franko.lviv.ua

Rainer PÖTTGEN*, Mar'yana LUKACHUK, and Rolf-Dieter HOFFMANN

Institut für Anorganische und Analytische Chemie and NRW Graduate School of Chemistry, Westfälische Wilhelms-Universität Münster, Wilhelm-Klemm-Straße 8, D-48149 Münster, Germany

E-mail: pottgen@uni-muenster.de

Contents

Symbols and abbreviations	2	4.1. Structure type NaZn ₁₃	39
1. Introduction	3	4.2. Structure type LaNi ₇ In ₆	39
2. Synthesis conditions	4	4.3. Structure type ThMn ₁₂	40
3. Ternary systems – compounds and phase relations	7	4.4. Structure type EuAg ₄ In ₈	40
3.1. R–3d-metal–In systems	7	4.5. Structure type Dy ₂ Pt ₇ In ₁₆	41
3.1.1. The R–Mn–In systems	7	4.6. Structure type YNi ₉ In ₂	42
3.1.2. The R–Fe–In systems	7	4.7. Structure type CaCo ₂ Al ₈	43
3.1.3. The R–Co–In systems	7	4.8. Structure type Yb ₂ Pd ₆ In ₁₃	44
3.1.4. The R–Ni–In systems	8	4.9. Structure type LaNi ₃ In ₆	45
3.1.5. The R–Cu–In systems	14	4.10. Structure type Th ₂ Ni ₁₇	45
3.1.6. The R–Zn–In systems	26	4.11. Structure type Ho ₄ Ni ₁₀ -Ga ₂₁	45
3.2. R–4d-metal–In systems	27	4.12. Structure type CeNi ₅ Sn	47
3.2.1. The R–Ru–In systems	27	4.13. Structure type Sm ₂ Co ₉ In ₃	48
3.2.2. The R–Rh–In systems	27	4.14. Structure type CeCu _{4.32} In _{1.68}	48
3.2.3. The R–Pd–In systems	28	4.15. Structure type YbAg ₂ In ₄	49
3.2.4. The R–Ag–In systems	29	4.16. Structure type HoCoGa ₅	49
3.2.5. The R–Cd–In systems	33	4.17. Structure type Tb ₆ Pt ₁₂ In ₂₃	49
3.3. R–5d-metal–In systems	33	4.18. Structure type Gd ₃ Pt ₄ In ₁₂	51
3.3.1. The R–Ir–In systems	34	4.19. Structure type Lu ₆ Co _{17.92} In ₁₄	52
3.3.2. The R–Pt–In systems	34	4.20. Structure type MgCu ₄ Sn	52
3.3.3. The R–Au–In systems	36	4.21. Structure type HoNi _{2.6} Ga _{2.4}	53
4. Structure types of ternary indides of rare-earth and transition metals	39	4.22. Structure type YNiAl ₄	54
		4.23. Structure type LaCoAl ₄	54

* Corresponding author.

4.24. Structure type Ho_2CoGa_8	55	4.52. The structure type CsCl	73
4.25. Structure type CePt_2In_2	56	4.53. Structure type $\text{LT-LaAg}_x\text{In}_{1-x}$	74
4.26. Structure type $\text{Ce}_2\text{Au}_3\text{In}_5$	57	4.54. Structure type $\text{Mo}_5\text{B}_2\text{Si}$	74
4.27. Structure type LaRuSn_3	58	4.55. Structure type $\text{Ce}_{12}\text{Pt}_7\text{In}$	75
4.28. Structure type $\text{Ce}_4\text{Ni}_7\text{In}_8$	58	4.56. Structure type $\text{Sm}_{12}\text{Ni}_6\text{In}$	76
4.29. Structure type $\text{La}_3\text{Au}_4\text{In}_7$	59	4.57. Structure type $\text{Ho}_6\text{Co}_2\text{Ga}$	76
4.30. Structure type anti- $\text{Hf}_2\text{Co}_4\text{P}_3$	59	4.58. Structure type $\text{Lu}_{14}\text{Co}_2\text{In}_3$	76
4.31. Structure type $\text{Pr}_5\text{Ni}_6\text{In}_{11}$	61	5. Geometrical relations of some $R_xT_y\text{In}_z$ structures	78
4.32. Structure type $\text{Ce}_8\text{Pd}_{24}\text{Sb}$	61	5.1. Structures of multiple substitution	82
4.33. Structure type PrCo_2Ga	61	5.2. Structures of intergrowth of small slabs	83
4.34. Structure type GdPt_2Sn	62	6. Chemical bonding in rare earth transition metal indides	94
4.35. Structure type MnCu_2Al	63	7. Chemical and physical properties	100
4.36. Structure type MgCuAl_2	63	7.1. Ternary equiatomic indides RTIn	101
4.37. Structure type PrNiIn_2	64	7.1.1. Magnetic and electronic properties	101
4.38. Structure type HfNiGa_2	64	7.1.2. Hydrogenation behavior	106
4.39. Structure type $\text{Ho}_{10}\text{Ni}_9\text{In}_{20}$	65	7.2. Indides $R_2T_2\text{In}$ with ordered U_3Si_2 or Zr_3Al_2 type structures	107
4.40. Structure type $\text{La}_6\text{Co}_{11}\text{Ga}_3$	66	7.3. Indium-rich indides with HoCoGa_5 or Ho_2CoGa_8 structures	110
4.41. Structure types Fe_2P	66	7.4. Cubic indides with MgCu_4Sn structure	114
4.42. Structure type TiNiSi	68	7.5. Ternary indides with CsCl superstructures or Heusler phases	118
4.43. Structure type CeCu_2	69	7.6. Other indides	121
4.44. The structure type CaIn_2	69	Acknowledgements	124
4.45. Structure type $\text{Lu}_3\text{Co}_{1.87}\text{In}_4$	69	References	124
4.46. Structure type AlB_2	70		
4.47. Structure type Mn_2AlB_2	71		
4.48. Structure type W_2CoB_2	71		
4.49. Structure type $\text{U}_2\text{Pt}_2\text{Sn}$	71		
4.50. Structure type Mo_2FeB_2	72		
4.51. Structure type $\text{Lu}_5\text{Ni}_2\text{In}_4$	72		

Symbols and abbreviations

AF	antiferromagnetism	K	Bloch–Grüneisen fitting parameter
B_C	critical magnetic field	LT	low temperature
B_{hf}	magnetic hyperfine field	M	metal
C, C_P	heat capacity	MM	metamagnetism
CF	crystal electric field	NCW	non-Curie–Weiss behavior
CN	coordination number	NQR	nuclear quadrupolar resonance
CP	coordination polyhedron	P	paramagnetism
d	d-electron	p	pressure
DOS	density-of-states	R	specific electrical resistivity coefficient
E_F	Fermi energy	R	rare earth metal
f	f-electron	rf	radio frequency
F	ferromagnetism	RT	room temperature
IV	intermediate valence	S	thermoelectric power
J	magnetic coupling constant	SG	space group
\mathbf{k}	magnetic propagation vector	T	transition metal

T_C	magnetic Curie temperature; superconducting transition temperature	ΔE_Q	quadrupole splitting parameter
T_N	magnetic Néel temperature	Θ	paramagnetic Curie temperature (Weiss constant)
T_{ord}	magnetic ordering temperature	Θ_D	Debye temperature
T_{SF}	magnetic spin fluctuation temperature	μ_B	Bohr magnetons
X	main group element of the 3rd, 4th, or 5th group	μ_{exp}	experimental magnetic moment
XPS	X-ray photoemission spectroscopy	μ_{sm}	experimental magnetic saturation magnetization
γ	electronic specific heat coefficient	ν	valence
Γ	experimental line width	ρ_0	electrical resistivity
δ	isomer shift	χ	magnetic susceptibility; absolute electronegativity

1. Introduction

Intermetallic rare earth (R)–transition metal (T)–indium compounds, i.e. indides have attracted considerable interest in recent years due to their peculiar crystal chemistry and intriguing physical properties. More than thirty years ago, the ternary indides with uranium and thorium as electropositive component, $UTIn$ ($T = Pd, Pt$) and $ThTIn$ ($T = Ni, Pd, Pt$), have been synthesized by Dwight et al. (1968). The first series of rare earth metal-based ternary indides, i.e. $RNiIn$, $RRhIn$, $RPdIn$, and $RPtIn$, have been synthesized in Genova by the Ferro group (Ferro et al., 1974a, 1974b) and characterized with respect to metallography and X-ray powder diffraction.

More detailed investigations of the ternary systems $R-T-In$ including construction of the complete isothermal sections, determination of crystal structures, and chemical bonding have been performed in the last 20 years by the groups of Kalychak in Lviv and Pöttgen in Münster. The phase relations in the systems with cobalt, nickel, and copper as transition metal component have recently been reviewed by Kalychak (1997, 1998a, 1999a). Especially the nickel-based systems are extremely rich in compounds. With the early rare earth metals, more than ten different intermetallics form in these systems. Physical properties of indides have been investigated by various groups of researchers.

The crystal chemistry and chemical bonding of the $R-T-In$ compounds strongly depend on the composition. The rare earth metal-rich compounds exhibit typical intermetallic structures with relatively large coordination numbers, as found in close packed arrangements. Compounds with a high transition metal content show a tendency for transition metal cluster formation (Kalychak et al., 2001). In the indium rich parts of the ternary phase diagrams, compounds with interesting indium substructures exist (Hoffmann and Pöttgen, 2000; Hoffmann et al., 2000). In the case of a low rare earth metal content, the transition metal and indium atoms form two- or three-dimensional $[T_xIn_y]$ networks, in which the rare earth metal atoms fill cages or channels. Many of these crystal structures are very complicated, however, in some cases they can easily be described by an intergrowth of various slabs of simple binary and/or ternary structure types.

The rare earth transition metal indides have not only attracted interest in the chemists community, but also the physicists have intensively investigated such materials, mainly with respect to the largely varying magnetic and electrical properties. The primary interest concerns ferromagnetic, intermediate-valent, and heavy fermion materials. Prominent examples are the 22 K ferromagnet EuRhIn (Pöttgen et al., 1999c), mixed-valent CeRhIn (Adroja et al., 1989), valence-fluctuating CeNiIn (Fujii et al., 1989; Kurisu et al., 1990), or the intermediate heavy-fermion system $\text{Ce}_5\text{Ni}_6\text{In}_{11}$ (Tang et al., 1995). Gadolinium based indides are currently under investigation due to their potential technological applications for magnetic refrigeration (Canepa et al., 2002b). Finally, it is worthwhile to mention the very recent investigations on the new heavy fermion materials Ce_2TIn_8 and CeTIn_5 ($T = \text{Co}, \text{Rh}, \text{Ir}$). These indides have been thoroughly investigated in the last two years (Hegger et al., 2000; Moshopoulou et al., 2001). Precise and detailed physical property investigations have been performed on large single crystals.

With an increasing interest in hydrogen storage materials, various ternary indides have been studied with respect to their hydride formation. The hydrogen absorption has a strong influence on the physical properties. A prominent example is valence fluctuating CeNiIn that exhibits ferromagnetic ordering upon hydrogenation to $\text{CeNiInH}_{1.8}$ (Chevalier et al., 2002).

In this chapter, we review the synthesis techniques and the crystal chemistry of rare earth–transition metal–indides. Furthermore, we focus on phase relations and physical properties and discuss structure–property relationships.

2. Synthesis conditions

Rare earth–transition metal–indides can be prepared directly from the elements. In view of the highly electropositive character of the rare earth metals, the use of large rare earth metal pieces is highly recommended in order to avoid surface contaminations, mostly by oxides. The air (humidity) sensitive rare earth metals lanthanum, cerium, praseodymium, neodymium, samarium, europium, and ytterbium must be kept in Schlenk tubes under dried argon. The argon can easily be dried by standard procedures (Brauer, 1981; Brauer and Herrmann, 2000). The transition metals are used in the form of pieces or wires, while most noble metals are available as powders or foils. Indium is commercially available in the form of tear drops or granules. These are very soft and ductile and can be easily cut mechanically. The reactions of the rare earth metals with a transition metal and indium are strongly exothermic. The rare earth metals are often available in the form of sublimed ingots. Direct use of such ingots can lead to shattering during the reaction. In many cases, it is useful to arc-melt pieces of the rare earth metal first in order to reduce the shattering.

A very fast and efficient synthesis technique is arc-melting. This technique can be used for most rare earth–transition metal–indides. On the laboratory scale, arc-melting can easily be performed on water-cooled copper chills or within a water-cooled conical copper crucible (Pöttgen et al., 1999b). A non-consumable cerium dioxide doped tungsten electrode is used and the welding generator should be equipped with a high-frequency supply. This avoids

touching the crucible or the sample allowing a contact-free ignition of the arc. With a miniaturized arc-melting furnace, samples up to 2 g can be synthesized. Larger copper crucibles can be used in order to melt small bars for physical property investigations. If only polycrystalline samples are obtained by arc-melting, annealing of the arc-melted buttons in a water-cooled silica ampoule in a high-frequency furnace (Niepmann et al., 2000) can significantly increase the crystallinity. This annealing technique is especially useful for high-melting temperature products.

Many of the ternary indides directly crystallize from the melt. Often small single crystals already form during the solidification process. As an example, in fig. 1 we present a scanning electron micrograph of an arc-melted button from the solid solution $\text{TmNi}_{1+x}\text{In}_{1-x}$ (Lukachuk et al., 2003). In most cases, however, the arc-melted buttons are annealed in evacuated, sealed silica tubes at temperatures between 700 and 1300 K in order to achieve homogenization. The samples can be wrapped in tantalum or zirconium foil in order to avoid a reaction with the ampoule material. These annealing procedures are very important for the study of the isothermal sections of the phase diagrams. Compounds that form peritectically can only be obtained this way as single phase materials.

If one of the reaction components has a comparatively low boiling temperature, significant evaporation can occur during the arc-melting procedures. This is especially the case for the rare earth metals samarium (boils at 2050 K), europium (1870 K), thulium (2000 K), and

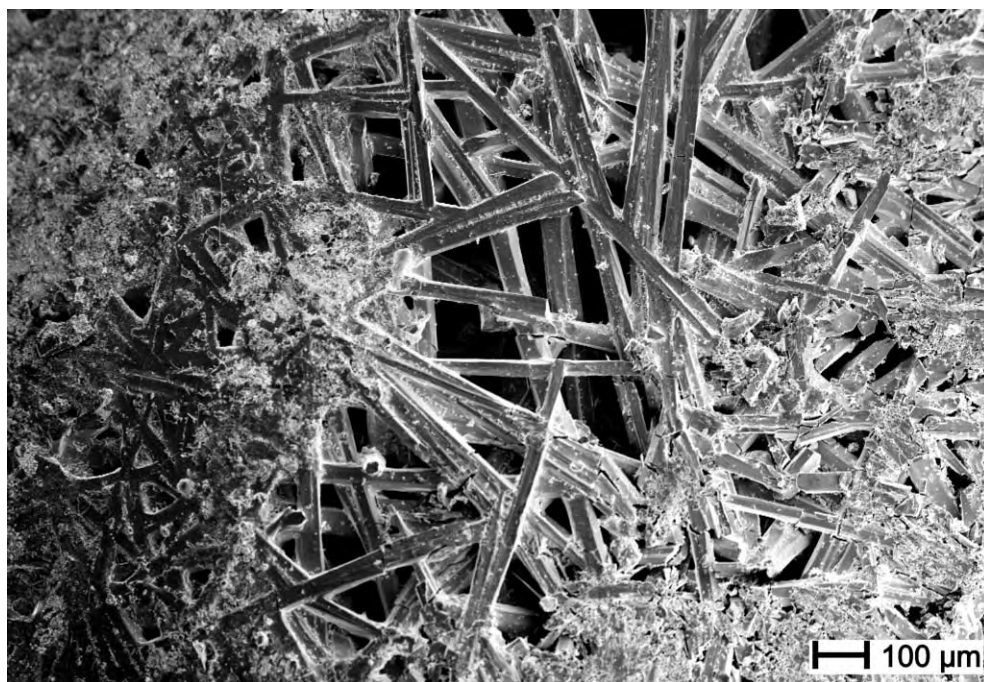


Fig. 1. Scanning electron micrograph of an arc-melted button taken from the solid solution $\text{TmNi}_{1+x}\text{In}_{1-x}$.

ytterbium (1470 K), and the transition metals manganese (2235 K), zinc (1180 K), and silver (2485 K). In these cases, the preparation technique needs to be modified. One possibility is high-frequency melting of the elements in a water-cooled sample chamber (Kußmann et al., 1998). Alumina, zirconium dioxide, or glassy carbon are suitable crucible materials. This special sample chamber is equipped with an observation window, which allows a direct observation of the reaction process. A large advantage of this technique is the relatively fast reaction procedure, which is nearly as fast as arc-melting. Typical annealing times are between one to four hours. In most cases, however, the high-frequency techniques lead to a better crystal quality.

In the case of europium and ytterbium as rare earth metal component, the synthesis conditions need to be more sophisticated. A significant problem arises, if europium or ytterbium with relatively low boiling temperatures (1870 K for Eu and 1470 K for Yb) are reacted with the high melting noble metals (e.g. melting temperature is 2045 K for Pt and 2240 K for Rh) and indium. In these cases, during an arc-melting procedure, europium or ytterbium might have already been evaporated before the noble metal melts. This leads to a significant loss of the rare earth metal component in such a quasi-open system. Europium and ytterbium based intermetallics are therefore synthesized in sealed inert metal tubes, mainly made of molybdenum, niobium, or tantalum (Corbett, 1983). Such tubes have small volumes (1–2 cm³).

Two different heating procedures can be used for reaction of the elements. The tantalum tubes can be sealed in evacuated silica tubes and annealed in conventional resistance furnaces. The better procedure is the annealing of the tubes in a water-cooled sample chamber of a high-frequency furnace (Pöttgen et al., 1999d). Again, the high-frequency annealing produces the better crystals. This way, the series of EuTIn and YbTIn intermetallics (Pöttgen and Johrendt, 2000; Pöttgen et al., 2001) have been synthesized in quantitative yields for structure determination and measurements of physical properties.

Each synthesis technique discussed above mostly yields polycrystalline samples. Single crystals have only a size of several tenths to a few hundreds of μm ; they can be used for single crystal structure determination. Larger single crystals for physical property investigations are not available with these techniques. They can be obtained in a different way. On a millimeter scale, single crystals can be grown in a tri-arc furnace equipped with the Czochralski technique. Suitable pieces can be cut from the crystals with a diamond wire saw. Crystal growth with the tri-arc technique is only possible for compounds that directly crystallize from the melt and where all components have comparable and high boiling temperatures.

A second technique is the growth of single crystals in an indium flux. Here, two different strategies may be applied. First it might be important to grow small single crystals from polycrystalline samples for X-ray structure determination. Suitable crucible materials for such indium fluxes are niobium, tantalum, and alumina or zirconium dioxide. Well-shaped single crystals of CeNiIn_2 (Zaremba et al., 2002b), $\text{Tb}_6\text{Pt}_{12}\text{In}_{23}$, and $\text{Dy}_2\text{Pt}_7\text{In}_{16}$ (Zaremba et al., 2002d) have recently been obtained with this technique. Larger single crystals can be grown by various metal flux techniques (Canfield and Fisk, 1992; Kanatzidis et al., 2004).

3. Ternary systems – compounds and phase relations

The ternary rare earth metal–transition metal–indium systems contain a vast number of individual intermetallic compounds. In this section we summarize the crystallographic data (lattice parameters) of all known indides. The compounds are grouped with respect to the *d* element component.

3.1. *R–3d-metal–In systems*

To date, the systems $R\text{--}\{\text{Co, Ni, Cu}\}\text{--In}$ have been studied most exhaustively. The isothermal sections of the systems $R\text{--Cu--In}$ have been constructed and published (Kalychak, 1998a). Other systems were investigated for the existence of isostructural compounds. With iron as transition metal component, only the Pr--Fe--In system has been studied. In the titanium, vanadium, and chromium systems Kalychak (2003) has studied only some alloys, which indicated that the components do not mix in the region of low contents of rare earth elements. The Pm--3d-metal--In systems have not been studied at all.

3.1.1. *The R–Mn–In systems*

The compounds with equiatomic composition RMnIn (Dhar et al., 2002b) crystallize with the cubic MgCu_2 type (SG $Fd\bar{3}m$, $a = 832.5$ pm for NdMnIn) and the hexagonal MgZn_2 type (SG $P6_3/mmc$, $a = 577.8$, $c = 941.2$ pm for GdMnIn ; $a = 573.4$, $c = 930.9$ pm for DyMnIn ; $a = 568.6$, $c = 926.0$ pm for ErMnIn , and $a = 574.1$, $c = 934.5$ pm for YMnIn). The isothermal sections of the phase diagrams of these ternary systems have not been investigated.

3.1.2. *The R–Fe–In systems*

Weitzer and Rogl (1990) proposed the partial isothermal section of the Pr--Fe--In phase diagram (fig. 2) and found the indide $\text{Pr}_6\text{Fe}_{13}\text{In}$ (structure type $\text{Nd}_6\text{Fe}_{13}\text{Si}$; SG $I4/mcm$, $a = 810.32(14)$, $c = 2352.75(89)$ pm). The other $R\text{--Fe--In}$ systems have been investigated in order to find isotypic $\text{R}_6\text{Fe}_{13}\text{In}$ indides. Two additional compounds, i.e. $\text{Nd}_6\text{Fe}_{13}\text{In}$ ($a = 808.8(1)$, $c = 2343.1(9)$ pm) and $\text{Sm}_6\text{Fe}_{13}\text{In}$ ($a = 806.5(1)$, $c = 2320.2(2)$ pm) with the same crystal structure have been found (Weitzer et al., 1993).

3.1.3. *The R–Co–In systems*

The ternary phase diagram Ce--Co--In has been constructed by investigating the isothermal section of the system at 870 K in the region of 0–33.3 atomic percent cerium and at 670 K in the region of 33.3–100 atomic percent cerium. According to Kalychak (1999b), only two ternary compounds, CeCoIn_5 and Ce_2CoIn_8 , exist in the region with high indium content (fig. 3). In the other $R\text{--Co--In}$ systems, the compounds with similar compositions were investigated and more than 120 ternary compounds have been found. The crystal structures for 68 of them have been determined by X-ray data. It was generally observed that in all ternary systems no solid solutions based on binary compounds exist, and ternary compounds form at constant stoichiometry showing practically no homogeneity ranges. The basic crystallographic data of all known ternary $\text{R}_x\text{Co}_y\text{In}_z$ compounds are listed in table 1.

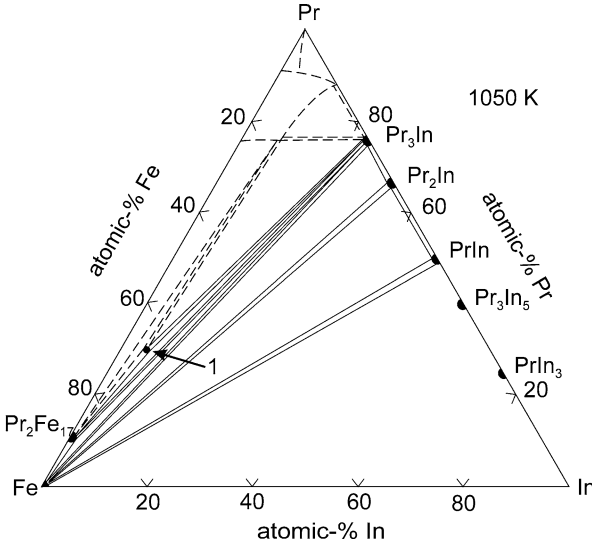


Fig. 2. Isothermal section of the phase diagram in the Pr-Fe-In system at 1050 K. 1 – $\text{Pr}_6\text{Fe}_{13}\text{In}$.

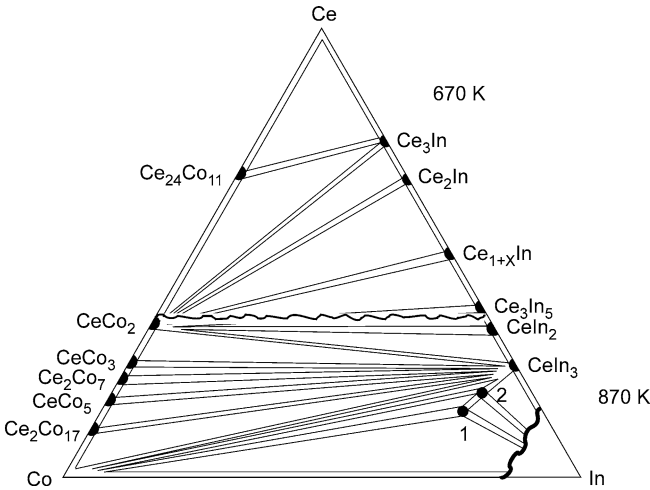


Fig. 3. Isothermal sections of the phase diagram in the Ce-Co-In system at 870 K and 670 K. 1 – CeCoIn_5 ; 2 – Ce_2CoIn_8 .

3.1.4. The R-Ni-In systems

The isothermal sections of the phase diagram of the ternary Ce-Ni-In system at 870 K and at 670 K in the region of 0–33.3 and of 33.3–100 atomic percent cerium, respectively, have been built. Twelve ternary intermetallics have been found in the Ce-Ni-In system (fig. 4) (Kalychak, 1998b). A small range of homogeneity was found for $\text{CeNi}_x\text{In}_{2-x}$, $x = 0.2-0.3$ (#9 in fig. 4), which is characteristic for the intermetallics with the AlB_2 structure. Furthermore, the crystal structure for ten more compounds has been studied. $\text{Ce}_4\text{Ni}_7\text{In}_8$ exists only above 870 K. The crystal structures of $\sim\text{Ce}_3\text{NiIn}_2$ and $\sim\text{Ce}_5\text{NiIn}_3$ are unknown. The ranges of homogeneity

Table 1
Crystallographic data of ternary R–Co–In compounds

Compound	Str. type	S.G.	<i>a</i> (pm)	<i>b</i> (pm)	<i>c</i> (pm)	Ref.
YCoIn ₅	HoCoGa ₅	<i>P4/mmm</i>	455.1(1)		743.3(2)	1
Y ₂ CoIn ₈	Ho ₂ CoGa ₈	<i>P4/mmm</i>	457.4(2)		1201.3(4)	1
YCo ₂ In	PrCo ₂ Ga	<i>Pmma</i>	502.7(2)	403.8(2)	710.8(2)	2
Y ₆ Co _{2.14} In _{0.86}	Ho ₆ Co ₂ Ga	<i>Immm</i>	950.6(5)	951.1(4)	999.2(3)	3
Y ₁₄ Co ₂ In ₃	Lu ₁₄ Co ₂ In ₃	<i>P4₂/nmc</i>	953.0(3)		2326.9(8)	4
LaCoIn ₅	HoCoGa ₅	<i>P4/mmm</i>	463.99(4)		761.51(6)	5
La ₆ Co ₁₃ In	Nd ₆ Fe ₁₃ Si	<i>I4/mcm</i>	810.2		2357.6	6
La ₁₂ Co ₆ In	Sm ₁₂ Ni ₆ In	<i>Im$\bar{3}$</i>	1016.5(3)			7
CeCoIn ₅	HoCoGa ₅	<i>P4/mmm</i>	460.1(1)		754.0(2)	1
Ce ₂ CoIn ₈	Ho ₂ CoGa ₈	<i>P4/mmm</i>	464.0(1)		1225.1(3)	1
PrCoIn ₅	HoCoGa ₅	<i>P4/mmm</i>	459.6(2)		750.3(3)	1
Pr ₂ CoIn ₈	Ho ₂ CoGa ₈	<i>P4/mmm</i>	460.5(1)		1219.3(4)	1
PrCo ₂ In	PrCo ₂ Ga	<i>Pmma</i>	511.9(3)	408.9(3)	719.7(3)	2
Pr ₁₂ Co ₆ In	Sm ₁₂ Ni ₆ In	<i>Im$\bar{3}$</i>	992.0(2)			7
NdCoIn ₅	HoCoGa ₅	<i>P4/mmm</i>	459.0(2)		750.2(3)	1
Nd ₂ CoIn ₈	Ho ₂ CoGa ₈	<i>P4/mmm</i>	460.8(1)		1217.2(3)	1
NdCo ₂ In	PrCo ₂ Ga	<i>Pmma</i>	509.6(3)	408.2(2)	715.8(4)	2
Nd ₁₂ Co ₆ In	Sm ₁₂ Ni ₆ In	<i>Im$\bar{3}$</i>	986.6(2)			7
Sm ₂ Co ₉ In ₃	Sm ₂ Co ₉ In ₃	<i>Cmmm</i>	2283.4(4)	502.0(1)	408.42(8)	8
SmCoIn ₅	HoCoGa ₅	<i>P4/mmm</i>	457.7(1)		746.3(3)	1
Sm ₂ CoIn ₈	Ho ₂ CoGa ₈	<i>P4/mmm</i>	458.3(1)		1210.1(4)	1
SmCo ₂ In	PrCo ₂ Ga	<i>Pmma</i>	508.0(3)	406.0(3)	712.7(3)	2
Sm ₆ Co ₂ In	Ho ₆ Co ₂ Ga	<i>Immm</i>	954.9	958.3	1006.8	9
Sm ₁₂ Co ₆ In	Sm ₁₂ Ni ₆ In	<i>Im$\bar{3}$</i>	978.6(3)			7
GdCoIn ₅	HoCoGa ₅	<i>P4/mmm</i>	456.7(1)		746.1(2)	1
Gd ₂ CoIn ₈	Ho ₂ CoGa ₈	<i>P4/mmm</i>	456.9(1)		1202.1(4)	1
GdCo ₂ In	PrCo ₂ Ga	<i>Pmma</i>	505.2(2)	405.5(1)	712.4(2)	2
Gd ₆ Co _{2.14} In _{0.86}	Ho ₆ Co ₂ Ga	<i>Immm</i>	954.4(5)	959.7(5)	1004.1(5)	3
Gd ₆ Co _{2.2} In _{0.8}	Ho ₆ Co ₂ Ga	<i>Immm</i>	950.1(3)	962.3(3)	1009.0(2)	10
Gd ₁₄ Co ₂ In ₃	Lu ₁₄ Co ₂ In ₃	<i>P4₂/nmc</i>	961.5(2)		2333.6(6)	4
Gd ₁₄ Co ₃ In _{2.7}	Gd ₁₄ Co ₃ In _{2.7}	<i>P4₂/nmc</i>	961.9(2)		2329.1(4)	11
TbCoIn ₅	HoCoGa ₅	<i>P4/mmm</i>	454.9(1)		742.5(2)	1
Tb ₂ CoIn ₈	Ho ₂ CoGa ₈	<i>P4/mmm</i>	456.8(1)		1200.8(2)	12
TbCo ₂ In	PrCo ₂ Ga	<i>Pmma</i>	503.3(1)	405.0(2)	712.2(2)	13
Tb ₆ Co _{2.14} In _{0.86}	Ho ₆ Co ₂ Ga	<i>Immm</i>	942.8(6)	945.0(8)	996.9(6)	3
Tb ₁₄ Co ₂ In ₃	Lu ₁₄ Co ₂ In ₃	<i>P4₂/nmc</i>	954.4(3)		2322.5(9)	4
DyCoIn ₅	HoCoGa ₅	<i>P4/mmm</i>	454.5(1)		741.8(2)	1
DyCo ₄ In	MgCu ₄ Sn	<i>F$\bar{4}3m$</i>	708.7(1)			14
Dy ₂ CoIn ₈	Ho ₂ CoGa ₈	<i>P4/mmm</i>	456.1(2)		1199.4(5)	1
DyCo ₂ In	PrCo ₂ Ga	<i>Pmma</i>	499.8(4)	403.4(4)	706.0(3)	2
Dy ₃ Co ₂ In ₄	Lu ₃ Co _{1.87} In ₄	<i>P$\bar{6}$</i>	786.7(2)		364.5(4)	15
Dy ₆ Co _{2.14} In _{0.86}	Ho ₆ Co ₂ Ga	<i>Immm</i>	940.1(5)	943.8(5)	993.8(7)	3
Dy ₁₄ Co ₂ In ₃	Lu ₁₄ Co ₂ In ₃	<i>P4₂/nmc</i>	950.0(3)		2300.2(9)	4
HoCoIn ₅	HoCoGa ₅	<i>P4/mmm</i>	454.7(1)		741.1(2)	1
HoCo ₄ In	MgCu ₄ Sn	<i>F$\bar{4}3m$</i>	706.8(2)			14
Ho ₂ CoIn ₈	Ho ₂ CoGa ₈	<i>P4/mmm</i>	454.0(2)		1198.4(4)	1
HoCo ₂ In	PrCo ₂ Ga	<i>Pmma</i>	499.3(3)	402.9(4)	705.4(3)	2

continued on next page

Table 1, *continued*

Compound	Str. type	S.G.	<i>a</i> (pm)	<i>b</i> (pm)	<i>c</i> (pm)	Ref.
Ho ₃ Co ₂ In ₄	Lu ₃ Co _{1.87} In ₄	<i>P</i> $\bar{6}$	786.6(1)		360.5(3)	15
Ho ₆ Co _{2.14} In _{0.86}	Ho ₆ Co ₂ Ga	<i>Immm</i>	934.8(6)	943.0(6)	990.6(9)	3
Ho ₁₄ Co ₂ In ₃	Lu ₁₄ Co ₂ In ₃	<i>P4</i> ₂ / <i>nmc</i>	945.9(2)		2291.3(8)	4
Er ₆ Co _{17.92} In ₁₄	Lu ₆ Co _{17.92} In ₁₄	<i>Pm</i> $\bar{3}$	866.3			16
ErCo ₄ In	MgCu ₄ Sn	<i>F</i> $\bar{4}3m$	704.9(1)			14
Er ₂ CoIn ₈	Ho ₂ CoGa ₈	<i>P4</i> / <i>mmm</i>	456.0(1)		1195.8(4)	1
Er ₁₀ Co ₉ In ₂₀	Ho ₁₀ Ni ₉ In ₂₀	<i>P4</i> / <i>nmm</i>	1325.3(2)		907.8(4)	17
Er ₃ Co ₂ In ₄	Lu ₃ Co _{1.87} In ₄	<i>P</i> $\bar{6}$	785.0(1)		358.3(2)	15
Er ₁₄ Co ₂ In ₃	Lu ₁₄ Co ₂ In ₃	<i>P4</i> ₂ / <i>nmc</i>	941.3(3)		2279.3(9)	4
TmCoIn ₅	HoCoGa ₅	<i>P4</i> / <i>mmm</i>	453.2(1)		738.7(3)	12
Tm ₆ Co _{17.92} In ₁₄	Lu ₆ Co _{17.92} In ₁₄	<i>Pm</i> $\bar{3}$	865.5(4)			18
TmCo ₄ In	MgCu ₄ Sn	<i>F</i> $\bar{4}3m$	704.2(1)			14
Tm ₂ CoIn ₈	Ho ₂ CoGa ₈	<i>P4</i> / <i>mmm</i>	454.4(1)		1193.4(4)	1
Tm ₁₀ Co ₉ In ₂₀	Ho ₁₀ Ni ₉ In ₂₀	<i>P4</i> / <i>nmm</i>	1316.6(5)		909.7(4)	17
Tm ₃ Co ₂ In ₄	Lu ₃ Co _{1.87} In ₄	<i>P</i> $\bar{6}$	784.3(1)		355.6(2)	15
Tm ₆ Co _{2.14} In _{0.86}	Ho ₆ Co ₂ Ga	<i>Immm</i>	928.8(3)	930.1(6)	979.3(4)	3
Tm ₁₄ Co ₂ In ₃	Lu ₁₄ Co ₂ In ₃	<i>P4</i> ₂ / <i>nmc</i>	936.8(3)		2269.1(9)	4
YbCoIn ₅	HoCoGa ₅	<i>P4</i> / <i>mmm</i>	455.90(7)		743.3(1)	19
LuCoIn ₅	HoCoGa ₅	<i>P4</i> / <i>mmm</i>	452.7		735.9	1
Lu ₆ Co _{17.92} In ₁₄	Lu ₆ Co _{17.92} In ₁₄	<i>Pm</i> $\bar{3}$	865.2(3)			16
LuCo ₄ In	MgCu ₄ Sn	<i>F</i> $\bar{4}3m$	702.9(1)			14
Lu ₁₀ Co ₉ In ₂₀	Ho ₁₀ Ni ₉ In ₂₀	<i>P4</i> / <i>nmm</i>	1316.0(1)		910.6(1)	17
Lu ₃ Co _{1.87} In ₄	Lu ₃ Co _{1.87} In ₄	<i>P</i> $\bar{6}$	781.4(2)		352.1(1)	15
Lu ₆ Co _{2.14} In _{0.86}	Ho ₆ Co ₂ Ga	<i>Immm</i>	923.8(3)	924.1(4)	972.7(4)	3
Lu ₁₄ Co ₂ In ₃	Lu ₁₄ Co ₂ In ₃	<i>P4</i> ₂ / <i>nmc</i>	933.3(2)		2263.3(4)	4

References:

- | | |
|--------------------------------|-----------------------------|
| 7. Kalychak et al. (1998) | 14. Sysa et al. (1988) |
| 1. Kalychak et al. (1989a) | 8. Baranyak et al. (1993) |
| 2. Kalychak and Zaremba (1994) | 9. Kalychak (2003) |
| 3. Kalychak et al. (1993b) | 10. Canepa et al. (2002a) |
| 4. Zaremba et al. (1992) | 11. Canepa et al. (2002b) |
| 5. Macaluso et al. (2002) | 12. Kalychak (1999a) |
| 6. Weitzer and Rogl (1990) | 13. Kalychak et al. (1993a) |
| | 15. Zaremba et al. (1989) |
| | 16. Zaremba et al. (1990) |
| | 17. Dubenskii et al. (1998) |
| | 18. Dubenskii et al. (1999) |
| | 19. Zaremba et al. (2003b) |

ity of the compounds with AIB₂ type structure have been established by Baranyak (1991). The compounds RNi_{0.33}In_{1.67} (*R* = La and Pr) show no homogeneity range, while the compounds with neodymium and samarium as *R* component have small homogeneity ranges with the compositions as stated in the formulae, RNi_{0.3–0.2}In_{1.7–1.8}.

In other ternary systems, *R*–Ni–In, compounds with the same compositions as in the Ce–Ni–In system have been studied. In contrast to the cobalt systems some compounds in the *R*–Ni–In systems have variable composition, i.e. they have extended homogeneity ranges or they form solid solutions. The equiatomic indides in the {Y, La, Ce, Pr, Nd, Sm, Gd, Tb, Dy, Ho, Er, and Tm}–Ni–In systems have been investigated by Ferro et al. (1974a). The other ternary indides *R*_{*x*}Ni_{*y*}In_{*z*} have been prepared for the first time by the Kalychak group. Nearly 180 ternary compounds exist at the thermal conditions mentioned above and the crystal structures have been determined for 127 of these nickel-based indides (table 2).

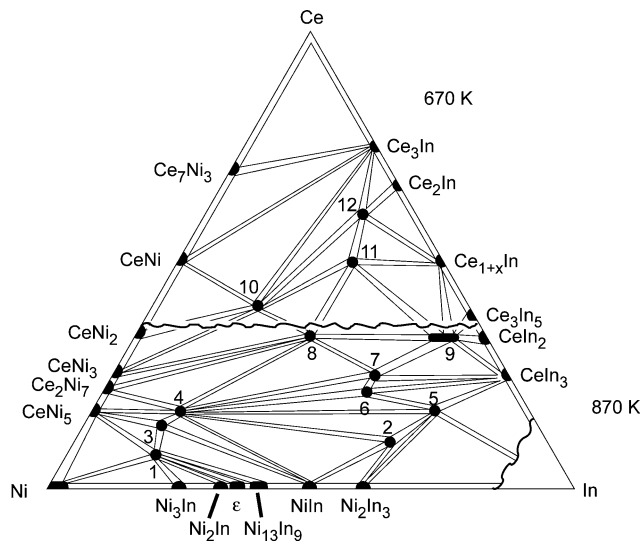


Fig. 4. Isothermal sections of the phase diagram in the Ce–Ni–In system at 870 K and 670 K. 1 – CeNi₉In₂; 2 – CeNi₃In₆; 3 – CeNi₅In; 4 – CeNi₄In; 5 – CeNiIn₄; 6 – Ce₅Ni₆In₁₁; 7 – CeNiIn₂; 8 – CeNiIn; 9 – CeNi_{0.3–0.2}In_{1.7–1.8}; 10 – Ce₂Ni₂In; 11 – ~Ce₃NiIn₂; 12 – ~Ce₅NiIn₃.

Table 2
Crystallographic data of ternary R–Ni–In compounds

Compound	Str. type	S.G.	<i>a</i> (pm)	<i>b</i> (pm)	<i>c</i> (pm)	Ref.
ScNi ₄ In	MgCu ₄ Sn	<i>F</i> 43 <i>m</i>	687.2(1)			1
ScNi ₂ In	MnCu ₂ Al	<i>Fm</i> 3 <i>m</i>	625.6			2
Sc ₂ Ni ₂ In	Mo ₂ FeB ₂	<i>P</i> 4/ <i>mbm</i>	716.79(1)		333.154(8)	3
YNi ₉ In ₂	YNi ₉ In ₂	<i>P</i> 4/ <i>mbm</i>	822.2(2)		482.7(2)	4
YNi ₄ In	MgCu ₄ Sn	<i>F</i> 43 <i>m</i>	703.4(1)			1
YNiIn ₂	MgCuAl ₂	<i>Cmcm</i>	431.4(2)	1040.6(5)	727.6(3)	5
YNiIn	Fe ₂ P	<i>P</i> 6̄2 <i>m</i>	748.6		378.4	6
YNi _{1–0.50} In _{1–1.50}	ZrNiAl	<i>P</i> 6̄2 <i>m</i>	747.4–756.6		377.3–380.5	7
Y ₂ Ni ₂ In	Mn ₂ AlB ₂	<i>Cmmm</i>	390.0(1)	1418.6(2)	369.4(1)	8
Y ₂ Ni _{2–x} In	Mo ₂ FeB ₂	<i>P</i> 4/ <i>mbm</i>	736.5(3)		367.9(3)	9
Y ₁₂ Ni ₆ In	Sm ₁₂ Ni ₆ In	<i>Im</i> 3̄	971.1(2)			10
LaNi ₇ In ₆	LaNi ₇ In ₆	<i>Ibam</i>	806.6(2)	924.8(2)	1246.5(2)	11
LaNi ₉ In ₂	YNi ₉ In ₂	<i>P</i> 4/ <i>mbm</i>	833.9(3)		487.7(2)	4
LaNi ₃ In ₆	LaNi ₃ In ₆	<i>Pmmn</i>	438.8(2)	757.4(4)	1211.0(7)	12
LaNi ₅ In	CeNi ₅ Sn	<i>P</i> 6 ₃ / <i>mmc</i>	495.7(2)		1996.9(5)	13
LaNi ₃ In ₂	HoNi _{2.6} Ga _{2.4}	<i>P</i> 6/ <i>mmm</i>	933.4(4)		435.6(2)	14
LaNiIn ₄	YNiAl ₄	<i>Cmcm</i>	448.4(4)	1688.5(4)	719.9(2)	15
			448.2(1)	1689.5(4)	722.1(1)	11
La ₄ Ni ₇ In ₈	Ce ₄ Ni ₇ In ₈	<i>Cmmm</i>	1475.7(5)	2418.7(7)	439.8(1)	16
La ₅ Ni ₆ In ₁₁	Pr ₅ Ni ₆ In ₁₁	<i>Cmmm</i>	1464.0(8)	1467.4(8)	443.9(2)	17
			1465(1)	1465.4(9)	444.1(3)	18
LaNi ₂ In	PrCo ₂ Ga	<i>Pmma</i>	525.4(1)	413.1(1)	716.9(1)	19
LaNiIn	Fe ₂ P	<i>P</i> 6̄2 <i>m</i>	761.3		403.5	6
LaNi _{0.5} In _{1.5}	AlB ₂	<i>P</i> 6/ <i>mmm</i>	483.7(1)		403.6(2)	20,21
La ₂ Ni ₂ In	Mo ₂ FeB ₂	<i>P</i> 4/ <i>mbm</i>	761.1(3)		391.8(2)	9
			762.7(3)		390.5(1)	22
La ₁₂ Ni ₆ In	Sm ₁₂ Ni ₆ In	<i>Im</i> 3̄	1020.9(1)			10

continued on next page

Table 2, *continued*

Compound	Str. type	S.G.	<i>a</i> (pm)	<i>b</i> (pm)	<i>c</i> (pm)	Ref.
CeNi ₉ In ₂	YNi ₉ In ₂	<i>P4/mbm</i>	825.0(2)		485.1(2)	4
			825.97(1)		484.66(2)	23
CeNi ₃ In ₆	LaNi ₃ In ₆	<i>Pmnn</i>	438.5(4)	753.7(4)	1206.0(1)	12
CeNi ₅ In	CeNi ₅ Sn	<i>P6₃/mmc</i>	489.4(2)		1987.8(5)	13
CeNi ₄ In	MgCu ₄ Sn	<i>F43m</i>	705.6(1)			1
CeNiIn ₄	YNiAl ₄	<i>Cmcm</i>	446.0(2)	1678.8(5)	722.0(2)	15
			445.9(1)	1676.7(2)	719.3(1)	24
Ce ₄ Ni ₇ In ₈	Ce ₄ Ni ₇ In ₈	<i>Cmmm</i>	1475.2(2)	2418.4(3)	439.51(8)	16
Ce ₅ Ni ₆ In ₁₁	Pr ₅ Ni ₆ In ₁₁	<i>Cmmm</i>	1460.0(4)	1460.1(3)	441.3(1)	17
			1457(1)	1458.4(9)	441.2(3)	18
CeNiIn ₂	PrNiIn ₂	<i>Cmcm</i>	440.78(4)	1834.3(1)	2178.8(2)	25
CeNiIn	Fe ₂ P	<i>P62m</i>	752.3		397.3	6
CeNi _{0.5} In _{1.5}	AlB ₂	<i>P6/mmm</i>	483.4(1)		392.8(2)	20
CeNi _{0.3-0.2} In _{1.7-1.8}	AlB ₂	<i>P6/mmm</i>	484.9-486.8(1)		395.9-392.9(1)	26
Ce ₂ Ni ₂ In	Mo ₂ FeB ₂	<i>P4/mbm</i>	749.9(2)		375.1(2)	9
			753.05(3)		372.23(2)	22
PrNi ₉ In ₂	YNi ₉ In ₂	<i>P4/mbm</i>	827.5(2)		487.1(2)	4
PrNi ₃ In ₆	LaNi ₃ In ₆	<i>Pmnn</i>	433.6(6)	753.9(2)	1204.3(6)	12
Pr ₂ Ni _{16.6} In _{0.4}	Th ₂ Ni ₁₇	<i>P6₃/mmc</i>	835.3		814.1	27
PrNi ₅ In	CeNi ₅ Sn	<i>P6₃/mmc</i>	491.9(1)		1993.6(6)	13
PrNi ₄ In	MgCu ₄ Sn	<i>F43m</i>	713.7(1)			1
PrNiIn ₄	YNiAl ₄	<i>Cmcm</i>	444.3(1)	1668.1(4)	719.3(2)	15
Pr ₄ Ni ₇ In ₈	Ce ₄ Ni ₇ In ₈	<i>Cmmm</i>	1475.6(4)	2418.9(6)	439.4(1)	16
Pr ₅ Ni ₆ In ₁₁	Pr ₅ Ni ₆ In ₁₁	<i>Cmmm</i>	1457.9(6)	1457.9(6)	440.0(1)	17
PrNi ₂ In	PrCo ₂ Ga	<i>Pmma</i>	518.0(3)	410.5(2)	710.0(3)	19
PrNiIn ₂	PrNiIn ₂	<i>Cmcm</i>	440.0(2)	1833.9(6)	2164.6(5)	28
PrNiIn	Fe ₂ P	<i>P62m</i>	754.1		395.0	6
PrNi _{0.5} In _{1.5}	AlB ₂	<i>P6/mmm</i>	483.6(1)		386.1(2)	20,21
Pr ₂ Ni ₂ In	Mo ₂ FeB ₂	<i>P4/mbm</i>	752.6(2)		381.7(1)	9
Pr ₁₂ Ni ₆ In	Sm ₁₂ Ni ₆ In	<i>Im3</i>	999.3(2)			10
NdNi ₉ In ₂	YNi ₉ In ₂	<i>P4/mbm</i>	826.2(3)		484.7(3)	4
NdNi ₃ In ₆	LaNi ₃ In ₆	<i>Pmnn</i>	434.3	752.2	1205.4	12
NdNi ₅ In	CeNi ₅ Sn	<i>P6₃/mmc</i>	491.1(1)		1989.9(6)	13
NdNi ₄ In	MgCu ₄ Sn	<i>F43m</i>	711.8(1)			1
NdNiIn ₄	YNiAl ₄	<i>Cmcm</i>	443.0(2)	1665.6(6)	717.8(2)	15
Nd ₄ Ni ₇ In ₈	Ce ₄ Ni ₇ In ₈	<i>Cmmm</i>	1475.4(4)	2418.9(6)	439.4(1)	16
Nd ₅ Ni ₆ In ₁₁	Pr ₅ Ni ₆ In ₁₁	<i>Cmmm</i>	1450.9	1451.7	438.0	17
			1455.9(3)	1453.3(3)	438.3(1)	29
NdNi ₂ In	PrCo ₂ Ga	<i>Pmma</i>	516.4(3)	409.4(3)	708.8(3)	19
NdNiIn ₂	PrNiIn ₂	<i>Cmcm</i>	438.0(1)	1833.5(4)	2151.6(5)	28
NdNiIn	Fe ₂ P	<i>P62m</i>	753.7		392.2	6
NdNi _{0.5} In _{1.5}	AlB ₂	<i>P6/mmm</i>	481.0(1)		378.2(2)	20
NdNi _{0.3-0.2} In _{1.7-1.8}	AlB ₂	<i>P6/mmm</i>	481.0-483.6(1)		378.2-379.5(1)	21
Nd ₂ Ni ₂ In	Mo ₂ FeB ₂	<i>P4/mbm</i>	751.4(2)		375.7(2)	9
Nd ₁₂ Ni ₆ In	Sm ₁₂ Ni ₆ In	<i>Im3</i>	993.8(2)			10
SmNi ₉ In ₂	YNi ₉ In ₂	<i>P4/mbm</i>	823.6(3)		483.3(3)	4
SmNi ₅ In	CeNi ₅ Sn	<i>P6₃/mmc</i>	488.8(1)		1982.7(3)	13
SmNi ₄ In	MgCu ₄ Sn	<i>F43m</i>	708.1(1)			1
Sm ₄ Ni ₇ In ₈	Ce ₄ Ni ₇ In ₈	<i>Cmmm</i>	1475.6(4)	2417.7(7)	439.3(1)	16
SmNiIn ₂	PrNiIn ₂	<i>Cmcm</i>	434.9(2)	1818.4(6)	2143.6(7)	28

continued on next page

Table 2, continued

Compound	Str. type	S.G.	<i>a</i> (pm)	<i>b</i> (pm)	<i>c</i> (pm)	Ref.
SmNiIn	Fe ₂ P	<i>P</i> 6̄2 <i>m</i>	750.3		388.0	6
SmNi _{1.0–0.7} In _{1.0–1.3}	ZrNiAl	<i>P</i> 6̄2 <i>m</i>	748.7–763.0		387.2–387.0	7
SmNi _{0.5} In _{1.5}	AlB ₂	<i>P</i> 6̄/ <i>mmm</i>	479.1(1)		373.6(1)	20
SmNi _{0.4–0.3} In _{1.6–1.7}	AlB ₂	<i>P</i> 6̄/ <i>mmm</i>	477.8–481.1(1)		374.1–373.3(1)	21
Sm ₂ Ni ₂ In	Mn ₂ AlB ₂	<i>Cmmm</i>	396.1(1)	1437.0(4)	377.1(2)	8
Sm ₂ Ni _{2–x} In	Mo ₂ FeB ₂	<i>P</i> 4/ <i>mbm</i>	744.8(2)		372.8(2)	9
Sm ₁₂ Ni ₆ In	Sm ₁₂ Ni ₆ In	<i>Im</i> 3̄	980.0(2)			10
EuNi ₇ In ₆	LaNi ₇ In ₆	<i>Ibam</i>	804.5	916.2	1239.6	30
EuNi ₉ In ₂	YNi ₉ In ₂	<i>P</i> 4/ <i>mbm</i>	824.6(3)		484.0(2)	4
EuNi ₃ In ₆	LaNi ₃ In ₆	<i>Pmmn</i>	433.8(2)	761.6(5)	1170.7(7)	30
EuNi ₅ In	CeNi ₅ Sn	<i>P</i> 6 ₃ / <i>mmc</i>	487.5(2)		1979.1(4)	13
EuNiIn ₄	YNiAl ₄	<i>Cmcm</i>	446.3(2)	1694.2(5)	720.2(2)	15
			447.31	1695.88	722.36	31
EuNiIn ₂	MgCuAl ₂	<i>Cmcm</i>	439.0(1)	1064.4(2)	767.3(2)	32
EuNi _{0.5} In _{1.5}	AlB ₂	<i>P</i> 6̄/ <i>mmm</i>	496.0(1)		393.3(1)	20
GdNi ₉ In ₂	YNi ₉ In ₂	<i>P</i> 4/ <i>mbm</i>	823.2(4)		483.4(4)	4
GdNi ₉ In ₂	CeMn ₆ Ni ₅	<i>P</i> 4/ <i>mbm</i>	821.2		482.1	33
GdNi ₄ In	MgCu ₄ Sn	<i>F</i> 4̄3 <i>m</i>	705.9(1)			1
GdNiIn ₂	MgCuAl ₂	<i>Cmcm</i>	433.5(2)	1045.2(5)	732.7(3)	5
GdNiIn	Fe ₂ P	<i>P</i> 6̄2 <i>m</i>	746.7		384.5	6
			748.9		383.2	34
GdNi _{1–0.65} In _{1–1.35}	ZrNiAl	<i>P</i> 6̄2 <i>m</i>	748.3–769.9		384.0–385.2	7
Gd ₂ Ni ₂ In	Mn ₂ AlB ₂	<i>Cmmm</i>	393.0(1)	1424.0(3)	371.7(2)	8
Gd ₂ Ni _{2–x} In	Mo ₂ FeB ₂	<i>P</i> 4/ <i>mbm</i>	742.9(1)		370.7(1)	9
Gd ₁₂ Ni ₆ In	Sm ₁₂ Ni ₆ In	<i>Im</i> 3̄	974.3(1)			10
TbNi ₉ In ₂	YNi ₉ In ₂	<i>P</i> 4/ <i>mbm</i>	821.2(4)		482.1(3)	4
TbNi ₄ In	MgCu ₄ Sn	<i>F</i> 4̄3 <i>m</i>	703.4(1)			1
TbNiIn ₂	MgCuAl ₂	<i>Cmcm</i>	432.8(2)	1042.3(2)	730.3(2)	5
TbNiIn	Fe ₂ P	<i>P</i> 6̄2 <i>m</i>	747.2		377.6	6
TbNi _{1.0–0.5} In _{1.0–1.5}	ZrNiAl	<i>P</i> 6̄2 <i>m</i>	744.7–765.6		380.1–3.777	7
Tb ₂ Ni ₂ In	Mn ₂ AlB ₂	<i>Cmmm</i>	392.1(1)	1421.7(4)	369.4(1)	8
Tb ₂ Ni _{2–x} In	Mo ₂ FeB ₂	<i>P</i> 4/ <i>mbm</i>	737.2(3)		368.2(3)	9
DyNi ₉ In ₂	YNi ₉ In ₂	<i>P</i> 4/ <i>mbm</i>	820.0(4)		481.5(3)	4
DyNi ₄ In	MgCu ₄ Sn	<i>F</i> 4̄3 <i>m</i>	701.2(1)			1
DyNiIn ₂	MgCuAl ₂	<i>Cmcm</i>	431.5(2)	1039.1(3)	730.6(3)	5
DyNiIn	Fe ₂ P	<i>P</i> 6̄2 <i>m</i>	746.2		377.0	6
DyNi _{1.0–0.6} In _{1.0–1.4}	ZrNiAl	<i>P</i> 6̄2 <i>m</i>	743.3–762.5		377.1–374.5	7
Dy ₂ Ni ₂ In	Mn ₂ AlB ₂	<i>Cmmm</i>	389.9(1)	1414.4(4)	366.2(2)	9
Dy ₂ Ni _{2–x} In	Mo ₂ FeB ₂	<i>P</i> 4/ <i>mbm</i>	735.0(3)		367.2(3)	9
HoNi ₉ In ₂	YNi ₉ In ₂	<i>P</i> 4/ <i>mbm</i>	819.0(3)		480.1(3)	4
HoNi ₄ In	MgCu ₄ Sn	<i>F</i> 4̄3 <i>m</i>	700.4(1)			1
Ho ₁₀ Ni ₉ In ₂₀	Ho ₁₀ Ni ₉ In ₂₀	<i>P</i> 4/ <i>nmn</i>	1328.6(3)		908.3(3)	35
HoNiIn	Fe ₂ P	<i>P</i> 6̄2 <i>m</i>	762.9		374.9	6
HoNi _{1–0.5} In _{1–1.5}	ZrNiAl	<i>P</i> 6̄2 <i>m</i>	744.2–766.1		374.6–383.2	7
Ho ₂ Ni ₂ In	Mn ₂ AlB ₂	<i>Cmmm</i>	389.9(1)	1413.9(4)	365.8(2)	8
Ho ₂ Ni _{2–x} In	Mo ₂ FeB ₂	<i>P</i> 4/ <i>mbm</i>	734.5(4)		366.7(3)	9
Ho ₅ Ni ₂ In ₄	Lu ₅ Ni ₂ In ₄	<i>Pbam</i>	1776.8(5)	788.8(3)	356.8(2)	36

continued on next page

Table 2, *continued*

Compound	Str. type	S.G.	<i>a</i> (pm)	<i>b</i> (pm)	<i>c</i> (pm)	Ref.
ErNi ₉ In ₂	YNi ₉ In ₂	<i>P4/mbm</i>	819.0(4)		480.1(3)	4
ErNi ₄ In	MgCu ₄ Sn	<i>F43m</i>	699.6(1)			1
Er ₁₀ Ni ₉ In ₂₀	Ho ₁₀ Ni ₉ In ₂₀	<i>P4/nmm</i>	1325.0(2)		907.5(3)	35
ErNiIn	Fe ₂ P	<i>P62m</i>	744.1		372.3	6
ErNi _{1-0.6} In _{1-1.4}	ZrNiAl	<i>P62m</i>	741.2–765.6		373.0–369.3	7
Er ₂ Ni ₂ In	Mn ₂ AlB ₂	<i>Cmmm</i>	389.3(1)	1411.0(4)	363.9(2)	8
Er ₂ Ni _{2-x} In	Mo ₂ FeB ₂	<i>P4/mbm</i>	731.0(3)		365.4(3)	9
Er ₅ Ni ₂ In ₄	Lu ₅ Ni ₂ In ₄	<i>Pbam</i>	1772.2(8)	786.6(4)	355.8(3)	36
TmNi ₄ In	MgCu ₄ Sn	<i>F43m</i>	699.3(1)			1
Tm ₁₀ Ni ₉ In ₂₀	Ho ₁₀ Ni ₉ In ₂₀	<i>P4/nmm</i>	1325.1(2)		906.0(2)	35
TmNiIn	Fe ₂ P	<i>P62m</i>	742.6		370.4	6
TmNi _{1-0.6} In _{1-1.4}	ZrNiAl	<i>P62m</i>	738.8–765.9		370.5–367.2	7
Tm ₂ Ni ₂ In	Mn ₂ AlB ₂	<i>Cmmm</i>	388.6(2)	1404.1(3)	361.3(2)	8
Tm ₂ Ni _{2-x} In	Mo ₂ FeB ₂	<i>P4/mbm</i>	729.3(4)		364.4(4)	9
Tm ₅ Ni ₂ In ₄	Lu ₅ Ni ₂ In ₄	<i>Pbam</i>	1765.3(6)	784.3(3)	354.2(3)	36
Tm _{5-x} Ni ₂ In _{1-x} <i>x</i> = 0.18	Mo ₅ B ₂ Si	<i>I4/mcm</i>	752.16		1315.9	37
Tm _{14-x} Ni ₃ In _{3+x} <i>x</i> = 0.52	own	<i>P4₂/nmc</i>	939.22		2251.2	37
YbNi ₄ In	MgCu ₄ Sn	<i>F43m</i>	697.5(1)			1
YbNiIn ₄	YNiAl ₄	<i>Cmcm</i>	439.8(1)	1660.6(5)	727.8(2)	15
LuNi ₄ In	MgCu ₄ Sn	<i>F43m</i>	699.7(1)			1
Lu ₁₀ Ni ₉ In ₂₀	Ho ₁₀ Ni ₉ In ₂₀	<i>P4/nmm</i>	1315.5(2)		899.3(2)	35
LuNiIn	ZrNiAl	<i>P62m</i>	740.8(1)		369.3(1)	38
LuNi _{1.1-0.65} In _{0.9-1.35}	ZrNiAl	<i>P62m</i>	738.1–749.0		369.1–374.2	7
Lu ₂ Ni ₂ In	Mn ₂ AlB ₂	<i>Cmmm</i>	385.5(1)	1400.5(4)	367.0(2)	8
Lu ₂ Ni _{2-x} In	Mo ₂ FeB ₂	<i>P4/mbm</i>	728.2(4)		363.6(3)	9
Lu ₅ Ni ₂ In ₄	Lu ₅ Ni ₂ In ₄	<i>Pbam</i>	1756.8(5)	779.8(2)	352.2(1)	36

References

- | | | |
|-----------------------------------|---------------------------------|----------------------------|
| 1. Zaremba et al. (1984) | 13. Baranyak et al. (1992) | 26. Kalychak (1998b) |
| 2. Dwight and Kimball (1987) | 14. Zaremba et al. (1993) | 27. Kalychak (1997) |
| 3. Pöttgen and Dronskowski (1996) | 15. Kalychak et al. (1988b) | 28. Zaremba et al. (2000c) |
| 4. Kalychak et al. (1984b) | 16. Baranyak et al. (1988a) | 29. Pöttgen et al. (1999a) |
| 5. Zaremba et al. (1987a) | 17. Kalychak et al. (1987) | 30. Zaremba et al. (2004) |
| 6. Ferro et al. (1974a) | 18. Tang et al. (1995) | 31. Pöttgen et al. (1996) |
| 7. Kalychak et al. (1995) | 19. Kalychak and Zaremba (1994) | 32. Kalychak et al. (1997) |
| 8. Zaremba et al. (1988) | 20. Baranyak et al. (1988b) | 33. Mulder et al. (1998) |
| 9. Kalychak et al. (1990) | 21. Baranyak (1991) | 34. Buschow (1975) |
| 10. Kalychak et al. (1998) | 22. Kaczorowski et al. (1996a) | 35. Zaremba et al. (1987b) |
| 11. Kalychak et al. (2001) | 23. Moze et al. (1995) | 36. Zaremba et al. (1991) |
| 12. Kalychak et al. (1985) | 24. Pöttgen (1995) | 37. Lukachuk et al. (2002) |
| | 25. Zaremba et al. (2002b) | 38. Sysa et al. (1988) |

3.1.5. *The R–Cu–In systems*

Isothermal sections of the phase diagrams of each *R*–Cu–In system have been built for the whole area of compositions. Only the Sc–Cu–In system has not been investigated. The {La, Ce, Pr, Nd, Sm}–Cu–In systems have been investigated at 870 K in the region of 0–33.3 atomic percent *R* and at 670 K in the region of 33.3–100 atomic percent *R*. The {Eu, Yb}–

Cu–In systems have been investigated at 670 K and the {Y, Gd, Tb, Dy, Ho, Er, Tm, Lu}–Cu–In systems have been investigated at 870 K. The existence of 13 compounds with equiatomic composition $RCuIn$ is confirmed (Kalychak et al., 1998), which were first investigated by Dwight (1976) in each system. $Yb_{0.4}Cu_2In_{0.6}$ reported by Felner and Nowik (1987) is also confirmed. The formation of homogeneity ranges is typical for the R –Cu–In systems and they are much broader than in the R –Ni–In systems. There exist 102 ternary compounds in the copper based systems under the thermal conditions mentioned above. The crystal structures have been investigated for 92 of them (table 3).

Table 3
Crystallographic data of ternary R –Cu–In compounds

Compound	Str. type	S.G.	a (pm)	b (pm)	c (pm)	Ref.
ScCu ₂ In	MnCu ₂ Al	$Fm\bar{3}m$	636.2(2)			1
Sc ₂ Cu ₂ In	U ₂ Pt ₂ Sn	$P4_2/mmm$	722.36(6)		689.55(9)	2
YCu _{5.1} In _{6.9}	ThMn ₁₂	$I4/mmm$	915.8(2)		539.8(1)	3
YCu ₄ In	MgCu ₄ Sn	$F\bar{4}3m$	719.1(1)			4
YCu _{4.64–4.00} In _{0.36–1.00}	MgCu ₄ Sn	$F\bar{4}3m$	707.5–719.1(2)			3
YCu ₂ In	MnCu ₂ Al	$Fm\bar{3}m$	660.1(1)			1,5
YCuIn	ZrNiAl	$P\bar{6}2m$	743.9(1)		394.6	4
YCu _{0.53–0.32} In _{1.47–1.68}	AlB ₂	$P6/mmm$	469.0(1)–470.9(1)		366.8(1)–365.3(1)	3
Y ₂ Cu ₂ In	Mo ₂ FeB ₂	$P4/mbm$	747.0(2)		376.5(2)	6
LaCu _{6.5} In _{6.5}	NaZn ₁₃	$Fm\bar{3}c$	1249.2(3)			1
LaCu ₉ In ₂	YNi ₉ In ₂	$P4/mbm$	859.7		507.7	7
LaCu _{5.23–4.25} In _{0.77–1.75}	CeCu _{4.38} In _{1.62}	$Pnmm$	1653.3–1706.2	1050.2– 1088.0	496.8–518.0	7,8
LaCu ₂ In	MnCu ₂ Al	$Fm\bar{3}m$	684.5(1) 685.4			1 5,9
LaCuIn	ZrNiAl	$P\bar{6}2m$	755		428	10
LaCu _{0.5} In _{1.5}	AlB ₂	$P6/mmm$	482.1(1)		402.5(2)	11
LaCu _{0.50–0.20} In _{1.50–1.80}	AlB ₂	$P6/mmm$	482.1–487.0		399.6–403.2	7
La ₂ Cu ₂ In	Mo ₂ FeB ₂	$P4/mbm$	778.9(2) 796.4		398.3(3) 390.6	6,7 12
Ce _{0.72} Cu _{8.80} In _{3.84}	NaZn ₁₃	$Fm\bar{3}c$	1248.2(1)			13,14
CeCu _{5.1} In _{6.9}	ThMn ₁₂	$I4/mmm$	926.3(2)		542.3(1)	15
CeCu _{9.0–8.0} In _{2.0–3.0}	YNi ₉ In ₂	$P4/mbm$	847.6–863.1(2)		498.8–511.7(2)	14
CeCu _{4.38} In _{1.62}	CeCu _{4.38} In _{1.62}	$Pnmm$	1716.9(6)	1090.8(4)	520.2(2)	8
CeCu _{5.1–4.2} In _{0.9–1.8}	CeCu _{4.38} In _{1.62}	$Pnmm$	1672.0–1701.9(4)	1060.0– 1080.9(3)	507.4–518.9(1)	14
CeCu ₂ In	MnCu ₂ Al	$Fm\bar{3}m$	678.5(1)			1,9
CeCuIn	ZrNiAl	$P\bar{6}2m$	749 749.0(1)		424 424.9(1)	10 14
CeCu _{0.5} In _{1.5}	AlB ₂	$P6/mmm$	481.8(1)		389.9(1)	11
CeCu _{0.8–0.4} In _{1.2–1.6}	AlB ₂	$P6/mmm$	480.4–483.5(1)		383.7–391.7(2)	14
Ce ₂ Cu ₂ In	Mo ₂ FeB ₂	$P4/mbm$	772.8(1) 773.68		391.6(2) 392.40	6,14 12
CeCu _{2–x} In _{2–y} ($x = y = 0.5$)	CaBe ₂ Ge ₂	$P4/nmm$	424.5(19)		1055.0(2)	13,14
PrCu _{5.1} In _{6.9}	ThMn ₁₂	$I4/mmm$	924.6(1)		541.5(1)	15
PrCu _{9.0–8.1} In _{2.0–2.9}	YNi ₉ In ₂	$P4/mbm$	858.6–859.7		508.9–510.7	16
PrCu _{4.38} In _{1.62}	CeCu _{4.38} In _{1.62}	$Pnmm$	1694.8(4)	1079.9(3)	515.4(1)	8

continued on next page

Table 3, *continued*

Compound	Str. type	S.G.	<i>a</i> (pm)	<i>b</i> (pm)	<i>c</i> (pm)	Ref.
PrCu _{5.1-4.2} In _{0.9-1.8}	CeCu _{4.38} In _{1.62}	<i>Pnmm</i>	1666.7–1694.8	1059.1– 1080.0	505.0–516.0	16
PrCu ₂ In	MnCu ₂ Al	<i>Fm$\bar{3}m$</i>	675.7(1)			1,9
PrCuIn	ZrNiAl	<i>P$\bar{6}2m$</i>	746		420	10
PrCu _{0.5} In _{1.5}	AlB ₂	<i>P6/mmm</i>	478.9(2)		381.2(3)	11
PrCu _{0.5-0.20} In _{1.50-1.80}	AlB ₂	<i>P6/mmm</i>	478.2–485.3		395.8–378.9	16
Pr ₂ Cu ₂ In	Mo ₂ FeB ₂	<i>P4/mbm</i>	767.8(1)		389.3(1)	6
NdCu _{5.1} In _{6.9}	ThMn ₁₂	<i>I4/mmm</i>	923.9(1)		542.3(1)	15
NdCu _{9.0-8.4} In _{2.0-2.6}	YNi ₉ In ₂	<i>P4/mbm</i>	852.1–853.7(2)		503.4–505.6(2)	17
NdCu _{4.38} In _{1.62}	CeCu _{4.38} In _{1.62}	<i>Pnmm</i>	1695.8(5)	1077.(3)	513.1(2)	8
NdCu _{4.9-4.0} In _{1.1-2.0}	CeCu _{4.38} In _{1.62}	<i>Pnmm</i>	1667.5–1692.4(5)	1060.5– 1081.2(4)	502.3–511.8(1)	17
NdCu ₄ In	MgCu ₄ Sn	<i>F$\bar{4}3m$</i>	729.3(1)			4
NdCu ₂ In	MnCu ₂ Al	<i>Fm$\bar{3}m$</i>	673.5(1)			1,9
NdCuIn	ZrNiAl	<i>P$\bar{6}2m$</i>	747		414	10
			745.9(2)		415.9(3)	17
NdCu _{0.5} In _{1.5}	AlB ₂	<i>P6/mmm</i>	478.4(1)		380.0(2)	11
NdCu _{0.7-0.3} In _{1.3-1.7}	AlB ₂	<i>P6/mmm</i>	477.3–481.3(1)		376.4–380.5(2)	17
Nd ₂ Cu ₂ In	Mo ₂ FeB ₂	<i>P4/mbm</i>	763.8(2)		387.7(1)	6
SmCu _{5.1} In _{6.9}	ThMn ₁₂	<i>I4/mmm</i>	920.2(1)		539.6(1)	15
SmCu _{9.0-8.0} In _{2.0-3.0}	YNi ₉ In ₂	<i>P4/mbm</i>	849.7–856.1(1)		500.0–509.4(1)	17
SmCu _{4.38} In _{1.62}	CeCu _{4.38} In _{1.62}	<i>Pnmm</i>	1658.0(7)	1058.2(4)	499.6(2)	17
SmCu ₄ In	MgCu ₄ Sn	<i>F$\bar{4}3m$</i>	722.4(1)			4
SmCu _{4.9-4.0} In _{0.1-1.0}	MgCu ₄ Sn	<i>F$\bar{4}3m$</i>	713.2–724.3(1)			17
SmCu ₂ In	MnCu ₂ Al	<i>Fm$\bar{3}m$</i>	673.2(1)			1
			668.5			5,9
SmCuIn	ZrNiAl	<i>P$\bar{6}2m$</i>	748		407	10
			742.1(1)		395.0(1)	4
SmCu _{0.5} In _{1.5}	AlB ₂	<i>P6/mmm</i>	470.4(1)		364.7(1)	11
SmCu _{0.6-0.2} In _{1.4-1.8}	AlB ₂	<i>P6/mmm</i>	474.7–481.3(1)		372.5–369.9(1)	17
Sm ₂ Cu ₂ In	Mo ₂ FeB ₂	<i>P4/mbm</i>	757.1(2)		382.3(1)	6
EuCu _{6.5} In _{6.5}	NaZn ₁₃	<i>Fm$\bar{3}c$</i>	1258.1(7)			1
EuCu _{8.5} In _{2.5}	YNi ₉ In ₂	<i>P4/mbm</i>	864.3(2)		515.6(2)	18
EuCuIn ₄	YNiAl ₄	<i>Cmcm</i>	449.3(2)	1693.5(5)	737.3(5)	19
EuCu _{0.5} In _{1.5}	AlB ₂	<i>P6/mmm</i>	494.2(1)		393.5(2)	11
GdCu _{5.1} In _{6.9}	ThMn ₁₂	<i>I4/mmm</i>	918.6(2)		541.2(2)	15
GdCu _{9.00-8.36} In _{2.00-2.64}	YNi ₉ In ₂	<i>P4/mbm</i>	849.2–856.5(2)		504.7–510.0(2)	20
GdCu ₄ In	MgCu ₄ Sn	<i>F$\bar{4}3m$</i>	722.7(1)			4
GdCu _{4.70-4.00} In _{0.30-1.00}	MgCu ₄ Sn	<i>F$\bar{4}3m$</i>	709.0–722.7(2)			20
GdCu ₂ In	MnCu ₂ Al	<i>Fm$\bar{3}m$</i>	664.1(2)			1
			664.3			5,9
GdCuIn	ZrNiAl	<i>P$\bar{6}2m$</i>	746.3(1)		399.6(1)	4
GdCu _{0.59-0.35} In _{1.41-1.65}	AlB ₂	<i>P6/mmm</i>	473.0–477.0(1)		369.2–367.5(1)	20
Gd ₂ Cu ₂ In	Mo ₂ FeB ₂	<i>P4/mbm</i>	752.8(2)		379.8(2)	6

continued on next page

Table 3, *continued*

Compound	Str. type	S.G.	<i>a</i> (pm)	<i>b</i> (pm)	<i>c</i> (pm)	Ref.
TbCu _{5,1} In _{6,9}	ThMn ₁₂	<i>I4/mmm</i>	917.2(2)		539.4(2)	15
TbCu ₅₋₄ In ₀₋₁	MgCu ₄ Sn	<i>F43m</i>	719.9(1)			4
TbCu ₅₋₄ In ₀₋₁	AuBe ₅ -MgCu ₄ Sn	<i>F43m</i>	704.1–719.9			21
TbCu ₂ In	MnCu ₂ Al	<i>Fm3m</i>	661.5(3)			1
			661.3			5,9
TbCuIn	ZrNiAl	<i>P62m</i>	745		397	10
			745.4(1)		396.4(2)	4
TbCu _{0,56-0,32} In _{1,44-1,68}	AlB ₂	<i>P6/mmm</i>	471.7–475.0(2)		366.6–363.8(2)	21
Tb ₂ CuIn ₃	AlB ₂	<i>P6/mmm</i>	470.2(1)		368.2(2)	22
Tb ₂ CuIn ₃ (at 3.8 K)	own	<i>Cmmm</i>	469.9(2)	813.9(2)	366.8(1)	22
Tb ₂ Cu ₂ In	Mo ₂ FeB ₂	<i>P4/mbm</i>	748.7(2)		377.2(2)	6
DyCu _{5,1} In _{6,9}	ThMn ₁₂	<i>I4/mmm</i>	916.3(2)		539.5(2)	15
DyCu ₄ In	MgCu ₄ Sn	<i>F43m</i>	718.4(1)			4
DyCu ₅₋₄ In ₀₋₁	AuBe ₅ -MgCu ₄ Sn	<i>F43m</i>	702.7–718.4			21
DyCu ₂ In	MnCu ₂ Al	<i>Fm3m</i>	659.3(1)			1
			659.4			5,9
DyCuIn	ZrNiAl	<i>P62m</i>	744		394	10
			743.8(2)		394.3(2)	4
DyCu _{0,65-0,32} In _{1,35-1,68}	AlB ₂	<i>P6/mmm</i>	470.6–473.8(1)		364.8–363.3(1)	21
Dy ₂ Cu ₂ In	Mo ₂ FeB ₂	<i>P4/mbm</i>	746.6(3)		374.6(2)	6
HoCu _{5,1} In _{6,9}	ThMn ₁₂	<i>I4/mmm</i>	915.4(2)		538.7(1)	15
HoCu ₄ In	MgCu ₄ Sn	<i>F43m</i>	718.3(1)			4
HoCu ₅₋₄ In ₀₋₁	AuBe ₅ -MgCu ₄ Sn	<i>F43m</i>	701.6–716.9			23
HoCu ₂ In	MnCu ₂ Al	<i>Fm3m</i>	651.1(1)			1
			657.6			5,9
HoCuIn	ZrNiAl	<i>P62m</i>	743.2(1)		389.4(1)	4,10
HoCu _{0,41-0,29} In _{1,59-1,71}	AlB ₂	<i>P6/mmm</i>	469.0–470.9		362.7–361.0	23
Ho ₂ Cu ₂ In	Mo ₂ FeB ₂	<i>P4/mbm</i>	744.1(2)		373.1(2)	6
ErCu _{5,1} In _{6,9}	ThMn ₁₂	<i>I4/mmm</i>	915.2(2)		539.0(2)	15
ErCu ₄ In	MgCu ₄ Sn	<i>F43m</i>	715.9(1)			4
ErCu ₅₋₄ In ₀₋₁	AuBe ₅ -MgCu ₄ Sn	<i>F43m</i>	700.3–715.9			23
ErCu ₂ In	MnCu ₂ Al	<i>Fm3m</i>	658.1(1)			1
			656.2			5,9
ErCu _{1,0-0,64} In _{1,0-1,36}	ZrNiAl	<i>P62m</i>	740.8(1)		398.3(1)	4,23
ErCu _{0,44-0,35} In _{1,56-1,65}	AlB ₂	<i>P6/mmm</i>	469.7		359.8	23
Er ₂ Cu ₂ In	Mo ₂ FeB ₂	<i>P4/mbm</i>	741.4(3)		372.3(2)	6
TmCu _{5,1} In _{6,9}	ThMn ₁₂	<i>I4/mmm</i>	915.0(21)		538.3(1)	15
TmCu ₄ In	MgCu ₄ Sn	<i>F43m</i>	715.3(1)			4
TmCu ₅₋₄ In ₀₋₁	AuBe ₅ -MgCu ₄ Sn	<i>F43m</i>	699.1–715.3			24
TmCu ₂ In	MnCu ₂ Al	<i>Fm3m</i>	653.9(2)			1
TmCuIn	ZrNiAl	<i>P62m</i>	739.8(1)		386.8(1)	4
TmCu _{1,0-0,56} In _{1,0-1,44}	ZrNiAl	<i>P62m</i>	739.9–739.1		386.8–394.3	24
TmCu _{0,4-0,3} In _{1,6-1,7}	AlB ₂	<i>P6/mmm</i>	469.4		359.5	24
Tm ₂ Cu ₂ In	Mo ₂ FeB ₂	<i>P4/mbm</i>	739.3(1)		369.6(1)	6
YbCu _{5,1} In _{6,9}	ThMn ₁₂	<i>I4/mmm</i>	921.9(2)		538.9(2)	15
YbCu ₄ In	MgCu ₄ Sn	<i>F43m</i>	714.6(1)			4
			715.75(6)			25
YbCu _{4,8-4,0} In _{0,2-1,0}	MgCu ₄ Sn	<i>F43m</i>	703.6–714.5(3)			26

continued on next page

Table 3, continued

Compound	Str. type	S.G.	<i>a</i> (pm)	<i>b</i> (pm)	<i>c</i> (pm)	Ref.
Yb ₂ Cu ₂ In	W ₂ CoB ₂	<i>Immm</i>	438.8(5)	574.30(6)	873.37(9)	27
Yb ₂ Cu ₂ In	Mo ₂ FeB ₂	<i>P4/mbm</i>	747.3		389.2	28
LuCu _{5.1} In _{6.9}	ThMn ₁₂	<i>I4/mmm</i>	914.0(2)		537.7(2)	24
LuCu ₄ In	MgCu ₄ Sn	<i>F43m</i>	714.4(1)			4
LuCu ₅₋₄ In ₀₋₁	AuBe ₅ -MgCu ₄ Sn	<i>F43m</i>	697.0(1)-714.4(1)			24
LuCu ₂ In	MnCu ₂ Al	<i>Fm3m</i>	650.9(2)			1
			651.4			5,9
LuCuIn	ZrNiAl	<i>P62m</i>	738.8(1)		378.9(1)	4
LuCu _{1.0-0.41} In _{1.0-1.59}	ZrNiAl	<i>P62m</i>	738.8(1)-736.4(1)		382.6(1)-392.3(1)	24
Lu ₂ Cu ₂ In	Mo ₂ FeB ₂	<i>P4/mbm</i>	736.4(1)		368.2(1)	6

References

- | | | |
|---------------------------------|----------------------------------|-------------------------------|
| 1. Kalychak et al. (1984a) | 10. Dwight (1976) | 20. Bakar and Kalychak (1990) |
| 2. Hulliger (1996) | 11. Baranyak et al. (1988b) | 21. Kalychak et al. (1989b) |
| 3. Kalychak and Bakar (1989) | 12. Kaczorowski et al. (1996a) | 22. Siouris et al. (2001) |
| 4. Sysa et al. (1988) | 13. Baranyak et al. (1990) | 23. Kalychak and Bakar (1994) |
| 5. Dwight and Kimball (1987) | 14. Baranyak and Kalychak (1991) | 24. Kalychak and Bakar (1996) |
| 6. Kalychak et al. (1990) | 15. Sysa et al. (1989) | 25. Kojima et al. (1990) |
| 7. Dmytrakh and Kalychak (1990) | 16. Kalychak (1998a) | 26. Kalychak et al. (1989a) |
| 8. Kalychak et al. (1988a) | 17. Baranyak and Kalychak (1993) | 27. Giovannini et al. (2001) |
| 9. Felner (1985) | 18. Sysa et al. (1994b) | 28. Tsujii et al. (2001) |
| | 19. Sysa and Kalychak (1993) | |

Six ternary compounds exist in the Y-Cu-In system (fig. 5); (Kalychak and Bakar, 1989). The crystal structures are all known. YCu_{4.64-4.00}In_{0.36-1.00} and YCu_{0.53-0.32}In_{1.47-1.68} have extended homogeneity ranges.

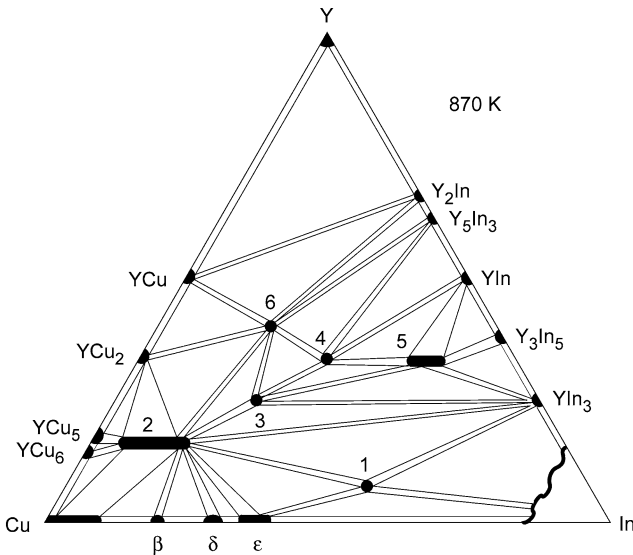


Fig. 5. Isothermal sections of the phase diagram in the Y-Cu-In system at 870 K. 1 - YCu_{5.1}In_{6.9}; 2 - YCu_{4.64-4.00}In_{0.36-1.00}; 3 - YCu₂In; 4 - YCuIn; 5 - YCu_{0.53-0.32}In_{1.47-1.68}; 6 - Y₂Cu₂In.

Eight ternary compounds exist in the La–Cu–In system (fig. 6) (Dmytrakh and Kalychak, 1990). The crystal structure of $\sim\text{LaCu}_2\text{In}_3$ is unknown. $\text{LaCu}_{5.2-4.3}\text{In}_{0.8-1.7}$ and $\text{LaCu}_{0.5-0.2}\text{In}_{1.5-1.8}$ have homogeneity ranges as stated in the formulæ. A small homogeneity region is also characteristic for LaCu_9In_2 .

Nine ternary indides have been discovered in the Ce–Cu–In system (fig. 7) (Baranyak and Kalychak, 1991). So far, only the crystal structure of $\sim\text{CeCu}_{4.2}\text{In}_{4.8}$ has not been de-

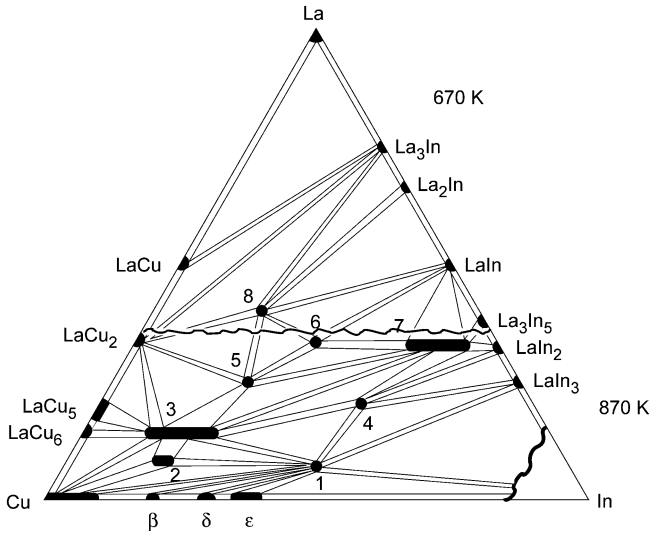


Fig. 6. Isothermal sections of the phase diagram in the La–Cu–In system at 870 K and 670 K. 1 – $\text{LaCu}_{6.5}\text{In}_{6.5}$; 2 – LaCu_9In_2 ; 3 – $\text{LaCu}_{5.23-4.25}\text{In}_{0.77-1.75}$; 4 – $\sim\text{LaCu}_2\text{In}_3$; 5 – LaCu_2In ; 6 – LaCuIn ; 7 – $\text{CaCu}_{0.5-0.2}\text{In}_{1.5-1.8}$; 8 – $\text{La}_2\text{Cu}_2\text{In}$.

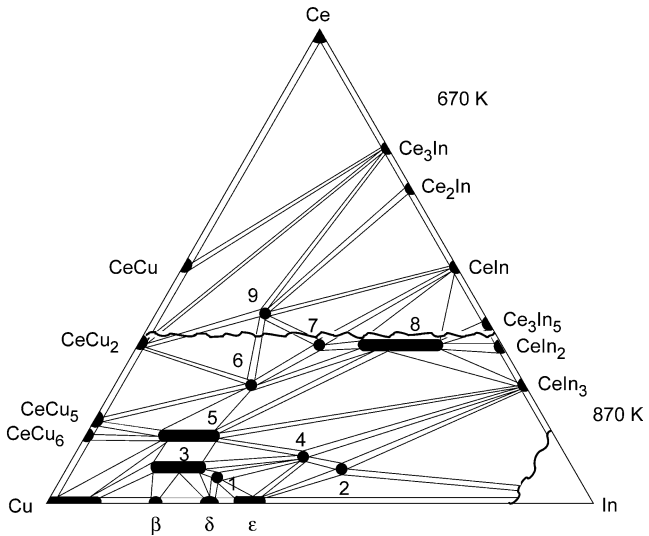


Fig. 7. Isothermal sections of the phase diagram in the Ce–Cu–In system at 870 K and 670 K. 1 – $\text{Ce}_{1-x}(\text{Cu}_{0.68}\text{In}_{0.32})_{12}\text{Cu}_{1-y}$ ($x = 0.22$; $y = 0.36$); 2 – $\text{CeCu}_{5.1}\text{In}_{6.9}$; 3 – $\text{CeCu}_{9.0-8.0}\text{In}_{2.0-3.0}$; 4 – $\sim\text{CeCu}_{4.2}\text{In}_{4.8}$; 5 – $\text{CeCu}_{5.1-4.2}\text{In}_{0.9-1.8}$; 6 – CeCu_2In ; 7 – CeCuIn ; 8 – $\text{CeCu}_{0.8-0.4}\text{In}_{1.2-1.6}$; 9 – $\text{Ce}_2\text{Cu}_2\text{In}$.

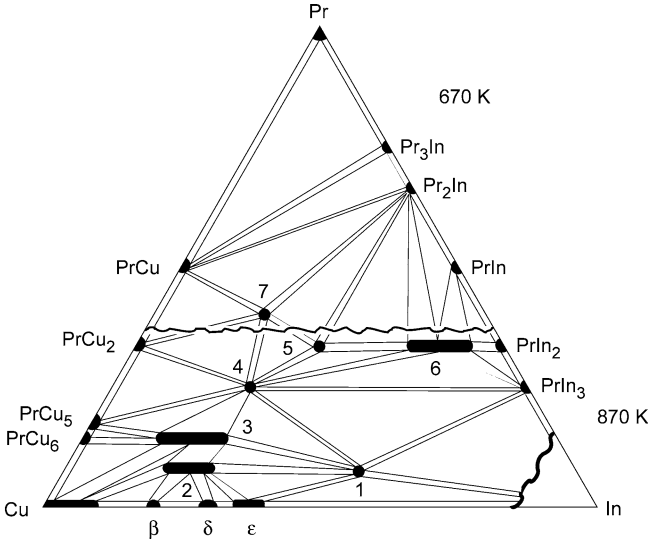


Fig. 8. Isothermal sections of the phase diagram in the Pr-Cu-In system at 870 K and 670 K. 1 - $\text{PrCu}_{5,1}\text{In}_{6,9}$; 2 - $\text{PrCu}_{9,0-8,1}\text{In}_{2,0-2,9}$; 3 - $\text{PrCu}_{5,1-4,2}\text{In}_{0,9-1,8}$; 4 - PrCu_2In ; 5 - PrCuIn ; 6 - $\text{PrCu}_{0,50-0,20}\text{In}_{1,50-1,80}$; 7 - $\text{Pr}_2\text{Cu}_2\text{In}$.

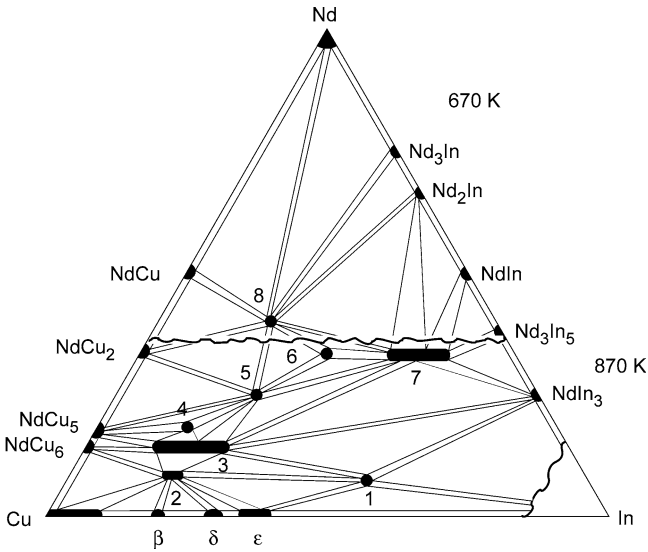


Fig. 9. Isothermal sections of the phase diagram in the Nd-Cu-In system at 870 K and 670 K. 1 - $\text{NdCu}_{5,1}\text{In}_{6,9}$; 2 - $\text{NdCu}_{9,0-8,4}\text{In}_{2,0-2,6}$; 3 - $\text{NdCu}_{4,9-4,0}\text{In}_{1,1-2,0}$; 4 - NdCu_4In ; 5 - NdCu_2In ; 6 - NdCuIn ; 7 - $\text{NdCu}_{0,7-0,3}\text{In}_{1,3-1,7}$; 8 - $\text{Nd}_2\text{Cu}_2\text{In}$.

terminated. Homogeneity regions are present in $\text{CeCu}_{9,0-8,0}\text{In}_{2,0-3,0}$, $\text{CeCu}_{5,1-4,2}\text{In}_{0,9-1,8}$, and $\text{CeCu}_{0,8-0,4}\text{In}_{1,2-1,6}$. $\text{CeCu}_{2-x}\text{In}_{2-y}$ is stable only above 870 K (Baranyak et al., 1990). A homogeneity range $\text{CeCu}_{6-x}\text{In}_x$ ($x = 0-1.75$) has been reported by Kasaya et al. (1996).

In the Pr-Cu-In system (fig. 8), seven ternary compounds and their crystal structures are known (Kalychak, 1998a). The indides $\text{PrCu}_{9,0-8,1}\text{In}_{2,0-2,9}$, $\text{PrCu}_{5,1-4,2}\text{In}_{0,9-1,8}$ and $\text{PrCu}_{0,5-0,2}\text{In}_{1,5-1,8}$ have homogeneity ranges as indicated in the formulæ.

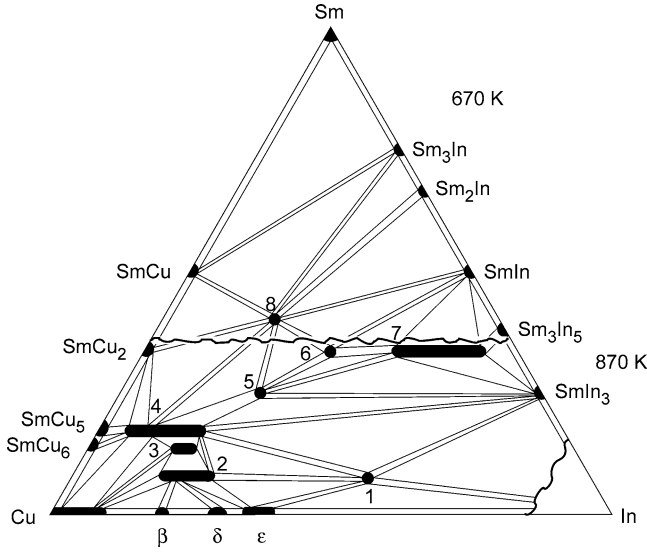


Fig. 10. Isothermal sections of the phase diagram in the Sm–Cu–In system at 870 K and 670 K. 1 – $\text{SmCu}_{5.1}\text{In}_{6.9}$; 2 – $\text{SmCu}_{9.0-8.0}\text{In}_{2.0-3.0}$; 3 – $\text{SmCu}_{4.38-4.0}\text{In}_{1.62}$; 4 – $\text{SmCu}_{4.9-4.0}\text{In}_{0.1-1.0}$; 5 – SmCu_2In ; 6 – SmCuIn ; 7 – $\text{SmCu}_{0.6-0.2}\text{In}_{1.4-1.8}$; 8 – $\text{Sm}_2\text{Cu}_2\text{In}$.

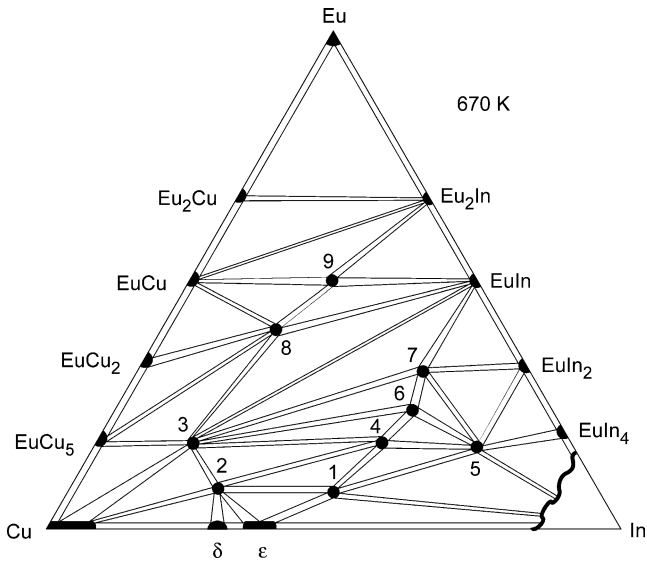


Fig. 11. Isothermal section of the phase diagram in the Eu–Cu–In system at 670 K. 1 – $\text{EuCu}_{6.5}\text{In}_{6.5}$; 2 – $\text{EuCu}_{8.5}\text{In}_{2.5}$; 3 – $\sim\text{EuCu}_4\text{In}$; 4 – $\sim\text{EuCu}_2\text{In}_3$; 5 – EuCuIn_4 ; 6 – $\sim\text{EuCuIn}_2$; 7 – $\text{EuCu}_{0.5}\text{In}_{1.5}$; 8 – $\sim\text{Eu}_2\text{Cu}_2\text{In}$; 9 – $\sim\text{Eu}_2\text{CuIn}$.

In the Nd–Cu–In system (fig. 9), eight ternary compounds with known crystal structures exist (Baranyak and Kalychak, 1993). $\text{NdCu}_{9.0-8.4}\text{In}_{2.0-2.6}$, $\text{NdCu}_{4.9-4.0}\text{In}_{1.1-2.0}$ and $\text{NdCu}_{0.7-0.3}\text{In}_{1.3-1.7}$ have extended homogeneity ranges with respect to Cu/In mixing.

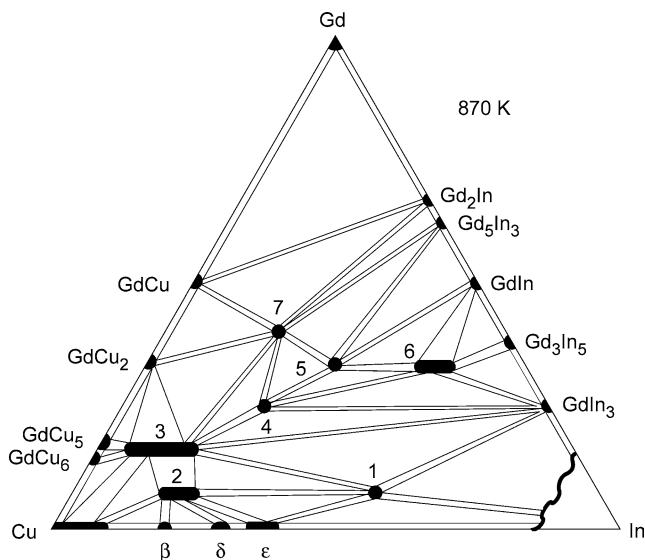


Fig. 12. Isothermal section of the phase diagram in the Gd-Cu-In system at 870 K. 1 - $\text{GdCu}_{5.1}\text{In}_{6.9}$; 2 - $\text{GdCu}_{9.00-8.36}\text{In}_{2.00-2.64}$; 3 - $\text{GdCu}_{4.70-4.00}\text{In}_{0.30-1.00}$; 4 - GdCu_2In ; 5 - GdCuIn ; 6 - $\text{GdCu}_{0.59-0.35}\text{In}_{1.41-1.65}$; 7 - $\text{Gd}_2\text{Cu}_2\text{In}$.

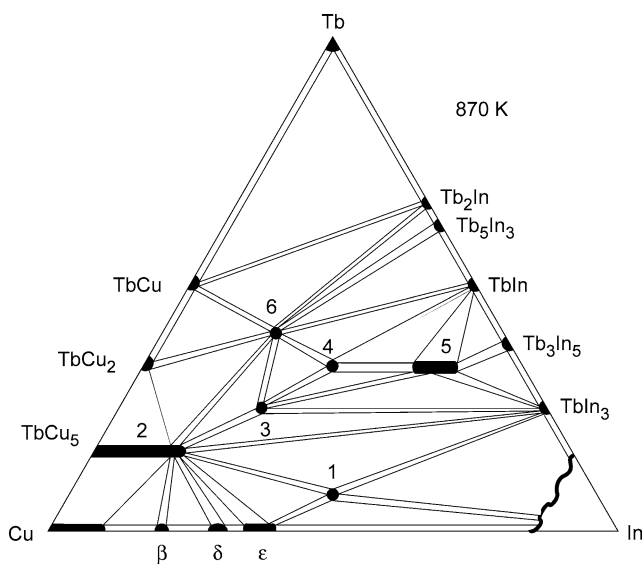


Fig. 13. Isothermal section of the phase diagram in the Tb-Cu-In system at 870 K. 1 - $\text{TbCu}_{5.1}\text{In}_{6.9}$; 2 - $\text{TbCu}_{5.4}\text{In}_{0.1}$; 3 - TbCu_2In ; 4 - TbCuIn ; 5 - $\text{TbCu}_{0.56-0.32}\text{In}_{1.44-1.68}$; 6 - $\text{Tb}_2\text{Cu}_2\text{In}$.

Eight ternary intermetallics have been found in the Sm-Cu-In system (fig. 10) (Baranyak and Kalychak, 1993). The crystal structures of these intermetallics have been determined. Homogeneity regions are present in $\text{SmCu}_{9.0-8.0}\text{In}_{2.0-3.0}$, $\text{SmCu}_{4.9-4.0}\text{In}_{1.1-2.0}$, and $\text{SmCu}_{0.6-0.2}\text{In}_{1.4-1.8}$.

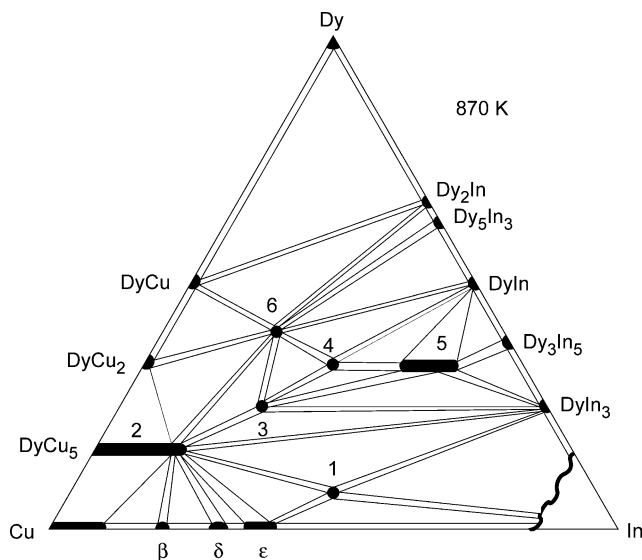


Fig. 14. Isothermal section of the phase diagram in the Dy–Cu–In system at 870 K. 1 – $\text{DyCu}_{5.1}\text{In}_{6.9}$; 2 – $\text{DyCu}_{5-4}\text{In}_{0-1}$; 3 – DyCu_2In ; 4 – DyCuIn ; 5 – $\text{DyCu}_{0.65-0.32}\text{In}_{1.35-1.68}$; 6 – $\text{Dy}_2\text{Cu}_2\text{In}$.

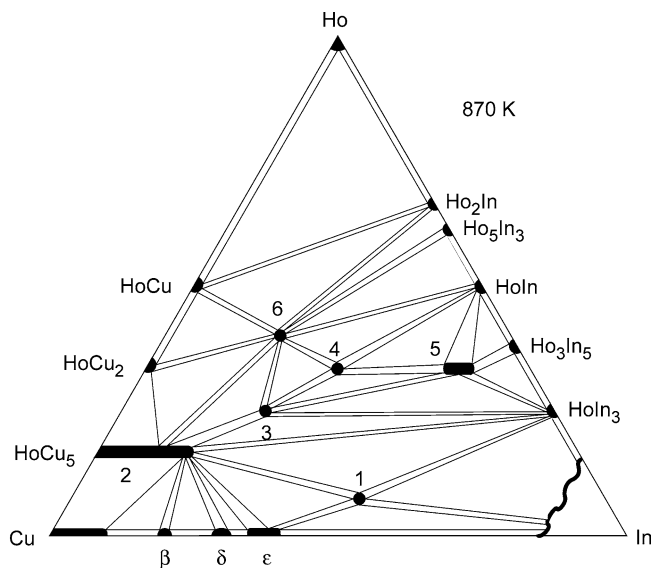


Fig. 15. Isothermal section of the phase diagram in the Ho–Cu–In system at 870 K. 1 – $\text{HoCu}_{5.1}\text{In}_{6.9}$; 2 – $\text{HoCu}_{5-4}\text{In}_{0-1}$; 3 – HoCu_2In ; 4 – HoCuIn ; 5 – $\text{HoCu}_{0.41-0.29}\text{In}_{1.59-1.71}$; 6 – $\text{Ho}_2\text{Cu}_2\text{In}$.

Nine compounds of practically constant stoichiometry in the Eu–Cu–In system (fig. 11) are known (Kalychak, 1998a). The crystal structures have been investigated for $\text{EuCu}_{6.5}\text{In}_{6.5}$, $\text{EuCu}_{8.5}\text{In}_{2.5}$, EuCuIn_4 , and $\text{EuCu}_{0.5}\text{In}_{1.5}$.

In the Gd–Cu–In system (fig. 12), seven ternary compounds exist (Bakar and Kalychak, 1990) and their crystal structures are known. $\text{GdCu}_{9.0-8.4}\text{In}_{2.0-2.6}$, $\text{GdCu}_{4.7-4.0}\text{In}_{0.3-1.0}$, and

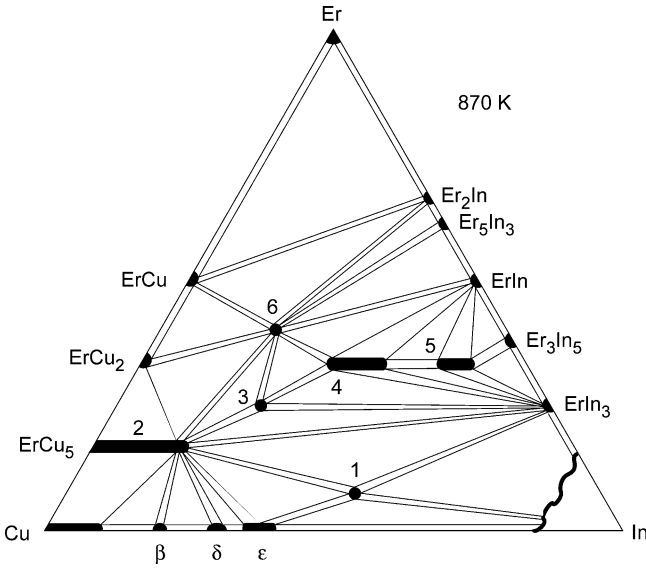


Fig. 16. Isothermal section of the phase diagram in the Er-Cu-In system at 870 K. 1 – $\text{ErCu}_{5,1}\text{In}_{6,9}$; 2 – $\text{ErCu}_{5-4}\text{In}_{0-1}$; 3 – ErCu_2In ; 4 – $\text{ErCu}_{1,0-0,64}\text{In}_{1,0-1,36}$; 5 – $\text{ErCu}_{0,44-0,35}\text{In}_{1,56-1,65}$; 6 – $\text{Er}_2\text{Cu}_2\text{In}$.

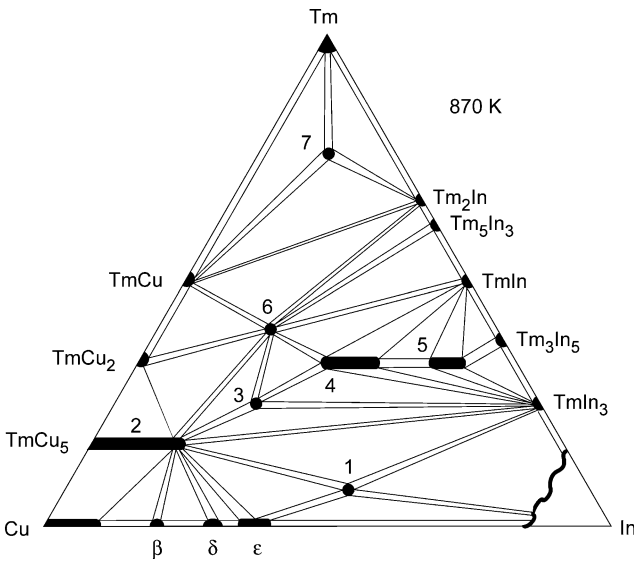


Fig. 17. Isothermal section of the phase diagram in the Tm-Cu-In system at 870 K. 1 – $\text{TmCu}_{5,1}\text{In}_{6,9}$; 2 – $\text{TmCu}_{5-4}\text{In}_{0-1}$; 3 – TmCu_2In ; 4 – $\text{TmCu}_{1,0-0,56}\text{In}_{1,0-1,44}$; 5 – $\text{TmCu}_{0,4-0,3}\text{In}_{1,6-1,7}$; 6 – $\text{Tm}_2\text{Cu}_2\text{In}$; 7 – $\sim\text{Tm}_6\text{CuIn}$.

$\text{GdCu}_{0,6-0,4}\text{In}_{1,4-1,6}$ have homogeneity ranges. Six ternary intermetals have been found in the Tb-Cu-In system (fig. 13) (Kalychak et al., 1989b) and their crystal structures have been determined. Binary TbCu_5 dissolves up to 16.7 atomic percent indium and a homogeneity range is present in $\text{TbCu}_{0,56-0,32}\text{In}_{1,44-1,68}$.

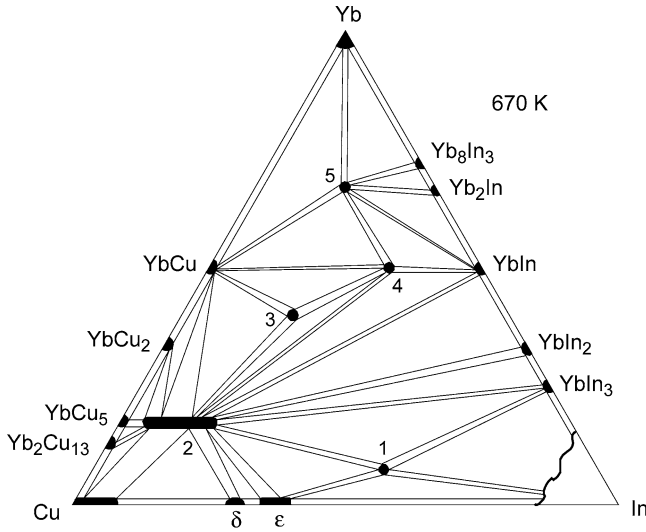


Fig. 18. Isothermal section of the phase diagram in the Yb–Cu–In system at 670 K. 1 – $\text{YbCu}_{5,1}\text{In}_{6,9}$; 2 – $\text{YbCu}_{4,8-4,0}\text{In}_{0,2-1,0}$; 3 – $\text{Yb}_2\text{Cu}_2\text{In}$; 4 – $\sim\text{Yb}_3\text{CuIn}_2$, 5 – $\sim\text{Yb}_4\text{CuIn}$.

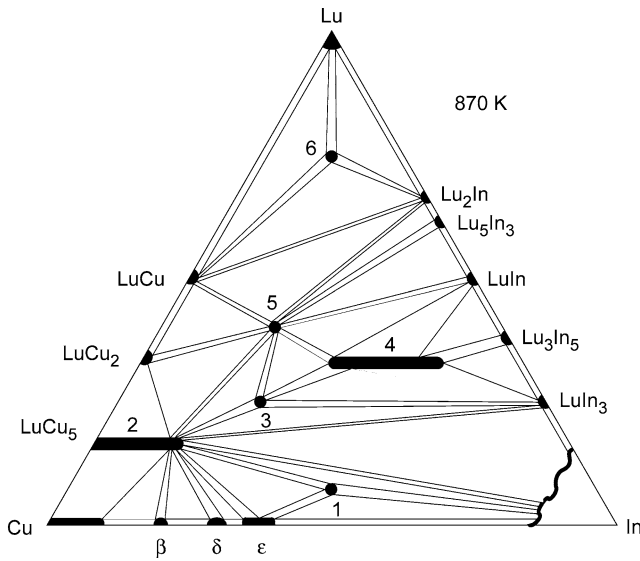


Fig. 19. Isothermal section of the phase diagram in the Lu–Cu–In system at 870 K. 1 – $\text{LuCu}_{5,1}\text{In}_{6,9}$; 2 – $\text{LuCu}_{5,4}\text{In}_{0-1}$; 3 – LuCu_2In ; 4 – $\text{LuCu}_{1,0-0,41}\text{In}_{1,0-1,59}$; 5 – $\text{Lu}_2\text{Cu}_2\text{In}$; 6 – $\sim\text{Lu}_6\text{CuIn}$.

The Dy–Cu–In system (fig. 14) is very similar to the system with terbium (fig. 13) (Kalychak et al., 1989b), except for the difference in the limits of the homogeneity range of $\text{DyCu}_{0,65-0,32}\text{In}_{1,35-1,68}$.

In the Ho–Cu–In system (fig. 15) five ternary indides have been found (Kalychak and Bakar, 1994) and their crystal structures have been established. HoCu₅ dissolves up to 16.7 atomic percent indium, while the homogeneity range for HoCu_{0.41–0.29}In_{1.59–1.71} is smaller.

Six ternary indides have been found in the Er–Cu–In system, whose phase diagram is shown in fig. 16 (Kalychak and Bakar, 1994). The crystal structures have been established for all compounds. Binary ErCu₅ dissolves up to 16.7 atomic percent indium and homogeneity regions are present in ErCu_{1.0–0.64}In_{1.0–1.36} and ErCu_{0.44–0.35}In_{1.56–1.65}.

Seven ternary compounds form in the Tm–Cu–In system (fig. 17; Kalychak and Bakar, 1996). A solid solution based on TmCu₅ extends up to 16.7 atomic percent indium into the ternary system. The crystal structures of all Tm–Cu–In indides have been determined. TmCu_{1.0–0.56}In_{1.0–1.44} with ZrNiAl type structure has an extended homogeneity range. TmCu_{0.4–0.3}In_{1.6–1.7} with AlB₂ structure, however, has a limited homogeneity range. The crystal structure of \sim Tm₆CuIn is unknown.

In the Yb–Cu–In system (fig. 18; Kalychak, 1998a), the crystal structures of YbCu_{4.8–4.0}In_{0.2–1.0}, YbCu_{5.1}In_{6.9}, and Yb₂Cu₂In (Giovannini et al., 2001; Tsujii et al., 2001) have been investigated. The crystal structures of two other compounds are still unknown.

In the Lu–Cu–In system (fig. 19), five ternary compounds (Kalychak and Bakar, 1996) exist with known crystal structures. LuCu₅ dissolves up to 16.7 at. percent indium and LuCu_{1.0–0.41}In_{1.0–1.59} has an extended homogeneity range. The crystal structure of \sim Lu₆CuIn is not known.

3.1.6. The R–Zn–In systems

In the R–Zn–In systems only the compounds of equiatomic composition have been investigated and they crystallize in the CaIn₂ or CeCu₂ (KHg₂) type. Their crystallographic data are listed in table 4.

Table 4
Crystallographic data of ternary R–Zn–In compounds

Compound	Str. type	S.G.	<i>a</i> (pm)	<i>b</i> (pm)	<i>c</i> (pm)	Ref.
LaZnIn	CaIn ₂	<i>P</i> 6 ₃ / <i>mmc</i>	479.6(3)		776.8(5)	1
CeZnIn	CaIn ₂	<i>P</i> 6 ₃ / <i>mmc</i>	478.7(3)		763.1(5)	1
PrZnIn	CaIn ₂	<i>P</i> 6 ₃ / <i>mmc</i>	478.6(3)		753.7(5)	1
NdZnIn	CaIn ₂	<i>P</i> 6 ₃ / <i>mmc</i>	471.9(3)		753.1(5)	1
SmZnIn	CaIn ₂	<i>P</i> 6 ₃ / <i>mmc</i>	469.7(3)		741.4(5)	1
EuZnIn	KHg ₂	<i>Imma</i>	482.3(1)	780.7(2)	827.6(2)	2
GdZnIn	CaIn ₂	<i>P</i> 6 ₃ / <i>mmc</i>	467.6(3)		733.5(5)	1
DyZnIn	CaIn ₂	<i>P</i> 6 ₃ / <i>mmc</i>	464.9(3)		723.9(5)	1
HoZnIn	CaIn ₂	<i>P</i> 6 ₃ / <i>mmc</i>	463.6(3)		721.4(5)	1
ErZnIn	CaIn ₂	<i>P</i> 6 ₃ / <i>mmc</i>	461.6(3)		718.4(5)	1
YbZnIn	CaIn ₂	<i>P</i> 6 ₃ / <i>mmc</i>	472.5(3)		738.2(5)	1
YbZnIn	KHg ₂	<i>Imma</i>	473.4	737.0	819.1	3

References

- Mazzone et al. (1982)
- Pöttgen (1996a)
- Dhar et al. (1995)

3.2. *R–4d-metal–In systems*

The isothermal sections of the phase diagrams of the *R–4d-metal–In* systems have not been studied prior to our own experimental investigations. Only the ternary compounds with equiatomic compositions in the *R–{Rh, Pd, Ag, Cd}–In* systems were known in the literature. The systems with zirconium, niobium, molybdenum, and technetium as *4d*-element component have not been studied to date. The *Pm–4d-metal–In* systems have not been investigated at all.

3.2.1. *The R–Ru–In systems*

The phase diagrams of the *R–Ru–In* systems have not been studied at the present time. According to Kurenbaeva et al. (2002), only CeRuIn_2 with MgCuAl_2 type structure, SG *Cmcm*, $a = 453.58(17)$, $b = 1000.27(23)$, $c = 767.73(12)$ pm is known.

3.2.2. *The R–Rh–In systems*

Several compounds with equiatomic and other simple stoichiometries have been studied. The isothermal sections of the phase diagrams for these ternary systems have not been investigated. The crystallographic data for the known compounds are listed in table 5. The structurally most peculiar compound in the *La–Rh–In* system is $\text{La}_{1.18}\text{Rh}_3\text{In}_2$ (Esmailzadeh et al., 2002), which crystallizes with an incommensurate structure.

Table 5
Crystallographic data of ternary *R–Rh–In* compounds

Compound	Str. type	S.G.	<i>a</i> (pm)	<i>b</i> (pm)	<i>c</i> (pm)	Ref.
YRhIn ₅	HoCoGa ₅	<i>P4/mmm</i>	459.6(2)		743.5(4)	1
YRhIn	Fe ₂ P	<i>P62m</i>	748		388	2
			747.7(1)		388.9(1)	3
LaRhIn ₅	HoCoGa ₅	<i>P4/mmm</i>	467.5(1)		759.6(4)	1
			467.68(3)		759.88(12)	4
La ₂ RhIn ₈	Ho ₂ CoGa ₈	<i>P4/mmm</i>	469.9(4)		1233.6(7)	5
			469.80(2)		1234.40(4)	6
LaRhIn ₂	MgCuAl ₂	<i>Cmcm</i>	448.2(1)	1025.7(1)	795.1(1)	7
LaRhIn	Fe ₂ P	<i>P62m</i>	761.8		412.3	2
			761.0		412.9	8
La ₂ Rh ₂ In	Mo ₂ FeB ₂	<i>P4/mbm</i>	763.62(8)		399.70(8)	9
			781.0(9)		394.3(1)	10
CeRhIn ₅	HoCoGa ₅	<i>P4/mmm</i>	464.9(1)		754.0(3)	1
			465.2		754.2	11
			465.6(2)		754.2(1)	12
Ce ₂ RhIn ₈	Ho ₂ CoGa ₈	<i>P4/mmm</i>	466.5(1)		1224.4(5)	13
			466.70(4)		1224.7(4)	6
CeRhIn ₂	MgCuAl ₂	<i>Cmcm</i>	446.0(1)	1017.3(2)	792.7(1)	5
CeRhIn	Fe ₂ P	<i>P62m</i>	755.5		405.5	14
			754.7		405.0	8
Ce ₂ Rh ₂ In	Mo ₂ FeB ₂	<i>P4/mbm</i>	758.74(3)		377.09(3)	9
			758.84(2)		377.09(1)	10
PrRhIn ₅	HoCoGa ₅	<i>P4/mmm</i>	464.2(1)		753.1(3)	1
PrRhIn ₂	MgCuAl ₂	<i>Cmcm</i>	444.03(1)	1013.1(1)	792.5(1)	4

continued on next page

Table 5, continued

Compound	Str. type	S.G.	<i>a</i> (pm)	<i>b</i> (pm)	<i>c</i> (pm)	Ref.
PrRhIn	ZrNiAl	<i>P62m</i>	755.6(2)		404.8(1)	15
Pr ₂ Rh ₂ In	Mo ₂ FeB ₂	<i>P4/mbm</i>	753.44		393.83	9
NdRhIn ₅	HoCoGa ₅	<i>P4/mmm</i>	463.6(2)		751.0(4)	1
			463.0(3)		750.2(6)	16
Nd ₂ RhIn ₈	Ho ₂ CoGa ₈	<i>P4/mmm</i>	464.0(3)		1217.1(6)	16
NdRhIn ₂	MgCuAl ₂	<i>Cmcm</i>	442.49(5)	1012.7(1)	789.3(1)	7
NdRhIn	Fe ₂ P	<i>P62m</i>	753.4		402.8	2
Nd ₂ Rh ₂ In	Mo ₂ FeB ₂	<i>P4/mbm</i>	751.47(3)		391.17(3)	9
SmRhIn ₅	HoCoGa ₅	<i>P4/mmm</i>	461.9(1)		745.8(1)	1
			461.8(4)		747.0(8)	5
Sm ₂ RhIn ₈	Ho ₂ CoGa ₈	<i>P4/mmm</i>	462.1(4)		1210.6(9)	5
SmRhIn ₂	MgCuAl ₂	<i>Cmcm</i>	438.1(1)	1009.3(1)	788.3(1)	7
SmRhIn	ZrNiAl	<i>P62m</i>	750.93(8)		397.52(4)	3
Sm ₂ Rh ₂ In	Mo ₂ FeB ₂	<i>P4/mbm</i>	745.89(5)		388.49(6)	9
EuRh ₂ In ₈	CaCo ₂ Al ₈	<i>Pbam</i>	1611.8(2)	1381.7(2)	436.44(6)	17
EuRhIn ₂	MgCuAl ₂	<i>Cmcm</i>	432.2(1)	1058.8(1)	805.5(2)	17
EuRhIn	TiNiSi	<i>Pnma</i>	744.4(1)	434.15(9)	845.5	14
GdRhIn ₅	HoCoGa ₅	<i>P4/mmm</i>	460.1(1)		744.5(3)	1
			460.9(4)		744.5(3)	5
Gd ₂ RhIn ₈	Ho ₂ CoGa ₈	<i>P4/mmm</i>	460.4(4)		1206.0(9)	5
GdRhIn ₂	MgCuAl ₂	<i>Cmcm</i>	435.0(1)	1013.3(3)	783.6(2)	19
GdRhIn	Fe ₂ P	<i>P62m</i>	749.8		393.6	2
TbRhIn ₅	HoCoGa ₅	<i>P4/mmm</i>	459.2(2)		742.6(4)	1
TbRhIn	ZrNiAl	<i>P62m</i>	748.0(2)		390.4(1)	3
DyRhIn ₅	HoCoGa ₅	<i>P4/mmm</i>	458.5(2)		741.4(3)	1
DyRhIn	Fe ₂ P	<i>P62m</i>	747.0		388.1	2
HoRhIn ₅	HoCoGa ₅	<i>P4/mmm</i>	458.3(2)		739.9(3)	1
HoRhIn	ZrNiAl	<i>P62m</i>	747.21(6)		385.72(3)	3
ErRhIn ₅	HoCoGa ₅	<i>P4/mmm</i>	457.6(2)		739.6(4)	1
ErRhIn	Fe ₂ P	<i>P62m</i>	746.1		383.7	2
			746.5(1)		384.01(9)	3
TmRhIn ₅	HoCoGa ₅	<i>P4/mmm</i>	457.4(1)		737.6(2)	1
YbRhIn ₅	HoCoGa ₅	<i>P4/mmm</i>	460.5(1)		745.7(3)	1
			459.52(6)		744.2(2)	20
YbRhIn ₄	LaCoAl ₄	<i>Pmma</i>	863.7(2)	422.5(1)	743.1(1)	19
YbRhIn	TiNiSi	<i>Pnma</i>	694.0(2)	413.5(1)	849.1(3)	3
LuRhIn	TiNiSi	<i>Pnma</i>	690.3(1)	413.12(8)	848.2(2)	3

References

- | | | |
|----------------------------|--------------------------------|--------------------------------|
| 1. Zaremba et al. (2000b) | 7. Zaremba et al. (2002a) | 14. Rossi et al. (1983) |
| 2. Ferro et al. (1974b) | 8. Adroja et al. (1989) | 15. Zaremba et al. (2000c) |
| 3. Lukachuk et al. (2003) | 9. Hulliger (1995b) | 16. Pagliuso et al. (2000) |
| 4. Macaluso et al. (2002) | 10. Kaczorowski et al. (1996a) | 17. Pöttgen and Kußmann (2001) |
| 5. Pagliuso et al. (2001a) | 11. Hegger et al. (2000) | 18. Pöttgen et al. (1999c) |
| 6. Macaluso et al. (2003) | 12. Moshopoulou et al. (2001) | 19. Hoffmann et al. (2000) |
| | 13. Thompson et al. (2001) | 20. Zaremba et al. (2003a) |

3.2.3. The R–Pd–In systems

Giovannini et al. (2003) have built the isothermal section of the Ce–Pd–In phase diagram at 1023 K (fig. 20). Besides the known ternary intermetallics CePdIn (Fe₂P type), CePdIn₂ (MgCuAl₂

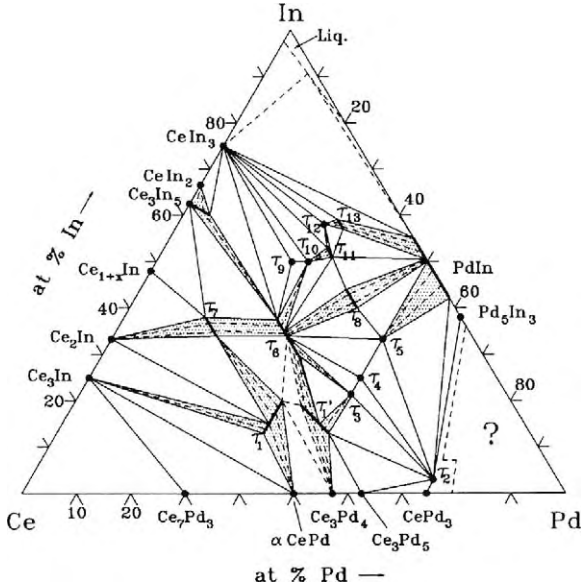


Fig. 20. Isothermal section of the phase diagram in the Ce–Pd–In system at 1023 K. τ_1 – left branch $\text{Ce}_{2+x}\text{Pd}_{1.85}\text{In}_{1-x}$; τ'_1 – right branch $\text{Ce}_{1.95}\text{Pd}_{2+x}\text{In}_{1-x}$; τ_2 – $\text{Ce}_8\text{Pd}_{24}\text{In}$; τ_3 – $\text{Ce}_4\text{Pd}_7\text{In}_3$; τ_4 – CePd_2In ; τ_5 – CePd_3In_2 ; τ_6 – CePdIn ; τ_7 – $\sim\text{Ce}_{47}\text{Pd}_{17}\text{In}_{36}$; τ_8 – CePd_2In_2 ; τ_9 – CePdIn_2 ; τ_{10} – $\sim\text{Ce}_{22}\text{Pd}_{28}\text{In}_{50}$; τ_{11} – $\sim\text{CePd}_2\text{In}_3$; τ_{12} – $\sim\text{Ce}_{15}\text{Pd}_{27}\text{In}_{58}$; τ_{13} – $\sim\text{Ce}_{12}\text{Pd}_{30}\text{In}_{58}$. Taken from Giovannini et al. (2003).

type), CePd_2In (GdPt_2Sn type), $\text{Ce}_8\text{Pd}_{24}\text{In}$ ($\text{Ce}_8\text{Pd}_{24}\text{Sb}$ type) and double-branched solid solutions $\text{Ce}_{1.95}\text{Pd}_{2+x}\text{In}_{1-x}$ and $\text{Ce}_{2+x}\text{Pd}_{1.85}\text{In}_{1-x}$, eight novel ternary compounds were revealed in the system. The isothermal sections of the phase diagrams of the other ternary systems have not been investigated, however, many ternary intermetallics have been discovered. The lattice parameters of these compounds are listed in table 6.

3.2.4. The R–Ag–In systems

Only the quasi-binary sections between the isostructural compounds RAg and RIn with CsCl type structure have been investigated. According to Ihrig et al. (1973), a continuous solid solution between the isostructural compounds LaAg and LaIn (CsCl type) occurs in the system La–Ag–In . Within the solid solution, a cubic-to-tetragonal distortion at low temperatures is observed. The transition temperature is a function of the composition and is the highest at 180 K for $\text{LaAg}_{0.5}\text{In}_{0.5}$. The structural deformation has been confirmed by Maetz et al. (1980). According to Ihrig and Methfessel (1976) the solid solution between CeAg and CeIn also shows a tetragonal distortion at low temperatures ($T \leq 40$ K). The structures and physical properties of the alloys within the solid solutions between RAg and RIn were studied by various authors (Sekizawa and Yasukōchi, 1964; Buschow et al., 1972). Data for $R = \text{Gd}$ (Yagasaki et al., 1978b, 1980), $R = \text{Tb}$ and Dy (Lal and Methfessel, 1981), and for $R = \text{Ho}$, Er , and Tm , show that above 8 K they have the cubic CsCl structure. According to Lal (1982), a tetragonal deformation occurs below 8 K for $\text{GdAg}_{0.5}\text{In}_{0.5}$. The crystallographic data of the other known compounds are given in table 7.

Table 6
Crystallographic data of the ternary R–Pd–In compounds

Compound	Str. type	S.G.	<i>a</i> (pm)	<i>b</i> (pm)	<i>c</i> (pm)	Ref.
ScPd ₂ In	MnCu ₂ Al	<i>Fm</i> $\bar{3}m$	672.3(2)			1
Sc ₂ Pd ₂ In	U ₂ Pt ₂ Sn	<i>P4</i> ₂ / <i>mmm</i>	749.8(2)		677.3(2)	2
Sc _{1-x} PdIn _x (<i>x</i> = 0–0.1)	CsCl	<i>Pm</i> $\bar{3}m$	328.2–324.6			3
YPd ₂ In	MnCu ₂ Al	<i>Fm</i> $\bar{3}m$	672.3			4
YPdIn	Fe ₂ P	<i>P</i> $\bar{6}2m$	764.9		381.9	5
Y ₂ Pd ₂ In	Mo ₂ FeB ₂	<i>P4/mbm</i>	767.23(3)		368.88(2)	6
La ₄ Pd ₁₀ In ₂₁	Ho ₄ Ni ₁₀ Ga ₂₁	<i>C2/m</i>	2314.3(2)	454.70(7)	1940.8(2)	7
				$\beta = 133.4(1)^\circ$		
La ₈ Pd ₂₄ In	Ce ₈ Pd ₂₄ Sb	<i>Pm</i> $\bar{3}m$	849.40			8
LaPdIn ₂	MgCuAl ₂	<i>Cmcm</i>	463.79(7)	1074.3(2)	746.4(2)	9
LaPd ₂ In	GdPt ₂ Sn	<i>P6</i> ₃ / <i>mmc</i>	464.45(7)		935.4(2)	10
LaPdIn	Fe ₂ P	<i>P</i> $\bar{6}2m$	772.9		413.3	5
La ₂ Pd ₂ In	Mo ₂ FeB ₂	<i>P4/mbm</i>	785.95(4)		397.48(3)	6
			786.9(1)		396.3(1)	11
Ce ₄ Pd ₁₀ In ₂₁	Ho ₄ Ni ₁₀ Ga ₂₁	<i>C2/m</i>	2308.2(1)	452.52(7)	1944.84(9)	7
				$\beta = 133.4(1)^\circ$		
Ce ₈ Pd ₂₄ In	Ce ₈ Pd ₂₄ Sb	<i>Pm</i> $\bar{3}m$	844.57			8
CePdIn ₂	MgCuAl ₂	<i>Cmcm</i>	462.10	1069.4	745.5	12
CePd ₂ In	GdPt ₂ Sn	<i>P6</i> ₃ / <i>mmc</i>	462.72(5)		919.75(5)	13
CePdIn	Fe ₂ P	<i>P</i> $\bar{6}2m$	769.8		407.9	5
Ce ₂ Pd ₂ In	Mo ₂ FeB ₂	<i>P4/mbm</i>	779.72(3)		392.37(3)	6
			781.3(4)		391.6(2)	11
Pr ₄ Pd ₁₀ In ₂₁	Ho ₄ Ni ₁₀ Ga ₂₁	<i>C2/m</i>	2303.8(1)	450.78(4)	1940.6(9)	7
				$\beta = 133.4(1)^\circ$		
PrPdIn ₂	HfNiGa ₂	<i>I4mm</i>	1397.7(1)		925.5(1)	9
PrPdIn	ZrNiAl	<i>P</i> $\bar{6}2m$	767.9		404.3	5
Pr ₂ Pd ₂ In	Mo ₂ FeB ₂	<i>P4/mbm</i>	777.54(5)		388.77(5)	6
			778.04(2)		388.15(1)	14
Nd ₄ Pd ₁₀ In ₂₁	Ho ₄ Ni ₁₀ Ga ₂₁	<i>C2/m</i>	2300.2(2)	449.8(6)	1937.8(2)	7
				$\beta = 133.3(1)^\circ$		
NdPdIn ₂	HfNiGa ₂	<i>I4mm</i>	1391.9(1)		922.42(9)	9
NdPdIn	ZrNiAl	<i>P</i> $\bar{6}2m$	768.3		399.7	5
Nd ₂ Pd ₂ In	Mo ₂ FeB ₂	<i>P4/mbm</i>	775.27(5)		385.84(5)	6
			774.92(2)		386.78(2)	14
Sm ₄ Pd ₁₀ In ₂₁	Ho ₄ Ni ₁₀ Ga ₂₁	<i>C2/m</i>	2295.6(2)	447.07(4)	1935.7(1)	7
				$\beta = 133.4(3)^\circ$		
SmPdIn ₂	HfNiGa ₂	<i>I4mm</i>	1383.8(1)		918.6(1)	9
SmPdIn	Fe ₂ P	<i>P</i> $\bar{6}2m$	765.6		393.4	5
Sm ₂ Pd ₂ In	Mo ₂ FeB ₂	<i>P4/mbm</i>	770.98(4)		380.44(3)	6
			770.09(5)		380.85(3)	14
EuPdIn ₄	YNiAl ₄	<i>Cmcm</i>	454.8(2)	1703.2(8)	738.0(3)	15
EuPdIn ₂	MgCuAl ₂	<i>Cmcm</i>	453.6(1)	1054.3(3)	785.3(2)	16
EuPdIn	Fe ₂ P	<i>P</i> $\bar{6}2m$	830.9		395.7	5
	TiNiSi	<i>Pnma</i>	747.4	446.4	852.9	17
			748.30(13)	447.20(8)	853.50(14)	18
Gd ₄ Pd ₁₀ In ₂₁	Ho ₄ Ni ₁₀ Ga ₂₁	<i>C2/m</i>	2293.3(2)	444.49(3)	1717.5(1)	7
				$\beta = 124.55(1)^\circ$		

continued on next page

Table 6, *continued*

Compound	Str. type	S.G.	<i>a</i> (pm)	<i>b</i> (pm)	<i>c</i> (pm)	Ref.
GdPdIn ₂	HfNiGa ₂	<i>I4mm</i>	1376.5(1)		915.6(1)	9
GdPd ₂ In	MnCu ₂ Al	<i>Fm3m</i>	675.6(2)			1
GdPdIn	Fe ₂ P	<i>P62m</i>	764.9		388.6	5
			764.7		388.6	19
Gd ₂ Pd ₂ In	Mo ₂ FeB ₂	<i>P4/mbm</i>	768.60(7)		375.52(6)	6
			768.29(3)		376.17(2)	14
TbPdIn ₂	HfNiGa ₂	<i>I4mm</i>	1368.5(1)		912.8(1)	9
TbPdIn	ZrNiAl	<i>P62m</i>	764.7		384.3	5
			764.16		384.34	20
Tb ₂ Pd ₂ In	Mo ₂ FeB ₂	<i>P4/mbm</i>	765.95(5)		372.43(4)	6
			766.36(2)		372.39(1)	14
DyPdIn ₂	HfNiGa ₂	<i>I4mm</i>	1368.63(7)		912.09(4)	9
DyPd ₂ In	MnCu ₂ Al	<i>Fm3m</i>	672.0(2)			1
DyPdIn	ZrNiAl	<i>P62m</i>	763.8		381.9	5
Dy ₂ Pd ₂ In	Mo ₂ FeB ₂	<i>P4/mbm</i>	764.38(4)		369.60(3)	6
			765.32(4)		369.37(2)	14
HoPdIn ₂	HfNiGa ₂	<i>I4mm</i>	1365.55(6)		911.00(8)	9
HoPdIn	ZrNiAl	<i>P62m</i>	762.9		378.8	5
Ho ₂ Pd ₂ In	Mo ₂ FeB ₂	<i>P4/mbm</i>	764.50(4)		366.55(4)	6
			764.04(3)		367.13(2)	14
ErPdIn ₂	HfNiGa ₂	<i>I4mm</i>	1362.09(8)		909.98(9)	9
ErPd ₂ In	MnCu ₂ Al	<i>Fm3m</i>	668.0(2)			1
ErPdIn	Fe ₂ P	<i>P62m</i>	763.2		375.4	5
	ZrNiAl	<i>P62m</i>	763.1		375.5	17
Er ₂ Pd ₂ In	Mo ₂ FeB ₂	<i>P4/mbm</i>	762.43(4)		364.47(4)	6
			763.29(2)		364.46(1)	14
TmPdIn ₂	HfNiGa ₂	<i>I4mm</i>	1356.80		908.37	9
TmPd ₂ In	MnCu ₂ Al	<i>Fm3m</i>	666.9(2)			1
TmPdIn	Fe ₂ P	<i>P62m</i>	762.8		372.6	5
Tm ₂ Pd ₂ In	Mo ₂ FeB ₂	<i>P4/mbm</i>	761.62(5)		361.97(5)	6
			762.25(2)		362.41(1)	14
Yb ₂ Pd ₆ In ₁₃	Yb ₂ Pd ₆ In ₁₃	<i>C2/m</i>	1677.0(1)	438.17(4)	1339.7(1)	21
				$\beta = 118.5(1)^\circ$		
YbPdIn ₄	YNiAl ₄	<i>Cmcm</i>	445.8(2)	1666.0(3)	747.3(2)	15
YbPdIn ₂	MgCuAl ₂	<i>Cmcm</i>	444.3(1)	1031.2(2)	779.9(2)	16
YbPdIn	Fe ₂ P	<i>P62m</i>	757.4		393.2	5
	ZrNiAl	<i>P62m</i>	757.3		393.3	17
Yb ₂ Pd ₂ In	Mo ₂ FeB ₂	<i>P4/mbm</i>	759.78(3)		364.05(2)	14, 22
LuPdIn ₂	HfNiGa ₂	<i>I4mm</i>	1353.66(9)		906.9(1)	9
LuPd ₂ In	MnCu ₂ Al	<i>Fm3m</i>	662.3(2)			1
LuPdIn	Fe ₂ P	<i>P62m</i>	762.9		368.4	5
Lu ₂ Pd ₂ In	Mo ₂ FeB ₂	<i>P4/mbm</i>	760.32(5)		358.34(5)	6
			760.46(4)		358.5(2)	14

References

- | | | |
|------------------------------|--------------------------------|------------------------------|
| 1. Dwight and Kimball (1987) | 8. Gordon and DiSalvo (1996) | 16. Galadzhun et al. (1999a) |
| 2. Hulliger (1996) | 9. Zaremba et al. (2004) | 17. Cirafici et al. (1985) |
| 3. Savitskiy et al. (1980) | 10. Xue et al. (1992) | 18. Pöttgen (1996b) |
| 4. Jorda et al. (1983) | 11. Kaczorowski et al. (1996b) | 19. Buschow (1975) |
| 5. Ferro et al. (1974a) | 12. Ijiri et al. (1996) | 20. Daniš et al. (2002) |
| 6. Hulliger and Xue (1994) | 13. Xue et al. (1993) | 21. Zaremba et al. (2002c) |
| 7. Zaremba et al. (2002a) | 14. Giovannini et al. (1998) | 22. Giovannini et al. (2001) |
| | 15. Hoffmann et al. (2000) | |

Table 7
Crystallographic data of ternary R–Ag–In compounds

Compound	Str. type	S.G.	<i>a</i> (pm)	<i>c</i> (pm)	Ref.
ScAg ₂ In	MnCu ₂ Al	<i>Fm</i> $\bar{3}m$	672.0		1
YAg _{3.5} In _{2.5}	YbAg ₂ In ₄	<i>Im</i> $\bar{3}$	1516.7		2
YAg ₂ In	MnCu ₂ Al	<i>Fm</i> $\bar{3}m$	691.4(15)		3
Y ₂ AgIn ₃	CaIn ₂	<i>P6</i> ₃ / <i>mmc</i>	474.9(2)	733.0(2)	4
LaAg _{5.4} In _{6.6}	ThMn ₁₂	<i>I4/mmm</i>	967.6(4)	574.5(3)	5
LaAg ₂ In	MnCu ₂ Al	<i>Fm</i> $\bar{3}m$	715.6(15)		3
La ₂ AgIn ₃	CaIn ₂	<i>P6</i> ₃ / <i>mmc</i>	491.5(1)	771.6(5)	4
La ₂ AgIn	CsCl	<i>Pm</i> $\bar{3}m$	387.5		6
La ₄ Ag ₃ In	La ₄ Ag ₃ In	<i>I4/mmm</i>	752 ^a	781 ^a	7
			755 ^b	779 ^b	7
CeAg _{5.4} In _{6.6}	ThMn ₁₂	<i>I4/mmm</i>	962.9(3)	569.9(5)	5
CeAg ₂ In	MnCu ₂ Al	<i>Fm</i> $\bar{3}m$	710.8(15)		3
Ce ₂ AgIn ₃	CaIn ₂	<i>P6</i> ₃ / <i>mmc</i>	490.1(2)	759.2(6)	4
Ce ₂ AgIn ^c	CsCl	<i>Pm</i> $\bar{3}m$	383.3		8
Ce ₂ AgIn ^d	δ -CuTi	<i>P4/mmm</i>	373.2	3.944	8
PrAg _{5.4} In _{6.6}	ThMn ₁₂	<i>I4/mmm</i>	966.9(3)	570.8(3)	5
PrAg ₂ In	MnCu ₂ Al	<i>Fm</i> $\bar{3}m$	707.5(15)		3
Pr ₂ AgIn ₃	CaIn ₂	<i>P6</i> ₃ / <i>mmc</i>	486.0(3)	754.8(5)	4
PrAg _{1-x} In _x (<i>x</i> = 0–0.7)	CsCl	<i>Pm</i> $\bar{3}m$	372.3–383.8		2
NdAg _{5.4} In _{6.6}	ThMn ₁₂	<i>I4/mmm</i>	965.0(2)	572.2(2)	5
NdAg ₂ In	MnCu ₂ Al	<i>Fm</i> $\bar{3}m$	704.4(15)		3
Nd ₂ AgIn ₃	CaIn ₂	<i>P6</i> ₃ / <i>mmc</i>	483.9(2)	750.1(3)	4
SmAg _{5.4} In _{6.6}	ThMn ₁₂	<i>I4/mmm</i>	963.4(5)	571.4(5)	5
SmAg _{3.5} In _{2.5}	YbAg ₂ In ₄	<i>Im</i> $\bar{3}$	1526.1		9
SmAg ₂ In	MnCu ₂ Al	<i>Fm</i> $\bar{3}m$	700.1(15)		3
Sm ₂ AgIn ₃	CaIn ₂	<i>P6</i> ₃ / <i>mmc</i>	481.3(3)	737.1(5)	4
EuAg _{5.4} In _{6.6}	ThMn ₁₂	<i>I4/mmm</i>	976.0(7)	571.0(4)	5
EuAg ₄ In ₈	EuAg ₄ In ₈	<i>P6/mmm</i>	992.5(6)	972.7(5)	10
EuAg _{0.5} In _{0.5}	CsCl	<i>Pm</i> $\bar{3}m$	390.4(3)		11
GdAg _{3.5} In _{2.5}	YbAg ₂ In ₄	<i>Im</i> $\bar{3}$	1521.7		2
GdAg ₂ In	MnCu ₂ Al	<i>Fm</i> $\bar{3}m$	696.5(15)		3
Gd ₂ AgIn ₃	CaIn ₂	<i>P6</i> ₃ / <i>mmc</i>	480.2(3)	732.3(4)	4
GdAg _{1-x} In _x (<i>x</i> = 0–0.5)	CsCl	<i>Pm</i> $\bar{3}m$	366.0–371.8		12
GdAg _{1-x} In _x (<i>x</i> = 0.6–1)	δ -CuTi	<i>P4/mmm</i>	374.2–383.0	371.1–364.0	12
TbAg _{3.5} In _{2.5}	YbAg ₂ In ₄	<i>Im</i> $\bar{3}$	1516.2		2
TbAg ₂ In	MnCu ₂ Al	<i>Fm</i> $\bar{3}m$	693.4(15)		3, 13
Tb ₂ AgIn ₃	CaIn ₂	<i>P6</i> ₃ / <i>mmc</i>	477.6(3)	730.9(5)	4
			479.3(2)	732.2(3)	14
TbAg _{1-x} In _x (<i>x</i> = 0–0.6)	CsCl	<i>Pm</i> $\bar{3}m$	361–369		15
Tb ₂ AgIn	CsCl	<i>Pm</i> $\bar{3}m$	370.2		16
DyAg _{3.5} In _{2.5}	YbAg ₂ In ₄	<i>Im</i> $\bar{3}$	1514.7		2
DyAg ₂ In	MnCu ₂ Al	<i>Fm</i> $\bar{3}m$	691.0(15)		3, 13

continued on next page

Table 7, *continued*

Compound	Str. type	S.G.	<i>a</i> (pm)	<i>c</i> (pm)	Ref.
Dy ₂ AgIn ₃	CaIn ₂	<i>P6₃/mmc</i>	475.6(4)	729.1(54)	2
Dy ₂ AgIn	CsCl	<i>Pm$\bar{3}m$</i>	368.5		16
HoAg _{3.5} In _{2.5}	YbAg ₂ In ₄	<i>Im$\bar{3}$</i>	1511.4		5
HoAg ₂ In	MnCu ₂ Al	<i>Fm$\bar{3}m$</i>	689.3(15)		3
Ho ₂ AgIn ₃	CaIn ₂	<i>P6₃/mmc</i>	475.3(2)	726.7(3)	4
Ho ₂ AgIn	CsCl	<i>Pm$\bar{3}m$</i>	366.6		16
ErAg _{3.5} In _{2.5}	YbAg ₂ In ₄	<i>Im$\bar{3}$</i>	1511.3		2
ErAg ₂ In	MnCu ₂ Al	<i>Fm$\bar{3}m$</i>	688.2(15)		3
Er ₂ AgIn ₃	CaIn ₂	<i>P6₃/mmc</i>	474.6(1)	721.8(3)	4
Er ₂ AgIn	CsCl	<i>Pm$\bar{3}m$</i>	365.1		16
TmAg _{3.5} In _{2.5}	YbAg ₂ In ₄	<i>Im$\bar{3}$</i>	1509.5		2
TmAg ₂ In	MnCu ₂ Al	<i>Fm$\bar{3}m$</i>	686.7(15)		3
Tm ₂ AgIn ₃	CaIn ₂	<i>P6₃/mmc</i>	473.1(2)	719.5(2)	4
Tm ₂ AgIn	CsCl	<i>Pm$\bar{3}m$</i>	362.9		16
YbAg _{5.4} In _{6.6}	ThMn ₁₂	<i>I4/mmm</i>	973.4(4)	570.9(3)	5
YbAg ₂ In ₄	YbAg ₂ In ₄	<i>Im$\bar{3}$</i>	1536.2(3)		17
LuAg _{3.5} In _{2.5}	YbAg ₂ In ₄	<i>Im$\bar{3}$</i>	1507.2		2
Lu ₂ AgIn ₃	CaIn ₂	<i>P6₃/mmc</i>	472.0(4)	720.7(5)	4

^aLattice parameters at 20 K.

^bLattice parameters at 100 K.

^cRT modification, CeAg_{*x*}In_{1-*x*}, *x* = 0.3–1, *a* = 386.0–378.0 pm at 300 K.

^dLT modification, CeAg_{*x*}In_{1-*x*}, *x* = 0.3–1, *a* = 374.1–377.1, *c* = 400.0–377.1 pm at 40 K.

References

- | | | |
|------------------------------|--------------------------------|-------------------------------|
| 1. Dwight and Kimball (1987) | 6. Ihrig et al. (1973) | 12. Lal (1982) |
| 2. Yagasaki et al. (1985) | 7. Maetz et al. (1980) | 13. André et al. (1992) |
| 3. Galera et al. (1984) | 8. Ihrig and Methfessel (1976) | 14. Semitelou et al. (1999) |
| 4. Sysa and Kalychak (1992) | 9. Galadzhun et al. (2000c) | 15. Cable et al. (1965) |
| 5. Sysa (1991) | 10. Sysa et al. (1994a) | 16. Lal and Methfessel (1981) |
| | 11. Sysa et al. (1994b) | 17. Sysa et al. (1998) |

3.2.5. The *R*–*Cd*–*In* systems

In the *R*–*Cd*–*In* systems, 10 ternary compounds with equiatomic composition have been found (Rossi et al., 1981). They crystallize with the hexagonal CaIn₂ type structure. The basic crystallographic data are listed in table 8.

3.3. *R*–*5d*–*metal*–*In* systems

No information has been found in the literature for phase equilibria and isothermal sections of ternary *R*–*5d*–*metal*–*In* systems. Only a few compounds with ideal compositions have been investigated. The systems with hafnium, tantalum, tungsten, rhenium, and osmium as *5d*-element have not been studied. The *Pm*–*5d*–*metal*–*In* systems have not been investigated at all.

Table 8
Crystallographic data of ternary R–Cd–In compounds according to Rossi et al. (1981)

Compound	Str. type	S.G.	<i>a</i> (pm)	<i>c</i> (pm)
LaCdIn	CaIn ₂	<i>P</i> 6 ₃ / <i>mmc</i>	493.6(3)	765.2(5)
CeCdIn	CaIn ₂	<i>P</i> 6 ₃ / <i>mmc</i>	494.3(3)	780.9(5)
PrCdIn	CaIn ₂	<i>P</i> 6 ₃ / <i>mmc</i>	490.7(3)	760.9(5)
NdCdIn	CaIn ₂	<i>P</i> 6 ₃ / <i>mmc</i>	488.9(3)	757.2(5)
SmCdIn	CaIn ₂	<i>P</i> 6 ₃ / <i>mmc</i>	486.6(3)	746.9(5)
GdCdIn	CaIn ₂	<i>P</i> 6 ₃ / <i>mmc</i>	484.5(3)	739.8(5)
DyCdIn	CaIn ₂	<i>P</i> 6 ₃ / <i>mmc</i>	481.9(3)	731.8(5)
HoCdIn	CaIn ₂	<i>P</i> 6 ₃ / <i>mmc</i>	480.5(3)	730.1(5)
ErCdIn	CaIn ₂	<i>P</i> 6 ₃ / <i>mmc</i>	479.6(3)	725.3(5)
YbCdIn	CaIn ₂	<i>P</i> 6 ₃ / <i>mmc</i>	494.8(3)	730.2(5)

Table 9
Crystallographic data of ternary R–Ir–In compounds

Compound	Str. type	S.G.	<i>a</i> (pm)	<i>c</i> (pm)	Ref.
LaIrIn ₅	HoCoGa ₅	<i>P</i> 4/ <i>mmm</i>	471.0(4)	762.5(6)	1
			468.97(6)	757.9(1)	2
La ₂ IrIn ₈	Ho ₂ CoGa ₈	<i>P</i> 4/ <i>mmm</i>	470.3(4)	1231.4(7)	1
			470.60(1)	1231.20(4)	3
CeIrIn ₅	HoCoGa ₅	<i>P</i> 4/ <i>mmm</i>	467.4(1)	750.1(5)	4
			466.8(1)	751.5(2)	5
Ce ₂ IrIn ₈	Ho ₂ CoGa ₈	<i>P</i> 4/ <i>mmm</i>	467.1(2)	1221.4(6)	5
			468.97(6)	1219.5(1)	3
NdIrIn ₅	HoCoGa ₅	<i>P</i> 4/ <i>mmm</i>	464.8(3)	747.7(6)	6
Nd ₂ IrIn ₈	Ho ₂ CoGa ₈	<i>P</i> 4/ <i>mmm</i>	464.7(3)	1213.9(6)	6
SmIrIn ₅	HoCoGa ₅	<i>P</i> 4/ <i>mmm</i>	463.4(3)	744.6(7)	1
Sm ₂ IrIn ₈	Ho ₂ CoGa ₈	<i>P</i> 4/ <i>mmm</i>	462.6(4)	1208.8(7)	1
GdIrIn ₅	HoCoGa ₅	<i>P</i> 4/ <i>mmm</i>	462.2(4)	741.3(8)	1
Gd ₂ IrIn ₈	Ho ₂ CoGa ₈	<i>P</i> 4/ <i>mmm</i>	461.5(4)	1203.4(7)	1

References

- Pagliuso et al. (2001a)
- Macaluso et al. (2002)
- Macaluso et al. (2003)
- Moshopoulou et al. (2001)
- Thompson et al. (2001)
- Pagliuso et al. (2000)

3.3.1. The R–Ir–In systems

So far, only some ternary intermetallics of compositions *R*IrIn₅ and *R*₂IrIn₈ are known. Their crystallographic data are listed in table 9.

3.3.2. The R–Pt–In systems

The ternary equiatomic *R*PtIn intermetallics are known for a long time. They have been originally investigated by Ferro et al. (1974b). Crystallographic data of all known ternary compounds are presented in table 10.

Table 10
Crystallographic data of ternary R–Pt–In compounds

Compound	Str. type	S.G.	<i>a</i> (pm)	<i>b</i> (pm)	<i>c</i> (pm)	Ref.
ScPt ₂ In	MgCu ₂ Al	<i>Fm</i> $\bar{3}m$	651.2			1
ScPtIn	ZrNiAl	<i>P</i> $\bar{6}2m$	754.6(1)		348.31(8)	2
YPt ₂ In	GdPt ₂ Sn	<i>P</i> 6 ₃ / <i>mmc</i>	453.9		891.9	3
YPtIn	Fe ₂ P	<i>P</i> $\bar{6}2m$	758.3		384.6	4
Y ₂ Pt ₂ In	Mo ₂ FeB ₂	<i>P</i> 4/ <i>mbm</i>	765.86(4)		367.68(4)	5
La ₃ Pt ₄ In ₁₃	Pr ₃ Rh ₄ Sn ₁₃	<i>Pm</i> $\bar{3}n$	981.2			6
LaPt ₄ In	MgCu ₄ Sn	<i>F</i> $\bar{4}3m$	764.8			7
LaPtIn ₄	YNiAl ₄	<i>Cmcm</i>	455.1(2)	1687.5(5)	738.3(2)	8
LaPt ₂ In ₂	CePt ₂ In ₂	<i>P</i> 2 ₁ / <i>m</i>	1024.3(3)	449.9(1)	1025.9(3)	9
				$\beta = 116.97(1)^\circ$		
LaPtIn ₃	LaRuSn ₃	<i>Pm</i> $\bar{3}n$	980.4(2)			8
LaPtIn	Fe ₂ P	<i>P</i> $\bar{6}2m$	769.5		412.5	4
La ₂ Pt ₂ In	Mo ₂ FeB ₂	<i>P</i> 4/ <i>mbm</i>	787.35(4)		394.33(4)	5
			788.1(1)		393.8(1)	10
Ce ₃ Pt ₄ In ₁₃	Pr ₃ Rh ₄ Sn ₁₃	<i>Pm</i> $\bar{3}n$	977.1			6
CePt ₄ In	MgCu ₄ Sn	<i>F</i> $\bar{4}3m$	760.2			7
CePt ₂ In ₂	CePt ₂ In ₂	<i>P</i> 2 ₁ / <i>m</i>	1018.9(6)	447.7(4)	1022.6(6)	9
				$\beta = 117.00(5)^\circ$		
CePtIn ₃	LaRuSn ₃	<i>Pm</i> $\bar{3}n$	977.0(2)			8
CePtIn	ZrNiAl	<i>P</i> $\bar{6}2m$	765.7		406.9	11
Ce ₂ Pt ₂ In	Mo ₂ FeB ₂	<i>P</i> 4/ <i>mbm</i>	780.38(3)		388.30(2)	5
			780.48(3)		388.08(2)	10
			779.8(1)		388.5(1)	8
Ce ₁₂ Pt ₇ In	Ce ₁₂ Pt ₇ In	<i>I</i> 4/ <i>mcm</i>	1210.2(1)		1454.2(2)	12
PrPt ₄ In	MgCu ₄ Sn	<i>F</i> $\bar{4}3m$	760.1			7
PrPt ₂ In ₂	CePt ₂ In ₂	<i>P</i> 2 ₁ / <i>m</i>	1015.2(4)	446.2(1)	1020.4(4)	9
				$\beta = 116.78(2)^\circ$		
PrPtIn ₃	LaRuSn ₃	<i>Pm</i> $\bar{3}n$	975.6(1)			8
PrPtIn	ZrNiAl	<i>P</i> $\bar{6}2m$	765.22		404.55	13
Pr ₂ Pt ₂ In	Mo ₂ FeB ₂	<i>P</i> 4/ <i>mbm</i>	777.6		386.95	5
Pr ₁₂ Pt ₇ In	Ce ₁₂ Pt ₇ In	<i>I</i> 4/ <i>mcm</i>	1197.6(1)		1447.8(2)	12
NdPt ₄ In	MgCu ₄ Sn	<i>F</i> $\bar{4}3m$	759.0			7, 14
NdPt ₂ In ₂	CePt ₂ In ₂	<i>P</i> 2 ₁ / <i>m</i>	1012.7(1)	444.6(1)	1019.3(1)	9
				$\beta = 116.71(1)^\circ$		
NdPtIn ₃	LaRuSn ₃	<i>Pm</i> $\bar{3}n$	973.1(1)			8
NdPtIn	Fe ₂ P	<i>P</i> $\bar{6}2m$	763.6		401.0	4
Nd ₂ Pt ₂ In	Mo ₂ FeB ₂	<i>P</i> 4/ <i>mbm</i>	776.39(3)		383.31(3)	5
Nd ₁₂ Pt ₇ In	Ce ₁₂ Pt ₇ In	<i>I</i> 4/ <i>mcm</i>	1190.1(1)		1447.1(2)	12
SmPt ₄ In	MgCu ₄ Sn	<i>F</i> $\bar{4}3m$	757.4			7
SmPtIn ₃	LaRuSn ₃	<i>Pm</i> $\bar{3}n$	970.9(1)			8
SmPtIn	ZrNiAl	<i>P</i> $\bar{6}2m$	758.95		395.40	13
Sm ₂ Pt ₂ In	Mo ₂ FeB ₂	<i>P</i> 4/ <i>mbm</i>	771.08(7)		378.96(5)	5
EuPt ₄ In	MgCu ₄ Sn	<i>F</i> $\bar{4}3m$	766.6			7
EuPtIn	TiNiSi	<i>Pnma</i>	746.94(8)	447.27(6)	843.46(9)	15
Gd ₃ Pt ₄ In ₁₂	Gd ₃ Pt ₄ In ₁₂	<i>P</i> $\bar{3}m1$	990.5(1)		1529.5(3)	16

continued on next page

Table 10, *continued*

Compound	Str. type	S.G.	<i>a</i> (pm)	<i>b</i> (pm)	<i>c</i> (pm)	Ref.
GdPt ₄ In	MgCu ₄ Sn	<i>F</i> $\bar{4}3m$	756.4			7
GdPt ₂ In	GdPt ₂ Sn	<i>P</i> $\bar{6}_3/mmc$	455.1		899.7	3
GdPtIn	Fe ₂ P	<i>P</i> $\bar{6}2m$	757.3		391.7	4
Gd ₂ Pt ₂ In	Mo ₂ FeB ₂	<i>P</i> $\bar{4}/mbm$	770.09(7)		373.48(6)	5
Gd ₁₂ Pt ₇ In	Ce ₁₂ Pt ₇ In	<i>I</i> $\bar{4}/mcm$	1160.1(3)		1447.2(4)	12
Tb ₆ Pt ₁₂ In ₂₃	Tb ₆ Pt ₁₂ In ₂₃	<i>C</i> $\bar{2}/m$	2834.6(4)	440.05(7) 112.37(1) ^o	1477.1(3)	17
Tb ₃ Pt ₄ In ₁₂	Gd ₃ Pt ₄ In ₁₂	<i>P</i> $\bar{3}m1$	988.65(9)		1524.0(1)	16
TbPt ₄ In	MgCu ₄ Sn	<i>F</i> $\bar{4}3m$	755.0			7
TbPt ₂ In	GdPt ₂ Sn	<i>P</i> $\bar{6}_3/mmc$	454.5		894.0	3
TbPtIn	ZrNiAl	<i>P</i> $\bar{6}2m$	759.3(1)		387.6(1)	2
Tb ₂ Pt ₂ In	Mo ₂ FeB ₂	<i>P</i> $\bar{4}/mbm$	767.72(4)		370.51(4)	5
Dy ₂ Pt ₇ In ₁₆	Dy ₂ Pt ₇ In ₁₆	<i>Cmnm</i>	1211.1(2)	1997.8(3)	439.50(6)	17
DyPt ₄ In	MgCu ₄ Sn	<i>F</i> $\bar{4}3m$	753.7			7
DyPt ₂ In	GdPt ₂ Sn	<i>P</i> $\bar{6}_3/mmc$	453.9		890.7	3
DyPtIn	Fe ₂ P	<i>P</i> $\bar{6}2m$	758		385	4
Dy ₂ Pt ₂ In	Mo ₂ FeB ₂	<i>P</i> $\bar{4}/mbm$	765.11(6)		367.67(5)	5
HoPt ₄ In	MgCu ₄ Sn	<i>F</i> $\bar{4}3m$	752.4			7
HoPt ₂ In	GdPt ₂ Sn	<i>P</i> $\bar{6}_3/mmc$	453.6		887.8	3
HoPtIn	ZrNiAl	<i>P</i> $\bar{6}2m$	758.13(1)		381.62(1)	2
Ho ₂ Pt ₂ In	Mo ₂ FeB ₂	<i>P</i> $\bar{4}/mbm$	765.45(6)		365.06(6)	5
Ho ₁₂ Pt ₇ In	Ce ₁₂ Pt ₇ In	<i>I</i> $\bar{4}/mcm$	1136.9(1)		1446.2(2)	12
ErPt ₄ In	AuCu ₃	<i>Pm</i> $\bar{3}m$	405.9			7
ErPt ₄ In	MgCu ₄ Sn	<i>F</i> $\bar{4}3m$	745.9			7
ErPtIn	Fe ₂ P	<i>P</i> $\bar{6}2m$	756.9		379.0	4
TmPt ₄ In	AuCu ₃	<i>Pm</i> $\bar{3}m$	404.5			7
TmPtIn	Fe ₂ P	<i>P</i> $\bar{6}2m$	756.0		378.0	4
YbPtIn ₄	YNiAl ₄	<i>Cmcm</i>	444.5(1)	1655.0(1)	751.6(1)	18
YbPtIn	ZrNiAl	<i>P</i> $\bar{6}2m$	753.8		376.5	19
			754.8(1)		376.6(1)	20
LuPtIn	Fe ₂ P	<i>P</i> $\bar{6}2m$	754.2		375.6	4

References

- | | | |
|------------------------------|---------------------------------|--------------------------------|
| 1. Dwight and Kimball (1987) | 7. Malik et al. (1990b) | 14. Blazina (1994) |
| 2. Galadzhun et al. (2000b) | 8. Galadzhun and Pöttgen (1999) | 15. Pöttgen (1996a) |
| 3. Dwight (1987) | 9. Zaremba et al. (2000a) | 16. Rodewald et al. (2002) |
| 4. Ferro et al. (1974b) | 10. Kaczorowski et al. (1996a) | 17. Zaremba et al. (2002d) |
| 5. Hulliger (1995a) | 11. Rossi et al. (1983) | 18. Zaremba et al. (2003b) |
| 6. Hundley et al. (2001) | 12. Galadzhun et al. (2003) | 19. Kaczorowski et al. (2000a) |
| | 13. Zaremba et al. (2001) | 20. Trovarelli et al. (2000) |

3.3.3. *The R–Au–In systems*

According to Marazza et al. (1975), the indides *RAu₂In* crystallize with tungsten (or CsCl) type structure. However, the latest investigations by Besnus et al. (1985, 1986) showed that these indides belong to the *MnCu₂Al* type. *YbAuIn* has a pronounced homogeneity range (Pöttgen and Grin, 1997). The crystallographic data are given in table 11.

Table 11
Crystallographic data of ternary R–Au–In compounds

Compound	Str. type	S.G.	<i>a</i> (pm)	<i>b</i> (pm)	<i>c</i> (pm)	Ref.
ScAu ₂ In	MnCu ₂ Al	<i>Fm</i> $\bar{3}m$	669.2			1
Sc ₂ Au ₂ In	U ₂ Pt ₂ Sn	<i>P4</i> ₂ / <i>mmm</i>	756.69(6)		695.63(9)	2
YAu ₂ In	CsCl MnCu ₂ Al	<i>Pm</i> $\bar{3}m$	344.3			3
		<i>Fm</i> $\bar{3}m$	689.3			4,5
YAuIn	Fe ₂ P	<i>P</i> $\bar{6}2m$	769.1(2)		390.7(1)	6
Y ₂ Au ₂ In	Mo ₂ FeB ₂	<i>P4</i> / <i>mbm</i>	783.5(2)		375.2(1)	7
			783.67(3)		374.40(2)	2
La ₃ Au ₄ In ₇	La ₃ Au ₄ In ₇	<i>I2</i> / <i>m</i>	460.42(5)	1389.5(1)	1039.6(2)	8
LaAu ₂ In	W tetragonal	<i>Im</i> $\bar{3}m$	356.0			3
		–	704.8		731.8	4,5
LaAuIn	Fe ₂ P	<i>P</i> $\bar{6}2m$	772.7(2)		431.5(1)	6
La ₂ Au ₂ In	Mo ₂ FeB ₂	<i>P4</i> / <i>mbm</i>	809.63(6)		399.98(5)	2
			809.9(1)		400.3(1)	9
CeAu _{3,5} In _{2,5}	YbAg ₂ In ₄	<i>Im</i> $\bar{3}$	1529.7			10
Ce ₂ Au ₃ In ₅	Ce ₂ Au ₃ In ₅	<i>Pmn</i> 2 ₁	465.27(8)	5348.3(9)	740.5(1)	11
CeAu ₂ In	W MnCu ₂ Al tetragon.-LT	<i>Im</i> $\bar{3}m$	354.4			3
		<i>Fm</i> $\bar{3}m$	709.0			4
		–	698.0		726.8	5
CeAuIn	Fe ₂ P	<i>P</i> $\bar{6}2m$	769.8(2)		425.6(1)	6
Ce ₂ Au ₂ In	Mo ₂ FeB ₂	<i>P4</i> / <i>mbm</i>	804.27(4)		394.59(3)	2
			804.74(3)		394.07(2)	9
Pr ₂ Au ₃ In ₅	Ce ₂ Au ₃ In ₅	<i>Pmn</i> 2 ₁	461.81(6)	5350.7(9)	742.2(1)	11
PrAu ₂ In	W MnCu ₂ Al tetragon.-LT	<i>Im</i> $\bar{3}m$	352.4			3
		<i>Fm</i> $\bar{3}m$	705.5			4
		–	699.3		718.4	5
PrAuIn	Fe ₂ P	<i>P</i> $\bar{6}2m$	770.0(2)		419.5(1)	6
Pr ₂ Au ₂ In	Mo ₂ FeB ₂	<i>P4</i> / <i>mbm</i>	800.25(4)		392.00(4)	2
Nd ₂ Au ₃ In ₅	Ce ₂ Au ₃ In ₅	<i>Pmn</i> 2 ₁	459.98(6)	5338.2(8)	740.7(1)	11
NdAu ₂ In	W MnCu ₂ Al tetragon.-LT	<i>Im</i> $\bar{3}m$	351.6			3
		<i>Fm</i> $\bar{3}m$	703.0			4
		–	690.2		706.0	5
NdAuIn	Fe ₂ P	<i>P</i> $\bar{6}2m$	771.9(2)		412.4(1)	6
Nd ₂ Au ₂ In	Mo ₂ FeB ₂	<i>P4</i> / <i>mbm</i>	797.60(4)		388.63(3)	2
Sm ₂ Au ₃ In ₅	Ce ₂ Au ₃ In ₅	<i>Pmn</i> 2 ₁	456.40(7)	5332.5(9)	739.4(1)	11
SmAu ₂ In	W MnCu ₂ Al	<i>Im</i> $\bar{3}m$	348.8			3
		<i>Fm</i> $\bar{3}m$	697.3			4,5
SmAuIn	Fe ₂ P	<i>P</i> $\bar{6}2m$	771.6(2)		404.3(1)	6
Sm ₂ Au ₂ In	Mo ₂ FeB ₂	<i>P4</i> / <i>mbm</i>	793.02(4)		382.82(3)	2
Eu ₂ Au ₃ In ₄	anti-Hf ₂ Co ₄ P ₃	<i>P</i> $\bar{6}2m$	1489.7(3)		454.90(7)	12
EuAuIn ₂	MgCuAl ₂	<i>Cmcm</i>	468.1(2)	1105.5(4)	753.5(4)	13
EuAuIn	TiNiSi	<i>Pnma</i>	755.2(2)	472.2(1)	842.3(2)	14
GdAu ₂ In	W MnCu ₂ Al	<i>Im</i> $\bar{3}m$	346.9			3
		<i>Fm</i> $\bar{3}m$	694.0			4,5
GdAuIn	Fe ₂ P ZrNiAl	<i>P</i> $\bar{6}2m$	769.3(2)		399.1(1)	6
		<i>P</i> $\bar{6}2m$	769.8(3)		397.8(2)	15

continued on next page

Table 11, *continued*

Compound	Str. type	S.G.	<i>a</i> (pm)	<i>b</i> (pm)	<i>c</i> (pm)	Ref.
GdAu _{0.44} In _{1.56}	CaIn ₂	<i>P6₃/mmc</i>	478.9(1)		740.3(1)	15
Gd ₂ Au ₂ In	Mo ₂ FeB ₂	<i>P4/mbm</i>	787.9(1)		379.9(1)	7
			786.88(6)		381.13(6)	2
TbAu ₂ In	W	<i>Im$\bar{3}m$</i>	345.5			3
	MnCu ₂ Al	<i>Fm$\bar{3}m$</i>	691.3			4,5
TbAuIn	Fe ₂ P	<i>P$\bar{6}2m$</i>	769.1(2)		395.1(1)	6
	ZrNiAl	<i>P$\bar{6}2m$</i>	770.18(11)		393.55(7)	16
Tb ₂ Au ₂ In	Mo ₂ FeB ₂	<i>P4/mbm</i>	785.1(1)		376.8(1)	7
			785.35(6)		376.58(6)	2
DyAu ₂ In	W	<i>Im$\bar{3}m$</i>	344.9			3
	MnCu ₂ Al	<i>Fm$\bar{3}m$</i>	688.5			4,5
DyAuIn	Fe ₂ P	<i>P$\bar{6}2m$</i>	768.6(2)		390.2(1)	6
	ZrNiAl	<i>P$\bar{6}2m$</i>	767.67(15)		392.19(10)	16
Dy ₂ Au ₂ In	Mo ₂ FeB ₂	<i>P4/mbm</i>	784.1(1)		373.9(1)	7
			782.48(6)		375.25(7)	2
HoAu ₂ In	W	<i>Im$\bar{3}m$</i>	343.7			3
	MnCu ₂ Al	<i>Fm$\bar{3}m$</i>	687.0			4,5
HoAuIn	Fe ₂ P	<i>P$\bar{6}2m$</i>	768.3(2)		387.7	6
	ZrNiAl	<i>P$\bar{6}2m$</i>	767.55(8)		389.20(5)	16
Ho ₂ Au ₂ In	Mo ₂ FeB ₂	<i>P4/mbm</i>	782.6(2)		371.7(1)	7
			781.34(3)		371.95(4)	2
ErAu ₂ In	CsCl	<i>Pm$\bar{3}m$</i>	343.0			3
	MnCu ₂ Al	<i>Fm$\bar{3}m$</i>	696.4			4,5
ErAuIn	Fe ₂ P	<i>P$\bar{6}2m$</i>	767.4(2)		384.7(1)	6
Er ₂ Au ₂ In	Mo ₂ FeB ₂	<i>P4/mbm</i>	781.2(3)		370.4(2)	7
			778.86(3)		370.86(3)	2
TmAu ₂ In	MnCu ₂ Al	<i>Fm$\bar{3}m$</i>	685.6			4,5
Tm ₂ Au ₂ In	U ₂ Pt ₂ Sn	<i>P4₂/mnm</i>	779.1(1)		734.8(2)	7
			777.95(4)		734.37(8)	2
YbAu ₂ In	CsCl	<i>Pm$\bar{3}m$</i>	342.8			3
	MnCu ₂ Al	<i>Fm$\bar{3}m$</i>	682.2			4,5
YbAuIn ₂	MgCuAl ₂	<i>Cmcm</i>	455.9(2)	1076.4(3)	755.2(2)	17
YbAuIn	Fe ₂ P	<i>P$\bar{6}2m$</i>	770.8(2)		402.7(1)	6
	ZrNiAl	<i>P$\bar{6}2m$</i>	769.8(1)		402.7(1)	18
YbAu _{1.27} In _{0.73}	ZrNiAl	<i>P$\bar{6}2m$</i>	772.3(3)		394.7(1)	18
Yb ₂ Au ₂ In	Mo ₂ FeB ₂	<i>P4/mbm</i>	783.03(5)		385.95(4)	2
			784.2(3)		384.7(2)	19
LuAu ₂ In	MnCu ₂ Al	<i>Fm$\bar{3}m$</i>	682.2			4,5
Lu ₂ Au ₂ In	U ₂ Pt ₂ Sn	<i>P4₂/mnm</i>	775.5(1)		728.7(1)	7

References

- | | | |
|------------------------------|-------------------------------|------------------------------|
| 1. Dwight and Kimball (1987) | 7. Pöttgen (1994) | 14. Pöttgen (1996b) |
| 2. Hulliger (1996) | 8. Galadzhun et al. (2000a) | 15. Pöttgen et al. (1998) |
| 3. Marazza et al. (1975) | 9. Kaczorowski et al. (1996a) | 16. Szytuła et al. (2002) |
| 4. Besnus et al. (1985) | 10. Galadzhun et al. (2000c) | 17. Galadzhun et al. (1999a) |
| 5. Besnus et al. (1986) | 11. Galadzhun et al. (1999b) | 18. Pöttgen and Grin (1997) |
| 6. Rossi et al. (1977) | 12. Hoffmann et al. (1999) | 19. Giovannini et al. (2001) |
| | 13. Hoffmann et al. (2000) | |

4. Structure types of ternary indides of rare-earth and transition metals

The various ternary R - d -metal–In indides, the corresponding structure types, and the lattice parameters have been listed in the previous section (tables 1–11). These ternary indides crystallize with 58 different structure types. 24 of them represent new structure types of intermetallic compounds. They have been determined first for these indium compounds. In the following paragraphs, we list the atomic coordinates and details on the coordination polyhedra.

4.1. *Structure type* NaZn_{13} (Shoemaker et al., 1952) (fig. 21). SG $Fm\bar{3}c$; $Z = 8$; $a = 1249.2(3)$ pm for $\text{LaCu}_{6.5}\text{In}_{6.5}$. 8La: $8a$ $1/4$ $1/4$ $1/4$; 8M1: $8b$ 0 0 0 ; 96M2: $96i$ 0 y z ($y = 0.1810$, $z = 0.1217$, $M1 = M2 = \text{Cu}_{0.5}\text{In}_{0.5}$) (Kalychak et al., 1984a). The CP of the lanthanum atoms have 24 vertices (CN = 24), for the M1 and M2 atoms of the mixed Cu–In sites the CP are icosahedra (CN = 12). The shortest distances are La–M 361.3 pm and M–M 272.7 pm. The isotopic compound with cerium shows defects on the cerium and copper sites: 6.14Ce: $8a$; 96(Cu_{0.68}In_{0.32}): $96i$ ($y = 0.1810$, $z = 0.1223$); 5.18Cu: $8b$. The composition of this compound is described by the formula $\text{Ce}_{1-x}(\text{Cu}_{0.68}\text{In}_{0.32})_{12}\text{Cu}_{1-y}$ with $x = 0.22$ and $y = 0.36$ (Baranyak et al., 1990).

4.2. *Structure type* LaNi_7In_6 (fig. 22). SG $Ibam$; $Z = 4$; $a = 806.6(2)$, $b = 924.8(2)$, $c = 1246.5(2)$ pm. 4La: $4a$ 0 0 $1/4$; 4Ni1: $4d$ 0 $1/2$ 0 ; 8Ni2: $8j$ x y 0 ($x = 0.0758$, $y = 0.2388$); 16Ni3: $16k$ x y z ($x = 0.6245$, $y = 0.08896$, $z = 0.17140$); 16In1: $16k$ ($x = 0.17351$, $y = 0.69254$, $z = 0.13737$); 8M: $8j$ ($x = 0.17391$, $y = 0.95635$, $M = 0.180\text{Ni} + 0.820\text{In}$). The CP of the lanthanum atoms have 20 vertices (CN = 20). The CP of the Ni1 atoms are icosahedra (CN = 12) and the Ni2 and Ni3 atoms are situated in defective icosahedra

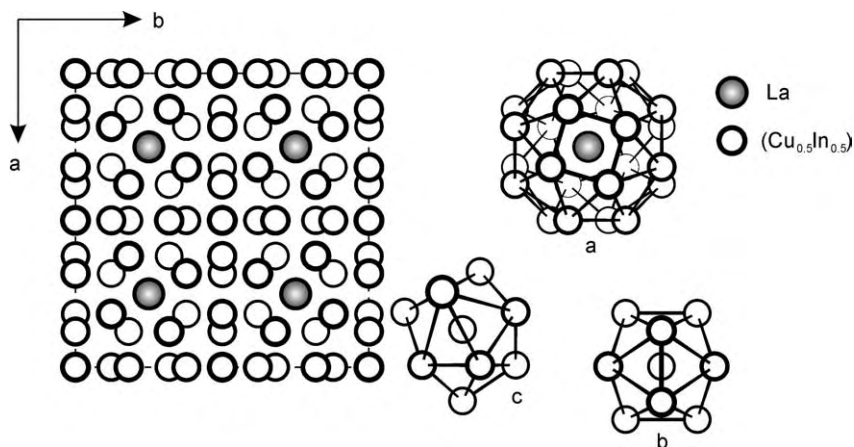


Fig. 21. Projection of the $\text{LaCu}_{6.5}\text{In}_{6.5}$ structure on the xy plane and coordination polyhedra of the atoms: La (a), M (b, c) ($M = \text{Cu}_{0.5}\text{In}_{0.5}$).

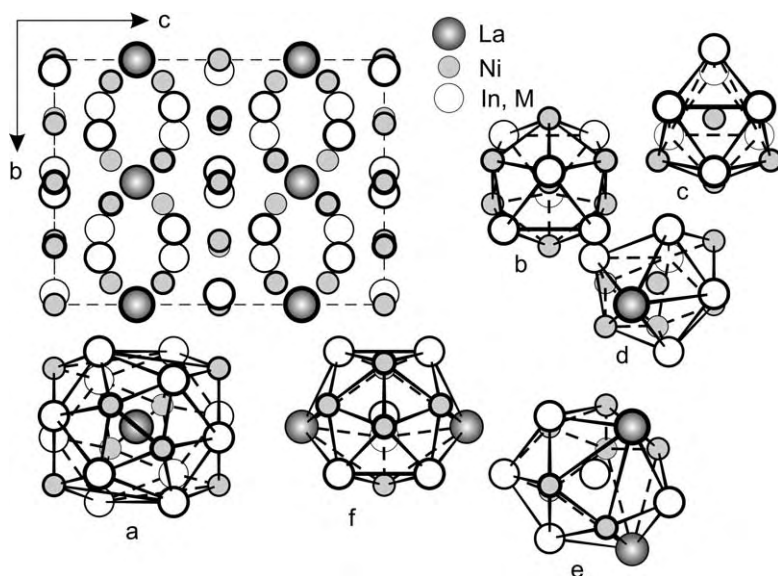


Fig. 22. Projection of the LaNi_7In_6 structure on the yz plane and coordination polyhedra of the atoms: La (a), Ni (b–e) and M (f) ($M = \text{Ni}_{0.18}\text{In}_{0.82}$).

(CN = 10 and 11, respectively). The CP of the indium atoms and the mixed site are distorted icosahedra with one additional atom (CN = 13). The shortest distances are La–In (346.6 pm), La– M (344.1 pm), Ni–Ni (249.2 pm), Ni–In (259.9 pm), Ni– M (266.1 pm), M – M (291.9 pm), M –In (298.1 pm), and In–In (324.6 pm) (Kalychak et al., 2001).

4.3. *Structure type ThMn_{12}* (Floriot et al., 1952) (fig. 23). SG $I4/mmm$; $Z = 2$; $a = 915.2(2)$, $c = 539.0(2)$ pm for $\text{ErCu}_{5.1}\text{In}_{6.9}$. 2Er : $2a\ 0\ 0\ 0$; $8M1$: $8f\ 1/4\ 1/4\ 1/4$; 8In : $8i\ x\ 0\ 0$ ($x = 0.3397$); $8M2$: $8j\ x\ 1/2\ 0$ ($x = 0.2968$) ($M1 = \text{Cu}_{0.850}\text{In}_{0.150}$; $M2 = \text{Cu}_{0.422}\text{In}_{0.578}$) (Sysa et al., 1989). The CP of the erbium atoms have 20 vertices (CN = 20), the CP of the $M1$ atoms are icosahedra (CN = 12), the CP of $M2$ atoms are polyhedra with 13 vertices, which derive from icosahedra (CN = 12 + 1). The indium atoms have polyhedra with 14 vertices, which can be described as hexagonal antiprisms with capped bases (CN = 12 + 2). The shortest distances are Er–In (310.9 pm), In–In (293.4 pm), and $M2$ – $M2$ (263.0 pm). Isostructural $\text{YbAg}_{5.4}\text{In}_{6.6}$ has the following distribution of the atoms: 2Yb : $2a$; 8Ag : $8i$ ($x = 0.339$); 8In : $8j$ ($x = 0.289$); $8(\text{Ag}_{0.35}\text{In}_{0.65})$: $8f$ (Sysa, 1991).

4.4. *Structure type EuAg_4In_8* (fig. 24). SG $P6/mmm$; $Z = 3$; $a = 992.5(6)$, $c = 972.7(5)$ pm. 1Eu : $1a\ 0\ 0\ 0$; 2Eu : $2d\ 2/3\ 1/3\ 1/2$; 12Ag : $12o\ x\ 2x\ z$ ($x = 0.1670$, $z = 0.2416$); 2In : $2e\ 0\ 0\ z$ ($z = 0.3434$); 4In : $4h\ 2/3\ 1/3\ z$ ($z = 0.1487$); 6In : $6i\ 1/2\ 0\ z$ ($z = 0.2764$); 6In : $6k\ x\ 0\ 1/2$ ($x = 0.3008$); 6In : $6j\ x\ 0\ 0$ ($x = 0.3469$) (Sysa et al., 1994a). The europium CP are face capped hexagonal prisms (CN = 20), the silver CP are icosahedra (CN = 12), the CP

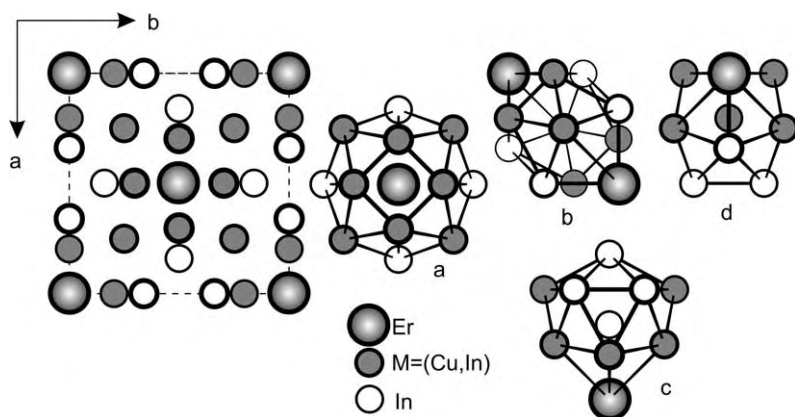


Fig. 23. Projection of the ErCu_{5.1}In_{6.9} structure on the *xy* plane and coordination polyhedra of the atoms: Er (a), M1 (b), M2 (d) and In(c) ($M1 = \text{Cu}_{0.85}\text{In}_{0.15}$, $M2 = \text{Cu}_{0.422}\text{In}_{0.578}$).

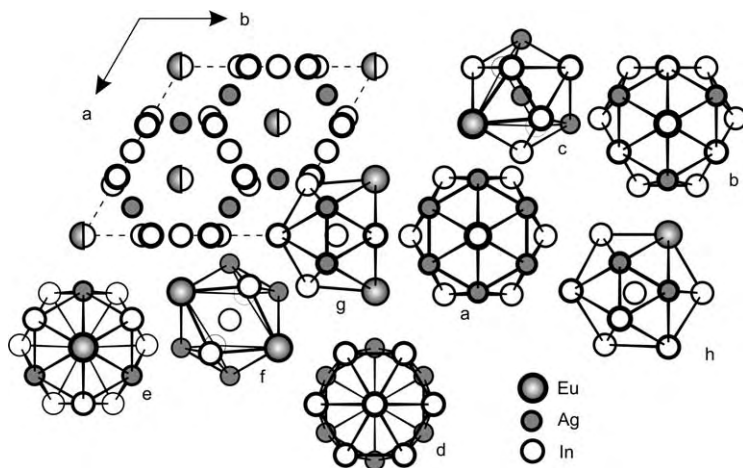


Fig. 24. Projection of the EuAg₄In₈ structure on the *xy* plane and coordination polyhedra of the atoms: Eu (a, b), Ag (c), and In (d-h).

of the In1, In2 and In5 atoms are base capped hexagonal antiprisms (CN = 14), and the CP of the In5 atoms are similar to the CP of the indium atoms in the ThMn₁₂ type. The CP for the In3 atoms are hybrids of the CP for the Cu2 atoms in the CaCu₅ structure and icosahedra (CN = 12). The In4 CP are distorted icosahedra (CN = 12). The shortest distances are Eu–In (334.0 pm), Ag–Ag (287.1 pm), Ag–In (288.2 pm), and In–In (289.3 pm).

4.5. Structure type Dy₂Pt₇In₁₆ (fig. 25). SG *Cmmm*; Z = 2; $a = 1211.1(2)$, $b = 1997.8(3)$, $c = 439.50(6)$ pm. 4Dy1: $4h\ x\ 0\ 1/2$ ($x = 0.82979$); 2Pt1: $2c\ 1/2\ 0\ 1/2$; 4Pt2: $4j\ 0\ y\ 1/2$

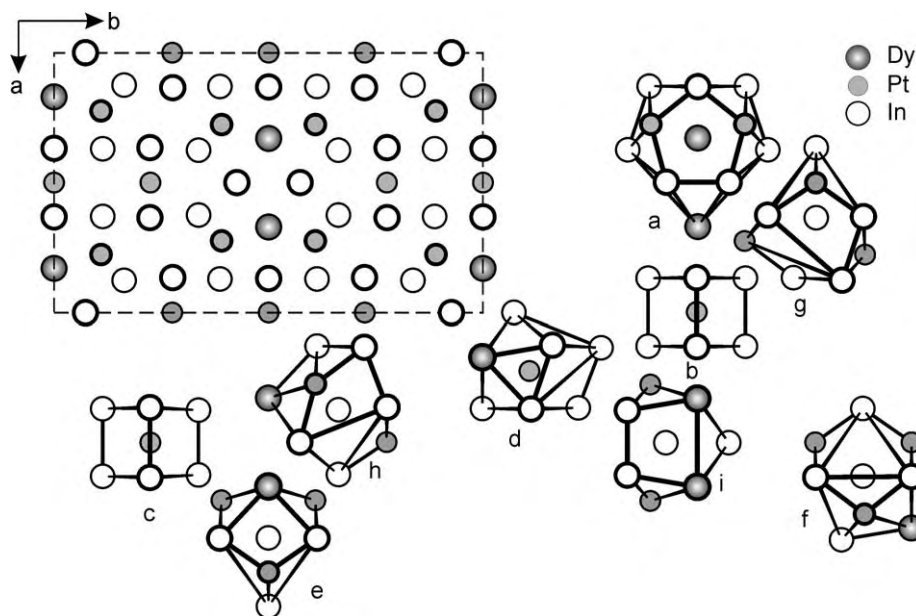


Fig. 25. The projection of the $\text{Dy}_2\text{Pt}_7\text{In}_{16}$ structure on the xy plane and coordination polyhedra of the atoms: Dy (a), Pt (b–d) and In (e–i).

($y = 0.27558$); $8\text{Pt}3: 8p \ x \ y \ 0$ ($x = 0.27619$, $y = 0.39055$); $4\text{In}1: 4g \ x \ 0 \ 0$ ($x = 0.63185$); $8\text{In}2: 8q \ x \ y \ 1/2$ ($x = 0.13008$, $y = 0.38679$); $8\text{In}3: 8p$ ($x = 0.13473$, $y = 0.27644$); $8\text{In}4: 8q$ ($x = 0.12466$, $y = 0.16317$); $4\text{In}5: 4i \ 0 \ y \ 0$ ($y = 0.92644$) (Zaremba, 2003d). The CP for Pt1 and Pt2 are cubes (CN = 8) and trigonal prisms for Pt3 with four additional equatorial atoms (CN = 10). For the indium atoms, In1 and In5, the CP are tetragonal prisms with three additional equatorial atoms (CN = 11). The 11-vertices polyhedron of In2 is similar to the In2 coordination in the structure of HoCoIn_5 . In1 and In2 have 11-vertices polyhedra and a trigonal prism with four additional equatorial atoms (CN = 10) occurs for the In4 atoms. The shortest distances are Pt–In (270.6 pm), In–In (298.5 pm), and Dy–Pt (316.7 pm).

4.6. *Structure type* YNi_9In_2 (fig. 26). SG $P4/m\bar{b}m$; $Z = 2$; $a = 822.2(2)$, $c = 482.7(2)$ pm. $2\text{Y}: 2a \ 0 \ 0 \ 0$; $8\text{Ni}1: 8j \ x \ y \ 1/2$ ($x = 0.195$, $y = 0.061$); $2\text{Ni}2: 2c \ 0 \ 1/2 \ 1/2$; $8\text{Ni}3: 8k \ x$, $1/2 + x$, z ($x = 0.326$, $z = 0.252$); $4\text{In}: 4g \ x$, $1/2 + x$, 0 ($x = 0.111$) (Kalychak et al., 1984b). The CP of the yttrium atoms have 20 vertices and they are similar to the thorium polyhedra in the ThMn_{12} type (CN = 20). The CP of the Ni1, Ni2, and Ni3 atoms are icosahedra (CN = 12). The indium atoms have 15 neighbors. The CP can be described as hexagonal antiprisms, in which one of the bases is capped by one atom and the opposite one by two atoms (CN = 15). The shortest distances are Y–Ni (294.0 pm), Ni–Ni (235.1 pm), Ni–In (269.0 pm), and In–In (258.2 pm).

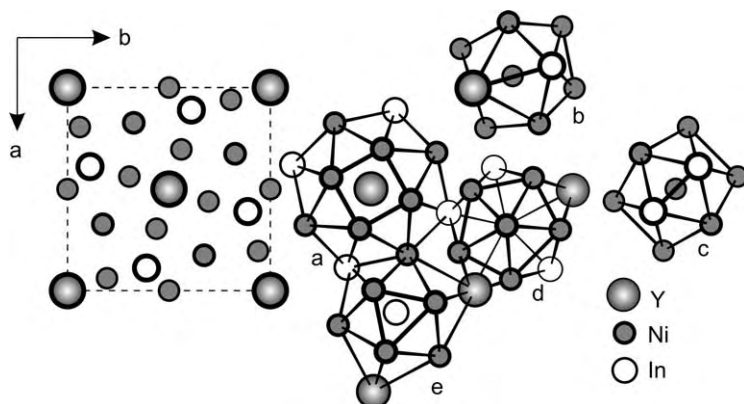


Fig. 26. Projection of the YNi₉In₂ structure on the *xy* plane and coordination polyhedra of the atoms: Y (a), Ni (b–d) and In (e).

4.7. Structure type *CaCo₂Al₈* (Czech et al., 1983) (fig. 27). SG *Pbam*; *Z* = 4; *a* = 1611.8(2), *b* = 1381.7(2), *c* = 436.44(6) pm for EuRh₂In₈. 4Eu: 4*h* *x* *y* 1/2 (*x* = 0.68057, *y* = 0.15683); 4Rh1: 4*h* (*x* = 0.90356, *y* = 0.34646); 4Rh2: 4*h* (*x* = 0.59524, *y* = 0.46552); 4In1: 4*g* *x* *y* 0 (*x* = 0.12249, *y* = 0.16704); 4In2: 4*g* (*x* = 0.31621, *y* = 0.44956); 2In3: 2*a*

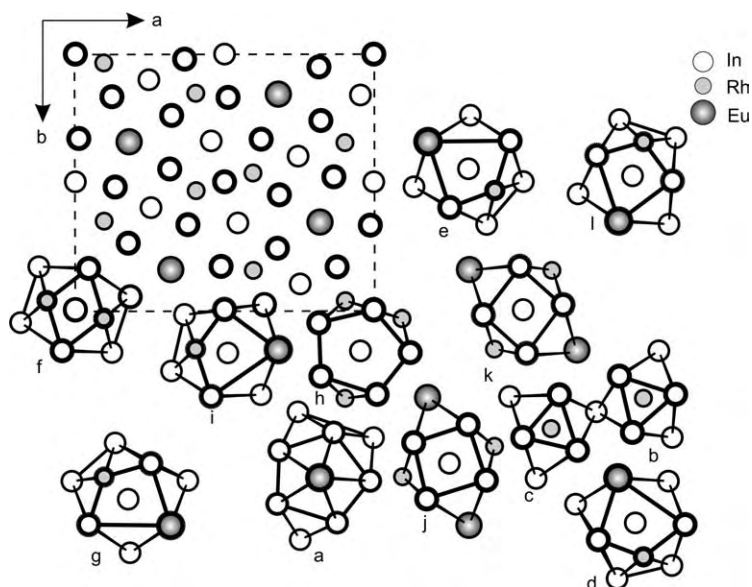


Fig. 27. Projection of the EuRh₂In₈ structure on the *xy* plane and coordination polyhedra of the atoms: Eu (a), Rh (b, c), and In (d–l).

0 0 0; 4In4: 4g ($x = 0.32275$, $y = 0.24019$); 4In5: 4h ($x = 0.95555$, $y = 0.16029$); 4In6: 4g ($x = 0.01161$, $y = 0.33048$); 4In7: 4h ($x = 0.74642$, $y = 0.39938$); 2In8: $2d$ 0 1/2 1/2; 4In9: 4g ($x = 0.36626$, $y = 0.02000$) (Pöttgen and Kußmann, 2001). The europium CP are pentagonal prisms, which are capped on the bases and on three rectangular faces (CN = 15). The Rh1 and Rh2 CP are trigonal prisms with capped rectangular faces (CN = 9). The In5 CP has a pentagonal prism with three additional atoms on the rectangular faces (CN = 13). The CP of the other indium atoms are distorted cuboctahedra (CN = 12). The shortest distances are Eu–In (336.2 pm), Eu–In (325.1 pm), Rh–In (260.2 pm), and In–In (288.0 pm).

4.8. *Structure type Yb₂Pd₆In₁₃* (fig. 28). SG $C2/m$; $Z = 2$; $a = 1677.0(1)$, $b = 438.17(4)$, $c = 1339.7(1)$ pm, $\beta = 118.53(1)^\circ$. 4Yb: 4i x 0 z ($x = 0.17731$, $z = 0.27207$); 2In1: $2a$ 0 0 0; 4In2: 4i ($x = 0.51062$, $z = 0.17241$); 4In3: 4i ($x = 0.79906$, $z = 0.46081$); 4In4: 4i ($x = 0.40763$, $z = 0.40093$); 4In5: 4i ($x = 0.29942$, $z = 0.12454$); 4In6: 4i ($x = 0.65290$, $z = 0.07570$); 4In7: 4i ($x = 0.99902$, $z = 0.32852$); 4Pd1: 4i ($x = 0.81896$, $z = 0.26369$); 4Pd2: 4i ($x = 0.88380$, $z = 0.08234$); 4Pd3: 4i ($x = 0.61206$, $z = 0.40484$) (Zaremba et al., 2002c). The CP of the ytterbium atoms are pentagonal prisms with five additional atoms on the equatorial rectangular faces (CN = 15). The CP for the palladium atoms are trigonal prisms with four additional atoms (CN = 10). For the indium atoms the CP are distorted cuboctahedra (CN = 12) for In1–In3 and In6. Tetragonal prisms with five additional equatorial atoms (CN = 13) are found for In4, while pentagonal prisms with five and four additional atoms occur for In5 and In7, (CN = 15 and 14), respectively. The shortest distances are Yb–In (323.0 pm), In–In (296.5 pm), and Pd–In (265.9 pm).

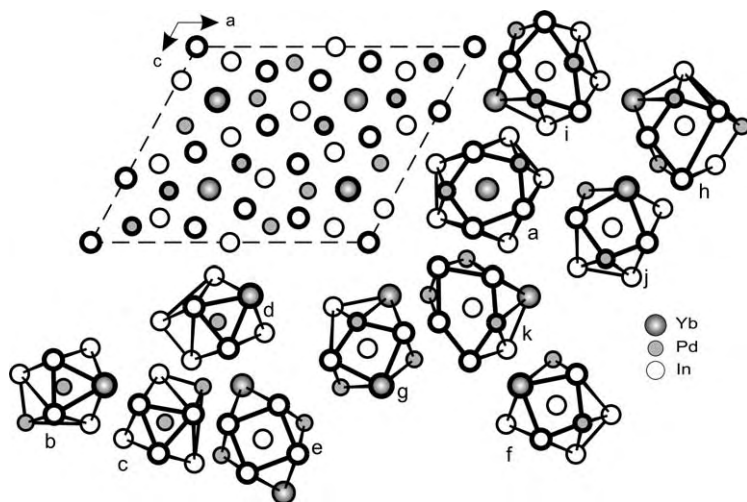


Fig. 28. Projection of the $Yb_2Pd_6In_{13}$ structure on the xz plane and coordination polyhedra of the atoms: Yb (a), Pd (b–d) and In (e–k).

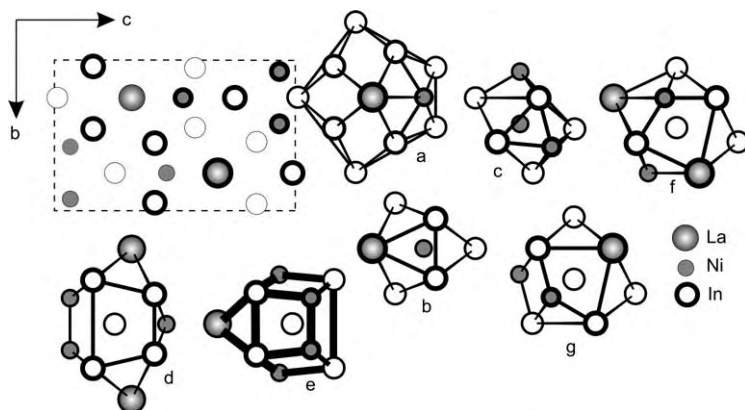


Fig. 29. Projection of the LaNi_3In_6 structure on the yz plane and coordination polyhedra of the atoms: La (a), Ni (b, c), and In (d–g).

4.9. *Structure type* LaNi_3In_6 (fig. 29). SG $Pm\bar{m}n$; $Z = 2$; $a = 438.8(2)$, $b = 757.4(4)$, $c = 1211.0(7)$ pm. 2La: $2a \ 1/4 \ 1/4 \ z$ ($z = 0.32187$); 2Ni1: $2b \ 1/4 \ 3/4 \ z$ ($z = 0.46597$); 4Ni2: $4e \ 1/4 \ y \ z$ ($y = 0.37642$, $z = 0.06560$); 2In1: $2a$ ($z = 0.25114$); 2In2: $2a$ ($z = 0.01173$); 4In3: $4e$ ($y = 0.44791$, $z = 0.58362$); 4In4: $4e$ ($y = 0.54299$, $z = 0.83908$) (Kalychak et al., 1985). The CP of the lanthanum atoms are face capped pentagonal prisms (CN = 17). Ni1 and Ni2 have trigonal prisms with three and four additional atoms (CN = 9 and 10). In1 and In2 have tetragonal prisms with five additional equatorial atoms (CN = 13) and In3 and In4 are situated in strongly distorted cuboctahedra (CN = 12). The shortest distances are La–Ni (338.0 pm), La–In (332.7 pm), Ni–In (256.0 pm), Ni–Ni (263.0 pm), and In–In (299.8 pm).

4.10. *Structure type* $\text{Th}_2\text{Ni}_{17}$ (Florio et al., 1956) (fig. 30). SG $P6_3/mmc$; $Z = 2$; $a = 835.3$, $c = 814.1$ pm for $\text{Pr}_2\text{Ni}_{16.0}\text{In}_{1.0}$. 2Pr1: $2d \ 1/3 \ 2/3 \ 3/4$; 2Pr2: $2b \ 0 \ 0 \ 1/4$; 12M1: $12k \ x \ 2x \ 0$ ($x = 0.1666$); 12M2: $12j \ x \ 0 \ 1/4$ ($x = 0.3300$); 6M3: $6g \ 1/2 \ 0 \ 0$; 4M4: $4f \ 1/3 \ 2/3 \ z$ ($z = 0.1100$) ($M = \text{Ni}_{0.94}\text{In}_{0.06}$) (Kalychak, 1997). The CP of the praseodymium atoms are face capped hexagonal prisms (CP = 20). The CP of the $M1$ and $M3$ atoms are distorted icosahedra (CN = 12). The CP of the $M2$ atoms have 13 vertices (CN = 13) and the $M4$ CP are base capped hexagonal antiprisms (CN = 14). The shortest distances are Pr–Ni (289.5 pm) and M – M (244.1 pm).

4.11. *Structure type* $\text{Ho}_4\text{Ni}_{10}\text{Ga}_{21}$ (Grin et al., 1979b) (fig. 31). SG $C2/m$; $Z = 2$; $a = 2314.3(2)$, $b = 454.70(7)$, $c = 1940.8(2)$ pm, $\beta = 133.43(1)^\circ$ for $\text{Ce}_4\text{Pd}_{10}\text{In}_{21}$. 4Ce1: $4i \ x \ 0 \ z$ ($x = 0.90482$, $z = 0.67701$), 4Ce2: $4i$ ($x = 0.71229$, $z = 0.83395$), 4Pd1: $4i$ ($x = 0.13471$, $z = 0.88679$), 4Pd2: $4i$ ($x = 0.9115$, $z = 0.8865$), 4Pd3: $4i$ ($x = 0.26770$, $z = 0.61427$), 4Pd4: $4i$ ($x = 0.47021$, $z = 0.60646$), 4Pd5: $4i$ ($x = 0.18294$, $z = 0.68821$), 2In1: $2b \ 0 \ 1/2 \ 0$, 4In2: $4i$ ($x = 0.06148$, $z = 0.95035$), 4In3: $4i$ ($x = 0.33085$, $z = 0.87224$), 4In4: $4i$ ($x = 0.76707$, $z = 0.70270$), 4In5: $4i$ ($x = 0.06836$, $z = 0.6986$), 4In6: $4i$ ($x = 0.5841$,

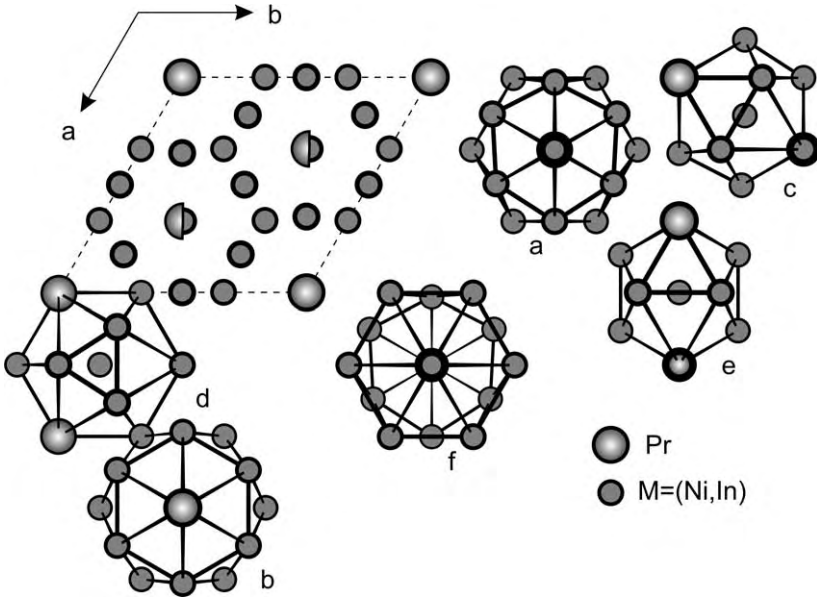


Fig. 30. Projection of the $\text{Pr}_2\text{Ni}_{16.0}\text{In}_{1.0}$ structure on the xy plane and coordination polyhedra of the atoms: Pr (a, b) and M (c-f) ($M = \text{Ni}_{0.94}\text{In}_{0.06}$).

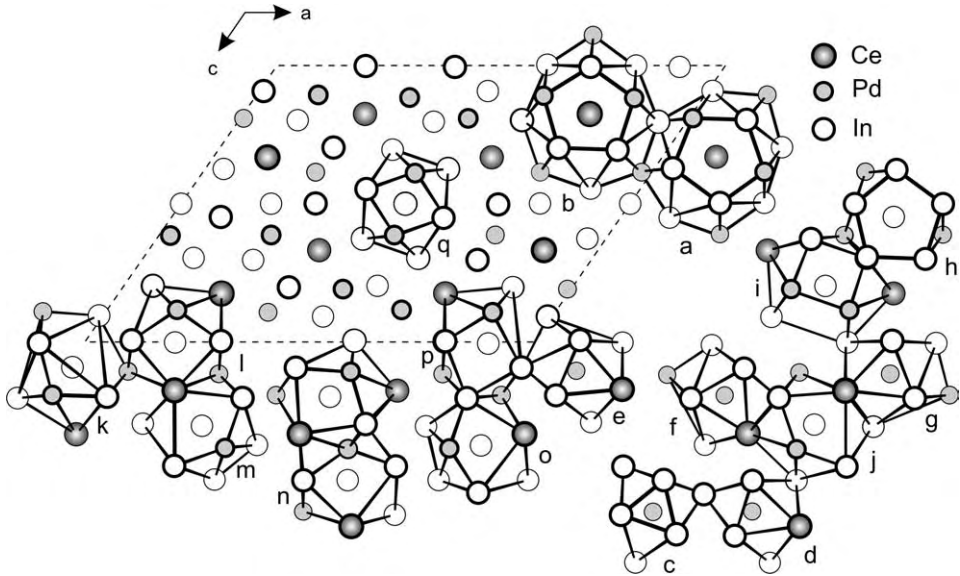


Fig. 31. Projection of the $\text{Ce}_4\text{Pd}_{10}\text{In}_{21}$ structure on the xz plane and coordination polyhedra of the atoms: La (a, b), Pd (c-g) and In (h-q).

$z = 0.5936$), 4In7: 4i ($x = 0.54379$, $z = 0.79579$), 4In8: 4i ($x = 0.41472$, $z = 0.8021$), 4In9: 4i ($x = 0.10453$, $z = 0.50274$), 4In10: 4i ($x = 0.69682$, $z = 0.49612$), 4In11: 4i ($x = 0.70030$, $z = 0.99949$) (Zaremba et al., 2003a). The CP of both cerium atoms are pentagonal prisms with five additional indium atoms located on opposite rectangular faces and three additional palladium atoms located on opposite edges (CN 18). Trigonal prisms with three or four additional atoms are characteristic for the palladium atoms (CN 9 and CN 10). For the indium atoms, distorted and defect icosahedra (CN 12 and CN 11) and 13-vertices polyhedra are typical. The shortest distances are Ce–Pd (331.3 pm), Ce–In (321.3 pm), Pd–In (269.4 pm), and Pd–Pd (312.4 pm).

4.12. *Structure type CeNi₅Sn* (Skolozdra et al., 1981) (fig. 32). SG $P6_3/mmc$; $Z = 4$; $a = 489.4(2)$, $c = 1987.8(5)$ pm for CeNi₅In. 2Ce1: $2c$ $1/3$ $2/3$ $1/4$; 2Ce2: $2a$ 0 0 0 ; 12Ni1: $12k$ x $2x$ z ($x = 0.8347$, $z = 0.1473$); 4Ni2: $4f$ $1/3$ $2/3$ z ($z = 0.5460$); 2Ni3: $2d$ $1/3$ $2/3$ $3/4$; 2Ni4: $2b$ 0 0 $1/4$; 4In: $4f$ ($z = 0.0856$) (Baranyak et al., 1992). The CP of the Ce1 atoms are face capped hexagonal prisms (CN = 20), the Ce2 polyhedra have 18 vertices (CN = 18) and the Ni1 CP are icosahedra (CN = 12). The Ni2 atoms have a 10-vertices polyhedron, which may be considered as a combination of an icosahedron and a trigonal prism (CN = 10). The Ni3 and Ni4 atoms have coordination number 12, while the indium atoms have a 14-vertices

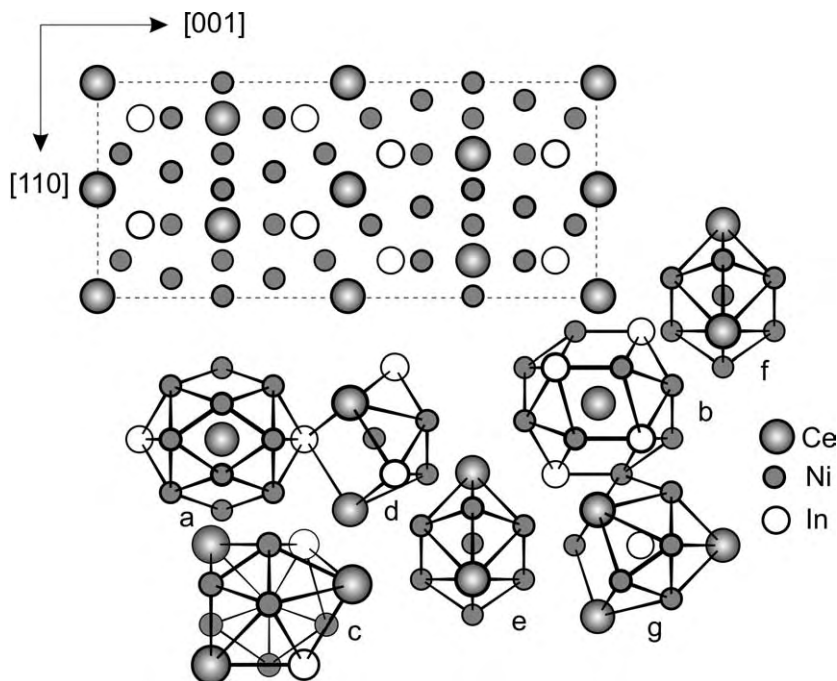


Fig. 32. Projection of the CeNi₅In structure in the orthohexagonal setting and coordination polyhedra of the atoms: Ce (a, b), Ni (c–f) and In (g).

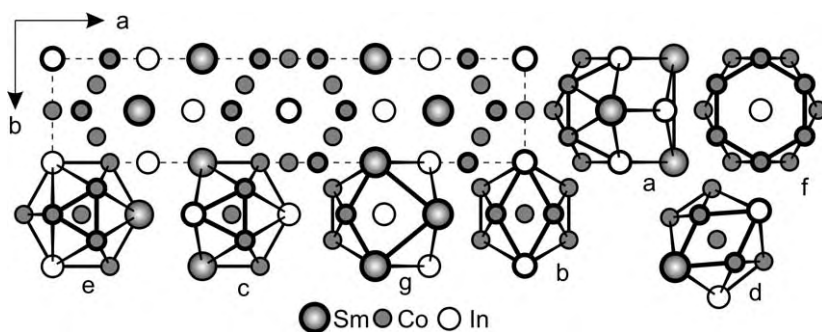


Fig. 33. Projection of the $\text{Sm}_2\text{Co}_9\text{In}_3$ structure on the xy plane and coordination polyhedra of the atoms: Sm (a), Co (b–e), and In (f, g).

polyhedron (CN = 14). The shortest distances are Ce–Ni (282.5 pm), Ce–In (326.8 pm), Ni–In (261.6 pm), and Ni–Ni (242.7 pm).

4.13. *Structure type $\text{Sm}_2\text{Co}_9\text{In}_3$* (fig. 33). SG $Cmmm$; $Z = 2$; $a = 2283.4(4)$, $b = 502.0(1)$, $c = 408.42(8)$ pm. 4Sm : $4g\ x\ 0\ 0$ ($x = 0.3166$); $2\text{Co}1$: $2c\ 1/2\ 0\ 1/2$; $4\text{Co}2$: $4g$ ($x = 0.1212$); $8\text{Co}3$: $8q\ x\ y\ 1/2$ ($x = 0.0931$, $y = 0.2490$); $4\text{Co}4$: $4g$ ($x = 0.4390$); $2\text{In}1$: $2a\ 0\ 0\ 0$; $4\text{In}2$: $4h\ x\ 0\ 1/2$ ($x = 0.2022$) (Baranyak et al., 1993). The CP of the samarium atoms are face capped pentagonal prisms (CN = 17). The Co1 (Co3) and Co4 atoms have a 12-vertices polyhedron similar to the Cu2 and Cu1 atoms in the CaCu_5 structure, (CN = 12), respectively. Co2 has a lower coordination number with an 11-vertices polyhedron. The In1 atoms have a face capped hexagonal prism (CN = 18) and the In2 atoms have a distorted cuboctahedron (CN = 12). The shortest distances are Sm–Co (279.5 pm), Sm–In (326.4 pm), and Co–Co (247.1 pm).

4.14. *Structure type $\text{CeCu}_{4.32}\text{In}_{1.68}$* (fig. 34). SG $Pnmm$; $Z = 8$; $a = 1716.9(6)$, $b = 1090.8(4)$, $c = 520.2(2)$ pm. $2\text{Ce}1$: $2a\ 0\ 0\ 0$; $2\text{Ce}2$: $2d\ 1/2\ 0\ 0$; $4\text{Ce}3$: $4g\ x\ y\ 0$ ($x = 0.7585$, $y = 0.3844$); $4\text{Cu}1$: $4g$ ($x = 0.4653$, $y = 0.3057$); $4\text{Cu}2$: $4g$ ($x = 0.3485$, $y = 0.1581$); $4\text{Cu}3$: $4g$ ($x = 0.1682$, $y = 0.0697$); $4\text{Cu}4$: $4g$ ($x = 0.0942$, $y = 0.4530$); $8\text{Cu}5$: $8h\ x\ y\ z$ ($x = 0.5913$, $y = 0.2534$, $z = 0.2503$); $8\text{Cu}6$: $8h$ ($x = 0.8424$, $y = 0.1344$, $z = 0.2540$); $4M1$: $4g$ ($x = 0.2193$, $y = 0.3003$); $4M2$: $4g$ ($x = 0.5871$, $y = 0.4616$); $4\text{In}1$: $4g$ ($x = 0.9474$, $y = 0.3085$); $4\text{In}2$: $4g$ ($x = 0.6927$, $y = 0.0795$) ($M1 = \text{Cu}_{0.50}\text{In}_{0.50}$; $M2 = \text{Cu}_{0.75}\text{In}_{0.25}$) (Kalychak et al., 1988a). The CP of the Ce1, Ce2, and Ce3 atoms are 20-, 18- and 19-vertices polyhedra, respectively. The first two are similar to the CP of the cerium atoms in the hexagonal CeNi_5In structure and the third one is a hybrid of both (CN = 20; 18; 19). The CP of Cu1, Cu5, Cu6, and M1 are distorted icosahedra (CN = 12), M2 is similar to the Ni3 and Ni4 CP in the CeNi_5In structure (CN = 12). Cu3 has only an 11-vertices polyhedron (CN = 11) and the Cu2 and Cu4 atoms each have a 10-vertices polyhedron, which is similar to those of the Ni2 atoms in CeNi_5In (CN = 10). The In1 and In2 CP are also identical to the indium CP in CeNi_5In (CN = 14). The shortest distances are Ce–Cu (298.6 pm), Ce–In (334.7 pm), Cu–Cu (254.9 pm), Cu–In (268.7 pm), and Cu–M1 (259.5 pm).

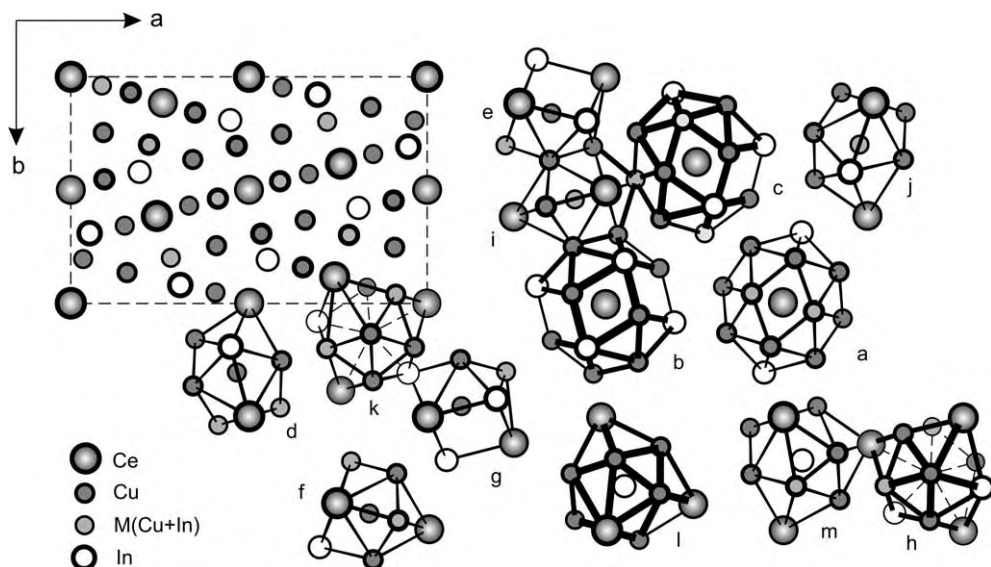


Fig. 34. Projection of the $\text{CeCu}_{4.32}\text{In}_{1.68}$ structure on the xy plane and coordination polyhedra of the atoms: Ce (a–c), Cu (d–i), $M1$ (j), $M2$ (k), and In (l, m) ($M1 = \text{Cu}_{0.50}\text{In}_{0.50}$; $M2 = \text{Cu}_{0.75}\text{In}_{0.25}$).

4.15. *Structure type* YbAg_2In_4 (fig. 35). SG $Im\bar{3}$; $Z = 24$; $a = 1536.2(3)$ pm. 24Yb: $24g$ $0\ y\ z$ ($y = 0.1984$, $z = 0.3149$); 11.8Ag1: $16f$ $x\ x\ x$ ($x = 0.1617$); 5.6Ag2: $16f$ ($x = 0.1448$); 18.2Ag3: $24g$ ($y = 0.2478$, $z = 0.0940$); 7.7Ag4: $24g$ ($y = 0.2164$, $z = 0.084$); 7.7Ag5: $48h$ $x\ y\ z$ ($x = 0.023$, $y = 0.0664$, $z = 0.0850$); 12In1: $12d$ $x\ 0\ 0$ ($x = 0.4089$); 12In2: $12e$ $x\ 0\ 1/2$ ($x = 0.1966$); 24In3: $24g$ ($y = 0.4038$, $z = 0.3497$); 48In4: $48h$ ($x = 0.2012$, $y = 0.1153$, $z = 0.3392$) (Sysa et al., 1998). The ytterbium CP are 16-vertices polyhedra, Ag1 and Ag2 have trigonal prisms with capped rectangular faces (CN = 9), Ag3 and Ag4 have distorted tetragonal antiprisms with a capped base (CN = 9), Ag5 has a 7-vertices polyhedron (CN = 7). In1 and In3 have icosahedra (CN = 12) and In2 and In4 have a 11-vertices polyhedron each (CN = 11). The shortest distances are Yb–Ag (329.5 pm), Yb–In (328.4 pm), Ag–Ag (240.7 pm), and In–In (277.7 pm).

4.16. *Structure type* HoCoGa_5 (Grin et al., 1979a) (fig. 36). SG $P4/mmm$; $Z = 1$; $a = 454.7(1)$, $c = 741.1(2)$ pm for HoCoIn_5 . 1Ho: $1a$ $0\ 0\ 0$; 1Co: $1b$ $0\ 0\ 1/2$; 1In1: $1c$ $1/2\ 1/2\ 0$; 4In2: $4h$ $0\ 1/2\ z$ ($z = 0.3051$) (Kalychak et al., 1989a). The holmium CP are cuboctahedra (CN = 12), the cobalt atoms have a cube-like coordination (CN = 8), the In1 atoms have cuboctahedra (CN = 12), and the In2 atoms have a defective cuboctahedron with coordination number 11. The shortest distances are Ho–In (320.6 pm), In–In (289.0 pm), and Co–In (269.4 pm).

4.17. *Structure type* $\text{Tb}_6\text{Pt}_{12}\text{In}_{23}$ (fig. 37). SG $C2/m$; $Z = 2$; $a = 2834.6(4)$, $b = 440.05(7)$, $c = 1477.1(3)$ pm, $\beta = 112.37(1)^\circ$. 4Tb1: $4i$ $x\ 0\ z$ ($x = 0.45413$, $z = 0.30114$); 4Tb2: $4i$

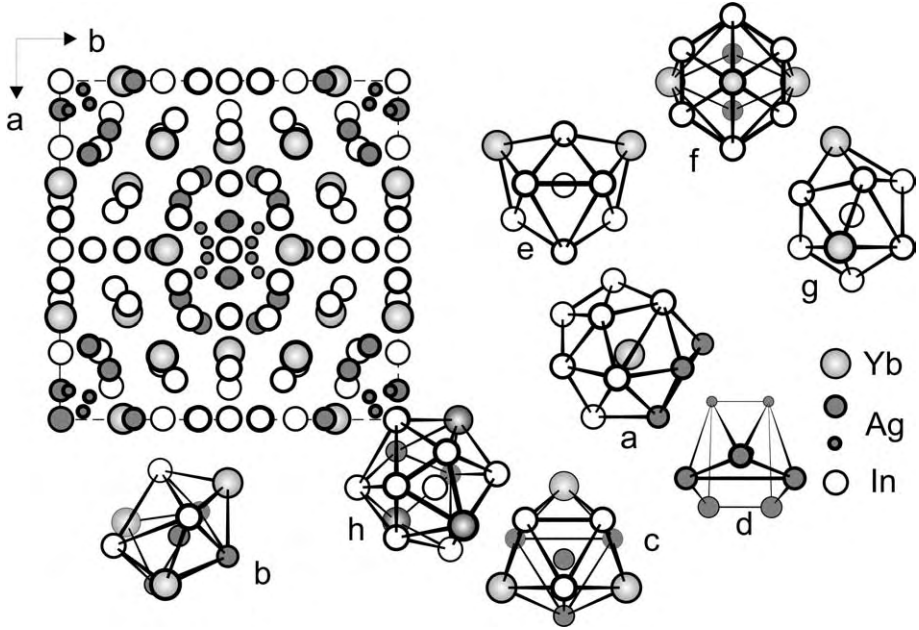


Fig. 35. Projection of the YbAg_2In_4 structure on the xy plane and coordination polyhedra of the atoms: Yb (a), Ag (b–d), and In (e–h). (To simplify the figure, the Ag5 atoms are not up to scale).

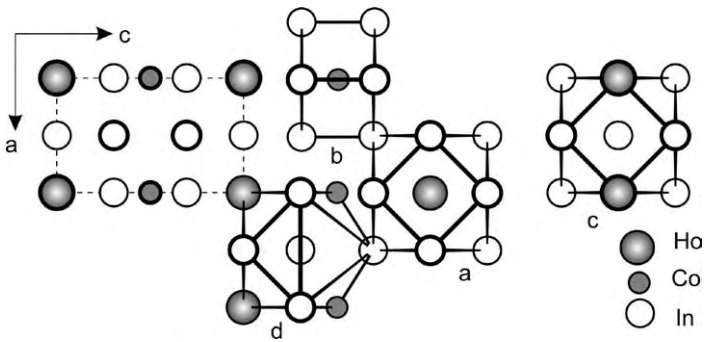


Fig. 36. Projection of the HoCoIn_5 structure on the xz plane and coordination polyhedra of the atoms: Ho (a), Co (b), and In (c, d).

($x = 0.82171$, $z = 0.92201$); 4Tb3: 4*i* ($x = 0.83410$, $z = 0.46938$); 4Pt1: 4*i* ($x = 0.25299$, $z = 0.36389$); 4Pt2: 4*i* ($x = 0.38127$, $z = 0.85045$); 4Pt3: 4*i* ($x = 0.32069$, $z = 0.08940$); 4Pt4: 4*i* ($x = 0.90070$, $z = 0.36563$); 4Pt5: 4*i* ($x = 0.96746$, $z = 0.14225$); 4Pt6: 4*i* ($x = 0.39081$, $z = 0.64133$); 4In1: 4*i* ($x = 0.40793$, $z = 0.04986$); 4In2: 4*i* ($x = 0.71338$, $z =$

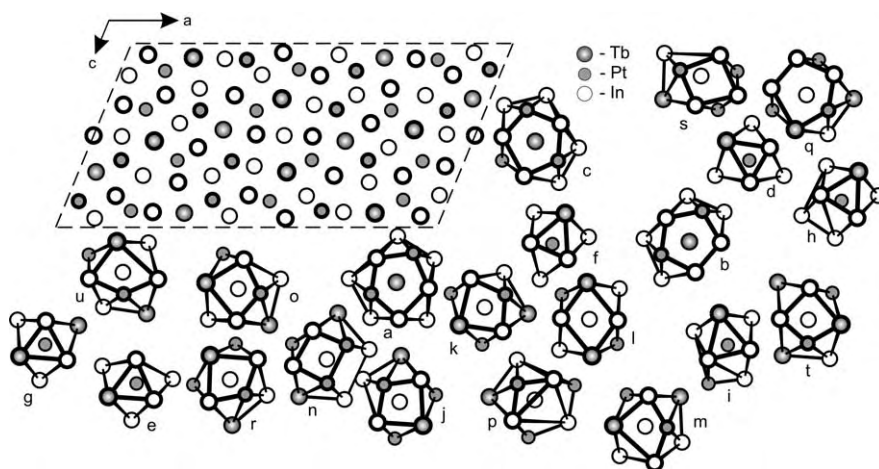


Fig. 37. Projection of the $\text{Tb}_6\text{Pt}_{12}\text{In}_{23}$ structure on the xz plane and coordination polyhedra of the atoms: Tb (a–c), Pt (d–i), and In (j–u).

0.43450); 2In3: $2c\ 0\ 0\ 1/2$; 4In4: $4i\ (x = 0.76219, z = 0.08351)$; 4In5: $4i\ (x = 0.14577, z = 0.27948)$; 4In6: $4i\ (x = 0.04543, z = 0.33334)$; 4In7: $4i\ (x = 0.94389, z = 0.93853)$; 4In8: $4i\ (x = 0.32641, z = 0.28166)$; 4In9: $4i\ (x = 0.87649, z = 0.17059)$; 4In10: $4i\ (x = 0.47123, z = 0.82555)$; 4In11: $4i\ (x = 0.42464, z = 0.49405)$; 4In12: $4i\ (x = 0.72732, z = 0.24450)$ (Zaremba et al., 2002d). The CP of the terbium atoms are pentagonal prisms with five (for Tb1 and Tb3, CN = 15) or four (for Tb2, CN = 14) additional atoms on the equatorial rectangles. The CP of the platinum atoms are trigonal prisms with three (for Pt1–Pt4, CN = 9) and four (for Pt5–Pt6, CN = 10) additional atoms on the equatorial rectangles. The indium atoms have distorted cuboctahedra (for In1–In4, In6, In9–In12), tetragonal prisms with five additional atoms on the equatorial rectangles (CN = 13 for In5). The In7 atoms are coordinated by an 11-vertices polyhedron similar to the In2 atoms in HoCoIn_5 . Pentagonal prisms with four additional atoms on the equatorial rectangles (CN = 14) occur for the In8 atoms. The shortest distances are In–In (290.2 pm), Tb–Pt (284.9 pm), and In–Pt (269.1 pm).

4.18. *Structure type* $\text{Gd}_3\text{Pt}_4\text{In}_{12}$ (fig. 38). SG $P\bar{3}m1$; $Z = 3$, $a = 990.5(1)$, $c = 1529.5(3)$ pm. 1Gd1: $1a\ 0\ 0\ 0$; 2Gd2: $2d\ 1/3\ 2/3\ z\ (z = 0.51246)$; 6Gd3: $6i\ x\ -x\ z\ (x = 0.49152, z = 0.19482)$; 6Pt1: $6i\ (x = 0.82826, z = 0.13791)$; 6Pt2: $6i\ (x = 0.50511, z = 0.38982)$; 2In1: $2c\ 0\ 0\ 0\ (z = 0.3741)$; 2In2: $2d\ (z = 0.8795)$; 6In3: $6g\ x\ 0\ 0\ (x = 0.65033)$; 6In4: $6i\ (x = 0.22110, z = 0.33341)$; 6In5: $6i\ (x = 0.11826, z = 0.17814)$; 6In6: $6i\ (x = 0.78757, z = 0.31395)$; 2In7: $2d\ (z = 0.0819)$; 6In8: $6h\ x\ 0\ 1/2\ (x = 0.71296)$ (Rodewald et al., 2002). The Gd1 and Gd2 atoms have CN 18. The Gd1 CP can be considered as a cuboctahedron with six additional atoms capping the rectangular faces. The CP of the Gd2 atoms are hexagonal prisms with six additional atoms. Gd3 with CN 15 has a low symmetry coordination. Both platinum sites are surrounded by tricapped trigonal prisms (CN 9). The coordination num-

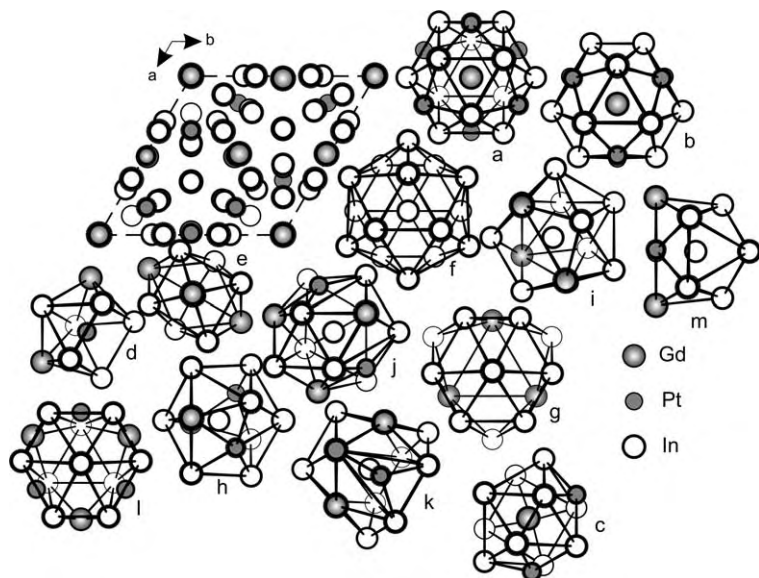


Fig. 38. Projection of the $Gd_3Pt_4In_{12}$ structure on the yz plane and coordination polyhedra of the atoms: Gd (a–c), Pt (d–e), and In (f–m).

bers for the eight crystallographically different indium sites vary from CN 12 to CN 16. In1 has exclusively indium neighbors, while all other indium atoms have gadolinium, platinum, and indium atoms in their coordination shell. All polyhedra contain fragments of icosahedra. The shortest distances are Gd–In (321.2 pm), Gd–Pt (299.2 pm), In–In (284.3 pm), and In–Pt (268.3 pm).

4.19. *Structure type* $Lu_6Co_{17.92}In_{14}$ (fig. 39). SG $Pm\bar{3}$; $Z = 1$; $a = 865.2(3)$ pm. 6Lu: $6g$ $1/2\ 0\ z$ ($z = 0.1824$); 1Co1: $1a\ 0\ 0\ 0$; 12Co2: $12j\ x\ 0\ z$ ($x = 0.1452$, $z = 0.2402$); 0.33Co3: $1b\ 1/2\ 1/2\ 1/2$; 2.70Co4: $6h\ 1/2\ y\ 1/2$ ($y = 0.287$); 1.56Co5: $6h$ ($y = 0.237$); 6In1: $6f\ x\ 0\ 1/2$ ($x = 0.3210$); 8In2: $8i\ x\ x\ x$ ($x = 0.2824$) (Zaremba et al., 1990). The lutetium CP are hexagonal antiprisms with capped faces (CN = 17). Co1 and Co2 have icosahedra (CN = 12), Co4 and Co5 have polyhedra with 12 vertices (CN = 12), which can be considered as strongly distorted icosahedra or cuboctahedra. Co3 has a tetrahexahedron (CN = 14). The In1 atoms have a 13-vertices polyhedron derived from an icosahedron and In2 has a distorted cuboctahedral coordination (CN = 12). The shortest distances are Lu–Lu (318.7 pm), Lu–In (314.1 pm), Co–Co (242.8 pm), Co–In (256.9 pm), and In–In (309.7 pm).

4.20. *Structure type* $MgCu_4Sn$ (Gladyshevskii et al., 1952) (fig. 40). SG $F\bar{4}3m$; $Z = 4$; $a = 705.6(1)$ pm for $CeNi_4In$. 4Ce: $4a\ 0\ 0\ 0$; 16Ni: $16e\ x\ x\ x$ ($x = 5/8$); 4In: $4c\ 1/4\ 1/4\ 1/4$ (Zaremba et al., 1984). The CP of the cerium and indium atoms have 16 vertices (CN = 16).

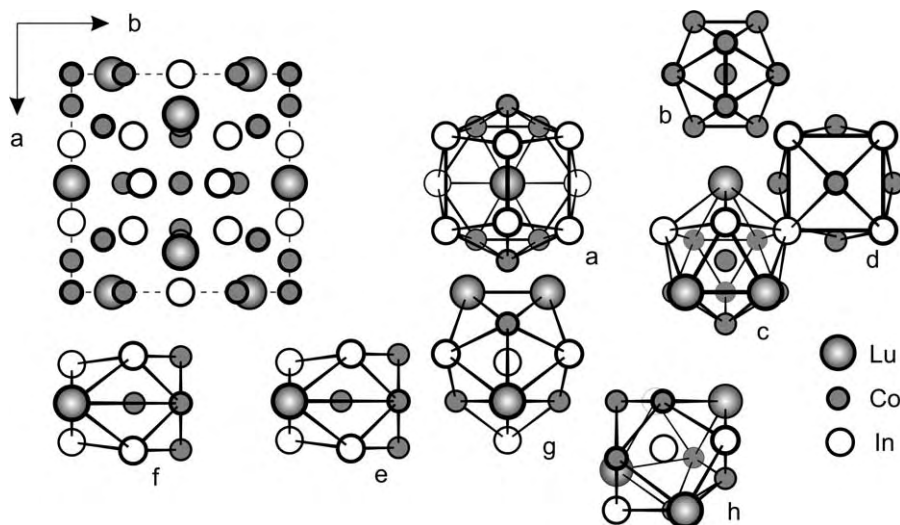


Fig. 39. Projection of the $\text{Lu}_6\text{Co}_{17.92}\text{In}_{14}$ structure on the xy plane and coordination polyhedra of the atoms: Lu (a), Co (b–f), and In (g, h).

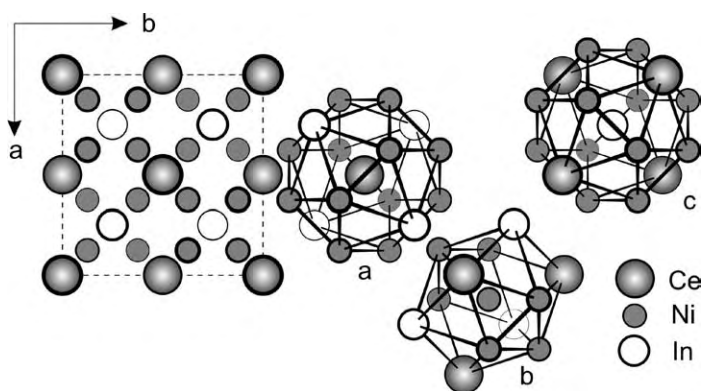


Fig. 40. Projection of the CeNi_4In structure on the xy plane and coordination polyhedra of the atoms: Ce (a), Ni (b), and In (c).

The nickel CP are icosahedra (CN = 12). The shortest distances are Ce–Ni (292.7 pm), Ce–In (305.7 pm), and Ni–Ni (249.7 pm).

4.21. *Structure type* $\text{HoNi}_{2.6}\text{Ga}_{2.4}$ (Grin et al., 1983) (fig. 41). SG $P6/mmm$; $Z = 3$; $a = 933.4(4)$, $c = 435.6(2)$ pm for LaNi_3In_2 . 1La1: $1a\ 0\ 0\ 0$; 2La2: $2d\ 1/3\ 2/3\ 1/2$; 6Ni: $6l\ x\ 2x\ 0$ ($x = 0.1783$); 6M: $6k\ x\ 0\ 1/2$ ($x = 0.2839$; $M = \text{Ni}_{0.48}\text{In}_{0.52}$); 3In: $3f\ 1/2\ 0\ 0$ (Zaremba et al., 1993). The La1 and La2 CP are face capped hexagonal prisms (CN = 20). The nickel

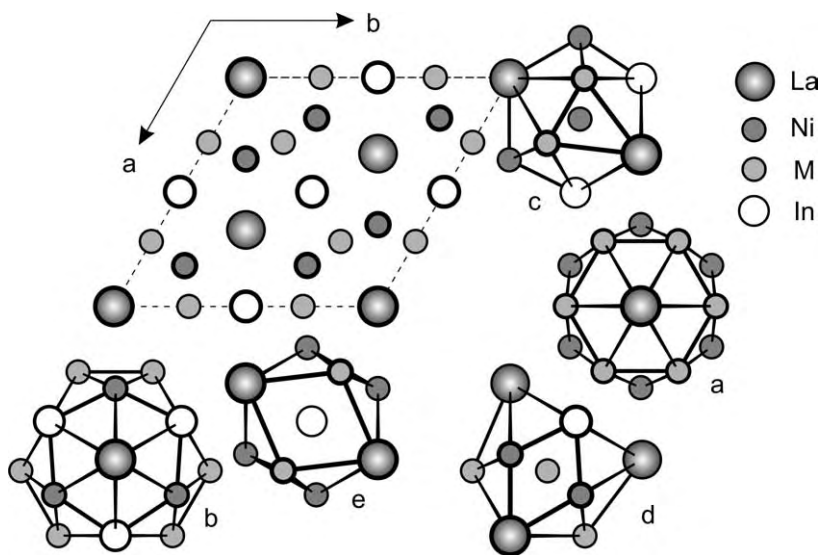


Fig. 41. Projection of the LaNi_3In_2 structure on the xy plane and coordination polyhedra of the atoms: La (a, b), Ni (c), M (d) with $M = \text{Ni}_{0.48}\text{In}_{0.52}$, and In (e).

polyhedra have only 11 vertices (one atom is missing when compared to the Cu_2 atoms in CaCu_5) ($\text{CN} = 11$), the M and indium atoms have a 12-vertices polyhedron each as the Cu_2 atoms in CaCu_5 ($\text{CN} = 12$). The shortest distances are La–Ni (288.2 pm), Ni– M (261.6 pm), M – M (265.0 pm), and M –In (296.9 pm).

4.22. *Structure type YNiAl_4* (Rykhail et al., 1972) (fig. 42). SG $Cmcm$; $Z = 4$; $a = 439.8(1)$, $b = 1660.6(5)$, $c = 727.8(2)$ pm for YbNiIn_4 . 4Yb : $4c\ 0\ y\ 1/4$ ($y = 0.12458$); 4Ni : $4c$ ($y = 0.77398$); $8\text{In}1$: $8f\ 0\ y\ z$ ($y = 0.31307$, $z = 0.04844$); $4\text{In}2$: $4c$ ($y = 0.92806$); $4\text{In}3$: $4b\ 0\ 1/2\ 0$ (Kalychak et al., 1988b). The ytterbium CP are face capped pentagonal prisms ($\text{CN} = 17$), the nickel atoms have trigonal prisms with capped rectangular faces ($\text{CN} = 9$). The In1, In2, and In3 atoms have distorted cuboctahedra ($\text{CN} = 12$). The shortest distances are Yb–In (326.0 pm), Ni–In (255.9 pm), and In–In (309.4 pm).

4.23. *Structure type LaCoAl_4* (Rykhail et al., 1977) (fig. 43). SG $Pmma$; $Z = 2$; $a = 863.7(2)$, $b = 422.5(1)$, $c = 743.1(1)$ pm for YbRhIn_4 . 2Yb : $2e\ 1/4\ 0\ z$ ($z = 0.3980$); 2Rh : $2e$ ($z = 0.8063$); $2\text{In}1$: $2a\ 0\ 0\ 0$; $2\text{In}2$: $2f\ 1/4\ 1/2\ z$ ($z = 0.0656$); $4\text{In}3$: $4j\ x\ 1/2\ z$ ($x = 0.0634$, $z = 0.6860$) (Hoffmann et al., 2000). The ytterbium CP are pentagonal prisms with capped bases and three capped rectangular faces ($\text{CN} = 15$). The rhodium atoms fill trigonal prisms with capped rectangular faces ($\text{CN} = 9$); In1–In3 have a distorted cuboctahedral coordination ($\text{CN} = 12$). The shortest distances are Yb–Rh (303.4 pm), Yb–In (325.0 pm), Rh–In (259.5 pm), and In–In (297.3 pm).

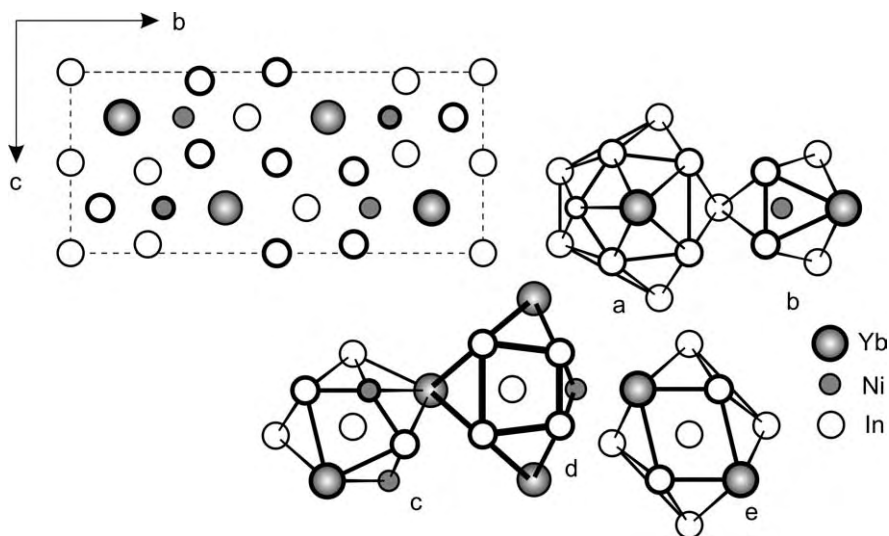


Fig. 42. Projection of the YbNiIn₄ structure on the yz plane and coordination polyhedra of the atoms: Yb (a), Ni (b), and In (c–e).

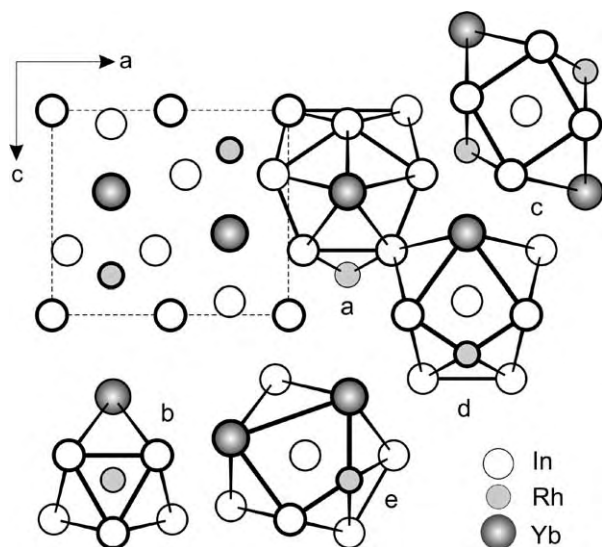


Fig. 43. Projection of the YbRhIn₄ structure on the xz plane and coordination polyhedra of the atoms: Yb (a), Rh (b), and In (c–e).

4.24. Structure type Ho_2CoGa_8 (Grin et al., 1979a) (fig. 44). SG $P4/mmm$; $Z = 1$; $a = 464.0(1)$, $c = 1225.1(3)$ pm for Ce_2CoIn_8 . $2Ce$: $2a\ 0\ 0\ z$ ($z = 0.3105$); $1Co$: $1a\ 0\ 0\ 0$; $2In1$: $2e\ 0\ 1/2\ 1/2$; $2In2$: $2h\ 1/2\ 1/2\ z$ ($z = 0.2962$); $4In3$: $4i\ 0\ 1/2\ z$ ($z = 0.1199$) (Kalychak et al., 1989a). The CP of the cerium, In1, and In2 atoms are cuboctahedra (CN = 12). The

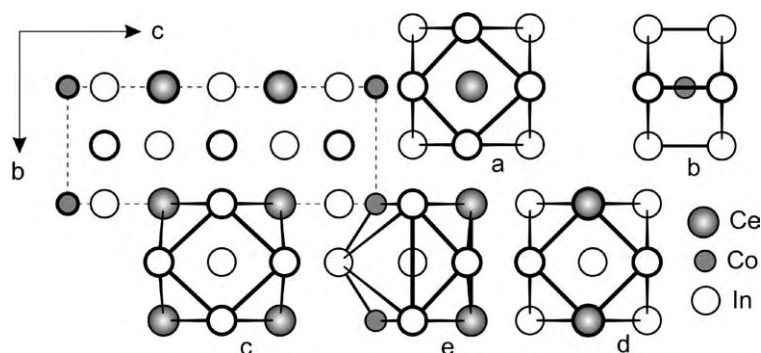


Fig. 44. Projection of the Ce_2CoIn_8 structure on the yz plane and coordination polyhedra of the atoms: Ce (a), Co (b), and In (c–e).

cobalt atoms have a compressed cube-like coordination (CN = 8) and In₃ has an 11-vertices polyhedron similar to the In₂ CP in HoCoGa₅. The shortest distances are Ce–In (328.2 pm), Co–In (274.6 pm), and In–In (293.8 pm).

4.25. *Structure type CePt₂In₂* (fig. 45). SG $P2_1/m$; $Z = 4$; $a = 1018.9(6)$, $b = 447.7(4)$, $c = 1022.6(6)$ pm, $\beta = 117.00(5)^\circ$; 2Ce1: $2e \times 1/4 z$ ($x = 0.0483$, $z = 0.7899$); 2Ce2: $2e$ ($x = 0.4020$, $z = 0.7106$); 2Pt1: $2e$ ($x = 0.0712$, $z = 0.1003$); 2Pt2: $2e$ ($x = 0.1574$, $z = 0.4189$);

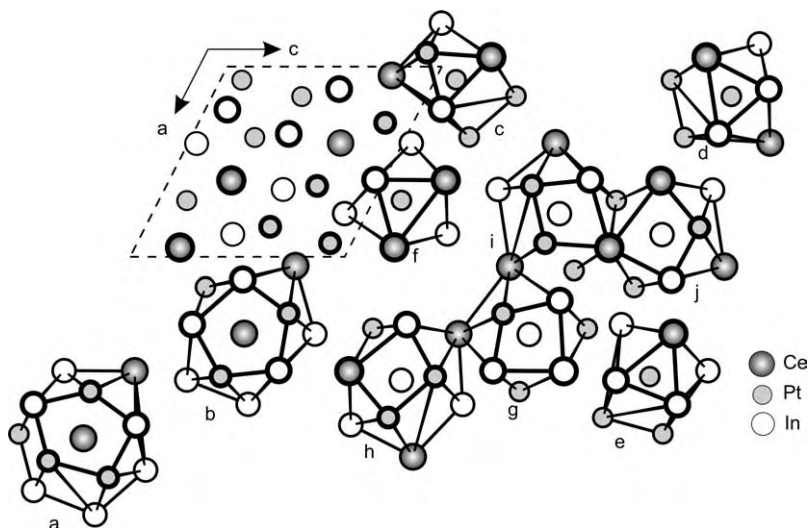


Fig. 45. Projection of the CePt_2In_2 structure on the xz plane and coordination polyhedra of the atoms: Ce (a, b), Pt (c–f), and In (g–j).

2Pt3: $2e$ ($x = 0.3731, z = 0.2975$); 2Pt4: $2e$ ($x = 0.7046, z = 0.1306$); 2In1: $2e$ ($x = 0.4045, z = 0.0408$); 2In2: $2e$ ($x = 0.6462, z = 0.5534$); 2In3: $2e$ ($x = 0.7740, z = 0.8972$); 2In4: $2e$ ($x = 0.8814, z = 0.4246$) (Zaremba et al., 2000a). The cerium CP are pentagonal prisms with six (Ce1, CN = 16) and five (Ce2, CN = 15) additional equatorial atoms. The platinum atoms have a trigonal prismatic coordination with four (Pt1–Pt3, CN = 10) or three (Pt4, CN = 9) equatorial atoms. Most indium atoms have a distorted cuboctahedral environment (CN = 12 for In1 and In4) or a cuboctahedron with an additional atom (CN = 13 for In2 and In3). The shortest distances are Ce–Pt (289.1 pm), Ce–In (328.8 pm), Pt–In (271.4 pm), and In–In (312.6 pm).

4.26. *Structure type* $Ce_2Au_3In_5$ (fig. 46). SG $Pmn2_1$; $Z = 8$; $a = 465.27(8), b = 5348.3(9), c = 740.5(1)$ pm. All atoms are in the Wyckoff position $2\ 0\ y\ z$: 2Ce1: $y = 0.11547, z = 0.9021$; 2Ce2: $y = 0.13424, z = 0.4008$; 2Ce3: $y = 0.28853, z = 0.4342$; 2Ce4: $y = 0.46181, z = 0.9379$; 2Ce5: $y = 0.61566, z = 0.9706$; 2Ce6: $y = 0.63459, z = 0.4696$; 2Ce7: $y = 0.78788, z = 0.4335$; 2Ce8: $y = 0.96172, z = 0.9330$; 2Au1: $y = 0.07123, z = 0.6410$; 2Au2: $y = 0.17904, z = 0.1412$; 2Au3: $y = 0.26207, z = 0.9340$; 2Au4: $y = 0.35112, z = 0.6848$; 2Au5: $y = 0.39911, z = 0.1849$; 2Au6: $y = 0.48762, z = 0.4344$; 2Au7: $y = 0.57116, z = 0.2328$; 2Au8: $y = 0.67868, z = 0.7340$; 2Au9: $y = 0.76202, z = 0.9382$; 2Au10: $y = 0.85087, z = 0.1898$; 2Au11: $y = 0.89903, z = 0.6893$; 2Au12: $y = 0.98763, z = 0.4380$; 2In1: $y = 0.02103, z = 0.1413$; 2In2: $y = 0.02176, z = 0.7327$; 2In3: $y = 0.07458, z = 0.2517$; 2In4: $y = 0.17539, z = 0.7530$; 2In5: $y = 0.22834, z = 0.2295$; 2In6: $y = 0.22884, z = 0.6401$; 2In7: $y = 0.31428, z = 0.9617$; 2In8: $y = 0.34894, z = 0.2992$; 2In9: $y = 0.40070, z = 0.7982$; 2In10: $y = 0.43593, z = 0.4613$; 2In11: $y = 0.52115, z = 0.7285$; 2In12: $y = 0.52145, z = 0.1421$; 2In13: $y = 0.57443, z = 0.6202$; 2In14: $y = 0.67524, z = 0.1202$; 2In15: $y = 0.72821, z = 0.2316$; 2In16: $y = 0.72873, z = 0.6393$; 2In17: $y = 0.81430, z = 0.9107$; 2In18: $y = 0.84922, z = 0.5793$; 2In19: $y = 0.90106, z = 0.0773$; 2In20: $y = 0.93558, z = 0.4087$ (Galadzhun et al., 1999b). The CP of the cerium atoms are pentagonal prisms with six equatorial atoms (CN = 16). The Au3, Au6, Au9, and Au12 atoms are coordinated by trigonal prisms with three capping atoms (CN = 9), while the other gold atoms have trigonal prisms with four equatorial atoms (CN = 10). In7, In10, In17,

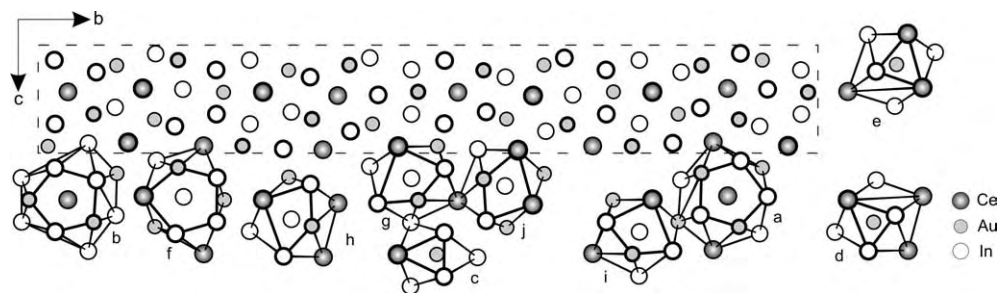


Fig. 46. Projection of the $Ce_2Au_3In_5$ structure on the yz plane and coordination polyhedra of the atoms: Ce (a, b), Au (c–e), and In (f–j). Only representative polyhedra are shown.

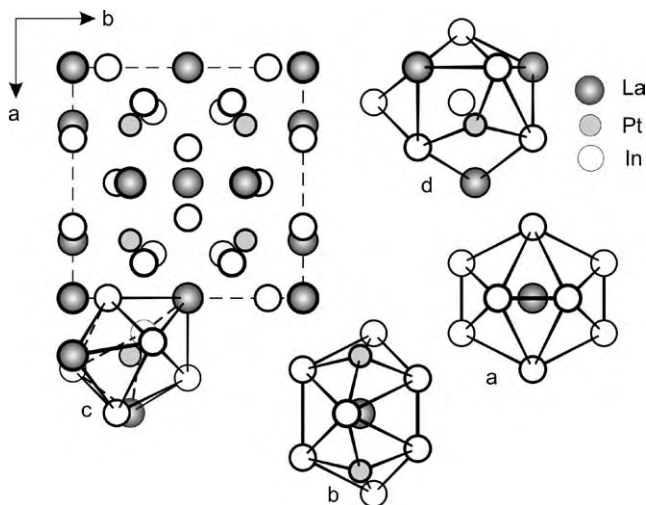


Fig. 47. Projection of the LaPtIn_3 structure on the xy plane and coordination polyhedra of the atoms: La (a, b), Pt (c), and In (d).

and In_{20} have pentagonal prisms with five equatorial atoms ($\text{CN} = 15$) and the coordination polyhedra of the other indium atoms are distorted cuboctahedra ($\text{CN} = 12$). The shortest distances are Ce–Au (305.6 pm), Ce–In (325.3 pm), Au–In (271.6 pm), and In–In (295.1 pm).

4.27. *Structure type LaRuSn_3* (Eisenmann and Schäfer, 1986) (fig. 47). SG $Pm\bar{3}n$; $Z = 8$; $a = 980.4$ pm; $1.81\text{La}1: 2a\ 0\ 0\ 0$; $6\text{La}2: 6c\ 1/2\ 1/4\ 0$; $8\text{Pt}: 8e\ 1/4\ 1/4\ 1/4$; $24\text{In}: 24k\ x\ y\ 0$ ($x = 0.15239$, $y = 0.30906$) for LaPtIn_3 (Galadzhun and Pöttgen, 1999). The $\text{La}1$ CP are icosahedra ($\text{CN} = 12$). $\text{La}2$ has a 16-vertices polyhedron, which can be described as a hexagonal prism built from platinum and indium atoms. The platinum atoms have a tricapped trigonal prismatic coordination ($\text{CN} = 9$) and the indium atoms occupy distorted cuboctahedra ($\text{CN} = 12$). The shortest distances are La–In (337.8 pm), Pt–In (269.4 pm), and In–In (298.8 pm).

4.28. *Structure type $\text{Ce}_4\text{Ni}_7\text{In}_8$* (fig. 48). SG $Cmcm$; $Z = 4$; $a = 1475.2(2)$, $b = 2418.4(3)$, $c = 439.51(8)$ pm; $4\text{Ce}1: 4g\ x\ 0\ 0$ ($x = 0.18413$); $8\text{Ce}2: 8p\ x\ y\ 0$ ($x = 0.17175$, $y = 0.17682$); $4\text{Ce}3: 4j\ 0\ y\ 1/2$ ($y = 0.39366$); $8\text{Ni}1: 8q\ x\ y\ 1/2$ ($x = 0.09462$, $y = 0.09494$); $8\text{Ni}2: 8p$ ($x = 0.64297$, $y = 0.05444$); $4\text{Ni}3: 4h\ x\ 0\ 1/2$ ($x = 0.62174$); $8\text{Ni}4: 8p$ ($x = 0.13832$; $y = 0.34612$); $4\text{In}1: 4j$ ($y = 0.19046$); $4\text{In}2: 4i\ 0\ y\ 0$ ($y = 0.08628$); $8\text{In}3: 8q$ ($x = 0.65787$, $y = 0.21613$); $2\text{In}4: 2d\ 0\ 0\ 1/2$; $2\text{In}5: 2b\ 1/2\ 0\ 0$; $8\text{In}6: 8q$ ($x = 0.22498$, $y = 0.40620$); $4\text{In}7: 4i$ ($y = 0.27729$) (Baranyak et al., 1988a). The CP of $\text{Ce}1$ and $\text{Ce}3$ are hexagonal prisms, which are capped on all faces ($\text{CN} = 20$) and $\text{Ce}2$ has a pentagonal prismatic coordination with additional atoms capping each face ($\text{CN} = 17$). $\text{Ni}1$ and $\text{Ni}2$ have trigonal prisms with four additional atoms ($\text{CN} = 10$), $\text{Ni}3$ has a strongly distorted cuboctahedron ($\text{CN} = 12$), and $\text{Ni}4$ has trigonal prisms with three additional atoms capping the rectangular faces ($\text{CN} = 9$). The $\text{In}1$ – $\text{In}7$ atoms have distorted cuboctahedra ($\text{CN} = 12$). The shortest dis-

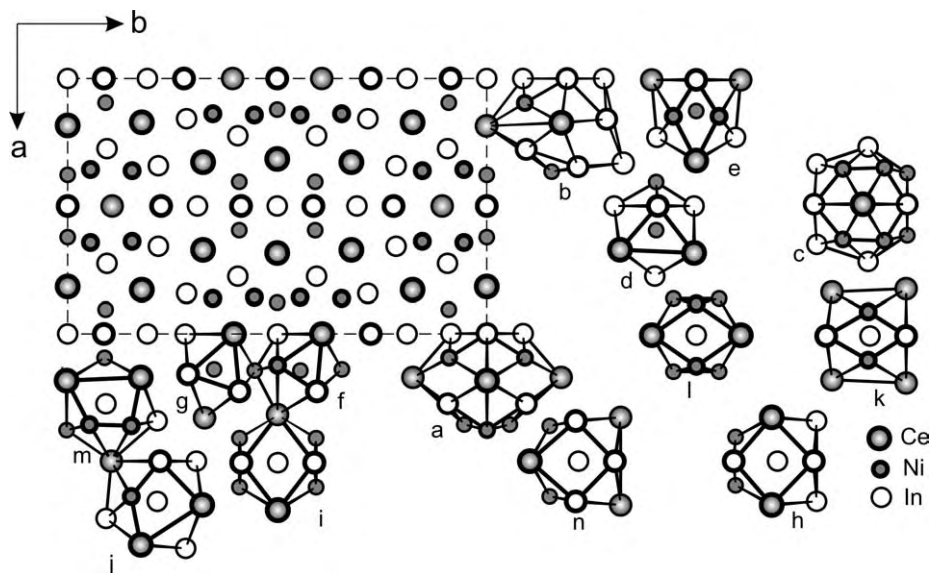


Fig. 48. Projection of the $Ce_4Ni_7In_8$ structure on the xy plane and coordination polyhedra of the atoms: Ce (a–c), Ni (d–g), and In (h–n).

tances are Ce–Ni (285.7 pm), Ce–In (333.3 pm), Ni–Ni (240.7 pm), Ni–In (248.6 pm), and In–In (303.9 pm).

4.29. *Structure type $La_3Au_4In_7$* (fig. 49). SG $I2/m$; $Z = 2$; $a = 460.42(5)$, $b = 1389.5(1)$, $c = 1039.6(2)$ pm, $\alpha = 90.77(1)^\circ$. $2La1: 2a\ 0\ 0\ 0$; $4La2: 4i\ 0\ y\ z$ ($y = 0.31110$, $z = 0.00504$); $4Au1: 4i$ ($y = 0.65405$, $z = 0.38435$); $4Au2: 4i$ ($y = 0.12836$, $z = 0.27750$); $2In1: 2b\ 0\ 0\ 1/2$; $4In2: 4i$ ($y = 0.32455$, $z = 0.35676$); $4In3: 4i$ ($y = 0.83943$, $z = 0.26837$); $4In4: 4i$ ($y = 0.50319$, $z = 0.21248$) (Galadzhun et al., 2000a). The La1 CP are hexagonal prisms with six equatorial atoms (CN = 18), La2 has pentagonal prisms with seven equatorial atoms (CN = 17), Au1 and Au2 have trigonal prisms with three and four equatorial atoms (CN = 9 and CN = 10), and In1–In4 have distorted cuboctahedra (CN = 12). The shortest distances are La–Au (332.7 pm), La–In (331.5 pm), Au–In (270.4 pm), and In–In (291.7 pm).

4.30. *Structure type anti- $Hf_2Co_4P_3$* (Ganglberger, 1968) (fig. 50). SG $P\bar{6}2m$; $Z = 4$; $a = 1489.7(3)$, $c = 454.90(7)$ pm for $Eu_2Au_3In_4$. $3Eu1: 3g\ x\ 0\ 1/2$ ($x = 0.8195$); $2Eu2: 2c\ 1/3\ 2/3\ 0$; $3Eu3: 3f\ x\ 0\ 0$ ($x = 0.4522$); $3Au1: 3f$ ($x = 0.1789$); $6Au2: 6k\ x\ y\ 1/2$ ($x = 0.6788$, $y = 0.5081$); $3Au3: 3f$ ($x = 0.6569$); $3In1: 3g$ ($x = 0.2807$); $6In2: 6j\ x\ y\ 0$ ($x = 0.8012$, $y = 0.6187$); $6In3: 6k$ ($x = 0.8762$, $y = 0.5265$); $1In4: 1a\ 0\ 0\ 0$ (Hoffmann et al., 1999). The Eu1 and Eu2 CP are face capped hexagonal prisms (CN = 20) and face capped pentagonal prisms for Eu3, CN = 18. The gold atoms have tricapped trigonal prisms (CN = 9) and the indium atoms have either distorted cuboctahedra (CN = 12 for In1–In3) or tricapped trigonal

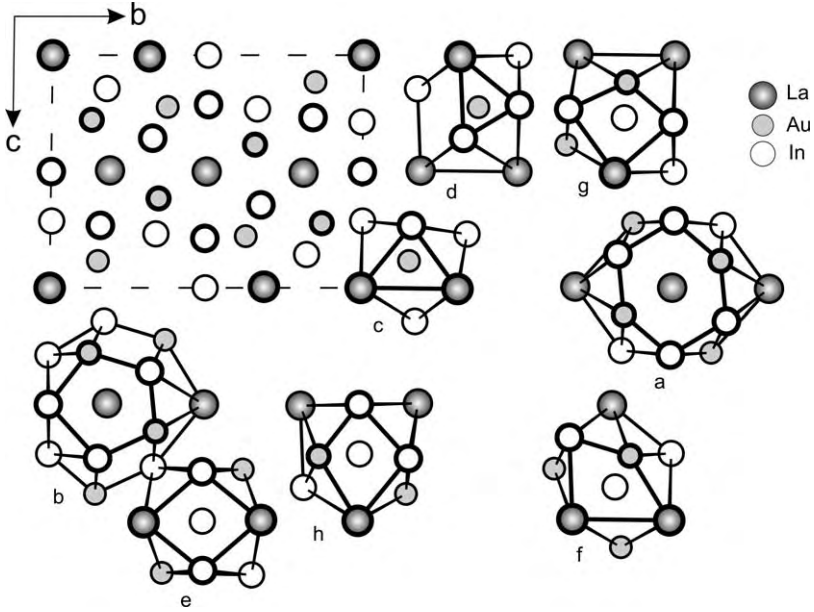


Fig. 49. Projection of the $\text{La}_3\text{Au}_4\text{In}_7$ structure on the yz plane and coordination polyhedra of the atoms: La (a, b), Au (c–d), and In (e–h).

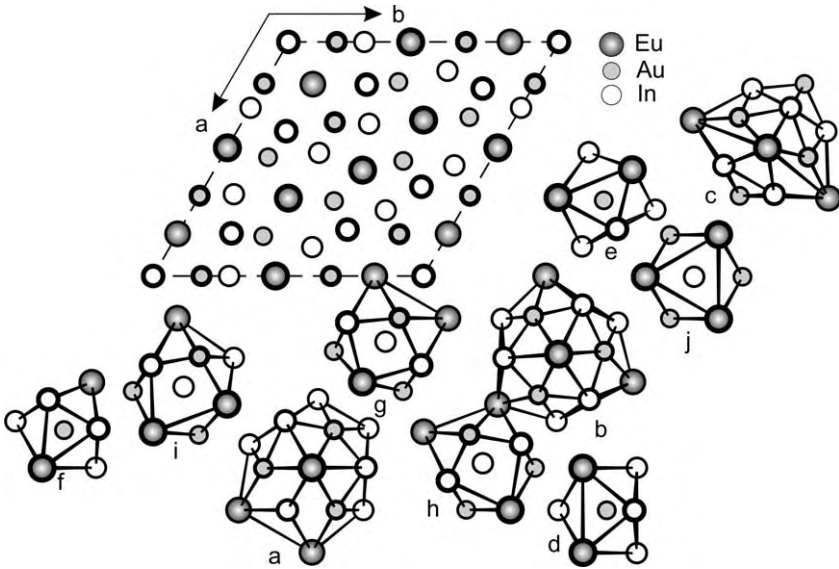


Fig. 50. Projection of the $\text{Eu}_2\text{Au}_3\text{In}_4$ structure on the xy plane and coordination polyhedra of the atoms: Eu (a–c), Au (d–f), and In (g–j).

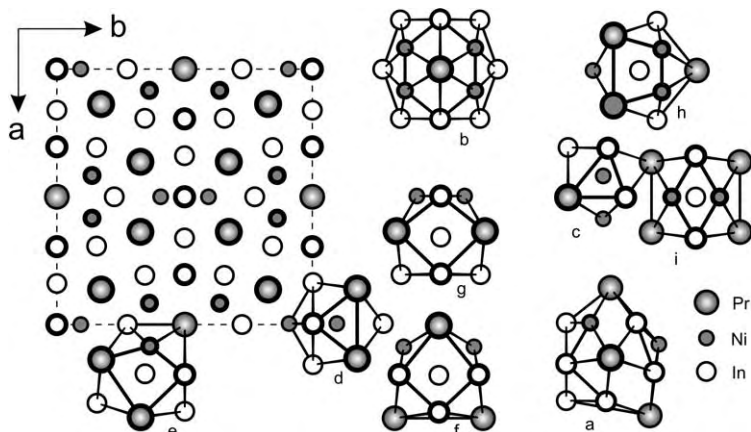


Fig. 51. Projection of the $\text{Pr}_5\text{Ni}_6\text{In}_{11}$ structure on the xy plane and coordination polyhedra of the atoms: Pr (a, b), Ni (c, d), and In (e–i).

prisms (In4 with CN = 9). The shortest distances are Eu–Au (304.9 pm), Eu–In (337.3 pm), Au–In (266.5 pm), and In–In (313.7 pm).

4.31. *Structure type* $\text{Pr}_5\text{Ni}_6\text{In}_{11}$ (fig. 51). SG $Cmmm$; $Z = 2$; $a = 1457.9(6)$; $b = 1457.9(6)$; $c = 440.0(1)$ pm. 8Pr1: $8p\ x\ y\ 0$ ($x = 0.36301$, $y = 0.32683$); 2Pr2: $2c\ 1/2\ 0\ 1/2$; 8Ni1: $8p\ (x = 0.41618, y = 0.13737)$; 4Ni2: $4j\ 0\ y\ 1/2$ ($y = 0.90655$); 8In1: $8q\ x\ y\ 1/2$; ($x = 0.30739$; $y = 0.15587$); 4In2: $4g\ x\ 0\ 0$ ($x = 0.69544$); 4In3: $4h\ x\ 0\ 1/2$ ($x = 0.16067$); 4In4: $4j\ (y = 0.72503)$; 2In5: $2a\ 0\ 0\ 0$ (Kalychak et al., 1987). The Pr1 CP are face capped pentagonal prisms similar to the Ce2 CP in $\text{Ce}_4\text{Ni}_7\text{In}_8$ (CN = 17), Pr2 has face capped hexagonal prisms (CN = 20), Ni1 and Ni2 have tricapped (CN = 9) or tetrapped (CN = 10) trigonal prisms, and the In1–In5 atoms have distorted cuboctahedra (CN = 12). The shortest distances are Pr–Ni (286.8 pm), Pr–In (322.0 pm), Ni–Ni (244.3 pm), Ni–In (258.1 pm), and In–In (298.3 pm).

4.32. *Structure type* $\text{Ce}_8\text{Pd}_{24}\text{Sb}$ (Gordon and DiSalvo, 1996) (fig. 52). SG $Pm\bar{3}m$; $Z = 1$; $a = 844.57$ pm for $\text{Ce}_8\text{Pd}_{24}\text{In}$; 8Ce: $8g\ x\ x\ x$ ($x = 0.25140$); 6Pd1: $6f\ x\ 1/2\ 1/2$ ($x = 0.25552$); 6Pd2: $6e\ x\ 0\ 0$ ($x = 0.31118$); 12Pd3: $12h\ x\ 1/2\ 0$ ($x = 0.26675$); 1In: $1a\ 0\ 0\ 0$. (Gordon et al., 1996). The cerium CP have 19 vertices (CN = 19), the Pd1 and Pd3 CP are slightly distorted cuboctahedra (CN = 12), Pd2 has base capped tetragonal antiprisms (CN = 10), and the indium atoms have tetrahexahedra (CN = 14). The shortest distances are Ce–Ce (419.9 pm), Ce–Pd (297.0 pm), Ce–In (367.8 pm), Pd–Pd (276.0 pm), and Pd–In (262.8 pm).

4.33. *Structure type* PrCo_2Ga (Yarmolyuk and Kripyakevich, 1976) (fig. 53). SG $Pmma$; $Z = 2$; $a = 503.3(1)$, $b = 405.0(2)$, $c = 712.2(2)$ pm for TbCo_2In . 2Tb: $2e\ 1/4\ 1/2\ z$

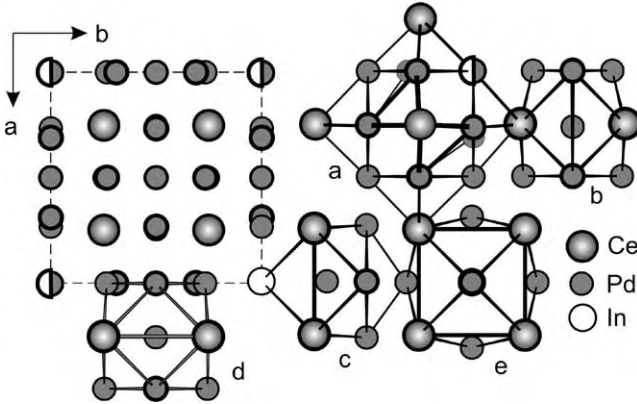


Fig. 52. Projection of the $\text{Ce}_8\text{Pd}_{24}\text{In}$ structure on the xy plane and coordination polyhedra of the atoms: Ce (a), Pd (b-d), and In (e).

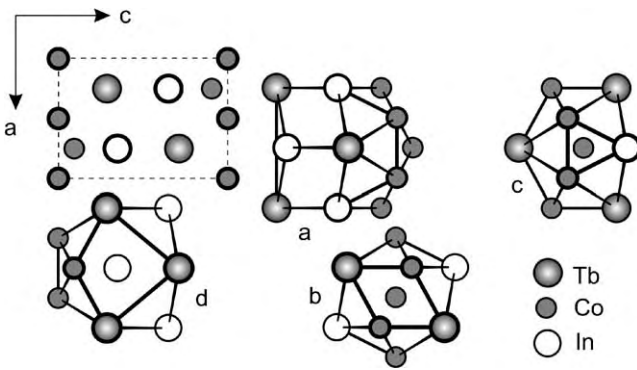


Fig. 53. Projection of the TbCo_2In structure on the xz plane and coordination polyhedra of the atoms: Tb (a), Co (b, c) and In (d).

($z = 0.28813$); $2\text{Co}1: 2b\ 0\ 0\ 0$; $2\text{Co}2: 2e\ (z = 0.9064)$; $2\text{In}: 2f\ 1/4\ 0\ z\ (z = 0.65061)$ (Kalychak et al., 1993a). The TbCo_2In structure differs from the PrCo_2Ga structure, because the indium atoms occupy the $\text{Co}1$ position $2f$ instead of the gallium position $2e$. The terbium CP are 17-vertices polyhedra, which are similar to the samarium CP in $\text{Sm}_2\text{Co}_9\text{In}_3$ ($\text{CN} = 17$). $\text{Co}1$ has a 12-vertices polyhedron, which is similar to the $\text{Cu}2$ CP in CaCu_5 ($\text{CN} = 12$) and $\text{Co}2$ has an 11-vertices polyhedron ($\text{CN} = 11$). The indium atoms have a distorted cuboctahedral coordination ($\text{CN} = 12$). Two more indium atoms at longer distances can be included in the coordination sphere, resulting in higher coordination numbers. These coordinations are similar to those in ZrNiAl and $\text{Lu}_3\text{Co}_{2-x}\text{In}_4$. The shortest distances are Tb-Co (272.8 pm), Tb-In (326.0 pm), Co-Co (247.5 pm), and Co-In (272.4 pm).

4.34. *Structure type GdPt_2Sn* (De Mooij and Buschow, 1984) (fig. 54). SG $P6_3/mmc$; $Z = 2$; $a = 464.45(7)$, $c = 935.4(2)$ pm for LaPd_2In . $2\text{La}: 2c\ 1/3\ 2/3\ 1/4$; $4\text{Pd}: 4f\ 1/3\ 2/3\ z\ (z = 0.5779)$; $2\text{In}: 2a\ 0\ 0\ 0$ (Xue et al., 1992). The lanthanum CP are 14-vertices polyhedra, which can be considered as distorted, base capped hexagonal prisms ($\text{CN} = 14$). The palladium coordination derives from an icosahedron, but with the reduced $\text{CN} = 11$. The indium atoms

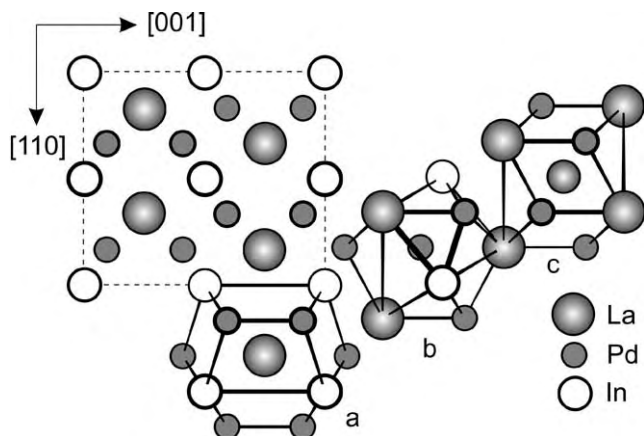


Fig. 54. Projection of the LaPd₂In structure in the orthohexagonal setting and coordination polyhedra of the atoms: La (a), Pd (b), and In (c).

have defective rhombododecahedra (CN = 12). The shortest interatomic distances are La–Pd (306.2 pm), La–In (355.8 pm), and Pd–In (277.7 pm). Similar atomic arrangements occur in LiCu₂Sn (Kripyakevich and Oleksiv, 1970) and ZrPt₂Al (Ferro et al., 1975). The series of RPt₂In ($R = \text{Gd, Tb, Dy, Ho, Y}$; Dwight, 1987) has mistakenly been ascribed to the ZrPt₂Al type, in which the $2a$ position is occupied by the R atoms and $2c$ by the indium atoms.

4.35. *Structure type MnCu₂Al* (Heusler, 1934) (fig. 55). SG $Fm\bar{3}m$; $Z = 4$; $a = 684.5(1)$ pm for LaCu₂In. 4La: $4b \frac{1}{2} \frac{1}{2} \frac{1}{2}$; 8Cu: $4c \frac{1}{4} \frac{1}{4} \frac{1}{4}$; 4In: $4a 0 0 0$ (Kalychak et al., 1984a). The CP of the three atomic sites are rhombododecahedra (CN = 14), if the atoms have similar radii. The CN14 CP occur for the larger size R and indium atoms in the RCu₂In structures, while the copper atoms have only CN 8 in the form of a cube, because the six copper atoms at 342.2 pm may not be included into the nearest coordination sphere. The shortest distances are La–Cu (296.4 pm), La–In (342.2 pm), and Cu–In (296.4 pm). In a first publication (Marazza et al., 1975), the tungsten or CsCl types have been assigned to the RAu₂In compounds. The later work (Besnus et al., 1985) correctly refers to the MnCu₂Al type.

4.36. *Structure type MgCuAl₂* (Perlitz and Westgren, 1943) (fig. 56). SG $Cmcm$; $Z = 4$; $a = 432.8(2)$, $b = 1042.3(2)$, $c = 730.3(2)$ pm for TbNiIn₂. 4Tb: $4c 0 y \frac{1}{4}$ ($y = 0.0705$);

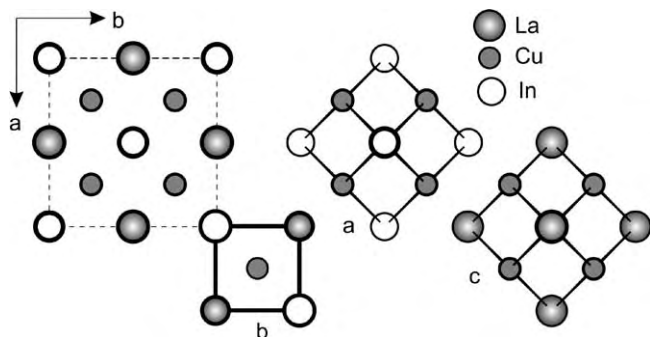


Fig. 55. Projection of the LaCu₂In structure on the xy plane and coordination polyhedra of the atoms: La (a), Cu (b), and In (c).

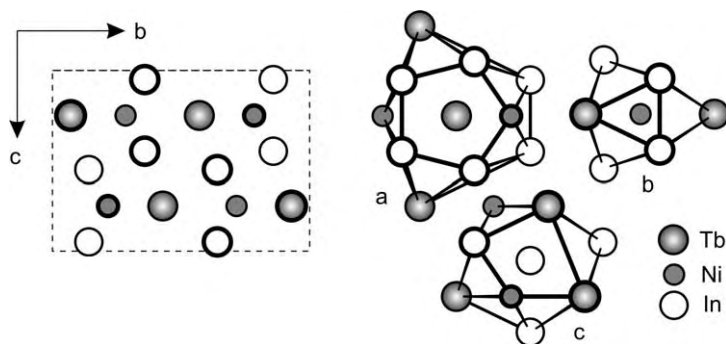


Fig. 56. Projection of the TbNiIn₂ structure on the yz plane and coordination polyhedra of the atoms: Tb (a), Ni (b), and In (c).

4Ni: $4c$ ($y = 0.7844$); 8In: $8f\ 0\ y\ z$; ($y = 0.3589$, $z = 0.0506$) (Zaremba et al., 1987a). The terbium CP are pentacapped pentagonal prisms (CN = 15). Two additional terbium atoms, which cap the prism bases, can be included in the coordination sphere of the terbium atoms. Their Tb–Tb distance corresponds to the lattice parameter a . The nickel CP are tricapped trigonal prisms (CN = 9); the indium atoms have a distorted cuboctahedral coordination (CN = 12). The shortest distances are Tb–Ni (299.1 pm), Tb–In (317.0 pm), Ni–In (265.6 pm), and In–In (290.7 pm).

4.37. *Structure type PrNiIn₂* (fig. 57). SG $Cmcm$; $Z = 20$; $a = 440.0(2)$, $b = 1833.9(6)$, $c = 2164.6(5)$ pm. 8Pr1: $8f\ 0\ y\ z$ ($y = 0.22883$, $z = 0.12764$); 8Pr2: $8f$ ($y = 0.43744$, $z = 0.07986$); 4Pr3: $4c\ 0\ y\ 1/4$ ($y = 0.46930$); 8Ni1: $8f$ ($y = 0.01428$, $z = 0.15791$); 8Ni2: $8f$ ($y = 0.34429$, $z = 0.53222$); 4Ni3: $4c$ ($y = 0.31569$); 8In1: $8f$ ($y = 0.06702$, $z = 0.04296$); 8In2: $8f$ ($y = 0.13635$, $z = 0.67518$); 8In3: $8f$ ($y = 0.19974$, $z = 0.53323$); 8In4: $8f$ ($y = 0.59918$, $z = 0.14383$); 4In5: $4c$ ($y = 0.10966$); 4In6: $4c$ ($y = 0.72458$) (Zaremba et al., 2000c). The Pr1–Pr3 CP are pentacapped pentagonal prisms (CN = 15), Ni1–Ni3 have tricapped trigonal prisms (CN = 9), and In1–In6 have distorted cuboctahedra (CN = 12). The shortest distances are Pr–Ni (281.1 pm), Pr–In (325.1 pm), Ni–In (263.1 pm), and In–In (301.8 pm).

4.38. *Structure type HfNiGa₂* (Markiv et al., 1988; Schlüter et al., 2003) (fig. 58). SG $I4mm$; $Z = 20$; $a = 1397.7(1)$, $c = 925.5(1)$ pm for PrPdIn₂. 8Pr1: $8d\ x\ 0\ z$ ($x = 0.71950$, $z = 0.61820$); 8Pr2: $8c\ x\ x\ z$ ($x = 0.703249$, $z = 0.63088$); 2Pr3: $2a\ 0\ 0\ z$ ($z = 0.01276$); 2Pr4: $2a$ ($z = 0.54244$); 8Pd1: $8d$ ($x = 0.78208$, $z = 0.97650$); 8Pd2: $8c$ ($x = 0.66014$, $z = 0.96880$); 4Pd3: $4b\ 0\ 1/2\ z$ ($z = 0.88810$); 16In1: $16e\ x\ y\ z$ ($x = 0.85917$, $y = 0.64726$, $z = 0.88008$); 8In2: $8d$ ($x = 0.83413$, $z = 0.28644$); 8In3: $8d$ ($x = 0.61702$, $z = 0.14024$); 8In4: $8c$ ($x = 0.86651$, $z = 0.78597$) for PrPdIn₂ (Zaremba et al., 2003c). The four crystallographically different praseodymium atoms have coordination numbers 16 (Pr4) and 17 (Pr1–Pr3) with quite irregular coordination polyhedra. This is also the case for the palladium atoms, which

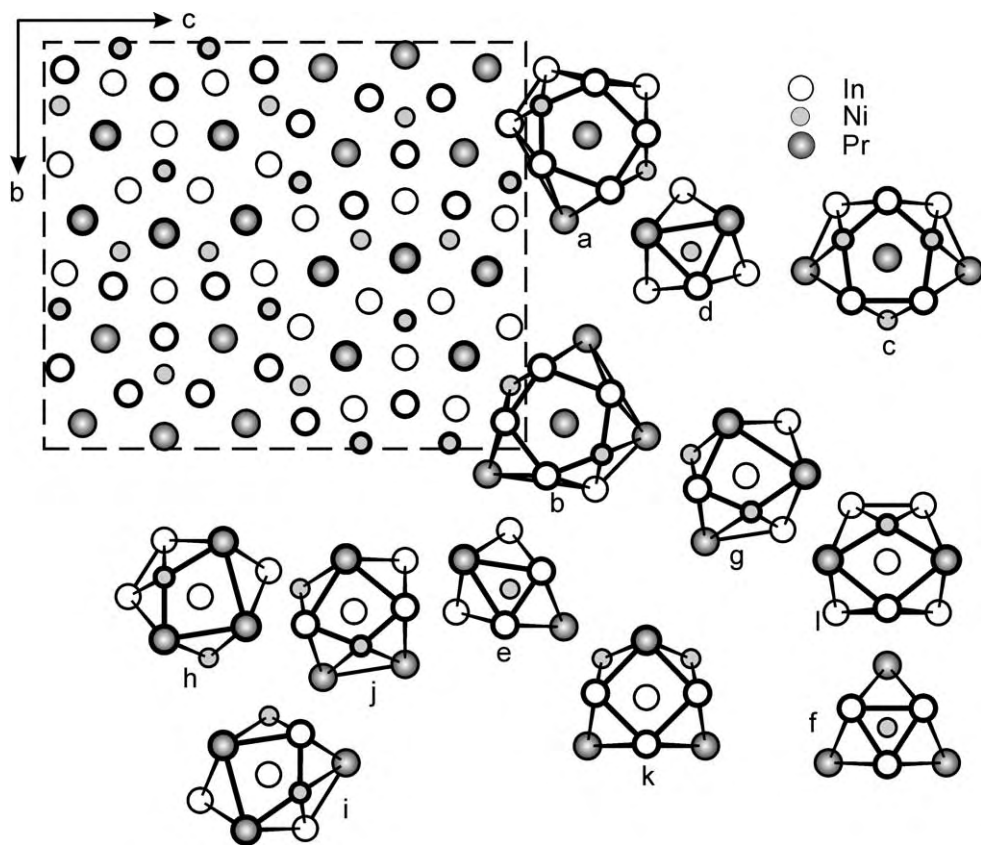


Fig. 57. Projection of the PrNiIn_2 structure on the yz plane and coordination polyhedra of the atoms: Pr (a–c), Ni (d–f), and In (g–l).

have CN 10 (Pd1 and Pd2) and CN 12 (Pd3). The coordination numbers for the In1–In4 atoms range from CN 13 to CN 15. All indium atoms have praseodymium, palladium, and indium neighbors. The shortest distances are Pr–Pd (306.4 pm), Pr–In (318.0 pm), Pd–In (276.0 pm), and In–In (304.5 pm).

4.39. *Structure type* $\text{Ho}_{10}\text{Ni}_9\text{In}_{20}$ (fig. 59). SG $P4/nmm$; $Z = 2$; $a = 1328.6(3)$, $c = 908.3(3)$ pm. $2\text{Ho}1: 2c \ 1/4 \ 1/4 \ z$ ($z = 0.6382$); $2\text{Ho}2: 2c$ ($z = 0.1696$); $8\text{Ho}3: 8i \ 1/4 \ y \ z$ ($y = 0.5277$, $z = 0.2324$); $8\text{Ho}4: 8j \ x \ x \ z$ ($x = 0.4538$, $z = 0.7334$); $2\text{Ni}1: 2a \ 1/4 \ 3/4 \ 0$; $8\text{Ni}2: 8i$ ($y = 0.0272$, $z = 0.5899$); $8\text{Ni}3: 8j$ ($x = 0.5948$, $z = 0.8997$); $8\text{In}1: 8g \ x \ y \ 0$ ($x = 0.0964$, $y = 0.9036$); $8\text{In}2: 8h \ x \ y \ 1/2$ ($x = 0.6207$, $y = 0.3793$); $8\text{In}3: 8i$ ($y = 0.0824$, $z = 0.9060$); $8\text{In}4: 8i$ ($y = 0.8654$, $z = 0.7659$); $8\text{In}5: 8j$ ($x = 0.3820$, $z = 0.4101$) (Zaremba et al., 1987b). The Ho1–Ho3 CP are pentagonal prisms with capped bases and four capped rectangular faces (CN = 16). The Ho4 atoms, however, have a completely face capped pen-

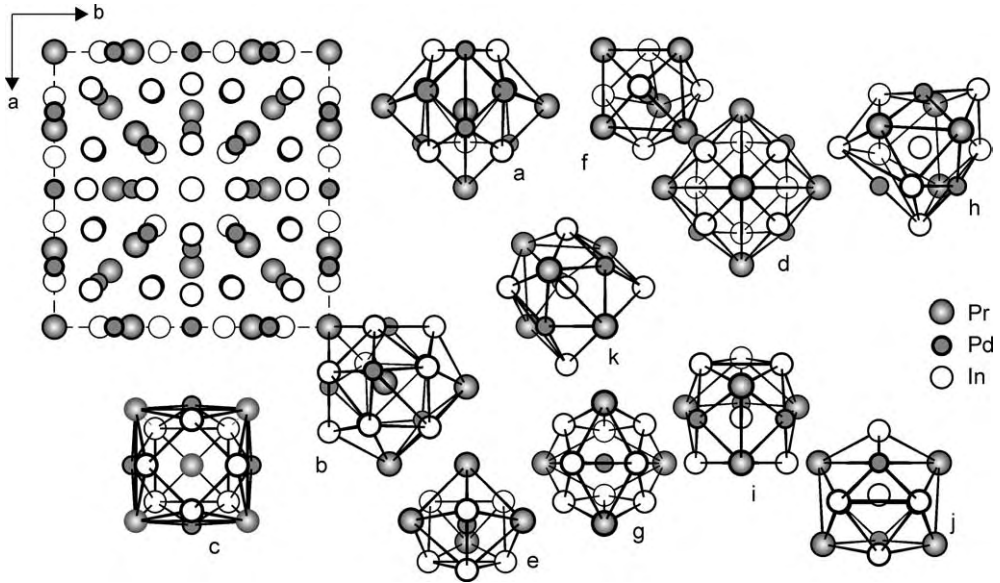


Fig. 58. Projection of the PrPdIn_2 structure on the xy plane and coordination polyhedra of the atoms: Pr (a–d), Pd (e–g), and In (h–k).

tagonal prism (CN = 17). Ni1 has a bisfenoid (CN = 8), Ni2 and Ni3 have distorted base capped tetragonal antiprisms (CN = 10). In1 and In2 have distorted cuboctahedra (CN = 12), while In3 and In5 have distorted cuboctahedra with an additional atom (CN = 13). In4 has a distorted icosahedral coordination (CN = 12). The shortest distances are Ho–Ni (288.7 pm), Ho–In (307.4 pm), Ni–In (262.1 pm), and In–In (296.9 pm).

4.40. *Structure type* $\text{La}_6\text{Co}_{11}\text{Ga}_3$ (Sichevich et al., 1985) is identical to $\text{Nd}_6\text{Fe}_{13}\text{Si}$ (Allemand et al., 1990) (fig. 60). SG $I4/mcm$; $Z = 4$; $a = 810.2$, $c = 2357.6$ pm for $\text{La}_6\text{Co}_{13}\text{In}$. 16La1: $16l \ x \ 1/2 + x \ z$ ($x = 0.1627$, $z = 0.1857$); 8La2: $8f \ 0 \ 0 \ z$ ($z = 0.8944$); 16Co1: $16l \ (x = 0.1795, z = 0.0585)$; 16Co2: $16k \ x \ y \ 0$ ($x = 0.0659, y = 0.2103$); 16Co3: $16l \ (x = 0.3856, z = 0.0936)$; 4Co4: $4d \ 0 \ 1/2 \ 0$; 4In: $4a \ 0 \ 0 \ 1/4$. The atomic coordinates are taken from the isostructural compound with lead $\text{Pr}_6\text{Fe}_{13}\text{Pb}$ (Weitzer et al., 1993). The La1 and La2 CP are pentacapped pentagonal prisms with one (CN = 16) and two (CN = 17) capped bases, Co1–Co4 have distorted icosahedra (CN = 12), and the indium atoms have base capped tetragonal antiprisms (CN = 10). The shortest distances are La–La (357.4 pm), La–Co (300.1 pm), La–In (339.2 pm), and Co–Co (240.7 pm).

4.41. *Structure types* Fe_2P (Rundqvist and Jellinek, 1959) and ZrNiAl (Kripyakevich et al., 1967) (fig. 61). These structures are related via their coloring of the atoms on the four Wyckoff positions. In the latter, the zirconium and aluminum atoms take the positions of the iron atoms in the Fe_2P structure. In the ternary indides of equiatomic composition RTIn ($T = \text{Ni, Cu}$,

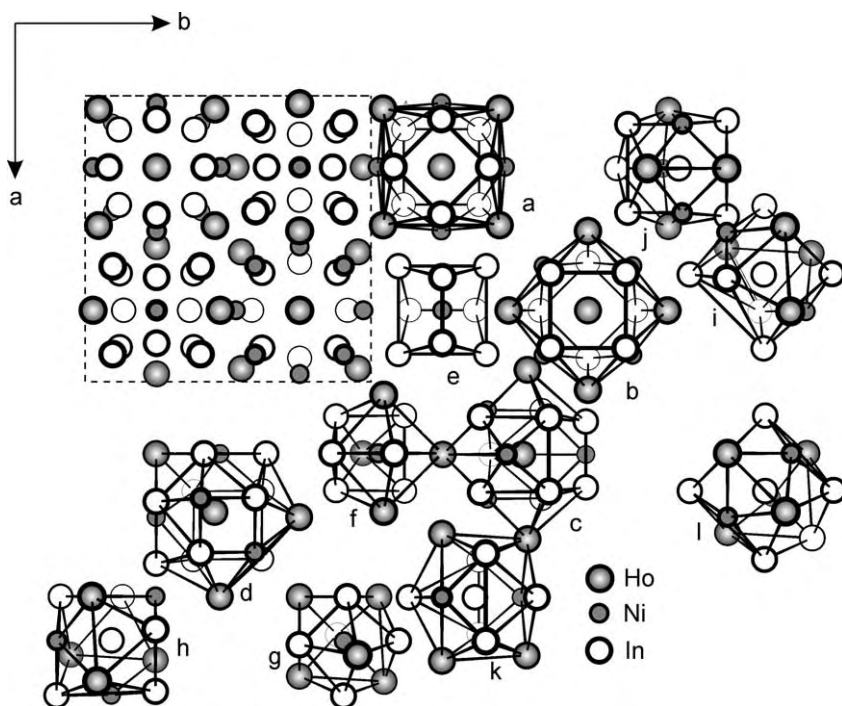


Fig. 59. Projection of the $\text{Ho}_{10}\text{Ni}_9\text{In}_{20}$ structure on the xy plane and coordination polyhedra of the atoms: Ho (a–d), Ni (e–g), and In (h–l).

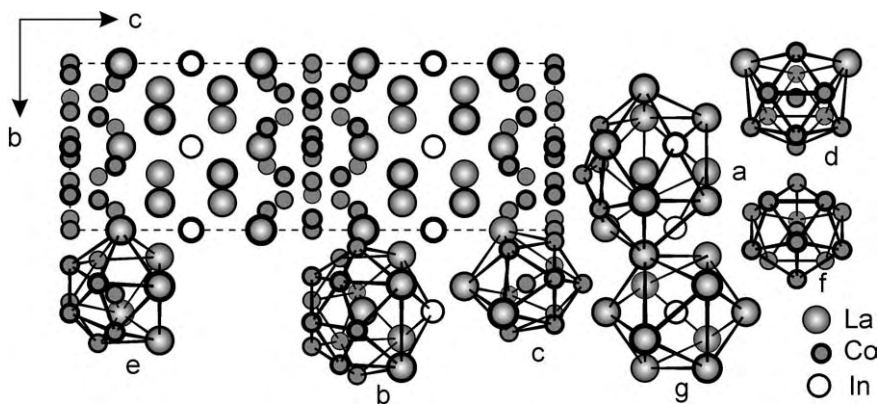


Fig. 60. Projection of the $\text{La}_6\text{Co}_{13}\text{In}$ structure on the yz plane and coordination polyhedra of the atoms: La (a, b), Co (c–f), and In (g).

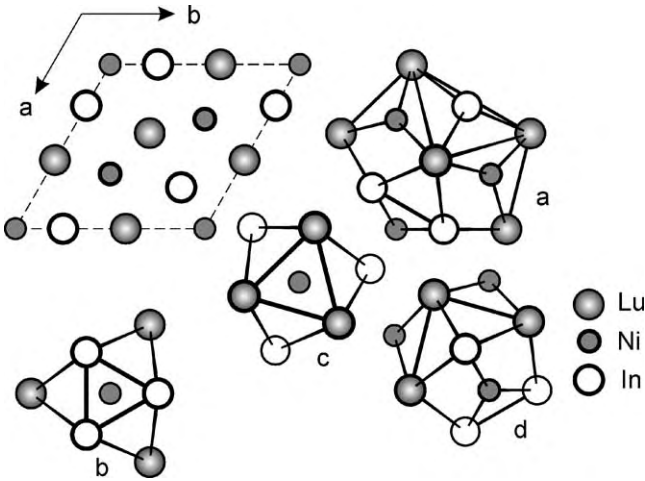


Fig. 61. Projection of the LuNiIn structure on the xy plane and coordination polyhedra of the atoms: Lu (a), Ni (b, c), and In (d).

Rh, Pd, Pt, Au) (Ferro et al., 1974a, 1974b; Buschow, 1975; Rossi et al., 1977) the transition metal and indium atoms are ordered. The structures can be ascribed to the ZrNiAl type; SG $P6_2m$; $Z = 3$; $a = 740.8(1)$, $c = 369.3(1)$ pm for LuNiIn. $3\text{Lu}: 3g \ x \ 0 \ 1/2$ ($x = 0.5824$); $1\text{Ni}1: 1b \ 0 \ 0 \ 1/2$; $2\text{Ni}2: 2c \ 1/3 \ 2/3 \ 0$; $3\text{In}: 3f \ x \ 0 \ 0$ ($x = 0.2517$) (Sysa et al., 1988). The CP of the lutetium atoms are pentagonal prisms with capped faces (CN = 17), the CP for the Ni1 and Ni2 atoms are tricapped trigonal prisms (CN = 9) and the indium atoms have distorted tetrahedra (CN = 14). The shortest distances are Lu–Ni (288.7 pm), Lu–In (306.3 pm), Ni–In (262.1 pm), and In–In (322.2 pm).

4.42. *Structure type TiNiSi* (Shoemaker and Shoemaker, 1965) (fig. 62). SG $Pnma$; $Z = 4$; $a = 748.30(13)$, $b = 447.20(8)$, $c = 853.50(14)$ pm for EuPdIn. $4\text{Eu}: 4c \ x \ 1/4 \ z$ ($x = 0.03494$, $z = 0.67695$); $4\text{Pd}: 4c$ ($x = 0.27153$, $z = 0.37356$); $4\text{In}: 4c$ ($x = 0.14172$, $z = 0.06247$) (Pöttgen, 1996b). The CP of the europium atoms are pentagonal prisms with six additional equatorial atoms and two atoms capping the bases (CN = 18); the palladium atoms have tricapped trigonal prisms (CN = 9) and the indium atoms are distorted cuboc-

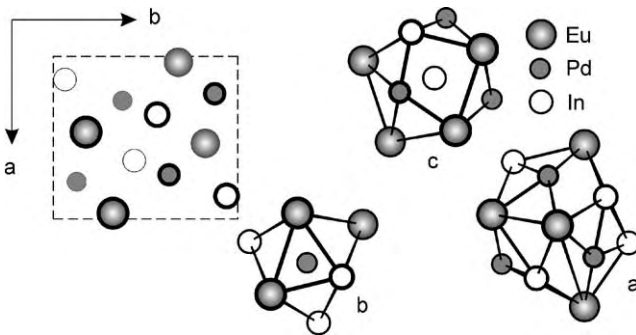


Fig. 62. Projection of the EuPdIn structure on the xy plane and coordination polyhedra of the atoms: Eu (a), Pd (b), and In (c).

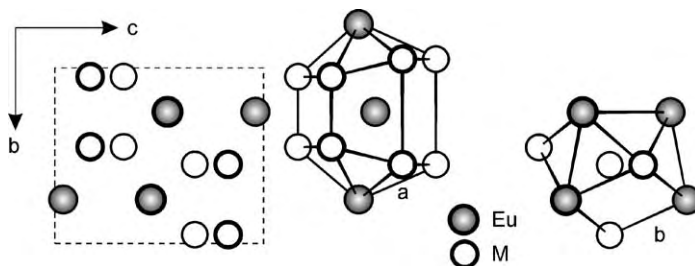


Fig. 63. Projection of the EuZnIn structure on the yz plane and coordination polyhedra of the atoms: Eu (a) and M (b) ($M = \text{Zn}_{0.50}\text{In}_{0.50}$).

tahedra (CN = 12). The shortest distances are Eu–In (314.6 pm), Eu–Pd (338.1 pm), and Pd–In (282.4 pm). The crystal structure of EuPdIn was also studied by Cirafici et al. (1985), however, the positions of the Pd and In atoms were not determined correctly.

4.43. *Structure type CeCu₂* (Larson and Cromer, 1961) (i.e. KHg_2 ; Duwell and Baenziger, 1955) (SG Imma ; $Z = 4$). For EuZnIn (fig. 63) $a = 482.3(1)$, $b = 780.7(2)$, $c = 827.6(2)$ pm (Pöttgen, 1996a). The europium atoms take the positions of cerium ($4e\ 0\ 1/4\ z$ ($z = 0.53763$)), while the zinc and indium atoms (M) statistically occupy the copper positions ($8h\ 0\ y\ z$ ($y = 0.0489$, $z = 0.1648$)).

4.44. *The structure type CaIn₂* (Iandelli, 1964) (SG $P6_3/mmc$; $Z = 2$) is characteristic for $R\text{ZnIn}$ (Mazzone et al., 1982) and $R\text{CdIn}$ (Rossi et al., 1981). The R atoms take the positions of the calcium atoms, while the zinc (cadmium) and indium atoms statistically occupy the positions of the indium atoms of CaIn_2 . For $R(\text{Ag}_{0.25}\text{In}_{0.75})_2$ the $4c$ position is occupied by a mixture ($M = \text{Ag}_{0.25}\text{In}_{0.75}$) with $z = 0.463$ (fig. 64) (Sysa and Kalychak, 1992). The shortest distances for $\text{Ce}(\text{Ag}_{0.25}\text{In}_{0.75})_2$ ($a = 490.1(2)$, $c = 759.2(6)$ pm) are Ce– M (326.5 pm) and M – M (288.5 pm).

4.45. *Structure type Lu₃Co_{1.87}In₄* (fig. 65). SG $P\bar{6}$; $Z = 1$; $a = 781.4(2)$, $c = 352.1(1)$ pm. 3Lu : $3k\ x\ y\ 1/2$ ($x = 0.2949$, $y = 0.0432$); $1\text{Co}1$: $1a\ 0\ 0\ 0$; $0.87\text{Co}2$: $1d\ 1/3\ 2/3\ 1/2$; $1\text{In}1$: $1e\ 2/3\ 1/3\ 0$; $3\text{In}2$: $3f\ x\ y\ 0$ ($x = 0.0744$, $y = 0.6650$) (Zaremba et al., 1989). The CP

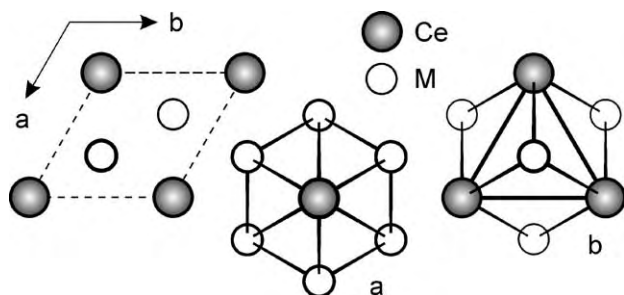


Fig. 64. Projection of the $\text{Ce}(\text{Ag}_{0.25}\text{In}_{0.75})_2$ structure on the xy plane and coordination polyhedra of the atoms: Ce (a) and M (b) ($M = \text{Ag}_{0.25}\text{In}_{0.75}$).

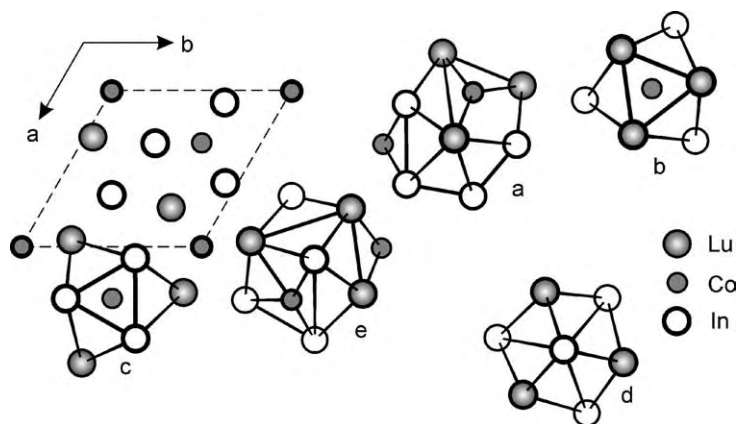


Fig. 65. Projection of the $\text{Lu}_3\text{Co}_{1.87}\text{In}_4$ structure on the xy plane and coordination polyhedra of the atoms: Lu (a), Co (b, c), and In (d, e).

of the lutetium atoms are pentagonal prisms with three additional equatorial atoms and two atoms capping the bases (CN = 15). The CP for the Co1 and Co2 atoms are tricapped trigonal prisms (CN = 9). The CP for the In1 atoms are trigonal prisms with additional atoms capping all faces (CN = 11) and the In2 atoms have distorted tetrahexahedra (CN = 14). The shortest distances are Lu–Co (278.3 pm), Lu–In (311.6 pm), Lu–Lu (352.1 pm), Co–In (267.7 pm), and In–In (293.5 pm).

4.46. *Structure type* AlB_2 (Hofmann and Jäniche, 1935). SG $P6/mmm$; $Z = 1$; $a = 481.8(1)$, $c = 389.9(1)$ pm for $\text{Ce}(\text{Cu}_{0.25}\text{In}_{0.75})_2$ (fig. 66). $1\text{Ce}: 1a\ 0\ 0\ 0$; $2M: 2d\ 1/3\ 2/3\ 1/2$ ($M = \text{Cu}_{0.25}\text{In}_{0.75}$) (Baranyak et al., 1988b). The CP of the cerium atoms are hexagonal prisms with capped bases (CN = 14), the M atoms ($0.25\text{Cu} + 0.75\text{In}$) have tricapped trigonal prisms (CN = 9). The shortest distances are Ce– M (339.6 pm) and M – M (278.2 pm). The AlB_2 structure of Tb_2CuIn_3 has been refined from neutron diffraction data (Siouris et al., 2001), i.e. $\text{Tb}(\text{Cu}_{0.25}\text{In}_{0.75})_2$.

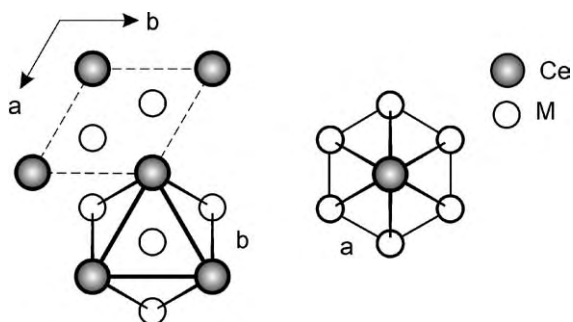


Fig. 66. Projection of the $\text{Ce}(\text{Cu}_{0.25}\text{In}_{0.75})_2$ structure on the xy plane and coordination polyhedra of the atoms: Ce (a) and M (b) ($M = \text{Cu}_{0.25}\text{In}_{0.75}$).

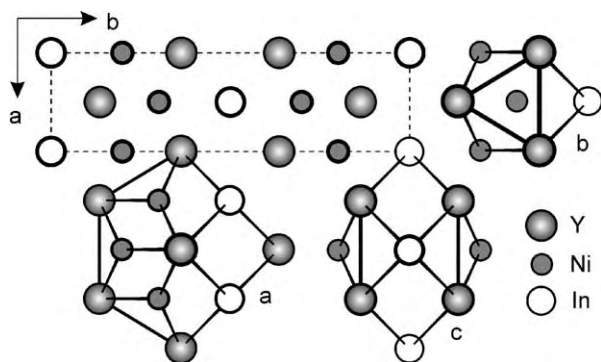


Fig. 67. Projection of the Y_2Ni_2In structure on the xy plane and coordination polyhedra of the atoms: Y (a), Ni (b), and In (c).

4.47. *Structure type* Mn_2AlB_2 (Becher et al., 1966). SG $Cmmm$; $Z = 2$; $a = 390.00(1)$, $b = 1418.6(2)$, $c = 369.4(1)$ pm for Y_2Ni_2In (fig. 67). $4Y$: $4j\ 0\ y\ 1/2$ ($y = 0.36364$); $4Ni$: $4i\ 0\ y\ 0$ ($y = 0.19892$); $2In$: $2a\ 0\ 0\ 0$ (Zaremba et al., 1988). The CP of the yttrium atoms are pentacapped pentagonal prisms (CN = 15), the nickel atoms have tricapped trigonal prisms (CN = 9), and the indium atoms have distorted tetrahexahedra (CN = 14). The shortest distances are Y–Y (390.0 pm), Y–Ni (282.8 pm), Y–In (331.0 pm), Ni–Ni (243.0 pm), and In–In (282.2 pm).

4.48. *Structure type* W_2CoB_2 (Rieger et al., 1966). SG $Immm$; $Z = 2$; $a = 438.8(5)$, $b = 574.30(6)$, $c = 873.37(9)$ pm for Yb_2Cu_2In (fig. 68). $4Yb$: $4j\ 1/2\ 0\ z$ ($z = 0.2962$); $4Cu$: $4h\ 0\ y\ 1/2$ ($y = 0.2138$); $2In$: $2a\ 0\ 0\ 0$ (Giovannini et al., 2001). The CP for the ytterbium atoms are pentacapped pentagonal prisms (CN = 15), for the copper atoms tricapped trigonal prisms (CN = 9), and distorted cuboctahedra (CN = 12) for the indium atoms. The shortest distances are Yb–Cu (306.5 pm), Yb–In (337.8 pm), and Cu–In (274.1 pm).

4.49. *Structure type* U_2Pt_2Sn (Gravereau et al., 1994). SG $P4_2/mnm$; $Z = 4$; $a = 779.1(1)$, $c = 734.8(2)$ pm for Tm_2Au_2In (fig. 69). $4Tm1$ $4g\ x\ y\ 0$ ($x = 0.3140$, $y = 0.6860$); $4Tm2$ $4f$

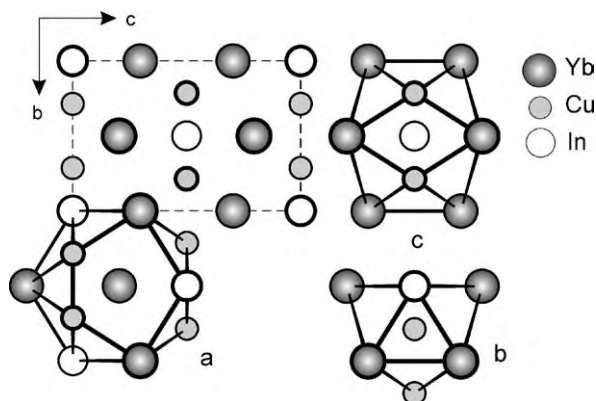


Fig. 68. Projection of the Yb_2Cu_2In structure on the yz plane and coordination polyhedra of the atoms: Yb (a), Cu (b), and In (c).

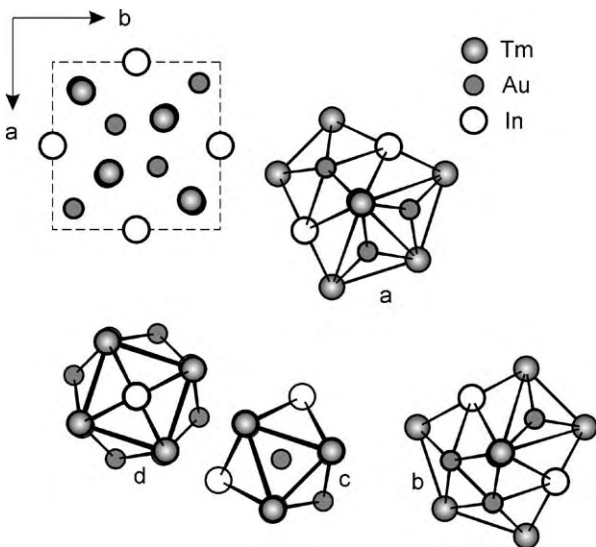


Fig. 69. Projection of the $\text{Tm}_2\text{Au}_2\text{In}$ structure on the *xy* plane and coordination polyhedra of the atoms: Tm (a, b), Au (c), and In (d).

$x x 0$ ($x = 0.1593$); $8\text{Au } 8j x x z$ ($x = 0.3719$, $z = 0.2216$); $4\text{In } 4d 0 1/2 1/4$ (Pöttgen, 1994). The CP for both thulium atoms are pentagonal prisms with capped faces (CN = 17), tricapped trigonal prisms for the gold atoms (CN = 9), and distorted tetrahedra (CN = 14) for the indium atoms. The shortest distances are Tm–Tm (368.6 pm), Tm–Au (285.3 pm), Tm–In (338.5 pm), Au–Au (282.3 pm), Au–In (307.2 pm), and In–In (367.4 pm).

4.50. *Structure type* Mo_2FeB_2 (Rieger et al., 1964). SG $P4/mbm$; $Z = 2$; $a = 749.9(2)$, $c = 375.1(2)$ pm for $\text{Ce}_2\text{Ni}_2\text{In}$ (fig. 70). 4Ce : $4h x 1/2 + x 1/2$ ($x = 0.1734$); 4Ni : $4g x 1/2 + x 0$ ($x = 0.3768$); 2In : $2a 0 0 0$ (Kalychak et al., 1990). The CP for the cerium atoms are pentagonal prisms, which are capped on all faces (CN = 17), the nickel atoms have tricapped trigonal prisms (CN = 9), and the indium atoms have tetrahedra (CN = 14). The shortest distances are Ce–Ce (367.8 pm), Ce–Ni (285.9 pm), Ce–In (334.8 pm), Ni–Ni (261.2 pm), Ni–In (297.3 pm), and In–In (375.1 pm). The samarium and the yttrium compounds with Mo_2FeB_2 type show defects on the nickel sites leading to the composition $R_2\text{Ni}_{2-x}\text{In}$ ($x = 0.22$). For $\text{Gd}_2\text{Ni}_{1.88}\text{In}$ the positions are: 4Gd : $4h$ ($x = 0.17529$); 3.56Ni : $4g$ ($x = 0.37990$); 2In : $2a 0 0 0$ (Kalychak et al., 1990).

4.51. *Structure type* $\text{Lu}_5\text{Ni}_2\text{In}_4$ (fig. 71). SG $Pbam$; $Z = 2$; $a = 1756.8(5)$, $b = 779.8(2)$, $c = 352.2(1)$ pm. $2\text{Lu}1$: $2a 0 0 0$; $4\text{Lu}2$: $4g x y 0$ ($x = 0.2197$, $y = 0.2458$); $4\text{Lu}3$: $4g$ ($x = 0.4137$, $y = 0.1170$); 4Ni : $4h x y 1/2$ ($x = 0.3020$, $y = 0.0220$); $4\text{In}1$: $4h$ ($x = 0.5676$, $y = 0.2071$); $4\text{In}2$: $4h$ ($x = 0.8477$, $y = 0.0747$) (Zaremba et al., 1991). The CP for the Lu1 and Lu3 atoms are pentagonal prisms with all faces capped (CN = 17), the Lu2 atoms have tetragonal prisms with capped faces (CN = 14), the nickel atoms have tricapped trigonal prisms (CN = 9), and the In1 and In2 atoms have distorted tetrahedra where some vertices

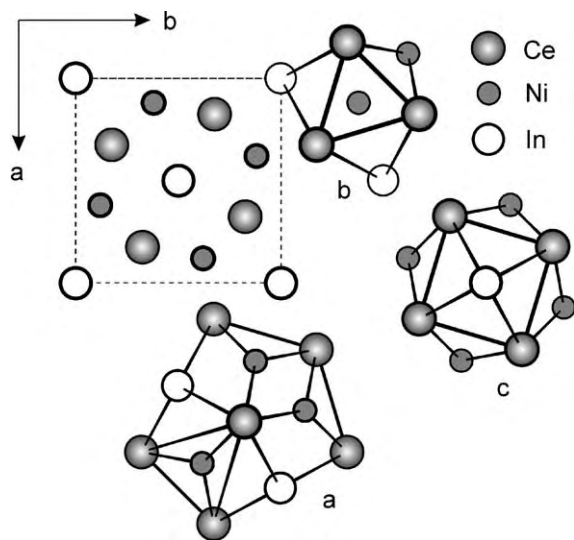


Fig. 70. Projection of the Ce_2Ni_2In structure on the xy plane and coordination polyhedra of the atoms: Ce (a), Ni (b), and In (c).

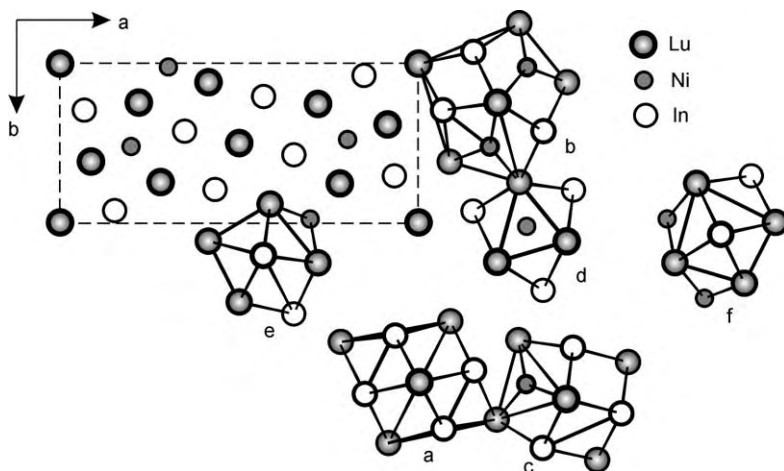


Fig. 71. Projection of the $Lu_5Ni_2In_4$ structure on the xy plane and coordination polyhedra of the atoms: Lu (a–c), Ni (d), and In (e, f).

are not occupied (reduced CN = 12 and 13, respectively). The shortest distances are Lu–Lu (334.8 pm), Lu–Ni (273.9 pm), Lu–In (311.9 pm), Ni–In (273.6 pm), and In–In (323.0 pm).

4.52. The structure type $CsCl$ is characteristic for the ternary indides RAg_xIn_{1-x} (Ihrig et al., 1973; Lal and Methfessel, 1981). The compounds belong to solid solutions of binary RAg and RIn , which both crystallize with the $CsCl$ type structure (fig. 72).

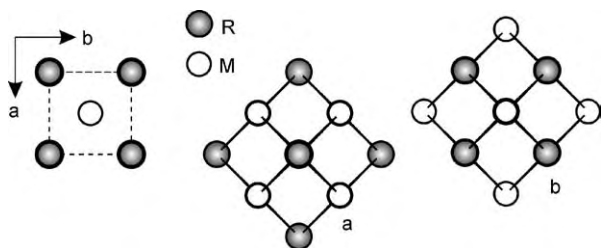


Fig. 72. Projection of the CsCl-type structure (for RAg_xIn_{1-x} compounds) on the xy plane and coordination polyhedra of the atoms: R (a) and M (b) ($M = Ag_xIn_{1-x}$).

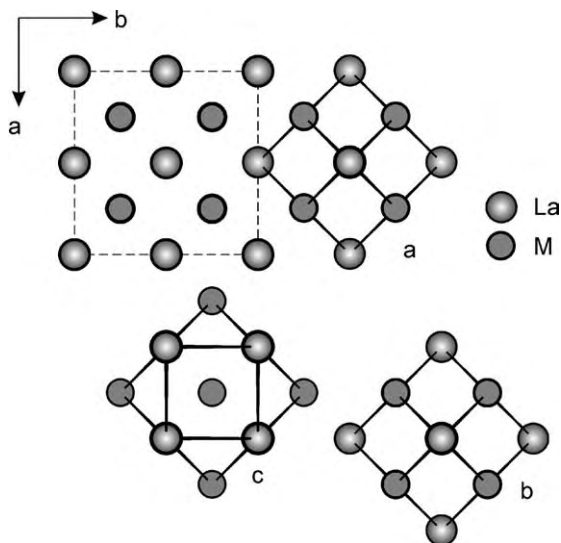


Fig. 73. Projection of the $LaAg_xIn_{1-x}$ structure on the xy plane and coordination polyhedra of the atoms: La (a-b) and M (c) ($M = Ag_xIn_{1-x}$).

4.53. Structure type $LT-LaAg_xIn_{1-x}$ ($x = 0.75-0.89$). SG $I4/mmm$; $Z = 4$; $a \cong 755$, $c \cong 780$ pm for $LaAg_{0.75}In_{0.25}$ (fig. 73). $4La1: 4d\ 0\ 1/2\ 1/4$; $4La2: 4e\ 0\ 0\ 1/4 - \varepsilon$; $8(Ag_xIn_{1-x}): 8h\ 1/4 + \delta\ 1/4 + \delta\ 0$; ε and δ are the atoms shifts in the tetragonal versus the cubic phase (Maetz et al., 1980). The CP for $La1$ and $La2$ are rhombododecahedra (CN = 14) and the CP for the mixed site (Ag_xIn_{1-x}) are cuboctahedra (CN = 12).

4.54. Structure type Mo_5B_2Si (Aronsson, 1958). SG $I4/mcm$; $Z = 4$; $a = 752.16(7)$, $c = 1315.9(1)$ pm for $Tm_{4.82}Ni_2In_{1.18}$ (fig. 74) (Lukachuk et al., 2002). $16Tm1: 16l\ x\ x + 1/2\ z$ ($x = 0.65841$, $z = 0.13672$); $4M: 4c\ 0\ 0\ 0$ ($M = Tm_{0.82}In_{0.18}$); $8Ni: 8h\ x\ x + 1/2\ 0$ ($x = 0.1298$); $4In2: 4a\ 0\ 0\ 1/4$. The CP of the $Tm1$ atoms are 16-vertices polyhedra (CN = 16). The CP of the M atoms are tetragonal prisms with nickel capped rectangular faces and indium capped bases (CN = 14). The nickel atoms have tricapped trigonal prisms (CN = 9) and the $In2$ atoms have a base capped tetragonal antiprism (CN = 10) as coordination polyhedra. The shortest distances are $Tm-Ni$ (282.5 pm), $Tm-In$ (320.1 pm), and $Ni-Ni$ (276.1 pm).

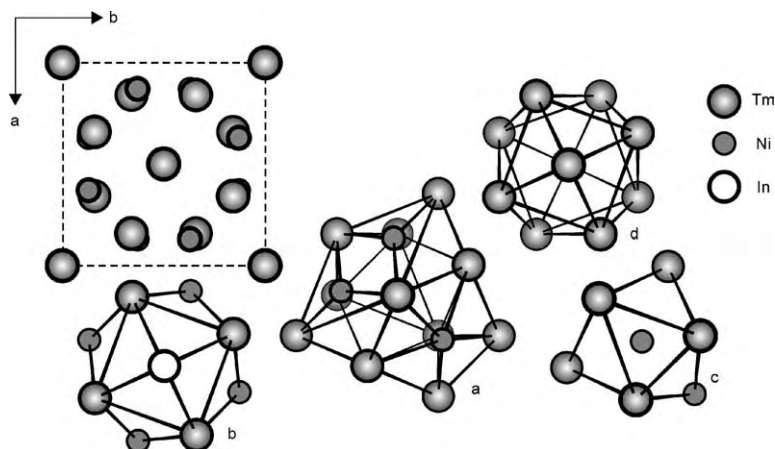


Fig. 74. Projection of the $\text{Tm}_{4.82}\text{Ni}_2\text{In}_{1.18}$ structure on the xy plane and coordination polyhedra of the atoms: Tm (a–b), Ni (c), and In (d).

4.55. Structure type $\text{Ce}_{12}\text{Pt}_7\text{In}$ (fig. 75). SG $I4/mcm$; $Z = 4$; $a = 1210.2(1)$, $c = 1454.2(2)$ pm. $32\text{Ce}1: 32m\ x\ y\ z$ ($x = 0.0711$, $y = 0.2082$, $z = 0.14222$); $8\text{Ce}2: 8g\ 0\ 1/2\ z$ ($z = 0.1392$); $8\text{Ce}3: 8h\ x\ x + 1/2\ 0$ ($x = 0.1753$); $16\text{Pt}1: 16l\ x\ x + 1/2\ z$ ($x = 0.17502$, $z = 0.19565$); $8\text{Pt}2: 8h$ ($x = 0.6245$); $4\text{Pt}3: 4a\ 0\ 0\ 1/4$; $4\text{In}: 4c\ 0\ 0\ 0$ (Galadzhun et al., 2003). The CP of the cerium atoms have 14 and 15 vertices (CN 14 and 15), the CP of Pt1 have nine vertices,

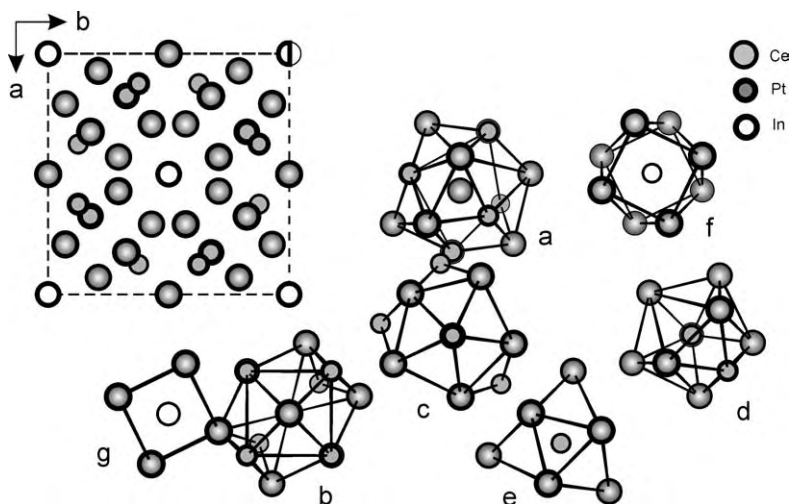


Fig. 75. Projection of the $\text{Ce}_{12}\text{Pt}_7\text{In}$ structure on the xy plane and coordination polyhedra of the atoms: Ce (a–c), Pt (d–f), and In (g).

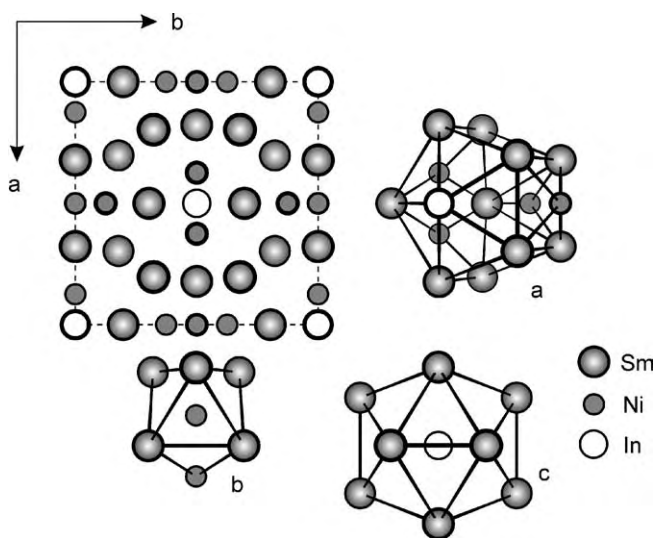


Fig. 76. Projection of the $\text{Sm}_{12}\text{Ni}_6\text{In}$ structure on the xy plane and coordination polyhedra of the atoms: Sm (a), Ni (b), and In (c).

the CP of Pt2 are tricapped trigonal prisms (CN 9), the CP of Pt3 are tetragonal antiprisms (CN 8), and for the indium atoms the CP are cubes (CN 8). The shortest distances are Ce–Pt (284.5 and 293.9 pm), Ce–Ce (322.3 pm), and Ce–In (337.1 pm).

4.56. *Structure type $\text{Sm}_{12}\text{Ni}_6\text{In}$* (fig. 76). SG $Im\bar{3}$; $Z = 2$; $a = 980.0(2)$ pm. 24Sm: $24g$ x y $1/2$ ($x = 0.6871$, $y = 0.1966$); 12Ni: $12e$ x 0 $1/2$ ($x = 0.8744$); 2In: $2a$ 0 0 0 (Kalychak et al., 1998). The CP for the samarium atoms are pentacapped pentagonal prisms (CN = 15), the nickel atoms have tricapped trigonal prisms (CN = 9), and the indium atoms have icosahedral coordination (CN = 12). The shortest distances are Sm–Sm (362.3 pm), Sm–Ni (266.1 pm), Ni–Ni (246.3 pm), and Sm–In (349.3 pm).

4.57. *Structure type $\text{Ho}_6\text{Co}_2\text{Ga}$* (Gladyshevskii et al., 1983). SG $Immm$; $Z = 4$; $a = 934.8(6)$, $b = 943.0(6)$, $c = 990.6(9)$ pm for $\text{Ho}_6\text{Co}_{2+x}\text{In}_{1-x}$ ($x = 0.135$) (fig. 77). 8Ho1: $8n$ x y 0 ($x = 0.2855$, $y = 0.1874$); 8Ho2: $8m$ x 0 z ($x = 0.3006$, $z = 0.3155$); 8Ho3: $8l$ 0 y z ($y = 0.2068$, $z = 0.2312$); 4Co1: $4j$ $1/2$ 0 z ($z = 0.1124$); 4Co2: $4g$ $1/2$ y $1/2$ ($y = 0.1260$); 2M: $2a$ 0 0 0 ; 2In: $2c$ 0 0 $1/2$ ($M = \text{Co}_{0.27}\text{In}_{0.73}$) (Kalychak et al., 1993b). The CP of the Ho1 and Ho2 atoms are pentagonal prisms with five and four additional atoms on the rectangular faces (CN = 15 and 14), and the CP for the Ho3 atoms are tetragonal prisms with five additional atoms (CN = 13). The CP of the Co1 and Co2 atoms are tricapped trigonal prisms (CN = 9), the M atoms have cubes (CN = 8), and the indium atoms center icosahedra (CN = 12). The shortest distances are Ho–Ho (336.7 pm), Ho–Co (274.2 pm), Ho–M (300.8 pm), Ho–In (330.0 pm), and Co–Co (222.7 pm).

4.58. *Structure type $\text{Lu}_4\text{Co}_2\text{In}_3$* (fig. 78). SG $P4_2/nmc$; $Z = 4$; $a = 933.3(2)$, $c = 2263.3(4)$ pm. 4Lu1: $4c$ $3/4$ $1/4$ z ($z = 0.1457$); 4Lu2: $4d$ $1/4$ $1/4$ z ($z = 0.2127$); 8Lu3:

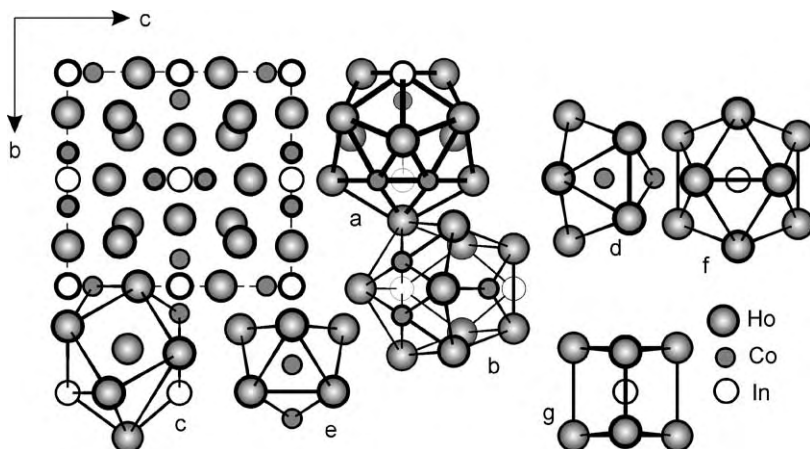


Fig. 77. Projection of the $\text{Ho}_6\text{Co}_{2.135}\text{In}_{0.865}$ structure on the yz plane and coordination polyhedra of the atoms: Ho (a-c), Co (d, e), In (f), and M (g) ($M = \text{Co}_{0.27}\text{In}_{0.73}$).

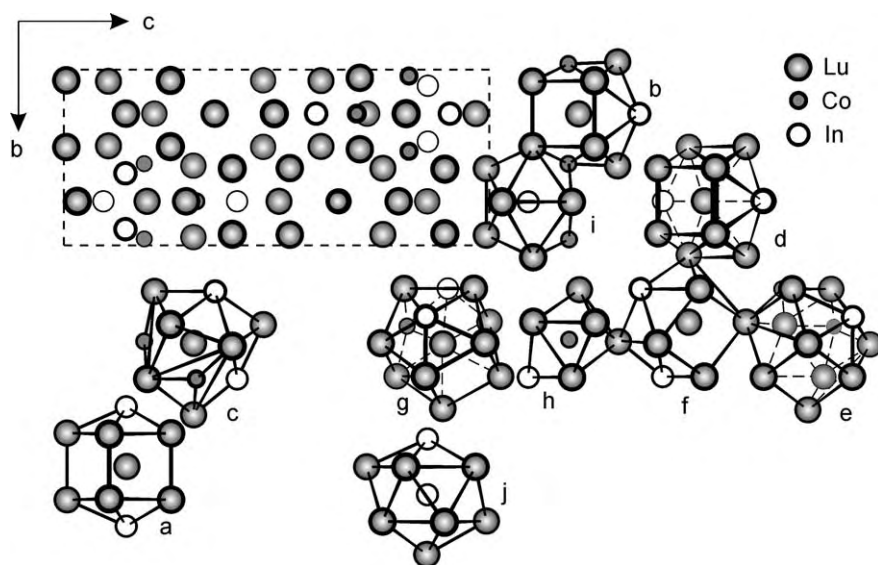


Fig. 78. Projection of the $\text{Lu}_{14}\text{Co}_2\text{In}_3$ structure on the yz plane and coordination polyhedra of the atoms: Lu (a-g), Co (h), and In (i, j).

$8g \frac{1}{4} y z$ ($y = 0.5467$, $z = 0.3045$); $8\text{Lu}4$: $8g$ ($y = 0.5595$, $z = 0.9945$); $8\text{Lu}5$: $8f x y \frac{1}{4}$ ($x = 0.5612$, $y = 0.4388$); $8\text{Lu}6$: $8g$ ($y = 0.4397$, $z = 0.4686$); $16\text{Lu}7$: $16h x y z$ ($x = 0.4375$, $y = 0.4342$, $z = 0.1045$); 8Co : $8g$ ($y = 0.5354$, $z = 0.1886$); $4\text{In}1$: $4c$

($z = 0.9072$); 8In_2 : $8g$ ($y = 0.4093$, $z = 0.8555$) (Zaremba et al., 1992). The CP of the Lu1 and Lu4 atoms are pentagonal prisms with additional atoms capping the bases (CN = 12), the CP of the Lu2 and Lu5 atoms are pentagonal prisms with capped bases and two additional atoms capping the rectangular faces (CN = 14). The Lu3 atoms have pentacapped pentagonal prisms (CN = 15) and the CP of the Lu6 and Lu7 atoms have 13-vertices. Except for the Lu1 atom, all lutetium CP contain fragments of icosahedra. The CP for the cobalt atoms are tricapped trigonal prisms (CN = 9) and the CP for In1 and In2 are icosahedra (CN = 12). The shortest distances are Lu–Lu (326.0 pm), Lu–Co (262.5 pm), Lu–In (284.8 pm), and Co–In (295.2 pm). The structure of $\text{Gd}_{14}\text{Co}_3\text{In}_{2.7}$ (SG $P4_2/nmc$; $Z = 4$; $a = 961.9(2)$, $c = 2329.1(4)$ pm) (Canepa et al., 2002b) is related to that of $\text{Lu}_{14}\text{Co}_2\text{In}_3$. It differs from the latter by the fact that the Co1 atoms occupy the $8g$ position only by 86%, and additional cobalt atoms occupy the $4d$ position and in the $4c$ position a statistical mixture ($\text{Co}_{0.31}\text{In}_{0.69}$) occurs instead of a pure indium occupancy, resulting in a different composition.

5. Geometrical relations of some $R_xT_y\text{In}_z$ structures

A significant number of structural relationships between indides (table 12) are known in the literature. Principally, structural relations can be investigated by various methods. One very concise way is establishing a group–subgroup relations based on the Bärnighausen formalism (Bärnighausen, 1980; Bärnighausen and Müller, 1996). Here, the evolution of atomic parameters can be followed up in going from high symmetry (given by an aristotype) to

Table 12

Structure–superstructure relationships between structure types of binary and ternary intermetallic indium compounds

Superstructure	Basic structure	Kind of superstructure (Kripyakevich, 1977)	Number of representatives	
			binary compounds	ternary compounds
AuCu	Cu	II	1	–
AuCu ₃	Cu	II	20	2
CsCl	W	II	13	12
MnCu ₂ Al	Fe ₃ Si (anti-BiF ₃)	II	–	50
CaIn ₂	AlB ₂	I	2	34
YNi ₉ In ₂	Ce(Mn _{0.45} Ni _{0.55}) ₁₁	II	–	19
CeCu _{4.32} In _{1.68}	CeCu ₆	I	–	5
YbAg ₂ In ₄	YbCd ₆ (YCd ₆)	II	–	11
MgCu ₄ Sn	AuBe ₅	II	–	40
MgCuAl ₂	PuBr ₃	II	–	11
ZrNiAl	Fe ₂ P	II	–	72
Lu ₃ Co _{1.87} In ₄	ZrNiAl	II	–	5
TiNiSi	KHg ₂ (CeCu ₂)	II	–	4
Mo ₂ FeB ₂	U ₃ Si ₂	II	–	65
U ₂ Pt ₂ Sn	Zr ₃ Al ₂	II	–	4
EuAg ₄ In ₈	SmZn _{12-x} ($x = 1$)	II	–	1
Nd ₆ Fe ₁₃ Si	La ₆ Fe ₁₁ Ga ₃	II	–	4

low symmetry (various superstructures). This is an excellent tool to analyze phase transitions. This concept, however, does not include structural similarities, in particular in the absence of a group–subgroup relation. Thus, it does not allow comparing and discussing those structures. Including atomic replacements widens the possibilities to compare structures (Kripyakevich, 1977). Another simplifying step is to look at the local environment in terms of slabs. The latter is known as chemical twinning of different structures (Aronsson et al., 1960; Andersson, 1983; Parthé and Chabot, 1984; Cenxual and Parthé, 1984; Parthé et al., 1985; Parthé, 1990; Parthé et al., 1993).

All ternary compounds of the rare earth metal–transition metal–indium systems with known crystal structure can be divided into three large groups depending on their position in the ternary system, i.e. on their composition. The first group comprises compounds within the triangle delineated by a transition metal, RM_2 , and elemental indium (fig. 79). The compounds crystallizing with NaZn_{13} , ThMn_{12} , $\text{Th}_2\text{Ni}_{17}$, YNi_9In_2 , EuAg_4In_8 , CeNi_5Sn , $\text{CeCu}_{4.38}\text{In}_{1.62}$, MgCu_4Sn , $\text{Lu}_6\text{Co}_{26-x}\text{In}_{14}$, YbAg_2In_4 , $\text{Nd}_6\text{Fe}_{13}\text{Si}$, $\text{Ce}_8\text{Pd}_{24}\text{Sb}$, and MnCu_2Al structure types belong to this group. In most cases, they have complex multilayer structures with at least one small lattice parameter of 480–500 pm. High values for the coordination numbers (CN) of all atom types and similar coordination polyhedra (CP) are typical for those structures.

The second range of compounds (fig. 79) is situated in the region with higher R content. It is limited by the compositions RM_2 – R_2M – In . The triangle includes the structure types HoCoGa_5 , Ho_2CoGa_8 , YNiAl_4 , MgCuAl_2 , $\text{Ce}_4\text{Ni}_7\text{In}_8$, $\text{Pr}_5\text{Ni}_6\text{In}_{11}$, ZrNiAl , AlB_2 , TiNiSi , $\text{Lu}_3\text{Co}_{1.87}\text{In}_4$, Mn_2AlB_2 , and Mo_2FeB_2 , as well as PrCo_2Ga and GdPt_2Sn , which lie on the

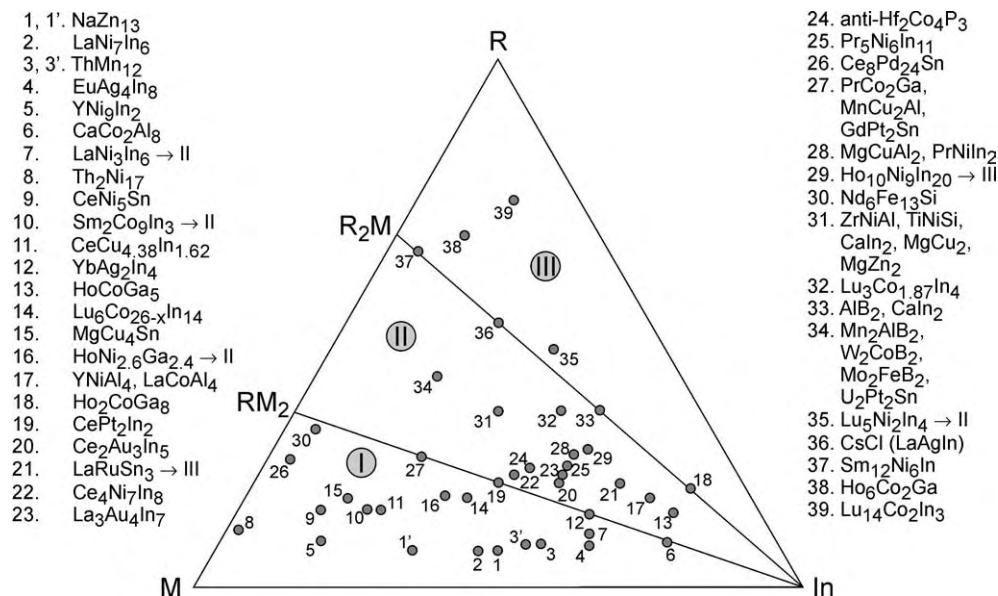


Fig. 79. Grouping of the various structure types within the systems R – M – In according to chemical composition.

boundary line. The shortest lattice parameter, ranging from ~ 360 to 420 pm, represents two layers of atoms and is typical for this group of compounds. The structure types $\text{Sm}_2\text{Co}_9\text{In}_3$, $\text{HoNi}_{2.6}\text{Ga}_{2.4}$, LaNi_3In_6 , and $\text{Lu}_5\text{Ni}_2\text{In}_4$ also belong to this group as far as the shortest lattice parameter is of concern. CaIn_2 and $\text{U}_2\text{Pt}_2\text{Sn}$, which are superstructures of AlB_2 and Zr_3Al_2 , respectively, have such short lattice parameters in their subcells.

The third and the smallest group (fig. 79), which is limited by the points $R_2M-R\text{-In}$, comprises the structures of $\text{Sm}_{12}\text{Ni}_6\text{In}$, $\text{Ho}_6\text{Co}_2\text{Ga}$, and $\text{Lu}_{14}\text{Co}_2\text{In}_3$. The $\text{Ho}_{10}\text{Ni}_9\text{In}_{20}$ type also belongs to this group, however, according to its stoichiometry, it belongs to the second group. These types are complex multilayer structures with the value of the shortest lattice parameter of 900 pm or more. Additional types in this group are $\text{Lu}_5\text{Ni}_2\text{In}_4$ and LaAgIn .

The structural relations between the types $\text{Lu}_3\text{Co}_{1.87}\text{In}_4$ and ZrNiAl , $\text{CeCu}_{4.38}\text{In}_{1.62}$ and CeCu_6 , YNi_9In_2 and $\text{Ce}(\text{Mn}_{0.45}\text{Ni}_{0.55})_{11}$, EuAg_4In_8 and SmZn_{11} (SmZn_{12-x} with $x = 1$), as well as YbCd_6 and YbAg_2In_4 will be discussed in this section.

As illustrated in fig. 80, the $\text{Lu}_3\text{Co}_{1.87}\text{In}_4$ structure (Zaremba et al., 1989) is formed by substitution of one transition metal atom by an indium atom on a single site in the structure type ZrNiAl , i.e. $R\text{NiIn}$, resulting in a change of the composition from " $R_3M_3X_3$ " to $R_3M_2X_4$. This requires a reduction of symmetry from $P\bar{6}2m$ to $P\bar{6}$ (Zumdick and Pöttgen, 1999). The coordination number of the indium atoms of this substituted site increases as compared with the CN of the M atoms in the ZrNiAl type structure from nine (tricapped trigonal prism) to 11 (pentacapped trigonal prism). Another related structure is Lu_3CoGa_5 . Grin and Gladyshevskii (1989) reported that the Lu_3CoGa_5 structure type (fig. 80, right-hand side) does not occur in indium-based systems. In this structure type, the substitution of the transition metal by a p -element takes place according to the scheme $R_3M_3X_3 \rightarrow R_3MX_5$, which allows preservation of the space group symmetry, $P\bar{6}2m$.

The structure of $\text{CeCu}_{4.38}\text{In}_{1.62}$ (Kalychak et al., 1988a) is a derivative of the CeCu_6 type (SG $Pnma$; $a = 811.2$, $b = 510.2$, $c = 1016.2$ pm) (Cromer et al., 1960). It consists of two unit cells of the latter compound, connected via a two-fold axis. As a result two lattice parameters of these structure types are similar ($b_{\text{CeCu}_{4.38}\text{In}_{1.62}} \approx c_{\text{CeCu}_6}$; $c_{\text{CeCu}_{4.38}\text{In}_{1.62}} \approx b_{\text{CeCu}_6}$) and the

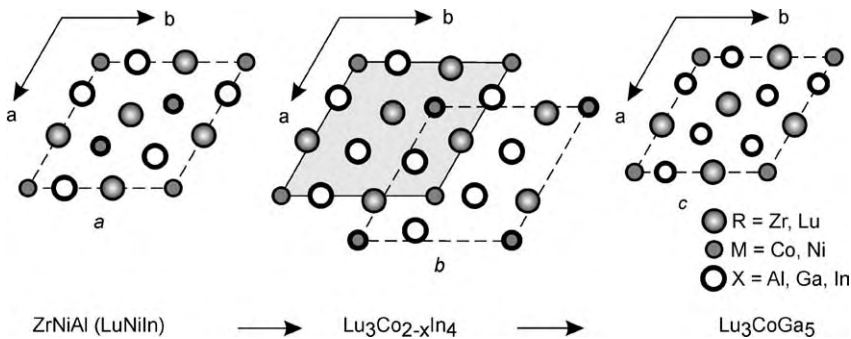


Fig. 80. Relations between the structure types ZrNiAl ($R_3M_3X_3$) (a), $\text{Lu}_3\text{Co}_{1.87}\text{In}_4$ ($R_3M_2X_4$) (b), and Lu_3CoGa_5 (R_3MX_5) (c). Note the origin shift of b in the original work (Zaremba et al., 1989).

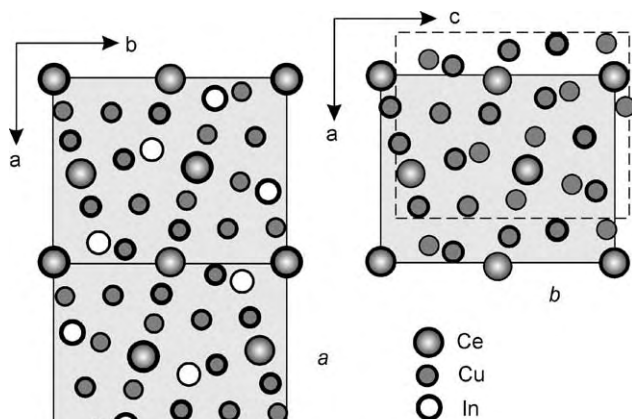


Fig. 81. Relations between the structure types $\text{CeCu}_{4.8}\text{In}_{1.62}$ (a) and CeCu_6 (b).

third in the $\text{CeCu}_{4.38}\text{In}_{1.62}$ type is about twice as large as the corresponding one in the CeCu_6 structure ($a_{\text{CeCu}_{4.38}\text{In}_{1.62}} \approx 2a_{\text{CeCu}_6}$) (fig. 81).

The structure of YNi_9In_2 (Kalychak et al., 1984b) is a superstructure of the $\text{Ce}(\text{Mn}_{0.45}\text{Ni}_{0.55})_{11}$ type (SG $P4/mbm$, $a = 834.8$, $c = 491.9$ pm) (Kalychak et al., 1975). In the latter the manganese and nickel atoms randomly occupy four Wyckoff positions. On the sites $2c$, $8k$, and $8j$, the atoms have CN 12 and their CP are slightly distorted icosahedra. The atoms on the $4g$ site have CN 15. In the YNi_9In_2 type, the large indium atoms occupy the site $4g$ and have a high CN with a 15-vertex coordination polyhedron, while the nickel atoms occupy the $2c$, $8k$, and $8j$ sites (fig. 26).

Due to their close relations we also review the structure types EuAg_4In_8 (fig. 24) (Sysa et al., 1994a) and SmZn_{11} (SG $P6/mmm$, $a = 897.4$, $c = 891.8$ pm) (Mason et al., 1970). The similarity of the lattice parameters, the identity of the space group, and the occupation of the same atomic sites with close values of the coordinates allow us to consider the EuAg_4In_8 structure as a superstructure of the SmZn_{11} type, where the silver and indium atoms are ordered on the sites of the zinc atoms. However, there is one significant difference concerning the composition. In the SmZn_{11} structure, the samarium atoms occupy additionally the sites $2c$ and $1b$ at 15 and 4%, respectively, and the sites $2e$ and $4h$ are occupied by zinc atoms only at 96 and 85%, while in the EuAg_4In_8 structure the latter are occupied by indium atoms at 100%. The defects result in the composition $\sim\text{SmZn}_{11}$ as compared to SmZn_{12} with full occupancies.

A similar relation is observed for the binary structure types YCd_6 (SG $Im\bar{3}$, $a = 1548.3$ pm) (Larson and Cromer, 1971) and YbCd_6 (SG $Im\bar{3}$, $a = 1565.8$ pm) (Palenzona, 1971), and ternary YbAg_2In_4 (Sysa et al., 1989). These structures are actually identical considering the lattice parameters, the space group symmetry, the sites, and the parameters of the atoms. In YbAg_2In_4 the smaller silver and indium atoms are ordered, thus, it represents a ternary ordered superstructure of the binary ones. However, there is a difference between the binary compounds: in YCd_6 one cadmium atom occupies the $24g$ site by about one third, and in

YbCd₆ one cadmium atom occupies the 16*f* site by about one half. These inconsistencies might be due to a variable stoichiometry or different qualities of the structure solution. On the other hand, in the ternary compound YbAg₂In₄, the silver atoms occupy the site 48*h* by about one sixth. It should be mentioned, that the mixed site occupancies actually do not result in a change of the general structural motif. This manifests the view of the structure-superstructure relationship at least in the sense of Kripyakevich (1977). The YbAg₂In₄ structure has one more peculiarity: the sites 16*f* and 24*g* are occupied by the atoms Ag1, Ag2, Ag3, and Ag4, respectively, on split positions, but with a total occupancy of 100%.

5.1. Structures of multiple substitution

The formation of the superstructures, in particular those of the second kind following the definition of Kripyakevich (1977), occurs by ordered substitution of one kind of atoms in the parent structure by two different atom types in a way that the total number of atoms per unit cell remains the same, i.e. ternary ordered variants of binary structures. Another variant for the formation of more complex structures from simple ones is the substitution of single atoms by pairs of atoms of another kind. This way, a more complex structure is obtained by multiple substitutions of larger atoms by pairs of atoms with smaller size. The indides with the structure types ThMn₁₂ (Sysa et al., 1989), EuAg₄In₈ (Sysa et al., 1994a), Th₂Ni₁₇ (Kalychak et al., 1997), and Sm₁₂Ni₆In (Kalychak et al., 1998) belong to this class of substitution structures for ternary indides. The first three structure types are obtained by multiple substitution of a part of the *R* atoms in the structure type CaCu₅ by pairs of smaller atoms. The geometrical relations take place according to the schemes described below (for simplification all atoms of smaller size are designated as *X*).

For the ThMn₁₂ type (Kripyakevich, 1977), (tetragonal symmetry), which is connected with the CaCu₅ type via $a_{\text{ThMn}_{12}} \cong \sqrt{3} a_{\text{CaCu}_5}$, $c_{\text{ThMn}_{12}} \cong a_{\text{CaCu}_5}$ and $V_{\text{ThMn}_{12}} \cong 4V_{\text{CaCu}_5}$: (CaCu₅ type) $4RX_5 = R_4X_{20} = R_2R'_2X_{20} \xrightarrow{2R=4X} R_2X_4X'_{20} = R_2X_{24} = 2RX_{12}$ (ThMn₁₂ type). For the structure type Th₂Ni₁₇ (hexagonal symmetry), for which $a_{\text{Th}_2\text{Ni}_{17}} \cong \sqrt{3} a_{\text{CaCu}_5}$, $c_{\text{Th}_2\text{Ni}_{17}} \cong 2c_{\text{CaCu}_5}$ and $V_{\text{Th}_2\text{Ni}_{17}} \cong 6V_{\text{CaCu}_5}$ we obtain: (CaCu₅ type) $6RX_5 = R_6X_{30} = R_4R'_2X_{30} \xrightarrow{2R=4X} R_4X_4X'_{30} = R_4X_{34} = 2R_2X_{17}$ (Th₂Ni₁₇ type). The structure type EuAg₄In₈, which also has hexagonal symmetry and lattice parameters similar to the Th₂Ni₁₇ type, has the same geometrical relation to the CaCu₅ type. However, the number of atoms of the *R* component, which are substituted by pairs of *X* atoms is different: (CaCu₅ type) $6RX_5 = R_6X_{30} = R_3R'_3X_{30} \xrightarrow{3R=6X} R_3X_6X'_{30} = R_3X_{36} = 3RX_{12}$ (EuAg₄In₈ type). Thus, for the formation of the ThMn₁₂ and EuAg₄In₈ types, half of the *R* atoms of the parent structure are replaced by pairs, and for the Th₂Ni₁₇ type only one third of the *R* atoms is replaced by *X*₂ pairs. Likewise, there is a close relationship between the types Th₂Ni₁₇ (SG *P6₃/mmc*, 38 atoms per unit cell) and EuAg₄In₈ (SG *P6/mmm*, 39 atoms per unit cell) with very close coordinates of the atoms and, accordingly, similar structural motifs. The EuAg₄In₈ structure is deduced from the Th₂Ni₁₇ type by a substitution of one of the two *R* atoms in site 2*b* 0 0 1/4 by two *X* atoms (in this case In) with the coordinates 0 0 *z* (*z* = 0.3434, site 2*e*) and a displacement of the other *R* atom to the

site $1a\ 0\ 0\ 0$. The geometrical scheme for the transformation is the following: (Th₂Ni₁₇ type)
 $2R_2X_{17} = R_4X_{34} = R_1R'_3X_{34} \xrightarrow{R=2X} R_3X_2X'_{34} = R_3X_{36} = 3RX_{12}$ (EuAg₄In₈ type).

The structure type Sm₁₂Ni₆In (cubic symmetry, 38 atoms per unit cell) can be analogously obtained from the Ho₆Co₂Ga type (orthorhombic pseudocubic symmetry, 36 atoms per unit cell) (Kalychak et al., 1993b; Grin and Gladyshevskii, 1989). The substitution involves two X atoms and two pairs of transition metal atoms M with $r_X > r_M$ and approximately identical volumes of the unit cells ($a_{\text{Sm}_{12}\text{Ni}_6\text{In}} \cong a_{\text{Ho}_6\text{Co}_2\text{Ga}} \cong b_{\text{Ho}_6\text{Co}_2\text{Ga}} \cong c_{\text{Ho}_6\text{Co}_2\text{Ga}}$). The geometrical scheme for the transformation is: (Ho₆Co₂Ga type) $4R_6M_2X = R_{24}M_8X_4 = R_{24}M_8X_2X'_2 \xrightarrow{2X=4M} R_{24}M_8M'_4X_2 = R_{24}M_{12}X_2 = 2R_{12}M_6X$ (Sm₁₂Ni₆In type).

We have already mentioned that the EuAg₄In₈ structure can be considered as a superstructure of the SmZn₁₁ type with the latter having defects on the zinc sites. However, another interpretation is also possible: EuAg₄In₈ (= RX_{12}) can be considered as a filled version of SmZn₁₁. The sites $2e$ and $4h$ with the zinc defects are fully occupied by the atoms of smaller size, thus SmZn₁₁ can be considered as a defect derivative of the EuAg₄In₈ type neglecting the R atoms on the sites $1b$ and $2c$, which are occupied only by 4 and 15%, respectively.

5.2. Structures of intergrowth of small slabs

A significant number of crystal structures occurring in binary and ternary indides can be considered as consisting of simple structural slabs in different ratios and arrangements. In most cases, these fragments are unit cells or fractions of unit cells of simple structures, which are formed in systems with indium or other metals, i.e. the slabs have real representatives among intermetallic compounds. In some cases, however, slabs are hypothetical and they occur only in combination with other slabs. Identical slabs, combined in different ratios, form homologous series of structure types. The so-called one-dimensional homologous series are the result of combining the slabs in one direction; two- and three-dimensional ones are obtained, if the combination of the slabs occurs within a plane or in all three directions, respectively. The slabs, which occur most often in the structures of indides, derive from the following structure types: tungsten (α -Fe), CsCl, AuCu₃, AlB₂, CaCu₅ (and its derivatives), CeMg₂Si₂, Zr₄Al₃, and a few others (Kripyakevich, 1977).

The analysis of the structures shows, that the slabs of α -Fe and AlB₂ are of special importance. The motif of tungsten (α -Fe; a body-centered cube) is frequently distorted in real structures; the tetragonal deformation ($c/a \geq 1$) corresponds to the structure of elemental indium (SG $I4/mmm$, $a = 325.12$, $c = 494.67$ pm) (Donohue, 1974). Such slabs frequently occur in indium-rich binary and ternary compounds. In the case when the atoms within the slab and at the vertices are different, we obtain slabs derived from cubic CsCl or tetragonal AuCu, most often with the composition $R\text{In}$. The phase diagrams of the binary systems $R\text{--In}$ (Yatsenko et al., 1983) reveal that binary compounds $R\text{In}$ with CsCl structure type mostly form directly from the melt and they have the highest melting points in these systems, i.e. they are thermodynamically very stable. This is confirmed by the experimental data for the heats of formation ΔH_{form} . Their theoretical estimations are given by Colinet (1995). Considering this, the presence of such slabs in complex structures is not surprising. These cubic or tetragonally distorted fragments can form layers or isolated columns in more complex struc-

tures. Another very important structural element of binary and ternary indides is a trigonal prism as the main constituent of trigonal and hexagonal structures. Unfilled prisms exist with the composition E (E is a rare earth, M , or X element) or centered by another atom with the composition $EE'2$, which corresponds to the motif of the AlB_2 structure (two prisms connected by a rectangular face). In ternary compounds with different degrees of deformation, these two structural elements, a cube (or a tetragonal prism) and a trigonal prism (empty or filled), are the basic slabs for the geometrical construction of the crystal structures of indium-rich compounds.

For crystal structures of compounds, that are rich in transition metal (compounds of group I according to fig. 79) it is possible to isolate fragments of more simple structures. The structure types $ThMn_{12}$, YNi_9In_2 , $CeNi_5Sn$, $CeCu_{4.38}In_{1.62}$, and $NdFe_{13}Si$ are among those. In figs. 82–92 we illustrate some of the interesting examples where complex structures can be presented as various combinations of simple fragments. The unit cells are outlined by dashed lines and the fragments with solid lines. In these figures, the R , $T(M)$, and $In(X)$ atoms are presented as large gray, small black, and medium unfilled circles, respectively.

In the tetragonal types $ThMn_{12}$ and YNi_9In_2 with very similar lattice parameters it is possible to isolate a unit cell of the $CeMg_2Si_2$ structure (SG $P4/mmm$, $a = 425.0$, $c = 576.5$ pm) (Kripyakevich, 1977) and in the first type, slabs of a hypothetical structure with a disordered arrangement of the atoms, and in the second type, a unit cell of the Zr_4Al_3 type

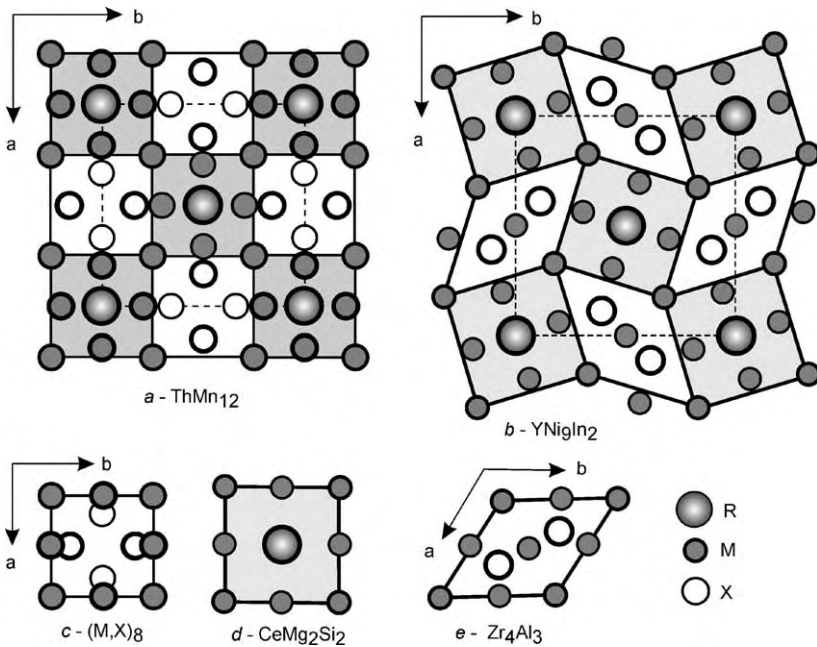


Fig. 82. Packing of slabs of the types $(M, X)_8$ (c) and $CeMg_2Si_2$ (d) in the $ThMn_{12}$ structure (a) and $CeMg_2Si_2$ and Zr_4Al_3 (e) in the YNi_9In_2 structure (b).

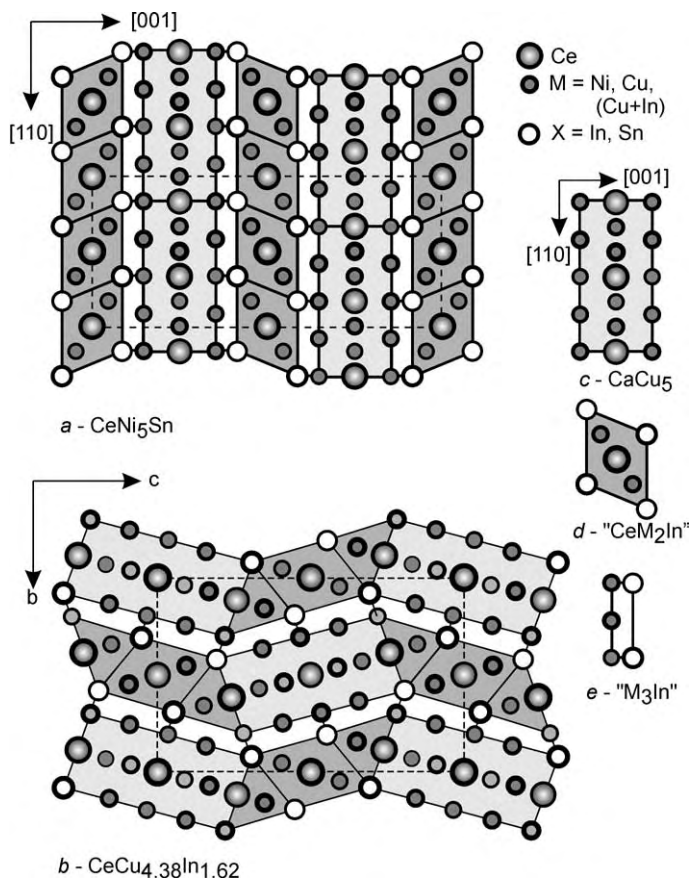


Fig. 83. Packing of slabs of the CaCu_5 type (c) and the hypothetical structures CeM_2In (d) and M_3In (e) in the structures of CeNi_5Sn (a) and $\text{CeCu}_{4.38}\text{In}_{1.62}$ (b).

(SG $P6/mmm$, $a = 543.3$, $c = 539.0$ pm) (Kripyakevich, 1977). In both structures, the ratio of the fragments is 2:2 (fig. 82). Then, the formulæ of the structure types are described for the ThMn_{12} type as follows: $(2\text{CeMg}_2\text{Si}_2) 2R(M, X)_4 + 2(M, X)_8 = R_2(M, X)_8 + (M, X)_{16} = R_2(M, X)_{24} = 2R(M, X)_{12}$ and for the YNi_9In_2 type: $(2\text{CeMg}_2\text{Si}_2)2RM_2M'/_2 + (2\text{Zr}_4\text{Al}_3)2M_5X_2 = R_2M_8 + M_{10}X_4 = R_2M_{18}X_4 = 2RM_9X_2$. The difference in the number of atoms in the Zr_4Al_3 type (7 atoms per unit cell) and in the hypothetical structure $(M, X)_8$ (8 atoms per unit cell) determines the difference in the compositions of ThMn_{12} and YNi_9In_2 .

The following two structure types, hexagonal CeNi_5Sn (Skolozdra and Komarovskaya, 1988) and orthorhombic $\text{CeCu}_{4.38}\text{In}_{1.62}$ (Kalychak et al., 1988a), also have similar metric ratios taking the orthohexagonal setting. Both types can be divided into identical fragments: a CaCu_5 related slab in the orthorhombic setting and two slabs of hypothetical compositions RM_2X and M_3X , or, taking into account the presence of statistical occupancies of atoms

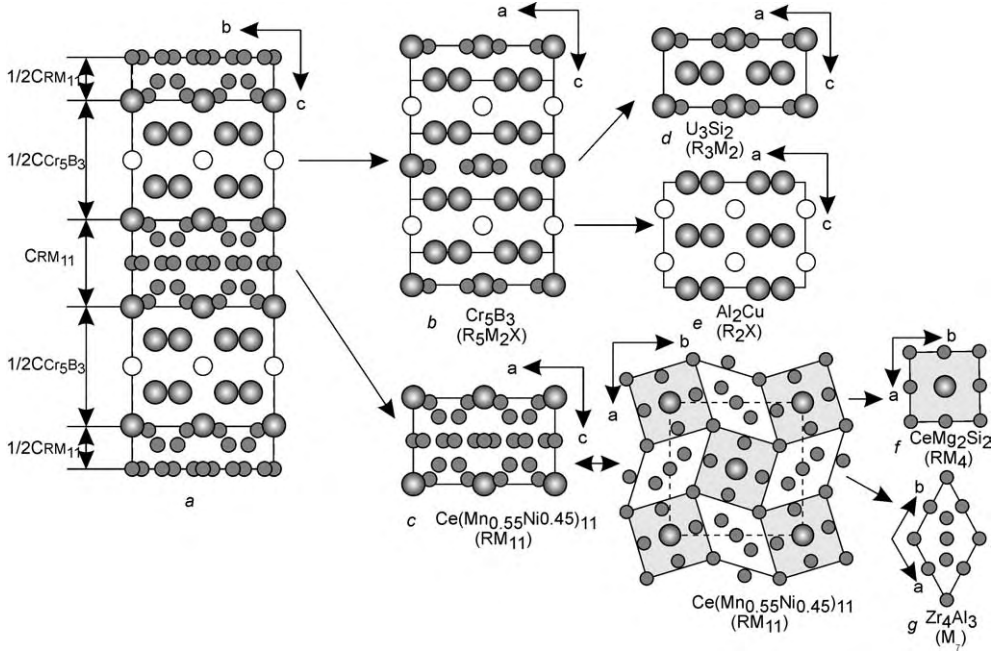


Fig. 84. Representation of the $\text{Nd}_6\text{Fe}_{13}\text{Si}$ structure type ($\text{La}_6\text{Co}_{13}\text{In}$) (a) as a packing of fragments of the Cr_5B_3 (R_5M_2X) (b) and $\text{Ce}(\text{Mn}_{0.55}\text{Ni}_{0.45})_{11}$ (RM_{11}) structures (c). The Cr_5B_3 structure (b) is an intergrowth of U_3Si_2 (R_3M_2) (d) and CuAl_2 (R_2X) (e) slabs. The structure of $\text{Ce}(\text{Mn}_{0.55}\text{Ni}_{0.45})_{11}$ consists of CeMg_2Si_2 (RM_4) (f) and Zr_4Al_3 (M_7) (g) related slabs.

(in particular in the $\text{CeCu}_{4.38}\text{In}_{1.62}$ type), they can be designated as (M, X). One unit cell of each type contains one slab of the CaCu_5 type ($R_2(M, X)_{10}$) in the orthohexagonal setting and 4 slabs of the hypothetical composition: $2R_2(M, X)_{10} + 4R(M, X)_3 + 4(M, X)_4 = R_4(M, X)_{20} + R_4(M, X)_{12} + (M, X)_{16} = R_8(M, X)_{48} = 8R(M, X)_6$. The main difference between the two types is that the arrangement of the slabs is linear (one-dimensional) for CeNi_5Sn and it is mosaic (two-dimensional) for $\text{CeCu}_{4.38}\text{In}_{1.62}$ (fig. 83).

The closely related structure types $\text{Nd}_6\text{Fe}_{13}\text{Si}$ and $\text{La}_6\text{Co}_{11}\text{Ga}_3$ (Weitzer et al., 1993; Sichevich et al., 1985) can be considered as intergrowth structures, which consist of $\text{Ce}(\text{Mn}_{0.55}\text{Ni}_{0.45})_{11}$ ($= RM_{11}$) (SG $P4/mbm$, $a \approx 830$, $c \approx 490$ pm) (Kalychak et al., 1975) (in systems with indium the YNi_9In_2 structure corresponds to it) and Cr_5B_3 (SG $I4/mcm$, $a \approx 760$, $c \approx 1400$ pm for Ho_5Ga_3) slabs with composition R_5M_2X (Grin and Gladyshevskii, 1989) in the ratio 2:1 (fig. 84). The composition of the compound is deduced as follows: $2 \cdot 2RM_{11} + 1 \cdot 4R_5M_2X = R_4M_{44} + R_{20}M_8X_4 = R_{24}M_{52}X_4 = R_6M_{13}X$ ($= \text{La}_6\text{Co}_{13}\text{In}$). As mentioned above, the RM_{11} structure is an intergrowth of the more simple types Zr_4Al_3 and CeMg_2Si_2 in the ratio 2:2, and the structure of Cr_5B_3 (Kuz'ma, 1983) is an intergrowth of the types CuAl_2 and U_3Si_2 in the ratio 1:2. The U_3Si_2 type structure itself consists of CsCl and AlB_2 related slabs (see below).

Considering the packing of slabs in the group *II* compounds (fig. 79), they can be divided into several subgroups with close structural relations. One subgroup consists of the types MgCuAl_2 (ternary indides $R\text{NiIn}_2$), YNiAl_4 ($R\text{NiIn}_4$), and LaNi_3In_6 ($R\text{Ni}_3\text{In}_6$) (Kalychak et al., 1985). All have orthorhombic symmetry and two approximately identical lattice parameters, which are close to ~ 440 and ~ 730 pm.

The structure of MgCuAl_2 is the simplest one of them; half of its unit cell is a basic building block for the formation of two other structures, YNiAl_4 and LaNi_3In_6 . In the YNiAl_4 type two of such fragments are separated by a chain of indium atoms and in the LaNi_3In_6 type the building block is sandwiched by two fragments of a hypothetical structure Ni_2In_4 in the form of distorted, empty octahedra (fig. 85).

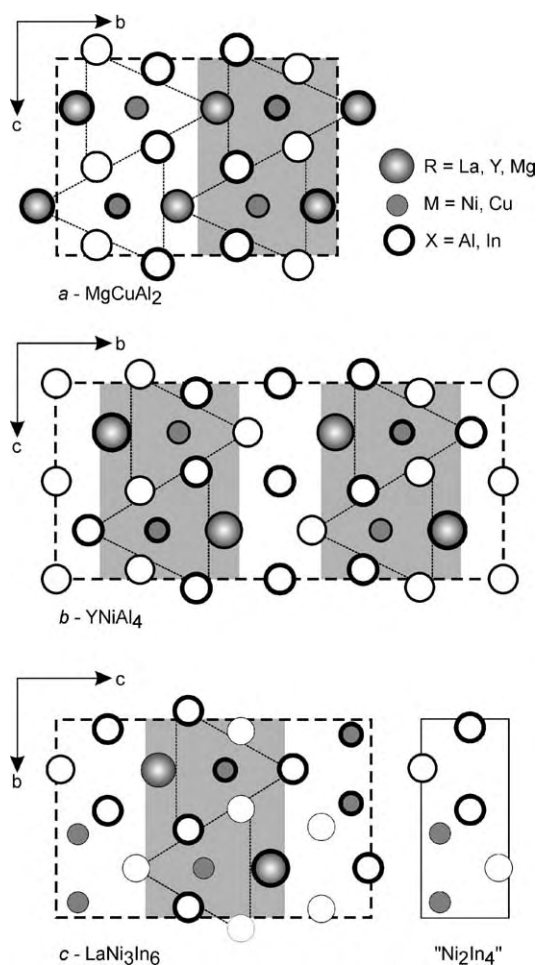


Fig. 85. Relations between the structures of MgCuAl_2 (a), YNiAl_4 (b), and LaNi_3In_6 (c). In each structure half of a MgCuAl_2 unit cell is shaded. The dotted lines outline the motif of the CaCu_5 type structure.

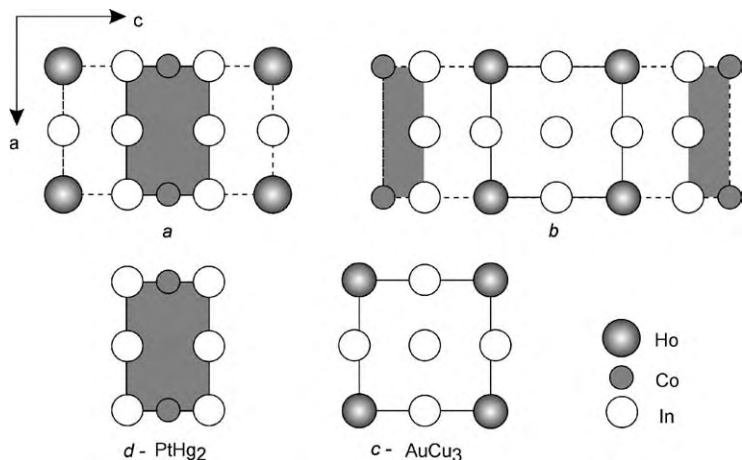


Fig. 86. The structures of HoCoIn_5 (HoCoGa₅ type) (a) and Ho_2CoIn_8 (Ho₂CoGa₈ type) (b). These are the members of a homologous series, based on AuCu_3 (HoIn₃) (c) and PtHg_2 (CoIn₂) (d) related slabs.

The next subgroup consists of tetragonal structure types with very similar *a* parameters: the HoCoGa_5 (Grin et al., 1979a) type for $R\text{CoIn}_5$ (Kalychak et al., 1989a) and the Ho_2CoGa_8 (Grin et al., 1979a) type for $R_2\text{CoIn}_8$ (Kalychak et al., 1989a). They are the members of a one-dimensional homologous series, which is based on AuCu_3 and PtHg_2 type slabs (Kripyakevich, 1977) and is described by the general formula $R_m M_n X_{3m+2n}$, where *m* and *n* are the number of AuCu_3 (composition RX_3) and PtHg_2 (composition MX_2) fragments per unit cell. For HoCoGa_5 , $m = n = 1$, and for Ho_2CoGa_8 , $m = 2$ and $n = 1$ (fig. 86).

The orthorhombic structures $\text{Pr}_5\text{Ni}_6\text{In}_{11}$ (Kalychak et al., 1987) and $\text{Ce}_4\text{Ni}_7\text{In}_8$ (Baranyak et al., 1988a) also have two approximately identical lattice parameters and in contrast to other structures of this group, they contain slabs of the CeMg_2Si_2 type (compounds of group I such as ThMn_{12} and YNi_9In_2 contain these fragments), AuCu_3 , CsCl, and variations of the CaCu_5 structure. The CaCu_5 slab in $\text{Pr}_5\text{Ni}_6\text{In}_{11}$ is ordered as in the superstructure of CeCo_3B_2 (SG $P6/mmm$, $a = 505.7$, $c = 303.6$ pm (Kuz'ma, 1983)). $\text{Ce}_4\text{Ni}_7\text{In}_8$ contains derivatives of the $\text{HoNi}_{2.6}\text{Ga}_{2.4}$ type (Grin and Gladyshevskii, 1989), which has representatives in the systems $R\text{-Ni-In}$. The intergrowth of these slabs is presented in fig. 87. The $\text{Pr}_5\text{Ni}_6\text{In}_{11}$ structure contains: $(4\text{CeMg}_2\text{Si}_2) 4R\text{Ni}_2\text{In}_2 + (2\text{AuCu}_3)2R\text{In}_3 + (2\text{CsCl})2R\text{In} + (2\text{CeCo}_3\text{B}_2)2R\text{Ni}_2\text{In}_3 = R_{10}\text{Ni}_{12}\text{In}_{22} = 2R_5\text{Ni}_6\text{In}_{11}$. The $\text{Ce}_4\text{Ni}_7\text{In}_8$ structure consists of: $(4\text{CeMg}_2\text{Si}_2) 4R\text{Ni}_2\text{In}_2 + (2\text{AuCu}_3)2R\text{In}_3 + (2\text{CsCl})2R\text{In} + (\text{structural fragments of the } \text{HoNi}_{2.6}\text{Ga}_{2.4} \text{ type}) 2R\text{Ni}_4\text{In}(\text{I}) + 2R\text{Ni}_2\text{In}_3(\text{II}) + 4R\text{Ni}_2\text{In}_{3-1}(\text{III}) = R_{16}\text{Ni}_{28}\text{In}_{32} = 4R_4\text{Ni}_7\text{In}_8 (= \text{Ce}_4\text{Ni}_7\text{In}_8)$.

The two orthorhombic structure types PrCo_2Ga (Grin and Gladyshevskii, 1989) and $\text{Sm}_2\text{Co}_9\text{In}_3$ (Baranyak et al., 1993) have two similar lattice parameters and similar fragments (fig. 88 a, b). $R\text{Ni}_2\text{In}$ and $R\text{Co}_2\text{In}$ (Kalychak et al., 1993c; Kalychak and Zaremba, 1994) crystallize with the PrCo_2Ga type. Both types have a larger transition metal content than the structures described above. They contain CaCu_5 type slabs (fig. 88 d) and fragments of the

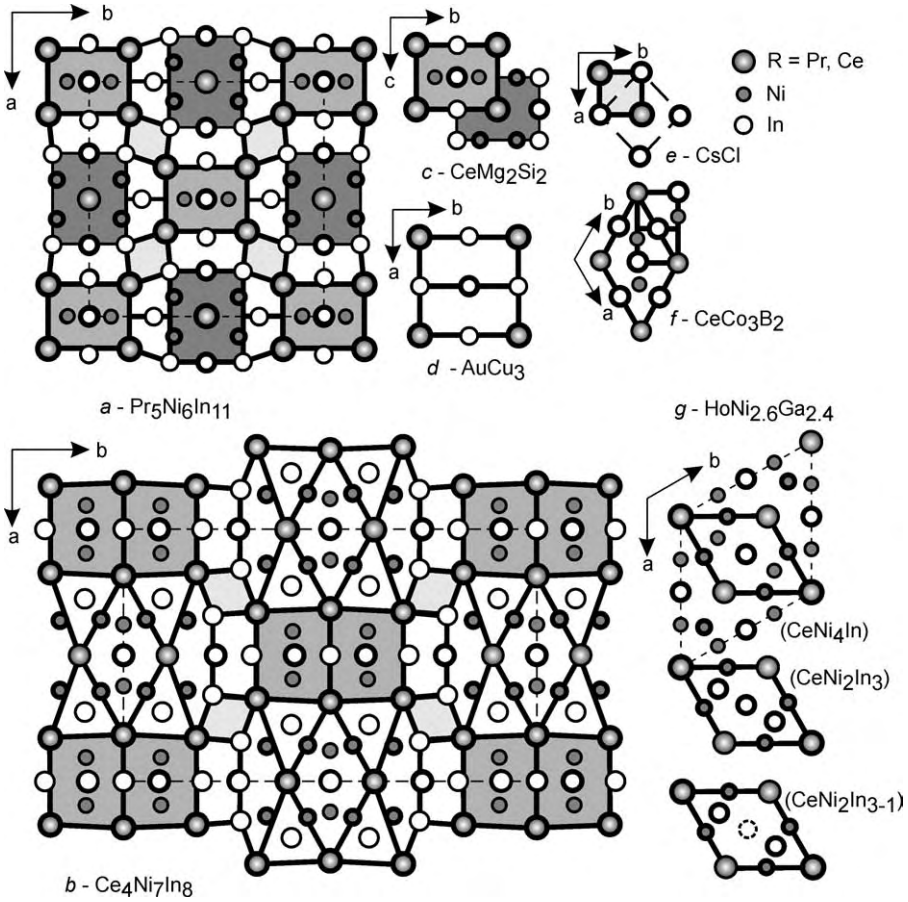


Fig. 87. The structures of $\text{Pr}_5\text{Ni}_6\text{In}_{11}$ (a) and $\text{Ce}_4\text{Ni}_7\text{In}_8$ (b). The various slabs derive from CeMg_2Si_2 (c), AuCu_3 (d), CsCl (e), and CeCo_3B_2 (f) in $\text{Pr}_5\text{Ni}_6\text{In}_{11}$. A larger slab of $\text{Ce}_4\text{Ni}_7\text{In}_8$ corresponds to the structure of $\text{HoNi}_{2.6}\text{Ga}_{2.4}$ (g).

CsCl type (fig. 88 c). The more complex structure of $\text{Sm}_2\text{Co}_9\text{In}_3$ (fig. 88 e) contains two unit cells of the HoCo_2Ga structure and a Co_5In slab with the motif of the CaCu_5 type. The compositions of the compounds are described by the formulae: for the HoCo_2Ga type (compound TbCo_2In): $(1\text{CsCl}) \text{TbIn} + (1\text{CaCu}_5) \text{TbCo}_4\text{In} = \text{Tb}_2\text{Co}_4\text{In}_2 = 2\text{TbCo}_2\text{In}$ and for the $\text{Sm}_2\text{Co}_9\text{In}_3$ type: $(2\text{CsCl}) 2\text{SmIn} + (2\text{CaCu}_5) 2\text{Sm}_{0.5}\text{Co}_4\text{In}_{1.5} + (2\text{CaCu}_5) 2\text{Sm}_{0.5}\text{Co}_5\text{In}_{0.5} = \text{Sm}_4\text{Co}_{18}\text{In}_6 = 2\text{Sm}_2\text{Co}_9\text{In}_3$.

Orthorhombic Mn_2AlB_2 (Becher et al., 1966) for $R_2\text{Ni}_2\text{In}$ (Zaremba et al., 1988), tetragonal Mo_2FeB_2 (Rieger et al., 1964) for $R_2\text{Cu}_2\text{In}$ and $R_2\text{Ni}_2\text{In}$ (Kalychak et al., 1990), and orthorhombic $\text{Lu}_5\text{Ni}_2\text{In}_4$ for $R_5\text{Ni}_2\text{In}_4$ (Zaremba et al., 1991) contain only CsCl and AlB_2

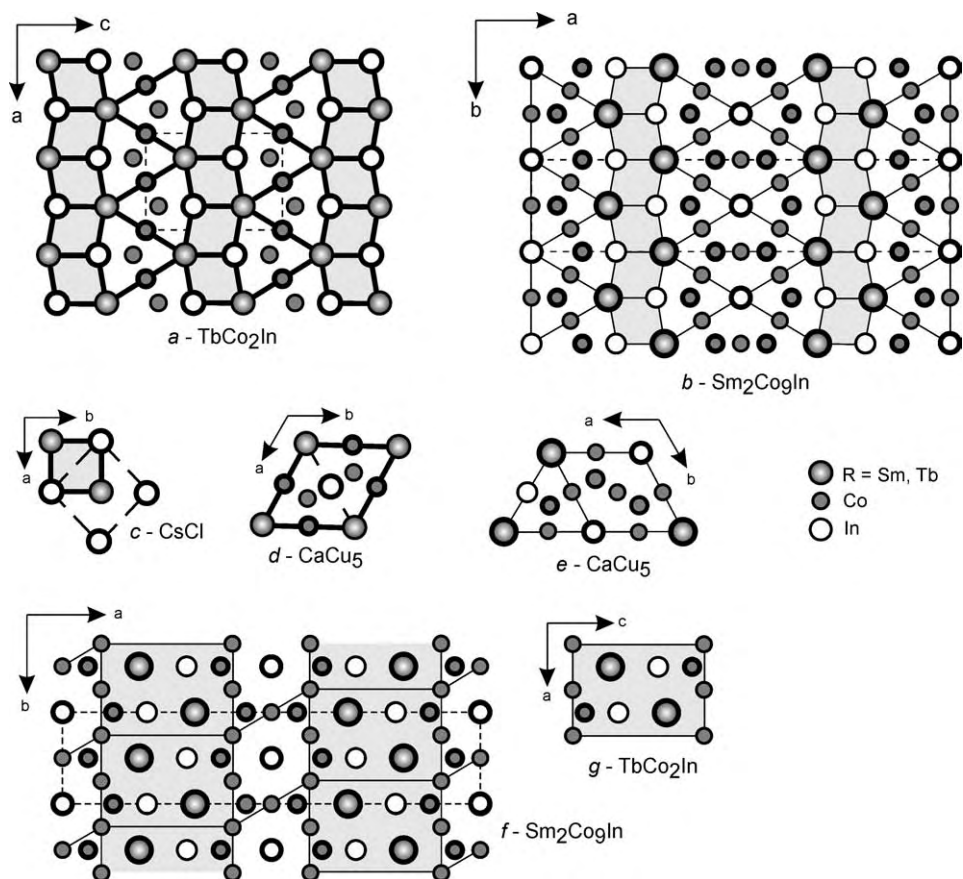


Fig. 88. Packing of CsCl (c) and CaCu_5 (d, e) related slabs in the structures of TbCo_2In (a) and $\text{Sm}_2\text{Co}_9\text{In}_3$ (b). The TbCo_2In (g) slabs in the $\text{Sm}_2\text{Co}_9\text{In}_3$ structure (f) are outlined at the bottom part of the figure.

related slabs. These structures have a similar value for the c lattice parameter, i.e. $\sim 360\text{--}370$ pm.

In addition, Mo_2FeB_2 and $\text{Lu}_5\text{Ni}_2\text{In}_4$ have a similar value for the b lattice parameter (~ 700 pm). Together, the structure types Mn_2AlB_2 and Cr_3AlB_4 (SG $Pmmm$, $a = 295.2$, $b = 809.1$, $c = 298.9$ pm (Kuzma, 1983)) form a one-dimensional homologous series based on CsCl (RX) and AlB_2 (RM_2) slabs as described by the general formula $R_{m+n}M_{2n}X_m$, where m and n are the numbers of CsCl and AlB_2 related slabs, respectively. For the Mn_2AlB_2 type, $m = n = 2$, and for Cr_3AlB_4 , $m = 1$ and $n = 2$ (Kuz'ma, 1983) (fig. 89 a, b). The Cr_3AlB_4 stacking sequence, however, is not known in the indium-based structures.

The structures of Mo_2FeB_2 and $\text{Lu}_5\text{Ni}_2\text{In}_4$ are the representatives of a two-dimensional homologous series formed by the same types and with the same general formula. For Mo_2FeB_2 ,

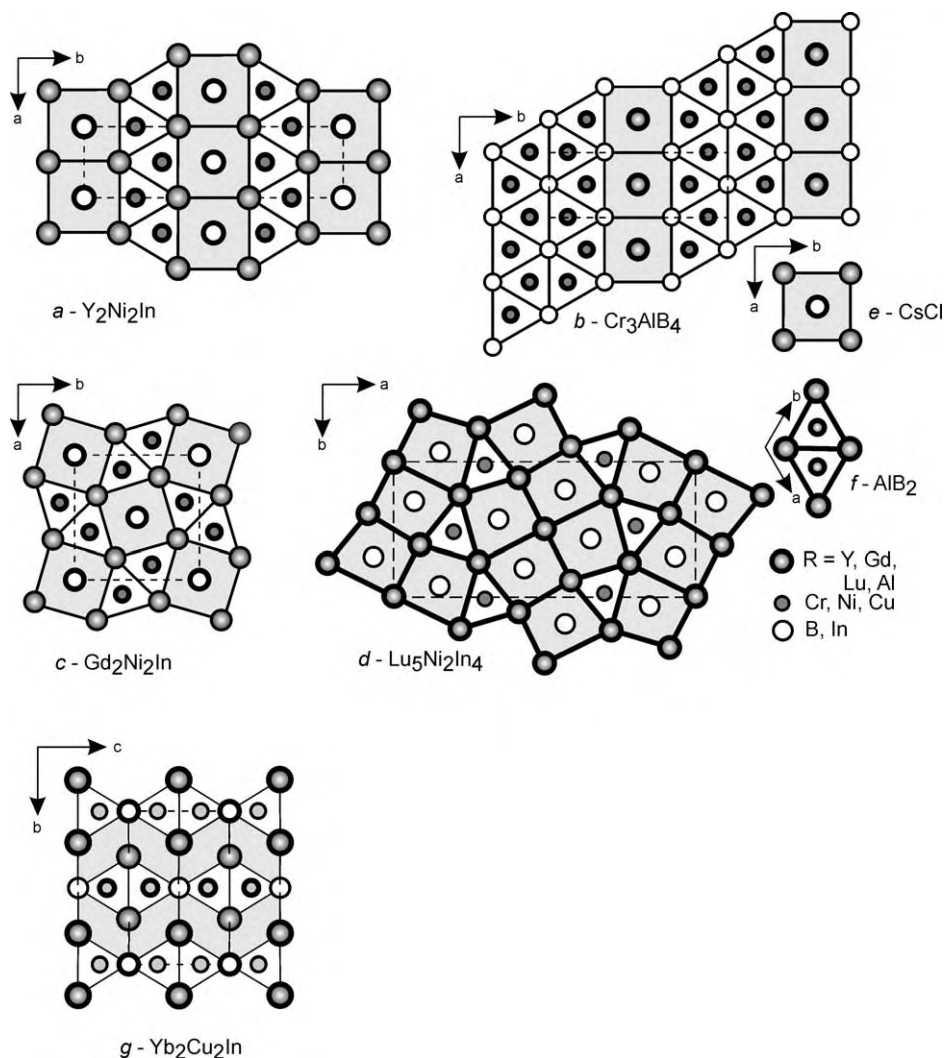


Fig. 89. The structure types Mn_2AlB_2 ($\text{Y}_2\text{Ni}_2\text{In}$) (a) and Cr_3AlB_4 (b) represent a one-dimensional series. The types Mo_2FeB_2 (c) and $\text{Lu}_5\text{Ni}_2\text{In}_4$ (d) represent a two-dimensional homologous series $R_{m+n}M_{2n}X_m$, based on CsCl (e) and AlB_2 (f) related slabs. AlB_2 slabs occur also in $\text{Yb}_2\text{Cu}_2\text{In}$ (g).

$m = n = 2$ and for $\text{Lu}_5\text{Ni}_2\text{In}_4$, $m = 8$, $n = 2$ (fig. 89 c, d). $\text{U}_2\text{Pt}_2\text{Sn}$ (Gravereau et al., 1994) is a ternary ordered version of the Zr_3Al_2 type (Kripyakevich, 1977). This latter structure is a representative of a three-dimensional homologous series of structures, based on the same slabs.

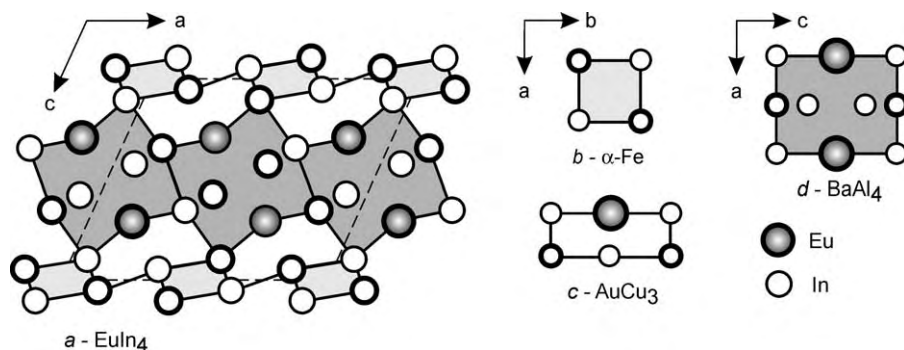


Fig. 90. The EuIn_4 structure (a) as an intergrowth of tungsten ($\alpha\text{-Fe}$) (b), AuCu_3 (c), and BaAl_4 (d) related slabs.

Among binary compounds in the systems $R\text{-In}$, the structure of EuIn_4 (Fornasini and Cirafici, 1990) consists of BaAl_4 (RX_4), AuCu_3 (RX_3), and $\alpha\text{-Fe}$ (X_2) related slabs. The formula of the compound is described by $R_{l+m}X_{4l+3m+n}$, where l , m , and n are the numbers of the respective slabs (fig. 90).

As mentioned above, a significant number of structure types, in which binary and ternary indides of rare earth elements crystallize, contain tetragonal motifs of the indium, CsCl , or AuCu structures and filled or empty trigonal prisms. In particular, binary rare earth metal indides crystallize with the structure types AuCu_3 , CaIn_2 , CeCu_2 , Ni_2In , Co_2Si , and EuIn_4 , and also some ternary indides, i.e. the structure types HoCoGa_5 , Ho_2CoGa_8 , YNiAl_4 , MgCuAl_2 , TiNiSi , AlB_2 , and to some degree GdPt_2Sn . From a purely geometrical point of view, all these structures consist of two different layers, which are stacked along the shortest lattice periods. Often these layers coincide with mirror planes in the structures. Depending on the nature of the rare earth element and the structure type, the shortest lattice parameters have values between 470 and 550 pm. The hexagonal structures of CaIn_2 , AlB_2 , or Ni_2In are viewed in the orthohexagonal settings. In fig. 91 (a–d) the geometrical elements of the structures are presented, and in fig. 91 (e–k) their packing in the real structures is shown.

The structure type of AuCu_3 with $a \sim 326$, $c \sim 461$ pm for GdIn_3 (fig. 87 d) can be considered as a packing of slabs of elemental indium (we remind that elemental indium has $a = 325$, $c = 494$ pm) and AuCu with composition $R\text{In}$ according to $R\text{In}_3 = R\text{In} + \text{In}_2$. In the hexagonal CaIn_2 , AlB_2 , and Ni_2In types, orthorhombic CeCu_2 and Co_2Si types, and monoclinic EuIn_4 type structures of binary indides of rare earth elements, depending on their composition, one can see tetragons of composition $R\text{In}$ (or $R_{1.5}\text{In}_{0.5}$ for compounds with a high rare earth metal content) and empty trigonal prisms of compositions In or $R_{0.5}\text{In}_{0.5}$ with a different degree of distortion. The formulae of the binary structure types are described by the sums of their constituents: AlB_2 ($2R\text{In} + 2\text{In} = 2R\text{In}_2$); CaIn_2 ($4R\text{In} + 4\text{In} = 4R\text{In}_2$); CeCu_2 ($4R\text{In} + 4\text{In} = 4R\text{In}_2$); Ni_2In ($4R_{1.5}\text{In}_{0.5} + 4R_{0.5}\text{In}_{0.5} = 4R_2\text{In}$); Co_2Si ($4R_{1.5}\text{In}_{0.5} + 4R_{0.5}\text{In}_{0.5} = 4R_2\text{In}$).

In the ternary structure types HoCoGa_5 and Ho_2CoGa_8 , formed only by filled tetragonal prisms In_2 and $R\text{In}$, also empty tetragonal prisms of composition In and transition metal filled

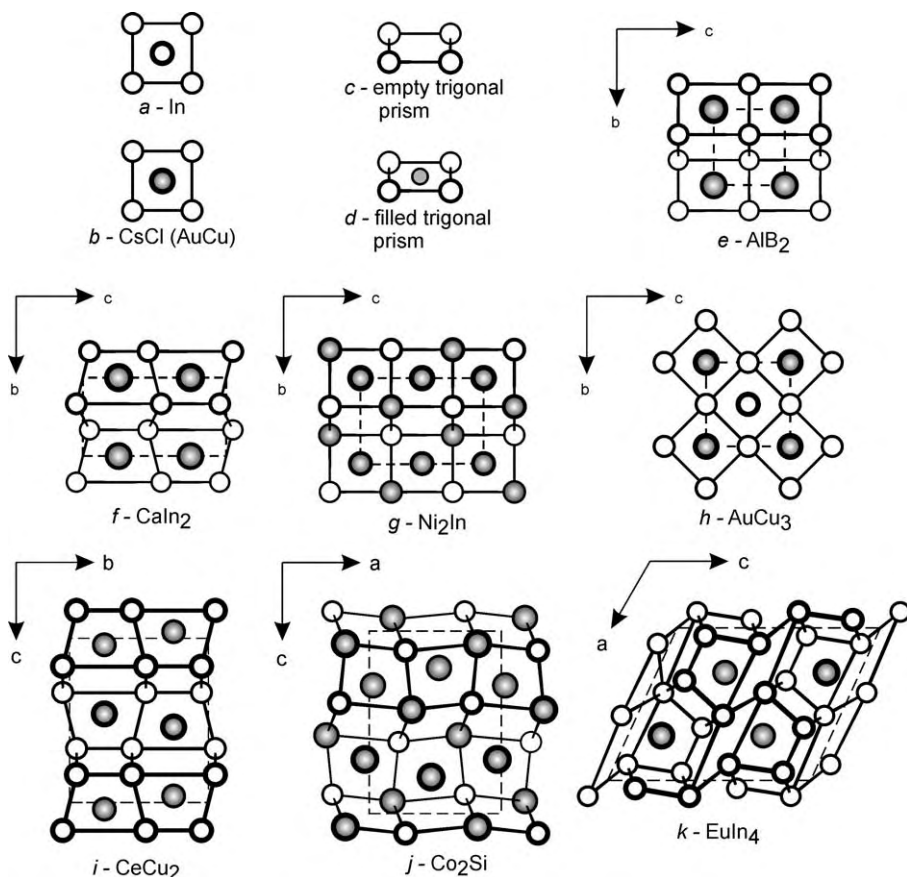


Fig. 91. Geometrical motifs of the structures of binary indides (*a-d*) and their packing in some structure types of binary compounds of the systems *R-In* (*e-k*).

tetragonal prisms exist (fig. 92 *a, b*). The formulæ of these structure types are: HoCoGa_5 ($1R\text{In} + 1\text{In}_2 + 1\text{CoIn} + 1\text{In} = R\text{CoIn}_5$); Ho_2CoGa_8 ($2R\text{In} + 2\text{In}_2 + 1\text{CoIn} + 1\text{In} = R_2\text{CoGa}_8$).

The structure types MgCuAl_2 and YNiAl_4 (fig. 92 *c* and *e*) can be considered as transition metal filled versions of binary compounds $R\text{In}_2$ (Hoffmann and Pöttgen, 2001). In contrast to binary structures of composition $R\text{In}_2$, only half of the trigonal prisms are filled by transition metal atoms. The difference between these two structure types is that in the MgCuAl_2 type a slab of tetragonal prisms $R\text{In}$ alternates with a slab of trigonal prisms, $\text{NiIn}_{0.5}$ and $\text{EIn}_{0.5}$ in the ratio 2:2 (*E* is an empty site). In the YNiAl_4 type, two slabs of tetragonal prisms In_2 and $R\text{In}$ alternate with one slab of trigonal prisms, $\text{NiIn}_{0.5}$ and $\text{EIn}_{0.5}$ (a ratio of 4:2 per unit cell) (fig. 92 *c, d*). The formulæ of the structure types are the following: YNiAl_4 ($4R\text{In} + 4\text{In}_2$

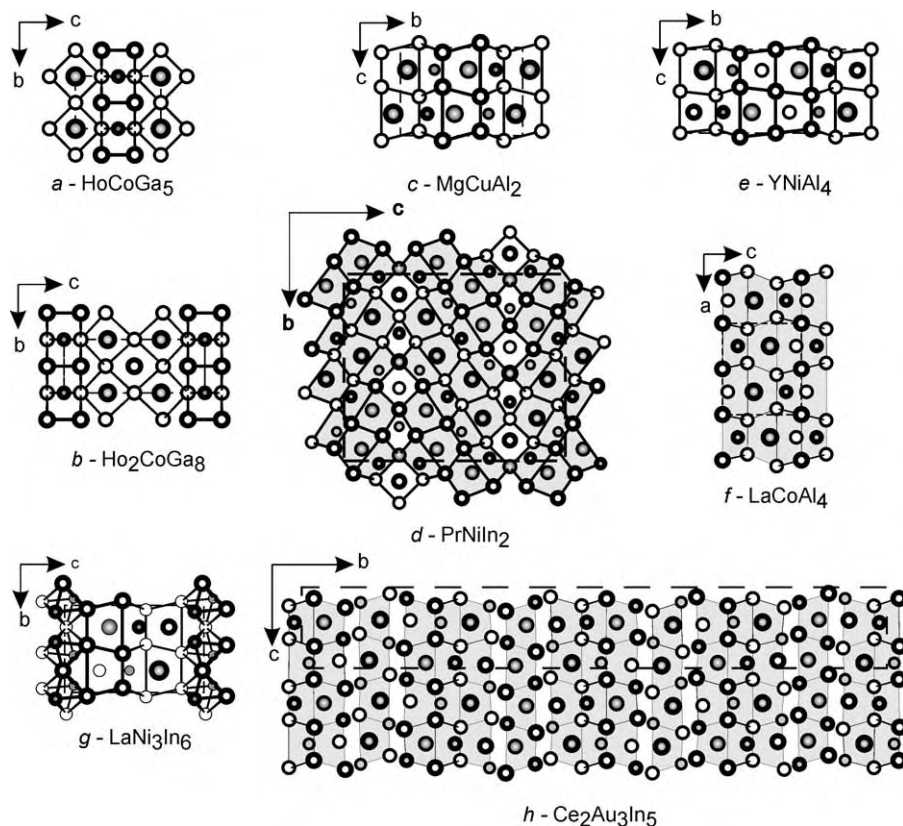


Fig. 92. Tetragonal and trigonal prisms in the structures of the ternary indides HoCoGa_5 (a), Ho_2CoGa_8 (b), MgCuAl_2 (c), PrNiIn_2 (d), YNiAl_4 (e), LaCoAl_4 (f), LaNi_3In_6 (g), and $\text{Ce}_2\text{Au}_3\text{In}_5$ (h).

$+ 4\text{NiIn}_{0.5} + 4\text{EIn}_{0.5} = \text{R}_4\text{Ni}_4\text{In}_{16} = 4\text{RNiIn}_4$); MgCuAl_2 ($4\text{RIn} + 4\text{NiIn}_{0.5} + 4\text{EIn}_{0.5} = \text{R}_4\text{Ni}_4\text{In}_8 = 4\text{RNiIn}_2$).

The LaNi_3In_6 type is formed by the geometrical elements RIn , In_2 , $\text{NiIn}_{0.5}$, and $\text{RIn}_{0.5}$. Furthermore, this structure type contains empty octahedra formed by nickel and indium atoms (fig. 92 g).

$\text{Ce}_2\text{Au}_3\text{In}_5$ (fig. 92 h) contains alternating slabs of LaCoAl_4 (fig. 92 f) and cutouts of MgCuAl_2 (fig. 92 c).

6. Chemical bonding in rare earth transition metal indides

The nature of chemical bonding in the various rare earth transition metal indides strongly depends on the composition. In fig. 93 we present the different structural varieties that occur

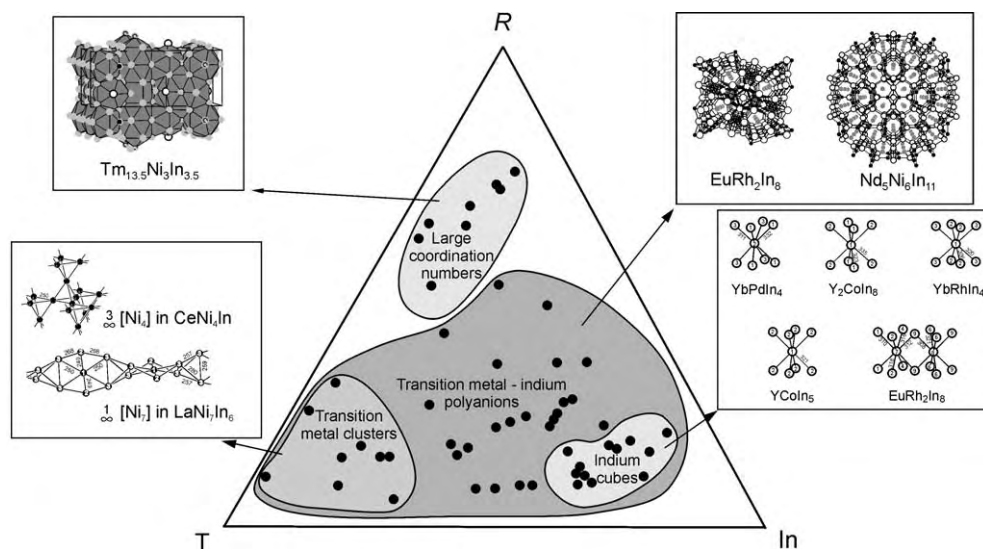


Fig. 93. Regions of different chemical bonding in the ternary systems rare earth metal–transition metal–indium. Characteristic examples for each structural family are shown as call-out.

in the ternary systems. As shown in fig. 93, two large families of compounds, drawn as islands within a generic ternary system, can be identified.

The most complicated structures occur in the region with high rare earth metal content. As an example we present the $Tm_{13.5}Ni_3In_{3.5}$ structure at the left-hand side of fig. 93. Due to the large size of the rare earth metal atoms, these structures are dominated by high coordination numbers. Depending on the rare earth metal content, the coordination numbers vary.

With the coordination numbers CN 12, CN14, CN15, and CN16, sometimes slightly distorted Frank–Kasper polyhedra occur (Frank and Kasper, 1958, 1959). In many cases, the packing of the different polyhedra is very complex. Mostly we observe interpenetrating polyhedra. Chemical bonding in these compounds is more or less isotropic. The shortest interatomic distances in such structures occur between the transition metal and indium atoms. These distances mostly are close to the sum of the covalent radii (Emsley, 1999) and one can assume strong T – In bonding. Nevertheless, in R -rich compounds, T – In interactions play only a subordinate role.

The second family of compounds has a larger transition metal and/or indium content. In all of these compounds T – In bonding is much more important than in the R -rich compounds. The transition metal atoms have broadly varying indium coordination. In compounds like $Ce_8Pd_{24}In$ (Gordon et al., 1996), only one indium atom is bonded to palladium. Such small fragments also occur in the rare earth metal rich compounds. Normally, the lowest coordination number for a transition metal by indium is three. In fig. 94 we present the various $RhIn_x$, $PdIn_x$, and $PtIn_x$ monomeric units in the ternary indides with rhodium, palladium, and platinum as transition metal component. With the other late transition metals similar

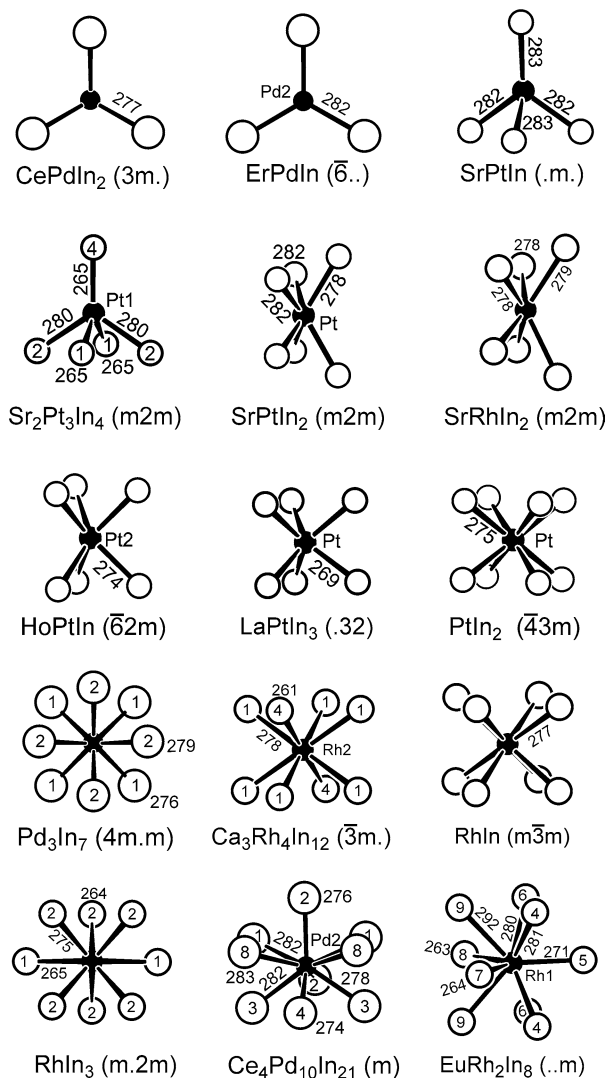


Fig. 94. Cutouts of RhIn_x, PdIn_x, and PtIn_x (x = 3–9) units in various binary and ternary indides. The rhodium, palladium, and platinum atoms are drawn as black circles, the indium atoms as open circles. Relevant interatomic distances in pm and atom labels are indicated. The site symmetries are given in parentheses. Note, that the alkaline earth and rare earth metal atoms are omitted for clarity.

units occur. The highest coordination number of the transition metal by indium is CN 9. The monomeric units are condensed via the indium atoms, which are shared by neighboring units. This way one gets two- or three-dimensional T_xIn_y polyanionic networks. As examples, we have drawn the polyanions, [Ni₆In₁₁] and [Rh₂In₈], of the Nd₅Ni₆In₁₁ (Pöttgen et al., 1999a) and EuRh₂In₈ (Pöttgen and Kußmann, 2001) structures in the upper right-hand part of fig. 93. The rare earth atoms are located in cavities or channels of the three-dimensional polyanions, while they separate layers in the case of two-dimensional networks.

There is not a uniform coloring scheme for the polyanions. The degree of T – T , T – In , and In – In contacts does not necessarily depend on the composition. In GdRhIn_2 (Hoffmann et al., 2000) there occur only Rh – In and In – In interactions within the three-dimensional $[\text{RhIn}_2]$ polyanion, while several Ni_2 dumb-bells (244 and 273 pm) occur in $\text{Nd}_5\text{Ni}_6\text{In}_{11}$ with quite similar composition.

The first very simple parameter that gives information about a potential charge transfer is the electronegativity. For most indides discussed in the present review, the rare earth element is the most electropositive and the late transition metal the most electronegative component, while the indium atoms play a mediate role. These differences in electronegativity lead to a significant filling of the transition metal d bands. The position of the transition metal d block is well below the Fermi level. Thus, the late transition metal atoms become negatively charged and consequently one obtains nickelides, aurides, and related species rather than indides.

We will discuss the situation of chemical bonding for the indides $RT\text{In}_2$ and for $\text{GdAu}_{0.44}\text{In}_{1.56}$ in more detail. With the alkaline earth elements, divalent europium, and divalent ytterbium, the Zintl phases $AE\text{In}_2$ ($AE = \text{Ca}, \text{Sr}, \text{Ba}$), EuIn_2 , and YbIn_2 exist (Iandelli, 1964). Chemical bonding in the binaries is relatively easy to understand. The more electropositive elements lose their two valence electrons and one consequently obtains In^- with a formal charge of -1 . The indium atoms thus acquire the electron configuration of the fourth group main element and indeed they form a network of slightly distorted, condensed tetrahedra similar to lonsdaleite (Donohue, 1974). An ionic formula splitting leads to an electron precise formulation $\text{Eu}^{2+}(\text{In}^-)_2$, etc. In ternary indides like EuPdIn_2 , EuAuIn_2 , or YbPdIn_2 , the indium substructure of binary EuIn_2 and YbIn_2 is retained in an orthorhombically distorted arrangement (fig. 95).

The transition metal atoms in the ternaries fill some of the triangles formed by the alkaline earth, europium, or ytterbium atoms. Since the late transition metal atoms are by far the most electronegative component of the $AET\text{In}_2$, EuTIn_2 , and YbTIn_2 compounds, they tend to fill their d bands. The europium atoms have already completely transferred their valence electrons to the indium network. The electrons filling the transition metal d band consequently originate from an oxidation of the indium network, resulting in longer In – In distances in the ternary indides (fig. 95). The MgCuAl_2 type structure (Perlitz and Westgren, 1943) of these indides is somewhat flexible with respect to the electron count. Such indides also exist with a trivalent rare earth metal, i.e. the series $RR\text{In}_2$ ($R = \text{La}, \text{Ce}, \text{Pr}, \text{Nd}, \text{Sm}$) (Zaremba et al., 2002a) and $R\text{NiIn}_2$ ($R = \text{Eu}$ – Dy) (Zaremba et al., 1987a; Kalychak et al., 1997). The crystal orbital overlap populations have been calculated for BaRhIn_2 (Hoffmann and Pöttgen, 2001). The Rh – In and In – In COOP curves show all bonding states above the Fermi level. Assuming a rigid band model, we can thus explain the existence of the $RR\text{In}_2$ series. For BaPtIn_2 , the Fermi energy already separates In – In bonding from antibonding states. So far, no $R\text{PtIn}_2$ indides are known.

Another possibility to obtain compounds with a trivalent rare earth element with CaIn_2 structure is the direct substitution of indium atoms by largely electronegative transition metal atoms. While a binary indide “ GdIn_2 ” with CaIn_2 structure is not known, such a structural arrangement is realized for $\text{GdAu}_{0.44}\text{In}_{1.56}$ (Pöttgen et al., 1998).

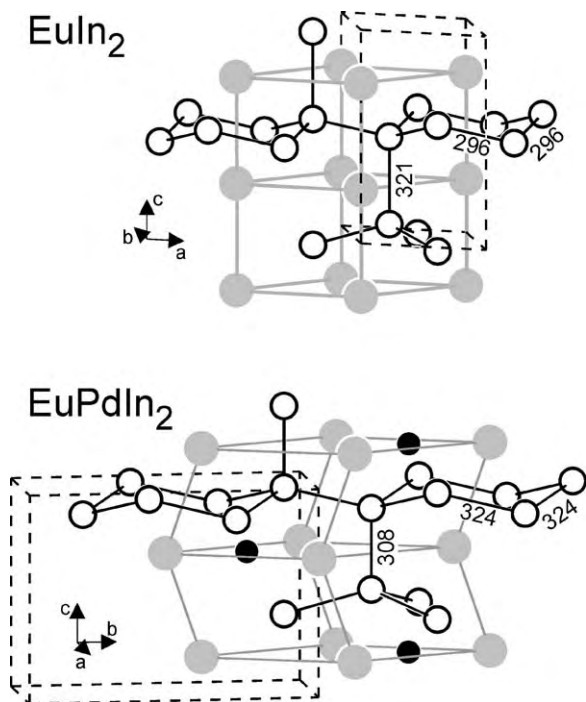


Fig. 95. The crystal structure of EuIn_2 and EuPdIn_2 . The europium, palladium, and indium atoms are drawn as gray, filled, and open circles, respectively. Selected bond lengths within the indium networks are given in pm.

In all rare earth metal–transition metal–indides with polyanionic networks there is a smaller range for the T –In than for the In–In distances. The T –In distances are mostly close to the sum of the covalent radii (Emsley, 1999). Many of the In–In distances compare well with those in tetragonal body-centered elemental indium, where each indium atom has four nearest indium neighbors at 325 pm and eight further neighbors at 338 pm (Donohue, 1974). Sometimes there are also longer In–In contacts, which still belong to the coordination spheres. Based on these distance criteria and the course of the crystal orbital overlap populations (Pöttgen and Dronskowski, 1996; Pöttgen et al., 1998), chemical bonding within the transition metal–indium networks is governed by strong T –In and In–In interactions (Landrum et al., 1998). The rare earth metal atoms have at least one short contact to the network and they are essentially electrostatically (ionically) bonded to the polyanion. This has been demonstrated for various europium and ytterbium intermetallics (Pöttgen and Johrendt, 2000; Pöttgen et al., 2001).

A special situation occurs for some of the cerium and ytterbium based compounds. Here, the $4f^{13}$ (Yb^{3+}) configuration is the hole analogue of $4f^1$ (Ce^{3+}). The degree of $4f$ state contribution at the Fermi energy has a drastic influence on the physical properties of these materials, leading to valence instabilities or heavy fermion behavior.

Two special situations of chemical bonding occur in the compounds with T –In polyanions, i.e. (i) clustering of the T atoms when the transition metal content is high (lower left-hand side

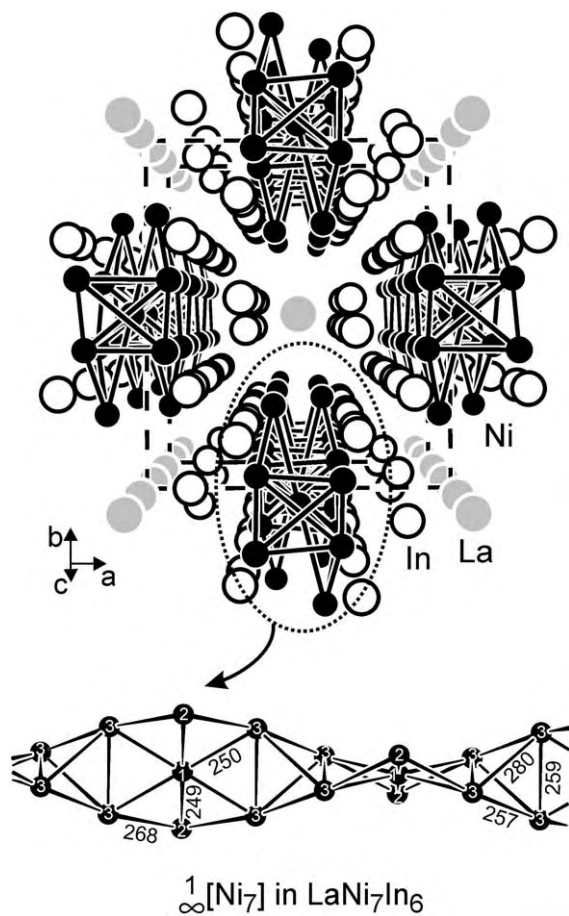


Fig. 96. Perspective view of the LaNi_7In_6 structure along the z axis. The one-dimensional $[\text{Ni}_7]$ cluster chain is emphasized. The lanthanum, nickel, and indium atoms are drawn as gray, filled, and open circles, respectively.

of fig. 93) and (ii) the formation of indium cubes at high indium content (lower right-hand side of fig. 93). A prominent example for such a cluster compound is LaNi_7In_6 (Kalychak et al., 2001) (fig. 96). The nickel d block in this cluster compound stays sharply localized well below the Fermi energy. The course of the gross Mulliken charges, La: +1.81, Ni: -0.94, and In: +0.80 characterizes LaNi_7In_6 as a nickelide. The Ni–Ni bonding and antibonding states are filled formally leading to a closed-shell interaction. The Ni–In and In–In interactions within the cluster chain are strongly bonding, while La–Ni and La–In interactions are much weaker. The small overlap populations and the course of the Mulliken charges fully justify the ionic formula splitting $\text{La}^{3+}[\text{Ni}_7\text{In}_6]^{3-}$ as a first approximation.

With increasing indium content, the indium substructures within the polyanionic networks gradually more resemble the structure of elemental indium. As emphasized at the lower right-hand part of fig. 93, these indium sub-units are more or less distorted bcc indium cubes with In–In distances in the range of elemental indium.

A very interesting situation is the comparison of chemical bonding in the ZrNiAl type intermetallics LaNiIn, CeNiIn, and NdNiIn with the corresponding hydrides $R_3Ni_3In_3H_4$, i.e. $RNiInH_{1.33}$ (Vajeeston et al., 2003). When hydrogen is introduced in the ZrNiAl type substructure, there occurs an anisotropic contraction of the structure along [001]. Force minimization, volume, and c/a optimizations have been performed by first-principles calculations. The theoretical data are in good agreement with the experimental ones. The hydrogen atoms are located in slightly distorted tetrahedral sites formed by three rare earth metal and one nickel atom, with short Ni–H distances. Since the tetrahedra are alternating face and corner sharing along the c axis, there occur very short H–H distances within the three hydrides (156–164 pm). The electronic structure calculations revealed significant ionic bonding for the Ni–H contacts and weak metallic bonding for the short H–H contacts. The electron distribution at the hydrogen atoms is polarized towards the rare earth metal and indium atoms, reducing the repulsion between the negatively charged hydrogen atoms. This further explains the short H–H distances. The density of states curves reveal metallic behavior for the three hydrides. Roughly speaking, there is an ionically bonded Ni–H species within a metallic matrix, a situation of chemical bonding that is very similar to the alkaline earth metal subnitrides (Simon and Steinbrenner, 1996).

The calculated bulk modulus for NdNiIn increases upon hydrogenation, leading to an enhancement of the overall bond strength in this hydride. The integrated crystal orbital Hamilton populations ICOHP's (Dronskowski and Blöchl, 1993) give a direct indication for the bond strength. For the ternary LaNiIn, the strongest bonding interactions were found for the Ni–In contacts followed by La–Ni. This situation is different for the hydride, where the Ni–H interactions are by far the strongest ones, followed by Ni–In. In comparison with LaNiIn, one observes a slight weakening of Ni–In and La–Ni bonding in the hydride LaNiInH_{1.33}.

7. Chemical and physical properties

In this section we discuss the chemical and various physical properties of rare earth–transition metal–intermetallics. Most of these intermetallics are light gray in polycrystalline form. Single crystals have metallic luster. Although the rare earth metals are relatively electropositive elements similar to the alkaline earth metals, there is a significant difference in the stability of the ternary compounds. Most rare earth–transition metal–intermetallics are stable in moist air over several months. There are only few exceptions, e.g. EuZnIn (Pöttgen, 1996a). The stability of the intermetallics, however, differs from that of the corresponding rare earth–transition metal–stannides. The latter can often be synthesized from a tin flux and the excess tin can be dissolved with diluted hydrochloric acid while the ternary stannide is not attacked. Several intermetallics are not stable under such conditions. In the following subsections we first discuss the properties of the extended families of equiatomic intermetallics $RTIn$ and those with the ordered U_3Si_2 or Zr_3Al_2 , $HoCoGa_5$, or Ho_2CoGa_8 , and $MgCu_4Sn$ type structures. These compounds have intensively been investigated with respect to their magnetic and electrical properties since they have comparably simple crystal structures. This facilitates the calculation of the electronic structure and various properties.

7.1. Ternary equiatomic indides $RTIn$

7.1.1. Magnetic and electronic properties

Short overviews on the unusual low-temperature properties of equiatomic $CeTX$ compounds were given by Adroja and Malik (1991) and Fujita et al. (1992). These microreviews focus on valence fluctuation and heavy fermion behavior. The $CeTIn$ indides are discussed together with the $CeTGe$ germanides and $CeTSn$ stannides. Those and most recent data on the indides are summarized here in the following paragraphs.

Single crystal magnetic susceptibility and electrical resistivity data reveal valence-fluctuating behavior for $CeNiIn$ with a significantly anisotropic Kondo effect, which arises from anisotropic c - f mixing along the a and c axes (Fujii et al., 1989). At 2 K, C/T reaches a value of 60 mJ/mol K^2 , which is ten times larger than that in $LaNiIn$ without $4f$ electrons. The physical properties of $CePdIn$ and $CeNiIn$ have been reviewed and compared to those of $UPdIn$ (Fujii et al., 1992).

The magnetic ordering in the Kondo-lattice compound $CePdIn$ has been investigated in detail by Brück et al. (1988). A transition to an antiferromagnetically ordered state has been observed at 1.65 K. In the temperature range 200 to 300 K, $CePdIn$ is a Curie–Weiss paramagnet and the experimental moment (table 13) indicated essentially trivalent cerium. Two maxima occur in the electrical resistivity curve and the Hall effect is anomalously large. Specific heat measurements show an electronic specific heat coefficient $\gamma = 123 \text{ mJ/mol K}^2$. All these features are reminiscent of low T_{SF} spin-fluctuating systems. Isotypic $LaPdIn$ becomes superconducting at 1.6 K. Single crystal magnetic susceptibility data of $CePdIn$ (Fujii et al., 1990) reveal a small peak at the Néel temperature in the c axis magnetic susceptibility, while no anomaly occurs for the a axis. The difference in the paramagnetic Curie temperatures Θ_a and Θ_c is 22 K. In contrast to the magnetic susceptibility data, both the a and c axis electrical resistivity show a double peak structure characteristic for a Kondo lattice system.

In contrast to the antiferromagnetic ordering in $CePdIn$, no sign for a magnetic phase transition is evident for the dense Kondo compound $CePtIn$ down to 50 mK (Fujita et al., 1988; Fujii et al., 1987; Maeno et al., 1987; Satoh et al., 1988, 1990). Specific heat data confirmed that $CePtIn$ is a heavy fermion system with $C/T \geq 0.5 \text{ J/mol K}^2$ below 1 K. Thus, the magnetic ground state of the $CeTIn$ compounds varies dramatically with T . This variation most likely arises from a change in the coupling constant J between the localized $4f$ electrons and the conduction electrons. The temperature dependence of the electrical resistivity of $CeTIn$ ($T = Ni, Pd, Pt$) was compared with those of $LaTIn$ ($T = Ni, Pd, Pt$). Subtracting the electrical resistivities of the lanthanum compounds, it was possible to extract the part of magnetic scattering for the cerium compounds (Fujii et al., 1987). The temperature dependence of the thermoelectric power is similar for the three indides. $CeNiIn$ has the highest absolute values with $50 \mu\text{V/K}$ near 120 K (Yamaguchi et al., 1990).

$CeRhIn$ (Adroja et al., 1989; Malik et al., 1990a) is a mixed-valent indide with $ZrNiAl$ type structure. The magnetic susceptibility shows a broad shoulder around 150 K which is a characteristic feature of intermediate-valent cerium compounds. The magnetic susceptibility behavior can be expressed via the Sales and Wohleben (1975) interconfiguration fluctuation model. The fit resulted in a spin fluctuation temperature of about 500 K. Due to strong magnetic scattering, also the electrical resistivity of $CeRhIn$ shows a broad maximum at about

Table 13
Magnetic properties of equiatomic rare earth metal–transition metal–indides

Compound	Magnetism	$\mu_{\text{exp}}/\mu_{\text{B}}$	$T_{\text{N}}, T_{\text{C}}/\text{K}$	Θ/K	$\mu_{\text{sm}}/\mu_{\text{B}}$	Ref.
GdNiIn	F	–	83	80	–	Buschow, 1975
GdNiIn	F	7.28	83	80	–	de Vries et al., 1985
CeCuIn	P	2.50	–	18	–	Malik et al., 1990a
GdCuIn	AF	7.90	20	20	–	de Vries et al., 1985
EuZnIn	AF	7.80(5)	8.0(5)	6(2)	4.8(1)	Müllmann et al., 1998
CePdIn	AF	2.58	1.8	–15	–	Maeno et al., 1987
CePdIn	AF	2.64	1.65	–41	0.72	Brück et al., 1988
EuPdIn	P	7.99	–	40	–	Cirafici et al., 1985
EuPdIn	MM	7.6(1)	13.0(5)	13(1)	5.9(1)	Pöttgen, 1996b
GdPdIn	F	12.0	102	96.5	7.0	Balanda et al., 2002
GdPdIn	F	–	102	103	–	Oesterreicher, 1977
GdPdIn	F	–	102	103	–	Buschow, 1975
GdPdIn	F	7.73	102	103	–	de Vries et al., 1985
TbPdIn	F	10.4	70, 27, 6	6	3.8	Balanda et al., 2002
TbPdIn	F	–	66	–	–	Nishigori et al., 1998
TbPdIn	F	9.73	74	60	–	Li et al., 2002
DyPdIn	F	11.0	34, 14	5.2	6.7	Balanda et al., 2002
DyPdIn	F	–	31	–	–	Nishigori et al., 1998
DyPdIn	F	10.5	38, 23	29	–	Li et al., 2002
HoPdIn	F	10.8	25, 6	7	7.7	Balanda et al., 2002
ErPdIn	F	9.7	12.3	1.6	6.0	Balanda et al., 2002
PrRhIn	F	3.69(5)	5.8(6)	–2.7(4)	1.60(5)	Zaremba et al., 2000c
EuRhIn	F	7.9(1)	22.0(5)	34(1)	6.7(1)	Pöttgen et al., 1999c
PrPtIn	P	3.53	–	–29	–	Zaremba et al., 2001
EuPtIn	MM	8.0(1)	16.0(5)	20(2)	7.0(1)	Müllmann et al., 1998
YbPtIn	AF	4.21	3.1	–16	1.6	Kaczorowski et al., 2000b
CeAuIn	AF	2.50	5.7	–10	–	Pleger et al., 1987
EuAuIn	MM	7.5(1)	21.0(5)	22(1)	5.9	Pöttgen, 1996b
GdAuIn	AF	8.2(1)	12.5(5)	–17(1)	2.0(1)	Pöttgen et al., 1998
TbAuIn	AF	9.8	35	–17	1.5	Szytuła et al., 2002
DyAuIn	AF	10.3	11	–6	3.2	Szytuła et al., 2002
HoAuIn	AF	10.1	4.8	–9	5.0	Szytuła et al., 2002

140 K. In contrast, LaRhIn behaves like a classical metal. The local magnetic susceptibility of ^{140}Ce in YRhIn, LaRhIn, CeRhIn, and GdRhIn was investigated using the time differential perturbed angular correlation method (Nyayate et al., 1990). The measurements reveal that the local magnetic susceptibility is highly reduced at low temperatures compared to that of the free Ce^{3+} ion.

Brück et al. (1993) studied the electronic properties of the solid solution $\text{CePd}_x\text{Rh}_{1-x}\text{In}$ for $x = 0, 0.2, 0.4, 0.6, 0.8, 0.85, 0.95,$ and 1. The properties continuously change from CeRhIn with unstable $4f$ moments towards CePdIn with localized $4f$ moments. This behavior was studied by magnetic susceptibility and magnetization measurements. At 4.2 K the magnetization at 35 T continuously increases from $x = 0$ to $x = 1$. The electronic specific heat coefficient γ increases with increasing palladium content and reaches a maximum before magnetic ordering sets in at $x = 0.8$. Thus, γ is 40 mJ/mol K² for CeRhIn and it is consid-

erably enhanced for $\text{CePd}_{0.2}\text{Rh}_{0.8}\text{In}$ (78 mJ/mol K^2). For $x = 0.4$ and $x = 0.6$, pronounced upturns are observed in C/T at low temperatures, yielding extrapolated values of about 280 and 700 mJ/mol K^2 . $\text{CePd}_{0.6}\text{Rh}_{0.4}\text{In}$ is a heavy fermion compound showing no sign of magnetic ordering above 300 mK.

CeCuIn remains paramagnetic down to 4.2 K (Malik et al., 1990a). Curie–Weiss behavior is observed above 40 K with an experimental magnetic moment of $2.50 \mu_{\text{B}}/\text{Ce}$ atom and $\Theta = 18 \text{ K}$. The temperature dependence of the electrical resistivity shows metallic behavior with a linear part between 100 and 300 K and a curvature below 100 K.

The electronic structures of mixed-valent CeNiIn and the 6.2 K antiferromagnet CeAuIn have experimentally been investigated via XPS measurements (Gondek et al., 2003). The nickel $3d$ and cerium $4f$ states are close to the Fermi level in CeNiIn , while only the Ce $4f$ states stay close to E_{F} in CeAuIn . The gold $5d$ band is presented by two peaks in the region between 3 and 5 eV below the Fermi energy. Interpretation of the cerium $3d$ spectra according to the Gunnarsson–Schönhammer (1983) theory reveal that the hybridization energy between the cerium $4f$ band and the conduction band is 144 meV in CeAuIn and 205 meV in CeNiIn . An overview on L_{III} X-ray absorption spectroscopy, including data on CeAuIn , is given by Wohlleben and Röhler (1984).

The electrical resistivities of the dense Kondo systems CeNiIn , CePdIn , and CePtIn have been measured under hydrostatic pressures up to 19 kbar (Kurisu et al., 1990). The Kondo temperature of CeNiIn and CePtIn shifts linearly with pressure to higher temperatures at rates of 2.3 and 1.5 K/kbar, respectively. For CePdIn , the pressures were not high enough to reach the CePtIn or CeNiIn state. Measurements of the elastic properties of CePdIn reveal that all elastic constants exhibit softening at low temperatures due to the crystal electric field effect and the antiferromagnetic ordering (Suzuki et al., 1990).

CeAuIn orders antiferromagnetically at 5.7 K as is evident from magnetic susceptibility and specific heat data (Pleger et al., 1987). The electronic specific heat coefficient γ is 30 mJ/mol K^2 . The temperature dependence of the electrical resistivity of CeAuIn shows a magnetic scattering contribution. Thermal conductivity measurements show values of 50 and 60 mW/cm K for LaAuIn and CeAuIn , respectively.

The magnetic properties of RPdIn with hexagonal ZrNiAl type structure have intensively been investigated. The compounds with Gd through Er as rare earth metal component show ferro- or ferrimagnetic ordering at comparatively high ordering temperatures (Oesterreicher, 1977; Nishigori et al., 1998). The recent investigations by Bałanda et al. (2002) are very detailed. These studies revealed additional magnetic phase transitions for the terbium, dysprosium, and holmium compound. The magnetization curves classify the RPdIn indides as soft ferromagnets with almost negligible hysteresis. Some of the RPdIn compounds are not easily magnetizable. Large magnetic anisotropy leads to different critical fields for this metamagnet. This behavior has been investigated in more detail for TbPdIn and DyPdIn in external fields up to 23 T. The critical fields are 5.2 and 15 T for TbPdIn and 3.2 T for DyPdIn at 4.2 K.

The magnetic structures of TbPdIn and DyPdIn were solved from powder neutron diffraction data (Javorský et al., 1998, 2000). TbPdIn is a non-collinear $\mathbf{k} = (0, 0, 0)$ ferromagnet with the terbium magnetic moments within the basal plane. For DyPdIn two different magnetic phases are observed. In the high-temperature phase, $15 \text{ K} < T < T_{\text{ord}}$, the dysprosium

magnetic moments order ferromagnetically along the c axis. Below 15 K, basal-plane components of the dysprosium moments show antiferromagnetic ordering with a propagation vector $\mathbf{k} = (1/2, 0, 1/2)$.

An independent investigation on TbPdIn and DyPdIn by Li et al. (2002) revealed different ordering temperatures as compared to the study by Bałanda et al. (2002). The ordering temperatures are slightly higher for both compounds and the second transition temperature for DyPdIn differs. The nature of these discrepancies remains unclear. One possibility is a difference in the sample preparation or a variable stoichiometry. The investigations by Li et al. (2002) further revealed that for both compounds the ground state is not a collinear ferromagnet, but some canted one with an antiferromagnetic component. The observed metastable magnetic properties are discussed in terms of the domain-wall pinning model. The AC magnetic susceptibility measurements on TbPdIn and DyPdIn by Nishigori et al. (1998) revealed spin-glass behavior. The spin-glass state arises from spin frustration due to the rare earth atoms forming a deformed Kagomé network.

The magnetic properties of SmPdIn with ZrNiAl structure were studied on large single crystals (Ito et al., 1995). SmPdIn orders ferromagnetically at $T_C = 54$ K. Isothermal magnetizations were measured at 4.5 K along the a and the c axis up to external fields of 5.5 T. The a axis is the easy magnetization axis, however, at 5.5 T the magnetization has reached only a value of $0.21 \mu_B/\text{Sm atom}$, roughly 30% of the saturation magnetization. Specific heat measurements on a polycrystalline sample revealed a magnetic entropy that is only 80% of the theoretical value, suggesting that also ferromagnetic ordering might be possible for SmPdIn.

The magnetic hyperfine interactions in GdNiIn, GdCuIn, and GdPdIn have been studied by ^{155}Gd Mössbauer spectroscopy (de Vries et al., 1985). Full hyperfine field splitting is observed at 4.2 K with hyperfine fields between 23.3 and 26.2 T at the gadolinium nuclei. The fitting parameters are listed in table 14.

The lattice parameters of TbPdIn have been refined from X-ray powder diffraction data as a function of temperature (Daniš et al., 2002). These experiments revealed a large anisotropy for the evolution of the a and c lattice parameter. A pronounced minimum occurs for the a parameter around 80 K, slightly higher than the magnetic ordering temperature of 66 K. The c lattice parameter shows a constant increase from low to high temperatures, but with a steeper increase below the ordering temperature. These studies agree well with the magnetization data which revealed the a axis as the easy magnetization axis.

The magnetic susceptibility of EuPdIn and YbPdIn has been measured in the temperature range 100 to 1000 K (Cirafici et al., 1985). While the europium atoms in EuPdIn are in a stable divalent oxidation state over the whole temperature range, a continuous increase of

Table 14
Hyperfine parameters derived from fitting of ^{155}Gd Mössbauer spectra of various GdTIn compounds

Compound	B_{hf}/T	$\Delta E_Q/\text{mms}^{-1}$	Γ/mms^{-1}	δ/mms^{-1}	Ref.
GdNiIn	23.3(1)	0.53(8)	0.76(4)	0.39(1)	de Vries et al., 1985
GdPdIn	24.0(1)	0.56(1)	0.68(4)	0.36(1)	de Vries et al., 1985
GdCuIn	26.2(12)	1.06(14)	0.71(7)	0.48(1)	de Vries et al., 1985
GdAuIn	18.4(2)	-0.707(4)	-	0.355(4)	Pöttgen et al., 1998

the ytterbium valence from 2.05 at 100 K to 2.55 at 1000 K is observed for YbPdIn. The intermediate-valent character of ytterbium is also evident from the specific heat data.

Single crystal magnetization data confirm the Néel temperature of 13 K for EuPdIn with TiNiSi type structure (Ito et al., 1998). The isothermal magnetizations along the a , b , and c axis exhibit three anomalies that are associated with metamagnetic transitions. The magnetic phase diagrams for all three axes have been established. According to the experimental data, EuPdIn has only a small magnetic anisotropy, in contrast to the $RPdIn$ indides with hexagonal ZrNiAl structure.

The influence of thorium substitution in YPdIn and GdPdIn has been studied by Buschow (1975). The lattice parameters correlate with the substitution. In the solid solution Gd_xTh_{1-x} -PdIn, the c parameter decreases while a increases with increasing x . The thorium substitution in YPdIn changes the Pauli susceptibility. In ferromagnetic GdPdIn the magnetic coupling drastically changes upon thorium substitution, resulting in a significant decrease of the paramagnetic Curie temperature.

YbPtIn is a Kondo lattice system, which orders antiferromagnetically at 3.1 K (Kaczorowski et al., 2000a, 2000b; Trovarelli et al., 2000). Successive spin reorientations at lower temperatures are evident from the specific heat and electrical resistivity data. According to the large electronic specific heat coefficient of $\gamma = 750$ mJ/mol K², YbPtIn can be classified as a heavy Fermion system. The complex magnetic behavior of YbPtIn arises from a topological frustration in the ytterbium atom substructure with trigonal symmetry. At 1.7 K and in an external field of 5 T, the magnetization tends towards saturation. The magnetic moment of $1.6 \mu_B$ /Yb atoms, however, is significantly smaller than the free ion value of $4 \mu_B$ for Yb³⁺.

The $EuTIn$ ($T = Zn, Rh, Pd, Pt, Au$) indides have intensively been studied by magnetization measurements, electrical resistivity data, and ¹⁵¹Eu Mössbauer spectroscopy with respect to their magnetic hyperfine interactions at low temperatures (Müllmann et al., 1998; Pöttgen, 1996a, 1996b; Pöttgen et al., 1999c). The basic magnetic data and the fitting parameters for the Mössbauer spectra are listed in tables 13 and 15, respectively. While EuZnIn is a simple antiferromagnet that is stable even in an external field of 5.5 T, metamagnetic transitions are observed for EuPdIn, EuPtIn, and EuAuIn. The ¹⁵¹Eu isomer shifts of the $EuTIn$ indides show a linear correlation with the shortest Eu–Eu distance (Pöttgen et al., 1999c). By comparing the $EuTIn$ indides with similar gallides, stannides, and germanides Müllmann et al. (2001) observed that the isomer shift indeed depends on the valence electron concentration.

The metallic indide PrRhIn ($105 \pm \mu\Omega$ cm at room temperature) orders ferromagnetically at 5.8(6) K with a saturation magnetic moment of $1.60(5) \mu_B/Pr$ at 2 K and 5.5 T (Zaremba et al.,

Table 15

Hyperfine parameters derived from fitting of ¹⁵¹Eu Mössbauer spectra of various EuTIn compounds (4.2 K data). From Müllmann et al. (1998)

Compound	B_{hf}/T	$\Delta E_Q/mms^{-1}$	Γ/mms^{-1}	δ/mms^{-1}
EuZnIn	20.1(3)	5	3.8(3)	-10.27(9)
EuRhIn	22.6(2)	8(1)	2.4	-7.9(1)
EuPdIn	22.2(1)	-2(1)	2.4(1)	-8.8(1)
EuAuIn	21.5(2)	8(1)	2.3	-9.7(4)
EuPtIn	23.1(2)	10(1)	2.3	-8.66(7)

2000c). In contrast, PrPtIn remains paramagnetic down to 1.7 K (Zaremba et al., 2001). The largely negative paramagnetic Curie temperature of -29 K may indicate antiferromagnetic ordering at much lower temperatures. SmPtIn orders ferromagnetically at 25 K. The saturation magnetization of $0.20 \mu_B/\text{Sm}$ at 1.7 K and 5 T is much smaller than expected for the free Sm^{3+} ion ($0.71 \mu_B$). PrRhIn and SmPtIn may be classified as soft ferromagnets.

The compounds RMnIn ($R = \text{Y, Nd, Gd, Dy, Er}$) are the first known manganese containing indides (Dhar et al., 2002a, 2002b). They crystallize with the structures of the cubic Laves phase MgCu_2 ($R = \text{Nd}$) or the hexagonal Laves phase MgZn_2 ($R = \text{Y, Gd, Dy, Er}$). Since with a composition RMnIn an ordered distribution of manganese and indium atoms in the corresponding sites is not possible in the structures of the Laves phases, we observe Mn/In statistics leading to spin-glass behavior. The manganese atoms carry a substantial magnetic moment, but no signature of long-range magnetic ordering is observed. This is supported by specific heat data. After subtraction of the free ion values of R^{3+} , magnetic moments of 5.3 and $1.7 \mu_B$ per manganese atom for GdMnIn and DyMnIn result. The spin-glass behavior is evident from differences in the zero-field cooling and field cooling data. Magnetization measurements reveal substantial coercive fields of 0.072 and 0.22 T for GdMnIn and DyMnIn, respectively. The magnetizations for GdMnIn and DyMnIn are smaller than those for the binary Laves phases GdMn_2 and DyMn_2 . Similar magnetic properties have been observed for ThMnIn with the cubic Laves phase structure. The latter indide shows a sharp ferromagnetic-like transition around 270 K, which may be ascribed to Mn–Mn interactions (Manfrinetti et al., 2000). The magnetic ground state is not clear. There are indications for possible ferromagnetic ordering or even a reentrant spin-glass like state, which most likely results from the Mn/In statistics.

The antiferromagnetic ground state of GdAuIn is stable at least up to 5.5 T (Pöttgen et al., 1998). The magnetization at that field and 4.2 K is $2.1 \mu_B/\text{Gd}$ atom. The ^{155}Gd Mössbauer spectra show one signal that is subject to quadrupole splitting. The ordering temperatures determined from the magnetic susceptibility measurements and the Mössbauer spectra agree well. Full magnetic hyperfine field splitting is detected at 4.2 K. The fitting parameters are listed in table 14.

The magnetic structures of RAuIn ($R = \text{Tb, Dy, Ho}$) were determined from neutron powder diffraction data (Szytuła et al., 2002). Antiferromagnetic ordering is evident from the temperature dependent magnetic susceptibility data (table 13). The magnetic ordering in TbAuIn and DyAuIn is described by the propagation vector $\mathbf{k} = (0, 0, 1/2)$, while two propagation vectors $\mathbf{k}_1 = (0, 1/2, 1/2)$ and $\mathbf{k}_2 = (0, 0, 1/2)$ are needed for HoAuIn. The magnetization isotherms at 1.9 K reveal metamagnetic transitions at critical fields of 2.05 T (TbAuIn), 1.5 T (DyAuIn), and 0.8 T (HoAuIn). For TbAuIn, spin-glass behavior occurs between the Néel temperature $T_N = 35$ K and the spin-freezing temperature T_{SG} of 58.5 K. TbAuIn is paramagnetic above 58 K. Susceptibility data of YbAuIn and YbPdIn indicate intermediate ytterbium valence (Zell et al., 1981). The valence/pressure dependence of both indides and of YbAu_2In has also been determined.

7.1.2. Hydrogenation behavior

Many of the equiatomic indides have intensively been studied with respect to their hydrogenation behavior. In the RNiIn series, only the indides with lanthanum, cerium, praseodymium,

and neodymium form hydrides, while no hydrogen incorporation is observed for those with yttrium and the heavy rare earth metals (Bulyk et al., 1999). The hydrogen insertion into LaNiIn, CeNiIn, and NdNiIn causes a pronounced anisotropic expansion of the unit cell along the *c* axis and results in volume increases up to 9%. The structures of LaNiInH_{2.0}, CeNiInH_{1.8}, and NdNiInH_{1.7} have been investigated by X-ray powder diffraction and the hydrogen desorption behavior was studied in detail. High-resolution neutron diffraction data led to a clear localization of the hydrogen atoms and they revealed extraordinary short H–H separations around 160 pm (Yartys et al., 2002). The chemical bonding situation in R₃Ni₃In₃H₄ (Vajeeston et al., 2003) was discussed in sect. 6 *Chemical Bonding*.

The hydrides CeNiInH_{1.0} and CeNiInH_{1.6} have been investigated by ¹H nuclear magnetic resonance (Ghoshray et al., 1993). The spectra show a narrow single line near 300 K but a Pake doublet at lower temperature. Fitting of the spectrum yields a proton–proton separation of 148(2) pm. Similar results have been obtained for PrNiInH_{1.29} (Sen et al., 1994; Sen et al., 1996).

Hydrogenation of intermediate-valent CeNiIn induces a ferromagnetic transition at $T_C = 6.8(2)$ K (Chevalier et al., 2002). Thus, the insertion of hydrogen forces a cerium valence transition from intermediate-valent to trivalent. CeNiInH_{1.8(1)}} is a Curie–Weiss paramagnet above 100 K with an experimental magnetic moment of 2.61 μ_B /Ce atom and $\Theta = 20$ K. In the ferromagnetically ordered state at 2 K and 2 T, the saturation magnetization of 1.31 μ_B is smaller than that of the free Ce³⁺ ion (2.14 μ_B), suggesting magnetic anisotropy. The first systematic investigations on the hydrogenation behavior of CeNiIn, however, have been performed by Sen et al. already in 1994. Quaternary hydrides of compositions CeNiInH_{*x*} (*x* = 0.5, 0.6, 0.67, 0.75, 1.0, 1.6) showed an increase of the magnetic moment on the cerium atoms from 1.73 μ_B /Ce for *x* = 0 to 2.36 μ_B /Ce for *x* = 1.6.

Mixed-valent CeRhIn forms a higher hydride CeRhInH_{1.55}, which is quite unstable and transforms to the lower hydride CeRhInH_{0.55} (Raj et al., 2002). The hexagonal ZrNiAl related host structure remains for the hydride in a somewhat expanded form. According to magnetic susceptibility measurements, cerium remains in a mixed-valent state also in the hydride; however, a definite shift towards Ce³⁺ is detected, as is evident from a reduction of the Kondo temperature. The hydride formation results in an increasing occupancy of the rhodium *d*-bands.

7.2. Indides R₂T₂In with ordered U₃Si₂ or Zr₃Al₂ type structures

The indides with the diamagnetic rare earth elements scandium, yttrium, lanthanum, and lutetium show Pauli paramagnetism, in agreement with the metallic conductivity. Plots of the magnetic data have so far only been published for Sc₂Ni₂In (Pöttgen and Dronskowski, 1996).

If a magnetic rare earth metal is introduced into these indides, various kinds of magnetic interactions occur. The basic magnetic data of these intermetallics are listed in table 16. The palladium and copper based cerium compounds Ce₂Pd₂In and Ce₂Cu₂In show extended homogeneity ranges Ce₂Pd_{2+*x*}In_{1–*x*} and Ce₂Cu_{2+*x*}In_{1–*x*} (Sampathkumaran and Mallik, 1996). The essential features of thermoelectric power (*S*) measurements of Ce₂Pd_{2.05}In_{0.95} resemble those of a heavy fermion system (Pinto et al., 1997). Magnetoresistivity data underline the important role of the Kondo effect.

Table 16
Magnetic properties of selected R_2T_2X intermetallics

Compound	Magnetism	μ_{exp}/μ_B	$T_N, T_C/\text{K}$	Θ/K	Ref.
Ce ₂ Cu ₂ In	MM	2.48	5.5	-7.7	Kaczorowski et al., 1996a
Gd ₂ Cu ₂ In	F	-	85.5	90	Fisher et al., 1999
Tb ₂ Cu ₂ In	F	-	81	77.2	Fisher et al., 1999
Dy ₂ Cu ₂ In	F/ AF	-	45.5; 22	46	Fisher et al., 1999
Ho ₂ Cu ₂ In	F	-	26.7	29	Fisher et al., 1999
Er ₂ Cu ₂ In	F	-	37	30	Fisher et al., 1999
Tm ₂ Cu ₂ In	F	-	29.5	21	Fisher et al., 1999
Ce ₂ Pd ₂ In	AF	2.9	4.3	12.3	Kaczorowski et al., 1996b
Ce ₂ Pd ₂ In	F	2.48(3)	~ 4.2	18(2)	Gordon et al., 1995
Ce ₂ Pd ₂ In	AF/F	2.34	4.3; 3.8	11	Giovannini et al., 1998
Ce ₂ Pd ₂ In	F	1.7	4	4	Hulliger and Xue, 1994
Pr ₂ Pd ₂ In	AF	3.55	5	-17	Giovannini et al., 1998
Pr ₂ Pd ₂ In	AF	3.54	5	1	Hulliger and Xue, 1994
Nd ₂ Pd ₂ In	AF	3.64	8	3	Giovannini et al., 1998
Nd ₂ Pd ₂ In	AF	3.57	7.5	4	Hulliger and Xue, 1994
Sm ₂ Pd ₂ In	AF	0.58	12; 9	-12	Giovannini et al., 1998
Gd ₂ Pd ₂ In	AF	8.15	20	-9	Giovannini et al., 1998
Gd ₂ Pd ₂ In	AF	7.95	21	-	Hulliger and Xue, 1994
Tb ₂ Pd ₂ In	AF	9.83	32	7	Giovannini et al., 1998
Tb ₂ Pd ₂ In	AF	9.7	31	-5	Hulliger and Xue, 1994
Dy ₂ Pd ₂ In	AF	10.47	12	-20	Giovannini et al., 1998
Dy ₂ Pd ₂ In	AF	10.45	12	-7	Hulliger and Xue, 1994
Ho ₂ Pd ₂ In	AF	10.4	8.5	-2	Giovannini et al., 1998
Ho ₂ Pd ₂ In	AF	10.60	8	-2	Hulliger and Xue, 1994
Er ₂ Pd ₂ In	AF	9.55	5.5	-5	Giovannini et al., 1998
Er ₂ Pd ₂ In	AF	9.65	5	-5	Hulliger and Xue, 1994
Tm ₂ Pd ₂ In	AF	7.32	3.8; 3.2	-22	Giovannini et al., 1998
Tm ₂ Pd ₂ In	AF	7.5	4	-2	Hulliger and Xue, 1994
Yb ₂ Pd ₂ In	IV	4.05	-	-104	Giovannini et al., 1998
Ce ₂ Pt ₂ In	P	2.49	-	-8.4	Kaczorowski et al., 1996a
Ce ₂ Au ₂ In	MM	2.48	3.2	-15.7	Kaczorowski et al., 1996a
Pr ₂ Au ₂ In	F	3.51	< 4	-7	Hulliger, 1996
Nd ₂ Au ₂ In	F	3.50	~ 36	11	Hulliger, 1996
Gd ₂ Au ₂ In	F	7.80	~ 83	85	Hulliger, 1996
Tb ₂ Au ₂ In	F	9.31	~ 73	76	Hulliger, 1996
Dy ₂ Au ₂ In	AF	10.4	24	27	Hulliger, 1996
Ho ₂ Au ₂ In	F	10.3	~ 20	6	Hulliger, 1996
Er ₂ Au ₂ In	F	9.47	19	7	Hulliger, 1996
Tm ₂ Au ₂ In	AF	7.50	6.5	-3	Hulliger, 1996

The antiferromagnetic structures of Pr₂Pd₂In and Nd₂Pd₂In have been refined from neutron powder diffraction data (Fischer et al., 2000). A modulated ordering of the praseodymium and neodymium magnetic moments with propagation vectors $\mathbf{k} = [0, 0, 1/2]$ and $[1/4, 1/4, 0]$ below the Néel temperatures $T_N = 5$ K and 8 K is evident for Pr₂Pd₂In and Nd₂Pd₂In, respectively.

Depending on the size of the transition metal, the ytterbium compounds Yb_2T_2In ($T = \text{Cu}, \text{Pd}, \text{Au}$) crystallize with two different structure types, i.e. the tetragonal Mo_2FeB_2 type for the gold and palladium compound and the orthorhombic W_2CoB_2 type for $\text{Yb}_2\text{Cu}_2\text{In}$ (Giovannini et al., 2001). Susceptibility, electrical resistivity, and heat capacity measurements revealed no magnetic order for any of these compounds. $\text{Yb}_2\text{Cu}_2\text{In}$ and $\text{Yb}_2\text{Au}_2\text{In}$ show stable divalent ytterbium while an intermediate ytterbium valence is detected for $\text{Yb}_2\text{Pd}_2\text{In}$. Divalent ytterbium in $\text{Yb}_2\text{Au}_2\text{In}$ was also reported by Hulliger (1996). $\text{Yb}_2\text{Cu}_2\text{In}$ has independently been investigated by Tsujii et al. (2001). This group prepared $\text{Yb}_2\text{Cu}_2\text{In}$ under high-pressure (3.5 GPa)–high-temperature (870 K) conditions and the properties determined for their sample are in good agreement with the results by Giovannini et al. (2001). A ^{170}Yb Mössbauer spectrum of $\text{Yb}_2\text{Pd}_2\text{In}$ at 4.2 K and 40 mK shows a single signal subject to quadrupole splitting, reflecting the non-cubic site symmetry of ytterbium (Bauer et al., 2003). The quadrupolar coupling parameter is 1.85 mm/s.

A very detailed investigation of the magnetic properties was performed for the series $R_2\text{Pd}_2\text{In}$ (Giovannini et al., 1998). The basic magnetic data are listed in table 16. As expected, the compounds with the diamagnetic lanthanum and lutetium atoms show Pauli-paramagnetism. Interesting results are the wide homogeneity range for $\text{Ce}_2\text{Pd}_{2+x}\text{In}_{1-x}$, which is comparable to the tin compound, $\text{Ce}_2\text{Pd}_{2+x}\text{Sn}_{1-x}$. The intermediate-valent behavior of $\text{Yb}_2\text{Pd}_2\text{In}$ is discussed in detail by Giovannini et al. (2001). Magnetization measurements show metamagnetic transitions for many of the $R_2\text{Pd}_2\text{In}$ compounds with critical fields around 1 T. Strong crystal field splitting occurs for $\text{Ce}_2\text{Pd}_2\text{In}$ (Kaczorowski et al., 1996b). The pressure dependence of the electrical resistivity and the heat capacity was investigated in detail.

The solid solution $\text{Ce}_2\text{Ni}_x\text{Pd}_{2-2x}\text{In}$ was studied for $x = 0-1$ (Ijiri and DiSalvo, 1996). The magnetic properties change gradually from ferromagnetic $\text{Ce}_2\text{Pd}_2\text{In}$ with $T_C = 4$ K to the temperature-independent paramagnet $\text{Ce}_2\text{Ni}_2\text{In}$. These changes are also evident from the behavior of the unit cell parameters and the evolution of the electrical resistivity behavior as functions of x .

Preliminary magnetic data for the series of $R_2\text{Rh}_2\text{In}$ compounds have been reported by Hulliger (1995b). The behavior of the unit cell volumes and the magnetic susceptibility data confirmed tetravalent cerium in $\text{Ce}_2\text{Rh}_2\text{In}$. For $\text{Pr}_2\text{Rh}_2\text{In}$ ($3.60 \mu_B$ and $\Theta = 14$ K) and $\text{Nd}_2\text{Rh}_2\text{In}$ ($3.55 \mu_B$) ferromagnetic transitions at $T_C = 13.5$ and ~ 10 K have been observed. The platinum based indides $\text{Pr}_2\text{Pt}_2\text{In}$ and $\text{Nd}_2\text{Pt}_2\text{In}$ order ferromagnetically at $T_C = 9.5$ and 17 K, respectively (Hulliger, 1995a). $\text{Tb}_2\text{Pt}_2\text{In}$ is an antiferromagnet ($T_N = 40$ K, $9.75 \mu_B$ and $\Theta = 33$ K). A metamagnetic transition occurs at 1.8 T and $T = 2.4$ K. This is also the case for $\text{Ho}_2\text{Pt}_2\text{In}$ ($T_N = 8$ K, $10.3 \mu_B$, $\Theta = 3$ K, $B_C = 0.4$ T, and $T = 2$ K). All these values are only preliminary data. As stated by Hulliger (1995a), the magnetic measurements were carried out on impurity-containing samples. The magnetic data of the $R_2\text{Au}_2\text{In}$ series have also been investigated (Hulliger, 1996). They are listed in table 16. $\text{Ce}_2\text{Au}_2\text{In}$ shows strong crystal field effects and the samarium sample probably contained a ferromagnetic impurity with a Curie temperature of 44 K.

The whole series of Ce_2T_2In ($T = \text{Ni}, \text{Cu}, \text{Rh}, \text{Pd}, \text{Pt}, \text{Au}$) indides has been investigated by Kaczorowski et al. (1996a, 1996b). The authors report structure refinements, magnetization measurements, and a detailed study of the electrical resistivity behavior. The magnetic

contribution to the electrical resistivity was evaluated by subtractions of the diamagnetic part derived from the isostructural lanthanum compounds. The detailed investigations led to a better understanding of the electronic structures of these interesting materials. Magnetization and specific heat measurements of Ce_2T_2In ($T = \text{Cu, Au, Pt}$) at extremely low temperatures gave further interesting results (Mock et al., 1997). $\text{Ce}_2\text{Cu}_2\text{In}$ and $\text{Ce}_2\text{Au}_2\text{In}$ show clear metamagnetic transition at 0.3 T. Spin-glass freezing below ~ 0.5 K is observed for $\text{Ce}_2\text{Pt}_2\text{In}$.

Cerium substitution by diamagnetic lanthanum, yttrium, or lutetium in $\text{Ce}_2\text{Rh}_2\text{In}$ and $\text{Ce}_2\text{Pd}_2\text{In}$ has been investigated by Mallik et al. (1997). Cerium L_{III} spectra revealed cerium valences of 3.07 in $\text{Ce}_2\text{Pd}_2\text{In}$, 3.07 in $\text{Y}_{1.6}\text{Ce}_{0.4}\text{Pd}_2\text{In}$, 3.0 in $\text{Lu}_{1.6}\text{Ce}_{0.4}\text{Pd}_2\text{In}$, 3.18 in $\text{Ce}_2\text{Rh}_2\text{In}$, and 3.20 in CeLaRh_2In . The large γ values (70–100 mJ/mol K^2 for $\text{Y}_{1.6}\text{Ce}_{0.4}\text{Pd}_2\text{In}$ and ~ 150 mJ/mol K^2 for $\text{Lu}_{1.6}\text{Ce}_{0.4}\text{Pd}_2\text{In}$) are attributable to heavy fermion behavior.

All $R_2\text{Cu}_2\text{In}$ indides order ferromagnetically with Curie temperatures between 26.7 and 85.5 K. Strong crystal field anisotropies result in T_C values that do not scale with the de Gennes function of the rare earth elements (Fisher et al., 1999). $\text{Dy}_2\text{Cu}_2\text{In}$ shows a second phase transition to an antiferromagnetic ground state at $T_N = 22$ K.

All $R_2\text{Pd}_2\text{In}$ indides are metallic conductors (Fischer et al., 2000). Anomalies at low temperatures indicate the onset of magnetic ordering. The electrical resistivity of $\text{Ce}_2\text{Cu}_2\text{In}$, $\text{Ce}_2\text{Au}_2\text{In}$, and $\text{Ce}_2\text{Pt}_2\text{In}$ has been measured as a function of temperature and pressure (Hauser et al., 1997). For the copper compound, the Néel temperature increases with increasing pressure, while for $\text{Ce}_2\text{Au}_2\text{In}$ T_N stays nearly constant in the pressure range investigated. Thus, the AF transition is hardly affected by the external pressure. For $\text{Ce}_2\text{Pt}_2\text{In}$ a rapid reduction of $N(E_F)$ with increasing pressure is observed. Additionally, the specific heat behavior of $\text{Ce}_2\text{Cu}_2\text{In}$, $\text{Ce}_2\text{Au}_2\text{In}$, and $\text{Ce}_2\text{Pt}_2\text{In}$ at various external fields has been measured. The high γ value of 500 mJ/mol K^2 for $\text{Ce}_2\text{Pt}_2\text{In}$ classifies this indide as a heavy-fermion system.

A detailed study of the electrical resistivity behavior of the La_2T_2In and Ce_2T_2In ($T = \text{Ni, Cu, Rh, Pd, Pt, Au}$) indides was performed by Kaczorowski et al. (1996a, 1996b). They evaluated the electrical resistivity data according to the modified Bloch–Grüneisen relation and derived the Debye temperatures (table 17).

7.3. Indium-rich indides with HoCoGa_5 or Ho_2CoGa_8 structures

The crystallographic data of CeCoIn_5 and Ce_2CoIn_8 have been published in 1987 by Kalychak et al. The isotypic rhodium and iridium indides have been synthesized in the form of large

Table 17

Parameters of the fits of the resistivities of La_2T_2In according to a modified Bloch–Grüneisen formula (Kaczorowski et al., 1996a, 1996b)

Compound	$\rho_0 / \mu\Omega \text{ cm}$	Θ_D / K	$R / \mu\Omega \text{ cm K}^{-1}$	$K / 10^{-7} \mu\Omega \text{ cm K}^{-3}$
$\text{La}_2\text{Ni}_2\text{In}$	52.5	118	0.578	9.9
$\text{La}_2\text{Cu}_2\text{In}$	25.9	114	0.413	6.1
$\text{La}_2\text{Rh}_2\text{In}$	32.0	119	0.268	5.1
$\text{La}_2\text{Pd}_2\text{In}$	91.8	130	0.964	12.5
$\text{La}_2\text{Pt}_2\text{In}$	42.4	104	0.707	14.3
$\text{La}_2\text{Au}_2\text{In}$	20.7	98	0.376	8.7

single crystals from indium fluxes in the last three years. Discovery of the heavy fermion state and superconductivity in these materials (Petrovic et al., 2001a, 2001b; Thompson et al., 2001) triggered large research programs. In the following paragraphs we summarize the recent results. The data are certainly not complete since several new publications already appeared after the completion of this manuscript.

Among the indides with HoCoGa_5 type structure, CeRhIn_5 (Hegger et al., 2000) has most intensively been investigated with respect to the magnetic and electrical properties. CeRhIn_5 is a heavy-fermion antiferromagnet with an ordering temperature of 3.8 K. Christianson et al. (2002a, 2002b) give a detailed report on the magnetotransport properties of CeRhIn_5 . Resistivity measurements revealed an anisotropy in the Kondo-derived magnetic scattering. The magnetoresistance of CeRhIn_5 is positive. Application of hydrostatic pressure induces a first-order-like transition from an unconventional antiferromagnetic to a superconducting state with $T_C = 2.1$ K (Hegger et al., 2000). The CeRhIn_5 structure contains a tetragonally distorted CeIn_3 slab. Taking the bulk modulus $B = 650$ kbar for binary CeIn_3 with Cu_3Au structure, the difference in the lattice parameters between cubic CeIn_3 at atmospheric pressure and the tetragonally distorted slab in CeRhIn_5 experiences a chemical pressure of approximately 14 kbar. As yttrium is substituted for cerium in the solid solution $\text{Ce}_{1-x}\text{Y}_x\text{RhIn}_5$, the Néel temperature is suppressed, yielding a quantum critical point at an yttrium concentration of $x = 0.38$ (Zapf et al., 2003).

The cerium compound CeRhIn_5 forms a solid solution $\text{Ce}_x\text{La}_{1-x}\text{RhIn}_5$ with the lanthanum compound LaRhIn_5 where the paramagnetic cerium atoms are substituted by diamagnetic lanthanum (Alver et al., 2001). Measurements of the de Haas–van Alphen effect for indides with $x = 0$ –1 reveal that the cerium $4f$ electrons remain localized. Such a behavior is typical of antiferromagnetic heavy fermion compounds. A detailed study of cerium site dilution by lanthanum was presented by Pagliuso et al. (2002) for CeRhIn_5 and Ce_2RhIn_8 . Magnetic susceptibility and low-temperature specific heat data are consistent with a smooth suppression of the Néel temperature by lanthanum doping. This is also the case within the solid solution $\text{Ce}_x\text{La}_{1-x}\text{CoIn}_5$ (Petrovic et al., 2002).

High pulsed magnetic fields up to 50 T have been used to observe the de Haas–van Alphen oscillations in ternary CeRhIn_5 (Cornelius et al., 2000). Specific heat data revealed an enhanced value of the electronic specific heat coefficient $\gamma = 420$ mJ/molK². The electronic and magnetic properties of CeRhIn_5 are anisotropic due to the quasi-two-dimensional character of the crystal structure. In addition, in isotypic CeIrIn_5 the de Haas–van Alphen oscillation has been observed. Due to the tetragonal structure, the topology of the Fermi surface is found to be nearly cylindrical (Haga et al., 2001; Shishido et al., 2002). Electronic structure calculations and the de Haas–van Alphen effect have been used to study the angular-dependent extrema areas and effective masses of CeRhIn_5 (Hall et al., 2001a). Detailed comparison between theory and experiment was given. The density of states shows a predominance of cerium $4f$ states at the Fermi energy. The DOS at E_F is quite large but does not indicate a significant structural instability. Time-of-flight neutron scattering data on large high quality single crystals of CeRhIn_5 gave evidence for two crystal field excitations at 6.9 and 23.6 meV (Christianson et al., 2002b).

Specific heat measurements on CeCoIn_5 and CeIrIn_5 in magnetic fields up to 32 T show only a weak field dependence suggesting that the large Sommerfeld coefficients of both indides are due to correspondingly large effective electron masses (Kim et al., 2001).

The compound Ce_2RhIn_8 is a heavy-fermion antiferromagnet (Cornelius et al., 2001) with a γ value around 400 mJ/molK^2 . The specific heat data at zero applied magnetic field are consistent with the existence of an anisotropic spin-density wave opening a gap in the Fermi surface of CeRhIn_5 . In contrast, Ce_2RhIn_8 shows behavior consistent with a simple antiferromagnetic magnon. The complex magnetic phase diagrams for CeRhIn_5 and Ce_2RhIn_8 studied by Cornelius et al. (2001) are shown in fig. 97. Furthermore, the complex magnetic behavior in the solid solution $\text{CeRh}_{1-x}\text{Ir}_x\text{In}_5$ and the pressure–temperature phase diagram of Ce_2RhIn_8 have intensively been studied (Nicklas et al., 2003a, 2003b; Pagliuso et al., 2001a, 2001b). Susceptibility measurements show experimental moments of 2.6 and $2.3 \mu_B/\text{Ce}$ atom for Ce_2RhIn_8 and Ce_2IrIn_8 , respectively (Ohara et al., 2003; Nicklas et al., 2003b), in agreement with trivalent cerium. The Θ values of -15 K and -85 K for $H\parallel c$ and $H\parallel a$ have been observed for Ce_2RhIn_8 and Ce_2IrIn_8 , indicating similar crystal field effects in both compounds. The isotopic praseodymium indides show magnetic moments close to $3.58 \mu_B$ as expected for Pr^{3+} . The indides $R_2\text{RhIn}_8$ and $R_2\text{IrIn}_8$ ($R = \text{La, Ce, Pr}$)

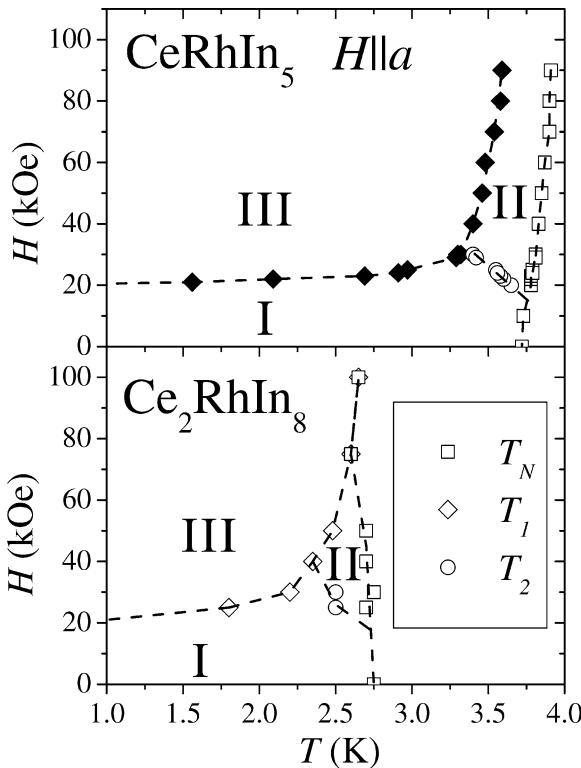


Fig. 97. Cumulative phase diagrams for CeRhIn_5 and Ce_2RhIn_8 for various applied fields along the a axis. From Cornelius et al. (2001). I, II, and III are different antiferromagnetic phases. Filled rhombi denote T_N .

are metallic conductors. The temperature dependence for the electrical resistivity of La_2RhIn_8 is somewhat peculiar and a quantitative understanding has not been achieved yet. The magnetic structure of Ce_2RhIn_8 has been solved from neutron powder diffraction data (Wei et al., 2001). Ce_2RhIn_8 is a collinear antiferromagnet with a propagation vector of $(1/2, 1/2, 0)$ and a staggered magnetic moment of $0.55(6) \mu_B$ per cerium atom at 1.6 K tilted by $38(2)^\circ$ from the tetragonal c axis.

The ^{115}In nuclear quadrupole resonance (NQR) measurements of CeRhIn_5 in the paramagnetic and in the antiferromagnetic states gave evidence for a spiral magnetic order of the cerium magnetic moments, which are incommensurate with the nuclear structure (Curro et al., 2000; Zheng et al., 2003). According to the ^{115}In NQR data of Kohori et al. (2000, 2001), non- s -wave superconductivity occurs in CeRhIn_5 . The magnetic dynamic indicates possible two-dimensional behavior. NQR is an ideal probe for the local magnetic fields as well as the dynamic behavior of the electronic system. Most investigations on the CeTIn_5 and Ce_2TIn_8 intermetallics have been performed on single crystalline materials. Nevertheless, for the NQR measurements on CeRhIn_5 , the crystals were ground to a fine powder in order to facilitate the penetration of the rf fields. Pressure-dependent ^{115}In NQR measurements of CeRhIn_5 were performed by Kawasaki et al. (2001, 2003) and Mito et al. (2001). The Néel temperature is reduced at $p \geq 1.23$ GPa with an emerging pseudogap behavior. Corresponding ^{115}In NQR data for CeIrIn_5 are available from Zheng et al. (2001).

Neutron powder diffraction data confirm the incommensurate magnetic structure of CeRhIn_5 (Wei et al., 2000). The magnetic propagation vector is $\mathbf{k} = (1/2, 1/2, 0.297)$ and temperature independent up to the Néel temperature. At 1.4 K a staggered magnetic moment of $0.264(4) \mu_B$ resides on the cerium atoms and spirals transversely along the c axis. The magnetic moments of the nearest cerium neighbors in the tetragonal basal plane show antiferromagnetic alignment. Magnetic neutron scattering data reveal anisotropic three-dimensional antiferromagnetic fluctuations with an energy scale of less than 1.7 meV for temperatures as high as $3T_C$ (Wei et al., 2002).

CeCoIn_5 has been investigated by means of ^{115}In and ^{59}Co nuclear magnetic resonance measurements above and below the superconducting state (Curro et al., 2001). The hyperfine field couplings of both ^{115}In and ^{59}Co are anisotropic and they exhibit a large change below 50 K arising from changes in the crystal field populations of the cerium atoms indicating localized f electrons. Measurements of the de Haas–van Alphen effect in CeCoIn_5 have been performed in the temperature range 20 to 500 mK and in applied fields up to 18 T. According to the angular-dependent measurements of the external Fermi surface areas, CeCoIn_5 has a more extreme two-dimensional surface than is found in isotypic CeRhIn_5 and CeIrIn_5 (Hall et al., 2001a, 2001b). The unconventional superconducting properties of CeCoIn_5 are strongly supported by point-contact spectra (Goll et al., 2003). The thermal expansion of CeCoIn_5 in zero field shrinks for the $[100]$ direction in the superconducting state, while it expands for $[001]$ (Takeuchi et al., 2002).

The thermal conductivity of CeCoIn_5 has been studied in a magnetic field rotating within the 2D planes (Izawa et al., 2001). These data clearly reveal fourfold symmetry for the thermal conductivity and indicate that the symmetry most likely belongs to dx^2-y^2 implying that the anisotropic antiferromagnetic fluctuation is relevant to the superconductivity. Independent

thermal conductivity studies were reported by Movshovich et al. (2001). DC magnetization measurements of a high-quality single crystal of CeCoIn₅ down to 50 mK showed a sharp magnetization jump with a small hysteresis at an upper critical field H_{C2} for both the a and c directions (Tayama et al., 2002; Sakakibara et al., 2003). These data revealed that the transition to the normal state is of first order. The magnetic phase diagram under magnetic field parallel to the a and c axes are presented. Low-temperature specific heat data in magnetic fields up to 8 T are presented by Ikeda et al. (2001). The solid solution CeRh_{1-x}Co_xIn₅ was recently investigated with respect to the magnetic and superconducting properties (Zapf et al., 2001; Majumdar et al., 2003). T_C increases and T_N decreases with increasing x .

High-field magnetization data revealed weak metamagnetism for CeIrIn₅ for the field along the [001] direction (Takeuchi et al., 2001). The critical field is around 42 T. In the [110] direction, the magnetization increases gradually up to 50 T. For CeRhIn₅, a two-step metamagnetic transition occurs at 2 and 50 T along [001]. Together with detailed specific heat measurements, the magnetic phase diagram of CeRhIn₅ has been constructed. The anisotropy in the magnetization data for both compounds is paralleled by the thermal expansion data along [100] and [001]. All data have been analyzed based on the CEF model. The splitting energies from the first ground state to the first and second excited states are 61 K and 300 K for the iridium and 68 and 330 K for the rhodium compound.

Besides the detailed investigations on the lanthanum and cerium compounds within this structural family, some magnetic data on the isotypic neodymium (Pagliuso et al., 2000) and gadolinium compounds (Pagliuso et al., 2001a) were reported. The basic magnetic data of these intermetallics are listed in table 18. For the neodymium compounds, good agreement has been observed for the transition temperatures detected from the magnetic susceptibility and specific heat measurements.

7.4. Cubic indides with MgCu₄Sn structure

The ternary indide YbCu₄In has a phase transition at 40 K (Felner et al., 1987; Kojima et al., 1990; Lawrence et al., 2001). This indide belongs to a series of Yb_xIn_{1-x}Cu₂ compounds

Table 18
Magnetic properties of tetragonal $RTIn_5$ and R_2TIn_8 indides (Pagliuso et al., 2000, 2001a)

Compound	Magnetism	μ_{exp}/μ_B	$T_N, T_C/K$	Θ/K
NdRhIn ₅	AF	3.66(3)	11	17
Nd ₂ RhIn ₈	AF	3.57(3)	10.7	14
NdIrIn ₅	AF	3.58(3)	13.75	18
Nd ₂ IrIn ₈	AF	3.60(3)	12.30	13
SmRhIn ₅	AF	–	15	–
Sm ₂ RhIn ₈	AF	–	15	–
SmIrIn ₅	AF	–	14.3	–
Sm ₂ IrIn ₈	AF	–	14.2	–
GdRhIn ₅	AF	8.0(1)	40	–69
Gd ₂ RhIn ₈	AF	7.4(1)	40	–73
GdIrIn ₅	AF	7.9(1)	42	–64
Gd ₂ IrIn ₈	AF	8.2(1)	41	–75

with structures derived from the cubic Laves phase MgCu_2 . A short overview on many experimental results and a comparison with other YbXCu_4 ($X = \text{semi-metal or transition metal}$) intermetallics was given recently by Sarrao (1999).

The valence transitions in these indides are accompanied by jumps in the unit cell size. Measurements of ^{119}Sn and ^{170}Yb Mössbauer spectra, neutron diffraction, magnetic susceptibility data, and X-ray absorption measurements at the ytterbium L_{III} edge were used for the study of the valence transition. The transition temperature changes with increasing applied pressure (De Teresa et al., 1996; Hedo et al., 2003). From the volume anomaly at the phase transition, the valence change of ytterbium is found to decrease at the rate $\Delta\nu \approx 0.0045 \text{ kbar}^{-1}$. It has been speculated that the first-order transition in YbCu_4In is a Mott transition between a high-temperature phase, in which localized moments are stabilized by the entropy term of the free energy, and a band-like diamagnetic ground state of the f electrons (Dzero et al., 2000). The magnetoresistance of YbCu_4In has been investigated in magnetic fields as high as 30 T (Immer et al., 1997). Applied pressure shifts the valence transition to lower temperatures. The studies revealed that a single energy scale is associated with the valence transition. *Filamentary* superconductivity was observed above 0.74 GPa and below $\sim 1.2 \text{ K}$ (Hedo et al., 2003).

Analyses of the $^{63,65}\text{Cu}$ NQR resonance frequency and the spin-lattice relaxation time microscopically prove the transition from the local moment state with stable trivalent ytterbium to the Fermi liquid state at the valence transition temperature of 40–50 K (Nakamura et al., 1990).

A time-of-flight neutron scattering study of YbCu_4In was performed to understand the diamagnetic scattering (Lawrence et al., 1999). The key result of the investigation is that the spin dynamics in the mixed valent phase are well described over a broad range of energy transfer ($10 < \Delta E < 150 \text{ meV}$) and incident energies ($35 < E_i < 150 \text{ meV}$) by a Lorentzian power spectrum, centered at $E_0 = 40 \text{ meV}$. The scattering for $\text{YbIn}_{0.3}\text{Ag}_{0.7}\text{Cu}_4$ is inelastic at low temperatures. The crystal field parameters were derived from inelastic neutron scattering data (Severing et al., 1990). The crystal field schemes of YbCu_4In and YbNi_4In are compared.

Neutron powder diffraction data of YbCu_4In revealed that the first order phase transition at 40 K is indeed isomorphic (Lawrence et al., 1996). No change in the crystal symmetry could be detected. An important point concerns the site disorder in the YbCu_4In structure. The diffraction line widths decrease systematically on going from polycrystalline samples with two transitions (40 and 70 K) to polycrystals with a single transition at 40 K to flux-grown single crystals with a sharp transition at 40 K. This is an important result, which clearly shows the influence of the sample type on the long-range ordering. The latter certainly influences the physical properties. An X-ray diffraction study of YbCu_4In up to 13 GPa gave no indication for a structural change (Oomi et al., 1994).

The series $\text{Yb}_x\text{In}_{1-x}\text{Cu}_2$ has intensively been studied in detail with respect to the ytterbium valence transition (Oesterreicher and Parker, 1977; Felner and Nowik, 1986; Felner et al., 1987; Sampathkumaran et al., 1987; Nowik et al., 1988; Kojima et al., 1989). For the solid solution $0.30 \leq x \leq 0.65$, a sharp $\text{Yb}^{2+} \rightarrow \text{Yb}^{3+}$ valence transition occurs at temperatures between 40 and 80 K. For comparison, the authors have also measured the magnetic susceptibility of $\text{Gd}_{0.4}\text{In}_{0.6}\text{Cu}_2$, $\text{Lu}_{0.4}\text{In}_{0.6}\text{Cu}_2$, and $\text{Yb}_{0.5}\text{In}_{0.5}\text{Ni}_2$. The gadolinium and ytterbium

compounds show paramagnetism down to 2 and 4.2 K, respectively, with stable trivalent rare earth atoms. High-field magnetization data on $\text{Yb}_x\text{In}_{1-x}\text{Cu}_2$ reveal metamagnetic transitions at 30 T (Shimizu et al., 1988; Yoshimura et al., 1988).

Ultraviolet and X-ray photoemission spectra of the solid solution $\text{Yb}_x\text{In}_{1-x}\text{Cu}_2$ at 293, 80, and 10 K show a valence transition of ytterbium between 293 and 80 K, much higher than the bulk transition temperature of about 40 K estimated from the magnetic susceptibility data (Ogawa et al., 1988). After subtraction of the Yb(II) surface contribution, the valence was estimated to be 2.63 at 293 K and 2.38 at 80 and 10 K, still much smaller than the bulk data. These measurements suggest that a surface region at least as thick as the XPS probing depth is strongly modified versus the bulk. A high-resolution photoemission study of YbCu_4In showed that the ytterbium 4*f* peak is located just below the Fermi level (Susaki et al., 2001). Temperature dependent measurements show a shift of the photoemission peak from -35 meV at 75 K to -40 meV at 7 K. The bare 4*f* level, which is close to the Fermi energy, is shifted downwards and the hybridization strength decreases from the high-temperature to the low-temperature phase. This picture of chemical bonding is supported by electronic band structure calculations for YbCu_4In and LuCu_4In (Takegahara and Kasuya, 1990).

$\text{Yb}_{0.4}\text{In}_{0.6}\text{Cu}_2$ exhibits a sharp valence transition at 50 K (Felner et al., 1987). Neutron diffraction data prove the absence of magnetic order down to 10 K. Specific heat data show a characteristic increasing of C_p at the transition temperature. Ytterbium L_{III} X-ray absorption spectra show a sudden change in the 4*f* electron occupancy. Based on these data, the ytterbium valence changes from 2.9 to 2.8 below the transition temperature. Furthermore, the authors investigated the influence of ytterbium/indium substitution by lanthanum, europium, and tin. The pressure effect on the valence transition of $\text{Yb}_{0.4}\text{In}_{0.6}\text{Cu}_2$ (electrical resistivity data up to 10 kbar) was measured by Kojima et al. (1988). The valence transition temperature decreases at a rate of -1.7 K/kbar.

Several other indides with the same structure, such as $\text{YbIn}_{1-x}\text{Ag}_x\text{Cu}_4$, have been investigated. Alloying YbInCu_4 with silver increases the temperature of the first-order isomorphic phase transition (Cornelius et al., 1997; Yoshimura et al., 1990). Within the solid solution $\text{YbIn}_{1-x}\text{Ag}_x\text{Cu}_4$, the valence phase transition temperature decreases with increasing pressure at a rate of -1.7 K/kbar for $x = 0$, -1.8 K/kbar for $x = 0.1$, and -1.9 K/kbar for $x = 0.2$ (Matsumoto et al., 1992). The crossover from a first order valence transition in YbInCu_4 to the dense Kondo lattice YbAgCu_4 was also monitored via the concentration dependence of the electronic specific heat coefficient, by electrical resistivity, magnetic susceptibility, and X-ray powder diffraction measurements (Pillmayr et al., 1992; Sarrao et al., 1996). ^{63}Cu NQR studies on YbInCu_4 , $\text{YbIn}_{0.9}\text{Ag}_{0.1}\text{Cu}_4$, and $\text{YbIn}_{0.9}\text{Au}_{0.1}\text{Cu}_4$ show a correlation between the increase of the valence transition temperature and a decrease of the NQR frequency (Kojima et al., 1992). The decrease of the frequency comes mainly from the electronic contribution, suggesting a change in the hybridization of the ytterbium 4*f* and the conduction electrons. The nickel-based indide YbNi_4In is an intermediate-valent compound as is evident from electrical resistivity, thermopower, and ytterbium L_{III} data (Koterlyn et al., 1991).

External pressure of $p \geq 0.8$ GPa suppresses the valence transition in $\text{Yb}_{0.8}\text{Y}_{0.2}\text{InCu}_4$ and induces weak ferromagnetism at the low Curie temperature of 1.7 K (Mitsuda et al., 2002). Although the ytterbium atoms are in the trivalent state, magnetization measurements reveal an extremely small ordered moment of $0.05 \mu_{\text{B}}/\text{Yb}$ atom, much smaller than the theoretical value of $4 \mu_{\text{B}}$ for Yb^{3+} . The whole system $\text{Yb}_{1-x}\text{Y}_x\text{InCu}_4$ ($0 \leq x \leq 1$) was studied with the copper nuclear quadrupole resonance technique, in order to investigate the valence transition and $4f$ electron spin dynamics in the diluted system (Nakamura and Shiga, 1995). The valence transition temperature decreases with increasing x and the NQR frequency at low temperatures is sensitively affected. Analyses of the nuclear spin-lattice relaxation time indicate that the stability of the low-temperature Fermi liquid state is related to the intersite coherence between the ytterbium $4f$ electrons. Magnetization and electrical resistivity measurements on YCu_4In and LuCu_4In with the diamagnetic rare earth metals indicate semimetal behavior (Nakamura et al., 1993b, 1994b).

Alloying of YbCu_4In in the series $\text{Yb}_{1-x}\text{R}_x\text{InCu}_4$ ($R = \text{Y, La, Ce, Lu}$) has been studied for various x values (Mushnikov et al., 2002). Correlating with the size of the rare earth elements, the lattice parameters increase with x for $R = \text{Y, La, and Ce}$, while they decrease for lutetium. The influence of alloying on the valence transition temperature is discussed. Zhang et al. (2002) investigated the ytterbium substitution by yttrium, lutetium, and zirconium.

GdCu_4In is a Curie–Weiss paramagnet with an experimental magnetic moment of $8.15 \mu_{\text{B}}/\text{Gd}$ atom and a paramagnetic Curie temperature of -45 K (Nakamura et al., 1993a). Although the large negative Θ indicates strong antiferromagnetic correlations, the Néel temperature is depressed down to 6.9 K. From the low-temperature specific heat data a typical lambda-type transition is evident at 6.9 K, however, the magnetic entropy reaches only a value of about 60%. Thus, short-range magnetic correlations persist at temperatures higher than T_{N} . These data can be explained in terms of magnetic frustration. The magnetization vs external field dependence increases monotonically and approaches a moment of $6.5 \mu_{\text{B}}/\text{Gd}$ atom at 4.2 K and 3.5 T, close to the saturation magnetization of $7 \mu_{\text{B}}$ for Gd^{3+} . The antiferromagnetic short-range correlations above the Néel temperature have also been studied in detail for the solid solution series $\text{Gd}_{1-x}\text{Lu}_x\text{Cu}_4\text{In}$, where part of the magnetic gadolinium atoms is substituted by diamagnetic lutetium (Nakamura et al., 1994a).

The nickel-based compound PrNi_4In has a diamagnetic ground state (Suzuki et al., 2003). A small upward curvature of the inverse magnetic susceptibility vs temperature dependence indicates a relatively large crystal electric field splitting. Magnetization data at 2 K in magnetic fields up to 30 T show a field-induced transition and a tendency to saturation above 20 T at a value of $\sim 2.4 \mu_{\text{B}}$, smaller than the expected moment of $3.2 \mu_{\text{B}}$ for Pr^{3+} .

Most of the platinum based compounds RPt_4In remain paramagnetic down to 4.2 K (Mallik et al., 1990b). The magnetic moments are close to the free ion values of the respective R^{3+} cations (table 19). Ferromagnetic ordering is detected for the europium and gadolinium compounds. In the magnetically ordered state, EuPt_4In and GdPt_4In exhibit full parallel spin alignment. Deviations from the trivalent oxidation states are evident for CePt_4In and EuPt_4In . The latter has a stable $4f^7$ configuration for the europium atoms, while the strongly negative paramagnetic Curie temperature of CePt_4In is indicative for intermediate valence or Kondo type interactions.

Table 19
Magnetic $R\text{Pt}_4\text{In}$ indides with MgCu_4Sn structure (Malik et al., 1990b)

Compound	Magnetism	$\mu_{\text{exp}}/\mu_{\text{B}}$	$T_{\text{N}}, T_{\text{C}}/\text{K}$	Θ/K	$\mu_{\text{sm}}/\mu_{\text{B}}$
LaPt_4In	P	—	—	—	—
CePt_4In	P	2.54	—	-255	—
PrPt_4In	P	3.63	—	-6	—
NdPt_4In	P	3.78	—	-8	—
SmPt_4In	NCW	—	—	—	—
EuPt_4In	P	7.56	53	66	7.3
GdPt_4In	P	8.03	20	16	6.9
TbPt_4In	P	10.13	—	5	—
DyPt_4In	P	10.83	—	4	—
HoPt_4In	P	—	—	—	—
ErPt_4In	P	—	—	—	—
TmPt_4In	P	7.85	—	0	—

7.5. Ternary indides with CsCl superstructures or Heusler phases

The binary intermetallics GdAg and GdZn form solid solutions $\text{GdAg}_{1-x}\text{In}_x$ and $\text{GdZn}_{1-x}\text{In}_x$ (Buschow et al., 1972; Lal, 1982; Larica and Guimarães, 1976; Oppelt et al., 1972; Alfieri et al., 1966). These compounds show ferromagnetic ordering above 100 K. The Curie temperatures within the solid solutions vary with the valence electron concentration. With the diamagnetic rare earth elements yttrium and lanthanum, the Pauli susceptibility also varies with the number of conduction electrons. A cubic-to-tetragonal phase transition is observed within the solid solution $\text{LaAg}_x\text{In}_{1-x}$ (Ihrig et al., 1973). The $\text{LaAg}_x\text{In}_{1-x}$ alloys have intensively been investigated by X-ray powder diffraction and magnetic susceptibility measurements. According to the experimental data, the phase transformation arises from a band Jahn–Teller effect. The magnetic data of the whole series of $\text{RAg}_{0.5}\text{In}_{0.5}$ ($R = \text{Gd}, \text{Tb}, \text{Dy}, \text{Ho}, \text{Er}, \text{Tm}, \text{Yb}$) compounds are listed in table 20 (Lal and Methfessel, 1981).

The series of terbium compounds $\text{TbAg}_{1-x}\text{In}_x$ has been investigated in detail with respect of the influence of the valence electron concentration on the magnetic structure (Cable et al., 1965; Yagasaki et al., 1978a). The Néel temperatures for $\text{TbAg}_{0.8}\text{In}_{0.2}$, $\text{TbAg}_{0.6}\text{In}_{0.4}$, $\text{TbAg}_{0.5}\text{In}_{0.5}$, and $\text{TbAg}_{0.4}\text{In}_{0.6}$ are 90, 57, 64, and 77 K, respectively. The magnetic structures were determined from neutron diffraction data. Also in the pseudo-binary system $\text{GdAg}_{1-x}\text{In}_x$, the type of magnetic ordering depends on the valence electron concentration (Sekizawa and Yasukōchi, 1966). With $x = 0.1, 0.8,$ and 0.9 antiferromagnetic ordering occurs, while samples with $x = 0.3, 0.5,$ and 0.7 order ferromagnetically. The basic magnetic data are summarized in table 20. Under hydrostatic pressure conditions, the Néel temperatures do not change with pressure within the experimental error, while the Curie temperatures shift to higher temperatures with increasing pressure (Yagasaki et al., 1978b).

The structural and magnetic properties of the whole series of Heusler type compounds RAu_2In ($R = \text{Y}, \text{La–Lu}$) has been investigated with great care by Besnus et al. (1985, 1986). The indides with lanthanum, cerium, praseodymium, and neodymium show a crystallographic transition from cubic to tetragonal as is evident from X-ray powder data. The transition temperature decreases from 355 K for LaAu_2In to 70 K for the neodymium compound. This

Table 20

Magnetic properties of rare earth metal–transition metal–indides with CsCl superstructures or Heusler type structure

Compound	Magnetism	$\mu_{\text{exp}}/\mu_{\text{B}}$	$T_{\text{N}}, T_{\text{C}}/\text{K}$	Θ/K	$\mu_{\text{sm}}/\mu_{\text{B}}$	Ref.
GdAg _{0.9} In _{0.1}	AF	8.4	132	−28	−	Sekizawa and Yasukōchi, 1966
GdAg _{0.8} In _{0.2}	F	7.9	40	42	1.1	Sekizawa and Yasukōchi, 1966
GdAg _{0.7} In _{0.3}	F	8.2	72	80	4.5	Sekizawa and Yasukōchi, 1966
GdAg _{0.5} In _{0.5}	F	8.1	122	126	6.6	Sekizawa and Yasukōchi, 1966
GdAg _{0.3} In _{0.7}	F	8.5	116	105	3.9	Sekizawa and Yasukōchi, 1966
GdAg _{0.2} In _{0.8}	AF	8.3	77	63	−	Sekizawa and Yasukōchi, 1966
GdAg _{0.1} In _{0.9}	AF	8.7	155	−8	−	Sekizawa and Yasukōchi, 1966
GdAg _{0.5} In _{0.5}	F	8.54	118	120	7.61	Lal and Methfessel, 1981
TbAg _{0.5} In _{0.5}	MM	9.91	66	70	7.94	Lal and Methfessel, 1981
DyAg _{0.5} In _{0.5}	MM	11.05	30	32	9.61	Lal and Methfessel, 1981
HoAg _{0.5} In _{0.5}	F	10.48	24	18.1	−	Lal and Methfessel, 1981
ErAg _{0.5} In _{0.5}	F	9.24	22	16.0	−	Lal and Methfessel, 1981
TmAg _{0.5} In _{0.5}	F	7.48	21	16.0	−	Lal and Methfessel, 1981
YbAg _{0.5} In _{0.5}	F	3.86	20	14.0	−	Lal and Methfessel, 1981
CeAg ₂ In	AF	2.54(2)	2.7(5)	−9(1)	−	Galera et al., 1984
PrAg ₂ In	P	3.63(3)	−	−16(2)	−	Galera et al., 1984
NdAg ₂ In	AF	3.68(3)	2.5(5)	−24(2)	−	Galera et al., 1984
SmAg ₂ In	AF	−	4.5(5)	−23(2)	−	Galera et al., 1984
GdAg ₂ In	AF	8.10(8)	10.0(5)	−56(5)	−	Galera et al., 1984
GdAg ₂ In	AF	8.10	10	−56	−	de Vries et al., 1985
TbAg ₂ In	AF	9.62(9)	8.8(5)	−29(2)	−	Galera et al., 1984
DyAg ₂ In	AF	10.33(10)	3.5(5)	−20(2)	−	Galera et al., 1984
HoAg ₂ In	AF	10.23(10)	< 2	−14(1)	−	Galera et al., 1984
ErAg ₂ In	AF	9.47(9)	< 2	−9.5(10)	−	Galera et al., 1984
TmAg ₂ In	P	7.33(7)	−	−5.0(5)	−	Galera et al., 1984
CeAu ₂ In	AF	2.56	1.2	−14	−	Pleger et al., 1987
CeAu ₂ In	AF	2.57	1	−15	1.05	Besnus et al., 1986
PrAu ₂ In	−	3.55	−	−5	1.03	Besnus et al., 1986
NdAu ₂ In	−	3.70	−	−8	1.78	Besnus et al., 1986
SmAu ₂ In	−	−	−	−	0.15	Besnus et al., 1986
GdAu ₂ In	AF	8.0	11.5	−14	6.8	Besnus et al., 1986
TbAu ₂ In	AF	9.7	8.2	−7	7.4	Besnus et al., 1986
DyAu ₂ In	AF	10.8	6.0	−5	7.8	Besnus et al., 1986
HoAu ₂ In	AF	10.8	2.6	−5	7.8	Besnus et al., 1986
ErAu ₂ In	−	9.63	−	−4	6.7	Besnus et al., 1986
TmAu ₂ In	−	7.06	−	−35	5.65	Besnus et al., 1986
YbAu ₂ In	IV	−	−	−	0.17	Besnus et al., 1986

structural transition has a drastic effect on the electrical behavior of these indides (abrupt change in the slope), but no observable effect on the magnetic data (table 20). The samarium and ytterbium compound show non-Curie–Weiss behavior. Specific heat data revealed a high γ coefficient of 130 mJ/mol K² for the cerium compound (Pleger et al., 1987).

The electrical resistivity of the intermediate-valent ytterbium compound YbAu₂In has been investigated under high-pressure conditions (Alami-Yadri et al., 1998) up to 8 GPa. The Kondo temperature decreases with increasing pressure, while the residual electrical resistiv-

ity increases in the same range. A minimum in $\rho(T)$ is observed at low temperatures. The pressure dependence can be ascribed to a Kondo hole effect.

The crystal field (CF) level scheme of YbPd_2In and HoPd_2In has been determined by inelastic neutron scattering experiments (Babateen et al., 1995): $W = 0.02673$; $X = 0.3543$ for HoPd_2In and $W = -0.5194$; $X = -0.7485$ for YbPd_2In . For the magnetization curves, satisfactory agreement is observed for the calculated and measured data.

The solid solution $\text{LaAg}_x\text{In}_{1-x}$ crystallizes with a CsCl type structure (Balster et al., 1975). This pseudobinary system undergoes a martensitic (displacive) crystal structure transition. At low temperature the X-ray powder patterns of polycrystalline samples show line splitting corresponding to a cubic-to-tetragonal transformation. The indium concentration $1 - x$ and thus the electron count per formula unit has a large influence on the transition temperature. This structural phase transition is revealed also in the temperature dependence of the electrical resistivity. For indium concentrations above 5% the curves show a pronounced hysteresis behavior.

The magnetic properties in the whole series of RAg_2In indides, except europium and ytterbium, have been investigated by Galera et al. (1984). The magnetic data are summarized in table 20. SmAg_2In shows Van Vleck behavior, while the other compounds behave as Curie–Weiss paramagnets, ordering antiferromagnetically at low temperatures. Most structural investigations were done by X-ray powder diffraction. Since silver and indium differ only by two electrons, the ordering between these atoms is hardly detectable by X-rays. The authors additionally performed neutron diffraction experiments for the cerium and neodymium compounds and found indications for at least partially ordered Ag/In sites. The RAg_2In indides are metallic conductors. Compounds with a rare earth element that orders magnetically show a steeper decrease of the electrical resistivity below the ordering temperature. The precise crystal field parameters for the cerium, praseodymium, and neodymium compounds have been determined from inelastic neutron scattering experiments.

The magnetic hyperfine interactions of the gadolinium magnetic moments in GdAg_2In have been investigated by magnetic susceptibility data (table 20) and ^{155}Gd Mössbauer spectroscopy (de Vries et al., 1985). The hyperfine parameters at 4.2 K are $\delta = 0.52(3)$ mm/s, $\Gamma = 0.66(5)$ mm/s and $B_{\text{hf}} = 24.8(8)$ T.

CeCu_2In shows interesting pressure dependent physical properties (Kagayama et al., 1994). A crossover from the heavy fermion state to an itinerant $4f$ state is induced by applying a pressure of 2 GPa. This change is associated with a large enhancement of the Kondo temperature. The data of the cerium compound are compared to those of LaCu_2In with the diamagnetic lanthanum atoms and binary CeCu_6 . The Heusler phases CeCu_2In and CeAg_2In form a solid solution $\text{CeAg}_{2-x}\text{Cu}_x\text{In}$ (Lahiouel et al., 1987). In this series, the hybridization continuously increases from the antiferromagnetic Kondo lattice CeAg_2In to the heavy fermion compound CeCu_2In . The electrical resistivities of diluted solutions $\text{La}_{1-x}\text{Ce}_x\text{InCu}_2$ and $\text{Y}_{1-x}\text{Ce}_x\text{InCu}_2$ can be decomposed into a single ion term plus a pair interaction term, which follows the Curie–Weiss law (Najib et al., 1988). Magnetization and specific heat measurements indicate antiferromagnetic correlations. Various single crystals of CeCu_2In have been grown (Önuki et al., 1987). Crystals with a slightly higher cerium content, $\text{Ce}_{1.06}\text{Cu}_2\text{In}$, show slightly varying magnetic and electrical properties. Thermal expansion measurements of single crystalline

CeCu₂In show isotropic behavior in the [100] and [110] directions as expected for a cubic material (Oomi et al., 1990). The thermal expansion coefficient of CeCu₂In below 100 K, however, is larger compared with that of LaCu₂In, which has no *f* electrons.

The lattice parameters of LaCu₂In and CeCu₂In have been measured under pressures up to 14 GPa by X-ray powder diffraction (Kagayama et al., 1990). Fine powders were prepared from Czochralski grown single crystals in an alcohol atmosphere in order to avoid oxidation of the material. In contrast to the differences reported for single crystals by Oomi et al. (1990), almost similar values for the bulk modulus and the expansion coefficient are reported for the LaCu₂In and CeCu₂In powder data.

7.6. Other indides

Most indides with a diamagnetic rare earth element, i.e. scandium, yttrium, lanthanum and lutetium, are Pauli paramagnetic. An example is the metallic conductor Sc₂Ni₂In (Pöttgen and Dronskowski, 1996).

Susceptibility measurements revealed intermediate-valent behavior for CeNi₉In₂ (Moze et al., 1995). The magnetic susceptibility is nearly temperature independent over the whole temperature range indicating that the cerium atoms do not carry a localized moment. This is also evident from the magnetization *vs* field dependence at 1.6 K, where only a moment of 0.06 μ_B per formula unit is detected at 12 T. The electrical resistivity data show metallic behavior and the absence of magnetic ordering at low temperatures. Isotypic GdNi₉In₂ ($\mu_{\text{exp}} = 8.35 \mu_B$ and $\Theta = -3.5$ K) orders presumably ferromagnetically below 2 K (Mulder et al., 1998). The values of the magnetization at 2 K are slightly higher than the corresponding value of the Brillouin function. The ¹⁵⁵Gd spectrum at 4.2 K shows a well resolved doublet at an isomer shift of 0.35 mm/s and a V_{zz} component of $6.9 \cdot 10^{21}$ V/m², reflecting the non-cubic site symmetry of gadolinium.

The properties of the solid solution Ce_{1-x}La_xCu₅In have been compared to the pure cerium compound which exhibits Kondo lattice properties with a specific heat coefficient $\gamma = 200$ mJ/mol K² (Tchoula Tchokonte et al., 2003). Susceptibility measurements gave no hint for magnetic ordering in the Ce_{1-x}La_xCu₅In indides. Resistivity data enabled the extraction of the Kondo temperature for the different compositions.

The palladium-rich hexagonal indide CePd₂In (Bianchi et al., 1995) orders antiferromagnetically at $T_N = 1.23$ K. A further spin rearrangement has been detected around 0.6 K. The temperature dependence of the magnetic susceptibility does not show significant crystal field effects. LaPd₂In with the diamagnetic lanthanum atoms was investigated for comparison. The electronic specific heat of the cerium compound is enhanced by a factor of five with respect to the lanthanum compound. LaPd₂In behaves like a classical metal while CePd₂In shows a Kondo minimum and a steep drop in electrical resistivity at the Néel temperature. The indium-rich compound CePdIn₂ with MgCuAl₂ structure orders ferromagnetically at 10 K (Ijiri et al., 1996). The saturation magnetization at 4.2 K is 1.6 μ_B /Ce atom, slightly reduced as compared to the expected *gJ* value of 2.14 μ_B for Ce³⁺ in a $J = 5/2$ state.

The heavy fermion antiferromagnet Ce₃Pt₄In₁₃ ($T_N = 0.95$ K) exhibits unusual Kondo behavior (Hundley et al., 2001) and it has an unusually large electronic contribution to the specific heat of about 1 J/mol K² at the Néel temperature. Thermoelectric power and Hall effect

measurements suggest that the RKKY and Kondo type interactions in $\text{Ce}_3\text{Pt}_4\text{In}_{13}$ are closely balanced. The isotopic compound $\text{La}_3\text{Pt}_4\text{In}_{13}$ with diamagnetic lanthanum is a conventional superconductor with $T_C = 3.3$ K.

The rare earth metal atoms in EuPdIn_2 and YbPdIn_2 are divalent (Galadzhun et al., 1999a). YbPdIn_2 shows a diamagnetic signal over the whole temperature range. The europium compound shows Curie–Weiss behavior (table 21) and orders ferromagnetically at 14.5(5) K. EuPdIn_2 shows negligible coercivity and remanent magnetization, classifying this indide as a soft ferromagnet. Both compounds are metallic conductors.

$\text{Eu}_2\text{Au}_3\text{In}_4$ with anti- $\text{Hf}_2\text{Co}_4\text{P}_3$ structure (Hoffmann et al., 1999) orders antiferromagnetically (table 21). Magnetization measurements at 2 K indicate a metamagnetic phase transition at a critical field of 0.5(2) T and a saturation magnetization of 5.95 μ_B/Eu atom at 5.5 T. $\text{Eu}_2\text{Au}_3\text{In}_4$ is a metallic conductor. The divalent character of europium in this indide was confirmed by ^{151}Eu Mössbauer data that show only one signal at an isomer shift of $-10.5(5)$ K. Hyperfine field splitting is observed below 10 K, however, due to the various europium sites in the structure, a fit of the spectra was not possible.

$\text{Gd}_6\text{Co}_{2.2}\text{In}_{0.8}$ with orthorhombic $\text{Ho}_6\text{Co}_2\text{Ga}$ structure shows complex magnetic behavior (Canepa et al., 2002a). Specific heat and magnetic susceptibility data reveal two magnetic transitions. At 34 K, the antiferromagnetic coupling changes to ferromagnetic and at 66 K a transition to a paramagnetic state occurs. The low magnetic moment of 6.8 μ_B in the paramagnetic state can be explained within the RKKY theory by a strong coupling of the conduction

Table 21
Magnetic properties of various ternary rare earth metal–transition metal–indides

Compound	Magnetism	μ_{exp}/μ_B	$T_N, T_C/\text{K}$	Θ/K	Ref.
Ce_2CuIn_3	P	2.49	–	–8	Siouris et al., 2000b
Pr_2CuIn_3	P	3.48	–	–3	Siouris et al., 2000b
Nd_2CuIn_3	AF	3.75	12	–12	Siouris et al., 2000b
Tb_2CuIn_3	AF	10.3	30	–72	Siouris et al., 2000b
Tb_2CuIn_3	AF	10.3	33(1)	–72	Siouris et al., 2001
Dy_2CuIn_3	AF	10.5	22	–30	Siouris et al., 2000b
Ho_2CuIn_3	AF	10.47	8	2	Siouris et al., 2000b
Tm_2CuIn_3	AF	10.55	9	23	Siouris et al., 2000b
CeNiIn_4	P	2.6(1)	–	4(1)	Pöttgen, 1995
$\text{Ce}_5\text{Ni}_6\text{In}_{11}$	AF	2.57(5)	0.63; 1.10	–8	Tang et al., 1995
CePd_2In	AF	2.69	1.23	–3	Bianchi et al., 1995
CePdIn_2	F	2.47(2)	10	16.5(15)	Ijiri et al., 1996
$\text{Ce}_3\text{Pt}_4\text{In}_{13}$	AF	2.64	0.95	–36	Hundley et al., 2001
$\text{Ce}_2\text{Au}_3\text{In}_5$	P	2.51(2)	–	–16(1)	Galadzhun et al., 1999b
$\text{Nd}_5\text{Ni}_6\text{In}_{11}$	AF	3.60(5)	11.4(1)	–18(1)	Pöttgen et al., 1999a
EuNiIn_4	AF	7.86(5)	16(1)	–8(1)	Pöttgen et al., 1996
EuPdIn_2	F	7.8(1)	14.5(5)	22(1)	Galadzhun et al., 1999a
$\text{Eu}_2\text{Au}_3\text{In}_4$	AF	7.88(5)	9.5(5)	4.0(5)	Hoffmann et al., 1999
$\text{Gd}_6\text{Co}_{2.2}\text{In}_{0.8}$	AF / F	6.82	34, 66	80.3	Canepa et al., 2002a
$\text{Gd}_{14}\text{Co}_3\text{In}_{2.7}$	AF	7.34	37	50	Canepa et al., 2002b
$\text{GdAu}_{0.44}\text{In}_{1.56}$	AF	7.8(1)	21.0(5)	–30(1)	Pöttgen et al., 1998

electrons with the localized magnetic moments. In the ferromagnetically ordered state, the magnetic moment of $4.81 \mu_B$ is far from the saturation value for the Gd^{3+} ion of $7 \mu_B$.

The complex metal-rich indide $Gd_{14}Co_3In_{2.7}$ orders antiferromagnetically at $T_N = 37$ K (Canepa et al., 2002b) and undergoes a metamagnetic phase transition at 1.4 T. The $2.65 \mu_B$ per gadolinium atom at the highest obtainable field of 9 T is even smaller than that of $Gd_6Co_{2.2}In_{0.8}$.

$CeNiIn_4$ shows Curie–Weiss behavior over the whole investigated temperature range (Pöttgen, 1995). No magnetic ordering could be detected down to 2 K. $CeNiIn_4$ is a good metallic conductor. In the solid solution $CeNiAl_{4-x}In_x$, the thermopower is significantly higher than in the parent compound (Poduska et al., 2000). Also, $EuNiIn_4$ is a Curie–Weiss paramagnet (table 21) with a Néel temperature of 16 K (Pöttgen et al., 1996). Magnetic ordering is already evident at 32 K in the ^{151}Eu Mössbauer spectra. In the region between 16 and 32 K the ^{151}Eu spectra can be fit as a superposition of a magnetically split and an unsplit component, while full magnetic hyperfine field splitting is detected below T_N with a hyperfine field of 26.4 T at 4.2 K at the europium nuclei.

$GdAu_{0.44}In_{1.56}$ with $CaIn_2$ structure orders antiferromagnetically 21.0(5) K (Pöttgen et al., 1998). The antiferromagnetic ground state is stable in high magnetic fields. The magnetization at 5 K and 5.5 T is $2.6(1) \mu_B/Gd$ atom. The ^{155}Gd Mössbauer spectrum shows a single signal at an isomer shift of 0.452 mm/s subject to quadrupole splitting of -0.842 mm/s. At 4.2 K a hyperfine field of 19.8 T is detected at the gadolinium nuclei.

$Ce_5Ni_6In_{11}$ is an intermediate heavy fermion material with a high electronic specific heat coefficient of $\gamma = 145 \pm 20$ mJ/mol K² (Tang et al., 1995). The heat capacity measurements reveal two magnetic transitions, both being of antiferromagnetic nature. Most likely the cerium atoms on the $2c$ Wyckoff position order at T_{N1} and those on the $8p$ position at T_{N2} . There is also evidence for weak magnetic coupling between the two cerium sites. $Nd_5Ni_6In_{11}$ is a 11.4 K antiferromagnet (Pöttgen et al., 1999a). Magnetization and specific heat measurements indicate a complex magnetic phase diagram with spin reorientations into three antiferro- and one ferromagnetic phase. $Nd_5Ni_6In_{11}$ is a metallic conductor with a specific electrical resistivity of $120 \mu\Omega$ cm at room temperature.

The magnetic ground states of the silver-based indides R_2AgIn_3 ($R = Pr, Nd, Tb, Ho, Er$) have been investigated (Siouris et al., 2000a). The silver and indium atoms in these indides are randomly distributed on the indium network of the $CaIn_2$ structure. Consequently, due to the structural disorder, many of these compounds show spin-glass behavior. Except for the terbium compound, neutron diffraction data revealed the absence of long-range magnetic ordering. The antiferromagnetic structure ($T_N = 42$ K) of Tb_2AgIn_3 was determined from neutron powder diffraction data. The magnetic unit cell corresponds to the orthohexagonal setting of the hexagonal nuclear structure. The magnetic moment of the terbium atoms is $5.9 \mu_B$ at 4.2 K (Semitelou et al., 1999).

The rare earth atoms are in a stable trivalent state in all R_2CuIn_3 compounds (Siouris et al., 2000b). The basic magnetic data are listed in table 21. No magnetic ordering has been observed for the cerium and praseodymium compounds, while antiferromagnetism is detected for the remaining indides. The magnetic structure of the collinear antiferromagnet Tb_2CuIn_3 was refined from neutron powder diffraction data (Siouris et al., 2001), with a magnetic unit

cell similar to Tb_2AgIn_3 . The terbium magnetic moments ($6.8 \mu_B$ at 3.8 K) are oriented along the c axis. According to the small almost linear increase of the magnetization isotherm at 5 K, the antiferromagnetic structure is stable in high external fields.

YbAg_2In_4 follows the Curie–Weiss law above 90 K with an experimental magnetic moment of $2.3 \mu_B/\text{Yb}$ atom, much smaller than the free ion value of $4.45 \mu_B$ for Yb^{3+} (Sysa et al., 1998). The low magnetic moment and the large negative paramagnetic Curie temperature ($\Theta = -86$ K) are both indicative for intermediate-valent ytterbium. When ytterbium is substituted by calcium, the compound becomes Pauli paramagnetic with a low magnetic susceptibility value of $0.8 \cdot 10^{-6} \text{ cm}^3/\text{g}$. Both indides are metallic conductors.

X-ray absorption L_{III} spectra indicated stable divalent europium in EuAg_4In_8 , while signals for Eu^{II} and Eu^{III} were observed for EuCuIn_4 and $\text{EuCu}_{6.5}\text{In}_{6.5}$ (Sysa et al., 1994a). A variety of indides $R\text{Ag}_6\text{In}_6$ with site occupancy variants of the tetragonal ThMn_{12} type have been analyzed with respect to their magnetic and electrical properties (Zaremba et al., 1999). $\text{CeAg}_{6.4}\text{In}_{5.6}$ and PrAg_6In_6 are paramagnets with experimental magnetic moments of $2.32 \mu_B/\text{Ce}$ ($\Theta = 3.84$ K) and $3.41 \mu_B/\text{Pr}$ ($\Theta = -2.83$ K), close to the free ion values of Ce^{3+} and Pr^{3+} . NdAg_6In_6 ($3.43 \mu_B/\text{Nd}$ and $\Theta = -2.15$ K) orders antiferromagnetically at 5 K. The magnetization curves increase almost linearly up to 5 T. These silver compounds are metallic conductors.

Acknowledgements

This work was financially supported by the Deutsche Forschungsgemeinschaft and the Fonds der Chemischen Industrie. We thank the Degussa-Hüls AG for several gifts of noble metals for our experimental investigations. M.L. is indebted to the NRW Graduate School of Chemistry for a PhD stipend. Ya.M.K. and V.I.Z. are grateful to the Deutsche Forschungsgemeinschaft and the Alexander von Humboldt Foundation for research stipends and the Ministry of Education and Science of Ukraine for financial support.

References

- Adroja, D.T., Malik, S.K., Padalia, B.D., Vijayaraghavan, R., 1989. *Phys. Rev. B* **39**, 4831.
- Adroja, D.T., Malik, S.K., 1991. *J. Magn. Magn. Mater.* **100**, 126.
- Alami-Yadri, K., Wilhelm, H., Jaccard, D., 1998. *Solid State Commun.* **108**, 279.
- Alfieri, G.T., Banks, E., Kanematsu, K., 1966. *J. Appl. Phys.* **37**, 1254.
- Allemand, J., Letant, A., Moreau, J.M., Nozières, J.P., Perrier de la Bathie, R., 1990. *J. Less-Common Met.* **166**, 73.
- Alver, U., Goodrich, R.G., Harrison, N., Hall, D.W., Palm, E.C., Murphy, T.P., Tozer, S.W., Pagliuso, P.G., Moreno, N.O., Sarrao, J.L., Fisk, Z., 2001. *Phys. Rev. B* **64**, 180402.
- Andersson, S., 1983. *Angew. Chem.* **95**, 67.
- André, G., Bažela, W., Oleś, A., Szytuła, A., 1992. *J. Magn. Magn. Mater.* **109**, 34.
- Aronsson, B., 1958. *Acta Chem. Scand.* **12**, 31.
- Aronsson, B., Bäckman, M., Rundqvist, S., 1960. *Acta Chem. Scand.* **14**, 1001.
- Babateen, M., Crangle, J., Fauth, F., Furrer, A., Neumann, K.-U., Ziebeck, K.R.A., 1995. *Physica B* **213–214**, 300.
- Bakar, A.M., Kalychak, Ya.M., 1990. *Tsvetnaya Metallurgiya* **1**, 99 (in Russian).

- Bafanda, M., Szytuła, A., Guillot, M., 2002. *J. Magn. Magn. Mater.* **247**, 345.
- Balster, H., Ihrig, H., Kockel, A., Methfessel, S., 1975. *Z. Phys. B* **21**, 241.
- Baranyak, V.M., Kalychak, Ya.M., Bruskov, V.A., Zavalij, P.Yu., Dmytrakh, O.V., 1988a. *Krystallografiya* **33**, 601 (in Russian).
- Baranyak, V.M., Dmytrakh, O.V., Kalychak, Ya.M., Zavalij, P.Yu., 1988b. *Neorg. Mater.* **24**, 873 (in Russian).
- Baranyak, V.M., Kalychak, Ya.M., Zavalij, P.Yu., Belsky, V.K., 1990. *Neorg. Mater.* **26**, 2316 (in Russian).
- Baranyak, V.M., 1991. PhD Thesis, Ivan Franko National University, Lviv (in Ukrainian).
- Baranyak, V.M., Kalychak, Ya.M., 1991. *Neorg. Mater.* **27**, 1235 (in Russian).
- Baranyak, V.M., Kalychak, Ya.M., Sysa, L.V., 1992. *Krystallografiya* **37**, 1022 (in Russian).
- Baranyak, V.M., Kalychak, Ya.M., 1993. *Ukr. Chem. J.* **59**, 139 (in Russian).
- Baranyak, V.M., Kalychak, Ya.M., Zavalij, P.Yu., 1993. *Krystallografiya* **38**, 268 (in Russian).
- Bärnighausen, H., 1980. *Commun. Math. Chem.* **9**, 139.
- Bärnighausen, H., Müller, U., 1996. Symmetriebeziehungen zwischen den Raumgruppen als Hilfsmittel zur straffen Darstellung von Strukturzusammenhängen in der Kristallchemie. University of Karlsruhe and University/GH Kassel, Germany.
- Becher, H.J., Krogmann, K., Peisker, E., 1966. *Z. Anorg. Allg. Chem.* **344**, 140.
- Bauer, E., Berger, St., Gabani, S., Hilscher, G., Michor, H., Paul, C., Giovannini, M., Saccone, A., Godart, C., Bonville, P., Aoki, Y., Sato, H., 2003. *Acta Phys. Polonica B* **34**, 367.
- Besnus, M.J., Kappler, J.P., Meyer, A., Sereni, J., Siaud, E., Lahiouel, R., Pierre, J., 1985. *Physica B* **130**, 240.
- Besnus, M.J., Kappler, J.P., Ravet, M.F., Meyer, A., 1986. *J. Less-Common Met.* **120**, 101.
- Bianchi, A.D., Felder, E., Schilling, A., Chernikov, M.A., Hulliger, F., Ott, H.R., 1995. *Z. Phys. B* **99**, 69.
- Blazina, N., 1994. *J. Alloys Compd.* **216**, 251.
- Brauer, G., 1981. *Handbuch der Präparativen Anorganischen Chemie*. Enke Verlag Stuttgart, Germany.
- Brauer, G., Herrmann, W.A., 2000. *Synthetic Methods of Organometallic and Inorganic Chemistry*. Thieme Verlag Stuttgart, New York.
- Brück, E., van Sprang, M., Klaasse, J.C.P., de Boer, F.R., 1988. *J. Appl. Phys.* **63**, 3417.
- Brück, E., Nakotte, H., Bakker, K., de Boer, F.R., de Châtel, P.F., Li, J.-Y., Kuang, J.P., Yang, F.-M., 1993. *J. Alloys Compd.* **200**, 79.
- Bulyk, I.I., Yartys, V.A., Denys, R.V., Kalychak, Ya.M., Harris, I.R., 1999. *J. Alloys Compd.* **284**, 256.
- Buschow, K.H.J., Oppelt, A., Dormann, E., 1972. *Phys. Stat. Sol.* **50**, 647.
- Buschow, K.H.J., 1975. *J. Less-Common Met.* **39**, 185.
- Cable, J.W., Koehler, W.C., Child, H.R., 1965. *J. Appl. Phys.* **36**, 1096.
- Canepa, F., Napoletano, M., Manfrinetti, P., Merlo, F., 2002a. *J. Alloys Compd.* **334**, 34.
- Canepa, F., Napoletano, M., Fornasini, M.L., Merlo, F., 2002b. *J. Alloys Compd.* **345**, 42.
- Canfield, P.C., Fisk, Z., 1992. *Philosoph. Mag. B: Phys. Condens. Matter* **65**, 1117.
- Cenzual, K., Parthé, E., 1984. *Acta Cryst. C* **40**, 1127.
- Chevalier, B., Kahn, M.L., Bobet, J.-L., Pasturel, M., Etourneau, J., 2002. *J. Phys.: Condens. Matter* **14**, L365.
- Christianson, A.D., Lacerda, A.H., Hundley, M.F., Pagliuso, P.G., Sarrao, J.L., 2002a. *Phys. Rev. B* **66**, 054410.
- Christianson, A.D., Lawrence, J.M., Pagliuso, P.G., Moreno, N.O., Sarrao, J.L., Thompson, J.D., Riseborough, P.S., Kern, S., Goremychkin, E.A., Lacerda, A.H., 2002b. *Phys. Rev. B* **66**, 193102.
- Cirafici, S., Palenzona, A., Canepa, F., 1985. *J. Less-Common Met.* **107**, 179.
- Colinet, C., 1995. *J. Alloys Compd.* **225**, 409.
- Corbett, J.D., 1983. *Inorg. Synth.* **22**, 15.
- Cornelius, A.L., Lawrence, J.M., Sarrao, J.L., Fisk, Z., Hundley, M.F., Kwei, G.H., Thompson, J.D., Booth, C.H., Bridges, F., 1997. *Phys. Rev. B* **56**, 7993.
- Cornelius, A.L., Arko, A.J., Sarrao, J.L., Hundley, M.F., Fisk, Z., 2000. *Phys. Rev. B* **62**, 14181.
- Cornelius, A.L., Pagliuso, P.G., Hundley, M.F., Sarrao, J.L., 2001. *Phys. Rev. B* **64**, 144411.
- Cromer, D.T., Larson, A.C., Roof, R.B., 1960. *Acta Cryst.* **13**, 913.
- Curro, N.J., Hammel, P.C., Pagliuso, P.G., Sarrao, J.L., Thompson, J.D., Fisk, Z., 2000. *Phys. Rev. B* **62**, R6100.
- Curro, N.J., Simovic, B., Hammel, P.C., Pagliuso, P.G., Sarrao, J.L., Thompson, J.D., Martins, G.B., 2001. *Phys. Rev. B* **64**, 180514.
- Czech, E., Cordier, G., Schaefer, H., 1983. *J. Less-Common Met.* **95**, 205.
- Daniš, S., Javorský, P., Rafaja, D., 2002. *J. Alloys Compd.* **345**, 10.
- De Mooij, D.B., Buschow, K.H.J., 1984. *J. Less-Common Met.* **102**, 113.

- De Teresa, J.M., Arnold, Z., del Moral, A., Ibarra, M.R., Kamarád, J., Adroja, D.T., Rainford, B.D., 1996. *Solid State Commun.* **99**, 911.
- De Vries, J.W.C., Thiel, R.C., Buschow, K.H.J., 1985. *J. Less-Common Met.* **111**, 313.
- Dhar, S.K., Manfrinetti, P., Palenzona, A., 1995. *Phys. Rev. B* **51**, 12464.
- Dhar, S.K., Manfrinetti, P., Palenzona, A., 2002a. *Solid State Commun.* **124**, 379.
- Dhar, S.K., Mitra, C., Manfrinetti, P., Palenzona, R., Palenzona, A., 2002b. *J. Phase Equilibria* **23**, 79.
- Dmytrakh, O.V., Kalychak, Ya.M., 1990. *Metally* **6**, 197 (in Russian).
- Donohue, J., 1974. *The Structures of the Elements*. Wiley, New York.
- Dronskowski, R., Blöchl, P.E., 1993. *J. Phys. Chem.* **97**, 8617.
- Dubenskii, V.P., Kalychak, Ya.M., Zaremba, V.I., Goreshnik, E.A., 1998. *J. Alloys Compd.* **280**, 199.
- Dubenskii, V.P., Kalychak, Ya.M., Zaremba, V.I., Lukachuk, M.O., Goreshnik, E.A., 1999. *J. Alloys Compd.* **284**, 228.
- Duwell, E.J., Baenziger, N.C., 1955. *Acta Cryst.* **8**, 705.
- Dwight, A.E., Mueller, M.H., Conner Jr., R.A., Downey, J.W., Knott, H., 1968. *Trans. Met. Soc. AIME* **242**, 2075.
- Dwight, A.E., 1976. In: *Proceedings of the Rare Earth Research Conference 12th, Colorado*, vol. **1**, p. 480.
- Dwight, A.E., 1987. *Mat. Res. Bull.* **22**, 201.
- Dwight, A.E., Kimball, C.W., 1987. *J. Less-Common Met.* **127**, 179.
- Dzero, M.O., Gorkov, L.P., Zvezdin, A.K., 2000. *J. Phys.: Condens. Matter* **12**, L711.
- Emsley, J., 1999. *The Elements*. Oxford University Press, Oxford.
- Eisenmann, B., Schäfer, H., 1986. *J. Less-Common Met.* **123**, 89.
- Esmailzadeh, S., Zaremba, V.I., Kalychak, Ya.M., Hoffmann, R.-D., Pöttgen, R., 2002. *Solid State Science* **4**, 93.
- Felner, I., 1985. *Solid State Commun.* **56**, 315.
- Felner, I., Nowik, I., 1986. *Phys. Rev. B* **33**, 617.
- Felner, I., Nowik, I., 1987. *J. Magn. Magn. Mater.* **63–64**, 615.
- Felner, I., Nowik, I., Vaknin, D., Potzel, U., Moser, J., Kalvius, G.M., Wortmann, G., Schmiester, G., Hilscher, G., Gratz, E., Schmitzer, C., Pillmayr, N., Prasad, K.G., de Waard, H., Pinto, H., 1987. *Phys. Rev. B* **35**, 6956.
- Ferro, R., Marazza, R., Rambaldi, G., 1974a. *Z. Metallkd.* **65**, 37.
- Ferro, R., Marazza, R., Rambaldi, G., 1974b. *Z. Anorg. Allg. Chem.* **410**, 219.
- Ferro, R., Marazza, R., Rambaldi, G., Saccone, A., 1975. *J. Less-Common Met.* **40**, 251.
- Fisher, I.R., Islam, Z., Canfield, P.C., 1999. *J. Magn. Magn. Mater.* **202**, 1.
- Fischer, P., Herrmannsdorfer, T., Bonelli, T., Fauth, F., Keller, L., Bauer, E., Giovannini, M., 2000. *J. Phys. Cond. Matter* **12**, 7089.
- Florio, J.V., Rundle, R.E., Snow, A.I., 1952. *Acta Cryst.* **5**, 449.
- Florio, J.V., Baenziger, N.C., Rundle, R.E., 1956. *Acta Cryst.* **9**, 367.
- Fornasini, M.L., Cirafici, S., 1990. *Z. Kristallogr.* **190**, 295.
- Frank, F.C., Kasper, J.S., 1958. *Acta Cryst.* **11**, 184.
- Frank, F.C., Kasper, J.S., 1959. *Acta Cryst.* **12**, 483.
- Fujii, H., Uwatoko, Y., Akayama, M., Satoh, K., Maeno, Y., Fujita, T., Sakurai, J., Kamimura, H., Okamoto, T., 1987. *Jap. J. Appl. Phys.* **26**, 549.
- Fujii, H., Inoue, T., Andoh, Y., Takabatake, T., Satoh, K., Maeno, Y., Fujita, T., Sakurai, J., Yamaguchi, Y., 1989. *Phys. Rev. B* **39**, 6840.
- Fujii, H., Nagasawa, M., Kawanaka, H., Inoue, T., Takabatake, T., 1990. *Physica B* **165**, 435.
- Fujii, H., Takabatake, T., Andoh, Y., 1992. *J. Alloys Compd.* **181**, 111.
- Fujita, T., Satoh, K., Maeno, Y., Uwatoko, Y., Fujii, H., 1988. *J. Magn. Magn. Mater.* **76–77**, 133.
- Fujita, T., Suzuki, T., Nishigori, S., Takabatake, T., Fujii, H., Sakurai, J., 1992. *J. Magn. Magn. Mater.* **108**, 35.
- Galadzhun, Ya.V., Pöttgen, R., 1999. *Z. Anorg. Allg. Chem.* **625**, 481.
- Galadzhun, Ya.V., Hoffmann, R.-D., Kotzyba, G., Künnen, B., Pöttgen, R., 1999a. *Eur. J. Inorg. Chem.*, 975.
- Galadzhun, Ya.V., Hoffmann, R.-D., Pöttgen, R., Adam, M., 1999b. *J. Solid State Chem.* **148**, 425.
- Galadzhun, Ya.V., Zaremba, V.I., Kalychak, Ya.M., Hoffmann, R.-D., Pöttgen, R., 2000a. *Z. Anorg. Allg. Chem.* **626**, 1773.
- Galadzhun, Ya.V., Zaremba, V.I., Piotrowski, H., Mayer, P., Hoffmann, R.-D., Pöttgen, R., 2000b. *Z. Naturforsch.* **55b**, 1025.
- Galadzhun, Ya.V., Kalychak, Ya.M., Zaremba, V.I., Stepień-Damm, J., Pietraszko, A., 2000c. In: *4th Internat. Conf. on f-elements*, Madrid, Spain, September 2000, p. 24.
- Galadzhun, Ya.V., Zaremba, V.I., Kalychak, Ya.M., Davydov, V., Pikul, A.P., Stepień-Damm, J., Kaczorowski, D., 2003. *J. Solid State Chem.*, submitted for publication.

- Galera, R.M., Pierre, J., Siaud, E., Murani, A.P., 1984. *J. Less-Common Met.* **97**, 151.
- Ganglberger, E., 1968. *Monatsh. Chem.* **99**, 566.
- Ghoshray, K., Bandyopadhyay, B., Mita Sen, Ghoshray, A., Chatterjee, N., 1993. *Phys. Rev. B* **47**, 8277.
- Giovannini, M., Michor, H., Bauer, E., Hilscher, G., Rogl, P., Ferro, R., 1998. *J. Alloys Compd.* **280**, 26.
- Giovannini, M., Bauer, E., Michor, H., Hilscher, G., Galatanu, A., Saccone, A., Rogl, P., 2001. *Intermetallics* **9**, 481.
- Giovannini, M., Saccone, A., Rogl, P., Ferro, R., 2003. *Intermetallics* **11**, 197.
- Gladyshevskii, E.I., Kripyakevich, P.I., Tesliuk, M.J., 1952. *Dokl. Akad. Nauk SSSR* **85**, 81 (in Russian).
- Gladyshevskii, R.E., Grin, Yu.N., Yarmolyuk, Ya.P., 1983. *Dopov. Akad. Nauk Ukr. RSR, Ser. A* **2**, 67 (in Ukrainian).
- Goll, G., von Löhneysen, H., Zapf, V.S., Bauer, E.D., Maple, M.B., 2003. *Acta Phys. Polonica B* **34**, 575.
- Gondek, L., Penc, B., Szytuła, A., Jezierski, A., Zygmunt, A., 2003. *Acta Phys. Polonica B* **34**, 1209.
- Gordon, R.A., Ijiri, Y., Spencer, C.M., DiSalvo, F.J., 1995. *J. Alloys Compd.* **224**, 101.
- Gordon, R.A., DiSalvo, F.J., 1996. *Z. Naturforsch. B* **51**, 52.
- Gordon, R.A., Jones, C.D.W., Alexander, M.G., DiSalvo, F.J., 1996. *Physica B* **225**, 23.
- Gravereau, P., Mirambet, F., Chevalier, B., Weill, F., Fournes, L., Laffargue, D., Bouree, F., Etourneau, J., 1994. *J. Mater. Chem.* **4**, 1893.
- Grin, Yu.N., Yarmolyuk, Ya.P., Gladyshevskii, E.I., 1979a. *Kristallografiya* **24**, 242 (in Russian).
- Grin, Yu.N., Yarmolyuk, Ya.P., Gladyshevskii, E.I., 1979b. *Dokl. Akad. Nauk SSSR* **245**, 1102 (in Russian).
- Grin, Yu.N., Yarmolyuk, Ya.P., Pecharsky, V.K., 1983. *Izv. Akad. Nauk SSSR, Metallurgy* **3**, 213 (in Russian).
- Grin, Yu.N., Gladyshevskii, R.E., 1989. *Gallidy: Spravochnik, Metallurgiya, Moscow, USSR* (in Russian).
- Gunnarsson, O., Schönhammer, K., 1983. *Phys. Rev. B* **28**, 4315.
- Haga, Y., Inada, Y., Harima, H., Oikawa, K., Murakawa, M., Nakawaki, H., Tokiwa, Y., Aoki, D., Shishido, H., Ikeda, S., Watanabe, N., Ōnuki, Y., 2001. *Phys. Rev. B* **63**, 060503(R).
- Hall, D., Palm, E.C., Murphy, T.P., Tozer, S.W., Petrovic, C., Miller-Ricci, E., Peabody, L., Li, C.Q.H., Alver, U., Goodrich, R.G., Sarrao, J.L., Pagliuso, P.G., Wills, J.M., Fisk, Z., 2001a. *Phys. Rev. B* **64**, 064506.
- Hall, D., Palm, E.C., Murphy, T.P., Tozer, S.W., Fisk, Z., Alver, U., Goodrich, R.G., Sarrao, J.L., Pagliuso, P.G., Ebihara, T., 2001b. *Phys. Rev. B* **64**, 212508.
- Hauser, R., Michor, H., Bauer, E., Hilscher, G., Kaczorowski, D., 1997. *Physica B* **230–232**, 211.
- Hedo, M., Uwatoko, Y., Matsumoto, T., Sarrao, J.L., Thompson, J.D., 2003. *Acta Phys. Polonica B* **34**, 1193.
- Hegger, H., Petrovic, C., Moshopoulou, E.G., Hundley, M.F., Sarrao, J.L., Fisk, Z., Thompson, J.D., 2000. *Phys. Rev. Lett.* **84**, 4986.
- Heusler, O., 1934. *Ann. Physik* **19**, 155.
- Hoffmann, R.-D., Pöttgen, R., Rosenhahn, C., Mosel, B.D., Künnen, B., Kotzyba, G., 1999. *J. Solid State Chem.* **145**, 283.
- Hoffmann, R.-D., Pöttgen, R., 2000. *Chem. Eur. J.* **6**, 600.
- Hoffmann, R.-D., Pöttgen, R., Zaremba, V.I., Kalychak, Ya.M., 2000. *Z. Naturforsch.* **55b**, 834.
- Hoffmann, R.-D., Pöttgen, R., 2001. *Chem. Eur. J.* **7**, 382.
- Hofmann, W., Jäniche, W., 1935. *Z. Phys. Chem. B* **31**, 214.
- Hulliger, F., Xue, B., 1994. *J. Alloys Compd.* **215**, 267.
- Hulliger, F., 1995a. *J. Alloys Compd.* **217**, 164.
- Hulliger, F., 1995b. *J. Alloys Compd.* **221**, L11.
- Hulliger, F., 1996. *J. Alloys Compd.* **232**, 160.
- Hundley, M.F., Sarrao, J.L., Thompson, J.D., Movshovich, R., Jaime, M., Petrovic, C., Fisk, Z., 2001. *Phys. Rev. B* **65**, 024401.
- Huppertz, H., Kotzyba, G., Hoffmann, R.-D., Pöttgen, R., 2002. *J. Solid State Chem.* **169**, 155.
- Iandelli, A., 1964. *Z. Anorg. Allg. Chem.* **330**, 221.
- Ihrig, H., Vigren, D.T., Kübler, J., Methfessel, S., 1973. *Phys. Rev. B* **8**, 4525.
- Ihrig, H., Methfessel, S., 1976. *Z. Physik B* **24**, 385.
- Ijiri, Y., DiSalvo, F.J., 1996. *J. Alloys Compd.* **233**, 69.
- Ijiri, Y., DiSalvo, F.J., Yamane, H., 1996. *J. Solid State Chem.* **122**, 143.
- Ikeda, S., Shishido, H., Nakashima, M., Settai, R., Aoki, D., Haga, Y., Harima, H., Aoki, Y., Namiki, T., Sato, H., Ōnuki, Y., 2001. *J. Phys. Soc. Jpn.* **70**, 2248.
- Immer, C.D., Sarrao, J.L., Fisk, Z., Lacerda, A., Mielke, C., Thompson, J.D., 1997. *Phys. Rev. B* **56**, 71.
- Ito, T., Ohkubo, K., Hirasawa, T., Takeuchi, J., Hiromitsu, I., Kurisu, M., 1995. *J. Magn. Magn. Mater.* **140**, 873.
- Ito, T., Nishigori, S., Hiromitsu, I., Kurisu, M., 1998. *J. Magn. Magn. Mater.* **177**, 1079.
- Izawa, K., Yamaguchi, H., Matsuda, Y., Shishido, H., Settai, R., Ōnuki, Y., 2001. *Phys. Rev. Lett.* **87**, 057002.

- Javorský, P., Svoboda, P., Nishigori, S., Hofmann, M., Stüsser, N., 1998. *Acta Phys. Slovaca* **48**, 767.
- Javorský, P., Nishigori, S., Svoboda, P., Hofmann, M., 2000. *Mater. Sci. Forum* **321**, 705.
- Jorda, J.L., Ishikawa, M., Hovestreydt, E., 1983. *J. Less-Common Met.* **92**, 155.
- Kaczorowski, D., Rogl, P., Hiebl, K., 1996a. *Phys. Rev. B* **54**, 9891.
- Kaczorowski, D., Giovannini, M., Hauser, R., Michor, H., Bauer, E., Hilscher, G., 1996b. *Czech. J. Phys.* **46**, 2063.
- Kaczorowski, D., Andraka, B., Pietri, R., Cichorek, T., Zaremba, V.I., 2000a. *Phys. Rev. B* **61**, 15255.
- Kaczorowski, D., Andraka, B., Zaremba, V.I., Marucha, Cz., 2000b. *Physica B* **281**, 44.
- Kagayama, T., Suenaga, K., Oomi, G., Ōnuki, Y., Komatsubara, T., 1990. *J. Magn. Magn. Mater.* **90–91**, 451.
- Kagayama, T., Oomi, G., Yagi, R., Iye, Y., Ōnuki, Y., Komatsubara, T., 1994. *J. Alloys Compd.* **207–208**, 271.
- Kalychak, Ya.M., Aksel'rud, L.G., Yarmolyuk, Ya.P., Bodak, O.I., Gladyshevskii, E.I., 1975. *Kristallografiya* **20**, 1045 (in Russian).
- Kalychak, Ya.M., Dmytrakh, O.V., Bodak, O.I., Ogryzlo, M.M., 1984a. *Dopov. Akad. Nauk Ukr. RSR, Ser. B* **1**, 34 (in Ukrainian).
- Kalychak, Ya.M., Aksel'rud, L.G., Zaremba, V.I., Baranyak, V.M., 1984b. *Dopov. Akad. Nauk Ukr. RSR. Ser. B* **8**, 37 (in Ukrainian).
- Kalychak, Ya.M., Gladyshevskii, E.I., Bodak, O.I., Dmytrakh, O.V., Kotur, B.Ya., 1985. *Krystallografiya* **30**, 591 (in Russian).
- Kalychak, Ya.M., Zavalij, P.Yu., Baranyak, V.M., Dmytrakh, O.V., Bodak, O.I., 1987. *Kristallografiya* **32**, 1021 (in Russian).
- Kalychak, Ya.M., Baranyak, V.M., Belsky, V.K., Dmytrakh, O.V., 1988a. *Dopov. Akad. Nauk Ukr. RSR. Ser. B* **9**, 40 (in Ukrainian).
- Kalychak, Ya.M., Baranyak, V.M., Zaremba, V.I., Zavalij, P.Yu., Dmytrakh, O.V., Bruskov, V.A., 1988b. *Krystallografiya* **33**, 1017 (in Russian).
- Kalychak, Ya.M., Bakar, A.M., 1989. *Izv. VUZ. Tsvetnaya Metallurgiya* **6**, 106 (in Russian).
- Kalychak, Ya.M., Zaremba, V.I., Baranyak, V.M., Bruskov, V.A., Zavalij, P.Yu., 1989a. *Metally* **1**, 209 (in Russian).
- Kalychak, Ya.M., Bakar, A.M., Gladyshevskii, E.I., 1989b. *Tsvetnaya Metallurgiya* **3**, 95 (in Russian).
- Kalychak, Ya.M., Zaremba, V.I., Baranyak, V.M., Zavalij, P.Yu., Bruskov, V.A., Sysa, L.V., Dmytrakh, O.V., 1990. *Neorg. Mater.* **26**, 94 (in Russian).
- Kalychak, Ya.M., Zaremba, V.I., Pecharsky, V.K., 1993a. *Z. Kristallogr.* **205**, 333.
- Kalychak, Ya.M., Zaremba, V.I., Zavalij, P.Yu., 1993b. *Z. Kristallogr.* **208**, 380.
- Kalychak, Ya.M., Zaremba, V.I., Baranyak, V.M., Pecharsky, V.K., 1993c. *Z. Kristallogr.* **205**, 335.
- Kalychak, Ya.M., Bakar, A.M., 1994. *Visnyk Lviv University, Ser. Khim.* **33**, 32 (in Ukrainian).
- Kalychak, Ya.M., Zaremba, V.I., 1994. *Krystallografiya* **39**, 923 (in Russian).
- Kalychak, Ya.M., Zaremba, V.I., Tyvanchuk, Yu.B., 1995. In: VI International Conference On Crystal Chemistry of Intermetallic Compounds, Lviv, Ukraine, September 26–29, 1995, p. 77.
- Kalychak, Ya.M., Bakar, A.M., 1996. *Visnyk Lviv University, Ser. Khim.* **36**, 52 (in Ukrainian).
- Kalychak, Ya.M., 1997. *J. Alloys Compd.* **262–263**, 341.
- Kalychak, Ya.M., Galadzhun, Ya.V., Stepień-Damm, J., 1997. *Z. Kristallogr.* **212**, 292.
- Kalychak, Ya.M., 1998a. *Metally* **4**, 110 (in Russian).
- Kalychak, Ya.M., 1998b. *Ukr. Chem. J.* **64**, 15.
- Kalychak, Ya.M., Zaremba, V.I., Stepień-Damm, J., Galadzhun, Ya.V., Aksel'rud, L.G., 1998. *Krystallografiya* **43**, 17 (in Russian).
- Kalychak, Ya.M., 1999a. *J. Alloys Compd.* **291**, 80.
- Kalychak, Ya.M., 1999b. *Visnyk Lviv University, Ser. Khim.* **38**, 70 (in Ukrainian).
- Kalychak, Ya.M., Zaremba, V.I., Galadzhun, Ya.V., Miliyanchuk, K.Y., Hoffmann, R.-D., Pöttgen, R., 2001. *Chem. Eur. J.* **7**, 5343.
- Kalychak, Ya.M., 2003. Unpublished.
- Kanatzidis, M.G., Pöttgen, R., Jeitschko, W., 2004. *Angew. Chem.*, in preparation.
- Kasaya, M., Satoh, N., Ono, A., 1996. In: *Proc. of the Internat. Conf. On Strongly Correlated Electron Systems*, Zürich, 19–22 August, p. 160.
- Kawasaki, Y., Ishida, K., Mito, T., Thessieu, C., Zheng, G.-Q., Kitaoka, Y., Geibel, C., Steglich, F., 2001. *Phys. Rev. B* **63**, 140501.
- Kawasaki, S., Mito, T., Zheng, G.-Q., Kawasaki, Y., Kitaoka, Y., Aoki, D., Haga, Y., Ōnuki, Y., 2003. *Acta Phys. Polonica B* **34**, 419.
- Kim, J.S., Alwood, J., Stewart, G.R., Sarrao, J.L., Thompson, J.D., 2001. *Phys. Rev. B* **64**, 134524.
- Kohori, Y., Yamato, Y., Iwamoto, Y., Kohara, T., 2000. *Eur. Phys. J. B* **18**, 601.
- Kohori, Y., Yamato, Y., Iwamoto, Y., Kohara, T., Bauer, E.D., Maple, M.B., Sarrao, J.L., 2001. *Phys. Rev. B* **64**, 134526.
- Kojima, K., Hayashi, H., Hihara, T., Kasamatsu, Y., 1988. *J. Magn. Magn. Mater.* **76–77**, 291.

- Kojima, K., Hayashi, H., Minami, A., Kasamatsu, Y., Hihara, T., 1989. *J. Magn. Magn. Mater.* **81**, 267.
- Kojima, K., Nakai, Y., Suzuki, T., Asano, H., Izumi, F., Fujita, T., Hihara, T., 1990. *J. Phys. Soc. Jpn.* **59**, 792.
- Kojima, K., Yabuta, H., Hihara, T., 1992. *J. Magn. Magn. Mater.* **104–107**, 653.
- Koterlyn, M.D., Morokhivsky, B.S., Scherba, I.D., Sysa, L.V., Kalychak, Ya.M., Lutziv, R.V., 1991. *Dopov. Akad. Nauk Ukr. RSR.* **5**, 65 (in Ukrainian).
- Kripyakevich, P.I., Markiv, V.Ya., Mel'nyk, Ya.V., 1967. *Dopov. Akad. Nauk Ukr. RSR, Ser. A* **29**, 750 (in Ukrainian).
- Kripyakevich, P.I., Oleksiv, G.I., 1970. *Dopov. Akad. Nauk Ukr. RSR, Ser. A* **1**, 63 (in Ukrainian).
- Kripyakevich, P.I., 1977. *Structure Types of Intermetallic Compounds. (Strukturnye Tipy Intermetallicheskikh Soedinenii)*. Nauka, Moscow, USSR (in Russian).
- Kurenbaeva, J.M., Tursina, A.I., Gribanov, A.V., Seropugin, Yu.D., Bodak, O.I., 2002. In: *Proc. of the VIII International Conference on Crystal Chemistry of Intermetallic Compounds Lviv, Ukraine, September 25–28*, p. 82.
- Kurusu, M., Takabatake, T., Fujii, H., 1990. *J. Magn. Magn. Mater.* **90–91**, 469.
- Kußmann, D., Hoffmann, R.-D., Pöttgen, R., 1998. *Z. Anorg. Allg. Chem.* **624**, 1727.
- Kuz'ma, Yu.B., 1983. *Crystal Chemistry of Borides. (Kristalloghimiya Boridov)*. Vishcha Shkola, Lviv, USSR (in Russian).
- Lahiouel, R., Pierre, J., Siaud, E., Galera, R.M., Besnus, M.J., Kappler, J.P., Murani, A.P., 1987. *Z. Phys. B* **67**, 185.
- Lal, H.B., Methfessel, S., 1981. *J. Magn. Magn. Mater.* **23**, 283.
- Lal, H.B., 1982. *J. Magn. Magn. Mater.* **30**, 192.
- Landrum, G.A., Hoffmann, R., Evers, J., Boysen, H., 1998. *Inorg. Chem.* **37**, 5754.
- Larica, C., Guimarães, A.P., 1976. *Phys. State Sol.* **77**, K11.
- Larson, A.C., Cromer, D.T., 1961. *Acta Cryst.* **14**, 73.
- Larson, A.C., Cromer, D.T., 1971. *Acta Cryst. B* **27**, 1875.
- Lawrence, J.M., Kwei, G.H., Sarrao, J.L., Fisk, Z., Mandrus, D., Thompson, J.D., 1996. *Phys. Rev. B* **54**, 6011.
- Lawrence, J.M., Osborn, R., Sarrao, J.L., Fisk, Z., 1999. *Phys. Rev. B* **59**, 1134.
- Lawrence, J.M., Riseborough, P.S., Booth, C.H., Sarrao, J.L., Thompson, J.D., Osborn, R., 2001. *Phys. Rev. B* **63**, 054427.
- Li, D.X., Shiokawa, Y., Nozue, T., Kamimura, T., Sumiyama, K., 2002. *J. Magn. Magn. Mater.* **241**, 17.
- Lukachuk, M., Kalychak, Ya.M., Pöttgen, R., Hoffmann, R.-D., 2002. In: *Proc. of the VIII International Conference on Crystal Chemistry of Intermetallic Compounds, Lviv, Ukraine, September 25–28, 2002*, p. 157.
- Lukachuk, M., Kalychak, Ya.M., Pöttgen, R., 2003. Unpublished.
- Macaluso, R.T., Sarrao, J.L., Pagliuso, P.G., Moreno, N.O., Goodrich, R.G., Browne, D.A., Fronczek, F.R., Chan, J.Y., 2002. *J. Sol. State Chem.* **166**, 245.
- Macaluso, R.T., Sarrao, J.L., Moreno, N.O., Pagliuso, P.G., Thompson, J.D., Fronczek, F.R., Hundley, M.F., Malinowski, A., Chan, J.Y., 2003. *Chem. Mater.* **15**, 1394.
- Maeno, Y., Takahashi, M., Fujita, T., Uwatoko, Y., Fujii, H., Okamoto, T., 1987. *Jap. J. Appl. Phys.* **26**, 545.
- Maetz, J., Muellner, M., Jex, H., Assmus, W., Takke, R., 1980. *Z. Physik B* **37**, 39.
- Majumdar, S., Balakrishnan, G., Lees, M.R., McK Paul, D., 2003. *Acta Phys. Polonica B* **34**, 1043.
- Malik, S.K., Adroja, D.T., Padalia, B.D., Vijayaraghavan, R., 1990a. *Physica B* **163**, 89.
- Malik, S.K., Vijayaraghavan, R., Adroja, D.T., Padalia, B.D., Edelstein, A.S., 1990b. *J. Magn. Magn. Mater.* **92**, 80.
- Mallik, R., Sampathkumaran, E.V., Dumschat, J., Wortmann, G., 1997. *Solid State Commun.* **102**, 59.
- Manfrinetti, P., Palenzona, A., Dhar, S.K., Mitra, C., Paulose, P.L., Pal, D., Ramakrishnan, S., 2000. *J. Magn. Magn. Mater.* **213**, 404.
- Marazza, R., Ferro, R., Rossi, D., 1975. *Z. Metallkd.* **66**, 110.
- Markiv, V.Ya., Belyavina, N.N., Zavodnik, V.E., 1988. *Dokl. Akad. Nauk Ukr. SSR, Ser. B* **6**, 51 (in Russian).
- Matsumoto, T., Shimizu, T., Yamada, Y., Yoshimura, K., 1992. *J. Magn. Magn. Mater.* **104–107**, 647.
- Mason, J.T., Harsha, K.S., Premo Chiotti, 1970. *Acta Cryst. B* **26**, 356.
- Mazzone, D., Rossi, D., Marazza, R., Ferro, R., 1982. *J. Less-Common Met.* **84**, 301.
- Mito, T., Kawasaki, S., Zheng, G.-Q., Kawasaki, Y., Ishida, K., Kitaoka, Y., Aoki, D., Haga, Y., Ōnuki, Y., 2001. *Phys. Rev. B* **63**, 220507.
- Mitsuda, A., Goto, T., Yoshimura, K., Zhang, W., Sato, N., Kosuge, K., Wada, H., 2002. *J. Phys. Chem. Solids* **63**, 1211.
- Mock, S., Faisst, A., von Lohneysen, H., 1997. *Phys. Rev. B* **56**, 335.

- Moshopoulou, E.G., Fisk, Z., Sarrao, J.L., Thompson, J.D., 2001. *J. Solid State Chem.* **158**, 25.
- Movshovich, R., Jaime, M., Thompson, J.D., Petrovic, C., Fisk, Z., Pagliuso, P.G., Sarrao, J.L., 2001. *Phys. Rev. Lett.* **86**, 5152.
- Moze, O., Mentink, S.A.M., Nieuwenhuys, G.H., Buschow, K.H.J., 1995. *J. Magn. Magn. Mater.* **150**, 345.
- Müllmann, R., Mosel, B.D., Eckert, H., Kotzyba, G., Pöttgen, R., 1998. *J. Solid State Chem.* **137**, 174.
- Müllmann, R., Ernet, U., Mosel, B.D., Eckert, H., Kremer, R.K., Hoffmann, R.-D., Pöttgen, R., 2001. *J. Mater. Chem.* **11**, 1133.
- Mulder, F.M., Thiel, R.C., Tung, L.D., Franse, J.J.M., Buschow, K.H.J., 1998. *J. Alloys Compd.* **264**, 43.
- Mushnikov, N.V., Goto, T., Ishikawa, F., Zhang, W., Yoshimura, K., Gaviko, V.S., 2002. *J. Alloys Compd.* **345**, 20.
- Najib, A., Pierre, J., Besnus, M.J., Haen, P., Murani, A.P., Siaud, E., 1988. *J. Magn. Magn. Mater.* **76–77**, 135.
- Nakamura, H., Nakajima, K., Kitaoka, Y., Asayama, K., Yoshimura, K., Nitta, T., 1990. *J. Phys. Soc. Jpn.* **59**, 28.
- Nakamura, H., Ito, K., Wada, H., Shiga, M., 1993a. *Physica B* **186–188**, 633.
- Nakamura, H., Ito, K., Uenishi, A., Wada, H., Shiga, M., 1993b. *J. Phys. Soc. Jpn.* **62**, 1446.
- Nakamura, H., Ito, K., Shiga, M., 1994a. *J. Phys.: Condens. Matter* **6**, 6801.
- Nakamura, H., Ito, K., Shiga, M., 1994b. *J. Phys.: Condens. Matter* **6**, 9201.
- Nakamura, H., Shiga, M., 1995. *Physica B* **206–207**, 364.
- Nicklas, M., Sidorov, V.A., Borges, H.A., Pagliuso, P.G., Petrovic, C., Fisk, Z., Sarrao, J.L., Thompson, J.D., 2003a. *Phys. Rev. B* **67**, 020506.
- Nicklas, M., Sidorov, V.A., Borges, H.A., Moreno, N.O., Pagliuso, P.G., Sarrao, J.L., Thompson, J.D., 2003b. *Acta Phys. Polonica B* **34**, 907.
- Niepmann, D., Prots', Yu.M., Pöttgen, R., Jeitschko, W., 2000. *J. Sol. State Chem.* **154**, 329.
- Nishigori, S., Hirooka, Y., Ito, T., 1998. *J. Magn. Magn. Mater.* **177–181**, 137.
- Nowik, I., Felner, I., Voiron, J., Beille, J., Najib, A., du Tremolet de Lacheisserie, E., Gratz, G., 1988. *Phys. Rev. B* **37**, 5633.
- Nyayate, M.N., Devare, S.H., Malik, S.K., Adroja, D.T., Devare, H.G., 1990. *Phys. Lett. A* **151**, 547.
- Oesterreicher, H., 1977. *J. Less-Common Met.* **55**, 131.
- Oesterreicher, H., Parker, F.T., 1977. *Phys. Rev. B* **16**, 5009.
- Ogawa, S., Suga, S., Taniguchi, M., Fujisawa, M., Fujimori, A., Shimizu, T., Yasuoka, H., Yoshimura, K., 1988. *Solid State Commun.* **67**, 1093.
- Ohara, S., Sakamoto, I., Shomi, T., Chen, G., 2003. *Acta Phys. Polonica B* **34**, 1243.
- Ōnuki, Y., Yamazaki, T., Kobori, A., Omi, T., Komatsubara, T., Takayanagi, S., Kato, H., Wada, N., 1987. *J. Phys. Soc. Jpn.* **56**, 4251.
- Oomi, G., Kagayama, T., Ōnuki, Y., Komatsubara, T., 1990. *Physica B* **163**, 557.
- Oomi, G., Kagayama, T., Kojima, K., Hihara, T., 1994. *J. Alloys Compd.* **207–208**, 282.
- Oppelt, A., Dormann, E., Buschow, K.H.J., 1972. *Internat. J. Magn.* **3**, 55.
- Pagliuso, P.G., Thompson, J.D., Hundley, M.F., Sarrao, J.L., 2000. *Phys. Rev. B* **62**, 12266.
- Pagliuso, P.G., Thompson, J.D., Hundley, M.F., Sarrao, J.L., Fisk, Z., 2001a. *Phys. Rev. B* **63**, 054426.
- Pagliuso, P.G., Petrovic, C., Movshovich, R., Hall, D., Hundley, M.F., Sarrao, J.L., Thompson, J.D., Fisk, Z., 2001b. *Phys. Rev. B* **64**, 100503(R).
- Pagliuso, P.G., Moreno, N.O., Curro, N.J., Thompson, J.D., Hundley, M.F., Sarrao, J.L., Fisk, Z., Christianson, A.D., Lacerda, A.H., Light, B.E., Cornelius, A.L., 2002. *Phys. Rev. B* **66**, 054433.
- Palenzona, A., 1971. *J. Less-Common Met.* **25**, 367.
- Parthé, E., Chabot, B., 1984. In: Gschneidner, K.A. Jr., Eyring, L. (Eds.), *Handbook on the Physics and Chemistry of Rare Earths*, vol. **6**. North-Holland, Amsterdam, p. 113.
- Parthé, E., Chabot, B., Cenzual, K., 1985. *Chimia* **39**, 164.
- Parthé, E., 1990. *Elements of Inorganic Structural Chemistry*. Pöge, Leipzig.
- Parthé, E., Gelato, L., Chabot, B., Penzo, M., Cenzual, K., Gladyshevskii, R.E., 1993. TYPIX – standardized data and crystal chemical characterization of inorganic structure types. In: *Gmelin Handbook of Inorganic and Organometallic Chemistry*, eighth ed. Springer-Verlag, Berlin.
- Perlitz, H., Westgren, A., 1943. *Ark. Kemi, Mineral. Geol. B* **16**, 1.
- Petrovic, C., Pagliuso, P.G., Hundley, M.F., Movshovich, R., Sarrao, J.L., Thompson, J.D., Fisk, Z., Monthoux, P., 2001a. *J. Phys.: Condens. Matter* **13**, L337.
- Petrovic, C., Movshovich, R., Jaime, M., Pagliuso, P.G., Hundley, M.F., Sarrao, J.L., Fisk, Z., Thompson, J.D., 2001b. *Europhys. Lett.* **53**, 354.
- Petrovic, C., Bud'ko, S.L., Kogan, V.G., Canfield, P.C., 2002. *Phys. Rev. B* **66**, 054534.

- Pillmayr, N., Bauer, E., Yoshimura, K., 1992. *J. Magn. Magn. Mater.* **104–107**, 639.
- Pinto, R.P., Amado, M.M., Braga, M.E., de Azevedo, M.M.P., Sousa, J.B., Etourneau, J., 1997. *J. Appl. Phys.* **81**, 4182.
- Pleger, H.R., Brück, E., Braun, E., Oster, F., Freimuth, A., Politt, B., Roden, B., Wohlleben, D., 1987. *J. Magn. Magn. Mater.* **63–64**, 107.
- Poduska, K.M., DiSalvo, F.J., Petříček, V., 2000. *J. Alloys Compd.* **308**, 64.
- Pöttgen, R., 1994. *Z. Naturforsch.* **49b**, 1525.
- Pöttgen, R., 1995. *J. Mater. Chem.* **5**, 769.
- Pöttgen, R., 1996a. *Z. Kristallogr.* **211**, 884.
- Pöttgen, R., 1996b. *J. Mater. Chem.* **6**, 63.
- Pöttgen, R., Dronskowski, R., 1996. *Z. Anorg. Allg. Chem.* **622**, 355.
- Pöttgen, R., Müllmann, R., Mosel, B.D., Eckert, H., 1996. *J. Mater. Chem.* **6**, 801.
- Pöttgen, R., Grin, Yu.N., 1997. *Z. Kristallogr. Suppl.* **12**, 136.
- Pöttgen, R., Kotzyba, G., Görlich, E.A., Łatka, K., Dronskowski, R., 1998. *J. Solid State Chem.* **141**, 352.
- Pöttgen, R., Hoffmann, R.-D., Kremer, R.K., Schnelle, W., 1999a. *J. Solid State Chem.* **142**, 180.
- Pöttgen, R., Gulden, T., Simon, A., 1999b. *GIT Labor-Fachzeitschrift* **43**, 133.
- Pöttgen, R., Hoffmann, R.-D., Möller, M.H., Kotzyba, G., Künnen, B., Rosenhahn, C., Mosel, B.D., 1999c. *J. Solid State Chem.* **145**, 174.
- Pöttgen, R., Lang, A., Hoffmann, R.-D., Künnen, B., Kotzyba, G., Müllmann, R., Mosel, B.D., Rosenhahn, C., 1999d. *Z. Kristallogr.* **214**, 143.
- Pöttgen, R., Johrendt, D., 2000. *Chem. Mater.* **12**, 875.
- Pöttgen, R., Kußmann, D., 2001. *Z. Anorg. Allg. Chem.* **627**, 55.
- Pöttgen, R., Johrendt, D., Kußmann, D., 2001. In: Gschneidner, K.A. Jr., Eyring, L. (Eds.), *Handbook on the Physics and Chemistry of Rare Earths*, vol. **32**, p. 453.
- Raj, P., Sathyamoorthy, A., Shashikala, K., Venkateswara Rao, C.R., Kundaliya, D., Malik, S.K., 2002. *J. Alloys Compd.* **345**, L1.
- Rieger, W., Nowotny, H., Benesovsky, F., 1964. *Monatsh. Chem.* **95**, 1502.
- Rieger, W., Nowotny, H., Benesovsky, F., 1966. *Monatsh. Chem.* **97**, 378.
- Rodewald, U.-Ch., Zaremba, V.I., Galadzhun, Ya.V., Hoffmann, R.-D., Pöttgen, R., 2002. *Z. Anorg. Allg. Chem.* **628**, 2293.
- Rossi, D., Ferro, R., Contardi, V., Marazza, R., 1977. *Z. Metallkd.* **68**, 493.
- Rossi, D., Marazza, R., Mazzone, D., Ferro, R., 1981. *J. Less-Common Met.* **78**, P1.
- Rossi, D., Mazzone, D., Marazza, R., Ferro, R., 1983. *Z. Anorg. Allg. Chem.* **507**, 235.
- Rundqvist, S., Jellinek, F., 1959. *Acta Chem. Scand.* **13**, 425.
- Rykhail, R.M., Zarechnyuk, O.S., Yarmolyuk, Ya.P., 1972. *Kristallografiya* **17**, 521 (in Russian).
- Rykhail, R.M., Zarechnyuk, O.S., Yarmolyuk, Ya.P., 1977. *Dopov. Akad. Nauk Ukr. RSR, Ser. A* **3**, 265 (in Ukrainian).
- Sakakibara, T., Tayama, T., Harita, A., Haga, Y., Shishido, H., Settai, R., Ōnuki, Y., 2003. *Acta Phys. Polonica B* **34**, 467.
- Sales, B.C., Wohlleben, D., 1975. *Phys. Rev. Lett.* **35**, 1240.
- Sampathkumaran, E.V., Nambudripad, N., Dhar, S.K., Vijayaraghavan, R., Kuentzler, R., 1987. *Phys. Rev. B* **35**, 2035.
- Sampathkumaran, E.V., Mallik, R., 1996. *Physica B* **223–224**, 316.
- Sarrao, J.L., Immer, C.D., Benton, C.L., Fisk, Z., Lawrence, J.M., Mandrus, D., Thompson, J.D., 1996. *Phys. Rev. B* **54**, 12207.
- Sarrao, J.L., 1999. *Physica B* **259**, 128.
- Satoh, K., Maeno, Y., Fujita, T., Uwatoko, Y., Fujii, H., 1988. *J. de Physique* **49**, 779.
- Satoh, K., Fujita, T., Maeno, Y., Uwatoko, Y., Fujii, H., 1990. *J. Phys. Soc. Jpn.* **59**, 692.
- Savitskiy, E.M., Poliakova, V.P., Urvachev, V.P., 1980. *Izv. Akad. Nauk SSSR, Metallurgy* **4**, 192.
- Schlüter, M., Heying, B., Pöttgen, R., 2003. *Z. Naturforsch. B* **58**, 16.
- Sekizawa, K., Yasukōchi, K., 1964. *Phys. Lett.* **11**, 216.
- Sekizawa, K., Yasukōchi, K., 1966. *J. Phys. Soc. Jpn.* **21**, 684.
- Semitelou, J.P., Siouris, J., Yakinthos, J.K., Schäfer, W., Schmitt, D., 1999. *J. Alloys Compd.* **283**, 12.
- Sen, M., Giri, S., Ghoshray, K., Bandyopadhyay, B., Ghoshray, A., Chatterjee, N., 1994. *Solid State Commun.* **89**, 327.
- Sen, M., Ghoshray, A., Ghoshray, K., Sil, S., Chatterjee, N., 1996. *Phys. Rev. B* **53**, 14345.
- Severing, A., Gratz, E., Rainford, B.D., Yoshimura, K., 1990. *Physica B* **163**, 409.
- Shimizu, T., Yoshimura, K., Nitta, T., Sakakibara, T., Goto, T., Mekata, M., 1988. *J. Phys. Soc. Jpn.* **57**, 405.
- Shishido, H., Settai, R., Araki, S., Ueda, T., Inada, Y., Kobayashi, T.C., Muramatsu, T., Haga, Y., Ōnuki, Y., 2002. *Phys. Rev. B* **66**, 214510.

- Shoemaker, D.P., Marsh, R.E., Ewing, F.J., Pauling, L., 1952. *Acta Cryst.* **5**, 637.
- Shoemaker, C.B., Shoemaker, D.P., 1965. *Acta Cryst.* **18**, 900.
- Sichevich, O.M., Lapunova, R.V., Sobolev, A.N., Grin, Yu.N., Yarmolyuk, Ya.P., 1985. *Kristallografiya* **30**, 1077 (in Russian).
- Simon, A., Steinbrenner, U., 1996. *J. Chem. Soc., Faraday Trans.* **92**, 2117.
- Siouris, J., Semitelou, J.P., Yakinthos, J.K., Schäfer, W., 2000a. *Physica B* **276–278**, 582.
- Siouris, I.M., Semitelou, J.P., Yakinthos, J.K., 2000b. *J. Alloys Compd.* **297**, 26.
- Siouris, I.M., Semitelou, J.P., Yakinthos, J.K., Schäfer, W., Arons, R.R., 2001. *J. Alloys Compd.* **314**, 1.
- Skolozdra, R.V., Mandzyk, V.M., Aksel'rud, L.G., 1981. *Kristallografiya* **26**, 480 (in Russian).
- Skolozdra, R.V., Komarovskaya, L.P., 1988. *Izv. Akad. Nauk SSSR, Metall* **2**, 214 (in Russian).
- Susaki, T., Fujimori, A., Okusawa, M., Sarrao, J.L., Fisk, Z., 2001. *Solid State Commun.* **118**, 413.
- Suzuki, T., Nohara, M., Fujita, T., Takabatake, T., Fujii, H., 1990. *Physica B* **165**, 421.
- Suzuki, H., Tsujii, N., Suzuki, O., Kitazawa, H., Abe, H., Imai, M., Kido, G., 2003. *Acta Phys. Polonica B* **34**, 1055.
- Sysa, L.V., Zaremba, V.I., Kalychak, Ya.M., Baranyak, V.M., 1988. *Visnyk Lviv University, Ser. Khim.* **29**, 32 (in Ukrainian).
- Sysa, L.V., Kalychak, Ya.M., Bakar, A.M., Baranyak, V.M., 1989. *Krystallografiya* **34**, 744 (in Russian).
- Sysa, L.V., 1991. *Visnyk Lviv University, Ser. Khim.* **31**, 15 (in Ukrainian).
- Sysa, L.V., Kalychak, Ya.M., 1992. *Metally* **3**, 126 (in Russian).
- Sysa, L.V., Kalychak, Ya.M., 1993. *Krystallografiya* **38**, 271 (in Russian).
- Sysa, L.V., Kalychak, Ya.M., Stets', I.N., Galadzhun, Ya.V., 1994a. *Krystallografiya* **39**, 821 (in Russian).
- Sysa, L.V., Kalychak, Ya.M., Galadzhun, Ya.V., 1994b. *Visnyk Lviv University, Ser. Khim.* **33**, 49 (in Ukrainian).
- Sysa, L.V., Kalychak, Ya.M., Galadzhun, Ya.V., Zaremba, V.I., Aksel'rud, L.G., Skolozdra, R.V., 1998. *J. Alloys Compd.* **266**, 17.
- Szytuła, A., Bązela, W., Gondek, Ł., Jaworska-Gołąb, T., Penc, B., Stüsser, N., Zygmunt, A., 2002. *J. Alloys Compd.* **336**, 11.
- Takegahara, K., Kasuya, T., 1990. *J. Phys. Soc. Jpn.* **59**, 3299.
- Takeuchi, T., Inoue, T., Sugiyama, K., Aoki, D., Tokiwa, Y., Haga, Y., Kindo, K., Ōnuki, Y., 2001. *J. Phys. Soc. Jpn.* **70**, 877.
- Takeuchi, T., Shishido, H., Ikeda, S., Settai, R., Haga, Y., Ōnuki, Y., 2002. *J. Phys.: Condens. Matter* **14**, 261.
- Tang, J., Gschneidner Jr., K.A., White, S.J., Roser, M.R., Goodwin, T.J., Corruccini, L.R., 1995. *Phys. Rev. B* **52**, 7328.
- Tayama, T., Harita, A., Sakakibara, T., Haga, Y., Shishido, H., Settai, R., Ōnuki, Y., 2002. *J. Phys. Chem. Solids* **63**, 1155.
- Tchoula Tchokonte, M.B., de V. Du Plessis, P., Strydom, A.M., Czopnik, A., Kaczorowski, D., 2003. *Acta Phys. Polonica B* **34**, 1309.
- Thompson, J.D., Movshovich, R., Fisk, Z., Bouquet, F., Curro, N.J., Fisher, R.A., Hammel, P.C., Hegger, H., Hundley, M.F., Jaime, M., Pagliuso, P.G., Petrovic, C., Phillips, N.E., Sarrao, J.L., 2001. *J. Magn. Magn. Mater.* **226–230**, 5.
- Trovarelli, O., Geibel, C., Cardoso, R., Mederle, S., Borth, R., Buschinger, B., Grosche, F.M., Grin, Yu.N., Sparn, G., Steglich, F., 2000. *Phys. Rev. B* **61**, 9467.
- Tsujii, N., Kitô, H., Kitazawa, H., Kido, G., 2001. *J. Alloys Compd.* **322**, 74.
- Vajeeston, P., Ravindran, P., Vidya, R., Kjekshus, A., Fjellvåg, H., Yartys, V.A., 2003. *Phys. Rev. B* **67**, 014101.
- Wei, B., Pagliuso, P.G., Sarrao, J.L., Thompson, J.D., Fisk, Z., Lynn, J.W., Erwin, R.W., 2000. *Phys. Rev. B* **62**, R14621.
- Wei, B., Pagliuso, P.G., Sarrao, J.L., Thompson, J.D., Fisk, Z., Lynn, J.W., 2001. *Phys. Rev. B* **64**, 020401(R).
- Wei, B., Aeppli, G., Lynn, J.W., Pagliuso, P.G., Sarrao, J.L., Hundley, M.F., Thompson, J.D., Fisk, Z., 2002. *Phys. Rev. B* **65**, 100505(R).
- Weitzer, F., Rogl, P., 1990. *J. Less-Common Met.* **167**, 135.
- Weitzer, F., Leithe-Jasper, A., Rogl, P., Hiebl, K., Noël, H., Wiesinger, G., Steiner, W., 1993. *J. Solid State Chem.* **104**, 368.
- Wohlleben, D., Röhrler, J., 1984. *J. Appl. Phys.* **55**, 1904.
- Xue, B., Schwer, H., Hulliger, F., 1992. *Acta Cryst. C* **48**, 2064.
- Xue, B., Hulliger, F., Baerlocher, Ch., Estermann, M., 1993. *J. Alloys Compd.* **191**, L9.
- Yagasaki, K., Fujii, H., Kadena, Y., Okamoto, T., 1978a. *J. Phys. Soc. Jpn.* **44**, 859.
- Yagasaki, K., Hidaka, Y., Fujii, H., Okamoto, T., 1978b. *J. Phys. Soc. Jpn.* **45**, 110.
- Yagasaki, K., Fujii, H., Fujiwara, H., Okamoto, T., 1980. *J. Phys. Soc. Jpn.* **49**, 250.

- Yagasaki, K., Uwatoko, Y., Fujii, H., Okamoto, T., 1985. *J. Magn. Magn. Mater.* **51**, 117.
- Yamaguchi, Y., Sakurai, J., Teshima, F., Kawanaka, H., Takabatake, T., Fujii, H., 1990. *J. Phys.* **2**, 5715.
- Yarmolyuk, Ya.P., Kripyakevich, P.I., 1976. *Dopov. Akad. Nauk Ukr. RSR, Ser. A* **1**, 86 (in Ukrainian).
- Yartys, V.A., Denys, R.V., Hauback, B.C., Fjellvåg, H., Bulyk, I.I., Riabov, A.B., Kalychak, Ya.M., 2002. *J. Alloys Compd.* **330–332**, 132.
- Yatsenko, S.P., Semyannikov, A.A., Shakarov, H.O., Fedorova, E.G., 1983. *J. Less-Common Met.* **90**, 95.
- Yoshimura, K., Nitta, T., Mekata, M., Shimizu, T., Sakakibara, T., Goto, T., Kido, G., 1988. *Phys. Rev. Lett.* **60**, 851.
- Yoshimura, K., Nitta, T., Shimizu, T., Mekata, M., Yasuoka, H., Kosuge, K., 1990. *J. Magn. Magn. Mater.* **90–91**, 466.
- Zanicchi, G., Mazzone, D., Contardi, V., Marazza, R., Rambaldi, G., Rossi, D., 1983. *Gaz. Chim. Italiana* **113**, 257.
- Zapf, V.S., Freeman, E.J., Bauer, E.D., Petricka, J., Sirvent, C., Frederick, N.A., Dickey, R.P., Maple, M.B., 2001. *Phys. Rev. B* **65**, 014506.
- Zapf, V.S., Frederick, N.A., Rogers, K.L., Hof, K.D., Ho, P.-C., Bauer, E.D., Maple, M.B., 2003. *Phys. Rev. B* **67**, 064405.
- Zaremba, V.I., Baranyak, V.M., Kalychak, Ya.M., 1984. *Visnyk Lviv University, Ser. Khim.* **25**, 18 (in Ukrainian).
- Zaremba, V.I., Zakharko, O.Ya., Kalychak, Ya.M., Bodak, O.I., 1987a. *Dopov. Akad. Nauk Ukr. RSR Ser. B* **12**, 44 (in Ukrainian).
- Zaremba, V.I., Belsky, V.K., Kalychak, Ya.M., Pecharsky, V.K., Gladyshevskii, E.I., 1987b. *Dopov. Akad. Nauk Ukr. RSR Ser. B* **3**, 42 (in Ukrainian).
- Zaremba, V.I., Bruskov, V.A., Zavali, P.Yu., Kalychak, Ya.M., 1988. *Neorg. Mater.* **24**, 409 (in Russian).
- Zaremba, V.I., Kalychak, Ya.M., Zavali, P.Yu., Sobolev, A.N., 1989. *Dopov. Akad. Nauk Ukr. RSR Ser. B* **2**, 38 (in Russian).
- Zaremba, V.I., Kalychak, Ya.M., Zavali, P.Yu., Zavadnik, V.E., 1990. *Krystallografiya* **35**, 493 (in Russian).
- Zaremba, V.I., Kalychak, Ya.M., Zavali, P.Yu., Bruskov, V.A., 1991. *Krystallografiya* **36**, 1415 (in Russian).
- Zaremba, V.I., Kalychak, Ya.M., Zavali, P.Yu., 1992. *Krystallografiya* **37**, 352 (in Russian).
- Zaremba, V.I., Kalychak, Ya.M., Pecharsky, V.K., Dmytrakh, O.V., 1993. *Neorg. Mater.* **29**, 1693 (in Russian).
- Zaremba, V.I., Kalychak, Ya.M., Galadzhun, Ya.V., Suski, W., Wochowski, K., 1999. *J. Solid State Chem.* **145**, 216.
- Zaremba, V.I., Galadzhun, Ya.V., Kalychak, Ya.M., Kaczorowski, D., Stepień-Damm, J., 2000a. *J. Alloys Compd.* **296**, 280.
- Zaremba, V.I., Galadzhun, Ya.V., Kaczorowski, D., Wolcyrz, M., 2000b. 13th Internat. Conf. Solid Compounds of Transition Elements, Stresa (Italy), April, 2000, P-C56.
- Zaremba, V.I., Kalychak, Ya.M., Dubenskii, V.P., Hoffmann, R.-D., Pöttgen, R., 2000c. *J. Solid State Chem.* **152**, 560.
- Zaremba, V.I., Galadzhun, Ya.V., Belan, B.D., Pikul, A., Stepień-Damm, J., Kaczorowski, D., 2001. *J. Alloys Compd.* **316**, 64.
- Zaremba, V.I., Dubenskii, V.P., Pöttgen, R., 2002a. *Z. Naturforsch.* **57b**, 798.
- Zaremba, V.I., Kalychak, Ya.M., Tyvanchuk, Yu.B., Hoffmann, R.-D., Möller, M.H., Pöttgen, R., 2002b. *Z. Naturforsch.* **57b**, 791.
- Zaremba, V.I., Dubenskii, V.P., Kalychak, Ya.M., Hoffmann, R.-D., Pöttgen, R., 2002c. *Sol. State Sci.* **4**, 1293.
- Zaremba, V.I., Kalychak, Ya.M., Dubenskii, V.P., Hoffmann, R.-D., Rodewald, U.-Ch., Pöttgen, R., 2002d. *J. Sol. State Chem.* **169**, 118.
- Zaremba, V.I., Rodewald, U.-Ch., Kalychak, Ya.M., Galadzhun, Ya.V., Kaczorowski, D., Hoffmann, R.-D., Pöttgen, R., 2003a. *Z. Anorg. Allg. Chem.* **629**, 434.
- Zaremba, V.I., Rodewald, U.-Ch., Hoffmann, R.-D., Kalychak, Ya.M., Pöttgen, R., 2003b. *Z. Anorg. Allg. Chem.* **629**, 1157.
- Zaremba, V.I., Rodewald, U.-Ch., Hoffmann, R.-D., Pöttgen, R., 2003c. *Z. Kristallogr. Suppl.* **20**, 160.
- Zaremba, V.I., 2003d. Unpublished.
- Zaremba, V.I., Kaczorowski, D., Rodewald, U.-Ch., Hoffmann, R.-D., Pöttgen, R., 2004. *Chem. Mater.* **16**, 466.
- Zell, W., Pott, R., Roden, B., Wohlleben, D., 1981. *Solid State Commun.* **40**, 751.
- Zhang, W., Sato, N., Yoshimura, K., Mitsuda, A., Sorada, K., Mitamura, H., Goto, T., Kosuge, K., 2002. *J. Phys. Chem. Solids* **63**, 1215.
- Zheng, G.-Q., Tanabe, K., Mito, T., Kawasaki, S., Kitaoka, Y., Aoki, D., Haga, Y., Ōnuki, Y., 2001. *Phys. Rev. Lett.* **86**, 4664.
- Zheng, G.-Q., Tanabe, K., Kawasaki, S., Kan, H., Kitaoka, Y., Aoki, D., Haga, Y., Ōnuki, Y., 2003. *Acta Phys. Polonica B* **34**, 435.
- Zumdick, M.F., Pöttgen, R., 1999. *Z. Kristallogr.* **214**, 90.

Chapter 219

UNCONVENTIONAL SUPERCONDUCTIVITY AND MAGNETISM IN LANTHANIDE AND ACTINIDE INTERMETALLIC COMPOUNDS

P. THALMEIER

*Max-Planck-Institut für Chemische Physik fester Stoffe, 01187 Dresden,
Germany*

G. ZWICKNAGL

*Institut für Mathematische Physik, Technische Universität Braunschweig,
38106 Braunschweig, Germany*

Contents

List of symbols	137	2.3.2. Specific heat and magnetotransport in the vortex phase: a genuine angular resolved method	175
List of acronyms	138	2.3.3. Detection of density wave type order parameters	178
1. Introduction	138	3. Ce-based heavy-fermion superconductors	183
2. Theory and techniques	142	3.1. CeM ₂ X ₂	184
2.1. Heavy quasiparticles in Ce, U compounds and their interactions	142	3.1.1. Electronic properties, Fermi surfaces and heavy quasiparticles	184
2.1.1. Kondo lattice model for Ce-compounds	143	3.1.2. Superconductivity and itinerant antiferromagnetism in CeCu ₂ Si ₂	189
2.1.2. Dual model for U-compounds	145	3.1.3. Pressure-induced superconductivity in CePd ₂ Si ₂ and CeNi ₂ Ge ₂	190
2.1.3. Fermi-liquid state and heavy quasiparticles: renormalized band theory	150	3.2. CeMIn ₅	191
2.1.4. Quasiparticle interactions and spin fluctuation theory	152	3.2.1. Electronic properties and Fermi surfaces	193
2.2. Order parameters and their coexistence in strongly correlated electron systems	157	3.2.2. Unconventional superconductivity in CeCoIn ₅	194
2.2.1. Order parameter classification	158	3.3. Superconductivity close to a quantum critical point	196
2.2.2. Pairing model for coexistence of SC and CDW/SDW	163	4. U-based heavy-fermion superconductors	198
2.2.3. Coupled gap equations and results for coexistence	165	4.1. Multicomponent heavy fermion superconductor UPt ₃	199
2.3. Methods to investigate the symmetry of order parameters	168	4.1.1. Dual model and heavy quasiparticles	200
2.3.1. Detection of superconducting order parameter symmetry	169		

4.1.2. Pairing and the spin-orbit coupling problem	203	4.4.5. Collective excitations in the ordered phase	243
4.1.3. Multicomponent superconducting order parameter	204	4.4.6. The superconducting state	243
4.1.4. Small moment AF order	205	4.5. Superconductivity in the non-Fermi liquid state of UBe_{13} and $U_{1-x}Th_xBe_{13}$	244
4.1.5. The superconducting state, coupled with AF order	206	4.5.1. Normal state and nFI properties of UBe_{13}	244
4.1.6. The critical field curves and Ginzburg-Landau theory	210	4.5.2. The 5f-ground state of U	245
4.1.7. The superconducting gap function	211	4.5.3. The superconducting state in UBe_{13}	245
4.1.8. Low temperature transport properties	213	4.5.4. Superconducting phase diagram of Th-doped crystals	246
4.1.9. NMR Knight shift results	214	5. Rare earth borocarbide superconductors	248
4.1.10. Magnetothermal properties in the vortex phase	215	5.1. Physical properties of the nonmagnetic borocarbides	250
4.2. Magnetic exciton mediated superconductivity in UPd_2Al_3	216	5.1.1. Evidence for electron-phonon superconductivity	251
4.2.1. AF structure and superconducting properties	217	5.1.2. Anomalous H_{c2} -behaviour	252
4.2.2. Electronic structure, Fermi surface and effective mass	219	5.1.3. Specific heat and thermal conductivity results	252
4.2.3. The dual model for UPd_2Al_3 and induced moment AF	221	5.2. Theoretical analysis of nonmagnetic borocarbides	253
4.2.4. Induced moments and magnetic exciton dispersion in UPd_2Al_3	222	5.2.1. Electronic structure of the borocarbides	253
4.2.5. Magnetic exciton anomalies in quasiparticle tunneling spectra	225	5.2.2. Nodal structure of the superconducting gap and impurity effects	254
4.2.6. Possible symmetries of the superconducting order parameter	227	5.2.3. Thermodynamics and transport in the vortex phase	256
4.2.7. UNi_2Al_3 : a possible triplet superconductor	228	5.3. Magnetic borocarbides	258
4.3. Ferromagnetism and superconductivity in UGe_2	229	5.3.1. Metamagnetism and IC-C lock-in transition in $HoNi_2B_2C$	259
4.3.1. Electronic structure and band magnetism	231	5.3.2. Weak ferromagnetism in $ErNi_2B_2C$	262
4.3.2. Coexistence of FM order and superconductivity under pressure	233	5.4. Coexistence of superconductivity and magnetic order	262
4.3.3. Theoretical scenarios for superconductivity in UGe_2	234	5.4.1. Coexistence of helical SDW, antiferromagnetism and superconductivity in $HoNi_2B_2C$	263
4.3.4. Symmetry properties of gap states and Ginzburg-Landau theory	235	5.4.2. Coexistence of superconductivity and weak ferromagnetism in $ErNi_2B_2C$	267
4.3.5. Microscopic approaches	236	6. Rare earth skutterudite superconductors	268
4.4. A case of 'hidden order' in URu_2Si_2	236	6.1. Electronic structure and HF behaviour of $PrOs_4Sb_{12}$	269
4.4.1. Electronic structure and 5f-states	237	6.2. Pr CEF states and antiferroquadrupolar order	269
4.4.2. Phase transitions, field and pressure dependence	238	6.3. The superconducting split transition	271
4.4.3. Theoretical models: localised vs. itinerant	240	6.4. Thermal conductivity in the vortex phase and multiphase superconductivity in $PrOs_4Sb_{12}$	272
4.4.4. High field phase diagram and metamagnetism	242		

6.5. Gap models for SC <i>A</i> - and <i>B</i> -phases of PrOs ₄ Sb ₁₂	274	Acknowledgements	277
7. Summary and outlook	276	References	277

List of symbols

$\alpha(T)$	ultrasonic attenuation	m_b	conduction electron band mass
$\alpha_0, \beta, \gamma_0$	Landau free energy parameters	m^*	effective quasiparticle mass
B	magnetic induction	M	magnetization
c, c^\dagger	conduction electron operators	M_Q	staggered magnetization
$C(T)$	specific heat	$N(E)$	quasiparticle DOS
δ	CEF splitting energy	N_n	normal state quasiparticle DOS at E_F
$\Delta(\mathbf{k})$	gap function (SC, SDW, etc.; singlet, triplet, etc.)	p	pressure
d(k)	vector of triplet gap functions	q	conduction electron wave vector
ε_f	f-level position	Q	nesting or ordering wave vector
$\epsilon_{\mathbf{k}}$	quasiparticle energy in the normal state	$\rho(T)$	electrical resistivity
$E_{\mathbf{k}}$	quasiparticle energy in the ordered state (SC, SDW, etc.)	$\rho_{\mathbf{Q}}$	conduction electron charge density
E_F	Fermi energy	s_Q	conduction electron spin density
$f(\mathbf{k})$	form factor of gap functions	σ	vector of Pauli matrices
$f(E_{\mathbf{k}})$	Fermi function	θ, ϕ	polar angles of H
f_L, f_{GL}	Landau and Ginzburg–Landau free energy density	ϑ, φ	polar angles of k
γ	linear specific heat (Sommerfeld) coefficient	t	nearest neighbor hopping matrix element
Γ	quasiparticle scattering rate	t'	next nearest neighbor hopping matrix element
$ G\rangle$	CEF state	T	temperature
η	SC vector order parameter	T^*	characteristic or ‘Kondo’ temperature of HF compound
H	magnetic field	T_c	superconducting transition temperature
H_{c2}	upper critical field of the superconductor	T_N	Néel temperature
I	residual on-site quasiparticle repulsion or contact exchange	T_1^{-1}	NMR relaxation rate
$J(\mathbf{q})$	effective interaction between quasiparticles or local moments	U	bare on-site Coulomb interaction
J	total angular momentum of f-shell	$u(\omega)$	local CEF susceptibility
$\kappa(T)$	thermal conductivity	v_F	Fermi velocity
k	Boltzmann constant	$\mathbf{v}_s(\mathbf{r})$	superfluid velocity field
k	conduction electron wave vector	V_l	effective quasiparticle interaction ($l = \text{angular momentum channel}$)
k_F	Fermi wave number	\bar{v}	average Fermi velocity in uniaxial crystal
λ	electron–phonon interaction	$\chi_n, \chi_s(T)$	static homogeneous ($\mathbf{q} = 0$) conduction electron spin susceptibility in normal and SC state
μ, μ_B	magnetic moment, Bohr magneton	$\chi(\mathbf{q}, \omega)$	magnetic susceptibilities for conduction electrons or localised moments
m	free electron mass		

x	impurity or dopant concentration	ω	frequency
$Y(T)$	Yoshida function	$\omega_E(\mathbf{q})$	magnetic exciton dispersion

List of acronyms

AF	antiferromagnetic	LDA	local density approximation
AFQ	antiferroquadrupolar	LSDA	local spin density approximation
ANNNI	anisotropic next nearest neighbor Ising	mf	mean field
ARPES	angle resolved photoemission spectroscopy	MFS	magnetic Fermi surface
BIS	Bremsstrahlung isochromat spectroscopy	nFl	non-Fermi liquid
BZ	Brillouin zone	n.n.	next neighbor
CDW	charge density wave	n.n.n.	next nearest neighbor
CEF	crystalline electric field	NCA	non-crossing approximation
dHvA	de Haas–van Alphen	NMR	nuclear magnetic resonance
DLRO	diagonal long range order	OAF	orbital antiferromagnet
DOS	density of states	ODLRO	off-diagonal long range order
e-e	electron–electron	OP	order parameter
e-h	electron–hole	PES	photoemission spectroscopy
e-p	electron–phonon	QCP	quantum critical point
FFLO	Fulde–Ferrell–Larkin–Ovchinnikov	qp	quasiparticle
FL	Fermi liquid	RPA	random phase approximation
FLEX	fluctuation exchange	RKKY	Ruderman–Kittel–Kasuya–Yoshida
FM	ferromagnet	SBF	symmetry breaking field
FS	Fermi surface	SC	superconductivity
GL	Ginzburg–Landau	SDW	spin density wave
HF	heavy fermion	SN	spin nematic
IC	incommensurate	s.o.	spin–orbit
INS	inelastic neutron scattering	WFM	weak ferromagnetism

1. Introduction

The Fermi liquid state in metals has two common instabilities. Superconductivity (SC) is due to pair formation of electrons and (spin-, charge-) density waves (CDW, SDW) are formed by pairing electrons and holes. Theoretically it has been suspected quite early that pair-wave functions other than s -wave as in conventional superconductors and density waves may exist. However it has taken surprisingly long to identify such ‘unconventional’ condensed pair states in real materials.

Now there is an abundance of non- s -wave superconductors which are frequently associated with anisotropic ‘nodal’ gap functions where the quasiparticle excitations of the SC state vanishes on points or lines on the Fermi surface. This leads to low temperature ‘power law’

behaviour in many physical quantities. Heavy fermion (HF) lanthanide and actinide superconducting compounds were the first that were supposed to have unconventional SC pair states mediated by low energy spin fluctuations. High T_c cuprates which exhibit d-wave superconductivity are the most prominent and important examples. But nodal SC have also been found among the ruthenates and organic salts.

Conventional CDW and SDW states are ubiquitous in metals with the commensurate SDW or antiferromagnetic (AF) order being the most common. Compounds with confirmed unconventional density waves so far are rather scarce and with certainty have only been found in organic metals and perhaps in uranium HF compounds and the 'pseudogap' phase of underdoped cuprates. This may in part be due to the difficulty detecting such 'hidden' order parameters which leave no signature in standard neutron or X-ray diffraction experiments.

In this review article we will summarize the knowledge on a class of unconventional superconductors and their competition and coexistence with magnetism and hidden order phases that has accumulated over the last decade. To be comprehensive we will restrict ourselves exclusively to intermetallic lanthanide (4f) and actinide (5f) systems. Except for occasional remarks we will leave out completely the cuprate, cobaltate and ruthenate superconductors which are beyond the scope of our work on intermetallic compounds. The oxide superconductors are mostly close to a Mott insulator transition and the underlying microscopic physics is very different from the intermetallic f-electron compounds. Although on the phenomenological level of SC and density wave order parameter classification and investigation strong similarities exist. Likewise we do not discuss unconventional organic superconductors. The focus here is on stoichiometric 4f- and 5f-compounds where the lanthanide or actinide atoms occupy regular sublattices. With the exception of rare earth borocarbides the compounds reviewed are heavy fermion metals to a varying degree. In our review we do not want to provide an exhausting compilation of the physical properties in this whole class of materials. We rather focus on a few important compounds where each displays an important aspect of unconventional SC and its relation to magnetism or hidden order that will be discussed in detail in its physical and theoretical implications.

The complex low temperature phase diagrams of the HF metals results from the partially filled f-shells of the lanthanide and actinide ions which preserve atomic-like character. Occupying the states according to Hund's rules leads to magnetic moments. In a crystal their rotational degeneracy is partly lifted by the crystalline electric field (CEF) and the hybridization with broad conduction bands of the outer shell electrons. As a result a large number of low-energy excitations appears. In the ideal Fermi liquid case these excitations correspond to heavy quasiparticles whose effective mass m^* is by orders of magnitude larger than the free electron mass m . The corresponding quasiparticle band width T^* is of the order meV for true HF metals. The mass enhancement is reflected in large increase of the specific heat γ -value, the Pauli susceptibility and the T^2 -coefficient of electrical resistivity. However close to a quantum critical point (QCP) which signifies the onset of density wave instabilities low temperature anomalies in these quantities appear which are characteristic signatures of a non-Fermi liquid state.

At this point, we emphasize that the Landau theory of Fermi liquids does not make assumptions concerning the microscopic nature of the ground state and the low-lying excitations, it merely gives a counting prescription. It does not address the question how these excitations emerge in an interacting electron system, this requires a microscopic treatment. Generally speaking heavy quasiparticles arise from the lifting of local degeneracies which result as a consequence of strong local correlations. Various mechanisms for heavy mass generation have been suggested. While in Ce compounds with well localised $4f^1$ -states the Kondo mechanism is appropriate, there is increasing evidence that the dual, i.e., partly localised and partly itinerant, nature of $5f$ -states is responsible for the mass renormalization in the U-compounds. In both scenarios it is assumed that the heavy quasiparticles predominantly have f -character.

Residual interactions among the quasiparticles lead to the pairing instabilities. Two candidates have been identified in HF compounds: Firstly pairing interactions via exchange of enhanced overdamped spin fluctuations of itinerant quasiparticles, presumably at an antiferromagnetic wave vector. This model is invoked for Ce-compounds, especially when SC appears near a quantum critical point. It may also contain some truth for the more itinerant U-HF compounds. However we now know for sure that in U-compounds with partly localised $5f$ electrons a different mechanism is at work: pairing mediated by the exchange of propagating internal excitations ('magnetic excitons') of the localised $5f$ subsystem. A variant of this mechanism may also be appropriate for the recently discovered Pr-skutterudite HF superconductor with quadrupolar instead of magnetic excitons involved.

A major topic of our review is the critical discussion of existing evidence for unconventional SC order parameters as witnessed frequently by the presence of nodal gap functions. Previously the identification of gap symmetries has been an elaborate guess work mostly built on indirect evidence from low temperature 'power laws'. This situation has dramatically improved in recent years with the advent of genuine angular resolved magnetothermal and magnetotransport experiments in the vortex phase. They exploit the Doppler shift of SC quasiparticle energies which leads to field-angle oscillations in specific heat and thermal conductivity. Their analysis may lead to an unambiguous determination of nodal positions of the gap functions which facilitates a strong restriction and sometimes unique determination of the possible gap symmetry.

Superconductivity in HF-compounds frequently coexists with (spin-)density waves. In some cases they may be of the unconventional (hidden order) type. We discuss the competition and coexistence behaviour of these order parameters and related physical effects. Since both order parameters appear in the itinerant quasiparticle system this is a subtle interplay of Fermi surface geometry, pairing potentials and gap structures which can only be schematically understood in simplified toy models.

Coexistence behaviour is much simpler in the relatively new class of rare earth borocarbide superconductors which have comparatively high T_c 's. Although as electron-phonon superconductors they are set aside from our main focus on HF systems, they have been included in this review for various reasons: Firstly magnetism and SC superconductivity are carried by different species of electrons which only interact weakly through contact exchange interaction leading to a small effect of the local moment molecular field on the SC conduction electrons. This can be nicely treated by perturbation theory and allows a much better understanding of

coexistence behaviour as compared to the HF systems. Also they provide the first example of homogeneous coexistence of SC and ferromagnetism for all temperatures below T_c . Secondly the nonmagnetic rare earth borocarbides have extremely large gap anisotropy ratios $\geq 10^2$ which means that they are essentially nodal superconductors. In fact nonmagnetic borocarbides are the first which have been identified to have a SC gap with point nodes that is of fully symmetric $s + g$ wave type. Surely the standard electron–phonon mechanism has to be supplemented by something else, perhaps anisotropic Coulomb interactions to achieve this unconventional behaviour of borocarbides.

Considering the wide range of phenomena and questions involved we have to be quite selective in our review. We will concentrate on the exciting developments in 4f/5f intermetallic materials of the past decade referring to the literature for the earlier work. A general introduction to strongly correlated electron systems is given in the textbooks of Fulde (1995) and Fazekas (1999). Various aspects of heavy fermion physics are described in the previous review articles by Stewart et al. (1984), Ott (1987), Ott and Fisk (1987), Fulde et al. (1988), Grewe and Steglich (1991), Thalmeier and Lüthi (1991) and Zwicknagl (1992) as well as in the monographs by Kuramoto and Kitaoka (2000) and Hewson (1993). Reviews which focus on theories of unconventional HF superconductors are Sigrist and Ueda (1991), Sauls (1994) and Joynt and Taillefer (2002) and the monograph by Mineev and Samokhin (1999). Reviews discussing the rare earth borocarbide magnetic superconductors are given in Hilscher and Michor (1999) and Müller and Narozhnyi (2001). Earlier reviews of coexistence of superconductivity and localised magnetism can be found in Fulde and Keller (1982), Fulde and Zwicknagl (1990) and Fischer (1990).

Since we will not discuss oxide or organic unconventional superconductors we would like to refer to a few review articles where parallel developments, especially on pairing mechanism and gap function symmetries are discussed for these classes of materials: van Harlingen (1995), Scalapino (1995), Izyumov (1999), Moriya and Ueda (2000), Yanase et al. (2003) and Tsuei and Kirtley (2000) for cuprates, Mackenzie and Maeno (2003) for ruthenates and Maki and Won (1996) and Lang and Müller (2003) for unconventional organic superconductors.

The present review focuses on chosen topics of high current interest. We therefore select specific materials which allow us to discuss physical effects and theoretical concepts in detail.

This article is organized as follows: In sect. 2 we review the basic theoretical concepts and experimental techniques to identify pair condensate order parameters, especially we discuss the important new tool of angular resolved methods for SC gap investigation. Section 3 deals with the Ce-based heavy fermion compounds. The central question there is the competition between magnetism and Fermi liquid states which may become superconducting. While superconducting ground states seem to occur rather rarely in Ce-based heavy fermion systems at ambient pressure they are common in their U-based counterparts discussed in sect. 4. The major challenge in this context is the investigation of the unconventional and often exotic pairing mechanism and the identification of the symmetry of superconducting order parameters which may coexist with (hidden) long-range order. The low-temperature phases of rare earth borocarbides are reviewed in sect. 5. Of particular interest are the unusual magnetic ordering phenomena which may coexist with very anisotropic electron–phonon superconductivity. Section 6 is devoted to the newly discovered superconducting rare earth skutterudite cage

compounds which may exhibit a quadrupolar pairing mechanism. We conclude in sect. 7 by giving a summary and an outlook.

2. Theory and techniques

The theoretical understanding of superconductivity and magnetism in the heavy fermion systems is still in the state of rather schematic or illustrative models without real predictive power. The difficulty arises on two levels. Firstly the normal state quasiparticles themselves can so far be described only within effective one particle renormalised band pictures with empirical input parameters. For some compounds like URu_2Si_2 and Ce-compounds close to the quantum critical point the SC transition even takes place in a state without well defined quasiparticles as witnessed by the observation of non-Fermi liquid (nFL) behaviour. Secondly the effective pairing interactions can only be described in an oversimplified way as in the spin fluctuation models and its variants. They commonly neglect the internal orbital structure of f-electron compounds due to the intra-atomic spin-orbit coupling and CEF potential. Attempts to include these terms have not been carried very far. Nevertheless it is important to understand these qualitative theories. We first discuss normal state quasiparticles, namely Kondo lattice models for Ce-compounds vs. dual 5f-electrons models for the U-compounds. Starting from this basis the renormalised band theory provides a way to describe the heavy quasiparticle bands within a Fermi liquid approach. From there approximate models for the effective pairing interactions may be obtained by standard many-body techniques. The symmetry classification of pairing order parameters is an important step to understand the nodal structure of the gap and solve the gap equations. Models for coexistence and competition of SC and density wave order parameters frequently observed in HF metals will also be discussed. Finally we make a survey of theoretical ideas and experimental methods to identify the nodal structure of SC and density type order parameters which is the most important ingredient to understand the physics of HF superconductors.

2.1. Heavy quasiparticles in Ce, U compounds and their interactions

A prerequisite for a microscopic theory of superconductivity in heavy-fermion compounds is a description of the normal state and of the low-energy excitations at low temperatures. We begin by reviewing the physical processes which lead to the high density of low-energy excitations reflected in the strongly enhanced specific heat. The corresponding microscopic many-body problems, i.e., the Kondo model and the dual model, can be solved for (effective) impurities but not for extended systems. The energy dispersion of the coherent quasiparticle states in a periodic lattice, however, can be calculated from an effective single-particle Hamiltonian where the effective and not necessarily local potential is devised to account for the relevant many-body effects. The residual interaction among the quasiparticles eventually leads to the instability of the normal Fermi liquid phase. We focus on Cooper pair formation induced by electron-electron interactions. Of particular importance are spin-fluctuation models which were adopted in the majority of papers during the past decade.

2.1.1. Kondo lattice model for Ce-compounds

The similarities in the behavior of Ce-based heavy-fermion systems to that of dilute magnetic alloys have led to the assumption that these systems are ‘Kondo lattices’ where the observed anomalous behavior can be explained in terms of periodically repeated resonant Kondo scattering. This ansatz provides a microscopic model for the formation of a singlet ground state and the existence of heavy quasiparticles. In addition, it explains why there is no magnetic pairbreaking associated with the presence of the f-electrons. An extensive review is given by Hewson (1993). The Kondo picture for the Ce-based heavy-fermion compounds is supported by the fact that both the thermodynamic properties at low temperatures (e.g., the specific heat, the magnetic susceptibility) as well as the temperature dependence of the spectroscopic data can be reproduced by an Anderson model with the same parameters (Gunnarsson and Schönhammer, 1983). The most direct evidence, however, comes from photoelectron spectroscopy. The characteristic features of a Kondo system can be summarized as follows (Allen, 1992; Malterre et al., 1996): At high temperatures, the combined PES/BIS spectra from photoemission and inverse photoemission exhibit two distinct peaks below and above the Fermi energy. These two features correspond to the valence transitions $f^n \rightarrow f^{n\pm 1}$, respectively. The changes in the occupation of the Ce 4f-shells are associated with energies of order eV. The high-temperature state can be modelled by weakly correlated conduction electrons which are weakly coupled to local f-moments. The f-derived low-energy excitations are those of a system of local moments. The direct manifestation of the low-energy scale is the appearance of a sharp peak in the f-spectral density near the Fermi energy when the temperature T is smaller than a characteristic (‘Kondo’) temperature T^* . In Ce systems, this many-body feature, i.e., the ‘Abrikosov–Suhl’ or ‘Kondo’ resonance, is centered at $E_F + kT^*$ slightly above the Fermi edge E_F with $T^* \simeq W \exp(\pi \varepsilon_f / N_f \Delta)$ up to a constant of order unity. Here W is the conduction band width, $\varepsilon_f < 0$ is the f-level position below the Fermi level $E_F \equiv 0$, N_f the f-level degeneracy and $\Delta = \pi |V|^2 N(E_F)$ is the hybridization or charge fluctuation width which can be estimated from the width of the transition $4f^1 \rightarrow 4f^0$ (V = hybridization matrix element, $N(E_F)$ = conduction electron DOS). This energy scale characterises the dynamical screening of the impurity spin by conduction electron spin fluctuations within a “screening cloud” that extends to distances $\sim \hbar v_F / kT^*$ away from the impurity. The evolution of the Kondo resonance with temperature was recently observed by high-resolution photoemission experiments. The spectra displayed in fig. 1 provide direct evidence for the presence of a Kondo resonance in the lattice. The resonance is a genuine many-body feature reflecting the small admixture of f^0 -configurations to the ground state and the low-lying excitations which are mainly built from f^1 -configurations. By hybridization with conduction states via transitions $f^1 \leftrightarrow f^0$, the local magnetic degeneracies of the singly occupied 4f-shells are lifted. The characteristic energy $kT^* \simeq 1\text{--}10$ meV which can be surprisingly close to the value of the corresponding dilute system sets the scale for the anomalous low-temperature behavior. The width and the overall weight of the resonance are of the order $\pi kT^* / N_f$ and $\pi kT^* / N_f \Delta = 1 - n_f \ll 1$, respectively. Here n_f denotes the occupation of the f^1 state which in the Kondo limit $\Delta \ll |\varepsilon_f|$ is slightly less than one due to the finite hybridization matrix element V with conduction electrons. Impurity model calculations based on the NCA approximation for the Anderson model indicate that the Kondo resonance states exist as long as $n_f \geq 0.85$. For smaller n_f due to

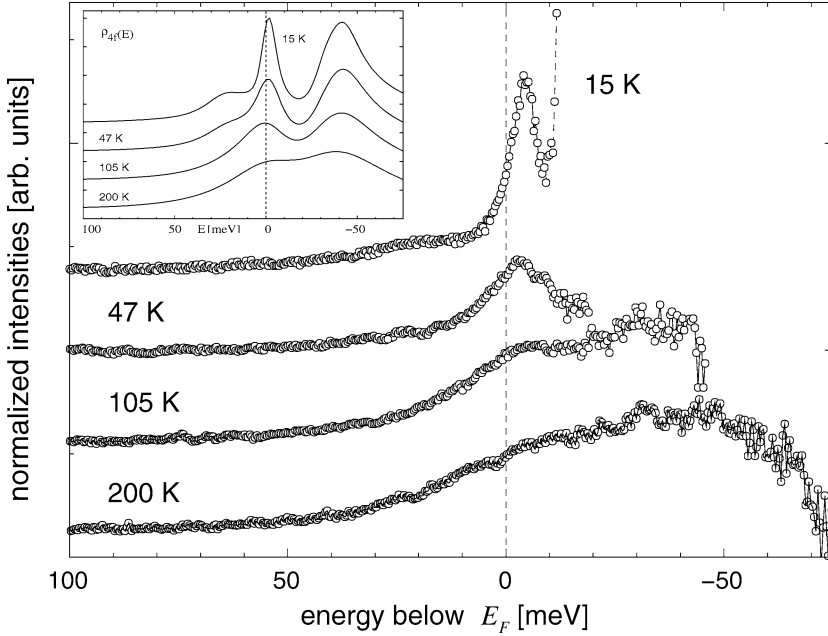


Fig. 1. PES spectra at various temperatures showing the appearance of the low temperature Kondo resonance in CeCu_2Si_2 . The inset shows 4f-spectral density $\rho_{4f}(E)$ of the impurity Anderson model calculated within NCA (Reinert et al., 2001).

larger V one enters the mixed valent regime. At sufficiently low temperatures $T \ll T^*$, the contribution of the narrow resonance peak to the thermodynamic and transport properties can be described in terms of a Landau theory with heavy fermionic quasiparticles as suggested by the renormalization group calculations for magnetic impurities immersed in a metallic host (Wilson, 1975). Based on the corresponding effective Hamiltonian Nozières (1974) introduced a narrow resonant phase shift to account for the impurity contribution to the low-energy properties.

The novel feature observed in stoichiometric Ce-compounds is the formation of narrow coherent bands of low-energy excitations (Garnier et al., 1997, 1998; Zwicknagl, 1999). Following this line of thought, heavy fermions arise from a decoherence-coherence crossover. The strong local correlations in Kondo lattices lead to an observable many-body effect, i.e., the change with temperature of the volume of the Fermi surface. At high temperatures, the f-degrees of freedom appear as localized magnetic moments, and the Fermi surface contains only the itinerant conduction electrons. At low temperatures, however, the f-degrees of freedom are now tied into itinerant fermionic quasiparticle excitations and accordingly, have to be included in the Fermi volume following Luttinger's theorem. Consequently the Fermi surface is strongly modified. This scenario (Zwicknagl, 1993) was confirmed experimentally by

measurements of the de Haas–van Alphen (dHvA) effect (Lonzarich, 1988; Aoki et al., 1993; Tautz et al., 1995).

Competition between the formation of (local) Kondo singlets and the lifting of degeneracies by long-range magnetic order is clearly evident in many Ce-based heavy fermion compounds. In the high-temperature regime the moments of the Ce 4f-shells are coupled by the RKKY interaction which can favor parallel as well as antiparallel orientation of the moments at neighboring sites. In the majority of cases, there is a tendency towards antiferromagnetic alignment although also ferromagnetic HF systems are known. Model calculations for two Kondo impurities (Jayprakash et al., 1981, 1982; Jones and Varma, 1987) showed that antiferromagnetic correlations between the magnetic sites weaken the Kondo singlet formation reducing the characteristic energy scale kT^* to rather small values. Since the latter plays the role of an effective Fermi energy for the heavy quasiparticles it is not surprising that the Fermi liquid description fails to be valid in systems with sufficiently strong antiferromagnetic correlations.

For Ce-based systems, the natural tuning parameter is the hybridization which measures the coupling between the strongly correlated f-electrons and the weakly correlated conduction states. This coupling, which can be increased by applying hydrostatic pressure or chemical pressure via proper element substitution, affects the f-electron system in two different ways. First, it is responsible for the indirect exchange interaction building up magnetic correlations between the moments at different sites. On the other hand, it leads to the formation of local singlets via the Kondo effect. The energy gain due to magnetic ordering follows a power law for weak hybridization whereas the Kondo temperature depends exponentially on the latter. Based on these considerations, Doniach (1977) suggested that for sufficiently weak hybridization the f-derived magnetic moments should order. With increasing hybridization, however, the magnetic ordering temperature should be suppressed and a Fermi liquid ground state characterized by Kondo-type correlations forms above a quantum critical point (QCP). At the QCP itself non-Fermi liquid behaviour is expected in the temperature dependence of physical quantities. The resulting schematic “Doniach phase diagram” has been widely used to understand qualitatively the variation with pressure of the anomalous low-temperature properties in heavy-fermion systems. It seems that in the majority of Ce-based heavy-fermion superconductors the superconducting phase develops in the vicinity of a quantum critical point.

2.1.2. *Dual model for U-compounds*

The Kondo picture, however, does not apply in the case of the actinide compounds. The difficulties with this model have been discussed in Cox and Zawadowski (1999). The difference between the Ce-based heavy-fermion compounds and their U-counterparts can be seen directly from the photoemission spectra (Allen, 1992). In U-based heavy-fermion compounds, the fingerprint character of the transitions $f^n \rightarrow f^{n\pm 1}$ is lost. Instead of the well-defined f-derived peaks familiar for the Ce systems, we encounter a rather broad f-derived feature. This fact shows that the f-valence in the actinide heavy-fermion systems is not close to integer value as it is the case in Ce-based compounds. In fact, the f-valence of the U ions has been discussed rather controversially.

There is growing evidence that actinide ions may have localized as well as delocalized 5f electrons. This picture which was suggested by susceptibility measurements (Schoenes et al., 1996) is supported by a great variety of experiments including, e.g., photoemission and neutron inelastic scattering experiments on UPd₂Al₃ (Takahashi et al., 1995; Metoki et al., 1998; Bernhoeft et al., 1998) as well as muon spin relaxation measurement in UGe₂ (Yaouanc et al., 2002). The assumption is further supported by quantum chemical calculations on uranocene U(C₈H₈)₂ (Liu et al., 1998) which exhibit a number of low-lying excitations which are due to intra-shell rearrangements of 5f-electrons. There is clear evidence that the presence of localized 5f-states is even responsible for the attractive interactions leading to superconductivity (Sato et al., 2001). In addition the dual model should allow for a rather natural description of heavy fermion superconductivity coexisting with 5f-derived magnetism.

The above-mentioned observations form the basis of the dual model which assumes the coexistence of both itinerant and localized 5f-electrons. The former hybridize with the conduction states and form energy bands while the latter form multiplets to reduce the local Coulomb repulsion. The two subsystems interact which leads to the mass enhancement of the delocalized quasiparticles. The situation resembles that in Pr metal where a mass enhancement of the conduction electrons by a factor of 5 results from virtual crystal field (CEF) excitations of localized 4f²-electrons (White and Fulde, 1981). The underlying hypothesis is supported by a number of experiments. Detailed Fermi surface studies for UGa₃ (Biasini, 2003) show that the experimental data cannot be explained by assuming all 5f-electrons to be itinerant nor by treating them as fully localized. The basic assumptions underlying the dual model were recently confirmed by measurements of the optical conductivity (Dressel et al., 2002) which show the evolution of the high effective mass at low temperatures. The formation of the heavy quasiparticles is also observed in ARPES (Denlinger et al., 2001).

The dual model provides a microscopic theory for the heavy quasiparticles in U-compounds. The method reproduces the dHvA data in UPt₃ (Zwicknagl et al., 2002) and UPd₂Al₃ (Zwicknagl et al., 2003). The calculation of the heavy bands proceeds in three steps schematically summarized in fig. 2. First, the band structure is determined by solving the Dirac equation for the self-consistent LDA potentials but excluding two U 5f ($j = 5/2$) states from forming bands. The choice of the itinerant and localized orbitals depends upon the symmetry of the crystal and the hybridization strengths. The localized 5f orbitals are accounted for in the self-consistent density and accordingly in the potential seen by the conduction electrons. The intrinsic bandwidth of the itinerant U 5f $j = 5/2$ electrons is taken from the LDA calculation while the position of the corresponding band center is chosen such that the density distribution of the conduction states as obtained within LDA remains unchanged. For UPt₃ and UPd₂Al₃, the f-occupancy per U atom for the delocalized 5f-electrons amounts to $n_f = 0.65$ indicating that we are dealing with a mixed valent situation. The calculations yield the dHvA frequencies which can be directly compared with experimental data. In the second step, the localized U 5f-states are calculated by diagonalizing the Coulomb matrix in the restricted subspace of the localized 5f-states. Assuming the jj -coupling scheme, the Coulomb matrix elements are calculated from the radial functions of the ab-initio band structure potentials. In a crystal, the degeneracies of the ground-state may be lifted by a CEF. This is in fact the case for UPd₂Al₃ where the resulting singlet ground state of the localized 5f² is given by

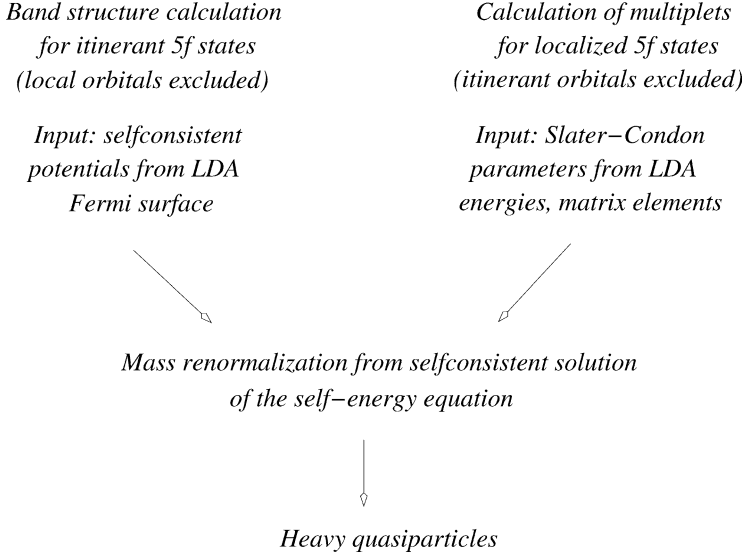


Fig. 2. Calculational scheme for heavy quasiparticles in U-based heavy-fermion compounds.

$|g\rangle = (1/\sqrt{2})(|J_z = 3\rangle + |J_z = -3\rangle)$ in the $J = 4$ subspace. The coupling between the localized and delocalized 5f-electrons is directly obtained from the expectation values of the Coulomb interaction H_C in the $5f^3$ -states. Finally, the renormalization of the effective masses which results from the coupling between the two 5f subsystems is determined. The enhancement factor is calculated from the self-consistent solution of the self-energy equation (White and Fulde, 1981) with the input taken from the ab-initio electronic structure calculations for the delocalized and the localized 5f-electrons.

The coexistence of itinerant and localized 5f-states is a consequence of the interplay between hybridization with the conduction electrons and local Coulomb correlations. This “partial localization” of the 5f-states is found in many actinide intermetallic compounds. The underlying microscopic mechanism is an area of active current research (Lundin et al., 2000; Söderlind et al., 2000). LDA calculations show that the hopping matrix elements for different 5f orbitals vary. But it is of interest to understand why only the largest one of them is important and why the other ones are suppressed.

Partial localization may arise from the competition between hopping and angular correlations. This can be seen by exact diagonalization of small clusters which model the U sites in heavy fermion compounds (Efremov et al., 2004). We keep only the degrees of freedom of the 5f shells, the conduction states being accounted for by (effective) anisotropic intersite hopping. The Hamiltonian reads

$$H = - \sum_{\langle nm \rangle, j_z} t_{j_z} (c_{j_z}^\dagger(n) c_{j_z}(m) + \text{h.c.}) + H_C, \quad (1)$$

where the first sum is over neighboring sites $\langle nm \rangle$. Furthermore $c_{j_z}^\dagger(n)$ ($c_{j_z}(n)$), creates (annihilates) an electron at site n in the $5f$ $j = 5/2$ state with $j_z = -5/2, \dots, 5/2$. We will consider two and three sites models. Since the relevant correlations are local the results for these small clusters are qualitatively similar to those of four-site models. The effective hopping between sites results from the hybridization of the $5f$ -states with the orbitals of the ligands and depends generally on the crystal structure. Rather than trying to exhaust all possible different lattice symmetries, we shall concentrate here on the special case that hopping conserves j_z . While this is certainly an idealization, it allows us to concentrate on our main interest, i.e., a study of the influence of atomic correlations on the renormalization of hybridization matrix elements. The parameters t_{j_z} ($= t_{-j_z}$) are chosen in accordance with density-functional calculations for bulk material which use $j j_z$ basis states. The local Coulomb interactions can be written in the form

$$H_C = \frac{1}{2} \sum_n \sum_{j_{z1}, \dots, j_{z4}} U_{j_{z1} j_{z2}, j_{z3} j_{z4}} c_{j_{z1}}^\dagger(n) c_{j_{z2}}^\dagger(n) c_{j_{z3}}(n) c_{j_{z4}}(n) \quad (2)$$

with Coulomb matrix elements

$$U_{j_{z1} j_{z2}, j_{z3} j_{z4}} = \delta_{j_{z1}+j_{z2}, j_{z3}+j_{z4}} \sum_J \langle \frac{5}{2} \frac{5}{2} j_{z1} j_{z2} | J J_z \rangle U_J \langle J J_z | \frac{5}{2} \frac{5}{2} j_{z3} j_{z4} \rangle. \quad (3)$$

Here J denotes the total angular momentum of two electrons and $J_z = j_{z1} + j_{z2} = j_{z3} + j_{z4}$. The sum is restricted by the antisymmetry of the Clebsch–Gordan coefficients $\langle \frac{5}{2} \frac{5}{2} j_{z1} j_{z2} | J J_z \rangle$ to even values $J = 0, 2, 4$. We use in the actual calculations U_J values which are determined from LDA wavefunctions for UPT_3 (Zwicky et al., 2002), i.e., $U_{J=4} = 17.21$ eV, $U_{J=2} = 18.28$ eV, and $U_{J=0} = 21.00$ eV. We expect $U_{J=4} < U_{J=2} < U_{J=0}$ always to hold for Coulomb interactions, independently of the chemical environment. In contrast, the relative order of the hopping matrix elements will vary strongly from one compound to the next. The average Coulomb repulsion of about 20 eV is irrelevant for the low-energy physics of the model. It simply restricts the relevant configurations to states such that each site is occupied either by 2 or 3 f electrons. The low-energy sector is exclusively determined by the differences of the U_J values, which are of the order of 1 eV and thus slightly larger than typical bare f -band widths. The latter are obtained, e.g., from LDA calculations for metallic uranium compounds like UPT_3 . Restricting the model to f^2 and f^3 configurations is equivalent to let the various $U_J \rightarrow \infty$ while their differences remain finite. To mimic the situation in the U-based heavy-fermion compounds we consider the intermediate valence regime. Note that in the absence of a magnetic field all states of the two-site model with five electrons will be at least doubly degenerate because of Kramers' degeneracy.

The Hamiltonian equation (1) conserves $\mathcal{J}_z = \sum_n J_z(n)$ where \mathcal{J}_z is the z -component of the total angular momentum of the system and the $J_z(n)$ refer to angular momentum projections on individual sites. We shall therefore characterize the eigenstates by their \mathcal{J}_z value. Since $t_{j_z} = t = \text{const}$ the system is rotationally invariant. Then \mathcal{J}^2 provides an additional good quantum number. Strong on-site correlations result in a considerable enhancement of anisotropies in the bare hopping matrix elements. This can lead to a localization of electrons

in orbitals with relatively weak hybridization. The latter is effectively reduced to zero in those cases.

In order to quantify the degree of localization or, alternatively, of the reduction of hopping of a given j_z orbital by local correlations, we calculate the ratio of the j_z -projected kinetic energy T_{j_z} and the bare matrix element t_{j_z} and obtain

$$\frac{T_{j_z}}{t_{j_z}} = \sum_{(nm), \pm} \langle \Psi_{\text{gs}} | (c_{\pm j_z}^\dagger(n) c_{\pm j_z}(m) + \text{h.c.}) | \Psi_{\text{gs}} \rangle. \quad (4)$$

The ground-state wavefunction $|\Psi_{\text{gs}}\rangle$ contains the strong on-site correlations. A small ratio of T_{j_z}/t_{j_z} indicates partial suppression of hopping for electrons in the $\pm j_z$ orbitals. Two kinds of correlations may contribute to that process. The first one is based on the reduction of charge fluctuations to atomic f^2 and f^3 configurations. This is a result for large values of U_J and can be studied by setting all U_J equal to a value much larger than the different t_{j_z} . The second one is due to differences in the U_J values, i.e., $U_{J=4} < U_{J=2} < U_{J=0}$. The differences in the U_J values are the basis of Hund's rules. Hopping counteracts Hund's rule correlations and vice versa. What we want to stress is the fact that those correlations can lead to a complete suppression of hopping channels except for the dominant one which shows only little change.

Results for the ratios T_{j_z}/t_{j_z} are shown in fig. 3 for a two-site model. As the relevant correlations are local the general results qualitatively agree with those found for a three-site cluster and four-site clusters (Pollmann and Zwicknagl, 2004). We can distinguish three different regimes with $\mathcal{J}_z = 15/2, 5/2$ and $3/2$, labeled I, II and III, respectively. One observes that in region I only the dominant hybridization of the $j_z = 3/2$ orbital survives while that

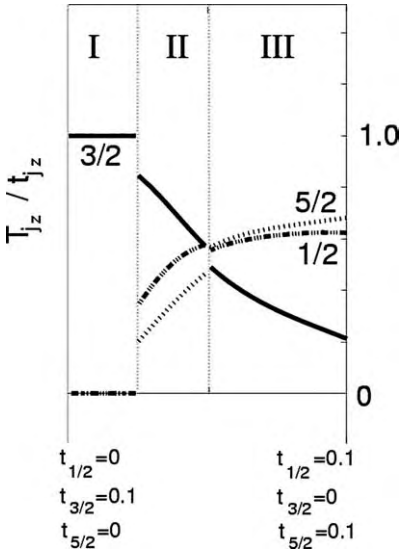


Fig. 3. Values T_{j_z}/t_{j_z} for the two-site cluster along the line connecting linearly the points written below the figure. Regions with $\mathcal{J}_z = 15/2, 5/2$ and $3/2$, are labeled with I, II and III, respectively (Efremov et al., 2004).

of the $j_z = 1/2$ and $j_z = 5/2$ orbitals is completely suppressed. On the other hand in regions II and III the correlation effects on different orbitals are not very different. These findings demonstrate that in particular Hund's rule correlations strongly enhance anisotropies in the hopping. For a certain range of parameters this may result in a complete suppression of the effective hopping except for the largest one, which remains almost unaffected. This provides a microscopic justification of partial localization of 5f-electrons which is observed in a number of experiments on U compounds and which is the basis for further model calculations described later.

2.1.3. *Fermi-liquid state and heavy quasiparticles: renormalized band theory*

Neither the Kondo model for Ce-based heavy-fermion systems nor the dual model for their U-based counterparts can be solved for extended systems described by lattice models. The excitation spectra of Ce metal in the α - and γ -phase were recently calculated applying the dynamical mean field theory (McMahan et al., 2003). The method yields a low-energy resonance but the experimentally observed change of the f-valence at the transition is not reproduced. A fully microscopic description is not available to describe experiments where inter-site effects become strongly manifest. Typical lattice effects are the formation of coherent heavy quasiparticle bands whose Fermi surfaces were observed experimentally.

The Landau–Fermi liquid (FL) theory assumes a one-to-one correspondence between the states of the complex interacting system and those of a gas of independent fermions which may move in an external potential (Landau, 1956, 1957, 1958; Abrikosov et al., 1975). The single-particle orbitals and energies are determined from an effective Hamiltonian. The characteristic properties of a system are reflected in an effective and not necessarily local potential V_{eff} which describes the field of the nuclei and the modifications arising from the presence of the other electrons. The essential many-body aspects of the problem are then contained in the prescription for constructing the effective potentials which have to be determined specifically for the problem under consideration.

The quasiparticle energies reflect the interaction among the fermions and therefore may be altered when the overall configuration is changed. A characteristic feature of interacting Fermi liquids is that the energy dispersion $\epsilon_\sigma(\mathbf{k})$ depends on how many other quasiparticles are present,

$$\epsilon_\sigma(\mathbf{k}) = E(\mathbf{k}) + \sum_{\mathbf{k}'\sigma'} f_{\sigma\sigma'}(\mathbf{k}, \mathbf{k}') \delta n_{\sigma'}(\mathbf{k}'). \quad (5)$$

Here $E(\mathbf{k})$ denotes the energy dispersion of a dilute gas of quasiparticles. In systems with strong correlations it cannot be calculated from the overlap of single-electron wave functions. The interactions among the quasiparticles are characterized by the matrix $f_{\sigma\sigma'}(\mathbf{k}, \mathbf{k}')$. The deviations from the equilibrium distribution are given by $\delta n_\sigma(\mathbf{k})$.

Interaction effects must be accounted for in considering those situations where the quasiparticle distribution function deviates from that of the equilibrium case. In the phenomenological Landau–FL theory the characteristic properties of the quasiparticles, which can hardly be calculated microscopically, are expressed in terms of parameters which are determined from

experiment. Examples are the effective potentials, the interaction potential and the scattering amplitudes. An important property of the quasiparticles is that they can be considered as ‘rigid’ with respect to low-energy and long-wavelength perturbations. Only such processes can be described within this theoretical framework.

The energy dispersion $E(\mathbf{k})$ of a dilute gas of noninteracting quasiparticles is parametrized by the Fermi wave vector \mathbf{k}_F and the Fermi velocity \mathbf{v}_F

$$E(\mathbf{k}) = \mathbf{v}_F(\hat{\mathbf{k}}) \cdot (\mathbf{k} - \mathbf{k}_F), \quad (6)$$

where $\hat{\mathbf{k}}$ denotes the direction on the Fermi surface. The key idea of the renormalized band method is to determine the quasiparticle states by computing the band structure for a given effective potential. Coherence effects which result from the periodicity of the lattice are then automatically accounted for. The quantities to be parametrized are the effective potentials which include the many-body effects. The parametrization of the quasiparticles is supplemented by information from conventional band structure calculations as they are performed for “ordinary” metals with weakly correlated electrons. The periodic potential leads to multiple-scattering processes involving scattering off the individual centers as well as the propagation between the centers which mainly depends on the lattice structure and is therefore determined by geometry. The characteristic properties of a given material enter through the information about single center scattering which can be expressed in terms of a properly chosen set of phase shifts $\{\eta_\nu^i(E)\}$ specifying the change in phase of a wave incident on site i with energy E and symmetry ν with respect to the scattering center. Within the scattering formulation of the band structure problem the values of the phase shifts at the Fermi energy $\{\eta_\nu^i(E_F)\}$ together with their derivatives $\{(d\eta_\nu^i/dE)_{E_F}\}$ determine the Fermi wave vectors \mathbf{k}_F and the Fermi velocity \mathbf{v}_F .

The calculation of realistic quasiparticle bands proceeds in several steps as schematically summarized in fig. 4. The first step is a standard LDA band structure calculation by means of which the effective single-particle potentials are self-consistently generated. The calculation starts, like any other ab-initio calculation, from atomic potentials and structure information. In this step, no adjustable parameters are introduced. The effective potentials and hence the phase shifts of the conduction states are determined from first principles to the same level as in the case of ‘ordinary’ metals. The f-phase shifts at the lanthanide and actinide sites, on the other hand, are described by a resonance type expression

$$\tilde{\eta}_f \simeq \arctan \frac{\tilde{\Delta}_f}{E - \tilde{\epsilon}_f} \quad (7)$$

which renormalizes the effective quasiparticle mass. One of the two remaining free parameters $\tilde{\epsilon}_f$ and $\tilde{\Delta}_f$ is eliminated by imposing the condition that the charge distribution is not significantly altered as compared to the LDA calculation by introducing the renormalization. The renormalized band method devised to calculate the quasiparticles in heavy-fermion compounds thus is essentially a one-parameter theory. We mention that spin-orbit and CEF splittings can be accounted for in a straightforward manner (Zwicknagl, 1992).

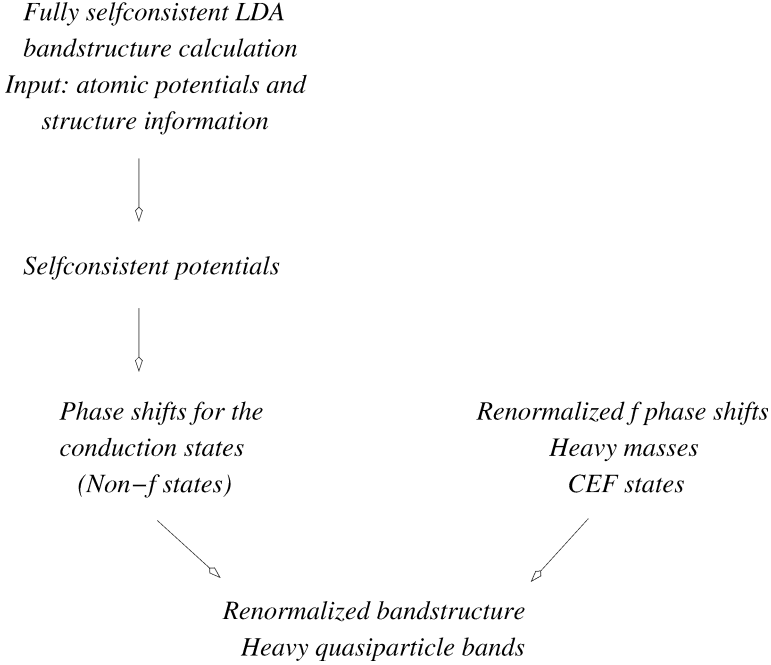


Fig. 4. Schematic summary of renormalized band calculation for metals with strongly correlated electrons.

2.1.4. *Quasiparticle interactions and spin fluctuation theory*

The low-energy excitations of heavy-fermion systems are described in terms of quasiparticle bands which yield the high density of states and specific heat γ -value. The preceding sections focussed on the case of a dilute gas of quasiparticles whose energy dispersion can be explicitly calculated by means of the renormalized band method. The many-body effects, however, lead to deviations from the picture of independent fermions which fill the rigid bands of the dilute gas of quasiparticles. An important consequence of the quasiparticle interactions is the instability of the normal Fermi liquid with respect to charge or spin density waves or superconductivity. In heavy-fermion compounds, quasiparticle interactions are strongly evident in the electronic compressibility whose values are comparable to those of a normal metal and do not reflect the enhancement of the specific heat. This experimental fact indicates that there must be a strong repulsion between two quasiparticles at the same lattice site.

The influence of the quasiparticle interactions on observable quantities is usually described in terms of a small set of interaction parameters. According to Landau, the compressibility κ_e and susceptibility χ_s are given by

$$\frac{\kappa_e}{\kappa_e^0} = \frac{m^*/m}{1 + F_0^s} \quad \text{and} \quad \frac{\chi_s}{\chi_s^0} = \frac{m^*/m}{1 + F_0^a}, \quad (8)$$

where κ_e^0 and χ_s^0 denote the compressibility and susceptibility of independent fermions of mass m . From $\kappa_e/\kappa_e^0 \simeq 1$ follows the order of magnitude estimate $F_0^s \simeq m^*/m \simeq 10^2\text{--}10^3$ for the spin-independent isotropic part of the quasiparticle interactions. The spin-dependent isotropic part of the interaction, on the other hand, is reflected in the enhancement of the spin susceptibility χ_s over χ_s^0 . From the observed value $\chi_s/\chi_s^0 \simeq m^*/m$ we infer that the enhanced spin susceptibility simply reflects the high density of quasiparticle states and that the corresponding Landau–FL parameter F_0^a plays only a minor role in heavy-fermion compounds. Although these results are not sufficient to specify the effective interaction in an anisotropic Fermi liquid they nevertheless impose important constraints on theoretical models.

In Landau–FL theory a two-particle scattering matrix $T_{\alpha\beta;\gamma\rho}(\mathbf{k}_1\mathbf{k}_2; \mathbf{k}_3\mathbf{k}_4)$ is introduced which describes the scattering of two quasiparticles with momenta $\mathbf{k}_3\mathbf{k}_4$ and spins $\gamma\rho$ into states with momenta $\mathbf{k}_1\mathbf{k}_2$ and spins $\alpha\beta$ on the Fermi surface. The superconducting transition in a Fermi liquid is determined by a singularity in the scattering matrix of two quasiparticles with opposite momenta at the Fermi surface (see fig. 5). Assuming rotational invariance in spin space the general scattering matrix $T_{\alpha\beta;\gamma\rho}$ can be expressed in terms of two scalar amplitudes. Conventional choices are either the singlet and triplet amplitudes in the particle–particle channel ($\gamma\rho \rightarrow \alpha\beta$), T_s and T_t or alternatively, the singlet and triplet amplitudes in one of the particle–hole channels, $T^{(s)}$ and $T^{(a)}$,

$$\begin{aligned} T_{\alpha\beta;\gamma\rho} &= -\frac{1}{2}(\sigma_2)_{\alpha\beta}(\sigma_2)_{\gamma\rho}T_s + \frac{1}{2}(\boldsymbol{\sigma}\sigma_2)_{\alpha\beta} \cdot (\boldsymbol{\sigma}\sigma_2)_{\gamma\rho}T_t \\ &= \delta_{\alpha\beta}\delta_{\gamma\rho}T^{(s)} + \boldsymbol{\sigma}_{\alpha\beta} \cdot \boldsymbol{\sigma}_{\gamma\rho}T^{(a)}, \end{aligned} \quad (9)$$

where σ_μ ; $\mu = 1\text{--}3$ denote the Pauli matrices. The two sets of scalar amplitudes are related by

$$\begin{aligned} T_s &= T^{(s)} - 3T^{(a)}; & T_t &= T^{(s)} + T^{(a)}; \\ T^{(s)} &= \frac{1}{4}(T_s + 3T_t); & T^{(a)} &= \frac{1}{4}(T_t - T_s). \end{aligned} \quad (10)$$

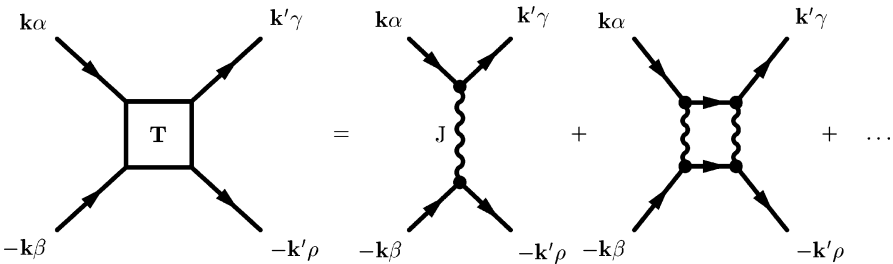


Fig. 5. Two-particle (e-e) scattering matrix $T_{\alpha\beta;\gamma\rho}(\mathbf{k}, -\mathbf{k}; \mathbf{k}', -\mathbf{k}')$ for quasiparticle scattering with initial momenta $\mathbf{k}', -\mathbf{k}'$ and spins $\gamma\rho$ to final momenta $\mathbf{k}, -\mathbf{k}$ and spins $\alpha\beta$. SC transition corresponds to singular pair scattering with opposite momenta. It is approximated by ladder diagrams involving the irreducible (with respect to e-e scattering) four-point vertex for the effective interaction (wiggly line) which is the central quantity in microscopic models of SC, see also fig. 6 and eqs. (12), (13).

The symmetries can be obtained directly from the symmetries of the two-particle Green's function. The Landau-FL parameters F_0^s and F_0^a are determined by the isotropic Fermi surface averages $A_0^{s,a} = \langle T^{s,a}(\mathbf{k}_1 \mathbf{k}_2; \mathbf{k}_1 \mathbf{k}_2) \rangle_{\text{FS}}$ of the two particle forward-scattering amplitude by $F_0^{s,a} = A_0^{s,a} [1 - A_0^{s,a}]^{-1}$. As mentioned above, the transition to the superconducting state is caused by a singularity in the scattering of a pair with opposite momenta $\mathbf{k}_3 = -\mathbf{k}_4 = \mathbf{k}'$ into pair states with $\mathbf{k}_1 = -\mathbf{k}_2 = \mathbf{k}$.

The Fermi liquid approach which attempts to construct phenomenological models for the scattering amplitude has been reviewed (Fulde et al., 1988; Zwicky, 1992). In the present review we shall rather concentrate on microscopic models for the effective pairing interaction.

Microscopic theories of superconductivity focus on the attractive interaction which results from the motion of the (heavy) quasiparticle through a polarizable medium. The theories can be divided into two major groups depending on whether the polarizable medium is distinct from the particles which are participating in the attraction or not. The BCS theory (Bardeen et al., 1957; Schrieffer, 1964) belongs to the former class. Here Cooper-pair formation is due to quasiparticle-phonon interactions which is appropriate for common metals. The spin fluctuation models assume that pairing is mediated by overdamped low lying magnetic excitations with a preferred wave vector in the itinerant electron system. The dual model for U-based heavy-fermion systems suggests a novel mechanism for the Cooper-pair formation, i.e., the exchange of weakly damped propagating magnetic excitons. In this case, the polarizable medium is provided by the CEF-split multiplets of the localized 5f-electrons. A model calculation for UPd₂Al₃ is presented in sect. 4.2, where we also compare theoretical predictions with experimental observations.

The majority of theoretical calculations for heavy-fermion systems adopts spin-fluctuation models for the quasiparticle attraction which belong to the second group. Early theoretical efforts (Anderson, 1984a; Valls and Tešanović, 1984) emphasized an analogy with superfluid ³He. Even though a quantitative microscopic theory of suprafluidity is still lacking for ³He it is generally accepted that spin fluctuations qualitatively explain observed features in ³He, in particular odd-parity spin-triplet pairing (Anderson, 1984b; Vollhardt and Wölfle, 1990). The influence of spin fluctuations on the Cooper pair formation in metals was studied first by Berk and Schrieffer (1966) and Layzer and Fay (1971, 1974). It has found its most prominent applications in HF systems (Miyake et al., 1986) and especially in the theory of high- T_c superconductors (Monthoux et al., 1991; Monthoux and Pines, 1994). The calculations proceed in close analogy to the strong-coupling theory of phonon-mediated superconductivity. At this point we have to add that the theory of spin fluctuation-mediated superconductivity does not have a natural small parameter which would allow for a systematic asymptotic expansion. In particular, there is no a priori justification for including only selected contributions in a diagrammatic expansion for the scattering matrix.

The pair scattering for two quasiparticles with opposite momenta at the Fermi surface is evaluated adopting the ladder approximation displayed in fig. 5. The problem is therefore reduced to finding the four-point vertex which is irreducible with respect to particle-particle scattering. The basic assumption is that the important structure in the scattering amplitudes comes from exchange of collective modes in the two particle-hole channels. The central quantity of these theories is the dynamic magnetic susceptibility $\chi(\mathbf{q}, \omega)$ which can be determined

– in principle – by inelastic neutron scattering. Close to a magnetic instability, the susceptibility diverges for $\omega \rightarrow 0$ at some wave vector \mathbf{Q} . This behaviour results from a singularity in the particle–hole scattering matrix which accounts for the dynamic effects of the induced spin polarizations. The strong particle–hole correlations affect the pair scattering amplitude in the particle–particle channel. In explicit calculations, the effective interaction associated with $\chi(\mathbf{q}, \omega)$ originates in a residual on-site quasiparticle repulsion (I) described by the single band Hubbard model for the heavy quasiparticle bands $\epsilon_{\mathbf{k}}$.

$$H_I = \sum_{\mathbf{k}, s} \epsilon_{\mathbf{k}} n_{\mathbf{k}} + I \sum_i n_{i\uparrow} n_{i\downarrow}. \quad (11)$$

This is also the starting point in the theory of high- T_c SC, albeit with bare Coulomb repulsion and 2D quasiparticle band. In the fluctuation exchange (FLEX) approach (Pao and Bickers, 1994; Dahm and Tewordt, 1995) the effective pair interactions and gap equations are obtained and solved self-consistently in the context of a strong coupling approach. For the complicated 3D Fermi surfaces of HF materials this is too difficult and one is restricted to nonretarded model calculations. In this context the effective interaction is obtained within the random phase approximation (RPA) for pairs of quasiparticles with opposite and equal spins from the diagrams displayed in fig. 6. To conserve rotational invariance in spin space the maximally crossed particle exchange contributions in fig. 6 have to be included. These terms were studied by Berk and Schrieffer (1966) who considered the influence of spin-fluctuations on singlet pairing. The case of triplet scattering was discussed by Nakajima (1973) for ^3He . He showed that sufficiently close to a magnetic instability, the complete set of diagrams yields an effective spin-dependent interaction which is rotationally invariant in spin space

$$H_{\text{eff}} = \frac{1}{2} \sum_{\mathbf{k}, \mathbf{k}'} J(\mathbf{k} - \mathbf{k}') \sigma_{\alpha\gamma} \cdot \sigma_{\beta\rho} c_{\mathbf{k}\alpha}^\dagger c_{-\mathbf{k}\beta}^\dagger c_{-\mathbf{k}'\rho} c_{\mathbf{k}'\gamma}, \quad (12)$$

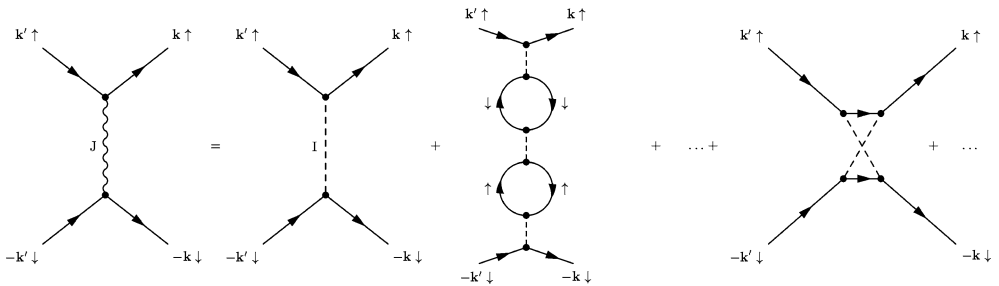


Fig. 6. RPA diagrams for the effective interaction $J(\mathbf{k} - \mathbf{k}')$ between quasiparticles with opposite spins. The bare instantaneous interaction is denoted by I (dashed line) as in eq. (11). Contribution from polarisation (bubble) diagrams contains odd number and from (maximally crossed) exchange diagrams contains any number of interaction lines (I). For equal quasiparticle spins the RPA yields only a sum of bubble diagrams with an even number of interaction lines.

where

$$J(\mathbf{q}) = -\frac{1}{2} \frac{I}{1 - I\chi_0(\mathbf{q})} \simeq -\frac{1}{2} I^2 \chi(\mathbf{q}) \quad \text{and} \quad \chi(\mathbf{q}) = \frac{\chi_0(\mathbf{q})}{1 - I\chi_0(\mathbf{q})}. \quad (13)$$

Here $\chi_0(\mathbf{q})$ is the static susceptibility of the non-interacting quasiparticles and $\chi(\mathbf{q})$ the RPA susceptibility of the interacting system. The approximation is valid for the enhanced spin fluctuation regime $I\chi_0(\mathbf{q}) \leq 1$. In this regime the effective pairing is therefore completely determined by the collective static magnetic susceptibility $\chi(\mathbf{q})$.

Assuming a spherical FS the appropriate basis function for the SC order parameter are spherical harmonics of angular momentum l . The interaction in the l -wave channel is given by ($P_l =$ Legendre polynomial)

$$V_l = a_l 2 \int_0^1 dx x P_l(1 - 2x^2) [-J(2k_F x)], \quad (14)$$

with $x = 1 - (q/2k_F)^2$ and $a_l = 3$ (l even) or $a_l = -1$ (l odd). If the effective interaction $-J(\mathbf{q})$ strongly peaks for small q ($x \simeq 1$), i.e., for FM spin fluctuations, the integrand is positive in this region and hence $V_l < 0$ for odd l and $V_l > 0$ for even l .

Assuming that in HF systems the quasiparticle interaction is mediated by FM spin fluctuations one would expect odd-parity SC order parameters. For UPt₃ however, the odd parity state was originally claimed to be inconsistent with the power law behavior observed in thermodynamic and transport properties at low temperatures. This statement was based on the assumption that the superconducting phase should be characterized by one of the symmetry-adapted order parameters which were derived in the limit of strongly coupled orbital and spin moment of the Cooper pair (Volovik and Gorkov, 1985; Ueda and Rice, 1985; Sigrist and Ueda, 1991). We shall comment on this subtle point in the next section.

The discovery of antiferromagnetic spin fluctuations in UPt₃ (Aeppli et al., 1987) prompted Miyake et al. (1986) to study the nature of pairing due to antiferromagnetic spin fluctuations. The authors consider pairing in a single-band model with the effective electron interaction of eq. (12) where the nonretarded interaction $-J(\mathbf{q})$ should have a maximum at an AF wave vector \mathbf{Q} , e.g., $\mathbf{Q} = (\frac{1}{2}, \frac{1}{2}, \frac{1}{2})$ or $\mathbf{Q} = (\frac{1}{2}, \frac{1}{2}, 0)$. In the vicinity of its maximum at \mathbf{Q} , $-J(\mathbf{q})$ is approximated by

$$-J(\mathbf{q}) = J_0 - J_1 \gamma_{\mathbf{q}}, \quad (15)$$

where J_0, J_1 are positive constants and the function $\gamma_{\mathbf{q}}$ has a minimum at $\mathbf{q} = \mathbf{Q}$. Examining this model for a parabolic single band Miyake et al. (1986) demonstrated that the resulting pairing interaction favors anisotropic even-parity SC order parameters in cubic symmetry ($V_l < 0$ for even $l > 0$). This turned out to be an influential result. Because of the general presence of AF spin fluctuations in HF metals it has led to the attitude to expect generally singlet (even parity) SC in these compounds.

There are, however, counter-examples like UPt₃ and UNi₂Al₃ with AF spin fluctuations and experimentally identified triplet order parameter. The prediction of only even parity unconventional pair states therefore seems to be an artefact of the simplifications inherent in the model. One obvious deficiency is the assumption of cubic symmetry and basis functions

adjusted for a spherical Fermi surface not appropriate for these compounds. More sophisticated versions of the model incorporating experimental data for the magnetic fluctuations via $\chi(\mathbf{q}, \omega)$ and realistic band structures for the quasiparticles failed to reproduce the symmetry of the superconducting order parameter in UPt₃. In particular, the calculations do not produce a multicomponent E_1 or E_2 order parameter as stable solution. This failure is discussed in detail in Heffner and Norman (1996). Also the generalizations of standard spin-fluctuation theory which account for orbital effects (Norman, 1994) do not resolve the difficulties encountered in real materials.

Aspects of strong coupling effects within spin-fluctuation theories, especially the pair breaking role of low frequency bosons have been discussed by Millis et al. (1988). More recently magnetically mediated superconductivity in materials close to a magnetic instability was investigated in a series of papers by Monthoux and Lonzarich (1999, 2001, 2002) and McHale and Monthoux (2003). A phenomenological form for the retarded generalized magnetic susceptibility $\chi(\mathbf{q}, \omega)$ defining the effective quasiparticle interaction is adopted

$$\chi(\mathbf{q}, \omega) = \frac{\chi_0 \kappa_0^2}{\kappa^2 + \hat{q}^2 - i \frac{\omega}{\eta(\hat{q})}}, \quad (16)$$

where κ and κ_0 are the inverse correlation lengths (in units of the inverse lattice constant) with and without strong magnetic correlations, respectively. The functions \hat{q}^2 and $\eta(\hat{q})$ are parametrized so as to directly compare ferromagnetic and antiferromagnetic spin fluctuations. The instability of the normal state is determined by solving the linearized Eliashberg equations which yield the transition temperatures T_c and the mass renormalization. The questions addressed include the influence of dimensionality on the robustness of magnetic pairing and the relative stability of d-wave versus p-wave pairing.

Pairing instabilities may also appear in the electron-hole (Peierls-) rather than electron-electron (Cooper-) channel leading to CDW/SDW type instabilities described by $T^{(s)}$ and $T^{(a)}$ in eq. (10). They are strongly favored if the Fermi surface shows the nesting property $\epsilon_{\mathbf{k}+\mathbf{Q}} = -\epsilon_{\mathbf{k}}$ characteristic for flat FS portions connected by the nesting vector \mathbf{Q} as shown later in fig. 7. In this case the on-site interaction term in the Hamiltonian equation (11) may be truncated in momentum space because the e-h scattering is dominated by processes with momentum transfer \mathbf{Q} . In mf approximation the effective CDW/SDW pairing Hamiltonian is given in eq. (33). To obtain the full variety of electron-hole pair states one needs more general microscopic interactions, replacing the on-site Hubbard model of eq. (11) by an extended Hubbard model which include inter-site Coulomb repulsion and exchange (Gulacsi and Gulacsi, 1987; Schulz, 1989; Ozaki, 1992).

2.2. Order parameters and their coexistence in strongly correlated electron systems

Degenerate interacting Fermi systems are prone to instabilities due to pair condensation. The Pauli principle requires that states have to be filled up to the Fermi energy E_F leading to a large kinetic energy. Rearranging the occupation of noninteracting states around the Fermi level may reduce the interaction energy considerably. The large on-site Coulomb interactions

will achieve this by reducing double occupancies of opposite spin states below the Hartree–Fock result. This leads to a strongly correlated electronic ground state which is ideally approached at low temperatures below a characteristic temperature scale T^* without breaking of spatial or internal symmetries. Excitations from this state may be described within the Landau–Fermi liquid (FL) picture with quasiparticles that have a strongly enhanced effective electron mass $m^* \gg m$. Eventually however this state will become unstable against formation of electron (Cooper-)pairs or electron–hole (Peierls-)pairs due to the residual screened interactions between the quasiparticles. In the former case gauge symmetry is broken leading to a superconducting (SC) state, in the latter spatial symmetries and possibly spin rotational and time reversal symmetry are broken leading to charge-density wave (CDW) or spin-density wave (SDW) states. Which state is more favorable depends on the momentum and energy dependence of residual quasiparticle interactions and on the geometric properties of the Fermi surface and usually cannot be predicted with confidence for real materials. The effective Hamiltonian obtained previously describing the low energy pairing correlations of quasiparticles is most frequently used for studying possible SC states. The condensation into pairs is described by a gap function $\Delta(\mathbf{k})$ which characterises both the type of broken symmetry state and its new quasiparticle excitations. Its experimental determination is therefore of central importance. Unfortunately this is a difficult task except in the isotropic case where $\Delta(\mathbf{k})$ is a constant. In this section we outline the possible type of pair states and gap functions and their symmetry classification. We also discuss simple models of coexistence of SC and CDW/SDW type order parameters based on 2D FS models with nesting properties.

2.2.1. Order parameter classification

Many physical properties of superconducting materials are directly determined by the symmetry of the SC order parameter. The possible types of order parameters are restricted by crystal symmetry. This fact provides a classification scheme for different superconducting states and, in addition, allows one to construct the superconducting classes by means of group theory.

Superfluids are characterized by off-diagonal long range order (ODLRO) which leads to nonvanishing correlations in the two-particle density matrix for large separations of particles at points $\mathbf{r}_1, \mathbf{r}_2$ and $\mathbf{r}'_1, \mathbf{r}'_2$,

$$\langle \mathbf{r}_1 s_1; \mathbf{r}_2 s_2 | \rho^{(2)} | \mathbf{r}'_1 s'_1; \mathbf{r}'_2 s'_2 \rangle \rightarrow \psi_{s_1, s_2}^*(\mathbf{r}_1, \mathbf{r}_2) \psi_{s'_1, s'_2}(\mathbf{r}'_1, \mathbf{r}'_2). \quad (17)$$

Here, \mathbf{r}_i, s_i denote the fermion positions and spins, respectively. In systems with strong spin–orbit (s.o.) interactions, the indices s_i refer to pseudo spins associated with Kramers degeneracy of conduction bands. The ordered phase is characterized by the order parameter ψ which is a complex pseudo-wave function always connected with a spontaneous breaking of U(1) gauge symmetry. In general, it depends on the center-of-mass and relative coordinates, $\mathbf{R} = \frac{1}{2}(\mathbf{r}_1 + \mathbf{r}_2)$, $\mathbf{r} = \mathbf{r}_1 - \mathbf{r}_2$ and the pseudo spins s_1 and s_2 , respectively. We shall restrict ourselves to homogeneous systems neglecting the dependence on the center-of-mass variable \mathbf{R} . Then the order parameter is a function of the relative coordinate \mathbf{r} only. Performing a Fourier transformation with respect to \mathbf{r} with $\psi_{s_1 s_2}(\mathbf{r}) \rightarrow \psi_{s_1 s_2}(\mathbf{k})$ and restricting the wave vector to the Fermi surface $\mathbf{k} = k_F(\hat{\mathbf{k}})\hat{\mathbf{k}}$ yields a pairing amplitude $\psi_{s_1 s_2}(\hat{\mathbf{k}})$ which depends upon the direction $\hat{\mathbf{k}}$ on the Fermi surface. In microscopic theories the gap function $\Delta_{s_1 s_2}$

which also determines the excitation spectrum is commonly used as order parameter. It is given by

$$\Delta_{s_1 s_2}(\hat{\mathbf{k}}) = - \sum_{\hat{\mathbf{k}}'_{s_3 s_4}} V_{s_1 s_2 s_3 s_4}(\hat{\mathbf{k}}, \hat{\mathbf{k}}') \psi_{s_3 s_4}(\hat{\mathbf{k}}'), \quad (18)$$

where V is the effective pairing interaction. For the spin fluctuation model we obtained $V_{s_1 s_2 s_3 s_4}(\mathbf{k}, \mathbf{k}') = -J(\mathbf{k} - \mathbf{k}') \sigma_{s_1 s_4} \sigma_{s_2 s_3}$ in eq. (12). Concerning the symmetry classification of the superconducting phases, one may use the gap function $\Delta_{s_1 s_2}$ or the pair amplitude $\psi_{s_1 s_2}$ as order parameter due to their identical transformation properties.

The fundamental property of $\psi_{s_1 s_2}$ or $\Delta_{s_1 s_2}$ is its behaviour as a two-fermion wave function in many respects. This expresses the fact that an ODLRO order parameter is not the thermal expectation value of a physical observable but rather a complex pseudo-wave function describing quantum phase correlations on the macroscopic scale of the SC coherence length. Its phase is a direct signature of the broken gauge invariance in the SC condensate. The Pauli principle then requires $\Delta_{s_1 s_2}$ to be antisymmetric under the interchange of particles

$$\Delta_{s_1 s_2}(\hat{\mathbf{k}}) = -\Delta_{s_2 s_1}(-\hat{\mathbf{k}}). \quad (19)$$

In addition, it transforms like a two-fermion wave function under rotations in position and spin space and under gauge transformations. The transformation properties yield a general classification scheme for the superconducting order parameter which is represented by a 2×2 -matrix in (pseudo-)spin space. It can be decomposed into an antisymmetric (s) and a symmetric (t) contribution according to $\mathbf{\Delta}(\hat{\mathbf{k}}) = \mathbf{\Delta}_s(\hat{\mathbf{k}}) + \mathbf{\Delta}_t(\hat{\mathbf{k}})$ with

$$\mathbf{\Delta}_s(\hat{\mathbf{k}}) = \phi(\hat{\mathbf{k}}) i \sigma_2 \quad \text{and} \quad \mathbf{\Delta}_t(\hat{\mathbf{k}}) = \sum_{\mu=1}^3 d_\mu(\hat{\mathbf{k}}) \sigma_\mu i \sigma_2, \quad (20)$$

where σ_μ denote the Pauli matrices. Antisymmetry $\mathbf{\Delta}(\hat{\mathbf{k}}) = -\mathbf{\Delta}^T(-\hat{\mathbf{k}})$ requires

$$\phi(\hat{\mathbf{k}}) = \phi(-\hat{\mathbf{k}}) \quad \text{and} \quad d_\mu(\hat{\mathbf{k}}) = -d_\mu(-\hat{\mathbf{k}}) \quad (21)$$

for the complex orbital functions $\phi(\hat{\mathbf{k}})$ and $d_\mu(\hat{\mathbf{k}})$ ($\mu = 1-3$). For brevity we will frequently write $\Delta(\hat{\mathbf{k}})$ for $\phi(\hat{\mathbf{k}})$ or $|\mathbf{d}(\hat{\mathbf{k}})|$. The physical meaning of the order parameters ϕ and \mathbf{d} for singlet and triplet state, respectively, is evident from the identity

$$\frac{1}{2} \text{Tr} |\mathbf{\Delta}_s(\hat{\mathbf{k}})|^2 = |\phi(\hat{\mathbf{k}})|^2 \quad \text{and} \quad \frac{1}{2} \text{Tr} |\mathbf{\Delta}_t(\hat{\mathbf{k}})|^2 = |\mathbf{d}(\hat{\mathbf{k}})|^2. \quad (22)$$

Therefore the modulus of ϕ and \mathbf{d} is a measure for the total gap amplitude of the Cooper pairs at a given point $\hat{\mathbf{k}}$ on the Fermi surface. In addition, the direction of the vector \mathbf{d} specifies the relative contributions of the three triplet pair states. The above relation holds for triplet states which satisfy $\mathbf{d}^* \times \mathbf{d} = 0$. They are called ‘unitary states’ because they are invariant under time reversal. In this case the vector \mathbf{d} defines a unique direction in spin space for every point on the Fermi surface.

The order parameter can be chosen either as purely antisymmetric Δ_s or purely symmetric Δ_t when spin-orbit interaction can be neglected. Then the total spin is a good quantum number and may be used to classify the pair states. Accordingly the states Δ_s and Δ_t are called spin singlet and spin triplet states, respectively. In crystals which have an inversion center, pair states can also be classified with respect to their parity as even-parity (Δ_s) and odd-parity states (Δ_t).

In the 4f- and 5f-based heavy fermion superconductors the spin-orbit interaction is strong. As a consequence classification according to physical pair spins cannot be used. If their high-temperature crystal structures, however, have an inversion center then classification according to parity is still possible. We note here that recently the first example of a HF superconductor (CePt₃Si) which lacks inversion symmetry was discovered (Bauer et al., 2004) and its theoretical implications were discussed by Frigeri et al. (2004).

The simplest even-parity state is the isotropic state encountered in ordinary superconductors. This state is often referred to as “s-wave state”. The isotropic order parameter does not depend on the direction $\hat{\mathbf{k}}$ and reduces to a complex constant $\phi = |\phi|e^{i\varphi}$. Its only degree of freedom is the Josephson phase φ . By far the most extensively studied examples of anisotropic pairing are the p-wave states realized in the superfluid phases of ³He, the d-wave pair state in high- T_c superconductors and the f-wave states in UPt₃ and SrRu₂O₄. The odd parity (p, f) states among these examples are characterised by more than one order parameter component with internal phase degrees of freedom which appear in addition to the overall Josephson phase.

The general classification scheme for superconducting order parameters proceeds from the behavior under the transformations of the symmetry group \mathcal{G} of the Hamiltonian. It consists of the crystal point group G , the spin rotation group $SU(2)$, the time-reversal symmetry group \mathcal{K} , and the gauge group $U(1)$. The latter two are, respectively, defined by

$$K \Delta(\hat{\mathbf{k}}) = \sigma_2 \Delta^*(-\hat{\mathbf{k}}) \sigma_2 \quad \text{and} \quad \Phi \Delta(\hat{\mathbf{k}}) = e^{i\varphi} \Delta(\hat{\mathbf{k}}). \quad (23)$$

Concerning rotations in \mathbf{k} - and spin space we distinguish two different cases: (1) If spin-orbit coupling is negligible spatial and spin rotations can be applied independently. For the elements $g \in G$ of the point group which act on $\hat{\mathbf{k}}$ one has

$$g \Delta(\hat{\mathbf{k}}) = \Delta(D_G^{(-)}(g)\hat{\mathbf{k}}), \quad (24)$$

where $D_G^{(-)}(g)$ is the three-dimensional representation of G in $\hat{\mathbf{k}}$ -space. For the elements $g \in SU(2)$ of the spin rotation group which act on the spin indices we obtain

$$g \Delta(\hat{\mathbf{k}}) = D_{(s)}^T(g) \Delta(\hat{\mathbf{k}}) D_{(s)}(g), \quad (25)$$

where $D_{(s)}(g)$ denotes the representation of $SU(2)$ for spin $\frac{1}{2}$. This transformation leaves even-parity states invariant. For odd-parity states where the order parameter can be represented by a vector \mathbf{d} in spin space the transformation gives a conventional orthogonal rotation of the \mathbf{d} -vector according to

$$g \mathbf{d}(\hat{\mathbf{k}}) = D_G^{(+)}(g) \mathbf{d}(\hat{\mathbf{k}}). \quad (26)$$

(2) In the presence of spin–orbit interaction the transformations of $\hat{\mathbf{k}}$ and the spin rotations are no longer independent. The spins are frozen in the lattice and the operations of the point group amount to simultaneous rotations in $\hat{\mathbf{k}}$ space and spin space:

$$g\mathbf{d}(\hat{\mathbf{k}}) = D_G^{(+)}(g)\mathbf{d}(D_G^{(-)}(g)\hat{\mathbf{k}}). \quad (27)$$

The appropriate choice of rotations corresponding to weak or strong spin–orbit coupling case is determined by microscopic considerations. Using the above transformation properties the singlet and triplet gap functions $\phi(\hat{\mathbf{k}})$ and $\mathbf{d}(\hat{\mathbf{k}})$, respectively, may further be decomposed into basis functions $\phi_r^n(\hat{\mathbf{k}})$ or $\mathbf{d}_r^n(\hat{\mathbf{k}})$ of the irreducible representations Γ (degeneracy index n) of $G \times \text{SU}(2)$ (weak s.o. coupling) or G (strong s.o. coupling).

The occurrence of long-range order at a phase transition described by an order parameter is most frequently associated with spontaneous symmetry breaking. The simplest superconductors where only gauge symmetry is broken are called *conventional*. In this case the SC order parameter has the same spatial symmetry as the underlying crystal, i.e., it transforms as a fully symmetric even parity singlet A_{1g} representation of G . It should be noted, however, that conventional is not a synonym for isotropic, for any G one can form A_{1g} representations from angular momentum orbitals of higher order l , for example, $l \geq 2$ for tetragonal and hexagonal symmetry and $l \geq 4$ for cubic symmetry. On the other hand, a superconductor with additional broken symmetries besides gauge symmetry is called *unconventional*. It can have either parity. Any odd-parity SC state which has broken inversion symmetry is unconventional in this sense. From the effective attractive interactions as eq. (12) obtained from model Hamiltonians like eq. (11) containing ‘high energy’ interaction parameters the symmetry can be obtained by directly minimizing the free energy and solving the resulting gap equations. These calculations depend on the model parameters and approximation schemes and cannot make predictions for real compounds.

The usual procedure described in detail in the next section to determine the symmetry of SC order parameters is to select plausible candidate states corresponding to irreducible representations (or mixtures) of the symmetry group, calculate the expected (temperature, field) behavior of physical quantities and compare the predictions with experiment. The selection of candidate states exploits Michel’s theorem (Michel, 1980) according to which stable points of the free energy should correspond to states which are invariant under subgroups of the full symmetry group. However the theorem was only proven for free energy expressions which are polynomial in the order parameter. As long as we work sufficiently close to the transition temperature, where a Ginzburg–Landau expansion is valid the systematic construction of gap functions in terms of basis functions which are invariant under subgroups is a useful guideline. Exhaustive lists of the superconducting classes for the relevant crystal symmetries were given by Volovik and Gorkov (1985), Ueda and Rice (1985), Blount (1985), Gorkov (1987), Sigrist and Ueda (1991), Annett (1990) and Ozaki and Machida (1985), Machida and Ohmi (1998), Machida et al. (1999) and references cited therein. A recent summary is found in the textbook of Mineev and Samokhin (1999).

Quite generally the results as given above can be divided into two groups (1, 2) according to their treatment of spin–orbit interaction. Group (1) treats the orbital and (pseudo-)spin degrees of freedom separately, while group (2) assumes that the spin of the Cooper pair is frozen in

the lattice. In mathematical terms: (1) assumes the symmetry group to be the direct product $G \times SU(2)$, while (2) considers the point group of the crystal to be the double group. The two schemes yield different predictions for the node structures. Treating the Cooper pair spin or \mathbf{d} as frozen in the lattice leads to odd-parity order parameters which vanish only in isolated points on the Fermi surface. This fact was first pointed out by Blount (1985) and is usually referred to as Blount's theorem. Even-parity states, on the other hand, have gap functions which may vanish on lines and at isolated points on the Fermi surface.

Blount's theorem seems to rule out odd-parity states in UPT_3 at first glance since there is strong evidence for node lines on the Fermi surface. As a consequence, the majority of early order parameter models for UPT_3 adopted multicomponent even-parity states. However the anisotropy of thermal conductivity, reversal of upper critical field anisotropy and Knight shift results in UPT_3 are better accounted for by an odd-parity order parameter. For an extensive discussion of this problem we refer to sect. 4.1. Another more recent case is UNi_2Al_3 where evidence for an odd parity state exists. It seems that Blount's theorem is not respected in real HF superconductors.

Concerning this ambiguity we add the following remark. Doubtlessly spin-orbit interaction plays an important role in U compounds. However, the energy $\xi_{so} \simeq 2$ eV associated with this relativistic effect is large compared to the HF quasiparticle band width $k_B T^* \simeq 10$ meV. In fact it is even larger than the hybridization energies, leading to separate 5f LDA bands belonging to different total angular momenta $j = 5/2$ and $7/2$ where the latter is almost empty (Albers et al., 1986). With respect to pair formation spin-orbit coupling is therefore to be treated as a high-energy effect. This suggests that spin-orbit coupling should be included already in the properties of the normal state quasiparticle states. The latter can be classified according to the pseudo spins connected with Kramers degeneracy of band states.

The transformation properties of the odd-parity order parameters under spatial rotations is reduced to considering the behavior of the quasiparticle states. To leading order in the small ratio kT^*/ξ_{so} we include the spin-orbit interaction in the calculation of the local atomic basis states, in a second step they are coherently superposed to form extended states. For bands derived from one doubly (Kramers-)degenerate orbital the elements of the point group should act only on the propagation vector. When the Cooper pairs, i.e., the two-particle states, are formed the orbital and spin degrees of freedom can be treated independently. With the spin-orbit interaction already included in the normal state quasiparticles one can use Machida's states derived for vanishing spin-orbit interaction.

The two different methods in treating the spin-orbit interaction have their counterparts in atomic physics. The scheme put forward by Volovik and Gor'kov parallels Russell-Saunders coupling where the orbital momenta and spins of the individual electrons are coupled to the total orbital momentum \mathbf{L} and total spin \mathbf{S} , respectively. These two quantities are coupled to form the total angular momentum $\mathbf{J} = \mathbf{L} + \mathbf{S}$. Including the spin-orbit interaction in the quasiparticle states, on the other hand, closely parallels jj -coupling.

The symmetry classification of density wave order parameters may proceed in a similar way. Charge and spin density are physical observables, hence the CDW/SDW order parameter describe diagonal long range order (DLRO) meaning that they correspond to expectation

values of diagonal elements in the one-particle density matrix according to

$$\langle \mathbf{r}s_1 | \rho^{(1)} | \mathbf{r}s_2 \rangle \rightarrow A_{s_1 s_2} \exp(i\mathbf{Q}\mathbf{r}), \quad (28)$$

where \mathbf{Q} is the wave vector of the density modulation and its amplitude is given by

$$A_{s_1 s_2} = \sum_{\mathbf{k}} F_{s_1 s_2}^{\mathbf{Q}}(\mathbf{k}) \quad \text{and} \quad F_{s_1 s_2}^{\mathbf{Q}}(\mathbf{k}) = \langle c_{\mathbf{k}s_1}^\dagger c_{\mathbf{k}+\mathbf{Q}s_2} \rangle. \quad (29)$$

The electron-hole pair amplitude $F_{\mathbf{Q}}(\mathbf{k})$ may again be decomposed into singlet (CDW) and triplet (SDW) components $\rho_{\mathbf{Q}}(\mathbf{k})$ and $\mathbf{s}_{\mathbf{Q}}(\mathbf{k})$, respectively, in analogy to SC pair amplitudes. Their corresponding gap functions are then given by the gap equations (cf. eq. (52))

$$\Delta_C(\mathbf{k}) = -I \langle \rho_{\mathbf{Q}}(\mathbf{k}) \rangle \quad \text{and} \quad \Delta_S(\mathbf{k}) = -I \langle s_{\mathbf{Q}}^z(\mathbf{k}) \rangle \quad (30)$$

for CDW and SDW (\mathbf{d} vector along z), respectively, where I is the on-site Hubbard interaction. Likewise the \mathbf{k} -dependence of gap functions may be classified according to the irreducible representations of the point group G with even and odd parity type when it contains the inversion symmetry. Several interesting aspects arise here: (1) Since gauge symmetry is obviously not broken its phase cannot be chosen arbitrarily, it rather is tied to the spatial transformation properties of the representation considered. Commonly the gap functions will either be real or imaginary for commensurate density waves. (2) On the other hand for electron-hole pairing there is no antisymmetry requirement hence the gap function for singlet (CDW) or triplet (SDW) can *both* be odd or even. (3) Conventional CDW and SDW states correspond to gap functions $\Delta_C(\mathbf{k})$ and $\Delta_S(\mathbf{k})$ which transform as fully symmetric (A_{1g}) representations, in the simplest case they are constants, independent of \mathbf{k} . In this case the amplitude of the CDW/SDW density modulation in real space obtained from the summation in eq. (29) is nonzero because the gap function does not change sign. If the gap functions belong to *nontrivial* representations, e.g., $d_{x^2-y^2}$ in two dimensions they do change sign and the sum in eq. (29) is zero, i.e., there is *no density modulation* although there is a ‘hidden’ order parameter $\Delta_C(\mathbf{k})$ or $\Delta_S(\mathbf{k})$ which characterizes the electron-hole condensate. Such states have been given the misleading name ‘unconventional density waves’ in analogy to the usage for SC states. These hidden order parameters have recently been under intense discussion for both underdoped cuprates, organic materials and U-HF systems.

2.2.2. Pairing model for coexistence of SC and CDW/SDW

In U-HF compounds the coexistence of SC and SDW order parameters is frequently observed. In a purely itinerant picture this phenomenon is well studied on the basis of a mean field (mf) pairing Hamiltonian which allows for both type of instabilities. It has first been proposed for SC/CDW coexistence (Bilbro and McMillan, 1976) and then for conventional SC/SDW (Machida, 1981; Machida and Matsubara, 1981) coexistence and later generalized to unconventional anisotropic gap functions for both SC and CDW/SDW (Kato and Machida, 1988; Thalmeier, 1994).

The effective mf Hamiltonian for pair formation in both electron–hole (e-h or Peierls) and electron–electron (e-e or Cooper) channels is given by

$$H = \sum_{\mathbf{k},s} \epsilon_{\mathbf{k}} c_{\mathbf{k}s}^{\dagger} c_{\mathbf{k}s} + H_{e-h} + H_{e-e}. \quad (31)$$

Introducing the charge and spin-densities (polarised along z)

$$\begin{aligned} \rho_{\mathbf{k}}(\mathbf{Q}) &= c_{\mathbf{k}\uparrow}^{\dagger} c_{\mathbf{k}+\mathbf{Q}\uparrow} + c_{\mathbf{k}\downarrow}^{\dagger} c_{\mathbf{k}+\mathbf{Q}\downarrow}, \\ s_{\mathbf{k}}(\mathbf{Q}) &= c_{\mathbf{k}\uparrow}^{\dagger} c_{\mathbf{k}+\mathbf{Q}\uparrow} - c_{\mathbf{k}\downarrow}^{\dagger} c_{\mathbf{k}+\mathbf{Q}\downarrow}, \end{aligned} \quad (32)$$

the electron–hole part can be separated in singlet (CDW) and triplet (SDW) part

$$H_{e-h} = - \sum_{\mathbf{k}} [\Delta_C(\mathbf{k}) \rho_{\mathbf{k}}(\mathbf{Q}) + \text{h.c.}] - \sum_{\mathbf{k}} [\Delta_S(\mathbf{k}) s_{\mathbf{k}}(\mathbf{Q}) + \text{h.c.}]. \quad (33)$$

Likewise the electron–electron part which, for example, is the mf approximation of eq. (12) is given by

$$H_{e-e} = - \sum_{\mathbf{k}} \Delta_{SC}^{ss'}(\mathbf{k}) [c_{\mathbf{k}s}^{\dagger} c_{-\mathbf{k}s'}^{\dagger} + \text{h.c.}]. \quad (34)$$

Here $\Delta_C(\mathbf{k})$, $\Delta_S(\mathbf{k})$ and $\Delta_{SC}^{ss'}$ are the CDW, SDW and SC gap functions which in general will depend on the momentum \mathbf{k} . The former two simply correspond to spin singlet (CDW) and triplet pairing (SDW) in the e-h channel. Analogously the superconducting gap matrix $\Delta_{SC}^{ss'}(\mathbf{k})$ may be decomposed into singlet and triplet parts described previously.

If only a single nonzero OP is present diagonalisation of H leads to quasiparticle excitations ($A \equiv C, S$)

$$E_{\mathbf{k}} = [\epsilon_{\mathbf{k}}^2 + (\Delta_{SC}^{\mathbf{k}})^2]^{1/2}; \quad \text{or} \quad E_{\mathbf{k}} = [\epsilon_{\mathbf{k}}^2 + (\Delta_A^{\mathbf{k}})^2]^{1/2}; \quad (35)$$

in the ordered phase. Here $\Delta_{SC}^{\mathbf{k}}$ represents $\phi(\mathbf{k})$ in the singlet case and $|\mathbf{d}(\mathbf{k})|$ in the (unitary) triplet case, respectively. The general case of coexisting order parameters and coupled gap equation is discussed below.

In the spirit of the Landau theory of 2nd order phase transitions one has to assume that each of the gap functions transforms as an irreducible representation of the underlying symmetry group which consists of gauge transformations $U(1)$, time reversal K , spin rotations $SU(2)$ and spatial transformations G as introduced before. For e-h pairing the former is preserved, for e-e pairing it is at least partly broken. If the gap functions belong to a fully symmetric or trivial representation (A_{1g} or Γ_1^+), i.e., if they are invariant under all spatial symmetry operations (including parity) of G then the condensed state describes a conventional CDW, SDW or superconductor, for all other representations the pair state is called unconventional as mentioned before. The most important difference in the two cases is due to their generally different nodal structure. Whereas for A_{1g} in general $|\Delta_i(\mathbf{k})| > 0$ ($i = A, SC$) and hence quasiparticle excitations are gapped, for the unconventional states frequently zeroes of the gaps $\Delta_i(\mathbf{k}) = 0$ or $\mathbf{d}(\mathbf{k}) = 0$ on points or lines on the Fermi surface are *possible* but not necessary. In the SC case one basically has two types of nodes: (i) Symmetry enforced gap nodes which always

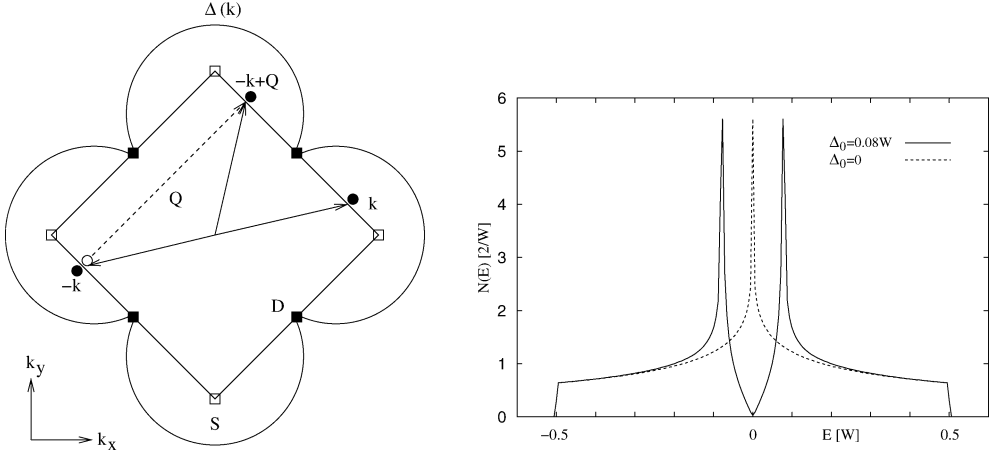


Fig. 7. Left panel: Cooper pairs $(-\mathbf{k}, \mathbf{k})$ and electron-hole (Peierls) pairs $(-\mathbf{k}, -\mathbf{k} + \mathbf{Q})$ for the n.n. tight binding Fermi surface (thick line) with perfect nesting vector \mathbf{Q} . Saddle points (S) of $\epsilon(\mathbf{k})$ at $(0, \pm\pi)$ and $(\pm\pi, 0)$ lead to DOS peak at the Fermi energy. Therefore unconventional pair states can only have nodes away from S, i.e., at the ‘Dirac’ points $D(\pm\frac{\pi}{2}, \pm\frac{\pi}{2})$ where the quasiparticle spectrum takes the form of eq. (54). This is the case for a $d_{x^2-y^2}$ -type gap function $\Delta(\mathbf{k})$ which is indicated schematically. Right panel: Corresponding quasiparticle DOS $N(E)$ ($W =$ tight binding band width) for normal state (dotted) and with $d_{x^2-y^2}$ -gap with amplitude Δ_0 . The Fermi level is at $E_F = 0$.

appear when the gap function transforms as an irreducible representation whose remaining symmetry group in the SC phase contains elements composed of spatial transformation and discrete gauge transformations and/or time reversal. (ii) Accidental nodes which depend on the specific choice of basis functions within a single representation or which appear as a result of superposition of different representations (‘hybrid gap functions’). Then gap nodes exist only for special superposition parameters (‘fine tuning’). Such nodes (or at least very large gap anisotropies $\Delta_{\max}(\mathbf{k}_{\max})/\Delta_{\min}(\mathbf{k}_{\min})$) may also be present in conventional superconductors where the hybrid gap function is constructed from fully symmetric representations A_{1g} of various degree and only U(1) symmetry is broken. Both types of nodes have been found and examples will be discussed in later sections. The precise conditions for the symmetry enforced gap nodes are discussed in Mineev and Samokhin (1999). On the other hand in some compounds, for example, borocarbides (sect. 5) and possibly skutterudites (sect. 6) the second type of SC gap nodes is observed. The quasiparticle spectrum of eq. (35) around the nodes defined by $\Delta_{\text{SC}}^{\mathbf{k}} = 0$ or $\Delta_{\text{A}}^{\mathbf{k}} = 0$ determines completely the low temperature physics of the ordered state. Knowledge about their position, multiplicity and dimension (points or lines) is therefore essential.

2.2.3. Coupled gap equations and results for coexistence

The interplay between superconductivity and antiferromagnetism has been in the focus of interest for a long time. The coexistence of the two ordering phenomena is well understood in those materials where they occur in different electronic subsystems which, in addition, are

not coherently coupled. Well-known examples are the Chevrel phases RMo_6S_8 , the rhodium borides RRh_4B_4 or the borocarbides $\text{RNi}_2\text{B}_2\text{C}$ where the influence of local moments of the lanthanide elements (R) on SC can be modelled by a molecular magnetic field acting on the SC conduction electrons (sect. 5). This results in a weaker pair interaction as compared to the paramagnetic phase and therefore leads to anomalies in the upper critical field H_{c2} below the onset of magnetic order.

The interplay of superconductivity with itinerant-electron magnetism where *both* SC and CDW/SDW are carried by conduction electrons continues to be a theoretical challenge. Qualitative phase diagrams reflecting the dominant order parameters and their mutual coexistence or expulsion have been derived within a mf approximation in order to interpret experiments. The concepts developed for transition metal alloys or organic superconductors have been extended to the case of heavy-fermion systems (Kato and Machida, 1988; Konno and Ueda, 1989). The basic assumption is that the long-range order, i.e., superconductivity or spin-density wave results from an instability of the Fermi surface of the strongly renormalized heavy quasiparticles. This assumption implies that we have at least an approximate separation of energy scales with $T_c(T_N) \ll T^*$ where T_c , and T_N denote the superconducting and magnetic transition temperatures while T^* is the HF quasiparticle band width.

Kato and Machida (1988) adopt a two-dimensional (t, t')-tight binding model for the quasiparticle bands resulting in a Fermi surface that exhibits nesting features with the commensurate wave vector $\mathbf{Q} = (\frac{1}{2}, \frac{1}{2}, 0)$. The effective interaction which consists of an on-site repulsion and an attractive pairing leads to both SDW and SC instabilities, the former supported by the nesting feature. The formation of a spin-density wave changes the symmetry of the system. This requires a modified classification scheme for the superconducting order parameters which can appear in a second order phase transition within the SDW state. The presence of both types of order parameters Δ_A ($A = C, S$) and Δ_{SC} may lead to induced SC pair amplitudes with pair momentum \mathbf{Q} which strongly influence the coexistence behaviour. The competing order parameters for various symmetry types are determined from coupled gap equations for $\Delta_A(\mathbf{k})$ and $\Delta_{\text{SC}}(\mathbf{k})$. In Kato and Machida (1988) the former was taken as constant (conventional SDW) while the latter allowed to belong to any nonconventional representation. In Thalmeier (1994) the coexistence study was generalised to include also unconventional density waves $\Delta_A(\mathbf{k})$. In the general case coexistence, competition as well as expulsion of the two order parameters may be observed.

For the tight binding model described above there are two types of coupled gap equations which are due to the different even/odd transformation properties of $\Delta_{\text{SC}}(\mathbf{k})$, $\Delta_A(\mathbf{k})$ under the two discrete transformations $\mathbf{k} \rightarrow -\mathbf{k}$ (inversion) and $\mathbf{k} \rightarrow \mathbf{k} + \mathbf{Q}$ (translation).

Case (I): there is no induced SC pairing with nonzero wave vector.

Case (II): a finite induced pairing amplitude $\langle c_{\mathbf{k}S_1} c_{\mathbf{k}+\mathbf{Q}S_2} \rangle$ for SC pairs with nonzero pair momentum exists.

Competition of SC and density wave pairs is much stronger in the second case because the induced pairing inevitably leads to a large loss in condensation energy.

In case I for the perfect nesting model ($t' = 0$) the gap equations are given simply by

$$1 = V \sum_{\mathbf{k}} \frac{f_{\text{SC}}(\mathbf{k})^2}{2E_{\mathbf{k}}} \tanh \frac{E_{\mathbf{k}}}{2T} \quad \text{and} \quad 1 = I \sum_{\mathbf{k}} \frac{f_A(\mathbf{k})^2}{2E_{\mathbf{k}}} \tanh \frac{E_{\mathbf{k}}}{2T}, \quad (36)$$

where $E_{\mathbf{k}} = [\epsilon_{\mathbf{k}}^2 + |\Delta_{\text{SC}}^{\mathbf{k}}|^2 + |\Delta_A^{\mathbf{k}}|^2]^{1/2}$ is the quasiparticle energy and the form factors $f_{\text{SC}}(\mathbf{k})$, $f_A(\mathbf{k})$ which correspond to irreducible basis functions of D_{4h} point group are defined via $\Delta_{\text{SC}}(\mathbf{k}) = \Delta_{\text{SC}}^0 f_{\text{SC}}(\mathbf{k})$ and $\Delta_A(\mathbf{k}) = \Delta_A^0 f_A(\mathbf{k})$. Furthermore interaction constants I and V determine whether SDW or SC transition happens first. In HF compounds frequently we have $T_N > T_c$. In this weakly competitive case coupled gap equations are formally the same as for each of the gap functions individually. They influence each other only through the quasiparticle energies where both gap functions appear. Numerical solution shows that for this case coexistence is always possible and (assuming $T_N > T_c$) the transition from SDW to SDW + SC coexistence phase happens always in a second order phase transition, irrespective how small T_c is.

In case II the gap equations are formally different from individual gap equations:

$$1 = V \sum_{\mathbf{k}} \frac{f_{\text{SC}}(\mathbf{k})^2}{4|\Delta_{\text{SC}}^{\mathbf{k}}|} \left(\frac{|\Delta_{\text{SC}}^{\mathbf{k}}| + |\Delta_A^{\mathbf{k}}|}{E_{\mathbf{k}}^+} \tanh \frac{E_{\mathbf{k}}^+}{2T} + \frac{|\Delta_{\text{SC}}^{\mathbf{k}}| - |\Delta_A^{\mathbf{k}}|}{E_{\mathbf{k}}^-} \tanh \frac{E_{\mathbf{k}}^-}{2T} \right),$$

$$1 = I \sum_{\mathbf{k}} \frac{f_A(\mathbf{k})^2}{4|\Delta_A^{\mathbf{k}}|} \left(\frac{|\Delta_A^{\mathbf{k}}| + |\Delta_{\text{SC}}^{\mathbf{k}}|}{E_{\mathbf{k}}^+} \tanh \frac{E_{\mathbf{k}}^+}{2T} + \frac{|\Delta_A^{\mathbf{k}}| - |\Delta_{\text{SC}}^{\mathbf{k}}|}{E_{\mathbf{k}}^-} \tanh \frac{E_{\mathbf{k}}^-}{2T} \right), \quad (37)$$

where the two quasiparticle bands $E_{\pm}^{\mathbf{k}} = [\epsilon_{\mathbf{k}}^2 + (|\Delta_{\text{SC}}^{\mathbf{k}}| \pm |\Delta_A^{\mathbf{k}}|)^2]^{1/2}$ are now split due to the presence of two order parameters. Numerical solutions for case II show a much more competitive behaviour of gap functions Δ_A and Δ_{SC} . If T_c is comparable in size to T_N the SDW state may be destroyed at T_c and replaced by the SC phase in a first order phase transition. For smaller T_c again a coexistence state SDW + SC appears in a second order phase transition but generally the order parameters in this regime show strong competition resulting in nonmonotonic temperature behaviour of gap functions.

The coexistence/competition behaviour of $\Delta_A(\mathbf{k})$ and $\Delta_S(\mathbf{k})$ is therefore quite different in cases I and II and it also depends strongly on the relative nodal structure of $\Delta_A(\mathbf{k})$ $\Delta_S(\mathbf{k})$. Generally speaking if their nodes are on the same positions on the FS (or if at least one of them is a conventional gap function without nodes) this enhances competition, nonmonotonic temperature behaviour and tendency to expulsion of one OP. On the other hand an ‘orthogonal’ nodal structure for both (e.g., d_{xy} symmetry for SDW and $d_{x^2-y^2}$ for SC) supports coexistence because the two gaps become maximal at different parts of the FS and this also favors monotonic temperature dependence of the gap amplitudes.

To illustrate this behaviour we briefly discuss an example which may be relevant to CeCu_2Si_2 . Qualitatively the complex phase diagram of CeCu_2Si_2 can be described by a simple mean-field model for a conventional spin density wave ground state (competing with d-wave superconductivity within a two band model proposed by Dahm (2001)). The calculated phase diagram displayed in fig. 8 shows that a state with d_{xy} symmetry can become stable within the SDW phase. This is in contrast to the pairing states with $d_{x^2-y^2}$ symmetry considered by Kato

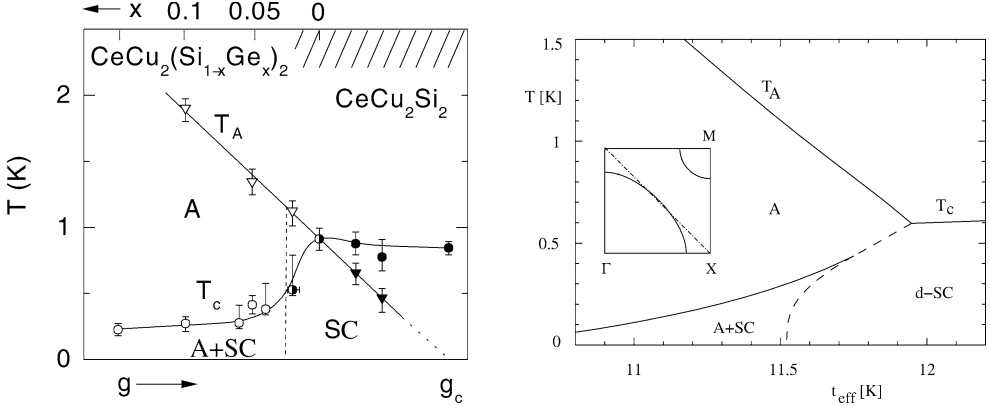


Fig. 8. Left panel: Experimental results for coexistence and competition between superconductivity and SDW in $\text{CeCu}_2(\text{Si}_{1-x}\text{Ge}_x)_2$ (Gegenwart et al., 1998). Ge substitution acts like a (negative) chemical pressure. Here A = SDW and SC is the superconducting state. T_A depends linearly on chemical pressure, hence $g \sim 1 - x$. Right panel: Two band model for A and d-SC order in mf theory from Steglich et al. (2001). Here A denotes a conventional SDW state with constant Δ_A and d-SC has $\Delta_{\text{SC}}(\mathbf{k}) = \Delta_{\text{SC}}^0 \sin k_x \sin k_y$; $A + \text{SC}$ denotes the coexistence region. Solid and dashed lines correspond to second and first order transitions, respectively. The effective tight-binding hopping integral is t_{eff} , it should also scale linearly with $1 - x$. Inset: FS topology with two bands. Dash-dotted line indicates location of SDW gapping.

and Machida (1988) in a one band model. The experimentally observed unusual stability of the $(A + \text{SC})$ phase might follow from the peculiar Fermi surface of the heavy quasiparticles displayed in fig. 18. This is suggested by model calculations which start from a more complex Fermi surface model. Assuming two well-separated sheets centered at Γ and M , respectively, allows for a solution where the SDW gaps exist only on part (centered around Γ) of the Fermi surface while the quasiparticles on the remaining parts (centered around M) condense into a superconducting state. The calculated temperature–‘pressure’ phase diagram (assuming that the electron band width $\sim t_{\text{eff}}$ scales linearly with pressure) is qualitatively in agreement with experimental results (Gegenwart et al., 1998) for CeCu_2Si_2 . Indeed the A -phase has now been identified as conventional SDW state with an incommensurate propagation vector $\mathbf{Q} = (0.22, 0.22, 0.55)$ and a moment of $0.1\mu_B$ per Ce-atom by neutron diffraction experiments (Stockert et al., 2004). The experimentally determined magnetic structure therefore requires a more refined treatment of the SDW/SC coexistence behaviour.

2.3. Methods to investigate the symmetry of order parameters

Phase transitions with the appearance of a spontaneous symmetry breaking are characterised by order parameters. In the spirit of Landau theory they belong to representations of the high temperature symmetry group and also characterise the class of remaining symmetries in the low-temperature phase. Furthermore they partly determine the type of possible excitations in the ordered phase which in turn influence the low-temperature thermodynamic and transport properties. The investigation of the order parameter symmetry is therefore of singular

importance. In the case of order parameters corresponding to expectation values of physical observables like spin- and charge densities this is in principle straightforward as they reveal their existence and symmetry in X-ray and neutron diffraction experiments. However for ‘hidden’ order, e.g., quadrupole ordering or ‘unconventional’ density waves (orbital antiferromagnetism) there is no large obvious signature in diffraction experiments and evidence for its presence has to be obtained indirectly by other means. The superconducting order parameter does not correspond to the expectation value of a classical observable but rather to the appearance of quantum mechanical phase rigidity of Cooper pairs on a macroscopic scale (the coherence length). For unconventional superconductors determination of the gap function dependence on the momentum of paired states is of fundamental importance. It is also extraordinarily difficult. The classical experimental techniques which we discuss in this section rely on the interpretation of temperature dependences of physical quantities obtained by *averaging* over the gap function momentum dependence and, therefore, the conclusion about their proper symmetry is always ambiguous. Recently a much more powerful method relying on the field angle resolved measurement of specific heat and thermal conductivity in the vortex phase for $T \ll T_c$ has been developed. It leads directly to the determination of the relative position of node lines and/or points of the SC gap function with respect to crystal axes. This leads to a strong reduction of the number of possible SC order parameters and possibly allows a unique determination. Therefore we devote an extra subsection to this new technique. On the other hand we shall not discuss phase sensitive methods based on Josephson tunneling which have been unsuccessful in HF compounds and point contact spectroscopy or μ SR methods due to their difficult interpretation. For unconventional density waves which also correspond to gap functions of nontrivial momentum dependence in the particle–hole channel, the field angle dependent investigation of magnetoresistance has similar potential but is less developed.

2.3.1. Detection of superconducting order parameter symmetry

In conventional electron–phonon superconductors with an almost isotropic gap numerous thermodynamic, static and dynamic transport measurements and also resonance methods can give information about the size of the superconducting gap. The SC transition affects these quantities in two ways: (i) the quasiparticle DOS exhibits a gap Δ with a square root singularity of the DOS: $N_s(E) = N_0 E / (E^2 - \Delta^2)^{1/2}$ ($E \geq \Delta$), (ii) coupling of external probe fields to the quasiparticles involves a coherence factor $\frac{1}{2}(1 \mp \Delta^2/EE')$ where \mp corresponds to perturbations even or odd under time reversal, respectively. In the former case (I) the DOS singularity and the vanishing coherence factor for $E \simeq \Delta$ compensate leading to a steep drop of the corresponding physical quantity, e.g., of ultrasonic attenuation below T_c . In the latter case (II) the coherence factor is unity and therefore a Hebel–Slichter type anomaly as, e.g., in the NMR-relaxation rate develops below T_c . At low temperatures ($T \ll T_c$) invariably experimental quantities determined by electron–hole excitations tend to zero exponentially due to the finite superconducting gap. Therefore the most obvious and seemingly easiest method to look for evidence of unconventional superconductivity is the search for deviations from the exponential low-temperature dependence. This strategy relies on the fact that nontrivial (unconventional) \mathbf{k} -dependent gap functions $\Delta(\mathbf{k})$ in many cases (though not always) exhibit node points or lines on the Fermi surface leading to a nonvanishing $N_s(E)$ for all

energies $E > 0$ even in the superconducting state. The asymptotic behaviour of $N_s(E)$ for $E/\Delta \ll 1$ is $\sim E^2$ for (first order) point nodes and $\sim E$ for line nodes. Then this should ideally lead to ‘power law’ behaviour $\sim T^n$ for physical quantities like specific heat, penetration depth, NMR relaxation rate and many others for $T \ll T_c$. The experimentally observed exponent n would then allow to determine whether $\Delta(\mathbf{k})$ has point nodes ($n = 3$), line nodes ($n = 2$) or both if the exponent n is in between, or whether gapless regions of the Fermi surface ($n = 1$) exist. For nondirectional quantities like $C(T)$ this would however say nothing about the position of nodes relative to the crystal axes. Unfortunately this picture is so oversimplified as to make it useless. Firstly, experimental determination of the exponent n very often includes temperatures where $T \ll T_c$ is not valid and more importantly impurity scattering in anisotropic superconductors has dramatic effects (Sigrist and Ueda, 1991; Fulde et al., 1988). In conventional superconductors Anderson’s theorem ensures that the low temperature thermodynamic properties are not affected by impurity scattering. On the other hand normal impurities for unconventional pairs act strongly pairbreaking. This is especially important in HF compounds where the normal state electrons are already strongly correlated and impurities act as unitary scattering centers. Their effect for anisotropic superconductors has originally been studied by Buchholtz and Zwicknagl (1981) for p-wave states and later extended and applied (Hirschfeld et al., 1986; Scharnberg et al., 1986; Schmitt-Rink et al., 1986; Hotta, 1993; Sun and Maki, 1995) for other cases like d-wave. In the unitary scattering limit a resonant residual quasiparticle DOS at low energies develops (Hirschfeld et al., 1986) invalidating the abovementioned power laws. On the other hand hybrid nodal superconductors like s + g wave type in borocarbides exhibit the opposite behaviour: Impurity scattering immediately leads to the opening of a gap (Yuan et al., 2003) with resulting low temperature exponential behaviour. It is therefore more reasonable to investigate the T -dependence of physical quantities depending on the gap anisotropy for the whole temperature range below T_c and compare with experiments, rather than looking at the often ill-defined and contradictory low- T power laws. This will be discussed now in a few cases.

Specific heat: The specific heat in the anisotropic SC state is given by an expression formally identical to the s-wave case:

$$C_s = 2k\beta \sum_{\mathbf{k}} \left(-\frac{\partial f_{\mathbf{k}}}{\partial E_{\mathbf{k}}} \right) \left[E_{\mathbf{k}}^2 + \frac{1}{2}\beta \frac{\partial \Delta_{\mathbf{k}}^2}{\partial \beta} \right] \quad \text{and} \quad \frac{\Delta C_s}{C_n} = \frac{3}{2} \frac{8}{7\zeta(3)} \frac{\langle f_{\mathbf{k}}^2 \rangle_{\text{FS}}}{\langle f_{\mathbf{k}}^4 \rangle_{\text{FS}}}, \quad (38)$$

where $\beta = 1/kT$, $E_{\mathbf{k}} = (\epsilon_{\mathbf{k}}^2 + \Delta_{\mathbf{k}}^2)^{1/2}$, $f_{\mathbf{k}} = f(E_{\mathbf{k}})$ is the Fermi function and $C_n = \gamma T$. The specific heat jump given by the second formula has the BCS value $\Delta C_s/C_n = 1.43$ for the isotropic s-wave gap. In fig. 9 model calculations for $C_s/\gamma T$ by Hasselbach et al. (1993) for all possible gap symmetries in tetragonal D_{4h} group are shown and compared with experimental results for URu_2Si_2 . The latter show remarkably linear behaviour over the whole experimental temperature range. It is obvious that a perfect fit is not possible with any gap representation and at low T a tendency for saturation due to an impurity induced residual DOS is visible. A comparison of theoretical and experimental $\Delta C(T_c)$ jumps however favors either a $E_u(1, 1)$ state $\Delta(\mathbf{k}) = \Delta(k_x + k_y)^2$ or B_{1g} state $\Delta(\mathbf{k}) = \Delta(k_x^2 - k_y^2)^2$ for which one has $2\Delta(0)/kT_c =$

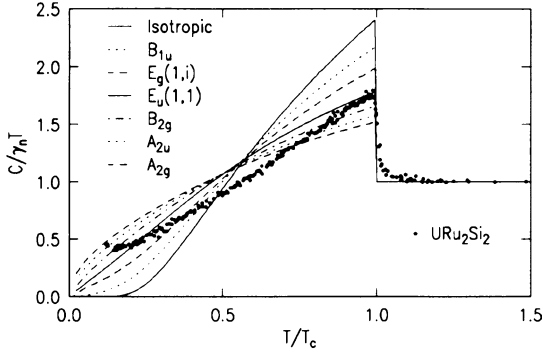


Fig. 9. Calculated specific heat for various superconducting order parameters in comparison to experimental results for URu₂Si₂ (Hasselbach et al., 1993). The specific heat jump $\Delta C_s(T_c)$ agrees best for $E_u(1, 1)$ or B_{1g} state.

Table 1

BCS ratio $2\Delta(0)/kT_c$ and specific heat ratio $\Delta C_s/C_n$ for some common order parameter models Einzel (2002) characterised by the gap form factor $f(\vartheta, \varphi)$ as function of polar angles of \mathbf{k} and normalised on the unit sphere ($a = 3\sqrt{3}/2$)

	Isotropic	Axial	Polar	E_{1g} (D_{6h})	E_{2u} (D_{6h})
$f(\vartheta, \varphi)$	1	$\sin \vartheta$	$\cos \vartheta$	$2 \sin \vartheta \cos \vartheta$	$a \sin^2 \vartheta \cos \vartheta$
$2\Delta(0)/kT_c$	3.52	4.06	4.92	4.22	4.26
$\Delta C_s/C_n$	1.43	1.19	0.79	1.00	0.97

4.92 or 5.14, respectively. Since the presence of nodes reduces T_c compared to s-wave case for the same gap amplitude the BCS ratio (table 1) is always larger for anisotropic SC. However for real compounds this increase may also be partly due to strong coupling effects. Likewise the ratio $\Delta C_s/C_n$ is always maximal for isotropic SC.

Thermal conductivity: The thermal conductivity tensor is a directional quantity depending on the orientation of temperature gradient and heat current. At low temperatures its anisotropy may contain important information on the relative position of nodal points or lines with respect to crystal axes. For example, this has proved decisive in the identification of the E_{2u} SC order parameter of UPt₃ (sect. 4.1). The uniaxial thermal conductivity tensor in the unitary scattering limit for a spherical Fermi surface is explicitly given (Norman and Hirschfeld, 1996; Kübert and Hirschfeld, 1998; Machida et al., 1999; Graf et al., 2000; Wu and Joynt, 2002) as

$$\frac{\kappa_i(T)}{\kappa_n} = \frac{9}{2\pi^2 T_c} \int_0^\infty d\omega \left(\frac{\omega}{T}\right)^2 \operatorname{sech}^2 \frac{\omega}{2T} K_i(\omega, T), \quad (39)$$

$$K_i(\omega, T) = \frac{\langle \hat{k}_i^2 \operatorname{Re}[\omega^2 - |\Delta_{\mathbf{k}}(T)|^2]^{1/2} \rangle}{\langle \operatorname{Re}[\omega^2 - |\Delta_{\mathbf{k}}(T)|^2]^{-1/2} \rangle},$$

where $\hat{k}_i = (\hat{\mathbf{i}} \cdot \hat{\mathbf{k}}) = \cos \theta_i$ and $\hat{\mathbf{i}}$ are the unit vectors along x, y, z axes.

At low temperatures the \mathbf{k} -averaging in $\kappa_i(T)$ is determined only by the quasiparticles close to the nodal region. Because of the direction cosines in the averages of eq. (39) coming from the quasiparticle velocities, κ_i depend on the position of the nodal points or lines with respect

to the axis $\hat{\mathbf{i}}$. When the nodal direction in \mathbf{k} -space is parallel to the direction $\hat{\mathbf{i}}$ of the heat current a large contribution to $\kappa_i(T)$ is obtained and a small one if it is perpendicular. This may lead to a uniaxial thermal conductivity anisotropy characterised by the ratio (Norman and Hirschfeld, 1996)

$$\frac{\kappa_c(0)}{\kappa_a(0)} = \lim_{\omega \rightarrow 0} \frac{\text{Re}\langle \hat{k}_z^2 [\omega^2 - |\Delta_{\mathbf{k}}(T)|^2]^{1/2} \rangle}{\text{Re}\langle \hat{k}_x^2 [\omega^2 - |\Delta_{\mathbf{k}}(T)|^2]^{1/2} \rangle}. \quad (40)$$

As discussed in sect. 4.1 this anisotropy ratio of thermal conduction has proved quite useful in the identification of the order parameter symmetry in UPT₃ (see fig. 31).

Ultrasonic attenuation: Sound attenuation has in addition to the propagation direction ($\hat{\mathbf{q}}$) another polarization ($\hat{\mathbf{e}}$) degree of freedom and may therefore give even more information on the gap nodes than the thermal conductivity. In HF metals sound attenuation can generally be considered in the hydrodynamic limit where $\omega\tau, ql \ll 1$ with q, ω denoting wave number and frequency (~ 100 MHz) of the sound wave respectively and $l = v_F\tau$ is the mean free path in the normal state. In this case conduction electrons act like a viscous medium to the sound waves and the attenuation coefficient may be expressed as a correlation function of the electronic stress tensor (Tsuneto, 1961; Kadanoff and Falko, 1964). Its evaluation for unconventional SC states using a quasiclassical approximation leads to (Machida et al., 1999; Graf et al., 2000)

$$\begin{aligned} \frac{\alpha_{ij}(T)}{\alpha_n} &= \frac{1}{2T} \int_0^\infty d\omega \text{sech}^2 \frac{\omega}{2T} A_{ij}(\omega, T), \\ A_{ij}(\omega, T) &= \frac{1}{\langle \Pi_{ij}^2 \rangle} \left\langle \Pi_{ij}^2 \frac{1}{\omega} \text{Re}[\omega^2 - |\Delta_{\mathbf{k}}(T)|^2]^{1/2} \right\rangle, \\ \Pi_{ij} &= \hat{k}_i \hat{k}_j - \frac{1}{3} \delta_{ij}. \end{aligned} \quad (41)$$

The projection factor Π_{ij} ($i = \text{polarisation}, j = \text{propagation direction}$) determines which of the quasiparticles having a $\hat{\mathbf{k}}$ -vector described by polar and azimuthal angles ϑ, φ contribute strongly to the attenuation. Consider two cases with $ij = ab$ where $\Pi_{ij}^2 \sim \sin^2(2\varphi)$ and $ij = ac$ with $\Pi_{ij}^2 \sim \sin^2(2\vartheta)$. The quasiparticle contribution to $\alpha_{ij}(T)$ therefore vanishes for nodal directions $\varphi = n(\frac{\pi}{2})$ and $\vartheta = n(\frac{\pi}{2})$, respectively. For example, if the gap has a node line in the basal plane ($\vartheta = \frac{\pi}{2}$) it gives maximal contribution to the attenuation for $ij = ab$ but minimal contribution for $ij = ac$. The same argument holds for point nodes on the c -axis where $\vartheta = 0, \pi$. This situation is indeed realized in the E_{2u} type B -phase of UPT₃ (sect. 4.1) and one can see in fig. 10 that the attenuation for ac configuration is much smaller than for ab . The anomalies around the split T_c are complicated and analyzed in Graf et al. (2000). Therefore polarization and propagation dependence of ultrasonic attenuation is a powerful method to distinguish between gap representations with different nodal structure. Finally it should be mentioned that collective modes in unconventional superconductors hardly contribute to the attenuation since one has an off-resonance situation due to $v_s \ll v_F$ (Kee et al., 2000).

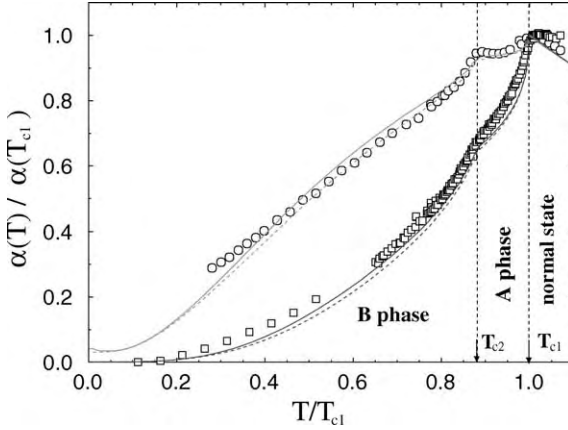


Fig. 10. Temperature dependence of ultrasonic attenuation in *B*-phase of UPt₃ for transverse waves with propagation along *a*-axis and polarisation along *b*-axis (*ab*: circles) or *c*-axis (*ac*: squares), from Graf et al. (2000). Here $T_{c1,2}$ denotes the split SC transition temperature.

NMR relaxation and Knight shift: In an external field nuclear spins exhibit a Larmor precession with a frequency ω_0 . In metals this is modified by the hyperfine coupling to conduction electrons which leads to spin-flip processes as witnessed by the NMR-relaxation rate T_1^{-1} and the Knight shift of the resonance frequency $\delta\omega_0$. A review of these important effects for HF superconductors is given by Tou et al. (2003). The relaxation rate T_1^{-1} is determined by the availability of resonant electron-hole excitations. In the normal state this leads to the Korringa law $T_{1n}^{-1} \sim T$. In the superconducting state the presence of $\Delta(\mathbf{k})$ should lead to a faster decrease with temperature depending on the type of node structure, i.e., the low energy behaviour of the quasiparticle DOS. According to Sigrist and Ueda (1991) for singlet pairs one has

$$\frac{T_{1n}}{T_1} = \frac{2}{N_n^2} \int_0^\infty dE \left(-\frac{\partial f}{\partial E} \right) N_s(E) N_s(E + \omega_0) \left[1 + \frac{|\langle \Delta_{\mathbf{k}} \rangle_{\text{FS}}|^2}{E(E + \omega_0)} \right]. \quad (42)$$

For *s*-wave pairs the type II-coherence factor together with the singular DOS leads to the appearance of the Hebel-Slichter peak. Because for unconventional pair states the Fermi surface average in eq. (42) vanishes, there is no difference between type I and II coherence factors and the relaxation rate is determined by the DOS alone. Because in the presence of nodes there is no divergence in $N_s(E)$ no Hebel-Slichter peak will appear below T_c . Its absence may therefore be taken as a sign of an unconventional pair state. Furthermore the low temperature behaviour of T_1^{-1} should be $\sim T^3$ for line nodes and $\sim T^5$ for point nodes. Invariably the former is observed in HF systems, often in conflict with ‘power laws’ of other quantities. A puzzling feature is the absence of any crossover for $T \ll T_c$ to Korringa behaviour in the impurity dominated gapless regime.

In addition to the relaxation the hyperfine interaction leads to a Knight shift of the resonance frequency given by

$$\delta\omega_0(T) \sim |\psi_0|^2 \chi_s(T) H, \quad (43)$$

where ψ_0 is the conduction electron wave function at the nucleus and $\chi_s(T)$ is the *spin* susceptibility of conduction electrons. Without spin-orbit coupling present in an *s*-wave singlet state

this drops to zero exponentially below T_c , leading to a pronounced T -dependence of $\delta\omega_0$. For a triplet SC state the condensate spin or the \mathbf{d} -vector of the pair can be freely rotated and $\chi_s(T)$ should not change leading to T -independent $\delta\omega_0$. Therefore the existence or non-existence of a T -dependent Knight shift below T_c is usually interpreted as direct evidence for singlet or triplet superconductivity, respectively. In the former case the Knight shift should be proportional to the Yoshida function given by the FS average

$$Y(T) = \left\langle \frac{1}{2T} \int_0^\infty d\epsilon \cosh^{-2} \frac{E_{\mathbf{k}}}{2T} \right\rangle_{\text{FS}} \quad (44)$$

with a low T behaviour $Y(T) \sim T^2$ for point nodes and $\sim T$ for line nodes. Unfortunately the situation may be completely changed under the presence of strong spin-orbit (s.o.) coupling, for both the conduction electrons themselves and for the conduction electron-impurity scattering. If the mean free path due to conduction electron-impurity s.o. scattering is much smaller than the coherence length, the Knight shift variation with temperature approaches zero also for singlet pairing (Abrikosov, 1988). On the other hand in a triplet pair state a conduction electron s.o. coupling may lead to the pinning of the triplet pair \mathbf{d} -vector along one of the crystal axis. Then the T -dependence of $\delta\omega_0$ should be very anisotropic, vanishing for $\mathbf{H} \perp \mathbf{d}$ and large for $\mathbf{H} \parallel \mathbf{d}$. A moderately anisotropic Knight shift is indeed found in UPt₃ (sect. 4.1). These complications make a quantitative analysis as for the previous quantities difficult, in fact it is rarely performed for HF compounds. The arguments for or against singlet or triplet pairing using Knight shift results should therefore be taken with caution.

Upper critical field: The temperature dependence and anisotropy of the upper critical field H_{c2} may contain important information both about the question of singlet vs. triplet pairing and the anisotropy of the gap function $\Delta(\mathbf{k})$. A general discussion of the problem within the semiclassical approach has been given in Rieck et al. (1991). Theoretical analysis in the context of a generalized Ginzburg-Landau theory depends very much on the crystal symmetry and order parameter model. It will be briefly discussed in sect. 4.1 for UPt₃. In this case the importance of uniaxial anisotropy to decide between singlet and triplet pairing has been realized (Choi and Sauls, 1991; Sauls, 1994; Yang and Maki, 1999). In a pure isotropic superconductor the upper critical field $H_{c2}(0)$ is limited by orbital effects leading to

$$\mu_B H_{c2}(0) = 0.693 T_c |dH_{c2}/dT|_{T_c}. \quad (45)$$

The actual critical field may be much lower caused by the effect of paramagnetic ‘Pauli-limiting’ due to the Zeeman energy of the Cooper pair. If the field is larger than $\mu_B H_P = \Delta_0/\sqrt{2} = 1.25 T_c$ the upper critical field is limited by the breaking up of singlet Cooper pairs. According to eq. (45) a large critical field slope should also lead to a larger $H_{c2}(0)$. In UPt₃ the opposite is true leading to a ‘crossing’ of $H_{c2}(T)$ curves for a - and c -directions. This led to the proposal that $H_{c2}(0)$ is strongly reduced by Pauli-limiting effects for field along c but not along a . This can only be explained by assuming triplet pairing with strongly pinned \mathbf{d} -vector parallel to c . As will be discussed in sect. 4.1 this interpretation is not undisputed. In addition to the question of the spin state a nontrivial \mathbf{k} -dependence of the gap should also lead to anisotropies in the upper critical field (slope) beyond those due to effective mass anisotropies.

This proved difficult or inconclusive for HF superconductors investigated so far (Keller et al., 1995).

2.3.2. *Specific heat and magnetotransport in the vortex phase: a genuine angular resolved method*

The classical methods to determine $\Delta(\mathbf{k})$ discussed above all suffer under the same major deficiency: the angular dependence, or at least nodal positions in \mathbf{k} -space are never determined directly. Instead the physical quantities investigated are obtained by *averaging* over the quasiparticle and hence gap energies in \mathbf{k} -space. And then it is hoped that the averaged quantities still show clear signatures depending on the gap symmetry. Naturally this leads to ambiguous results for any one method and only a comparison of all gap models for a number of methods may lead to a conclusion on the gap symmetry.

However, recently a new and powerful method has been established that is able to locate directly the nodal positions of the SC gap in \mathbf{k} -space (Izawa et al., 2001, 2001a, 2002). In this method the *field-angle* dependence of specific heat or thermal conductivity is investigated. Typical oscillations are observed whose periodicity, phase and shape give direct information on the type of nodes (point- or line-like) and their direction in \mathbf{k} -space. Therefore possibilities for allowed gap functions can be much more restricted. Notice however that still the full \mathbf{k} -dependence of $\Delta(\mathbf{k})$ cannot be determined.

At the heart of this method is the ‘Volovik effect’ in the vortex state of the superconductor, it was first proposed by Volovik (1993) for d-wave superconductors. There it was shown that for nodal gap functions a continuum of quasiparticle states exists outside the vortex cores which dominate the specific heat and can easily carry a thermal current even perpendicular to the vortex lines. These states are due to quasiparticles channeling out of the vortex core region through the nodal points or lines. This is an important new aspect as compared to conventional nodeless gap functions where one has only bound states in the vortex core. For the quasiclassical limit $\xi_0 k_F \gg 1$ they also form a quasi-continuum but they can carry a heat current only parallel to the vortex direction. The theory of magnetothermal transport has subsequently been developed by many authors (Barash et al., 1997; Kübert and Hirschfeld, 1998; Vekhter et al., 2001; Won and Maki, 2000; Dahm et al., 2000; Won and Maki, 2001a, 2001b). The Volovik effect can nicely be explained within the quasiclassical picture where momentum (\mathbf{k}) and position (\mathbf{r}) coordinates commute and the quasiparticle energy $E(\mathbf{k}, \mathbf{r})$ and occupation $f(\mathbf{k}, \mathbf{r})$ depends on both variables. The dependence on \mathbf{r} comes from the fact that the energy of quasiparticles channeling into the inter-vortex region gets Doppler shifted due to the \mathbf{r} -dependent superfluid velocity field $\mathbf{v}_s(\mathbf{r})$. This leads to $E(\mathbf{k}, \mathbf{r}) = E(\mathbf{k}) - \mathbf{v}_s(\mathbf{r}) \cdot \mathbf{k}$. Here $E(\mathbf{k})$ is the zero-field quasiparticle energy and the second term is the Doppler shift energy. This position dependent shift leads to a finite residual DOS which will depend both on field magnitude and direction:

$$\frac{N_s(E, \mathbf{H})}{N_n} \simeq \frac{1}{\Delta} \langle \langle |E - \mathbf{v}_s(\mathbf{r}) \cdot \mathbf{k}| \rangle \rangle. \quad (46)$$

The double average is performed both over the velocity field coordinate \mathbf{r} and the quasiparticle momentum \mathbf{k} . It will depend on the direction of the magnetic field $\mathbf{H}(\theta, \phi)$ with respect to

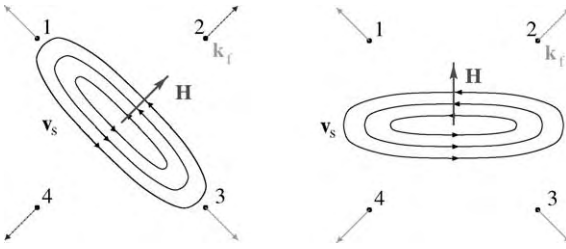


Fig. 11. Illustration of the Volovik effect (Vekhter et al., 2001). \mathbf{k}_i ($i = 1-4$) denote the nodal directions of the gap. Left: Field \mathbf{H} along nodal direction where \mathbf{v}_s is orthogonal to $\mathbf{k}_2, \mathbf{k}_4$; these nodal directions do not contribute to the Doppler shift, the residual DOS will be at minimum. Right: Field along antinodal direction, all \mathbf{k}_i ($i = 1-4$) directions contribute to the Doppler shift, the residual DOS is maximal.

the nodal directions (θ and ϕ are polar and azimuthal angles of \mathbf{H} with respect to the c -axis). An illustration of this direction dependence is given in fig. 11. The variation of the field angles (θ, ϕ) is therefore expected to lead to a periodic variation in $N(E, \theta, \phi)$ and hence in the specific heat and thermal conductivity components. Oscillations will be strongest (i) in the low temperature limit $T \ll \tilde{v}\sqrt{eH} \ll \Delta(0)$ when only quasiparticles from the nodal regions contribute to the residual DOS and (ii) if the node structure is not smeared to much by impurity scattering, i.e., one is in the ‘superclean limit’ with $(\Gamma\Delta)^{1/2} \ll \tilde{v}\sqrt{eH}$ where Γ is the impurity scattering rate and $\tilde{v} = \sqrt{v_a v_c}$ with v_a and v_c giving the Fermi velocities along a - and c -axis in uniaxial symmetry. This limit can also be expressed as $\Gamma/\Delta \ll H/H_{c2} \ll 1$. For hybrid nodal gaps such as $s + g$ wave gap in the borocarbides the superclean condition should be replaced by $\Gamma \ll T \ll \tilde{v}\sqrt{eH}$ due to the completely different effect of impurities in this case (sect. 5). Including the effect of impurity scattering one obtains for the residual DOS at the Fermi level (Won and Maki, 2000):

$$\begin{aligned} \frac{N_s(0, \mathbf{H})}{N_n} &= \text{Re}[g(0, \mathbf{H})], \\ g(0, \mathbf{H}) &= \left\langle \frac{C_0 - ix}{\sqrt{(C_0 - ix)^2 + f^2}} \right\rangle, \\ C_0 &= \frac{\Gamma}{\Delta g(0, \mathbf{H})}. \end{aligned} \quad (47)$$

Here $f(\mathbf{k}) = \Delta(\mathbf{k})/\Delta$ and $x = |\mathbf{v}_s \cdot \mathbf{k}|/\Delta$ are the normalized gap function and Doppler shift energy, respectively, while C_0 is a normalized scattering rate. The above condition for the superclean limit can be expressed as $C_0 \ll x$.

The averaging is performed by restricting the \mathbf{k} -integration to the node region (since $T \ll \Delta$) and approximating the \mathbf{r} -integration over the superfluid velocity field of the vortex lattice by that of a single vortex (assuming $H \ll H_{c2}$) with cutoff $d = 1/\sqrt{eH}$ given by the half-distance between two vortices (Won and Maki, 2001a). It is important to note that the averaging of the Doppler shift energy has to be done simultaneously in \mathbf{r} and \mathbf{k} . The field (angle-)dependent specific heat C_s , spin susceptibility χ_s and superfluid density are then given by

$$\frac{C_s(\mathbf{H})}{\gamma T} = \frac{\chi_s(\mathbf{H})}{\chi_n} = g(0, \mathbf{H}) \quad \text{and} \quad \frac{\rho_s(\mathbf{H})}{\rho_s(0)} = 1 - g(0, \mathbf{H}). \quad (48)$$

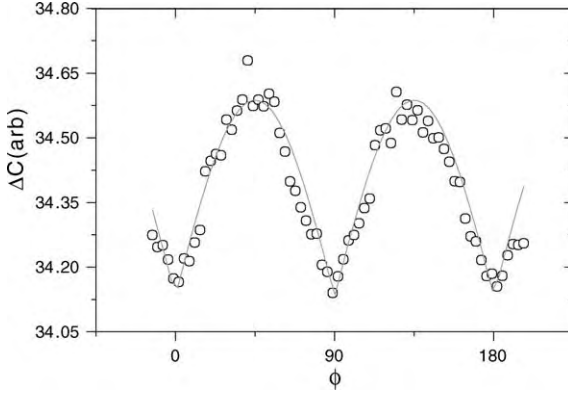


Fig. 12. Specific heat oscillation $\Delta C(\phi)$ in $\text{YNi}_2\text{B}_2\text{C}$ for field \mathbf{H} in the ab -plane as function of the azimuthal field angle ϕ . Full line is a fit using a phenomenological cusp function (Park et al., 2003).

The explicit expression for $C_s(H, \theta, \phi)$ depends on the node structure of $\Delta(\mathbf{k})$ and is obtained as

$$C_s(H, \theta, \phi)/\gamma T = \frac{\tilde{v}\sqrt{eH}}{\Delta} I(\theta, \phi). \quad (49)$$

Where for example for the d-wave order parameter with $f(\mathbf{k}) = \cos(2\varphi)$ and two orthogonal line nodes parallel to c one has for planar magnetic field (Won and Maki, 2000)

$$I\left(\frac{\pi}{2}, \phi\right) \simeq 0.95 + 0.028 \cos(4\phi). \quad (50)$$

Thus the specific heat should exhibit a four-fold oscillation with field rotation in the ab -plane with a minimum in the nodal and the maximum in the anti-nodal direction. The amplitude of the oscillation is not large because of the \mathbf{k} -averaging in eq. (47) along the node line. It may be larger for a gap function with point nodes as in the case of borocarbides which is discussed in detail in sect. 5. This has been experimentally investigated by Park et al. (2003) as shown in fig. 12. It also shows the typical cusp-like minima of point nodes as opposed to smooth minima observed for gap functions with line nodes. The smoothing is also due to the additional averaging along the line node. A most significant result is the observed \sqrt{H} dependence of the specific heat magnitude which is also a fingerprint of nodal superconductivity (fig. 55). However one must keep in mind that this should be observed for $H \ll H_{c2}$, a global approximate behaviour over the whole field range as sometimes found in conventional superconductors has no relation to the above effect.

Similar field-angle dependence of thermal conductivity can be calculated starting from the Ambegaokar–Griffin formula generalized to anisotropic gap functions. In the d-wave case one obtains in the superclean limit (Won and Maki, 2000).

$$\frac{\kappa_{xx}}{\kappa_n} = \frac{2}{\pi} \langle x \rangle^2 = \frac{2}{\pi} \frac{\tilde{v}^2 e H}{\Delta^2} I\left(\frac{\pi}{2}, \phi\right)^2. \quad (51)$$

Due to the magnetic field there is also an off-diagonal ‘thermal Hall conductivity’ κ_{xy} which has been identified in high- T_c compounds (Ocana and Esquinazi, 2002). The four-fold oscil-

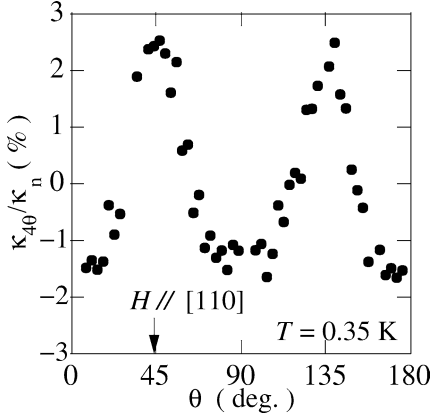


Fig. 13. Thermal conductivity $\kappa_{xx}(\phi)$ for field in the ab -plane as function of the azimuthal angle ϕ for CeCoIn₅ (Izawa et al., 2001a). A four-fold oscillation compatible with $d_{x^2-y^2}$ SC state is clearly seen.

lations in $\kappa_{xx}(\phi)$ have been found in the HF superconductor CeCoIn₅ with node directions $\phi = 0, \frac{\pi}{2}$ corresponding to maxima in $\kappa_{xx}(\phi)$ in the anti-nodal directions $\phi = \pm \frac{\pi}{4}$ as shown in fig. 13. This lead to the proposal of a $d_{x^2-y^2}$ gap functions as in high- T_c compounds. For this geometry, where both field and heat current are in the ab -plane, there is also a term that shows a two-fold rotation $\sim \cos(2\phi)$ which is possibly due to the heat current contribution of vortex core states. This contribution is zero or finite for heat current perpendicular or parallel to vortex lines, respectively. Therefore a more favorable geometry is to rotate the field around the heat current direction, e.g., measuring κ_{zz} as function of the azimuthal angle for a given polar angle θ . In this case only oscillations due to the nodes should appear. Various examples will be discussed later (sects. 4.1, 5 and 6).

Finally we note that the field angle-oscillations in specific heat and thermal conductivity cannot be explained by normal state Fermi surface effects. Calculations based on the Kubo formula indicate that the angle variation of thermal conductivity is determined by the anisotropy of the gap function and not by that of the Fermi velocity which enters only as secondary effect. This can be checked experimentally by measuring the angle dependence in the *normal* state for fields above H_{c2} . Also the (planar) angle dependence of H_{c2} is usually of a few percent and for fields $H \ll H_{c2}$ this does not contribute significantly to the angle dependence of the thermal conductivity.

The field angle dependence of specific heat and thermal transport in the vortex phase have revolutionized the investigation of superconducting gap structure in nodal superconductors. Many ambiguities from the previous methods which have persisted over years have been resolved in a short time. This method certainly has enormous potential, it remains to be seen whether it can also be tried for other quantities, e.g., ultrasonic attenuation in the vortex phase as function of magnetic field direction.

2.3.3. Detection of density wave type order parameters

Density wave order parameters are of ‘diagonal long range order’ (DLRO) type and correspond to the expectation value of a physical observable, i.e., the charge or spin density op-

erator in eq. (32). Their gap functions for e-h pair states are determined by self-consistent equations formally identical to the BCS gap equations as obvious from eq. (36). The physical meaning of the gap function in the e-h pairing case becomes clear by calculating the expectation values of charge (C) and spin (S) densities in eq. (32):

$$\langle \rho_{\mathbf{Q}} \rangle = \sum_{\mathbf{k}} \Delta_C(\mathbf{k}) F(\mathbf{k}) \quad \text{and} \quad \langle M_{\mathbf{Q}}^z \rangle = \sum_{\mathbf{k}} \Delta_S(\mathbf{k}) F(\mathbf{k}) \quad (52)$$

with $F(\mathbf{k}) = \tanh(E_{\mathbf{k}}/2T)/2E_{\mathbf{k}}$ and $E_{\mathbf{k}} = \sqrt{\epsilon(\mathbf{k})^2 + \Delta_i(\mathbf{k})^2}$ ($i = C, S$) denoting the quasi-particle energy and the gap functions $\Delta_i(\mathbf{k})$ are given by eq. (30).

Conventional density waves: In the conventional ‘s-wave’ CDW and SDW case with \mathbf{k} -independent gap functions $\Delta_{C,S}(\mathbf{k}) = \Delta$ the sum in eq. (52) leads to a finite charge or spin density Fourier component for the modulation vector \mathbf{Q} . This also holds for a fully symmetric (A_{1g}) gap function which is \mathbf{k} -dependent but satisfies $\Delta(g\mathbf{k}) = \Delta(\mathbf{k})$ for any group element $g \in G$. Due to nonvanishing $\langle \rho_{\mathbf{Q}} \rangle$ and $\langle M_{\mathbf{Q}}^z \rangle$ conventional CDW and SDW states are straightforward to identify because macroscopic densities either couple to the electric and magnetic fields of external probes or, as in the case of CDW, lead to observable distortions of the underlying crystal lattice. In neutron and (magnetic) X-ray diffraction experiments one can therefore observe additional lattice or magnetic superstructure Bragg reflections that originate in the scattering from density modulations $\langle \rho_{\mathbf{Q}} \rangle \cos(\mathbf{Q} \cdot \mathbf{r})$ and $\langle M_{\mathbf{Q}}^z \rangle \cos(\mathbf{Q} \cdot \mathbf{r})$. This is the standard method to observe broken spatial and time reversal symmetries, i.e., structural and magnetic phase transitions. There are also numerous other physical quantities, both static and dynamic which are affected by the appearance of conventional CDW and SDW modulations for which we refer to the book by Grüner (1994) and references cited therein.

Unconventional density waves: These order parameters also correspond to DLRO of density operators but the gap functions $\Delta_{\mathbf{k}}$ now belong to a nontrivial representation of G sometimes called ‘unconventional density waves’. In this case there will be elements $g \in G$ with $\Delta(g\mathbf{k}) = -\Delta(\mathbf{k})$ signifying a sign change of $\Delta_i(\mathbf{k})$ between different sectors of \mathbf{k} -space. Under these circumstances cancellation in eq. (52) occurs and macroscopic charge and spin-densities $\langle \rho_{\mathbf{Q}} \rangle$ and $\langle M_{\mathbf{Q}}^z \rangle$ vanish even though the order parameter corresponds to a physical observable (therefore the name convention for these states is misleading). A more formal proof of this cancellation effect was given in Thalmeier (1994). Now one has a perplexing situation of ‘hidden order’. Although there is a condensation of e-h pairs associated with quasiparticle energies and thermodynamic signatures similar to conventional (s-wave) CDW and SDW, the order parameter cannot be identified by the usual diffraction type experiments. This makes the search for such ‘hidden order’ a difficult task, and in fact it has not been unambiguously successful in any specific material. Some of the most prominent candidates for unconventional density waves are: the HF compound URu_2Si_2 (Ikeda and Ohashi, 1998) to be discussed in sect. 4.4; the underdoped pseudo-gap phase of high- T_c materials (Benfatto et al., 2000; Chakravarty et al., 2001); and the organic conductors (Dóra and Virosztek, 2001; Basletic et al., 2002; Korin-Hamzic et al., 2002), especially Bechgaard-salts (Maki et al., 2003a, 2003b). To discuss the properties of unconventional CDW and SDW e-h pair states and

their physical signature we restrict ourselves in the following to the 2D tight binding model with nearest neighbor (n.n.) hopping which in this respect is the only model so far investigated in any detail. In this case the tight-binding band $\epsilon_{\mathbf{k}} = -2t(\cos k_x + \cos k_y)$ has the important perfect nesting property $\epsilon_{\mathbf{k} \pm \mathbf{Q}} = -\epsilon_{\mathbf{k}}$ leading to parallel Fermi surface sections at half filling ($E_F = 0$) as shown in fig. 7. This also leads to a singular behaviour of the DOS according to $N(0) \sim \ln(t/|\epsilon|)$ due to the saddle points (S) of $\epsilon_{\mathbf{k}}$ at $\mathbf{k} = (0, \pm\pi)$ and $(\pm\pi, 0)$. The various possibilities of density wave and superconducting pair states assuming three types of interactions ($U =$ on-site Coulomb, $V =$ n.n. Coulomb, $J =$ n.n. exchange) were studied and classified (Gulacsi and Gulacsi, 1987; Schulz, 1989; Ozaki, 1992). From the many possible phases the most important ones are conventional s-SC, s-CDW, SDW, and unconventional d-SC, d-CDW, SDW states. Historically the latter two states have also been called orbital antiferromagnet (OAF) and spin-nematic (SN) states, respectively (Nersesyan and Vachnadze, 1989; Nersesyan et al., 1991; Gorkov and Sokol, 1992) which points to their physical origin in staggered charge or spin currents on the 2D square lattice, respectively. Their pairing amplitudes or gap functions have a d-wave like \mathbf{k} -dependence given by

$$\Delta_{C,S}^d(\mathbf{k}) = i \Delta_0 (\cos k_x - \cos k_y) \quad (53)$$

and illustrated in fig. 7. The d-wave gaps have nodes which are located at the four ‘Dirac’ points (D) $\mathbf{k} = (\pm\frac{\pi}{2}, \pm\frac{\pi}{2})$. The node points are in ‘orthogonal’ (rotated by $\frac{\pi}{4}$) configuration to the saddle points (S) because at the latter with their singular DOS the gap value of a density wave state (and also SC state) has to achieve maximum value to be stable. In other words the ordered state consists mostly of e-h pairs $(\mathbf{k}, \mathbf{k} + \mathbf{Q})$ with \mathbf{k} close to the saddle point regions. This allows one to study the problem in a simplified continuum theory (Schulz, 1989; Thalmeier, 1996). As indicated the phase of gap functions for d-density waves with commensurate nesting \mathbf{Q} is not arbitrary. Because of the symmetry $\Delta_{C,S}^d(\mathbf{k})^* = -\Delta_{C,S}^d(\mathbf{k})$ the gap function has to be purely imaginary. Due to this property the ordered states are connected with staggered persistent charge (C) or spin (S) currents around the lattice plaquettes. In real space the pattern of currents at the lattice links is indicated in fig. 14.

As a means of identification of d-density wave states one then has to look for signatures of persistent currents in the ground state and for evidence of nodes in the quasiparticle excitation spectrum in thermodynamic and (magneto-)transport properties.

Neutron diffraction: For d-CDW the charge currents break time reversal symmetry while the spin-currents in d-SDW do not (under time reversal both current and spin direction are reversed leaving the spin current invariant), they do, however, break spin rotational symmetry. Therefore d-CDW states may lead to the appearance of staggered *orbital* moments. Because the currents are spread out over a whole plaquette, the generated magnetic fields are of the order ~ 10 G associated with orbital moments $\sim 10^{-2} \mu_B$ per plaquette. The contribution to elastic and inelastic neutron cross section has been discussed (Chakravarty et al., 2001) in context with the d-CDW scenario for the spin gap phase of underdoped cuprates (Chakravarty et al., 2001a), but it is generally valid for the tight binding model used here. While the scattering from spin moments is determined by the form factor $g(\mathbf{q})$ of atomic electron densities which falls off moderately fast with momentum transfer \mathbf{q} , the scattering cross section from

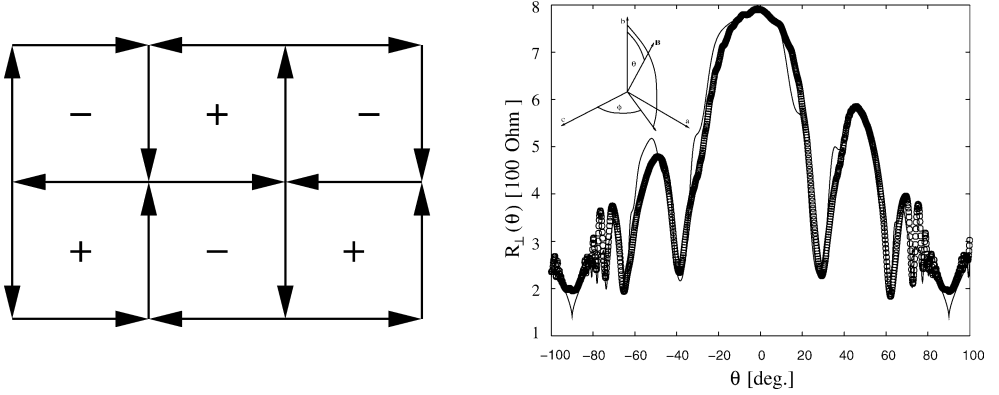


Fig. 14. Left: Illustration of staggered charge or spin current pattern in the square lattice for d-CDW or d-SDW. Right: Magnetoresistance ($\mathbf{j} \perp ac$ -plane) oscillations in the low temperature d-CDW state of the organic quasi-1D conductor α -(BEDT-TTF) $_2$ KHg(SCN) $_4$. The oscillations result from the Landau quantisation of energy levels eq. (55) around the nodal Dirac points in fig. 7. The circles are from experiment ($T = 1.4$ K, $B = 15$ T, $\phi = 45^\circ$), and the full line from d-CDW calculations (Maki et al., 2003a).

orbital moments is determined by the orbital current distribution $\mathbf{j}(\mathbf{q})$, namely proportional to $|\langle \mathbf{j}(\mathbf{q}) \rangle|^2 / q^2 \sim 1/q^4$ which falls off much more quickly with momentum transfer due to the spread-out orbital moment density. Although this method would be rather straightforward it is quantitatively difficult due to the small orbital moment size and only applicable for d-CDW.

A more indirect but more versatile method consists in looking for signatures of the gap nodes in the d-density wave states. For low temperatures $T \ll \Delta$ the nodal regions dominate thermodynamics and transport properties. Specific heat and thermal conductivity is equivalent to that of d-SC which have been discussed before. Susceptibility and frequency dependent electrical conductivity however are characteristic for the d-density wave states. Of course there is no vortex phase and the Doppler shift method cannot be applied.

Giant diamagnetism: The susceptibility has been analysed in detail (Nersesyan and Vachnadze, 1989; Nersesyan et al., 1991). Strong anomalies in the diamagnetic susceptibility for both d-CDW and -SDW are predicted at low fields. This is due to the peculiar conical or ‘relativistic’ quasiparticle spectrum around the nodal Dirac points (D) in fig. 7. For $T \ll \Delta_0$ the spectrum can be linearized and consists of two bands

$$E_{\pm}(\mathbf{k}) = \pm \sqrt{v_F^2 k_x^2 + v_{\Delta}^2 k_y^2} \quad (54)$$

with $v_F = 2\sqrt{2}ta$ and $v_{\Delta} = \sqrt{2}\Delta_0a$ giving the group velocity perpendicular and parallel to the original Fermi surface in fig. 7, respectively, which are related to the effective mass via $m^* = \Delta_0/2v_Fv_{\Delta}$. Here the lower band (–) is completely filled and the upper band (+) empty, thus the Fermi surface in the ordered state ($\Delta_0 > 0$) consists of two inequivalent points $\mathbf{k}_{1,2} = (\frac{\pi}{2}, \pm \frac{\pi}{2})$, the other Dirac points are equivalent since \mathbf{Q} is now a reciprocal lattice vector. The

linearization corresponds to restricting to a $(2 + 1)$ -dimensional continuum field theory of chiral massless relativistic fermions with ‘anisotropic’ velocities v_F and v_Δ (Nersisyan and Vachnadze, 1989). The quasiparticle DOS close to the Fermi level $E_F = 0$ is given by $N(E) = |E|/(\pi v_F v_\Delta)$ therefore one has low- T power laws $C \sim T^2/(t \Delta_0)$ and $\chi_P^\parallel \sim \mu_B^2 T/\Delta_0$ for the specific heat and the in-plane spin susceptibility. The most striking effect however should appear in the diamagnetic susceptibility anomaly caused by the persistent plaquette currents. This is obtained through the relativistic Landau quantisation of the spectrum which leads to Landau levels

$$E_n^\pm = \pm \sqrt{|\Omega_\perp| n} \quad \text{and} \quad \Omega_\perp = 2eH_\perp v_F v_\Delta / c \quad (55)$$

which have a degeneracy $\nu(H) = |eH|/2\pi c$ (c = speed of light) per unit area. Furthermore, $H_\perp = H \cos \theta$ where θ = polar field angle with respect to the plane normal vector $\hat{\mathbf{n}}$. This equation holds for fields with $\sqrt{|\Omega_\perp|} \ll \Delta_0$. From eq. (55) the H -dependent total energy is obtained leading to a (2D) diamagnetic susceptibility

$$\chi_{2D} \sim \frac{\sqrt{\Delta_0}}{|H|^{1/2}} \cos^{3/2} \theta \quad (56)$$

which predicts an enhancement factor of $(\Delta_0/\Omega_c) \gg 1$ compared to the normal state diamagnetic susceptibility. The divergence in eq. (56) will be arrested below a tiny crossover field where 3D behaviour due to interlayer hopping sets in and perfect diamagnetism with $\chi_{3D}(H \rightarrow 0) = -1/4\pi$ will be approached. Thus for temperatures $T \ll \Delta_0$ and almost zero field the staggered currents of d-CDW or SDW should achieve a similar perfect screening effect as supercurrents in the d-SC state.

The conical quasiparticle spectrum and associated ‘relativistic’ Landau quantisation should also leave its mark on the (magneto-)resistance which we only briefly mention since so far it has only been applied to d-CDW candidates among quasi-1D organic conductors. In this case a finite carrier concentration ($|E_F| > 0$) should be present. This is achieved by including a finite next-nearest-neighbor (n.n.n.) hopping element t' in the model. It does not appear in the linearized spectrum eq. (55) however. Analogous to the susceptibility, the magnetoresistance is determined by the Landau levels of the d-CDW state leading to typical oscillations (fig. 14) in its angular dependence which have been identified in two examples (Dóra et al., 2002; Basletic et al., 2002; Maki et al., 2003a).

Finite frequency probes: Finally we discuss finite frequency probes for d-DW states like optical conductivity (Yang and Nayak, 2002). It exhibits non-Drude like behaviour at low frequencies because of arbitrary low excitation energies for $\mathbf{q} = 0$ interband ($E_- \leftrightarrow E_+$) transitions at the nodal (Dirac) points. For perfect nesting ($E_F = 0$) at low temperatures one obtains (for $\omega\tau \gg 1$, τ = quasiparticle lifetime)

$$\sigma(\omega, T) = (\ln 2)e^2 \alpha T \delta(\omega) + \frac{1}{8}e^2 \alpha \left| f\left(-\frac{\omega}{2}\right) - f\left(+\frac{\omega}{2}\right) \right|, \quad (57)$$

where $\alpha \simeq (v_F/v_\Delta)$ and f denotes the Fermi function. The first part is the Drude term and the second is the interband term which should extend to arbitrary low frequencies and contribute

to the d.c. conductivity because of the vanishing gap at the node points. The weight of the Drude peak vanishes for $T \rightarrow 0$ while the interband contribution stays finite at zero frequency. Since the thermal conductivity has only a Drude contribution, the Wiedemann–Franz law $\kappa \sim \sigma T$ should be strongly violated in the d-DW state and one would rather expect $\kappa \sim \sigma T^2$. This result holds as long as $E_F < kT$ and also for finite quasiparticle scattering rate $\Gamma = 1/\tau$ if $\Gamma < E_F$. In addition the d-DW state may lead to anomalous field dependence of electrical and thermal Hall conductivity.

The peculiar excitation spectrum eq. (55) of a d-DW should also leave its imprint in the inelastic neutron scattering cross section (Chakravarty et al., 2001) which is proportional to the imaginary part of the dynamical spin susceptibility.

3. Ce-based heavy-fermion superconductors

The discovery of superconductivity in CeCu_2Si_2 by Steglich et al. (1979) initiated the rapid development of heavy fermion physics. For nearly two decades, this material was the only Ce-based heavy-fermion superconductor at ambient pressure. Only recently, superconductivity at ambient pressure was found in the new class of heavy-fermion materials $\text{Ce}_n\text{M}_m\text{In}_{3n+2m}$ where M stands for the transition metal ion Co, Ir or Rh and $m = 1$ while $n = 1$ or $n = 2$ (Thompson et al., 2001). Typical examples are CeCoIn_5 (Petrovic et al., 2001b) and CeIrIn_5 (Petrovic et al., 2001a).

The SC phases are characterized by BCS-type pair correlations among the heavy quasiparticles. In addition the strong on-site correlations introduced by the partially filled Ce-4f shells are reflected in several aspects. Firstly, the SC gap functions are anisotropic due to the local quasiparticle repulsion. Secondly, the competition between the non-magnetic Fermi liquid state and magnetically ordered phases leads to pronounced strong-coupling effects. They highlight the complex low-frequency dynamics in these systems which result from the competition between Kondo effect and long-range magnetic order.

The main emphasis of the current experimental and theoretical studies is on the fundamental question which factors actually determine the low-temperature phases, i.e., when does a Ce compound become a heavy-fermion superconductor or why does it order magnetically. The subtle interplay between Kondo effect and long-range magnetic order can be monitored experimentally in pressure studies where isostructural relatives of the heavy-fermion superconductors are tuned from magnetic phases at ambient pressure to superconducting states. Similar behavior is found in doping experiments where constituents of the metallic host are successively replaced. Examples for pressure-induced superconductors are CeCu_2Ge_2 (Jaccard et al., 1992), CePd_2Si_2 (Grosche et al., 1996; Mathur et al., 1998), CeNi_2Ge_2 (Grosche et al., 2000) and CeRh_2Si_2 (Movshovich et al., 1996), CeSn_3 (Walker et al., 1997) and CeIn_3 (Grosche et al., 1996).

Finally, a different type of competition between superconductivity and magnetic order may be realized in CeCu_2Si_2 . In this compound, the strongly renormalized Fermi liquid seems to be unstable with respect to the formation of both superconducting pairs and an (incommensurate)

spin-density wave. The actual ground state depends sensitively on the composition of the sample.

In the present section, we review the properties of the stoichiometric Ce compounds exhibiting competition between heavy-fermion superconductivity and long-range magnetic order. We shall not discuss the highly complex phase diagrams obtained in alloy systems. In addition, we summarize recent attempts at a theoretical description of the complex low-frequency dynamics resulting from the competition between Kondo effect and RKKY interaction.

3.1. CeM_2X_2

The archetype heavy-fermion superconductor $CeCu_2Si_2$ as well as the pressure-induced superconductors $CeCu_2Ge_2$, $CePd_2Si_2$, $CeNi_2Ge_2$ and $CeRh_2Si_2$ crystallize in the tetragonal $ThCr_2Si_2$ structure. The unit cell is shown in fig. 15. The isostructural compounds CeM_2X_2 with $M = Ru, Ni, Pd, Cu, Ag, Au$ and $X = Si, Ge$ exhibit a great variety of possible ground states and have been extensively studied to clarify the interplay between the formation of magnetic order and heavy fermion behavior.

3.1.1. *Electronic properties, Fermi surfaces and heavy quasiparticles*

To study the electronic structure, we compare the results for two different models treating the Ce 4f degrees of freedom as localized (atomic-like) states and as delocalized yet strongly renormalized electrons. The first procedure provides a good quantitative description of the properties at elevated temperatures, high excitation energies, and above the metamagnetic transition. The latter ansatz yields a model for the Fermi liquid state.

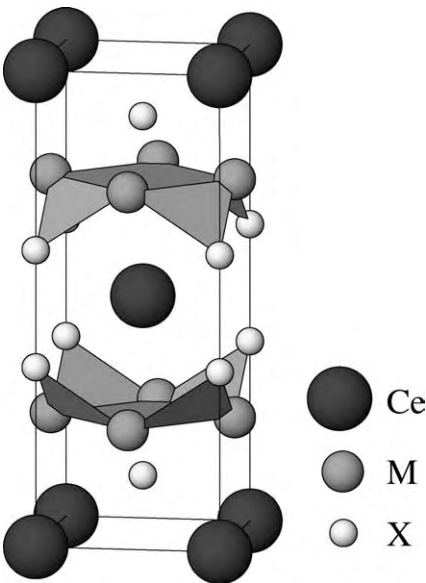


Fig. 15. Conventional unit cell of the $ThCr_2Si_2$ structure of CeM_2X_2 where $M = Cu, Ni, Ru, Rh, Pd, Au, \dots$ and $X = Si, Ge$. This is also the unit cell of URu_2Si_2 (sect. 4.4).

With respect to the electronic properties, the compounds CeM_2X_2 fall into two distinct categories, the key feature being the presence or absence of transition metal d-states at the Fermi level. We apply this criterion to classify the CeM_2X_2 compounds exhibiting superconductivity. The first group is formed by CePd_2Si_2 , CeNi_2Ge_2 and CeRh_2Si_2 which have a large conduction electron density of states at the Fermi level. A well-studied model for the normal state of these systems is provided by CeRu_2Si_2 which we shall consider in detail below. The macroscopic properties of this compound closely resemble those of CeNi_2Ge_2 and CePd_2Si_2 . The general conclusions derived for CeRu_2Si_2 should therefore apply also to the pressure-induced superconductors. The second group is given by CeCu_2Si_2 and CeCu_2Ge_2 where the metal d-bands are filled.

The low-temperature behavior of CeRu_2Si_2 is well described by a paramagnetic Fermi liquid with weak residual interactions. The relevant low-energy excitations are heavy quasiparticles as inferred from the linear specific heat coefficient $\gamma \simeq 350 \text{ mJ/mol K}^2$ (Steglich et al., 1985). The electronic structure was calculated both for the local moment regime at high temperatures and for the Fermi liquid state. Both types of calculations start from ab-initio crystal potentials which are determined self-consistently within the LDA. Details of the calculation can be found in Runge et al. (1995). In the local moment regime, the Fermi surface is determined exclusively by the conduction states. The strongly renormalized Fermi liquid state, on the other hand, is described by the renormalized band method using $\Delta_f \simeq 10 \text{ K}$ in eq. (7) for the intrinsic width of the quasiparticle band. The value is consistent with inelastic neutron data (Regnault et al., 1988) as well as thermopower and specific heat data (Steglich, 1985). CEF effects are accounted for by adopting a Γ_7 ground state. The details of the calculation are described in Zwicky (1992).

The renormalized band scheme gives the correct Fermi surface topology for CeRu_2Si_2 and thus consistently explains the measured dHvA data (Zwicky et al., 1990; Zwicky, 1993). The Fermi surface consists of five separate sheets among which are four closed hole surfaces centered around the Z-point. The remaining one is a complex multiply-connected surface where extremal orbits of rather different character exist. In particular, one can find typical particle-like orbits as well as others for which a hole picture would be more appropriate. The agreement between calculated and experimental results with respect to general topology is rather good (for further details see (Zwicky, 1992, 1993)).

The character of quasiparticles in CeRu_2Si_2 varies quite strongly over the Fermi surface. There are three Z-centered hole ellipsoids with rather light quasiparticles. The states on the pillow-shaped Z-centered hole surface displayed in fig. 16, however, have predominantly f-character and therefore yield the dominant contribution to the specific heat. Experimentally, one finds heavy and light quasiparticles coexisting on the multiply-connected sheet.

The validity of the Fermi liquid picture is concluded from a comparison of the effective masses on the fourth pillow-shaped sheet as given in table 2. From the large linear specific heat the renormalized band scheme deduces a characteristic energy $kT^* \simeq 10 \text{ K}$ which in turn implies heavy masses of the order of $m^*/m \simeq 100$. This value was confirmed by experiments (Albessard et al., 1993; Aoki et al., 1993; Tautz et al., 1995) where the ψ orbit with $m^*/m \simeq 120$ was observed. The corresponding Fermi surface cross section is in agreement with estimates from the renormalized band theory. This proves that the heavy quasiparticles

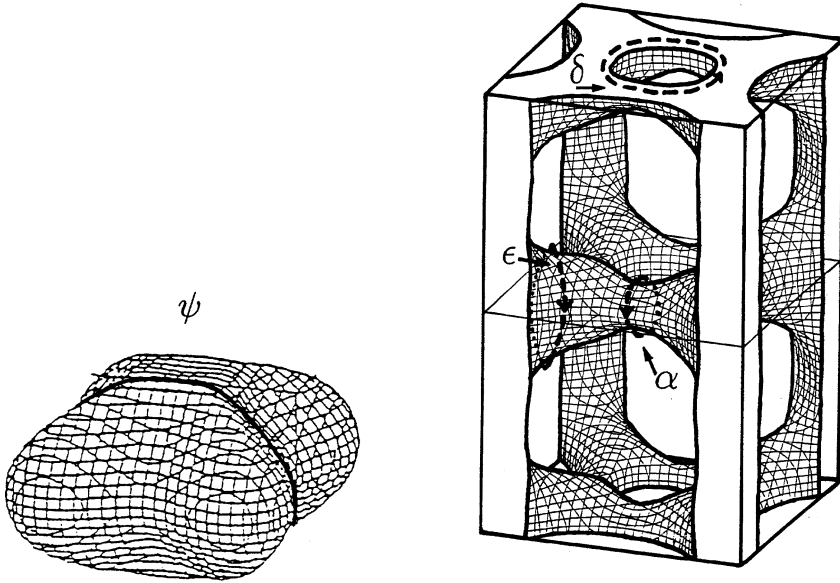


Fig. 16. CeRu_2Si_2 : Fermi surface sheets for quasiparticles with f-character. The labels ψ and α , δ , ϵ refer to the branches observed in dHvA experiments (Lonzarich, 1988; Albessard et al., 1993). Left: Hole surface centered around the Z-point of the Brillouin zone with effective mass $m^* \sim 100m$ which dominates the specific heat γ -value. For localized f-electrons at elevated temperatures, the hole surface expands extending to the boundaries of the Brillouin zone while the multiply connected electron-like surface shrinks. The expansion of ψ is confirmed by photoemission experiments. Right: Multiply-connected electron-like sheet.

Table 2

CeRu_2Si_2 : Effective masses of the heavy quasiparticles. Comparison of experiment (Albessard et al., 1993) and theory (Zwicknagl et al., 1990). The heavy quasiparticles explain the specific heat at low temperatures. There are no further low-energy excitations involved

ψ	Experiment	Theory (approx.)
area [MG]	53.6	62
m^*/m	120	100

exhaust the low-energy excitations associated with the f-states in HF systems. The shape of the Fermi surface of heavy quasiparticles implies the existence of nesting vectors. This fact suggests that the Fermi liquid state might become unstable with respect to particle-hole pairing, leading for example to the formation of a SDW state.

The change in the volume of the Fermi surface when going from $T \ll T^*$ to $T \gg T^*$ is observed by comparing the Fermi surface of CeRu_2Si_2 to that of its ferromagnetic isostructural counterpart CeRu_2Ge_2 where the f-states are clearly localized. In a series of beautiful experiments (King and Lonzarich, 1991) it was demonstrated that the Fermi surfaces of these two compounds are rather similar. However, the enclosed Fermi volume is smaller in the case

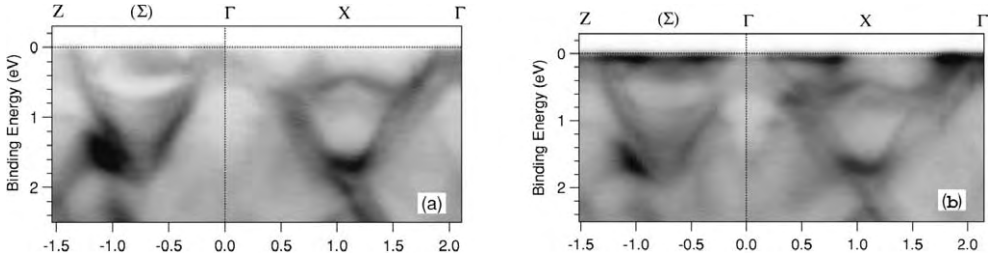


Fig. 17. Photoemission results for LaRu_2Si_2 (a) in comparison to CeRu_2Si_2 (b) at $T = 25$ K above the Kondo temperature $T^* = 15$ K of CeRu_2Si_2 . Band structures are similar for both compounds (Denlinger et al., 2001).

of CeRu_2Ge_2 , the difference being roughly one electron per unit cell. More direct evidence is provided by recent photoemission experiments (see fig. 17). Denlinger et al. (2001) have shown that at temperatures around 25 K, the Fermi surface of CeRu_2Si_2 , is that of its counterpart LaRu_2Si_2 which has no f-electrons.

The similarity of the Fermi surface topologies for localized and itinerant Ce 4f states is a characteristic feature of the CeM_2X_2 systems with partially filled M d-bands. In addition, we mention that the topology of the Fermi surface for the heavy quasiparticles is qualitatively reproduced by standard band structure calculations based on the LDA (Zwicknagl, 1988).

This, however, is not the case for CeCu_2Si_2 . As the Cu d-bands are filled there are only two major two-fold degenerate bands crossing the Fermi energy, and the effective hybridization becomes rather anisotropic. To calculate the quasiparticle bands in CeCu_2Si_2 by means of the renormalized band method, we adopt the doublet-quartet CEF scheme suggested by Goremychkin and Osborn (1993). The ground state is separated from the excited quartet by $\delta \simeq 340$ K.

The results for the Fermi surface (Zwicknagl and Pulst, 1993; Pulst, 1993) can be summarized as follows: two separate sheets of the Fermi surface for heavy and light quasiparticles are found. The light quasiparticles have effective masses of the order of $m^*/m \simeq 5$. They can be considered as weakly renormalized conduction electrons and the corresponding Fermi surface is rather similar to the LDA prediction (Harima and Yanase, 1991). The observed Fermi surface cross sections (Hunt et al., 1990) can be explained by both the renormalized band structure as well as by the LDA bands. There is, however, a characteristic difference between the Fermi surfaces for the light quasiparticles as derived from the two schemes: The LDA calculation predicts a small closed surface centered around the Γ -point which is absent in the dHvA-experiment although the corresponding cross sections are rather small and the masses are expected to be light.

Of particular interest are heavy quasiparticles of effective masses $m^*/m \simeq 500$ which are found on a separate sheet. The topology of this surface is rather different from the corresponding LDA result as can be seen from fig. 18. It mainly consists of columns parallel to the tetragonal axis and small pockets. The topology of the Fermi surface suggests that the strongly correlated Fermi liquid state should become unstable at sufficiently low temperatures. Firstly, it exhibits pronounced nesting features which may eventually lead to the formation of a ground

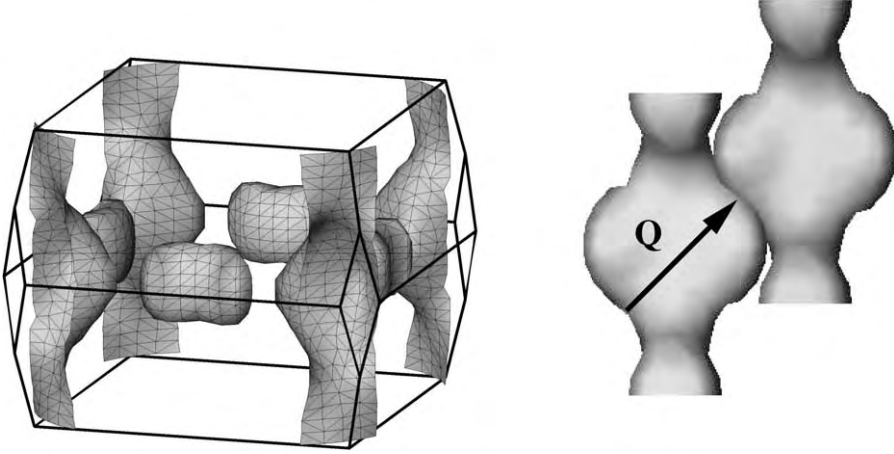


Fig. 18. CeCu_2Si_2 : Left: FS of heavy quasiparticles ($m^*/m \simeq 500$) calculated by using the renormalized band method. It consists of ellipsoids and modulated columns which are oriented parallel to the tetragonal axis. The calculations adopt the CEF scheme suggested by Goremychkin and Osborn (1993) consisting of a singlet ground state separated from an excited quartet by a CEF splitting $\delta \sim 340$ K. Therefore $\delta \gg T^* \simeq 10$ K (obtained from the γ -value). Consequently quasiparticle properties are strongly anisotropic. The topology of the renormalized band FS differs qualitatively from LDA results. Right: Enlarged FS columns exhibiting nesting in a column with a nesting vector $\mathbf{Q} = (0.23, 0.23, 0.52)$ (Zwicky and Pulst, 1993).

state with a spin density modulation. This will be discussed in detail below. Secondly, the topology of this surface depends rather sensitively on the position of the Fermi energy. The band filling and hence the f -valence are critical quantities. Reducing the f -occupancy from the initial value of $n_f \simeq 0.95$ by $\sim 2\%$ leads to changes in the topology as shown by Pulst (1993) and Zwicky and Pulst (1993). As a result, the quasiparticle density of states (DOS) should exhibit rather pronounced structures in the immediate vicinity of the Fermi energy which, in turn, can induce instabilities (Kaganov and Lifshits, 1979).

An external magnetic field couples to the f -degrees of freedom. It leads to a Zeeman splitting of order $\mu_{\text{eff}}B$ of the heavy quasiparticle bands and hence can move the structures in the DOS relative to the Fermi energy. The effective moment μ_{eff} of the f -states which contains the CEF effects depends on the direction of the external magnetic field. From the renormalized band calculation we determine the values of the critical magnetic fields when the pronounced structures are moved to the Fermi energy. Due to CEF effects on the f -states this critical value of the external magnetic field will depend upon its orientation. The explicit values of the critical fields B_{crit}^c and B_{crit}^a for field directions parallel to the c - and a -axes as listed in table 3 agree rather well with the observed critical magnetic fields for the transition into the ‘ B -phase’ (see fig. 19).

Having discussed the basic electronic structure of the CeM_2X_2 heavy fermion compounds we now turn to their low-temperature properties.

Table 3

Low-temperature values of the critical magnetic fields for the transition into the high-field ‘ B -phase’. Comparison with experiment of the renormalized band prediction for the approximate critical magnetic fields for field directions along the tetragonal axis (B_{crit}^c) and in the basal plane (B_{crit}^a) (Zwicknagl and Pulst, 1993)

Critical field	Renormalized bands	Experiment
B_{crit}^a [T]	8.0	7.0
B_{crit}^c [T]	6.5	4.0

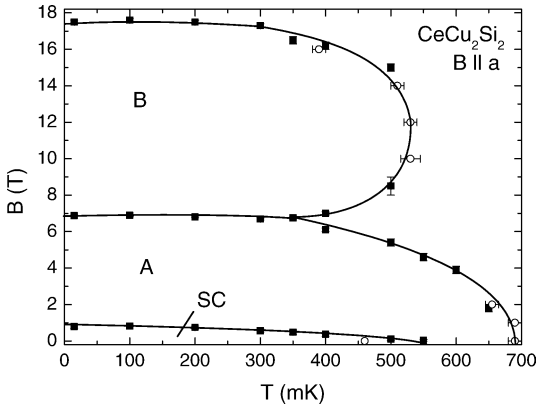


Fig. 19. B - T phase diagram of CeCu_2Si_2 for $B \parallel a$. The original version of this phase diagram is from Bruls et al. (1994) while the completed version is from Weickert et al. (2004). For this sample the A-phase is expelled from the SC region (no co-existence).

3.1.2. Superconductivity and itinerant antiferromagnetism in CeCu_2Si_2

CeCu_2Si_2 exhibits highly complex phase diagrams at low temperatures. This fact partially results from an extreme sensitivity of the physical properties with respect to variations of the stoichiometry. Thorough investigations of the ternary chemical phase diagram (for a review see Steglich et al. (2001)) showed that the actual ground state is mainly determined by the average occupation of the non-f sites surrounding the Ce-ion.

Apart from the composition, the phases are strongly affected by magnetic fields. The B - T -phase diagram (Bruls et al., 1994) for a high-quality single-crystal is displayed in fig. 19. The phase transitions were deduced from anomalies in thermodynamic quantities including the elastic constants, thermal expansion and magnetostriction coefficients. In the low temperature regime, there is a SC phase surrounded by a phase ‘A’ which becomes unstable in high magnetic fields. Similar phase diagrams are obtained from resistivity measurements, e.g. (Steglich et al., 2000a). In addition to these ‘A-SC-type’ crystals, there exist also ‘A-type’ systems which do not superconduct as well as ‘SC-type’ compounds where the A-phase is suppressed (fig. 8). The high-field phase B , on the other hand, is present in all three cases. It is interesting to note that the transition into the B -phase occurs close to the calculated critical fields B_{crit}^a and B_{crit}^c listed in table 3. At these values, the Fermi surface of the heavy quasiparticles is expected to change drastically.

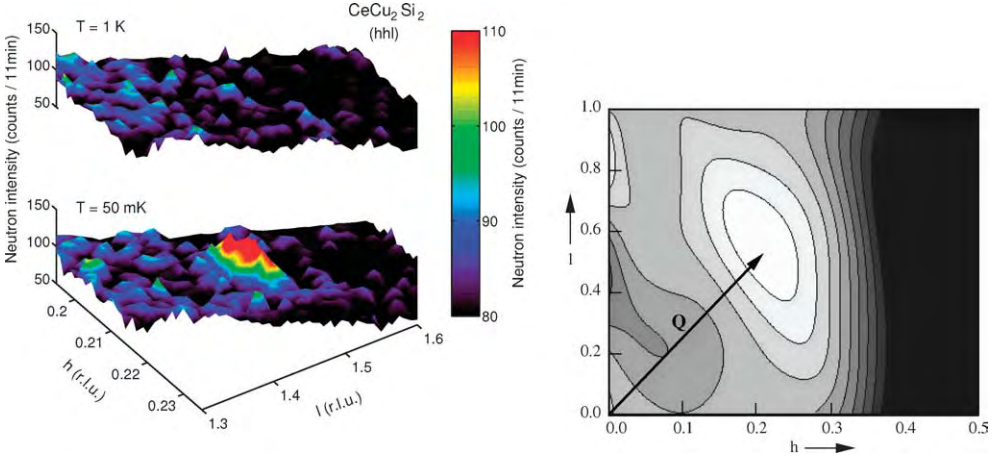


Fig. 20. Left panel: Neutron diffraction intensity in CeCu_2Si_2 at temperatures above and below the A -phase transition temperature T_A . Incommensurate peak corresponds to $\mathbf{Q} = (0.215, 0.215, 0.53)$ (Stockert et al., 2004). Right panel: Nesting of heavy FS columns (fig. 18) leads to a peak in the static susceptibility $\chi(\mathbf{q})$ at $\mathbf{q} = \mathbf{Q}$. The intensity map of $\chi(\mathbf{q})$ (value increasing from dark to bright) in the reciprocal (h, h, l) -plane as calculated for the renormalized bands at $T = 100$ mK. The *experimental* \mathbf{Q} at 50 mK from the left panel shows perfect agreement with the calculated maximum position of $\chi(\mathbf{q})$.

Much effort has been devoted to the characterization of the A -phase which originally had the appearance of another ‘hidden order’ phase. However later the spin density wave character first inferred from resistivity results (Gegenwart et al., 1998) was supported by specific heat and high-resolution magnetization measurements (Steglich et al., 2000). The transition temperature T_A is suppressed by increasing the 4f-conduction electron hybridization and eventually vanishes. This can be achieved by applying hydrostatic pressure or choosing a few percent excess of Cu. The ordered moments are expected to be rather small. The propagation vector \mathbf{Q} can be estimated by extrapolation from neutron diffraction studies in single-crystalline $\text{CeCu}_2(\text{Si}_{1-x}\text{Ge}_x)_2$. The central result is that the wave vector of the magnetic order changes only slightly with the Ge concentration while the ordered moment per Ce site, however, decreases strongly from $\mu \simeq 0.5\mu_B$ for $x = 0.5$ to $\mu \simeq 0.1\mu_B$ for $x = 0$.

Recent neutron scattering experiments (Stockert et al., 2004) (fig. 20) for the stoichiometric compound ($x = 0$) show a spin density wave which forms below $T_N \simeq 0.7$ K. The experimental propagation vector \mathbf{Q} is close to $(0.215, 0.215, 0.53)$ and the ordered moment amounts to $\mu \simeq 0.1\mu_B$. The instability of the Fermi liquid state with respect to the SDW state follows from the nesting properties of the heavy quasiparticle surface shown in fig. 18 which leads to a peak at $\mathbf{q} = \mathbf{Q}$ in the static susceptibility $\chi(\mathbf{q})$ with \mathbf{Q} close to the above experimental value (fig. 20).

3.1.3. Pressure-induced superconductivity in CePd_2Si_2 and CeNi_2Ge_2

The compounds CeNi_2Ge_2 and CePd_2Si_2 offer the possibility for studies of the antiferromagnetic instability in a heavy-fermion system. In the vicinity of the quantum critical point, non-

Fermi liquid behaviour and superconductivity are observed. At ambient pressure, CePd₂Si₂ orders in an antiferromagnetic structure below a Néel temperature $T_N \simeq 8.5$ K. The magnetic structure is characterized by a propagation vector $\mathbf{Q} = (1/2, 1/2, 0)$. The ordered moment lying in the basal plane is reduced to $\sim 0.66\mu_B$ by CEF effects and possibly Kondo screening (van Dijk et al., 2000). The coefficient of the linear specific heat $\gamma \simeq 250$ mJ/mol K² and the quasielastic line width suggest a Kondo temperature $T^* \simeq 10$ K which is close to the Néel temperature T_N . The interplay between the Kondo effect and the RKKY interaction is reflected in the depression of T_N with increasing pressure. The antiferromagnetic order is suppressed by a critical pressure p_c between 28 and 29.5 kbar. There is a superconducting phase between 23 and 33 kbar with a maximum $T_c \simeq 290$ K close to p_c . This fact indicates that the appearance of superconductivity should be related to the magnetic instability (Demuer et al., 2001).

CeNi₂Ge₂ has a slightly smaller lattice constant than CePd₂Si₂ and exhibits non-Fermi liquid behavior at ambient pressure (Gegenwart et al., 1999). No phase transition is found down to lowest temperatures. However magnetic correlations appear gradually with decreasing temperature (Fak et al., 2000). They have a characteristic energy of 4 meV and an incommensurate wave vector $\mathbf{Q} = (0.23, 0.23, 0.5)$ which is rather similar to the ordering vector in CeCu₂Ge₂. They also exhibit quasi-two-dimensional character with strong correlations between moments in the [110] planes. The electronic structure was recently studied by angle-resolved photoemission (Ehm et al., 2001). The low-temperature data ($T \simeq 20$ K) exhibit strongly dispersing bands in agreement with LDA band structure calculations. Close to the Fermi level two features with high spectral intensity can be distinguished one of which has predominantly Ni-3d character. The other one can be assigned to a non-dispersive Kondo resonance. These findings indicate that CeNi₂Ge₂ is in the intermediate temperature regime below the single-site Kondo temperature T^* and above the coherence temperature where extended heavy band states form. The magnetic moments of the Ce ions are already screened by the Kondo effect as indicated by the f-spectral weight at the Fermi level. The coherence between the sites in the periodic lattice, on the other hand, is not yet fully developed.

Traces of possible superconductivity at ambient pressure have been found in resistivity measurements (Steglich et al., 1997; Gegenwart et al., 1999; Grosche et al., 2000). The preliminary phase diagram (Braithwaite et al., 2000) shows that the transition temperature T_c goes through a maximum around 30 kbar and vanishes above 65 kbar. The upper critical field data $H_{c2}(T)$ of the system under pressure are analyzed by comparing them with calculated curves assuming weak coupling in the clean limit. The analysis reveals two interesting points. First, the values of H_{c2} at low temperatures considerably exceed the Pauli limit which indicates the possibility of triplet pairing. Second, the initial slope $(-dH_{c2}/dT)_{T=T_c}$ exhibits only a weak decrease in the range between 0 kbar and 23 kbar which is much weaker than the change expected from the variation of the specific heat.

3.2. CeMIn₅

The compounds CeMIn₅ (M = Co, Ir, Rh) are a newly reported family of heavy fermion systems (Hegger et al., 2000; Petrovic et al., 2001a) which exhibit a superconducting transition

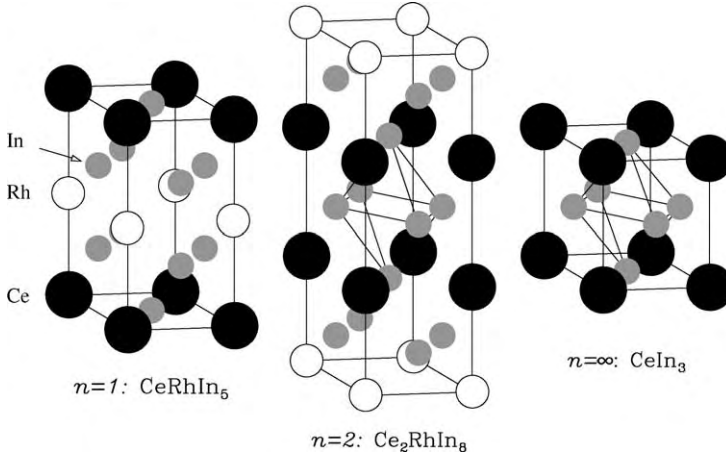


Fig. 21. Unit cell of typical $Ce_nM_mIn_{3n+2m}$ (here for $M = Rh$) compounds which are built from n ‘ $CeIn_3$ ’ and m ‘ MIN_2 ’ subunits stacked along the tetragonal axis. $CeCoIn_5$ has $n = 1$.

at comparatively high temperatures. The values of the critical temperatures reach $T_c = 2.3$ K in $CeCoIn_5$ (Petrovic et al., 2001b). We mention that the isostructural compound $PuCoGa_5$ is the first Pu-based superconductor with $T_c = 18.5$ K (Sarrao et al., 2003). The discovery of this new class of heavy-fermion compounds has opened a way to systematically investigate the evolution from the antiferromagnetic to superconducting state as a function of pressure.

The structurally layered compounds $CeMIn_5$ crystallize in the tetragonal $HoCoGa_5$ -structure (Grin et al., 1979) which is displayed in fig. 21. They belong to the broader family of materials $Ce_nM_mIn_{3n+2m}$ which can be considered as built from ‘ $CeIn_3$ ’ and ‘ MIN_2 ’ layers stacked along the tetragonal c -axis. The infinite-layer parent $CeIn_3$ crystallizes in the cubic $AuCu_3$ structure. The layering introduces pronounced anisotropies in the electronic and structural properties which, in turn, influence the magnetic and superconducting properties as well as the behavior in the quantum critical regime. Varying the stacking sequence, i.e., the parameters n and m , allows for a study of the general role on dimensionality in the competition between the various ground states.

The subsequent section is mainly devoted to the properties of the $n = m = 1$ materials commonly referred to as single-layer systems. We begin, however, by briefly summarizing the properties of the infinite-layer parent $CeIn_3$. At ambient pressure it orders antiferromagnetically at $T_N \simeq 10$ K with an ordering vector $\mathbf{Q} = (0.5, 0.5, 0.5)$ (Morin et al., 1988) and an ordered moment of $0.4\mu_B$. The magnetic ordering temperature decreases monotonically with pressure. In a narrow range around a critical pressure $p_c = 2.6$ GPa resistivity vanishes below the onset temperature at 0.2 K. Recent measurements of T_1^{-1} and the ac-susceptibilities (Kawasaki et al., 2002) confirm the bulk character of superconductivity. The results, however, yield a much lower value $T_c = 95$ mK than the onset temperature. The absence of the coherence peak is taken as evidence of an unconventional pair state.

The single-layer ($n = 1$) members with $M = \text{Rh, Ir, Co}$ and the bilayer ($n = 2$) member with $M = \text{Rh}$ can be considered as pressure variants of the parent CeIn_3 . This is suggested by the lattice constants of CeIn_3 ($a = 4.689 \text{ \AA}$), CeRhIn_5 ($a = 4.652 \text{ \AA}$, $c = 7.542 \text{ \AA}$), CeIrIn_5 ($a = 4.668 \text{ \AA}$, $c = 7.515 \text{ \AA}$), CeCoIn_5 ($a = 4.62 \text{ \AA}$, $c = 7.56 \text{ \AA}$) and Ce_2RhIn_8 ($a = 4.665 \text{ \AA}$, $c = 12.244 \text{ \AA}$). Like the parent, the compounds CeRhIn_5 and Ce_2RhIn_8 order antiferromagnetically at ambient pressure and become pressure-induced superconductors. The magnetic ordering temperatures T_N , however, are reduced while the superconducting transition temperatures T_c are an order of magnitude higher than the maximum value found in CeIn_3 . CeIrIn_5 ($T_c = 0.4 \text{ K}$) and CeCoIn_5 ($T_c = 2.3 \text{ K}$) become superconducting at ambient pressure.

Structure data as well as pressure studies indicate that superconductivity in CeMIn_5 occurs close to a quantum critical point (QCP). The lattice parameters suggest that the antiferromagnetic compound CeRhIn_5 and the superconductor CeCoIn_5 fall on different sides of the QCP in the Doniach phase diagram.

Finally we want to add two comments. The layered crystal structure of the materials seems to suggest that the compounds may be approximately described as 2-dimensional systems. However, this is not justified in view of magnetic properties. Neutron scattering data on CeRhIn_5 and Ce_2RhIn_8 have shown that these materials are magnetically 3-dimensional despite their layered structure. The Fermi surface topologies of the alloys $\text{Ce}_x\text{La}_{1-x}\text{RhIn}_5$ (Alver et al., 2001) are found to be nearly independent of the composition parameter x .

3.2.1. *Electronic properties and Fermi surfaces*

The electronic properties of the CeMIn_5 compounds have been studied theoretically by band structure calculations based on the LDA. Of particular interest are the Fermi surfaces which can be directly compared with experimental dHvA data. The central result is the confirmation of the qualitative picture that Ce 4f-degrees of freedom should be considered as localized moments in CeRhIn_5 (at ambient pressure) while a description in terms of itinerant, strongly renormalized fermions is more appropriate in CeIrIn_5 and CeCoIn_5 . The conclusions are based on the following findings by Shishido et al. (2002) and references therein: For the reference compound LaRhIn_5 without f-electrons the Fermi surface as well as the effective masses of the quasiparticles are well described by the LDA band structure. The quasi-two-dimensional character reflects the tetragonal lattice structure. The topology of the main Fermi surfaces is also in good agreement with that of the Ce-counterpart CeRhIn_5 indicating the localized nature of the Ce-4f electron in this system. A detailed quantitative comparison between calculated and measured cross-sections, however, is difficult due to the complicated antiferromagnetic structure. Angle-resolved photoemission experiments (Fujimori et al., 2003) performed at 15 K showed rather small 4f weight close to E_F . The presence of the localized 4f-states in CeRhIn_5 is reflected in the rather large quasiparticle masses m^* which are enhanced by a factor 7–9 over those of LaRhIn_5 . The Fermi surfaces of LaRhIn_5 and the localised 4f-compound CeRhIn_5 are highly different from those of the HF systems CeIrIn_5 and CeCoIn_5 which are reasonably well explained by the itinerant 4f-band model.

Let us now turn to the properties of the 4f-electrons in the local moment regime. In the tetragonal CEF the degeneracy of the 4f $j = 5/2$ state is lifted. The level scheme has been determined using susceptibility and thermal expansion coefficient data for CeRhIn_5 , CeIrIn_5

and CeCoIn_5 (Takeuchi et al., 2001; Shishido et al., 2002). In all three compounds, the CEF ground state has predominantly $j_z = \pm 5/2$ -character while the first and second excited states are mainly derived from $j_z = \pm 3/2$ - and $j_z = \pm 1/2$ -states. However the CEF level schemes differ with respect to their excitation energies. In the Rh and Ir systems, the $j = 5/2$ -manifold is split into three Kramers doublets with the excitation energies $E(\pm \frac{3}{2}) \sim 60$ K and $E(\pm \frac{1}{2}) \sim 300$ K whereas these excited states are (almost) degenerate in the Co-compound separated by ~ 150 K from the ground state.

Finally, we mention angle-resolved photoemission studies of CeRhIn_5 and CeIrIn_5 (Fujimori et al., 2002a, 2003). The spectral contributions from the ligand states, i.e., from the Rh, Ir and In states, agree rather well with the results of LDA band structure calculations. However, no feature originating from the Ce 4f-states is observed near the Fermi level. This fact may have an explanation within the Kondo scenario: The experiments were carried out at $T = 14$ K which is already equal to the estimated Kondo temperature of CeIrIn_5 given by $T^* \simeq 15$ K.

3.2.2. Unconventional superconductivity in CeCoIn_5

CeCoIn_5 appears to be a typical heavy-fermion material. The effective magnetic moment of $\sim 2.59\mu_B$ as determined at high temperatures ($T > 200$ K) from a polycrystalline average is consistent with the free-ion value for $\text{Ce}^{3+} + (2.54\mu_B)$. The $\rho(T)$ dependence is rather weak above a characteristic temperature $T^* \simeq 30$ K. The crossover to a coherent state is reflected in a rapid decrease at lower temperatures. The electronic contribution to the low-temperature specific heat in the normal state ($T > 2.3$ K) varies linearly $C \sim \gamma T$ with a large coefficient $\gamma \sim 350$ mJ/mol K² indicating substantial mass renormalization (Petrovic et al., 2001a). The normal Fermi liquid becomes unstable at $T_c = 2.3$ K where the heavy quasiparticles form Cooper pairs. This can be seen from the discontinuity in the specific heat with $\Delta C(T_c)/\gamma T_c \simeq 5$ as shown in fig. 22. The enhancement over the universal BCS values for isotropic SC points to pronounced strong coupling effects. The BCS value of 1.43 for isotropic superconductors should be considered as an upper bound on weak-coupling theory which is reduced for anisotropic pair states as obvious from table 1.

The superconducting state seems to be of unconventional d-wave singlet type. The presence of line nodes is inferred from the power-law behavior exhibited by various thermodynamic and transport properties at low temperatures. The latter include the specific heat (Petrovic et al., 2002; Hegger et al., 2000) and NMR relaxation rate (Kohori et al., 2001; Zheng et al., 2001). The most direct evidence, however, is provided by thermal conductivity measurements in a magnetic field rotating within the a - b plane (Izawa et al., 2001; Matsuda and Izawa, 2003) (fig. 13). In addition, the observation of a zero-bias conductance anomaly in point-contact spectroscopy supports the hypothesis of an unconventional pair state (Goll et al., 2003). This is also suggested by the Knight shift measurements of Kohori et al. (2001) which give support for an even singlet SC order parameter with line nodes such as the $d_{x^2-y^2}$ gap function deduced from the above thermal conductivity results or the d_{xy} gap function according to specific heat results (Aoki et al., 2004).

The properties of this unconventional superconductor are of great interest. A first issue is the sensitivity to nonmagnetic impurities which are expected to act as strong pairbreakers. Substitution of Ce-ions with La-ions results in a depression of the transition tempera-

ture T_c (Petrovic et al., 2002). However the measured T_c -reduction is weaker than the value expected for isotropic (s-wave) scatterers in a $d_{x^2-y^2}$ -state. This suggests that La-substitution introduces anisotropic scattering. Anisotropies in the scattering matrix element may strongly reduce pairbreaking as compared with pure s-wave scattering (Fulde and Zwicknagl, 1990; Fulde et al., 1988). The upper critical field H_{c2} is simply reduced by the impurities while its anisotropy remains unaltered.

A magnetic field can suppress superconductivity by acting on the orbits of the charged quasiparticles and by acting on their spins. Both mechanisms determine the upper critical magnetic field $H_{c2}(T)$ which separates the normal state for $H > H_{c2}(T)$ from the superconducting vortex phase at $H < H_{c2}(T)$. The relative importance of the two depairing effects determines the order of the phase transition in a type-II superconductor. While the omnipresent and usually dominating orbital pairbreaking is associated with a second order phase transition, a first order transition is anticipated for dominant spin depairing. In superconductors with sufficiently weak orbital pairbreaking a change from second order at $T_0 < T \leq T_c$ to first order at $T < T_0$ should be observed (for a review see Saint-James et al. (1969)). The crossover, however, was not observed in conventional superconductors due to the presence of strong spin-orbit scattering. CeCoIn₅ appears to be an ideal candidate for the observation of the first order phase transition in a magnetic field. Firstly, it is a very clean type-II superconductor where the orbital pairbreaking is rather weak due to the high effective mass of the quasiparticles. Secondly, the magnetic susceptibility is enhanced which further lowers the Chandrasekhar-Clogston field. The first order phase transition at T_0 shown in the phase diagram of fig. 22 was originally inferred from a step in thermal conductivity by Izawa et al. (2001). It is reflected in a pronounced sharpening of both the specific heat and thermal expansion, a large magnetoelastic effect and a steplike change in the sample volume (Bianchi et al., 2002).

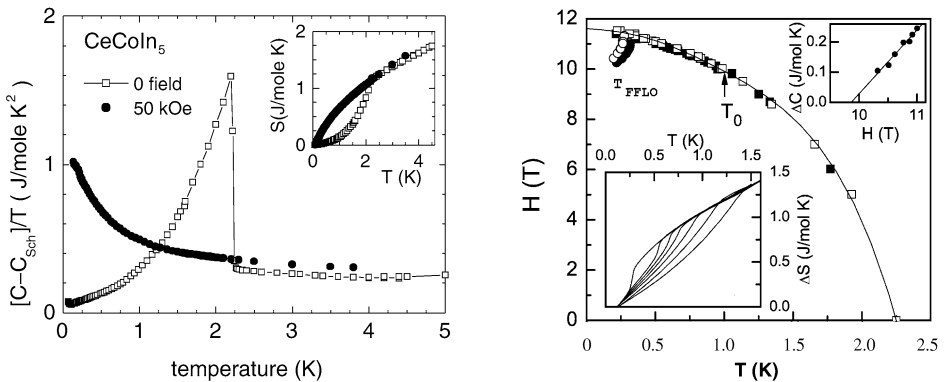


Fig. 22. Left panel: Linear specific heat coefficient of CeCoIn₅ vs temperature, for zero field anomalous nFI behaviour is observed. $\Delta C(T_c)/\gamma T_c \simeq 5$ is strongly enhanced over the isotropic BCS value 1.43. Inset shows corresponding entropies. Right panel: H_{c2} curve from specific heat data. At $T_0 \simeq 1.1$ K the transition changes from second to first order. Lower inset shows entropy gain as function of T starting from 0.13 K, for increasing field (right to left: 8.6 T–11.4 T) a step is evolving. Upper inset shows specific heat jump at the transition line T_{FFLO} to the Fulde–Ferrell–Larkin–Ovchinnikov state (Bianchi et al., 2003).

The change from the second-order nature of the transition observed at zero and low magnetic field to first order at high fields occurs at $T_0 \simeq 1.1 \text{ K} = 0.48T_c$. This value should be compared with the estimate of $0.33T_c$ deduced from the Chandrasekhar–Clogston field of a d-wave order parameter and the orbital critical field obtained from extrapolating the behavior close to the zero-field transition to low temperatures.

The structure of the flux line lattice which forms at low temperatures in the presence of an external magnetic field is of particular interest. A comprehensive review of this topic for s-wave superconductors has been given by Brandt (1995). An ideal isotropic type-II superconductor favors the hexagonal flux lattice. However, as the energy gain with respect to the square lattice is only 2%, relatively weak perturbations like FS or gap anisotropies may lead to distorted hexagonal or even square vortex lattices. CeCoIn₅ is a clean type-II superconductor for which one anticipates a rather complex variation with magnetic field of the flux line lattice. Recent small-angle neutron scattering experiments (Eskildsen et al., 2003) have imaged the vortex lattice of CeCoIn₅. At low fields, a hexagonal lattice is observed. The latter undergoes a “phase transition” to a square lattice when the field is increased. The orientation of the square flux line lattice relative to the crystal lattice is consistent with the expectations for the suggested d-wave order parameter. The square lattice for d-wave superconductors has been predicted theoretically by Won and Maki (1995) and Berlinsky et al. (1995). Finally at low temperatures and close to H_{c2} specific heat measurements (Bianchi et al., 2003) seem to indicate the presence of another inhomogeneous phase for both *a*- and *c*-field directions which was interpreted as the long-sought Fulde–Ferrell–Larkin–Ovchinnikov (FFLO) phase which is characterised by Cooper pairs with finite net momentum. The FFLO phase for d-wave SC order parameter of CeCoIn₅ was studied theoretically in Won et al. (2004).

3.3. Superconductivity close to a quantum critical point

The symmetry and mechanism of SC in the CeMIn₅ compounds have not yet been identified in any comprehensive way. However there are strong indications of unconventional order parameters. The interest in the SC of these compounds results from the observation that under pressure and chemical substitution the SC pair correlations develop in the vicinity of a QCP. Recently a few U-compounds have been found which fall also in this class. Theories to describe SC at the QCP are at present highly controversial and will be discussed there to some extent (sect. 4.3).

Here we shall briefly focus on the genuine QCP phenomenon in Ce-systems and its theoretical description. The compounds under consideration have a tendency to AF order. Two different scenarios are discussed for the transition from the HF state to a phase with long-range magnetic order.

The first approach views the magnetic order as itinerant magnetism of the heavy quasi-particle system. The theory starts on the Fermi liquid side which is characterized by a large Fermi surface including the *f*-degrees of freedom. The low-energy excitations are fermionic quasiparticles and their collective excitations. Close to the QCP, the static susceptibility is assumed to diverge at a specific wave vector \mathbf{Q} which signifies the transition to a spin density wave state. The quasiparticles are strongly scattered by spin fluctuations along “hot lines”

which are connected by \mathbf{Q} . This scattering modifies the low-temperature thermodynamic and transport properties which exhibit anomalous scaling relations close to QCP. They differ from those of the familiar Fermi liquid and therefore are at the focus of experimental interest. The theoretical derivation of the QCP scaling relations proceeds in close analogy to the spin-fluctuation theory of ferromagnetism (Moriya, 1985) starting from the self-consistent RPA expression for the magnetic susceptibility of the heavy Fermi liquid (Moriya and Takimoto, 1995). The theory was recast in the renormalization group language (Hertz, 1976; Millis, 1993). The ansatz yields scaling relations for the specific heat, the susceptibility, and the Wilson ratio which differ from the well-known Fermi liquid results (Continentino, 2001; Sachdev, 1999). The scaling behavior obtained for various different models and many non-Fermi liquid compounds are summarized in Stewart (2001). The anomalous transport properties exhibited by metals near antiferromagnetic quantum phase transitions are of particular interest in the experimental study of Ce-based heavy fermion systems. The theory (Rosch, 1999) exploits the fact that in the vicinity of the magnetic instability the magnetic susceptibility reduces to the simple form

$$\chi^{-1}(\mathbf{q}, \omega) \simeq \frac{1}{(q_0\xi)^2} + \omega_{\mathbf{q}} - \frac{i\omega}{\Gamma} \quad (58)$$

with

$$\frac{1}{(q_0\xi)^2} \simeq r + c\left(\frac{T}{\Gamma}\right)^{3/2} \quad \text{and} \quad \omega_{\mathbf{q}} \simeq \frac{1}{q_0^2}(\mathbf{q} - \mathbf{Q})^2. \quad (59)$$

Here r measures the (almost T -independent) distance from the quantum critical point, Γ denotes the characteristic energy scale of the fluctuations and c, q_0 are constants. The frequency magnetic $\omega_{\mathbf{q}}$ vanishes at the ordering vector \mathbf{Q} of the magnetic structure. In the dirty limit the variation with temperature of the resistivity is given by

$$\rho(T) = \rho(0) + \Delta\rho(T) \quad \text{with} \quad \Delta\rho(T) \sim T^{3/2}. \quad (60)$$

In the clean limit, on the other hand, the transport is dominated by the carriers with the longest life times, i.e., by the quasiparticles far away from the ‘hot’ regions on the Fermi surface yielding $\rho(T) \sim T^2$. Equation (60) is valid only at very low temperatures $T/\Gamma < 1/\hat{\rho}_0$ where $\hat{\rho}_0$ denotes the residual resistivity ratio $\hat{\rho}_0 = \rho(0)/\rho(273 \text{ K})$. At intermediate temperatures $1/\hat{\rho}_0 < T/\Gamma < 1/\sqrt{\hat{\rho}_0}$ the resistivity rises linearly with temperature

$$\Delta\rho(T) \sim T\sqrt{\hat{\rho}_0}. \quad (61)$$

The important feature of the weak-coupling picture as described above is that Γ , which is related to the characteristic energy of the Fermi liquid phase still plays the role of the scaling energy. This fact is not surprising since only parts of the Fermi surface contribute to the anomalous properties. One should note however that this theory is not fully self-consistent because the AF fluctuation wave vector is not connected with any FS feature since the latter is assumed as spherical.

The loss of the energy scale Γ is a characteristic feature of an alternative scenario which emphasizes the role of local correlations in quantum critical behavior (Si et al., 1999, 2001;

Coleman, 1999). The dynamical competition between the Kondo and RKKY interactions is analyzed by an extension (Smith and Si, 2000; Chitra and Kotliar, 2000) of the dynamical mean-field theory (see (Georges et al., 1996) and references therein). The resulting momentum-dependent susceptibility has the general form

$$\chi^{-1}(\mathbf{q}, \omega) = M(\omega) + J(\mathbf{q}), \quad (62)$$

where the spin fluctuation self energy $M(\omega)$ is calculated from the effective impurity problem. A zero-temperature phase transition will occur when $\chi(\mathbf{q}, \omega = 0)$ diverges. Anomalous behavior is expected whenever the (effective) local dynamics has an anomalous frequency dependence. Different scenarios are discussed in Si (2001). We finally mention that the compound YbRh_2Si_2 (where Yb has one f-hole instead of one f-electron as in Ce) has been identified as one of the most promising and cleanest QCP systems where these theoretical models can be tested (Custers et al., 2003).

4. U-based heavy-fermion superconductors

Heavy Fermion superconductivity is found more frequently in intermetallic U-compounds than in Ce-compounds. This may be related to the different nature of heavy quasiparticles in U-compounds where the 5f-electrons have a considerable, though orbitally dependent, degree of delocalisation. The genuine Kondo mechanism is not appropriate for heavy quasiparticle formation as is the case in Ce-compounds. This may lead to more pronounced delocalised spin fluctuations in U-compounds which mediate unconventional Cooper pair formation as discussed in sect. 2. The AF quantum critical point scenario invoked for Ce compounds previously also does not seem to be so important for U-compounds with the possible exception of UGe_2 . On the other hand AF order, mostly with small moments of the order $10^{-2}\mu_B$ is frequently found to envelop and coexist with the SC phase in the $B-T$ plane.

A common trait of U-compounds is the varying degree of localisation of 5f-electrons. It has recently become clear that Fermi surface properties of, e.g., UPt_3 (Zwicknagl et al., 2002) and UPd_2Al_3 (Zwicknagl et al., 2003) can be well described by treating two of the three 5f-electrons as localised in orbitals of specific symmetry and small CEF splitting of the order of meV. This approach also leads to a natural mechanism for the formation of heavy quasiparticles via the scattering of delocalised 5f-electrons by the internal CEF excitations of the localised 5f-electrons. This type of ‘dual model’ seems much closer to the truth than either a purely delocalised LDA type description which fails to explain the large masses or Kondo lattice models with fully localised 5f-states whose associated Kondo type anomalies above the Kondo temperature in transport and thermodynamics are not present in U-compounds.

In the following we will discuss to some length a number of prominent examples of U-compounds which have extensively been investigated experimentally and partly theoretically, mostly in the context of phenomenological Ginzburg–Landau (GL) theories or BCS type theories with magnetic effective pairing interactions. One is however far from being able to predict the spin state (parity) or even symmetry type of the gap function. Simple models

of AF spin fluctuations would predict singlet even parity gap functions but well characterised examples of triplet odd parity U-superconductors exist.

Indeed the hexagonal compound UPt_3 (Stewart et al., 1984) exhibits triplet pairing and it sticks out as the most interesting case of unconventional SC with a multicomponent order parameter whose degeneracy is lifted by a symmetry breaking field due to the small moment AF order. On the other hand in UPd_2Al_3 (Geibel et al., 1991a) SC coexists with large moment AF and probably spin singlet pairing is realised, it also exhibits a new kind of magnetic pairing mechanism mediated by propagating magnetic exciton modes. The sister compound UNi_2Al_3 (Geibel et al., 1991) is an example of coexistence of large moment AF with a SC triplet order parameter. In URu_2Si_2 (Palstra et al., 1985) the SC order parameter symmetry is still undetermined. The interest in this compound is focused more on the enveloping phase with a ‘hidden’ order parameter presumably of quadrupolar type or an ‘unconventional’ SDW. The oldest cubic U-HF superconductor UBe_{13} (Ott et al., 1983) and its thorium alloy $U_{1-x}Th_xBe_{13}$ is also the most mysterious one. While for the pure system there is a single SC phase of yet unknown symmetry, in the small Th concentration range two distinct phases exist which may either correspond to two different SC order parameters or may be related to a coexistence of SC with a SDW phase. In addition in UBe_{13} SC order appears in a state with clear non-Fermi liquid type anomalies. More recently the coexistence of ferromagnetism and SC in UGe_2 (Saxena et al., 2000) has been found. This is the only case of U-compounds where quantum critical fluctuations might be involved in the SC pair formation. Due to the FM polarisation the triplet gap function contains only equal spin pairing.

4.1. Multicomponent heavy fermion superconductor UPt_3

The intermetallic compound UPt_3 which crystallizes in the hexagonal Ni_3Sn structure is regarded as the archetype of a strongly correlated Fermi liquid. The existence of heavy quasiparticles is inferred from enhanced thermodynamic and transport coefficients, for example $\gamma \sim 420$ mJ/(mol U K²) (Frings et al., 1983) and anisotropic Pauli-like susceptibility $\chi_c \sim 50 \cdot 10^{-9}$ m³/(mol U) and $\chi_{a,b} \sim 100 \cdot 10^{-9}$ m³/(mol U) (Frings et al., 1983; Stewart et al., 1984). In addition, the resistivity rises quadratically with temperature with a T^2 -coefficient $A \simeq 0.49$ $\mu\Omega$ /(cm K²) (Taillefer and Lonzarich, 1988). The formation of the coherent heavy Fermi liquid state is clearly seen in the optical conductivity (Marabelli et al., 1987; Degiorgi, 1999; Dressel et al., 2002) and in the dynamical magnetic susceptibility as measured by neutron scattering (Bernhoeft and Lonzarich, 1995). Direct evidence for the existence of heavy quasiparticles comes from the observation of quantum oscillations (Taillefer et al., 1987; Taillefer and Lonzarich, 1988; McMullen et al., 2001; Kimura et al., 1998) where Fermi surfaces and effective masses up to $m^* = 135m$ were determined. The average dHvA mass enhancement $m^*/m_b \simeq 20$ compared to the band mass m_b is found to be consistent with the specific heat enhancement $\gamma_{exp}/\gamma_{calc} = 17$ (Norman et al., 1988). These results prove convincingly that UPt_3 in its normal state is a heavy Fermi liquid.

The normal Fermi liquid state becomes unstable at low temperatures. At $T_N \simeq 5.8$ K an antiferromagnetic phase with extremely small ordered moments $\mu \simeq 0.035\mu_B/U$ develops (Heffner et al., 1989; Hayden et al., 1992; Lussier et al., 1996). The most exciting phenomena are associated with the superconducting state. The existence of two clearly

distinct transition temperatures $T_{c1} = 530$ mK and $T_{c2} = 480$ mK (Fisher et al., 1989; Brison et al., 1994) implies that the superconducting phases are characterized by a multi-component order parameter. The discontinuities in the specific heat at the superconducting transitions show that the Cooper pairs are formed by the heavy quasiparticles of the normal heavy Fermi liquid state.

From this we conclude that a quantitative theory for the origin of the heavy quasiparticles in UPt_3 is a prerequisite for a detailed understanding of the fascinating low-temperature properties of this compound.

4.1.1. *Dual model and heavy quasiparticles*

Although a comprehensive picture of the low temperature ordered phases of UPt_3 has emerged, a complete theoretical understanding of the origin of 5f-derived heavy quasiparticles is still missing. The number of itinerant U 5f-electrons as well as the microscopic mechanism yielding the high effective masses are still controversial. It has been considered a success of the LDA that de Haas–van Alphen (dHvA) frequencies can be related to the areas of extremal orbits on the Fermi surface obtained by band-structure calculation which treats the U 5f-states as itinerant (Albers et al., 1986; Norman et al., 1988). From these findings, however, one should not conclude that the U 5f-states are ordinary weakly correlated band states. The calculated energy bands are much too broad for explaining the effective masses while on the other hand, they are too narrow to fit the photoemission data (Allen, 1992).

The key feature is likely the dual nature of the U 5f-states, i.e., the presence of both localized and delocalized U 5f-electrons. The theoretical investigation proceeds in three steps. Firstly, band-structure calculations have been performed starting from the self-consistent LDA potentials but excluding the U 5f $j = 5/2$, $j_z = \pm 5/2$ and $j_z = \pm 1/2$ states from forming bands. The localized 5f-orbitals are accounted for in the self-consistent density and likewise in the potential seen by the conduction electrons. The 5f-bands are calculated by solving the Dirac equation (Albers et al., 1986). The intrinsic bandwidth of the itinerant U 5f $j = 5/2$, $j_z = \pm 3/2$ is taken from the LDA calculation while the position of the corresponding band center is chosen such that the density distribution of the conduction states as obtained within LDA remains unchanged. The resulting position of the f-band relative to the calculated Pt d-states is consistent with photoemission data. It was found that the U 5f-bands with $j_z = \pm 3/2$ hybridize strongly near the Fermi level so that the f occupancy per U atom for the delocalized 5f-electrons amounts to $n_f = 0.65$ indicating that we are dealing with a mixed valent situation. The theoretical Fermi surface shown in fig. 23 is formed by two bands which are doubly degenerate and which are derived from the 5f $|j = 5/2, j_z = \pm 3/2\rangle$ states. The thermodynamically most important orbit is assigned to the Γ -centered strongly anisotropic electron surface shown in the left part of fig. 23. The A-centered part of the Fermi surface shown in the right part of fig. 23 has open orbits spanning the entire Brillouin zone for magnetic fields oriented along the a -direction in the basal plane. This feature is consistent with magnetoresistance measurements (McMullen et al., 2001). Now we turn to the discussion of the localized U 5f-states. The multiplet structure of the localized f^2 -states is calculated by diagonalizing the Coulomb matrix. The spin-orbit splitting is rather large and therefore a jj -coupling scheme is used. This simplification gives six 2-particle states built from $|j = 5/2, j_z = \pm 5/2\rangle$ and

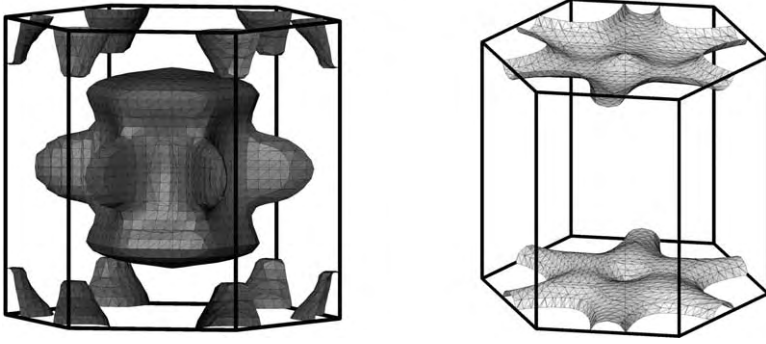


Fig. 23. UPt₃: FS of heavy quasiparticles as calculated within the dual model (Zwicknagl et al., 2002). One of the U 5f-electrons ($j = 5/2, j_z = 3/2$) is treated as itinerant and is included in the FS while the remaining two are localized. Then two bands contribute to the FS. Left: Γ -centered heavy electron sheet which dominates γ . Right: A-centered open orbit sheet consistent with magnetoresistance results (McMullen et al., 2001).

$|j = 5/2, j_z = \pm 1/2\rangle$. The resulting eigenstates are generally no longer eigenstates of the total angular momentum \mathbf{J}^2 , but remain eigenstates of J_z . The Coulomb matrix elements are calculated following Condon and Shortley (1957). Inputs are the Slater–Condon parameters F^K (Coulomb integrals) and G^K (exchange integrals) which are evaluated with the radial function $R_{f,5/2}^U(r)$ for U which is determined from a self-consistent band structure potential. Diagonalization of the matrix yields a doubly degenerate ground-state $J_z = \pm 3$ which must be an eigenstate of $J = 4$. Note that the Pauli principle permits even values of J only, i.e., $J = 0, 2, 4$ in our case. The states $|j = 5/2, j_z = 5/2; J = 4, J_z = \pm 3\rangle$ have an overlap of 0.865 with the Hund’s rule ground-state 3H_4 derived from the LS-coupling scheme. Therefore the choice of jj vs. LS coupling should only weakly affect the results obtained for the ground-state multiplet. The two-fold degeneracy of the ground-state is lifted by a CEF yielding the two singlet states

$$\begin{aligned} |\Gamma_3\rangle &= \frac{1}{\sqrt{2}}(|J = 4; J_z = 3\rangle + |J = 4; J_z = -3\rangle), \\ |\Gamma_4\rangle &= \frac{1}{\sqrt{2}}(|J = 4; J_z = 3\rangle - |J = 4; J_z = -3\rangle). \end{aligned} \quad (63)$$

Note that $|\Gamma_4\rangle$ has also been suggested as ground state of UPd₂Al₃ (Grauel et al., 1992; Böhm et al., 1992). The excited eigenstates of the Coulomb matrix are neglected, they are assumed to be separated by a rather high excitation energy from the ground state. The coupling between the localized and delocalized f-electrons is directly obtained from the expectation values of the Coulomb interaction H_C (eq. (2)) in the 5f³-states yielding the transition matrix element

$$|M| = \left| \left\langle f^1; \frac{5}{2}, \frac{3}{2} \right| \otimes \langle \Gamma_4 | H_C | \Gamma_3 \rangle \otimes \left| f^1; \frac{5}{2}, \frac{3}{2} \right\rangle \right| = 0.19 \text{ eV}. \quad (64)$$

Finally, we determine the mass enhancement which arises from the scattering of the itinerant U 5f-electrons due to virtual excitations of the localized f² subsystem. The latter are

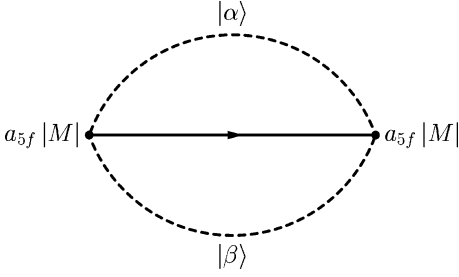


Fig. 24. Self energy due to virtual CEF excitations $|\alpha\rangle \leftrightarrow |\beta\rangle$ leading to the enhanced m^* . Full line and dashed bubble represent conduction electron propagator and local 5f susceptibility of eq. (66), respectively. The selfconsistent solution of eq. (65) yields the leading order in an expansion in terms of the small ratio δ/W^* (δ = CEF-splitting, W^* = effective conduction band width). Input parameters: matrix element $a_{5f}|M|$, DOS $N(E)$ and (effective) CEF splitting δ . The former two are determined from first principles calculations while δ is taken from experiment.

characterized by a CEF splitting energy δ while the relevant energy scale for the ‘itinerant’ 5f-states is set by the effective band width W^* . To leading order in the ratio δ/W^* the mass enhancement m^*/m_b is obtained from the fluctuation exchange (FLEX) contribution to the band self energy as shown in fig. 24 in close analogy to the case of Pr metals (White and Fulde, 1981). This leads to an expression

$$\frac{m^*}{m_b} = 1 - \left(\frac{\partial \Sigma}{\partial \omega} \right)_{\omega=0}, \quad (65)$$

$$\Sigma(i\omega_n) = a_{5f}^2 |M|^2 T \sum_{n'} \chi(i\omega_n - i\omega_{n'}) g(i\omega_{n'}),$$

where ω_n are Matsubara frequencies, m_b is the LDA band mass and a_{5f} denotes the 5f weight of conduction electron states close to E_F . Furthermore the local 5f susceptibility and conduction electron propagator are given, respectively, by

$$\chi(i\omega_n - i\omega_{n'}) = \tanh \frac{\delta}{2T} \frac{2\delta}{\delta^2 - (i\omega_n - i\omega_{n'})^2}, \quad (66)$$

$$g(i\omega_n) = \int dE \frac{N(E)}{i\omega_n - E - \Sigma(i\omega_n)}.$$

Here $2N(E)$ is the total electronic DOS obtained from the LDA bandstructure with two of the 5f-electrons kept localised.

This calculation procedure leads to a good agreement of theoretical and observed quasiparticle masses (Zwicknagl et al., 2002) for the main Fermi surface sheets. The results are summarized in fig. 25 as well as in table 4. If the dependence upon the wave vector \mathbf{k} is neglected one obtains an isotropic enhancement of the effective mass m^* over the band mass m_b . The explicit evaluation requires as input parameters the density of states and the f-weight per spin and U-atom at the Fermi energy, $N(0)$ and $4a_{5f}^2$, respectively, as well as the average energy δ of CEF excitations. Solving for the selfconsistent conduction electron propagator with the input determined from the ab-initio calculations of the electronic structure ($N(0) \simeq 15.5$ states/(eV cell), $|M|^2 = 0.036$ eV², $4a_{5f}^2 = 0.13$) and the estimate $\delta \simeq 20$ meV we finally obtain the effective masses listed above.

The dual model and its partial 5f localisation scenario therefore provides for a satisfactory explanation for both the FS structure and mass renormalisation of the heavy quasiparticles observed in UPt₃. The physical reason for the strongly orbital dependent effect of local electron

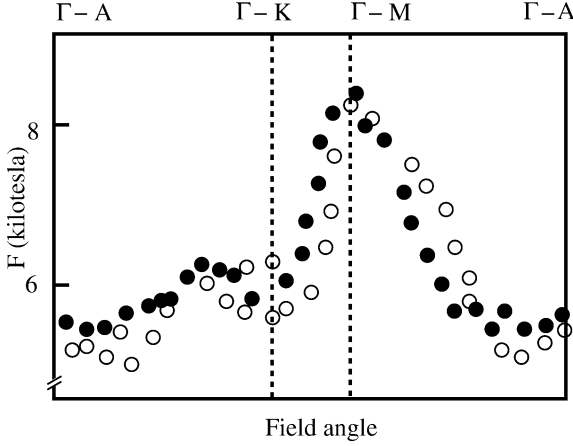


Fig. 25. UPt₃: dHvA cross sections of heavy quasiparticle FS (Γ -centered closed sheet in fig. 23 from experiment (filled symbols) (Kimura et al., 1998) and from dual model calculation (Zwicknagl et al., 2002) (empty symbols). Field direction is turned from c -direction (Γ -A) to a -direction (Γ -K) and then rotated in the basal plane from a -direction to b -direction (Γ -M) and finally turned back to c -direction. The calculated splitting for magnetic field orientations in the a - c -plane (Γ -A to Γ -K sector) is indeed observed in recent dHvA experiments (McMullen et al., 2001).

Table 4

Mass renormalisation in UPt₃ from dHvA experiments and dual model calculations for field along hexagonal symmetry directions

m^*/m	c	a	b
Experiment	110	82	94
Theory	128	79	104

correlations on the different LDA hybridization matrix elements has been investigated separately (sect. 2). Finally we want to point out that the prescribed way of treating the 5f-electrons in UPt₃ is also applicable to other uranium compounds, notably UPd₂Al₃ (sect. 4.2).

4.1.2. Pairing and the spin-orbit coupling problem

There is little doubt that UPt₃ is an unconventional superconductor with a multicomponent superconducting order parameter. Theoretical models which have been proposed are reviewed by Sauls (1994) and Joynt and Taillefer (2002) and will be discussed in the next section. Here we shall briefly comment on the issue of the importance of spin-orbit coupling in the pairing scheme. In all theoretical treatments the superconducting phases of UPt₃ are characterized by BCS-type gap functions $\Delta_{s1,s2}(\hat{\mathbf{k}})$ which satisfies the antisymmetry relation eq. (19). The wave vector $\mathbf{k} = k_F(\hat{\mathbf{k}})\hat{\mathbf{k}}$ is restricted to the Fermi surface since the coherence length ξ_0 is much larger than the interatomic distance or, equivalently, the Fermi wave length $\lambda_F = 2\pi/k_F$ satisfies

$$\xi_0 = \frac{\hbar v_F}{k T_c} \gg \lambda_F. \quad (67)$$

As a consequence, the gap function $\mathbf{\Delta}(\hat{\mathbf{k}})$ is a matrix function of $\hat{\mathbf{k}}$ only or its corresponding polar and azimuthal angles ϑ and φ . We have neglected indices for interband pairing because the available phase space is much smaller than in the case of intraband pairs.

The indices s_1, s_2 refer to the (pseudo-)spin labels of the quasiparticles. Due to the large spin-orbit interaction the quasiparticle states are no longer eigenstates of the spin. In the absence of an external magnetic field the states $|\mathbf{k}s\rangle$ and $|-\mathbf{k}-s\rangle$ show Kramers degeneracy. In UPt_3 , the crystal structure has inversion symmetry. This fact implies that all four quasiparticle states $|\mathbf{k}s\rangle, |-\mathbf{k}s\rangle, |\mathbf{k}-s\rangle$ and $|-\mathbf{k}-s\rangle$ are degenerate. As a result, the superconducting order parameter can be decomposed into the contributions

$$\begin{aligned} \text{even-parity (pseudo-spin singlet, } S = 0): \quad \Delta_{s_1 s_2}(\mathbf{k}_F) &= \Delta(\mathbf{k}_F)(i\sigma_y)_{s_1 s_2}, \\ \text{odd-parity (pseudo-spin triplet, } S = 1): \quad \Delta_{s_1 s_2}(\mathbf{k}_F) &= \Delta(\mathbf{k}_F) \cdot (i\sigma\sigma_y)_{s_1 s_2}. \end{aligned} \quad (68)$$

Because the energy splitting of $j = 5/2$ and $j = 7/2$ states due to spin-orbit coupling is larger than the bandwidth due to hybridization and overlap (Albers et al., 1986) their mixing can be neglected. Consequently the pseudospin indices s_1, s_2 are good quantum numbers and effectively the classification of the gap function can proceed as for the weak spin-orbit coupling case (sect. 2).

4.1.3. Multicomponent superconducting order parameter

The hexagonal heavy Fermion compound UPt_3 can justly be called the flagship of unconventional superconductivity, despite having a critical temperature less than one Kelvin. It is set aside from all other unconventional superconductors so far because it exhibits *two* superconducting phase transitions which have to be interpreted as a direct signature of the fact that the SC order parameter is a complex vector with more than one component. In all other unconventional superconductors, e.g., in high- T_c compounds the order parameter is still a complex scalar as in ordinary superconductors, albeit belonging to a nontrivial (but one-dimensional) representation of the symmetry group as witnessed by nodes in the anisotropic gap function. Only recently another example of a multicomponent superconductor, the Pr-skutterudite compound $\text{PrOs}_4\text{Sb}_{12}$ (sect. 6), may have been found. The exciting discovery of the split SC transitions in UPt_3 at $T_{c1} = 530$ mK and $T_{c2} = 480$ mK in specific heat measurements by Fisher et al. (1989) has led to an enormous amount of experimental and theoretical work on UPt_3 whose historical evolution has been described in detail in a recent review by Joynt and Taillefer (2002). Therefore in the following discussion we shall restrict to the essential aspects of SC in UPt_3 . The additional small moment AF observed in UPt_3 ($T_N = 5.8$ K, $\mu = 0.035\mu_B$) plays a key role in the identification of the SC order parameter since the in-plane staggered magnetization acts as a symmetry breaking field (SBF) to the SC multicomponent order parameter. The SBF is believed to be responsible for the appearance of two SC transitions which otherwise would merge into one, in fact this has later been proven by specific heat pressure experiments (Trappmann et al., 1991) on the SC $T_{c1,2}(p)$ and by complementary neutron diffraction under pressure (Hayden et al., 1992). Naturally there are also two critical-field curves. They intersect at a tetracritical point in the B - T plane that is present for all field directions. Therefore one can identify three distinct SC phases A, B, C in the B - T plane (fig. 29) corresponding to different choices of the orientation of the complex vector SC-order parameter. These phase boundaries have first been identified by ultrasound velocity measurements (Bruls et al., 1990) and have been confirmed using the

same method (Adenwalla et al., 1990). Subsequently many different methods like thermal expansivity (van Dijk et al., 1993; van Dijk, 1994), field dependent specific heat (von Löhnneysen, 1994), etc. have yielded equivalent B - T phase diagrams. An important observation is a crossover of the anisotropy ratio of upper critical fields as function of temperature indicating that H_{c2} shows Pauli limiting for $\mathbf{H} \parallel c$ but not for $\mathbf{H} \perp c$ (Shivaram et al., 1987; Choi and Sauls, 1991). Again the asymptotic ($T \ll T_c$) low temperature behaviour of thermodynamic and transport coefficients, most notably thermal conductivity (Lussier et al., 1996; Graf et al., 1999) with power law behaviour points to a gap function with nodes. The precise node structure is different for the three phases due to the internal degrees of freedom for a multicomponent order parameter. Despite the wealth of experimental results on UPt_3 there is no unequivocal consensus on the symmetry and node structure of the superconducting gap. The many different proposals that have been put forward at various times are summarized in Joynt and Taillefer (2002). Here we restrict to the most commonly accepted E_{2u} (f-wave) model for the order parameter which was originally proposed by Choi and Sauls (1991), Sauls (1994) and in the form used here by Norman and Hirschfeld (1996). This odd parity spin triplet order parameter is consistent with ^{195}Pt Knight shift measurements and the observed linear in T -dependence of the thermal conductivity for both a - and c -directions. The corresponding B -phase (e.g., $H = 0$, $T < T_{c2}$) has a gap function with an equatorial node line and polar second order node points. The anisotropic paramagnetic limiting of the upper critical field suggests that its \mathbf{d} -vector is pinned along the c -axis by an anisotropy potential due to spin-orbit coupling. This interpretation is however in conflict with a nearly isotropic constant Knight shift for larger fields (Kitaoka et al., 2000). Further investigations, notably field-angle dependent thermal conductivity experiments are necessary to confirm the node structure of the E_{2u} model.

The underlying normal heavy fermion state of UPt_3 , which was the first system where heavy quasiparticles have directly been seen in dHvA oscillations (Taillefer and Lonzarich, 1988), has been described above. It was argued that the picture of heavy quasiparticle mass generation in 5f-metals has to be revised. This is due to a considerably different degree of localisation of 5f-electrons in different orbital states as opposed to the simple LDA picture which assumes complete delocalisation for all 5f-orbitals.

4.1.4. Small moment AF order

UPt_3 crystallizes in the hexagonal MgCd_3 structure (D_{6h} point group) and has two inequivalent U-sites with C_{3v} site symmetry. As in most other U-based superconductors the SC phase is embedded in an antiferromagnetic phase with very small moments ($\mu = 0.035\mu_B$). The commensurate AF order of hcp UPt_3 with moments parallel to the hexagonal b -axis is indicated in fig. 26. The D_{6h} six-fold symmetry of the paramagnetic phase is reduced to an orthorhombic D_{2h} symmetry by the AF order with modulation vector $\mathbf{Q} = (\frac{1}{2}, 0, 0)$. Although the AF intensity shows mean field behaviour $\sim (T_N - T)$ (Aeppli et al., 1988), AF Bragg peaks retain a finite width pointing to imperfect AF ordering with a correlation length of $\xi_{\text{AF}} \sim 150 \text{ \AA}$. Only below 50 mK ξ_{AF} starts to diverge (Koike et al., 1998) and true long range magnetic order develops at 28 mK according to specific heat measurements (Schuberth et al., 1992). Still in the imperfect ordered regime the Bragg intensity starts to decrease below the superconducting

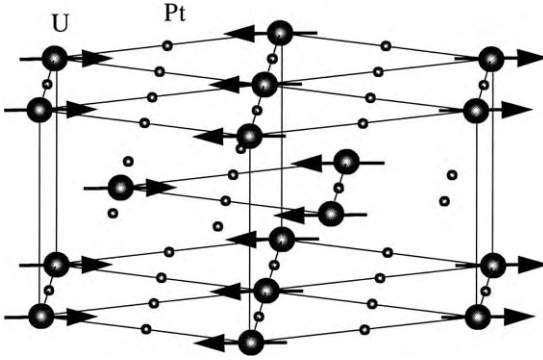


Fig. 26. Crystal structure and AF magnetic structure of UPt_3 below $T_N = 5.8$ K. The hexagonal axis defines the c direction and the moments are oriented along $\mathbf{b} \perp \mathbf{a}$ (using orthogonal $\mathbf{a}, \mathbf{b}, \mathbf{c}$ lattice vectors where $a = b = 5.764 \text{ \AA}$ and $c = 4.884 \text{ \AA}$). Hexagonal planes are separated by $c/2$. The AF order leads to a doubling of the unit cell along \mathbf{b} (moment direction) resulting in orthorhombic (D_{2h}) symmetry of the AF crystal.

transition (Aeppli et al., 1988) which signifies a coupling of superconducting and AF order parameters, this has also been observed in URu_2Si_2 , UPd_2Al_3 and UNi_2Al_3 (Metoki, 2001). Thus the small moment AF itself is a rather unconventional magnetic state but in the following discussions its influence on the superconducting state will be treated as ordinary AF order though with small moment.

4.1.5. The superconducting state, coupled with AF order

The exceptional nature of the superconducting state was already obvious from the two specific heat jumps first observed by Fisher et al. (1989) of comparable size indicating two SC transitions at $T_{c1,2}$. Later it was shown (Trappmann et al., 1991) that under hydrostatic pressure the two transitions merge at a critical pressure of $p_c \simeq 3.8$ kbar (fig. 27). It is important to note that above p_c the two transitions do not separate again. Together with the pressure dependence of the AF moments observed in neutron diffraction (Hayden et al., 1992) this gives a clue about the nature of the two superconducting transitions as well as the role of AF order. If the two transitions would correspond to two SC phases whose order parameters belong to one-dimensional representations with accidentally close transition temperatures then one would expect simply a crossing of $T_{c1,2}(p)$ at p_c , there would be no symmetry reason why the two transitions should merge above p_c as is actually seen in fig. 28. The observation (Hayden et al., 1992) that the magnetic moment vanishes at about the same critical pressure (fig. 28) then suggests a natural scenario: at large hydrostatic pressure $p > p_c$ which preserves hexagonal symmetry the SC order parameter belongs to a two-dimensional hexagonal representation, E_1 or E_2 , i.e., it is a complex 2-component vector $\boldsymbol{\eta} = (\eta_1, \eta_2) = (|\eta_1|, |\eta_2|e^{i\Phi})e^{i\varphi}$ rather than a complex scalar $\eta e^{i\varphi}$ as for one-dimensional representations associated with a single T_c . Here φ is the overall Josephson-phase of the order parameter and Φ is an intrinsic phase which is a novel feature of the 2-component order parameter. At pressures $p < p_c$ the AF moments appear, since they are aligned in the b -direction they reduce hexagonal symmetry to orthorhombic symmetry. The AF order parameter acts as a symmetry breaking field (SBF), any small coupling between the AF and SC order parameters will then lead to a splitting of T_c into $T_{c1,2}$ which are associated with two SC order parameters of different symmetry with respect to the orthorhombic group. Therefore the small moment magnetism with

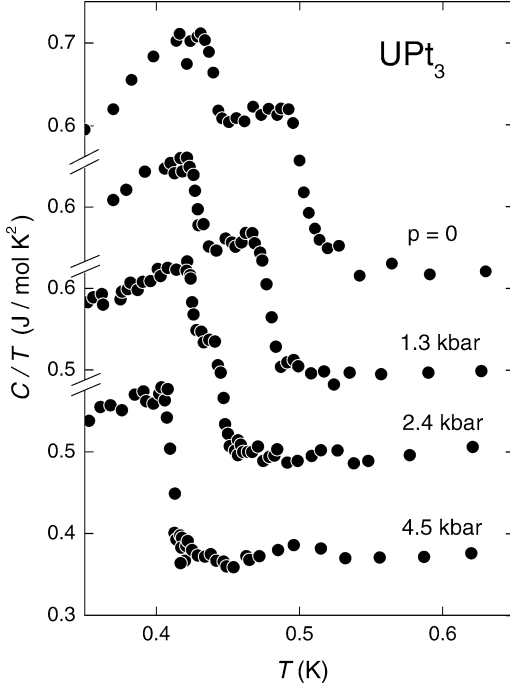


Fig. 27. Disappearance of the double-peak structure of specific heat under hydrostatic pressure (Trappmann et al., 1991) from which the pressure dependence of $T_{c1,2}(p)$ shown in fig. 28 is obtained.

its easy-plane anisotropy is a lucky coincidence which helps to unveil the complex vector nature of the SC order parameter. This scenario may generically be described within the Landau theory characterised by a free energy density (Machida et al., 1989; Hess et al., 1989; Joynt, 1990)

$$f_L(\boldsymbol{\eta}, \mathbf{M}_Q) = \alpha_0(T - T_c)\boldsymbol{\eta} \cdot \boldsymbol{\eta}^* + \beta_1(\boldsymbol{\eta} \cdot \boldsymbol{\eta}^*)^2 + \beta_2|\boldsymbol{\eta} \cdot \boldsymbol{\eta}|^2 - \gamma_0\mathbf{M}_Q^2(\eta_x^2 - \eta_y^2). \quad (69)$$

Here $\mathbf{M}_Q = M_Q\hat{\mathbf{y}}$ is the AF order parameter which has already reached saturation in the SC temperature range, furthermore a shift of the critical temperature $T_c \sim M_Q^2$ has already been included in T_c . There are two fourth order terms characterized by the Landau parameters β_1 , β_2 as compared to only one in the case of a scalar SC order parameter. The last term is a phenomenological coupling of the SBF to the E-type SC order parameter. This type of theory is the same for each of the even or odd two-dimensional E-representations. The different \mathbf{k} -dependence of the respective SC-gap function enters only via the parameters of the Landau free energy in eq. (69) where $\alpha_0, \beta_1 > 0$. The ratio β_2/β_1 selects the SC ground state in the two-dimensional manifold of possible order parameters $\boldsymbol{\eta}$. First we discuss the decoupled case $\gamma_0 = 0$ where a single transition at T_c into a state belonging to that manifold takes place. Then all possible SC ground states have $|\eta_1| = |\eta_2| \equiv |\eta|$. For $-1 < \beta_2/\beta_1 < 0$ the ‘unitary’ state with intrinsic phase $\Phi = 0$ is stable whereas for $\beta_2/\beta_1 > 0$ the ‘non-unitary’ state with $\Phi = \pm\frac{\pi}{2}$ and $\boldsymbol{\eta} \times \boldsymbol{\eta}^* \neq 0$ is the stable one, which is the case in UPt₃. The SBF splits the degenerate

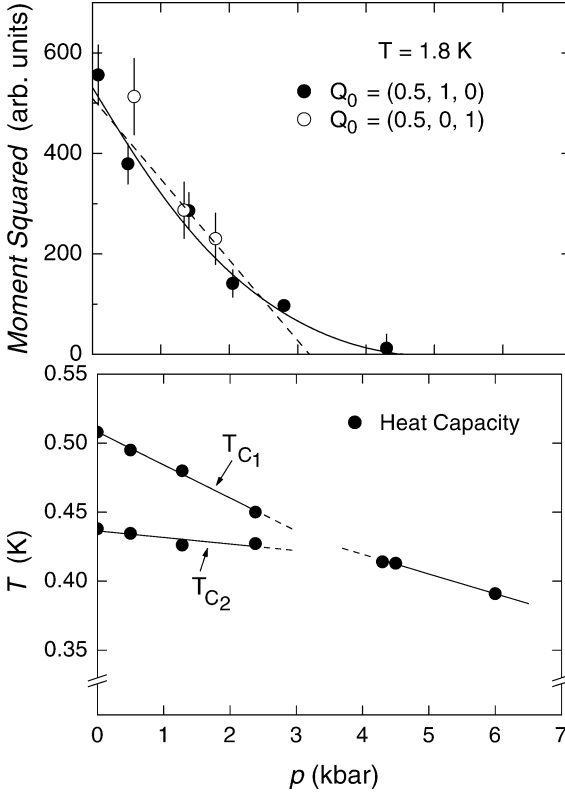


Fig. 28. Reduction of the squared AF moment in UPt_3 with hydrostatic pressure p (above), it vanishes at a critical pressure of $p_c \simeq 3.8$ kbar. Simultaneously the SC T_c splitting is reduced and also vanishes at p_c staying zero for larger pressures (Hayden et al., 1992). This supports the idea that a two-fold degenerate SC order parameter (e.g., E_{2u}) is split by an AF symmetry breaking field according to eqs. (69), (70).

E-representations through the last term in eq. (69). Whereas at low temperature the stable state is determined by the fourth order terms, close to T_{c1} the second order terms $\sim \gamma_0 > 0$ dominate and favor a single component state, only below T_{c2} will the second component be nonzero. One has two phases (A) $\eta = \eta(1, 0)$ below T_{c1} and (B) $\eta = \eta(1, ai)$ below T_{c2} . The $T_{c1,2}$ -splitting and the difference in amplitudes ($a < 1$) in the B-phase are determined by the Landau parameters according to

$$\begin{aligned} \Delta T_c &= T_{c1} - T_{c2} = \left(1 + \frac{\beta_1}{\beta_2}\right) \lambda_0 T_c, \\ a &= \left(1 - \frac{\beta_1}{\beta_2} \lambda_0\right) / \left(1 + \frac{\beta_1}{\beta_2} \lambda_0\right), \\ \lambda_0 &= \frac{\gamma_0 M_{\mathbf{Q}}^2}{\alpha_0 T_c}. \end{aligned} \quad (70)$$

Using the somewhat smaller transition temperatures $T_{c1,2}$ of van Dijk (1994) with $\Delta T_c = 0.054$ K (fig. 29) one obtains for the dimensionless coupling parameter of SC and AF order

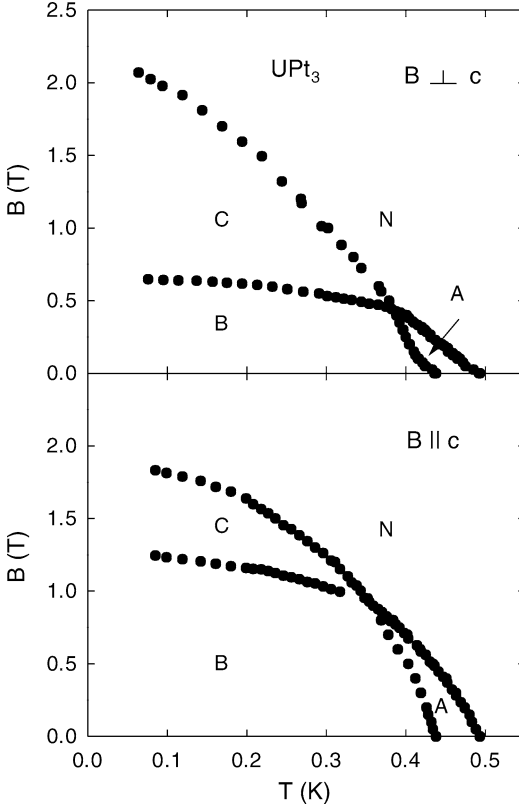


Fig. 29. Superconducting B - T phase diagram as obtained from thermal expansion and magnetostriction (van Dijk et al., 1993; van Dijk, 1994). Critical field curves cross at a tetracritical point which is present for all field directions, therefore three distinct SC phases $A(1, 0)$, $B(1, i)$ and $C(0, 1)$ with different E_{2u} order parameters η exist.

parameters $\lambda_0 = 0.038$. The smallness of this parameter is primarily due to the small AF moment in UPt_3 . If it would be only slightly larger the lower B -phase of UPt_3 would be completely suppressed and only one SC transition would be observable. Furthermore one has $\frac{\beta_1}{\beta_2} = \frac{T_c - T_{c2}}{\lambda_0 T_c} \simeq 2$ and the amplitude ratio $a = 0.86$ which will be set to 1 in the following. The ratio of the SC specific heat jumps at $T_{c1,2}$ is given by

$$\frac{\Delta_2 C}{\Delta_1 C} = \frac{T_{c2}}{T_{c1}} \left(1 + \frac{\beta_2}{\beta_1} \right). \quad (71)$$

Here $\Delta_i C$ ($i = 1, 2$) are both counted from the normal state. Using the experimental values this also leads to a ratio $\frac{\beta_1}{\beta_2} = 2$. This type of phenomenological theory can be extended to include also the pressure dependence (Thalmeier et al., 1991). From the two different slopes of $T_{c1,2}$ vs. pressure one may infer a magnetic Grüneisen parameter $\Omega_M = -(\partial \ln M_{\mathbf{Q}}^2 / \partial \epsilon_v) = -385$ which is in reasonable agreement with $\Omega_M = -260$ as determined directly from the pressure dependence of Bragg intensities which are $\sim M_{\mathbf{Q}}^2$. This gives further support that the AF order provides the SBF that leads to the observed splitting into $(1, 0)$ and $(1, i)$ superconducting phases at zero field.

4.1.6. The critical field curves and Ginzburg–Landau theory

Naturally the two superconducting transitions at $T_{c1,2}$ will lead to two different critical field curves $H_{c2}^{1,2}$ which have been investigated by experimental methods mentioned before. The most obvious feature is a crossing of the critical field curves at a tetracritical point for all field directions. As a consequence there are three distinct SC regions in the H – T plane with phases A (high T , low H), B (low T , low H) and C (low T , high H). This important result has first been obtained by Bruls et al. (1990) with ultrasonic experiments. In fig. 29 we show the phase diagram for $H \perp c$ and $H \parallel c$ obtained by van Dijk (1994) using thermal expansion measurements. Its most important properties may be summarized as follows: (i) The existence of a tetracritical point (T_t, H_t). Purely thermodynamical analysis of its vicinity (Yip et al., 1991) leads to the conclusion that if all four phase boundaries meeting at (T_t, H_t) are of second order, relations between their slopes and the specific heat jumps across them exist. They were confirmed by van Dijk (1994) which proved the second order nature of transitions. The change of slopes leads to pronounced kinks in the phase boundaries for $H \parallel a$. (ii) Defining the upper critical field $H_{c2}(T)$ as the upper phase boundary in fig. 29 for a, c directions one notices a reversal of the a – c anisotropy ratio $H_{c2}^a(T)/H_{c2}^c(T)$ as function of temperature. This ratio is < 1 for $T/T_c > 0.4$ and > 1 for $T/T_c < 0.4$. This reversal has been advanced as a major argument for spin triplet pairing by Sauls (1994). For the explanation of the structure of the A, B, C phase diagram an appropriate Ginzburg–Landau theory for a SC 2-component vector order parameter has to be constructed (Machida et al., 1989; Hess et al., 1989). It is obtained by adding all appropriate hexagonal invariants formed from η_j and its covariant gradient operators $D_j = \partial_j - iA_j$ with \mathbf{A} denoting the vector potential corresponding to the field \mathbf{B} given in units of $\phi_0/2\pi$ where $\phi_0 = \frac{hc}{2e}$ is the flux quantum. The homogeneous terms of the GL free energy density are again given by eq. (69) to which we have to add the gradient terms

$$\begin{aligned}
 f_G(\boldsymbol{\eta}, \mathbf{M}_\mathbf{Q}) = & K_1(|D_x\eta_1|^2 + |D_y\eta_2|^2) + K_2(|D_x\eta_2|^2 + |D_y\eta_1|^2) \\
 & + K_3(D_x\eta_1 D_y^*\eta_2^* + D_x\eta_2 D_y^*\eta_1^* + \text{c.c.}) + K_4(|D_z\eta_1|^2 + |D_z\eta_2|^2) \\
 & - \kappa M_\mathbf{Q}^2(|D_x\eta_1|^2 - |D_y\eta_1|^2 + |D_x\eta_2|^2 - |D_y\eta_2|^2). \quad (72)
 \end{aligned}$$

The expression for the total GL free energy density $f_{\text{GL}} = f_L + f_G$ is valid for both E_1 and E_2 type order parameters of odd and even parity but in the whole section we restrict discussion to the most likely E_{2u} case. The last term in eq. (72) with $K_M = \kappa M_\mathbf{Q}^2$ describes the coupling of the SBF to the gradients of the SC order parameter. In a conventional GL theory for a scalar order parameter one has only one GL parameter $K = \frac{hc}{2m^*}$ determined by the effective electron mass. For the vector order parameter $\boldsymbol{\eta}$ one has altogether 5 parameters. It is therefore obvious that a GL theory for a multicomponent superconductor has little real predictive power, but it may be used as a convenient frame for qualitative discussion. In weak coupling BCS theory the coefficients K_i can be expressed as angular averages of Fermi velocities (Sauls, 1994) which leads to the conclusion that in the E_{2u} -case one has $K_2, K_3 \ll K_1$. In this case the terms mixing η_x and η_y can be neglected and the solution of the linearized GL-equations corresponding to eqs. (69), (72) lead to two parallel critical field curves without the term

$\sim K_M$ for all directions of the field. The tetracritical point in this model is therefore entirely due to the coupling of gradient terms $D_{x,y}\eta_i$ to the SBF where the sign of κ is negative, i.e., it has to be opposite to that of γ in the homogeneous coupling term of eq. (69) in order to obtain a crossing at T_t . Using eq. (72) and the quadratic part of eq. (69) one obtains the critical field curves

$$\begin{aligned} H_{c2}^1 &= \frac{\phi_0}{2\pi} \frac{\alpha_0(T_{c1} - T)}{\sqrt{(K_1 + K_M)K_4}}, \\ H_{c2}^2 &= \frac{\phi_0}{2\pi} \frac{\alpha_0(T_{c2}^0 - T)}{\sqrt{(K_1 - K_M)K_4}}. \end{aligned} \quad (73)$$

Here $T_{c2}^0 > T_{c2}$ is the second transition temperature without inclusion of quartic terms of eq. (69) (Machida et al., 1989). For fields parallel to the c -axis similar expressions hold with $\sqrt{(K_1 \pm K_M)K_4}$ replaced by $(K_1 \pm K_M)$. Ignoring K_M for the moment the a - c anisotropy of H_{c2}^1 is given by a slope ratio $H_{c2}^{1c}/H_{c2}^{1a} = \sqrt{K_4/K_1} = \sqrt{\langle v_c^2 \rangle / \langle v_a^2 \rangle} = \sqrt{m_a/m_c}$. The experimental slope ratio 1.64 is indeed exactly equal to the root of the mass anisotropy $m_a/m_c = 2.7$ as obtained from transport measurements. The linearized version of the E_{2u} model has however no natural explanation for the slope changes ($B \perp c$) at the tetracritical point. On the other hand it explains the basic observation of the three (A, B, C) phases in the B - T plane for all field directions. In addition to the low- (or zero-)field phases (A, B) discussed before a high field phase (C) with an order parameter $\boldsymbol{\eta} = |\eta|(0, 1)$ appears which is stabilized by the gradient coupling term $\sim K_M$.

4.1.7. The superconducting gap function

A detailed understanding of thermodynamics and transport properties requires the \mathbf{k} -dependent gap functions of the three phases. Their node structure determines the low temperature behaviour of thermodynamic and transport coefficients. The most commonly proposed triplet f -wave gap function with E_{2u} symmetry is given by

$$\mathbf{d}(\mathbf{k}) = \eta_1 [k_z \hat{\mathbf{z}}(k_x^2 - k_y^2) + \eta_2 (2k_z \hat{\mathbf{z}} k_x k_y)]. \quad (74)$$

The orientation of the \mathbf{d} -vector is assumed to be \mathbf{k} -independent and pinned along the hexagonal c -axis ($\hat{\mathbf{z}}$) by an anisotropy potential acting on the (Kramers degeneracy) pseudo spin of the heavy quasiparticles which has its origin in the spin-orbit coupling of 5 f -electrons. This pinning effect leads to a large paramagnetic limiting effect for $\mathbf{B} \parallel \mathbf{d}, \hat{\mathbf{z}}$ and to no effect for $\mathbf{B} \perp \mathbf{d}, \hat{\mathbf{z}}$ which was suggested (Graf et al., 2000) as origin of the crossover in the a - c upper critical field anisotropy mentioned before. This is claimed as strong evidence for triplet pairing (Graf et al., 2000) and as argument against the singlet d -wave (E_{1g}) gap function. Defining $\mathbf{d}(\mathbf{k}) = \Delta(\mathbf{k})\hat{\mathbf{z}} = \Delta(\vartheta, \varphi)\hat{\mathbf{z}}$ where ϑ, φ are the polar and azimuthal angles of \mathbf{k} one has explicitly the following E_{2u} gap functions (without normalization) for the A, B ($a = 1$) and C phases ($\Delta_0 \equiv |\eta_{1,2}|$)

$$\begin{aligned} A(1, 0): \quad \Delta(\vartheta, \varphi) &= \Delta_0 k_z (k_x^2 - k_y^2) = \Delta_0 \cos \vartheta \sin^2 \vartheta \cos(2\varphi), \\ B(1, i): \quad \Delta(\vartheta, \varphi) &= \Delta_0 k_z (k_x + ik_y)^2 = \Delta_0 \cos \vartheta \sin^2 \vartheta \exp(2i\varphi), \\ C(0, 1): \quad \Delta(\vartheta, \varphi) &= 2\Delta_0 k_z k_x k_y = \Delta_0 \cos \vartheta \sin^2 \vartheta \sin(2\varphi). \end{aligned} \quad (75)$$

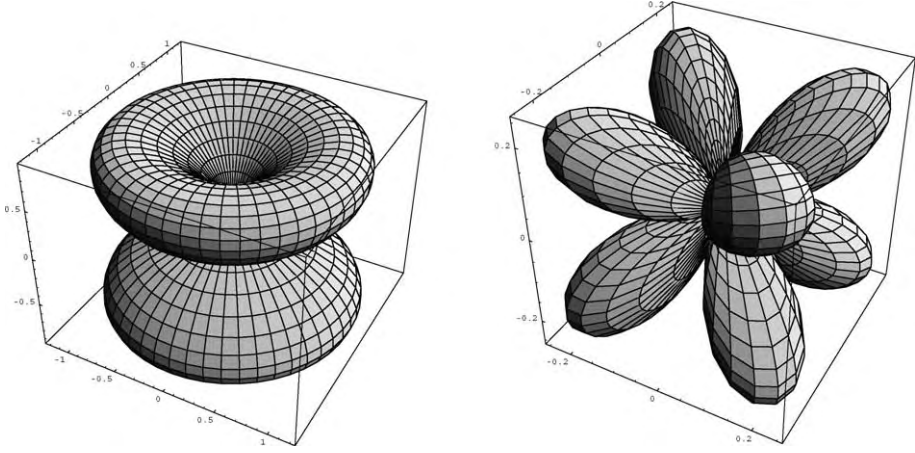


Fig. 30. Spherical plots of $|\Delta(\vartheta, \varphi)|$ for B -phase (left) and C -phase (right). B -phase has node line $\vartheta = \frac{\pi}{2}$ ($k_z = 0$) and 2nd order node points along c -axis ($\vartheta = 0, \pi$). C -phase has additional node lines at $k_x = 0, k_y = 0$ ($\varphi = 0, \frac{\pi}{2}$) (Yang and Maki, 1999).

An angular plot of these gap functions is shown in fig. 30 which also exhibits their node structure described in the caption. In the above equation the equal amplitude approximation $a = 1$ was made for the B -phase which leads to a gap with full rotational symmetry around c . As an effect of the SBF which leads to $a < 1$ the rotational symmetry is slightly broken, one has to multiply the (B -phase) gap function by a factor $(1 - \epsilon^2 \sin^2(2\varphi))^{1/2}$ with four-fold symmetry around c and $\epsilon^2 = 1 - a^2 = 0.26$. The node structure is unchanged, it consists of an equatorial line node and two second order node points at the poles. Both contribute to the linear behaviour of the quasiparticle DOS $N(E)$ for $E \ll \Delta_0$. It was calculated (Yang and Maki, 2001) including the effect of impurity scattering which quickly leads to a residual DOS $N(0)$. Indeed in UPt_3 large residual γ values are usually obtained by extrapolation from temperatures above the magnetic ordering at 28 mK. Finally one should note that the presence of a node line is not required by symmetry if one assumes the strong spin-orbit coupling case (Blount, 1985), it is rather a result of a special choice of the E_{2u} order parameter in the allowed subspace. Forming a linear combination of all possible E_{2u} representations there are in general only point nodes. However, as argued above and in sect. 2, the weak spin-orbit coupling case is more realistic in the effective quasiparticle pseudo spin picture for UPt_3 and then the appearance of node lines is natural. It is obvious from fig. 30 and eq. (75) that the non-unitary B -phase has fewer nodes than the unitary A - or C -phases. This general feature of non-unitary phases means that they are preferred as stable low temperature states in unconventional SC because fewer nodes lead to a larger condensation energy.

The ratio of fourth order Landau coefficients $\beta_1/\beta_2 \simeq 2$ was taken as evidence for the weak coupling nature of superconductivity. Therefore the question arises whether it is possible to calculate the symmetry of the order parameter within a microscopic weak coupling Hamiltonian starting from an on-site effective quasiparticle interaction which is repulsive. Such

attempts have originally been made without the inclusion of the orbital degeneracy of U-5f states and within one band models with the static susceptibility tensor used as an input. However, not surprisingly the gap functions obtained are sensitive to the input function and also the E_{2u} gap function is not the favored one (Norman, 1991, 1994) in such models. Attempts to include orbital degrees of freedom to remedy this situation have been made (Norman, 1994). As mentioned before it has now become clear that 5f-states in UPt₃ have also a dual nature, partly localised in 5f² configurations and partly itinerant states which have heavy masses due to renormalisation by low lying CEF excitations of the 5f²-states. It is therefore possible that, as in the case of UPd₂Al₃, exchange of localised 5f² excitation modes play an essential role for the formation of unconventional Cooper pairs in UPt₃.

4.1.8. Low temperature transport properties

The quasiparticle energies vanish at the nodes of the superconducting gap. Therefore the low temperature ($T \ll T_c$) behaviour of thermodynamic and transport coefficients may give information on the node structure. Specific heat analysis has proved of little use due to the presence of the huge 28 mK peak caused by the onset of true long range magnetic order of the small moments. Thermal conductivity measurements for $0.1 < T/T_{c2} < 0.3$ (Lussier et al., 1996) have been more succesful. The temperature dependence in this asymptotic regime requires the presence of node lines and/or second order node points, furthermore comparison of the anisotropy ratio $\kappa_c(T)/\kappa_a(T)$ shown in fig. 31 with the calculated ones (Norman and Hirschfeld, 1996) gives good agreement for the E_{2u} gap function of the B-phase in eq. (75). Extrapolation for zero temperature leads to a ratio ~ 0.5 contrary to the older E_{1g} model which extrapolates to zero. This difference is due to the presence of second order node points with $\Delta(\vartheta) \sim \vartheta^2$ or $(\pi - \vartheta)^2$ at the poles in the E_{2u} case. Finally for $T/T_{c2} < 0.1$ one reaches

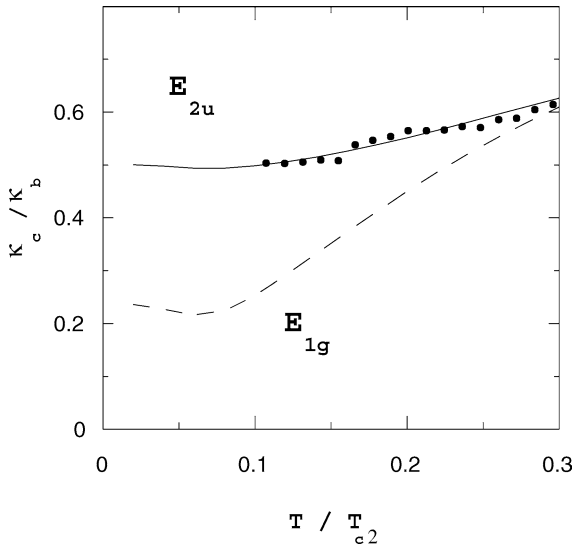


Fig. 31. Anisotropy ratio κ_c/κ_b of thermal conductivities as function of the reduced temperature. Data from (Lussier et al., 1996).

the gapless regime where the pair breaking energy scale $\sqrt{\hbar\Gamma kT} > kT$ with Γ denoting the normal state impurity scattering rate. In this case a behaviour $\kappa/T \sim \alpha + \beta T^2$ is predicted (Graf et al., 1996) in good agreement with observations (Suderow et al., 1997).

4.1.9. NMR Knight shift results

The Knight shift (KS) in the superconducting regime is a direct measure of the change $\delta\chi_s$ in the spin susceptibility of the SC condensate. It can be measured by μ SR or NMR experiments. In the latter the NMR resonance frequency is shifted due to the contact interaction of nuclear and electronic spin moment (sect. 2). Ideally when spin–orbit coupling can be neglected, the KS should drop to zero for a singlet SC state and should be unchanged for a triplet state. Spin–orbit coupling complicates the interpretation and may lead to only a partial reduction for a singlet state and an observable anisotropic reduction in the triplet state (Mineev and Samokhin, 1999). In the latter case for a rigid $\mathbf{d}(\mathbf{k})$ with respect to \mathbf{H} one has for the susceptibility tensor ($i, j = x, y, z$):

$$\chi_{sij} = \chi_n \int \frac{d\Omega}{4\pi} [(P_{ij}^\perp(\mathbf{k}) + Y(\hat{\mathbf{k}}, T)P_{ij}^\parallel(\mathbf{k}))], \quad (76)$$

where χ_n is the normal state spin susceptibility (assumed isotropic for simplicity). Furthermore $P_{ij}^\parallel(\mathbf{k}) = d_i^*(\mathbf{k})d_j^*(\mathbf{k})/|\mathbf{d}(\mathbf{k})|^2$ and $P_{ij}^\perp(\mathbf{k}) = [\delta_{ij} - P_{ij}^\parallel(\mathbf{k})]$ are the projectors to the direction parallel and perpendicular to $\mathbf{d}(\mathbf{k})$, respectively, and $Y(\hat{\mathbf{k}}, T)$ is related to the Yoshida function of sect. 2.

In the strong spin–orbit coupling case with the \mathbf{d} -vector pinned along c one would expect a suppression of the KS for \mathbf{H} applied parallel to the c direction due to the effect of $Y(\hat{\mathbf{k}}, T)$ but not for $\mathbf{H} \perp c$, i.e., for \mathbf{H} in the hexagonal plane. The Knight shift should therefore be quite anisotropic for pinned \mathbf{d} -vector. However it was found (Tou et al., 1996, 1998;

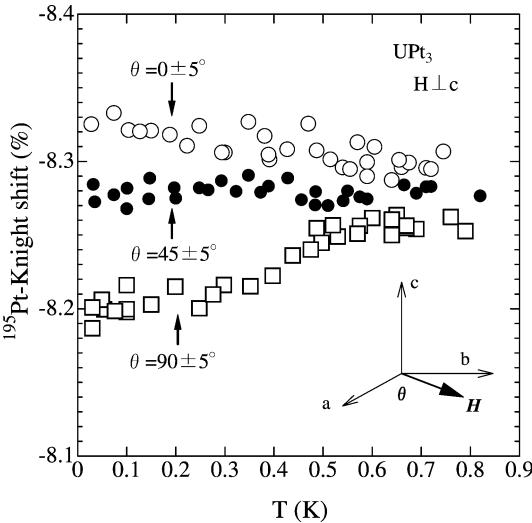


Fig. 32. Anisotropic Knight shift for field in the hexagonal plane ($H = 0.19$ T) (Kitaoka et al., 2000). The field angle dependence of $\sim 1\%$ of the Knight shift is possibly a sign of weak \mathbf{d} -vector pinning by the SBF.

Kitaoka et al., 2000) that for large fields (in the C -phase) there is almost no change for both field directions. This was interpreted as evidence that the weak spin-orbit coupling case is realized in UPT_3 . In this case the \mathbf{d} -vector may be rotated by the field. For large fields it is always perpendicular to \mathbf{H} and therefore no KS reduction will take place. On the other hand for low fields (in the B -phase) it may be pinned by the SBF (parallel to a) and therefore rotation of \mathbf{H} in the hexagonal ab -plane will produce an anisotropic Knight shift as shown in fig. 32. The weak spin-orbit coupling scenario has also been theoretically investigated (Ohmi and Machida, 1996, 1996a). On the other hand this interpretation seems to be in conflict with the anisotropic paramagnetic limiting which leads to the reversal for the upper critical field anisotropy as explained before. This discrepancy has so far not been resolved.

4.1.10. Magnetothermal properties in the vortex phase

The a - c anisotropy of the zero-field thermal conductivity in the B -phase has provided a major argument for the E_{2u} SC order parameter with its second order nodal points at the poles. These node points (and also the equatorial node line) have, however, not been seen directly until now. As explained in sect. 2 magnetothermal conductivity or specific heat measurements in the vortex phase as function of field angles can provide such direct evidence. Due to the comparatively low T_c of UPT_3 experiments have to be done at 50 mK or below, so far they have not been performed. Calculations of the field angle dependence for the B -phase (Maki and Thalmeier, 2003) and the C -phase (Thalmeier and Maki, 2003a) have been carried out however. For simplicity we discuss only the former since the modulus of the gap function in the B -phase is isotropic in the hexagonal plane according to eq. (75). This means that specific heat and c -axis thermal conductivity κ_{zz} depend only on the polar field angle θ . They are given in the low temperature and superclean limit of sect. 2 by $(\tilde{v} = (v_a v_c)^{1/2})$

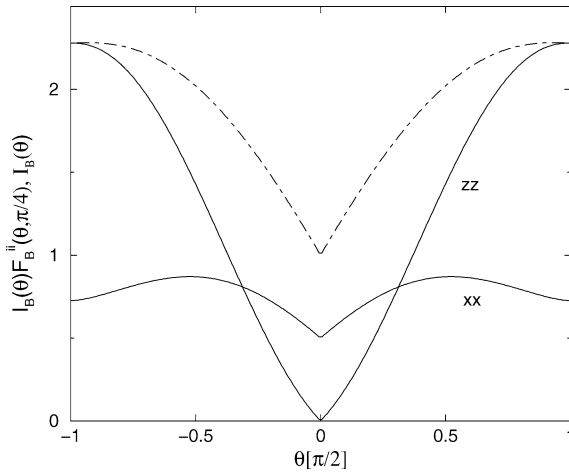


Fig. 33. Angular dependence of specific heat (dot-dashed) and thermal conductivity κ_{ii} ($i = x, z$) on polar field angle θ . Cusps at $\theta = 0$ are due to polar node points of the gap in eq. (75). While κ_{zz} is independent of ϕ , κ_{xx} is shown for $\phi = \frac{\pi}{4}$ (Thalmeier and Maki, 2003a).

$$\begin{aligned}
\frac{C_s(\theta)}{\gamma T} &= \frac{1}{\sqrt{3}} \tilde{v} \sqrt{eH} I_B(\theta), \\
\frac{\kappa_{zz}(\theta)}{\kappa_n} &= \frac{2}{3} \frac{\tilde{v}^2}{\Delta^2} (eH) I_B(\theta) F_B^{zz}(\theta), \\
I_B(\theta) &= \alpha \sin \theta + \frac{2}{\pi} E(\sin \theta),
\end{aligned} \tag{77}$$

where $F_B^{zz}(\theta) = \sin \theta$ and $E(\sin \theta)$ is the complete elliptic integral. The θ -dependent factors in the above equation are shown in fig. 33. Sharp cusps for $\theta = 0, \pi$ are indeed seen in these functions which, if observed in the corresponding specific heat $C_s(\theta)$ and thermal conductivity $\kappa_{zz}(\theta)$, would constitute a direct and unambiguous proof for the polar node points in the B -phase of UPt_3 . Likewise the equatorial line node of the B -phase will lead to a flat minimum (without a cusp) for $\theta = \frac{\pi}{2}$ in $\kappa_{xx}(\theta)$. Observing these features in UPt_3 as ultimate proof for the node structure is an experimental challenge.

4.2. Magnetic exciton mediated superconductivity in UPd_2Al_3

Among the U-based HF superconductors UPd_2Al_3 (Geibel et al., 1991a) is a rather special case. In this HF compound with a moderate $\gamma = 140 \text{ mJ/mol K}^2$ there is also AF order below $T_N = 14.3 \text{ K}$ with almost atomic size local moments ($\mu = 0.85\mu_B$) in contrast to the small moments in other U-compounds. The entropy release is $\Delta S(T_N) = 0.67R \ln 2$ per mole, much larger than in the itinerant SDW sister compound UNi_2Al_3 . The AF order coexists with superconductivity below $T_c = 1.8 \text{ K}$. This suggests that in addition to the heavy itinerant quasiparticles nearly localised 5f-electrons should be present. They result from the dominating $5f^2$ configuration of the U^{4+} ion (Grauel et al., 1992). This dual nature of 5f-electrons is even more obvious than in UPt_3 as is seen from various experimental investigations like susceptibility (Grauel et al., 1992), Knight shift (Feyerherm et al., 1994) and optical measurements (Dressel et al., 2002). The former exhibit a pronounced a - c axis anisotropy (Grauel et al., 1992) shown in fig. 34 with a much larger $\chi_a(T)$ whose T -dependence is very reminiscent of CEF-effects.

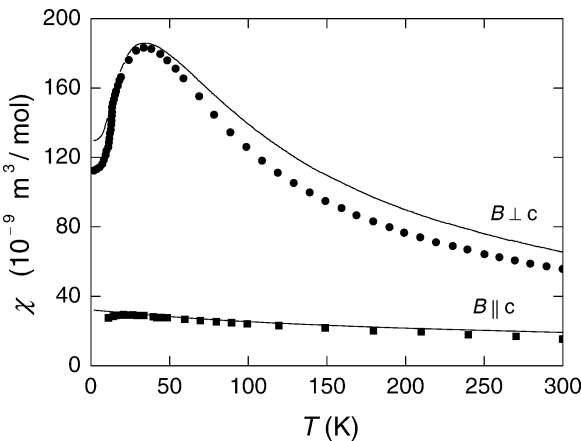


Fig. 34. Magnetic susceptibility of UPd_2Al_3 for field parallel to a - and c -axis. The pronounced maximum for $\chi_{\perp}(T)$ is a typical signature of CEF split localised 5f-states (Grauel et al., 1992). The full line is a fit using a U^{3+} CEF level scheme containing singlet ground state and first excited state (33 K).

A CEF scheme with two low lying singlets split by δ was proposed for the $5f^2$ localized states. Later investigations (Shiina, 2001) indicate that the first excited state is rather a doublet with $\delta = 6$ meV. Since the ground state is a singlet the local $5f$ -moment magnetism must be of the induced type caused by the mixing with the excited doublet via inter-site exchange. A direct confirmation of this dual nature of $5f$ -electrons in UPd_2Al_3 was obtained from inelastic neutron scattering (INS) (Mason and Aeppli, 1997) which found excitations that originate in local CEF transitions of energy δ and disperse into bands of ‘magnetic excitons’ due to intersite exchange. This band extends up to 8 meV and along the c direction the modes are propagating with little damping. Later high resolution INS experiments (Sato et al., 1997, 1997a; Bernhoeft et al., 1998; Bernhoeft, 2000) have shown that below T_c a resonance like structure in the dynamical structure function of localised moments appears which is linked to the superconducting quasiparticles. Complementary tunneling experiments probe the response of the itinerant quasiparticles and their superconducting gap. In a breakthrough experiment this has been achieved the first time for a HF superconductor using an epitaxially grown $\text{UPd}_2\text{Al}_3\text{-AlO}_x\text{-Pb}$ tunneling device (Jourdan et al., 1999). Typical strong coupling features in the tunneling DOS have been observed which appear at an energy related to the excitations of local moments seen in INS. Together both experiments strongly suggest that the magnetic excitons identified in INS are the bosonic ‘glue’ which binds the electrons together to Cooper pairs (Sato et al., 2001). This is a new mechanism for superconductivity distinctly different from both the electron–phonon and spin fluctuation mechanism known sofar. The pairing potential is mediated by a propagating boson (the magnetic exciton) as in the former but depends on the spin state of conduction electrons as in the latter. It is the main purpose of this section to present the evidence for this important new mechanism for unconventional superconductivity. Before considering this in detail we summarize some essential physical facts known about UPd_2Al_3 .

4.2.1. AF structure and superconducting properties

The AF magnetic structure of UPd_2Al_3 consists of FM ordered hexagonal planes with moments ($\mu = 0.83\mu_B$) in $[100]$ direction and stacked antiferromagnetically along the c -axis (Krimmel et al., 1992; Kita et al., 1994). It corresponds to an AF wave vector $\mathbf{Q} = (0, 0, \frac{1}{2})$ (in r.l.u.) and is shown in fig. 35. As expected from the large a – c anisotropy of the susceptibility in fig. 34 the AF structure does not change in applied magnetic fields \mathbf{H} along c . For fields in the easy ab -plane the hexagonal in-plane anisotropy is much smaller and moment reorientation can be seen. The magnetic B – T phase diagram has been determined by Kita et al. (1994) and no effects of the superconducting transition at $T_c = 1.8$ K on the magnetic structure has been found supporting the idea of two separate superconducting (itinerant) and magnetic (localised) $5f$ -subsystems.

The superconducting state of UPd_2Al_3 has been investigated by thermodynamic and transport measurements (Caspary et al., 1993; Hessert et al., 1997; Hiroi et al., 1997), NMR (Tou et al., 1995; Matsuda et al., 1997), μSR experiments (Feyerherm et al., 1994) and tunneling studies (Jourdan et al., 1999). Despite this great effort the symmetry of the order parameter is not reliably known sofar.

The upper critical field exhibits flattening for low temperatures which has been interpreted as a Pauli limiting effect and hence evidence for singlet pairing (Hessert et al., 1997). The

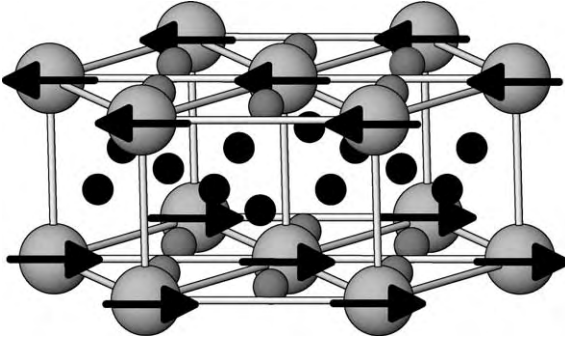


Fig. 35. Conventional unit cell of UPd_2Al_3 ($a = 5.350 \text{ \AA}$, $c = 4.185 \text{ \AA}$) and simple AF magnetic structure with propagation vector $\mathbf{Q} = (0, 0, \frac{1}{2})$. The large and small grey spheres in hexagonal planes correspond to the U and Pt atoms, respectively, intercalated by Al atoms (small black spheres).

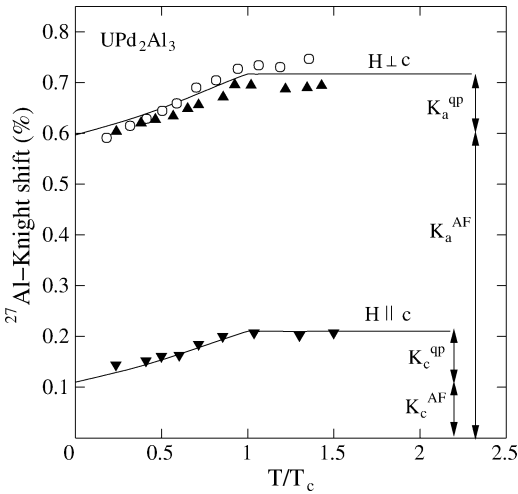


Fig. 36. ^{27}Al Knight shift from NMR below T_c (Kitaoka et al., 2000). The arrows indicate the suggested separation in localised (AF) and itinerant quasiparticle (qp) contributions. The AF and qp parts cannot be independently determined experimentally. Therefore the complete suppression of K^{qp} is a conjecture.

angular dependence $H_{c2}(\theta)$, where θ is the polar angle, changes dramatically from $T = 1.5 \text{ K}$ to $T = 0.5 \text{ K}$ which was interpreted as a gradual change from d-wave to s-wave character of the order parameter when temperature is lowered. Within this picture the effect of background AF order was ignored which may not be permissible because the critical fields for localized 5f-spin reorientation are of the same order as H_{c2} (Grauel et al., 1992; Kita et al., 1994).

The Knight shift in the SC phase is a direct probe for the reduction of the spin susceptibility $\chi_s(T)$ in the SC state (Tou et al., 2003). Ideally there should be a complete suppression of $\chi_s(T)$ for singlet pairing and no effect for triplet pairing (sects. 2 and 4.1). This picture is however complicated by the effect of spin-orbit coupling which may lead to intermediate cases. The result for $\Delta K_s(T)$ as obtained from ^{27}Al NMR experiments (Tou et al., 1995) is shown in fig. 36. Although a reduction is clearly visible, large (anisotropic) residual Knight shift values remain. This is attributed to the localized 5f-susceptibility which cannot be independently determined. Therefore these results and similar ones from μSR experiments (Feyrherm et al., 1994) are difficult to interpret. It is not possible to say with certainty how strong

the Knight shift caused by the itinerant quasiparticles is actually reduced in the SC phase. But the conclusion concerning singlet pairing seems unaffected by this ambiguity.

The ^{27}Al NMR relaxation rate T_1^{-1} was found to exhibit a T^3 behaviour in the SC state over four orders of magnitude down to $0.1T_c$ (Tou et al., 1995) where the gap amplitude will be constant. This means that $\Delta(\mathbf{k})$ should have a node line implying a low quasiparticle energy DOS $N_s(E) \sim |E|$. This conclusion was confirmed by ^{105}Pd NMR/NQR experiments (Matsuda et al., 1997) which also observed a T^3 behaviour of the relaxation rate and the absence of a coherence peak immediately below T_c was noticed, both facts are naturally explained by the existence of a node line in $\Delta(\mathbf{k})$.

Commonly in HF compounds the low temperature behaviour of the specific heat is not easily explained by simple models that involve only the topology of gap nodes. Very often residual γ -values exist where they should not due to node points or lines in $\Delta(\mathbf{k})$. This is ascribed to the presence of a residual density of states induced by impurity scattering. Extracting the true low temperature behaviour of the electronic specific heat C_s is also complicated by the presence of nuclear terms due to the hyperfine splitting which lead to a low temperature upturn $\sim \alpha T^{-2}$. This situation has also been encountered in UPd_2Al_3 . Originally the existence of a residual γ -value was concluded in Caspary et al. (1993) but later measurements extending to lower temperatures (Sato, 1993) have shown that the data can be well fitted without the residual γ but assuming instead a dominant T^2 term in $C_S(T)$ which is compatible with the node line hypothesis for UPd_2Al_3 . It is not known yet whether the field dependence of $C_S(T, H)$ is dominated by field induced $\gamma(H) \sim \sqrt{H}$ expected in the presence of nodes.

Thermal conductivity measurements for parallel heat current and field lying in the hexagonal plane (Hiroi et al., 1997) have shown a dominating temperature dependence $\kappa(T) \sim T^2$ and a linear behaviour $\kappa(T, H) \sim H$ at low temperatures. This is again in agreement with the existence of node lines in $\Delta(\mathbf{k})$. However their exact position on the FS is not yet known. This has to be investigated by field-angle dependent thermal conductivity measurements which has been successful in this task in other unconventional superconductors as described in sect. 2.

4.2.2. *Electronic structure, Fermi surface and effective mass*

In LDA type electronic band structure calculations for intermetallic U-compounds all 5f-electrons are treated in the same way and their degree of (de-)localisation is not much different. This is in contradiction to the behaviour observed in UPd_2Al_3 just as described above. Nevertheless LDA calculations give usually reasonable results for the Fermi surface topology. This can be understood in the context of model calculations as a result of many body correlations. For example within the Anderson lattice model it may be shown that the Fermi volume comprises both the f-electrons and conduction electrons ('Luttinger's theorem'), even in the Kondo limit when the f-electron is localised (Fazekas, 1999). Therefore it looks as if the Fermi wave vector, and more generally the Fermi surface is the same as if both type of electrons were delocalised. This is indeed assumed in LDA calculations for UPd_2Al_3 which we discuss now. FS sheets and associated angle dependent de Haas-van Alphen (dHvA) frequencies have first been calculated by Sandratskii and Kübler (1994), Knöpfle et al. (1996) and compared to the experimental dHvA results (Inada et al., 1995). Similar calculations (Inada et al., 1999) obtain the same main FS sheets but differ in the positions of smaller sheets.

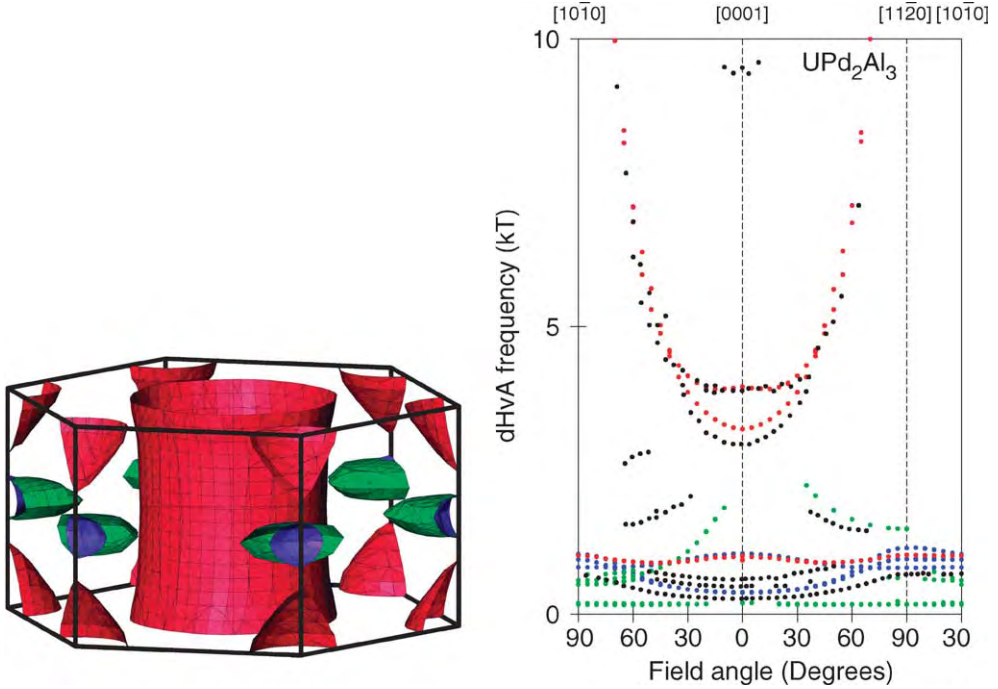


Fig. 37. Left panel: Fermi surface of UPd₂Al₃ calculated within the dual approach method (Zwicknagl et al., 2003). The main cylinder part has also a heavy mass with $m^* = 19\text{--}33m$. Right panel: Comparison of experimental dHvA frequencies (black symbols) from (Inada et al., 1999) and calculated frequencies (color symbols compatible with FS sheets on left panel) from the dual approach model (Zwicknagl et al., 2003). Large parabola corresponds to the main FS cylinder.

The larger sheets are also those with experimentally found heavy masses, which the LDA calculation naturally cannot explain. The largest sheet which also has the strongest 5f-admixture is shown in fig. 37 in the AF Brillouin zone. It has the shape of a corrugated cylinder if one ignores the hexagonal in-plane anisotropy. In the subsequent model calculations we assume this simplified FS for UPd₂Al₃ and neglect all other sheets. The LDA approach to the 5f-electronic structure does not include the different degree of localisation evident from experiments discussed before. Progress in the treatment of partial localisation of 5f-electrons has recently been made for a number of U-compounds including UPt₃ (Zwicknagl et al., 2002) (sect. 4.1) and UPd₂Al₃ (Zwicknagl et al., 2003). Due to the strong spin-orbit coupling 5f-electrons occupy total angular momentum orbitals $|j = 5/2, j_z\rangle$. The two localised 5f-electrons are put into $j_z = \pm 5/2$ and $j_z = \pm 1/2$ localized states and the remaining $j_z = \pm 3/2$ states are included in the LDA basis of band electrons. This treatment is justified by the larger hybridization of the $j_z = \pm 3/2$ orbitals as compared to $j_z = \pm 1/2, \pm 5/2$ already on the LDA level. It has been shown within model calculations (Efremov et al., 2004) that intra-atomic correlations strongly increase the orbital dependence of the effective hybridization, leading to

Table 5
Effective masses for $\mathbf{H} \parallel c$

FS sheet	m^*/m (exp.)	m^*/m (theory)
ζ	65	59.6
γ	33	31.9
β	19	25.1
ϵ_2	18	17.4
ϵ_3	12	13.4
β	5.7	9.6

Notation for FS sheets and experimental values from Inada et al. (1999). Theoretical values from Zwicknagl et al. (2003).

the dual character of the 5f-electrons (sect. 2). Although two of the 5f-electrons are localised, the Fermi surface obtained from this calculation shows good agreement with the experimental results of the dHvA experiments. They are presented in fig. 37 together with the theoretical calculations.

This is reassuring for the dual 5f model approach, however the FS is also in good agreement with standard LDA calculations as discussed before. The decisive advantage of the former is that it also provides a basically parameter free explanation for the mass enhancement which cannot be obtained within LDA. The enhancement is due to the coupling of the delocalised with the localised 5f-electrons characterised by a matrix element $\alpha = 2a_{5f}M$. As explained below the latter are split into two low lying CEF singlet states with an excitation energy δ which is known from INS. Then the global mass enhancement factor (m^*/m_b) (independent of the FS sheet) with respect to the band mass m_b may be calculated according to eqs. (65), (66) as in the case of UPt₃. The comparison of experimental and theoretical total mass enhancement m^*/m is presented in table 5.

4.2.3. The dual model for UPd₂Al₃ and induced moment AF

The dual model for UPd₂Al₃ which comprises both localised 5f² electrons with total angular momentum \mathbf{J} and itinerant heavy 5f-electrons created by $c_{\mathbf{k}\sigma}^\dagger$ is described by the model Hamiltonian

$$\begin{aligned}
 H &= H_c + H_{\text{CEF}} + H_{ff} + H_{cf}, \\
 H &= \sum_{\mathbf{k}\sigma} \epsilon_{\mathbf{k}\sigma} c_{\mathbf{k}\sigma}^\dagger c_{\mathbf{k}\sigma} + \delta \sum_i |e\rangle\langle e|_i - \sum_{\langle\langle ij \rangle\rangle} J_{ff}(ij) \mathbf{J}_i \mathbf{J}_j - 2I_0(g-1) \sum_i \mathbf{s}_i \mathbf{J}_i,
 \end{aligned} \tag{78}$$

where

$$\epsilon_{\mathbf{k}\sigma} = \epsilon_\perp(\mathbf{k}_\perp\sigma) - 2t_\parallel \cos k_z \tag{79}$$

is a model for the heavy conduction band energies whose FS is a corrugated cylinder along the hexagonal c -axis. Here t_\parallel is the effective hopping along c which determines the amount of corrugation. The form of the dispersion $\perp c$ is not important. The localised 5f²-electrons show a CEF splitting $\delta = 6$ meV into a singlet ground state $|g\rangle$ and an excited singlet $|e\rangle$ at δ . The remaining terms describe a superexchange J_{ff} between localised and an on-site

exchange $I = I_0(g - 1)$ between itinerant and localised 5f-electrons. The total effective inter-site exchange has therefore an additional RKKY contribution:

$$J(\mathbf{q}) = J_{ff}(\mathbf{q}) + I_0^2(g - 1)^2 \chi_e(\mathbf{q}). \quad (80)$$

Here $\chi_0(\mathbf{q})$ is the conduction electron susceptibility. $J(\mathbf{q})$ may be fitted to the experimentally observed magnetic excitations.

4.2.4. Induced moments and magnetic exciton dispersion in UPd_2Al_3

First we consider the magnetism of the localised 5f moments without dynamic effects of coupling to itinerant 5f-electrons. In a nonmagnetic singlet ground state system with $\langle g | \mathbf{J} | g \rangle \equiv 0$ the moments have to be induced via nondiagonal matrix elements $\langle e | J_x | g \rangle = -i \langle e | J_y | g \rangle = \frac{1}{2} \alpha$ between ground state and excited state singlets. In UPd_2Al_3 the maximum of $J(\mathbf{q})$ is at the AF wave vector $\mathbf{Q} = (0, 0, \frac{1}{2})$ with $J_e \equiv J(\mathbf{Q})$. In the resulting AF state the CEF ground state will then be a superposition of $|g\rangle$ and $|e\rangle$. This type of magnetism is well known for Pr-metal and its compounds where one has two CEF split singlets from the $Pr^{3+}(4f^2)$ configuration (Jensen and Mackintosh, 1991). This induced moment AF is only possible if the control parameter

$$\xi = \frac{\alpha^2 J_e}{2\delta} \quad (81)$$

exceeds a critical value, i.e., $\xi > \xi_c = 1$. Then the Néel temperature T_N and saturation moment $\langle J \rangle_0$ oriented along the a -axis (x -direction) are given by

$$T_N = \frac{\delta}{2 \tanh^{-1}(\frac{1}{\xi})} \quad \text{and} \quad \langle J \rangle_0 = \frac{1}{2} \alpha \frac{1}{\xi} (\xi^2 - 1)^{1/2}. \quad (82)$$

When ξ is only slightly larger than $\xi_c = 1$ ($T_N/\delta \ll 1$) the saturation moment will be $\sim \alpha \exp(-\delta/2T_N)$ and hence decreases exponentially for small T_N . This is the major difference from the usual local moment AF where the saturation moment is independent of T_N .

The signature of singlet–singlet induced moment magnetism is the existence of a paramagnetic excitation that grows soft on approaching T_N . The excitation spectrum is obtained from the dynamical local moment susceptibility

$$\chi_{ij;\alpha\beta}^{\lambda\mu}(\tau) = -\langle T \{ J_{i\alpha}^{\lambda}(\tau) J_{j\beta}^{\mu}(0) \} \rangle, \quad (83)$$

where i, j = lattice site, λ, μ = AF sublattices (A, B) and $\alpha, \beta = x, y, z$ denotes Cartesian components. Within RPA its Fourier transform is obtained as

$$\chi(\mathbf{q}, \omega) = [\mathbf{1} - \mathbf{u}(\omega) \mathbf{J}(\mathbf{q})]^{-1} \mathbf{u}(\omega). \quad (84)$$

Here $\chi(\mathbf{q}, \omega)$ and the single ion dynamical susceptibility $\mathbf{u}(\omega)$ are tensors in both sublattice (A, B) and transverse (xy) Cartesian coordinates. The poles of eq. (84) determine the collective excitations of 5f-local moments. In the paramagnetic phase they are given by the *magnetic exciton* dispersion

$$\omega_E(\mathbf{q}) = \delta \left[1 - \frac{\alpha^2 J(\mathbf{q})}{2\delta} \tanh \frac{\beta}{2} \delta \right]. \quad (85)$$

The physical origin and nature of magnetic excitons is illustrated in the inset of fig. 38 and described in the caption. When T_N is approached the exciton energy at \mathbf{Q} (PM zone boundary or AF zone center) becomes soft as a precursor to the appearance of the AF moment according to

$$\omega_E(\mathbf{Q}, T) = \frac{1}{2} \left(\frac{\delta}{T_N} \right)^2 \left(\xi - \frac{1}{\xi} \right) (T - T_N). \quad (86)$$

Below T_N an induced staggered moment leading to two magnetic sublattices appears. Its saturation value is given by eq. (82). Then $\mathbf{Q} = (0, 0, \frac{1}{2})$ becomes the center of the new AF Brillouin zone $[\frac{\pi}{2c}, -\frac{\pi}{2c}]$. In reality the softening of $\omega_E(\mathbf{Q}, T)$ will be arrested at a finite value at T_N by Curie type contributions to the static susceptibility which contribute to the AF instability but not to the exciton dispersion. Therefore a magnetic excitation gap at \mathbf{Q} will appear. Below T_N the dispersion is somewhat modified due to the effect of the molecular field, however for ξ only marginally above the critical value this modification is not important. This is indeed the case for the dual model of UPd_2Al_3 where $T_N/\delta = 0.22$ and hence $\xi = 1.015$. The magnetic exciton dispersion including the molecular field and exchange anisotropy has been derived (Thalmeier, 2002) and compared to the experimental results obtained in INS experiments (Mason and Aeppli, 1997). In this work the excitations were measured up to 10 meV in the whole BZ and it was found that well defined propagating modes exist along the hexagonal c^* -axis. For wave vector in the hexagonal plane $\perp c^*$ the line width of excitations was found to be much bigger. No excitation gap at the AF zone center \mathbf{Q} could be identified in these early experiments. This conclusion had to be revised in later high resolution experiments around \mathbf{Q} as discussed below. The comparison to the theoretical calculation using a parametrized exchange function $J(\mathbf{q})$ was given in Thalmeier (2002) and is shown in fig. 38. There the extended BZ was used which allows one to plot only the acoustic mode. It should be mentioned that it is not clear whether the dip at the K-point is realistic because the line width of magnetic excitons becomes rather large.

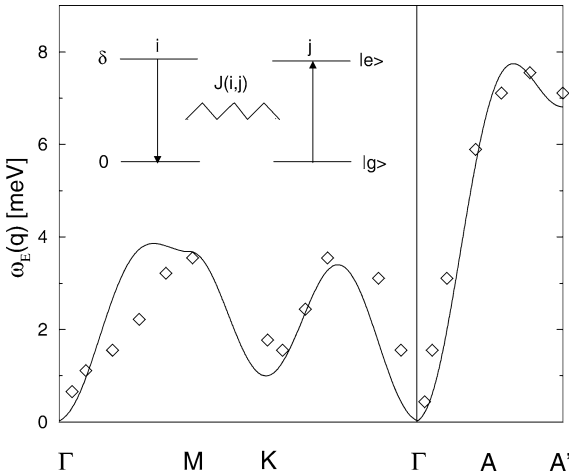


Fig. 38. Magnetic exciton dispersion of UPd_2Al_3 in the AF BZ. The diamonds are data from Mason and Aeppli (1997). The solid line is a calculation using a generalized version of eq. (85) with an appropriate model for the exchange function $J(\mathbf{q})$ (Thalmeier, 2002). The inset illustrates the principle of magnetic (Frenkel)-exciton propagation: A CEF singlet-singlet excitation (δ) propagates between lattice sites i, j through the action of intersite exchange $J(i, j)$ and thereby acquires a dispersion $\omega_E(\mathbf{q})$.

The damping of magnetic exciton modes has two sources: (i) Intrinsic dynamical effects in the localised moment system beyond RPA, e.g., damping by thermal fluctuations in the singlet occupation. (ii) Extrinsic damping due to the coupling to conduction electrons described by the last term in eq. (78). For low temperatures the latter is the dominating part. In addition it leads to a renormalized exciton mode frequency. Both effects can be described in extending the previous RPA approach including the last coupling term in eq. (78). This leads to coupled RPA equations (Buyers and Holden, 1985), the solution for the localised dynamical susceptibility is given by

$$\chi(\mathbf{q}, \omega) = \frac{u(\omega)}{1 - J_{ff}(\mathbf{q})u(\omega) - I^2 u(\omega)\chi_e(\omega)} \quad (87)$$

with

$$u(\omega) = \frac{\alpha \langle S \rangle}{\delta - \omega} \quad \text{and} \quad \chi_e(\omega) = \frac{1}{i\omega - \Gamma}, \quad (88)$$

where $u(\omega)$ is the single ion local moment susceptibility and $\chi_e(\omega) \equiv \chi_e(\mathbf{Q}, \omega)$ is the low frequency conduction electron susceptibility at $\mathbf{q} = \mathbf{Q}$ and Γ is a phenomenological damping rate. If one neglects its imaginary part and uses $\chi_e(\mathbf{q}) \sim \Gamma^{-1}$ for $\mathbf{q} \simeq \mathbf{Q}$ then, with eqs. (88), (80) the poles of eq. (87) again lead to the undamped magnetic exciton dispersion $\omega_E(\mathbf{q})$ of eq. (85). Inclusion of the imaginary part of $\chi_e(\omega)$ leads to a shift of the mode frequency and a damping. For a large coupling constant I , a part of the spectral weight of the magnetic exciton is shifted to low energies leading to an additional quasielastic peak.

The INS intensity is then proportional to the *localised* 5f-dynamical structure factor $S(\mathbf{q}, \omega) = \frac{1}{\pi} (1 + n(\omega)) \text{Im} \chi(\mathbf{q}, \omega)$ where $n(\omega) = (\exp(\beta\omega) - 1)^{-1}$ is the Bose factor. The experimental high resolution magnetic INS intensity for wave vectors close to \mathbf{Q} as obtained by Sato et al. (1997, 1997a), Bernhoeft et al. (1998) is shown in fig. 39. At the AF vector \mathbf{Q} above T_c (2.5 K) one can observe a strongly broadened inelastic peak at around 1.5 meV which is interpreted as the (upward) shifted magnetic exciton energy. In addition, as a signature of the strong coupling to conduction electrons one observes a quasielastic peak around $\hbar\omega \simeq 0$. The full line is a calculation of $S(\mathbf{Q}, \omega)$ using eq. (87) for $\chi(\mathbf{q}, \omega)$ and taking I and $\omega_E(\mathbf{Q})$ as adjustable parameters. The INS intensity was also measured for other wave vectors close to \mathbf{Q} along c^* . Repeating the same fitting procedure one may determine the *unrenormalized* magnetic exciton dispersion $\omega_E(\mathbf{q})$ which is shown in the inset of fig. 39. Obviously the magnetic excitons have a gap at the AF zone center of about 1 meV. As mentioned before in the original experiments (Mason and Aeppli, 1997) this gap was not identified due to insufficient resolution. In the singlet-singlet CEF model, even including a uniaxial anisotropy of the exchange, this relatively large gap cannot be explained. Its most probable origin is an arrested softening of $\omega_E(\mathbf{Q}, T)$ due to higher lying CEF states.

In fig. 39 another important feature is obvious: As temperature is lowered below $T_c = 1.8$ K the quasielastic peak evolves into a low energy inelastic peak. This is due to the appearance of the SC quasiparticle gap function $\Delta(\mathbf{k})$ which possibly may have node lines or points. Its influence on the conduction electron susceptibility may be described in a simple manner by shifting the diffusive pole at $-i\Gamma$ in $\chi_e(\omega)$ to $-i\Gamma + \Delta_{av}$ where the real part corresponds

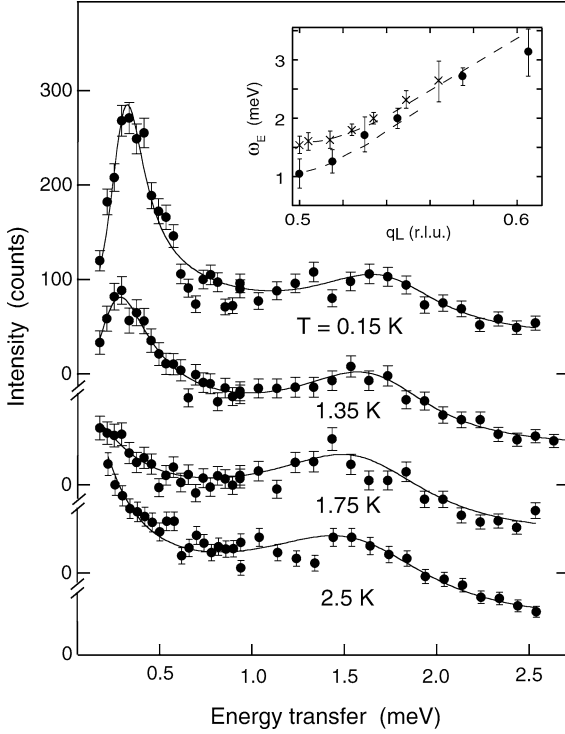


Fig. 39. INS spectrum for various temperatures above and below $T_c = 1.8$ K (Sato et al., 2001). The momentum transfer was varied around the AF point $\mathbf{q} = (0, 0, q_L)$. The solid line is the result of a calculation using eq. (87) from which the magnetic exciton energy $\omega_E(\mathbf{q})$ is determined for every \mathbf{q} . The result is shown in the inset for $T = 2.5$ K (crosses) and $T = 0.15$ K (circles).

to the \mathbf{k} -averaged SC gap. The calculated intensity in the SC phase (e.g., at $T = 0.15$ K) is then again shown as a full line from which the size of $\Delta_{av} \simeq \omega_E(\mathbf{Q})$ shows that magnetic exciton energy and SC gap are almost degenerate, which means that there will be a strong mixing of magnetic excitons with SC quasiparticle excitations. This explains why the lower peak appears with a large intensity.

4.2.5. Magnetic exciton anomalies in quasiparticle tunneling spectra

The near degeneracy of SC gap and magnetic exciton energy suggests that the latter might play a role in the formation of Cooper pairs in UPd_2Al_3 . Knowing only the INS results this would only be a hypothesis. However in a breakthrough experiment (Jourdan et al., 1999) the first SC quasiparticle tunneling in a HF system by using epitaxially grown UPd_2Al_3 was achieved. This experiment is complementary to INS measurements as it probes the itinerant 5f-electrons. The resulting tunneling spectra which ideally are proportional to the SC quasiparticle DOS are shown in fig. 40. The tunneling current is parallel to the c -axis and a real gap is seen in dI/dV in this direction. Therefore, if node lines of $\Delta(\mathbf{k})$ exist they should be perpendicular to the c -axis at k_z positions where the velocity $v_c(k_z)$ vanishes. The most striking result is the presence of typical ‘strong coupling anomalies’ around 1 meV which are well known from ordinary electron–phonon superconductors like Pb. These anomalies are connected to

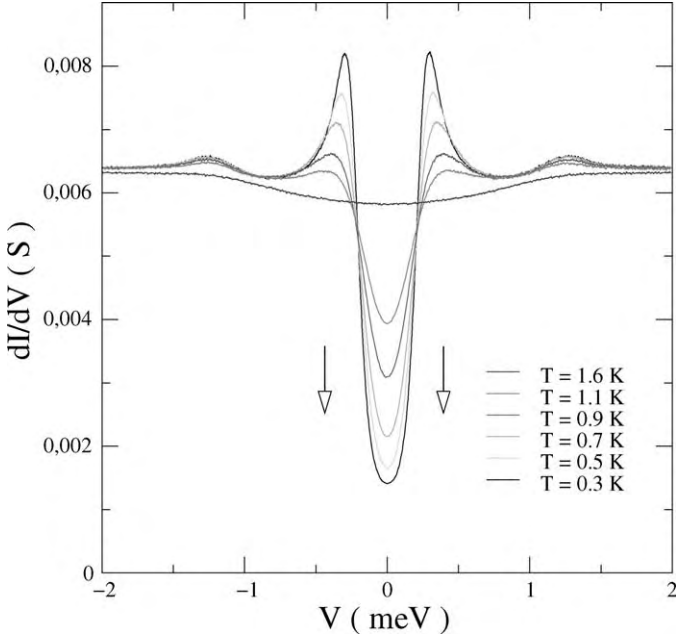


Fig. 40. Differential conductivity dI/dV of a c -axis oriented $\text{UPd}_2\text{Al}_3\text{-AlO}_x\text{-Pb}$ tunneling contact as function of the voltage across the tunneling contact for different temperatures (Jourdan et al., 1999). At low temperatures dI/dV is proportional to the quasiparticle DOS. The arrows indicate a monotonic depending of the SC-gap related minimum at $V = 0$ with decreasing temperature.

the frequency spectrum of the exchanged boson which is responsible for the formation of Cooper pairs in UPd_2Al_3 . The Debye energy of UPd_2Al_3 $k\theta_D = 13$ meV is much too large to be connected with the observed modulation around 1 meV, however it agrees perfectly with the magnetic exciton energy $\omega_E(\mathbf{Q})$ found by INS (inset of fig. 39). Furthermore the average gap energy and mode energy determined in INS are of the same order. This leads to the conclusion that UPd_2Al_3 is a magnetic exciton mediated strong coupling superconductor. This is the first time that a non-phononic mechanism for superconductivity has been proven in a direct way by identifying the non-phononic boson (magnetic exciton) that provides the ‘glue’ for the formation of Cooper pairs in UPd_2Al_3 . These arguments can be made more quantitative by using Eliashberg theory to calculate the SC quasiparticle DOS. The retarded effective potential due to magnetic exciton exchange can be described by a factorized ansatz

$$V_E(\mathbf{q}, \omega) = \frac{V_0\omega_0}{(\omega - \omega_E(\mathbf{Q}))^2 + \omega_0^2} f(\mathbf{k})f(\mathbf{k}') \quad (89)$$

which exhibits a maximum at the observed exciton frequency $\omega_E(\mathbf{Q})$ with a width ω_0 and strength V_0 . Here $\mathbf{q} = \mathbf{k}' - \mathbf{k}$ and $f(\mathbf{k})$ is the form factor which describes the \mathbf{k} -dependence of the superconducting singlet gap function $\Delta(\mathbf{k}) = \Delta f(\mathbf{k})$. For an isotropic conventional

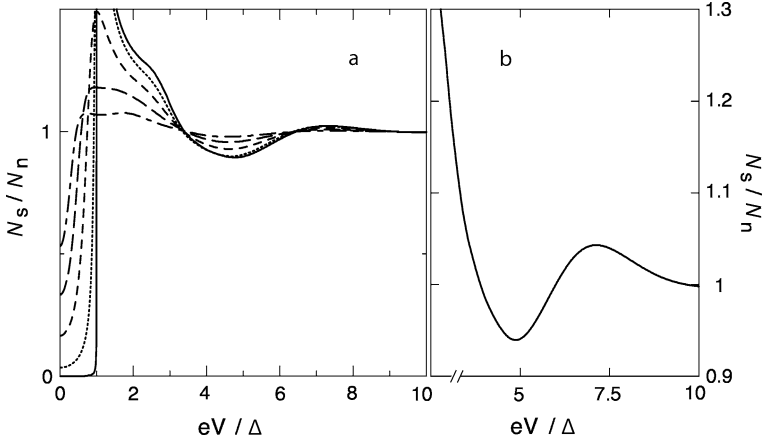


Fig. 41. Calculated tunneling DOS N_s using isotropic Eliashberg equations and the retarded potential of eq. (89). N_n is the DOS in the normal state. (a) The various lines correspond to temperatures $T/T_c = 0.25, 0.6, 0.9, 0.95$ from top to bottom at $eV/\Delta = 2$. (b) Enlarged strong coupling anomaly due to magnetic exciton exchange for $T = 0.25T_c$ (Sato et al., 2001).

e-p superconductor $f(\mathbf{k}) \equiv 1$. As explained in the next section in UPd_2Al_3 the gap function should have a node line perpendicular to the c -axis. For tunneling current along c the tunneling DOS can be determined from the *isotropic* Eliashberg equations using eq. (89) if one replaces $f(\mathbf{k})$ by the averaged constant $\langle f(\mathbf{k})^2 \rangle_{\text{FS}}^{1/2}$ which may then be absorbed into the coupling strength V_0 that is adjusted to obtain the experimental T_c . The result of this analysis is shown in fig. 41 which nicely explains the experimental results in fig. 40, especially: (i) The width of the gap does not depend much on temperature but is rather filled up with increasing temperature. This is characteristic for a strong coupling superconductor, the ratio $2\Delta/T_c = 5.6$ obtained here is rather high and agrees well with the ratio $2\Delta/T_c = 6$ obtained previously from the analysis of INS spectra. (ii) In the calculated tunneling DOS of fig. 41 typical modulations above the gap due to the retardation of the potential in eq. (89) appear at a voltage that corresponds to the magnetic exciton energy at \mathbf{Q} which is about 1 meV.

4.2.6. Possible symmetries of the superconducting order parameter

The existence of node lines of $\Delta(\mathbf{k})$ in UPd_2Al_3 was suggested by various thermodynamic properties discussed previously. Other evidence was proposed by Bernhoeft (2000) where it is claimed that the symmetry property $\Delta(\mathbf{k} \pm \mathbf{Q}) = \pm \Delta(\mathbf{k})$ has to be fulfilled to explain the large intensity of the low energy quasiparticle-like peak in fig. 39. This implies a node line orthogonal to the c -axis which is compatible with the appearance of a gap in the c -axis tunneling geometry as used for fig. 40. In the ansatz of eq. (89) the energy and momentum dependences are factorized and therefore the form factor $f(\mathbf{k})$, i.e., gap function symmetry is put in by hand. Considering the presence of a strong AF ordered moment $\parallel x$ -axis the appropriate symmetry group is orthorhombic D_{2h} . The simplest spin singlet even parity irreducible

representation appropriate for the FS with cylindrical symmetry (fig. 37) has the form

$$\Delta(\mathbf{k}) = \Delta \cos k_z \quad \text{with } A_{1g}(\Gamma_1^+)\text{-symmetry.} \quad (90)$$

This gap function is independent of k_x and k_y . A more general $\Delta(\mathbf{k})$ with the same symmetry can be obtained by multiplying eq. (90) with any fully symmetric function $f_{\Gamma_1^+}(k_x, k_y)$. $\Delta(\mathbf{k})$ has the required behaviour under the transformation $\mathbf{k} \rightarrow \mathbf{k} \pm \mathbf{Q}$ and it has a node line at the AF zone boundary $k_z = \pm \frac{1}{2}Q_z = \pm \frac{\pi}{2c}$. A theoretical investigation of possible gap functions based on a nonretarded weak coupling theory of the magnetic exciton mediated pair potential was undertaken in Thalmeier (2002). It was found that due to the CEF-anisotropy and the action of the AF local moment order the degeneracy of odd parity triplet states is lifted and one of them would be favored against the above even parity singlet state. However this may be due to the neglect of retardation which is not a good approximation for UPd₂Al₃ as evident from the previous discussion. As mentioned before Pauli limiting of H_{c2} and Knight shift reduction below T_c favor an even parity A_{1g} (singlet) state. Recently a strong coupling theory has been presented by McHale et al. (2004).

As in the borocarbides the gap function will be modified by the background magnetic order due to the reconstruction of Bloch states close to the magnetic Bragg planes $k_z = \pm \frac{1}{2}Q_z$. The AF modified gap function for the even parity state is given by eq. (117) which in the present case reduces to

$$\Delta(\mathbf{k}) = \Delta \cos k_z \left(\frac{\cos^2 k_z}{\lambda_{\text{AF}}^2 + \cos^2 k_z} \right)^{1/2}. \quad (91)$$

Here the dimensionless interaction parameter $\lambda_{\text{AF}} = (I\langle J \rangle_0)/(\alpha W_{\parallel})$ describes the strength of the AF influence on $\Delta(\mathbf{k})$. It is interesting to note that despite the presence of a node line the above order parameter is fully symmetric (A_{1g}) because it is invariant under all symmetry transformations of the *magnetic* unit cell. Thus in a strict sense UPd₂Al₃ cannot be called a superconductor with unconventional gap symmetry, although the novel magnetic exciton mechanism certainly is unconventional. Various possible nodal structures in addition to eq. (90) have been discussed by Thalmeier and Maki (2002) in the context of magnetothermal properties and experiments were performed by Watanabe et al. (2004).

4.2.7. UNi₂Al₃: a possible triplet superconductor

The HF superconductor UNi₂Al₃ (Geibel et al., 1991) ($\gamma = 120 \text{ mJ/K}^2 \text{ mol}$) is isostructural to its hexagonal sister compound UPd₂Al₃ (fig. 35) but it has rather different physical properties. It exhibits an incommensurate SDW below $T_m = 4.6 \text{ K}$ ($\mu = 0.2\mu_B$) with a modulation wave vector $\mathbf{Q}_m = (0.39, 0, 0.5)$, like in UPd₂Al₃ the moments are pointing to n.n. along the a direction of the hexagonal plane. Superconductivity sets in below $T_c = 1.2 \text{ K}$ and coexists with magnetic order. The T -dependence of $1/T_1$ in NMR (Kyogaku et al., 1993) and the small entropy release of $\Delta S = 0.12R \ln 2$ at T_m (Tateiwa et al., 1998) points to an itinerant character of magnetic order in contrast to UPd₂Al₃ ($\Delta S = 0.67R \ln 2$) which exhibits local moment magnetism of the induced type with large ordered moment. This view is supported by INS experiments (Gaulin et al., 2002) which do not show any evidence for propagating collective

modes in the SDW state unlike the magnetic exciton mode discussed previously for UPd₂Al₃. The magnetic excitation spectrum in UNi₂Al₃ consists of quasielastic spin fluctuations for all wave vectors and its energy width of about 6 meV corresponds to the coherence temperature ~ 80 K associated with the γ value. For temperatures not too close to T_m the spin fluctuations are centered around odd multiples of the commensurate AF wave vector $\mathbf{Q} = (0, 0, 0.5)$ and also extending along ridges in q_x -direction.

From the spin fluctuation spectrum of UNi₂Al₃ observed in INS which is located around an AF Bragg point one might expect it should be a textbook example of spin fluctuation mediated superconductivity. However as in the case of UPt₃ the spin singlet pairing predicted by AF spin fluctuation type theories (Miyake et al., 1986) is probably not realised. According to the ²⁷Al-Knight shift measurements of (Ishida et al., 2002) which did not observe any drop in the spin susceptibility below T_c UNi₂Al₃ should have a spin triplet SC order parameter. This is supported by the observed lack of Pauli paramagnetic limiting effect on $H_{c2}(T)$ (Sato et al., 1996). As in the case of UPd₂Al₃ the position of gap nodes is not known with certainty, but NMR results suggest the presence of a node line in UNi₂Al₃ as in UPd₂Al₃. In the simplest scenario then the latter might correspond to the singlet gap function of eq. (90) while the former has one of the triplet gap functions.

$$\mathbf{d}(\mathbf{k}) = \Delta \hat{d} \sin k_z. \quad (92)$$

With the possibilities $\hat{d} = \hat{x}, \hat{y}, \hat{z}$ due to the AF orthorhombic symmetry. These gap functions have all an equatorial node line at $k_z = 0$. Confirmation of the node structure has to await the results of angle resolved magnetotransport or specific heat measurements in the vortex phase and for a confirmation of the spin state the Knight shift measurements on high quality single crystals are necessary.

4.3. Ferromagnetism and superconductivity in UGe₂

The possibility of coexisting ferromagnetism (FM) and superconductivity was first considered by Ginzburg (1957) who noted that this is only possible when the internal FM field is smaller than the thermodynamic critical field of the superconductor. Such a condition is hardly ever fulfilled except immediately below the Curie temperature T_C where coexistence has been found in a few superconductors with local moment FM and $T_C < T_c$ such as ErRh₄B₄ and HoMo₆S₈. If the temperature drops further below T_C the internal FM molecular field rapidly becomes larger than H_{c2} and SC is destroyed. The reentrance of the normal state below T_C has indeed been observed in the above compounds. The only compound known so far where local moment FM coexists homogeneously with SC for all temperatures below T_c is the borocarbide compound ErNi₂B₂C (Canfield and Bud'ko, 1996) (sect. 5). The competition between FM and superconductivity becomes more interesting if FM order is due to itinerant electrons which also form the SC state. In Hartree-Fock approximation the Stoner condition for the reduced interaction constant $\lambda = IN(0) = 1 - S^{-1} \geq 1$ (S = Stoner parameter, I = exchange constant) of conduction electrons determines the existence of itinerant FM order. If the interaction is slightly above the critical value $\lambda_c = 1$ one has weak FM order such as in ZrZn₂ with large longitudinal ferromagnetic spin fluctuations. Fay and Appel (1980) have shown

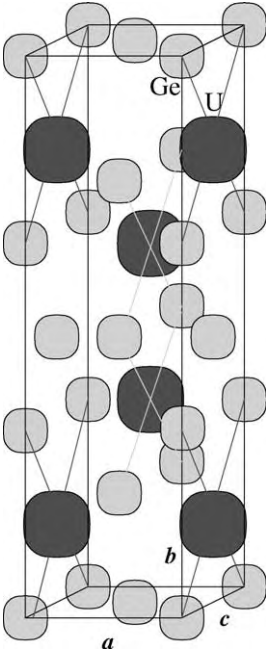


Fig. 42. Conventional orthorhombic unit cell of UGe_2 with lattice parameters given by $a = 3.997 \text{ \AA}$, $b = 15.039 \text{ \AA}$ and $c = 4.087 \text{ \AA}$. U atoms (large spheres) form zig-zag lines along a .

that in this case p-wave superconductivity may actually be mediated by the exchange of FM spin fluctuations and coexist with the small FM moments. According to this theory p-wave superconductivity should exist on both (FM and PM) sides of the critical value $\lambda_c = 1$ for some range of the interaction parameter λ . Until recently this remained only a theoretical scenario. The discovery of unconventional superconductivity under pressure in the itinerant FM UGe_2 (Saxena et al., 2000) and later for FM URhGe (Aoki et al., 2001) and the 3d FM ZrZn_2 (Pfleiderer, 2001) under ambient pressure has opened this field to experimental investigation.

It became quickly clear however that the physics of UGe_2 is not as simple as suggested by the FM spin fluctuation model. Firstly the maximum of SC T_c occurs at a pressure where the FM moment per U is still $1\mu_B$ as compared to $1.5\mu_B$ at ambient pressure thus λ_c should still be far from the critical value where spin fluctuations are important. Secondly the SC phase diagram is not approximately symmetric around the critical value as expected but the region of SC lies completely inside the FM phase. This problem has been further investigated by resistivity measurements (Huxley et al., 2001) where an additional phase within the FM region appeared at lower temperature witnessed by a resistivity anomaly. Its critical temperature $T_x(p)$ precisely hits the maximum of the SC $T_c(p)$ curve as seen in fig. 43. The x -phase has been associated with a combined CDW/SDW transition. This is also suggested by electronic structure calculations (Shick and Pickett, 2001) which show nesting features of the Fermi states. In addition the main FS sheet consists mostly of majority spin ($m_s = \uparrow$, $m_l = 0$) electrons. Therefore the SC pairs must have triplet character. It is suggestive that the unconventional Cooper pairing then appears close to the quantum critical point of the alleged CDW/SDW

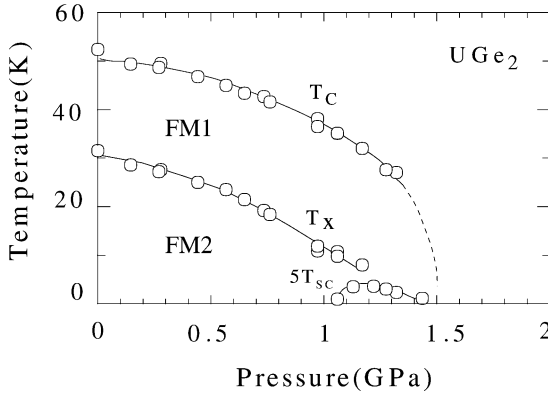


Fig. 43. Pressure–temperature phase diagram of UGe_2 from resistivity measurements. T_C = FM Curie temperature, T_x = boundary of new x -phase. T_{SC} = superconducting transition temperature (note scale enhancement) with optimum pressure at $p_m = 1.25$ GPa. Ferromagnetic FM1 and FM2 regions have different moments ($\approx 1\mu_B$ and $1.45\mu_B$ at low T , respectively) (Kobayashi et al., 2001).

transition and therefore T_c should rather be associated with the T_x transition instead of the FM transition at T_C . However so far no indication of a CDW/SDW order parameter below T_x has been identified in neutron diffraction (Kernavanois et al., 2001) and the subject remains open.

Various theoretical scenarios for UGe_2 have been formulated. In the context of Ginzburg–Landau theories the symmetries of possible SC order parameters and their coupling to the FM have been discussed, e.g., Machida and Ohmi (2001), Mineev (2002). However, as already mentioned in the context of UPt_3 the predictive power of such theories is limited. The traditional approach of microscopic theories invoking FM spin fluctuations has been extended beyond Hartree–Fock with the inclusion of mode coupling terms in order to explain the asymmetric phase diagram around the critical coupling strength (Kirkpatrick et al., 2001). The new aspect of the T_x transition line was introduced by Watanabe and Miyake (2002) who, in order to comply with the experimental evidence from Kernavanois et al. (2001), interpret it as a crossover line into a region of enhanced SDW/CDW fluctuations rather than an ordered phase. When $T_x(p)$ approaches zero these fluctuations then would mediate formation of a triplet p-wave SC state.

4.3.1. Electronic structure and band magnetism

The itinerant FM UGe_2 crystallizes in the base-centered orthorhombic ZrGa_2 type structure (Cmmm) which is shown in fig. 42. It may be viewed consisting of antiphase zig-zag U chains running along the a -axis. This is also the easy axis for the FM moments ($\mu = 1.43\mu_B$ per formula unit) below the Curie temperature of $T_C = 52$ K at ambient pressure. Magnetization and susceptibility are extremely anisotropic (Önuki et al., 1992) corresponding to almost Ising like behaviour of U-moments. The specific heat coefficient is $\gamma = 32$ mJ/mol K² which corresponds to an enhancement factor of 2.7 as compared to the band mass (Shick and Pickett, 2001). This points to some degree of mass renormalization by dynamic correlation effects. Individual masses observed in dHvA experiments exhibit an enhancement factor of $m^*/m \simeq 15$ –25 compared to the free electron mass. Therefore UGe_2 is an itinerant 5f metal with sizable correlation effects but has an order of magnitude smaller effective masses than real U-heavy fermion metals.

The electronic band structure of UGe_2 has first been calculated within the LDA + U approach (Shick and Pickett, 2001) where $U \simeq 0.7$ eV is a strongly screened on-site Coulomb interaction that was fitted to reproduce the proper FM ground state moment of $1.43\mu_B$. On the other hand this value is too small to reproduce the observed photoemission spectrum. The calculated Fermi surface has a main sheet which mostly consists of ($m_l = 0, m_s = \uparrow$)-states. Bands crossing the Fermi energy have mostly U-5f majority spin character, indicating almost complete polarisation, i.e., strong FM. The LDA + U Fermi surface also displays a nesting feature for $\mathbf{Q} = (0.45, 0, 0)$ (in r.l.u.) which is due to bands that have little dispersion along b , i.e., perpendicular to the zig-zag U chains. The proper easy axis for FM moment and a strong magnetocrystalline anisotropy of the moment due to spin-orbit coupling was also correctly found. These calculations describe the ambient pressure strong band ferromagnetism in UGe_2 which is still far from the superconducting pressure region with reduced moments.

A more recent theoretical investigation of the collapse of the FM state under hydrostatic pressure and the simultaneous appearance of another instability has been given in Yaresko and Thalmeier (2004). In this study a relativistic LSDA calculation was performed for isotropically compressed lattice constants simulating the application of hydrostatic pressure p . The experimental lattice constants corresponding to $p = 0$ are given in fig. 42. In agreement with the experimental results a FM ground state with the a -axis as easy axis is obtained. However the U spin ($-1.39\mu_B$) and orbital ($1.94\mu_B$) magnetic moments partly compensate leading to a total moment of only $0.55\mu_B$ significantly smaller than the experimental value ($1.43\mu_B$). This was the main reason for performing the above mentioned LDA + U calculation. However the LSDA calculation reproduces quite well the angular dependence of the cross section of a major FS sheet with an area of $F \simeq 9$ kT. The calculated cyclotron masses are about 8 m and smaller than the experimental values of 15.5 m. This confirms that UGe_2 has itinerant 5f-electrons with only moderately strong correlations.

The hydrostatic pressure simulation shows that FM U moments decrease continuously with pressure until at compression factor $x = 0.94$ only a nonmagnetic solution is obtained (fig. 44). The magnetocrystalline anisotropy energy $E_{\mathbf{M}\parallel a} - E_{\mathbf{M}\parallel b}$ also decreases upon compression. On the other hand the DOS $N(0)$ first increases to a maximum at $x \sim 0.98$ and then decreases again. In order to check whether a tendency to a CDW/SDW instability exists which might be related to the empirical observation of the T_x phase boundary inside FM the staggered static susceptibility within LSDA has been calculated (Yaresko and Thalmeier, 2004). It is given by

$$\chi_{0\alpha}(\mathbf{q}, 0) = \sum_{ij, \mathbf{k}} [f(\epsilon_{i\mathbf{k}}) - f(\epsilon_{j\mathbf{k}+\mathbf{q}})] \frac{|M_{i\mathbf{k}, j\mathbf{k}+\mathbf{q}}^\alpha|^2}{\epsilon_{i\mathbf{k}} - \epsilon_{j\mathbf{k}+\mathbf{q}}}, \quad (93)$$

where $\epsilon_{i\mathbf{k}}$ are the band energies, $M_{i\mathbf{k}, j\mathbf{k}+\mathbf{q}}^\alpha$ are the transition matrix elements ($\alpha = \parallel, \perp \mathbf{M}$) and $f(\epsilon)$ is the Fermi function. The q_z wave-number dependence of $\chi_{0\perp}$ and $\chi_{0\parallel}$ has been calculated as function of the lattice compression. Whereas $\chi_{0\perp}(q_z)$ shows monotonic decrease with compression $\chi_{0\parallel}(q_z)$ is very sensitive to lattice constant change, it develops a strong enhancement at small wave vector at the same intermediate compression $x = 0.98$ where $N(0)$ also is at its maximum. This is an indication that for an intermediate compression (smaller

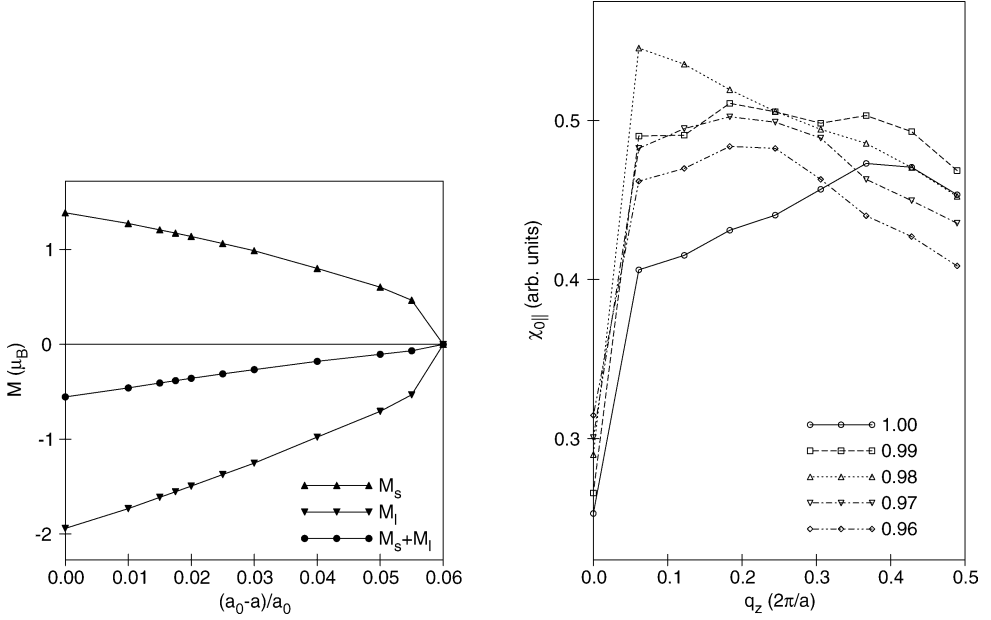


Fig. 44. Left panel: Calculated pressure dependence of spin (M_S), orbital (M_L) and total moment ($M_S + M_L$). Right panel: Pressure dependence of calculated longitudinal susceptibility. The steep drop at $q_z = 0$ is caused by the loss of intra-band transitions due to finite q_z resolution. The enhancement of $\chi_{0||}$ under pressure for small q_z suggests the evolution of a SDW instability within the FM phase (Yaresko and Thalmeier, 2004).

than the critical compression $x = 0.94$ where FM vanishes) UGe_2 has a tendency to develop a long wavelength longitudinal SDW-like instability. It is possible that the tendency towards instability for the susceptibility associated with an unconventional SDW is even stronger. However it should be noted that the susceptibility enhancement does not correspond to any obvious nesting in the FS sheets obtained in LSDA calculations. This raises the question whether the observed nesting feature in the LDA + U FS of Shick and Pickett (2001) has a real physical significance to the alleged hidden order phase.

4.3.2. Coexistence of FM order and superconductivity under pressure

The experimental phase diagram of FM collapse under pressure and simultaneous appearance of superconductivity is shown in fig. 43. The critical pressure for disappearance of FM order is $p_{c2} = 16\text{--}17$ kbar. The SC phase appears between $p_{c1} = 10$ kbar and $p_{c2} = 16$ kbar which is also the critical pressure for the FM-PM transition. The critical temperature $T_x(p)$ of the x -phase hits the maximum of $T_c(p)$ at the optimum pressure $p_m = 12.5$ kbar. As mentioned before the nature of the order parameter in the x -phase remains elusive. The coincidence of maximum T_c with vanishing x -phase order parameter suggests that the collective bosonic excitations of the x -phase which supposedly become soft at p_m mediate superconductivity and not quantum critical FM spin fluctuations which are absent due to the persisting large FM

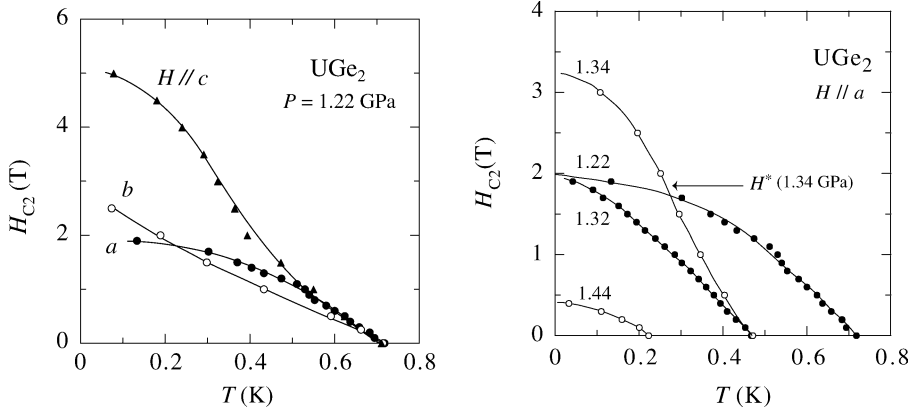


Fig. 45. Left panel: H_{c2} -curves for pressure close to p_m and field along the crystal axes. Right panel: H_{c2} for field parallel to easy a -axis at four different pressures below and above $p_m = 1.25$ GPa. Unusual H_{c2} at 1.34 GPa leads to SC reentrance as function of pressure for low temperature (Kobayashi et al., 2001).

molecular field. Associated with the $T_x(p)$ phase boundary is an abrupt first order change of the magnetic moment $\mu(p)$ around p_m whose different size distinguishes the FM2 region ($\mu(0) \simeq 1.45\mu_B$) from the FM1 region ($\mu(p_m) \simeq 1\mu_B$) (Pfleiderer and Huxley, 2002). The connection between SC and the x -phase is also witnessed by the anomalous upper critical field behaviour around p_m which displays a reentrance behaviour as function of pressure seen in fig. 45. Apparently close to the T_x line the superconducting state is strongly stabilized as shown by the dramatically increased value of $H_{c2}(0)$. The existence of phases with ‘hidden order parameters’ which show up in thermodynamic and transport coefficients but do not appear as spin- or charge-density modulations in neutron diffraction is not uncommon for U-compounds. As discussed in the next section URu_2Si_2 has a similar phase. Two kinds of proposals for such hidden order may be considered: (i) If the U 5f-electrons have a partly localised character as in the latter case the hidden order may be of quadrupolar or more generally multipolar character. (ii) If 5f-electrons are strongly itinerant, as apparently in UGe_2 , one may have an unconventional density wave order parameter which has been introduced in sect. 2. These phases have \mathbf{k} -dependent gap functions which do not belong to identity representations as in the CDW/SDW case. This type of order has also been proposed for the yet unidentified x -phase in UGe_2 and its coexistence behaviour with FM and unconventional superconductivity was studied (Varelogiannis et al., 2003).

4.3.3. Theoretical scenarios for superconductivity in UGe_2

From the previous discussion of experimental evidence the superconducting mechanism via ferromagnetic fluctuations can be ruled out since the ferromagnetic polarization at p_m where T_c is largest is still 65% of the maximum value at ambient pressure (Pfleiderer and Huxley, 2002). Therefore models based on the FM quantum critical point scenario that follow the original work of Fay and Appel (1980) are not relevant for UGe_2 . On the other hand the phe-

nomenclological classification of possible SC order parameters based on Landau expansion of the free energy is simplified by the remaining large spin polarisation of conduction electrons, only spin triplet pairing is possible in order to avoid the effect of the large exchange field.

4.3.4. Symmetry properties of gap states and Ginzburg–Landau theory

Triplet pair states are characterised by the vector gap function $\mathbf{d}(\mathbf{k})$ defined in sect. 2. Due to the constraint of equal (pseudo-)spin pairing (i.e., $\Delta_{\uparrow\downarrow} \equiv 0$) the \mathbf{d} -vector is confined to the bc -plane perpendicular to the FM moment \mathbf{M}_0 which is parallel to the easy a -axis. The gap function can be written as (Machida and Ohmi, 2001; Fomin, 2001)

$$\mathbf{d}(\mathbf{k}) = f(\mathbf{k})\boldsymbol{\eta} = f(\mathbf{k})(\hat{\mathbf{b}} + i\hat{\mathbf{c}}). \quad (94)$$

Here $\boldsymbol{\eta} = (\eta_x, \eta_y, \eta_z) = (0, 1, i)$ is the vector order parameter and $f(\mathbf{k})$ the orbital part which transforms as a representation of the (approximate) tetragonal group. As in the case of UPT₃ it is assumed that the pseudo spins describing the Kramers degeneracy of quasiparticle states are only weakly coupled to the orbital momentum, then $f(\mathbf{k})$ may belong to any tetragonal representation which have typical point or line node structures. Presently there is no experimental information on the nodes. The equal spin pairing state is nonunitary, i.e., it breaks time reversal symmetry. This property is directly enforced by the nearly complete FM polarisation. Therefore the Cooper pairs have a net spin moment $\mathbf{S} = i\mathbf{d}(\mathbf{k}) \times \mathbf{d}(\mathbf{k})^*$ which aligns with the ordered FM moment. In a Ginzburg–Landau expansion of the free energy it is sufficient to consider only the aligned component $\eta_+ = \eta_y + i\eta_z$ and neglect $\eta_- = \eta_x^*$ because of the large \mathbf{M}_0 even around the critical pressure. The total GL functional should then only be expanded in terms of η_+ and should also not contain \mathbf{M}_0 explicitly except in the vector potential. One obtains (Machida and Ohmi, 2001) for \mathbf{H} along the a -axis ($\|\mathbf{M}_0$),

$$f_{\text{GL}} = \alpha_0(T - T_c)|\eta_+|^2 + \frac{1}{2}\beta|\eta_+|^4 + K_1\left(\frac{d\eta_+}{dy}\right)^2 + \left(\frac{2\pi}{\phi_0}\right)^2 K_2(M_0 + \mu_0 H)^2 y^2 |\eta_+|^2 \quad (95)$$

because in this case the magnetic induction in the FM state is given by $\mathbf{B} = (\mu_0 H + M, 0, 0)$. Similar expressions hold for \mathbf{H} along c - and b -axis. Minimization of eq. (95) leads to the critical field curves close to T_c . The term $\sim M_0^2 |\eta_+|^2$ only renormalizes T_c . Then one obtains the upper critical fields $H_{c2}^a \sim (T_c - T)$ and $H_{c2}^{b,c} \sim (T_c - T)^{1/2}$. The remarkable root singularity for $H_{c2}^{b,c}$ at T_c is due to the presence of a finite FM moment. Experimentally the critical field curves are quite anomalous close to the optimal pressure p_m although different exponents for different field directions are not observed, the H_{c2}^c -curve, however, does show an anomalous strong upturn around $0.5T_c$ (Kobayashi et al., 2001), see fig. 45. In any case a proper theory of H_{c2} has to include the influence of the hidden order parameter close to maximum T_c (fig. 43). The symmetry considerations of this section gave some constraints one should expect to hold for the SC order parameter, however the simple Landau theory approach only indicates that H_{c2} should behave anomalous, without being able to give a quantitative account close to the optimum T_c .

4.3.5. *Microscopic approaches*

Aside from the FM QCP scenarios now known to be irrelevant for UGe_2 (Pfleiderer and Huxley, 2002) little theoretical investigation has been undertaken so far with the exception of Watanabe and Miyake (2002). This theory starts from the assumption that $T_x(p)$ represents the phase boundary of a coupled (conventional) CDW-SDW transition. Because of the strong background FM polarisation these two order parameters have to appear simultaneously. Inversely, if one is close to the critical pressure p_m their critical fluctuations will be coupled to fluctuations in the FM polarisation by a mode–mode coupling term in the free energy, which couples the amplitudes of FM, CDW and SDW fluctuations at the commensurate nesting vector \mathbf{Q} of a n.n.n. tight binding model used for the majority bands of UGe_2 . The strong coupling theory for this mechanism has been used to calculate H_{c2} and apparently qualitative anomalies like those close to p_m (fig. 45) are obtained.

However, no evidence for CDW or SDW formation central to this theory has been seen below T_x so far. On the other hand in specific heat measurements a pronounced anomaly $\Delta C(T_x)$ at 1.15 GPa suggests that $T_x(p)$ is a real phase line (Tateiwa et al., 2003). This leads one to the natural suggestions that one should look for more general particle–hole pairing (‘unconventional density wave’) discussed in sects. 2 and 4.4 as an alternative for the phase below T_x since they do not lead to charge or magnetic superstructures (Varelogiannis et al., 2003).

4.4. *A case of ‘hidden order’ in URu_2Si_2*

This moderate HF compound ($\gamma = 110 \text{ mJ/mol K}^2$) has mystified both experimentalists and theorists alike since the discovery of AF order at T_m and another still unidentified (‘hidden order’) phase at T_0 which both seem to appear at the same temperature $T_0 = T_m = 17.5 \text{ K}$, at least for annealed samples. In addition the compound becomes a nodal superconductor below $T_c \simeq 1.2 \text{ K}$ (Palstra et al., 1985; Schlabitz et al., 1986; de Visser et al., 1986). The simple tetragonal AF order with wave vector $\mathbf{Q} = (0, 0, \frac{\pi}{c})$ has tiny moments $\mu \simeq 0.02\mu_B$ along c -axis (Broholm et al., 1987; Walker et al., 1993) which are of the same order as in UPt_3 . However, unlike in UPt_3 , very large thermodynamic effects, e.g., in specific heat ($\Delta C/T_0 \simeq 300 \text{ mJ/mol K}^2$), thermal expansion, etc., occur which are hard to reconcile with the small ordered moments. The pronounced anomalies at T_0 were interpreted as evidence for the presence of a second ‘hidden order’ parameter which cannot be seen in neutron or X-ray diffraction. Many different types of models for hidden order have been proposed, where the 5f-electrons of URu_2Si_2 are considered as essentially localized (Santini and Amoretti, 1994), or itinerant (Ikeda and Ohashi, 1998) or, of dual nature (Okuno et al., 1998; Sikkema et al., 1996). In the former case local quadrupoles of the CEF states are supposed to show staggered order below T_0 akin to the many examples of such order in 4f-compounds. Quadrupolar order does not break time reversal symmetry and cannot be directly seen by neutron diffraction. The small dipolar moments are considered as an unrelated secondary order parameter with accidentally the same transition temperature. In the itinerant models the order parameter is due to an unconventional pairing in the particle–hole channel leading to an unconventional SDW which has vanishing moment in the clean limit and also does not break time reversal invariance. The small staggered moments may then be induced in the condensate

due to impurity scattering. Finally in the dual models one assumes a localised singlet–singlet system in interaction with the itinerant electrons to cause induced moment magnetism with small moments but large anomalies.

In all models it was previously taken for granted that both the primary ‘hidden’ order parameter and AF order coexist homogeneously within the sample. However, hydrostatic and uniaxial pressure experiments (Amitsuka et al., 1999, 2002) have radically changed this view, showing that the order parameters exist in different parts of the sample volume; the tiny AF moment is not intrinsic but due to the small AF volume fraction under ambient pressure. Applying hydrostatic pressure or lowering the temperature increases the AF volume fraction and hence the ordered moment until it saturates at an atomic size moment of $0.4\mu_B/U$. This means that the evolution of AF arises from the increase of AF volume with pressure rather than the increase of the ordered moment μ per U-atom. This interpretation is supported by the observation of a comparatively weak increase of T_0 with pressure (Amitsuka et al., 1999).

4.4.1. Electronic structure and 5f-states

Inelastic neutron scattering (Park et al., 2002) using the time-of-flight method has shown that the valence state in URu_2Si_2 is U^{3+} corresponding to $5f^2$, judging from the observation of the ${}^3H_4 \rightarrow {}^3F_2$ transition of this configuration. In tetragonal (D_{4h}) symmetry the nine-fold degenerate 3H_4 multiplet should be split by the CEF potential into five singlets and two doublets. There is indeed an indication of four strongly broadened CEF transitions at energies ranging from $\delta = 5$ meV to 159 meV. However, the data are not sufficient to determine the CEF potential and states. There is a transition at 49 meV which might be associated with the $\Gamma_3 - \Gamma_5^1$ transition from the Γ_3 ground state which has been invoked in the model of Santini and Amoretti (1994). Earlier, low energy triple axis INS (Broholm et al., 1991) has shown that the transitions have a considerable dispersion. In addition the c -axis susceptibility exhibits clear CEF anomalies from which a CEF level scheme has been derived (Santini and Amoretti, 1994). However the result is not unique and the overall splitting obtained is by a factor two smaller as compared to the above INS results. In this analysis the low energy group of CEF states consists of three singlets shown in table 6.

The clear evidence for CEF states supports the view of mostly localised 5f-states in URu_2Si_2 . This raises the question of the origin of HF behaviour in this compound. The specific heat coefficient in the low temperature ordered (magnetic + hidden) phase is reduced to

Table 6

Model for low lying CEF states in URu_2Si_2 (tetragonal structure as in fig. 15). The complete CEF level system for concentrated URu_2Si_2 is comprised of five singlets (the low lying states are listed with ϵ and γ being adjustable parameters) and two doublets. The dilute ($x \ll 1$) $Th_{1-x}U_xRu_2Si_2$ system may have a different single-ion CEF level scheme with a doublet ground state (Amitsuka and Sakakibara, 1994)

Symmetry	CEF-state	Energy (meV)
Γ_3	$ 0\rangle = \frac{1}{\sqrt{2}}(2\rangle + -2\rangle)$	0
Γ_1^1	$ 1\rangle = \epsilon(4\rangle + -4\rangle) + \gamma 0\rangle$	3.8
Γ_2	$ 2\rangle = \frac{1}{\sqrt{2}}(4\rangle - -4\rangle)$	9.6

only a moderate $\gamma = 64 \text{ mJ/mol K}^2$, 40% of the paramagnetic value and only one tenth that of typical HF values. Magnetoresistance measurements have shown that URu₂Si₂ is a compensated metal without open orbits (Ohkuni et al., 1999). Three of the closed Fermi surface sheets have been determined by dHvA experiments (Ohkuni et al., 1999). Their moderately heavy masses are in the range $m^* = 8\text{--}25 m$ which are, however, still larger by a factor ten as compared to the LDA band masses. For a nonmagnetic 5f singlet ground-state system as given in table 6 there is no Kondo mechanism to generate heavy quasiparticles. It is tempting to assume that rather the same mechanism as recently proposed for UPt₃ (Zwicknagl et al., 2002) and UPd₂Al₃ (Zwicknagl et al., 2003) is important: mass renormalization through virtual excitations within a pair of low lying 5f singlet states which leads to (White and Fulde, 1981)

$$\frac{m^*}{m_b} = 1 + N(0) \frac{2\alpha^2 I^2}{\delta}, \quad (96)$$

where $\alpha = \langle 0|J_z|1\rangle$ is a dipolar matrix element, I is the one-site exchange and δ the singlet–singlet splitting. This is a simplified version of the mass renormalisation in eqs. (65), (66) with $\alpha \equiv 2a_{5f}|M|$. For several singlet pairs as in the present case one has a sum of such contributions. As discussed for UPt₃ for realistic parameters of U-compounds this mechanism may easily lead to a mass enhancement factor $\frac{m^*}{m_b} \simeq 10$ which would be an appropriate value for URu₂Si₂.

4.4.2. Phase transitions, field and pressure dependence

The discrepancy between small AF moment in URu₂Si₂ and large thermodynamic anomalies has led to the postulation of a hidden (non-dipolar) order parameter. The crucial questions about its nature are: (i) Is the order primarily involving the localised 5f-CEF split states or the heavy itinerant conduction electrons. (ii) Does the hidden order parameter break time reversal invariance or not. In the former case it may induce AF as secondary order parameter, in the latter the two order parameters are unrelated and their appearance at the same temperature $T_m = T_0$ has to be considered as accidental.

The continuous phase transition at T_0 is clearly seen in a large specific heat anomaly which becomes more pronounced in a magnetic field (fig. 46). The magnetic entropy contained in this peak is orders of magnitude larger compared to other magnetic U-compounds and alloys if one scales it with the AF ordered moment (Amitsuka et al., 2002) which proves that it must be connected to a hidden order parameter. A similar behaviour is seen in thermal expansion (Mentink et al., 1997) along a, however, the tetragonal symmetry below T_0 is preserved and no superstructure evolves (Kernavanois et al., 1999). The shape of specific heat and thermal expansion anomalies and their sharpening in an external field is reminiscent of antiferroquadrupolar (AFQ) phase transitions due to localised f-electrons known in the 4f-Ce-hexaborides and *Tm*-intermetallics. A quadrupolar order parameter is even under time reversal and is expected to be in competition with the dipolar AF order.

Pressure experiments have indeed found this competition. It is evident from the comparison of the pressure dependent ordered AF moment, and the position and intensity of ²⁹Si-NMR satellites. While the former increases continuously with pressure, the splitting which is proportional to the local 5f-moment is pressure independent, however, the split satellite intensity

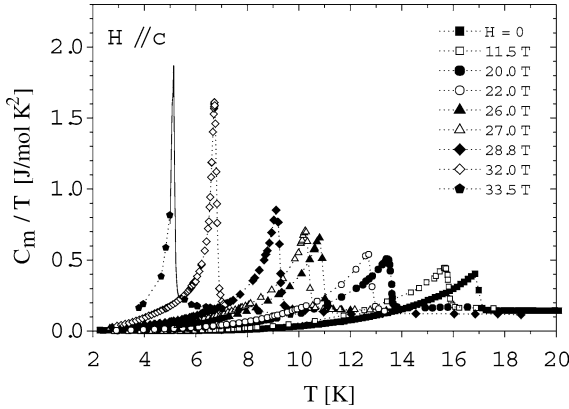


Fig. 46. Magnetic specific heat C_m/T of URu_2Si_2 for fields up to 33.5 T (Jaime et al., 2002).

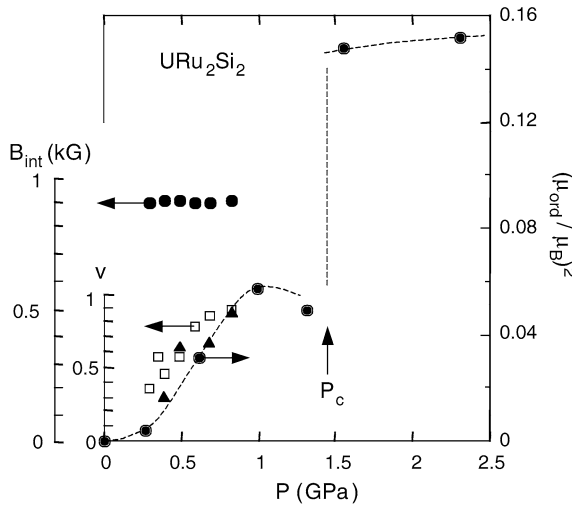


Fig. 47. Evolution of AF Bragg intensity (full circles, right scale) with hydrostatic pressure. Full circles (leftmost scale) denote internal staggered field B_{int} from ^{29}Si NMR. Triangles and squares denote AF volume fraction v from the same experiment (Amitsuka et al., 2002).

which is a measure of the AF volume fraction also increases with pressure (fig. 47). Analysis of these results show that the AF moment per magnetic U-site $\mu_{\text{AF}} \simeq 0.25\mu_{\text{B}}/U$ is not small. It is the small AF volume fraction at ambient pressure which leads to the small overall ordered moment of $0.03\mu_{\text{B}}$. As pressure increases the ordered moment also increases due to the increase in AF volume which continuously replaces the volume fraction with the hidden order. The replacement is complete at $p \simeq 1$ GPa. Somewhat above at p_c another phase transition takes place in the complete AF-phase leading to a sudden increase of the on-site U-moment, however we note that this has not been observed in magnetic X-ray diffraction experiments. The observed moderate increase of T_m with pressure (Amitsuka et al., 1999) is compatible with the observation of a pressure independent U-moment. Subsequent uniaxial pressure experiments (Yokoyama et al., 2002) have shown that only the [100] or [110] uniaxial pressure

in the tetragonal plane leads to the increase of the AF volume fraction or destruction of the hidden order, whereas the [001] uniaxial pressure has little effect. This anisotropic behaviour under pressure suggests that the hidden order parameter is associated with the tetragonal four-fold symmetry plane.

4.4.3. Theoretical models: localised vs. itinerant

We shall not recount the many attempts to explain the broken symmetry states of URu_2Si_2 but rather concentrate on two typical examples that seem to be compatible with the recent important results of the pressure investigations just described.

4.4.3.1. *AFQ order of local induced quadrupole moments.* The competitive behaviour of AF and hidden order points to even time reversal symmetry of the latter. If one assumes that the localised 5f electrons are involved in the hidden order then the already mentioned AFQ order in the singlet CEF level scheme is the most obvious choice. This model was proposed by Santini and Amoretti (1994) and Santini (1998) and is also the most well studied one. It is an entirely localised 5f-model and is defined by the Hamiltonian

$$H = \sum_i \sum_{k,q} B_k^q O_k^q(i) + K \sum_{i \in A, j \in B} Q(i)Q(j) - \sum_i g\mu_B J_z(i)H \quad (97)$$

whose terms represent CEF potential in Stevens operator representation, quadrupolar interactions and Zeeman energy, respectively. K is an effective quadrupolar inter-site exchange mediated by conduction electrons, similar as in 4f-systems (Thalmeier and Lüthi, 1991). The CEF parameters B_k^q are obtained from fitting to the susceptibility which leads to the CEF states in table 6. Since the ground state is a singlet, quadrupole order can only appear as *induced* order, i.e., nondiagonal matrix elements $\langle \Gamma_3 | Q | \Gamma_1^1 \rangle \neq 0$ must be present. This is possible for quadrupole operators $Q_{\Gamma_3} = (J_x^2 - J_y^2)$ or $Q_{\Gamma_3} = (J_x J_y + J_y J_x)$. Naively this would be compatible with uniaxial pressure results which show that the hidden order parameter is most sensitive to strains within the tetragonal xy -plane. Mean field calculations were performed with eq. (97) based on the above CEF scheme under the assumption of two sublattice AFQ ordering. They give a qualitatively correct behaviour of the specific heat, thermal expansion, nonlinear and anisotropic susceptibility and magnetization. For example, the thermal expansion exhibits step like anomalies at $T_0(H)$ which increase with field strength. This is reproduced by the model since in tetragonal symmetry ($i = a, c$) $\alpha_i = g_i \partial \langle O_2^0 \rangle / \partial T$ where $Q = O_2^0 = 3J_z^2 - J(J+1)$ and g_i is an effective magnetoelastic coupling constant. Close to T_0 this is proportional to the growth rate $\partial \langle Q \rangle^2 / \partial T$ which leads to jumps in thermal expansion coefficient $\alpha_a = (1/a)(\partial a / \partial T)$ etc. reminiscent of those in the specific heat.

In principle the AFQ order parameter may also lead to a lattice superstructure with the AFQ vector \mathbf{Q} via magnetoelastic coupling terms. This has not been found (Kernavanois et al., 1999) but may simply be too small to observe as it is the case in other AFQ compounds like CeB_6 . More disturbing is the fact that in the AFQ state an external field in the ab -plane should also induce a field dependent staggered magnetization which has not been observed either.

In the AFQ hidden order model there is no natural connection to an AF order parameter. For this purpose a dipolar interaction term has to be introduced (Santini, 1998) and the resulting magnetic ordering temperature T_m is unrelated to T_0 , if they are equal this has to be interpreted as accidental. In the light of the new pressure experiments it seems that they are close at ambient pressure, slightly favoring AFQ order. For $p > 0$ $T_0(p)$ and $T_m(p)$ cross at the critical pressure p_c , stabilizing the AF local moment phase for $p > p_c$. At ambient pressure local stress around crystal imperfections might already lead to a small AF volume fraction which then increases upon applying external pressure. Such a situation may be phenomenologically described by a Landau free energy ansatz (Shah, 2000)

$$f_L = \alpha_0(T - T_0(p))Q^2 + \beta Q^4 + \alpha'_0(T - T_m(p))m^2 + \beta'm^4 + \gamma_0 m^2 Q^2, \quad (98)$$

where the last term is a coupling term for AF (m) and AFQ (Q) order parameters. For $\gamma_0 > 0$ the two order parameters are in competition. If $T_m(p)$ and $T_0(p)$ are close the inclusion of inhomogeneities might then lead to a phase separation where m and Q order parameters exist in macroscopically separate volume fractions. The Landau approach has been extended by including the strain coordinates to analyze neutron diffraction results under uniaxial pressure (Yokoyama et al., 2003).

Although the AFQ scenario for the hidden order parameter seems most attractive for the explanation of macroscopic anomalies at T_0 there is no direct experimental proof. This would require the observation of either (i) the induced AF magnetic order in an external field or (ii) direct signature of 5f-orbital order in resonant X-ray scattering as, e.g., in the AFQ phase of CeB₆ (Nakao et al., 2001).

4.4.3.2. *Hidden order as unconventional density wave.* A complementary view of hidden order in URu₂Si₂ starts from a completely itinerant view of 5f-electrons by describing them within a multiband extended Hubbard model (Ikeda and Ohashi, 1998, 1999). Naturally this approach is unable to account for the CEF signatures in specific heat, susceptibility and similar quantities. In this model the large jump $\Delta C(T_0)$ is due to a condensation of electron–hole pairs (sect. 2). Unlike conventional CDW or SDW states however the pair states belong to nontrivial anisotropic representations of the symmetry group, similar to Cooper pairs in unconventional superconductors. The symmetry classification of unconventional electron–hole pair states and their stability analysis is given in (Gulacsi and Gulacsi, 1987; Schulz, 1989; Ozaki, 1992). In full generality this has only been done for n.n. tight binding models with perfect nesting property of 2D conduction bands $\epsilon_{\mathbf{k}\pm\mathbf{Q}} = -\epsilon_{\mathbf{k}}$ and $\mathbf{Q} = (\frac{1}{2}, \frac{1}{2}, 0)$. In the low energy corner of the U – V phase diagram (U , V = on-site and n.n. Coulomb interaction, respectively) the stable state is an unconventional triplet particle–hole pair condensate ('d-SDW'). In contrast to a common SDW where the gap function $\Delta^s(\mathbf{k}) = \text{const}$ is momentum independent, in the d-wave case one has $\Delta^d_{s_1s_2}(\mathbf{k}) = \Delta^d(\mathbf{k})\sigma^z_{s_1s_2}$ with

$$\Delta^d(\mathbf{k}) = i\Delta_0^d(\cos k_x - \cos k_y). \quad (99)$$

The order parameter is purely imaginary because it is connected with persistent commensurate spin currents around lattice plaquettes. This state breaks spin rotational symmetry but not time reversal symmetry because the latter inverses both current and spin direction leaving the order

parameter invariant. The staggered magnetic moment in the s- or d-wave case is given by

$$M_Q^z = \sum_{\mathbf{k}\sigma} \sigma \langle c_{\mathbf{k}\sigma}^\dagger c_{\mathbf{k}+\mathbf{Q}\sigma} \rangle = \sum_{\mathbf{k}} \frac{\Delta^{d,s}(\mathbf{k})}{2E(\mathbf{k})} \tanh \frac{E(\mathbf{k})}{2T}, \quad (100)$$

where $E_{\mathbf{k}} = [\epsilon_{\mathbf{k}}^2 + \Delta_{\mathbf{k}}^2]^{1/2}$ is the quasiparticle energy which is fully symmetric in both s, d cases. Therefore $M_Q^z > 0$ for conventional s-SDW but $M_Q^z \equiv 0$ for d-SDW case since the sign change in eq. (99) as function of \mathbf{k} makes the integral in eq. (100) vanish for d-SDW (this notation convention is a misnomer since $M_Q^z \equiv 0$ means that there is precisely *no* ‘spin density’ in the d-wave case).

Despite the vanishing staggered moment in the d-SDW state there is a large BCS-like specific heat anomaly similar to the conventional s-SDW case. Therefore the d-SDW state would naturally explain the most prominent property of the hidden order phase in URu₂Si₂. The tiny moments would then immediately appear at the hidden order transition ($T_m \equiv T_0$) around impurities, either through the creation of a s-SDW component by a proximity effect (Ikeda and Ohashi, 1998, 1999) or through anisotropic exchange interactions of the condensate with magnetic impurities (Virosztek et al., 2002). In the latter case the temperature dependence of the staggered moment can be explained. The phase separation of hidden order and staggered micromagnetism is then again seen as a consequence of the sample defects and inhomogeneous impurity concentration.

4.4.4. High field phase diagram and metamagnetism

Besides pressure, magnetic fields also destroy the hidden order as can be seen from the progressive $T_0(B)$ -reduction in fig. 46. The corresponding critical field line forms the boundary to the hidden order phase (I) in fig. 48. Assuming the AFQ hidden order model of URu₂Si₂ there is an important difference to other known AFQ compounds which have a *degenerate* CEF ground state like cubic Γ_8 in CeB₆. There $T_0(B)$ first *increases* with field strength due to the lifting of orbital degeneracy. Since in URu₂Si₂ $T_0(B)$ decreases monotonously this is a strong argument for the induced AFQ order in a singlet–singlet system. At low temperatures the hidden order phase is destroyed at a field $B_0(0) = 36.1$ T. For $B > B_0(0)$ $M(B)$

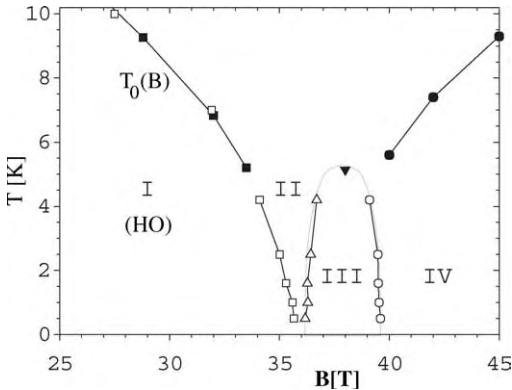


Fig. 48. B - T phase diagram of hidden order (HO) phase (I), metamagnetic phase (III) and high field phase (IV). Open symbols correspond to resistivity anomalies and filled symbols to specific heat maxima. For zero field $T_0 = 17.5$ K (HO) (Jaime et al., 2002).

exhibits multistep metamagnetic behaviour (Sugiyama et al., 1999) which may in principle be explained by the AFQ model as a field induced crossing of singlet CEF levels (Santini, 1998) complemented by the effect of inter-site exchange interactions. Originally it was thought that the metamagnetic transition extends to temperatures much higher than T_0 (Sugiyama et al., 1999). Recent pulsed field experiments (Jaime et al., 2002) have shown however that the metamagnetic phase is much more confined (region III in fig. 48). Alternatively this region has also been interpreted as reentrant hidden order phase (Harrison et al., 2003). Finally above $40T$ one reaches a moment of $1.5\mu_B/U$ which is much larger than the zero field value at high pressure, hence at high field not only the AF volume fraction is maximal but also the magnetic ground state of U^{4+} has a larger moment. The structure of magnetic phases in the high field regime is still unknown.

4.4.5. *Collective excitations in the ordered phase*

Inelastic neutron scattering has perhaps provided the most convincing evidence that the localised 5f-electron picture is a good starting point for URu_2Si_2 . In this case the dipolar CEF transition from the singlet ground state $|0'\rangle$ to excited singlet $|2'\rangle$ with dipolar matrix element $\alpha = \langle 0'|J_z|2'\rangle$ should disperse into a collective ‘magnetic exciton’ band. Here the primes indicate that the corresponding singlet states in table 6 are modified due to the presence of AF order which mixes the unprimed states with higher CEF states, without this mixing obviously α would vanish. These magnetic excitons have indeed been found (Broholm et al., 1991) as well propagating modes in a large part of the tetragonal BZ. They may be described by a similar expression as magnetic excitons for UPd_2Al_3 . The relatively large matrix element $\alpha = 1.2$ obtained from fitting to experimental results (Broholm et al., 1991) is not in contradiction to the small overall AF moment, since the latter is only an effect of the small AF volume fraction. The $|0'\rangle$ to $|1'\rangle$ singlet excitation has no dipolar matrix element, it is the excitation whose softening is governed by the quadrupolar matrix element $\alpha_Q = \langle 0'|Q|1'\rangle$ leading to the induced AFQ (hidden) order at T_0 . This quadrupolar mode does not directly appear in the dipolar response function and the INS cross section. It has been suggested that its presence can be seen indirectly through an influence on the dipolar excitation (Santini et al., 2000).

4.4.6. *The superconducting state*

As in other U-HF compounds the superconducting state in URu_2Si_2 with $T_c = 1.4$ K is embedded in the AF phase and here in addition in the hidden order phase with $T_0 \gg T_c$. Although there are a number of signatures for an unconventional pair state, it has attracted much less attention than the hidden order phase, possibly because there is no direct evidence for a multicomponent SC order parameter (Thalmeier, 1991). The evidence for gap anisotropy is obtained from various low temperature power laws for specific heat (Hasselbach et al., 1993) ($\sim T^2$) and NMR relaxation rate (Matsuda et al., 1996) ($\sim T^3$) which suggests the presence of line nodes. A plot of C/T vs. T is shown in fig. 9 in comparison with theoretical curves (Hasselbach et al., 1993) obtained for gap functions allowed in the Landau theory of tetragonal superconductors (Volovik and Gorkov, 1985). The region of experimental linear T behaviour in C/T is surprisingly large. This cannot be explained within a Landau approach which is restricted to the vicinity of T_c . In addition the reduced specific heat jump $\Delta C(T_c)$ as com-

pared to a constant gap supports the existence of a gap anisotropy with line nodes. This is also the conclusion from point contact spectroscopy (Hasselbach et al., 1992). The upper critical field curves of URu₂Si₂ show two anomalies (Keller et al., 1995): First the anisotropy ratio $B_{c2}^a/B_{c2}^c = 4$ is large, it cannot be fully explained by the anisotropy of Pauli limiting fields given by $\sqrt{\chi_c/\chi_a} \simeq \sqrt{5}$, orbital effects due to effective mass anisotropy must be involved. Furthermore, a distinct upward curvature of B_{c2}^a is observed, similar to critical fields in the borocarbide superconductors where it was associated with two band effects or alternatively anisotropic Fermi velocities. The effect of AF on B_{c2} should be negligible due to its small volume fraction.

As discussed in sect. 2 the observation of the dHvA effect far in the vortex phase ($B \ll B_{c2}$) is a sure signature of nodal superconductivity. Although oscillations of the three Fermi surface sheets in URu₂Si₂ have been seen below B_{c2} (Ohkuni et al., 1999) the amplitude falls off quite rapidly with B , especially for field along c . Therefore, these experiments are not able to confirm the existence of nodes in $\Delta(\mathbf{k})$.

4.5. Superconductivity in the non-Fermi liquid state of UBe₁₃ and U_{1-x}Th_xBe₁₃

This cubic compound was discovered rather early (Ott et al., 1983, 1984) as a superconducting HF system. The U atom in this structure is embedded in an icosahedral cage of 12 Be-atoms. A global understanding of the normal state and symmetry breaking in both superconducting and magnetic state is still elusive. Firstly ‘pure’ UBe₁₃ crystals do not have the highest quality as compared to, e.g., UPt₃ so that the symmetry of the anisotropic SC gap functions has not been identified, furthermore the Th-doped crystals U_{1-x}Th_xBe₁₃ show a perplexing variety of SC and possibly also magnetic phases whose microscopic origin and order parameter symmetries are not understood. The $T-x$ phase diagram of U_{1-x}Th_xBe₁₃ has been investigated with a variety of methods and the most detailed results have been obtained using the thermal expansion method (Kromer et al., 1998, 2000, 2002) (fig. 50). The most important question concerns the nature of the low temperature phase (C) at intermediate doping ($0.02 < x < 0.045$). This phase may either be a nonunitary SC phase with condensate magnetic moments due to unconventional Cooper pairs (Sigrist and Rice, 1989) or a phase with coexisting anisotropic SC and a SDW type phase suggested by Kromer et al. (1998) on experimental grounds and already proposed in a theory by Kato and Machida (1987). In the former case one has to assume a crossing of two SC phases with two independent order parameters as function of the Th-concentration (Sigrist and Ueda, 1991) and in the latter a crossing of a SC and SDW phase line. Already in the normal state UBe₁₃ is a rather anomalous metal, e.g., non-Fermi-liquid (nFl) behaviour has been observed and attributed to a multichannel Kondo effect.

4.5.1. Normal state and nFl properties of UBe₁₃

The 5f-electron level in UBe₁₃ is close to the Fermi level as seen from photoemission results. Therefore the HF-behaviour which sets in below a fluctuation temperature of $T^* \simeq 8-25$ K does not correspond well to the Kondo picture which requires 5f states to lie sufficiently removed from the Fermi energy. Nevertheless the Kondo model in its single and multichannel

version has been employed for this HF compound. The specific heat coefficient is strongly enhanced with $\gamma \simeq 1 \text{ J/mol K}^2$. Furthermore resistivity, specific heat and thermal expansion reveal the presence of a second low energy scale with $T_m \simeq 2 \text{ K}$ where these quantities exhibit an additional maximum anomaly. This proves that at T_m a coherent Landau–FL state has not yet evolved and that the superconducting transition at $T_c \simeq 0.9 \text{ K}$ in UBe_{13} happens within a strongly anomalous nFI state. In fact if superconductivity is suppressed by a strong magnetic field the γ value shows a roughly logarithmic increase with decreasing temperature typical for a nFI state. No saturation of $\gamma(T)$ is observed down to lowest temperatures (Helfrich, 1996). In most other U-HF compounds superconductivity is embedded in a weakly AF state. Despite a number of attempts no long range AF order has been found in UBe_{13} , μSR measurements set an upper limit of $10^{-3} \mu_B$ for the moments on U-sites.

4.5.2. *The 5f-ground state of U*

The observed normal state nFI behaviour raises the still controversial question of the magnetic ground state of U-atoms in UBe_{13} . The high temperature susceptibilities do not allow to distinguish between a $5f^3$ - and $5f^2$ -state of U. In the former case proposed in Felten et al. (1986) a Kramers degenerate magnetic Γ_6 CEF ground state and two excited Γ_8 quartets at 180 K and still higher energy were inferred from analysis of specific heat which exhibits a CEF Schottky anomaly around 80 K. In this case the HF state would be due to a conventional Kondo mechanism involving the magnetic Γ_6 localised doublet. However this picture is in conflict with the pronounced nFI anomalies mentioned above. Indeed the nFI behaviour was taken as direct evidence for a $5f^2$ configuration with a nonmagnetic Γ_3 doublet ground state which has a nonvanishing quadrupolar moment (Cox, 1987, 1988) whose fluctuations scatter conduction electrons. The effective Hamiltonian is of the two-channel Kondo type which leads to an overcompensation of quadrupolar moments and therefore to typical logarithmic nFI anomalies in specific heat and susceptibility at low temperatures (Schlottmann and Sacramento, 1993; Zvyagin, 2000). The Γ_3 quadrupolar model would predict a positive nonlinear magnetic susceptibility in χ_3 with considerable anisotropy at low temperatures, instead the opposite, namely almost isotropic, negative $\chi_3(T)$ was found (Ramirez et al., 1994). This suggests that the ground state is a magnetic Kramers doublet Γ_6 . To explain nFI behaviour one either has to invoke a magnetic multichannel Kondo effect or closeness to a quantum critical point in UBe_{13} .

4.5.3. *The superconducting state in UBe_{13}*

The T_c values for superconductivity which occurs in the nFI state depend considerably on the type of sample. There are two classes with ‘high’ T_c ($\simeq 0.9 \text{ K}$) and ‘low’ T_c ($\simeq 0.75$) which, however, are not much different in their impurity content. Low temperature ‘power law’ dependencies give conflicting information on the node structure of the gap and no firm conclusion on whether spin singlet or triplet pairing is realized in UBe_{13} can be drawn. Therefore, these results will not be discussed further here although an axial order parameter with point nodes seems to be favored. The most direct evidence obtained so far for unconventional superconductivity is connected with the giant ultrasonic absorption anomaly observed directly

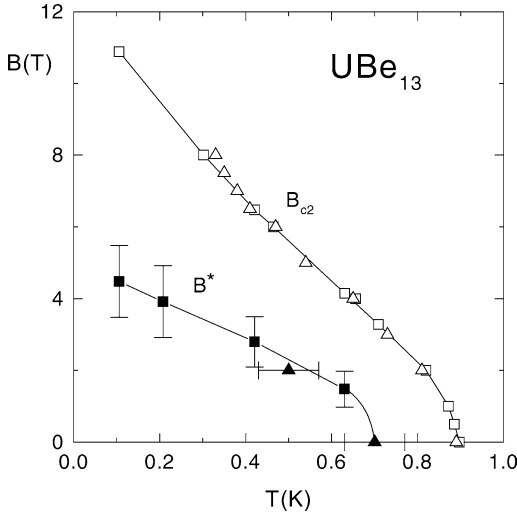


Fig. 49. Upper critical field B_{c2} and magnetic anomaly line B^* obtained from specific heat (squares) and thermal expansion (triangles) experiments (Helfrich, 1996; Kromer et al., 1998) for a ‘high’ T_c sample.

below T_c (Golding et al., 1985; Müller et al., 1986) which was attributed to collective modes or domain-wall damping due to a multicomponent order parameter (Sigrist and Ueda, 1991).

The B - T phase diagram of UBe_{13} presented in fig. 49 has quite anomalous appearance: The upper critical field curve $B_{c2}(T)$ shows an inflection point around 0.45 K, furthermore deep in the superconducting regime another anomaly line $B^*(T)$ starting at $T_L = 0.7$ K has been identified both by specific heat (Helfrich, 1996) and thermal expansion measurements (Kromer et al., 1998, 2000). This line might be connected to the onset of magnetic correlations which, however, do not lead to long range order. This interpretation is supported by recent thermal expansion results (Kromer et al., 2000) who have shown that the line can be followed as function of Th-doping and eventually, according to this picture, long range SDW order appears above a Th concentration of $x_{c1} = 0.02$.

4.5.4. Superconducting phase diagram of Th-doped crystals

The T - x superconducting phase diagram of the thorated $\text{U}_{1-x}\text{Th}_x\text{Be}_{13}$ -crystals ($x \leq 0.10$) whose most recent version (Kromer et al., 2002), is shown in fig. 50 has attracted enormous interest because it was taken as strong evidence for unconventional superconductivity. Mainly two observations favored an interpretation in terms of exclusively SC phase transitions into SC phases denoted A , B and C in fig. 50: (i) At $x_{c1} = 0.02$ a cusp-like increase of T_c into T_{c1} occurs with seemingly different T_c pressure coefficients below and above x_{c1} , suggesting that SC phases below T_c (A , $x < x_{c1}$) and T_{c1} (B , $x > x_{c1}$) are different. (ii) Below T_{c2} for $x_{c1} < x < x_{c2}$ with $x_{c2} = 0.045$ a second superconducting transition into phase C takes place which was inferred from the sudden increase of slope in H_{c1} (Rauchschwalbe et al., 1987). Furthermore in phase C magnetic moments $\mu \simeq 10^{-3}$ per U site appear according to μSR results (Heffner et al., 1990). This lead to the suggestion that the SC order parameter in the

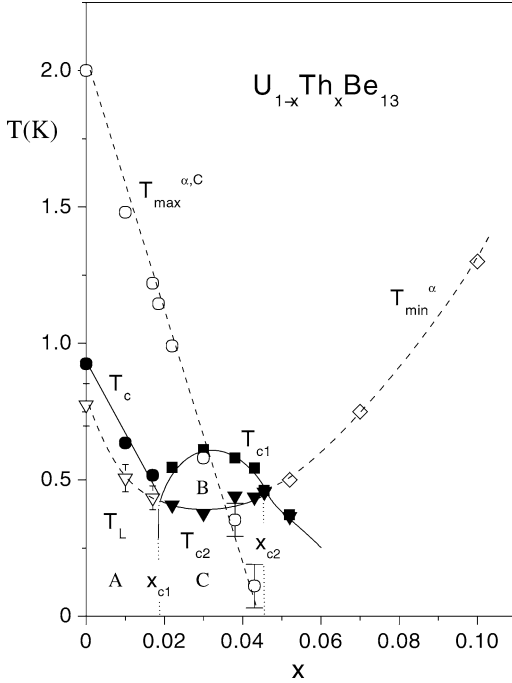


Fig. 50. Superconducting phase diagram of $U_{1-x}Th_xBe_{13}$ for $x < 0.10$ (Kromer et al., 2002). Full lines and symbols: thermodynamic phase boundaries; broken lines and open symbols: lines of anomalies. T_L and T_{min}^{α} denote line of anomalies from minimum in the thermal expansion coefficient $\alpha(T)$, $T_{max}^{\alpha,C}$ is the line of anomalies from the maximum in $C(T)$ and $\alpha(T)$. A, B and C denote distinct SC phases in the T_c -crossing model.

C phase is nonunitary, i.e., Cooper pairs carry a magnetic moment which appears around impurity sites.

These observations lead to a scenario within the Ginzburg–Landau theory approach based on the basic assumption of a crossing of $T_c(\Gamma_1, x)$ and $T_c(\Gamma_5, x)$ of two different superconducting order parameters at the critical concentration x_{c1} (Sigrist and Ueda, 1991). They belong to cubic O_h representations Γ_1 (fully symmetric) and Γ_5 (three-fold orbital degeneracy), though different pairs of representations are also possible. Below x_{c1} (and hence also for stoichiometric UBe_{13}) $T_c(\Gamma_5, x) > T_c(\Gamma_1, x)$ and the unconventional Γ_5 (A) SC state is stable. Above x_{c1} the opposite inequality holds and the conventional Γ_1 (B) SC phase is stable immediately below T_{c1} . For lower temperature when the size of the SC order parameter increases the fourth order mixing terms in the GL functional favor a mixed $\Gamma_1 \oplus \Gamma_5$ SC state (C) which becomes stable below the transition at T_{c2} . For a specific region in the parameter space of the GL functional the mixed state may be nonunitary and therefore lead to Cooper pairs with magnetic moments. For further increase of Th-concentration enhanced pair breaking eventually leads again to a decreasing $T_c(\Gamma_1, x)$ and a second crossing at x_{c2} appears.

However, the results of recent detailed thermal expansion experiments including additional Th-concentrations have challenged this $T_c(\Gamma_5, x) - T_c(\Gamma_1, x)$ crossing interpretation (Kromer, 2000; Kromer et al., 2000, 2002). Firstly, investigation of additional Th dopings has shown that pressure dependence of T_c and T_{c1} is not really different outside the critical region around x_{c1} . More importantly, however, a new line of anomalies T_L (dashed line in fig. 50)

has been found that starts at the aforementioned anomaly for UBe_{13} in fig. 49 ($B^* = 0$) and continues until it merges with T_{c2} for $x > x_{c1}$ and then even beyond x_{c2} . For $x = 0$ T_L was interpreted as onset temperature of magnetic correlations. The thermal expansion anomaly at T_L becomes ever sharper when x approaches x_{c1} which suggests increasing magnetic correlation length until finally at x_{c1} at the real phase transition line T_{c2} a true SDW state has evolved which continues beyond x_{c2} . In this picture then the phases *A* and *B* are the same superconducting phases and *C* is characterised by coexistence of the superconducting *B*-phase with the SDW state which also is responsible for the observed small moments ($10^{-3}\mu_B$), there is no need to assume an exotic nonunitary SC order parameter in the *C*-phase. The evolution of a SDW state within the SC phase has already been proposed by Kato and Machida (1987). However in this picture the increased slope of H_{c1} below T_{c2} has no obvious explanation. Furthermore the sudden drop of flux creep rate by several orders of magnitude below T_{c2} in phase *C* (Dumont and Mota, 2002) can be explained in the crossing scenario where the nonunitary nature of *C* provides an efficient mechanism for flux pinning (Sigrist and Agterberg, 1999). Indeed the drop in the flux creep rate is not observed for pure UBe_{13} below T_L (Mota and Cichorek, 2003).

In thermal expansion investigations it also became clear that the additional temperature scale T_{max} is continuously reduced with increasing Th-concentration. Amazingly it hits T_{c1} exactly at its maximum and (observed for $B > B_{c2}$) vanishes at x_{c2} as shown by the dashed T_{max} line in fig. 50. If this energy scale is due to magnetic excitations it suggests a close connection to the mechanism of Cooper pairing.

The discussion in this section has necessarily been rather qualitative as there is no developed microscopic theory for this complex behaviour where indeed SC and perhaps SDW order evolve in an incoherent nonstoichiometric HF metal with pronounced nFI behaviour.

5. Rare earth borocarbide superconductors

The superconducting class of layered transition metal borocarbides $\text{RNi}_2\text{B}_2\text{C}$ was discovered (Nagarajan et al., 1994; Cava et al., 1994) and investigated rather recently. Here R stands either for nonmagnetic Y, Lu and Sc or for lanthanide elements in a magnetic R^{3+} state. Several excellent reviews are available already (Hilscher and Michor, 1999; Müller and Narozhnyi, 2001), mostly focusing on the material physics and chemistry of these compounds. The crystal structure shown in fig. 51 is body centered tetragonal (space group I4/mmm). It consists of R-C rock salt type planes separated by Ni_2B_2 layers built from NiB_4 tetrahedra and stacked along the *c*-axis. More general structures with more than one R-C layer are possible (Hilscher and Michor, 1999) but will not be discussed further. The nonmagnetic borocarbides have relatively high T_c 's around 15 K as seen in fig. 51. There is evidence that the superconducting mechanism is primarily of the electron-phonon (e-p) type although this cannot explain the large anisotropy of the SC gap. At first sight the layered structure is similar to the high- T_c cuprates. However, unlike the copper oxide planes the Ni_2B_2 planes show buckling (fig. 51, left panel), as a consequence the electronic states at the Fermi level in the borocarbides do not have quasi-2D $d_{x^2-y^2}$ character and, therefore, have much weaker

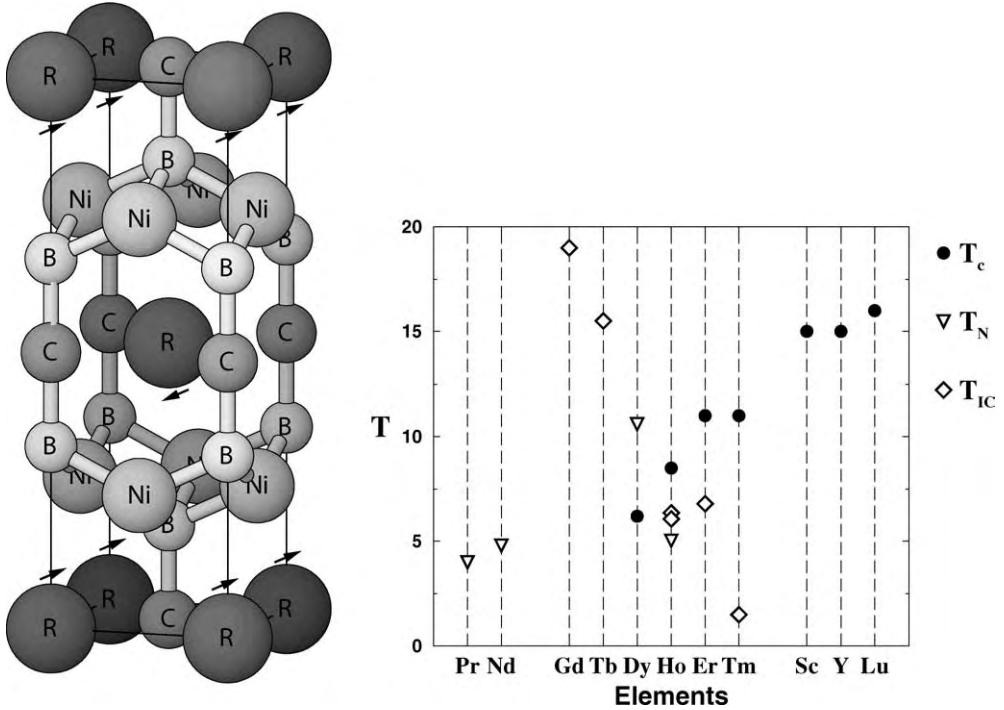


Fig. 51. Left: Tetragonal crystal structure ($I4/mmm$) of $\text{RNi}_2\text{B}_2\text{C}$. Low temperature AF2 magnetic structure with $[110]$ easy axis is indicated by arrows. $a = b = 3.52 \text{ \AA}$ and $c = 10.53 \text{ \AA}$ for $R = \text{Ho}$. Reciprocal lattice vectors are given by $2a^*$, $2b^*$ and $2c^*$ where $a^* = \frac{2\pi}{a}$, etc. Right: Magnetic (T_{IC} : incommensurate magnetic structure, T_N : simple AF structure) and superconducting (T_c) transition temperatures in Kelvin for the $\text{RNi}_2\text{B}_2\text{C}$ series.

correlations excluding the possibility of AF spin-fluctuation mediated superconductivity. The nonmagnetic borocarbides serve as a kind of reference point to separate the fascinating effects of AF and SC order parameter coupling in the magnetic $\text{RNi}_2\text{B}_2\text{C}$. However, the former have their own peculiarities which are not yet completely understood. Foremost, despite their alleged electron-phonon nature, $\text{LuNi}_2\text{B}_2\text{C}$ and $\text{YNi}_2\text{B}_2\text{C}$ have strongly anisotropic gap functions and low energy quasiparticle states as evident from specific heat and thermal conductivity. Furthermore an anomalous upturn in H_{c2} has been observed. The magnetic $\text{RNi}_2\text{B}_2\text{C}$ are an excellent class of materials to study the effects of competition of magnetic order and superconductivity for the following reasons: The T_c 's are relatively high and their size relative to T_N varies systematically across the R-series. Especially interesting are the cases of $\text{RNi}_2\text{B}_2\text{C}$ with $R = \text{Dy}$, Ho and Er where T_c and T_N (or T_{IC}) are not too different, leading to strong competition of the magnetic and SC order parameters. Furthermore the superconducting condensate and magnetic moments are carried by different types of electrons, namely itinerant 3d-electrons for the Ni_2B_2 layers and localized R^{3+} 4f-electrons for the R-C layers, respectively. Finally they are well separated and their coupling which is of the local exchange

type can be treated in a controlled perturbative way somewhat akin to the situation in the well known classes of Chevrel phase (Fischer, 1990) and ternary compound (Fischer and Maple, 1982) magnetic superconductors.

The antiferromagnetic molecular field establishes a periodic perturbation characterized by a length scale of the order of the Fermi wavelength $k_F^{-1} \ll \xi_0$. This implies that the spatial extent of the Cooper pairs extends over many periods of the staggered molecular field. The latter is therefore effectively averaged to zero and does not suppress superconductivity via an orbital effect. The system is invariant under the combined operation of time inversion followed by a translation with a lattice vector which allows to form Cooper pairs in a spin singlet state with vanishing (crystal) momentum in the antiferromagnetic lattice. This pair-state can be considered as a natural generalization of the pairing in time-reversed states encountered in usual nonmagnetic superconductors to which it reduces in the limit of vanishing staggered magnetization. The magnetic order does not lead to depairing (Fulde and Keller, 1982).

For detailed investigation it is necessary to gain a clear understanding of the magnetic phases of $\text{RNi}_2\text{B}_2\text{C}$. A theory of the rich metamagnetic phases in the B - T phase diagram of $\text{HoNi}_2\text{B}_2\text{C}$ and $\text{DyNi}_2\text{B}_2\text{C}$ is a necessary prerequisite to comprehend the interaction effects of the two order parameters in these compounds.

The investigation of alloy series of magnetic R^{3+} dissolved in the nonmagnetic borocarbides allows one to study the pair breaking effects due to incoherent exchange scattering and its associated de Gennes scaling of T_c . One also observes ‘inverse’ de Gennes scaling (Müller and Narozhnyi, 2001), i.e., the suppression of T_c by *nonmagnetic* impurities like Lu and Y in the *magnetic* $\text{RNi}_2\text{B}_2\text{C}$ superconductors which shows quite similar behaviour as function of the impurity concentration although its underlying physics is very different.

5.1. Physical properties of the nonmagnetic borocarbides

The nonmagnetic $\text{YNi}_2\text{B}_2\text{C}$ and $\text{LuNi}_2\text{B}_2\text{C}$ compounds with comparatively high T_c of 16.5 K and 15.5 K serve as reference systems for the more difficult systems $\text{RNi}_2\text{B}_2\text{C}$ with both magnetic and superconducting phases. The electron–phonon nature of superconductivity in $\text{YNi}_2\text{B}_2\text{C}$ and $\text{LuNi}_2\text{B}_2\text{C}$ is inferred from a substantial s-wave character of the order parameter as witnessed by the appearance of a moderate Hebel–Slichter peak in the ^{13}C NMR relaxation rate (Mizuno et al., 1999). On the other hand the gap function is strongly anisotropic as can be seen both from temperature and field dependence of thermodynamic and transport quantities. At low temperatures one observes a specific heat $C_s \sim T^3$ (Hilscher and Michor, 1999) and thermal conductivity $\kappa_{xx} \sim T$ (Boaknin et al., 2001) and $\kappa_{zz} \sim T^\alpha$ ($\alpha \sim 2-3$) indicating the presence of gap nodes (Izawa et al., 2002a). More precisely, within experimental accuracy, there must be at least a gap anisotropy of $\Delta_{\min}/\Delta_{\max} \leq 10^{-2}$ (Izawa et al., 2002a). For an electron–phonon superconductor this would be the largest anisotropy ever observed. This conjecture is also supported by a \sqrt{H} field dependence (Nohara et al., 1997) of the low temperature specific heat and the linear H dependence of the thermal conductivity κ_{xx} for \mathbf{H} along [001] (Boaknin et al., 2001). Since in the latter case the heat current is perpendicular to the vortices this proves that quasiparticles must be present in the inter-vortex region. This is also required to explain the observation of dHvA oscillations far in the vortex phase. Experimental

evidence therefore demands a nodal gap function for borocarbides and the $s + g$ wave model proposed in Maki et al. (2002) fulfils the requirements. In addition it explains recent results on ultrasonic attenuation which also confirmed the existence of gap nodes in the cubic plane (Watanabe et al., 2003). In the following we will address the question of electron–phonon coupling strength, isotope effect and positive curvature in the upper critical field. Furthermore power law behaviour of the electronic specific heat and thermal conductivity as function of temperature and in addition their field-angle dependence $C_s(T, \mathbf{H})$ and $\kappa_{ij}(T, \mathbf{H})$ for $T \ll T_c$ in the vortex phase allows to discuss the nodal structure of the SC gap.

5.1.1. Evidence for electron–phonon superconductivity

The classical argument in favor of the e-p mechanism is the observation of an isotope effect characterized by the isotope exponent for a specific atom with mass M as given by $\alpha_M = -d \ln T_c / d \ln M$. However, this cannot be applied easily to complex layered superconductors, as evident from the existence of an isotope effect in the nonphononic cuprate superconductors with nonoptimal doping. A boron isotope effect has been found in $\text{YNi}_2\text{B}_2\text{C}$ ($\alpha_B = 0.2$) and $\text{LuNi}_2\text{B}_2\text{C}$ ($\alpha_B = 0.11$) much smaller than the BCS value $\alpha_M = 0.5$ and a nonphononic origin for α_B originating in the influence of boron on the charge density in the B_2Ni_2 layers has, therefore, been suggested (Drechsler et al., 2001).

The most direct support for the phonon mediated Cooper pairing is due to scanning tunneling spectroscopy (Martinez-Samper et al., 2003) which has shown the existence of a strong coupling signature in the tunneling DOS due to a soft optical phonon close to the FS nesting wave vector \mathbf{Q} . The e-p coupling constant was derived as $\lambda = 0.5\text{--}0.8$ which is compatible with the value $\lambda = 0.53$ obtained from resistivity data.

Additional support for the electron phonon mechanism comes from the comparison of thermodynamic ratios $\Delta(T_c)/\gamma T_c$ and $\Delta(0)/kT_c$ calculated in strong coupling theory and the phonon spectra measured by inelastic neutron scattering (Hilscher and Michor, 1999). The strong coupling corrections of the above ratios to their BCS values are related to the logarithmic moments $\bar{\omega}$ of the phonon DOS $F(\omega)$ or more precisely of the $\alpha^2 F(\omega)$ Eliashberg function. These moments may be directly obtained from the INS phonon DOS or indirectly from the above ratios. A comparison shows a reasonable agreement between the moments with a $T_c/\bar{\omega}$ ratio characteristic for moderately strong coupling electron phonon superconductivity. The moments are, however, much smaller than the Debye energies obtained from the phonon specific heat which again indicates that certain low lying optical phonon modes play a special role for the coupling. By varying temperature it has been found that these are soft optical phonon modes along the $[q_x, 0, 0]$ direction which involve primarily the vibration of the heavy Y or Lu atoms. The softening occurs at $q_x \sim 0.55$ (in r.l.u. of $2\pi/a$) which corresponds to a nesting vector of the Fermi surface (Dugdale et al., 1999) where the \mathbf{q} -dependent electronic susceptibility which determines the renormalized phonon frequency becomes strongly enhanced. The special role of these optical phonons for the strong coupling effects is underlined by the moment ratio $(\bar{\omega}_{\text{YNi}_2\text{B}_2\text{C}}^{\alpha^2 F} / \bar{\omega}_{\text{LuNi}_2\text{B}_2\text{C}}^{\alpha^2 F}) \sim 1.5 \sim (M_{\text{Lu}}/M_{\text{Y}})^{1/2}$ rather than being equal to the square root of the unit cell masses which would only be 1.16.

5.1.2. Anomalous H_{c2} -behaviour

The upper critical field in nonmagnetic $\text{LuNi}_2\text{B}_2\text{C}$ and $\text{YNi}_2\text{B}_2\text{C}$ compounds shows a peculiar positive (upward) curvature below T_c . This phenomenon is also observed in various other layered superconductors. Within the standard Ginzburg–Landau description of H_{c2} for isotropic single band superconductors the slope is determined by the Fermi velocity and only a negative curvature is possible. A positive curvature can be obtained by assuming a strong anisotropy of the Fermi velocity (Drechsler et al., 2001) which may be simplified to a two band model with two Fermi velocities. The upper critical field for the two band model may be calculated within the linearized version of Eliashberg theory (Shulga et al., 1998). In this way a fit for the experimental H_{c2} -curves using a two band Fermi velocity ratio of $v_{F1} : v_{F2} = 0.97 : 3.7$ ($\text{LuNi}_2\text{B}_2\text{C}$) and $0.85 : 3.8$ ($\text{YNi}_2\text{B}_2\text{C}$) can be obtained. It also has to be assumed that there is strong e-p coupling in the v_{F1} band and sizable coupling between v_{F1} and v_{F2} bands. It should be noted that the presence of magnetic impurity scattering may change the picture (Shulga and Drechsler, 2001) because an increasing scattering rate decreases the positive curvature. Thus the extraction of a unique set of parameters for the two band model from the positive H_{c2} curvature seems difficult. As expected for uniaxial crystal structures, there is an a - c anisotropy of H_{c2} but surprisingly there is also a strong four-fold anisotropy within the tetragonal ab -plane (Metlushko et al., 1997) which cannot be due to FS effects on the level of the effective mass approximation, it rather should be taken as another indication of the large gap anisotropy in the ab -plane.

5.1.3. Specific heat and thermal conductivity results

The low temperature dependence of the specific heat is apparently described by a power law behaviour $C_s \sim T^n$ with n between 2 and 3 (Hilscher and Michor, 1999). Thermal conductivity κ_{xx} (Boaknin et al., 2001) clearly exhibits T -linear behaviour for $T \ll T_c$ suggesting the presence of nodal lines or second order node points as introduced below which would be compatible with $n = 2$ for the specific heat. Furthermore the investigation of field (and field-angle) dependence of $C_s(T, \mathbf{H})$ and $\kappa_{ij}(T, \mathbf{H})$ ($i, j = x, y, z$) is a powerful method to obtain information on the quasiparticle spectrum and hence on the anisotropy properties of the gap function (sect. 2). In a conventional superconductor with isotropic gap the quasiparticles at low temperature are confined to the vortex core where they form closely spaced bound states with an energy difference Δ^2/E_F much smaller than kT . Therefore, they can be taken as a cylinder of normal state electrons of diameter ξ_0 (coherence length) which gives a field independent contribution $\xi_0^2 \gamma T$ per vortex to the linear specific heat. Then in the vortex phase $\gamma(H)$ is predicted to scale with the number of vortex lines which is $\sim H$. However in superconductors with nodes the quasiparticles with momenta in the node direction can tunnel into the inter-vortex region and then their energy is Doppler shifted by the supercurrents around the vortex by an amount $\delta E = m\mathbf{v}_F \cdot \mathbf{v}_s$. As shown by Volovik (1993) this leads to a finite residual quasiparticle DOS at zero energy given by

$$N_s(0)/N_n = K \sqrt{\frac{H}{H_{c2}}}, \quad (101)$$

where K is a constant and N_n the normal state DOS. As found later the DOS also depends on the relative angle of the field with respect to the nodal positions of the gap function. The DOS in eq. (101) leads then to a \sqrt{H} behaviour of the specific heat (Nohara et al., 1997) and also for $\kappa_{zz}(H)$ for temperatures larger than the quasiparticle scattering rate. Thermal conduction perpendicular to the vortex lines ($\mathbf{H} \parallel c$) as given by $\kappa_{xx}(H)$ that starts immediately above H_{c1} for $T \ll T_c$ can only result from the presence of extended quasiparticle states outside the vortex cores and hence is a direct proof for the presence of nodal regions in the gap. To draw similar conclusions from the specific heat it is necessary to observe the \sqrt{H} behaviour for $H \ll H_{c2}$ and in connection the infinite slope of $\gamma(H)$ for $H \rightarrow 0$. The Doppler shift picture of magnetothermal properties is only an approximation. A comparison with exact quasiclassical calculations has been given in Dahm et al. (2002) and Nakai et al. (2004).

5.2. Theoretical analysis of nonmagnetic borocarbides

We briefly discuss the electronic structure and associated FS topology which is also important for the magnetic borocarbides. Our main topic here is the explanation of the quasi-unconventional SC low temperature behaviour of nonmagnetic Lu- and Y-borocarbides which may be understood within a hybrid s + g wave model for the SC gap function.

5.2.1. Electronic structure of the borocarbides

The crystal structure of the borocarbides is of a layered type which might one lead to expect quasi 2D features in the electronic bands. Calculations by various groups (Mattheis, 1994; Pickett and Singh, 1994; Rosner et al., 2001) have shown however that they have definitely 3D character which is also suggested by the rather isotropic resistivity (Fisher et al., 1997). Conduction states are composed of wide Ni-B-N-sp bands and narrow (~ 3 eV) Ni-3d bands centered about 2eV below the Fermi level which is close to a local peak of the DOS in LuNi₂B₂C and YNi₂B₂C. The DOS peak generally decreases when Lu is replaced by progressively lighter R atoms which leads to a correspondingly smaller T_c . This also agrees with the observation that substitution of Ni with Co (hole-doping) or with Cu (electron-doping) decreases T_c (Gangopadhyay and Schilling, 1996; Schmidt and Braun, 1997) because the Fermi level moves away from the local peak position. Unlike in the cuprates all Ni 3d-states in the borocarbides contribute to conduction bands at the Fermi surface which therefore consists of many sheets. In LuNi₂B₂C the main sheet exhibits an important nesting feature (Dugdale et al., 1999). FS lobes along [110] direction in the tetragonal plane are connected by a nesting vector $\mathbf{Q} = (0.55, 0, 0)$. This in turn leads to a peak structure in the staggered susceptibility $\chi(\mathbf{q})$ (Rhee et al., 1995) at $\mathbf{q} = \mathbf{Q}$. In the RNi₂B₂C the effective magnetic RKKY interaction $J(\mathbf{q})$ is proportional to $\chi(\mathbf{q})$ and therefore a -axis incommensurate magnetic order with modulation vector \mathbf{Q} is seen in Gd, Tb, Ho, Er and Tm-borocarbides which coexists with c -axis spiral order in HoNi₂B₂C (sect. 5.3). Further evidence of the importance of the nesting at \mathbf{Q} comes from the presence of a pronounced Kohn anomaly at wave vector \mathbf{Q} in the phonon dispersion of LuNi₂B₂C (Dervenagas et al., 1995). Finally the previous conjecture of strongly different Fermi velocities in the two band model has been confirmed in electronic structure calculations for YNi₂B₂C (Rosner et al., 2001).

5.2.2. Nodal structure of the superconducting gap and impurity effects

As explained before, thermodynamics and transport behaviour points to an extremely anisotropic or nodal gap function in the nonmagnetic borocarbides. A gap function compatible with reported experiments was proposed in Maki et al. (2002). It is a hybrid $s + g$ wave gap which is fully symmetric (A_{1g}) under the tetragonal group D_{4h} and has the form

$$\Delta(\mathbf{k}) = \frac{1}{2}\Delta(1 - \sin^4 \vartheta \cos(4\phi)), \quad (102)$$

where ϑ, ϕ are the polar and azimuthal angle in \mathbf{k} -space, respectively. This gap function has four second order node points at $(\vartheta, \phi) = (\frac{\pi}{2}, 0), (\frac{\pi}{2}, \pi)$ and $(\frac{\pi}{2}, \pm\frac{\pi}{2})$ (fig. 52) which dominate the quasiparticle DOS for $E \ll \Delta$ where

$$\frac{N_s(E)}{N_n} = \frac{\pi}{4} \frac{|E|}{\Delta}. \quad (103)$$

The form of $\Delta(\mathbf{k})$ implies a fine tuning of s and g amplitudes. At its *second order* node points there is no sign change of the gap function and therefore the derivative is also zero. The resulting linear quasiparticle DOS then leads to the observed low temperature specific heat

$$\frac{C_s}{\gamma T} = \frac{27}{4\pi} \zeta(3) \left(\frac{T}{\Delta} \right), \quad (104)$$

where γ is the Sommerfeld constant. The presence of nodal points in the hybrid $s + g$ wave gap function has no intrinsic symmetry reason but is due to a ‘fine-tuning’ of s - and g -wave amplitudes in eq. (102). For $\text{YNi}_2\text{B}_2\text{C}$ this is realised to an astonishing degree of $\Delta_{\min}/\Delta_{\max} \leq 0.01$. There is presently no microscopic explanation for this fine tuning but a phenomenological justification for the stability of an $s + g$ wave order parameter for a wide range of pair potentials has been given (Yuan and Thalmeier, 2003).

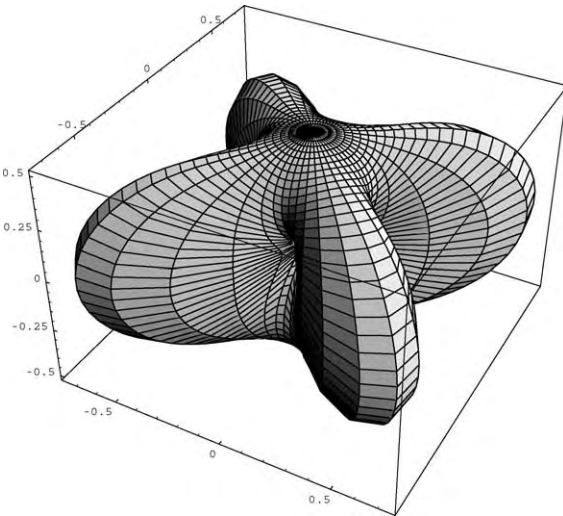


Fig. 52. Polar plot of the anisotropic SC gap function $\Delta(\mathbf{k})$ of the $s + g$ model. Nodal points are along $[100]$ and $[010]$ directions (Maki et al., 2002).

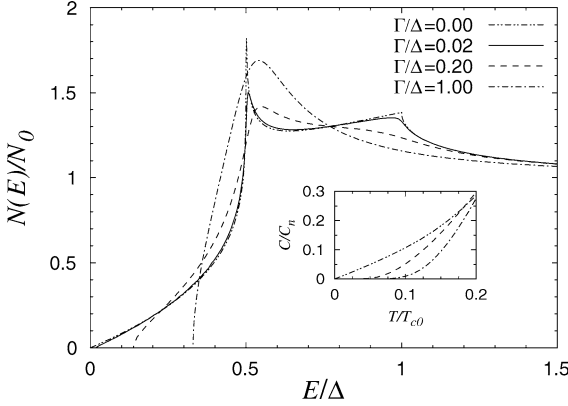


Fig. 53. Normalised quasiparticle DOS for s + g wave gap in pure $\text{YNi}_2\text{B}_2\text{C}$ ($\frac{\Gamma}{\Delta} = 0$, full line) and for various scattering strengths Γ in the Born limit (for unitary limit results are quite similar). Induced excitation gap ω_g increases monotonically with Γ . The inset shows the low temperature specific heat (Yuan et al., 2003).

The nodal s + g wave gap function has a surprising behaviour when normal impurity scattering is taken into account (Yuan et al., 2003). For nodal gap functions belonging to a single nontrivial representation, like a d-wave gap there is a strong difference between scattering in the Born limit (small phase shift) and unitary limit (phase shift $\frac{\pi}{2}$). In the latter resonance scattering leads to the appearance of a residual zero field DOS resulting in a finite specific heat coefficient for $T < \Gamma$ ($\Gamma =$ quasiparticle scattering rate). In the hybrid s + g wave case, quite the opposite behaviour, i.e., gap opening by impurity scattering, is observed which is almost identical for Born limit and unitary limit. The quasiparticle DOS including impurity scattering is given by

$$\frac{N_s(E)}{N_n} = \text{Im} \left\langle \frac{i\tilde{\omega}_n}{\sqrt{\tilde{\omega}_n^2 + \tilde{\Delta}_{\mathbf{k}}^2}} \right\rangle_{i\omega_n \rightarrow E+i\delta}, \quad (105)$$

where $\tilde{\omega}_n = \omega_n + i\Sigma_0$ and $\tilde{\Delta}_{\mathbf{k}} = \Delta_{\mathbf{k}} + \Sigma_1$ are the Matsubara frequency and gap function renormalised by impurity scattering which leads to diagonal and nondiagonal self energies Σ_0 and Σ_1 , respectively. For $\omega \rightarrow 0$ one finds $\tilde{\Delta} \rightarrow \frac{1}{2}\Delta + \Gamma$ where Γ is the scattering rate. In other words an energy gap ω_g immediately opens up for finite Γ as can be observed in fig. 53 which scales approximately as $\omega_g(\Gamma) = \Gamma / (1 + \frac{2\Gamma}{\Delta})$. Thus the s + g wave fine tuning is destroyed by impurity scattering and nodal quasiparticles are removed for temperatures $T < \Gamma$. This would lead to a crossover to exponential low temperature behaviour in the specific heat. Indeed this gap creation was observed in Pt-substituted $\text{Y}(\text{Ni}_{1-x}\text{Pt}_x)_2\text{B}_2\text{C}$ with $x = 0.2$ by Nohara et al. (1997) as shown in fig. 55. This remarkable behaviour, which is exactly opposite to the d-wave case where residual states at the Fermi level are created, can be traced back to the different character of first order nodes (d-wave) where the gap function changes sign and second order nodes (s + g wave) where the angular derivatives of $\Delta(\vartheta, \varphi)$ also vanish and no sign change of the gap occurs. In the first case the effect of impurity scattering averages out in the gap equation, in the second it does not, leading to a finite excitation gap ω_g .

5.2.3. Thermodynamics and transport in the vortex phase

As discussed in sect. 2 the Volovik effect leads to a momentum *and* position dependent Doppler shift of the quasiparticle energies caused by the supercurrent flowing around the vortices. The corresponding DOS change depends both on the field strength and field direction with respect to nodal positions. For the gap model of eq. (102) the residual field induced DOS is given by Won et al. (2003), Thalmeier and Maki (2003b)

$$\frac{N_s(0)}{N_n} = \frac{C_s}{\gamma T} = \frac{\tilde{v}\sqrt{eH}}{2\Delta} I(\theta, \phi), \quad (106)$$

$$I(\theta, \phi) = \frac{1}{2} \{ (1 - \sin^2 \theta \sin^2 \phi)^{1/2} \} + \{ (1 - \sin^2 \theta \cos^2 \phi)^{1/2} \},$$

where $\tilde{v} = \sqrt{v_a v_c}$ and $I(\frac{\pi}{2}, \phi) = \max(|\sin \phi|, |\cos \phi|)$. This function has a cusp-like minimum at $\phi = n\frac{\pi}{2}$ when \mathbf{H} is sweeping over the node points. Also the residual DOS exhibits naturally the experimentally observed \sqrt{H} behaviour. For the calculation of thermal conductivity in the vortex phase of the $s + g$ wave superconductor one has to be aware that impurity scattering immediately opens a gap $\omega_g \simeq \Gamma$. To have nodal quasiparticles for transport available one must fulfil $\omega_g \simeq \Gamma < T$. On the other hand to have an appreciable oscillation amplitude one must still be in the low temperature limit $\Gamma < T \ll \tilde{v}\sqrt{eH} \ll \Delta$. The angle dependence of the c -axis thermal conductivity in the leading order is then given by

$$\frac{\kappa_{zz}}{\kappa_n} \simeq \frac{2}{\pi} \frac{\tilde{v}\sqrt{eH}}{\Delta} I(\theta, \phi), \quad (107)$$

i.e., in this limit to leading order it is completely determined by the angular dependent residual DOS. To determine the proper nodal positions from the maxima/minima of $\kappa_{zz}(\theta, \phi)$ it is important that the low temperature limit is reached.

The angular dependence of the c -axis thermal conductivity has been investigated in detail in (Izawa et al., 2002a). The geometry with heat current along c and \mathbf{H} conically swept around c is shown in the inset of fig. 54. For the in-plane field ($\theta = \frac{\pi}{2}$) pronounced cusps in $\kappa_{zz}(\frac{\pi}{2}, \phi)$ appear for $\phi = 0, \pm\pi/2$ in $\kappa_{zz}(\frac{\pi}{2}, \phi)$ as is visible in fig. 54. This is a typical signature for the existence of point nodes in the gap in the direction of the tetragonal [100] and [010] axes. When the polar field angle θ decreases the oscillations in $\kappa_{zz}(\theta, \phi)$ as function of azimuthal field angle ϕ are rapidly diminished. This behaviour is indeed predicted from eq. (106) as shown in fig. 54. A similar calculation for a d_{xy} -gap function $\Delta(\phi) = \Delta(\varphi) = \Delta \sin(2\varphi)$ which has line nodes in the same directions may be performed (Thalmeier and Maki, 2003b). In this case no cusp appears and the amplitude of $\kappa_{zz}(\theta, \phi)$ oscillation in ϕ is almost independent of θ . This speaks strongly in favor of the $s + g$ wave order parameter as the correct model for $\text{YNi}_2\text{B}_2\text{C}$ and possibly $\text{LuNi}_2\text{B}_2\text{C}$. It is the first confirmed case of a superconductor with (second order) node points in the gap functions. The only other known candidate is UPt_3 whose E_{2u} gap function in the B -phase is supposed to have point nodes at the poles (sect. 4.1). Similar experiments as in fig. 54 have yet to be performed for this compound. The point nodes of $\text{YNi}_2\text{B}_2\text{C}$ were found to lie along the tetragonal axis, this means that the $s + g$ gap function in fig. 52 is rotated by 45 degrees compared to the one used in Maki et al. (2002). According to eq. (106) the ϕ dependence of the specific heat is determined by the same angular function

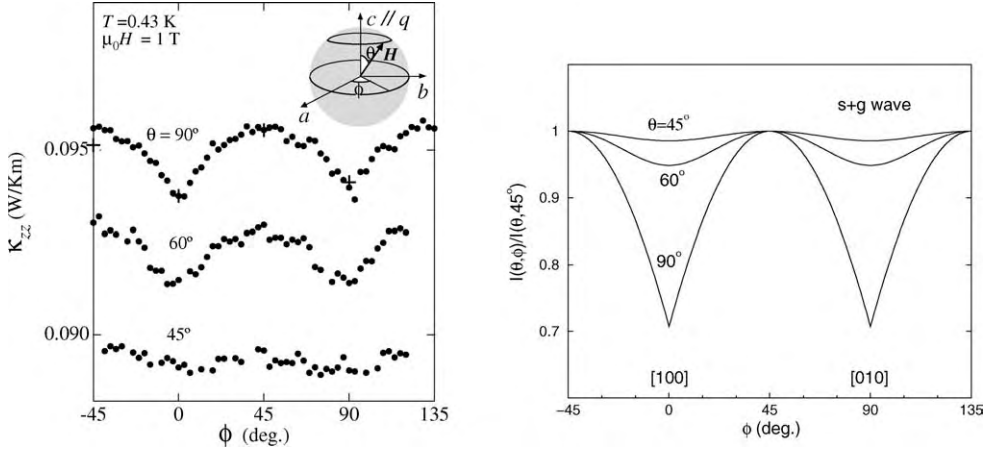


Fig. 54. Left: Experimental c -axis thermal conductivity of $\text{YNi}_2\text{B}_2\text{C}$ as function of azimuthal field angle ϕ for various polar field angles θ (Izawa et al., 2002). The inset shows the field geometry with \mathbf{H} being swept around c by varying ϕ and keeping θ constant. Right: Theoretical normalized ϕ -dependence of angular function $I(\theta, \phi)$ which determines κ_{zz} according to eqs. (106), (107) (Thalmeier and Maki, 2003b).

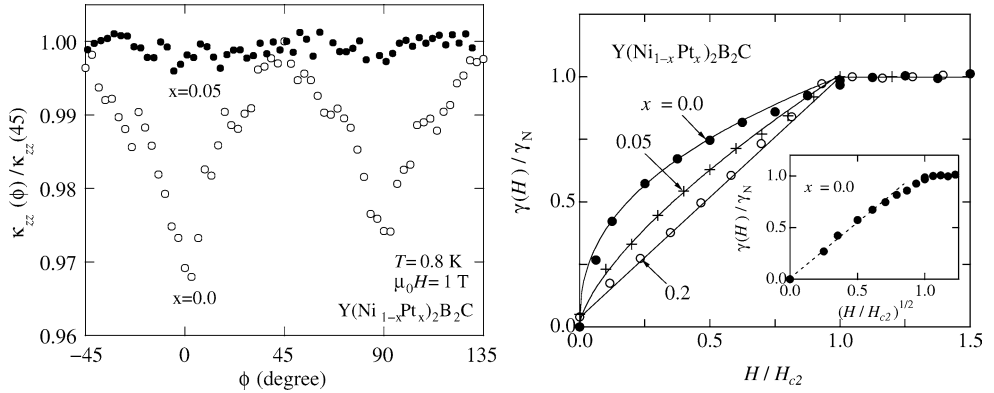


Fig. 55. Left panel: Cusp-like four-fold oscillations in $\kappa_{zz}(90^\circ, \phi)$ of $\text{YNi}_2\text{B}_2\text{C}$ due to $s + g$ wave point nodes are completely destroyed by 5% Pt-doping (Kamata, 2003). Right panel: Transition from \sqrt{H} -behaviour of $\gamma(H)$ for the nodal SC at $x = 0$ to linear in H behaviour for $x = 0.2$ when a large gap has opened (Nohara et al., 1997).

and cusps should also appear there. This was indeed observed (Park et al., 2002) (fig. 12). In the Pt-substituted compound $\text{Y}(\text{Ni}_{1-x}\text{Pt}_x)_2\text{B}_2\text{C}$ already $x = 0.05$ is sufficient to destroy the angular oscillations in $\kappa_{zz}(\theta, \phi)$ (Kamata, 2003) which is again due to the rapid gap-opening for $s + g$ wave and destruction of nodal regions by impurity scattering as shown in fig. 55.

In this section we have shown abundant experimental evidence that the nonmagnetic $\text{YNi}_2\text{B}_2\text{C}$ and possibly $\text{LuNi}_2\text{B}_2\text{C}$ have anisotropic gap functions with point nodes that can

be described by a hybrid $s + g$ wave order parameter. As a consequence the simple electron–phonon type pairing mechanism originally envisaged for the borocarbides certainly has to be supplemented, for example, by strongly anisotropic Coulomb interactions, to account for the strongly anisotropic gap function found there.

5.3. Magnetic borocarbides

The magnetic 4f-electrons of lanthanides and the superconducting 3d-electrons of Ni are well separated in the RC layers and Ni_2B_2 layers of $\text{RNi}_2\text{B}_2\text{C}$. The coupling between magnetic and superconducting order parameters is weak enough to be treated as a perturbation but still strong enough to lead to pronounced effects on the SC properties. The magnetic and superconducting transition temperatures T_m and T_c of the series are shown in fig. 51. We will first discuss some of the basic observations in the series with focus on the Ho and Er borocarbides where coexistence of both order parameters is most interesting. The size of T_m and the influence of magnetism on T_c are both governed by the de Gennes factor $dG = (g - 1)^2 J(J + 1)$ where g is the Landé factor and J the total angular momentum of the R^{3+} ion. The former suggests the RKKY interaction via Ni 3d conduction electrons of intervening Ni_2B_2 layers as the coupling mechanism for the 4f moments in RC layers. The magnetic structures exhibit a great variety which has been described and tabulated in Lynn et al. (1997) and Müller and Narozhnyi (2001) and the following general features are observed: (i) Both commensurate (C) and incommensurate (IC) magnetic order parameters are present. (ii) For Dy, Ho the commensurate AF structure consists of ferromagnetically ordered ab -planes stacked along the c -axis. (iii) In IC structures one has two possibly coexisting type of modulations: helical modulation of stacked FM planes along the c -axis or SDW type (both longitudinal and transverse) modulation within each ab -plane with a modulation vector \mathbf{Q} close to the FS nesting vector. (iv) The easy axis selected by the CEF potential is $[110]$ (Ho, Dy), $[100]$ (Er) or $[001]$ (Tm).

As an example the low temperature $\text{HoNi}_2\text{B}_2\text{C}$ commensurate AF2 structure is indicated in fig. 51. In the RKKY mechanism IC modulation vectors should result from the maxima of the static electronic susceptibility $\chi(\mathbf{q})$ which has been approximately calculated by Rhee et al. (1995). It exhibits a pronounced peak at the nesting vector \mathbf{Q} of the Fermi surface which is indeed quite close to observed a -axis magnetic modulation vectors $\mathbf{Q}_a = (0.55, 0, 0)$ of the Gd, Tb, Ho and Er borocarbide compounds. On the other hand in $\text{HoNi}_2\text{B}_2\text{C}$ only a flat maximum is observed for wave vectors $\mathbf{q} = (0, 0, q_z)$ close to the AF vector $\mathbf{Q}_{\text{AF}} = (0, 0, 0.5)$ so that the observed helically modulated structures along \mathbf{c}^* should not be associated with any FS nesting feature. For theoretical model calculations of stable magnetic structures it is a more sensible approach to parametrize the long range RKKY exchange interactions and compare the results with the experimentally determined field-angle dependent phase diagram at low temperature. This has been most successfully done for $\text{HoNi}_2\text{B}_2\text{C}$ (Amici and Thalmeier, 1998) and $\text{ErNi}_2\text{B}_2\text{C}$ (Jensen, 2002). Four of the $\text{RNi}_2\text{B}_2\text{C}$ ($\text{R} = \text{Dy}, \text{Ho}, \text{Er}, \text{Tm}$) show coexistence of superconductivity and magnetic order. As mentioned before $\text{HoNi}_2\text{B}_2\text{C}$ and $\text{DyNi}_2\text{B}_2\text{C}$ (Winzer et al., 1999) display the most spectacular interaction between superconductivity and magnetic order as already suggested by close transition temperatures T_m and T_c (fig. 51). On the other hand in $\text{ErNi}_2\text{B}_2\text{C}$ and $\text{TmNi}_2\text{B}_2\text{C}$ the SC vortex state exhibits an anomalous behav-

four connected with the magnetic order. In the following we will discuss mainly $\text{HoNi}_2\text{B}_2\text{C}$ and $\text{ErNi}_2\text{B}_2\text{C}$ where most of the work has been performed so far.

5.3.1. Metamagnetism and IC-C lock-in transition in $\text{HoNi}_2\text{B}_2\text{C}$

The metamagnetism of $\text{HoNi}_2\text{B}_2\text{C}$ has been investigated theoretically in considerable detail (Amici and Thalmeier, 1998; Amici et al., 2000). First we discuss the 4f-magnetism of $\text{HoNi}_2\text{B}_2\text{C}$. This problem has two related aspects. For zero field the first IC magnetic phase with $\mathbf{Q} = (0, 0, 0.45)$ appears at $T_{IC} = 6$ K which has a helical modulation of the moment of FM ab -planes along c . At $T_N = 5$ K a lock-in transition occurs to the simple AF with wavevector \mathbf{Q}_{AF} and $[110]$ easy axis which is the stable low temperature structure. In addition an a -axis modulation with wave vector \mathbf{Q}_a exists which will be neglected here. The application of a magnetic field \mathbf{H} at an angle θ with respect to the easy axis leads to the appearance of additional phases as witnessed by metamagnetic transition steps in the magnetization curve (Canfield et al., 1997) and shown in the inset of fig. 56. At these steps some of the FM layers with moments pointing roughly opposite to the field direction align with the easy axis closest to the field direction, this leads to a stacking of FM planes with a resulting net magnetic moment. Following the magnetization steps as function of θ one can construct the metamagnetic phase diagram (fig. 56). The observed magnetic high-field phases are listed in the caption of fig. 56.

The metamagnetism of $\text{HoNi}_2\text{B}_2\text{C}$ is caused by two conflicting interactions, namely tetragonal CEF potential and the RKKY-interaction. Whereas the first tries to align the moments along the easy axis as determined by the CEF potential the second one prefers a helical modulation of moments with a wavevector that minimizes the exchange energy. The favored structure results from a compromise and may change with temperature and external field. The

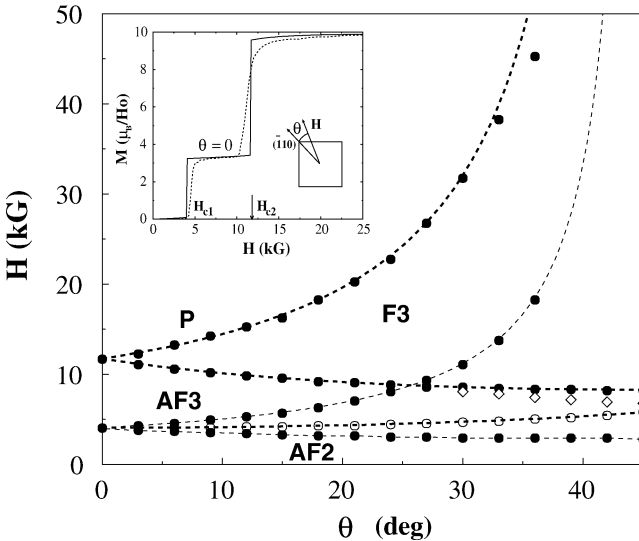


Fig. 56. Inset: Experimental (dashed line) and theoretical magnetization $M(H)$ (full line) for $\text{HoNi}_2\text{B}_2\text{C}$ with \mathbf{H} in the ab -plane at angle $\theta = 0$ with respect to the easy $[110]$ axis. Following the calculated magnetization steps as function of θ leads to the theoretical H - θ phase diagram shown in the main figure (Amici and Thalmeier, 1998). The stacking sequence of FM planes along c in the unit cell of magnetic phases is given by AF2($\uparrow\downarrow$), AF3($\uparrow\downarrow\uparrow$) (ferromagnetic), F3($\uparrow\uparrow\rightarrow$) (noncollinear). P(\uparrow) is the homogeneously magnetised phase. The weak dashed lines denote theoretically possible intermediate phase boundaries not observed experimentally.

CEF potential is obtained from inelastic neutron scattering experiments (Gasser et al., 1996; Cavadini et al., 2003) by fitting the observed energies and intensities of CEF transitions to the predictions of an extended point charge model of the tetragonal CEF which determines the parameters of the model Hamiltonian H_{CEF} . Then the CEF energies and wave functions may be obtained explicitly. For Ho^{3+} ($J = 8$) the 17 singlet and doublet CEF states split into two groups: A group of 13 states with energies > 10 meV which is irrelevant in the interesting temperature range and four low lying tetragonal CEF states consisting of a ground state singlet Γ_4 (0 meV) and excited doublet Γ_5^* (0.15 meV) and another singlet Γ_1 (0.32 meV). The interacting Ho 4f-states are then described by

$$H_M = \sum_i [H_{\text{CEF}}(\mathbf{J}_i) - \mu_B g \mathbf{J}_i \mathbf{B}] - \frac{1}{2} \sum_{ij} J(ij) \mathbf{J}_i \mathbf{J}_j, \quad (108)$$

where the first part describes the CEF potential and Zeeman energy ($g = 5/4$ for Ho^{3+}) and the second term the effective RKKY exchange interaction which is to be fitted empirically to reproduce the critical fields and temperatures of the metamagnetic phase diagram. In mean field (mf) approximation the dimensionless magnetization \mathbf{m}_i has to fulfil the self-consistency relations

$$\mathbf{m}_i(\mathbf{B}_i^e, T) = \text{Tr}(e^{\beta H_{mf}}(\mathbf{J}_i, \mathbf{B}_i^e) \mathbf{J}_i); \quad \mathbf{B}_i^e(\{\mathbf{m}_l\}, T) = g \mu_B + \sum_j J(i, j) \mathbf{m}_j, \quad (109)$$

here i runs over all moments \mathbf{m}_i in the magnetic unit cell in a given magnetic structure and \mathbf{B}_i^e is the effective field experienced by the moment. Because the ab -planes are FM ordered (neglecting the \mathbf{Q}_a -modulation) these mf-equations may be solved within a simplified quasi one-dimensional model where only structures are considered that correspond to a different stacking of FM planes along c . Structures with unit cell sizes of up to 29 layers have been considered. Of all structures that are solutions of eq. (109) the stable one at a given field and temperature has to minimize the Helmholtz free energy per volume

$$f_H = f_G(\mathbf{B}) + \frac{B^2}{8\pi} - \frac{\mathbf{H} \cdot \mathbf{B}}{4\pi} = f_G(\mathbf{B}) + 2\pi M^2 - \frac{H^2}{8\pi}, \quad (110)$$

where $\mathbf{B} = \mathbf{H} + 4\pi \mathbf{M}$ is assumed to be homogeneous throughout the sample with the homogeneous magnetization per volume given by $\mathbf{M} = (g \mu_B / v_c) \bar{\mathbf{m}}_i$. The bar indicates the average over all moments and v_c is the chemical unit cell volume. The effective exchange parameters between 0th and i th FM layer, $J_i = \sum_{\{j_i\}} J(0, j)$ (j_i runs over all the sites of the i th layer) are considered to be empirical parameters that are determined from the critical fields of the metamagnetic steps, from T_{IC} and from the requirement that the 1D Fourier transform $J(q_z)$ of J_i has a maximum close to the IC modulation vector \mathbf{Q} . This empirically determined exchange function $J(q_z)$ is shown in the inset of fig. 57. In this way most of the metamagnetic phases observed in $\text{HoNi}_2\text{B}_2\text{C}$ and the field angle have been explained within the CEF-RKKY-exchange model eq. (108) as shown in fig. 56 (Amici and Thalmeier, 1998). The exchange parameters derived theoretically in this work have been confirmed experimentally by Cavadini et al. (2003). However some discrepancies remain, especially it was found later

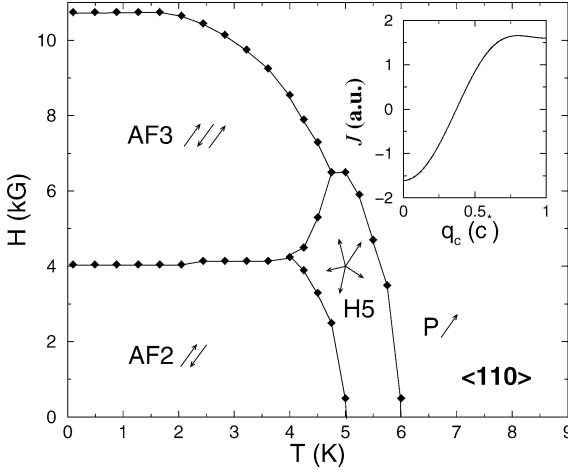


Fig. 57. Calculated magnetic H - T phase diagram of $\text{HoNi}_2\text{B}_2\text{C}$ for field along the easy direction $\langle 110 \rangle$. Arrows indicate FM ordered ab -planes (easy axis $[110]$) with stacking sequence along c . The inset shows the RKKY exchange function obtained from metamagnetic critical fields with a maximum around $0.8c^*$ that corresponds to the H5 helix with $T_{\text{IC}} = 6$ K. The lock-in transition to the simple AF2 phase appears at $T_N = 5$ K (Amici et al., 2000).

(Campbell et al., 2000; Detlefs et al., 2000) that in the high-field phase F3($\uparrow\uparrow\rightarrow$) the ab -planes are no longer FM ordered so that the simplified one-dimensional model is insufficient for high fields, but it is completely adequate for studying the coexistence behaviour with superconductivity since $H_{c2}(0) \simeq 0.8T$ for $\text{HoNi}_2\text{B}_2\text{C}$ is below the critical field where the ($\uparrow\uparrow\rightarrow$) phase appears.

The inter-layer exchange parameters J_i with $i = 0-3$, or exchange function $J(q_z)$ obtained in the analysis of metamagnetism can now be used to predict the B - T phase diagram for \mathbf{H} along the easy axis $[110]$ without invoking any further empirical parameters. The solution of eq. (109) for finite temperature leads to the phase diagram shown in fig. 57. The first phase that appears at T_{IC} is determined by the maximum gain in exchange energy, it is a long wavelength commensurate helix phase H5 (FM moment of ab -plane rotating around the c -axis) with wave vector $\mathbf{Q}_{\text{H5}} = 0.802\mathbf{c}^*$ which is not too far from the true IC wave vector $\mathbf{Q} = 0.9\mathbf{c}^*$ observed in neutron diffraction. To approximate the true IC phase even better with high order C phases, one had to include still more interlayer interactions, the free energies of these phases are, however, extremely close. When temperature decreases below T_{IC} the moments $\mathbf{m}_i(T)$ increase and the CEF contribution to the free energy which grows with fourth power of the moment size becomes more important. Because it favours alignment with the easy axis directions $[110]$, etc. the helix phase becomes less favorable and finally at $T_N = 5$ K a lock-in transition to the simple commensurate AF phase takes place. There are indications from magnetic X-ray diffraction that an intermediate lock-in to another C -phase above T_N may exist because a splitting of the IC satellite Bragg peak was observed. Such behaviour is well known from 1D ANNNI models that exhibit devil's staircase behaviour (Bak and von Boehm, 1980). At temperatures below 4 K application of a magnetic field along the easy axis finally leads to a metamagnetic transition from the AF2 phase ($\uparrow\downarrow$) to the ferrimagnetic AF3 phase with unit cell ($\uparrow\downarrow\uparrow$) (fig. 57).

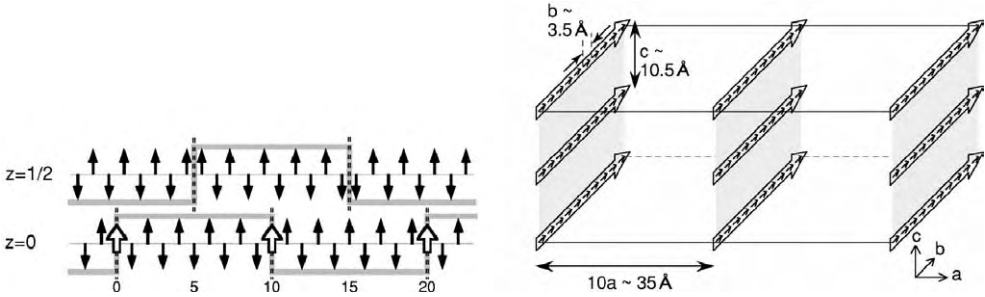


Fig. 58. Left panel: WFM structure of $\text{ErNi}_2\text{B}_2\text{C}$ showing the AF moment ordering (easy axis $[1010]$) along a -direction for two layers ($z = 0, 1/2$) along c . Moments residing in $z = 0$ antiphase boundaries order ferromagnetically (open arrows) below T_{WFM} . Right panel: Overall WFM structure is composed of FM sheets in bc -plane stacked along a (shaded in grey and corresponding to open arrows in left panel) (Kawano-Furukawa et al., 2002).

5.3.2. Weak ferromagnetism in $\text{ErNi}_2\text{B}_2\text{C}$

This compound becomes superconducting at $T_c = 11$ K and develops a transversely polarised SDW of Er moments below $T_{\text{IC}} = 6$ K with a propagation vector $\mathbf{Q} = (0.533, 0, 0)$ corresponding to the FS nesting vector and a moment $\mu = 7.8\mu_B$ and an easy axis $[100]$. Magnetization measurements (Canfield and Bud'ko, 1996) have shown that below $T_{\text{WFM}} = 2.3$ K a remnant magnetization exists due to the transition to a weak ferromagnetic (WFM) state with an average moment of $\mu_{\text{WFM}} = 0.33\mu_B/\text{Er}$ which persist to lowest temperatures. Therefore $\text{ErNi}_2\text{B}_2\text{C}$ is the first example of true microscopic SC/FM coexistence for all temperatures below T_c . The origin of the WFM phase has been investigated with neutron diffraction and its structure was determined (Kawano et al., 1999; Kawano-Furukawa et al., 2002). On lowering the temperature from T_N the SDW exhibits a 'squaring up' witnessed by magnetic satellite peaks and finally breaks up into commensurate AF sections separated by antiphase boundaries as shown in fig. 58. In every second layer along c the boundaries are located between the Er-bonds creating first disordered moments which finally below T_{WFM} order ferromagnetically. Because only the $z = 0$ and equivalent layers of the $\text{ErNi}_2\text{B}_2\text{C}$ bcc structure carry the FM moment one obtains an *average* FM bulk moment of $\mu_{\text{WFM}} = (2/40)M_{\text{sat}} = 0.39\mu_B$ which is close to the moment from magnetization measurements. The overall WFM structure (fig. 58) of $\text{ErNi}_2\text{B}_2\text{C}$ can be viewed as FM sheets in the bc -plane with easy axis b and stacked along a . The large stacking distance along a is the origin of the bulk WFM moment of $0.33\mu_B/\text{Er}$. As in the case of $\text{HoNi}_2\text{B}_2\text{C}$ metamagnetic transitions appear for applied field in the ab -plane. They have been explained by a similar model (Jensen, 2002) including dipolar interactions. The stable zero field structure has the observed modulation vector with $|\mathbf{Q}| = 11/20$.

5.4. Coexistence of superconductivity and magnetic order

Coexistence behaviour has been studied both for stoichiometric compounds Er, Tm, Dy and Ho borocarbides as well as for pseudo-quarternary compounds $\text{R}_{1-x}\text{R}'_x\text{Ni}_2\text{B}_2\text{C}$ where R, R' are different lanthanide atoms or compounds $\text{R}(\text{Ni}_{1-x}\text{M}_x)_2\text{B}_2\text{C}$ with M denoting another transition metal atom. In the stoichiometric compounds the interaction of both order parameters

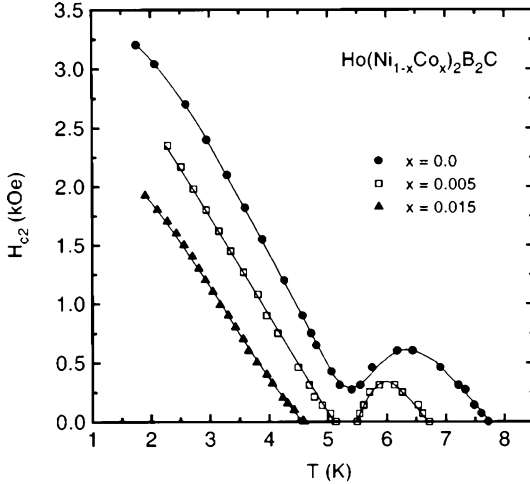


Fig. 59. Upper critical field curves for $\text{HoNi}_2\text{B}_2\text{C}$ ($x = 0$) and Co-substituted compounds. For $x = 0$ one observes near reentrance around $T_N \simeq 5.3$ K. For $x = 0.005$ the reduced T_c leads to real reentrance and for $x = 0.015$ finally T_c falls below T_N and ordinary H_{c2} behaviour sets in Schmidt and Braun (1997).

is most dramatically seen in the upper critical field H_{c2} -anomalies, especially for $\text{HoNi}_2\text{B}_2\text{C}$ with an almost reentrant behaviour visible in fig. 59. Reentrance can finally be achieved by replacing Ni with Co around $x = 0.005$. According to sect. 5.2 this reduces the DOS at the Fermi level. As seen in fig. 59, this results in a lower T_c and destabilizes the superconducting order parameter against magnetic order, finally for $x > 0.0075$ Co reentrance disappears and superconductivity exists only below the lock-in transition at T_N which remains almost unchanged. The main effect of M substitution for Ni is therefore a T_c tuning by variation of the DOS. Lanthanide substitution like $\text{R}' = \text{Ho}$ or Dy instead of $\text{R} = \text{Lu}$ or Y has a more subtle effect. For relatively small concentrations x of the magnetic R ions T_c is reduced as expected from the Abrikosov Gor'kov pair breaking theory by paramagnetic impurities in a nonmagnetic host superconductor, in this case $\text{LuNi}_2\text{B}_2\text{C}$. The pair breaking, like T_m in the magnetic borocarbides, is then controlled by the de Gennes factor dG . This leads to a reduction of T_c linear in $x \cdot dG$. For large concentrations ($x > 0.5$) of magnetic ions however this concept breaks down dramatically. In fact for $x = 1$ $\text{DyNi}_2\text{B}_2\text{C}$ is superconducting and one observes a kind of 'inverse' de Gennes scaling of the transition temperature with $(1 - x)dG$ corresponding to the concentration $(1 - x)$ of *nonmagnetic* Lu impurities in the *antiferromagnetic* host superconductor $\text{DyNi}_2\text{B}_2\text{C}$ which also act like pair breakers.

5.4.1. Coexistence of helical SDW, antiferromagnetism and superconductivity in $\text{HoNi}_2\text{B}_2\text{C}$

In this subsection we discuss a microscopic model (Amici, 1999; Amici et al., 2000) which successfully describes the most interesting coexistence behaviour found in $\text{HoNi}_2\text{B}_2\text{C}$. A more phenomenological approach based on GL theory has also been presented for $\text{Ho}_{1-x}\text{Dy}_x\text{Ni}_2\text{B}_2\text{C}$ in Doh et al. (1999). Firstly these compounds should more appropriately be called superconducting magnets because the magnetic and superconducting energy scales given by $E_m = kT_m$ and $E_{SC} = k^2T_c^2/E_F$ differ strongly. If $T_m \simeq T_c$ as in the present case then $E_{SC}/E_m = kT_c/E_F \simeq 10^{-2}$. This is due to the fact that only a fraction kT_c/E_F of con-

duction electrons participates in the pair formation whereas the exchange energy of all localised spins is involved in the magnetic ordering. Thus *local moment* magnetic order energetically completely dominates superconductivity whose influence on the former will therefore be neglected (Amici and Thalmeier, 2001). In fact in our previous discussion this was implicitly assumed by neglecting the effect of superconductivity on the RKKY interaction via the conduction electron susceptibility. This is justified because the latter would only be affected for $|\mathbf{q}| \leq \xi_0^{-1}$ ($\xi_0 = \text{SC coherence length}$), and we discuss the competition with AF order or IC phases with modulation vectors close to \mathbf{Q}_{AF} .

The really important microscopic coupling is then caused by the appearance of the ordered 4f local moments. According to their magnetic structure they exert an additional periodic potential on the conduction electrons. For the AF or helix structure the local 4f moments are described by

$$\langle S_{\mathbf{R}_i} \rangle = S(T) (\hat{\mathbf{a}} \cos(\mathbf{Q} \cdot \mathbf{R}_i) + \hat{\mathbf{b}} \sin(\mathbf{Q} \cdot \mathbf{R}_i)), \quad (111)$$

where $S(T)$ is the size of the ordered moments and \mathbf{Q} the helix wave vector with $\mathbf{Q} = \mathbf{Q}_{\text{AF}}$ in the AF case. The exchange interaction between the conduction and 4f-electrons then leads to an additional spin dependent periodic potential

$$H_{cf} = \frac{1}{2} IS \sum_{\mathbf{k}} (c_{\mathbf{k}+\mathbf{Q}\downarrow}^\dagger c_{\mathbf{k}\uparrow} + c_{\mathbf{k}-\mathbf{Q}\uparrow}^\dagger c_{\mathbf{k}\downarrow}). \quad (112)$$

The exchange constant I may be estimated from the RKKY expression $I^2 N(E_F) dG \simeq kT_m$ by using $N(E_F) = 4.8 \text{ eV}^{-1}$ resulting in $I \simeq 5 \text{ meV}$. The periodic exchange potential of eq. (112) has important effects on the conduction electron states, the original band energies $\epsilon_{\mathbf{k}}$ and Bloch states $c_{\mathbf{k}}$ are strongly modified close to the magnetic Bragg planes at $\pm\mathbf{Q}$ and at $\mathbf{c}^* \pm \mathbf{Q}$. The modified magnetic bands and Bloch states are obtained by a unitary transformation (Herring, 1966) which mixes states (\mathbf{k}, \uparrow) and $(\mathbf{k} + \mathbf{Q}, \downarrow)$ where each pair is decoupled from the others. This leads to magnetic Bloch states given by

$$c_{\mathbf{k}+}^\dagger = u_{\mathbf{k}} c_{\mathbf{k}\uparrow}^\dagger + v_{\mathbf{k}} c_{\mathbf{k}+\mathbf{Q}\downarrow}^\dagger; \quad c_{\mathbf{k}-}^\dagger = v_{-\mathbf{k}} c_{\mathbf{k}-\mathbf{Q}\uparrow}^\dagger + u_{-\mathbf{k}} c_{\mathbf{k}\downarrow}^\dagger \quad (113)$$

with the dispersion of the magnetic band given by

$$\tilde{\epsilon}_{\mathbf{k}\pm} = \frac{1}{2}(\epsilon_{\mathbf{k}} + \epsilon_{\mathbf{k}\pm\mathbf{Q}}) + \frac{1}{2}(\epsilon_{\mathbf{k}} - \epsilon_{\mathbf{k}\pm\mathbf{Q}}) \left(1 + \frac{I^2 S^2}{(\epsilon_{\mathbf{k}} - \epsilon_{\mathbf{k}\pm\mathbf{Q}})^2} \right)^{1/2}. \quad (114)$$

The $(u_{\mathbf{k}}, v_{\mathbf{k}})$ satisfy appropriate orthonormality conditions and fulfil the relation

$$u_{\mathbf{k}}^2 - v_{\mathbf{k}}^2 = \left(\frac{(\epsilon_{\mathbf{k}} - \epsilon_{\mathbf{k}+\mathbf{Q}})^2}{(\epsilon_{\mathbf{k}} - \epsilon_{\mathbf{k}+\mathbf{Q}})^2 + 4I^2 S^2} \right)^{1/2}. \quad (115)$$

Far away from magnetic Bragg planes $|\epsilon_{\mathbf{k}} - \epsilon_{\mathbf{k}+\mathbf{Q}}| \gg IS$ this leads to $u_{\mathbf{k}} \sim 1$ and $v_{\mathbf{k}} \sim 0$ and $\tilde{\epsilon}_{\mathbf{k}\pm} \sim \epsilon_{\mathbf{k}\pm}$ so that the original band states and energies are recovered with (\mathbf{k}, \pm) reducing to $(\mathbf{k}, \uparrow\downarrow)$ Bloch states. An illustration of the reconstructed FS is shown in fig. 60. Although the effect of the exchange potential eq. (112) is confined to a small region of \mathbf{k} -vectors with $\delta k_{\perp} \leq IS/v_F$ counted from the magnetic Bragg planes, this modification proves important for

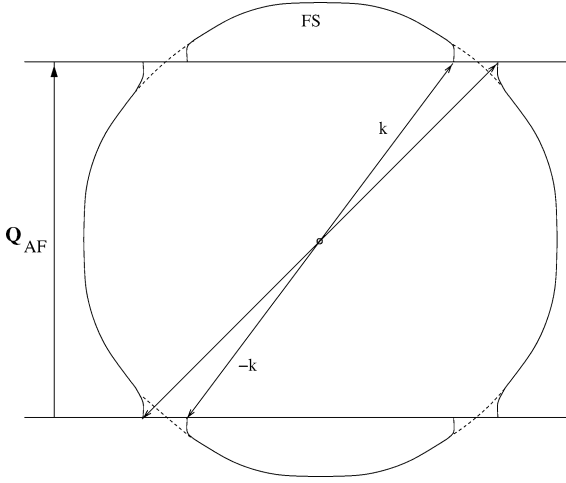


Fig. 60. Schematic view of Fermi surface (FS) reconstruction around magnetic Bragg planes connected by \mathbf{Q} according to eq. (114). This leads to strong modification of SC pair potential for conduction electron states with momenta \mathbf{k} , $-\mathbf{k}$ as indicated.

superconducting properties. From the previous consideration on superconducting and magnetic energy scales it is clear that the Cooper pairs have to be constructed from the *magnetic* Bloch states. This implies that the BCS pair Hamiltonian which is expressed in terms of nonmagnetic band states has to be transformed to the new magnetic basis states. For the AF structure this has been done in Zwicky and Fulde (1981) and for the more general helix phase in Morosov (1996, 1996a). Therefore, in addition to the modification eq. (114) of band energies, the nonmagnetic BCS pair potential $V_{\mathbf{k},\mathbf{k}'}$ will be replaced by an effective pair potential between magnetic Bloch states:

$$\tilde{V}_{\mathbf{k},\mathbf{k}'} = (u_{\mathbf{k}}^2 - v_{\mathbf{k}}^2)V_{\mathbf{k},\mathbf{k}'}(u_{\mathbf{k}'}^2 - v_{\mathbf{k}'}^2). \quad (116)$$

According to eq. (115) $\tilde{V}_{\mathbf{k},\mathbf{k}'}$ vanishes if \mathbf{k} or \mathbf{k}' are located on a Bragg plane. Naturally the BCS gap equations then lead to a modified gap function. To keep the discussion of magnetic effects simple we neglect the g-wave part in eq. (102) and assume an originally isotropic s-wave gap Δ . This should not influence the qualitative coexistence behaviour. Then the above equation leads to an additional \mathbf{k} -dependence originating in the exchange potential eq. (112) which is confined to the immediate vicinity of the Bragg planes. It is given by

$$\begin{aligned} \Delta(\mathbf{k}, T) &= (u_{\mathbf{k}}^2 - v_{\mathbf{k}}^2)\Delta(T), \\ \Delta(T) &= \int_0^{\omega_D} d\epsilon \left(V \int_{\text{MFS}} \frac{dS'}{(2\pi)^3} \frac{(u_{\mathbf{k}'}^2 - v_{\mathbf{k}'}^2)^2}{|\nabla_{\mathbf{k}'} \tilde{\epsilon}_{\mathbf{k}'}|} \right) \frac{\Delta(T)F(T)}{\sqrt{\epsilon^2 + \Delta^2(T)}}, \end{aligned} \quad (117)$$

where $F_{\mathbf{k}}(T) = [1 - 2f_{\mathbf{k}}(T)]$ and the inner integration is taken over the reconstructed magnetic Fermi surface (MFS) corresponding to $\tilde{\epsilon}_{\mathbf{k}}$. Obviously the modified gap function $\Delta(\mathbf{k}, T)$ vanishes on node lines $\perp c$ lying on the Bragg planes and accordingly the self-consistent gap equation for $\Delta(T)$ will lead to a reduced magnitude of the gap due to the factor in the numerator of the integral in brackets. However, note that no sign change in the modified gap function

$\Delta(\mathbf{k}, T)$ occurs when \mathbf{k} crosses a node line, it still belongs to a fully symmetric A_{1g} representation of the underlying AF magnetic structure. Since $(u_{\mathbf{k}}^2 - v_{\mathbf{k}}^2) \simeq 1$ almost everywhere except in the immediate vicinity of Bragg planes ($\delta k_{\perp}/k_F \leq ISN(E_F)$) the reduction of the gap amplitude is not large and helix order may coexist with superconductivity. For the special AF case this is known already from Baltensperger and Strässler (1963) and the helix case with general modulation vector \mathbf{Q} is not very different because it only has two more Bragg planes than the AF case. The second equation has the formal appearance of the BCS gap equation, however, the expression in parentheses has to be interpreted as an effective electron-phonon interaction $V_e(T)$ or dimensionless $\lambda_e(T) = N(E_F)V_e(T)$ which itself depends on the temperature via $S(T)$. Its reduction from the nonmagnetic background value $\lambda = N(E_F)V$ is due to the reconstruction of electronic states confined close to the Bragg planes. Therefore it may be treated as a perturbation linear in the small parameter $IS(T)/E_F$. One obtains

$$\delta\lambda(T) = \lambda - \lambda_e(T) = -\frac{V}{8\pi\hbar^2} \frac{k_r}{v_r v_z} IS(T) \quad (118)$$

for a FS piece without nesting features which is cut by a pair of Bragg planes with a FS radius k_r at the intersection and radial and parallel velocities v_r and v_z , respectively. For a helical structure with two pairs of Bragg planes at $\pm\frac{1}{2}\mathbf{Q}$ and $\pm\frac{1}{2}(\mathbf{c}^* - \mathbf{Q})$ one has to add two corrections as in eq. (118) with different FS parameters. The main effect of the interaction of magnetic order and superconductivity described by eq. (112) has now been condensed into eq. (118). The physical consequences of the reduction of λ due to magnetic order are a reduced superconducting T_c and condensation energy which results in an anomaly in $H_{c2}(T)$ that is directly correlated with the appearance of the local moment order parameter $S(T)$. The upper critical field anomaly may approximately be calculated by using an appropriately modified BCS expression and including the magnetization response of the local moments:

$$\begin{aligned} H_{c2}^{[110]}(T) &= B_{c2}[\lambda_e(T), T] - M^{[110]}(T), \\ H_{c2}^{[001]}(T) &= B_{c2}[\lambda_e(T), T], \end{aligned} \quad (119)$$

where $B_{c2}(\lambda_e(T), T) = B_{c2}^0(\lambda_e(T)) \cdot [1 - (T/T_c(\lambda_e(T)))^2]$ is the BCS expression modified due to the T -dependence of the effective e-p coupling. The magnetization for the [001] direction can be neglected because the 4f moments of CEF states are well constrained within the easy ab -plane. Using eqs. (118), (119) with an appropriate set of parameters for $\text{HoNi}_2\text{B}_2\text{C}$ the calculated upper critical field is shown in fig. 61. It clearly shows a pronounced depression of $H_{c2}(T)$ when magnetic order sets in. As discussed before there is no big difference in the effect of helical order (below T_{IC}) and commensurate AF order (below T_N), the overall depression is simply controlled by the increase of $S(T)$ when T decreases. At this point we mention again that in our discussion of coexistence behaviour the a^* -incommensurate magnetic modulation has been neglected. This is fully justified according to hydrostatic pressure experiments by Dertinger (2001) where it has been shown that: (i) while the a^* satellite intensity in ND decreases with pressure and vanishes at $p > 0.7$ GPa, (ii) the reentrance minimum in H_{c2} becomes even more pronounced. This proves that the a^* -modulation of moments plays no important role in the reentrance behaviour of SC, contrary to what has been claimed by many

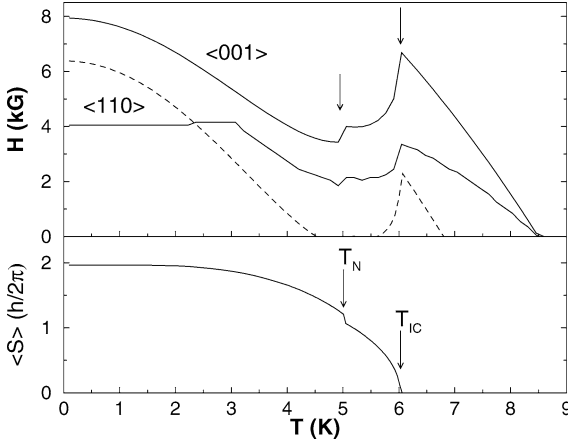


Fig. 61. Lower panel: Size of the magnetic order parameter (local moment amplitude) (S) vs. temperature for the helix (H5) phase below T_{IC} and the AF2 phase below T_N . Upper panel: H_{c2} for two symmetry directions. For $\langle 110 \rangle$ the plateau is caused by the transition to the ferrimagnetic AF3 phase in fig. 56. The dashed line is H_{c2} along $\langle 001 \rangle$ with a reduced background T_c that simulates the effect of doping on the reentrance behaviour (Amici et al., 2000).

previous investigations. The $[110]$, $[001]$ anisotropy of H_{c2} is due to the different magnetization response in both directions. For field lying in the easy plane $H_{c2}(T)$ exhibits a plateau which is due to the appearance of the ferrimagnetic AF3 phase above the first critical field in fig. 57. This phase has a net magnetic moment that cannot coexist with superconductivity. If the nonmagnetic background e-p coupling λ is reduced by about 10% the resulting reduction in T_c and condensation energy leads to a reentrance behaviour of $H_{c2}(T)$ as shown by the dashed curve. These features described by the theory of Amici et al. (2000), namely depression, anisotropy (plateau) and reentrance behaviour have all been observed experimentally in $\text{HoNi}_2\text{B}_2\text{C}$, the latter under Co-substitution of Ni which reduces T_c as shown in fig. 59.

5.4.2. Coexistence of superconductivity and weak ferromagnetism in $\text{ErNi}_2\text{B}_2\text{C}$

At the SDW transition of $\text{ErNi}_2\text{B}_2\text{C}$ ($T_{IC} = 6$ K) a similar but much less pronounced dip in H_{c2} as in $\text{HoNi}_2\text{B}_2\text{C}$ is observed indicating the coexistence of both types of order. Even more exciting is the observation of WFM order below $T_{\text{WFM}} = 2.3$ K which coexists with SC ($T_c = 11$ K) to the lowest temperatures. This first confirmed example of microscopic FM/SC coexistence has therefore attracted a lot of attention. Established theories (Ginzburg, 1957) predict that thermodynamic coexistence in type II superconductors is only possible when the internal FM field $H_{\text{int}} \sim 4\pi M$ is smaller than H_{c2} (Fischer, 1990). In $\text{ErNi}_2\text{B}_2\text{C}$ due to the large FM layer spacing (fig. 58) one estimates from μ a small $H_{\text{int}} \sim 0.5$ kG which is of the same order as H_{c1} and much smaller than $H_{c2} \sim 15$ kG (Canfield and Bud'ko, 1996). Despite its smallness H_{int} does have a very peculiar effect: For applied fields H with orientation θ_a close to the c -axis the perpendicular internal field along the a direction rotates the effective field of the vortex phase to an angle θ_v towards the a -axis. Thus the vortex lattice will show a misalignment with the applied field by a small angle $\theta_v - \theta_a$. This effect has been found experimentally by Yaron et al. (1996). Theoretically this effect was considered in the context of a Ginzburg–Landau theory including the terms corresponding WFM order parameter and the coupling to SC (Ng and Varma, 1997). Since the London penetration depth λ is 26 times larger than the FM layer spacing in fig. 58 (Kawano-Furukawa et al., 2001) it can still be

justified to use an averaged FM moment density of saturation value $0.34\mu_B$. The tilt angle $\theta_v - \theta_a$ of vortices becomes larger at lower temperature in agreement with theoretical predictions. If the internal field H_{int} is at least somewhat larger than H_{c1} another exotic transition to a spontaneous vortex phase in zero applied field may take place. In this phase the internal field spontaneously forms a vortex lattice oriented along the a direction. Low field magnetization measurements and small angle neutron scattering experiments (Kawano-Furukawa et al., 2001) seem to support such a possibility but the issue is not settled.

6. Rare earth skutterudite superconductors

The new heavy fermion superconductor $\text{PrOs}_4\text{Sb}_{12}$ which has been discovered recently (Bauer et al., 2002) is potentially of similar interest as UPt_3 because it represents the second example of multiphase superconductivity (Izawa et al., 2003) with a critical temperature $T_c = 1.85$ K. This material belongs to the large class of RT_4X_{12} skutterudite cage compounds (R = alkaline earth, rare earth or actinide; T = Fe, Ru or Os and X = P, As or Sb) which have a bcc-filled skutterudite structure with tetrahedral space group T_h^4 (fig. 62). In this structure large voids formed by tilted T_4X_{12} octahedrons can be filled with R atoms. They are however rather loosely bound and therefore may have large anharmonic oscillations ('rattling') in the cage. In addition if equivalent equilibrium positions are present tunneling split states may exist. Both effects may lead to interesting low temperature elastic and transport phenomena, i.e., thermoelectric effects (Sales et al., 1996; Sales, 2003). Depending on the cage-filling atom this large class of compounds displays also a great variety of interesting effects of strong electron correlation. Mixed valent and heavy fermion behaviour, magnetic and quadrupolar order, non-Fermi liquid and Kondo insulating behaviour has been found, see Bauer et al. (2002), Sales (2003) and references cited therein. Recently the SC in non-stoichiometric skutterudites $\text{Pr}(\text{Os}_{1-x}\text{Ru}_x)\text{Sb}_{12}$ has been investigated

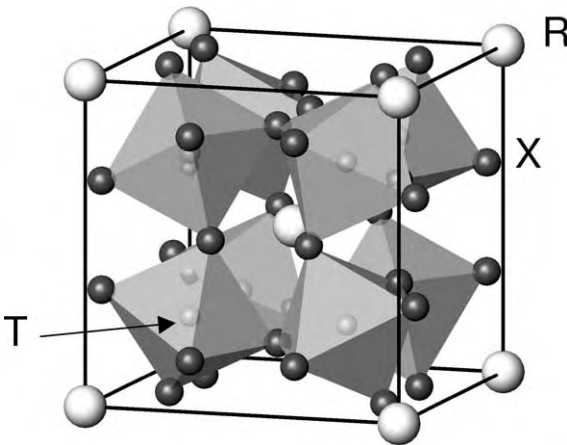


Fig. 62. Cubic crystal structure of filled skutterudite RT_4X_{12} . R atoms: large circles, X atoms: middle size circles, T atoms: small circles located in the center of TX_8 octahedra (grey). For $\text{PrOs}_4\text{Sb}_{12}$ the lattice constant is $a = 9.3017$ Å.

throughout the whole concentration range of $0 \leq x \leq 1$ (Frederick et al., 2003). While for $x = 0$ one has an unconventional HF superconductor the $x = 1$ compound $\text{PrRu}_4\text{Os}_{12}$ on the other hand is a conventional SC with $T_c \simeq 1$ K. The type of SC changes at $x \simeq 0.6$ where the transition temperature $T_c(x)$ has a minimum value of 0.75 K. Here we will focus, however, exclusively on the HF multiphase superconductivity in $\text{PrOs}_4\text{Sb}_{12}$ ($x = 0$).

6.1. Electronic structure and HF behaviour of $\text{PrOs}_4\text{Sb}_{12}$

The LDA + U band structure and Fermi surface of $\text{PrOs}_4\text{Sb}_{12}$ has been investigated by Sugawara et al. (2002) and compared with dHvA results. Three FS sheets, two of them closed and approximately spherical were identified both experimentally and in the calculation. Their dHvA masses are $m^* = 2.4\text{--}7.6m$, this is considerably higher than the calculated LDA + U band masses ranging from $m_b = 0.65\text{--}2.5m$. The observed dHvA masses however are still much too small compared to the thermal effective mass m^* estimated from the extrapolated γ -value of the linear specific heat. One obtains (Vollmer et al., 2003) $\gamma = 313$ mJ/mol K² leading to an estimate of $m^* = 50m$. This places $\text{PrOs}_4\text{Sb}_{12}$ among the heavy fermion metals, the first one ever observed for a Pr-compound with its $4f^2$ electronic configuration, the estimated quasiparticle bandwidth is $T^* \simeq 10$ K (Bauer et al., 2002) which is in the same range as the lowest CEF splittings. Therefore, the low temperature behaviour of $C(T)$, $\chi(T)$ and $\rho(T)$ is determined by both CEF effects and heavy quasiparticle formation and it is difficult to separate them (Maple et al., 2002). The latter is rather anomalous for a HF system since the A -coefficient in $\rho(T) = \rho_0 + AT^2$ is smaller by two orders of magnitude compared to other HF systems. The susceptibility is largely dominated by localised $4f^2$ CEF states and from the high temperature behaviour an effective Pr^{3+} moment $\mu = 2.97\mu_B$ is obtained.

6.2. Pr CEF states and antiferroquadrupolar order

The CEF level scheme of Pr^{3+} is determined by a CEF potential with tetrahedral T_h symmetry. For a long time it was thought that it is equivalent to that of other cubic point groups like T_d or O_h . However, it was shown recently (Takegahara et al., 2001) that this is incorrect. Due to the absence of two types of symmetry operations the CEF potential is rather given by

$$H_{\text{CEF}} = W \left[x \left(\frac{O_4}{F(4)} \right) + (1 - |x|) \left(\frac{O_6^c}{F(6)} \right) + y \left(\frac{O_6^t}{F^t(6)} \right) \right], \quad (120)$$

where $O_4 = O_4^0 + 5O_4^4$, $O_6^c = O_6^0 - 21O_6^4$ and $O_6^t = O_6^2 - O_6^6$ are Steven's operators and for Pr^{3+} $F(4) = 60$, $F(6) = 1260$ and $F^t(6) = 30$. For the cubic groups O_h and T_d we have $y = 0$ and there is only one CEF parameter x , aside from the overall scale W , then H_{CEF} reduces to the well known form. However in tetrahedral symmetry T_h in general a second CEF parameter $y \neq 0$ appears. The consequences were analysed in detail in Takegahara et al. (2001), specifically the Γ_1 , Γ_2 states of the cubic CEF case will be mixed into two inequivalent Γ_1 singlets of T_h and likewise Γ_4 , Γ_5 of O_h will be mixed to become two inequivalent Γ_4 triplets of T_h where the degree of mixing depends on y . The experimental determination of the Pr^{3+} CEF level scheme has been performed under

the restriction $y = 0$ (i.e., assuming the cubic CEF potential), therefore, we keep the original notation of states. With this restriction the level scheme has been determined by fitting $\chi(T)$ and also directly by inelastic neutron scattering (Maple et al., 2002). The latter leads to a level scheme $\Gamma_3(0 \text{ K})$, $\Gamma_5(8.2 \text{ K})$, $\Gamma_4(133.5 \text{ K})$, $\Gamma_1(320 \text{ K})$, which is close to the one obtained from $\chi(T)$. The ground state is a nonmagnetic (non-Kramers) doublet with a quadrupole moment and quadrupole matrix elements connecting to the first excited triplet state. An alternative CEF level scheme has been proposed (Aoki et al., 2002; Tayama et al., 2003) from specific heat and magnetization experiments. It has a singlet ground state without magnetic nor quadrupole moment, namely $\Gamma_1(0 \text{ K})$, $\Gamma_5(6 \text{ K})$, $\Gamma_4(65 \text{ K})$ and $\Gamma_3(111 \text{ K})$. The splitting energy δ ($\simeq 6\text{--}8.2 \text{ K}$) of ground state to first excited state is also seen as a pronounced zero field Schottky anomaly sitting on top of the superconducting transition. Application of a field above the SC $H_{c2}(0) = 2.2 \text{ T}$ suppresses the Schottky anomaly.

However, at larger fields of $H \simeq 4 \text{ T}$ a new and sharper one appears at lower temperatures possibly signifying the stabilization of a long range antiferroquadrupolar ordered phase (Aoki et al., 2001, 2002; Vollmer et al., 2003; Maple et al., 2003). This is summarized in the phase diagram shown in the left part of fig. 63. A detailed analysis of AFQ long range order in the high field region has been given by Shiina (2004). It is helpful to compare with other known AFQ ordered 4f systems, where $\text{Ce}_{1-x}\text{La}_x\text{B}_6$ is certainly the most well studied one (Shiina

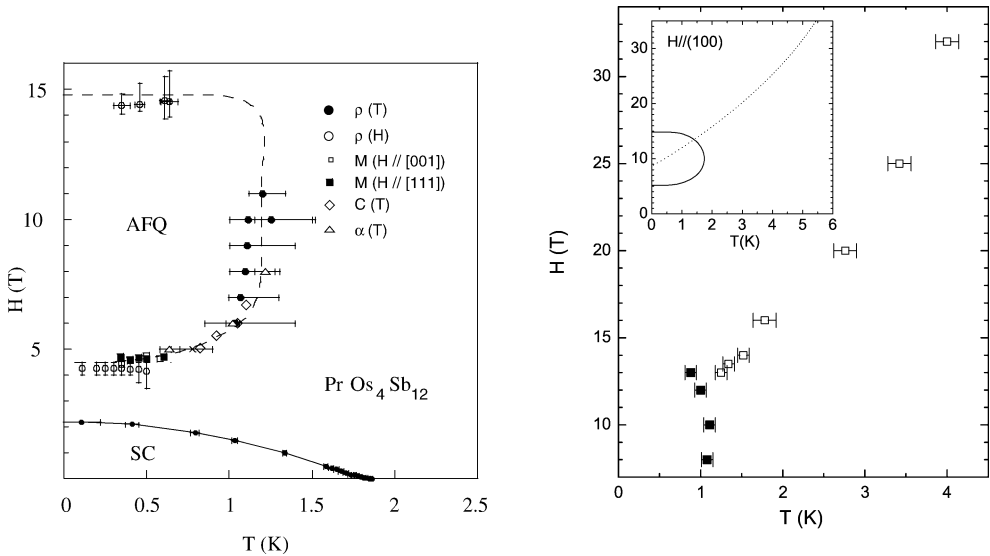


Fig. 63. Left panel: Complete B - T phase diagram (Maple et al., 2002) with SC regime and region of field induced order parameter which is presumably of antiferroquadrupolar (AFQ) type. Data are obtained from resistivity (ρ), magnetization (M), specific heat (C) and thermal expansion (α) measurements. Right panel: High magnetic field phase diagram (Aoki et al., 2003) with upper part of AFQ phase (full squares) and line of high field Schottky anomaly from the Γ_1 - Γ_5 crossing. The inset shows calculation for tetrahedral CEF model.

et al., 1997). It has a Γ_8 quartet as CEF ground state which carries both quadrupole and magnetic moment. Both spontaneous AFQ and AF order are therefore observed with $T_Q > T_N$ and we consider only the former. For $x = 0.5$ the AFQ phase diagram (Nakamura et al., 1997) is quite similar to that of fig. 63, namely the AFQ phase is only induced in finite field and $T_Q(H)$ increases with field. In the $\text{Ce}_{1-x}\text{La}_x\text{B}_6$ system the AFQ order has been identified by observing the induced secondary AF order which is induced by a homogeneous field H in the ordered AFQ background. This can be done by neutron diffraction and NMR experiments. Recent neutron diffraction results (Kohgi et al., 2003) suggest that the CEF ground state is singlet Γ_1 and the AFQ order parameter is of $O_{yz} = J_y J_z + J_z J_y$ type. Additional high field measurements on $C(T, H)$ for different field directions (Rotundu et al., 2003) also give strong evidence for the Γ_1 ground state scenario and for a Γ_1 - Γ_5 level crossing as origin of the field induced AFQ phase (fig. 63, right panel).

The existence of a nonmagnetic (Γ_1 or Γ_3) ground state in $\text{PrOs}_4\text{Sb}_{12}$ leads one to speculate about the origin of the observed HF behaviour since the usual Kondo lattice mechanism as in Ce-intermetallic compounds which demands a Kramers degenerate magnetic ground state cannot be at work here. In the case that Γ_3 were realised one might conjecture that instead of the exchange scattering one has aspherical Coulomb scattering from the quadrupolar degrees of freedom of the nonmagnetic Γ_3 ground state. As discussed for the isoelectronic U^{4+} -configuration in UBe_{13} in sect. 4.5 this is described by a multichannel Kondo Hamiltonian for the quadrupolar pseudo-spin. It can lead to a partial screening of the Γ_3 -quadrupole below a quadrupolar Kondo temperature T^* . At even lower temperatures logarithmic non-Fermi liquid anomalies in thermodynamic quantities should develop due to the partial screening. This cannot be confirmed due to the intervening SC transition. Therefore this quadrupolar HF mechanism for $\text{PrOs}_4\text{Sb}_{12}$ is only a conjecture. If a singlet Γ_1 ground state is realised as suggested by neutron diffraction and high field $C(T, H)$ results mentioned before one has to invoke another mechanism for heavy mass generation which is similar to the one implied in U-compounds like UPd_2Al_3 (Zwicknagl et al., 2003). It is due to mass renormalisation by the low lying Γ_1 - Γ_5 excitation, i.e., contrary to the previous scenario it is caused by off-diagonal parts of the conduction electron-CEF level interaction.

6.3. The superconducting split transition

The SC specific heat jump is superposed on the Schottky anomaly from the lowest CEF excitation at δ . Nevertheless its detailed analysis provides clear evidence for a split SC transition (Bauer et al., 2002; Vollmer et al., 2003) at $T_{c1} = 1.85$ K and $T_{c2} = 1.75$ K as shown in fig. 64. The total jump of both transitions amounts to $\Delta_{\text{SC}}C/\gamma T_c \simeq 3$ which exceeds the BCS value 1.43 for a single transition considerably. It also proves that the SC state is formed from the heavy quasiparticles that cause the enhanced γ -value. A T_c -splitting of similar size also was clearly seen in thermal expansion measurements (Oeschler et al., 2003, 2004). The two superconducting transitions in fig. 64 are reminiscent of the split transition in UPt_3 (sect. 4.1, fig. 27). There a two-fold orbitally degenerate SC state is split by weak AF order that reduces the hexagonal symmetry to orthorhombic. This also leads to two critical field curves in the B - T phase diagram. In $\text{PrOs}_4\text{Sb}_{12}$ no such symmetry breaking field exists and the split

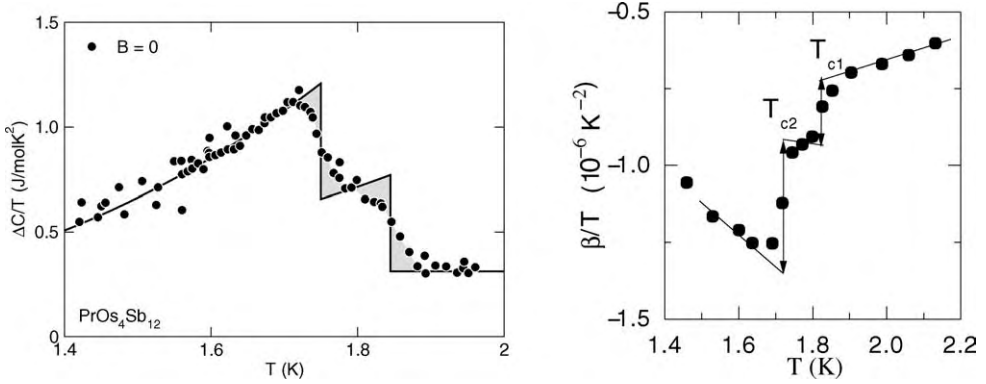


Fig. 64. Left panel: Electronic specific heat $\Delta C/T$ vs. temperature (Vollmer et al., 2003). Solid line is an entropy conserving construction leading to SC transitions at $T_{c1} = 1.85$ K and $T_{c2} = 1.75$ K. Total specific heat jump $\Delta C_{SC}/\gamma T_c \simeq 3$. Right panel: Corresponding jumps in the volume thermal expansion at $T_{c1,2}$ (Oeschler et al., 2003, 2004).

transition has to belong to two different T_h representations of the SC order parameter or combinations thereof as discussed below. The critical field curves associated with $T_{c1,2}$ have been investigated with magnetization (Tayama et al., 2003) and specific heat measurements (Measson et al., 2004) from which practically parallel curves are obtained. Only the upper critical field corresponding to T_{c1} with $H_{c2}(0) \simeq 2.2T$ is shown in fig. 63.

As usual in the early stage of investigation different experiments gave inconclusive results on the question of the nature of gap anisotropy. The low temperature specific heat exhibits a $C_s(T) \sim T^n$ power law in a rather reduced range between 0.65 K and 1.2 K which points to some kind of nodal state. In Sb-NQR experiments (Kotegawa et al., 2003) the nuclear spin lattice relaxation $1/T_1$ rate was determined. It has an itinerant quasiparticle contribution that contains information on the SC nodal state below T_c and in addition a localised contribution from broadened CEF excitations which decreases exponentially for temperatures $T \ll \Delta$. There is no unique way to separate these contributions, this problem is similar to the two Knight shift contributions in the case of UPd₂Al₃ (sect. 4.2) with its isoelectronic 5f² localised states. The NQR measurements did not show any evidence for a coherence peak below T_c which points to an unconventional SC state, for lower temperatures an exponential decay of T_1^{-1} , in conflict with the existence of gap nodes was reported. However, this result depends critically on the subtraction procedure of the localised contribution.

6.4. Thermal conductivity in the vortex phase and multiphase superconductivity in $PrOs_4Sb_{12}$

The experiments on field-angle dependent thermal conductivity described in sect. 2 are a more powerful method to investigate the SC state. This method achieved the determination of critical field curves and the associated $B-T$ phase diagram in $PrOs_4Sb_{12}$ (Izawa et al., 2003) and at the same time the nodal structure of the gap function has at least been partly clarified. The same geometry as for borocarbides (sect. 5) with conical field rotation around the heat current

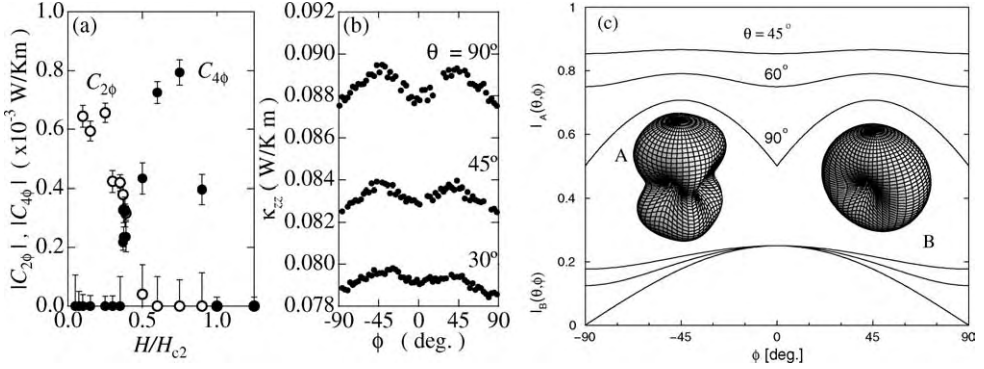


Fig. 65. (a) Field dependence of the four-fold ($C_{4\phi}$) and two-fold ($C_{2\phi}$) amplitudes of $\kappa_{zz}(\phi)$ oscillations in (b) as function of field strength at $T = 0.52$ K. Sharp transition at $H^* = 0.4H_{c2}$ from two-fold to four-fold oscillation is seen. (b) Four-fold oscillations from experiment for different polar field angle θ (Izawa et al., 2003). (c) Calculated angular variation of κ_{zz} as function of azimuthal field angle ϕ exhibiting four-fold (A) and two-fold (B) oscillations ($\theta =$ polar field angle). The inset shows polar plots of A- and B-phase gap functions with four- and two-point nodes, respectively (Maki et al., 2003c).

direction parallel to a cubic [001] axis was used and measurements in the whole temperature range from 0.3 K up to T_{c1} were performed. The azimuthal angle dependence of κ_{zz} was found to be approximately of the empirical form

$$\kappa_{zz}(\theta, \phi, H, T) = \kappa_0 + C_{2\phi}(\theta, H, T) \cos 2\phi + C_{4\phi}(\theta, H, T) \cos 4\phi \quad (121)$$

containing both two-fold and four-fold rotations in ϕ . The ϕ dependence for $H = 1.2T$ is shown in fig. 65 for a few polar angles θ . It exhibits clearly a dominating four-fold oscillation. Since the amplitude rapidly decreases with θ similar as in the borocarbides this may be interpreted as evidence for *point nodes* in $\Delta(\mathbf{k})$ along the [100] and [010] cubic axes. Surprisingly, when the field is lowered to $H^* = 0.8T \ll H_{c2}$ a rather sudden change from a four-fold to a two-fold oscillation in ϕ as shown in fig. 65 is observed which is interpreted as at transition to a different SC state with only two point nodes along [010]. The second critical field H^* can be followed to higher temperatures, although with rapidly decreasing oscillation amplitudes $C_{2\phi}$ and $C_{4\phi}$. Apparently the second critical field curve $H^*(T)$ ends at the lower critical temperature T_{c2} observed already in the second specific heat jump at zero field.

This allows one to construct a B - T phase diagram for $\text{PrOs}_4\text{Sb}_{12}$ shown in fig. 66. Most importantly one has two distinct regions with A- and B-phase superconductivity characterised by four and two point nodes along cubic axis [100] and [010]. In the applied geometry the field is swept around the [001] axis, and therefore possible nodes along this direction cannot be detected. Additional experiments with a sweep axis orthogonal to [001] would be necessary. Furthermore, three different domains (orientation of the node directions) of A- and B-phase are possible. Apparently for the sample investigated a specific domain has been selected, possibly by internal strain effects. From the B - T phase diagram in fig. 66 we conclude that $\text{PrOs}_4\text{Sb}_{12}$ is the second pure multiphase HF superconductor found after UPt_3 . There is, how-

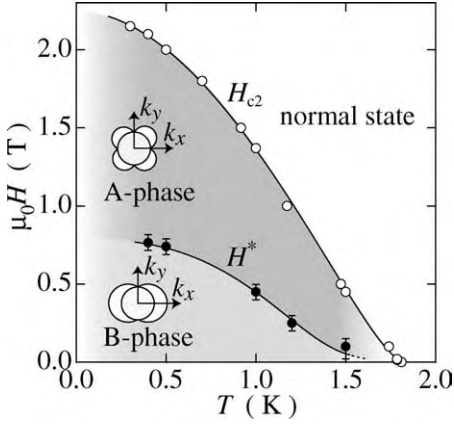


Fig. 66. B - T phase diagram of $\text{PrOs}_4\text{Sb}_{12}$ exhibiting B -phase with two-fold symmetry and A -phase with four-fold symmetry in a cubic plane. The A -phase and B -phase gap symmetries are indicated. They have four and two point nodes in a cubic plane, respectively (Izawa et al., 2003).

ever, no crossing of critical field lines and no corresponding tetracritical point in $\text{PrOs}_4\text{Sb}_{12}$ as was observed in fig. 29 for UPt_3 .

6.5. Gap models for SC A - and B -phases of $\text{PrOs}_4\text{Sb}_{12}$

The observation of a different nodal structure in the A - and B -phases raises the question of the symmetry of the gap function in $\text{PrOs}_4\text{Sb}_{12}$. Various proposals have been made in (Maki et al., 2003c; Goryo, 2003; Miyake et al., 2003; Ichioka et al., 2003) based on an empirical approach and compatible with the observed point nodes. The gap function may be expanded in terms of basis functions $\psi_i^\Gamma(\mathbf{k})$ which transform like representations Γ of the crystal symmetry group ($i = 1-d$ is the degeneracy index, the index l denoting the degree of Γ is suppressed). So far there is no information from NMR Knight shift or H_{c2} -Pauli limiting effects whether $\text{PrOs}_4\text{Sb}_{12}$ has spin singlet or triplet pairing. In the singlet case the gap function should then be given by

$$\Delta(\mathbf{k}) = \sum_{\Gamma, i} \eta_i^\Gamma \psi_i^\Gamma(\mathbf{k}) \equiv \Delta f(\mathbf{k}), \quad (122)$$

where the form factor $f(\mathbf{k})$ is normalized to one and Δ is the temperature dependent maximum gap value. In the spirit of the Landau theory only a *single* representation with the highest T_c should be realized and for $T \geq T_c$ the free energy may then be expanded in terms of possible invariants of the order parameter components (Volovik and Gorkov, 1985) η_i^Γ which are determined by Landau parameters $\alpha^\Gamma(T)$ and β_i^Γ . The node structure is then fixed by the specific symmetry class of $\Delta(\mathbf{k})$ defined by the set of η_i^Γ . However the pure second ($l = 2$) and fourth ($l = 4$) degree representations in tetragonal T_h symmetry which are given in table 7 cannot realize a gap function with the observed nodal structure, and therefore, one has to consider the possibility of hybrid order parameter models. A striking example of such a hybrid gap function ($s + g$ wave model) has already been discussed in the previous section for the nonmagnetic borocarbide superconductor $\text{Y}(\text{Lu})\text{Ni}_2\text{B}_2\text{C}$. The symmetry classification of

Table 7
Even parity basis functions for SC gap in tetrahedral (T_h) symmetry

d	Γ	$\psi_i^{\Gamma}(\mathbf{k})$	$\psi_i^{\prime\Gamma}(\mathbf{k})$
1	$A(\Gamma_1)$	1	$k_x^4 + k_y^4 + k_z^4$
2	$E(\Gamma_2, \Gamma_3)$	$(2k_z^2 - k_x^2 - k_y^2, k_x^2 - k_y^2)$	$(2k_z^4 - k_x^4 - k_y^4, k_x^4 - k_y^4)$
3	$T(\Gamma_5)$	$(k_y k_z, k_z k_x, k_x k_y)$	$(k_y k_z k_x^2, k_z k_x k_y^2, k_x k_y k_z^2)$

Symbols used: $\psi_i^{\Gamma}(\mathbf{k})$ and $\psi_i^{\prime\Gamma}(\mathbf{k})$ ($i = 1-d$) are second ($l = 2$) and fourth degree ($l = 4$) basis functions, respectively, d denotes the degeneracy and Γ_2 and Γ_3 are complex conjugate combinations of E_1 and E_2 components.

table 7 suggests the following simple proposal for a hybrid gap function $\Delta(\mathbf{k}) = \Delta f(\mathbf{k})$ for $\text{PrOs}_4\text{Sb}_{12}$ which has the observed nodes along the cubic axis, excluding the still hypothetical ones along [001]:

$$\begin{aligned} A\text{-phase} \quad \Delta(\mathbf{k}) &= \Delta(1 - k_x^4 - k_y^4), \\ B\text{-phase} \quad \Delta(\mathbf{k}) &= \Delta(1 - k_y^4). \end{aligned} \quad (123)$$

According to table 7 A - and B -phase are superpositions of A and E representations with planar and axial symmetry, respectively. They are three-fold degenerate and particular domains with nodes in the $k_x k_y$ -plane (A) or along k_y (B) have been chosen. This selection might be realised due to internal strains in the SC sample. Polar plots of A , B -phase gap functions are shown in the inset of fig. 65(c). The magnetothermal conductivity in the vortex state of phases A , B in the limit $\Gamma < T \ll \Delta$ can be calculated as described in sect. 2 and the result for κ_{zz} is, up to logarithmic corrections

$$\frac{\kappa_{zz}}{\kappa_n} \simeq \frac{2}{\pi} \frac{v\sqrt{eH}}{\Delta} I_{A,B}(\theta, \phi) \quad (124)$$

with the angular dependent functions $I_i(\theta, \phi)$ ($i = A, B$) given by

$$\begin{aligned} I_A(\theta, \phi) &= \frac{1}{2}[(1 - \sin^2 \theta \sin^2 \phi)^{1/2} + (1 - \sin^2 \theta \cos^2 \phi)^{1/2}], \\ I_B(\theta, \phi) &= \frac{1}{4}(1 - \sin^2 \theta \sin^2 \phi)^{1/2}. \end{aligned} \quad (125)$$

For in plane field ($\theta = \pi/2$) one has $I_A(\theta, \phi) = \frac{1}{2}(|\sin \phi| + |\cos \phi|)$ and $I_B(\theta, \phi) = \frac{1}{4}|\cos \phi|$, their leading Fourier components vary like $\cos 4\phi$ and $\cos 2\phi$, respectively, in accordance with the empirical expressions in eq. (121). However, the above equations really predicts cusps at $\phi = n(\pi/2)$ (fig. 65(c)) analogous to the situation in the borocarbides and not the smooth minima as seen in fig. 65(b). Therefore, the existence of cusps cannot be safely inferred from the experimental results in fig. 65, this would necessitate measurements at lower temperatures. Also experiments with variation of the polar angle θ have to be performed to check the possible existence of node points along [001]. Finally μSR experiments show indications of the presence of magnetic moments in the SC phase which is interpreted, similarly as in $\text{U}_{1-x}\text{Th}_x\text{Be}_{13}$ as evidence for a nonunitary triplet SC state (Aoki et al., 2003). This has also been claimed from a recent penetration depth study (Chia et al., 2003).

As a preliminary conclusion it seems clear that $\text{PrOs}_4\text{Sb}_{12}$ is a very unconventional multi-phase HF superconductor of potentially the same interest as UPt_3 . Recalling that heavy quasiparticles are presumably caused by coupling with virtual quadrupolar excitations from the nonmagnetic $5f$ ground state one is led to speculate that SC in $\text{PrOs}_4\text{Sb}_{12}$ might also imply the presence of an unprecedented pairing mechanism based on the exchange of quadrupolar fluctuations. In addition to the spin-fluctuation and magnetic-exciton exchange mechanism this would be the third possibility for Cooper pair formation at work in heavy fermion compounds. However, at the moment the quadrupolar SC mechanism in $\text{PrOs}_4\text{Sb}_{12}$ is still a conjecture.

7. Summary and outlook

During the past decade a number of exciting and often unanticipated broken symmetry states and associated physical effects have been discovered in lanthanide and actinide intermetallic compounds. Prominent among them are superconductivity characterized by highly anisotropic unconventional order parameters and superconductivity coexisting with ferromagnetic order as well as the hidden order of unconventional density waves. A further example is the inhomogeneous superconducting phase appearing in an applied field which has been predicted theoretically a long time ago. A general hallmark of these systems is the coexistence and the competition of various different cooperative phenomena such as superconductivity and itinerant spin density wave magnetism.

The wealth of experimental data is only partly understood. To describe the low-temperature ordered phases, the determination of the type and symmetry of order parameters is of central importance. The latter restrict the possible excitations in the ordered phases and hence determine the low-temperature properties. Order parameters given in terms of expectation values of physical observables like spin- and charge-densities can be directly measured, e.g., by X-ray and neutron diffraction. The magnetic phases in lanthanide and actinide compounds are therefore rather well characterized. This, however, is not the case for hidden order like quadrupolar ordering or unconventional density waves.

Superconductivity corresponds to an off-diagonal long range order parameter which is not directly observable and it is not surprising that the type of pairing is still a matter of controversy in many heavy fermion compounds. Considerable progress has, however, been made recently in detecting unconventional order parameter symmetries. Angle-resolved studies of thermodynamic and transport properties in the vortex phase determine the position of the order parameter nodes relative to the crystal axes. These results help to strongly reduce the number of symmetry-allowed superconducting candidate states.

Important information about the material properties relevant for superconductivity is gained from the temperature and frequency dependence of thermodynamic and transport properties. Experiments indicate severe deviations from the universal behavior predicted by weak-coupling BCS theory. The current theoretical analysis of experimental data which relies on standard weak-coupling theory can yield only qualitative results. A quantitative treatment must account for strong-coupling effects. This, however, requires a microscopic picture of the normal state, i.e., the quasiparticles and their interactions.

A microscopic picture for the strongly renormalized quasiparticles has finally emerged for the actinide compounds. The hypothesis of the dual character of the 5f-electrons is translated into a calculational scheme which reproduces both the Fermi surfaces and the effective masses determined by dHvA experiments without adjustable parameter. The method yields also a model for the residual interaction leading to the various instabilities of the normal phase. The next step will be to develop an appropriate Eliashberg-type theory. The dual model approach should also provide insight into the mysterious hidden order phases of U-compounds.

In Ce-based compounds, the Cooper pairs are formed by heavy quasiparticles with predominantly 4f-character which arise through the Kondo effect in the periodic lattice. This picture has been confirmed in detail by dHvA and high-resolution photoemission studies. The strongly renormalised quasiparticles can be successfully reproduced by a semiphenomenological ansatz. Despite the efforts to implement modern many-body methods for strong correlations into realistic electronic structure calculations there is still no general concept for quantitative microscopic calculations. In particular, the subtle interplay between local and intersite effects continues to challenge theorists. The latter may lead to long-range order of local moments while the former favor the formation of a Fermi liquid state at low temperatures.

Many heavy fermion materials are on the verge of magnetic instability. By application of pressure and magnetic field, these materials can be tuned through a quantum critical point from a metallic antiferromagnet into a paramagnet. This may also trigger a transition to an unconventional SC state. Much effort has been devoted to the study of the behavior in the vicinity of the quantum critical point. Experimental data exhibit universality with unusual critical exponents. The theoretical picture, however, is highly controversial at present.

Superconductivity, magnetism and hidden order in lanthanide and actinide compounds pose an ongoing challenge. These compounds serve as model systems to study strong correlations in a broader context.

Acknowledgements

We have benefitted from discussions and suggestions from many colleagues, especially we would like to thank for collaboration and support from J.W. Allen, A. Amici, N.E. Christensen, T. Dahm, P. Fulde, K. Izawa, G.G. Lonzarich, K. Maki, Y. Matsuda, E. Runge, N. Sato, R. Shiina, F. Steglich, G. Varelogiannis, H. Won, A. Yaresko, and Q. Yuan.

G. Zwirnagl would like to acknowledge hospitality of the Max Planck Institute for Chemical Physics of Solids, Dresden.

References

- Abrikosov, A.A., 1988. *Fundamentals of the Theory of Metals*. North-Holland, Amsterdam.
- Abrikosov, A.A., Gorkov, L.P., Dzyaloshinski, I.E., 1975. *Methods of Quantum Field Theory in Statistical Physics*. Dover, New York.
- Adenwalla, S., Lin, S.W., Ran, Q.Z., Zhao, Z., Ketterson, J.B., Sauls, J.A., Taillefer, L., Hinks, D.G., Levy, M., Sarma, B.K., 1990. *Phys. Rev. Lett.* **65**, 2298.
- Aeppli, G., Bucher, E., Broholm, C., Kjems, J.K., Baumann, J., Hufnagel, J., 1988. *Phys. Rev. Lett.* **60**, 615.

- Aeppli, G., Goldman, A.I., Shirane, G., Bucher, E., Lux-Steiner, M.-C., 1987. *Phys. Rev. Lett.*, **808**.
- Albers, R., Boring, A.M., Christensen, N.E., 1986. *Phys. Rev. B* **33**, 8116.
- Albessard, A.K., Ebihara, T., Umehara, I., Satoh, K., Ōnuki, Y., Aoki, H., Uji, S., Shimizu, T., 1993. *Physica B* **186–188**, 147.
- Allen, J.W., 1992. Resonant Photoemission of Solids with Strongly Correlated Electrons. In: *Synchrotron Radiation Research: Advances in Surface and Interface Science*, vol. 1. Plenum Press, New York, chapter 6, p. 253.
- Alver, U., Goodrich, R.G., Harrison, N., Hall, D.W., Palm, E.C., Murphy, T.P., Tozer, S.W., Pagliuso, P.G., Moreno, N.O., Sarrao, J.L., Fisk, Z., 2001. *Phys. Rev. B* **64**, 180402-1.
- Amici, A., 1999. Magnetic order and superconductivity in $\text{HoNi}_2\text{B}_2\text{C}$ and related borocarbide compounds, PhD thesis, Technical University, Dresden.
- Amici, A., Thalmeier, P., 1998. *Phys. Rev. B* **57**, 10648.
- Amici, A., Thalmeier, P., 2001. Rare earth transition metal borocarbides (nitrides): Superconducting, magnetic and normal state properties. In: Müller, K.-H., Narozhnyi, V. (Eds.), *NATO Science Series II*, vol. **14**. Kluwer Academic Publishers, Dordrecht, p. 297.
- Amici, A., Thalmeier, P., Fulde, P., 2000. *Phys. Rev. Lett.* **84**, 1800.
- Amitsuka, H., Sakakibara, T., 1994. *J. Phys. Soc. Jpn.* **63**, 736.
- Amitsuka, H., Sato, M., Metoki, N., Yokohama, M., Kuwahara, K., Sakakibara, T., Morimoto, H., Kawarazaki, S., Miyako, Y., Mydosh, J.A., 1999. *Phys. Rev. Lett.* **83**, 5114.
- Amitsuka, H., Yokoyama, M., Miyazaki, S., Tenya, K., Sakakibara, T., Higemoto, W., Nagamine, K., Matsuda, K., Kohori, Y., Kohara, T., 2002. *Physica B* **312–313**, 390.
- Anderson, P.W., 1984a. *Phys. Rev. B* **30**, 1549.
- Anderson, P.W., 1984b. Basic Notions of Condensed Matter Physics. In: *Frontiers in Physics*, vol. **55**. Benjamin, New York.
- Annett, J.F., 1990. *Adv. Phys.* **39**, 83.
- Aoki, D., Huxley, A., Ressouche, E., Braithwaite, D., Flouquet, J., Brison, J.-P., Lhotel, E., 2001. *Nature* **413**, 613.
- Aoki, H., Uji, S., Albessard, A.K., Ōnuki, Y., 1993. *Phys. Rev. Lett.* **71**, 2110.
- Aoki, Y., Namiki, T., Ohsaki, S., Saha, S.R., Sugawara, H., Sato, H., 2002. *J. Phys. Soc. Jpn.* **71**, 2098.
- Aoki, Y., Tsuchiya, A., Kanayama, T., Saha, S.R., Sugawara, H., Sato, H., Higemoto, W., Koda, A., Ohishi, K., Nishiyama, K., Kadono, R., 2003. *Phys. Rev. Lett.* **91**, 067003.
- Aoki, H., Sakakibara, T., Shishido, H., Settai, R., Ōnuki, Y., Miranović, P., Machida, K., 2004. *J. Phys. Condens. Matter.* **16**, L13.
- Bak, P., von Boehm, J., 1980. *Phys. Rev. B* **21**, 5297.
- Baltensperger, W., Strässler, S., 1963. *Phys. Condens. Mater.* **1**, 20.
- Barash, Y.S., Svidzinskii, A.A., Mineev, V.P., 1997. *JETP Lett.* **65**, 638.
- Bardeen, J., Cooper, L.N., Schrieffer, J.R., 1957. *Phys. Rev.* **108**, 1175.
- Basletic, M., Korin-Hamzic, B., Maki, K., 2002. *Phys. Rev. B* **65**, 235117.
- Bauer, E.D., Frederick, N.A., Ho, P.-C., Zapf, V.S., Maple, M.B., 2002. *Phys. Rev. B* **65**, 100506(R).
- Bauer, E., Hilscher, G., Michor, H., Paul, C., Scheidt, E.W., Griбанov, A., Seropegin, Y., Noel, H., Sigrist, M., Rogl, P., 2004. *Phys. Rev. Lett.* **92**, 027003.
- Benfatto, L., Caprara, S., Castro, C.D., 2000. *Eur. Phys. J. B* **17**, 95.
- Berk, N., Schrieffer, J.R., 1966. *Phys. Rev. Lett.* **17**, 433.
- Berlinsky, A.J., Fetter, A.L., Franz, M., Kallin, C., Soininen, P.I., 1995. *Phys. Rev. Lett.* **75**, 2200.
- Bernhoeft, N., 2000. *Eur. Phys. J. B* **13**, 685.
- Bernhoeft, N., Lonzarich, G.G., 1995. *J. Phys.: Condens. Matter.* **7**, 7325.
- Bernhoeft, N., Sato, N., Roessli, B., Aso, N., Hiess, A., Lander, G.H., Endoh, Y., Komatsubara, T., 1998. *Phys. Rev. Lett.* **81**, 4244.
- Bianchi, A., Movshovich, R., Capan, C., Lacerda, A., Pagliuso, P.G., Sarrao, J.L., 2003. *Phys. Rev. Lett.* **18**, 187004.
- Bianchi, A., Movshovich, R., Oeschler, N., Gegenwart, P., Steglich, F., Thompson, J.D., Pagliuso, P.G., Sarrao, J.L., 2002. *Phys. Rev. Lett.* **89**, 137002.
- Biasini, M., 2003. *J. Magn. Magn. Mater.*, submitted for publication.
- Bilbro, G., McMillan, W.L., 1976. *Phys. Rev. B* **14**, 1887.
- Blount, E., 1985. *Phys. Rev. B* **32**, 2935.
- Boaknin, E., Hill, R.W., Proust, C., Lupien, C., Taillefer, L., Canfield, P.C., 2001. *Phys. Rev. Lett.* **87**, 237001.
- Böhm, A., Grauel, A., Sato, N., Schank, C., Geibel, C., Komatsubara, T., Weber, G., Steglich, F., 1992. *Int. J. Mod. Phys. B* **7**, 34.
- Braithwaite, D., Fukuhara, T., Demuer, A., Sheikin, I., Kambe, S., Brison, J.-P., Maezawa, K., Naka, T., Flouquet, J., 2000. *J. Phys.: Condens. Matter.* **12**, 1339.
- Brandt, E.H., 1995. *Rep. Prog. Phys.* **58**, 1465.

- Brisson, J.-P., Keller, N., Lejay, P., Tholence, J.L., Huxley, A., Bernhoeft, N.R., Buzdin, A., Fak, B., Flouquet, J., Schmidt, L., Stepanov, A., Fisher, R.A., Phillips, N.E., Vettier, C., 1994. *Physica B* **199–200**, 70.
- Broholm, C., Kjems, J.K., Buyers, W.J.L., Matthews, P., Palstra, T.T.M., Menovsky, A.A., Mydosh, J.A., 1987. *Phys. Rev. Lett.* **58**, 1467.
- Broholm, C., Lin, H., Matthews, P.T., Mason, T.E., Buyers, W.J.L., Collins, M.F., Menovsky, A.A., Mydosh, J.A., Kjems, J.K., 1991. *Phys. Rev. B* **43**, 12809.
- Bruls, G., Weber, D., Wolf, B., Thalmeier, P., Lüthi, B., de Visser, A., Menovsky, A.A., 1990. *Phys. Rev. Lett.* **65**, 2294.
- Bruls, G., Wolf, B., Finsterbusch, D., Thalmeier, P., Kouroudis, I., Sun, W., Assmus, W., Lüthi, B., Lang, M., Gloos, K., Steglich, F., Modler, R., 1994. *Phys. Rev. Lett.* **72**, 1754.
- Buchholtz, L.J., Zwicknagl, G., 1981. *J. Phys. Condens. Matter* **23**, 5788.
- Buyers, W.J.L., Holden, T.M., 1985. In: *Handbook on the Physics and Chemistry of the Actinides*, vol. 2. Elsevier Science Publishers B.V., Amsterdam, p. 239, chapter 4.
- Campbell, A.J., Paul, D.M., McIntyre, G.J., 2000. *Phys. Rev. B* **61**, 5872.
- Canfield, P.C., Bud'ko, S.L., 1996. *Physica C* **262**, 249.
- Canfield, P.C., Bud'ko, S.L., Cho, B.K., Lacerda, A., Farrell, D., Johnston-Halperin, E., Kalatsky, V., Pokrovsky, V.L., 1997. *Phys. Rev. B* **55**, 970.
- Caspary, R., Hellmann, P., Keller, M., Wassilew, C., Köhler, R., Sparn, G., Schank, C., Geibel, C., Steglich, F., Phillips, N.E., 1993. *Phys. Rev. Lett.* **71**, 2146.
- Cava, R.J., Tagaki, H., Zandbergen, H.W., Krajewski Jr, J.J., Peck, W.F., Siegrist, T., Batlogg, B., van Dover, R.B., Felder, R.J., Mizuhashi, K., Lee, J.O., Eisaki, H., Uchida, S., 1994. *Nature* **367**, 252.
- Cavadini, N., Schneider, M., Allenspach, P., Canfield, P.C., Bourges, P., 2003. *Europhys. Lett.* **63**, 597.
- Chakravarty, S., Kee, H.-Y., Nayak, C., 2001. *Int. J. Mod. Phys. B* **15**, 2901.
- Chakravarty, S., Laughlin, R.B., Morr, D.K., Nayak, C., 2001a. *Phys. Rev. B* **63**, 94503.
- Chia, E.E., Salamon, M.B., Sugawara, H., Sato, H., 2003. *Phys. Rev. Lett.* **91**, 247003.
- Chitra, R., Kotliar, G., 2000. *Phys. Rev. Lett.* **84**, 3678.
- Choi, C., Sauls, J.A., 1991. *Phys. Rev. Lett.* **66**, 484.
- Coleman, P., 1999. *Physica B* **259–261**, 353.
- Condon, E.U., Shortley, G.H., 1957. *The Theory of Atomic Spectra*. Cambridge University Press, Cambridge.
- Continentino, M.A., 2001. *Quantum Scaling in Many-Body Systems*. World Scientific Publishing, Singapore.
- Cox, D.L., 1987. *Phys. Rev. Lett.* **59**, 1240.
- Cox, D.L., 1988. *J. Magn. Magn. Mater.* **76–77**, 53.
- Cox, D.L., Zawadowski, A., 1999. *Exotic Kondo Effects in Retals: Magnetic Ions in a Crystalline Electric Field and Tunnelling Centres*. Taylor and Francis.
- Custers, J., Gegenwart, P., Wilhelm, H., Neumaier, K., Tokiwa, Y., Trovarelli, O., Geibel, C., Steglich, F., Pepin, C., Coleman, P., 2003. *Nature* **424**, 524.
- Dahm, T., 2001, unpublished.
- Dahm, T., Graser, S., Iniotakis, C., Schopohl, N., 2002. *Phys. Rev. B* **66**, 144515.
- Dahm, T., Maki, K., Won, H., 2000. cond-mat/0006301.
- Dahm, T., Tewordt, L., 1995. *Phys. Rev. Lett.* **74**, 793.
- de Visser, A., Kayzel, F.E., Menovsky, A.A., Franse, J.J.M., van der Berg, J., Nieuwenhuys, G.J., 1986. *Phys. Rev. B* **34**, 8168.
- Degiori, L., 1999. *Rev. Mod. Phys.* **71**, 687.
- Demuer, A., Sheikin, I., Brathwaite, D., Fak, B., Huxley, A., Saymon, S., Flouquet, J., 2001. *J. Magn. Magn. Mater.* **226–230**, 17.
- Denlinger, J.D., Gweon, G.-H., Allen, J.W., Olson, C.G., Maple, M.B., Sarrao, J.L., Armstrong, P.E., Fisk, Z., Yamagami, H., 2001. *J. Electron Spectrosc. Relat. Phenom.* **117–118**, 347.
- Dertinger, A., 2001. *Supraleitung und Magnetismus in Holmium-Nickel-Borkarbid vom Strukturtyp LuNi₂B₂C*, PhD thesis, University of Bayreuth.
- Dervenagas, P., Bullock, M., Zarestky, J., Canfield, P.C., Chao, B.K., Harmon, B.N., Goldman, A.I., Stassis, C., 1995. *Phys. Rev. B* **52**, 9839.
- Detlefs, C., Bourdarot, F., Bourlet, P., Dervenagas, P., Bud'ko, S.L., Canfield, P.C., 2000. *Phys. Rev. B* **61**, R14916.
- Doh, H., Sigrist, M., Cho, B., Lee, S.-I., 1999. *Phys. Rev. Lett.* **83**, 5350.
- Doniach, S., 1977. *Physica B* **91**, 231.
- Dóra, B., Maki, K., Korin-Hamzic, B., Basletic, M., Virosztek, A., Kartsovnik, M.V., Müller, H., 2002. *Europhys. Lett.* **60**, 737.
- Dóra, B., Virosztek, A., 2001. *Eur. Phys. J. B* **22**, 169.
- Drechsler, S.-L., Rosner, H., Shulga, S.V., Opahle, I., Eschrig, H., Freudenberger, J., Fuchs, G., Nenkov, K., Müller, K., Bitterlich, H., Löser, W., Behr, G., Lipp, D., Gladun, A., 2001. *Physica C* **364–365**.
- Dressel, M., Kasper, N., Petukhov, K., Gorshunov, B., Grüner, G., Huth, M., Adrian, H., 2002. *Phys. Rev. Lett.* **88**, 186404.

- Dugdale, S.B., Alam, M.A., Wilkinson, I., Hughes, R.J., Fisher, I.R., Canfield, P.C., Jarlborg, T., Santi, G., 1999. *Phys. Rev. Lett.* **83**, 4824.
- Dumont, E., Mota, A.C., 2002. *Phys. Rev. B* **65**, 144519.
- Efremov, D., Hasselmann, N., Runge, E., Fulde, P., Zwicky, G., 2004. *Phys. Rev. B* **69**, 115114.
- Einzel, D., 2002. *J. Low Temp. Phys.* **126**, 867.
- Ehm, D., Reinert, F., Nicolay, G., Schmidt, S., Hüfner, S., Claessen, R., Eyert, V., Geibel, C., 2001. *Phys. Rev. B* **64**, 235104.
- Eskildsen, M.R., Dewhurst, C.D., Hoogenboom, B.W., Petrovic, C., Canfield, P.C., 2003. *Phys. Rev. Lett.* **90**, 187001.
- Fak, B., Flouquet, J., Lapertot, G., Fukuhara, T., Kadowaki, H., 2000. *J. Phys. Condens. Matter.* **12**, 5423.
- Fay, D., Appel, J., 1980. *Phys. Rev. B* **22**, 3173.
- Fazekas, P., 1999. *Lecture Notes on Electron Correlations and Magnetism*. In: *Series in Modern Condensed Matter Physics*, vol. **5**. World Scientific, Singapore.
- Felten, R., Steglich, F., Weber, G., Rietschel, H., Gompf, F., Renker, B., Beuers, J., 1986. *Europhys. Lett.* **2**, 323.
- Feyerherm, R., Amato, A., Gygax, F.N., Schenck, A., Geibel, C., Steglich, F., Sato, N., Komatsubara, T., 1994. *Phys. Rev. Lett.* **73**, 1849.
- Fischer, O., 1990. In: *Magnetic Superconductors*, vol. **5**. North-Holland, Amsterdam.
- Fischer, O., Maple, M.B. (Eds.), 1982. In: *Topics in Current Physics*, vols. **32** and **34**. Springer Verlag, Berlin.
- Fisher, I.R., Cooper, J.R., Canfield, P.C., 1997. *Phys. Rev. B* **56**, 10820.
- Fisher, R.A., Kim, S., Woodfield, B.F., Phillips, N.E., Taillefer, L., Hasselbach, K., Flouquet, J., Giorgi, A.L., Smith, J.L., 1989. *Phys. Rev. Lett.* **62**, 1411.
- Fomin, I.A., 2001. *JETP Lett.* **74**, 111.
- Frederick, N.A., Do, T.D., Ho, P.-C., Butch, N.P., Zapf, V.S., Maple, M.B., 2003. *Phys. Rev. B* **69**, 024523.
- Frigeri, P., Agterberg, D., Koga, A., Sigrist, M., 2004. *Phys. Rev. Lett.* **92**, 097001.
- Frings, P.H., Franse, J.J.M., deBoer, F.R., Menovsky, A.A., 1983. *J. Magn. Magn. Mater.* **31-34**, 240.
- Fujimori, S., Ino, A., Okane, T., Fujimori, A., Harima, H., Aoki, D., Ikeda, S., Shishido, H., Haga, Y., Tokiwa, Y., Ōnuki, Y., 2002a. *Physica B* **312-313**, 132.
- Fujimori, S., Okane, T., Okamoto, J., Mamiya, K., Muramatsu, Y., Fujimori, A., Harima, H., Aoki, D., Ikeda, S., Shishido, H., Tokiwa, Y., Haga, Y., Ōnuki, Y., 2003. *Phys. Rev. B* **67**, 144507.
- Fulde, P., 1995. *Electron Correlations in Molecules and Solids*, 3rd ed. Springer Verlag, Berlin.
- Fulde, P., Keller, J., 1982. *Theory of magnetic superconductors*. In: *Superconductivity in Ternary Compounds*. In: *Topics of Current Physics*, vol. **34**. Springer, Berlin.
- Fulde, P., Keller, J., Zwicky, G., 1988. *Theory of heavy fermion systems*. In: *Seitz, F., Turnbull, D., Ehrenreich, H. (Eds.), Solid State Physics*, vol. **41**. Academic Press, New York, p. 1.
- Fulde, P., Zwicky, G., 1990. *Pairbreaking in superconductors*. In: *Bednorz, J.G., Müller, K.A. (Eds.), Earlier and Recent Aspects of Superconductivity*, vol. **90**. Springer-Verlag, Heidelberg.
- Gangopadhyay, A.K., Schilling, J.S., 1996. *Phys. Rev. B* **54**, 10107.
- Garnier, M., Purdie, D., Breuer, K., Hengsberger, M., Baer, Y., 1997. *Phys. Rev. B* **56**, R11399.
- Garnier, M., Purdie, D., Breuer, K., Hengsberger, M., Baer, Y., 1998. *Phys. Rev. B* **58**, 3515.
- Gasser, U., Allenspach, P., Fauth, F., Henggeler, W., Mesot, J., Furrer, A., Rosenkranz, S., Vorderwisch, P., Buchgeister, M., 1996. *Z. Phys. B* **101**, 345.
- Gaulin, B.D., Mao, M., Wiebe, C.R., Qiu, Y., Shapiro, S.M., Broholm, C., Lee, S.-H., Garrett, J.D., 2002. *Phys. Rev. B* **66**, 174520.
- Gegenwart, P., Kromer, F., Lang, M., Sparn, G., Geibel, C., Steglich, F., 1999. *Phys. Rev. Lett.* **82**, 1293.
- Gegenwart, P., Langhammer, C., Geibel, C., Helfrich, R., Lang, M., Sparn, G., Steglich, F., Horn, R., Donnevert, L., Link, A., Assmus, W., 1998. *Phys. Rev. Lett.* **81**, 1501.
- Geibel, C., Schank, C., Thies, S., Kitazawa, H., Bredl, C.D., Böhm, A., Rau, M., Grauel, A., Caspary, R., Helfrich, R., Ahlheim, U., Weber, G., Steglich, F., 1991a. *Z. Phys. B* **84**, 1.
- Geibel, C., Thies, S., Kaczorowski, D., Mehner, A., Grauel, A., Seidel, B., Ahlheim, U., Helfrich, R., Petersen, K., Bredl, C.D., Steglich, F., 1991. *Z. Phys.* **83**, 305.
- Georges, A., Kotliar, G., Krauth, W., Rozenberg, M.J., 1996. *Rev. Mod. Phys.* **68**, 13.
- Ginzburg, V., 1957. *JETP* **4**, 153.
- Golding, B., Bishop, D.J., Batlogg, B., Haemmerle, W.H., Fisk, Z., Smith, J.L., Ott, H.R., 1985. *Phys. Rev. Lett.* **55**, 2479.
- Goll, G., von Löhneysen, H., Zapf, V.S., Bauer, E.D., Maple, M.B., 2003. *Acta Phys. Pol.* **34**, 575.
- Goremychkin, E.A., Osborn, R., 1993. *Phys. Rev. B* **47**, 14280.
- Gorkov, L., 1987. *Sov. Sci. Rev. Sect. A* **9**, 1.
- Gorkov, L.P., Sokol, A., 1992. *Phys. Rev. Lett.* **69**, 2586.
- Goryo, J., 2003. *Phys. Rev. B* **67**, 184511.

- Graf, M.J., Yip, S.-K., Sauls, J.A., 1996. *Phys. Rev. B* **53**, 15147.
- Graf, M.J., Yip, S.-K., Sauls, J.A., 1999. *J. Low Temp. Phys.* **114**, 257.
- Graf, M.J., Yip, S.-K., Sauls, J.A., 2000. *Phys. Rev. B* **62**, 14393.
- Grael, A., Böhm, A., Fischer, H., Geibel, C., Köhler, R., Modler, R., Schank, C., Steglich, F., Weber, G., 1992. *Phys. Rev. B* **46**, 5818.
- Grewe, N., Steglich, F., 1991. Heavy fermions. In: *Handbook on the Physics and Chemistry of Rare Earths*, vol. **14**. Elsevier Science Publishers B.V., Amsterdam, p. 343.
- Grin, Yu.N., Yarmolyuk, Ya.P., Gladyshevskii, E.I., 1979. *Sov. Phys. Crystallogr.* **24**, 137.
- Grosche, F.M., Agarwal, P., Julian, S.R., Wilson, N.J., Haselwimmer, R.K.W., Lister, S.J.S., Mathur, N.D., Carter, F.V., Saxena, S.S., Lonzarich, G.G., 2000. *J. Phys. Condens. Matter.* **12**, L533.
- Grosche, F.M., Julian, S.R., Mathur, N.D., Lonzarich, G.G., 1996. *Physica B* **223–224**, 50.
- Grüner, G., 1994. *Density waves in solids*. Frontiers in Physics. Addison-Wesley.
- Gulacsi, Z., Gulacsi, M., 1987. *Phys. Rev. B* **36**, 699.
- Gunnarsson, O., Schönhammer, K., 1983. *Phys. Rev. B* **28**, 4315.
- Harima, H., Yanase, A., 1991. *J. Phys. Soc. Jpn.* **60**, 21.
- Harrison, N., Jaime, M., Mydosh, J.A., 2003. *Phys. Rev. Lett.* **90**, 096402.
- Hasselbach, K., Kirtley, J.R., Flouquet, J., 1993. *Phys. Rev. B* **47**, 509.
- Hasselbach, K., Kirtley, J.R., Lejay, P., 1992. *Phys. Rev. B* **46**, 5826.
- Hayden, S.M., Taillefer, L., Vettier, C., Flouquet, J., 1992. *Phys. Rev. B* **46**, 8675.
- Heffner, R.H., Cooke, D.W., Giorgi, A.L., Hutson, R.L., Schillaci, M.E., Remp, H.D., Smith, J.L., Willis, J.O., MacLaughlin, D.E., Boekman, C., Licht, R.L., Oostens, J., Denison, A.B., 1989. *Phys. Rev. B* **39**, 11345.
- Heffner, R.H., Norman, M.R., 1996. *Commun. Cond. Matter. Phys.* **17**, 361.
- Heffner, R.H., Smith, J.L., Willis, J.O., Birrer, P., Baines, C., Gygax, F.N., Hitti, B., Lippelt, E., Ott, H.R., Schenck, A., Knetsch, E.A., Mydosh, J.A., MacLaughlin, D.E., 1990. *Phys. Rev. Lett.* **65**, 2816.
- Hegger, H., Petrovic, C., Moshopoulou, E.G., Hundley, M.F., Sarrao, J.L., Fisk, Z., Thompson, J.D., 2000. *Phys. Rev. Lett.* **84**, 4986.
- Helfrich, C., 1996. PhD thesis, TU Darmstadt.
- Herring, C., 1966. In: *Magnetism, A Treatise on Modern Theory and Materials*, vol. **IV**. Academic Press, New York.
- Hertz, J.A., 1976. *Phys. Rev. B* **14**, 1165.
- Hess, D.W., Tokuyasu, T.A., Sauls, J.A., 1989. *J. Phys. Condens. Matter.* **1**, 8135.
- Hessert, J., Huth, M., Jourdan, M., Adrian, H., Rieck, C.T., Scharnberg, K., 1997. *Physica B* **230–232**, 373.
- Hewson, A.C., 1993. *The Kondo Problem to Heavy Fermions*. Cambridge University Press.
- Hilscher, G., Michor, H., 1999. In: *Studies in High Temperature Superconductors*, vol. **28**. Nova Science Publishers, pp. 241–286.
- Hiroi, M., Sera, M., Kobayashi, N., Haga, Y., Yamamoto, E., Ōnuki, Y., 1997. *J. Phys. Soc. Jpn.* **66**, 1595.
- Hirschfeld, P., Vollhardt, D., Wölfle, P., 1986. *Solid State Commun.* **59**, 111.
- Hotta, T., 1993. *J. Phys. Soc. Jpn.* **62**, 278.
- Hunt, M., Meeson, P., Probst, P.A., Reinders, P., Springford, M., Assmus, W., Sun, W., 1990. *J. Phys. C* **2**, 6859.
- Huxley, A., Sheikin, I., Ressouche, E., Kernavanois, N., Braithwaite, D., Calemczuk, R., Flouquet, J., 2001. *Phys. Rev. B* **63**, 144519-1.
- Ichioka, M., Nakai, N., Machida, K., 2003. *J. Phys. Soc. Jpn.* **72**, 1322.
- Ikeda, H., Ohashi, Y., 1998. *Phys. Rev. Lett.* **81**, 3723.
- Ikeda, H., Ohashi, Y., 1999. *Phys. Rev. Lett.* **82**, 5173.
- Inada, Y., Ishiguro, A., Kimura, J., Sato, N., Sawada, A., Komatsubara, T., Yamagami, H., 1995. *Physica B* **206–207**, 33.
- Inada, Y., Yamagami, H., Haga, Y., Sakurai, K., Tokiwa, Y., Honma, T., Yamamoto, E., Ōnuki, Y., Yanagisawa, T., 1999. *J. Phys. Soc. Jpn.* **68**, 3643.
- Ishida, K., Okamoto, K., Kawasaki, Y., Kitaoka, Y., Troarelli, O., Geibel, C., Steglich, F., 2002. *Phys. Rev. Lett.* **89**, 107202.
- Izawa, K., Kamata, K., Nakajima, Y., Matsuda, Y., Watanabe, T., Nohara, M., Takagi, H., Thalmeier, P., Maki, K., 2002a. *Phys. Rev. Lett.* **89**, 137006.
- Izawa, K., Nakajima, Y., Goryo, J., Matsuda, Y., Osaki, S., Sugawara, H., Sato, H., Thalmeier, P., Maki, K., 2003. *Phys. Rev. Lett.* **90**, 1170013.
- Izawa, K., Takahashi, H., Yamaguchi, H., Matsuda, Y., Suzuki, M., Sasaki, T., Fukase, T., Yoshida, Y., Settai, R., Ōnuki, Y., 2001a. *Phys. Rev. Lett.* **86**, 2653.
- Izawa, K., Yamaguchi, H., Matsuda, Y., Shishido, H., Settai, R., Ōnuki, Y., 2001. *Phys. Rev. Lett.* **87**, 05700.
- Izawa, K., Yamaguchi, H., Sasaki, T., Matsuda, Y., 2002. *Phys. Rev. Lett.* **88**, 027002.
- Izyumov, Y.A., 1999. *Phys. Usp.* **42**, 215.
- Jaccard, D., Behnia, K., Sierro, J., 1992. *Phys. Lett. A* **163**, 475.

- Jaime, M., Kim, K.H., Jorge, G., McCall, S., Mydosh, J.A., 2002. *Phys. Rev. Lett.* **89**, 287201.
- Jayprakash, C., Krishna-murthy, H.-R., Wilkins, J.W., 1981. *Phys. Rev. Lett.* **47**, 737.
- Jayprakash, C., Krishna-murthy, H.-R., Wilkins, J.W., 1982. *J. Appl. Phys.* **53**, 2142.
- Jensen, J., 2002. *Phys. Rev. B* **65**, 140514.
- Jensen, J., Mackintosh, A.R., 1991. *Rare Earth Magnetism Structures and Excitations*. Clarendon Press, Oxford.
- Jones, B., Varma, C.M., 1987. *J. Magn. Magn. Mater.* **63–64**, 251.
- Jourdan, M., Huth, M., Adrian, H., 1999. *Nature* **398**, 47.
- Joynt, R., 1990. *J. Phys. Condens. Matter* **2**, 3415.
- Joynt, R., Taillefer, L., 2002. *Rev. Mod. Phys.* **74**, 235.
- Kadanoff, L., Falko, C., 1964. *Phys. Rev. A* **136**, A1170.
- Kaganov, M.I., Lifshits, I.M., 1979. *Sov. Phys. Usp.* **22**, 904.
- Kamata, K., 2003. Master's thesis, University of Tokyo.
- Kato, M., Machida, K., 1987. *J. Phys. Soc. Jpn.* **56**, 2136.
- Kato, M., Machida, K., 1988. *Phys. Rev. B* **37**, 1510.
- Kawano-Furukawa, H., Habuta, E., Nagata, T., Nagao, M., Yoshizawa, H., Furukawa, N., Takeya, H., Kadowaki, K., 2001. *cond-mat/0106273*.
- Kawano-Furukawa, H., Takeshita, H., Ochiai, M., Nagata, T., Yoshizawa, H., Furukawa, N., Takeya, H., Kadowaki, K., 2002. *Phys. Rev. B* **65**, 180508.
- Kawano, H., Takeya, H., Yoshizawa, H., Kadowaki, K., 1999. *J. Phys. Chem. Solids* **60**, 1053.
- Kawasaki, S., Mito, T., Kawasaki, Y., Zheng, G.-Q., Kitaoka, Y., Shishido, H., Araki, S., Settai, R., Ōnuki, Y., 2002. *Phys. Rev. B* **66**, 054521.
- Kee, H.-Y., Kim, Y.B., Maki, K., 2000. *Phys. Rev. B* **62**, 5877.
- Keller, N., Brison, J.-P., Lejay, P., Tholence, J.L., Huxley, A., Schmidt, L., Buzdin, A., Flouquet, J., 1995. *Physica B* **206–207**, 568.
- Kernavainis, N., de Réotier, P.D., Yaouanc, A., Sanchez, J.-P., Liß, K.D., Lejay, P., 1999. *Physica B* **259–261**, 648.
- Kernavainis, N., Grenier, B., Huxley, A., Ressouche, E., Sanchez, J.-P., Flouquet, J., 2001. *Phys. Rev. B* **64**, 174509.
- Kimura, N., Komatsubara, T., Aoki, D., Ōnuki, Y., Haga, Y., Yamamoto, E., Aoki, H., Harima, H., 1998. *J. Phys. Soc. Jpn.* **67**, 2185.
- King, C.A., Lonzarich, G.G., 1991. *Physica B* **171**, 161.
- Kirkpatrick, T.R., Belitz, D., Vojta, T., Narayanan, R., 2001. *Phys. Rev. Lett.* **87**, 127003.
- Kita, H., Dönni, A., Endoh, Y., Kakurai, K., Sato, N., Komatsubara, T., 1994. *J. Phys. Soc. Jpn.* **63**, 726.
- Kitaoka, Y., Tou, H., Ishida, K., Kimura, N., Ōnuki, Y., Yamamoto, E., Haga, Y., Maezawa, K., 2000. *Physica B* **281–282**, 878.
- Knöpfle, K., Mavromaras, A., Sandratskii, L.M., Kübler, J., 1996. *J. Phys. Condens. Matter* **8**, 901.
- Kobayashi, T.C., Hanazono, K., Tateiwa, N., Amaya, K., Haga, Y., Settai, R., Ōnuki, Y., 2001. *cond-mat/0107548*.
- Kohgi, M., Iwasa, K., Nakajima, M., Metoki, N., Araki, S., Bernhoeft, N., Mignot, J.-M., Gukasov, A., Sato, H., Aoki, Y., Sugawara, H., 2003. *J. Phys. Soc. Jpn.* **72**, 1002.
- Kohori, Y., Yamato, Y., Iwamoto, Y., Kohara, T., Bauer, E.D., Maple, M.B., Sarrao, J.L., 2001. *Phys. Rev. B* **64**, 134526.
- Koike, Y., Metoki, N., Kimura, N., Yamamoto, E., Haga, Y., Ōnuki, Y., Maezawa, K., 1998. *J. Phys. Soc. Jpn.* **67**, 1142.
- Konno, R., Ueda, K., 1989. *Phys. Rev. B* **40**, 4329.
- Korin-Hamzic, B., Basletic, M., Maki, K., 2002. *Europhys. Lett.* **59**, 298.
- Kotegawa, H., Yogi, M., Imamura, Y., Kawasaki, Y., Zheng, G.-Q., Kitaoka, Y., Ohsaki, S., Sugawara, H., Aoki, Y., Sato, H., 2003. *Phys. Rev. Lett.* **90**, 027001.
- Krimmel, A., Fischer, P., Roessli, B., Maletta, H., Geibel, C., Schank, C., Grauel, A., Loidl, A., Steglich, F., 1992. *Z. Phys. B* **86**, 161.
- Kromer, F., 2000. PhD thesis, TU Dresden.
- Kromer, F., Helfrich, R., Lang, M., Steglich, F., Langhammer, C., Bach, A., Michels, T., Kim, J.S., Stewart, G.R., 1998. *Phys. Rev. Lett.* **81**, 4476.
- Kromer, F., Lang, M., Oeschler, N., Hinze, P., Langhammer, C., Steglich, F., 2000. *Phys. Rev. B* **62**, 12477.
- Kromer, F., Oeschler, N., Tayama, T., Tenya, K., Cichorek, T., Lang, M., Steglich, F., Kim, J.S., Stewart, G.R., 2002. *J. Low Temp. Phys.* **126**, 815.
- Kübert, C., Hirschfeld, P.J., 1998. *Solid State Commun.* **105**, 459.
- Kuramoto, Y., Kitaoka, Y., 2000. Dynamics of Heavy Electrons. In: *International Series of Monographs in Physics*, vol. **105**. Clarendon Press, Oxford.
- Kyogaku, M., Kitaoka, Y., Asayama, K., Geibel, C., Schank, C., Steglich, F., 1993. *J. Phys. Soc. Jpn.* **62**, 4016.
- Landau, L.D., 1956. *Sov. Phys. JETP* **3**, 920.
- Landau, L.D., 1957. *Sov. Phys. JETP* **32**, 59.
- Landau, L.D., 1958. *Sov. Phys. JETP* **35**, 97.
- Lang, M., Müller, J., 2003. Organic superconductors. In: *The Physics of Superconductors*, vol. 2. Springer-Verlag. *cond-mat/0302157*.
- Layzer, A., Fay, D., 1971. *Int. J. Mag.* **1**, 135.
- Layzer, A., Fay, D., 1974. *Solid State Commun.* **14**, 599.

- Liu, W., Dolg, M., Fulde, P., 1998. *Inorg. Chem.* **37**, 1067.
- Lonzarich, G.G., 1988. *J. Magn. Magn. Mater.* **76/77**, 1.
- Lundin, U., Sandalov, I., Eriksson, O., Johansson, B., 2000. *Phys. Rev. B* **62**, 16370.
- Lussier, B., Ellman, B., Taillefer, L., 1996. *Phys. Rev. B* **53**, 5145.
- Lynn, J.W., Skanthakumar, S., Huang, Q., Sinha, S.K., Hossain, Z., Gupta, L.C., Nagarajan, R., Godart, C., 1997. *Phys. Rev. B* **55**, 6548.
- Machida, K., 1981. *J. Phys. Soc. Jpn.* **50**, 2195.
- Machida, K., Matsubara, T., 1981. *J. Phys. Soc. Jpn.* **50**, 3231.
- Machida, K., Nishira, T., Ohmi, T., 1999. *J. Phys. Soc. Jpn.* **68**, 3364.
- Machida, K., Ohmi, T., 1998. *J. Phys. Soc. Jpn.* **65**, 4018.
- Machida, K., Ohmi, T., 2001. *Phys. Rev. Lett.* **86**, 850.
- Machida, K., Ozaki, M., Ohmi, T., 1989. *J. Phys. Soc. Jpn.* **58**, 4116.
- Mackenzie, A.P., Maeno, Y., 2003. *Rev. Mod. Phys.* **75**, 657.
- Maki, K., Thalmeier, P., 2003. *Physica C* **388**, 521.
- Maki, K., Won, H., 1996. *J. Phys. I France* **6**, 2317.
- Maki, K., Thalmeier, P., Won, H., 2002. *Phys. Rev. B* **65**, 140502(R).
- Maki, K., Dóra, B., Kartsovnik, M., Virosztek, A., Korin-Hamzic, B., Basletic, M., 2003a. *Phys. Rev. Lett.* **90**, 256402.
- Maki, K., Dóra, B., Virosztek, A., 2003b. *AIP Conf. Proc.* **659**, 10.
- Maki, K., Won, H., Thalmeier, P., Yuan, Q., Izawa, K., Matsuda, Y., 2003c. *Europhys. Lett.* **64**, 496.
- Malterre, D., Griioni, M., Baer, Y., 1996. *Adv. Phys.* **45**, 299.
- Maple, M.B., Ho, P.-C., Frederick, N.A., Zapf, V.S., Yuhasz, W.M., Bauer, E.D., 2003. *Acta Phys. Pol. B* **34**, 919.
- Maple, M.B., Ho, P.-C., Zapf, V.S., Frederick, N.A., Bauer, E.D., Yuhasz, W.M., Woodward, F.M., Lynn, J.W., 2002. *J. Phys. Soc. Jpn.* **71** (Suppl.), 23.
- Marabelli, F., Wachter, P., Franse, J.J.M., 1987. *J. Magn. Magn. Mater.* **63-64**, 377.
- Martinez-Samper, P., Suderow, H., Vieira, S., Brison, J.-P., Luchier, N., Lejay, P., Canfield, P.C., 2003. *Phys. Rev. B* **64**, 020503.
- Mason, T.E., Aeppli, G., 1997. *Mat.-Fys. Meddelelser* **45**, 231.
- Mathur, N.D., Grosche, F.M., Julian, S.R., Walker, I.R., Freye, D.M., Haselwimmer, R.K.W., Lonzarich, G.G., 1998. *Nature* **394**, 39.
- Matsuda, K., Kohori, Y., Kohara, T., 1996. *J. Phys. Soc. Jpn.* **65**, 679.
- Matsuda, K., Kohori, Y., Kohara, T., 1997. *Phys. Rev. B* **55**, 15223.
- Matsuda, Y., Izawa, K., 2003. *Acta Phys. Pol. B* **34**, 579.
- Mattheis, L.F., 1994. *Phys. Rev. B* **49**, R13279.
- McHale, P., Monthoux, P., 2003. *Phys. Rev. B* **67**, 214512.
- McHale, P., Fulde, P., Thalmeier, P., 2004. *Phys. Rev. B* **70**, 014513.
- McMahan, A.K., Held, K., Scalettar, R.T., 2003. *Phys. Rev. B* **67**, 075108.
- McMullen, G.J., Julian, S.R., Doiron-Leyraud, N., Huxley, A., Bergemann, C., Flouquet, J., Lonzarich, G.G., 2001, in preparation.
- Measson, M.-A., Braithwaite, D., Flouquet, J., Seyfarth, G., Brison, J.-P., Lhotel, E., Paulsen, C., Sugawara, H., Sato, H., 2004. *cond-mat/0402681*.
- Mentink, S.A.M., Wyder, U., Perenboom, J.A.A.J., de Visser, A., Menovsky, A.A., Nieuwenhuys, G.J., Mydosh, J.A., Mason, T.E., 1997. *Physica B* **230-232**, 74.
- Metlushko, V., Welp, U., Koshelev, A., Aranson, I., Crabtree, G.W., Canfield, P.C., 1997. *Phys. Rev. Lett.* **7917**, 1738.
- Metoki, N., 2001. *J. Phys. Soc. Jpn.* **70**, 11.
- Metoki, N., Haga, Y., Koike, Y., Ōnuki, Y., 1998. *Phys. Rev. Lett.* **80**, 5417.
- Michel, L., 1980. *Rev. Mod. Phys.* **52**, 617.
- Millis, A.J., 1993. *Phys. Rev. B* **48**, 7183.
- Millis, A.J., Sachdev, S., Varma, C.M., 1988. *Phys. Rev. B* **37**, 4975.
- Mineev, V.P., 2002. *Phys. Rev. B* **66**, 134504.
- Mineev, V.P., Samokhin, K.V., 1999. *Introduction to Unconventional Superconductivity*. Gordon and Breach Science Publishers.
- Miyake, K., Kohno, H., Harima, H., 2003. *J. Phys. Condens. Matter.* **15**, L275.
- Miyake, K., Schmitt-Rink, S., Varma, C.M., 1986. *Phys. Rev. B* **34**, 6554.
- Mizuno, K., Saito, T., Fudo, H., Koyama, K., Endo, K., Deguchi, H., 1999. *Physica B* **259-261**, 594.
- Monthoux, P., Balatsky, A.V., Pines, D., 1991. *Phys. Rev. Lett.* **67**, 3448.
- Monthoux, P., Lonzarich, G.G., 1999. *Phys. Rev. B* **59**, 14598.
- Monthoux, P., Lonzarich, G.G., 2001. *Phys. Rev. B* **63**, 054529.
- Monthoux, P., Lonzarich, G.G., 2002. *Phys. Rev. B* **66**, 224504.
- Monthoux, P., Pines, D., 1994. *Phys. Rev. B* **49**, 4261.
- Morin, P., Vettier, C., Flouquet, J., Konczykowski, M., Lasailly, Y., Mignot, J.-M., Welp, U., 1988. *J. Low Temp. Phys.* **70**, 377.

- Moriya, T., 1985. *Spin Fluctuations in Itinerant Electron Magnets*. Springer-Verlag, Berlin.
- Moriya, T., Takimoto, T., 1995. *J. Phys. Soc. Jpn.* **64**, 960.
- Moriya, T., Ueda, K., 2000. *Adv. Phys.* **49**, 555.
- Morosov, A.I., 1996. *Sov. Phys. JETP* **83**, 1084.
- Morosov, A.I., 1996a. *Sov. Phys. JETP Lett.* **63**, 734.
- Mota, A.C., Cichorek, T., 2003, in preparation.
- Movshovich, R., Graf, T., Mandrus, D., Thompson, J.D., Smith, J.L., Fisk, Z., 1996. *Phys. Rev. B* **53**, 8241.
- Müller, K.-H., Narozhnyi, V.N., 2001. *Rep. Prog. Phys.* **64**, 943.
- Müller, V., Maurer, D., Scheidt, E.W., Roth, C., Lüders, K., Bucher, E., Bömmel, H.E., 1986. *Solid State Commun.* **57**, 319.
- Nagarajan, N., Mazumda, C., Hossain, Z., Dhar, S.K., Gopalakrishnan, K.V., Gupta, L.C., Godart, C., Padalia, B.D., Vijayaraghavan, R., 1994. *Phys. Rev. Lett.* **72**, 274.
- Nakai, N., Miranović, P., Ichioka, M., Machida, K., 2004. *cond-mat/0403589*.
- Nakajima, S., 1973. *Prog. Theor. Phys.* **50**, 1101.
- Nakamura, S., Suzuki, O., Goto, T., Sakatsume, S., Matsumara, T., Kunii, S., 1997. *J. Phys. Soc. Jpn.* **66**, 552.
- Nakao, H., Magishi, K., Wakabayashi, Y., Murakami, Y., Koyama, K., Hirota, K., Endoh, Y., Kunii, S., 2001. *J. Phys. Soc. Jpn.* **70**, 2892.
- Nersesyan, A.A., Japaridze, G.I., Kimeridze, I.G., 1991. *J. Phys. Condens. Matter* **3**, 3353.
- Nersesyan, A.A., Vachnadze, G.E., 1989. *J. Low Temp. Phys.* **77**, 293.
- Ng, T.K., Varma, C.M., 1997. *Phys. Rev. Lett.* **78**, 3745.
- Nohara, M., Isshiki, M., Takagi, H., Cava, R.J., 1997. *J. Phys. Soc. Jpn.* **66**, 1888.
- Norman, M.R., 1991. *Phys. Rev. B* **43**, 6121.
- Norman, M.R., 1994. *Phys. Rev. B* **50**, 6904.
- Norman, M.R., Albers, R.C., Boring, A.M., Christensen, N.E., 1988. *Solid State Commun.* **68**, 245.
- Norman, M.R., Hirschfeld, P.J., 1996. *Phys. Rev. B* **53**, 5706.
- Nozières, P., 1974. *J. Low Temp. Phys.* **17**, 31.
- Ocana, R., Esquinazi, P., 2002. *Phys. Rev. B* **66**, 064525.
- Oeschler, N., Gegenwart, P., Steglich, F., Frederick, N.A., Bauer, E.D., Maple, M.B., 2003. *Acta Phys. Pol. B* **34**, 959.
- Oeschler, N., Weickert, F., Gegenwart, P., Thalmeier, P., Steglich, F., Bauer, E.D., Maple, M.B., 2004. *Phys. Rev. B* **69**, 235108.
- Ohkuni, H., Inada, Y., Tokiwa, Y., Sakurai, K., Settai, R., Honma, T., Haga, Y., Yamamoto, E., Ōnuki, Y., Yamagami, H., Takahashi, S., Yanagisawa, T., 1999. *Philos. Magazine B* **79**, 1045.
- Ohmi, T., Machida, K., 1996. *J. Phys. Soc. Jpn.* **65**, 4018.
- Ohmi, T., Machida, K., 1996a. *J. Phys. Soc. Jpn.* **65**, 3456.
- Okuno, Y., Narikiyo, O., Miyake, K., 1998. *J. Phys. Soc. Jpn.* **67**, 2469.
- Ōnuki, Y., Ukon, I., Yun, S.W., Umeharaha, I., Satoh, K., Fukuhara, T., Sato, H., Takayanagi, S., Shikama, M., Ochiai, A., 1992. *J. Phys. Soc. Jpn.* **61**, 293.
- Ott, H.R., 1987. In: Brewer, D.F. (Ed.), *Prog. Low Temp. Phys.*, vol. **XI**. Elsevier, Amsterdam, p. 215.
- Ott, H.R., Fisk, Z., 1987. In: *Handbook on the Physics and Chemistry of the Actinides*, vol. **5**. North-Holland, p. 85.
- Ott, H.R., Rudigier, H., Fisk, Z., Smith, J.L., 1983. *Phys. Rev. Lett.* **50**, 1595.
- Ott, H.R., Rudigier, H., Rice, T.M., Ueda, K., Fisk, Z., Smith, J.L., 1984. *Phys. Rev. Lett.* **82**, 1915.
- Ozaki, M., 1992. *Int. J. Quantum Chem.* **42**, 55.
- Ozaki, M., Machida, K., 1985. *Prog. Theor. Phys.* **74**, 221.
- Palstra, T.T.M., Menovsky, A.A., vandenBerg, J., Dirkmaat, A.J., Res, P.H., Nieuwenhuys, G.J., Mydosh, J.A., 1985. *Phys. Rev. Lett.* **55**, 2727.
- Pao, C.H., Bickers, N.E., 1994. *Phys. Rev. Lett.* **72**, 1870.
- Park, J.-G., McEwen, K.A., Bull, M.J., 2002. *Phys. Rev. B* **66**, 094502.
- Park, T., Salamon, M.B., Choi, E.M., Kim, H.J., Lee, S.-I., 2003. *Phys. Rev. Lett.* **90**, 177001.
- Petrovic, C., Movshovich, R., Jaime, M., Pagliuso, P.G., Hundley, M.F., Sarrao, J.L., Fisk, Z., Thompson, J.D., 2001a. *Europhys. Lett.* **53**, 354.
- Petrovic, C., Pagliuso, P.G., Hundley, M.F., Movshovich, R., Sarrao, J.L., Thompson, J.D., Fisk, Z., Monthoux, P., 2001b. *J. Phys.: Condens. Matter* **13**, L337.
- Petrovic, C., Bud'ko, S.L., Kogan, V.G., Canfield, P.C., 2002. *Phys. Rev. B* **67**, 054534.
- Pfleiderer, C., 2001. *J. Magn. Magn. Mater.* **226–230**, 23.
- Pfleiderer, C., Huxley, A.D., 2002. *Phys. Rev. Lett.* **89**, 147005.
- Pickett, W.E., Singh, D.J., 1994. *Phys. Rev. Lett.* **72**, 3702.
- Pollmann, F., Zwicky, G., 2004, unpublished.
- Pulst, U., 1993. PhD thesis, TH Darmstadt.
- Ramirez, A.P., Chandra, P., Coleman, P., Fisk, Z., Smith, J.L., Ott, H.R., 1994. *Phys. Rev. Lett.* **73**, 3018.
- Rauchschwalbe, U., Steglich, F., Stewart, G.R., Giorgi, A.L., Fulde, P., Maki, K., 1987. *Europhys. Lett.* **3**, 751.
- Regnault, L.P., Erkelens, W.A.C., Rossat-Mignot, J., Lejay, P., Flouquet, J., 1988. *Phys. Rev. B* **38**, 4481.

- Reinert, F., Ehm, D., Schmidt, S., Nicolay, G., Hühner, S., Kroha, J., Trovarelli, O., Geibel, C., 2001. *Phys. Rev. Lett.* **87**, 106401.
- Rhee, J.Y., Wang, X., Harmon, B.N., 1995. *Phys. Rev. B* **51**, 15585.
- Rieck, C.T., Scharnberg, K., Schopohl, N., 1991. *J. Low Temp. Phys.* **84**, 381.
- Rosch, A., 1999. *Phys. Rev. Lett.* **82**, 4280.
- Rosner, H., Drechsler, S.-L., Koepfner, K., Opahle, I., Eschrig, H., 2001. Rare earth transition metal borocarbides (nitrides): Superconducting, magnetic and normal state properties. In: Müller, K.-H., Narozhnyi, V. (Eds.), NATO Science Series II. Kluwer Academic Publishers, Dordrecht.
- Rotundu, C.R., Tsuji, H., Takano, Y., Andracka, B., Sugawara, H., Aoki, Y., Sato, H., 2003. *cond-mat/0305182*.
- Runge, E., Albers, R.A., Christensen, N.E., Zwicknagl, G., 1995. *Phys. Rev. B* **51**.
- Sachdev, S., 1999. *Quantum Phase Transitions*. Cambridge University Press.
- Saint-James, D., Thomas, E.J., Sarma, G., 1969. *Type II Superconductivity*. Pergamon Press, Oxford.
- Sales, B.C., 2003. In: *Handbook on the Physics and Chemistry of the Rare Earths*, vol. **33**. Elsevier, chapter 211, p. 1.
- Sales, B.C., Mandrus, D., Williams, R.K., 1996. *Science* **272**, 1325.
- Sandratskii, L.M., Kübler, J., 1994. *Phys. Rev. B* **50**.
- Santini, P., 1998. *Phys. Rev. B* **57**, 5191.
- Santini, P., Amoretti, G., 1994. *Phys. Rev. Lett.* **73**, 1027.
- Santini, P., Amoretti, G., Caciuffo, R., Bourdarot, F., Fak, B., 2000. *Phys. Rev. Lett.* **85**, 654.
- Sarrao, J.L., Thompson, J.D., Moreno, N.O., Morales, L.A., Wastin, F., Rebizan, J., Boulet, P., Colineau, E., Lander, G.H., 2003. *J. Phys. Condens. Matter* **15**, 52775.
- Sato, N., 1993, unpublished.
- Sato, N., Aso, N., Lander, G.H., Roessli, B., Komatsubara, T., Endoh, Y., 1997. *J. Phys. Soc. Jpn.* **66**, 1884.
- Sato, N., Aso, N., Lander, G.H., Roessli, B., Komatsubara, T., Endoh, Y., 1997a. *J. Phys. Soc. Jpn.* **66**, 2981.
- Sato, N.K., Aso, N., Miyake, K., Shiina, R., Thalmeier, P., Varelogiannis, G., Geibel, C., Steglich, F., Fulde, P., Komatsubara, T., 2001. *Nature* **410**, 340.
- Sato, N., Koga, N., Komatsubara, T., 1996. *J. Phys. Soc. Jpn.* **65**, 1555.
- Sauls, J.A., 1994. *Adv. Phys.* **43**, 113.
- Saxena, S.S., Agarwal, P., Ahilan, K., Grosche, F.M., Haselwimmer, R.K.W., Steiner, M.J., Pugh, E., Walker, I.R., Julian, S.R., Monthoux, P., Lonzarich, G.G., Huxley, A., Shelkin, I., Braithwaite, D., Flouquet, J., 2000. *Nature* **406**, 587.
- Scalapino, D.J., 1995. *Phys. Rep.* **250**, 329.
- Scharnberg, K., Walker, D., Monien, H., Tewordt, L., Klemm, R., 1986. *Solid State Commun.* **60**, 535.
- Schlabbitz, W., Baumann, J., Politt, B., Rauchschalbe, U., Mayer, H.M., Ahlheim, U., Bredl, C.D., 1986. *Z. Phys. B* **52**, 171.
- Schlottmann, P., Sacramento, P., 1993. *Adv. Phys.* **42**, 641.
- Schmidt, H., Braun, H.F., 1997. *Phys. Rev. B* **55**, 8497.
- Schmitt-Rink, S., Miyake, K., Varma, C.M., 1986. *Phys. Rev. Lett.* **57**, 2575.
- Schoenes, J., Vogt, O., Löhle, J., Hulliger, F., Mattenberger, K., 1996. *Phys. Rev. B* **53**, 14987.
- Schrieffer, J.R., 1964. *Theory of Superconductivity*. Benjamin, Reading, MA.
- Schuberth, E.A., Strickler, B., Andres, K., 1992. *Phys. Rev. Lett.* **68**, 117.
- Schulz, H., 1989. *Phys. Rev. B* **39**, 2940.
- Shah, N., 2000. *Phys. Rev. B* **61**, 564.
- Shick, A.B., Pickett, W.E., 2001. *Phys. Rev. Lett.* **86**, 300.
- Shiina, R., 2001. Private communication.
- Shiina, R., 2004. *J. Phys. Soc. Jpn.* **73**, 2257.
- Shiina, R., Shiba, H., Thalmeier, P., 1997. *J. Phys. Soc. Jpn.* **66**, 1741.
- Shishido, H., Settai, R., Aoki, D., Ikeda, S., Nakawaki, H., Nakamura, N., Iizuka, T., Inada, Y., Sugiyama, K., Takeuchi, T., Kindo, K., Kobayashi, T.C., Haga, Y., Harima, H., Aoki, Y., Namiki, T., Sato, H., Ōnuki, Y., 2002. *J. Phys. Soc. Jpn.* **71**, 162.
- Shivaram, B.S., Jeong, Y.H., Rosenbaum, T.F., Hinks, D.G., Schmitt-Rink, S., 1987. *Phys. Rev. B* **35**, 5372.
- Shulga, S.V., Drechsler, S.-L., 2001. Rare earth transition metal borocarbides (nitrides): Superconducting, magnetic and normal state properties. In: Müller, K.-H., Narozhnyi, V. (Eds.), NATO Science Series II. Kluwer Academic Publishers, Dordrecht.
- Shulga, S.V., Drechsler, S.-L., Fuchs, G., Müller, K.H., Winzer, K.H., Heinecke, M., Krug, K., 1998. *Phys. Rev. Lett.* **80**, 1730.
- Si, Q., 2001. *J. Magn. Magn. Mater.* **226–230**, 30.
- Si, Q., Rabello, S., Ingersent, K., Smith, J.L., 2001. *Nature* **413**, 804.
- Si, Q., Smith, J.L., Ingersent, K., 1999. *Int. J. Mod. Phys. B* **13**, 2331.
- Sigrist, M., Agterberg, D., 1999. *Prog. Theor. Phys.* **102**, 965.
- Sigrist, M., Rice, T.M., 1989. *Phys. Rev. B* **39**, 2200.
- Sigrist, M., Ueda, K., 1991. *Rev. Mod. Phys.* **63**, 239.

- Sikkema, A.E., Buyers, W.J.L., Affleck, I., Gan, J., 1996. *Phys. Rev. B* **54**, 9322.
- Smith, J.L., Si, Q., 2000. *Phys. Rev. B* **61**, 5184.
- Söderlind, P., Ahuja, R., Eriksson, O., Johansson, B., Wills, J.M., 2000. *Phys. Rev. B* **61**, 8119.
- Steglich, F., 1985. In: Kasuya, T., Saso, T. (Eds.), *Theory of Heavy Fermions and Valence Fluctuations*. Springer-Verlag, Berlin, p. 3.
- Steglich, F., Aarts, J., Bredl, C.D., Lieke, W., Meschede, D., Franz, W., Schäfer, H., 1979. *Phys. Rev. Lett.* **43**, 1892.
- Steglich, F., Gegenwart, P., Geibel, C., Hinze, P., Lang, M., Langhammer, C., Sparn, G., Tayama, T., Trovarelli, O., Sato, N., Dahm, T., Varelogiannis, G., 2001. In: *More is Different – Fifty Years of Condensed Matter Physics*. Princeton University Press, p. 191, chapter 13.
- Steglich, F., Gegenwart, P., Geibel, C., Hinze, P., Lang, M., Langhammer, C., Sparn, G., Trovarelli, O., 2000a. *Physica B* **280**, 349.
- Steglich, F., Gegenwart, P., Helfrich, R., Langhammer, C., Hellmann, P., Donnevert, L., Geibel, C., Lang, M., Sparn, G., Assmus, W., Stewart, G.R., Ochiai, A., 1997. *Z. Phys. B* **103**, 235.
- Steglich, F., Rauchschalbe, U., Gottwick, U., Mayer, H.M., Sparn, G., Grewe, N., Poppe, U., 1985. *J. Appl. Phys.* **57**, 3054.
- Steglich, F., Sato, N., Tayama, T., Lühmann, T., Langhammer, C., Gegenwart, P., Hinze, P., Geibel, C., Lang, M., Sparn, G., Assmus, W., 2000. *Physica C* **341–348**, 691.
- Stewart, G.R., 2001. *Rev. Mod. Phys.* **73**, 797.
- Stewart, G.R., Fisk, Z., Willis, J.O., Smith, J.L., 1984. *Phys. Rev. Lett.* **52**, 679.
- Stockert, O., Faulhaber, E., Zwicknagl, G., Stuesser, N., Jeevan, H., Cichorek, T., Loewenhaupt, R., Geibel, C., Steglich, F., 2004. *Phys. Rev. Lett.* **92**, 136401.
- Suderow, H., Brison, J.P., Huxley, A., Flouquet, J., 1997. *J. Low Temp. Phys.* **108**, 11.
- Sugawara, H., Osaki, S., Saha, S.R., Aoki, Y., Sato, H., Inada, Y., Shishido, H., Settai, R., Ōnuki, Y., Harima, H., Oikawa, K., 2002. *Phys. Rev. B* **66**, 220504(R).
- Sugiyama, K., Nakashima, M., Ohkuni, H., Kindo, K., Haga, Y., Haga, Y., Honma, T., Yamamoto, E., Ōnuki, Y., 1999. *J. Phys. Soc. Jpn.* **68**, 3394.
- Sun, Y., Maki, K., 1995. *Europhys. Lett.* **32**, 335.
- Taillefer, L., Lonzarich, G.G., 1988. *Phys. Rev. Lett.* **60**, 1570.
- Taillefer, L., Newbury, R., Lonzarich, G.G., Fisk, Z., Smith, J.L., 1987. *J. Magn. Magn. Mater.* **63–64**, 372.
- Takahashi, T., Sato, N., Yokoya, T., Chainani, A., Morimoto, T., Komatsubara, T., 1995. *J. Phys. Soc. Jpn.* **65**, 156.
- Takegahara, K., Harima, H., Yanase, A., 2001. *J. Phys. Soc. Jpn.* **70**, 1190.
- Takeuchi, T., Inoue, T., Sugiyama, K., Aoki, D., Tokiwa, Y., Haga, Y., Kindo, K., Ōnuki, Y., 2001. *J. Phys. Soc. Jpn.* **70**, 877.
- Tateiwa, N., Kobayashi, T.C., Amaya, K., Haga, Y., Settai, R., Ōnuki, Y., 2003. *Acta Phys. Pol. B* **34**, 515.
- Tateiwa, N., Sato, N., Komatsubara, T., 1998. *Phys. Rev. B* **58**, 11131.
- Tautz, F.S., Julian, S.R., McMullen, G.J., Lonzarich, G.G., 1995. *Physica B* **206–207**, 29.
- Tayama, T., Sakakibara, T., Sugawara, H., Aoki, Y., Sato, H., 2003. *J. Phys. Soc. Jpn.* **72**, 1516.
- Thalmeier, P., 1991. *Phys. Rev. B* **44**, 7120.
- Thalmeier, P., 1994. *Z. Phys. B* **95**, 39.
- Thalmeier, P., 1996. *Z. Phys. B* **100**, 387.
- Thalmeier, P., 2002. *Eur. Phys. J. B* **27**, 29.
- Thalmeier, P., Lüthi, B., 1991. In: *Handbook on the Physics and Chemistry of Rare Earths*, vol. **14**. North-Holland, Amsterdam, p. 225, chapter 96.
- Thalmeier, P., Maki, K., 2002. *Europhys. Lett.* **58**, 119.
- Thalmeier, P., Maki, K., 2003a. *Phys. Rev. B* **67**, 092510.
- Thalmeier, P., Maki, K., 2003b. *Acta Phys. Pol. B* **34**, 557.
- Thalmeier, P., Wolf, B., Weber, D., Bruls, G., Lüthi, B., Menovskiy, A.A., 1991. *Physica C* **175**, 61.
- Thompson, J.D., Movshovich, R., Fisk, Z., Bouquet, F., Curro, N.J., Fisher, R.A., Hammel, P.C., Hegger, H., Hundley, M.F., Jaime, M., Pagliuso, P.G., Petrovic, C., Phillips, N.E., Sarrao, J.L., 2001. *J. Magn. Magn. Mater.* **226–230**, 5.
- Tou, H., Ishida, K., Kitaoka, Y., 2003. *cond-mat/0308562*.
- Tou, H., Kitaoka, Y., Asayama, K., Geibel, C., Schank, C., Steglich, F., 1995. *J. Phys. Soc. Jpn.* **64**, 725.
- Tou, H., Kitaoka, Y., Ishida, K., Asayama, K., Kimura, N., Ōnuki, Y., Yamamoto, E., Haga, Y., Maezawa, K., 1998. *Phys. Rev. Lett.* **80**, 3129.
- Tou, H., Kitaoka, Y., Kimura, N., Ōnuki, Y., Yamamoto, E., Maezawa, K., 1996. *Phys. Rev. Lett.* **77**, 1374.
- Trappmann, T., von Löhneysen, H., Taillefer, L., 1991. *Phys. Rev. B* **43**, 13714.
- Tsuei, C.C., Kirtley, J.R., 2000. *Rev. Mod. Phys.* **72**, 969.
- Tsuneto, T., 1961. *Phys. Rev.* **121**, 406.
- Ueda, K., Rice, T.M., 1985. *Phys. Rev. B* **31**, 7114.
- Valls, O.T., Tešanović, Z., 1984. *Phys. Rev. Lett.* **53**, 1497.
- van Dijk, N.H., 1994. *Dilatometry of heavy-fermion superconductors*, PhD thesis, Universiteit van Amsterdam.

- van Dijk, N.H., de Visser, A., Franse, J.J.M., Holtmeier, S., Taillefer, L., Flouquet, J., 1993. *Physica B* **186–188**, 267.
- van Dijk, N.H., Fak, B., Charvolin, T., Lejay, P., Mignot, J.-M., 2000. *Phys. Rev. B* **61**, 8922.
- van Harlingen, D.J., 1995. *Rev. Mod. Phys.* **67**, 515.
- Varelogiannis, G., Thalmeier, P., Tsonis, S., 2003. *cond-mat/0306106*.
- Vekhter, I., Hirschfeld, P.J., Nicol, E.J., 2001. *Phys. Rev. B* **64**, 064513.
- Virosztek, A., Maki, K., Dóra, B., 2002. *Int. J. Mod. Phys. B* **16**, 1667.
- Vollhardt, D., Wölfe, P., 1990. *The Superfluid Phases of ^3He* . Taylor and Francis, New York.
- Vollmer, R., Faißt, A., Pfeleiderer, C., von Löhneysen, H., Bauer, E.D., Ho, P.-C., Maple, M.B., 2003. *Phys. Rev. Lett.* **90**, 57001.
- Volovik, G.E., 1993. *JETP Lett.* **58**, 469.
- Volovik, G.E., Gorkov, L.P., 1985. *Sov. Phys. JETP* **61**, 843.
- von Löhneysen, H., 1994. *Physica B* **197**, 551.
- Walker, I.R., Grosche, F.M., Freye, D.M., Lonzarich, G.G., 1997. *Physica C* **282**, 303.
- Walker, M.B., Buyers, W.J.L., Tun, Z., Que, W., Menovsky, A.A., Garrett, J.D., 1993. *Phys. Rev. Lett.* **71**, 2630.
- Watanabe, S., Miyake, K., 2002. *J. Phys. Soc. Jpn.* **71**, 2489.
- Watanabe, T., Izawa, K., Kasahara, Y., Haga, Y., Ōnuki, Y., Thalmeier, P., Maki, K., Matsuda, Y., 2004. *cond-mat/0405211*.
- Watanabe, T., Nohara, M., Hanaguri, T., Takagi, H., 2003, submitted for publication.
- Weickert, F. et al., 2004, unpublished.
- White, R., Fulde, P., 1981. *Phys. Rev. Lett.* **47**, 1540.
- Wilson, K.G., 1975. *Rev. Mod. Phys.* **47**, 773.
- Winzer, K., Peng, Z., Krug, K., 1999. *Physica B* **259–261**, 586.
- Won, H., Maki, K., 1995. *Europhys. Lett.* **30**, 421.
- Won, H., Maki, K., 2000. *cond-mat/0004105*.
- Won, H., Maki, K., 2001a. *Europhys. Lett.* **56**, 729.
- Won, H., Maki, K., 2001b. *Vortices in Unconventional Superconductors and Superfluids*. Springer, Berlin.
- Won, H., Maki, K., Haas, S., Oeschler, N., Weickert, F., Gegenwart, P., 2004. *Phys. Rev. B* **69**, 180504.
- Won, H., Yuan, Q., Thalmeier, P., Maki, K., 2003. *Brazilian J. Phys.* **33**.
- Wu, W.C., Joynt, R., 2002. *Phys. Rev. B* **65**, 104502.
- Yanase, Y., Jujo, T., Nomura, T., Ikeda, H., Hotta, T., Yamada, K., 2003. *Phys. Reports* **387**, 1.
- Yang, G., Maki, K., 1999. *Europhys. Lett.* **48**, 208.
- Yang, G., Maki, K., 2001. *Eur. Phys. J. B* **21**, 61.
- Yang, X., Nayak, C., 2002. *Phys. Rev. B* **65**, 064523.
- Yaouanc, A., de Réotier, P.D., Gubbens, P.C.M., Kaiser, C.T., Menovsky, A.A., Mihalik, M., Cottrell, S.P., 2002. *Phys. Rev. Lett.* **89**, 147001.
- Yaresko, A., Thalmeier, P., 2004. *J. Magn. Magn. Mater.* **272–276**, e391.
- Yaron, U., Gammel, P.L., Ramirez, A.P., Huse, D.A., Bishop, D.J., Goldman, A.I., Stassis, C., Canfield, P.C., Mortensen, K., Eskildsen, M.R., 1996. *Nature* **382**, 236.
- Yip, S.-K., Li, T., Kumar, P., 1991. *Phys. Rev. B* **43**, 2742.
- Yokoyama, M., Amitsuka, H., Tenya, K., Watanabe, K., Kawarazaki, S., Yoshizawa, H., Mydosh, J.A., 2003. *cond-mat/0311199*.
- Yokoyama, M., Amitsuka, H., Watanabe, K., Kawarazaki, S., Yoshizawa, H., Mydosh, J.A., 2002. *J. Phys. Soc. Jpn.* **71** (Suppl.), 264.
- Yuan, Q., Chen, H.-Y., Won, H., Lee, S., Maki, K., Thalmeier, P., Ting, C.S., 2003. *Phys. Rev. B* **68**, 174510.
- Yuan, Q., Thalmeier, P., 2003. *Phys. Rev. B* **68**, 174501.
- Zheng, G.-Q., Tanabe, K., Mito, T., Kawasaki, S., Kitaoka, Y., Aoki, D., Haga, Y., Ōnuki, Y., 2001. *Phys. Rev. Lett.* **86**, 4664.
- Zvyagin, A.A., 2000. *Phys. Rev. B* **63**, 014503.
- Zwicknagl, G., 1988. *J. Magn. Magn. Mater.* **76–77**, 16.
- Zwicknagl, G., 1992. *Adv. Phys.* **41**, 203.
- Zwicknagl, G., 1993. *Phys. Scripta T* **49**, 34.
- Zwicknagl, G., 1999. *Physica B* **259–261**, 1105.
- Zwicknagl, G., Fulde, P., 1981. *Z. Phys. B* **43**, 23.
- Zwicknagl, G., Pulst, U., 1993. *Physica B* **186**, 895.
- Zwicknagl, G., Runge, E., Christensen, N.E., 1990. *Physica B* **163**, 97.
- Zwicknagl, G., Yaresko, A., Fulde, P., 2002. *Phys. Rev. B* **65**, 081103(R).
- Zwicknagl, G., Yaresko, A., Fulde, P., 2003. *Phys. Rev. B* **68**, 052508.

Chapter 220

CIRCULARLY POLARIZED LUMINESCENCE SPECTROSCOPY FROM LANTHANIDE SYSTEMS

James P. RIEHL

*Department of Chemistry, University of Minnesota Duluth,
1039 University Drive, Duluth, MN 55812-3020, USA*

Gilles MULLER

*Department of Chemistry, San Jose State University,
One Washington Square, San Jose, CA 95192-0101, USA*

Contents

List of symbols	290	3.1.2. Time-resolved CPL instrumentation	307
1. Introduction	291	3.2. Experimental and statistical limitations of CPL measurements	308
2. Theoretical aspects	292	3.3. Artifacts in CPL measurements	310
2.1. General theory	292	3.4. CPL calibration and standards	310
2.2. Circularly polarized luminescence from rigid samples: theory	293	4. Survey of recent experimental results (CPL)	311
2.3. Circularly Polarized Luminescence from solutions: theory	296	4.1. Lanthanide complexes with achiral ligands	311
2.4. CPL intensity calculations, selection rules, and spectra-structure correlations	298	4.1.1. CPL from racemic mixtures fol- lowing circularly polarized excita- tion	312
2.5. Circularly polarized luminescence from racemic mixtures: theory	300	4.1.1.1. Steady-state measurements	312
2.6. Theoretical aspects of time-resolved cir- cularly polarized luminescence	301	4.1.1.2. Racemization kinetics from CPL measurements	321
2.6.1. Time-resolved CPL from racemic mixtures: chemical racemization	301	4.1.1.3. CPL measurements in rigid sol-gels	322
2.6.2. Time-resolved CPL from racemic mixtures: excited state energy transfer	302	4.1.2. CPL from racemic mixtures: dif- ferential excited-state quenching	323
2.6.3. Time-resolved CPL from racemic mixtures: differential excited state quenching	302	4.1.3. CPL from racemic mixtures: per- turbation of the equilibrium	330
2.7. Circularly polarized luminescence from perturbed racemic equilibria	304	4.1.3.1. Perturbation of the racemic equilibrium as a structural probe	332
3. Experimental measurement	305	4.2. Lanthanide complexes with chiral ligands	333
3.1. CPL instrumentation	305	4.2.1. Chiral DOTA-based ligands	335
3.1.1. Steady-state CPL instrumentation	305	4.2.2. Chiral complexes with three-fold symmetry	341

4.2.3. Chiral complexes of low or no symmetry	343	5.1. Theoretical aspects	351
4.2.3.1. Mixed ligand systems.	346	5.2. MCPL experimental results from luminescent lanthanide systems	351
4.2.3.2. Other chiral mixtures.	348	6. Summary	353
4.3. CPL from Lanthanide (III) ions in biological systems	349	Acknowledgements	353
5. Magnetic Circularly Polarized Luminescence	350	References	354

List of symbols

\mathcal{A} , \mathcal{B} , and \mathcal{C}	Faraday terms in MCPL	M^{ng}	magnetic-dipole transition moment vector
b_0	external magnetic field strength		
B/τ	measure of the reduction of $g_{\text{lum}}^L(\lambda)$ due to energy transfer	MCPL	acronym for <i>Magnetic Circularly Polarized Luminescence</i>
CD	acronym for <i>Circular Dichroism</i>	n	emitting state
CPL	acronym for <i>Circularly Polarized Luminescence</i>	\mathcal{N} and \mathcal{g}	set of degenerate Zeeman levels
		N	total number of lanthanide complexes present
D^{gn}	dipole strength		
e	intermediate state	$N^L(t)$	total number of emitting molecules
$e^{A(t)}$	probability that an initial excitation of an A (or Δ) complex remains on an A (or Δ) molecule at time t	$N_L(\Delta)$	number of Δ enantiomers that absorb left circularly polarized light
		$N_R(\Delta)$	number of Δ enantiomers that would absorb right circularly polarized light
$f_\sigma(\lambda)$	normalized lineshape function		
f_{MCPL} and f'_{MCPL}	MCPL lineshape and its first derivative	$N_L(A)$	number of A enantiomers that would absorb left circularly polarized light
g	ground state		
g_{abs}	absorption dissymmetry ratio		
g_{lum}	luminescence dissymmetry ratio (or factor)	$N_n(\Omega, t)$	number of molecules in the emitting state $ n\rangle$ at time t
I	total emission intensity	$N_e^\pi(\Omega_0)$	electric dipole absorption
I_L	left circularly polarized light intensity	P^{gn}	electric-dipole transition moment vector
I_R	right circularly polarized light intensity	R	right circular polarization
		R^{gn}	rotatory (or rotational) strength
J	total angular momentum quantum number	t	time
		W_{gn}^σ	transition probability
k_0	excited state decay rate	ΔI	differential emission intensity
k_{rac}	racemization rate	ΔJ	change in angular momentum quantum number
$k_q^{\Delta Q}$ and $k_q^{A Q}$	diastereomeric bimolecular quenching rate constants	ΔN_L	differential population ($A - \Delta$) of excited enantiomers that would result from left circularly polarized excitation
L	left circular polarization		
m^{gn}	imaginary magnetic dipole transition moment	ΔW_{gn}	differential transition probability

ε_L	extinction coefficient for left circularly polarized light	λ'	excitation wavelength or absorption wavelength
ε_R	extinction coefficient for right circularly polarized light	μ^{gn}	electric dipole transition moment
η_n	fraction of molecules that end up in state $ n\rangle$	$\vec{\mu}^{\text{eg}}$	absorption transition vector
$\eta(\Omega, t)$	time dependence of the orientational distribution	π	state of linear polarization
η_g	enantiomeric excess in the ground state	σ	state of polarization
η_n	enantiomeric excess in the emitting state	σ_d	standard deviation
θ	twist angle between N_4 and O_4 planes	φ	PEM induced phase shift
λ	wavelength or emission wavelength	ϕ^{gn}	Angle between the electric-dipole ($ P_{\text{gn}} $) and magnetic-dipole ($ M_{\text{ng}} $) transition moment vectors
		ω	frequency of emission
		Ω	orientation
		Ω_0	orientation at the time of excitation ($t = 0$)

1. Introduction

The very first report of the detection of circular polarization in the emission of a chiral molecular system was by Samoilov in 1948 who was studying crystals of sodium uranyl acetate, $\text{Na}[\text{UO}_2(\text{CH}_3\text{COO})_3]$ (Samoilov, 1948). This species crystallizes in the $P2_13$ space group allowing for two enantiomeric forms, and the circular polarization is so large that it was easily detected with simple static optics. In the 1960s Professor Oosterhof and coworkers at the University of Leiden in The Netherlands published the first measurement from solution of the intrinsic circular polarization in the luminescence from a chiral organic molecule, namely, trans-b-hydrindanone, and from a resolved chiral transition metal complex, $[\text{Cr}(\text{ethylenediamine})_3]^{3-}$ (Emeis and Oosterhof, 1967, 1971). The extent of circular polarization from these systems is not nearly as large as the $\text{Na}[\text{UO}_2(\text{CH}_3\text{COO})_3]$ crystal, but advances in optics and electronics allowed for the detection of much smaller polarization values. In 1974, Luk and Richardson at the University of Virginia were the first to report the measurement of CPL from chiral complexes in solution containing a lanthanide ion (Luk and Richardson, 1974). It was quickly recognized that the luminescence from intraconfigurational $f \leftrightarrow f$ transitions of the lanthanide (III) ions that were magnetic-dipole allowed often showed very large circular polarization. Since the mid 1970s applications involving the measurement of circular polarization from molecular systems to chiral luminescent lanthanide complexes have dominated the use of this spectroscopic technique.

In this article we will refer to the measurement of the net circular polarization in the luminescence as *Circularly Polarized Luminescence* and use the acronym CPL. This is now the most widely used term to describe this spectroscopic technique, but in the older literature one finds circularly polarized emission (CPE), emission circular intensity differentials (ECID), or the somewhat more specific terms of circularly polarized fluorescence (CPF) or circularly

polarized phosphorescence (CPP). All of these terms refer to the spontaneous emission of circularly polarized light by chiral, or so-called "optically active" systems. A chiral molecule is one in which the mirror image isomers are not superimposable. From a molecular symmetry point of view, molecules belonging to point groups that do not contain mirror planes or an inversion center are chiral. All interactions involving light with chiral molecules discriminate between the two possible circular polarizations (left = L and right = R). In the absence of a perturbing static electric or magnetic field, the light emitted by a molecular chromophore will be partially circularly polarized only if the emitting species is chiral.

There have been several reviews published on the general use of CPL to study chiral molecular systems. Steinberg wrote the first review on CPL spectroscopy emphasizing applications to biochemical systems (Steinberg, 1975), and Richardson and Riehl published a review of CPL in 1977 (Richardson and Riehl, 1977) and an updated review in 1986 (Riehl and Richardson, 1986). Brittain published a review of the use of CPL to study chiral lanthanide complexes in 1989 (Brittain, 1989). Several other recent articles describing various general aspects of CPL measurements and CPL theoretical principles are also available (Riehl and Richardson, 1993; Riehl, 1993, 2000; Maupin and Riehl, 2000). In this article we will review the various applications of CPL to the study of lanthanide complexes, as well as provide an up-to-date assessment of the state of theory and instrumentation. We will emphasize both the qualitative and quantitative molecular information that has so far been obtained from this technique, and discuss the future of CPL as a reliable probe of the molecular stereochemistry of lanthanide complexes.

2. Theoretical aspects

2.1. General theory

In CPL spectroscopy one is interested in measuring the difference in the emission intensity (ΔI) of left circularly polarized light (I_L) versus right circularly polarized light (I_R). By convention this difference is defined as follows

$$\Delta I \equiv I_L - I_R. \quad (1)$$

Just as in ordinary luminescence measurements, the determination of absolute emission intensities is quite difficult, so it is customary to report CPL measurements in terms of the ratio of the difference in intensity, divided by the average total luminescence intensity

$$g_{\text{lum}} = \frac{\Delta I}{\frac{1}{2}I} = \frac{I_L - I_R}{\frac{1}{2}(I_L + I_R)}, \quad (2)$$

g_{lum} is referred to as the luminescence dissymmetry ratio (or factor). The extra factor of $\frac{1}{2}$ in eq. (2) is included to make the definition of g_{lum} consistent with the previous definition of the related quantity in circular dichroism, CD, namely, g_{abs}

$$g_{\text{abs}} = \frac{\Delta \varepsilon}{\varepsilon} = \frac{\varepsilon_L - \varepsilon_R}{\frac{1}{2}(\varepsilon_L + \varepsilon_R)}, \quad (3)$$

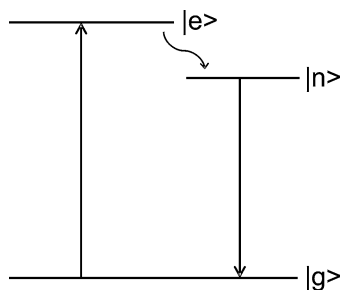


Fig. 1. Schematic energy level diagram for luminescence.

where in this equation ε_L and ε_R denote, respectively, the molar absorption coefficients for left and right circularly polarized light, and ε has always been explicitly defined as an average quantity.

We refer to the simple energy level diagram given in fig. 1. The time dependence of the intensity of emitted light of polarization σ , at a particular wavelength, λ , for a specific transition $n \rightarrow g$ of a molecule with orientation Ω (in the laboratory frame) may be expressed in terms of the transition probability, W_{gn}^σ , as follows

$$I_\sigma(\lambda, t) = (\hbar c/\lambda) N_n(\Omega, t) W_{gn}^\sigma(\Omega) f_\sigma(\lambda), \quad (4)$$

where $N_n(\Omega, t)$ denotes the number of molecules in the emitting state $|n\rangle$ at time t , and $f_\sigma(\lambda)$ is a normalized lineshape function. The number of molecules in the emitting state with orientation Ω depends on the orientation at the time of excitation ($t = 0$) with respect to the polarization π and direction of the excitation beam

$$N_n(\Omega, t) = N_e^\pi(\Omega : \Omega_0, t) \eta_n, \quad (5)$$

η_n denotes the fraction of molecules that end up in state $|n\rangle$ that were initially prepared in the intermediate state $|e\rangle$ by the excitation beam. This quantity is assumed to be independent of orientation. We consider here only the two limiting cases for the orientational distribution; the so-called “frozen” limit appropriate for crystals, glasses, rigid sol-gels, and solutions of very high viscosity, or *isotropic* appropriate for most solution measurements where we assume that the orientational distribution of emitting species is random. No intermediate cases have been reported, since the long radiative lifetimes of the luminescent lanthanide ions usually ensures that, in solution, the emitting species have had sufficient time to scramble any initial photoselected orientational distribution.

2.2. Circularly polarized luminescence from rigid samples: theory

In the frozen limit we set $\Omega = \Omega_0$. The differential intensity of left minus right circularly polarized light may now be expressed as follows

$$\Delta I(\lambda, t) = (\hbar c/\lambda) N_n(\Omega_0, t) \Delta W_{gn}(\Omega_0) f_\sigma(\lambda), \quad (6)$$

where we have introduced the differential transition probability ΔW_{gn}

$$\Delta W_{gn}(\Omega_0) \equiv W_{gn}^L(\Omega_0) - W_{gn}^R(\Omega_0). \quad (7)$$

The probability of emitting a right or left circularly polarized photon may be related in the usual way to molecular transition matrix elements through Fermi's Golden Rule. Under the assumption that the emitted light is being detected in the laboratory **3** direction, and allowing for electric dipoles and magnetic dipoles in the expansion of the molecule-radiation interaction Hamiltonian we obtain the following expressions

$$W_{\text{gn}}^L(\Omega_0) = K(\lambda^3)[|\mu_1^{\text{gn}}|^2 + |\mu_2^{\text{gn}}|^2 + |m_1^{\text{gn}}|^2 + |m_2^{\text{gn}}|^2 - 2i(\mu_1^{\text{gn}}m_1^{\text{gn}} + \mu_2^{\text{gn}}m_2^{\text{gn}})], \quad (8)$$

$$W_{\text{gn}}^R(\Omega_0) = K(\lambda^3)[|\mu_1^{\text{gn}}|^2 + |\mu_2^{\text{gn}}|^2 + |m_1^{\text{gn}}|^2 + |m_2^{\text{gn}}|^2 + 2i(\mu_1^{\text{gn}}m_1^{\text{gn}} + \mu_2^{\text{gn}}m_2^{\text{gn}})], \quad (9)$$

where **1** and **2** refer to laboratory axes and the electric dipole transition moment, μ^{gn} , and the imaginary magnetic dipole transition moment m^{gn} are defined as follows

$$\begin{aligned} \mu_1^{\text{gn}} &\equiv \langle g|\mu_1|n\rangle, \\ m_1^{\text{gn}} &\equiv \langle g|m_1|n\rangle. \end{aligned} \quad (10)$$

The differential transition rate is, therefore,

$$\Delta W_{\text{gn}}(\Omega_0) = K(\lambda^3)[2i(\mu_1^{\text{gn}}m_1^{\text{gn}} + \mu_2^{\text{gn}}m_2^{\text{gn}})]. \quad (11)$$

The condition for this quantity to be non-zero is that the chromophore of interest must have a non-zero magnetic and electric transition dipole moment along the same molecular direction. In the absence of perturbing external fields, this is only true for molecules that are chiral. Expressions that include higher order multipole contributions to eqs. (8), (9), and (11) can be found in previous theoretical descriptions of CPL theory (Riehl and Richardson, 1976a, 1986).

The final connection between molecular properties and experimental observables requires knowledge of the orientational distribution of the emitting molecules with respect to the direction and polarization of the excitation light and the direction of detection, and the time dependence of this distribution. Substituting eq. (5) into eq. (6) we obtain the following general expression

$$\Delta I^\pi(\lambda, t) = \eta_n(\hbar c/\lambda)N_e^\pi(\Omega_0, t)\Delta W_{\text{gn}}(\Omega_0)f_{\text{CPL}}(\lambda). \quad (12)$$

Note that we have a superscript, π , to indicate the polarization of the excitation beam, and also added a subscript to the lineshape function. As indicated above all CPL measurements are made relative to the total luminescence intensity which we may express using similar formalism as

$$I^\pi(\lambda, t) = \eta_n(\hbar c/\lambda)N_e^\pi(\Omega_0, t)W_{\text{gn}}(\Omega_0)f_{\text{TL}}(\lambda) \quad (13)$$

and

$$W_{\text{gn}}(\Omega_0) = K(\lambda^3)[|\mu_1^{\text{gn}}|^2 + |\mu_2^{\text{gn}}|^2 + |m_1^{\text{gn}}|^2 + |m_2^{\text{gn}}|^2]. \quad (14)$$

Equations (12) and (13) along with the transition probabilities given in eqs. (11) and (14) may be substituted into eq. (2) in order to relate the molecular transition moments (in the lab frame!) to the observable, g_{lum} . In sect. 2.2 we discuss the orientational averaging necessary to relate the molecular to laboratory coordinate system for randomly oriented samples. We will

not continue with any more specific theoretical development of CPL from “frozen” solutions or crystals in this section, but finish this discussion with some consequences of the formulas presented above for CPL measurements from lanthanide ions.

In order to measure CPL from crystals, the crystal system must be at least uniaxial with the optic axis oriented along the direction of emission detection, so that circularly polarized luminescence may be propagated through the crystal without scattering which leads to depolarization. Of course, the other requirement is that the emitting complex must be chiral. As we will discuss in sect. 2.5, it is also possible to study *racemic* systems containing an equal number of opposite mirror image isomers (enantiomers), if one uses a circularly polarized excitation beam to generate a non-racemic excited (emitting) state. Obviously, the circularly polarized excitation beam also must propagate along a crystal axis in which the two orthogonal directions are equivalent. These requirements have severely limited the use of CPL to study crystalline materials.

We also note the complicated dependence of luminescence intensity on molecular orientation and polarization of the excitation beam as given by eqs. (12) and (14). For chromophores with well-defined transition directions, one needs to know the orientation and direction of the excitation beam relative to the direction of emission detection in order to fully describe, and perhaps, exploit the polarization dependence of the emission. The circular and linear polarization properties of absorption and emission transitions of individual crystal field transitions of lanthanide (III) ions in crystals have been used to help assign the symmetry of the initial and final states (Hopkins et al., 1998; Berry et al., 1988). Meskers et al. (1993) have also measured the linear polarization in the luminescence from $[\text{Eu}(2,6\text{-pyridine-dicarboxylate})_3]^{3-}$ in a viscous glycerol/water mixture where it was assumed that no reorientation occurred during the excited state lifetime of Eu(III). This complex has almost exact D_3 symmetry, so, for example, the luminescent crystal field components in the $^5D_0 \rightarrow ^7F_1$ transition have the polarization properties listed in table 1. In this complex, the C_3 -axis defines the molecular z -axis, so by using linearly polarized excitation at right angles to the direction of emission detection, a non-isotropic orientational distribution of excited complexes was generated. From the linear polarization of the luminescence, it was not only possible to identify the symmetry of the individual crystal field states, but it was also possible to estimate the percentage magnetic dipole and electric dipole character of the transitions. By knowing the direction of the $\pi \rightarrow \pi^*$ absorption of the pyridine ring, the angle that the aromatic plane made with the z -axis was also determined. This experiment was possible because of the high symmetry of the complex,

Table 1
Experimental and theoretical polarizations and assignment of the emissive $^5D_0 \rightarrow ^7F_1$ transition of $[\text{Eu}(\text{DPA})_3]^{3-}$ ^a

Free ion	Transition		Experimental p_{lum} (standard error < 0.01)		Theoretical p_{lum}	
	D_3	λ (nm)	$\lambda_{\text{exc}} = 465.8$ nm	$\lambda_{\text{exc}} = 290$ nm	μ_x, μ_y^b	μ_z^b
$^5D_0 \rightarrow ^7F_1$	$A_1 \rightarrow A_2$	590.0	+0.26	-0.07	+1/3	-1/2
	$A_1 \rightarrow E$	594.0	-0.10	+0.05	-1/7	+1/3

^aFrom reference (Meskers et al., 1993).

^bTransition moment in absorption.

and the simplicity (i.e. small J) of the Eu(III) states which results in this case in individual (i.e. non-overlapping) crystal field transitions.

The results presented in the previous paragraph demonstrate that it might be necessary in the study of CPL from lanthanides imbedded in frozen solutions or rigid matrices, to be concerned with the presence of a photoselected orientational distribution of emitting species that is not random, even if the ground state orientational distribution is random. The key result here is that different components of the emission transition vectors may contribute unequally to the observable, g_{lum} . In principle, this would allow one to investigate the chirality of molecular transitions along specific molecular directions, but to date this has not been exploited. In this case, there also may be a dependence on the magnitude of CPL on laboratory excitation and emission geometry, and, perhaps more importantly, the luminescence may also be partially linearly polarized. As discussed in sect. 3.3, it is experimentally difficult to measure circular polarization in the presence of linear polarization in the emission. It is often possible, however, to eliminate the effects of linear polarization by careful experimental design.

2.3. Circularly Polarized Luminescence from solutions: theory

We restrict the discussion here to the measurement of CPL from randomly oriented molecular samples such as occur in liquid solutions. Of course, as described above, even if the ground state distribution is randomly oriented (isotropic), the emitting state may not be, due to the photoselection of the emitting sample by the excitation beam. We will denote an averaged orientational distribution by brackets $\langle \dots \rangle$. Substitution of eqs. (5) and (11) into eq. (6), and allowing for an ensemble of orientations we obtain the following

$$\Delta I(\lambda, t) = \left(\frac{2i\hbar c\eta_n}{\lambda} \right) K(\lambda^3) \langle N_e^\pi(\Omega : \Omega_0, t) [\mu_1^{\text{gn}} m_1^{\text{gn}} + \mu_2^{\text{gn}} m_2^{\text{gn}}] \rangle f_\sigma(\lambda). \quad (15)$$

We may formally separate the time dependence of the orientational distribution, $\eta(\Omega, t)$, from the number of molecules excited at time $t = 0$ by an excitation pulse as follows

$$N_e^\pi(\Omega : \Omega_0, t) = N_e^\pi(\Omega_0) \eta(\Omega, t). \quad (16)$$

Assuming electric dipole absorption, $N_e^\pi(\Omega_0)$ may be calculated from knowledge of the initial distribution, and direction and polarization of the excitation beam

$$N_e^\pi(\Omega_0) = \kappa^2 |\vec{\mu}^{\text{eg}} \cdot \vec{\pi}|^2 \quad (17)$$

where $\vec{\mu}^{\text{eg}}$ is the absorption transition vector. Final expressions for the formal relationship between the time-dependent circularly polarized luminescence intensity or g_{lum} require knowledge of experimental geometry, and $\eta(\Omega, t)$.

For purposes of illustration, we examine here the most common situation of random (isotropic) ground state distributions, and 90° excitation/emission geometry with unpolarized excitation. If the emission is detected in the laboratory $\mathbf{3}$ direction, then the excitation is polarized in the $\mathbf{13}$ plane. Equation (17) may then be written as

$$N_e^\pi(\Omega_0) = \kappa^2 [|\mu_1^{\text{eg}}|^2 + |\mu_3^{\text{eg}}|^2] \quad (18)$$

and the final formal expression is obtained by substituting this result into eq. (15).

$$\Delta I(\lambda, t) = \left(\frac{2i\hbar c\eta_n\kappa^2}{\lambda} \right) K(\lambda^3) \left([|\mu_1^{\text{eg}}|^2 + |\mu_3^{\text{eg}}|^2]_0 [\mu_1^{\text{gn}} m_1^{\text{gn}} + \mu_2^{\text{gn}} m_2^{\text{gn}}]_i \eta(\Omega, t) \right) f_\sigma(\lambda). \quad (19)$$

This equation is written, of course, in the laboratory coordinate frame, and the orientational average requires knowledge of the absorption and emission transition dipole directions in the molecular coordinate system. The average may be evaluated through the use of Euler matrix terms in the standard manner (Riehl and Richardson, 1976a). The reader is referred to previous publications in which various excitation emission geometries and molecular transition moments have been evaluated (Riehl and Richardson, 1976a, 1986).

Since the emission lifetimes of the luminescent lanthanide (III) ions are normally long (μsec to msec), it is appropriate to assume that in solution the orientational distribution of emitting species is completely random. In this case, the orientational average in eq. (19) reduces to the following “isotropic” limit.

$$g_{\text{lum}}(\lambda) = 4i \frac{f_{\text{CPL}}(\lambda)}{f_{\text{TL}}(\lambda)} \left[\frac{\vec{\mu}^{\text{gn}} \cdot \vec{m}^{\text{gn}}}{|\vec{\mu}^{\text{gn}}|^2} \right]. \quad (20)$$

We note again that the magnetic dipole operator is pure imaginary, and the multiplication by i results in a *real* value. In the denominator of eq. (20) we have also neglected the magnetic dipole transition moments in eq. (14) compared to the usually larger electric dipole moments. This equation is sometimes written as

$$g_{\text{lum}}(\lambda) = 4 \frac{f_{\text{CPL}}(\lambda)}{f_{\text{TL}}(\lambda)} \left[\frac{\text{Im}(\vec{\mu}^{\text{gn}} \cdot \vec{m}^{\text{gn}})}{|\vec{\mu}^{\text{gn}}|^2} \right]. \quad (21)$$

Often the imaginary nature of this quantity is simply ignored or omitted. In some applications the complete numerator and denominator of eq. (21) are integrated over a “band”, and results are reported in terms of the ratio, G_{lum} , of an integrated rotatory (or rotational) strength R^{gn} and dipole strength, D^{gn} .

$$G_{\text{lum}} = \frac{4R^{\text{gn}}}{D^{\text{gn}}} = \frac{4 \int_{\text{band}} f_{\text{CPL}}(\omega) \text{Re}(\vec{\mu}^{\text{gn}} \cdot \vec{m}^{\text{gn}}) \omega^{-4} d\omega}{\int_{\text{band}} f_{\text{TL}}(\omega) |\vec{\mu}^{\text{gn}}|^2 \omega^{-4} d\omega}, \quad (22)$$

where we have converted these equations to frequency (or energy), and we note that all of the multiplicative factors except for the frequency (or wavelength) dependence divide out. For the usually very sharp transitions seen for lanthanide (III) complexes, this integration over a band is seldom performed.

One final simplification is the assumption that the lineshapes for total luminescence and circularly polarized luminescence are identical. This is appropriate for the usually sharp isolated pure electronic transitions that are often the target of CPL measurements. In this case we rewrite eq. (21) as follows

$$g_{\text{lum}}(\lambda) = 4 \left[\frac{\text{Re}(\vec{\mu}^{\text{gn}} \cdot \vec{m}^{\text{gn}})}{|\vec{\mu}^{\text{gn}}|^2} \right] = 2 \frac{\Delta I(\lambda)}{I(\lambda)} \quad (23)$$

and make the final connection between theory and experiment.

2.4. CPL intensity calculations, selection rules, and spectra-structure correlations

Although there have been a number of reports of the calculation of CPL (and CD) intensities for various lanthanide complexes using the formalism presented above, it is not yet the case that the sign and magnitude of the differential emission or absorption of a chiral complex can be calculated reliably from knowledge of structure only. There have been a number of publications in which a parametric model has been used to match experimentally determined energy levels, and dipole and rotatory strengths on lanthanide complexes with D_3 symmetry (May et al., 1987, 1992; Berry et al., 1988; Moran and Richardson, 1992; Hopkins et al., 1996). Overall these model calculations have been fairly successful in matching the experimental values; however, it is observed that the calculated rotatory strengths, in particular, are quite sensitive to the quality of the wavefunctions used in the simulation and modeling.

The form of eq. (23) leads to several general conclusions concerning CPL spectroscopy. Since allowed magnetic dipole transition moments are usually much smaller in magnitude than allowed electric dipole transition moments, it makes sense to study emissive transitions that are formally electric dipole forbidden, but magnetic dipole allowed. Intraconfigurational $f \leftrightarrow f$ transitions are, indeed, formally LaPorte (parity) forbidden, and transitions that satisfy the formal selection rules of $\Delta J = 0, \pm 1$ (except $0 \leftrightarrow 0$) are magnetic dipole allowed (Richardson, 1980). These transitions may pick up electric dipole intensity from admixture of the odd-parity $4f^{N-1}5d$ and $4f^{N-1}ng$ configurations, and odd-parity multipole-ligand interactions. Since the electric dipole intensity is in the denominator of eq. (23), a larger value will often be obtained for g_{lum} if the transition is weak. This is essentially the paradox of CPL (and CD) spectroscopy, namely, that g_{lum} may be quite large for magnetic dipole allowed transitions that are electric dipole forbidden, but these transitions have very low total intensity, and therefore are more difficult to measure. A list of selected magnetic-dipole allowed emissive transitions of the luminescent lanthanide (III) ions are given in table 2.

It is unfortunate that there is to date no generally applicable spectra-structure correlations for CPL measurements from lanthanide (III) complexes. However, the number of chiral lanthanide complexes with well-understood geometry and solution dynamics is increasing, al-

Table 2
Selected magnetic dipole allowed emissive transitions of the lanthanide (III) ions

Lanthanide (III) ion	Emission transition	Approximate wavelength
Sm(III)	$^4G_{5/2} \rightarrow ^6H_{7/2}$	580 nm
	$^4G_{5/2} \rightarrow ^6H_{5/2}$	560 nm
Eu(III)	$^5D_0 \rightarrow ^7F_1$	590 nm
Gd(III)	$^8S_{7/2} \rightarrow ^6P_{7/2}$	312 nm
Tb(III)	$^5D_4 \rightarrow ^7F_3$	625 nm
	$^5D_4 \rightarrow ^7F_4$	580 nm
	$^5D_4 \rightarrow ^7F_5$	540 nm
Dy(III)	$^4F_{9/2} \rightarrow ^6H_{11/2}$	650 nm
Yb(III)	$^2F_{5/2} \rightarrow ^2F_{7/2}$	980 nm

lowing for considerable progress in relating structural or solvent characteristics to CPL measurements. In particular, Bruce et al. have analyzed and correlated the magnitude of CPL from Eu(III) complexes with C_4 symmetry, and related the magnitude of CPL to the polarizability of axial ligands and to the internal square antiprism twist angle (Bruce et al., 2002).

It is, in fact, for the higher symmetry lanthanide complexes that one would expect to find some reliable correlation between absolute stereochemistry and the CPL spectrum. Hilmes and Riehl were able to measure the CPL and CD for a number of transitions of the nine coordinate tris-terdentate complex of Eu(III) with 2,6-pyridine-dicarboxylate (dipicolinic acid \equiv DPA) through perturbation of a racemic equilibrium by added chiral agents, or by the use of circularly polarized excitation (see sect. 2.5) (Hilmes et al., 1988; Hilmes and Riehl, 1986). This complex is known to possess D_3 symmetry in the solid, and presumably in aqueous solution. They compared their results to those of Morley et al. (1982c) and Sen et al. (1981) who measured, respectively, the CPL, and CD of a particular chiral crystal of $\text{Na}_3\text{Eu}(\text{oxydiacetate} \equiv \text{ODA})_3 \cdot 2\text{NaClO}_4 \cdot 6\text{H}_2\text{O}$ which was determined by X-ray crystallography to have a Δ -configuration around the central Eu(III) ion. [A Δ -configuration is defined such that if the complex is viewed along the principal C_3 axis, the coordinated ligands are clockwise oriented as they go away from the observer.] A summary of the spectroscopic results are given in table 3. Çoruh et al. (1988b) noted that the signs of all the magnetic dipole transitions for $[\text{Eu}(\text{DPA})_3]^{3-}$ were uniformly opposite to those of $[\text{Eu}(\text{ODA})_3]^{3-}$, and the magnitudes were similar. They concluded that the complex that they were examining had the Λ -configuration. This conclusion has not as yet been verified with other Eu(III) complexes with local D_3 symmetry. As described in sect. 4.1.3.1, other much more empirical correlations of the sign of the observed CPL to various aspects of molecular structure have been attempted without much success.

Table 3

Absorption (g_{abs}) and luminescence (g_{lum}) dissymmetry ratios for selected transitions of a chiral crystal of $\Delta\text{-Na}_3[\text{Eu}(\text{ODA})_3] \cdot 2\text{NaClO}_4 \cdot 6\text{H}_2\text{O}^a$

Absorption		Emission	
Transition	g_{abs}	Transition	g_{lum}
$^5D_0 \leftarrow ^7F_0$	not observed	$^5D_0 \rightarrow ^7F_0$	not observed
$^5D_1 \leftarrow ^7F_0$	-4.60×10^{-1}	$^5D_0 \rightarrow ^7F_1$	-1.44×10^{-1}
$^5D_2 \leftarrow ^7F_0$	(a) -6.60×10^{-2} (b) -1.00×10^{-2}	$^5D_0 \rightarrow ^7F_2$	-3.30×10^{-2} (b) no CPL detected
$^5D_0 \leftarrow ^7F_1$	-1.70×10^{-1}	$^5D_0 \rightarrow ^7F_3$	(a) -1.10×10^{-1} (b) -1.05×10^{-1}
$^5D_1 \leftarrow ^7F_1$	large negative	$^5D_0 \rightarrow ^7F_4$	(a) $+2.10 \times 10^{-2}$ (b) $+1.50 \times 10^{-2}$
$^5D_2 \leftarrow ^7F_1$	(a) large negative (b) large negative		

^aFrom references (Morley et al., 1982c) and (Sen et al., 1981).

2.5. Circularly polarized luminescence from racemic mixtures: theory

One of the most useful applications of CPL spectroscopy has been in the study of racemic mixtures (Hilmes and Riehl, 1983). This experiment is possible, because, even though the ground state is racemic, i.e. equal concentrations of the two possible enantiomeric structures, the emitting state can sometimes be photoprepared in a significantly enantiomerically enriched state (non-racemic) by differential absorption of circularly polarized excitation. If the racemization (interconversion) rate of the excited state is less than the emission rate, then the emission will be circularly polarized. We consider a racemic sample containing equal concentrations of Λ and Δ enantiomers. The preferential absorption of circularly polarized light is related to the CD through the absorption dissymmetry ratio g_{abs} which was defined in eq. (3). Rewriting this equation for the CD of the Δ enantiomer we obtain the following

$$g_{\text{abs}}^{\Delta} = \frac{\Delta\varepsilon}{\varepsilon} = \frac{\varepsilon_L(\Delta) - \varepsilon_R(\Delta)}{\frac{1}{2}(\varepsilon_L(\Delta) + \varepsilon_R(\Delta))}. \quad (24)$$

The number of Δ enantiomers that absorb left circularly polarized light, $N_L(\Delta)$ is proportional to $\varepsilon_L(\Delta)$, and similarly for $\varepsilon_R(\Delta)$. Thus, we may make the following substitution

$$g_{\text{abs}}^{\Delta} = \frac{N_L(\Delta) - N_R(\Delta)}{\frac{1}{2}(N_L(\Delta) + N_R(\Delta))} \quad (25)$$

since all of the proportionality constants cancel. The number of Δ enantiomers that would absorb right circularly polarized light is exactly equal to the number of Λ enantiomers that would absorb left circularly polarized light, i.e. $N_R(\Delta) = N_L(\Lambda)$. This substitution yields the following

$$g_{\text{abs}}^{\Delta} = \frac{N_L(\Delta) - N_L(\Lambda)}{\frac{1}{2}[N_L(\Delta) + N_L(\Lambda)]} = \frac{2\Delta N_L}{N_L}. \quad (26)$$

ΔN_L is the differential population ($\Lambda - \Delta$) of excited enantiomers that would result from left circularly polarized excitation.

In general, an exact description of CPL from racemic mixtures requires consideration of the competition between racemization and emission (Hilmes and Riehl, 1983). Under the assumption that racemization is much slower than emission, we may write the following expression for CPL from a racemic mixture under left circularly polarized excitation as follows

$$g_{\text{lum}}^L(\lambda) = 4i \frac{f_{\text{CPL}}(\lambda)\Delta N_L}{f_{\text{TL}}(\lambda)N_L} \left[\frac{\vec{\mu}^{\text{gn}}(\Lambda) \cdot \vec{m}^{\text{gn}}(\Lambda)}{|\vec{\mu}^{\text{gn}}(\Lambda)|^2} \right]. \quad (27)$$

Substituting from above we obtain the following expression

$$g_{\text{lum}}^L(\lambda) = \frac{1}{2} g_{\text{abs}}^{\Lambda}(\lambda') g_{\text{lum}}^{\Lambda}(\lambda), \quad (28)$$

where we have explicitly labeled the excitation wavelength as λ' . Examination of eq. (28) shows that the measurement of CPL from racemic mixtures depends on the product of the CD and CPL. Since the measurement of g_{lum} is generally limited to magnitudes greater than 10^{-4} , the magnitude of the intrinsic dissymmetry ratios must usually be greater than approximately

10^{-2} for this unique measurement to be feasible. Since $f \leftrightarrow f$ transitions that obey magnetic dipole selection rules often are associated with large dissymmetry ratios, both the excitation and emissive transition should involve these transitions if possible.

2.6. Theoretical aspects of time-resolved circularly polarized luminescence

The measurement of the time dependence of g_{lum} may be used to probe various chiral aspects of excited state energetics, molecular dynamics, and reaction kinetics. Although there are some time-dependent circular polarization effects due to molecular reorientations that parallel time-dependent linear polarization measurements, the most interesting studies are those that involve the time-dependence of intrinsic molecular chirality. For a sample containing one chiral luminescent lanthanide chromophore, it might be the case that there are processes that affect chirality occurring on the same time scale as emission that could be probed by time-dependent CPL. To date, however, there have been no reports of such studies, and all of the time-dependent CPL measurements have involved racemic mixtures.

2.6.1. Time-resolved CPL from racemic mixtures: chemical racemization

We consider again the case that a non-racemic excited state of a racemic mixture is generated by use of a circularly polarized excitation beam. Neglecting orientational effects, and assuming a concentration sufficiently dilute (< 0.01 M) that excited state energy transfer between enantiomers does not occur (Sokolnicki et al., 2002), we may derive the following expression for the time-dependence of the excited state population following an excitation pulse of left circularly polarized light

$$\Delta N^L(t) = \Delta N^L(0) \exp(-2k_{\text{rac}}t - k_0t), \quad (29)$$

where k_{rac} is the racemization rate and k_0 is the excited state decay rate. The total number of emitting molecules excited by left circularly polarized excitation decays as

$$N^L(t) = N^L(0) \exp(-k_0t). \quad (30)$$

Allowing for the time-dependence of the excited state population, we may substitute eqs. (29) and (30) into eq. (27), and express the time-dependence of the luminescence dissymmetry as follows

$$g_{\text{lum}}^L(t) = g_{\text{lum}}^L(0) \exp(-2k_{\text{rac}}t). \quad (31)$$

This technique has been used in a studies in which the decay of $g_{\text{lum}}^L(\lambda)$ has been analyzed to extract racemization rate constants (Metcalf et al., 1990c; Glover-Fischer et al., 1998; Metcalf et al., 1991).

It is also possible to extract dynamic information concerning racemization rates through measurement of steady-state CPL (Belair et al., 2000; Mondry et al., 1994). Again neglecting time-dependent orientational effects and excited state energy transfer, one may integrate eqs. (29) and (30) over long times and obtain the following result

$$g_{\text{lum}}^L(\lambda) = \frac{1}{2} g_{\text{abs}}^A(\lambda') g_{\text{lum}}^A(\lambda) \left(\frac{k_0}{2k_{\text{rac}} + k_0} \right). \quad (32)$$

This equation has the expected limiting behavior. If $k_{\text{rac}} \ll k_0$ then the result of eq. (28) is obtained, and if $k_{\text{rac}} \gg k_0$ then the magnitude of $g_{\text{lum}}^L(\lambda)$ becomes negligibly small.

2.6.2. Time-resolved CPL from racemic mixtures: excited state energy transfer

A complete description of CPL from racemic mixtures must include the possibility of excited state energy transfer. Transfer of energy between identical enantiomers, of course, has no effect on the excited state differential population, transfer between opposite enantiomers will decrease the excited state population and, therefore, $g_{\text{lum}}^L(\lambda)$. There have been several reports of CPL from lanthanide complexes dissolved in rigid sol-gels, that have been interpreted in terms of possible effects of excited state energy transfer on measured CPL (Huskowska et al., 2000; Sokolnicki et al., 2002, manuscript in preparation). These sol-gels are made by slow evaporation of dilute samples, but the final concentrations of lanthanide complexes are quite high, so that intermolecular energy transfer effects may be important. Assuming that structural racemization does not occur, Sokolnicki et al. (2002) showed that the differential excited state concentration may be expressed as

$$\Delta N_n(t) = \Delta N_n(0)e^{-k_0 t} e^{A(t)}, \quad (33)$$

where

$$A(t) = - \int_0^t N k_{et}(t) dt. \quad (34)$$

N is the total number of lanthanide complexes present, and $e^{A(t)}$ is the probability that an initial excitation of an Λ (or Δ) complex remains on an Λ (or Δ) molecule at time t . In the derivation of this result, it was also assumed that the energy transfer rate between identical enantiomers was the same as between opposite enantiomers. Determination of the form of $e^{A(t)}$ depends on the particular energy transfer mechanism, and various assumptions concerning intermolecular orientation and distances.

So far no one has interpreted any time-resolved results as being due to effects of diminishing of CPL due to energy transfer. The results that have appeared involved "steady-state" measurements. Substitution of eqs. (33) and (30) into eq. (27), and integrating over long times as above yields the following result

$$g_{\text{lum}}^L(\lambda) = \frac{1}{2} g_{\text{abs}}^{\Lambda}(\lambda') g_{\text{lum}}^{\Lambda}(\lambda) \int_0^{\infty} e^{-k_{em} t} e^{A(t)} dt = \frac{1}{2} g_{\text{abs}}^{\Lambda}(\lambda') g_{\text{lum}}^{\Lambda}(\lambda) B/\tau. \quad (35)$$

The term B/τ , which is defined by eq. (35), is a measure of the reduction of $g_{\text{lum}}^L(\lambda)$ due to energy transfer. This term is approximately zero if racemization due to energy transfer is fast compared to the emission lifetime, and equal to 1 if no racemization occurs due to excited state energy transfer.

2.6.3. Time-resolved CPL from racemic mixtures: differential excited state quenching

We consider here the schematic energy level diagram given in fig. 2. In this experiment an unpolarized or linearly polarized beam excites a racemic mixture to an emitting state. Since the

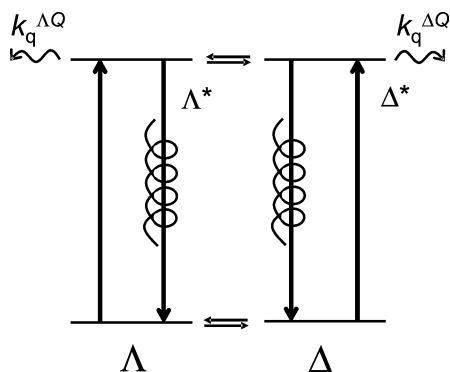


Fig. 2. Schematic energy level diagram showing enantioselective excited-state quenching of a racemic mixture.

excitation beam is not circularly polarized the initial concentration of the two excited enantiomers is equal, i.e. $[\Delta^*]_0 = [\Lambda^*]_0$. The solution under study also contains a chiral quencher molecule, Q , and the interaction of the quencher with the excited enantiomers is such that one of the enantiomers is quenched at a faster rate than the other. This, of course, results in an excited state that becomes increasingly chiral as time passes from an initial excitation pulse.

It is easy to show that the time-dependence of the excited state population of the two enantiomers may be expressed as (Metcalf et al., 1990a)

$$[\Delta^*](t) = [\Delta^*]_0 e^{-(k_0 + k_q^{\Delta Q})t}, \quad (36)$$

$$[\Lambda^*](t) = [\Lambda^*]_0 e^{-(k_0 + k_q^{\Lambda Q})t}, \quad (37)$$

where $k_q^{\Delta Q}$ and $k_q^{\Lambda Q}$ the *diastereomeric* bimolecular quenching rate constants. In this experiment we have two emitting species, thus we can write the following equation describing the time-dependence of the enantiomeric excess

$$\eta^*(t) = \frac{[\Lambda^*](t) - [\Delta^*](t)}{[\Lambda^*](t) + [\Delta^*](t)} \quad (38)$$

and substituting from eqs. (36) and (37) we obtain

$$\eta^*(t) = \frac{[\Lambda^*]_0 e^{-(k_0 + k_q^{\Lambda Q})t} - [\Delta^*]_0 e^{-(k_0 + k_q^{\Delta Q})t}}{[\Lambda^*]_0 e^{-(k_0 + k_q^{\Lambda Q})t} + [\Delta^*]_0 e^{-(k_0 + k_q^{\Delta Q})t}} \quad (39)$$

since $[\Delta^*]_0 = [\Lambda^*]_0$, after some cancellation we get

$$\eta^*(t) = \frac{e^{-k_q^{\Lambda Q}t} - e^{-k_q^{\Delta Q}t}}{e^{-k_q^{\Lambda Q}t} + e^{-k_q^{\Delta Q}t}} = \tanh\left(\frac{1}{2}k_d[Q]t\right), \quad (40)$$

where

$$k_d = k_q^{\Lambda Q} - k_q^{\Delta Q}. \quad (41)$$

In this case the time-dependence of g_{lum} is given through the time-dependence of the enantiomeric excess

$$g_{\text{lum}}(\lambda, t) = g_{\text{lum}}^{\Lambda}(\lambda)\eta^*(t) = g_{\text{lum}}^{\Lambda}(\lambda) \tanh\left(\frac{1}{2}k_d[Q]t\right). \quad (42)$$

Therefore, one may fit the time-dependence of g_{lum} to a hyperbolic tangent function to determine k_d . Note from the denominator of eq. (39), that, for this system, the total luminescence decay is described as a biexponential, and it is sometimes easier to determine the individual diastereomeric decay constants from a biexponential analysis.

Just as above, it is possible to determine the “steady-state” result for this differential quenching by integrating over long times. The final result is

$$g_{\text{lum}}(\lambda) = g_{\text{lum}}^{\Lambda} \frac{(k_q^{\Lambda Q} - k_q^{\Delta Q})[Q]}{2k_0(k_q^{\Lambda Q} + k_q^{\Delta Q})[Q]} \quad (43)$$

which again has the correct limiting result; if there is no difference in quenching rates, there will be no CPL observed.

2.7. Circularly polarized luminescence from perturbed racemic equilibria

The addition of chiral complexes to a solution containing a racemic mixture may lead to a perturbation of the ground state equilibrium without changing the local structure of the complexes involved. This perturbation, which is sometimes referred to as the “Pfeiffer effect” leads to an enantiomeric excess in the ground state, η_g , defined in analogy to eq. (38) as follows

$$\eta_g = \frac{[\Lambda] - [\Delta]}{[\Lambda] + [\Delta]}, \quad (44)$$

where the square brackets in this equation denote ground state concentrations. It is easy to see that the measured absorption or luminescence dissymmetry factors for a perturbed equilibrium may be related to the values that one would obtain if the solution contained a pure enantiomer by the following equations

$$g_{\text{abs}}(\lambda') = \eta_g g_{\text{abs}}^{\Lambda}(\lambda'), \quad (45)$$

$$g_{\text{lum}}(\lambda) = \eta_n g_{\text{lum}}^{\Lambda}(\lambda), \quad (46)$$

where we have introduced the symbol, η_n , to indicate the enantiomeric excess in the emitting state, and we explicitly denoted the absorption wavelength as λ' , and the emission wavelength as λ . In the absence of enantioselective excited state processes, one expects that the enantiomeric excess in the emitting and ground states are equal

$$\eta \equiv \eta_n = \eta_g. \quad (47)$$

Using this substitution in eqs. (45) and (46) and rewriting eq. (28) we have the following set of three equations with three unknowns

$$\begin{aligned} g_{\text{abs}}(\lambda') &= \eta g_{\text{abs}}^A(\lambda'), \\ g_{\text{lum}}(\lambda) &= \eta g_{\text{lum}}^A(\lambda), \\ g_{\text{lum}}^L(\lambda) &= \frac{1}{2} g_{\text{abs}}^A(\lambda') g_{\text{lum}}^A(\lambda). \end{aligned} \quad (48)$$

If one can measure the CD of a perturbed racemic solution at the same wavelength (λ') that one uses for circularly polarized excitation of a racemic mixture, and also measures the CPL of the perturbed racemic equilibrium at wavelength, λ , then one can not only determine the enantiomeric excess, but also the dissymmetry ratios of the pure enantiomeric complexes even if they can not be resolved. Application of this procedure is described in sect. 4.1.3.1.

3. Experimental measurement

3.1. CPL instrumentation

3.1.1. Steady-state CPL instrumentation

Unlike CD spectrometers, there are no commercial instruments available for the detection of CPL and, therefore, the research groups involved in this measurement over the last thirty have designed and built their own instruments (Brittain, 1991, 1989, 1997a, 1998, 2000; Riehl and Richardson, 1993, 1986; Schippers et al., 1982). All of these various custom-built instruments use the same basic optical design as described below, in which the circular polarizations are detected by conversion to linear polarization by a modulated quarter wave retarder/advancer. The earlier instruments used a lock-in amplifier to determine the extent of circular polarization in the emission, the more modern instruments use various methods of gated photon counting. Photon counting techniques have been shown to be much more stable, and not susceptible to the electronic problems (e.g., ground loops) associated with the small net signal usually seen in CPL spectroscopy.

To illustrate the basic design of a CPL spectrometer we present a short description of the CPL instrument used in our laboratory at the University of Minnesota Duluth. A schematic diagram for this instrument is illustrated in fig. 3. This instrument is designed to measure "steady-state" CPL. As can be seen in this figure, the source of excitation in this instrument is either a continuous wave (CW) dye laser (Coherent 599) pumped by a CW argon-ion laser (Coherent Innova 70-4), the argon-ion laser without the dye laser, or a CW 450 watt xenon arc lamp. In our experimental set-up, the laser beam is situated below the sample and emission light path, and is reflected through the sample quartz fluorescence cuvette with polished surfaces. In addition, the polarization of the laser beam is aligned along the direction of emission (laboratory **3** axis) so that the luminescence detected at 90° will not be linearly (**1** or **2**) polarized. The presence of linear polarization in the emission beam has been known to cause artifacts in the detection of circular polarization (see sect. 3.3). This precise experimental alignment is not important when the emission is isotropic, but it is extremely important for

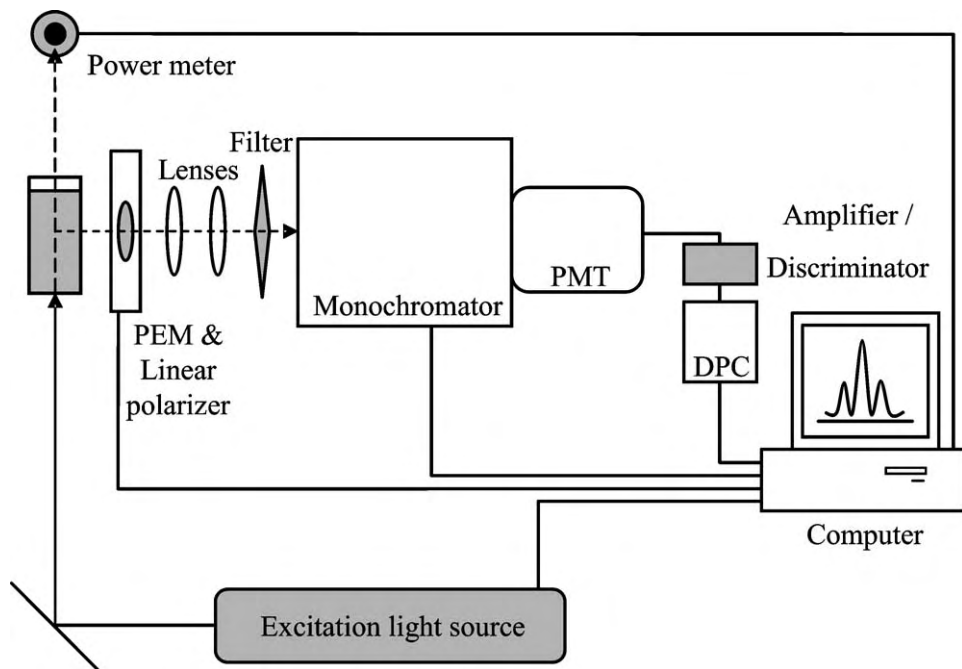


Fig. 3. Schematic diagram for instrumentation used to measure circularly polarized luminescence.

slowly rotating or oriented systems in which the emission could be linearly polarized (Field et al., 2003; Riehl and Richardson, 1986). It should be mentioned that the incident excitation beam may be linearly polarized, circularly polarized, or unpolarized, and that unpolarized or circularly polarized excitation at 90° may lead to linear polarization in the emission even if the ground state distribution of emitting species is isotropic.

The design of CPL instrumentation is based on an ordinary fluorescence instrument with the addition of a circular analyzer between the emitting sample and the emission monochromator. The circular analyzer is composed of a photo-elastic (or elasto-optic) modulator (PEM) followed by a high-quality linear polarizer. The PEM is composed of an isotropic clear optical material that becomes anisotropic on application of a periodic stress. PEMs that operate around 50 kHz are commercially available (Hinds Int., Eugene, OR) and in this application act as a dynamic quarter-wave polarization modulator. During one half-cycle of the modulation left circularly polarized light is converted to linearly polarized light which then passes through the linear polarizer, and then, during the other half-cycle, right circularly polarized light is passed on to the monochromator. Thus, the monochromator sees light with only one polarization throughout the modulator cycle, which is a necessity due to the polarization sensitivity of monochromators. In polarization-sensitive detection experiments it is obviously necessary to minimize sources of depolarization. Thus, for example, one normally places no optical elements between the sample compartment and the PEM. These precautions are es-

pecially important in CPL measurements owing to the fact that the difference in intensities between the left and right circularly polarized emitted light are 10 to 100 times less than that detected in linearly polarized luminescence measurements.

In order for the PEM to act as a quarter-wave device over the entire UV-visible spectral region, it must be driven at the appropriate amplitude corresponding to the detection wavelength by employing an inexpensive digital-to-analog (D/A) interface, and setting the appropriate voltage for the PEM controller. Another possibility may be by coupling the wavelength drive of the emission monochromator to the PEM controller. After passing through the PEM and linear polarizer, the emitted light travels through an appropriate filter to eliminate scattered excitation and other stray light, and a suitable lens is used to focus the beam onto the entrance slits of the emission monochromator. Detection is accomplished by a thermoelectrically cooled photomultiplier tube (PMT) operating in photon-counting mode. In the case of near-IR detection, a liquid N₂ cooled PMT is used. As shown in fig. 3, the output of the PMT can either be analyzed for a DC voltage which is a direct measurement of relative total luminescence in arbitrary units, or directed to an amplifier/discriminator which outputs photopulses to a custom-built differential photon counter (DPC). This latter was designed and constructed at the University of Leiden, The Netherlands, under the supervision of H.P.J.M. Dekkers (Schippers, 1982). In this case, the leading edge of the 50 kHz reference signal from the PEM controller is used to define a time window centered on the peak of the modulation reference signal. During the "open" time of this variable time window, photopulses are directed into two separate counters. One of the counters counts every pulse that passes through the time-window, and the other (up/down) counter adds the photo-pulses that enter the gate when left circularly polarized light is passing through the PEM and subtracts the pulses when right circularly polarized light intensity is being measured. Thus one counter contains a number proportional to I , and the other counter contains a number proportional to ΔI . These two quantities can be used to obtain g_{lum} (see eq. (2)). Perhaps the most difficult aspect of this gated-counter technique is the requirement that the time windows for left and right circular polarization detection must be positioned properly, have a high temporal resolution, and be exactly equal in width (Schippers, 1982). The computer used in this experimental setup monitors the DC voltage and differential photon count, steps the excitation and emission monochromators, and stores and displays g_{lum} values and total emission signals as a function of wavelength. These functions are accomplished using commercially available digital and analog input/output boards.

3.1.2. *Time-resolved CPL instrumentation*

The measurement of the time dependence of the emitted circular polarization is complicated by the inherent time variation of the PEM modulator, and the important requirement that the time windows corresponding to the detection of left and right circular polarization following a pulsed excitation be sampled equally. Blok et al. reported the modification of a commercial fluorescence spectrometer to measure time-dependent CPL (Blok et al., 1990). Metcalf et al. (1989) have briefly described their photon counting based time-resolved CPL instrumentation, and Rexwinkel et al. (1993c) have published a detailed account of their instrumentation in

which time resolution approaching nanoseconds could be obtained. An instrument using an analog detection system has also been described (Schauerte et al., 1995).

There have been two approaches to the sampling issue, one method is to ensure that the excitation pulses are positioned appropriately by coupling of the timing of the excitation pulse with the modulator cycle (Metcalf et al., 1989), the other is to have the excitation pulses occur randomly throughout the modulation cycle (Rexwinkel et al., 1993c; Blok et al., 1990). The photon counting detection system of Rexwinkel et al. (1993c) is composed of 2048 decay channels that are adjustable to time windows of 50 ns to 1 s. Just as described above, two counters associated with the total counts and differential counts are used, and the content of the counters are transferred into computer memory through high-speed direct memory access. The optical components of these instruments are essentially the same as the “steady-state” instrument described above.

3.2. Experimental and statistical limitations of CPL measurements

The use of photon-counting techniques in combination with sinusoidal variation of stress-induced polarization modulation imposes quantifiable limitations on the accuracy and precision of CPL measurements. We consider first the optical characteristics of the PEM. The phase difference (φ) between the two orthogonal crystal axes of the PEM is related to the sinusoidally varying periodic stress ($\sin \alpha t$) through the following Bessel function

$$\varphi = \sin(\sin \alpha t). \quad (49)$$

The stress modulation and polarization modulation are plotted in fig. 4. We also plot in this figure a square wave signal corresponding to a time-window (gate) equal to 50% of the half-period that would correspond to detection of left and right circularly polarized emitted photons. As one can see, only at the peaks of the modulation cycles is the PEM acting as an exactly quarter-wave advancing ($+90^\circ$) or retarding (-90° or $+270^\circ$) optical element. Clearly, the smaller the time-window, the more closely photons passing through the PEM are being properly selected, and the more accurate is the measurement. With a time-window corresponding to 50% of the modulation cycle, one is not counting 50% of the available photons, and reducing the time-window even smaller for more accurate measurements has obvious consequences, and makes the time for the measurement even longer.

Assuming perfect operating conditions, one can show that for a 50% window that the intrinsic error associated with the PEM in the measurement of g_{lum} is less than 3% (Kemp, 1969).

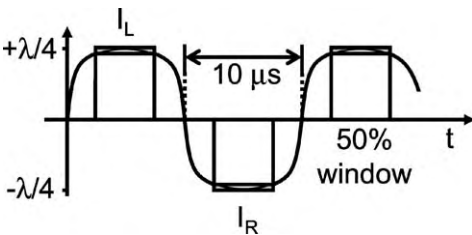


Fig. 4. Variation of applied stress and induced polarization modulation as a function of time. The square wave signal corresponds to a time-window equal to 50% of the half-period.

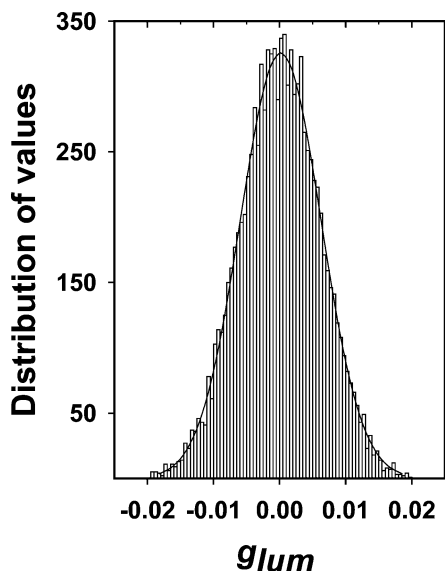


Fig. 5. The distribution of g_{lum} values obtained for 10,000 measurements from $[Eu(DPA)_3]^{3-}$ complex in aqueous solution.

For highly luminescent samples, the error may be reduced by decreasing the time-window (the error is approximately 1% for a 20% window) (Schippers and Dekkers, 1981), or one might be justified in simply “correcting” the value to account for this known effect. Obviously, there are other sources of error in polarization measurements of this type. The PEM itself is not a perfect optical element, and other elements including linear polarizers, sample containers, filters, mirrors, etc. all lead to sources of error. One also needs to consider the statistical nature of these measurements as described below, and, as a result, g_{lum} values obtained with 50% time-windows are usually presented as obtained without correction.

One of the principal advantages of the use of photon-counting methods over analog methods for detection and analysis of CPL is the statistical nature of these measurements. In fig. 5 we plot the distribution of g_{lum} results obtained for a sample measurement. Schippers has shown that the observed spread in g_{lum} values is what one expects from Poisson statistics (Schippers, 1982). The standard deviation, σ_d , of a particular measurement of g_{lum} in which a total of N photons were counted is as follows

$$\sigma_d = \sqrt{\frac{2}{N}}. \quad (50)$$

The data presented in fig. 5 is for 10,000 measurements of g_{lum} for $N = 1 \times 10^5$, thus we calculate a standard deviation of 4.5×10^{-3} which should be compared to the experimental σ_d of 6.1×10^{-3} . Obviously, if the instrument is working properly it is easy to determine the standard deviation for a particular measurement, or if a particular precision is required, the number of photons that must be counted may be predetermined.

Although selected transitions involving lanthanide (III) ions in chiral rigid complexes often exhibit large g_{lum} values, it is often the case that one is interested in studying racemic or

other types of mixtures, in which the circularly polarized component of the emitted light represents only a small fraction of the total emitted light intensity. The CPL spectrometers which have been constructed are able to determine g_{lum} with a sensitivity of approximately 1 part in 10^4 – 10^5 , depending on the total light intensity. From the discussion above, one can easily see that the time required for a CPL measurement is dependent on the intensity of luminescence of the system studied, and the “chirality” of the transition being analyzed. For example, using eq. (45), in order to measure g_{lum} with a standard deviation of 1×10^{-4} , a total of 2×10^8 photon pulses must be counted. As a consequence, accurate g_{lum} measurements can be achieved in a short time for highly luminescent systems for transitions associated with large g_{lum} values, while in the case of weakly luminescent samples with small g_{lum} values, a much longer collection time is required for the same percent error. These arguments, of course, pertain only to measurement at one wavelength. For measurement of a CPL spectrum, one must decide whether to collect data for approximately the same amount of time at each wavelength to present spectra in which the relative error at each wavelength point is the same, or to collect the same number of photon pulses at each wavelength so that the absolute error at each point is the same. This choice is usually accomplished in the controlling software.

3.3. *Artifacts in CPL measurements*

It has long been recognized that the main source of artifacts in CPL measurements is the passing of linearly polarized light through the very slightly birefringent PEM (Riehl and Richardson, 1986; Dekkers et al., 1985). Even though this birefringence is usually small ($< 5\%$), it may lead to a signal of comparable magnitude to many true CPL signals, since linear polarization is usually a much larger effect. Luminescence that is 10% linearly polarized may be converted by this effect to circular polarization of say 0.5%, which is often larger than the true signal.

Some success has been obtained in eliminating linear polarization effects by rotating the PEM and linear polarizer such that the birefringent axis of the PEM is parallel to the plane of polarization of the emitted light; however, it is our experience that one can only be confident of the accuracy of a CPL measurement by ensuring that the emitted light contains no linearly polarized component in the plane perpendicular to the emission direction. As described in sect. 3.1, one way of accomplishing this is to use a 90° excitation/emission geometry with a linearly polarized beam oriented parallel to the direction of emission detection. It is the case, however, that to date, no one has observed linear polarization in the luminescence from lanthanide (III) ions in ordinary solutions. This is due to the nature of the electronic transitions involved, and the fact that the lifetimes of the luminescent lanthanide ions are long, allowing for any initial photoselected orientational distribution to randomize in the time between excitation and emission.

3.4. *CPL calibration and standards*

In the analog detection of CPL, the differential emission intensity, ΔI , is assumed to be proportional to the output of the lock-in amplifier, and the total emission intensity, I , is proportional to a DC output voltage. These are generally independent measurements, so that a

Table 4

Signs and magnitudes of the g_{lum} values for several transitions of the CPL standard tris(3-trifluoroacetyl-d-camphorato)europium(III) complex, $[\text{Eu}(\text{facam})_3]$, in anhydrous DMSO^a

Emission transition	Approximate wavelength	g_{lum} value
$^5\text{D}_0 \rightarrow ^7\text{F}_1$	588.24 nm	-0.25
$^5\text{D}_0 \rightarrow ^7\text{F}_1$	595.24 nm	-0.78
$^5\text{D}_0 \rightarrow ^7\text{F}_2$	613.50 nm	+0.072

^aFrom reference (Schippers, 1982).

determination of g_{lum} requires the use of a calibration standard. One of the main advantages of the photon counting method is that g_{lum} is determined directly, so that, in principal, no independent calibration is necessary.

It is obviously important that one be sure that the magnitude and sign of the CPL signal are being measured accurately. Although there have been efforts at standardization and calibration using variable quarter-wave plates (Steinberg and Gafni, 1972), or passing unpolarized light through solutions of known CD (Barnett et al., 1979), the most common approach is to use a solution containing a chiral species of known CPL. Brittain was the first to suggest the use of the commercially available NMR chiral shift reagent tris(3-trifluoroacetyl-d-camphorato)europium (III), $\text{Eu}(\text{facam})_3$, as a CPL standard (Brittain, 1980). This complex is available in high purity, is readily soluble in DMSO, and may be excited either by a UV source around 350 nm or Ar-ion laser excitation at 345 nm. This complex has also been used by Schippers (1982), and the results reported in this reference are reproduced in table 4. As can be seen, three different Eu(III) transitions are observed with variable signs and magnitudes. It should be noted that Maupin has noted that the chirality of lanthanide facam complexes in DMSO are quite sensitive to the presence of water, so that care should be taken to ensure dry complex and dry solvent when using this species as a CPL standard (Maupin, 1999).

4. Survey of recent experimental results (CPL)

Since the last complete review of CPL spectroscopy (Riehl and Richardson, 1986) there have been approximately 150 articles published involving this technique with the vast majority being concerned with lanthanide (III) ions. In this section we will review the various types of applications of CPL to the study of the molecular and electronic structure of chiral systems containing lanthanide ions. We will attempt to be as complete as possible concerning work appearing since this last full review, but we will also include some of the earlier work in order to put some of the more recent results in context.

4.1. Lanthanide complexes with achiral ligands

In order for a luminescent lanthanide (III) ion to emit circularly polarized light, it must be in a chiral environment. In sect. 4.2 we will describe CPL measurements in which the chirality is due to the chirality induced in lanthanide (III) coordination due to the fact that the ligands

surrounding the lanthanide ion are themselves chiral. In this section we describe studies involving lanthanide complexes with ligands that are *not* chiral (*achiral*). If one mixes together non-chiral ligands with lanthanide ions which, of course, are not chiral, then the solution or solid that is formed can have no net chirality. As we will see below, however, the complexes that are formed may be of such a symmetry that mixtures are formed of opposite chirality. If a pair of molecular species are formed in equal concentration that are mirror images of each, the solution is said to be racemic, i.e. it contains a racemic mixture of enantiomers. This system has no optical rotation, no circular dichroism, and no CPL, unless one is able to generate an enantio-enriched population through some chemical or optical technique.

The simplest way to prepare the enantiomers for chiroptical study would be to physically separate the species through recrystallization or other classical chemical separation techniques. This is a well known process for racemic transition metal complexes. Enantiomeric complexes can be prepared, separated, and solutions of individual enantiomers studied by the various chiroptical techniques. This is much more problematic for lanthanide complexes, since the ligands are generally very labile. The first CPL results for a chiral complex of a luminescent lanthanide ion containing achiral ligands that has been resolved and studied in solution has just been reported (Cantuel et al., 2004). The much more common situation is the generation of enantioenriched excited states from racemic mixtures either by employing circularly polarized excitation, enantioselective quenching, or perturbation of a ground state equilibrium through the addition of chiral agents. These experiments are described in the next sections.

4.1.1. CPL from racemic mixtures following circularly polarized excitation

4.1.1.1. *Steady-state measurements.* As presented in sect. 2.6.1, CPL spectroscopy has been shown to be a particularly useful technique for studying chiral lanthanide complexes that occur in solution as racemic mixtures, but do not completely interconvert during the emitting state lifetime. The use of a left circularly polarized excitation beam results in a preferential excitation of one of the two possible enantiomers over the other. Excitation with right circularly polarized light gives the exactly opposite effect. This experiment relies upon differential absorption to generate a non-racemic excited state, so that if possible one should excite the species of interest at a wavelength corresponding to a magnetic-dipole allowed transition. A list of selected magnetic-dipole allowed absorptions of the luminescent lanthanides are given in table 5. In table 6 we list the racemic lanthanide complexes for which CPL has been reported either through circularly polarized excitation, or by perturbation of the ground state equilibrium.

Perhaps, the best example of this kind of experimental study are the numerous reports involving the 9-coordinate complex of lanthanide (III) ions with 2,6-pyridine-dicarboxylate = dipicolinic acid = DPA. These complexes are known to possess almost exact D_3 symmetry, and as such occur in solution as racemic mixtures of complexes with Λ and Δ helicity. It has been demonstrated that the CPL lineshape and the magnitude of the luminescence dissymmetry ratios, $g_{\text{lum}}(\lambda)$, of a 3.5:1 mixture of dipicolinic acid (DPA) to Tb(III) in aqueous solution excited with circularly polarized light were independent of pH in the range 7.0–8.8, additional ligand, or upon a 4-fold dilution (Hilmes et al., 1985;

Table 5
Selected magnetic dipole allowed absorptions of the luminescent lanthanide (III) ions

Lanthanide (III) ion	Absorption transition	Approximate wavelength
Nd(III)	$^4G_{7/2} \leftarrow ^4I_{9/2}$	526 nm
	$^4G_{9/2} \leftarrow ^4I_{9/2}$	514 nm
	$^4G_{11/2} \leftarrow ^4I_{9/2}$	465 nm
Sm(III)	$^4G_{5/2} \leftarrow ^6H_{5/2}$	560 nm
Eu(III)	$^5D_1 \leftarrow ^7F_0$	526 nm
	$^5D_1 \leftarrow ^7F_1$	535 nm
	$^5D_1 \leftarrow ^7F_2$	557 nm
	$^5D_2 \leftarrow ^7F_2$	488 nm
	$^5D_2 \leftarrow ^7F_1$	472 nm
Dy(III)	$^4I_{15/2} \leftarrow ^6H_{15/2}$	457 nm
Yb(III)	$^2F_{5/2} \leftarrow ^2F_{7/2}$	980 nm

Hilmes and Riehl, 1986). This study, which was the first example of CPL from a racemic 9-coordinate tris lanthanide complex, namely $[Tb(DPA)_3]^{3-}$, showed that an optically active species was indeed formed in aqueous solution, and was not labile on the time scale of Tb(III) emission from the 5D_4 excited state (~ 4 msec). This result may be explained by the high stability of the complexes formed between Tb(III) ion and DPA ligands. The observation of a CPL signal from complexes of DPA with Eu(III), Dy(III), or Sm(III) has also been reported, while for the Pr(III) complex, the lack of sufficient CD at the excitation wavelength is probably responsible for the absence of any measurable CPL signal.

CPL following circularly polarized excitation has also been observed for lanthanide (III) complexes with chelidamic acid (CDA) (Metcalf et al., 1990b), and oxydiacetic acid (ODA) (Hilmes and Riehl, 1986) when the metal:ligand ratio was greater than 1:3, but not for complexes with iminodiacetic acid (IDA) (Hilmes and Riehl, 1986). By analogy with $[Eu(DPA)_3]^{3-}$, the chiroptical measurements from $[Eu(CDA)_3]^{6-}$ complexes demonstrated that this species also exists as a racemic mixture of structural enantiomers, Δ - $[Eu(CDA)_3]^{6-}$ and Λ - $[Eu(CDA)_3]^{6-}$ in basic aqueous solution that do not racemize on the emission lifetime. The lack of measurable CPL in the case of the complexes with IDA may be explained by facial coordination of the ligands to the metal ion in the tri-capped trigonal prism geometry, resulting in *achiral* C_{3v} symmetry, instead of the meridional geometry observed for DPA and ODA that gives D_3 symmetry. Although CPL has been observed for $[Dy(ODA)_3]^{3-}$, no CPL was detected in aqueous solution for ODA complexes with Eu(III), Tb(III), or Sm(III) even though these species are known to possess D_3 symmetry in the solid state (Albertsson and Elding, 1977). These types of experiments are successful only if the differential excited state population is maintained during the excited state lifetime. Indeed, for the ODA complexes, Dy(III) has the shortest lived emitting state (approximately 0.07 ms in D_2O), while for the Sm(III) and Eu(III) compounds, the lifetime is longer by a factor of 2 and 14, respectively. Thus these results have been interpreted in terms of complete racemization of all of the complexes except $[Dy(ODA)_3]^{3-}$. It must be noted that it might be the case that the solution structure of the

Table 6

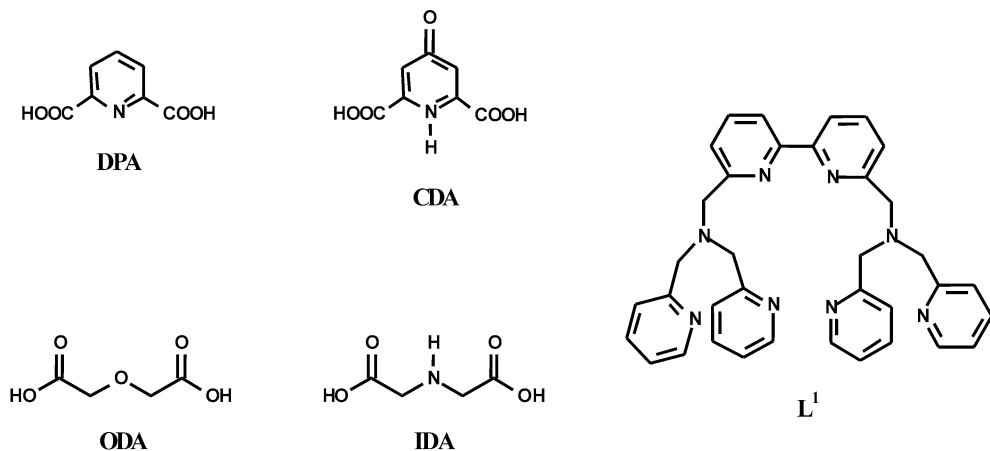
List of the racemic lanthanide (III) complexes for which CPL measurements have been reported, following circularly polarized excitation and/or perturbation of the ground state equilibrium by an added chiral agent (Pfeiffer effect)

Racemic lanthanide complex	Sample description		Reference
[Eu(DPA) ₃] ³⁻ DPA = dipicolinic acid	D ₂ O	circularly polarized excitation	(Hilmes and Riehl, 1987) (Hilmes et al., 1985) (Hilmes and Riehl, 1986) (Metcalf et al., 1990b) (Riehl, 1996)
	<u>rigid sol-gels</u>		(Huskowska et al., 2000) (Sokolnicki et al., 2002)
	H ₂ O	Pfeiffer effect	(Çoruh et al., 1988b) (Huskowska and Riehl, 1995) (Muller and Riehl, 2004)
[Sm(DPA) ₃] ³⁻	D ₂ O	circularly polarized excitation	(Hilmes and Riehl, 1986) (Hilmes et al., 1985)
[Yb(DPA) ₃] ³⁻	D ₂ O	Pfeiffer effect	(Maupin et al., 2000)
[Tb(DPA) ₃] ³⁻	H ₂ O, D ₂ O	circularly polarized excitation	(Hilmes and Riehl, 1986) (Hilmes et al., 1985) (Wu et al., 1989)
	H ₂ O	Pfeiffer effect	(Huskowska and Riehl, 1995) (Muller and Riehl, 2004) (Riehl, 1996) (Wu et al., 1989)
[Dy(DPA) ₃] ³⁻	H ₂ O, D ₂ O	circularly polarized excitation	(Çoruh et al., 1988b) (Hilmes et al., 1985) (Hilmes and Riehl, 1986) (Hilmes et al., 1988)
	H ₂ O, D ₂ O	Pfeiffer effect	(Çoruh et al., 1988b) (Hilmes and Riehl, 1986) (Hilmes et al., 1988) (Wu et al., 1989)

continued on next page

Table 6, *continued*

Racemic lanthanide complex	Sample description		Reference
[Eu(PEDPA) ₃] ³⁻ PEDPA = 4-phenyl-ethylnyl-dipicolinic acid	H ₂ O	circularly polarized excitation	(Belair et al., 2000)
	rigid sol-gels		(Sokolnicki et al., manuscript in preparation)
[Eu(CDA) ₃] ⁶⁻ CDA = chelidamic acid	D ₂ O	circularly polarized excitation	(Metcalf et al., 1990b)
[Dy(ODA) ₃] ³⁻ ODA = oxydiacetic acid	D ₂ O	circularly polarized excitation	(Hilmes and Riehl, 1986)
[Eu(ODA) ₃] ³⁻	rigid sol-gels	circularly polarized excitation	(Huskowska et al., 2000)
[Tb(ODA) ₃] ³⁻	H ₂ O, D ₂ O	Pfeiffer effect	(Parac-Vogt et al., 2002)
[Dy(L ¹)Cl ₂] ⁻ L ¹ = 6,6'-bis[bis(2-pyridylmethyl)amino-methyl]-2,2'-bipyridine	H ₂ O	circularly polarized excitation	(Gawryszewska et al., manuscript in preparation)
[Eu(bpyO ₂) ₄] ³⁻ bpyO ₂ = 2,2'-bipyridine-1,1'-dioxide	anhydrous MeCN	circularly polarized excitation	(Huskowska and Riehl, 2000)
[Eu(ceDOTA)] ⁻ ceDOTA = RRRR/SSSS-tetra(alpha-carboxyethyl)DOTA	D ₂ O	circularly polarized excitation	(Muller et al., 2002b)
[Dy(N ₄ P ₄ Bz ₄)] ⁻ [Eu(N ₄ P ₄ Bz ₄)] ⁻ , [Tb(N ₄ P ₄ Bz ₄)] ⁻ [Eu(N ₄ P ₄ Me ₄)] ⁻ , [Tb(N ₄ P ₄ Me ₄)] ⁻ [Eu(N ₄ P ₃ Me ₃ RMe ₂)] ⁻ , [Tb(N ₄ P ₃ Me ₃ RMe ₂)] ⁻ [1,4,7,10-tetraazacyclododecane-1,4,7,10-tetrayltetrakis(methylene)]tetrakis[a-b]-phosphinic acid a = phenyl, N ₄ P ₄ Bz ₄ b = methyl, N ₄ P ₄ Me ₄ N ₄ P ₃ Me ₃ RMe ₂ = [[10-[2-(dimethylamino)-2-oxoethyl]-1,4,7,10-tetraazacyclododecane-1,4,7-triyl]tris(methylene)]tris[methyl]-phosphinic acid	H ₂ O	circularly polarized excitation	(Luck et al., 2001) (Huskowska et al., 1997)
[Eu(TTHA)] ³⁻ TTHA = triethylenetetraaminehexaacetic acid	D ₂ O	circularly polarized excitation	(Mondry et al., 1994)

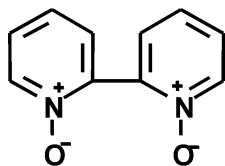


complexes with the slightly larger central lanthanide ion might not have a chiral structure in solution (Scheme 1).

Another recent study involving the use of circularly polarized excitation is for the compound $[\text{Eu}(\text{L}^1)\text{Cl}_2]\text{Cl}$ with the ligand 6,6'-bis[bis(2-pyridylmethyl)amino-methyl]-2,2'-bipyridine (Dossing et al., 2002; Gawryszewska et al., manuscript in preparation). Luminescence measurements have shown the existence of two forms in aqueous and MeOH solutions, where one of them ($[\text{Eu}(\text{L}^1)\text{Cl}]^{2+}$) appears to involve exchange of a Cl^- ion by a solvent molecule in the form $[\text{Eu}(\text{L}^1)\text{Cl}_2]^+$. To confirm the presence of a racemic mixture, use of the Eu(III) complex was not possible, because the species presumably racemizes during the Eu(III) emitting state lifetime. By looking at the complex with the Dy(III) ion, which has a shorter lifetime than the related Eu(III) compound, it was possible to record a CPL spectrum (fig. 6). Variation of the excitation polarization from right to left circular polarization produced an oppositely signed CPL spectrum of about equal magnitude as expected.

This technique has also been used to study a number of racemic lanthanide complexes with approximate C_4 or D_2 symmetries in solution. The ligand 2,2'-bipyridine-1,1'-dioxide (bpyO_2) (Scheme 2) forms 8-coordinate tetrakis lanthanide complexes in anhydrous acetonitrile (Huskowska and Riehl, 2000; Huskowska et al., 2002). Based on high-resolution luminescence studies and X-ray diffraction analysis, the solution structure of $[\text{Eu}(\text{bpyO}_2)_4](\text{ClO}_4)_3$ is probably distorted from the D_4 symmetry observed for the La(III) analog in the solid state and, thus, has an overall geometry of D_2 . This symmetry also results in a system composed of enantiomers, entirely consistent with the CPL results given in fig. 7.

Lanthanide complexes with macrocyclic ligands such as those based on 1,4,7,10-tetraazacyclododecane or polyaminocarboxylates have been studied extensively by CPL spectroscopy. These complexes often possess large stability constants in aqueous solution and, moreover, present interesting chiroptical properties. There have been a number of reports of CPL

bpyO₂

Scheme 2.

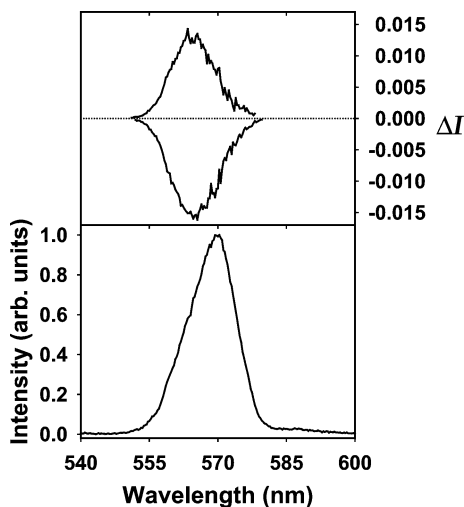


Fig. 6. Circularly polarized luminescence (upper curve) and total luminescence (lower curve) spectra for the ${}^6\text{H}_{13/2} \leftarrow {}^4\text{F}_{9/2}$ transition of a 0.001 M aqueous solution of $[\text{Dy}(\text{L}^1)\text{Cl}_2]^+$ at pH = 7, following left and right circularly polarized 476-nm excitation (Gawryszewska et al., manuscript in preparation).

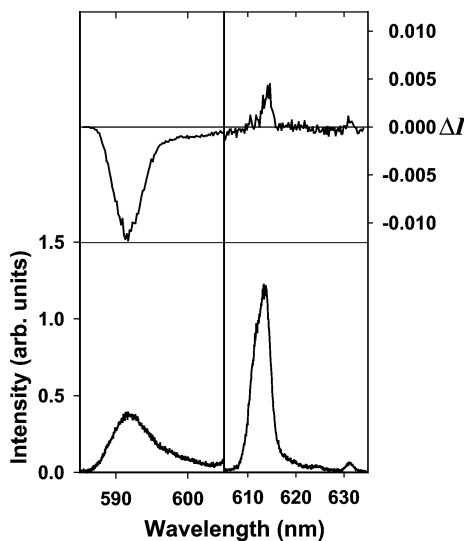


Fig. 7. Circularly polarized luminescence (upper curve) and total luminescence (lower curve) spectra for the ${}^7\text{F}_1 \leftarrow {}^5\text{D}_0$ (left) and ${}^7\text{F}_2 \leftarrow {}^5\text{D}_0$ (right) transitions of $[\text{Eu}(\text{bpyO}_2)_4]^{3+}$ in MeCN at 295 K, following left circularly polarized 553.7-nm excitation (Huskowska and Riehl, 2000).

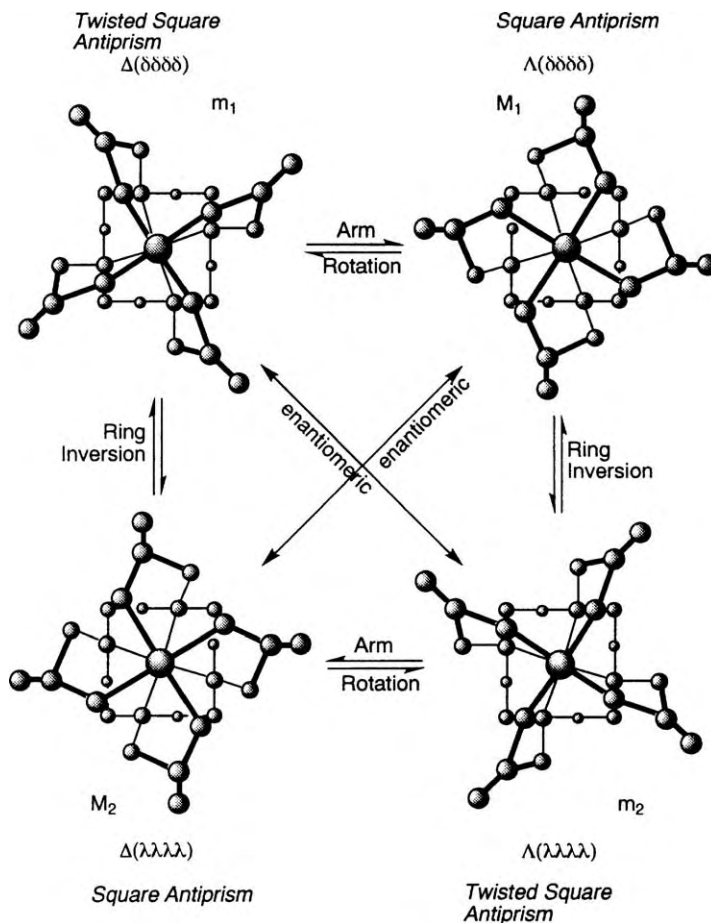


Fig. 8. Pictorial representation of the isomers of lanthanide complexes of DOTA-based ligands, showing the possible exchange mechanism (Dickins et al., 1998a).

following circularly polarized excitation of racemic complexes involving DOTA-type ligands (DOTA = 1,4,7,10-tetraazacyclododecane-1,4,7,10-tetraacetic acid), although no CPL has been detected from complexes of lanthanides with DOTA itself in aqueous solution presumably due to rapid racemization. As depicted in fig. 8, upon complexation with a lanthanide ion, square anti-prism (SAP) or twisted square antiprism (TSAP) structures are formed with a vacant coordination site in the “cap” position which is typically occupied by a solvent molecule. In these structures two distinct type of chiral stereochemistry are present. In analogy with D_3 or C_3 symmetry species, the sense of rotation of the pendant “arms” is denoted Λ or Δ depending upon if the arms rotate clockwise (Δ) or counterclockwise (Λ) as one proceeds down the direction of the C_4 axis. There is also chirality (or helicity) associated with

the non-planar 12 member ring. If one looks along the line connecting the coordinated nitrogens, the carbon atoms either have a right-handed (+ NCCN torsion angle) (δ) or left handed ($-\text{NCCN}$ torsion angle) (λ) twist. Since in this ligand there are four connecting segments, the full description of the molecular stereochemistry must include the overall helicity of the arms, and the helicity of the four segments. Since for this ligand all the segments are connected, however, one finds only $\delta\delta\delta\delta$ or $\lambda\lambda\lambda\lambda$ conformations. The ring conformations are further coupled to the arm configuration, so that the $\Delta(\delta\delta\delta\delta)$ and $\Lambda(\lambda\lambda\lambda\lambda)$ enantiomers of $[\text{Eu}(\text{DOTA})]^-$ have a TSAP structure, whereas the $\Delta(\lambda\lambda\lambda\lambda)$ and $\Lambda(\delta\delta\delta\delta)$ enantiomers have a SAP geometry (Dickins et al., 1998a).

As shown in fig. 8, complexes with these DOTA-type ligands racemize by inverting both the helicity of the pendant arms as well as the helicity of the ring conformation. We also show in this figure the equilibrium between the SAP and TSAP structures. It has been shown that when the pendant arms attached to the ring nitrogens are not α -substituted, arm rotation can lead to interconversion of TSAP (twisted square anti-prism) and SAP (square anti-prism) isomers, as well as a change in absolute configuration ($\Delta \leftrightarrow \Lambda$). However, for the complex formed between Eu(III) and *RRRR/SSSS*-tetra(α -carboxyethyl)DOTA ($[\text{Eu}(\text{ceDOTA})]^-$), and for other structurally related complexes, the only process that effectively interconverts these two isomers at ambient temperature is cyclen ring inversion as illustrated schematically in fig. 9 (Muller et al., 2002b). Verification that the solution prepared from this ligand was indeed a racemic mixture, was made by measuring the circularly polarized luminescence following circularly polarized excitation. An exactly opposite value was obtained when the excitation beam was converted from left to right circular polarization. This confirms that the structure in solution is chiral and does not racemize completely on the luminescence time-scale. The same technique has been used to examine a series of phosphinate macrocyclic complexes of Eu(III), Tb(III), and Dy(III) with octadentate ligands derived from the 1,4,7,10-tetraazacyclododecane ring: $\text{N}_4\text{P}_4\text{Bz}_4$, $\text{N}_4\text{P}_4\text{Me}_4$ and $\text{N}_4\text{P}_3\text{Me}_3\text{RMe}_2$ (Scheme 3) (Huskowska et al., 1997; Luck et al., 2001).

It has generally been observed that the overall chirality of the electronic transitions from these DOTA-type lanthanide complexes appears to be quite sensitive to the square antiprism

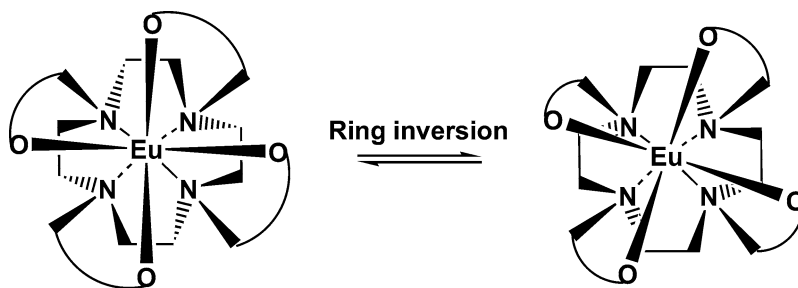
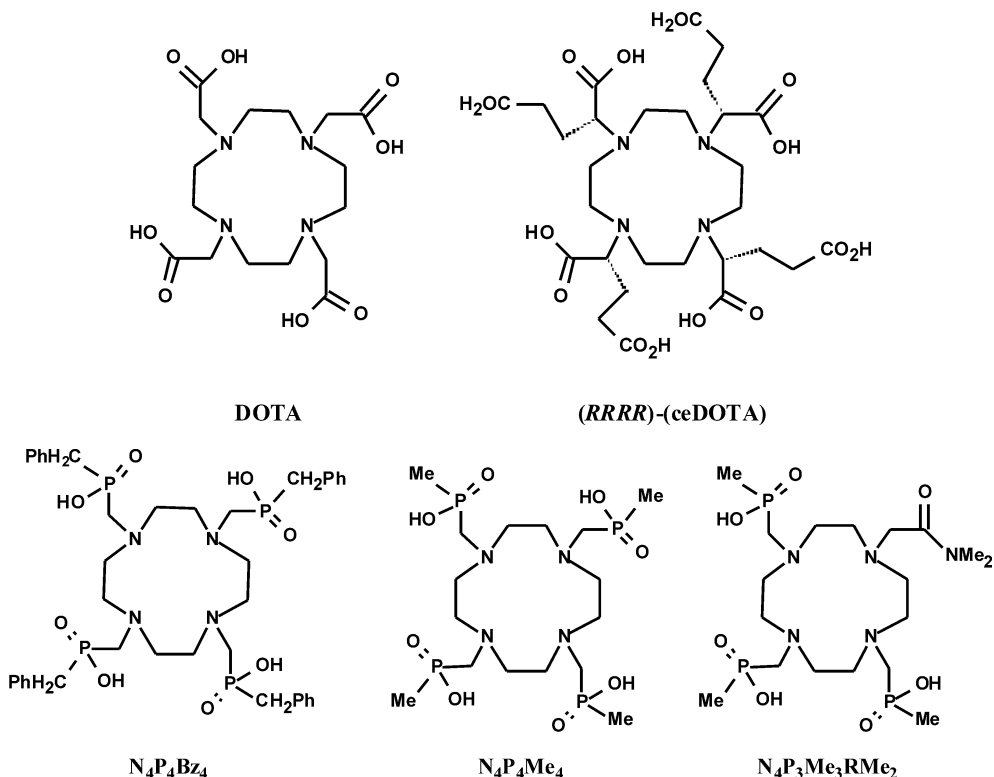


Fig. 9. Pictorial representation of the possible ring inversion that interconverts the two isomers of the complex $[\text{Eu}(\text{ceDOTA})]^-$. The coordinated water molecule, located above the plan of the four oxygen atoms, has been omitted for clarity (Muller et al., 2002b).



Scheme 3.

twist angle associated with the coordinated atoms, and relatively insensitive to the helicity of the ring (Bruce et al., 2002, 2001). Some generalizations concerning the averaged solution structure of these complexes may be possible from the magnitude of the observed effect. Using a simple model, it has been predicted that a twist angle of 22.5° would yield the largest g_{lum} (Bruce et al., 2002). Examination of the sharp crystal field splitting and large g_{lum} for the Tb(III) complexes of the three DOTA-phosphinates described above, suggested that the overall average chiral structure of these three complexes were very similar. The CPL spectra of the related compounds with the Eu(III) ion had quite small values for g_{lum} (fig. 10), even though the excitation wavelength corresponded to a magnetic dipole allowed transition, whereas the excitation of the Tb(III) complexes did not (Huskowska et al., 1997). These important variations suggested that there were differences between the emitting state structures of the Eu(III) and Tb(III) complexes. For comparison, the opposite trend was observed for the g_{lum} values when studying the same transitions on the Tb(III) and Eu(III) complexes with the DPA ligand (Hilmes and Riehl, 1986; Hilmes et al., 1985), consistent with the selection rules for the excitation transition used.

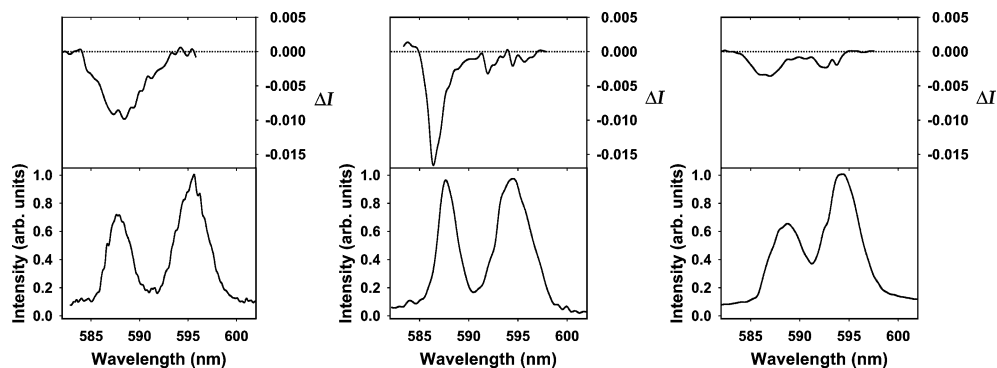
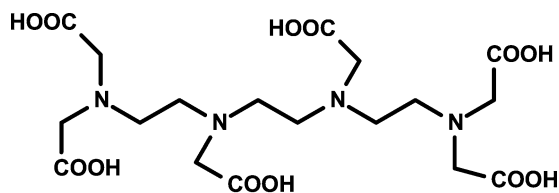


Fig. 10. Circularly polarized luminescence (upper curve) and total luminescence (lower curve) spectra for the ${}^7F_1 \leftarrow {}^5D_0$ transition of aqueous solutions of $[\text{Eu}(\text{N}_4\text{P}_4\text{Bz}_4)]^-$ (left), $[\text{Eu}(\text{N}_4\text{P}_4\text{Me}_4)]^-$ (middle), and $[\text{Eu}(\text{N}_4\text{P}_3\text{RMe}_2)]^-$ (right), following circularly polarized 555-nm excitation (Huskowska et al., 1997).

Circularly polarized excitation has also been a useful technique for studying solution complexes of lanthanides with achiral ligands of low symmetry. For example, CPL was observed from solutions of Eu(III) with triethylenetetraaminehexaacetic acid (TTHA) following circularly polarized excitation (Mondry et al., 1994). The spectroscopic studies of 1 : 1 solutions of Eu(III) with TTHA, corroborated by the X-ray diffraction analysis of the Gd(III) complex and temperature and pressure dependence of the ${}^7F_0 \rightarrow {}^5D_0$ excitation spectrum, clearly showed the presence of two distinct species corresponding to the dimer and monomer complexes (Maupin et al., 2001). Presumably, each of these species exists in solution as a racemic mixture. In the dimer species, the inner coordination sphere contains three nitrogen and six oxygen donors from TTHA (Scheme 4), while in the monomer there are four nitrogen and five oxygen donors.



TTHA

Scheme 4.

4.1.1.2. *Racemization kinetics from CPL measurements.* Experiments concerned with the enantiomer interconversion processes were carried out on the $[\text{Eu}(\text{TTHA})]^{3-}$ compound in neutral aqueous solution (Mondry et al., 1994). It has been demonstrated that the CPL spectrum of this system shows only a very slight temperature dependence from 283 to 353 K,

indicating that the complex does not undergo significant rearrangement that would lead to racemization in this temperature range. In these experiments it is assumed that the excited state lifetime is independent of temperature, and any decrease in g_{lum} is due to the increased racemization at elevated temperatures. The interpretation of these experiments is somewhat complicated by the fact that there is an equilibrium between two species that also changes with temperature (Mondry et al., 1994). By comparison, g_{lum} values measured for $[\text{Eu}(\text{DPA})_3]^{3-}$ in aqueous solution decreased by a factor of 4 or 5 when the temperature was increased from 293 to 353 K (Metcalf et al., 1990c). The estimated value of the activation energy for enantiomeric conversion for $[\text{Eu}(\text{DPA})_3]^{3-}$ was $E_a = 48.9$ kJ/mol using a simple Arrhenius analysis for k_{rac} determined in the steady state mode (eq. (31)) (Belair et al., 2000), or 50.7 kJ/mol derived from k_{rac} determined by time-resolved CPL studies (Glover-Fischer et al., 1998). This is about two times lower than the one corresponding value obtained for the complex with TTHA, $E_a = 96.1$ kJ/mol in D_2O (Mondry et al., 1994).

It should be mentioned that these types of measurements are only possible if the ligand-solvent or bound ligand-free ligand exchange processes are slow compared to optical enantiomer interconversions, and the complex remains intact on the time scale of these possible stereochemical transformations. The excited-state racemization kinetic may also be influenced by the nature of the solvent, as observed for $[\text{Eu}(\text{DPA})_3]^{3-}$ (Metcalf et al., 1990c) and $[\text{Eu}(\text{CDA})_3]^{6-}$ (Metcalf et al., 1990b). The racemization rates are respectively 1.44 and 4.70 times faster in H_2O than D_2O at 293 K, indicating relatively important complex-solvent interactions attributable to solvent mass and hydrogen-bonding capabilities. This solvent dependence is greater for $[\text{Eu}(\text{CDA})_3]^{6-}$ than for $[\text{Eu}(\text{DPA})_3]^{3-}$ reflecting stronger complex-solvent interactions via the 4-oxo substituent on each CDA ligand. Further studies have been carried out in ethylene glycol- H_2O mixture and in non-aqueous solvents such as methanol, ethanol, and acetonitrile (Glover-Fischer et al., 1998). The slower racemization rate and higher activation energy observed for $[\text{Eu}(\text{DPA})_3]^{3-}$ in ethylene glycol- H_2O solution than in H_2O or D_2O was attributed to the higher viscosity of the ethylene glycol- H_2O solvent mixture, while the experiments performed in non-aqueous solvent solutions show no evidence of enantiomer interconversion processes over time periods as long as 6 ms, at temperature up to 313–333 K.

4.1.1.3. *CPL measurements in rigid sol-gels.* In order to measure CPL from racemic mixtures without having to be concerned with competition from chemical racemization, a number of studies have been reported in which the racemic lanthanide complexes have been imbedded in rigid sol-gels (Sokolnicki et al., 2002; Huskowska et al., 2000). In this work it has been shown that at low concentrations in the sol-gel, the CPL results obtained for $[\text{Eu}(\text{DPA})_3]^{3-}$ are approximately the same as obtained in aqueous solution at room temperature, consistent with the observation that under these conditions racemization may be neglected. A somewhat surprising result was that at higher concentrations a reproducible decrease in g_{lum} was observed. This concentration dependent effect was ascribed to racemization due to excited state energy transfer. A theoretical description of this phenomena is presented in sect. 2.6.2. A resonance energy transfer occurring between opposite enantiomer will result in a decrease in $|g_{\text{lum}}|$, while a transfer between identical enantiomers will not have any effect on the CPL signal. Results have also been reported for the concentration dependence of g_{lum} for $[\text{Eu}(\text{bpyO}_2)_4]^{3+}$,

and an energy transfer model based on a diagrammatic Green's function approach (Gochanour and Fayer, 1981) has been used to estimate Förster critical transfer distances, R_0 , from the concentration dependence (Sokolnicki et al., 2002). A large value of the critical transfer distance ($R_0 = 69 \text{ \AA}$), was determined for $[\text{Eu}(\text{bpyO}_2)_4]^{3+}$, and a somewhat more reasonable value of 24 \AA was determined for $[\text{Eu}(\text{DPA})_3]^{3-}$. These results were obtained under the assumptions that the complexes remain intact in the sol-gel, and are evenly distributed through the matrix. There is evidence for some structural modifications, and for some clustering of complexes in sol-gel cavities that would impact the results reported above.

In order to verify the suggestion that no CPL was detected for $[\text{Eu}(\text{ODA})_3]^{3-}$ in solution because of racemization during the emission lifetime, this complex was also prepared and studied in a sol-gel. Small, oppositely signed g_{lum} results were obtained (-0.0063 and $+0.0043$ at 592.6 nm) following left and right circularly polarized excitation (Huskowska et al., 2000), but a concentration dependent study was not performed. It should be noted that preparation of strain-free sol-gels of sufficient quality for these types of polarization measurements are difficult, and one can not completely eliminate effects due to sample alignment, orientation, or depolarization of the circularly polarized excitation and emission.

4.1.2. CPL from racemic mixtures: differential excited-state quenching

As described in sect. 2.6.3, there have been a number of recent studies concerned with interconverting racemic mixtures in which a non-racemic excited state has been generated by differential quenching of one enantiomer over the other by an added chiral quencher. This has been commonly referred to *enantioselective quenching*, although the discriminatory interactions leading to the difference in excited state populations are properly described as *diastereomeric* interactions. A summary of the enantioselective quenching systems is given in table 7. In these experiments, optically active quenchers such as transition-metal complexes (Metcalf et al., 1990b; Morita et al., 2000; Maupin et al., 1996, 1998a; Glover-Fischer et al., 1995; Bolender et al., 1994, 1993; Metcalf et al., 1993; Rexwinkel et al., 1992a, 1992b, 1993a, 1993b; Glover et al., 1992; Çoruh et al., 1991; Richardson et al., 1991; Metcalf et al., 1990a, 1989; Wu et al., 1991), transition metal-nucleotide complexes (Stockman et al., 1996; Metcalf et al., 1992), metalloproteins (Meskers and Dekkers, 2001; Meskers et al., 1998a, 1996, 1998b; Meskers and Dekkers, 1998a), vitamin B₁₂ derivatives (Meskers and Dekkers, 1998b, 1999a, 1999b, 2001), organic dye molecules (Meskers and Dekkers, 1997) or dicopper trefoil knots (Meskers et al., 2000) have been used. Almost all of the studies have used the tris complexes of lanthanide(III) with DPA and CDA ligands. These complexes are known to be quite emissive and have luminescent transitions with large g_{lum} values, and, therefore, emit light with a high degree of circular polarization. This makes it possible to detect even small enantiomeric excesses in the excited state.

The first quencher used for this purpose was the resolved tris(1,10-phenanthroline)ruthenium(II) complex, $[\text{Ru}(\text{phen})_3]^{2+}$ (Metcalf et al., 1990a, 1989). The enantioselective excited-state quenching of $[\text{Tb}(\text{DPA})_3]^{3-}$, $[\text{Eu}(\text{DPA})_3]^{3-}$, and $[\text{Dy}(\text{DPA})_3]^{3-}$ by resolved- $[\text{Ru}(\text{phen})_3]^{2+}$ has provided important information regarding the structure and excited state energetics of the racemic donor and chiral acceptor molecules (e.g., size, shape, electrostatic

Table 7
List of the enantioselective quenching systems used

Enantioselective quenching system	Racemic system	Solvent	Reference
a. Δ -(+)-Co(en) ₃ ³⁺ en = ethylenediamine = 1,2-diaminoethane	[Eu(CDA) ₃] ⁶⁻ [a] CDA = chelidamic acid	H ₂ O, D ₂ O	(Metcalf et al., 1990b)
b. Δ -(-)-Co(en) ₃ ³⁺			
c. Δ -Co(en) ₂ (<i>R,R</i> -chxn) ³⁺ <i>R,R</i> -chxn = trans-1 <i>R</i> ,2 <i>R</i> -diaminocyclohexane	[Eu(CDA) ₃] ⁶⁻ [b, c, d, e] [Tb(CDA) ₃] ⁶⁻ [b, c, d, e]	H ₂ O	(Metcalf et al., 1993)
d. Δ -Co(en)(<i>R,R</i> -chxn) ₂ ³⁺	[Eu(DPA) ₃] ³⁻ [b, c, d, e]		
e. Δ -Co(<i>R,R</i> -chxn) ₃ ³⁺	DPA = dipicolinic acid		
f. Δ -Co(en) ₂ (bpy) ³⁺ bpy = 2,2'-bipyridine	[Tb(DPA) ₃] ³⁻ [b, c, d, e]		
g. Δ -Co(en) ₂ (phen) ³⁺ phen = 1,10-phenanthroline	[Eu(DPA) ₃] ³⁻ [a] [Tb(DPA) ₃] ³⁻ [a, i]	H ₂ O, D ₂ O	(Metcalf et al., 1990a)
h. Δ -Co(phen) ₃ ³⁺			
i. Δ -Co(phen) ₃ ³⁺	[Eu(DPA) ₃] ³⁻ [a, b] [Tb(DPA) ₃] ³⁻ [a, b]		(Glover et al., 1992)
	[Eu(DPA) ₃] ³⁻ [a, b, f, g] [Tb(DPA) ₃] ³⁻ [a, b, f, g]		(Richardson et al., 1991)
j. Δ -($\lambda\lambda\lambda$)-Co(<i>R,R</i> -chxn) ₃ ³⁺	[Eu(DPA) ₃] ³⁻ [i]	H ₂ O, D ₂ O,	(Glover-Fischer et al., 1995)
k. Δ -($\delta\delta\delta$)-Co(<i>R,R</i> -chxn) ₃ ³⁺	[Tb(DPA) ₃] ³⁻ [i]	H ₂ O/Ethylene Glycol	
l. Δ -($\lambda\lambda\delta$)- and/or Δ -($\lambda\delta\delta$)-[Co(<i>R,R</i> -chxn) ₂ (<i>S,S</i> -chxn)] ³⁺			
m. Δ -($\lambda\delta\delta$)-Co(<i>R,R</i> -chxn)(<i>S,S</i> -chxn) ₂ ³⁺			
n. Δ -($\lambda\lambda\lambda$)-Co(<i>R,R</i> -chxn) ₃ ³⁺ -mc -mc = mono-capped	[Eu(DPA) ₃] ³⁻ [i, j, k, l] [Tb(DPA) ₃] ³⁻ [i, j, k, l]	H ₂ O	(Bolender et al., 1994)
o. Δ -($\lambda\lambda\lambda$)-Co(<i>R,R</i> -chxn) ₃ ³⁺ -bc -bc = bi-capped	[Eu(DPA) ₃] ³⁻ [i, j, k, l, m, n] [Tb(DPA) ₃] ³⁻ [i, j, k, l, m, n]	H ₂ O	(Bolender et al., 1993)

continued on next page

Table 7, *continued*

Enantioselective quenching system	Racemic system	Solvent	Reference
p. Δ -(+)-Ru(phen) ₃ ²⁺	[Tb(DPA) ₃] ³⁻ [q]	H ₂ O, MeOH	(Maupin et al., 1998a)
q. Δ -(-)-Ru(phen) ₃ ²⁺			(Maupin et al., 1996)
r. Δ -(+)-Ru(bpy) ₃ ²⁺	[Eu(DPA) ₃] ³⁻ [p, q, r] [Tb(DPA) ₃] ³⁻ [p, q, r]	H ₂ O	(Metcalf et al., 1990a)
	[Dy(DPA) ₃] ³⁻ [q] [Tb(DPA) ₃] ³⁻ [q]	H ₂ O, D ₂ O, MeOH, CD ₃ OD	(Rexwinkel et al., 1993a)
	[Tb(DPA) ₃] ³⁻ [q]	H ₂ O, D ₂ O, MeOH	(Rexwinkel et al., 1992a, 1992b, 1993b)
	[Tb(DPA) ₃] ³⁻ [p, q]	H ₂ O, H ₂ O/MeOH	(Çoruh et al., 1991) (Metcalf et al., 1989)
	[Eu(DPA) ₃] ³⁻ [p, q] [Tb(DPA) ₃] ³⁻ [p, q]	H ₂ O	(Meskers and Dekkers, 1997) (Wu et al., 1991)
t. Δ -(<i>a</i>)- and Δ -(<i>e</i>)-Cr(H ₂ O) ₄ (ATP) ATP = adenosine triphosphate	[Eu(DPA) ₃] ³⁻ [t, u, v] [Tb(DPA) ₃] ³⁻ [t, v]	H ₂ O	(Stockman et al., 1996)
u. Δ -(<i>a</i>)-Cr(H ₂ O) ₄ (ATP)			
v. Δ -(<i>e</i>)-Cr(H ₂ O) ₄ (ATP) <i>a</i> = pseudo-axial orientation <i>e</i> = pseudo-equatorial orientation			
Δ - and Δ -endo-Rh(H ₂ O) ₃ (ATP)	[Eu(DPA) ₃] ³⁻	H ₂ O	(Stockman et al., 1996)
Δ - and Δ -exo-Rh(H ₂ O) ₃ (ATP)	[Tb(DPA) ₃] ³⁻		
Δ - and Δ -(<i>a/e</i>)-Rh(H ₂ O) ₄ (ATP)			

continued on next page

Table 7, *continued*

Enantioselective quenching system	Racemic system	Solvent	Reference
Co(NH ₃) ₄ (ntp) ntp = triphosphate nucleotide Co(NH ₃) ₄ (ndp) ndp = diphosphate nucleotide	[Eu(DPA) ₃] ³⁻ [Tb(DPA) ₃] ³⁻	D ₂ O	(Metcalf et al., 1992)
Metalloproteins: cytochrome c, cytochrome c-550, azurin, amicyanin, plastocyanin M44K azurin, wt azurin, amicyanin, plastocyanin cytochrome c, wt cytochrome c-550	[Eu(DPA) ₃] ³⁻ [Tb(DPA) ₃] ³⁻	H ₂ O	(Meskers and Dekkers, 2001) (Meskers et al., 1998a) (Meskers et al., 1998b) (Meskers et al., 1996) (Meskers and Dekkers, 1998a)
Vitamin B ₁₂ and derivatives cyanocobalamin = vitamin B ₁₂ = CNCbl, aquacobalamin = vitamin B _{12a} = H ₂ OCbl ⁺ , hydroxocobalamin = HOCbl, dicyanocobinamide = (CN) ₂ Cbi, heptamethyl ester of dicyanocobyrinic acid = (CN) ₂ Cby(OMe) ₇ cyanocobalamin = vitamin B ₁₂ = CNCbl, aquacobalamin = vitamin B _{12a} = H ₂ OCbl ⁺ , dicyanocobinamide = (CN) ₂ Cbi	[Eu(DPA) ₃] ³⁻ [Tb(DPA) ₃] ³⁻ [Eu(DPA) ₃] ³⁻ [La(DPA) ₃] ³⁻ [Tb(DPA) ₃] ³⁻ [Nd(DPA) ₃] ³⁻ [Gd(DPA) ₃] ³⁻	H ₂ O	(Meskers and Dekkers, 2001) (Meskers and Dekkers, 1999a) (Meskers and Dekkers, 1999b)

continued on next page

Table 7, *continued*

Enantioselective quenching system	Racemic system	Solvent	Reference
cyanocobalamin = vitamin B ₁₂ = CNCbl, aquacobalamin = vitamin B _{12a} = H ₂ OCbl ⁺	[Tb(DPA) ₃] ³⁻		(Meskers and Dekkers, 1998b)
Rhodamine 6G, Rhodamine B, Uro, MeUro (+)- and (-)- K ·2Cu·2PF ₆	[Tb(DPA) ₃] ³⁻ [Eu(DPA) ₃] ³⁻ [Tb(DPA) ₃] ³⁻	MeOH H ₂ O/MeCN	(Meskers and Dekkers, 1997) (Meskers et al., 2000)
Λ-(+)-Co(en) ₃ ³⁺ l-EDDS = (S,S')-ethylenediamine-N,N'- disuccinic acid d-EDDS = (R,R')-ethylenediamine-N,N'- disuccinic	[Tb(d-EDDS)] ⁻ [Tb(l-EDDS)] ⁻ measured separately	H ₂ O	(Morita et al., 2000)

charge distributions, stereochemical dynamics, or electronic state structures) as well as the stability of the diastereomeric encounter complexes that are formed, and other structural and energetic aspects of the energy transfer process. Studies have been carried out on solution samples in which the kinetics of the quenching reactions have been examined under variable temperature, pressure, ionic strength, solvent type, and solution viscosity conditions (Metcalf et al., 1990c; Glover-Fischer et al., 1998; Maupin et al., 1998a, 1996; Glover-Fischer et al., 1995; Rexwinkel et al., 1992a, 1992b, 1993a, 1993b; Çoruh et al., 1991). All those experiments have been very helpful in developing a better understanding of the characteristics of the observed chiral recognition/discrimination.

One of the more interesting results from these studies is the solvent dependence seen in the excited-state quenching of lanthanide (III) DPA complexes by $[\text{Ru}(\text{phen})_3]^{2+}$. Since in this case both donor and acceptor have D_3 symmetry, we can properly label the mutual interactions as being heterochiral ($\Delta\Lambda$ or $\Lambda\Delta$) or homochiral ($\Delta\Delta$ or $\Lambda\Lambda$). For this system it has been shown that heterochiral quenching is more efficient in methanol solution, whereas in water solution, homochiral quenching is the faster process (Rexwinkel et al., 1992b, 1993a). Analysis of the temperature dependence of the quenching kinetics in the two solvents has demonstrated that the competition between enthalpy and entropy effects is the driving force of the chiral discriminatory interactions. From all of these data, it was concluded that differential entropy effects control the overall quenching kinetics in methanol and favor heterochiral versus homochiral quenching. Differential enthalpy controls the quenching kinetics in aqueous solutions and favors heterochiral quenching. It is perhaps important to note that changing of the sign of g_{lum} from positive to negative by switching achiral solvents does not violate any symmetry considerations, since as stated above, the fundamental interactions are diastereomeric in nature and not enantiomeric. Comparative studies of enantioselective quenching in water and methanol solutions of the $[\text{Tb}(\text{DPA})_3]^{3-}/[\text{Ru}(\text{phen})_3]^{2+}$ system under variable pressure conditions have also been performed (Maupin et al., 1998a, 1996). It was observed that the rate of this enantioselective quenching process increased with pressure when the reaction was carried out in water, but decreased with pressure in methanol. The origin of the observed differences between the quenching in methanol versus aqueous solution has been attributed to different structural aspects of the solvated diastereomeric encounter pairs formed in these two solvents. A negative volume of activation in water is consistent with a close approach of donor: acceptor species without much solvent rearrangements. A positive volume of activation in methanol has been interpreted as being due to methanol molecules having to leave the interstitial spaces surrounding the $[\text{Ru}(\text{phen})_3]^{2+}$ before the donor can attain the close distance necessary for energy transfer to occur.

In addition to resolved $[\text{Ru}(\text{phen})_3]^{2+}$ complex, other enantiomerically pure transition-metal complexes have been examined as quenchers for either $[\text{Ln}(\text{DPA})_3]^{3-}$ or $[\text{Ln}(\text{CDA})_3]^{6-}$ ($\text{Ln} = \text{Eu}(\text{III})$ or $\text{Tb}(\text{III})$) in aqueous solution. These include resolved optical isomers of $[\text{Co}(\text{en})_3]^{3+}$, $[\text{Co}(\text{en})_2(\text{R,R-chxn})]^{3+}$, $[\text{Co}(\text{en})(\text{R,R-chxn})_2]^{3+}$, or $[\text{Co}(\text{R,R-chxn})_3]^{3+}$ (where en = ethylenediamine and R,R-chxn = trans-1R,2R-diaminocyclohexane) (Glover-Fischer et al., 1995; Metcalf et al., 1993). These studies have shown that the structural changes as well as the additional number of chiral centers in the coordinated ligands, brought by the substitution of R,R-chxn for en ligands had considerable effect on the degree and sense of chi-

Table 8
Ratio of the rate parameters for Λ -[Ln(L)₃]³⁻ versus Δ -[Ln(L)₃]³⁻ (L = DPA and CDA) quenching by resolved optical isomers of Co(II) complexes in aqueous solution^a

Racemic lanthanide complexes	Resolved quenchers	k_q^- / k_q^{+b}
[Eu(DPA) ₃] ³⁻	Λ -[Co(en) ₃] ³⁺ en = ethylenediamine	0.78
DPA = dipicolinic acid	Λ -[Co(en) ₂ (<i>R,R</i> -chxn)] ³⁺	1.67
	<i>R,R</i> -chxn = trans-1 <i>R</i> ,2 <i>R</i> -diaminocyclohexane	
	Λ -[Co(en)(<i>R,R</i> -chxn) ₂] ³⁺	3.02
	Λ -[Co(<i>R,R</i> -chxn) ₃] ³⁺	4.01
[Eu(CDA) ₃] ⁶⁻	Λ -[Co(en) ₃] ³⁺	0.75
CDA = chelidamic acid	Λ -[Co(en) ₂ (<i>R,R</i> -chxn)] ³⁺	1.33
	Λ -[Co(en)(<i>R,R</i> -chxn) ₂] ³⁺	2.01
	Λ -[Co(<i>R,R</i> -chxn) ₃] ³⁺	2.77
[Tb(DPA) ₃] ³⁻	Λ -[Co(en) ₃] ³⁺	0.87
	Λ -[Co(en) ₂ (<i>R,R</i> -chxn)] ³⁺	1.58
	Λ -[Co(en)(<i>R,R</i> -chxn) ₂] ³⁺	2.57
	Λ -[Co(<i>R,R</i> -chxn) ₃] ³⁺	3.40
[Tb(CDA) ₃] ⁶⁻	Λ -[Co(en) ₃] ³⁺	0.71
	Λ -[Co(en) ₂ (<i>R,R</i> -chxn)] ³⁺	1.42
	Λ -[Co(en)(<i>R,R</i> -chxn) ₂] ³⁺	2.00
	Λ -[Co(<i>R,R</i> -chxn) ₃] ³⁺	3.21

^aFrom references (Glover-Fischer et al., 1995) and (Metcalf et al., 1993).

^b k_q^- and k_q^+ denote the homochiral and heterochiral quenching constants, respectively.

ral recognition between [Ln(DPA)₃]³⁻ or [Ln(CDA)₃]⁶⁻ and those quenchers. These quenching results are summarized in table 8. It was noted that the [Co(*R,R*-chxn)₃]³⁺ complexes were the most efficient quenchers and, also, showed the strongest enantioselectivity in their quenching actions. To date these latter represent the largest observed degree of enantioselectivity in dynamic excited-state quenching processes in solution. The ratio of the rate parameters for Λ -[Ln(DPA)₃]³⁻ versus Δ -[Ln(DPA)₃]³⁻ quenched by Δ -($\lambda\lambda\lambda$)-[Co(*R,R*-chxn)₃]³⁺ was 4.01 and 3.40 for Eu(III) and Tb(III), respectively (table 8).

Among the search of new chiral quenchers for the enantioselective quenching of [Ln(DPA)₃]³⁻, the use of vitamin B₁₂ derivatives (Meskers and Dekkers, 1999a, 1999b) has shown that the intermolecular forces contribute to the stability of the encounter complexes and, also, that the H-bonding interactions between the carboxylate groups of the DPA ligand and the amide hydrogens of the corrinoid play an important role, as suggested by NMR and CD studies. On the other hand, the quenching of [Ln(DPA)₃]³⁻ by biomolecules such as vitamin B₁₂ derivatives or metalloproteins (c-type cytochrome (Meskers and Dekkers, 1998a; Meskers et al., 1998b, 1996)) can be used to probe structural aspects of complexation reactions of corrinoids with proteins or, in the near future, to study enantioselectivity in the luminescence of metal containing membrane proteins (Meskers and Dekkers, 2001).

4.1.3. CPL from racemic mixtures: perturbation of the equilibrium

In the two previous subsections, we have described experiments involving CPL from racemic solutions in which either a non-racemic emitting state is prepared by circularly polarized excitation or a time-dependent optically enriched excited state is generated through enantioselective quenching by an added chiral species. A third possibility is the preparation of a non-racemic emitting state by disturbance of the ground state racemic equilibrium by an added chiral substance, a phenomenon which has been called the Pfeiffer effect. The first examples of the measurement of the CPL from perturbed racemic solution involving a lanthanide complex have been reviewed by Brittain (1989). Brittain and coworkers showed that a variety of chiral species such as tartrate substrates, amino acids, or sugar derivatives, may cause a perturbation of the D_3 equilibrium between Λ - and Δ -[Tb(DPA) $_3$] $^{3-}$. Additional experiments (Hilmes and Riehl, 1986; Huskowska and Riehl, 1995; Wu et al., 1989; Çoruh et al., 1988b; Hilmes et al., 1988) have shown that the nature of this equilibrium shift was an outer-sphere interaction between the racemic lanthanide complex and the added chiral agent. It is important in this type of experiment to compare the CPL spectra from the Pfeiffer-perturbed system with the "pure" enantiomer generated in excess by a circularly polarized excitation beam. If the total emission and CPL lineshape are identical as shown in fig. 11, then one can assume that the structure of the emitting species is the same in the racemic mixture and the Pfeiffer-active systems. These types of measurements have been extended to Eu(III), Dy(III), and Yb(III) complexes of DPA (Çoruh et al., 1988b; Huskowska and Riehl, 1995; Hilmes et al., 1988; Maupin et al., 2000).

The experiments described above have led to the conclusion that the chiral-induced equilibrium shift could be induced in the lanthanide (III) complex by a combination of electrostatic and hydrophobic interactions. Hydrogen bonding effects appear to be less important as suggested by experiments carried out under variable pH, temperature, concentration, solvent type, and solution dielectric constant conditions. By analogy to the associated/dissociated equilibrium shift models of Schipper (1978) in which the source of the equilibrium perturbation is attributed to a free energy of mixing, Brittain (1981) and Wu et al. (1989) attempted to ascertain the complex mechanism responsible for this type of Pfeiffer effect. However, their conclusions were opposite as they concluded that the [Tb(DPA) $_3$] $^{3-}$ complex interacted with the

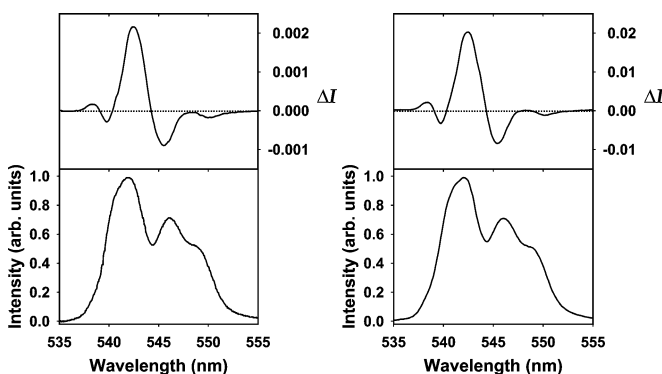


Fig. 11. Circularly polarized luminescence (upper curve) and total luminescence (lower curve) spectra for the ${}^7F_5 \leftarrow {}^5D_4$ transition of [Tb(DPA) $_3$] $^{3-}$ (left) and of 0.014 M [Tb(DPA) $_3$] $^{3-}$ after addition of 0.14 M of L-histidine (right) in aqueous solution, following circularly polarized 488-nm excitation and excitation at 488 nm, respectively (Wu et al., 1989).

chiral probe, L-histidine, in the associated and in the dissociated models, respectively. An explanation of this difference of behavior might be due to the experimental conditions concerning the dependence of g_{lum} on the ratio of chiral substrate (N_p) to complex (N). Indeed, it has recently been shown by CD or CPL spectroscopy that these chiral discrimination interactions involving the $[\text{Tb}(\text{ODA})_3]^{3-}$ /L-proline (Parac-Vogt et al., 2002) or $[\text{Tb}(\text{DPA})_3]^{3-}$ /L-proline benzyl ester (Muller and Riehl, 2004) system exhibit the behavior predicted by the associated model. Compared to the $[\text{Tb}(\text{DPA})_3]^{3-}$ /L-histidine system where the ratio of N_p/N did not exceed 10, the new experiments were carried out on solutions with ratios up to 40.

As presented in sect. 2.7, if one is able to measure CPL from a racemic mixture at wavelength λ using circularly polarized excitation at wavelength λ' , the CD of a perturbed system also at λ' , and the CPL from the same perturbed system at λ , then one should be able to determine the enantiomeric excess, and the g_{lum} and g_{abs} values for transitions of the pure enantiomers, even though they may not be separable by ordinary chemical means. This has been accomplished for $[\text{Dy}(\text{DPA})_3]^{3-}$ (Hilmes et al., 1988). In this work it was possible to measure the CPL of a racemic solution of this complex using a circularly polarized 457.9 nm Ar-ion laser line, and measure the CD at 457.9 nm of a solution of this complex which contained 0.075 M L-histidine. The CPL of this latter solution was also measured. These three experimental measurements are reproduced in fig. 12. The most difficult measurement of the three is the measurement of the CD, since the intraconfigurational $f \rightarrow f$ absorptions are so weak. The results displayed were obtained using a pathlength of 5 cm. From these three measurements, it was determined that the addition of 0.075 M L-histidine resulted in an enantiomeric excess of 3.7%. The magnitude of the dissymmetry ratios for the enantiomeric complexes were also determined, however, this analysis alone does not yield the specific sign of g_{lum} or g_{abs} for a specific enantiomer. These measurements were also reported for the same complex in the

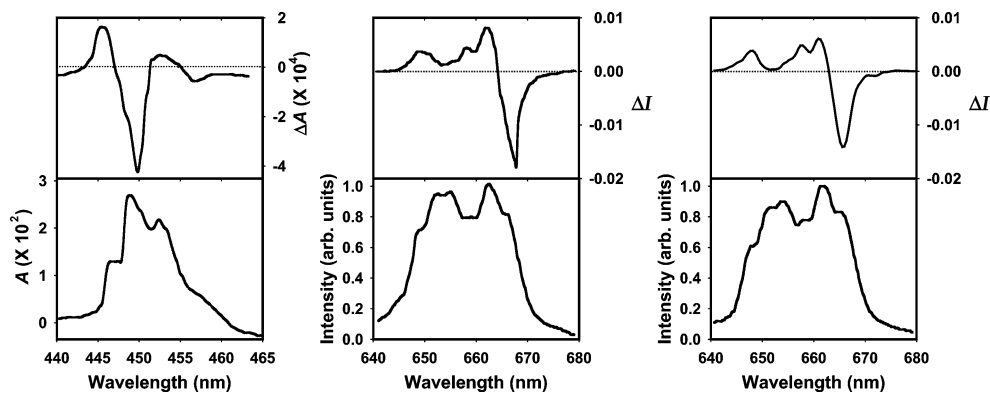
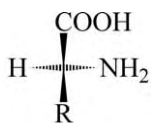


Fig. 12. Circular dichroism (upper curve) and absorption (lower curve) spectra (left), for the ${}^4I_{15/2} \leftarrow {}^6H_{15/2}$ transition of an aqueous solution of 5 : 1 L-histidine: $[\text{Dy}(\text{DPA})_3]^{3-}$ at pH = 3. Circularly polarized luminescence (upper curve) and total luminescence (lower curve) spectra for the ${}^6H_{11/2} \leftarrow {}^4F_{9/2}$ transition of $[\text{Dy}(\text{DPA})_3]^{3-}$ at pH = 3 (middle) and of a 5 : 1 L-histidine : $[\text{Dy}(\text{DPA})_3]^{3-}$ aqueous solution (right), following circularly polarized 457.9-nm excitation and excitation at 488 nm, respectively (Hilmes et al., 1988).

presence of 4.5M (+)-dimethyl-L-tartrate (Çoruh et al., 1988b). It can be seen that the CPL spectra for the racemic and perturbed equilibria are very similar. In this case the enantiomeric excess was estimated to be 37%. If one makes the reasonable assumption that the addition of the same amount of (+)-dimethyl-L-tartrate to other tris lanthanide (III) complexes with DPA results in the same enantiomeric excess, dissymmetry ratios for enantiomers for these other complexes may also be determined from eqs. (45) and (46).

4.1.3.1. *Perturbation of the racemic equilibrium as a structural probe.* Since the luminescence dissymmetry factors for the magnetic dipole allowed transitions of a number of lanthanide complexes are often quite large and easily measurable, it has been suggested that the perturbation of a ground state racemic equilibrium might be useful as a reliable structural indicator for chiral species. This practical use of CPL spectroscopy, of course, hinges on the ability to relate the created enantiomeric excess to some structural characteristic of the perturber molecule. This effort is further complicated by the inherent difficulty in the nomenclature of chiral molecules as expressed by Professor S.F. Mason "The principal nomenclature systems [*for chiral molecules*] are artificial in the sense that two analogous enantiomers with the same configurational label do not necessarily have the same absolute stereochemical form, nor need be related chemically, by interconversions, or physically, by the sign of their optical rotation properties" (Mason, 1982).

An obvious target for this kind of analysis is the perturbation of the racemic equilibria by L-amino acids, since the L, D nomenclature used for these molecules is based on the common structure indicated in Scheme 5.



L-amino acid Scheme 5.

Under physiological pH conditions (6–7) these are perhaps more correctly written as their zwitterionic form. There has been a number of studies in which various amino acids have been added to racemic solutions of $[\text{Tb}(\text{DPA})_3]^{3-}$ or $[\text{Eu}(\text{DPA})_3]^{3-}$ (Yan et al., 1982; Brittain, 1981; Huskowska and Riehl, 1995). Although the early work indicated that L-amino acids all gave the same sign for the CPL from selected transitions of the DPA complexes, more recent work has shown that such a simple structural picture is unfortunately not correct (Muller and Riehl). It does appear from this work that simple substitutions of similar groups lead to similar results. For example, in table 9 we show results for the luminescence dissymmetry values obtained from an aqueous solution of $[\text{Tb}(\text{DPA})_3]^{3-}$ in which the amino acids L-histidine, L-histidine methyl ester, and L-histidine benzyl ester have been added. One can conclude from this limited set of data that minor modifications of the alkyl group do not change the overall chirality of the perturbation.

Table 9

Luminescence dissymmetry ratio values (g_{lum}) in the spectral range of the ${}^5\text{D}_4 \rightarrow {}^7\text{F}_5$ transition for 0.01 M $[\text{Tb}(\text{DPA})_3]^{3-}$ after addition of 0.05 M of several amino acids in aqueous solution at pH = 7^a

Amino acid	g_{lum} value ($\lambda_{\text{em}} = 543 \text{ nm}$, $\lambda_{\text{exc}} = 293 \text{ nm}$)
L-histidine	+0.00039
L-histidine methyl ester	+0.00373
L-histidine benzyl ester	+0.00850

^aFrom reference (Muller and Riehl, 2004).

Just as in the development of other spectroscopic-based methods at determining chiral structure, the exploitation of the perturbation of racemic equilibria is based on very small differential effects. In the specific experiments involving neutral amino acids, the presumably outer sphere association is very weak, and the difference between the diastereomeric association constants is very small. There have been several other attempts at using the perturbation of the racemic equilibrium of DPA complexes as diagnostic of chiral structure. For example, Brittain has attempted to correlate the sign of the CPL to some element of the chiral structure of monosaccharide aldose sugars (Brittain, 1984), but in a more quantitative study using modern instrumentation it has been shown that, in fact, no simple correlation is evident in the CPL results from racemic $[\text{Tb}(\text{DPA})_3]^{3-}$ into which simple or complex sugars have been added (Huskowska and Riehl, 1995).

Although there has been some progress in understanding the nature of the equilibrium shift induced by added chiral agents to racemic equilibria (Huskowska and Riehl, 1995; Schipper, 1978; Wu et al., 1989), no one has yet “designed” a system based on specific consideration of the possible intermolecular interactions in which differences in diastereomeric perturbations would be expected to be maximized. Various speculations concerning the importance of hydrogen bonding, coulombic forces, π -stacking, steric factors, hydrophobic effects, etc. have been considered, but only in attempts to understand empirical observations. To be useful in determination of unknown chirality, and to develop a useful tool for determining molecular chirality, a more rational process of designing racemic complexes, and possibly chemical derivitization of target chiral molecules will probably be necessary.

4.2. Lanthanide complexes with chiral ligands

If the ligands surrounding a luminescent lanthanide ion are chiral due to, for example, an asymmetric carbon atom, then the luminescence from the lanthanide ion must be chiral. The “source” of the circular polarization of a particular transition may be due to vicinal effects associated with the chiral center(s) or due to a net chiral configuration about the lanthanide ion due to the influence of the chiral center(s). It is impossible to completely separate these two contributions, but it is generally believed that due to the short range nature of f-orbitals, that the effect of chiral centers in non-coordinating atoms is negligible compared to the chiral arrangement of ligands surrounding the luminescent center. Much of the experimental work involving lanthanide complexes with chiral ligands is, therefore, mostly a study of the chiroptical properties of the chiral configuration caused by the fact that the ligands are chiral.

Table 10
List of the enantiopure lanthanide complexes for which CPL measurements have been reported

Enantiopure lanthanide complex	Sample description	Reference
[Eu(DOTMPhA)] ³⁺ [Dy(DOTMPhA)] ³⁺	H ₂ O, D ₂ O	(Dickins et al., 1999)
[Yb(DOTMPhA)] ³⁺	MeOH/D ₂ O	(Dickins et al., 1999) (Maupin et al., 2000)
[Tb(DOTMPhA)] ³⁺	H ₂ O, D ₂ O, MeCN, MeOH	(Dickins et al., 1999) (Dickins et al., 1997a) (Morita et al., 2002b) (Rau and Morita, 2001)
	Xerogels	(Morita et al., 2002b) (Morita et al., 2003)
[Nd(DOTMPhA)] ³⁺	D ₂ O	(Rau and Morita, 2001)
[Eu(DOTMBrPhA)] ³⁺ [Tb(DOTMBrPhA)] ³⁺	H ₂ O, D ₂ O	(Dickins et al., 1999)
[Yb(DOTMBrPhA)] ³⁺	MeOH/D ₂ O, D ₂ O	(Dickins et al., 1999) (Maupin et al., 2000) (Maupin et al., 1998b)
[Eu(DOTMCNPhA)] ³⁺ [Tb(DOTMCNPhA)] ³⁺	H ₂ O, D ₂ O	(Dickins et al., 1999)
[Eu(DOTMCO ₂ MePhA)] ³⁺ [Tb(DOTMCO ₂ MePhA)] ³⁺	H ₂ O, D ₂ O	(Dickins et al., 1999)
1,4,7,10-tetrakis-[(<i>S</i> or <i>R</i>)-1-(1-[<i>a</i> - d]phenyl)ethylcarbamoylmethyl]-1,4,7,10- tetraazacyclododecane a = phenyl (Ph), DOTMPhA or (phen) ₄ b = 4-bromophenyl (<i>p</i> -Br-Ph), DOTMBrPhA c = 4-cyanophenyl (<i>p</i> -CN-Ph), DOTMCNPhA d = 4-phenyl (<i>p</i> -CO ₂ Me-Ph), DOTMCO ₂ MePhA		
[Yb(DO3MPhA)(PdPorph)] ³⁺ [Nd(DO3MPhA)(PdPorph)] ³⁺	CD ₃ OD/D ₂ O, EtOH	(Beeby et al., 2000) (Maupin et al., 2000)
DO3MPhA-based palladium porphyrin derivative		
[Yb(Rphen) ₃ (phenan)] ³⁺ 1,4,7,10-tetraacetamide- <i>N</i> -(2- phenanthridinylmethyl)- <i>N'</i> , <i>N''</i> , <i>N'''</i> -tris[(1 <i>S</i> or <i>R</i>)-1- phenylethyl]-1,4,7,10-tetraazacyclododecane	MeOH/D ₂ O, D ₂ O	(Maupin et al., 2000) (Maupin et al., 1998b)
[Eu(DOTM1NpA)] ³⁺ [Eu(DOTM2NpA)] ³⁺	MeOH	(Dickins et al., 1998a) (Dickins et al., 1997b)
1,4,7,10-tetrakis-[(<i>S</i> or <i>R</i>)-1-(1 or 2- naphthyl)ethylcarbamoylmethyl]-1,4,7,10- tetraazacyclododecane		
18% Er ³⁺ -doped GMO (β' -phase) GMO = ferroelectric Gd ₂ (MoO ₄) ₃	Crystal	(Herren and Morita, 1996)
Na ₃ [Tb(ODA) ₃] ODA = oxydiacetic acid	Crystal	(Morita et al., 2003)
Na ₃ [Gd _{1-x} Tb _x (ODA) ₃]·2NaBF ₄ ·6H ₂ O (<i>x</i> = 0.2)	Crystal	(Morita et al., 2002a)

In table 10 we list the enantiopure lanthanide complexes for which CPL measurements have been reported.

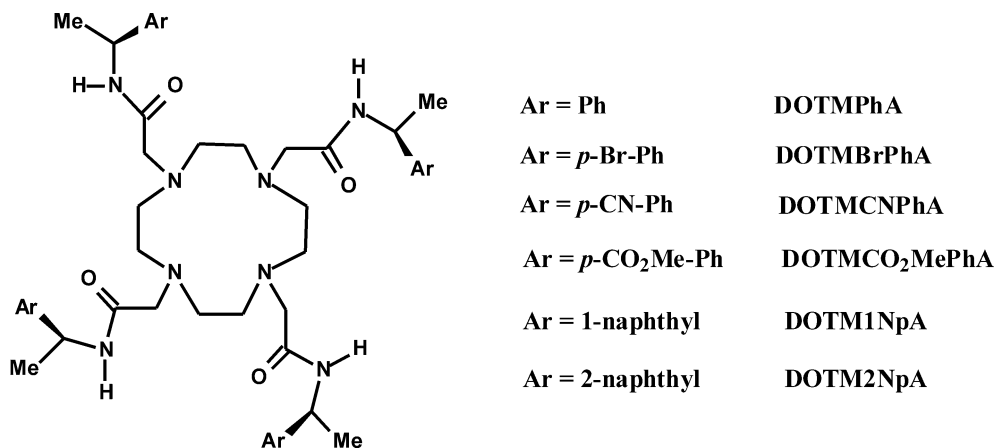
In the previously described studies on racemic mixtures, one had to circularly polarize an excitation beam at a wavelength corresponding to an $f \rightarrow f$ absorption in order to generate a significantly enantio-enriched excited state concentration, in order to see CPL. For enantiopure chiral complexes, one needs only to generate species in their emitting state, so it is very often the case that indirect excitation through ligand absorption and radiationless energy transfer to excited lanthanide (III) states is much more effective at generating luminescence. This is due, of course to the weakness of direct $f \rightarrow f$ absorption transitions. As stated above, for a pure chiral complex, g_{lum} will not depend upon the polarization of the exciting light. It might be possible to modulate the intensity of the luminescence due to preferential absorption of linear or circular polarized light, particularly for oriented systems, but to date no experiments of this type on pure chiral species have appeared in the literature. If a species is composed of an inherently chiral absorption chromophore, A_R , and an inherently chiral luminescent chromophore, L_R , then one might expect to see a difference in intensity between $A_R : L_R$ versus $A_S : L_R$ due to differences in energy transfer efficiency. This has been incorrectly referred to in the literature as “chiral energy transfer”, but is actually due to differences in diastereomeric interactions which can often be explained in terms of different donor: acceptor distances in the diastereomeric complexes.

In general, all of the fundamental principles concerning spectral overlap, absorption strength, etc., that are critical to understanding the ligand to metal energy transfer process in the design of luminescent lanthanide complexes, also apply to the luminescence from chiral complexes.

4.2.1. Chiral DOTA-based ligands

In sect. 4.1 we described a series of experiments concerning the measurement of CPL from racemic mixtures of complexes containing DOTA type ligands. As described previously, there is chirality associated with the pendant arms, and chirality associated with the 12 member ring (Scheme 6). In these structures, the introduction of a chiral center in the pendant arm α or β to the ring nitrogen may influence the sense of rotation (clockwise or counterclockwise) of the pendant arms, and result in a C_4 chirality that can be partially or completely locked.

It has been demonstrated that the C_4 -symmetric chiral tetraamide ligand, 1,4,7,10-tetrakis-[(*S*)-1-(1-phenyl)ethylcarbamoylmethyl]-1,4,7,10-tetraazacyclododecane ($Ar = Ph$, DOTM-PhA), and its *para*-substituted derivatives (DOTMBrPhA, DOTMCNPhA, and DOTMCO₂MePhA where $Ar = p\text{-Br-Ph}$, $p\text{-CN-Ph}$, and $p\text{-CO}_2\text{Me-Ph}$, respectively) give enantiomeric lanthanide (III) complexes that do not readily undergo interconversion of the Δ/Λ isomers in the temperature range 220–320 K and, also, exist as one predominant isomer in aqueous solution (Dickins et al., 1999, 1997a). The crystal structures of the Eu(III) complexes with both enantiomers of DOTMPhA lead to formation of one single isomer in which the chirality is controlled by the absolute configuration at the remote chiral carbon center (*S* and *R* give $\Delta(\lambda\lambda\lambda\lambda)$ and $\Lambda(\delta\delta\delta\delta)$, respectively) (Dickins et al., 1999, 1997a). These structural conclusions have been based on X-ray crystallographic analysis and NMR studies of these



Scheme 6.

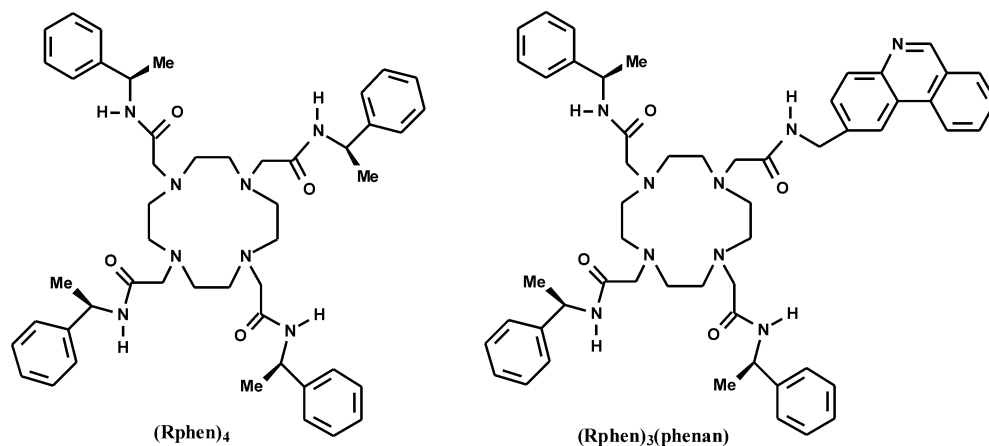
compounds. Confirmation and additional details concerning the chiroptical and structural properties in solutions containing these complexes have been provided by CPL spectroscopy (Maupin et al., 2000, 1998b; Dickins et al., 1999, 1997a). It was shown, for example, that the CPL spectra obtained were independent of the polarization of the excitation beam (left-, right-, or plane-polarized light). This is consistent with the presence of only one species in solution as indicated by NMR and X-ray crystallographic studies. As expected, complexes prepared with ligands of opposite chirality yield mirror image CPL spectra.

As noted above, the energetic and spectral properties that are important in the design of lanthanide-based luminescent species are also important in the development of chiral luminescent complexes. It has been shown, for example, that Tb(III) complexes with DOTMPhA or DOTMBrPhA are more emissive, due to the absence of efficient quenching processes, than the related complexes with Dy(III), Eu(III), and Yb(III) (Dickins et al., 1999, 1997a). However, all of these species exhibit strong circularly polarized luminescence following either direct excitation of the lanthanide (III) ion or indirect sensitization through the ligand absorption bands in aqueous solution. The g_{lum} values of (*R*)-[Ln(DOTMPhA)]³⁺ or (*R*)-[Ln(DOTMBrPhA)]³⁺ at, e.g., 548, 657, 995, or 590 nm are -0.25 , $+0.35$, $+0.18$, or -0.12 in the spectral range of the ⁵D₄ → ⁷F₅ (Tb(III)), ⁴F_{9/2} → ⁶H_{11/2} (Dy(III)), ²F_{5/2} → ²F_{7/2} (Yb(III)), or ⁵D₀ → ⁷F₁ (Eu(III)) transitions, which are particularly well-suited for CPL measurements since they satisfy magnetic-dipole selection rules, $\Delta J = 0, \pm 1$. It should be mentioned that the sign of the observed CPL was the same for all of the Eu(III) and Tb(III) analogues complexes in (*S*)- or (*R*)-[Ln(DOTMPhA)]³⁺ in which different aryl substituents such as naphthyl (Dickins et al., 1998a, 1998b, 1997b), or phenyl and its *para*-substituted derivatives (Dickins et al., 1999, 1997a) on the pendant arms have been studied. Such behavior is consistent with the adoption of an identical structure for each complex that has the same absolute configuration in the helicity of the pendant arm and the macrocyclic ring, and, therefore, indicates that the sign and magnitude of the CPL is controlled primarily by

this aspect of chiral structure. As stated above, this is controlled by the absolute configuration at the remote chiral carbon center: *S* and *R* give $\Delta(\lambda\lambda\lambda\lambda)$ and $\Lambda(\delta\delta\delta\delta)$, respectively.

An interesting and potentially useful result on these DOTA-ligand based systems is the observation that the sign and magnitude of the CPL is essentially “fixed” when only three of the pendant arms are chiral (Maupin et al., 2000, 1998b). Similar CPL spectra have been recorded for the enantiomeric pair of (*RRRR*)- Λ or (*SSSS*)- Δ -[Ln(phen)₄]³⁺ (where (phen)₄ = DOTMPhA) and (*RRR*)- Λ or (*SSS*)- Δ -[Ln(Rphen)₃(phenan)]³⁺ (Ln(III) = Eu, Tb, and Yb) in which one of the chiral amine groups has been substituted by an achiral phenanthridine group (see Scheme 7). Total luminescence and circularly polarized luminescence spectra of the Yb(III) complexes are plotted in fig. 13 (Maupin et al., 2000).

Although the experiments described above have been conducted on enantiopure tetraamide complexes, existing as one isomeric species in solution, it is possible to gain structural in-



Scheme 7.

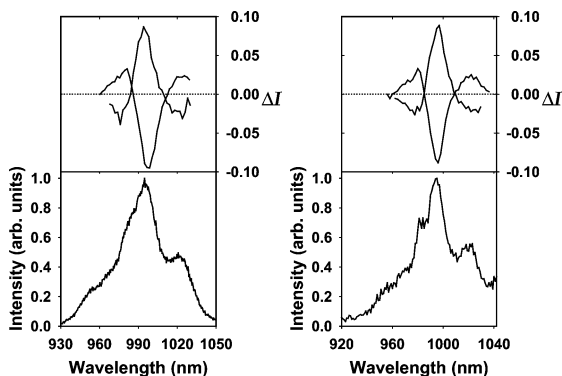


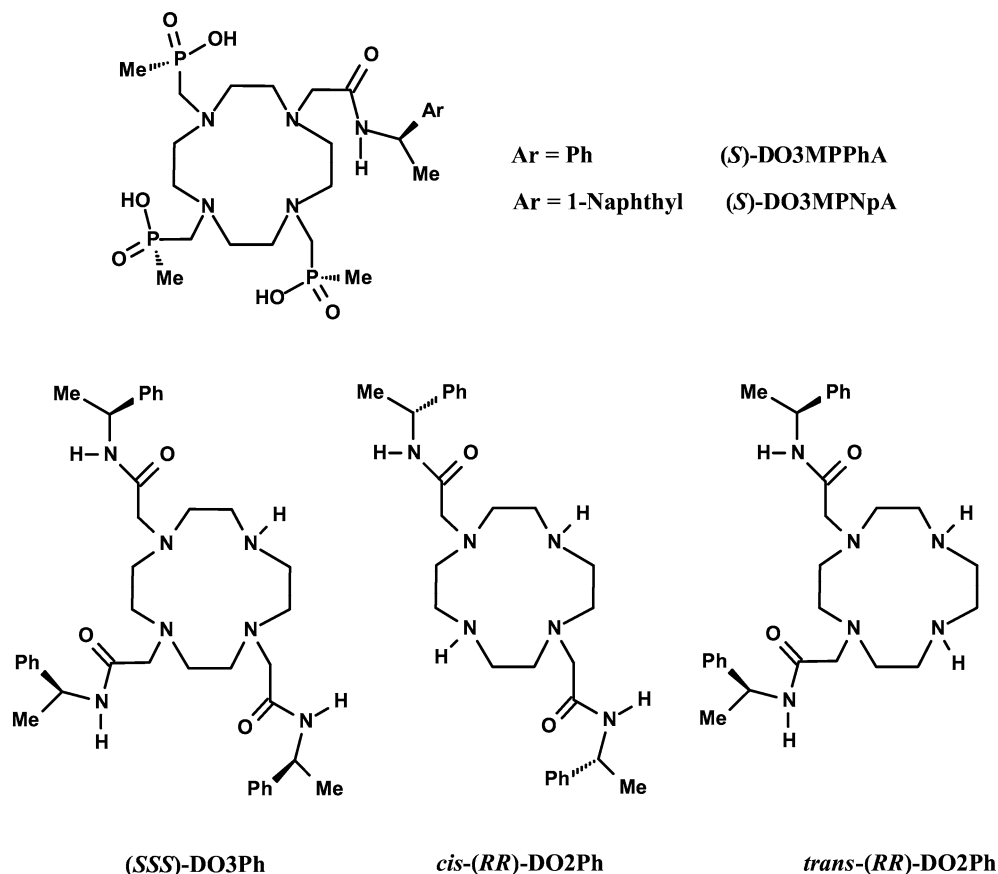
Fig. 13. Circularly polarized luminescence (upper curve) and total luminescence (lower curve) spectra for the ${}^2F_{7/2} \leftarrow {}^2F_{5/2}$ transition of solutions of (*RRRR*)- Λ and (*SSSS*)- Δ -[Yb(phen)₄]³⁺ (where (phen)₄ = DOTMPhA) in a MeOH/D₂O mixture (left), and (*RRR*)- Λ and (*SSS*)- Δ -[Yb(Rphen)₃(phenan)]³⁺ in an acidified MeOH/D₂O mixture (right), following excitation at 260 and 355 nm, respectively (Maupin et al., 2000).

formation from related compounds which exist as two non-interconverting diastereomers. Examples of such ligands are the chiral monoamidetrtris(phosphinates), DO3MPPhA and DO3MPNpA, in which one of the phosphinate groups has been replaced with a chiral amide substituent (α -phenylethyl and α -1-naphthylethyl) (Aime et al., 1998). Thus, the introduction of a chiral center possessing a *S* configuration at the carbon atom into the amide group leads to the formation of two diastereomeric complexes, (*S*-*SSS*)/(*S*-*RRR*), in ratios of 2 : 1 and 4 : 1, respectively. Observation of similar CPL spectra for Eu(III) and Tb(III) complexes of these two ligands indicated that the helicity and probably the macrocyclic ring conformation are determined by the configuration of the chiral carbon center in the amide group. This conclusion is based on the fact that the two diastereomers have identical ring conformations and pendant arm layout and, therefore, the observed CPL is due to the contribution from both isomers. If the two diastereomers had enantiomeric ring conformations and pendant arm layout, the CPL from the minor isomer would have been canceled by the CPL from the major. As a consequence, the magnitude of g_{lum} should have been higher for [Tb(DO3MPNpA)] compared to [Tb(DO3MPPhA)] with respect to the ratio difference between these complexes (4 : 1 and 2 : 1). The g_{lum} values amounted to +0.17 and +0.18 at 543 and 540 nm ($^5D_4 \rightarrow ^7F_5$ transition) for [Tb(DO3MPPhA)] and [Tb(DO3MPNpA)], respectively (Aime et al., 1998). Therefore, the two diastereomers in each system only differ in the configuration at each of the three phosphorus centers: (*RRR*) and (*SSS*). On the other hand, the ratio of the two diastereomers is modulated by the size of the remote chiral group as pointed out by NMR studies for DO3MPPhA and DO3MPNpA (2 : 1 for α -phenylethyl and 4 : 1 for α -naphthylethyl) (Scheme 8) (Aime et al., 1998).

As discussed briefly in sect. 2.4, these C_4 symmetric species have been a prime target for the development of useful correlations between CPL spectrum and chemical structure (Bruce et al., 2002). The sign and magnitude of CPL for this class of complexes have been correlated to the degree of helical twist of the complex, the nature of the ligand field, and the polarizability of the axial donor group. The local helicity at the lanthanide (III) center has been related to the angle, ϕ^{gn} , between the electric-dipole ($|P_{gn}|$) and magnetic-dipole ($|M_{ng}|$) transition moment vectors and, therefore, the rotatory strength, R_{gn} , associated with a given transition between two states g and n as described below.

$$R^{gn} = |P^{gn}| |M^{ng}| \cos \phi^{gn}. \quad (51)$$

The rotatory strength has been shown to have a $\sin 2\theta \cos 2\theta$ (or $\sin 4\theta$) dependence, where θ is the twist angle between the N_4 and O_4 planes. It is, therefore, predicted to vanish at 0° , 45° , or 90° and to be maximum at $\pm 22.5^\circ$ for square-antiprismatic complexes (fig. 14). This latter value is closer to twist angles determined by crystallographic analysis for twisted square antiprismatic isomers ($\sim 28^\circ$) than those associated with regular square antiprismatic species ($\sim 40^\circ$) (Parker et al., 2002). Another factor which may perturb the size of the twist angle is the degree of conformational rigidity in the complex. Indeed, the CPL will reflect the time-averaged local helicity around the lanthanide (III) ion. For example, the magnitude of g_{lum} has been shown to increase with an increase in the degree of conformational rigidity of the complex (Bruce et al., 2002). The tetramide complex, (*SSSS*)-[Eu(DOTMPhA)(solvent)] $^{3+}$, which does not readily undergo interconversion of the Δ/Λ isomers in the temperature range



Scheme 8.

220–320 K exhibited the highest value, while the triamide and the isomeric 1,4 and 1,7 diamide compounds showed lower values (table 11). It has been demonstrated by NMR studies that in these latter systems there were exchange processes involving the interconversion of isomeric species. Finally, the authors have concluded from their NMR, CD, and CPL experiments that it is for the more polarizable axial donors that the affinity of that axial donors for the lanthanide (III) ion and g_{lum} values are greater and smaller, respectively (Dickins et al., 2003; Bruce et al., 2002, 2001; Di Bari et al., 2000). This study has been conducted on a series of eight- and nine-coordinate axially symmetric complexes based on DOTA derivatives bearing phosphonate, phosphinate, or carboxamide groups. In particular, the detailed analysis of the Eu(III) total luminescence and CPL sign and magnitude changes for (SSSS)-[Eu(DOTMPPhA)(solvent)]³⁺ showed that the more polarizable axial donors (e.g., DMSO > EtOH > H₂O) gave the higher intensity ratios of ⁵D₀ → ⁷F₂ to ⁵D₀ → ⁷F₁ transi-

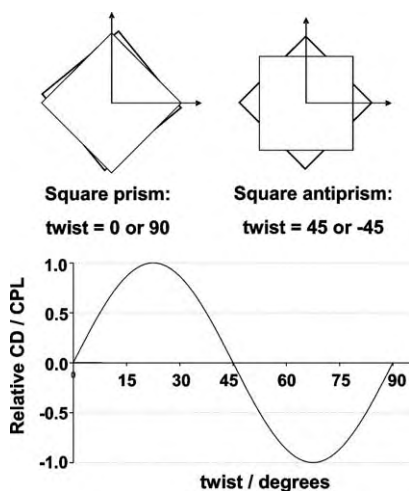


Fig. 14. Correlation of the effect of twist angle in axially symmetric eight- and nine-coordinate antiprismatic lanthanide complexes on their CPL or CD intensity (Bruce et al., 2002).

Table 11

Luminescence dissymmetry ratio values (g_{lum}) in the spectral range of the $^5D_0 \rightarrow ^7F_1$, 7F_2 , and 7F_4 , transitions for di-, tri-, and tetra-amide Eu(III) triflate complexes in acetonitrile solution at 295 K^a

Lanthanide complex ^b	g_{lum}/λ (nm)		
	$^5D_0 \rightarrow ^7F_1$	$^5D_0 \rightarrow ^7F_2$	$^5D_0 \rightarrow ^7F_4$
<i>cis</i> -(<i>RR</i>)-[Eu(DO2Ph)(H ₂ O) ₂] ³⁺	+0.013 (594)	-0.017 (613)	+0.022 (685)
<i>trans</i> -(<i>RR</i>)-[Eu(DO2Ph)(H ₂ O) ₂] ³⁺	+0.02 (594)	-0.013 (613)	+0.025 (685)
(<i>SSSS</i>)-[Eu(DOTMPPhA)(MeCN)] ³⁺	-0.06 (594)	+0.03 (614)	-0.11 (688)
(<i>SSSS</i>)-[Eu(DOTMPPhA)(H ₂ O)] ^{3+c}	-0.09 (594)	+0.08 (614)	-0.10 (688)
(<i>SSS</i>)-[Eu(DO3Ph)(H ₂ O) ₂] ³⁺	-0.05 (593)	+0.03 (612)	-0.06 (685)

^aFrom reference (Bruce et al., 2002).

^bSee text for nomenclature.

^cRecorded in H₂O.

tions ($2.8 > 1.0 > 0.6$) and the smaller g_{lum} values ($0 < +0.03 < +0.08$ at 614 nm) (Bruce et al., 2002).

DOTA-based ligands have also been used to prepare chiral complexes of Yb(III) and Nd(III) for the measurement of CPL in the near-IR. CPL from the $^2F_{5/2} \rightarrow ^2F_{7/2}$ transition of Yb(III) at about 980 nm, and from the $^4F_{3/2} \rightarrow ^4I_{9/2}$ and $^4F_{3/2} \rightarrow ^4I_{11/2}$ transitions of Nd(III) centered at 880 and 1060 nm, respectively, have been reported (Maupin et al., 2000; Beeby et al., 2000; Maupin et al., 1998b). CPL from Yb(III) complexes with the ligands DOTMPPhA and DOTMBrPhA have been studied in some detail. Although the conclusions from these CPL studies were consistent with results obtained previously from related complexes with Eu(III) and Tb(III) ions, the measurement of CPL in the near-IR may be particularly suited for the development of chiral luminescent probes of biological molecules. Indeed, helical tetraamide complexes of Yb(III) as well as of Eu(III) and Tb(III), bearing an

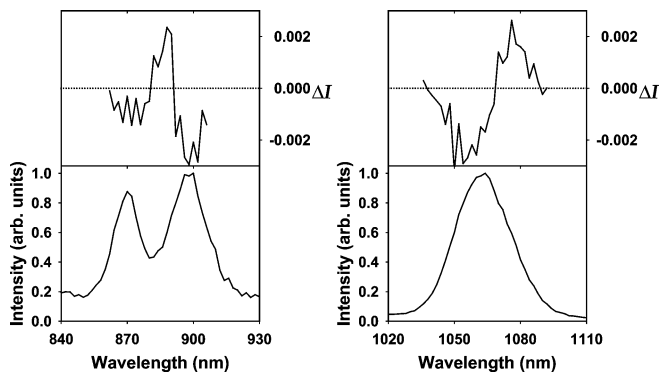


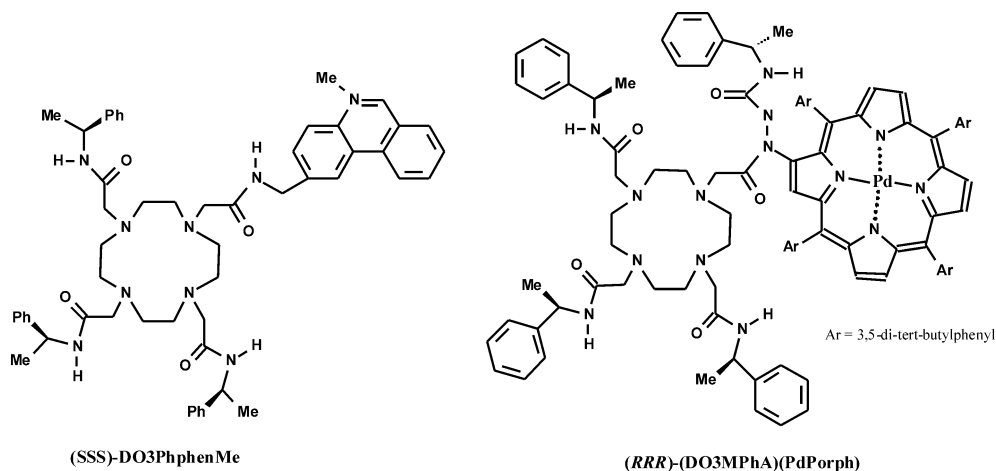
Fig. 15. Circularly polarized luminescence (upper curve) and total luminescence (lower curve) spectra for the ${}^4I_{9/2} \leftarrow {}^4F_{3/2}$ (left) and ${}^4I_{11/2} \leftarrow {}^4F_{3/2}$ (right) transitions of $(RRR)\text{-[Nd(DO3MPhA)(PdPorph)]}^{3+}$ in EtOH at 295 K, following excitation at 415 nm (Maupin et al., 2000).

N-methylphenanthridinium group ($[\text{Ln}(\text{DO3PhphenMe})]^{4+}$) have been shown to selectively bind to DNA (Bobba et al., 2001; Govenlock et al., 1999).

The CPL spectra plotted in fig. 15 are the first examples of small, but measurable, CPL based on the luminescence in the near-IR region from a chiral Nd(III) complex incorporating a Pd-centered porphyrin moiety, $(RRR)\text{-[Nd(DO3MPhA)(PdPorph)]}^{3+}$ (Maupin et al., 2000). In particular, it has been shown that the Pd-porphyrin chromophore sensitizes the near-IR emission from Nd(III) and Yb(III) which are enhanced either in the presence of a nucleic acid and in the absence of oxygen (Beeby et al., 2000). Another new development of using CPL is based on the structural changes resulting from the binding of anions (e.g., carbonate, phosphate, acetate, malonate) to the lanthanide center from coordinately unsaturated chiral lanthanide (III) complexes such as $[\text{Eu}(\text{DO3Ph})]^{3+}$ and $[\text{Eu}(\text{DO3PhphenMe})]^{4+}$ (Bruce et al., 2000; Parker, 2000; Dickins et al., 1998b). Upon coordination of the added anion to the lanthanide(III) ion, a new anion-bound complex was formed in which the helical twist about the center was modified and thus led to a different CPL spectrum. As a consequence, CPL spectroscopic measurements can be used as a probe of luminescent lanthanide complexes as sensory systems for anion binding in aqueous solution (Scheme 9).

4.2.2. Chiral complexes with three-fold symmetry

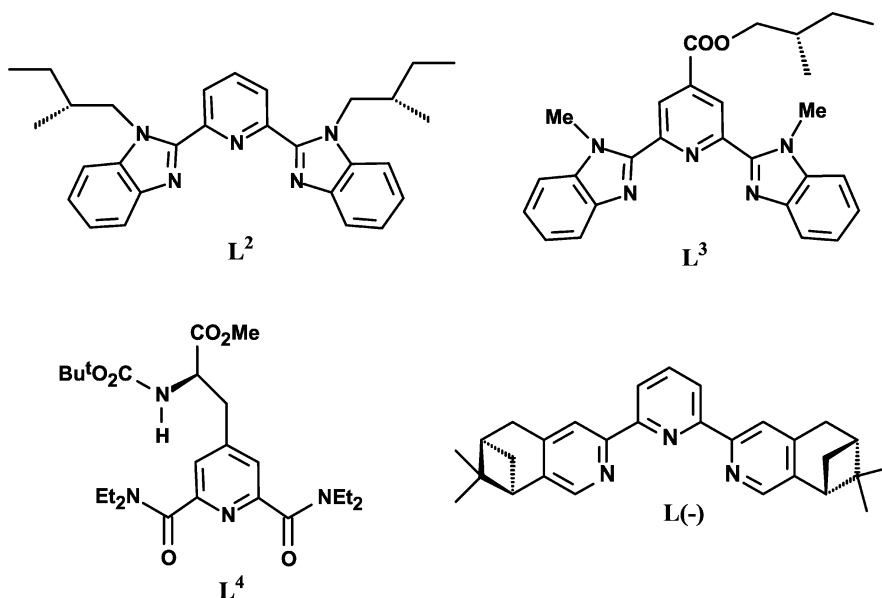
It is well known that triple-helical nine-coordinate complexes using achiral ligands are inherently chiral but they usually appear as racemic mixtures both in the solid state and in solution (Bünzli and Piguet, 2002). Since the high lability of the lanthanide (III) ions favors easy racemization of the triple helical complexes, it is possible to produce edifices in which the chirality is brought about by the ligands, a method that can only be used if the diastereomers have a large enough energy difference. During the last two years, the CPL technique has been used to probe the chiroptical properties of such systems with chiral tridentate aromatic ligands derived from 2,6-pyridine-dicarboxylic acid, bis(benzimidazole)pyridine, and terpyridine derivatives. The purpose of these studies was to attempt to quantify the importance of the helical wrapping of the ligand strand contribution and, therefore, the influence of this latter on the diastereomeric induction. Although the X-ray crystallographic analysis has shown that there is little or no helical arrangement of the ligand strands upon complexation of



Scheme 9.

2,6-bis[(1-*S*-neopentylbenzimidazol-2-yl)]-pyridine to lanthanide(III) in 1 : 3 Eu : L^2 complex (Muller et al., 2001a) the study of this system as well as of 1 : 1 and 1 : 2 complexes gave a better understanding about the influence of the helical wrapping on the chiroptical properties (Muller et al., 2003b). It should be mentioned that the steric hindrance generated by the presence of the bulky chiral neopentyl group precludes the wrapping of one of the three ligands in a helical way, as was usually observed for related 1 : 3 compounds (Muller et al., 2001a) while the ligand adopts a meridional planar coordination to the lanthanide (III) ion in the 1 : 1 complex (Scheme 10) (Muller et al., 2003b).

CPL comparative studies have been performed on anhydrous MeCN solutions of [Eu(NO₃)₃(L^2)(MeCN)], [Eu(ClO₄)₂(L^2)₂]⁺, and one with a Eu : L^2 ratio of 1 : 34 in which 20% and 80% of the Eu(III) ion are in the form of the 1 : 3 and 1 : 2 complexes, respectively (Muller et al., 2003b). The measured CPL of [Eu(NO₃)₃(L^2)(MeCN)] was due to the remote asymmetric centers' influence on chiral coordination, while for the 1 : 2 and 1 : 3 complexes, the structural contribution from the chiral helicate intervened also, as corroborated by the specific rotary dispersion values. Indeed, a little structural contribution effect (4–5 deg dm² mol⁻¹) has been evidenced for 1 : 2 complexes (33.9–35.2 deg dm² mol⁻¹) with respect to that generated by the sum of the two ligand molecules (15.1 deg dm² mol⁻¹ for the free ligand) (Muller et al., 2001a). Finally, the CPL data are consistent with the presence of a small diastereomeric excess in solution as indicating by the dependence of these latter on the polarization of the excitation light. Further experiments such as luminescence titration or temperature dependence of the ⁵D₀ ← ⁷F₀ excitation spectrum have demonstrated that the 1 : 3 and 1 : 2 species coexist in solution for a Eu : L^2 ratio of 1 : 34, in line with the observation of two CPL effects on the spectrum of this solution (Muller et al., 2003b). A similar conclusion has been found for a 10⁻³ M-solution of [Eu(ClO₄)₂(L^2)₂]⁺ in which 3% of the Eu(III) ion is in the form of the 1 : 1 species, as well as for related 1 : 3 complexes with the ligands 2,6-bis[(1-methylbenzimidazol-2-yl)]-pyridine-4-carboxylate (L^3) (Muller et al., 2002c) or



Scheme 10.

3-[2,6-bis(diethylcarbamoyl)pyridine-4-yl]-*N*-(tert-butoxycarbonyl)alanine ester (L^4) (Muller et al., 2001b). However, the CPL spectra of $[Eu(L)_3]^{3+}$ with both enantiomers, $L(+)$ and $L(-)$, of the terdentate chiral C_2 -symmetric ligand ‘dipino-[5,6:5'',6'']-fused-2,2':6',2''-terpyridine were independent of the polarization of the excitation beam, which confirms the presence of only one diastereomer in solution as pointed out by NMR (Muller et al. 2002a, 2003a). Moreover, Eu(III) and Tb(III) complexes with both enantiomers, $L(+)$ and $L(-)$, showed mirror image CPL spectra, respectively (fig. 16). The resultant emitted light is polarized in a direction determined by the helicity of the metal ion, which in turn is controlled by the absolute configuration at the remote carbon centers in the pinene moieties. This latter case is the first example of diastereoselective formation of lanthanide (III) triple helical complexes with a terdentate chiral C_2 -symmetric ligand.

4.2.3. Chiral complexes of low or no symmetry

CPL studies have also been used to investigate the solution structures of Eu(III) 1:1 complexes of chiral 18-crown-6 ligands in which the chirality is derived from stereospecific placement of methyl groups onto the crown ring (Metcalf et al., 1988, 1986). In particular, Eu(III) nitrate and chloride complexes of (2*R*,3*R*)-2,3- or (2*S*,6*S*)-2,6-dimethyl-1,4,7,10,13,16-hexaoxacyclooctadecane (L^5) and (2*R*,3*R*,11*R*,12*R*)-2,3,11,12- or (2*S*,6*S*,11*S*,15*S*)-2,6,11,15-tetramethyl-1,4,7,10,13,16-hexaoxacyclooctadecane (L^6), $[Eu(L)(X)_2]^+$ ($X = NO_3^-$ and Cl^-), have been studied in trifluoroethanol (TFE) solution (Metcalf et al., 1988) (Scheme 11). Although the opposite CPL sign observed for the *R*- and *S*-type com-

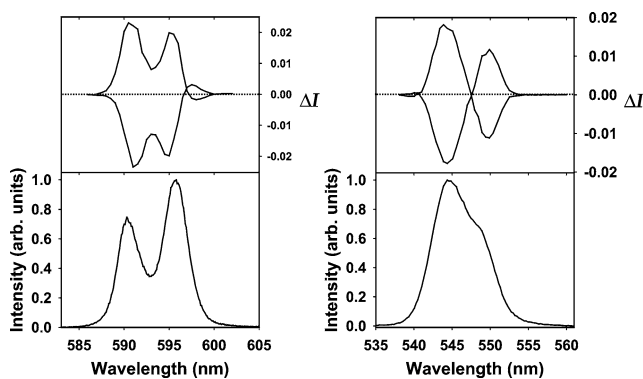
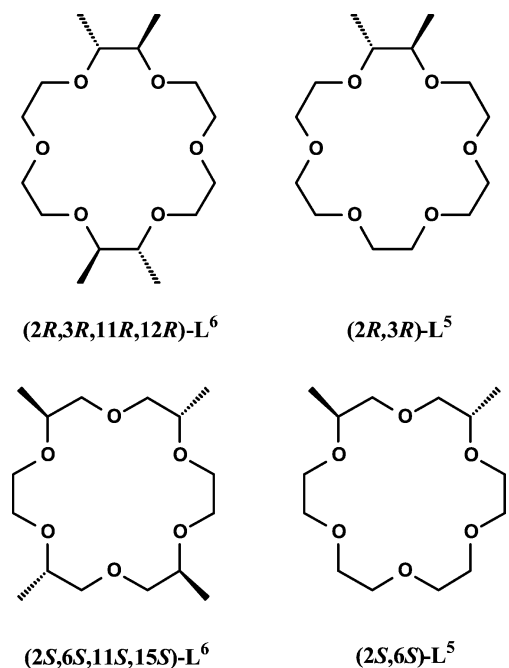
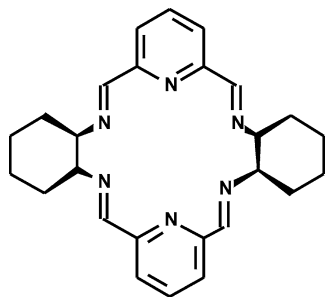


Fig. 16. Circularly polarized luminescence (upper curve) and total luminescence (lower curve) spectra of the two Eu- and Tb-containing compounds with both enantiomeric ligands, L(+) and L(-), in dry MeCN at 295 K, following excitation at 376 (left) and 373 nm (right). Left: ${}^7F_1 \leftarrow {}^5D_0$ transition, Eu(III); right: ${}^7F_5 \leftarrow {}^5D_4$ transition, Tb(III) (Muller et al., 2003a).



Scheme 11.

plexes resulted from the opposite absolute configuration of the chiral centers, its magnitude for the *R*-type systems was twice that of the corresponding *S*-type complexes indicated that the chirality also arose from conformational and configurational contributions. This magnitude difference has been explained by the greater importance of the steric interactions of the methyl substituents in the *R*-type crowns (methyl groups two atoms apart) which resulted in a larger twist of the crown ether ligands than in the *S*-type systems (methyl groups four atoms apart). Comparison of the CPL spectra of the Eu(III) nitrate and chloride complexes have shown that the complex chirality might be influenced by the nature of the anion. The

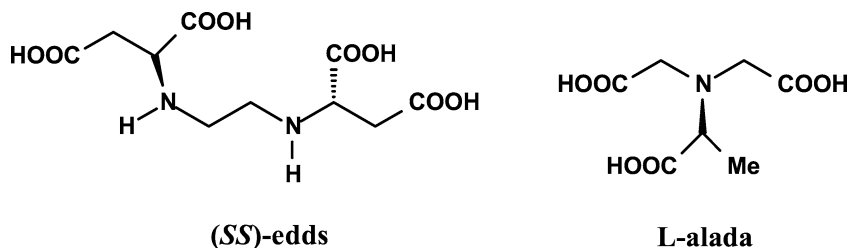
**(RR)-pydach**

Scheme 12.

optical activity of the nitrate complexes also contained a configurational contribution due to the chiral arrangement of the opposing bidentate coordinated nitrates, while the analogous Eu(III) chloride complexes did not contain such contribution. This arrangement, formed by the opposing nitrate chelate rings, has been described as a dissymmetric two-bladed propeller in which the nitrate twist angle was influenced by the steric interactions of the methyl groups onto the crown ring. As a consequence, the nitrate configurational contribution has been found more significant (larger nitrate twist angles) in the D_2 -symmetric tetramethyl crown systems than in the C_2 -symmetric dimethyl crown compounds, because of the more even spacing of the methyls around the macrocyclic ring (greater steric interactions). A similar pattern has been found for the metal transition complexes with these ligands as pointed out by the CD study (Dyer et al., 1986).

CPL investigations on Eu(III) and Tb(III) nitrate complexes with the chiral D_2 -symmetric ligand 4*R*,9*R*,19*R*,24*R*-3,10,18,25,31,32-hexaazapentacyclo[25.3.1.1.0.0]-dotriaconta-1-(31),2,10,12,14,16(32),17,25,27,29-decaene (*RR*-pydach) (Scheme 12) and its *SS*-pydach enantiomer have shown that the strong measured CPL, $g_{lum} = -0.19$ at 596 nm ($^5D_0 \rightarrow ^7F_1$ transition), was only due to the twisted conformation (Tsubomura et al., 1992). In the case of the complexes, $[Ln(RR\text{-pydach})]^{3+}$ and $[Ln(SS\text{-pydach})]^{3+}$, there was no evidence of a contribution from coordinated nitrate anions on the complex chirality as previously observed. The complex structures which have been characterized by NMR and luminescence spectroscopy have suggested that the nitrate anions were not coordinated to the lanthanide (III) ion in these species and, also, that approximately three water molecules were bound to the metal center.

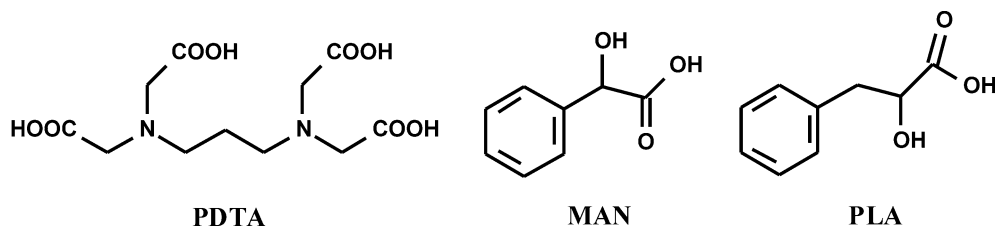
Chiroptical structures of lanthanide (III) complexes with chiral amino-polycarboxylate ligands such as (*S,S*)- and (*R,R*)-ethylenediamine-*N,N'*-disuccinic acid (edds) and L-alaninediacetate (alada) (Scheme 13) have been characterized by CPL (Murata et al., 1996). In particular, CPL spectra of nine-coordinate lanthanide(III) complexes of the hexadentate (*S,S*)-edds in aqueous solution have revealed strong and weak but measurable signal for Eu(III) or Tb(III) and Dy(III) or Sm(III) ions, respectively (Morita et al., 2000; Murata et al., 1988). The optical activity of these systems has been explained by conformational effects induced by the arrangement of the ligand coordinated to the metal ion, and by the asymmetric atoms in the ligand. As a comparison, the CPL lineshape and its mag-



Scheme 13.

nitude were different in the lanthanide(III)-L-alada system (Murata et al., 1996) which can be understood by a structural consideration. In an alada complex, the lanthanide (III) ion is coordinated to two tetradentate ligands and one or two water molecules, whereas in an edds complex, the metal ion is bound to one hexadentate ligand and three water molecules, leading to different symmetry fields. The presence of water molecules in the inner coordination sphere of these compounds has been assumed by analogy to the structure of Tb(III) complexes with ethylenediamine-tetraacetate (edta) and nitrilotriacetate (nta) ligands (Horrocks and Sudnick, 1979).

4.2.3.1. *Mixed ligand systems.* CPL measurements have also been performed on so-called *mixed-ligand* lanthanide systems in which a luminescent lanthanide ion is presumably coordinated to more than one type of ligand with one or more of the ligands being optically active. For example, the formation of Tb(PDTA) *mixed-ligand* complexes (PDTA = *R*-, *S*-, and *R,S*-1,2-propanediaminetetraacetic acid) with selected α -hydroxycarboxylic acids such as the *R*-, *S*- and *R,S*-isomers of both mandelic (MAN) and 3-phenyllactic (PLA) (Scheme 14) acids have been investigated (Brittain, 1997b). The results from these studies were interpreted by the authors in terms of the influence of differential steric interactions, originating from perturbations in ligand conformations, accompanying the formation of the [Tb(PDTA)(MAN)] complex and, therefore, influencing the lineshape of its resulting CPL signal. No such effects were observed in the case of [Tb(PDTA)(PLA)], but the measured CPL signal in this case was found to be the sum of the PDTA and PLA contributions.



Scheme 14.

Table 12

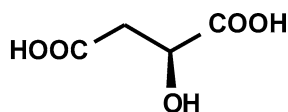
List of lanthanide (III) complexes containing ligands of more than one type in which CPL has been reported since the last general review of Riehl and Richardson (1986)

Complex	Reference
Tb(III)(PDTA)(MAN)	(Brittain, 1997b)
Tb(III)(PDTA)(PLA)	
PDTA = 1,2-propanediaminetetraacetate MAN = mandelic acid PLA = phenyllactic acid	
Tb(III)(<i>R</i> -PDTA)(AC)	(Spaulding et al., 1986)
Tb(III)(<i>R,R</i> -CDTA)(AC)	
<i>R</i> -PDTA = (<i>R</i>)-1,2-propanediaminetetraacetate <i>R,R</i> -CDTA = (<i>R,R</i>)-trans-1,2-cyclohexanediamine-tetraacetic acid AC = various achiral carboxylic acids	
Tb(III)(EDDS)(AC)	
EDDS = (<i>S,S</i>)-ethylenediamine- <i>N,N'</i> -disuccinic acid AC = various achiral carboxylic acids	(Spaulding and Brittain, 1985)
Eu(III)(<i>R</i> -methyl- <i>p</i> -tolyl-sulfoxide)(β -diketone)	(Brittain and Johnson, 1985)
(1 : 1 and 1 : 2 adducts of various β -diketones were investigated)	

In a previous review article, CPL measurements from mixed-ligand lanthanide complexes appearing in the literature prior to 1985 have been tabulated. In table 12 we list the publications involving CPL from these types of systems that have appeared since this last review.

In the interpretation of CPL results from *mixed-ligand* lanthanide complexes, one must be concerned with the possibility that the luminescence originates from a complicated distribution of species, and not simply a complex composed of ligands in the exact stoichiometry that the solution was prepared. It is always the case that the measurement of CPL for solutions in which the distribution of chiral species is undetermined is liable to misinterpretation. To illustrate this point, we consider the results obtained for an aqueous solution of Eu(III) in which two equivalents of DPA and one equivalent of L-malic acid (L-mal) (Scheme 15) have been added (Riehl, 1994; Hilmes and Riehl, 1987; Riehl, 1992).

In figs. 17 and 18 we plot, the total luminescence and CPL for a solution of Eu(III), DPA and L-mal prepared with a ratio of 1 : 2 : 1.82. We have taken care here not to plot these two spectra on the same figure, because it has been shown that the total luminescence comes almost exclusively from the very stable racemic-[Eu(DPA)₃]³⁻ complex, but this racemic mixture exhibits no CPL. The weak CPL given in fig. 18, however, originates from some



L-mal

Scheme 15.

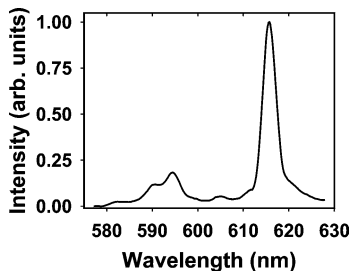


Fig. 17. Total luminescence spectrum for the ${}^7F_1 \leftarrow {}^5D_0$ and ${}^7F_2 \leftarrow {}^5D_0$ transitions of an aqueous solution of Eu(III), DPA and L-mal prepared with a ratio of 1:2:1.82 at pH = 8.1, following excitation at 476.5 nm (Hilmes and Riehl, 1987).

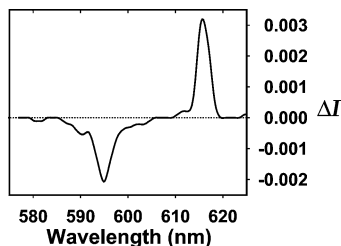
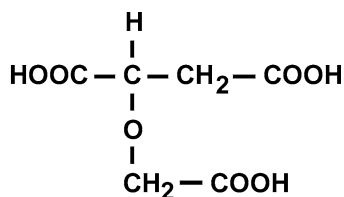


Fig. 18. Circularly polarized luminescence for the ${}^7F_1 \leftarrow {}^5D_0$ and ${}^7F_2 \leftarrow {}^5D_0$ transitions of an aqueous solution of Eu(III), DPA and L-mal prepared with a ratio of 1:2:1.82 at pH = 8.1, following circularly polarized 476.5-nm excitation (Hilmes and Riehl, 1987).

unknown weakly luminescent distribution of complexes containing L-mal, H_2O , DPA and Eu(III). Clearly, it would be a mistake to divide the value for ΔI from fig. 18 by I from fig. 17 to determine a g_{lum} value for some "mixed-ligand" complex of fixed stoichiometry.

4.2.3.2. Other chiral mixtures. It is obviously difficult to obtain useful detailed structural information from CPL measurements from lanthanide complexes with a mixture of ligands, some of which may be chiral, or in situations in which one chiral ligand may form multiple solution species. In general, unless there is additional structural information available, the measurement of CPL from these systems can only indicate that the average solution structure is chiral, and intact to some extent on the emission timescale. A tabulation of CPL results on various lanthanide (III) systems composed of mixtures of ligands that appeared prior to 1985 has been given in a previous review article (Riehl and Richardson, 1986). Two more recent studies will be briefly described here. A CPL study of Eu(III) complexes of chiral Schiff base ligands derived from the condensation of substituted salicylaldehydes with amino alcohols in a ratio of 1:1 has shown that oligomers are formed in solution under the conditions used, and the results were, therefore, not interpretable in terms of a simple solution structure (Calienni and Brittain, 1986). A similar situation was encountered in a CPL study of Tb(III) complexes with tetradentate *S*-carboxymethoxysuccinic acid (CMOS) (Scheme 16) (Brittain et al., 1991). In this work, the concentration dependence of the observed CPL has been related to the polynuclear nature of the complexes formed in solution, although, again, no specific structural information could be obtained.

For the first ten to fifteen years of CPL spectroscopy, a fairly large number of papers were published in which the main purpose of the work was to determine whether or not the solution species formed exhibited circularly polarized luminescence, and was therefore, chiral



CMOS

Scheme 16.

and stable on the emission lifetime. Variation of ligand ratios, ligand structure, solvent, etc. were used in a general way to probe the sources of chirality and some elements of solution structure. This pioneering work exploited the lability and variable coordination properties of lanthanide complexes. Within the last fifteen years, however, the field of CPL spectroscopy from lanthanide complexes that warrants publication, has been focused almost exclusively on complexes of well-defined structure or solution speciation.

4.3. CPL from Lanthanide (III) ions in biological systems

Although the measurement of CPL from lanthanide ions associated with biomolecular systems has great potential as a local probe of chirality around metal binding sites, the number of applications of CPL to such chiral systems reported to date has been quite limited. CPL from Tb(III) and Eu(III) have been used to probe conformational changes in calcium-binding (Çoruh and Riehl, 1991, 1992; Çoruh et al., 1988a; Riehl and Çoruh, 1991) and iron-binding proteins (Abdollahi et al., 1996). Whereas, CD measurements on proteins are widely used to obtain macromolecular features of secondary and tertiary structure (e.g., % alpha-helicity), CPL measurements from lanthanides may yield very local information concerning the chiral environment of the metal ion. In these works, Tb(III) and Eu(III) are bound to the Ca or Fe binding sites of the proteins calmodulin (CaM), parvalbumin (Parv), trypsin (Tryp) or transferrin (Tf), lactoferrin (Lf), and ovotransferrin (ovoTf), respectively. In particular, the differences in lineshape and magnitude of the CPL spectra from Tb(III) bound to Tf or Lf and ovoTf have been explained by structural changes of the binding sites of these systems (Abdollahi et al., 1996). In the case of the calcium-binding proteins, it has been shown that the CPL spectra for EF-hand proteins such as CaM and Parv are very similar and, therefore, the coordination environments in these proteins are very closely related, as already pointed out by structural studies. On the other hand, the sign and splitting pattern for other protein classes such as intestinal calcium-binding proteins (e.g., Tryp) are different. In this work, the sequence of binding and conformational changes induced by the addition of metal ion to the CaM in buffered aqueous media could be followed by variation in the magnitude of the CPL signal (Çoruh and Riehl, 1991, 1992; Çoruh et al., 1988a). These results need to be interpreted in the context of differential binding affinities, as compared to Ca(II). The generally accepted order of binding for Tb(III) or Eu(III) is I and II, and then III and IV as corroborated by competitive and sequential binding experiments in which g_{lum} was monitored (Çoruh and Riehl, 1991, 1992). Ca(II) binds in the order III and IV, then I and II. The

variation of g_{lum} with added lanthanide ion has been used to confirm previous CD results, namely, that CaM has essentially reached its final conformation after the binding of two metal ions and, also, that the environment of the second two sites is not as chiral as the first two. It should be mentioned that all bound lanthanide ions contribute to the CPL signal and that the results must be interpreted in terms of the average coordination environment of all four sites.

As implied in the previous discussions, a single CPL spectrum is often representative of several independent contributions either from different emitting species or from multiple conformations of these latter that exist simultaneously in the solution. As a consequence, these overlapping contributions do not allow the obtaining of individual information from the different emitting species present in the solution. One way to resolve this lack of information, in situations where the number of distinct species is small, might be to use a technique based on the determination of time-resolved CPL as already employed for enantioselective quenching of lanthanide luminescence, as a probe of energy-transfer dynamics in rare-earth doped crystals (Eu(III) ions in YAG, LaF₃, and LaAlO₃ crystals) (Reid, 1990), or in the study of biomolecules such as reduced nicotinamide adenine dinucleotide (NADH) bound to horse liver alcohol dehydrogenase (LADH) (Schauerte et al., 1995, 1992). It has been demonstrated that each emitting species has its own characteristic decay time associated with its electronically excited state and, therefore, can be used to obtain information on the individual CPL contribution of each luminophore. For example, a time-resolved CPL study of a mixture of Tb(III)/transferring and Tb(III)/conalbumin have demonstrated that it was possible to distinguish the two luminophores contributing for the overall CPL signal that differ by only 7% in lifetime and have a difference in g_{lum} factors of only 0.05 (Schauerte et al., 1996).

5. Magnetic Circularly Polarized Luminescence

Whereas only species that are "chiral" exhibit circularly polarized luminescence in the absence of an external magnetic field, all luminescence will be circularly polarized when detected axial (i.e. parallel) to an external magnetic field. This technique is commonly referred to as Magnetic Circularly Polarized Luminescence (MCPL), or alternatively as Magnetic Circularly Polarized Emission (MCPE), or Magnetic Induced Circular Emission (MICE). A general theoretical description of MCPL has been presented by Riehl and Richardson (1976b), and other theoretical descriptions of MCPL are available (Wagnière, 1984; Hipps, 1977, 1978; Schatz et al., 1978). A number of the early experimental applications of this technique have been discussed in previous review articles (Richardson and Riehl, 1977; Riehl and Richardson, 1986). The reader is referred to these articles for a more complete description of this spectroscopic technique. MCPL instrumentation is virtually identical to the instrumentation presented in sect. 3.1 with the addition of external magnetic field oriented in the direction of emission detection. Instruments specifically designed for MCPL measurements have also been described (Hipps and Crosby, 1977; Schultheiss and Gliemann, 1986).

5.1. Theoretical aspects

As shown in sect. 2.1, in natural CPL spectroscopy, the final formal relationships connecting experimental measurements and molecular transition matrix elements are developed so that comparison can be made with natural CD spectroscopy. The theoretical description of MCPL spectroscopy has been based on previous development of the much more widely used Magnetic Circular Dichroism (MCD) technique (Stephens, 1970; Dooley and Dawson, 1984). MCD is the measurement of the differential absorption of circularly polarized light in the direction of (axial to) the imposed external magnetic field. An external magnetic field will lead to splitting of Zeeman level degeneracies, and field strength-dependent mixing of ground and excited electronic states. The splitting of initial state Zeeman levels will also cause the spectra to be temperature dependent due to Boltzmann distribution among these closely spaced levels. Because of these complicated effects, the analysis of experimental MCD and MCPL spectra has traditionally been accomplished by resolving the resultant spectrum into the so-called Faraday \mathcal{A} , \mathcal{B} and \mathcal{C} terms. \mathcal{A} terms are associated with the appearance of a first derivative lineshape due to the fact that a degenerate state has been split so that one component absorbs or emits predominantly left circular polarization and the other component absorbs or emits predominantly right circular polarization. \mathcal{C} terms are associated with the temperature dependent part of the spectrum, and the rest of the spectrum is defined as a \mathcal{B} term.

In analogy with eq. (12) we may relate the differential emission intensity to the Faraday \mathcal{A} , \mathcal{B} and \mathcal{C} terms for MCPL from a transition $\mathcal{N} \rightarrow \mathcal{G}$ in which the magnetic field induced Zeeman splitting is much less than the line width, as follows

$$\Delta I(\lambda) = \left(\frac{\hbar c \eta_{\mathcal{N}}}{2\lambda} \right) \left(K(\lambda^3) \left\{ \mathcal{A}(\mathcal{N} \rightarrow \mathcal{G}) f'_{\text{MCPL}}(\lambda) / \hbar \right. \right. \\ \left. \left. + [\mathcal{B}(\mathcal{N} \rightarrow \mathcal{G}) + \mathcal{C}(\mathcal{N} \rightarrow \mathcal{G}) / kT] f_{\text{MCPL}}(\lambda) \right\} b_0 \right). \quad (52)$$

\mathcal{N} and \mathcal{G} in this equation refer to the set of degenerate Zeeman levels, f_{MCPL} and f'_{MCPL} refer, respectively, to the MCPL lineshape and its first derivative, and b_0 denotes the external magnetic field strength. Just as in the case for natural CPL, more specific expressions relating molecular transition moments in the laboratory or molecular coordinate system may be derived given an experimental geometry. Some common results may be found in the review by Richardson and Riehl (1977).

5.2. MCPL experimental results from luminescent lanthanide systems

In table 13 we list the applications of MCPL to lanthanide systems that have been reported. Applications of this technique in solids have focused on its use as a probe of Zeeman level degeneracy as a probe of site symmetry (Schwartz et al., 1977), or in studies interested in examining the field-induced mixing of electronic states as shown in recent applications of MCPL measurements from Tb(III) and Ho(III) doped into garnets (Valiev et al., 2002a, 2002b).

In an early study, Brittain and Richardson have examined the effect of an axial magnetic field on the energy levels of Eu(III) (Richardson and Brittain, 1981), and used the results

Table 13
List of the lanthanide systems for which MCPL measurements have been reported

Lanthanide complex or compound	Sample description	Reference
EuCl ₃	0.10 M in DMF and MeOH	(Foster et al., 1983) (Stephens et al., 1986)
Eu(NO ₃) ₃	Dissolved in various protic and aprotic solvents	(Stephens et al., 1986)
[Eu(DPA) ₃] ³⁻ DPA = dipicolinic acid	0.10 M in H ₂ O	(Foster and Richardson, 1983)
[Eu(ODA) ₃] ³⁻ ODA = oxydiacetic acid		
[Eu(IDA) ₃] ³⁻ IDA = iminodiacetic acid		
[Eu(MIDA) ₃] ³⁻ MIDA = methyl-iminodiacetic acid		
[Eu(EDTA)] ¹⁻	25 mM in D ₂ O	(Schultheiss and Gliemann, 1986)
[Eu(citrate) ₂] ³⁻	50 mM in D ₂ O	(Schultheiss and Gliemann, 1986)
[Eu(2,2'-bipyridine-1,1'-dioxide) ₄] ³⁺	0.25 mM in nitromethane	(Morita et al., 1992)
[Eu(fod) ₃]	2.0 mM in H ₂ O	(Morita et al., 1992)
Fod = 6,6,7,7,8,8,8-heptafluoro-2,2-dimethyl-3,5-octanedionate	0.67 mM in DMF	(Richardson and Brittain, 1981)
[Eu(thd) ₃] thd = 2,2,6,6-tetramethyl-3,5-heptanedionate	0.67 M in DMF	(Richardson and Brittain, 1981)
[Eu(dbm) ₃] dpm = dibenzoylmethanate		
[Eu(Bzac) ₃] Bzac = 1-benzoylacetonate		
[Eu(2,2'-bipyridine) ₂] ³⁺	2.0 mM in DMSO	(Morita et al., 1992)
[Eu(facam) ₃] facam = 3-(trifluoromethyl-hydroxymethylene)-d-camphorato	Dissolved in poly(methylmethacralate) at 77 K	(Morita et al., 1988)
[Eu(β-diketonates a-d) ₃] a. 1,1,1,5,5,5-hexafluoro-2,4-pentanedionato b. 1,1,1-trifluoro-2,4-pentanedionato c. 1,3-bis(3-pyridyl)-1,3-propanedionato d. 4,4,4-trifluoro-1-(2-furyl)-1,3-butanedionato	0.01 M in DMF	(Foster et al., 1983)
Cs ₂ [NaTbCl ₆]	Crystal	(Schwartz et al., 1977)
Cs ₂ [NaEuCl ₆]	Crystal	(Morley et al., 1982a)
Cs ₂ [NaPrCl ₆]	Crystal	(Morley et al., 1982b)
Y ₃ Al ₅ O ₁₂ :Tb ³⁺	5% doped crystal	(Valiev et al., 2002a)
Y ₃ Al ₅ O ₁₂ :Ho ³⁺		(Valiev et al., 2002b)

to gain information concerning whether or not the Eu(III) complex possessed axial symmetry (i.e. a C_n axis where $n > 2$). Similar studies have been undertaken on 9-coordinate tris terdentate complexes in aqueous (Foster and Richardson, 1983) and non-aqueous solutions (Foster et al., 1983), a tetrakis bidentate complex (Morita et al., 1992), and other less symmetric systems as given in table 13.

6. Summary

Although still limited to a very few laboratories around the world, the measurement of the usually small net circular polarization in the luminescence from chiral species containing lanthanide ions can now be accomplished with a high degree of sensitivity and reliability. Recent advances in instrumentation, such as the ability to measure the time-dependence of g_{lum} , should allow for additional applications of this technique in the microsecond to millisecond time frame. This time domain is an interesting one since structural changes associated with many important biological processes are known to occur on this time scale. Instrumental improvements, such as the use of array detectors, should allow for significant advances in the time required to collect an accurate CPL spectrum. This will, of course, help to eliminate some observed photochemical degradation which is a common problem when trying to measure the CPL from systems using indirect UV excitation. It is certainly possible to envisage the development of circularly polarized luminescence imaging as an important tool for biological applications, and the detection of circular polarization in the luminescence from single molecules containing luminescent lanthanide ions could provide a unique probe of individual molecular dynamics.

As described throughout this chapter, CPL is becoming increasingly useful as a probe of the existence of chiral lanthanide structures, and as an indicator of changes in chiral structure. However, there are currently no reliable correlations relating specific aspects of chiral structure to CPL measurements. The development of such spectra-structure correlations is key to the advancement of this technique as a useful probe of the stereochemistry of chiral lanthanide systems.

Acknowledgements

The authors gratefully acknowledge the many students and collaborators who have contributed to our research efforts in the CPL spectroscopy of lanthanide systems. Special recognition is given to Dr. Frederick L. Richardson, Dr. Harry P.J.M. Dekkers, Dr. Janina Legendziewicz, and Dr. David Parker for many years of fruitful collaboration. G.M. express his gratitude to Dr. Jean-Claude G. Bünzli for his support and guidance during his doctoral studies, and JPR wishes to recognize the contributions of his former doctoral students Dr. Christine L. Maupin, Dr. Nursen Çoruh, and Dr. Gary L. Hilmes. The authors also thank Mrs. Françoise C. Muller for her technical help in the preparation of the manuscript.

References

- Abdollahi, S., Harris, W.R., Riehl, J.P., 1996. *J. Phys. Chem.* **100**, 1950–1956.
- Aime, S., Botta, M., Dickins, R.S., Maupin, C.L., Parker, D., Riehl, J.P., Williams, J.A.G., 1998. *J. Chem. Soc., Dalton Trans.*, 881–892.
- Albertsson, J., Elding, L.I., 1977. *Acta Crystallogr. B* **33**, 1460–1469.
- Barnett, C.J., Drake, A.F., Mason, S.F., 1979. *Bull. Soc. Chim. Belg.* **88**, 853–862.
- Beeby, A., Dickins, R.S., FitzGerald, S., Govenlock, L.J., Maupin, C.L., Parker, D., Riehl, J.P., Siligardi, G., Williams, J.A.G., 2000. *Chem. Commun.*, 1183–1184.
- Belair, S.D., Maupin, C.L., Logue, M.W., Riehl, J.P., 2000. *J. Luminesc.* **86**, 61–66.
- Berry, M.T., Schwieters, C., Richardson, F.S., 1988. *Chem. Phys.* **122**, 125–139.
- Blok, P.M.L., Schakel, P., Dekkers, H.P.J.M., 1990. *Meas. Sci. Technol.* **1**, 126–130.
- Bobba, G., Dickins, R.S., Kean, S.D., Mathieu, C.E., Parker, D., Peacock, R.D., Siligardi, G., Smith, M.J., Williams, J.A.G., Geraldès, C.F.G.C., 2001. *J. Chem. Soc., Perkin Trans.* **2**, 1729–1737.
- Bolender, J.P., Metcalf, D.H., Richardson, F.S., 1993. *Chem. Phys. Lett.* **213**, 131–138.
- Bolender, J.P., Metcalf, D.H., Richardson, F.S., 1994. *J. Alloys Compd.* **207–208**, 55–58.
- Brittain, H.G., 1980. *J. Am. Chem. Soc.* **102**, 3693–3698.
- Brittain, H.G., 1981. *Inorg. Chem.* **20**, 3007–3013.
- Brittain, H.G., 1984. *J. Chem. Soc., Dalton Trans.*, 1367–1370.
- Brittain, H.G., 1989. *J. Coord. Chem.* **20**, 331–347.
- Brittain, H.G., 1991. *Pract. Spectrosc.* **12**, 179–200.
- Brittain, H.G., 1997a. *Microchem. J.* **57**, 137–148.
- Brittain, H.G., 1997b. *Chirality* **9**, 583–592.
- Brittain, H.G., 1998. *J. Pharm. Biomed. Anal.* **17**, 933–940.
- Brittain, H.G., 2000. *Appl. Spectrosc. Rev.* **35**, 175–201.
- Brittain, H.G., Johnson, C.R., 1985. *Inorg. Chem.* **24**, 4465–4469.
- Brittain, H.G., Kelty, S.P., Peters, J.A., 1991. *J. Coord. Chem.* **23**, 21–32.
- Bruce, J.I., Dickins, R.S., Govenlock, L.J., Gunnlaugsson, T., Lopinski, S., Lowe, M.P., Parker, D., Peacock, R.D., Perry, J.J.B., Aime, S., Botta, M., 2000. *J. Am. Chem. Soc.* **122**, 9674–9684.
- Bruce, J.I., Parker, D., Lopinski, S., Peacock, R.D., 2002. *Chirality* **14**, 562–567.
- Bruce, J.I., Parker, D., Tozer, D.J., 2001. *J. Chem. Soc., Chem. Commun.*, 2250–2251.
- Bünzli, J.-C.G., Piguet, C., 2002. *Chem. Rev.* **102**, 1897–1928.
- Calienni, J.J., Brittain, H.G., 1986. *Inorg. Chim. Acta* **116**, 163–169.
- Cantuel, M., Bernardinelli, G., Muller, G., Riehl, J.P., Piguet, C., 2004. *Inorg. Chem.* **43**, 1840–1849.
- Çoruh, N., Hilmes, G.L., Riehl, J.P., 1988a. *J. Luminesc.* **40–41**, 227–228.
- Çoruh, N., Hilmes, G.L., Riehl, J.P., 1988b. *Inorg. Chem.* **27**, 3647–3651.
- Çoruh, N., Riehl, J.P., 1991. *Collect. Czech. Chem. Commun.* **56**, 3028–3031.
- Çoruh, N., Riehl, J.P., 1992. *Biochemistry* **31**, 7970–7976.
- Çoruh, N., Wu, S., Hilmes, G.L., Riehl, J.P., 1991. *Lanthanide Actinide Res.* **3**, 357–365.
- Dekkers, H.P.J.M., Moraal, P.F., Timper, J.M., Riehl, J.P., 1985. *Appl. Spectrosc.* **39**, 818–821.
- Di Bari, L., Pintacuda, G., Salvadori, P., Dickins, R.S., Parker, D., 2000. *J. Am. Chem. Soc.* **122**, 9257–9264.
- Dickins, R.S., Howard, J.A.K., Maupin, C.L., Moloney, J.M., Parker, D., Peacock, R.D., Riehl, J.P., Siligardi, G., 1998a. *New J. Chem.* **22**, 891–899.
- Dickins, R.S., Gunnlaugsson, T., Parker, D., Peacock, R.D., 1998b. *Chem. Commun.*, 1643–1644.
- Dickins, R.S., Howard, J.A.K., Lehmann, C.W., Moloney, J.M., Parker, D., Peacock, R.D., 1997a. *Angew. Chem. Int. Ed. Engl.* **36**, 521–523.
- Dickins, R.S., Howard, J.A.K., Maupin, C.L., Moloney, J.M., Parker, D., Riehl, J.P., Siligardi, G., Williams, J.A.G., 1999. *Chem. Eur. J.* **5**, 1095–1105.
- Dickins, R.S., Howard, J.A.K., Moloney, J.M., Parker, D., Peacock, R.D., Siligardi, G., 1997b. *Chem. Commun.*, 1747–1748.
- Dickins, R.S., Parker, D., Bruce, J.I., Tozer, D.J., 2003. *J. Chem. Soc., Dalton Trans.*, 1264–1271.
- Dooley, D.M., Dawson, J.H., 1984. *Coord. Chem. Rev.* **60**, 1–66.
- Dossing, A., Sokolnicki, J., Riehl, J.P., Legendziewicz, J., 2002. *J. Alloys Compd.* **341**, 150–155.
- Dyer, R.B., Metcalf, D.H., Ghirardelli, R.G., Palmer, R.A., Holt, E.M., 1986. *J. Am. Chem. Soc.* **108**, 3621–3629.
- Emeis, C.A., Oosterhof, L.J., 1967. *Chem. Phys. Lett.* **1**, 129–132, errata 268.
- Emeis, C.A., Oosterhof, L.J., 1971. *J. Chem. Phys.* **54**, 4809–4819.

- Field, J.E., Muller, G., Riehl, J.P., Venkataraman, D., 2003. *J. Am. Chem. Soc.* **125**, 11808–11809.
- Foster, D.R., Richardson, F.S., 1983. *Inorg. Chem.* **22**, 3996–4002.
- Foster, D.R., Richardson, F.S., Vallarino, L.M., Shillady, D., 1983. *Inorg. Chem.* **22**, 4002–4009.
- Gawryszewska, P., Sokolnicki, J., Dossing, A., Riehl, J.P., Muller, G., Legendziewicz, J., Manuscript in preparation.
- Glover, D.P., Metcalf, D.H., Richardson, F.S., 1992. *J. Alloys Compd.* **180**, 83–92.
- Glover-Fischer, D.P., Metcalf, D.H., Bolender, J.P., Richardson, F.S., 1995. *Chem. Phys.* **198**, 207–234.
- Glover-Fischer, D.P., Metcalf, D.H., Hopkins, T.A., Pugh, V.J., Chisdes, S.J., Kankare, J., Richardson, F.S., 1998. *Inorg. Chem.* **37**, 3026–3033.
- Gochanour, C.R., Fayer, M.D., 1981. *J. Phys. Chem.* **85**, 1989–1994.
- Govenlock, L.J., Mathieu, C.E., Maupin, C.L., Parker, D., Riehl, J.P., Siligardi, G., Williams, J.A.G., 1999. *J. Chem. Soc., Chem. Commun.*, 1699–1700.
- Herren, M., Morita, M., 1996. *J. Luminesc.* **66–67**, 268–271.
- Hilmes, G.L., Çoruh, N., Riehl, J.P., 1988. *Inorg. Chem.* **27**, 1136–1139.
- Hilmes, G.L., Riehl, J.P., 1983. *J. Phys. Chem.* **87**, 3300.
- Hilmes, G.L., Riehl, J.P., 1986. *Inorg. Chem.* **25**, 2617–2622.
- Hilmes, G.L., Riehl, J.P., 1987. *Inorg. Chim. Acta* **129**, 123–125.
- Hilmes, G.L., Timper, J.M., Riehl, J.P., 1985. *Inorg. Chem.* **24**, 1721–1723.
- Hipps, K.W., 1977. *Chem. Phys.* **23**, 451–463.
- Hipps, K.W., 1978. *J. Phys. Chem.* **82**, 602–605.
- Hipps, K.W., Crosby, G.A., 1977. *Proc. Soc. Photo-Opt. Instrum. Eng.* **112**, 132–137.
- Hopkins, T.A., Bolender, J.P., Metcalf, D.H., Richardson, F.S., 1996. *Inorg. Chem.* **35**, 5356–5362.
- Hopkins, T.A., Metcalf, D.H., Richardson, F.S., 1998. (1998) *Inorg. Chem.* **37**, 1401–1412.
- Horrocks, W.d.J., Sudnick, D.R., 1979. *J. Am. Chem. Soc.* **101**, 334–340.
- Huskowska, E., Gawryszewska, P., Legendziewicz, J., Maupin, C.L., Riehl, J.P., 2000. *J. Alloys Compd.* **303–304**, 325–330.
- Huskowska, E., Maupin, C.L., Parker, D., Williams, J.A.G., Riehl, J.P., 1997. *Enantiomer* **2**, 381–395.
- Huskowska, E., Riehl, J.P., 1995. *Inorg. Chem.* **34**, 5615–5621.
- Huskowska, E., Riehl, J.P., 2000. *J. Luminesc.* **86**, 137–146.
- Huskowska, E., Turowska-Tyrk, I., Legendziewicz, J., Riehl, J.P., 2002. *New J. Chem.* **26**, 1461–1467.
- Kemp, J.C., 1969. *J. Opt. Soc. Am.* **59**, 950–954.
- Luck, R.L., Maupin, C.L., Parker, D., Riehl, J.P., Williams, J.A.G., 2001. *Inorg. Chim. Acta* **317**, 331–337.
- Luk, C.K., Richardson, F.S., 1974. *J. Am. Chem. Soc.* **96**, 2006–2009.
- Mason, S.F., 1982. *Molecular Optical Activity and the Chiral Discriminations*. Cambridge University Press, Cambridge.
- Maupin, C.L., 1999. Ph.D. Dissertation. Michigan Technological University, Houghton.
- Maupin, C.L., Dickins, R.S., Govenlock, L.J., Mathieu, C.E., Parker, D., Williams, J.A.G., Riehl, J.P., 2000. *J. Phys. Chem. A* **104**, 6709–6717.
- Maupin, C.L., Meskers, S.C.J., Dekkers, H.P.J.M., Riehl, J.P., 1996. *J. Chem. Soc., Chem. Commun.*, 2457–2458.
- Maupin, C.L., Meskers, S.C.J., Dekkers, H.P.J.M., Riehl, J.P., 1998a. *J. Phys. Chem. A* **102**, 4450–4455.
- Maupin, C.L., Mondry, A., Leifer, L., Riehl, J.P., 2001. *J. Phys. Chem. A* **105**, 3071–3076.
- Maupin, C.L., Parker, D., Williams, J.A.G., Riehl, J.P., 1998b. *J. Am. Chem. Soc.* **120**, 10563–10564.
- Maupin, C.L., Riehl, J.P., 2000. In: Lindon, J.C., Trantner, G.E., Holmes, J.L. (Eds.), *Encyclopedia of Spectroscopy and Spectrometry*. Academic Press, New York, pp. 319–326.
- May, P.S., Metcalf, D.H., Richardson, F.S., Carter, R.C., Miller, C.E., Palmer, R.A., 1992. *J. Luminesc.* **51**, 249–268.
- May, P.S., Reid, M.F., Richardson, F.S., 1987. *Mol. Phys.* **62**, 341–364.
- Meskers, S.C.J., Dekkers, H.P.J.M., 1997. *J. Alloys Compd.* **250**, 332–335.
- Meskers, S.C.J., Dekkers, H.P.J.M., 1998a. *Enantiomer* **3**, 95–102.
- Meskers, S.C.J., Dekkers, H.P.J.M., 1998b. *J. Am. Chem. Soc.* **120**, 6413–6414.
- Meskers, S.C.J., Dekkers, H.P.J.M., 1999a. *Spectrochim. Acta A* **55**, 1857–1874.
- Meskers, S.C.J., Dekkers, H.P.J.M., 1999b. *Spectrochim. Acta A* **55**, 1837–1855.
- Meskers, S.C.J., Dekkers, H.P.J.M., 2001. *J. Phys. Chem. A* **105**, 4589–4599.
- Meskers, S.C.J., Dekkers, H.P.J.M., Rapenne, G., Sauvage, J.-P., 2000. *Chem. Eur. J.* **6**, 2129–2134.
- Meskers, S.C.J., Dennison, C., Canters, G.W., Dekkers, H.P.J.M., 1998a. *J. Biol. Inorg. Chem.* **3**, 663–670.
- Meskers, S.C.J., Riehl, J.P., Dekkers, H.P.J.M., 1993. *Chem. Phys. Lett.* **216**, 241–246.

- Meskers, S.C.J., Ubbink, M., Canters, G.W., Dekkers, H.P.J.M., 1996. *J. Phys. Chem.* **100**, 17957–17969.
- Meskers, S.C.J., Ubbink, M., Canters, G.W., Dekkers, H.P.J.M., 1998b. *J. Biol. Inorg. Chem.* **3**, 463–469.
- Metcalf, D.H., Bolender, J.P., Driver, M.S., Richardson, F.S., 1993. *J. Phys. Chem.* **97**, 553–564.
- Metcalf, D.H., Carter, R.C., Ghirardelli, R.G., Palmer, R.A., 1986. *Inorg. Chem.* **25**, 2175–2180.
- Metcalf, D.H., Carter, R.C., Ghirardelli, R.G., Palmer, R.A., 1988. *Inorg. Chem.* **27**, 405–407.
- Metcalf, D.H., Snyder, S.W., Demas, J.N., Richardson, F.S., 1990a. *J. Am. Chem. Soc.* **112**, 5681–5695.
- Metcalf, D.H., Snyder, S.W., Demas, J.N., Richardson, F.S., 1990b. *J. Phys. Chem.* **94**, 7143–7153.
- Metcalf, D.H., Snyder, S.W., Demas, J.N., Richardson, F.S., 1990c. *J. Am. Chem. Soc.* **112**, 469–479.
- Metcalf, D.H., Snyder, S.W., Demas, J.N., Richardson, F.S., 1991. *Eur. J. Inorg. Sol. St. Chem.* **28**, 65–68.
- Metcalf, D.H., Snyder, S.W., Wu, S., Hilmes, G.L., Riehl, J.P., Demas, J.N., Richardson, F.S., 1989. *J. Am. Chem. Soc.* **111**, 3082–3083.
- Metcalf, D.H., Stewart, J.M.M., Snyder, S.W., Grisham, C.M., Richardson, F.S., 1992. *Inorg. Chem.* **31**, 2445–2455.
- Mondry, A., Meskers, S.C.J., Riehl, J.P., 1994. *J. Luminesc.* **62**, 17–23.
- Moran, D.M., Richardson, F.S., 1992. *Inorg. Chem.* **31**, 813–818.
- Morita, M., Gamou, K., Takada, K., Senba, Y., Rau, D., Iwamura, M., 2002a. *MCLC S&T, Section B: Non-linear Optics* **29**, 303–308.
- Morita, M., Herren, M., Ansay, T., Rau, D., 2000. *J. Luminesc.* **87–89**, 976–979.
- Morita, M., Ozawa, T., Tsubomura, T., 1992. *J. Luminesc.* **53**, 495–498.
- Morita, M., Rau, D., Iwamura, M., 2003. *Seikei Daigaku Kogaku Kenkyu Hokoku* **40**, 7–9.
- Morita, M., Rau, D., Kai, T., 2002b. *J. Luminesc.* **100**, 97–106.
- Morita, M., Sawabe, K., Nishimura, E., Eguchi, K., 1988. *J. Luminesc.* **40–41**, 889–890.
- Morley, J.P., Faulkner, L.R., Richardson, F.S., 1982a. *J. Chem. Phys.* **77**, 1710–1733.
- Morley, J.P., Faulkner, L.R., Richardson, F.S., Schwartz, R.W., 1982b. *J. Chem. Phys.* **77**, 1734–1749.
- Morley, J.P., Saxe, J.D., Richardson, F.S., 1982c. *Mol. Phys.* **47**, 379–406.
- Muller, G., Bünzli, J.-C.G., Riehl, J.P., Suhr, D., von Zelewsky, A., Mürner, H.-R., 2002a. *J. Chem. Soc., Chem. Commun.*, 1522–1523.
- Muller, G., Bünzli, J.-C.G., Schenk, K.J., Piguët, C., Hopfgartner, G., 2001a. *Inorg. Chem.* **40**, 2642–2651.
- Muller, G., Kean, S.D., Parker, D., Riehl, J.P., 2002b. *J. Phys. Chem. A* **106**, 12349–12355.
- Muller, G., Mamula, O., Bünzli, J.-C.G., Mürner, H.-R., Riehl, J.P., 2003a. In: *226th ACS National Meeting*, New York, NY, United States, September 7–11.
- Muller, G., Maupin, C.L., Riehl, J.P., Birkedal, H., Piguët, C., Bünzli, J.-C.G., 2003b. *Eur. J. Inorg. Chem.*, 4065–4072.
- Muller, G., Riehl, J.P., 2004. Unpublished results.
- Muller, G., Riehl, J.P., Schenk, K.J., Hopfgartner, G., Piguët, C., Bünzli, J.-C.G., 2002c. *Eur. J. Inorg. Chem.*, 3101–3110.
- Muller, G., Schmidt, B., Jiricek, J., Hopfgartner, G., Riehl, J.P., Bünzli, J.-C.G., Piguët, C., 2001b. *J. Chem. Soc., Dalton Trans.*, 2655–2662.
- Murata, K., Herren, M., Eguchi, K., Morita, M., 1996. *J. Alloys Compd.* **233**, 44–51.
- Murata, K., Morita, M., Eguchi, K., 1988. *J. Luminesc.* **42**, 227–234.
- Parac-Vogt, T.N., Binnemans, K., Görller-Walrand, C., 2002. *J. Chem. Soc., Dalton Trans.*, 1602–1606.
- Parker, D., 2000. *Coord. Chem. Rev.* **205**, 109–130.
- Parker, D., Dickins, R.S., Puschmann, H., Crossland, C., Howard, J.A.K., 2002. *Chem. Rev.* **102**, 1977–2010.
- Rau, D., Morita, M., 2001. *J. Luminesc.* **94–95**, 283–288.
- Reid, M.F., 1990. *J. Luminesc.* **45**, 384–386.
- Rexwinkel, R.B., Meskers, S.C.J., Dekkers, H.P.J.M., Riehl, J.P., 1992a. *J. Phys. Chem.* **96**, 5725–5733.
- Rexwinkel, R.B., Meskers, S.C.J., Dekkers, H.P.J.M., Riehl, J.P., 1993a. *J. Phys. Chem.* **97**, 13519–13526.
- Rexwinkel, R.B., Meskers, S.C.J., Riehl, J.P., Dekkers, H.P.J.M., 1992b. *J. Phys. Chem.* **96**, 1112–1120.
- Rexwinkel, R.B., Meskers, S.C.J., Riehl, J.P., Dekkers, H.P.J.M., 1993b. *J. Phys. Chem.* **97**, 3875–3884.
- Rexwinkel, R.B., Schakel, P., Meskers, S.C.J., Dekkers, H.P.J.M., 1993c. *Appl. Spectrosc.* **47**, 731–740.
- Richardson, F.S., 1980. *Inorg. Chem.* **19**, 2806–2812.
- Richardson, F.S., Brittain, H.G., 1981. *J. Am. Chem. Soc.* **103**, 18–24.
- Richardson, F.S., Metcalf, D.H., Glover, D.P., 1991. *J. Phys. Chem.* **95**, 6249–6259.
- Richardson, F.S., Riehl, J.P., 1977. *Chem. Rev.* **77**, 773–792.
- Riehl, J.P., 1992. In: *Strek, W. (Ed.), Int. Sch. Excited States Transition Elem., 2nd, Meeting Date 1991*. World Scientific, Singapore, pp. 241–246.
- Riehl, J.P., 1993. In: *Purdie, N., Brittain, H.G. (Eds.), Analytical Applications of Circular Dichroism*. Elsevier, Amsterdam.

- Riehl, J.P., 1994. In: Purdie, N., Brittain, H.G. (Eds.), *Analytical Applications of Circular Dichroism*. Elsevier Science B.V., pp. 207–240. Chapter 7.
- Riehl, J.P., 1996. *Acta Phys. Pol. A* **90**, 55–62.
- Riehl, J.P., 2000. In: Lindon, J.C., Trantner, G.E., Holmes, J.L. (Eds.), *Encyclopedia of Spectroscopy and Spectrometry*. Academic Press, New York, pp. 243–249.
- Riehl, J.P., Çoruh, N., 1991. *Eur. J. Solid State Inorg. Chem.* **28**, 263–266.
- Riehl, J.P., Richardson, F.S., 1976a. *J. Chem. Phys.* **65**, 1011–1021.
- Riehl, J.P., Richardson, F.S., 1976b. *J. Chem. Phys.* **66**, 1988–1998.
- Riehl, J.P., Richardson, F.S., 1986. *Chem. Rev.* **86**, 1–16.
- Riehl, J.P., Richardson, F.S., 1993. *Methods Enzymol.* **226**, 539–553.
- Samoilov, B.N., 1948. *J. Exp. Theor. Phys.* **18**, 1030.
- Schatz, P.N., Mowery, R.L., Krausz, E.R., 1978. *Mol. Phys.* **35**, 1537–1557.
- Schauerte, J.A., Gafni, A., Steel, D.G., 1996. *Biophys. J.* **70**, 1996–2000.
- Schauerte, J.A., Schlyer, B.D., Steel, D.G., Gafni, A., 1995. *Proc. Natl. Acad. Sci. USA* **92**, 569–573.
- Schauerte, J.A., Steel, D.G., Gafni, A., 1992. *Proc. Natl. Acad. Sci. USA* **89**, 10154–10158.
- Schipper, P.E., 1978. *J. Am. Chem. Soc.* **100**, 1079–1084.
- Schippers, P.H., 1982. Ph.D. Dissertation, University of Leiden, The Netherlands, pp. 12–25, Chapter 1.
- Schippers, P.H., Dekkers, H.P.J.M., 1981. *Anal. Chem.* **53**, 778–782.
- Schippers, P.H., van den Beukel, A., Dekkers, H.P.J.M., 1982. *J. Phys. E* **15**, 945–950.
- Schultheiss, R., Gliemann, G., 1986. *J. Luminesc.* **35**, 261–266.
- Schwartz, R.W., Brittain, H.G., Riehl, J.P., Yeakel, W., Richardson, F.S., 1977. *Mol. Phys.* **34**, 361–374.
- Sen, A.C., Chowdhury, M., Schwartz, R.W., 1981. *J. Chem. Soc., Faraday Trans. 2* **77**, 1293–1300.
- Sokolnicki, J., Legendziewicz, J., Muller, G., Riehl, J.P., 2004. Manuscript in preparation.
- Sokolnicki, J., Legendziewicz, J., Riehl, J.P., 2002. *J. Phys. Chem. B* **106**, 1508–1514.
- Spaulding, L., Brittain, H.G., 1985. *Inorg. Chim. Acta* **110**, 197–203.
- Spaulding, L., Brittain, H.G., O'Connor, L.H., Pearson, K.H., 1986. *Inorg. Chem.* **25**, 188–193.
- Steinberg, I., 1975. In: Chen, I.R.F., Edelhoch, H. (Eds.), *Biochemical Fluorescence: Concepts*, vol. 1. Marcel-Dekker, New York.
- Steinberg, I., Gafni, A., 1972. *Rev. Sci. Instrum.* **43**, 409–413.
- Stephens, E.M., Foster, D.R., Richardson, F.S., 1986. *J. Less-Common Met.* **126**, 389–394.
- Stephens, P.J., 1970. *J. Chem. Phys.* **52**, 3489–3516.
- Stockman, T.G., Kleivickis, C.A., Grisham, C.M., Richardson, F.S., 1996. *J. Mol. Recognit.* **9**, 595–606.
- Tsubomura, T., Yasaku, K., Sato, T., Morita, M., 1992. *Inorg. Chem.* **31**, 447–450.
- Valiev, U.V., Rustamov, U.R., Sokolov, B.Y., 2002a. *Phys. Sol. State* **44**, 278–281.
- Valiev, U.V., Rustamov, U.R., Sokolov, B.Y., Nekvasil, V., Rupp, R.A., Fally, M., Amin, I., 2002b. *Phys. Stat. Sol.* **231**, 98–105.
- Wagnière, G., 1984. *Chem. Phys. Lett.* **110**, 546–551.
- Wu, S., Bedard, T.C., Riehl, J.P., 1991. *Collect. Czech. Chem. Commun.* **56**, 3025–3027.
- Wu, S., Hilmes, G.L., Riehl, J.P., 1989. *J. Phys. Chem.* **93**, 2307–2310.
- Yan, F., Copeland, R.A., Brittain, H.G., 1982. *Inorg. Chem.* **21**, 1180–1185.

Chapter 221

LANTHANIDE-CONTAINING COORDINATION POLYMERS

Olivier GUILLOU* and Carole DAIGUEBONNE

Laboratoire de Chimie du Solide et Inorganique Moléculaire, UMR 6511 CNRS –
INSA Rennes, Institut National des Sciences Appliquées, 20 Avenue des Buttes de
Cöesmes, 35043 Rennes, France

E-mail: {olivier.guillou,carole.daiguebonne}@insa-rennes.fr

Contents

List of acronyms	359	3.5. Coordination polymers based on benzene polycarboxylate derivatives	386
1. Introduction	360	3.6. Coordination polymers based on other ligands	389
2. Coordination polymers containing transition metal ions	362	3.6.1. Coordination polymers with carboxylate ligands	389
3. Lanthanide-containing coordination polymers	365	3.6.2. Coordination polymers with sulfoxide ligands	395
3.1. Coordination polymers based on the (btc) ³⁻ ligand	368	3.7. Synthetic routes	396
3.2. Coordination polymers based on the (bdc) ²⁻ ligand	375	3.8. Coordination polymers containing polyhydroxo-lanthanide complexes	397
3.3. Coordination polymers based on the (btcc) ⁴⁻ ligand	380	4. Conclusion and outlooks	401
3.4. Coordination polymers based on the (bhc) ⁶⁻ ligand	382	References	402

List of acronyms

bdc	1,4 benzene dicarboxylate	pda	1,4-phenylendiacetate
BTB	4,4',4''-benzene-1,3,5-triyl-tribenzoate	pdcc	3,5-pyrazoledicarboxylate
btc	1,3,5 benzene tricarboxylate	ppa	N-(4-pyridinylmethyl)-4-pyridinecarboxamide
btcc	1,2,4,5 benzene tetracarboxylate	rac-L	rac-1,2-bis(ethylsulfanyl)ethane
bhc	benzene hexacarboxylate	XRD	X-Ray Diffraction
IRMOF	Iso Reticular Metal Organic Framework	TGA	ThermoGravimetric Analysis
meso-L	meso-1,2-bis(ethylsulfanyl)ethane	TDXD	Temperature Dependent X-ray Diffraction
ndc	2,6-naphthalenedicarboxylate	BET	Brunauer Emmett Teller
ox	oxalate		

* Corresponding author.

1. Introduction

The assembly of metal-organic infinite framework via the coordination of metal ions by multi-functional organic ligands is a field of increasing interest. Work along this line is motivated by the concept that molecular-based coordination polymers have potential technological applications such as opto-electronic or magnetic devices and microporous materials for shape- and size-selective separations and catalysis. The advantage of these metal-organic open frameworks is to allow a wide choice in various parameters including diverse electronic properties and coordination geometry of the metal ions as well as versatile functions and topologies of the organic ligands. So, specific electronic or structural characteristics of the metal ion can be translated into bulk properties for solid state compounds. In this context, there has been current interest in synthesizing stable polymeric coordination open frameworks with transition metal ions. The lanthanide ions owing to their very similar chemical and structural properties but very different physical properties from one to the other could lead to materials exhibiting tunable properties via the choice of the rare earth ion.

We would like to report here the state of the art in this rapidly emerging field of research.

This review is devoted to coordination polymers. These are built up from metal ions and multi-functional organic ligands. Examples of such polymeric coordination frameworks are known for a long time. Until recently they have been generally studied because of their interesting molecular topologies and crystal packing motifs (Batten and Robson, 1998; O'Keeffe et al., 2000), their interest as molecular precursor for condensed phases, or their expected magnetic properties. As an illustration of this, one may consider the oxalate based coordination polymers. The well-known honeycomb-like molecular motif of the hydrated oxalato lanthanide(III) is drawn on fig. 1.

Actually, these oxalato lanthanide compounds have been extensively studied for structural (Hansson, 1970, 1973; Hansson and Albertsson, 1968; Michaelides et al., 1988; Kahwa et al., 1984; Watanabe and Nagashima, 1971; Bataille et al., 1999; Bataille and Louër, 1999), magnetic (Larionova et al., 1998; Decurtins et al., 1998; Mörtl et al., 2000) purposes as well as for their interest as molecular precursors for condensed phases usable as magnets (Nag and Roy, 1976a, 1976b), high temperature superconducting ceramics (Jongen et al., 1999) or pigments (Trollet et al., 1997; Romero et al., 1995).

Due to the variety of the existing coordination polymers and of their potential applications, the literature describing them is very abundant and dispersed. Therefore performing an exhaustive review of all the reported coordination polymers is out of the scope of this article.

There is currently a renewed interest in that field partly because of the nano-technologies emergence. Actually the design of nano-porous open frameworks is a factor of this revival (Yaghi et al., 1996, 2004; Serpaggi et al., 1999) because these compounds are anticipated to exhibit good efficiency as far as size selective separation, catalysis and gas storage are concerned (Eddaoudi et al., 2002).

One of the major challenges in that field is to maintain the host framework integrity in the absence of guest molecules in order to allow reversible access to the cavities within the host. As one can notice, the requirements for the choice of the binding organic ligand are

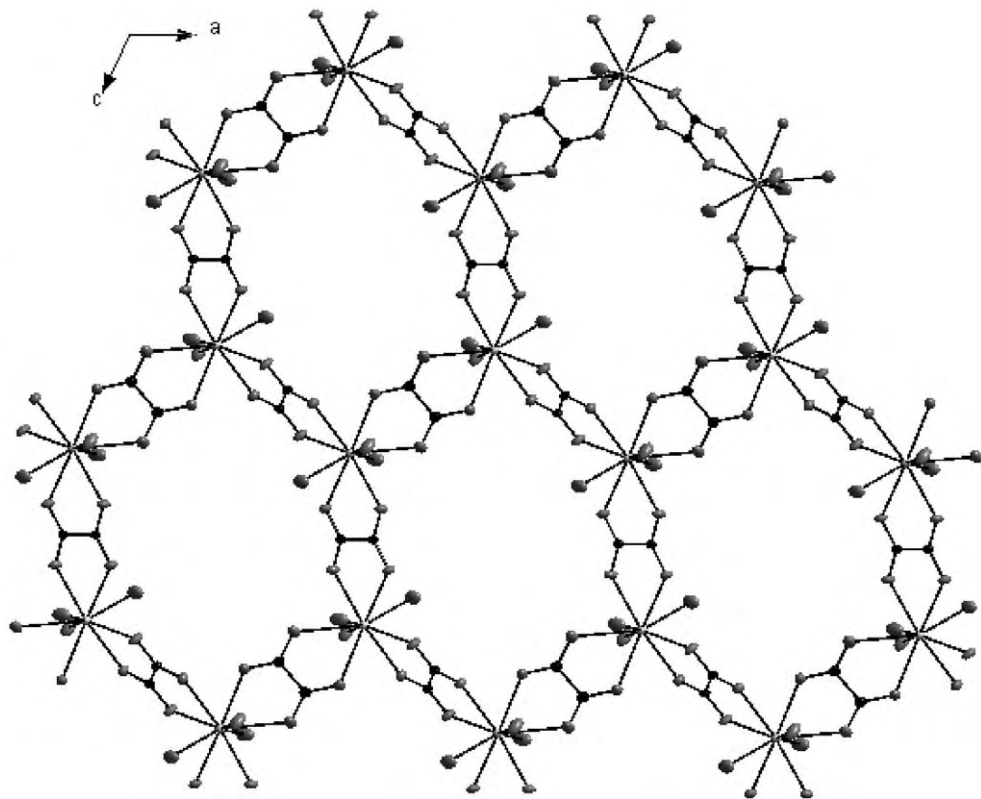
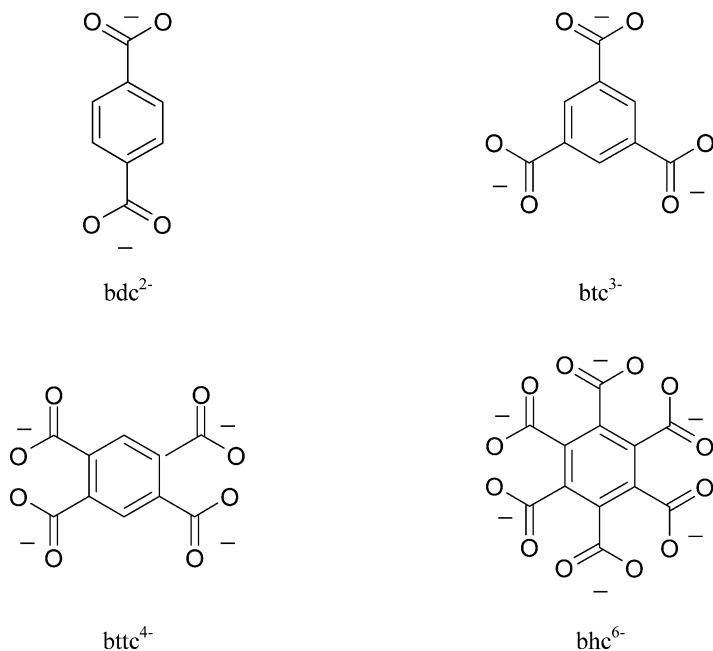


Fig. 1. Projection view along the b -axis of $\text{Er}_2(\text{C}_2\text{O}_4)_3 \cdot 10\text{H}_2\text{O}$: monoclinic, $P2_1/a$, $a = 9.9451(2) \text{ \AA}$, $b = 9.6170(2) \text{ \AA}$, $c = 10.9270(2) \text{ \AA}$, $\beta = 114.24(1)^\circ$. Redrawn from Hansson (1970).

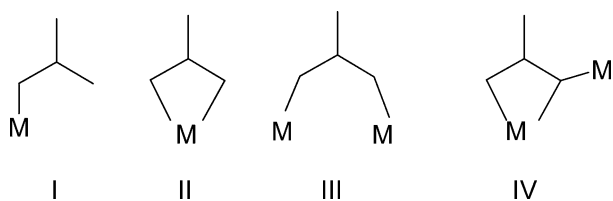
its chemical and thermal robustness, its topological properties and its functionality. Those requirements are fulfilled by the benzene-polycarboxylate ligands (see scheme 1).

Indeed, these ligands are rigid, planar, very stable thermally and chemically and they have non negligible structuring effect thanks to π -stacking. Furthermore their carboxylato functional groups present a very good affinity with most of metallic cations and, due to their numerous possible coordination modes (see scheme 2), they allow one to expect a great structural diversity. At last, most of them are commercially available and cheap what is an asset for further industrial applications.

This review is essentially devoted to the coordination polymers which have been synthesized for their potential technological applications or which could obviously be of interest as far as technological applications are concerned. As a consequence, polymeric complexes based on benzene-poly-carboxylates ligands and their derivatives will be described in more details. The paragraph dealing with coordination polymers containing transition metal ions is mainly



Scheme 1. Some extensively used benzene-polycarboxylate anionic ligands.



Scheme 2. Coordination modes presented by the carboxylato groups.

an illustration of what one can expect when designing a lanthanide-containing coordination polymer.

2. Coordination polymers containing transition metal ions

Actually very numerous transition elements ions containing coordination polymers have been described. Some of them are listed in table 1.

From this table, it is clear that this class of ligands has led to numerous structurally different compounds exhibiting various physical properties. Describing each of them is out of the scope of this article and we will focus only on the noticeable $[\text{Cu}_3(\text{btc})_2(\text{H}_2\text{O})_3]_n$ tri-dimensional compound reported by Chui et al. in 1999 (Chui et al., 1999). This compound, thermally stable up to 240°C , present a 3D system of channels with a pore diameter of 1 nanometer and an

Table 1

Non-exhaustive list of transition element (or main group element) based coordination polymers with benzene polycarboxylate ligands

Chemical formula	Metal ion	Dimensionality	Reference
1,4 benzene dicarboxylate (bdc)			
V(OH)(bdc)·0.75(bdcH ₂)	V ³⁺	3D	Barthelet et al., 2002
Zn ₃ (bdc) ₃ ·6(CH ₃ OH)	Zn ²⁺	3D	Li, H. et al., 1998
1,3,5 benzene tricarboxylate (btc)			
Zn ₂ (btc)(NO ₃)·(H ₂ O)(C ₂ H ₅ OH) ₅	Zn ²⁺	3D	Yaghi et al., 1997a
Ni ₅ (btc) ₂ (Hbtc) ₂ (C ₅ H ₅ N) ₁₅ (H ₂ O) ₅ ·xH ₂ O·yC ₄ H ₉ OH·zC ₅ H ₅ N	Ni ²⁺	1D	Prior and Rosseinsky, 2000
Co(Hbtc)(C ₅ H ₅ N) ₂ ·2/3C ₅ H ₅ N	Co ²⁺	2D	Yaghi et al., 1995
Mn ₃ (btc) ₂	Mn ²⁺	3D	Gutschke et al., 1996
Cu ₃ (btc) ₂ (C ₃ H ₃ N ₂ CH ₃) ₆ (H ₂ O)·xH ₂ O with x = 7 or 16	Cu ²⁺	2D	Cheng et al., 2001
M(Hbtc)(H ₂ O) ₂ ·(H ₂ O) _{0.5}	Sr ²⁺ , Ba ²⁺	2D	Plater et al., 1998
Ca(Hbtc)·2H ₂ O	Ca ²⁺	2D	Plater et al., 1997
Ni ₃ (btc) ₂ (H ₂ O) ₁₂	Ni ²⁺	1D	Yaghi et al., 1996 Daiguebonne et al., 2003
1,2,4,5 benzene tetracarboxylate (btcc)			
V ₂ (OH) ₄ [C ₆ H ₂ (CO ₂) ₄]·4H ₂ O	V ³⁺	3D	Barthelet et al., 2003
V(OH)[C ₆ H ₂ (CO ₂) ₂ (COOH) ₂]·H ₂ O	V ³⁺	3D	Barthelet et al., 2003
Cu ₂ (btcc)(H ₂ O) ₄ ·2H ₂ O	Cu ²⁺	2D	Cao et al., 2002a
Ni ₂ (2,2'-bipy) ₂ (OH) ₂ (H ₂ btcc)	Ni ²⁺	1D	Li, Y. et al., 2003
Co ₂ (btcc)(H ₂ O) ₁₈	Co ²⁺	1D	Robl and Hentschel, 1991a
benzene hexacarboxylate (bhc)			
Co ₃ (bhc)·18H ₂ O	Co ²⁺	1D	Robl and Hentschel, 1991b
Al ₂ (bhc)·16H ₂ O	Al ³⁺	3D	Giacovazzo et al., 1973

accessible porosity of nearly 40% in the solid. Unlike classical zeolites, the channel linings can be chemically functionalized. An extended view of its asymmetric unit and a projection view of the polymer framework are shown in fig. 2.

This example emphasizes the potentiality of the benzene polycarboxylate ligands. However some other coordination polymers containing transition metal ions deserve to be highlighted.

So is the compound Cu₃(BTB)₂(H₂O)₃·(DMF)₉(H₂O)₂ described in 2001 by O.M. Yaghi et al. (Chen et al., 2001), where H₃BTB stands for 4,4',4''-benzene-1,3,5-triyl-tribenzoic acid. This compound present large circular pores (16.4 Å in diameter) in which voluminous amounts of gases and organic solvents can be reversibly sorbed. It is thermally stable up to 250 °C. A view of the polymeric framework is reported in fig. 3.

The H₃BTB ligand is topologically rather similar to benzene polycarboxylate. In particular it is rigid. Some other coordination polymers built with flexible ligands are worth noticing. That is in particular the case of the two 3D networks obtained by reaction of Ag⁺ with pyridyl type ligands (Tong et al., 2002). A perspective view of the 3D network of the compound

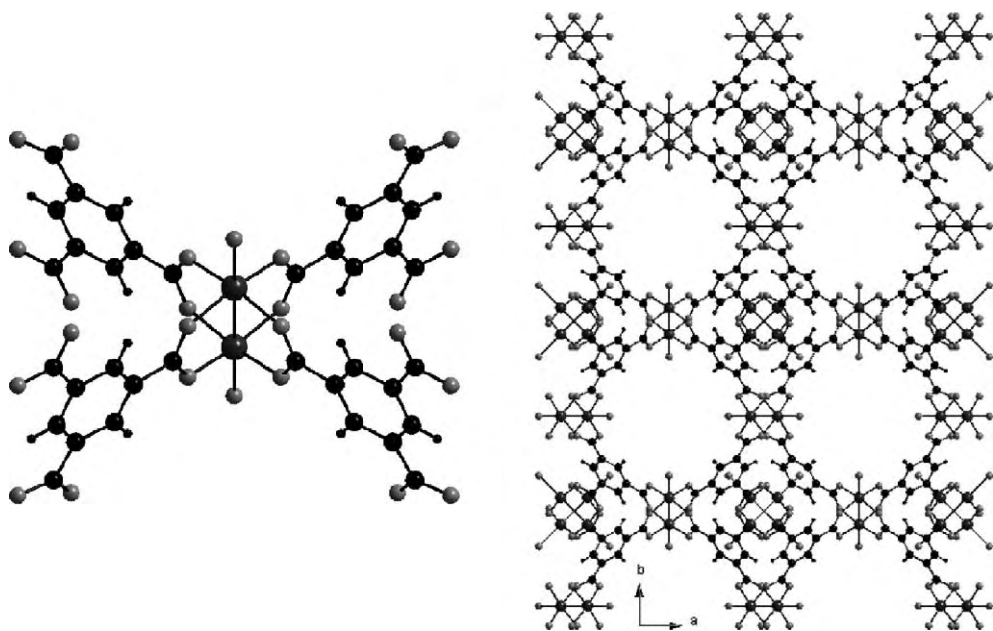


Fig. 2. (Left) view of the extended asymmetric unit of $[\text{Cu}_3(\text{btc})_2(\text{H}_2\text{O})_3]_n$: cubic, $\text{Fm}\bar{3}\text{m}$, $a = 26.343(5)$ Å. Redrawn from Chui et al. (1999). (Right) $[\text{Cu}_3(\text{btc})_2(\text{H}_2\text{O})_3]_n$ polymer framework viewed down the $[001]$ direction showing nanochannels with fourfold symmetry. Crystallization water molecules have been omitted for clarity.

$[\text{Ag}_2(\text{ppa})_2(\text{ox})] \cdot 9\text{H}_2\text{O}$ where ppa stands for N-(4-pyridinylmethyl)-4-pyridinecarboxamide and ox for oxalate is drawn in fig. 4.

This compound can be described as 2D $[\text{Ag}(\text{ppa})]_n$ infinite layers pillared by (ox) ligands as connectors. Unfortunately this compound is only structurally described and there is no information about its thermal stability nor about its microporous character.

To complete this short overview about coordination polymers containing transition metal ion, it is worthwhile pointing to recent works demonstrating that the construction of coordination polymers by employing rigid organic building-blocks binding metallic clusters provide an effective strategy to form robust hosts possessing porosity (Eddaoudi et al., 2001; Zhao et al., 2002). For instance, the third compound reported in fig. 5 is one of the highest porous metal-organic frameworks reported so far (Eddaoudi et al., 2002): 91% of the crystal volume is open space.

This compound which can be described as a cubic 3D network of zinc–oxygen clusters connected by molecular struts exhibits a density lower than any previously reported crystalline material (around 0.2 g cm^{-3}) and has been synthesized for its predicted useful properties for gas storage. It belongs to a family of sixteen metal-organic frameworks with the same network topology but various functionalities and pore sizes. This family has been systematically designed and for instance, the pore size is varied from 3.8 Å and 28.8 Å. One member of

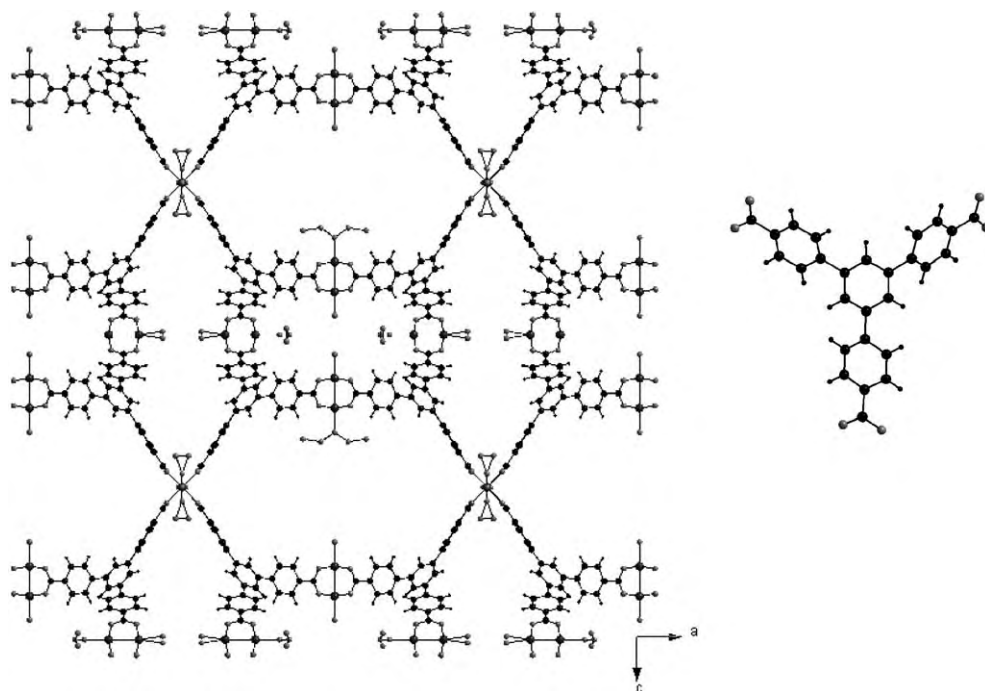


Fig. 3. (Left) projection view along the b -axis of the polymeric network of $\text{Cu}_3(\text{BTB})_2(\text{H}_2\text{O})_3 \cdot (\text{DMF})_9(\text{H}_2\text{O})_2$: cubic, $\text{Im}\bar{3}$, $a = 26.946(2)$ Å. Redrawn from Chen et al. (2001). (Right) view of the BTB^{3-} ligand (4,4',4''-benzene-1,3,5-triyl tribenzoate).

the family exhibits a high capacity for methane storage. All the sixteen compounds are rather stable thermally (up to 400 °C).

3. Lanthanide-containing coordination polymers

Despite the impressive development of the field of coordination polymers containing transition metal ions, the analogous chemistry involving the lanthanide ions remains much less developed. This is a priori rather surprising because the lanthanide ions are the largest family of chemically similar elements in the periodic table. So in principle, it must be possible to design coordination polymers with tunable physical properties by an appropriate choice of the lanthanide ion. However the relatively high cost of the lanthanide ions implies the design of materials with very specific properties. Indeed if the substitution of the lanthanide ion by a main group or a transition metal ion is possible without changing the physical properties, then there is no economical interest. For instance it seems worthless to synthesize lanthanide containing functionalized coordination polymers except if the lanthanide ion plays an essen-

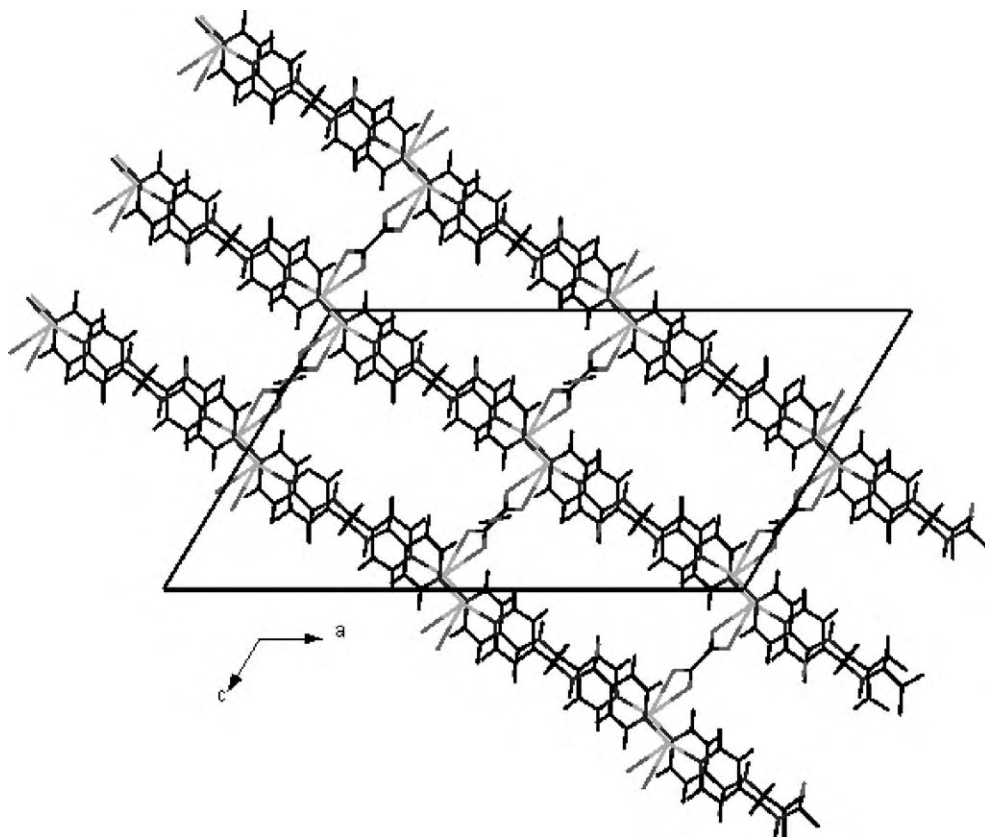


Fig. 4. Projection view from the b -axis direction of the 3D coordination network of $[\text{Ag}_2(\text{ppa})_2(\text{ox})]\cdot 9\text{H}_2\text{O}$: monoclinic, $C2/c$, $a = 28.947(8) \text{ \AA}$, $b = 8.617(3) \text{ \AA}$, $c = 16.307(6) \text{ \AA}$, $\beta = 121.07(1)^\circ$. Redrawn from Tong et al. (2002).

tial role in the chemical process. That is why, before designing a material one should think about the targeted physical properties.

Three physical properties are generally targeted in the field of lanthanide coordination polymers: the magnetic properties, the optical properties and the catalytic properties.

Much work has been done in the field of extended networks involving rare-earth ions and exhibiting interesting magnetic properties. These works were based on the observations that some lanthanide ions can present the higher local spin moments and the higher anisotropies of the periodic table. Unfortunately the inner character of the lanthanide ion magnetic orbitals leads to very poor overlap and extremely low coupling as far as coordination compounds are concerned (Decurtins et al., 1998; Daiguebonne et al., 1998, 2001b; Guillou et al., 1992a, 1992b, 1992c; Kahn and Guillou, 1993; Oushoorn et al., 1996). This field of research remains active and interesting because the mechanisms of the 4f-4f and 4f-3d interactions are still

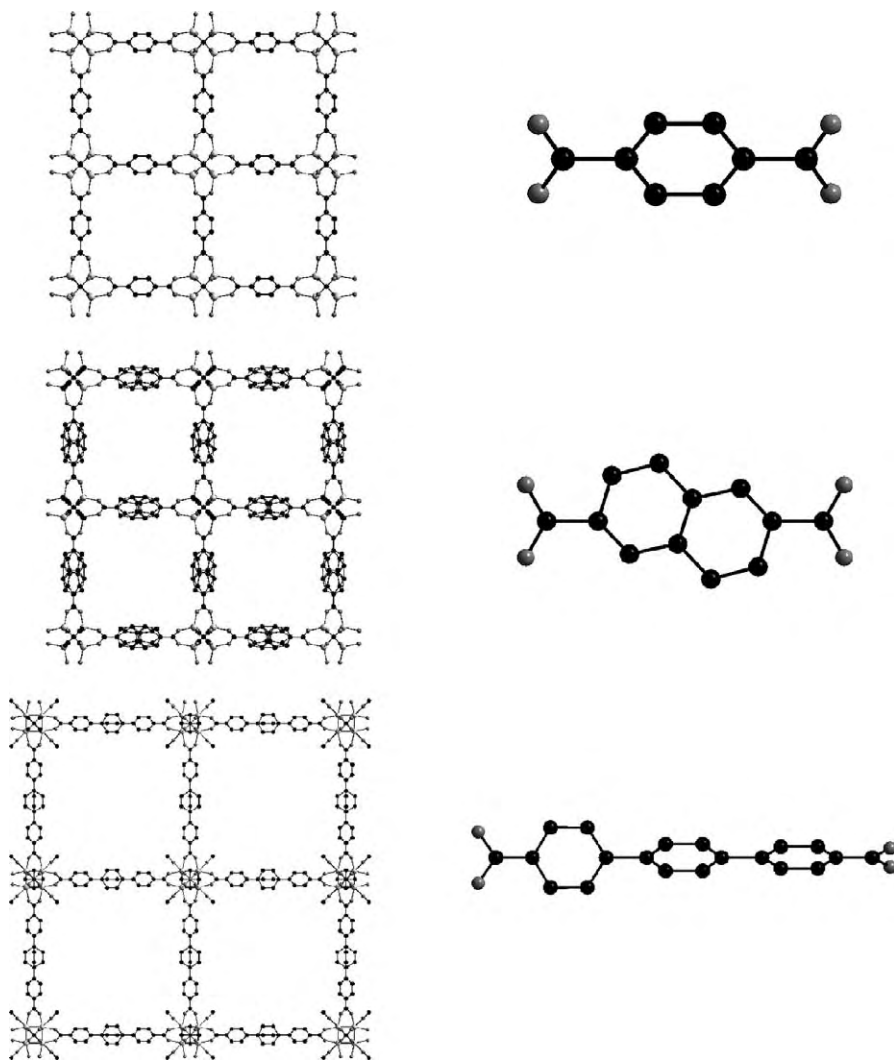


Fig. 5. (Left) projection view of the open networks of three of the sixteen IRMOF compounds. Redrawn from Eddaoudi et al. (2002). (Right) view of the corresponding ligands. (Up) the IRMOF-1 compound: cubic, $Fm\bar{3}m$, $a = 25.8320(2)$ Å. (Middle) the IRMOF-8 compound: cubic, $Fm\bar{3}m$, $a = 30.0915(3)$ Å. (Bottom) the IRMOF-16 compound: cubic, $Pm\bar{3}m$, $a = 21.4903(2)$ Å.

misunderstood (Decurtins et al., 1998; Sutter et al., 1998, 1999; Costes et al., 1998; Liu et al., 1998; Sanada et al., 1998; Rizzi et al., 2002) (for a recent review see reference (Benelli and Gatteschi, 2002)). So, to the best of our knowledge, magnetic materials seems not to be a driving force for the design of lanthanide based coordination polymers.

On the other hand, lanthanide ions are well known for their unique optical properties. These properties are extensively used in numerous fields such as laser amplifiers (Adam, 2002; Kuriki et al., 2002) or electroluminescent materials (Kido and Okamoto, 2002) for instance. Coordination polymers could be very interesting as far as optical properties are concerned. Indeed they are transparent and the rare earth ions distribution can be perfectly controlled by an appropriate choice of the ligand while in plastic or glasses they are generally statistically dispersed. The prerequisites of such coordination polymers exhibiting optical properties are obviously the following: the material must be thermally rather stable, solvent molecules must be avoided and the inter-metallic distances must be carefully adjusted in order to allow the best efficiency for the targeted application.

Some lanthanide ions have also well-known catalytic properties. For instance, the Sm(II) ion is extensively used in asymmetric catalysis (Iananaga et al., 2002) and cerium and praseodymium, thanks to their III/IV valences, are used in many depollution processes ("Catalysis by Ceria and Related Materials", 2002). This second class of application seems to be very promising as far as coordination polymers are concerned. The prerequisites for these applications are clearly a high thermal stability, a porous network and a chemical availability of the lanthanide ions.

From this rapid overview it appears that the benzene polycarboxylates and their derivatives could be good ligands for the design of 3D networks exhibiting catalytic or optical properties depending on the inserted lanthanide ion(s). Indeed benzene polycarboxylates are thermally stable, their carboxylato coordinating groups have good affinity with the hard acid character (according to Pearson's definition) of the lanthanide ions. That is probably why they are involved in many studies related to lanthanide coordination polymers (see table 2).

From the above table it appears that it is rather difficult to control the dimensionality of the obtained material. This is inherent to the use of both lanthanide ions and ligands presenting coordinating carboxylato groups.

Indeed, contrary to transition metal ions, lanthanide ions, due to the inner character of their 4f valence orbitals, exhibit very little preference in bonding direction (Karraker, 1970). The bonds between lanthanide ions and ligands are essentially ionic and the spatial arrangement of the ligand around the lanthanide ions are mainly due to steric hindrance and inter-ligand interactions. Further more it is well known that the carboxylate ions presents several coordination modes (see scheme 2) (Ouchi, 1988).

The lack of structuring effect from lanthanide ions and the flexibility of the coordinating carboxylate groups are responsible of the structural diversity observed.

3.1. Coordination polymers based on the $(btc)^{3-}$ ligand

As an illustration of this structural diversity one can consider the five Er^{3+} -containing coordination polymers which are reported in table 2. All five can be obtained in aqueous media by reacting an Er^{3+} salt with the sodium salt of 1,3,5-benzene-tricarboxylic acid (Dauguebonne et al., 2000b). As can be seen in fig. 6, where the molecular motifs of these five compounds are reported, despite their similar chemical formulae they present very different structural types.

The first compound, namely $Er(btc) \cdot 6H_2O$ (fig. 6(a)) has been synthesized by slow diffusion through water and presents a structure consisting in the juxtaposition of parallel ribbon-

Table 2

List of lanthanide based coordination polymers with benzene polycarboxylate ligands. Only structurally characterized compounds have been reported

Chemical formula	Lanthanide	Dimensionality	References
1,4 benzene dicarboxylate (bdc)			
Er ₄ (bdc) ₆ ·6H ₂ O	Er	3D	Pan et al., 2001
Ln ₂ (bdc) ₃ ·4H ₂ O	Tb and Er	3D	Reneike et al., 1999a; Li, H. et al., 1998; Pan et al., 2001
Ln ₂ (bdc) ₃ (H ₂ O) ₆	Er	3D	Deluzet et al., 2003
Tb(bdc)(NO ₃) ₂ ·2DMF	Tb	3D	Reneike et al., 1999b
1,3,5 benzene tricarboxylate (btc)			
Er(btc)(H ₂ O) ₅ ·H ₂ O	Er, Sm	1D	Zhi-Bang et al., 1990 Daiguebonne et al., 2002
Lu(btc)(H ₂ O) ₅ ·4H ₂ O	Lu	1D	Zhi-Bang et al., 1991
Gd(btc)(H ₂ O) ₃ ·1.5H ₂ O	Gd, Er, Sm	2D	Daiguebonne et al., 1998, 2000a, 2002
Er(btc)(H ₂ O) ₅ ·3.5H ₂ O	Er	1D	Daiguebonne et al., 1999
Y(btc)(H ₂ O) ₆	Y, Er, Sm	1D	Daiguebonne et al., 1999, 2002
Er ₃ (btc) ₃ (H ₂ O) ₈ ·4H ₂ O	Er	1D	Daiguebonne et al., 2000a
1,2,4,5 benzene tetracarboxylate (btcc)			
Eu ₂ (btcc)(H ₂ O) ₄ ·4H ₂ O	Eu	3D	Wu, C.D. et al., 2002
Yb ₄ (btcc) ₃ (H ₂ O) ₈ ·6H ₂ O	Yb	3D	Cao et al., 2002b
Er ₈ (btcc) ₆ (H ₂ O) ₁₆ ·16H ₂ O	Er	3D	Cao et al., 2002b
Tb ₂ (btcc)(H ₂ O) ₂ ·4H ₂ O	Tb	3D	Cao et al., 2002b
Ce(Hbtcc)·H ₂ O	Ce	1D	Yaghi et al., 1997b
benzene hexacarboxylate (bhc)			
Ln ₂ (bhc)(H ₂ O) ₁₀ ·4H ₂ O	Y, Er	1D	Deluzet and Guillou, 2003; Robl and Hentschel, 1992
Ln ₂ (bhc)(H ₂ O) ₆	La–Er	3D	Chui et al., 2001
Ln ₂ (bhc)(H ₂ O) ₄ ·H ₂ O	Tm–Lu	3D	Chui et al., 2001
Tm ₂ (bhc)(μ-H ₂ O) ₂ (H ₂ O) ₂	Tm	3D	Chui et al., 2001
La ₂ (bhc)(H ₂ O) ₉ ·2H ₂ O	La	3D	Wu, L.P. et al., 1996

like molecular motifs spreading along the \vec{a} direction. The Er³⁺ ion is nine coordinated by six oxygen atoms from water molecules as well as by three oxygen atoms from three carboxylato groups. Free carboxylato groups are facing Er³⁺ ions from adjacent ribbons forming an hydrogen bonds network with coordinated water molecules and so ensuring the cohesion of the crystal packing. One may note that there is no crystallization water molecule in this compound.

An other 1D coordination polymer has been described which presents the same global chemical formula Er(btc)(H₂O)₅·H₂O (Zhi-Bang et al., 1990). In this compound there are only five coordinated water molecules, the sixth one being a crystallization water molecule whereas in the previous compound the six water molecules were coordinated to the lanthanide ion. The structure can be described as parallel chains spreading along the \vec{b} axis (see fig. 6(b)). The molecular chains stacks in such a way that phenyl groups superimpose along the \vec{b} axis.

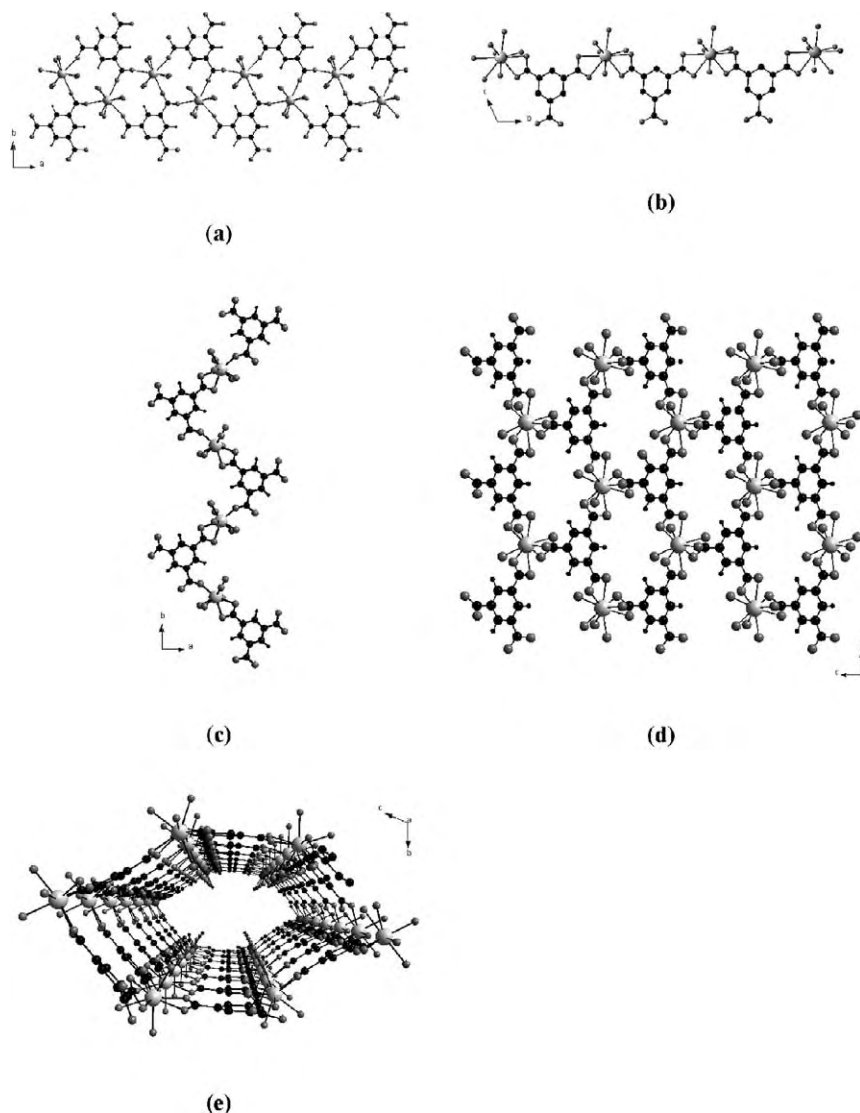


Fig. 6. Molecular motifs of the five $\text{Er}(\text{btc})\cdot n\text{H}_2\text{O}$ coordination polymers already reported. Redrawn from Daiguebonne et al. (2000b). (a) Perspective view along the *c*-axis of $\text{Er}(\text{btc})\cdot 6\text{H}_2\text{O}$: monoclinic, *Cc*, $a = 11.373(2)$ Å, $b = 17.850(3)$ Å, $c = 7.130(1)$ Å, $\beta = 119.14(3)^\circ$. (b) Projection view along the *a*-axis of the chain-like molecular motif of $\text{Er}(\text{btc})(\text{H}_2\text{O})_5\cdot\text{H}_2\text{O}$: triclinic, $\text{P}\bar{1}$, $a = 7.631(2)$ Å, $b = 9.965(2)$ Å, $c = 11.219(2)$ Å, $\alpha = 106.98(2)^\circ$, $\beta = 103.52(2)^\circ$, $\gamma = 107.50(2)^\circ$. (c) Projection along the *c*-axis of $\text{Er}(\text{btc})(\text{H}_2\text{O})_5\cdot 3.5\text{H}_2\text{O}$: monoclinic, *C2/c*, $a = 14.740(2)$ Å, $b = 16.987(2)$ Å, $c = 14.459(1)$ Å, $\beta = 118.754(9)^\circ$. (d) Projection along the *a*-axis of $\text{Er}(\text{btc})(\text{H}_2\text{O})_3\cdot 1.5\text{H}_2\text{O}$: monoclinic, *C2/c*, $a = 20.454(2)$ Å, $b = 9.973(1)$ Å, $c = 15.251(2)$ Å, $\beta = 125.68(1)^\circ$. (e) Projection along the *a*-axis of $\text{Er}_3(\text{btc})_3(\text{H}_2\text{O})_8\cdot 4\text{H}_2\text{O}$: triclinic, $\text{P}\bar{1}$, $a = 9.988(2)$ Å, $b = 15.656(3)$ Å, $c = 19.698(3)$ Å, $\alpha = 110.77(2)^\circ$, $\beta = 100.63(2)^\circ$, $\gamma = 100.58(2)^\circ$.

The Er^{3+} ions are nine coordinated by four oxygen atoms from two bidentate carboxylato groups and by five oxygen atoms from water molecules.

The third mono-dimensional compound, $\text{Er}(\text{btc})(\text{H}_2\text{O})_5 \cdot 3.5(\text{H}_2\text{O})$ (fig. 6(c)), has been obtained as single crystals by slow diffusion in an agarose gel. It can also be obtained as a precipitated powder by direct reaction between Er^{3+} and $(\text{btc})^{3-}$ in water. Its structure consists in the juxtaposition of molecular zig-zag chain-like motifs spreading along the \vec{b} axis. The Er^{3+} ion is only eight coordinated by five oxygen atoms from water molecules as well as by three oxygen atoms from carboxylato groups. The cohesion of the crystal structure is once more ensured by an hydrogen bond network but the chains are disposed in such a way that the π systems of the btc^{3-} ligands overlap. Crystallization water molecules are filling the inter-chain space as one can see on fig. 7.

This compound, when dehydrated by heating, leads to a bi-dimensional compound with a chemical formula $\text{Er}(\text{btc})(\text{H}_2\text{O})_3 \cdot 1.5(\text{H}_2\text{O})$ (fig. 6(d)). It presents a crystal structure which consists in the juxtaposition of bi-dimensional honeycomb-like molecular motifs spreading parallel to the $(\vec{b}, \vec{a} + \vec{c})$ plane where one corner out of two is occupied by an Er^{3+} ion and the other by the center of a phenyl ring. The Er^{3+} ions are nine coordinated by three oxygen atoms from water molecules and six oxygen atoms from three carboxylato groups. In this structure it is worth noting that all the carboxylato groups are bidentate (mode II). The planes are connected together via an hydrogen bond network and the phenyl rings are superimposed in such a way that their π systems interact. This compound may also be obtained via a slow diffusion through an agarose gel medium.

Dehydrating further this compound leads to $\text{Er}_3(\text{btc})_3(\text{H}_2\text{O})_8 \cdot 4\text{H}_2\text{O}$. Its structure consists in the juxtaposition of parallel tubes with hexagonal section spreading along the a -axis (fig. 6(e)). Each tube is constituted by cyclic honeycomb-like molecular motifs similar to those already described for the previous compound. Tubes are held together via an hydrogen bonds network. The chemical formula of this compound is a little bit more complicated than those previously described because there is three crystallographically different Er^{3+} ions in the structure. Two out of the three are nine coordinated by six oxygen atoms from three carboxylato groups (mode II) and three oxygen atoms from coordinated water molecules, while the third Er^{3+} ion is only eight coordinated by six oxygen atoms from three carboxylato groups and two water molecules. The crystallization water molecules are localized inside the tubes. The diameter of the tubes is roughly 11 Å. This compound can also be obtained thanks to a gel diffusion method.

As one can notice from these five structural descriptions, the structuring role of the ligand is predominant and the topology of the crystal structure is mainly due to hydrogen bonds and overlaps of the π systems. The structural diversity seems also to be a consequence of the versatility of the coordinating carboxylato groups. As an example the different coordinating modes encountered in these five structures are listed in table 3.

It can also be noticed that the third compound described, namely $\text{Er}(\text{btc})(\text{H}_2\text{O})_5 \cdot 3.5(\text{H}_2\text{O})$, presents a pseudo 3D structure via hydrogen bonds. However it is not a microporous solid precursor. Indeed, when dehydrated this compound reversibly rearrange leading successively to the honeycomb-like compound and then to the hexagonal-tube like structure. This last compound finally leads to an anhydrous compound which unfortunately has not yet

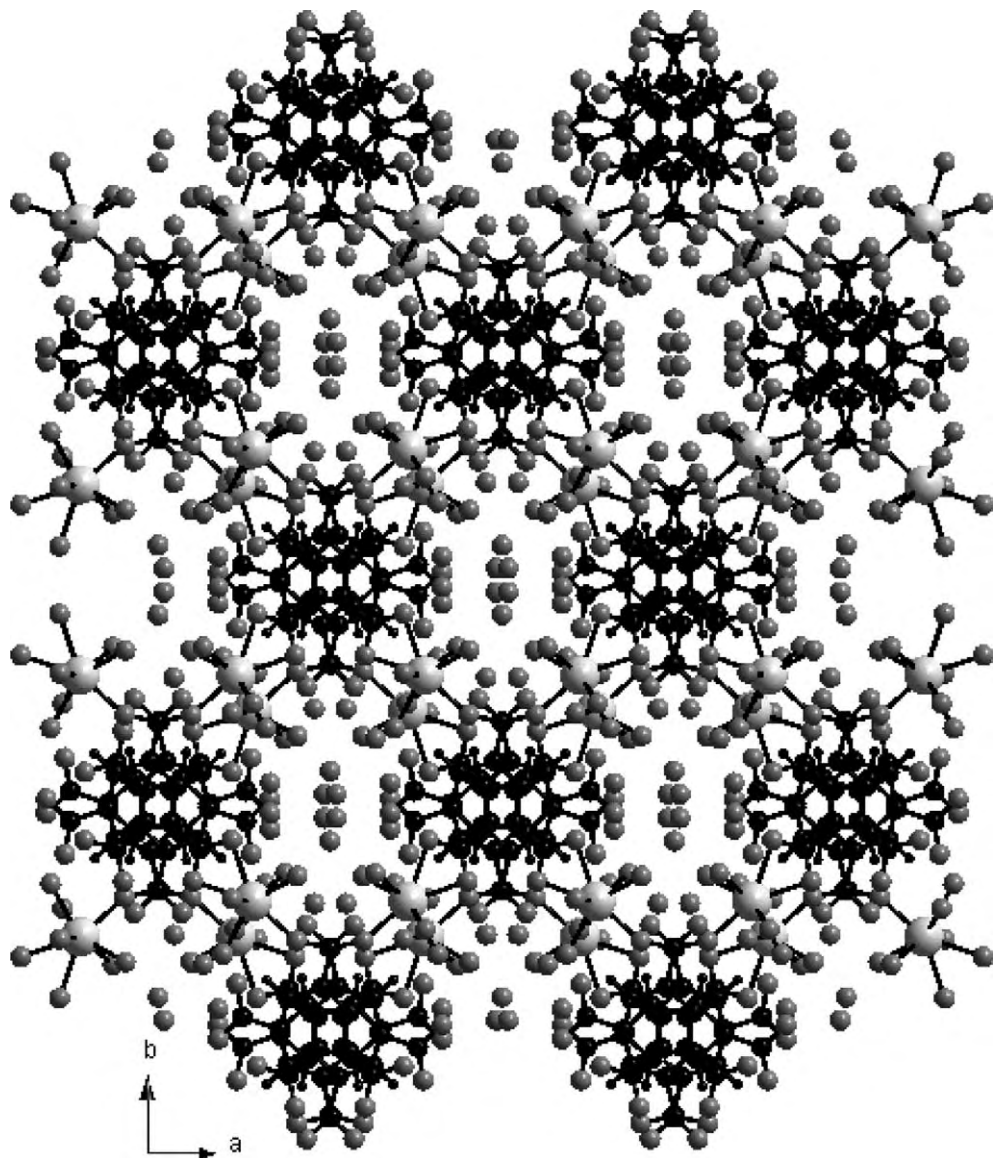


Fig. 7. Projection view along the c -axis of the pseudo-3D polymeric network of $\text{Er}(\text{btc})(\text{H}_2\text{O})_5 \cdot 3.5\text{H}_2\text{O}$ with the crystallization water molecules inside the cavities. Redrawn from Daiguebonne et al. (1999).

been structurally characterized. By re-hydration of this anhydrous compound one can re-obtain the zig-zag chain-like structure. This cycle of hydration/dehydration is symbolized in fig. 8.

Table 3
 Coordination modes of the carboxylato groups in the previously described benzene dicarboxylate based coordination polymers. See scheme 2 for a definition of the coordination modes I, II and III

Complexes	Number of oxygen atoms involved in bonding mode			Coordination numbers
	I	II	III	
Er(btc)(H ₂ O) ₃ ·1.5H ₂ O	0	6	0	9
Er(btc)(H ₂ O) ₅ ·3.5H ₂ O	1	2	0	8
Er(btc)(H ₂ O) ₅ ·H ₂ O	0	2	0	9
Er(btc)(H ₂ O) ₆	1	0	2	9
Er ₃ (btc) ₃ (H ₂ O) ₈ ·4H ₂ O				
Er1	0	6	0	8
Er2	0	6	0	9
Er3	0	6	0	9

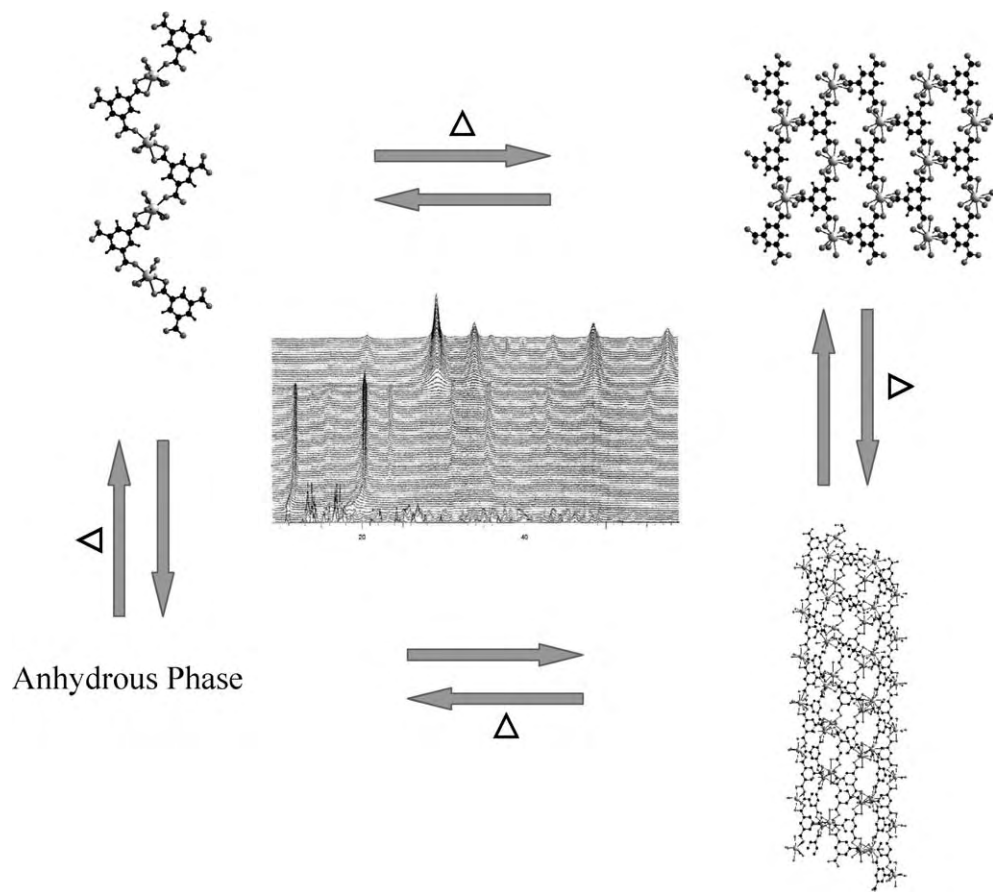


Fig. 8. Hydration/dehydration cycle of the Er(btc)-*n*H₂O compounds.

The anhydrous compound, whose chemical formula is $\text{Er}(\text{btc})$, has not been structurally characterized because of its lack of crystallinity and its physical properties have not been explored in details. This family is characteristic of the problem encountered when trying to construct molecular based microporous materials, that is obstruction of the pores by interpenetration of networks or collapse of the structure upon removal of the guest molecules intercalated in the cavities. This problem is, of course, also present for coordination polymers based on transition elements but it is much more crucial for lanthanide-based materials. Indeed, lanthanide ions present a high coordination number (generally ranging between 7 and 12) and their coordination sphere most often contains some solvent molecules. These coordination water molecules, when removed upon dehydration, lead to structural rearrangements and, sometimes, to a loss of the microporous character.

Another compound with chemical formula $\text{Eu}_3(\text{H}_2\text{O})(\text{OH})_6(\text{btc})\cdot 3\text{H}_2\text{O}$ has been reported recently (Serre and Férey, 2002) (see fig. 9). It has been obtained via an hydrothermal synthesis. The crystal structure has been solved on the basis of an XRD diagram of the polycrystalline powder. It displays a 3D structure and consists in inorganic layers linked together by

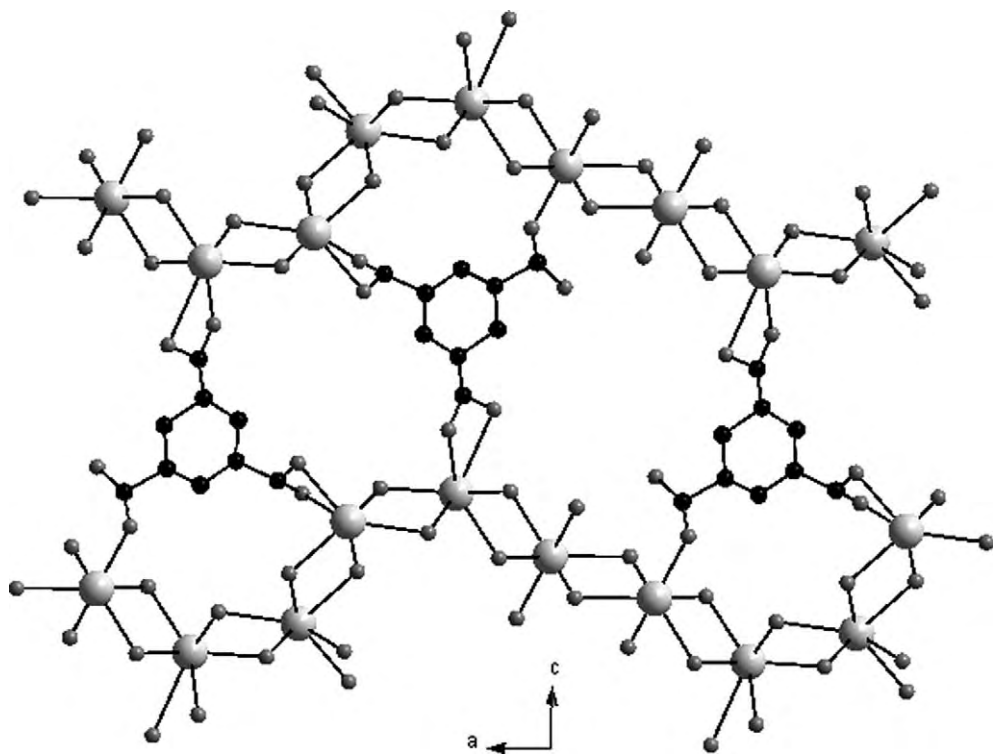


Fig. 9. Projection along the b -axis of $\text{Eu}(\text{H}_2\text{O})(\text{OH})_6(\text{btc})\cdot 3\text{H}_2\text{O}$: monoclinic, $P2_1$, $a = 17.640(1) \text{ \AA}$, $b = 3.689(2) \text{ \AA}$, $c = 12.385(1) \text{ \AA}$, $\beta = 91.247(4)^\circ$. Redrawn from Serre and Férey (2002).

(btc)³⁻ ions. The inorganic layers are built up from chains of europium polyhedra consisting of face-sharing europium polyhedra linked through μ_3 -hydroxo groups or oxygen atoms from carboxylates. Two out of the three crystallographically independent Eu³⁺ ions are surrounded by seven μ_3 -hydroxo groups and two oxygen atoms from a bidentate carboxylato group (mode II) while the third Eu³⁺ ion is surrounded by seven μ_3 -hydroxo groups and an oxygen atom from a monodentate carboxylato group (mode I). It completes its coordination sphere by a μ_2 -oxygen atom from a water molecule.

The thermal behavior of this compound has been studied by TGA and TDXD. Several phase transitions have been observed but none of these phases has been characterized. The removal of the crystallization and coordination water molecules is reversible. A BET nitrogen adsorption measurement has been performed on the solid dehydrated at 250 °C and revealed a low surface area ($\cong 15 \text{ m}^2 \text{ g}^{-1}$) probably due to a loss of the initial crystal structure upon dehydration.

Very recently, the same group has submitted an other paper describing the synthesis and the crystal structure of a three-dimensional anhydrous compound with chemical formula: $R(\text{btc})$ with $R = \text{Pr-Er}$ or Y (Serre et al., 2004). This compound has been obtained via hydrothermal synthesis and the crystal structure has been solved upon X-ray powder diffraction diagram data. The rare-earth ions are eight coordinated by eight oxygen atoms from carboxylato groups, that is, no coordination water molecule is present. All oxygen atoms from btc^{3-} are bound to R^{3+} ions. Two out of the three carboxylato groups present coordination mode IV while the third one is bridging (mode III) (see fig. 10). This compound presents a one-dimensional inorganic sub-network related to the 3D network via $(\text{btc})^{3-}$ ligand.

As all the oxygen atoms are already bound and no water molecule belongs to the R^{3+} ion coordination sphere, there is no structural rearrangement upon heating and the crystal structure remains unchanged upon 500 °C. At last, the optical emissions of doped isostructural compounds ($\text{Y}_{1-x}\text{R}_x(\text{btc})$ with $R = \text{Eu, Tb}$ or Dy and $x \sim 2\%$) have been studied. Very efficient red, green and blue emission respectively have been observed. As a concluding remark, one should notice that this anhydrous phase is different from the one obtained by de-hydration of the tube-like compound previously described.

3.2. Coordination polymers based on the $(\text{bdc})^{2-}$ ligand

The benzene-1,4-dicarboxylic acid (H_2bdc) is a bifunctional rod-like ligand which has lead to numerous interesting compounds by association with transition metal ions. Some interesting coordination polymers have been reported as well. The first one has been described in 1999 (Reneike et al., 1999a) and its chemical formula is $\text{Tb}_2(\text{bdc})_3 \cdot (\text{H}_2\text{O})_4$. It has been synthesized via an hydrothermal method. Its crystal structure is three-dimensional. As can be seen in fig. 11, each Tb^{3+} ion is eight coordinated by six oxygen atoms from six bridging carboxylato groups (mode III) and two oxygen atoms from two coordination water molecules. Each $(\text{bdc})^{2-}$ ligand is coordinated to four Tb^{3+} ion. Therefore, all oxygen atoms from carboxylato groups are bounded to Tb^{3+} ions.

Furthermore, there is no crystallization water molecule inside the structure. The projection view along the b -axis reported in fig. 11 emphasize the porosity of the structure. The

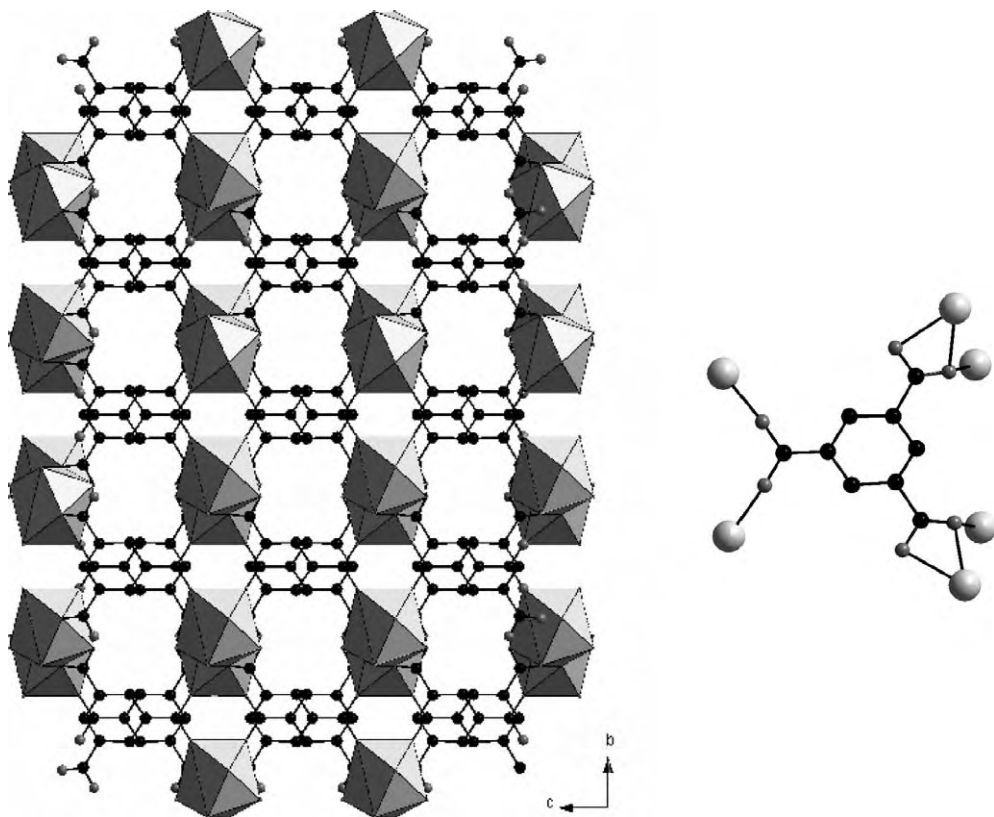


Fig. 10. (Left) projection along the a -axis of the polymeric network of $R(\text{btc})$: monoclinic, $C2/m$, $a = 6.941(1) \text{ \AA}$, $b = 14.700(1) \text{ \AA}$, $c = 8.488(1) \text{ \AA}$, $\beta = 107.73(1)^\circ$. The R^{3+} ion are represented in polyhedral representation. Re-drawn from Serre et al. (2004). (Right) coordination modes of the three carboxylato groups in $\text{Ln}(\text{btc})$.

microporous character of this compound as been checked by TGA and TDXD. These measurements reveal that the coordination water molecules can be evacuated under vacuum at 115°C and that the resulting anhydrous solid is thermally stable up to 450°C . Unfortunately neither the crystal structure of the anhydrous compound nor its porosity have been reported.

The luminescent lifetime of the anhydrous compound has also been studied but no definitive result was obtained. The authors concluded this paper saying that the anhydrous microporous phase presenting 1D channels can be potentially considered as luminescent probe for detecting small molecules. That is the reason why two years later another group published another paper on this family. In this paper (Pan et al., 2001) the synthesis, via hydrothermal method, and the crystal structure (see fig. 12) of a compound with chemical formula $\text{Er}_4(\text{bdc})_6 \cdot 6\text{H}_2\text{O}$ are described.

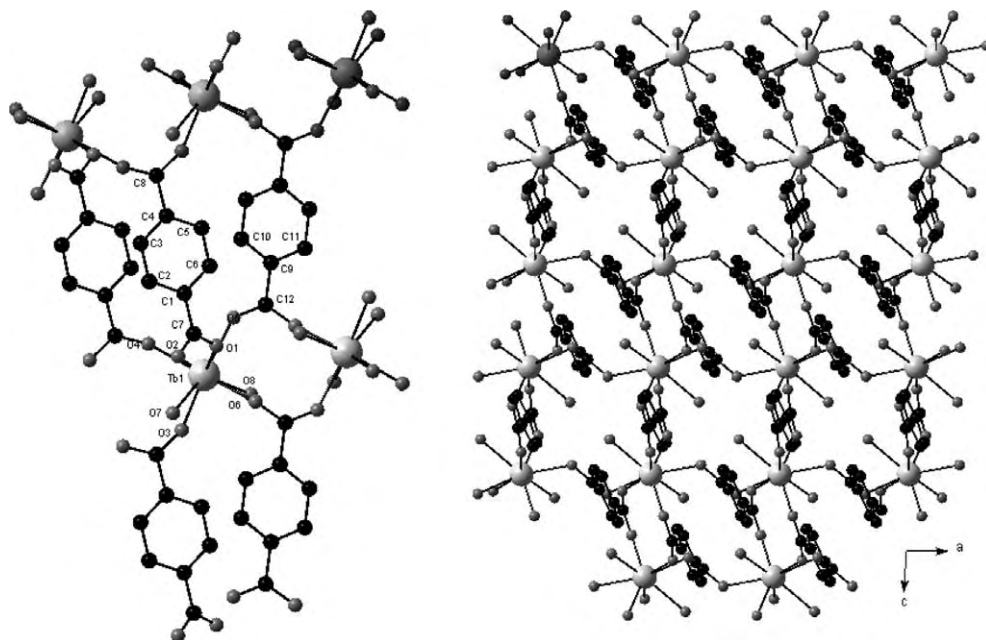


Fig. 11. (Left) extended asymmetric unit of $\text{Tb}_2(\text{bdc})_3 \cdot 4\text{H}_2\text{O}$: triclinic, $P\bar{1}$, $a = 6.1420(2)$ Å, $b = 10.0694(1)$ Å, $c = 10.0956(3)$ Å, $\alpha = 102.247(2)^\circ$, $\beta = 91.118(1)^\circ$, $\gamma = 101.518(2)^\circ$. Redrawn from Reneike et al. (1999a). (Right) projection view along the b -axis of $\text{Tb}_2(\text{bdc})_3 \cdot 4\text{H}_2\text{O}$.

In this structure there are four crystallographically independent Er^{3+} ions. The local coordination geometry around the first one is a dodecahedron which consists in six oxygen atoms from six $(\text{bdc})^{2-}$ groups and two from water molecules. The coordination polyhedron around the second Er^{3+} ion is a capped trigonal prism which contains five carboxylate oxygen and two water oxygen atoms. The coordination environments of the last two Er^{3+} ions are pentagonal pyramidal. The pentagonal planes are composed of four carboxylate oxygen atoms and a water oxygen atom, and the two apical sites are occupied by two oxygen atoms from another carboxylate ion. A projection view along the a -axis of the polymeric network is presented in fig. 13.

The thermal behavior has been studied by TGA and TDXD measurements which revealed that $\text{Er}_4(\text{bdc})_6 \cdot 6\text{H}_2\text{O}$ transforms upon dehydration (up to 300°C) into $\text{Er}_4(\text{bdc})_6$. This anhydrous compound then re-hydrates in $\text{Er}_2(\text{bdc})_3 \cdot 4\text{H}_2\text{O}$ which is isostructural with the Tb(III) compound previously described. The anhydrous compound is stable up to 500°C but its crystal structure has not been characterized.

Another compound with formula $\text{Er}_2(\text{bdc})_3(\text{H}_2\text{O})_6$ has also been reported (Deluzet et al., 2003). Contrary to the two previous ones, it has been obtained by slow diffusion through gel. Its crystal structure is three-dimensional and can be described as the succession of erbium ion planes linked by terephthalato organic groups (see fig. 14).

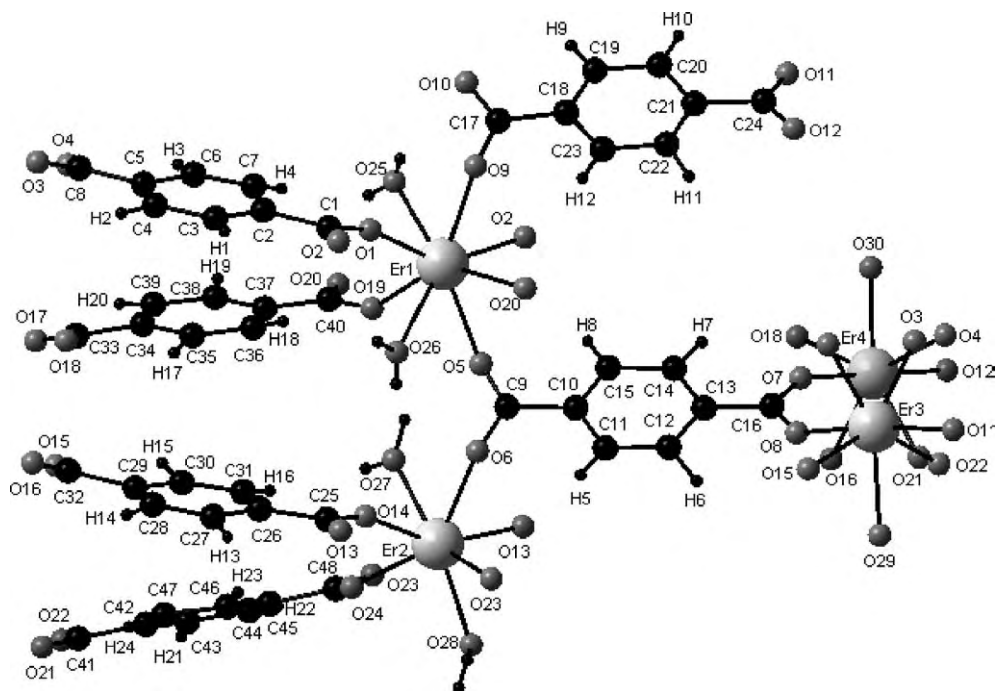


Fig. 12. Extended asymmetric unit of $\text{Er}_4(\text{bdc})_6 \cdot 6\text{H}_2\text{O}$: orthorhombic, Pbca , $a = 9.661(2) \text{ \AA}$, $b = 26.224(3) \text{ \AA}$, $c = 37.863(3) \text{ \AA}$. Redrawn from Pan et al. (2001).

The Er^{3+} ions are eight coordinated by three oxygen atoms from coordination water molecules and five oxygen atoms from carboxylate groups. There is no crystallization water molecule in this structure. Unfortunately this interesting compound has not yet been thermally studied because of its poor availability. Indeed it has only been obtained as single crystals dispersed in gel.

Another terephthalate-based coordination polymer has been described (Reneike et al., 1999b). It has been obtained once more thanks to hydrothermal methods in methanol/DMF medium. Its chemical formula is $\text{Tb}(\text{bdc})(\text{NO}_3) \cdot 2\text{DMF}$. Its crystal structure is reported in fig. 15. The Tb^{3+} ions are eight-coordinated by eight oxygen atoms. Four out of the eight are from four carboxylate monodentate groups belonging to four different $(\text{bdc})^{2-}$ ligand, two out of the eight are from coordinated DMF and the last two are from a bidentate NO_3^- ion.

The framework can be described as chains spreading along the c -axis. In these chains the Tb^{3+} ions are linked together via bridging carboxylate groups and the chains are cross-linked by $(\text{bdc})^{2-}$ entities to form a three-dimensional framework. As can be seen from fig. 15, this three-dimensional network presents no void. In order to create some the authors have removed the coordinated DMF molecules. The X-ray powder diffrac-

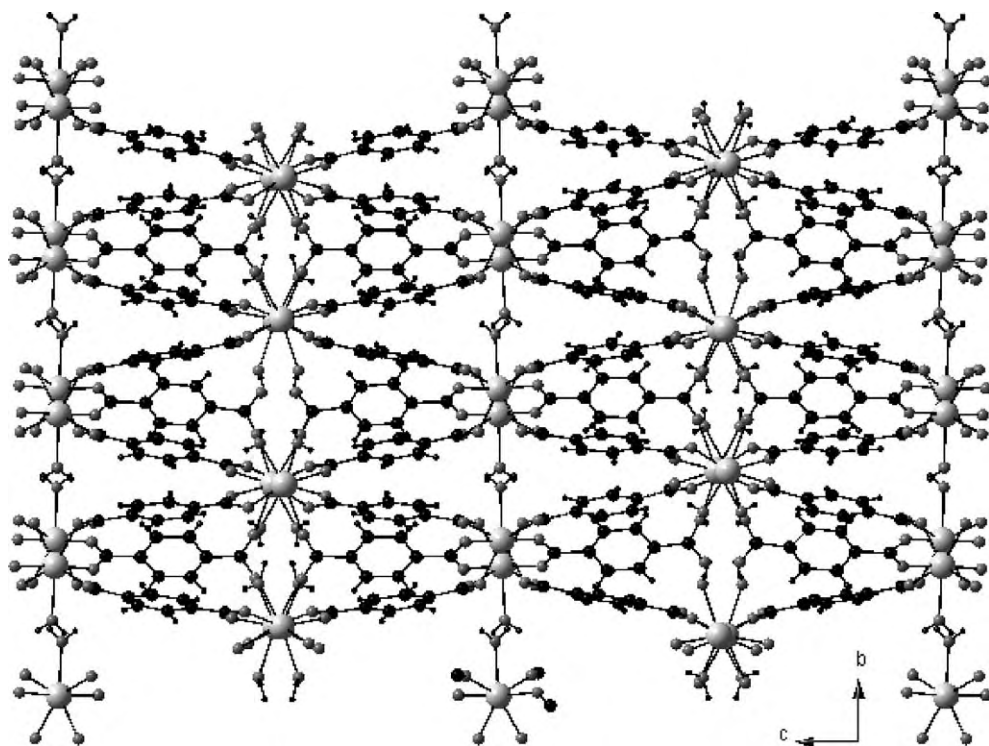


Fig. 13. Projection view along the a -axis of the polymeric network of $\text{Er}_4(\text{bdc})_6 \cdot 6\text{H}_2\text{O}$.

tion diagram show significantly broadened lines and did not allow any structural characterization. However this desolvated phase shows a rather interesting thermal stability (up to 300°C) and presents some interesting properties as far as gas sorption is considered.

Some other terephthalate-containing compounds have been obtained thanks to hydrothermal synthesis. The chemical formulae of these compound are $\text{Eu}_2(\text{H}_2\text{O})_2(\text{OH})_4(\text{bdc})$ and $\text{Eu}_2(\text{OH})_4(\text{bdc})$ (Serre et al., 2002). Their crystal structures (see fig. 16) are closely related to those of $\text{Eu}(\text{OH})_3$. Oxygen atoms of the inorganic sheets are either water molecules, hydroxo groups or oxygen atoms from the dicarboxylate ligand. In both structure elongated hydrophobic channels are present but with no real porosity. By TGA and TDXD it has been shown that both structures are related by an hydration/dehydration process. During the dehydration the coordination water molecules are removed and the monodentate carboxylato groups become bidentate. This results in a slight contraction of the Eu–Eu distances (Eu–Eu distances are roughly 13.8 \AA in the hydrated phase and 11.4 \AA in the dehydrated one).

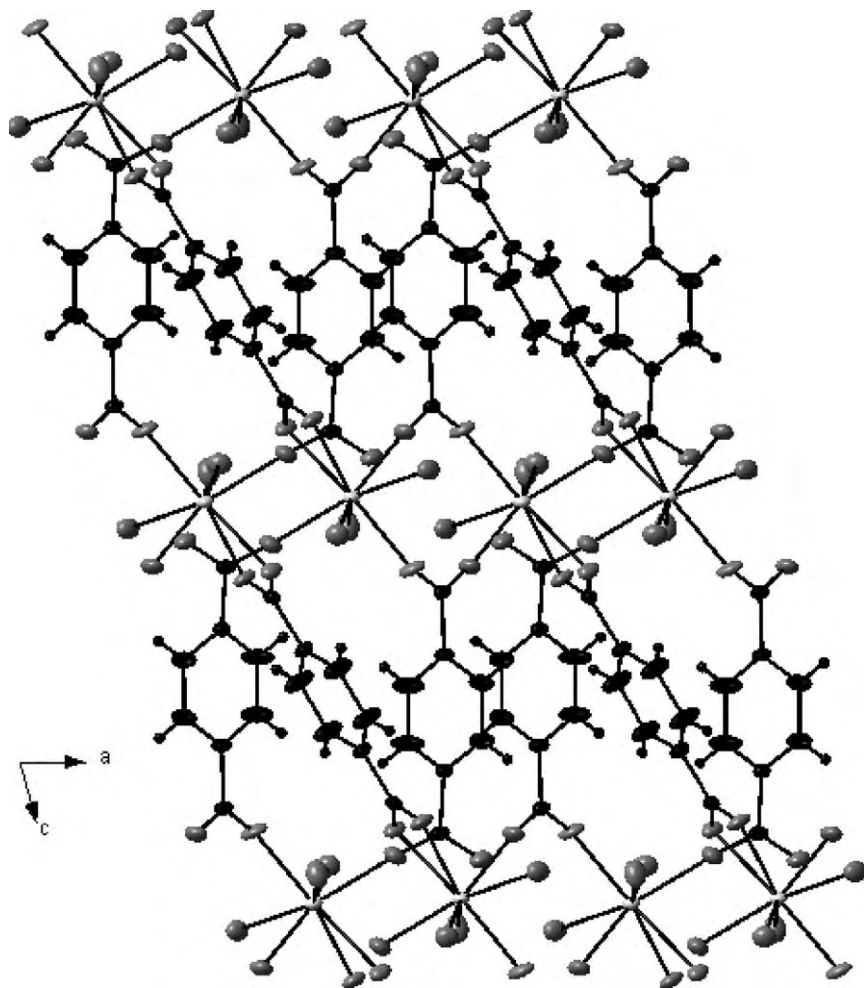


Fig. 14. Projection view along the b -axis of $\text{Er}_2(\text{bdc})_3(\text{H}_2\text{O})_6$: triclinic, $P\bar{1}$, $a = 7.8373(1) \text{ \AA}$, $b = 9.5854(2) \text{ \AA}$, $c = 10.6931(2) \text{ \AA}$, $\alpha = 68.78(1)^\circ$, $\beta = 70.87(2)^\circ$, $\gamma = 75.33(1)^\circ$. Redrawn from Deluzet et al. (2003).

3.3. Coordination polymers based on the $(\text{btc})^{4-}$ ligand

Several 1,2,4,5-benzene-tetracarboxylate containing coordination polymers have already been described. The oldest one was reported in a very short crystallographic paper (Yaghi et al., 1997b). It has been obtained via hydrothermal synthesis. Its chemical formula is $\text{Ce}(\text{Hbtc}) \cdot \text{H}_2\text{O}$ and its crystal structure is represented in fig. 17. The Ce^{3+} ions are surrounded by nine oxygen atoms. One out of the nine belongs to the coordinated water molecule while the eight others are from carboxylato groups from four different $(\text{Hbtc})^{3-}$ entities. The co-

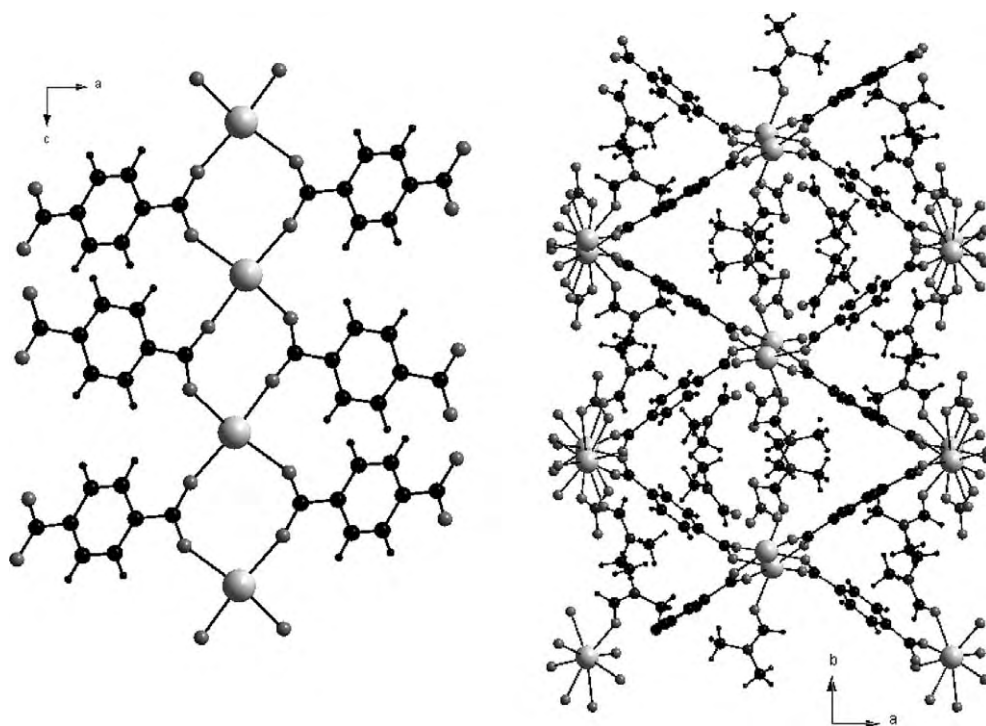


Fig. 15. (Left) projection view of the chains spreading along the c -axis of $\text{Tb}(\text{bdc})(\text{NO}_3)\cdot 2\text{DMF}$: monoclinic, $P2_1/c$, $a = 17.5986(1) \text{ \AA}$, $b = 19.9964(3) \text{ \AA}$, $c = 10.5454(2) \text{ \AA}$, $\beta = 91.283(1)^\circ$. NO_3^- and DMF groups have been omitted for clarity. Redrawn from Reneike et al. (1999b). (Right) projection view along the c -axis of the polymeric network of $\text{Tb}(\text{bdc})(\text{NO}_3)\cdot 2\text{DMF}$.

ordination modes adopted by the carboxylato groups are modes II, III and IV. Despite its three-dimensionality and the absence of crystallization water molecules, no further study has been undertaken until now.

More recently two other groups have published the synthesis and crystal structures of several other compounds. All of them have been obtained via hydrothermal methods and are three-dimensional.

The chemical formula of the first one is $[\text{Eu}_2(\text{btc})(\text{H}_2\text{btc})\text{H}_2\text{O}]\cdot 4\text{H}_2\text{O}$ (Wu, C.D. et al., 2002). Its crystal structure is reported in fig. 18. Eu^{3+} ions are nine coordinated by eight oxygen atoms from carboxylato groups belonging to six different $(\text{btc})^{4-}$ or $(\text{H}_2\text{btc})^{2-}$ ligands and the other one from a water molecule. The 3D structure presents channels spreading along the b -axis and filled by eight crystallization water molecules per unit cell. The magnetic properties have been studied but present no particular interest, as expected. The thermal behavior has also been studied. It shows that an anhydrous phase obtained upon heating is stable up to 400°C . Unfortunately no crystal structure of this anhydrous phase has been solved.

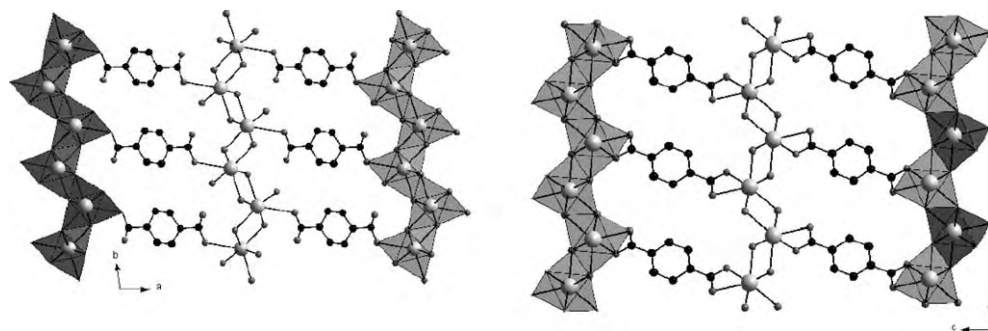


Fig. 16. (Left) projection view along the c -axis of the polymeric network of $\text{Eu}_2(\text{H}_2\text{O})_2(\text{OH})_4(\text{bdc})$: triclinic, $\bar{P}1$, $a = 13.190(1) \text{ \AA}$, $b = 7.185(1) \text{ \AA}$, $c = 3.718(1) \text{ \AA}$, $\alpha = 120.452(1)^\circ$, $\beta = 87.630(1)^\circ$, $\gamma = 97.650(1)^\circ$. The Eu^{3+} ions are represented in polyhedral representation. Redrawn from Serre et al. (2002). (Right) projection view along the a -axis of the polymeric network of $\text{Eu}_2(\text{OH})_4(\text{bdc})$: triclinic, $\bar{P}1$, $a = 3.6773(7) \text{ \AA}$, $b = 6.257(1) \text{ \AA}$, $c = 11.969(2) \text{ \AA}$, $\alpha = 91.01(3)^\circ$, $\beta = 97.53(3)^\circ$, $\gamma = 91.03(3)^\circ$. The Eu^{3+} ions are represented in polyhedral representation. Redrawn from Serre et al. (2002).

At last, three other coordination polymers based on 1,2,4,5-benzene-tetracarboxylate have been reported in the same publication by Cao et al. (2002b), namely $\text{Yb}_4(\text{btcc})_3(\text{H}_2\text{O})_8 \cdot 6\text{H}_2\text{O}$, $\text{Er}_8(\text{btcc})_6(\text{H}_2\text{O})_{16} \cdot 16\text{H}_2\text{O}$ and $\text{Tb}_2(\text{btcc})(\text{H}_2\text{btcc})(\text{H}_2\text{O})_2 \cdot 4\text{H}_2\text{O}$. All three have been obtained via hydrothermal methods and all three present a three-dimensional network with channels accommodating guest water molecules (see fig. 19). The thermal behavior of these compounds has been studied by TGA. In all cases it is possible to remove the water molecules and the resulting anhydrous phases are fairly stable. No crystal structure of these anhydrous phases has been reported.

As a concluding remark regarding $(\text{H}_2\text{btcc})^{2-}$ -containing coordination polymers, we would like to underline that the usual versatility of the carboxylate groups is reinforced in this ligand by its partial protonation. It is also worth noting that up to now, all the reported lanthanide-based coordination polymers obtained with this ligand are 3D.

3.4. Coordination polymers based on the $(\text{bhc})^{6-}$ ligand

To conclude this overview of the benzene-polycarboxylate based coordination polymers we now consider compounds built from benzene-hexacarboxylate containing compounds. As can be seen from table 2, there are several examples of such compounds. One is mono-dimensional and its chemical formula is $R_2(\text{bhc})(\text{H}_2\text{O})_{10} \cdot 4\text{H}_2\text{O}$ (Deluzet and Guillou, 2003; Robl and Hentschel, 1992). It has been obtained twice, with Y^{3+} and Er^{3+} , in gel media. Its crystal structure can be described as chain-like molecular motifs spreading along the \vec{a} axis. The rare-earth ion is eight coordinated by five oxygen atoms from water molecules and three oxygen atoms from three monodentate carboxylate groups. The six carboxylate groups are monodentate and the second oxygen atom remains free. The cohesion of the crystal structure is insured both by a complex network of hydrogen bonds and by interactions between the phenyl rings (see fig. 20).

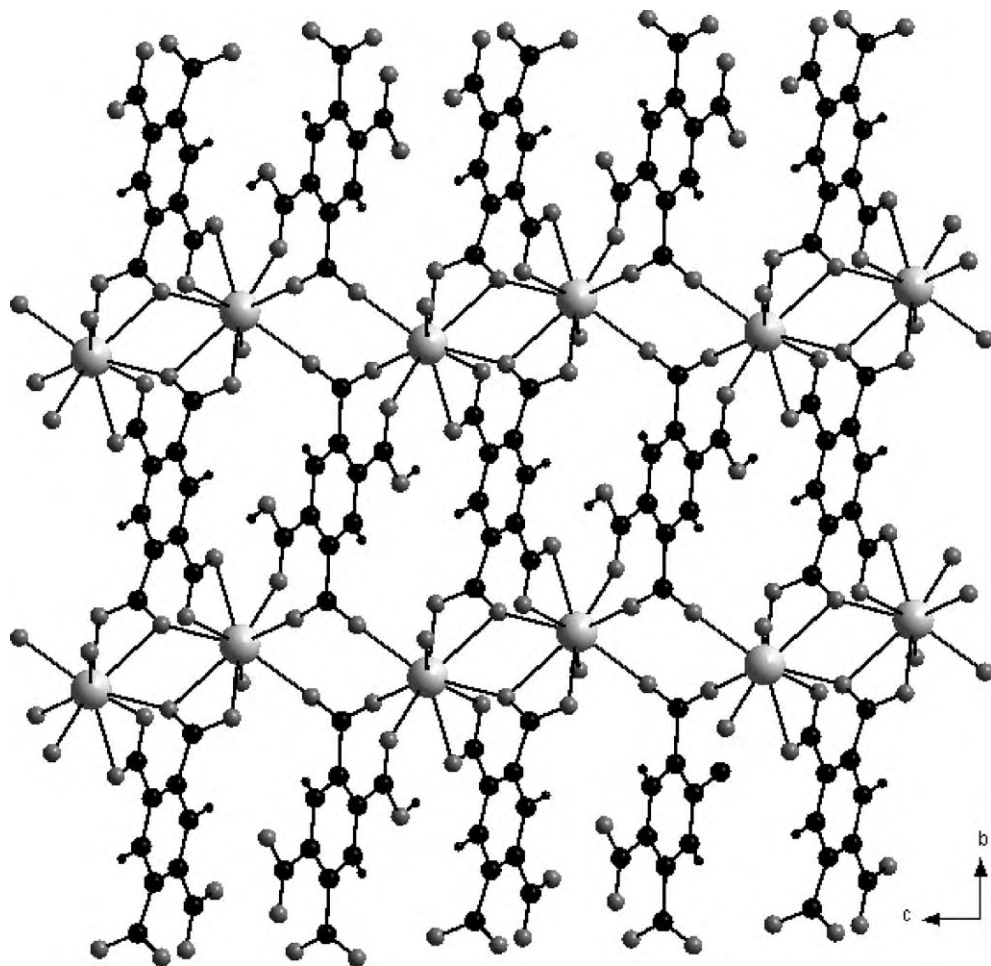


Fig. 17. Projection view along the a -axis of the three-dimensional network of $\text{Ce}(\text{Hbtc})\cdot\text{H}_2\text{O}$: triclinic, $P\bar{1}$, $a = 6.419(2)$ Å, $b = 9.414(2)$ Å, $c = 9.604(3)$ Å, $\alpha = 88.49(2)^\circ$, $\beta = 74.68(2)^\circ$, $\gamma = 76.68(2)^\circ$. Redrawn from Yaghi et al. (1997b).

Another compound has been structurally described (Wu, L.P. et al., 1996). Its chemical formula is $[\text{La}_2(\text{bhc})(\text{H}_2\text{O})_9]\cdot 2\text{H}_2\text{O}$. It has been obtained via a soft hydrothermal synthesis (the solution was sealed in a glass tube which was left for two days in a water bath at 40°C). Its crystal structure is 3D. There are two crystallographically independent La^{3+} ions. Both are nine coordinated. One by five water molecules plus four oxygen atoms from carboxylate groups while the other is linked to only four water molecules and five oxygen atoms from carboxylate groups. One out of the six mellitate carboxylate groups is free while the five others are bidentate or monodentate (see fig. 21). Two crystallization water molecules

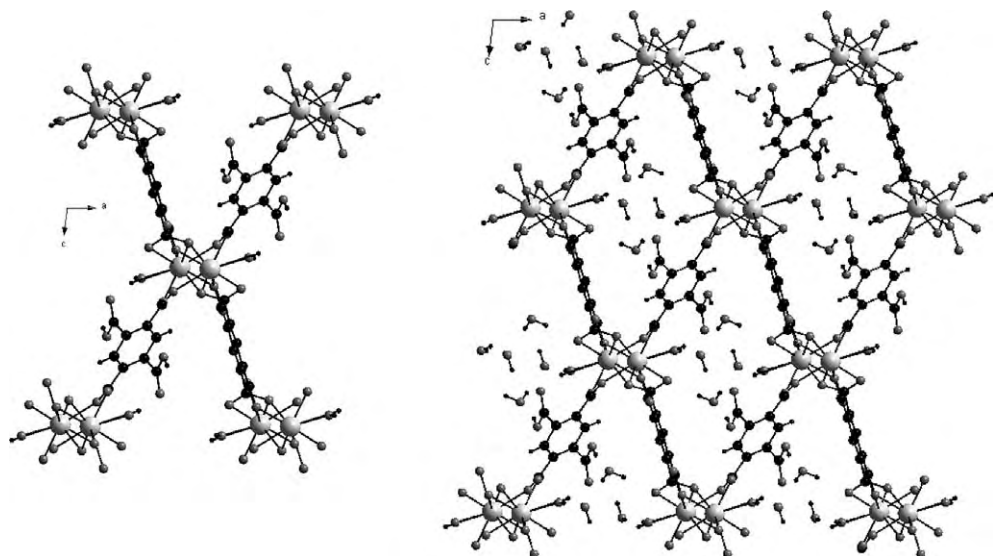


Fig. 18. (Left) projection view along the b -axis of $[\text{Eu}_2(\text{btc})(\text{H}_2\text{btc})(\text{H}_2\text{O})]\cdot 4\text{H}_2\text{O}$ molecular motif: monoclinic, $P2_1/n$, $a = 10.7562(2)$ Å, $b = 7.2075(2)$ Å, $c = 17.2180(5)$ Å, $\beta = 97.072(2)^\circ$. Redrawn from Wu, C.D. et al. (2002). (Right) projection view along the b -axis of the polymeric network of $[\text{Eu}_2(\text{btc})(\text{H}_2\text{btc})(\text{H}_2\text{O})]\cdot 4\text{H}_2\text{O}$.

are localized inside the cavities. No thermal study has been performed. However, even if this hydrated crystal structure seems promising (it is 3D and contains a light lanthanide ion) for catalytic purposes, one should notice that three out of the twelve oxygen atoms of the mellitate anion are free and available for a crystallographic rearrangement upon dehydration.

At last three other 3D frameworks containing rare-earth mellitates have recently been published (Chui et al., 2001). They all have been obtained by hydrothermal methods. Indeed, the authors of this publication think that hydrothermal conditions can lead to compounds with a lower level of hydration compared to ambient conditions. Actually the three new coordination polymers therein described present at most only one crystallization water molecule as evidenced by their chemical formulae: $\text{Ln}_2(\text{bhc})(\text{H}_2\text{O})_6$ with $\text{Ln} = \text{La}-\text{Er}$, $\text{Ln}_2(\text{bhc})(\text{H}_2\text{O})_4\cdot(\text{H}_2\text{O})$ with $\text{Ln} = \text{Tm}-\text{Lu}$ and $\text{Tm}_2(\text{bhc})(\mu\text{-H}_2\text{O})_2(\text{H}_2\text{O})_2$. Projection views of their molecular networks are presented in fig. 22.

The nine coordinated lanthanide ion in compounds $R_2(\text{bhc})(\text{H}_2\text{O})_6$ with $\text{Ln} = \text{La}-\text{Er}$ (left) is surrounded by three coordination water molecules and four carboxylato groups from four different mellitate anions (two bidentate and two mono dentate). The crystal structure present some channels spreading along the \vec{c} -axis filled with coordinated water molecules. Dehydration of these polymers is impossible because they loose their crystallinity above 100°C .

More interesting are the compounds $R_2(\text{bhc})(\text{H}_2\text{O})_4\cdot(\text{H}_2\text{O})$ with $R = \text{Tm}-\text{Lu}$ (middle). They crystallize in a tetragonal space group and the smaller lanthanide ions are only seven coordinated by two water molecules and five monodentate carboxylato groups from four dif-

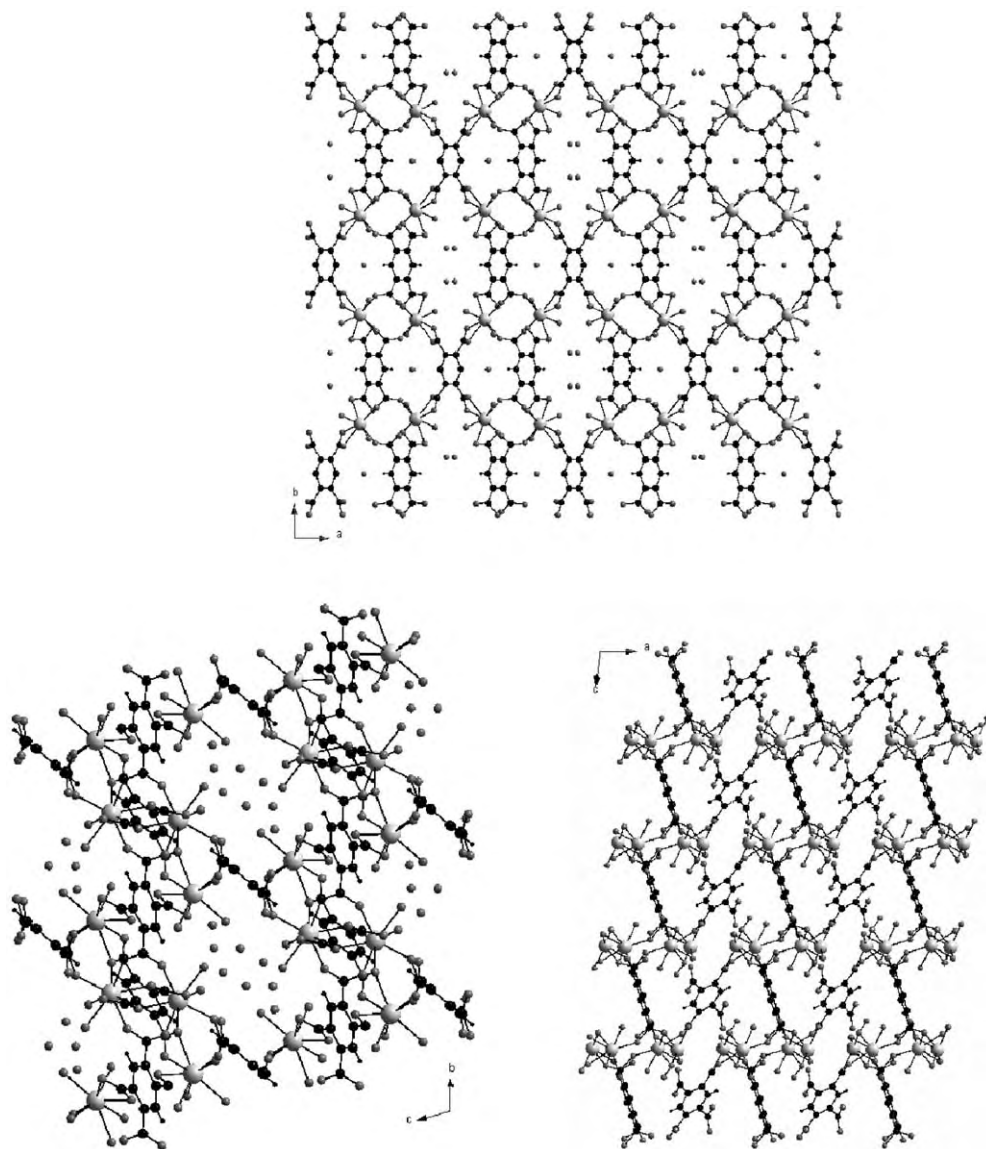


Fig. 19. (Left) projection view along the c -axis of the polymeric network of $\text{Yb}_4(\text{bttc})_3(\text{H}_2\text{O})_8 \cdot 6\text{H}_2\text{O}$: monoclinic, $C2/m$, $a = 20.8119(5)$ Å, $b = 17.6174(1)$ Å, $c = 5.7252(2)$ Å, $\beta = 92.32(1)^\circ$. Redrawn from Cao et al. (2002b). (Middle) projection view along the a -axis of the polymeric network of $\text{Er}_8(\text{bttc})_6(\text{H}_2\text{O})_{16} \cdot 16\text{H}_2\text{O}$: triclinic, $P\bar{1}$, $a = 9.6739(5)$ Å, $b = 11.0039(5)$ Å, $c = 11.5523(6)$ Å, $\alpha = 104.83(1)^\circ$, $\beta = 91.0(1)^\circ$, $\gamma = 114.26(1)^\circ$. Redrawn from Cao et al. (2002b). (Right) projection view along the b -axis of the polymeric network of $\text{Tb}_2(\text{bttc})(\text{H}_2\text{bttc})(\text{H}_2\text{O})_2 \cdot 4\text{H}_2\text{O}$: monoclinic, $P2_1/c$, $a = 10.725(1)$ Å, $b = 7.1693(9)$ Å, $c = 17.158(2)$ Å, $\beta = 97.11(2)^\circ$. Redrawn from Cao et al. (2002b).

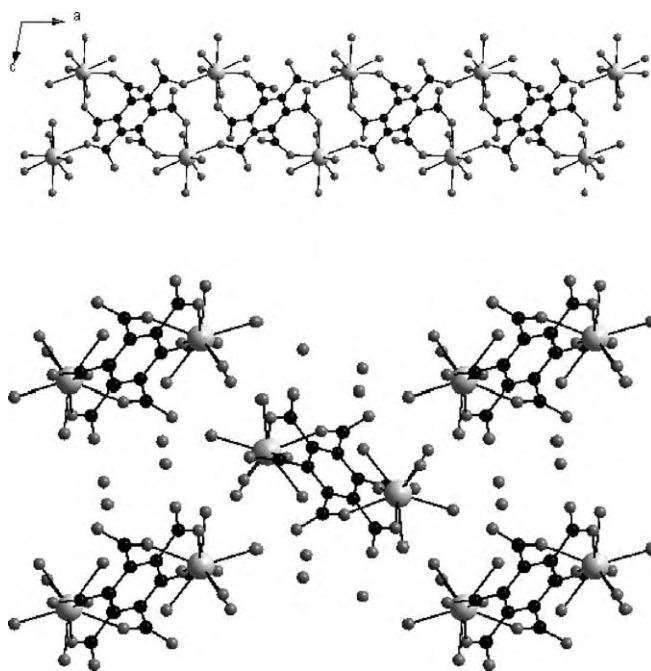


Fig. 20. (Left) projection view along the b -axis of the molecular motif of $\text{Er}_2(\text{bhc})(\text{H}_2\text{O})_{10} \cdot 4\text{H}_2\text{O}$: monoclinic, $P2_1/n$, $a = 8.4499(1) \text{ \AA}$, $b = 9.2595(2) \text{ \AA}$, $c = 16.2911(4) \text{ \AA}$, $\beta = 100.3390(8)^\circ$. Redrawn from Deluzet and Guillou (2003). (Right) projection view along the a -axis of the crystal packing of $\text{Er}_2(\text{bhc})(\text{H}_2\text{O})_{10} \cdot 4\text{H}_2\text{O}$.

ferent mellitate anions. The bound water molecules point toward the center of the channels spreading along the \bar{c} -axis. The crystallization water molecule is disordered and lies at the center of the largest cavity. Once more the framework is lost upon dehydration.

Finally, the eight coordinated Tm^{3+} ion in the compound $\text{Tm}_2(\text{bhc})(\mu\text{-H}_2\text{O})_2(\text{H}_2\text{O})_2$ (right) is surrounded by one terminal coordinated water molecule, five monodentate carboxylate groups and two bridging coordination water molecules. This last water molecule leads to dimeric units $[\text{Tm}_2(\mu\text{-H}_2\text{O})_2]$. No dehydration experiment is reported.

As can be seen from the previous examples much work is in progress in the field of lanthanide-containing coordination polymers involving benzene polycarboxylates as ligands. Before concluding this section we would like to cite two other interesting results involving ligands which can be considered as derivatives of these benzene polycarboxylates.

3.5. Coordination polymers based on benzene polycarboxylate derivatives

In the above-described crystal structures the intermetallic distances are a little bit too short if optical properties are to be targeted. Furthermore the porosity of the three-dimensional compounds should be enhanced for gas storage or molecular separation applications. The design of the two compounds described hereafter has been motivated by these observations.

The first one has been obtained thanks to gel diffusion methods by reacting an Er^{3+} ion with 2,6-naphtalenedicarboxylate (see scheme 3) (Deluzet et al., 2003). Its chemical formula is $\text{Er}_2(\text{ndc})_3(\text{H}_2\text{O})_6$ where $(\text{ndc})^{2-}$ stands for 2,6-naphtalenedicarboxylate.

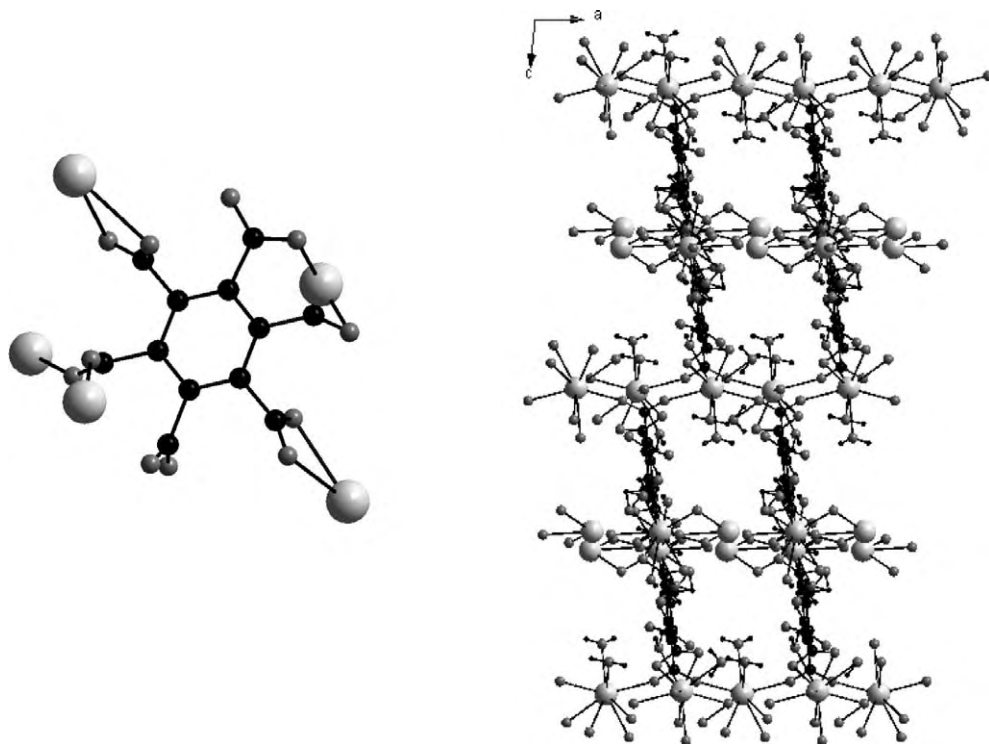


Fig. 21. (Left) the coordination environment of the $(bhc)^{6-}$ ligand in $La_2(bhc)(H_2O)_9 \cdot 2H_2O$. (Right) projection view along the b -axis of the crystal structure of $La_2(bhc)(H_2O)_9 \cdot 2H_2O$: monoclinic, $P2_1/n$, $a = 6.723(4) \text{ \AA}$, $b = 11.368(5) \text{ \AA}$, $c = 29.813(4) \text{ \AA}$, $\beta = 95.851(3)^\circ$. Redrawn from Wu, L.P. et al. (1996).

Its crystal structure is exactly the same than the one of the compound obtained in similar conditions with terephthalate (see fig. 23), namely $Er_2(bdc)_3(H_2O)_6$. The crystal structure can also be described as a succession of Er^{3+} ions planes connected by organic ligand planes. The only difference between the two structures lies in the inter inorganic plane distances. As an example the distances between two Er^{3+} ions connected through a 2,6-naphthalenedicarboxylate ligand is roughly 12 \AA while the distances between two Er^{3+} ions connected through a terephthalate ligand was 10 \AA . This result illustrates the tunability of the crystallographic arrangement by the choice of the ligand. However, in this particular case, the goal was not reached. Indeed, the intermetallic distances in the inorganic planes remains almost unchanged because of the bridging coordination mode of the carboxylato groups.

The second compound (Pan et al., 2003) has been obtained via hydrothermal methods by reacting a lanthanide ion with 1,4-phenylendiacetate (see scheme 3). The chemical formula of the obtained coordination polymer is $Ln_2(pda)_3(H_2O) \cdot 2H_2O$ with $Ln = La$ or Er and $(pda)^{2-} = 1,4\text{-phenylendiacetate}$. Its extended structure consists of $Ln\text{-COO}$ triple helices cross-linked through $\text{-CH}_2\text{C}_6\text{H}_4\text{CH}_2\text{-}$ spacers of the $(pda)^{2-}$ anions, showing 1D open chan-

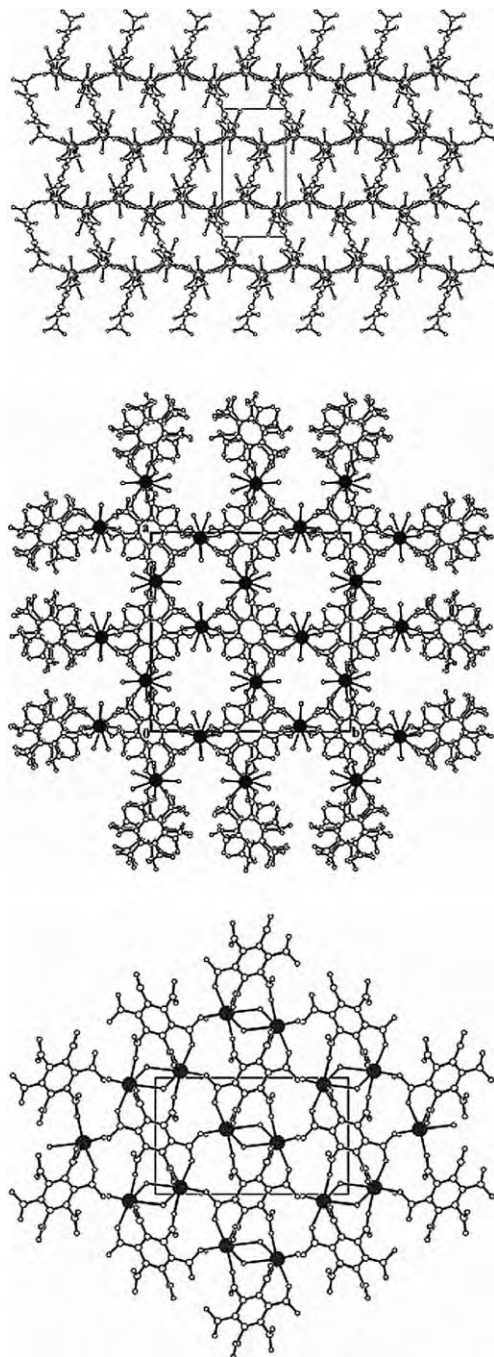
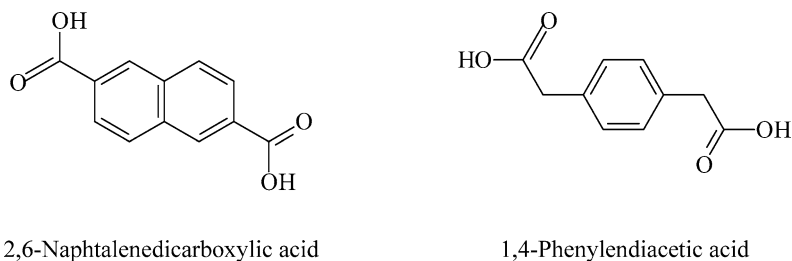


Fig. 22. (Left) projection view along the c -axis of the crystal structure of $\text{Ln}_2(\text{bhc})(\text{H}_2\text{O})_6$: orthorhombic, Pnmm , $a = 13.642(2) \text{ \AA}$, $b = 6.769(1) \text{ \AA}$, $c = 10.321(2) \text{ \AA}$. Redrawn from Chui et al. (2001). (Middle) projection view along the c -axis of the crystal structure of $\text{Ln}_2(\text{bhc})(\text{H}_2\text{O})_4 \cdot (\text{H}_2\text{O})$: tetragonal, P4/ncc , $a = 18.443(3) \text{ \AA}$, $c = 10.374(2) \text{ \AA}$. Redrawn from Chui et al. (2001). (Right) projection view along the a -axis of the crystal structure of $\text{Tm}_2(\text{bhc})(\mu\text{-H}_2\text{O})_2(\text{H}_2\text{O})_2$: monoclinic, $\text{P2}_1/\text{c}$, $a = 5.781(1) \text{ \AA}$, $b = 14.840(1) \text{ \AA}$, $c = 8.920(1) \text{ \AA}$, $\beta = 93.46(1)^\circ$. Redrawn from Chui et al. (2001).



Scheme 3.

nels along the crystallographic *c*-axis (see fig. 24). These channels accommodate the guest and coordinated water molecules. This compound can be dehydrated leading to $\text{Ln}_2(\text{pda})_3$ which has been assumed to present almost the same crystal structure than its hydrated precursor on the basis of X-ray powder diffraction diagrams. It reversibly bind water reforming $\text{Ln}_2(\text{pda})_3(\text{H}_2\text{O}) \cdot 2\text{H}_2\text{O}$. This dehydrated phase is stable up to 450 °C. The effective pore window size has been estimated to roughly 3.4 Å. These results demonstrate the feasibility of achieving well defined porous and stable lanthanide-organic framework with coordinatively unsaturated metal sites. Such systems would be well suited for the study of size- and shape-selective catalysis of organic reactions known to be catalyzed by lanthanide Lewis acids (Shibasaki et al., 1999; Imamoto, 1994).

3.6. Coordination polymers based on other ligands

Numerous other lanthanide coordination polymers have been designed with ligands which are neither rigid, nor unsaturated (Starynowicz and Meyer, 2000; Wu, Y. et al., 2002; Long et al., 2001; Alleyne et al., 2001; Wan et al., 2003; Feil-Jenkins et al., 1995). Some interesting results are highlighted in this section.

3.6.1. Coordination polymers with carboxylate ligands

Let us so consider $[\text{R}(\text{C}_9\text{H}_9\text{O}_6)(\text{H}_2\text{O})_2]_2 \cdot 5\text{H}_2\text{O}$ where $\text{C}_9\text{H}_9\text{O}_6$ stands for the *cis,cis*-1,3,5-cyclohexanetricarboxylate anion (Pan et al., 2000a; Daignebonne et al., 2001b) and *R* for Y and Dy–Yb. This ligand is rather interesting because it can be compared with the chemically similar 1,3,5-benzene-tricarboxylate. Comparing this structure with the various crystal structures obtained with $(\text{btc})^{3-}$ emphasizes the important role of the ligand. Indeed, whereas all the crystal structures involving $(\text{btc})^{3-}$ were mono- or bi-dimensional, the crystal structure of this compound is three-dimensional (see fig. 25). Unfortunately, analogous compounds with the lighter lanthanides have not been structurally characterized.

These compounds exhibit large channels along the three crystallographic axes filled with crystallization water molecules. The guest water molecules can be removed and the host structure has been claimed to remain unchanged. Unfortunately there is no direct evidence of this because of a lack of crystallinity. The anhydrous compound is thermally reasonably stable (up to 250 °C). Nevertheless the dehydrated compound can reversibly bind water.

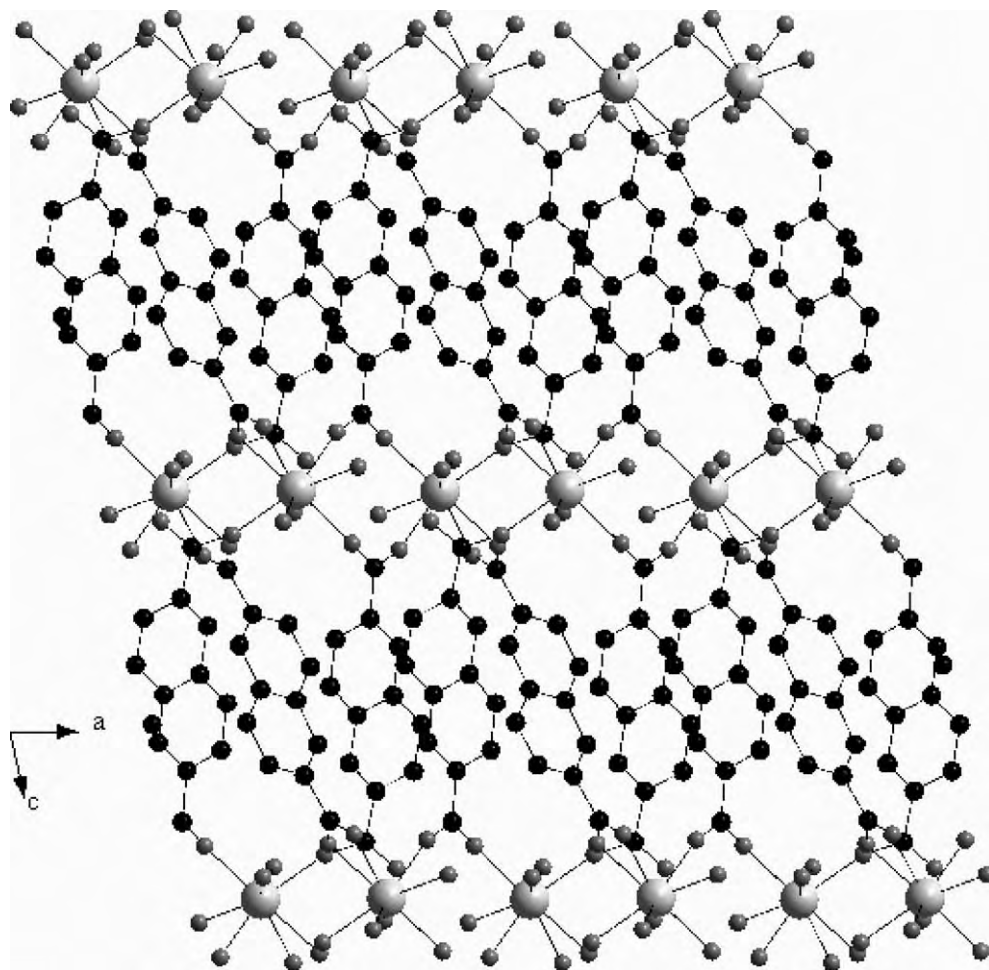


Fig. 23. Projection view along the b -axis of the crystal structure of $\text{Er}_2(\text{ndc})_3(\text{H}_2\text{O})_6$; triclinic, $\bar{P}1$, $a = 7.9891(3) \text{ \AA}$, $b = 9.5539(4) \text{ \AA}$, $c = 12.4286(6) \text{ \AA}$, $\alpha = 75.99(1)^\circ$, $\beta = 74.82(1)^\circ$, $\gamma = 75.89(2)^\circ$. Redrawn from Deluzet et al. (2003).

Another example is the $\{[\text{La}_2(\text{adipate})_3(\text{H}_2\text{O})_4] \cdot 6\text{H}_2\text{O}\}_n$ in which the adipate ligand is a long chain dicarboxylate (Kiritsis et al., 1998) ($\text{C}_6\text{H}_8\text{O}_4$) (see fig. 26).

This compound is remarkable because it is one of the first 3D molecular-based microporous materials using flexible multidentate ligand. Furthermore it is not irreversibly destroyed upon removal of its crystallization solvent molecules. Unfortunately adsorption studies showed that the specific area of the dehydrated compound was only $8 \text{ m}^2 \text{ kg}^{-1}$ and therefore that the porous host structure was not retained. The dehydrated compound is stable up to 300°C .

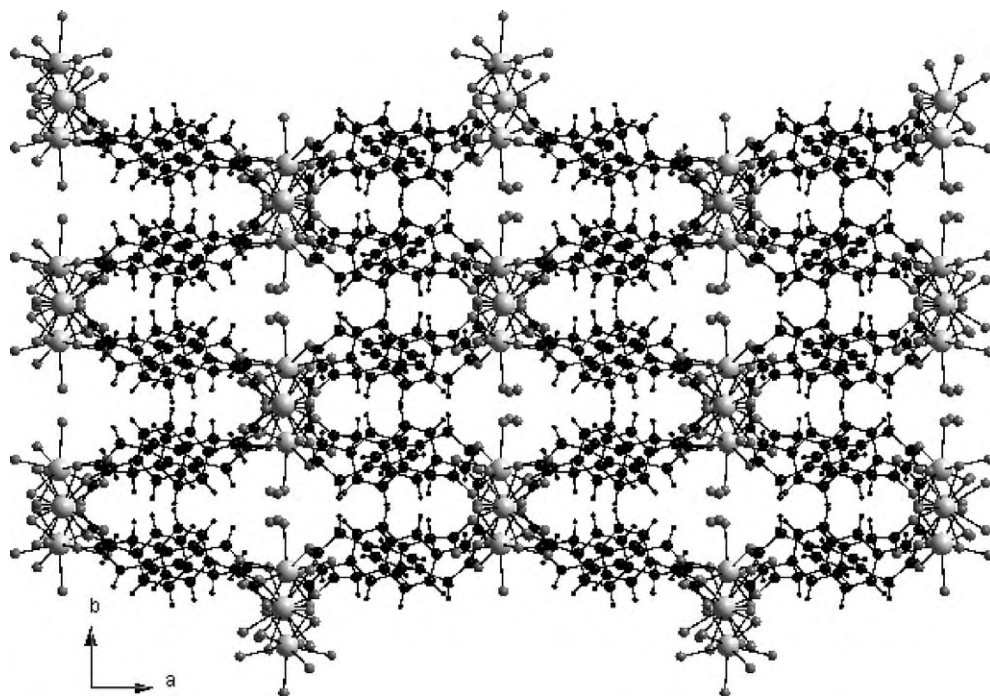


Fig. 24. Projection view along the c -axis of the crystal structure of $\text{Ln}_2(\text{pda})_3(\text{H}_2\text{O}) \cdot 2\text{H}_2\text{O}$: monoclinic, $P2_1/c$, $a = 21.6200(2) \text{ \AA}$, $b = 9.9719(1) \text{ \AA}$, $c = 14.0453(1) \text{ \AA}$, $\beta = 91.58(1)^\circ$. Redrawn from Pan et al. (2003).

This compound is rather interesting in the sense that it is one of the rare three-dimensional compounds based on a flexible ligand.

Very recently the same groups have reported the synthesis and the crystal structure of analogous compounds involving smaller lanthanide ions ($\text{Nd}^{3+} - \text{Yb}^{3+}$) (Dimos et al., 2002). The chemical formulae of these compounds are $R_2(\text{adipate})_3(\text{H}_2\text{O})_4 \cdot x\text{H}_2\text{O}$ with x ranging from 1.5 to 0. All the compounds were obtained thanks to slow diffusion in silica gel media. They also report, in the same paper, the crystal structure of $\text{La}(\text{C}_7\text{H}_{10}\text{O}_4)(\text{C}_7\text{H}_{11}\text{O}_4)(\text{H}_2\text{O}) \cdot \text{H}_2\text{O}$. All these compounds are three-dimensional and present channels filled with crystallization water molecules that can be reversibly removed. The thermal stability of these compound is unfortunately relatively low.

Much work as also been performed with the succinate ($[\text{O}_2\text{C}-(\text{CH}_2)_2-\text{CO}_2]^{2-}$) or glutarate ($[\text{O}_2\text{C}-(\text{CH}_2)_3-\text{CO}_2]^{2-}$) ligands (Serpaggi and Férey, 1998, 1999, 2003). All of them have been obtained via hydrothermal methods. As can be seen on fig. 27, these compounds exhibit rather large channels filled with water molecules. There are, however, very few information about their thermal behavior.

The same group has very recently synthesized and structurally characterized a new three-dimensional porous rare-earth carboxylate with chemical formula $\text{Eu}_2(\text{O}_2\text{C}-\text{C}_{10}\text{H}_{14}-\text{CO}_2)_3$ (Millange et al., 2004). This compound has been obtained under hydrothermal conditions

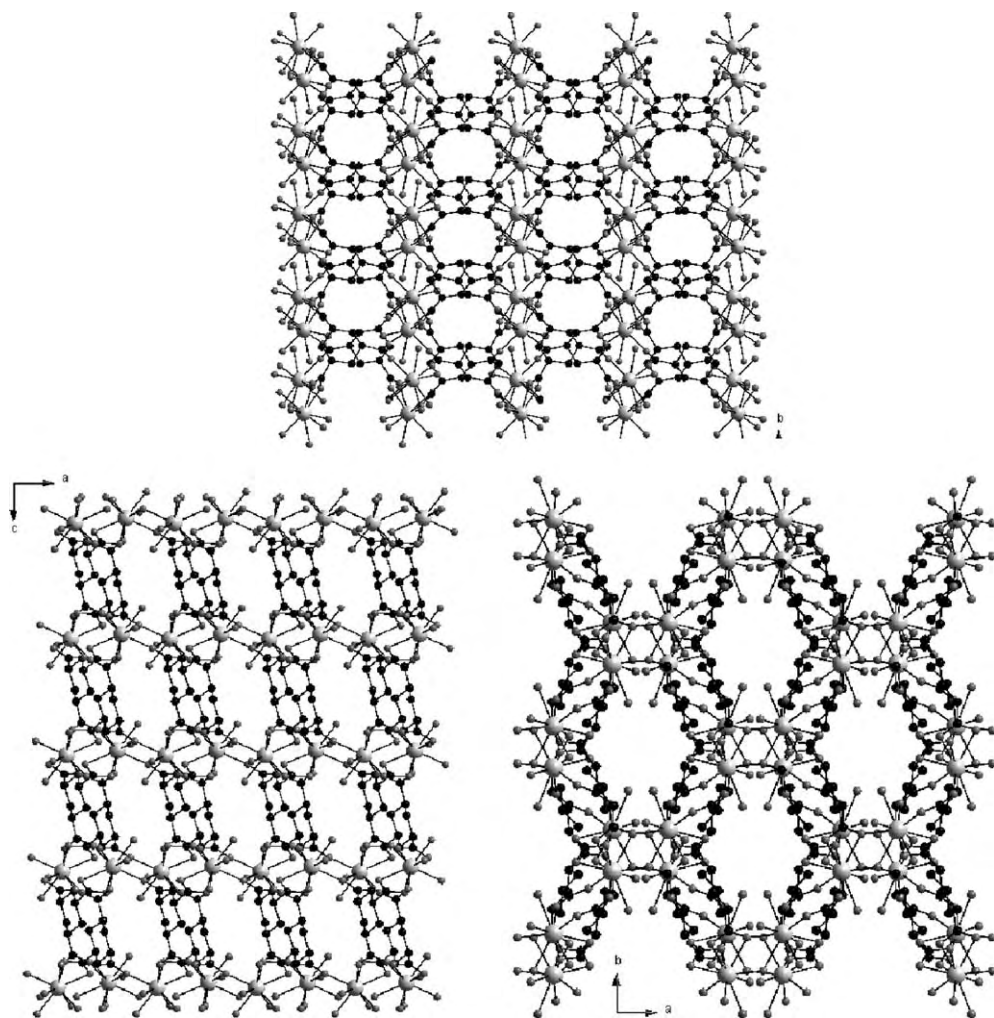


Fig. 25. (Left) projection view along the a -axis of $[\text{Er}(\text{C}_9\text{H}_9\text{O}_6)(\text{H}_2\text{O})_2]_2 \cdot 5\text{H}_2\text{O}$: monoclinic, $C2/c$, $a = 13.394(2) \text{ \AA}$, $b = 12.2501(9) \text{ \AA}$, $c = 15.922(2) \text{ \AA}$, $\beta = 92.09(1)^\circ$. Crystallization water molecules have been omitted for emphasizing the cavities. Redrawn from Daignebonne et al. (2001a). (Middle) projection view along the b -axis of $[\text{Er}(\text{C}_9\text{H}_9\text{O}_6)(\text{H}_2\text{O})_2]_2 \cdot 5\text{H}_2\text{O}$. Crystallization water molecules have been omitted for emphasizing the cavities. (Right) projection view along the c -axis of $[\text{Er}(\text{C}_9\text{H}_9\text{O}_6)(\text{H}_2\text{O})_2]_2 \cdot 5\text{H}_2\text{O}$. Crystallization water molecules have been omitted for emphasizing the cavities.

from aqueous mixtures of europium nitrate and 1,3-adamantanedicarboxylic acid. Its three-dimensional structure consists in chains built up from face-sharing nine-coordinated europium polyhedra connected by 1,3-adamantanedicarboxylate ligands. It exhibits rather large ($\approx 17 \text{ \AA}^2$) anhydrous channels (see fig. 28).

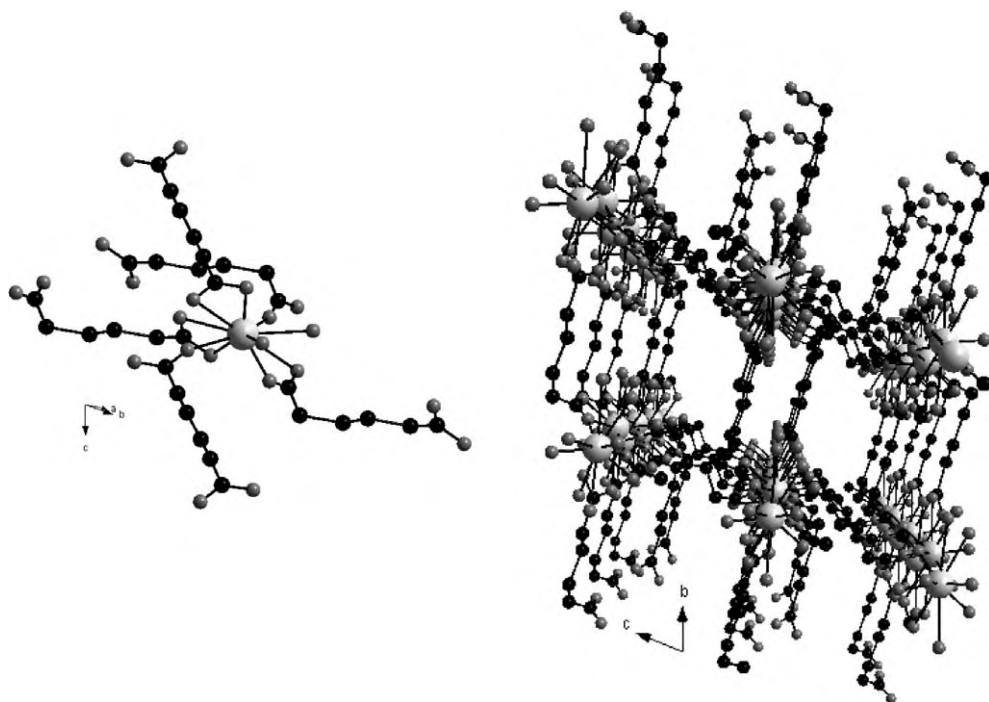


Fig. 26. (Left) view of the coordination environment of $\{La_2(adipate)_3(H_2O)_4 \cdot 6H_2O\}_n$: Triclinic, $P\bar{1}$, $a = 9.239(2)$ Å, $b = 9.790(2)$ Å, $c = 7.09(1)$ Å, $\alpha = 68.04(1)^\circ$, $\beta = 84.49(1)^\circ$, $\gamma = 62.01(1)^\circ$. Redrawn from Kiritsis et al. (1998). (Right) projection view along the a -axis of the crystal packing of $\{La_2(adipate)_3(H_2O)_4 \cdot 6H_2O\}_n$. Crystallization water molecules have been omitted for clarity.

The inner part of these channels is made of adamantane molecules which stack along the \vec{c} -axis and point toward the center of the channels. The anhydrous character of this compound, which is probably due to the hydrophobic character of the adamantane, implies several original properties. In particular, as there is no water molecule, the crystal structure remains unchanged up to 300°C . A Langmuir surface area of $65\text{ m}^2\text{ g}^{-1}$ has been measured, in agreement with the presence of a small accessible porosity. The isostructural Y^{3+} compound doped with Eu^{3+} has been prepared and the characteristic blue luminescence of Eu^{3+} ions has been observed at room temperature.

Finally, we turn our attention to the compounds synthesized via hydrothermal methods by reaction of a lanthanide nitrate with 3,5-pyrazoledicarboxylic acid (hereafter denoted H_3pdc) (Pan et al., 2000b). See scheme 4.

Three families of isostructural compounds have been obtained depending on the lanthanide ion involved. The most interesting feature in that beautiful crystallo-chemical work is that the highly asymmetric coordination patterns of the ligand leads to crystal structures belonging to acentric space groups. The authors of this publication suggest that it should be possible

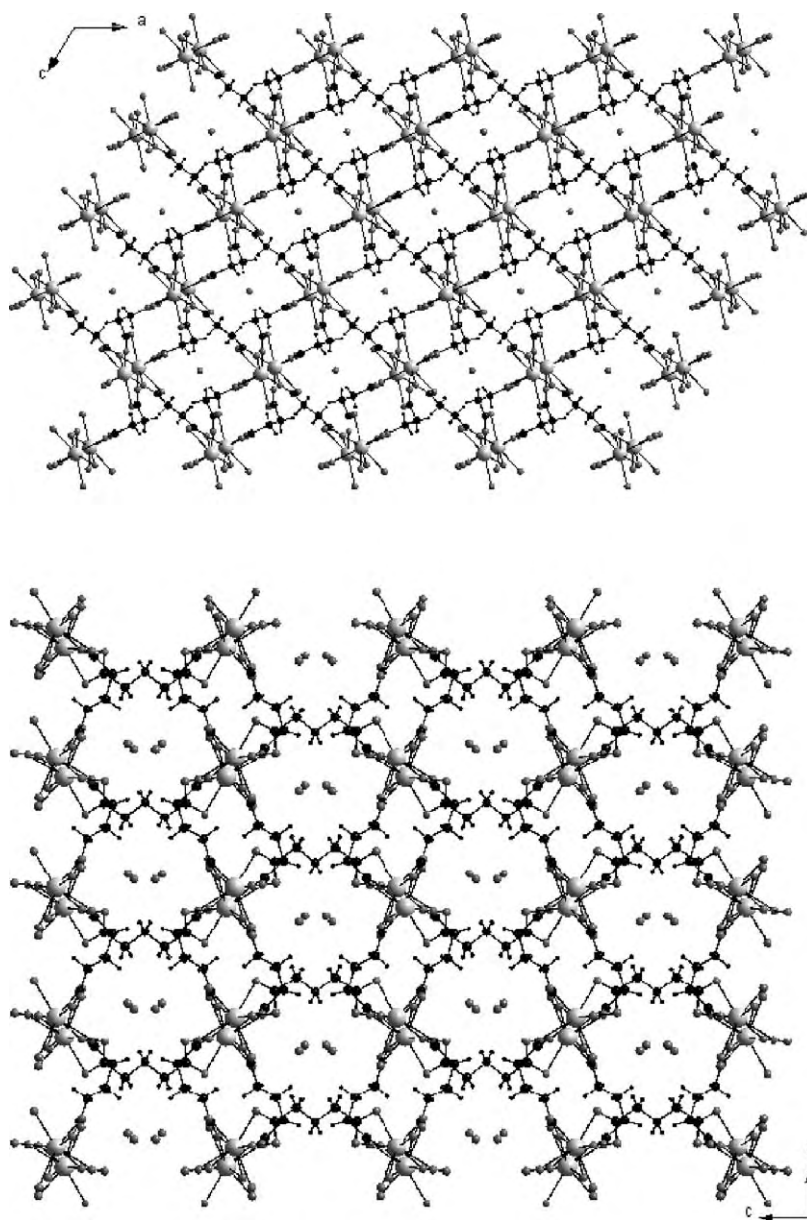


Fig. 27. (Left) projection view along the b -axis of the crystal packing of $[\text{Pr}(\text{H}_2\text{O})_2]_2[\text{O}_2\text{C}(\text{CH}_2)_2\text{CO}_2]_3 \cdot \text{H}_2\text{O}$: monoclinic, $C2/c$, $a = 20.2586(1) \text{ \AA}$, $b = 7.9489(1) \text{ \AA}$, $c = 13.9716(4) \text{ \AA}$, $\beta = 121.64(2)^\circ$. (Right) projection view along the a -axis of the crystal packing of $[\text{Ln}(\text{H}_2\text{O})_2]_2[\text{O}_2\text{C}(\text{CH}_2)_3\text{CO}_2]_3 \cdot 4\text{H}_2\text{O}$: monoclinic, $C2/c$, $a = 8.1174(1) \text{ \AA}$, $b = 15.1841(2) \text{ \AA}$, $c = 19.8803(4) \text{ \AA}$, $\beta = 93.76(2)^\circ$. Redrawn from Serpaggi and Férey (1998, 1999, 2003).

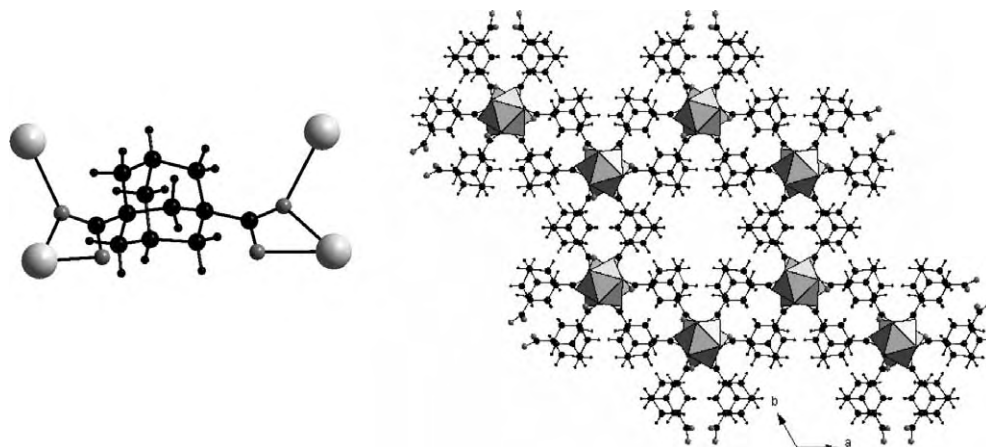
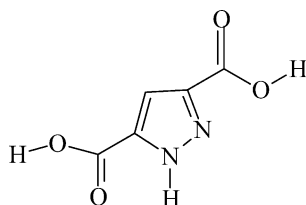


Fig. 28. (Left) coordination modes of the carboxylate groups in $\text{Eu}_2(\text{O}_2\text{C}-\text{C}_{10}\text{H}_{14}-\text{CO}_2)_3$: hexagonal, $P63$ cm, $a = 16.4660(1)$ Å, $c = 7.7375(1)$ Å. (Right) projection view along the c -axis of the network of $\text{Eu}_2(\text{O}_2\text{C}-\text{C}_{10}\text{H}_{14}-\text{CO}_2)_3$. The Ln^{3+} ion are represented in polyhedral representation. Redrawn from Millange et al. (2004).



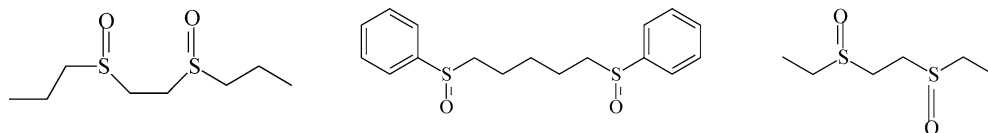
Scheme 4. 3,5-Pyrazoledicarboxylic acid.

to design new materials for non-linear optical devices using lanthanides in association with an asymmetric ligand. Actually, the little preference in bond direction of the lanthanide ions constitute an asset for the design of acentric coordination polymers.

3.6.2. Coordination polymers with sulfoxide ligands

It is also worth citing the work of X.-H. Bu et al. devoted to the synthesis of lanthanide containing coordination polymers with flexible disulfoxide ligands (Bu et al., 2002a, 2002b; Li, J.R. et al., 2004a, 2004b). The use of this type of flexible ligands leads to unprecedented molecular networks. Some of these ligands are represented in scheme 5.

This work actually offers new perspectives for the development of novel coordination polymers with unusual properties. The magnetic properties of one of these compounds has been measured. As expected they are not very exciting. On the opposite the luminescent properties of some compounds have been studied and seems to be rather interesting. As an example the structure of one of these compounds with chemical formula



Scheme 5. Some sulfinyl ligands used in (Bu et al., 2002a, 2002b; Li, J.R. et al., 2004a, 2004b).

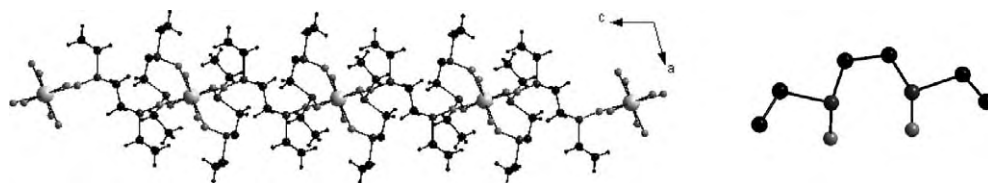


Fig. 29. (Left) projection view of the crystal structure of the $\{[\text{Tb}(\mu\text{-meso-L})(\text{rac-L})_2(\text{CH}_3\text{OH})_2](\text{ClO}_4)_3\}$: monoclinic, $C2/c$, $a = 19.976(8)$ Å, $b = 11.584(5)$ Å, $c = 19.242(8)$ Å, $\beta = 105.83(1)^\circ$. Redrawn from Li, J.R. et al. (2004a). (Right) scheme of the $(\mu\text{-meso-L})$ ligand.

$\{[\text{Tb}(\mu\text{-meso-L})(\text{rac-L})_2(\text{CH}_3\text{OH})_2](\text{ClO}_4)_3\}$ with meso-L = meso-1,2-bis(ethylsulfinyl)ethane is presented in fig. 29.

This structure can be described as the juxtaposition of chain-like molecular motifs. The emission spectrum of this compound contains four bands. The intensity of the hypersensitive ${}^5\text{D}_4 \rightarrow {}^7\text{F}_5$ transition is close to six times that of the other transitions. These results, according to the authors, show that the complex has excellent single color properties. Unfortunately the thermal stability of this class of compounds is rather low and decomposition occurs upon heating around 200°C .

3.7. Synthetic routes

Two main synthesis methods have been used in order to design lanthanide-containing coordination polymers, namely the diffusion through gels and hydrothermal conditions. We would like to briefly describe both and try to highlight their respective advantages and drawbacks.

Let us first consider the more commonly used method: the synthesis under hydrothermal conditions. There is an increasing interest for this technique (Feng and Xu, 2000). This interest is essentially due to inherent advantages such as a high reactivity of reactants, an easy control of solution or interface reactions, the formation of metastable and original condensed phases, a reduced air pollution and a low energy consumption.

Most of the above described coordination polymers have been obtained thanks to hydrothermal methods. Typically, they consist in synthesizing the coordination polymers in a Teflon-lined Parr bomb under relatively high temperatures. The reaction occurs at high temperature (typically between 150°C and 250°C) and elevated pressure (autogenous pressure). As far as lanthanide coordination polymers are concerned, this synthetic method seems to lead to materials exhibiting high dimensionality and low hydration rate (Cao et al., 2002b). That is why

these methods have been up to now extensively used in order to obtain molecular precursors for three-dimensional microporous materials.

The main drawback of this method is the difficult separation of the targeted product(s) from the resulting powder that may sometimes also contains remaining reactants and by-products. Moreover, it is sometimes impossible to get single crystal and the structural characterization is therefore difficult.

The alternative way of synthesis is the slow diffusion of the reactants through a gel medium. This slow diffusion is necessary because of the inherent insolubility of the coordination polymers.

Typically the gel is poured in the bottom of a U-shaped tube. Then solutions of the reactants are poured into the vertical parts of the U-shaped tube and allowed to slowly diffuse at room temperature and ambient pressure. The gel can be either a physical gel such as agarose or a chemical gel such as silica gel.

This technique presents great advantages as long as single crystals of metastable phases are needed. Actually, for the systems which have been explored both by hydrothermal and gel diffusion methods, the latter leads to more numerous polymorphic phases than the former. As an illustration of its efficiency one can consider the three-dimensional $R_2(C_2O_4)_3 \cdot 18H_2O$ which is represented in fig. 30. This compound has been first synthesized by Watanabe et al. in 1971 (Watanabe and Nagashima, 1971) but has never been structurally described despite the great number of works devoted to lanthanide oxalate compounds. Its crystal structure has been solved only recently (Camara et al., 2003) thanks to single crystals obtained by slow diffusion in gels.

This method has also allowed obtaining single crystal of all the phases encountered during the reversible dehydration process of $Ln(btc)(H_2O)_5 \cdot 3.5H_2O$ compounds except, of course, the resulting anhydrous one. These three different phases have been obtained by varying only the density of the gel medium (Daiguebonne et al., 2000b) (see fig. 31).

The obvious main drawback of this method is the separation of the products. Indeed, it is sometimes difficult to isolate the desired product from the gel medium. This problem is overcome when the desired phase can be obtained by a thermal treatment of the hydrated phase obtained by direct precipitation. In such cases, the gel methods are only used for structural characterization purposes and the availability of the material is ensured.

3.8. Coordination polymers containing poly-hydroxo-lanthanide complexes

As for coordination polymers containing transition metal ions, it could be of interest to design coordination polymers in which the metallic sites would be no longer occupied by simple ions but by polynuclear species. This could result in an increase of the porosity, as is the case for transition metal ions. Furthermore, the topology of the polynuclear species themselves could play a structuring role. To the best of our knowledge, there is only very few examples of such materials. This is essentially due to the difficult synthesis of lanthanide only containing polynuclear species. Actually the first poly-hydroxo-lanthanide complexes have been reported (Zak et al., 1994; Giester et al., 1997) and there is now several other poly-hydroxo-lanthanide

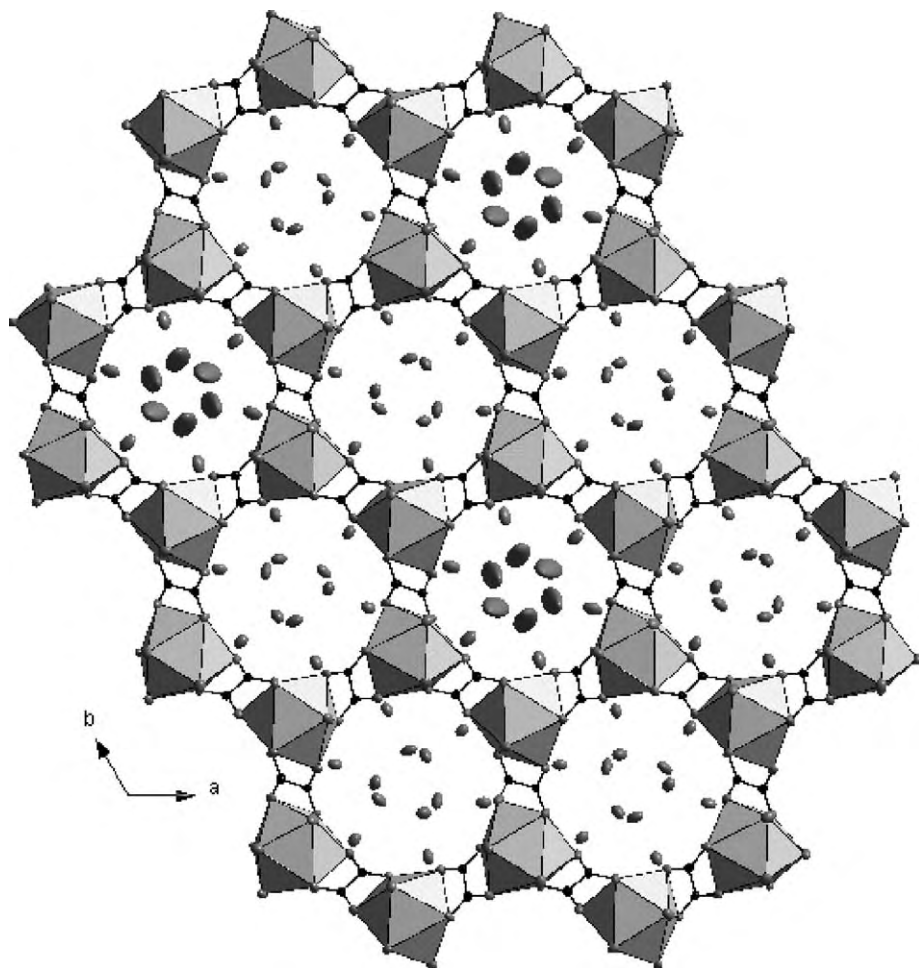


Fig. 30. Projection view along the b -axis of the crystal structure of $\text{Ln}_2(\text{C}_2\text{O}_4)_3 \cdot 18\text{H}_2\text{O}$: trigonal, $R\bar{3}$, $a = 30.869(1) \text{ \AA}$, $c = 7.2307(2) \text{ \AA}$. Redrawn from Camara et al. (2003).

complexes described in the literature and having various nuclearity (Zheng and Wang, 2000; Zheng, 2003). These species have been obtained by controlled hydrolysis. This control is, in most cases, ensured by organic ligands such as aminoacids. In some cases the use of bifunctionalized amino acids has led to extended frameworks in one pot syntheses (Ma et al., 2000a, 2000b). As an illustration of these beautiful works one can cite (Wang et al., 2001) the $[\text{Er}_4(\mu_3\text{-OH})_4(\text{C}_5\text{H}_9\text{NO}_4)_3(\text{H}_2\text{O})_8](\text{ClO}_4)_5 \cdot 6\text{H}_2\text{O}$ where $\text{C}_5\text{H}_9\text{NO}_4$ is glutamic acid (see scheme 6). A projection view of the 3D molecular framework is presented in fig. 32.

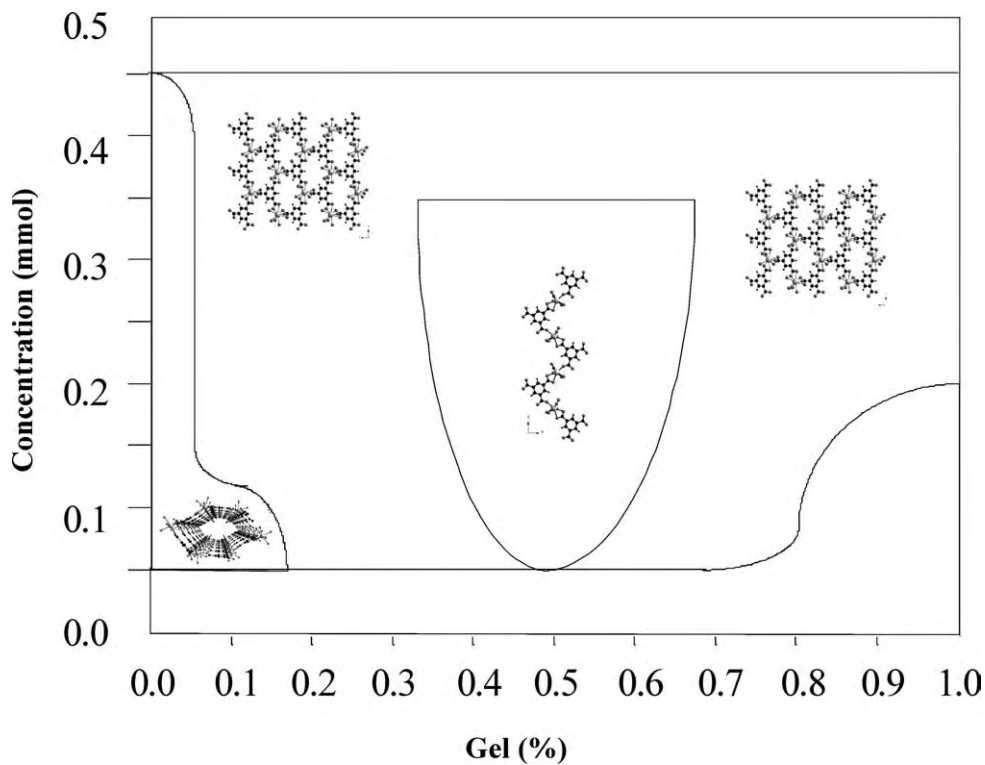
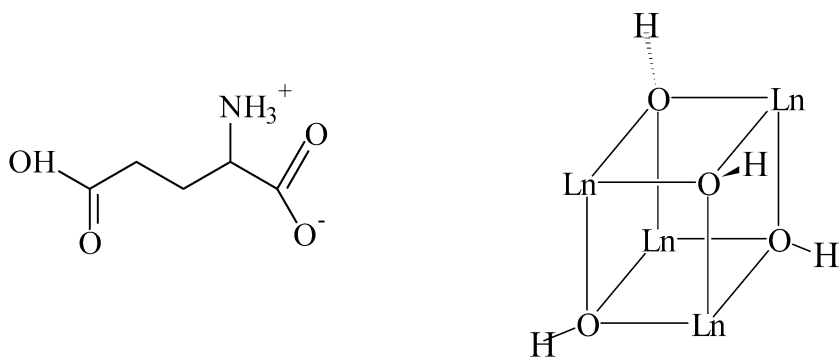


Fig. 31. Predominance phase diagram versus the concentration of the gel medium and of the solutions of reactants. Redrawn from Daiguebonne et al. (2000b).



Zwitterionic structure of glutamic acid.

Tetranuclear lanthanide-hydroxo species.

Scheme 6.

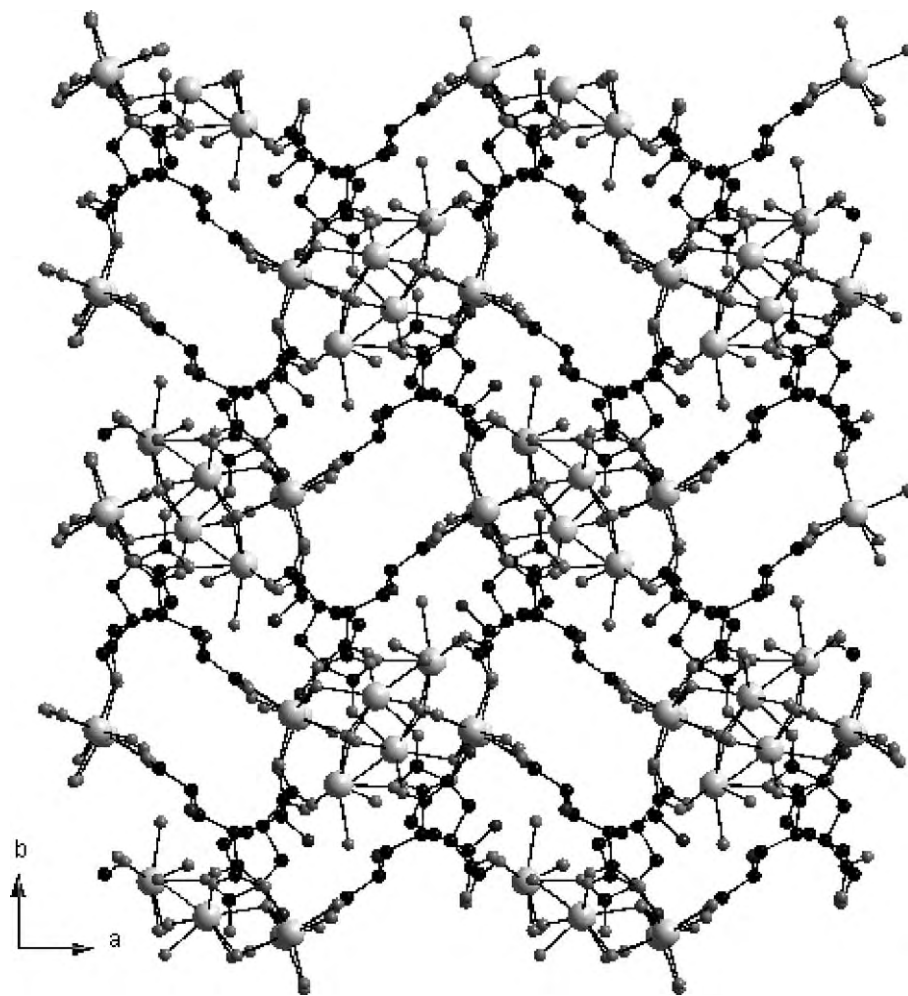


Fig. 32. Projection view along the c -axis of the crystal structure of $[\text{Er}_4(\mu_3\text{-OH})_4(\text{C}_5\text{H}_9\text{NO}_4)_3(\text{H}_2\text{O})_8](\text{ClO}_4)_5 \cdot 6\text{H}_2\text{O}$: orthorhombic, $P2_12_12_1$, $a = 14.6190(2) \text{ \AA}$, $b = 17.2110(1) \text{ \AA}$, $c = 21.2150(1) \text{ \AA}$. Redrawn from Wang et al. (2001).

This compound has been obtained in water by a self assembling strategy. Its extended solid state structure is composed of the cubane-like $[\text{Er}(\mu_3\text{-OH})_4]^{8+}$ cluster (see scheme 6) inter-linked by the carboxylate groups of the glutamate ligands. The molecular networks are positively charged and five perchlorate anions per asymmetric unit are ensuring electric neutrality of the crystal arrangement. These perchlorate anions are localized in the channels as well as the six guest water molecules. The aperture of the channels has been evaluated to be around 35 \AA^2 .

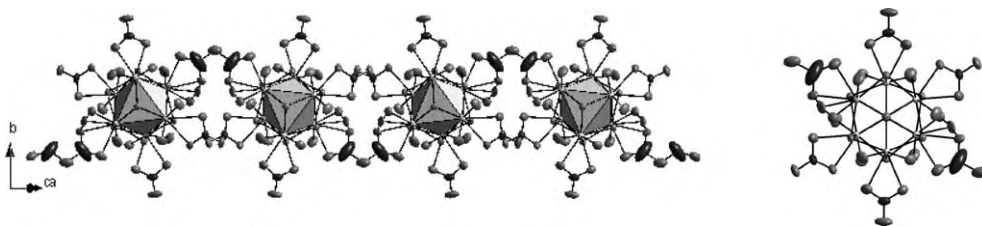


Fig. 33. (Left) projection view of the chain-like molecular motif of $[\text{Er}_6(\mu_6\text{-O})(\mu_3\text{-OH})_8(\text{NO}_3)_4(\text{H}_2\text{O})_{11}(\text{OH})(\text{ONONO}_2)]\text{Cl}_3 \cdot 2\text{H}_2\text{O}$: monoclinic, $C2/c$, $a = 16.4039(2) \text{ \AA}$, $b = 16.1017(2) \text{ \AA}$, $c = 14.0453(2) \text{ \AA}$, $\beta = 96.35(1)^\circ$. Redrawn from Mahé et al. (2004). (Right) the octahedral molecular motif of the cluster.

The main drawbacks of this compound are obviously the high positive charges borne by the molecular network as well as by the tetranuclear cluster core. Indeed, the perchlorate anions localized inside the channels cannot be removed upon heating and therefore this compound is definitely not porous. Moreover the high positive charge (8+) of by the tetranuclear species induces a very low chemical stability. As a matter of fact, these tetranuclear species are highly unstable and their use as isolated precursors is impossible. That is why the reported extended networks involving such poly-hydroxo-lanthanide clusters have all been obtained via a one-pot synthesis. This is an important disadvantage as long as molecular design is concerned.

However some poly-hydroxo-lanthanides with a smaller charge have been synthesized (Zak et al., 1994; Giester et al., 1997; Chane-Ching et al., 2002). Their general chemical formula is $\text{Ln}_6(\mu_6\text{-O})(\mu_3\text{-OH})_6(\text{NO}_3)_6(\text{H}_2\text{O})_{12} \cdot (\text{NO}_3)_2(\text{H}_2\text{O})_n$. They are stable in non-protogenous polar solvents such as DMF or DMSO and may so be used as chemical precursors (Mahé et al., 2004). Such a hexanuclear cluster, as well as a 1D coordination polymer involving it are presented on fig. 33. This result shows that it is possible to build extended molecular networks involving poly-hydroxo-lanthanide complexes as metallic cores. Unfortunately these hexanuclear species are not stable in water or less toxic solvents and this constitute an important disadvantage as far as industrial applications are targeted.

4. Conclusion and outlooks

This review demonstrates that despite the rapid emergence of metal-organic frameworks much remains to do in the field of lanthanide-containing coordination polymers. Actually, to the best of our knowledge, there is no compound fully characterized structurally, chemically and physically. However there are numerous interesting and promising results which demonstrate the great potentiality of these materials. Their more promising potential applications, namely optical or catalytic applications, will be, for sure, strong driving forces for the development of this field. Indeed, even if, up to now, there is no identified industrially interesting such material, the works described here show that it must be possible to design some. Before concluding this review we would like to emphasize some potential applications for the lanthanide-containing coordination polymers.

From a synthetic point of view, the design of highly porous lanthanide coordination polymers, stable at reasonably high temperature and containing metallic sites available for catalytic reactions, remains a challenge. Such a compound could find its application in depollution processes for instance. Several synthetic strategy may be used: the use of longer ligands of course but also the use of polynuclear metallic species or of complex bridging units involving, for instance, transition metal ion or main group metal ions complexes.

3D compounds could also be of interest for the design of optical devices. Indeed, in coordination polymers, inter-lanthanide distances can be controlled. This allows the synthesis of compounds with a high content in lanthanide ions. Furthermore the chemical likeness of the lanthanide ions allows the synthesis of hetero di-lanthanide compounds with a very good random distribution of the two rare earths. This property could be used for diluting the optically active lanthanide in a given framework or for enhancing optical properties thanks to up-conversion phenomena for instance.

Finally, the use of flexible ligands for designing 1D lanthanide coordination polymers could be of interest as far as the synthesis of polymers with interesting optical properties and exhibiting a thermoplastic behavior is considered.

References

- Adam, J.L., 2002. *Chem. Rev.* **102**, 2461–2476.
- Alleyne, B.D., Williams, A.R., Hall, L.A., White, A.J.P., Williams, D.J., 2001. *Inorg. Chem.* **40**, 1045–1051.
- Barthelet, K., Marrot, J., Riou, D., Férey, G., 2002. *Angew. Chem. Intl. Ed. Engl.* **41**, 281–284.
- Barthelet, K., Riou, D., Férey, G., 2003. *Inorg. Chem.* **42**, 1739–1743.
- Bataille, T., Louër, D., 1999. *Acta Cryst.* **55**, 1760–1762.
- Bataille, T., Auffrédic, J.P., Louër, D., 1999. *Chem. Mater.* **11**, 1559–1567.
- Batten, S.R., Robson, R., 1998. *Angew. Chem. Intl. Ed. Engl.* **37**, 1460–1494.
- Benelli, C., Gatteschi, D., 2002. *Chem. Rev.* **102**, 2369–2387.
- Bu, X.H., Weng, W., Li, J.R., Chen, W., Zhang, R.H., 2002a. *Inorg. Chem.* **41**, 413–415.
- Bu, X.H., Weng, W., Du, M., Chen, W., Li, J.R., Zhang, R.H., Zhao, L.J., 2002b. *Inorg. Chem.* **41**, 1007–1010.
- Camara, M., Daiguebonne, C., Boubekour, K., Roisnel, T., Gérard, Y., Baux, C., Le Dret, F., Guillou, O., 2003. *C. R. Chimie* **6**, 405–415.
- Cao, R., Shi, Q., Sun, D., Hong, M., Bi, W., Zhao, Y., 2002a. *Inorg. Chem.* **41**, 6161–6168.
- Cao, R., Sun, D., Liang, Y., Hong, M., Shi, Q., Tatsumi, K., 2002b. *Inorg. Chem.* **41**, 2087–2094.
- Chane-Ching, J.-Y., Guillou, O., Mahé, N., 2002. Synthèse et dispersion d'entités hexanucléaires de praséodyme, French Patent n° 02 14451.
- Chen, B., Eddaoudi, M., Hyde, S.T., O'Keeffe, M., Yaghi, O.M., 2001. *Science* **291**, 1021–1023.
- Cheng, D., Khan, M.A., Houser, R.P., 2001. *Inorg. Chem.* **40**, 6858–6859.
- Chui, S.S.-Y., Lo, S.M.-F., Charmant, J.P.H., Orpen, A.G., Williams, I.D., 1999. *Science* **283**, 1148–1150.
- Chui, S.S.-Y., Siu, A., Feng, X., Zhang, Z.Y., Mak, T.C.W., Williams, I.D., 2001. *Inorg. Chem. Commun.* **4**, 467–470.
- Costes, J.P., Dupuis, A., Laurent, J.P., 1998. *J. Chem. Soc., Dalton Trans.*, 735–736.
- Daiguebonne, C., Gérard, Y., Guillou, O., Lecerf, A., Boubekour, K., Kahn, O., Kahn, M.L., 1998. *J. Alloys & Compds*, 275–277, 50–53.
- Daiguebonne, C., Guillou, O., Gérard, Y., Lecerf, A., Boubekour, K., 1999. *Inorg. Chim. Acta* **284**, 139–145.
- Daiguebonne, C., Guillou, O., Boubekour, K., 2000a. *Inorg. Chim. Acta* **304**, 161–169.
- Daiguebonne, C., Guillou, O., Boubekour, K., 2000b. Structural diversity in lanthanide complex chemistry: the Ln^{3+} - TMA^{3-} - H_2O system. In: *Transworld Research Network: Recent Res. Devel. Inorganic Chem.*, pp. 165–183.

- Daiguebonne, C., Guillou, O., Boubekeur, K., 2001a. *J. Alloys & Compnds*, **324**–324, 199–203.
- Daiguebonne, C., Guillou, O., Kahn, M.L., Kahn, O., Oushoorn, R.L., Boubekeur, K., 2001b. *Inorg. Chem.* **40**, 176–178.
- Daiguebonne, C., Gérault, Y., Le Dret, F., Guillou, O., Boubekeur, K., 2002. *J. Alloys & Compnds* **344**, 179–185.
- Daiguebonne, C., Deluzet, A., Camara, M., Boubekeur, K., Audebrand, N., Gérault, Y., Baux, C., Guillou, O., 2003. *Crystal Growth and Design* **3**, 1015–1020.
- Decurtins, S., Gross, M., Schmalte, H.W., Ferlay, S., 1998. *Inorg. Chem.* **37**, 2443–2449.
- Deluzet, A., Guillou, O., 2003. *Acta Cryst. C* **59**, m277–m279.
- Deluzet, A., Maudez, W., Daiguebonne, C., Guillou, O., 2003. *Crystal Growth and Design* **3**, 475–479.
- Dimos, A., Tsaousis, D., Michaelides, A., Skoulika, S., Golhen, S., Ouahab, L., Didierjean, C., Aubry, A., 2002. *Chem. Mater.* **14**, 2616–2622.
- Eddaoudi, M., Kim, J.S., Wachter, J., Chae, H.K., O’Keeffe, M., Yaghi, O.M., 2001. *J. Amer. Chem. Soc.* **123**, 4368–4369.
- Eddaoudi, M., Kim, J.S., Rosi, N., Vodak, D., Wachter, J., O’Keeffe, M., Yaghi, O.M., 2002. *Science* **295**, 469–472.
- Feil-Jenkins, J.F., Nash, K.L., Rogers, R.D., 1995. *Inorg. Chim. Acta* **236**, 67–74.
- Feng, S., Xu, R., 2000. *Acc. Chem. Res.* **34**, 239–247.
- Giacovazzo, C., Menchetti, C., Scordari, F., 1973. *Acta Cryst. B*, 26–31.
- Giester, G., Unfried, P., Zak, Z., 1997. *J. Alloys & Compnds* **257**, 175–181.
- Guillou, O., Bergerat, P., Kahn, O., Bakalbassis, E., Boubekeur, K., Batail, P., Guillot, M., 1992a. *Inorg. Chem.* **31**, 110–114.
- Guillou, O., Kahn, O., Oushoorn, R.L., Boubekeur, K., Batail, P., 1992b. *Inorg. Chim. Acta*, 198–200, 119–131.
- Guillou, O., Oushoorn, R.L., Kahn, O., Boubekeur, K., Batail, P., 1992c. *Angew. Chem. Intl. Ed. Engl.* **31**, 626–628.
- Gutschke, S.O.H., Molinier, M., Powell, A.K., Winpenny, R.E.P., Wood, P.T., 1996. *Chem. Commun.*, 823–824.
- Hansson, E., 1970. *Acta Chem. Scand.* **24**, 2969–2982.
- Hansson, E., 1973. *Acta Chem. Scand.* **27**, 823–834.
- Hansson, E., Albertsson, J., 1968. *Acta Chem. Scand.* **22**, 1682–1716.
- Iananaga, J., Furuno, H., Hayano, T., 2002. *Chem. Rev.* **102**, 2211–2225.
- Imamoto, T., 1994. *Lanthanide in Organic Synthesis*. Academic Press, New York.
- Jongen, N., Lemaître, J., Bowen, P., Hofmann, H., 1999. *Chem. Mater.* **11**, 712–718.
- Kahn, O., Guillou, O., 1993. Magnetic properties of molecular compounds containing Ln(III) and Cu(II) ions. In: O’Connor, C.J. (Ed.), *Research Frontiers in Magnetochemistry*, pp. 179–200.
- Kahwa, I.A., Fronczek, F.R., Selbin, J., 1984. *Inorg. Chim. Acta* **82**, 161–166.
- Karraker, D.G., 1970. *J. Chem. Educ.* **47**, 424–430.
- Kido, J., Okamoto, Y., 2002. *Chem. Rev.* **102**, 2357–2368.
- Kiritsis, V., Michaelides, A., Skoulika, S., Golhen, S., Ouahab, L., 1998. *Inorg. Chem.* **37**, 3407–3410.
- Kuriki, K., Koike, Y., Okamoto, Y., 2002. *Chem. Rev.* **102**, 2347–2356.
- Larionova, J., Mombelli, B., Sanchiz, J., Kahn, O., 1998. *Inorg. Chem.* **37**, 679–684.
- Li, H., Davis, C.E., Groy, T.L., Kelley, D., Yaghi, O.M., 1998. *J. Amer. Chem. Soc.* **120**, 2186–2187.
- Li, J.R., Bu, X.H., Zhang, R.H., 2004a. *Inorg. Chem.* **43**, 237–244.
- Li, J.R., Bu, X.H., Zhang, R.H., Duan, C.Y., Wong, K.M.C., Yam, V.W.W., 2004b. *New J. Chem.* **28**, 261–265.
- Li, Y., Hao, N., Lu, Y., Wang, E., Kang, Z., Hu, C., 2003. *Inorg. Chem.* **42**, 3119–3124.
- Liu, J., Meyers, E.A., Cowan, J.A., Shore, S.G., 1998. *J. Chem. Soc., Chem. Commun.*, 2043–2044.
- Long, D.L., Blake, A.J., Champness, N.R., Wilson, C., Schröder, M., 2001. *J. Amer. Chem. Soc.* **123**, 3401–3402.
- Ma, B.Q., Zhang, D.S., Gao, S., Jin, T.Z., Yan, C.H., Xu, G.X., 2000a. *Angew. Chem. Intl. Ed. Engl.* **39**, 3644–3646.
- Ma, B.Q., Zhang, D.S., Gao, S., Jin, T.Z., Yan, C.H., 2000b. *New J. Chem.* **24**, 251–252.
- Mahé, N., Guillou, O., Daiguebonne, C., Gérault, Y., Caneschi, A., Sangregorio, C., Chane-Ching, J.-Y., Car, P.E., Roisnel, T., 2004. *Inorg. Chem.*, submitted for publication.
- Michaelides, A., Skoulika, S., Aubry, A., 1988. *Mat. Res. Bull.* **23**, 579–585.
- Millange, F., Serre, C., Marrot, J., Gardant, N., Pelle, F., Férey, G., 2004. *J. Mater. Chem.*, in press.
- Mörtl, K.P., Sutter, J.P., Golhen, S., Ouahab, L., Kahn, O., 2000. *Inorg. Chem.* **39**, 1626–1627.
- Nag, K., Roy, A., 1976a. *Therm. Acta* **17**, 247–251.
- Nag, K., Roy, A., 1976b. *J. Inorg. Nucl. Chem.* **38**, 1983–1987.

- O'Keeffe, M., Eddaoudi, M., Li, H., Renneke, T.M., Yaghi, O.M., 2000. *J. Sol. State Chem.* **152**, 3–20.
- Ouchi, A., 1988. *Coord. Chem. Rev.* **92**, 29–43.
- Oushoorn, R.L., Boubekour, K., Batail, P., Guillou, O., Kahn, O., 1996. *Bull. Soc. Chim. Fr.* **133**, 777–782.
- Pan, L., Huang, X., Li, J., Wu, Y., Zheng, N., 2000a. *Angew. Chem. Intl. Ed. Engl.* **39**, 527–530.
- Pan, L., Woodlock, E.B., Wang, X., 2000b. *Inorg. Chem.* **39**, 4174–4178.
- Pan, L., Zheng, N., Wu, Y.-M., Han, S., Yang, R., Huang, X., Li, J., 2001. *Inorg. Chem.* **40**, 828–830.
- Pan, L., Adams, K.M., Hernandez, H.E., Wang, X., Zheng, C., Hattori, Y., Kaneko, K., 2003. *J. Amer. Chem. Soc.* **125**, 3062–3067.
- Plater, M.J., Howie, R.A., Roberts, A.J., 1997. *Chem. Commun.*, 893–894.
- Plater, M.J., Roberts, A.J., Marr, J., Lachowski, E.E., Howie, R.A., 1998. *J. Chem. Soc., Dalton Trans.*, 797–802.
- Prior, T.J., Rosseinsky, M.J., 2000. *Cryst. Eng. Comm.* **24**.
- Renneke, T.M., Eddaoudi, M., Fehr, M., Kelley, D., Yaghi, O.M., 1999a. *J. Amer. Chem. Soc.* **121**, 1651–1657.
- Renneke, T.M., Eddaoudi, M., O'Keeffe, M., Yaghi, O.M., 1999b. *Angew. Chem. Intl. Ed. Engl.* **38**, 2590–2594.
- Rizzi, A.C., Calvo, R., Baggio, R., Garland, M.T., Pena, O., Percec, M., 2002. *Inorg. Chem.* **41**, 5609–5614.
- Robl, C., Hentschel, S., 1991a. *Mat. Res. Bull.* **26**, 1355–1362.
- Robl, C., Hentschel, S., 1991b. *Z. Naturforsch* **46**, 1188–1192.
- Robl, C., Hentschel, S., 1992. *Z. Naturforsch* **47**, 1561–1564.
- Romero, S., Mosset, A., Trombe, J.C., 1995. *Eur. J. Inorg. Chem.* **32**, 1053–1063.
- Sanada, T., Suzuki, T., Yoshida, T., Kaisaki, S., 1998. *Inorg. Chem.* **37**, 4712–4717.
- Serpaggi, F., Férey, G., 1998. *J. Mater. Chem.* **8**, 2737–2741.
- Serpaggi, F., Férey, G., 1999. *Microporous and Mesoporous Materials* **32**, 311–318.
- Serpaggi, F., Férey, G., 2003. *J. Mol. Struct.* **656**, 201–206.
- Serpaggi, F., Luxbacher, T., Cheetham, A.K., Férey, G., 1999. *J. Sol. State Chem.* **145**, 580–586.
- Serre, C., Férey, G., 2002. *J. Mater. Chem.* **12**, 3053–3057.
- Serre, C., Millange, F., Marrot, J., Férey, G., 2002. *Chem. Mater.* **14**, 2409–2415.
- Serre, C., Millange, F., Thouvenot, C., Gardant, N., Pelle, F., Férey, G., 2004. *J. Mater. Chem.*, submitted for publication.
- Shibasaki, M., Yamada, K.I., Yoshikawa, N., 1999. *Lanthanide Lewis acids catalysis*. In: Yamamoto, H. (Ed.), *Lewis Acids in Organic Synthesis*, New York.
- Starynowicz, P., Meyer, G., 2000. *Angew. Chem. Intl. Ed. Engl.* **626**, 2441–2442.
- Sutter, J.P., Kahn, M.L., Golhen, S., Ouahab, L., Kahn, O., 1998. *Chem. Eur. J.* **4**, 571–576.
- Sutter, J.P., Kahn, M.L., Kahn, O., 1999. *Adv. Mater.* **10**, 863–865.
- Tong, M.-L., Wu, Y.-M., Ru, J., Chen, X.M., Chang, H.-C., Kitagawa, S., 2002. *Inorg. Chem.* **41**, 4846–4848.
- Trollet, D., Romero, S., Mosset, A., Trombe, J.C., 1997. *C. R. Acad. Sci. Paris, Sér. II b.* **325**, 663–670.
- Trovarelli, A. (Ed.), 2002. *Catalysis by Ceria and Related Materials*. Imperial College Press, London.
- Wan, Y., Zhang, L., Jin, L., Gao, S., Lu, S., 2003. *Inorg. Chem.* **42**, 4985–4994.
- Wang, R., Liu, H., Carducci, M.D., Jin, T., Zheng, C., Zheng, Z., 2001. *Inorg. Chem.* **40**, 2743–2750.
- Watanabe, M., Nagashima, K., 1971. *J. Inorg. Nucl. Chem.* **33**, 3604–3608.
- Wu, C.-D., Lu, C.-Z., Yang, W.-B., Lu, S.-F., Zhuang, H.-H., Huang, J.-S., 2002. *Eur. J. Inorg. Chem.*, 797–800.
- Wu, L.P., Munakata, M., Yakamoto, M., Kuroda-Sowa, T., Maekawa, M., 1996. *J. Coord. Chem.* **37**, 361–369.
- Wu, Y., Zheng, N., Yang, R., Xu, H., Ye, E., 2002. *J. Mol. Struct.* **610**, 181–186.
- Yaghi, O.M., Li, G., Li, H., 1995. *Nature* **378**, 703–706.
- Yaghi, O.M., Li, H., Groy, T.L., 1996. *J. Amer. Chem. Soc.* **118**, 9096–9101.
- Yaghi, O.M., Davis, C.E., Li, G., Li, H., 1997a. *J. Amer. Chem. Soc.* **119**, 2861–2868.
- Yaghi, O.M., Li, H., Groy, T.L., 1997b. *Z. Kristallographie* **212**, 457–458.
- Yaghi, O.M., Li, G., Li, H., 2004. *Nature* **378**, 703–706.
- Zak, Z., Unfried, P., Giester, G., 1994. *J. Alloys & Compds* **205**, 235–242.
- Zhao, Y., Ju, J., Chen, X.M., Li, X., Wang, R., Mai, Z., 2002. *J. Sol. State Chem.* **165**, 182–186.
- Zheng, Z., 2003. *Chemtracts – Inorg. Chem.* **16**, 1–12.
- Zheng, Z., Wang, R., 2000. *Comm. Inorg. Chem.* **22**, 1–30.
- Zhi-Bang, D., Zhong-Sheng, J., Ge-Cheng, W., Jia-Zan, N., 1990. *J. Huaxue (J. Struct. Chem.)* **9**, 64–69.
- Zhi-Bang, D., Ge-Cheng, W., Zhong-Sheng, J., Jia-Zan, N., 1991. *J. Less Comm. Metals* **171**, L1–L3.

Chapter 222

CUTTING DNA AND RNA

Makoto KOMIYAMA*

Research Center for Advanced Science and Technology, The University of Tokyo,
Komaba, Tokyo 153-8904, Japan

E-mail: komiyama@mkomi.rcast.u-tokyo.ac.jp

Contents

1. Introduction	406	6. RNA hydrolysis by lanthanide ions and their complexes	426
1.1. Roles of DNA and RNA in living organisms	406	6.1. Catalysis by lanthanide(III) ions	426
1.2. Importance of non-enzymatic scission of DNA and RNA	406	6.2. Lanthanide complexes for RNA hydrolysis	427
1.3. Lanthanide ions for molecular biology and biotechnology	408	7. Kinetic analysis on the RNA hydrolysis	428
2. Discovery of DNA hydrolysis by Ce(IV)	409	8. Mechanism of RNA hydrolysis by lanthanide ions	430
2.1. The finding of DNA hydrolysis by lanthanide(III) trichloride	409	9. DNA hydrolysis vs. RNA hydrolysis	431
2.2. Remarkable catalysis by Ce(IV)	410	10. Strategy for site-selective scission of DNA and RNA	431
2.3. Evidence for the hydrolytic scission of DNA	411	11. Covalent strategy for site-selective scission of DNA	433
2.4. Cooperation of Ce(IV) and Pr(III) for faster DNA hydrolysis	414	12. Non-covalent strategy for site-selective DNA scission	434
2.5. Cleavage of plasmid DNA	414	12.1. Gap strategy for site-selective DNA scission	434
3. Homogeneous Ce(IV) complexes for DNA hydrolysis	414	12.2. Bulge structures for site-selective DNA scission	436
3.1. Ce(IV)/saccharide complexes	415	12.3. Catalytic effect of a Ce(IV) hydroxide gel on the hydrolysis of gap and bulge sites	438
3.2. Ce(IV)/EDTA complex and its equivalents	415	12.4. Covalent conjugates of oligoamine and acridine for the promotion of gap-selective DNA hydrolysis by Ce(IV)/EDTA complex	438
4. Mechanistic analysis of DNA hydrolysis by Ce(IV)	416	12.5. Hybridization of covalent and non-covalent strategies for improved site-selective DNA scission	440
4.1. Kinetic analysis	416	13. Covalent strategy for site-selective RNA hydrolysis	442
4.2. Spectroscopic studies	419		
4.3. Quantum-chemical studies on the catalytically active $[\text{Ce}^{\text{IV}}_2(\text{OH})_4]^{4+}$ cluster and its complex with phosphodiester	423		
5. Proposed mechanism for the DNA hydrolysis by Ce(IV)	424		

* Fax: +81-3-5452-5209.

14. Non-covalent strategy for site-selective RNA scission	444	15. Conclusions	451
14.1. Novel RNA cutters	444	Acknowledgements	452
14.2. Two-site RNA cutters for SNPs genotyping	448	References	452

1. Introduction

1.1. Roles of DNA and RNA in living organisms

As most of the readers probably know well, DNA and RNA are important biopolymers which are responsible for the storage and expression of genetic information. Both are composed of nucleosides and phosphate, which are connected alternately (fig. 1). In RNA, there exists a hydroxyl group at the 2'-position of ribose. In DNA, however, it is replaced by hydrogen atom. In both DNA and RNA, a nucleobase is attached to the 1'-position of ribose. The nucleobases used for DNA are adenine (A), guanine (G), thymine (T), and cytosine (C). In RNA, uracil (U) is used in place of T, and the other three nucleobases are the same as those used for DNA (A, G, and C). Significantly, adenine selectively forms a Watson–Crick base pair with T (or U in RNA), and G selectively forms a pair with C. This is the most important rule in molecular biology, and most of the functions of DNA and RNA are interpretable in terms of this selective base-pair formation. In living organisms, DNA stores the information on

- (i) what kinds of amino acids are used to compose a protein,
- (ii) how many are they, and
- (iii) in what order are they arranged.

This information determines the structures and properties of the protein. Typical examples of important proteins are enzymes, receptors, and antibodies, which carry out the desired biofunctions. When the genetic information of DNA is transferred to proteins, the necessary small part of DNA is copied to a kind of RNA (messenger RNA), which is ultimately used as template for producing the protein. In addition to messenger RNA, there are two other important RNAs named transfer RNA and ribosomal RNA.

When we prepare a desired protein by using biotechnology, the DNA of a living organism (e.g., *Escherichia coli*) is altered and the information on our target protein is incorporated into this DNA. There are two key steps in this technique: (i) site-selective scission of DNA and (ii) connection of DNA fragments. At present, both steps are successfully carried out by using naturally occurring enzymes. In the near future, however, we will need new tools that can accomplish even what these enzymes cannot do. As described in this manuscript, rare earth metal ions show remarkable activity for the hydrolysis of DNA and RNA, and should play very important roles in this field.

1.2. Importance of non-enzymatic scission of DNA and RNA

Non-enzymatic hydrolysis of DNA and RNA has been attracting interest, mainly because it is essential for further developments in biotechnology, molecular biology, therapy, and rel-

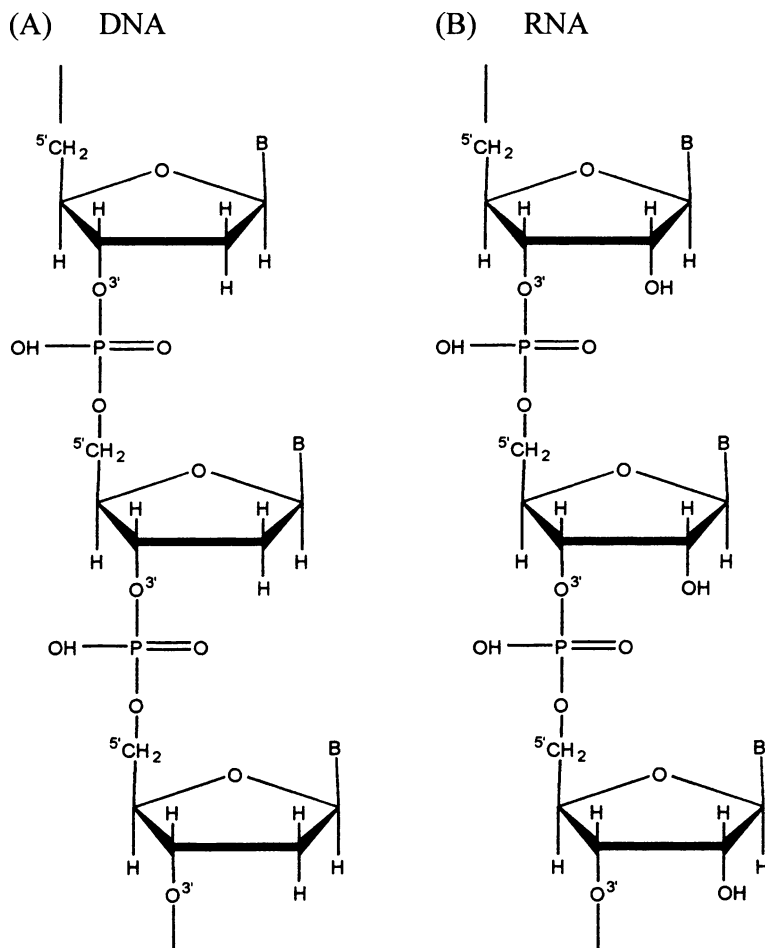


Fig. 1. Structures of DNA and RNA.

evant fields (Copeland et al., 2002; Franklin, 2002; Komiyama et al., 2001; Sreedhara and Cowan, 2001; Komiyama et al., 1999; Williams et al., 1999; Komiyama and Sumaoka, 1998; Hegg and Burstyn, 1998; Trawick et al., 1998; Oivanen et al., 1998). In present biotechnology, DNAs of bacteria and viruses are cut at a predetermined site by using naturally occurring enzymes named “restriction enzymes”. These enzymes recognize a specific sequence of DNA and cut the DNA at this location. The DNA fragment which conveys the information on the target protein is incorporated into this DNA. In this step, another enzyme (ligase) is used to connect the DNA fragments. At present, we are using very small DNA for this technology (the so-called plasmid DNA which contains 4–5000 nucleotides). Thus the site-specificity of these restriction enzymes is sufficient for site-selective scission of DNA at the target site. In

order to widen the scope of applications in the near future, however, we must deal with the DNAs of higher animals and plants. Can we directly apply the present method thereto? The answer is absolutely “no”. One of the most critical points is too low site-specificity of natural restriction enzymes. Most of them recognize a specific sequence comprised of 4 or 6 DNA bases. On average, the scission site of these restriction enzymes should be present at every 4^4 (= 256) or 4^6 (= 4096) DNA bases. These site-specificities are too low to cut the huge DNAs of higher living organisms at the desired site. For example, the DNA of human beings is composed of more than 10^9 DNA bases. If this DNA is treated with a 6-base recognizing restriction enzyme, scission will occur at more than 10^5 sites. Thus, artificial restriction enzymes with much higher specificity and able to selectively hydrolyze huge DNAs at the target positions, are crucially important (Komiyama et al., 2001, 1999; Komiyama and Sumaoka, 1998; Komiyama, 1995).

Artificial enzymes for sequence-selective RNA scission are also important. If only one RNA can be selected from many others in cells and is cleaved at the desired site, this should open the way to new RNA science. Regulation of the expression of a specific gene in cells, advanced therapy, and RNA manipulation are promising. However, none of the naturally occurring ribonucleases shows such a high sequence-selectivity. The so-called ribozymes are well suited for these purposes (Cech et al., 1981). However, these “semi-artificial” enzymes, based on RNA framework, do not necessarily fulfill all the requirements for versatile applications. The following factors sometimes impose limitations:

- (1) ribozymes are easily destroyed by the ribonucleases in living cells,
- (2) the scission occurs only at the specific sequences in RNA, and
- (3) RNAs having complicated tertiary structures are difficult to cleave (ribozymes are highly ordered macromolecules and cause significant steric hindrance against them).

In contrast, “completely artificial ribonucleases” are designed and synthesized according to the functions and properties we need, and thus factors (1)–(3) can be minimized. Furthermore, even non-natural functional groups can be easily incorporated in these man-made catalysts.

In order to prepare such artificial enzymes, catalysts for the scission of DNA and RNA are necessary. However, the phosphodiester linkages in them are enormously stable. The intrinsic half-life of the phosphodiester linkage in DNA at pH 7 and 25 °C is estimated to be 200 million years (Takasaki and Chin, 1993)! Although RNA is more reactive than DNA due to intramolecular attack by 2'-OH, the corresponding value is as large as 1000 years. In order to hydrolyze these stable linkages without using natural enzymes, a great deal of efforts have been made in various laboratories. Varieties of organic and inorganic catalysts for the hydrolysis of activated phosphoesters (e.g., bis(p-nitrophenyl)phosphate) were designed and studied in detail in 1960–1990, and the information on the mechanisms of their catalysis was accumulated. Yet, non-enzymatic hydrolysis of DNA was impossible, and RNA could not be hydrolyzed at reasonable rates.

1.3. *Lanthanide ions for molecular biology and biotechnology*

Some of the readers might wonder how and why lanthanide ions are related to biotechnology. Certainly, there was little interaction with this field until the early 1990s. In 1992–1993, it

Table 1
Remarkable catalytic activities of lanthanide ions for the hydrolysis of DNA and RNA

Nucleic acid	Half-life of phosphodiester linkage		The most active species
	Without catalyst	With lanthanide ion	
DNA	200 million years	a few hours	Ce(IV)
RNA	1000 years	a few minutes	Tm(III), Yb(III), Lu(III)

was found that these metal ions are highly effective for the hydrolysis of DNA (Matsumoto and Komiyama, 1992; Komiyama et al., 1993; Shiiba et al., 1993) and RNA (Matsumoto and Komiyama, 1992; Morrow et al., 1992). The results are shown in table 1 (Komiyama et al., 1994a, 1995). These findings represented a breakthrough in the relevant fields, since we could for the first time obtain very efficient scissors for cutting DNA and RNA. Accordingly, this opened the way to the preparation of artificial enzymes for the sequence-selective scission of DNA and RNA. Significantly, only lanthanide ions exhibit these remarkable catalytic properties, indicating that rare earth metals have more specific properties than previously understood. Why are lanthanide ions so eminent for the hydrolysis of DNA and RNA? How can they be applied to biotechnology? What can we expect in the future? These are the main themes of this review.

2. Discovery of DNA hydrolysis by Ce(IV)

2.1. *The finding of DNA hydrolysis by lanthanide(III) trichloride*

In 1992, the authors found that various lanthanide(III) salts are active for the hydrolysis of phosphodiester linkages in DNA (Matsumoto and Komiyama, 1992). Even linear (non-supercoiled) DNA was hydrolyzed at pH 7. This catalytic activity was quite important and attractive, since none of the catalysts previously reported could hydrolyze linear DNAs (several catalysts could hydrolyze supercoiled plasmid DNA, but they were inactive for the hydrolysis of linear DNAs: *vide infra*). Non-lanthanide ions, e.g., Mg(II), Zn(II), Co(II), Al(III), Fe(III), showed no measurable activity, and thus the remarkable catalysis for the hydrolysis of DNA is restricted to lanthanide ions. These findings built a bridge between biochemistry and rare earth chemistry.

More importantly, among the lanthanide(III) salts investigated, CeCl₃ was overwhelmingly ($> 10^3$ fold) more active than were the trichloride salts of other lanthanide(III) ions. Only this Ce(III) salt hydrolyzes non-supercoiled DNA under physiological conditions within a day. At pH 7 and 50 °C, for example, the half-life of phosphodiester linkage in dinucleotides (e.g., TpT, GpG, and others) is decreased to only a few hours. Thus, the acceleration of DNA hydrolysis by this metal salt is 10^{12} fold, which is enormous. This is the first hydrolysis of non-supercoiled DNA which was accomplished at reasonable rates without using naturally occurring enzymes. The rate of DNA hydrolysis was almost independent of the kind of nucleic acid bases in substrate DNA, showing that they do not directly participate in the catalysis. Consistently, oligonucleotides were hydrolyzed almost randomly throughout their strands

without no significant base-preference. Both single-stranded DNAs and double-stranded ones were hydrolyzed at almost the same rates.

2.2. Remarkable catalysis by Ce(IV)

Soon after the DNA hydrolysis by CeCl_3 was discovered, its catalytic mechanism was investigated in detail (Komiyama et al., 1994a, 1995; Takasaki and Chin, 1994). First, it was found that molecular oxygen is necessary for this metal salt to show remarkable catalytic activity. When oxygen was removed by repeated freeze-and-thaw cycles and the reaction with CeCl_3 was carried out under nitrogen atmosphere, the DNA substrate was hardly hydrolyzed (the scission rate was similar to the value for other lanthanide trichlorides). Furthermore, the ionic state of the Ce in the reaction mixtures was investigated by redox-titration experiments. A given amount of FeSO_4 was added to the mixtures, and the resultant solutions were back titrated with $\text{Ce}(\text{NH}_4)_4(\text{SO}_4)_4$ using *o*-phenanthroline as an indicator (its Fe(II) complex is red, while the Fe(III) complex is light-purple). It was shown that significant amounts of Ce(IV) were present in the reaction mixtures and that the rate of DNA hydrolysis linearly increased with increasing concentration of Ce(IV). Apparently, the active species is this tetravalent ion, which is formed by the oxidation of the Ce(III) with molecular oxygen. Furthermore, this fact satisfactorily explained why CeCl_3 was overwhelmingly more active than the other lanthanide(III) salts.¹ As is well known, only Ce can take both the trivalent state and the tetravalent state which are stable enough to exist in water under normal conditions.

It was also found that Ce(IV) salts (e.g., $\text{Ce}(\text{NH}_4)_2(\text{NO}_3)_6$) are also sufficiently active for DNA hydrolysis. The catalytic activity was comparable with that accomplished by CeCl_3 in presence of molecular oxygen. Still more importantly, molecular oxygen was not required at all when these salts were used as starting materials, and the catalysis was efficient even in its total absence. Thus we could conclude that, in the DNA hydrolysis by CeCl_3 , molecular oxygen is used only for the preparation of the catalytically active Ce(IV) species from the Ce(III) in the starting materials. The catalytic processes themselves do not require molecular oxygen at all. The salt $\text{Ce}(\text{NH}_4)_2(\text{NO}_3)_6$ is commercially available and easily soluble in water, and thus very convenient for practical purposes. After the finding of DNA hydrolysis by Ce(IV), various metal ions, including Ti(IV) and Zr(IV), were investigated in terms of their activities for DNA hydrolysis. They were found to be active but their catalytic effect was not sufficient. Even today, Ce(IV) is still the sole catalyst which can promptly hydrolyze linear DNAs irrespective of the DNA sequences.

Monophosphates such as adenosine 3'-monophosphate and guanosine 5'-monophosphate are also hydrolyzed by Ce(IV) (Miyama et al., 1997). The reactions are still faster than

¹ On the catalysis by CeCl_3/O_2 system, another mechanism involving dinuclear Ce(IV) species as the active species was proposed (Takasaki and Chin, 1994). There, the two Ce(IV) ions are bridged by $-\text{O}-\text{O}-$ group which is derived from molecular oxygen, and this group is the nucleophile for the reaction. However, this mechanism is unlikely, since molecular oxygen is not necessary to the catalytic process as described in text. Note that this mechanism is entirely different from the one described in sect. 5, although both involve dinuclear Ce(IV) species. In the mechanism proposed in sect. 5, the metal-bound hydroxide is the nucleophile and thus no molecular oxygen is required for the catalysis.

DNA hydrolysis. As an application of this catalysis, the phosphomonoesters at the 3'- or 5'-termini of DNA were removed by Ce(IV). Here, the internal phosphodiester linkages were kept rather intact. The selectivity of the terminal monoester hydrolysis, with respect to the phosphodiester hydrolysis, was notably increased by using concentrated Hepes and Tris buffer solutions. In doing so, the terminal phosphates were selectively removed from DNA with the main strands kept intact. The removal of the terminal monophosphate is one of the most fundamental processes in biotechnology and is currently accomplished by using naturally occurring phosphomonoesterase. The lanthanide(III) ions are far less active than Ce(IV). Lanthanide(III) ions also hydrolyze the phosphate esters other than DNA and DNA (Hay and Govan, 1990; Breslow and Zhang, 1994; Morrow et al., 1995; Matsumura and Komiyama, 1997).

2.3. Evidence for the hydrolytic scission of DNA

Although Ce(IV) is a well-known oxidant, the scission of DNA by Ce(IV) proceeds totally via hydrolysis of the phosphodiester linkages. No oxidative damage of either the nucleobases or the ribose occurs during the scission. This is really the most important advantage of the Ce(IV) catalysis, since the resultant fragments can be directly applicable to biotechnology. There, DNA is cut by a hydrolytic process with restriction enzymes, and the resultant fragments are transformed and/or combined by using enzymes. If the scission is accomplished by oxidative cleavage of ribose, for example, DNA can be certainly cut, but the fragments do not accept various enzymatic reactions and thus cannot be easily used any more.

The first important evidence is the results of ^1H NMR spectroscopy and HPLC analysis on the products. In the cleavage of dinucleotides (TpT, GpG, and others), the products were only nucleosides. No release of nucleobases to the solutions was detected although it should take place if the reaction were involving oxidative cleavage of the ribose. It is conclusive that the phosphodiester linkages were hydrolyzed by Ce(IV) and the monophosphates at the termini of the resultant fragments were further removed by the phosphomonoesterase activity of Ce(IV). In polyacrylamide gel electrophoresis, the fragments obtained by the scission of oligonucleotides with Ce(IV) completely comigrated with the fragments which were prepared by the digestion with naturally occurring nucleases.

Direct evidence of hydrolytic scission of oligonucleotides is presented in fig. 2 where the DNA fragments are manipulated using enzymes (Sumaoka et al., 1998). When oligonucleotides were labeled at 5'-end by radioactive ^{32}P and cleaved by $\text{Ce}(\text{NH}_4)_2(\text{NO}_3)_6$, a pair of fragments were formed for the scission at each of the phosphodiester linkages in the DNA substrate (see lane 3 in fig. 2(A)). One of these fragments has a monophosphate at its terminus and the other has an OH terminus. A pair of fragments were isolated from the gel, and each of them was treated by terminal deoxynucleotidyl transferase (TdT), as shown in fig. 2(B). This enzyme attaches a nucleoside to the fragment if an OH terminus is present at the 3'-end. When the slower fragment ($5'\text{P}^*-\text{T}_{17}-3'\text{s}$) was incubated with unlabeled 2', 3'-dideoxyadenosine-5'-triphosphate (ddCTP) in the presence of this enzyme, a new band having a smaller mobility than $5'\text{P}^*-\text{T}_{17}-3'\text{s}$ was quantitatively formed (compare lane 2 with lane 3 which refers to the fragment before the enzymatic treatment). Apparently, this fragment has a 3'-OH terminus

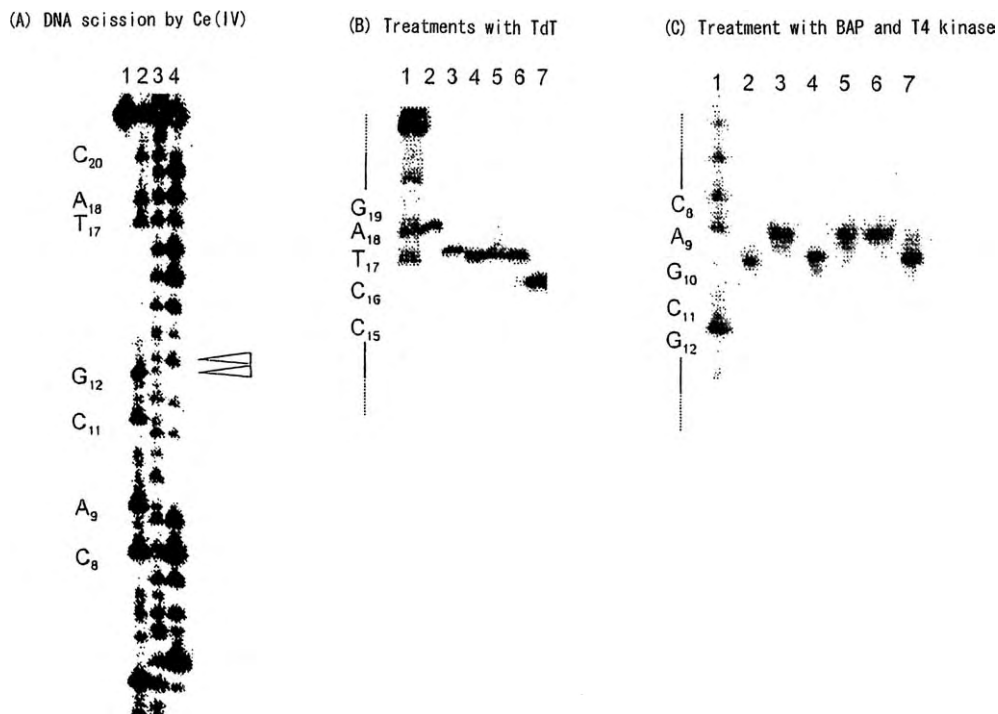


Fig. 2. Autoradiographs of a denaturing 20% polyacrylamide gel electrophoresis for Ce(IV)-induced hydrolysis of 22-mer DNA (A) and for the enzymatic treatment of the resultant fragments (B) and (C): the scales on the left-hand side show the nucleotides at the termini. (A): The 5'-end of the ^{32}P -labeled DNA oligomer. Lane 1, control; lane 2, Maxam-Gilbert A + G; lane 3, reaction with $\text{Ce}(\text{NH}_4)_2(\text{NO}_3)_6$; lane 4, DNase I. A typical pair of the fast and the slow fragments is designated by open arrows. Reaction conditions for lane 3: $[\text{Ce}(\text{IV})] = 1 \text{ mM}$ at pH 7 (Hepes buffer) and 37°C for 24 h. (B): The 5'-end of the ^{32}P -labeled fragments. Lane 1, Maxam-Gilbert A + G; lanes 2 and 3, $5'\text{P}^*-\text{T}_{17}-3's$; lanes 4 and 5, $5'\text{P}^*-\text{T}_{17}-3'f$; lanes 6 and 7, $5'\text{P}^*-\text{C}_{16}-3's$. Lanes 2, 4, and 6, treated with TdT; lanes 3, 5, and 7, untreated. (C): The 3'-end of the ^{32}P -labeled fragments. Lane 1, Maxam-Gilbert C + T; lanes 2-4, $5'f-\text{G}_{10}-3'\text{P}^*$; lanes 5-7, $5's-\text{G}_{10}-3'\text{P}^*$. Lanes 2 and 5, untreated; lanes 3 and 6, treated with BAP; lanes 4 and 7, treated with T4 kinase.

and a 2', 3'-dideoxycytidine moiety was enzymatically introduced thereto (the upper part of fig. 3(A)). In contrast, the slower fragment ($5'\text{P}^*-\text{T}_{17}-3'f$) was not susceptible to the enzymatic reaction, since it has a 3'-phosphate terminus (compare lanes 4 and 5 in fig. 2(B); see also the lower part of fig. 3(A)). Totally consistently, the slower fragment $5'\text{P}^*-\text{C}_{16}-3's$ (lane 7), which is one-nucleotide shorter than $5'\text{P}^*-\text{T}_{17}-3's$ and has a 3'-OH terminus, was elongated by the treatment with this enzyme (lane 6). The mobility of the product was virtually the same as that of $5'\text{P}^*-\text{T}_{17}-3's$.

In figs. 2(C) and 3(B), the fragments were labeled at the 3'-end, and the susceptibility of the fragments to two enzymes was examined. As was the case in the 5'-end labeled oligonucleotides, a pair of fragments, corresponding to the monophosphate terminus and

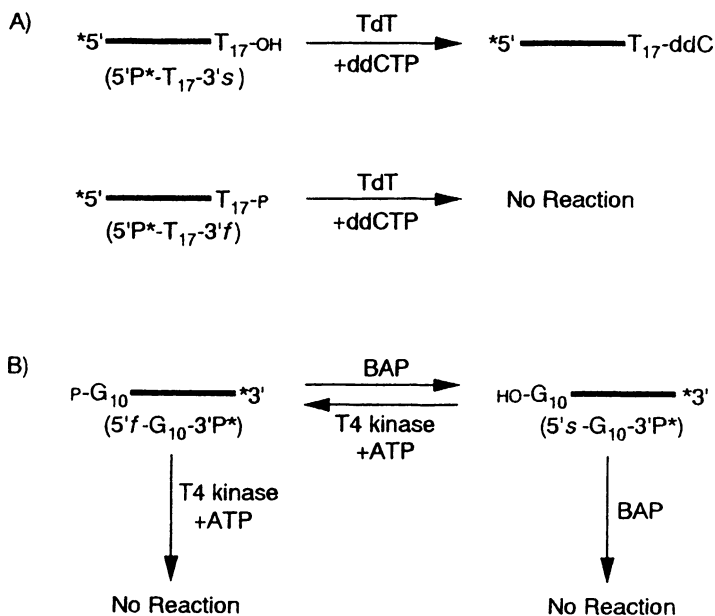


Fig. 3. Enzymatic manipulation of the fragments obtained by the hydrolysis of DNA (22-mer) with $\text{Ce}(\text{NH}_4)_2(\text{NO}_3)_6$: (A) 5'-end of ^{32}P -labeled fragments and (B) 3'-end of ^{32}P -labeled fragments.

the OH terminus, were formed for the scission at each of the phosphodiester linkages. The faster fragment $5'\text{f-G}_{10}\text{-3'P}^*$ was treated with bacterial alkaline phosphatase (BAP) which removes the terminal monophosphate if any. A new band of smaller mobility was quantitatively produced (compare lane 3 with lane 2 in fig. 2(C)). The mobility of the band was identical with that of the slower counterpart $5'\text{s-G}_{10}\text{-3'P}^*$ (lane 5). In contrast, the mobility of $5'\text{s-G}_{10}\text{-3'P}^*$ was unchanged on the BAP treatment (lane 5 vs. lane 6). Apparently, $5'\text{f-G}_{10}\text{-3'P}^*$ has a phosphate residue at the 5'-end, and it is removed by BAP. On the other hand, $5'\text{s-G}_{10}\text{-3'P}^*$ has an OH terminus. These arguments were furthermore confirmed by the following results. When $5'\text{s-G}_{10}\text{-3'P}^*$ (lane 5) was reacted with ATP in the presence of T4 polynucleotide kinase (T4 kinase), a phosphate residue was successfully attached to its 5'-end (lane 7). Note that the fragment flows faster since a negative charge is attached. The mobility of the product was exactly identical with that of $5'\text{f-G}_{10}\text{-3'P}^*$ in lane 2. As expected, the mobility of $5'\text{f-G}_{10}\text{-3'P}^*$ was unchanged, when it was treated with the combination of T4 kinase and ATP (compare lanes 2 and 4). Accordingly, upon the treatment with three enzymes (alkaline phosphatase, polynucleotide kinase, and terminal deoxynucleotidyl transferase), the DNA fragments obtained by using $\text{Ce}(\text{IV})$ were quantitatively transformed into the form expected for each of the enzymes (fig. 3). It is clear that the DNA fragment is completely free from any chemical damages (e.g., oxidative cleavage of the ribose) during the scission by $\text{Ce}(\text{IV})$. Otherwise, the fragments should not be susceptible to these natural enzymes, since enzymes strictly discriminate between normal

scission-products and abnormal ones. These results establish the potential of Ce(IV) as a tool in biotechnology, since the DNA fragments can be modulated at will by using various enzymes. As described above, the enzymatic transformation of the fragments, prepared by using restriction enzymes, into the desired forms is the key in the current and future biotechnology.

2.4. Cooperation of Ce(IV) and Pr(III) for faster DNA hydrolysis

Interestingly, the activity of $\text{Ce}(\text{NH}_4)_2(\text{NO}_3)_6$ for DNA hydrolysis is substantially enhanced when PrCl_3 is added to the mixture (Takeda et al., 1996). At $[\text{Ce}(\text{NH}_4)_2(\text{NO}_3)_6]/[\text{PrCl}_3] = 2$, the DNA hydrolysis is 10 times as fast as that induced by $\text{Ce}(\text{NH}_4)_2(\text{NO}_3)_6$ alone (the Pr(III) itself is virtually inactive under the reaction conditions employed). Notable synergetic cooperation is operative. This bimetallic system is the most active among all the catalysts for DNA hydrolysis ever reported. Mixed hydroxo-clusters are formed in situ from Ce(IV) and Pr(III) in the reaction mixtures, and the catalysis occurs therein. Assumedly, the Pr(III) ion in this mixed cluster provides its metal-bound water as the acid catalyst, and promotes the removal of the leaving OH of the DNA fragment. Under the reaction conditions (pH 7), the Pr(III)-bound water ($\text{p}K_a \sim 9$) mostly remains undissociated, and is superior as acid catalyst to the Ce(IV)-bound water. Although the $[\text{Ce}^{\text{IV}}(\text{H}_2\text{O})_n]^{4+}$ ion is intrinsically a very strong acid (the $\text{p}K_a$ for the first deprotonation is around 0), it loses three protons at pH 0–4 and is only a weak acid at pH 7 where the reactions are achieved.

Nd(III) can be also used, and significant cooperativity with Ce(IV) is observed. However, other lanthanide(III) ions are completely ineffective for this purpose, and rather suppress the catalytic activity of the Ce(IV). All non-lanthanide ions show no measurable effects on the catalytic activity of Ce(IV).

2.5. Cleavage of plasmid DNA

Plasmid DNA has a super-coiled structure and is activated by strain and other factors. The cleavage experiments of these DNAs are very convenient to achieve in chemical laboratories and we can learn much from them (Basile et al., 1987; Schnaith et al., 1994; Hashimoto and Nakamura, 1996; Hettich and Schneider, 1997). However, there are many catalysts which cleave plasmid DNA but cannot cut linear DNA. For example, lanthanide(III) ions are very active for the hydrolysis of this DNA, but cannot hydrolyze linear DNA so efficiently. It will take many years to hydrolyze linear DNA completely. On the contrary, the Ce(IV) ion does not cleave plasmid DNA so efficiently, although it rapidly hydrolyzes linear DNA as described above. Thus, sufficient care must be paid when the results on the catalysis for plasmid cleavage are extrapolated to the catalysis for the hydrolysis of linear DNA.

3. Homogeneous Ce(IV) complexes for DNA hydrolysis

Although Ce(IV) ion is very active for DNA hydrolysis, it easily forms metal hydroxide gel at physiological pH, and makes the system heterogeneous. This property has been imposing sig-

nificant limitations to practical applications of its catalytic effect. To solve this problem, many attempts were made to prepare Ce(IV) complexes which are homogeneous and catalytically active at pH 7.

3.1. *Ce(IV)/saccharide complexes*

Selected sugar derivatives form homogeneous complexes with Ce(IV) (Kajimura et al., 1998). Ribose, isomaltose, sugar alcohols, and dextran are especially effective. These sugar derivatives are electrically neutral and, probably because of this fact, the catalytic activity of Ce(IV) is little deteriorated by the complex formation. Similarly as in the catalysis by Ce(IV) hydroxide gel, the products of the hydrolysis of dinucleotides are mostly nucleosides (the monophosphates in the nucleoside phosphates are removed by the phosphomonoesterase activity of the Ce(IV) complex).

Quite interestingly and importantly, the synergism between Ce(IV) and Pr(III) described above (sect. 2.4) is also operating in these homogeneous solutions, and the catalytic activity of homogeneous Ce(IV)/dextran system was synergistically promoted by Pr(III). The activity for DNA hydrolysis shows a maximum at the [Ce(IV)]/[Pr(III)] ratio of 2. Other lanthanide ions also synergetically promoted the DNA hydrolysis by the Ce(IV)/dextran system.

3.2. *Ce(IV)/EDTA complex and its equivalents*

The homogeneous Ce(IV) complex was prepared by using ethylenediamine-N,N,N',N'-tetraacetate (EDTA), which is being most widely used as metal-binding ligand (Igawa et al., 2000). Another negatively charged ligand 5-methyl-2-hydroxy-1,3-xylenediamine-N,N,N',N'-tetraacetate was also usable (Branum et al., 2001). These complexes are sufficiently stable around pH 7 and exhibit notable catalytic activity for DNA hydrolysis.

It is noteworthy that the Ce(IV)/EDTA complex shows remarkable substrate specificity (see table 2). The catalysis of this complex is effective only for the hydrolysis of polynucleotides and oligonucleotides which are longer than tetranucleotides. Neither dinucleotides nor trinucleotides are hydrolyzed at all. Because of this fact, this complex had been for a long time believed to be inactive for DNA hydrolysis. Its catalytic effect for the hydrolysis of oligonucleotides was discovered in 2000 (Igawa et al., 2000). In addition to size-specificity, this complex clearly differentiates between single-stranded DNA and double-stranded one. Thus, single-stranded DNA is efficiently hydrolyzed by this complex, but double-stranded DNA is hardly cleaved. As described in sect. 12, these specificities are the origin of site-selective scission of DNA by using gap- or bulge-structures. In these structures, the target sites in the substrate DNA are kept single-stranded but the other parts form double-strands with appropriate oligonucleotide additives. When these structures are treated with the Ce(IV)/EDTA complex, the target sites are selectively hydrolyzed and thus the desired site-selective scission of DNA is successfully accomplished.

The remarkable substrate specificity of the Ce(IV)/EDTA complex is highly in contrast with non-specific properties of heterogeneous gels of Ce(IV) hydroxide, obtained by the addition

Table 2
Substrate-specificity of the Ce(IV)/EDTA complex and Ce(IV) hydroxide gel for DNA hydrolysis^a

Substrate	Catalyst	
	Ce(IV)/EDTA complex	Ce(IV) hydroxide gel
XpX	No	Yes
XpXpX	No	Yes
pXpXpX	Yes	Yes
XpXpXpX	Yes	Yes
larger oligonucleotide	Yes	Yes
double-strands	No	Yes

^aX = nucleoside.

of Ce(NH₄)₂(NO₃)₆ to buffered solutions in absence of EDTA. These heterogeneous gels efficiently hydrolyze all dinucleotides, trinucleotides, tetranucleotides, and polynucleotides. They hardly distinguish between single-stranded DNA and double-stranded one, and hydrolyze both of them at almost the same rates (see table 2).

The catalytic ability of the Ce(IV)/EDTA complex is notably promoted by cooperative effect with oligoamines such as ethylenediamine, diethylenetriamine, triethylenetetramine, spermine, and spermidine (Sumaoka et al., 2001). The synergism is conclusive, since all the oligoamines are completely inactive for DNA hydrolysis in the absence of the Ce(IV) complex. For example, 100 mM of ethylenediamine accelerated the DNA hydrolysis by more than 50 fold. Spermine is still more efficient for this cooperation in that it is effective at much smaller concentrations (e.g., 1 mM). The concentration of ethylenediamine must be 10 mM or larger in order to accelerate the reaction sufficiently. In a proposed mechanism, the positively charged oligoamines bind to the DNA and stabilize the negatively charged transition state of DNA hydrolysis through Coulomb interactions.

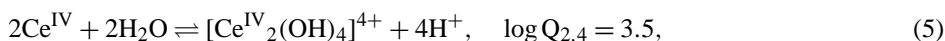
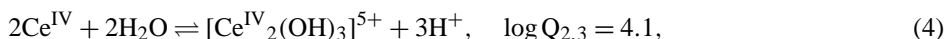
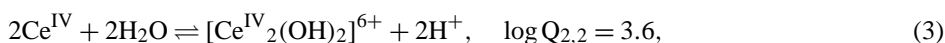
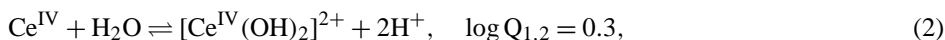
4. Mechanistic analysis of DNA hydrolysis by Ce(IV)

4.1. Kinetic analysis

One of the most significant obstacles for detailed kinetic analysis of DNA hydrolysis by Ce(NH₄)₂(NO₃)₆ is the formation of Ce(IV) hydroxide gel at physiological pH. Accordingly, the species responsible for the catalysis can not be easily pinned down and the mechanism of catalysis by Ce(IV) is not clear. However, we found that homogeneous Ce(IV) solutions can be obtained from Ce(NH₄)₂(NO₃)₆ when the pH is 2.5 or lower. The absence of any colloidal particles in these solutions was confirmed by light-scattering photometry. At least, there were no particles of diameter 15 Å or larger. Even in these acidic solutions, DNA hydrolysis by Ce(IV) proceeds efficiently and the rate is not much different from that at pH 7. The rate constant for the hydrolysis of thymidylyl(3'-5')thymidine (TpT) by Ce(NH₄)₂(NO₃)₆ (10 mM) at pH 2.0 and 50 °C is $6.3 \times 10^{-4} \text{ min}^{-1}$, whereas the value at pH 7.0 is $3.2 \times 10^{-3} \text{ min}^{-1}$. In both cases, the product is only thymidine. No oxidative cleavage was observed as long as the

pH was not too low (e.g., pH < 1). Apparently, essential features of the hydrolysis of TpT by $\text{Ce}(\text{NH}_4)_2(\text{NO}_3)_6$ in these acidic solutions are similar to those at pH 7, and thus the catalytic mechanism in acidic solutions should be comparable with that in neutral solutions. The redox titration showed that all the Ce(IV) ions in the solutions retain their tetravalent states throughout the DNA hydrolysis. This result further confirmed the absence of any redox reaction in the mixtures.

In the reaction mixtures, the solvolysis of Ce(IV) occurs as shown in eqs. (1)–(6), and there exist six Ce(IV)-derived species ($[\text{Ce}^{\text{IV}}]^{4+}$, $[\text{Ce}^{\text{IV}}(\text{OH})]^{3+}$, $[\text{Ce}^{\text{IV}}(\text{OH})_2]^{2+}$, $[\text{Ce}^{\text{IV}}_2(\text{OH})_2]^{6+}$, $[\text{Ce}^{\text{IV}}_2(\text{OH})_3]^{5+}$, $[\text{Ce}^{\text{IV}}_2(\text{OH})_4]^{4+}$, and $[\text{Ce}^{\text{IV}}_6(\text{OH})_{12}]^{12+}$). By using the equilibrium constants available, the concentrations of all these species were calculated, and the dependence of the rate of DNA hydrolysis on these values was investigated.



Under typical reaction conditions, the concentrations of these species are in the following order: $[\text{Ce}^{\text{IV}}(\text{OH})_2]^{2+} > [\text{Ce}^{\text{IV}}_2(\text{OH})_4]^{4+} \gg [\text{Ce}^{\text{IV}}(\text{OH})]^{3+} > [\text{Ce}^{\text{IV}}_2(\text{OH})_3]^{5+} \gg [\text{Ce}^{\text{IV}}_6(\text{OH})_{12}]^{12+} \gg [\text{Ce}^{\text{IV}}_2(\text{OH})_2]^{6+} \approx [\text{Ce}^{\text{IV}}]^{4+}$.

The pseudo-first-order rate constant k_{obs} monotonously increases with increase in the initial concentration of $\text{Ce}(\text{NH}_4)_2(\text{NO}_3)_6$ (cf. the open circles in fig. 4(A)). Here, the pH was kept constant at 2.0. All the experimental points fairly fit solid line (vi) corresponding to the equilibrium concentration of the bimetallic hydroxo-cluster $[\text{Ce}^{\text{IV}}_2(\text{OH})_4]^{4+}$. The dotted line (iv) showing the equilibrium concentration of $[\text{Ce}^{\text{IV}}_2(\text{OH})_2]^{6+}$ has a similar shape as line (vi). These two species are the candidates for the catalytically active species. On the other hand, line (i) for $[\text{Ce}^{\text{IV}}]^{4+}$, line (ii) for $[\text{Ce}^{\text{IV}}(\text{OH})]^{3+}$, line (iii) for $[\text{Ce}^{\text{IV}}(\text{OH})_2]^{2+}$, and line (v) for $[\text{Ce}^{\text{IV}}_2(\text{OH})_3]^{5+}$ are too flat to model the experimental data, while line (vii) for $[\text{Ce}^{\text{IV}}_6(\text{OH})_{12}]^{12+}$ is too steep. These species cannot be the active species. Note that the shapes of these lines are concretely determined only by the $Q_{x,y}$ values, pH, and $[\text{Ce}(\text{NH}_4)_2(\text{NO}_3)_6]_0$. On the other hand, the positions of lines are vertically movable by varying the catalytic rate constants of the corresponding species.

The pH dependence of the rate constant of hydrolysis is shown by the open circles in fig. 4(B) ($[\text{Ce}(\text{NH}_4)_2(\text{NO}_3)_6]_0$ is kept constant at 10 mM). The profile is rather flat from pH 1.4 to 2.1. All the experimental points are consistent with the shapes of the theoretical lines for the equilibrium concentrations of $[\text{Ce}^{\text{IV}}(\text{OH})_2]^{2+}$ (iii), $[\text{Ce}^{\text{IV}}_2(\text{OH})_4]^{4+}$ (vi), and $[\text{Ce}^{\text{IV}}_6(\text{OH})_{12}]^{12+}$ (vii). The concentrations of the other four species rapidly decrease with increasing pH and are inconsistent with the experimental data. Of the seven Ce(IV) derived

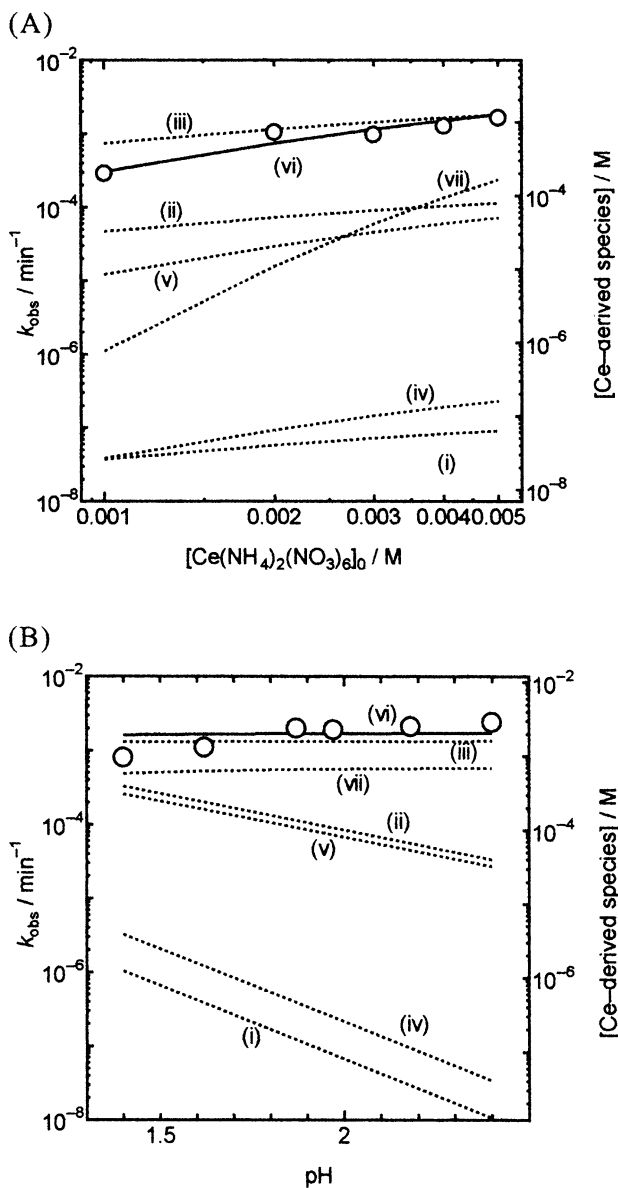


Fig. 4. Logarithm plots of the pseudo first-order rate constant of the TpT hydrolysis at 50 °C vs. (A) the initial concentration of $\text{Ce}(\text{NH}_4)_2(\text{NO}_3)_6$ and (B) pH. The pH was kept constant at 2.0 in (A), whereas $[\text{Ce}(\text{NH}_4)_2(\text{NO}_3)_6]_0$ was constant at 10 mM in (B). The solid line (vi) is the theoretical one showing the concentration of the proposed active species $[\text{Ce}^{IV}_2(\text{OH})_4]^{4+}$ (right ordinate). The dotted lines are the theoretical ones for (i) $[\text{Ce}^{IV}]^{4+}$; (ii) $[\text{Ce}^{IV}(\text{OH})]^{3+}$; (iii) $[\text{Ce}^{IV}(\text{OH})_2]^{2+}$; (iv) $[\text{Ce}_2^{IV}(\text{OH})_2]^{6+}$; (v) $[\text{Ce}_2^{IV}(\text{OH})_3]^{5+}$, and (vii) $[\text{Ce}_6^{IV}(\text{OH})_{12}]^{12+}$. All theoretical lines were calculated using the equilibrium constants in eqs. (1)–(6).

species in the mixtures, only the tetracationic bimetallic hydroxo-cluster $[\text{Ce}^{IV}_2(\text{OH})_4]^{4+}$ agrees with both independent analyses described in figs. 4(A) and 4(B). It is concluded that this species is not probably the active catalytic species in the DNA hydrolysis promoted by $\text{Ce}(\text{NH}_4)_2(\text{NO}_3)_6$.

A similar kinetic analysis of the hydrolysis of cyclic adenosine 3',5'-monophosphate (cAMP) by $\text{Ce}(\text{NH}_4)_2(\text{NO}_3)_6$ indicated that the $[\text{Ce}^{\text{IV}}_2(\text{OH})_4]^{4+}$ cluster is also the active catalytic species. This cyclic phosphate is an important biomaterial which is responsible for cell-to-cell communication. The hydrolysis of cAMP has many common features with DNA hydrolysis. First, both cAMP and DNA are enormously stable (the half-lives of the phosphodiester linkages in the absence of catalysts are estimated to be 400 thousand (Chin and Zou, 1987) and 200 million years, respectively). Second, the hydrolyses of both compounds are remarkably accelerated by Ce(IV) ion by 10^{12} – 10^{13} fold (Sumaoka et al., 1992, 1994). Thirdly, only Ce(IV) is effective for these reactions. Fourthly, both reactions proceed via the attack by OH^- (or its relevant species) as external nucleophile. The only notable difference between them is the fact that cAMP is hydrolyzed more promptly than DNA because of its ring strain. These results further confirm the proposal that the dinuclear Ce(IV) cluster $[\text{Ce}^{\text{IV}}_2(\text{OH})_4]^{4+}$ should be responsible for the catalytic DNA hydrolysis.

4.2. Spectroscopic studies

Why is Ce(IV) so active for DNA hydrolysis? What factors differentiate this metal ion from other lanthanide ions and non-lanthanide ions? Do the f-orbitals of Ce(IV) take significant roles in the catalysis? These questions are critically important for practical applications of this catalysis and also from the viewpoints of pure rare earth chemistry. In order to answer them, core-level photoelectron spectroscopy (Shigekawa et al., 1996), as well as EXAFS (extended X-ray absorption fine structure) and XANES (X-ray absorption near edge structure) measurements (Shigekawa et al., 1999), were carried out. The spectroscopic analysis was simplified by using diphenyl phosphate (DPP) in place of DNA, and the EXAFS and the XANES measurements were carried out on the samples frozen in liquid nitrogen.

Core-level spectroscopy was made on the phosphorus atom of DPP in various lanthanide complexes. This method provides the energy levels of atomic orbitals of the P atom. When the electron density on this atom is decreased and the atomic orbitals are stabilized, the corresponding binding energy should be increased. As shown in fig. 5, the binding energy of the $2p$ orbitals in the Ce(IV) complex is considerably greater than those for the complexes with La(III), Eu(III), Lu(III), and other non-lanthanide ions. Apparently, the Ce(IV) ion withdraws electrons from the phosphodiester linkage to a far greater extent than do the other metal ions, and increases the binding energy of the orbitals of the phosphorus atom far more drastically. As a result, the electrophilicity of the phosphodiester linkage in the Ce(IV) complex is exceptionally promoted. The superiority of Ce(IV) for the activation of DNA has been for the first time spectroscopically evidenced. Undoubtedly, this factor should be one of the origins of remarkable catalysis of Ce(IV) for DNA hydrolysis.

Detailed analysis of these core-level spectra further indicates that the phosphodiester is simultaneously coordinated to two Ce(IV) ions in the Ce(IV) complex, which is highly activated. As depicted in fig. 6, the $P2p$ signals of the DPP in the Ce(IV) complexes are composed of two components (P_H and P_L : each peak is further split into a spin-doublet). When the Ce(IV)/DPP ratio is 1:1, the peak P_L of the lower energy is predominant (b). Here, the phosphodiester linkage is bound to one Ce(IV) ion. Thus it is activated but only slightly.

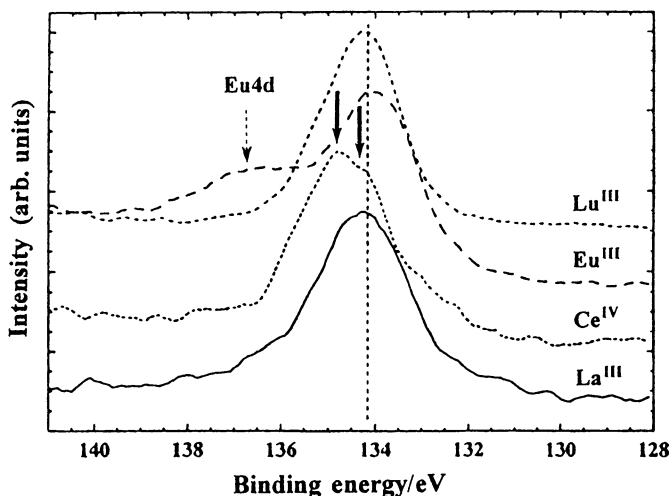


Fig. 5. Core-level spectra for the $P2p$ orbital of the diphenyl phosphate (DPP) in the La(III), Ce(IV), Eu(III), and Lu(III) complexes. $[\text{lanthanide ion}]_0/[\text{DPP}]_0 = 10$. The two bold arrows correspond to P_H and P_L in fig. 6.

Consistently, DNA hydrolysis hardly takes place under these conditions. As the Ce(IV)/DPP ratio increases (c)–(e), the intensity of the P_H signal, which has a higher energy, gradually increases. This signal corresponds to the DPP which is coordinated to two Ce(IV) ions in the hydroxo-cluster and is exceptionally activated by the two metal ions. Exactly as expected, the remarkable DNA hydrolysis occurs under conditions where Ce(IV) is in excess with respect to DNA (twofold or more). These arguments are further substantiated by the EXAFS spectra reported on fig. 7. In the absence of DPP ((a) and (b)), the Ce(IV) ions form metal hydroxo-clusters (and gel as they aggregate). Accordingly, the signal for the Ce–Ce distance is clearly observed at 3.6 Å (cf. the broken line). The signal at around 2.0 Å is assignable to the Ce–O bond. On addition of DPP, the signal for the Ce–Ce distance rapidly weakens and virtually vanishes for a Ce/DPP ratio of 1:1 (c). Since the 1:1 Ce(IV)/DPP complex exists as an independent species, without aggregation, the Ce–Ce signal at 3.6 Å is absent. When the Ce(IV)/DPP ratio becomes larger than one, however, the Ce–Ce signal appears again and its intensity gradually increases with increasing Ce/DPP ratio ((d) and (e)). Here, two Ce(IV) ions are simultaneously interacting with one DPP molecule, and located in a close proximity. Thus, these two Ce(IV) ions are bound to each other, giving rise to the Ce–Ce signal. These spectroscopic analyses completely agree with the conclusion of a kinetic study showing that $[\text{Ce}^{\text{IV}}_2(\text{OH})_4]^{4+}$ is the active species for DNA hydrolysis (see sect. 4.1). Furthermore, these results are also consistent with the conclusion of quantum-chemical studies.

That electron-transfer from phosphate to the Ce(IV) ion occurs is further supported by L_3 -XANES spectroscopy. In the Ce(IV)/DPP complex, there is 0.67 electron in the 4f orbitals of the Ce ion, although these orbitals should be empty in completely tetravalent Ce. This electron probably flows into the 4f orbitals from the surroundings. Consistently, the corresponding electron-transfer to the metal(III) ions is not observed in the DPP complexes of Ce(III) and other lanthanide(III) ions. As described above, the enormous activity of the Ce(IV) for DNA

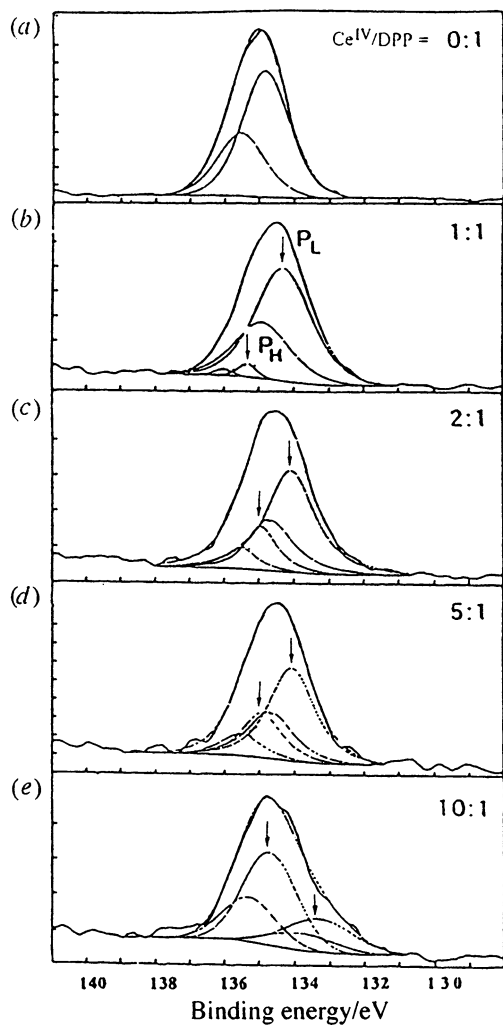


Fig. 6. Core-level spectra of the $P2p$ orbital of DPP in the Ce(IV)/DPP mixtures of different molar ratios. The peaks P_H and P_L correspond to the doublet signals of higher and lower binding energies, respectively.

hydrolysis is primarily ascribed to its dominant electron-accepting capability. These analyses further show that this specific property is derived from the stability of the trivalent state of Ce. The lanthanide(III) ions cannot efficiently accept the electrons from DNA, since their divalent states are too unstable.

When the Ce(IV)/DPP complex is formed, a new state appears near the Fermi level (fig. 8). Neither free DPP nor Ce(IV) hydroxo cluster (without DPP) has any density of state around the Fermi level. This suggests that the electron-transfer from the phosphate to the Ce(IV) ion occurs, at least partially, through hybrid orbitals, which are formed from the 4f-orbitals of the Ce(IV) and the orbitals of the phosphorus atom (and/or of the oxygen atom) in the phosphate

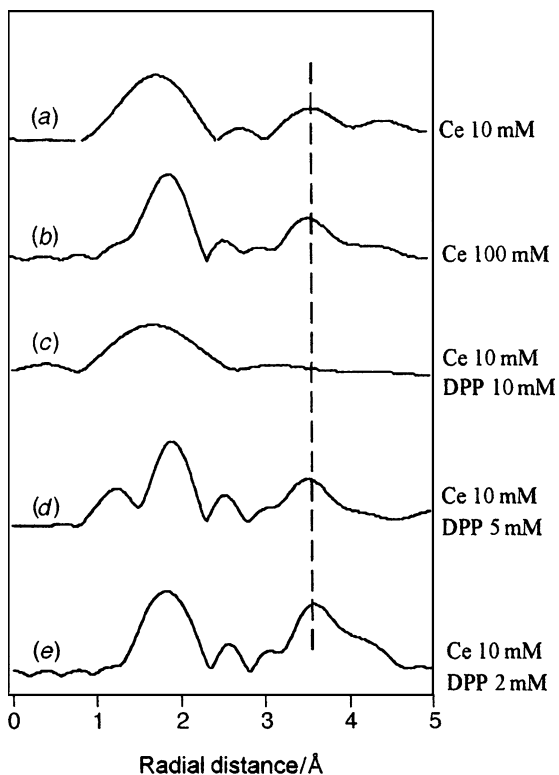


Fig. 7. EXAFS spectra for the Ce(IV)/DPP systems. The dotted line corresponds to the Ce-Ce distance.

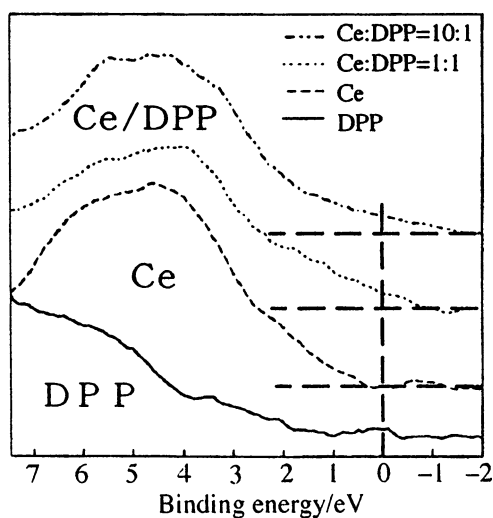


Fig. 8. X-ray photoelectron spectra near the Fermi-level in the Ce(IV)/DPP systems.

residue. Since the 4f orbitals of Ce(IV) are lower in energy than those of the lanthanide(III) ions, they can efficiently interact with the orbitals of the phosphate. The 5d orbitals of Ce(IV) could also participate to the hybrid orbitals. This mixing of the orbitals (as well as the resultant electron transfer) can be another factor for the activation of DNA by Ce(IV).

4.3. *Quantum-chemical studies on the catalytically active $[\text{Ce}^{\text{IV}}_2(\text{OH})_4]^{4+}$ cluster and its complex with phosphodiester*

The structures of various species responsible for DNA hydrolysis were investigated by using *ab initio* quantum chemical calculations. The optimized structure of $[\text{Ce}^{\text{IV}}_2(\text{OH})_4]^{4+}$ (the catalytically active species) is presented in fig. 9(A). This species is sufficiently stable, since the two Ce(IV) ions therein are bridged by two hydroxide groups. This dinuclear cluster is highly symmetric; the two Ce(IV) atoms and the two bridging OH groups (both the oxygen atoms and the hydrogen atoms) are located in one plane. Furthermore, the whole structure of the cluster has C_2 symmetry, the axis going through the two O-atoms of the OH groups. The distance between the two Ce(IV) atoms is 3.848 Å. This value is fairly in accord with the Ce–Ce distance (3.6 Å) in the 2:1 Ce(IV) complex of diphenyl phosphate (DPP), which was determined by the EXAFS study (see sect. 4.2). The structure of the catalytically active species, which was proposed above mainly in terms of both kinetic studies and spectroscopic analyses, has been further substantiated. It is noteworthy that a bimetallic Ce(IV) cluster of the same

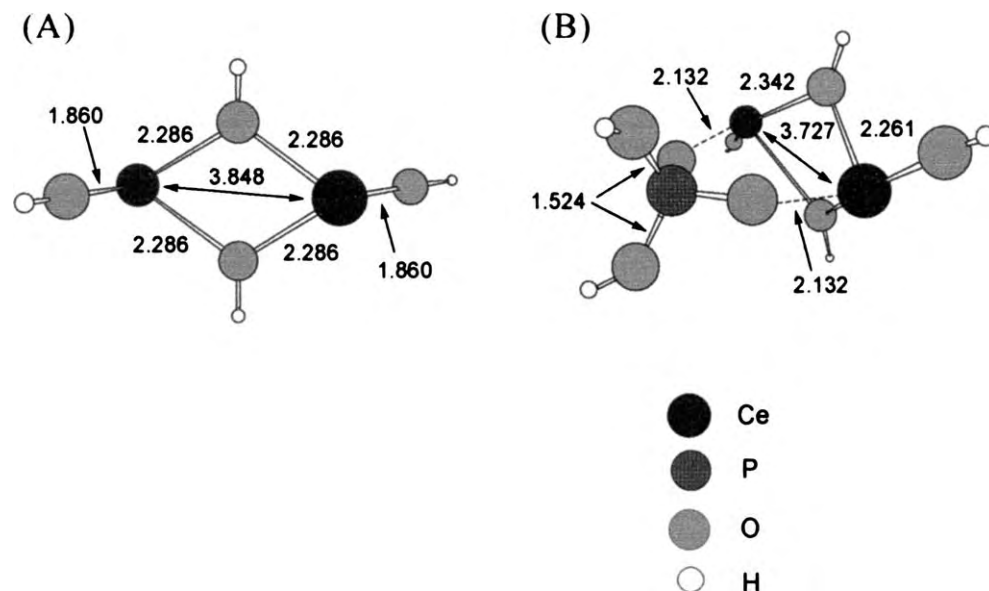


Fig. 9. The optimized structures determined by *ab initio* quantum-chemical calculations. (A) $[\text{Ce}^{\text{IV}}_2(\text{OH})_4]^{4+}$ involving two OH bridges. (B) 1:1 complex between H_2PO_4^- (a model compound of the phosphodiester in DNA) and $[\text{Ce}^{\text{IV}}_2(\text{OH})_4]^{4+}$. Bond lengths and interatomic distances are given in Å.

composition is quite unstable when there exists only one OH bridge between the two Ce(IV) atoms. Upon optimizing the geometry of this bimetallic cluster by quantum-chemical calculations, the OH-bridge was spontaneously broken and accordingly the cluster decomposed to two $[\text{Ce}^{\text{IV}}(\text{OH})_2]^{2+}$ molecules.

In order to obtain information on the catalytic process, the structure of the complex between DNA and this active species was also calculated. As a model compound of DNA, monoanionic phosphate H_2PO_4^- was employed. This choice is based on the fact that the phosphodiester group of DNA mostly exists as a monoanion under the reaction conditions where the kinetic studies were carried out (pH 1.4–2.5; sect. 4.1). The $\text{p}K_{\text{a}}$ value of the phosphodiester linkage of TpT is 0.4, according to a titration monitored by ^{31}P -NMR. Figure 9(B) shows the optimized structure of the complex between H_2PO_4^- and the $[\text{Ce}^{\text{IV}}_2(\text{OH})_4]^{4+}$ cluster (in fig. 9(A)). This complex is sufficiently stable, and the free energy change for its formation, evaluated by the theoretical calculations, is $-20.31 \text{ kcal mol}^{-1}$. The two oxygen atoms of H_2PO_4^- are coordinated to each of the two Ce(IV) atoms, and the Ce–O distance for both bonds is 2.13 Å. Upon complex formation, the Ce–Ce distance (3.73 Å) is almost unchanged, although the symmetric structure of the bimetallic Ce(IV) cluster is slightly distorted. These results are completely consistent with the core-level spectroscopy (fig. 6) showing that the activated Ce(IV) complex involves simultaneous coordination of phosphodiester to two Ce(IV) ions. The charge (+2.57) on the phosphorus atom in this complex is remarkably greater than the value for free H_2PO_4^- (+1.89), confirming that the electrons on this atom are notably withdrawn by the Ce(IV) ions. As a result, the electrophilicity of this reaction center is enhanced.

For the purpose of comparison, calculations were also carried out on the 1:2 complex between one H_2PO_4^- molecule and two $[\text{Ce}^{\text{IV}}(\text{OH})_2]^{2+}$ clusters. In the optimized structure of this ternary system, each of the two oxygen atoms of H_2PO_4^- is coordinated to either one of these two $[\text{Ce}^{\text{IV}}(\text{OH})_2]^{2+}$ molecules. The Ce–O distances are 2.20 Å. These two $[\text{Ce}^{\text{IV}}(\text{OH})_2]^{2+}$ clusters behave as independent species, the distance between these two Ce atoms being 6.63 Å. This 1:2 complex is quite unstable in comparison with the 1:1 complex between H_2PO_4^- and the dinuclear $[\text{Ce}^{\text{IV}}_2(\text{OH})_4]^{4+}$ cluster shown on fig. 9(B). The free energy change for its formation is only $-11.04 \text{ kcal mol}^{-1}$, whereas the corresponding value for the latter complex is $-20.31 \text{ kcal mol}^{-1}$. The charge on the P atom is +2.50, which is smaller by 0.07 unit than the value for the complex of the bimetallic cluster $[\text{Ce}^{\text{IV}}_2(\text{OH})_4]^{4+}$. This conclusion is consistent with the results presented in fig. 4. In order to achieve sufficient catalytic efficiency for DNA hydrolysis, the dinuclear Ce(IV) cluster $[\text{Ce}^{\text{IV}}_2(\text{OH})_4]^{4+}$ is essential both for the formation of a stable complex with the DNA substrate and for sufficient activation of the scissile phosphodiester linkage.

5. Proposed mechanism for the DNA hydrolysis by Ce(IV)

The hydrolysis of DNA proceeds as a two-step reaction. In the first step, one hydroxide ion attacks the phosphorus atom, forming a pentacoordinated intermediate. In the second step, the 5'-OH of 2'-deoxyribonucleotide is removed from the phosphorus atom through the scission of the P–O(2') bond (in non-enzymatic hydrolysis, the P–O(3') scission can also take place).

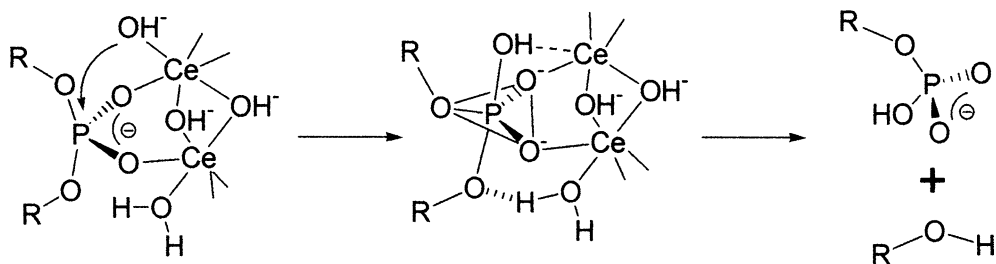


Fig. 10. Proposed mechanism for the hydrolysis of phosphodiester by the bimetallic hydroxo-cluster $[\text{Ce}^{\text{IV}}_2(\text{OH})_4]^{4+}$.

The Ce(IV) ion accelerates this process 10^{12} fold. The proposed mechanism of DNA hydrolysis by the bimetallic cluster $[\text{Ce}^{\text{IV}}_2(\text{OH})_4]^{4+}$ is schematically depicted on fig. 10. First, the phosphate residue is coordinated to the two Ce(IV) ions in $[\text{Ce}^{\text{IV}}_2(\text{OH})_4]^{4+}$; the apparent association constant between Ce(IV) and TpT was determined to be 10^3 M^{-1} at pH 2.0 and 50°C . As clearly evidenced by both spectroscopic and theoretical studies (cf. sects. 4.2 and 4.3), the electrons of the scissile phosphodiester linkage are strongly withdrawn by the Ce(IV) ions. Furthermore, the orbitals of this phosphate are mixed with the orbitals of the Ce(IV), and form new hybrid-orbital(s). These two factors greatly activate the phosphodiester linkage and make it highly susceptible to the attack by various nucleophiles.

Then, this phosphodiester group is attacked by the hydroxide ion coordinated to one of the two Ce(IV) ions in the $[\text{Ce}^{\text{IV}}_2(\text{OH})_4]^{4+}$ cluster. Although this metal-bound hydroxide ion is a rather weak nucleophile, the phosphodiester group is so much activated that this reaction can be efficient. Furthermore, the metal-bound hydroxide ion is located in quite a suitable position for the nucleophilic attack. The two Ce(IV) ions in the bimetallic cluster have many coordination water molecules, and at least one of them lies most appropriately for the purpose. Finally, the positive charges, accumulated in the Ce(IV) hydroxo cluster, stabilize the negatively charged transition state of DNA during its hydrolysis (the transition state is more negatively charged than the initial state, and is stabilized to a greater extent by the adjacent positive charges). Because of these factors, the pentacoordinated intermediate is efficiently formed.

In the breakdown of the intermediate, the water bound to Ce(IV) functions as acid catalyst. With this catalysis, the alkoxide ion of 5'-OH can be promptly removed from the phosphorus atom. Otherwise, the leaving group is poor and hard to be removed. Consistently, the DNA hydrolysis by Ce(IV) is accompanied by a notable D_2O solvent isotope effect ($k_{\text{H}_2\text{O}}/k_{\text{D}_2\text{O}} = 2.2\text{--}2.4$). The proton transfer is, at least partially, rate limiting. The large coordination-number of the Ce(IV) ions in the bimetallic cluster is favorable for this acid catalysis, exactly as described above for the first step of DNA hydrolysis (formation of the pentacoordinated intermediate). This mechanism is proposed on the basis of the kinetic analysis in acidic solutions. When DNA hydrolysis is carried out at around pH 7, similar acid-base cooperation by Ce(IV)-bound water molecule and the corresponding hydroxide should occur in higher aggregates of $[\text{Ce}^{\text{IV}}_2(\text{OH})_4]^{4+}$.

6. RNA hydrolysis by lanthanide ions and their complexes

6.1. Catalysis by lanthanide(III) ions

RNA bears a hydroxyl group at the 2'-position of ribose. When it is hydrolyzed, this group functions as intramolecular nucleophile, and attacks the adjacent phosphorus atom. As the result, a pentacoordinated intermediate is formed. Then, the 5'-OH of ribonucleotide is removed from the P atom in the intermediate, and 2',3'-cyclic monophosphate is formed as the covalent intermediate. In the following step, this cyclic monophosphate is hydrolyzed, and the RNA hydrolysis is completed. Thus the reaction mechanism of RNA hydrolysis is entirely different from that of DNA hydrolysis which involves intermolecular attack by external nucleophile towards the P atom. The intramolecular reaction in RNA hydrolysis is so efficient that RNA hydrolysis is far faster (10^5 – 10^6 fold) than DNA hydrolysis. Nevertheless, RNA is sufficiently stable under physiological conditions, and it is not easy to hydrolyze it efficiently without using enzymes (in the absence of catalysts, the half-life of the phosphodiester linkage in RNA is estimated to be around 1000 years). The catalysts for RNA must be enormously active. In order to hydrolyze RNA within an hour, for example, the catalyst must accelerate the reaction by 10^7 -fold or more. In spite of a number of attempts, sufficiently fast non-enzymatic hydrolysis of RNA was unsuccessful for a long period of time.

In 1992, it was discovered that lanthanide ions are extraordinarily active for RNA hydrolysis (Matsumura and Komiyama, 1992). With the use of lanthanide trichlorides, diribonucleotides are completely hydrolyzed at pH 7 within 30 min. Although several catalysts for RNA hydrolysis were previously reported, lanthanide(III) ions greatly exceed any of them in the catalytic activity. Thus these findings attracted significant interest from chemists and biochemists. All the lanthanide(III) ions are active, but the catalytic activity monotonically increases with increasing atomic number as depicted in fig. 11 (Matsumura and Komiyama, 1997). Thus, the last three lanthanide ions (Tm(III), Yb(III), and Lu(III)) are especially active. When $[\text{LuCl}_3]_0 = 5 \text{ mM}$ at pH 7 and 30°C , for example, more than half of adenylyl(3'-5')adenosine (ApA) disappears in 5 min, and 1:1 mixture of adenosine (A) and its monophosphates (A2'p + A3'p) is formed. The reaction intermediate, adenosine 2',3'-cyclic monophosphate (A > p), is rapidly hydrolyzed by the Lu(III) ion to A2'p or A3'p, and not much accumulated. The pseudo first-order rate constant for the disappearance of ApA is $3 \times 10^{-3} \text{ s}^{-1}$ (half-life = 3.8 min), and the acceleration is almost 10^8 fold. The reaction rate is not much dependent on the kind of substrate. The hydrolysis rate is proportional to $[\text{LuCl}_3]_0$. Interestingly, Ce(IV), which is overwhelmingly the best ion for DNA hydrolysis, is not exceptionally active for RNA hydrolysis (its activity is comparable with that of Tb(III)).

Oligoribonucleotides are also efficiently hydrolyzed by lanthanide(III) ions. The scission occurs randomly without any specific base-preference, as is the case in the DNA hydrolysis by Ce(IV). When $[\text{LuCl}_3]_0 = 10 \text{ mM}$ at pH 7.5 and 30°C , substrate RNAs are almost completely degraded into small fragments within 1 h. The termini of the RNA fragments are either the 2'- or 3'-monophosphates, and the 2',3'-cyclic monophosphate termini are hardly formed because they are rapidly hydrolyzed to the monophosphates. It is noteworthy that the rate of RNA hydrolysis by lanthanide ions is drastically dependent on the pH of the solution. With LuCl_3 ,

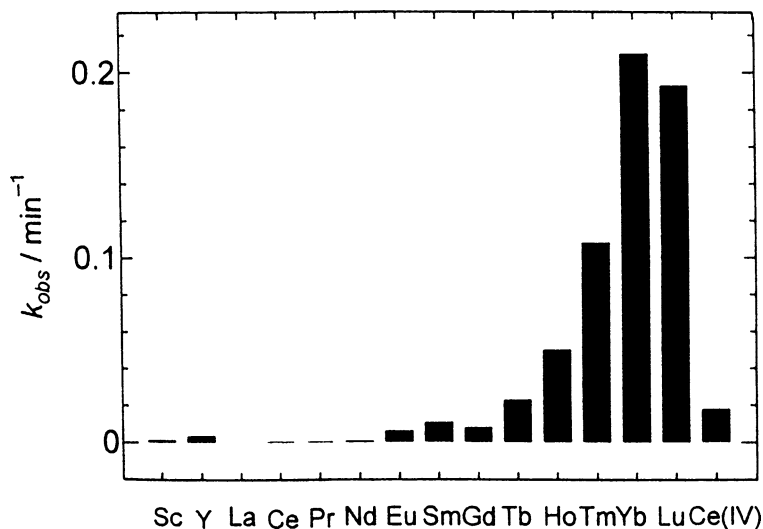


Fig. 11. Activities of a series of lanthanide(III) ions for RNA hydrolysis at pH 7 (substrate = ApA).

the RNA hydrolysis at pH 8 is 300-fold faster than that at pH 7; the slope of the logarithm of rate constant vs. pH is around 2.5, reflecting the formation of catalytically active dinuclear metal hydroxide cluster (*vide infra*). In order to obtain reproducible results, the pH of the reaction mixture must be very carefully controlled.

6.2. Lanthanide complexes for RNA hydrolysis

Immediately after the remarkable catalytic ability of lanthanide(III) ions for RNA hydrolysis was found, a number of attempts were made to prepare their complexes and extend the scope of the applications of this catalysis. The lanthanide complexes of iminodiacetate (in fig. 12(A)) and acetylacetonate are obtainable simply by mixing the metal salt with the corresponding ligand (Sumaoka et al., 1995). The lanthanide complexes of Schiff-base macrocycles (fig. 12(B)) are prepared by refluxing the corresponding diamine and dialdehyde in the presence of the metal salts (Morrow et al., 1992). So-called “texaphyrins” (expanded porphyrins involving five nitrogen atoms; fig. 12(C)) (Magda et al., 1994, 1997) and derivatives of tetraazacyclododecane (fig. 12(D)) (Chin and Morrow, 1994) are also available.

The mixtures of LaCl_3 and hydrogen peroxide efficiently hydrolyze RNA. The active species is a trimeric aggregate of the dinuclear complex $[\text{La}(\text{O}-\text{O})_3\text{La}]$ (Komiya et al., 1996). In the hydrolysis of an activated phosphodiester [bis(4-nitrophenyl) phosphate (BNPP)] by the same combination, however, monomeric $[\text{La}(\text{O}-\text{O})_2\text{La}]^{2+}$ is the active species (Takasaki and Chin, 1995). The catalytic mechanism (and thus the catalytic species) is strongly dependent on the substrate.

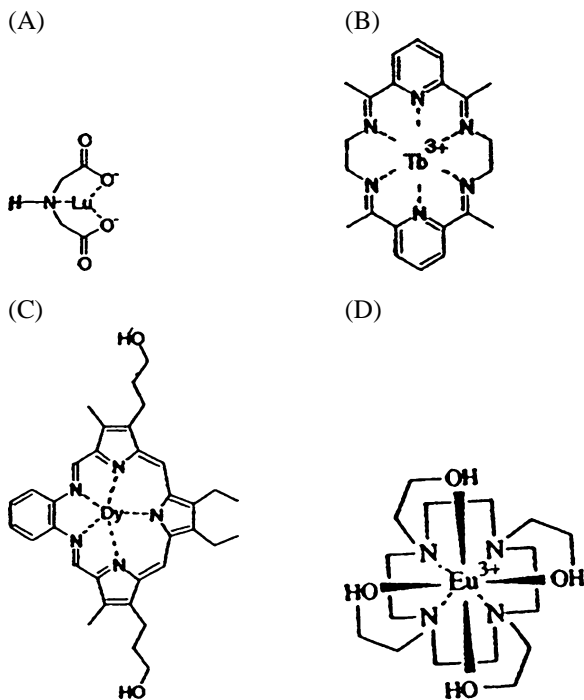
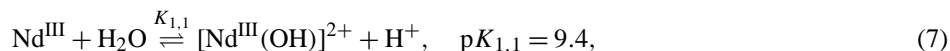


Fig. 12. Typical lanthanide complexes used for RNA hydrolysis.

7. Kinetic analysis on the RNA hydrolysis

The Nd(III)-induced hydrolysis of adenylyl(3'-5')adenosine (ApA) has been kinetically analyzed in detail (Matsumura and Komiyama, 1997). In the reaction mixtures, solvolysis of Nd(III) occurs and there exist three Nd(III)-derived species: free Nd^{3+} , $[\text{Nd}^{\text{III}}(\text{OH})]^{2+}$, and $[\text{Nd}^{\text{III}}_2(\text{OH})_2]^{4+}$ (see eqs. (7) and (8)). The equilibrium concentration of each species can be calculated by using the $K_{1,1}$ and $K_{2,2}$ values, and the dependence of the reaction rate on the concentration of these species has been investigated.

As shown in fig. 13, the logarithm of the rate of RNA hydrolysis steeply increases with increasing pH, up to pH 8, and then reaches a plateau. The slope in the steep region is greater than 2. The experimental points fairly fit the theoretical line (the solid line) which shows the equilibrium concentration of $[\text{Nd}^{\text{III}}_2(\text{OH})_2]^{4+}$. The other species never satisfy the experimental results. Undoubtedly, this bimetallic cluster is the active species for the RNA hydrolysis. In order to hydrolyze RNA efficiently, the bimetallic structure is essential, as is the case in DNA hydrolysis. The concentration of this active species is strongly dependent on pH, since it is accompanied by the release of two protons. Because of this, the rate of RNA hydrolysis by lanthanide(III) ions is so highly pH dependent.



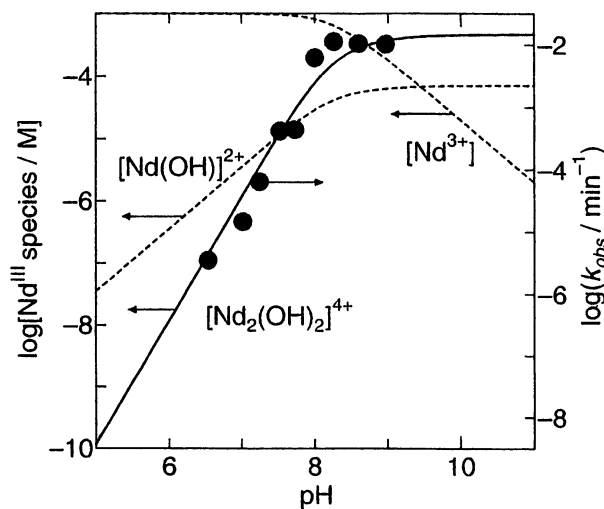


Fig. 13. The pH-dependence of the rate of ApA hydrolysis by NdCl_3 (1 mM) at 30°C . The closed circles are the experimental points, whereas the curved lines show the equilibrium concentration of the Nd(III)-derived species.

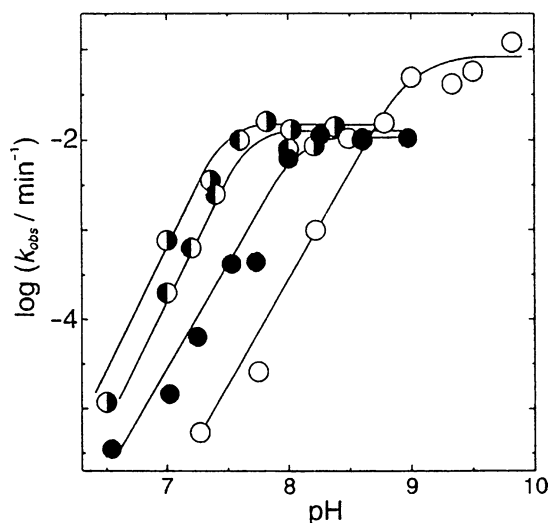


Fig. 14. The pH-dependence of the rate of ApA hydrolysis by various lanthanide(III) chlorides (1 mM) at 30°C . \circ – La(III); \bullet – Nd(III); \ominus – Tb(III); \oplus – Lu(III). Only typical results are presented here, since the shapes of the profiles for all the lanthanide(III) ions are similar and their positions monotonically shift towards lower pH with increasing atomic number.



The pH-rate constant profiles for the RNA hydrolysis by all the other lanthanide(III) ions have similar shapes, and are composed of (i) a steep straight line at lower pH and (ii) a plateau at the higher pH values (see fig. 14). The straight line corresponds to the formation of the active species $[\text{R}^{\text{III}}_2(\text{OH})_2]^{4+}$, whereas its formation is completed in the plateau region at higher pH. As the atomic number of lanthanide ion increases, these profiles gradually shift towards the lower pH side. Accordingly, the concentration of the active species at pH 7 increases with

increasing atomic number. For example, Tm(III), Yb(III), and Lu(III) mostly exist under the form of bimetallic active species ($[\text{R}^{\text{III}}_2(\text{OH})_2]^{4+}$) at pH 7. As a result, these metal ions are quite active for RNA hydrolysis in neutral solutions. However, most of La(III) ions are in their monomeric form at pH 7, with only a small fraction incorporated into the active form $[\text{La}^{\text{III}}_2(\text{OH})_2]^{4+}$. Thus, Tm(III), Yb(III), and Lu(III) are superior to the others, when RNA hydrolysis is carried out under physiological pH. In alkaline solutions, however, even La(III) ions mostly exist under the active form and are sufficiently active.

8. Mechanism of RNA hydrolysis by lanthanide ions (fig. 15)

The first step in RNA hydrolysis is the intramolecular nucleophilic attack of the phosphorus atom by the 2'-OH of ribose. This step is activated by the coordination of the phosphodiester linkage in RNA to the lanthanide(III) ion in the bimetallic cluster $[\text{R}^{\text{III}}_2(\text{OH})_2]^{4+}$, since the electrons are withdrawn by the metal ion from the phosphorus atom. This electron withdrawal promotes the electrophilicity of the P atom, although it is not so drastic as the effect achieved by the Ce(IV) in DNA hydrolysis (cf. sect. 5). Furthermore, the hydroxide ion bound to another lanthanide(III) ion in the bimetallic cluster functions as a general base catalyst, and enhances the electrophilicity of the 2'-OH by removing its proton. Alternatively, the 2'-OH is directly coordinated to this metal ion, and its dissociation to alkoxide ion is facilitated. In this way, both the nucleophilic center (the oxygen in the 2'-OH) and the electrophilic center (the phosphorus atom) are simultaneously activated by the bimetallic cluster, and thus the intramolecular nucleophilic attack proceeds efficiently.

The breakdown of the resultant pentacoordinated intermediate is rate limiting, since the first step is an intramolecular reaction facilitated by a favorable activation entropy term. In this step, the metal-bound water functions as a general acid catalyst. The water bound to the lanthanide(III) ions has a $\text{p}K_a$ in the range 8–9, which should be further decreased in the bimetallic clusters since the second trivalent ion should further withdraw electrons from the

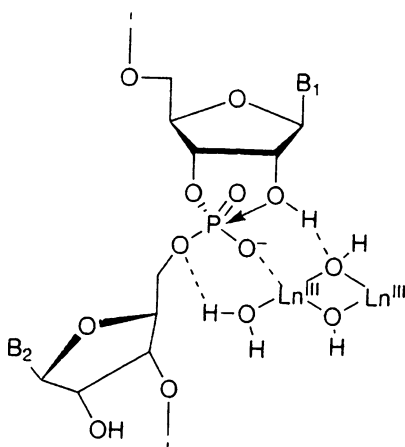


Fig. 15. Proposed mechanism of the lanthanide(III)-induced RNA hydrolysis.

first one. This is quite appropriate for RNA hydrolysis carried out around pH 7. When the apparent activities of various acid catalysts are compared with each other at a predetermined pH, the activity increases as the pK_a gets closer to the pH. Alternatively, the metal ion itself in the cluster acts as the acid catalyst. In this way, the general acid catalysis cooperates with the general base catalysis in the hydroxo clusters, resulting in the prompt hydrolysis of RNA.

9. DNA hydrolysis vs. RNA hydrolysis

Which factor makes the Ce(IV) ion best for DNA hydrolysis? Why are lanthanide(III) ions so efficient for RNA hydrolysis? The energy diagram for the uncatalyzed (alkaline) hydrolysis of DNA is virtually symmetric, and the heights of the first-barrier (for the formation of pentacoordinated intermediate) and the second-barrier (for the removal of leaving group from the reaction intermediate) are almost the same. Under these conditions, the primary requirement for an efficient catalysis is to lower the energy barrier of the first step (otherwise, the first step is rate limiting, even when the second step is accelerated). Furthermore, the catalyst can stabilize the pentacoordinated intermediate with respect to the initial state. The Ce(IV) ion satisfactorily fulfills both of these requirements, since it efficiently activates DNA by both (i) withdrawing the electrons from the phosphate in the “two-metal activation” and (ii) mixing its f-orbitals with those of the phosphate. Accordingly, the second-barrier is lowered with respect to the initial state. In contrast with these remarkable effects, the lanthanide(III) ions cannot withdraw electrons so efficiently and their activation of DNA is much poorer. Yet it is noteworthy that even lanthanide(III) ions are far better than non-lanthanide ions.

In RNA hydrolysis, however, the second energy barrier, the removal of leaving group from the pentacoordinated intermediate, is considerably higher than the first energy barrier. Here, the promotion of the second step should directly accelerate the whole reaction. The lanthanide(III) ions are suitable for promoting the second step as acid catalysts, since they have many (8 or 9) coordination water molecules with pK_a values close to the pH of the reaction mixtures. These metal-coordinated water molecules exist in large amounts at pH 7 and have sufficiently large activity as acid catalyst. According to Brønsted rule for acid/base catalysis, the activity of an acid catalyst increases with decreasing pK_a . At the same time, these metal ions withdraw electrons and promote the first step, which of course also contributes to facilitate the RNA hydrolysis as is the case in DNA hydrolysis.

10. Strategy for site-selective scission of DNA and RNA

As described in the introduction section, one of the goals of non-enzymatic hydrolysis of DNA and RNA is to prepare artificial enzymes for site-selective scission of them. With these new tools, we can develop novel biotechnology and therapy, which are impossible with the use of naturally occurring enzymes. Now that we have lanthanide ions as efficient molecular scissors on DNA and RNA, what we should do next for the site-selective scission is to let these scissors work at the desired site in DNA and RNA substrates.

The strategies for sequence-selective scission of DNA and RNA hitherto proposed are divided into the following two categories. In the first one (“covalent strategy”), a catalyst for the hydrolysis of phosphodiester linkages in DNA and RNA is covalently attached to oligonucleotides that are complementary with DNA and RNA substrates (fig. 16(A)). Accordingly, the molecular scissors are placed near the target phosphodiester linkage, and cleave this linkage selectively. Peptide nucleic acids (PNAs), DNA-binding proteins, and other organic or inorganic molecules are also available as the sequence-recognizing moieties. If necessary, they can be chemically modified to provide the desired physicochemical and/or biological properties (e.g., increased permeability through cell membranes or strong resistance against enzymatic cleavage). There is no limitation in their molecular design.

Another methodology for sequence-selective scission is “non-covalent strategy”, in which the target phosphodiester linkage is differentiated from the other linkages in the substrate in terms of intrinsic reactivity (fig. 16(B)). For example, as described below, a single-stranded fragment in substrate DNA is much more susceptible to hydrolysis by the Ce(IV)/EDTA complex than is the double-stranded fragment. Accordingly, the target phosphodiester linkage is selectively hydrolyzed by placing this linkage in a single-stranded fragment and the other linkages in double-stranded fragments. Here we do not have to immobilize the molecular scissors on any sequence-recognizing moiety. The scission is selective because of the difference in the intrinsic reactivity, even though the scissors are freely moving around in the solutions. If the target site can be activated by some non-covalent interactions, the selectivity can be improved. The non-covalent activation of the target site in RNA by acridine-modified DNA (see sect. 13) is a typical example.

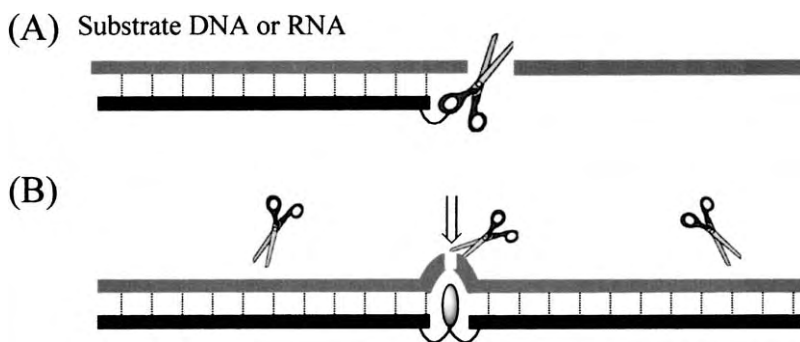


Fig. 16. Two strategies for site-selective scission of DNA and RNA: (A) “covalent strategy” in which lanthanide complexes are covalently linked near the target phosphodiester linkages by using oligonucleotides that are complementary with the DNA and RNA substrates, and (B) “non-covalent strategy”, in which the target phosphodiester linkage is activated by some non-covalent interactions and differentiated from the others in the substrate in terms of intrinsic reactivity. The black ribbons show the oligonucleotides (or their equivalents) used for the artificial enzymes to recognize the target sites.

11. Covalent strategy for site-selective scission of DNA

Artificial enzymes for site-selective scission of DNA were prepared by hybridizing the Ce(IV)/iminodiacetate complex with oligonucleotides (fig. 17(A)) (Komiyama et al., 1994b, 1994c). First, the oligonucleotide which is complementary to the DNA substrate was prepared on an automated synthesizer, and an amino group was attached to its 5'-end by using the commercially available phosphoramidite monomer. This modified oligonucleotide was reacted with an activated urea derivative bearing a diethyl iminodiacetate. Finally, the ethyl esters in

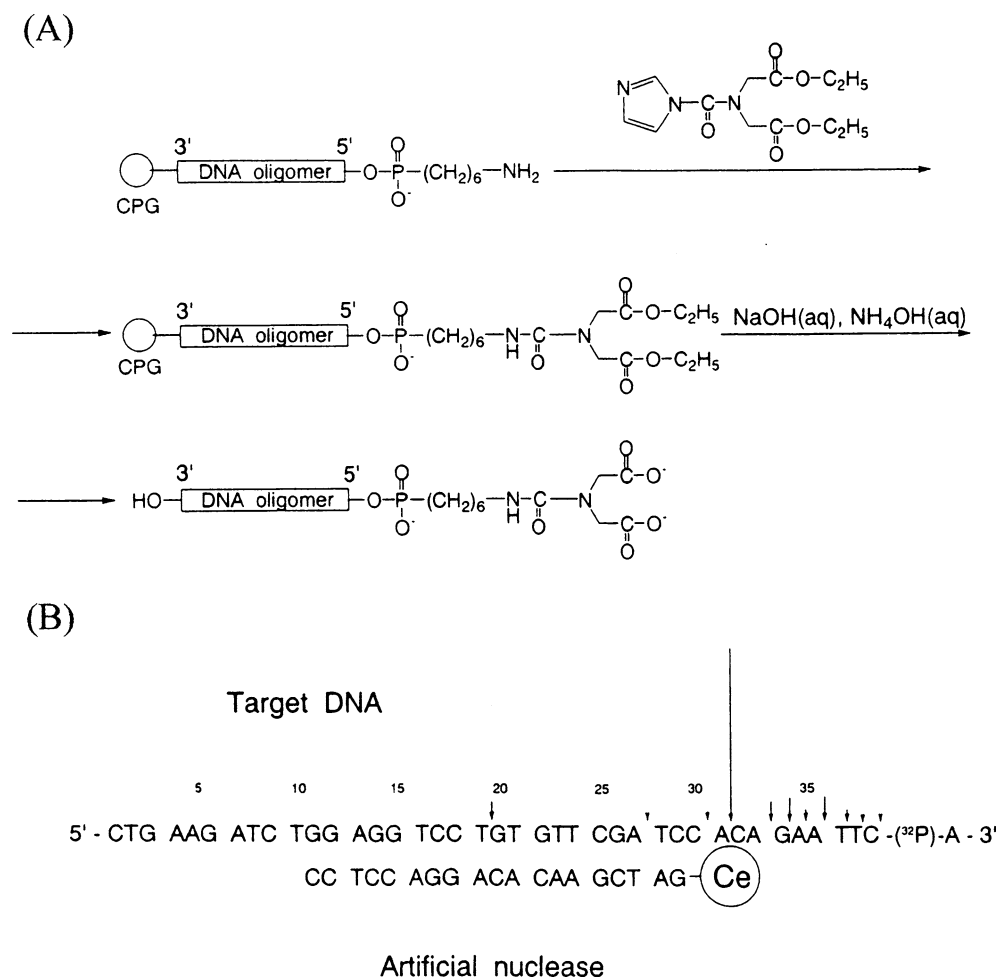


Fig. 17. Typical artificial enzyme for sequence-selective DNA hydrolysis. (A) The procedure for its preparation and (B) the site-selective scission pattern.

the intermediate which was protecting the iminodiacetate group were hydrolyzed under alkaline conditions. By these procedures, an iminodiacetate group was bound to the 5'-end of the oligonucleotide via a urea linkage. As shown in fig. 17(B), the Ce(IV) complex in this artificial restriction enzyme selectively hydrolyzed the target phosphodiester linkage of the DNA substrate, since this linkage was placed exactly near the catalytically active species in the substrate/catalyst complex.

The length and the sequence of oligonucleotides used to recognize the target sequence in these artificial restriction enzymes are freely chosen so that the sequence-specificity of these artificial enzymes can be increased as needed. In the above example, a 19-mer oligonucleotide was used, and thus the target sequence should appear at every 4¹⁹ nucleobases. This number is more than 50 fold greater than the number of total nucleobases in the DNA of human beings. In other words, even in this huge DNA, the scission site of this sequence-selective artificial restriction enzyme should come out at most only once. If necessary, site-specificity can be easily increased by increasing the length of oligonucleotide which is obtained by an automated synthesizer. The scission of DNA is totally hydrolytic, and thus the fragments obtained are successfully transformed into desired forms by using natural enzymes (e.g., alkaline phosphatase, polynucleotide kinase, and terminal deoxynucleotidyl transferase) (Sumaoka et al., 1998). The match between these artificial restriction enzymes and the current biotechnology is straightforward.

12. Non-covalent strategy for site-selective DNA scission

In contrast with “covalent strategy” described above, “non-covalent strategy” involves no covalent fixation of lanthanide complexes to oligonucleotides. The advantages of this strategy are (i) the simplicity of their preparation procedures and (ii) versatility and freedom of their molecular design. We do not need ligands which bind lanthanide ions to sequence-recognizing moiety. These factors are certainly advantageous for various applications, although notable efforts are necessary to achieve sufficiently high site-selectivity in the scission.

12.1. *Gap strategy for site-selective DNA scission (Kitamura and Komiyama, 2002)*

The Ce(IV)/EDTA complex preferentially hydrolyzes single-stranded DNA over double-stranded DNA (see sect. 3.2). This specificity indicates that the target site in the DNA substrate will be site-selectively hydrolyzed if this linkage is placed in single-stranded portion and the other linkages are kept in double-stranded portion. In order to satisfy this situation, gap structures were formed in the DNA substrate by using two shorter oligonucleotides which are complementary with some part of the substrate DNA. When these three components form duplexes in the reaction mixtures, most part of the DNA substrate is present in double strands but only a small designated part (the target site for the scission) is kept single-stranded.

Figure 18 shows typical gel electrophoresis patterns for the scission of gap structures by the Ce(IV)/EDTA complex. In absence of oligonucleotide additive, the whole part of the substrate DNA (50-mer) is single-stranded and thus this DNA is cut almost randomly without

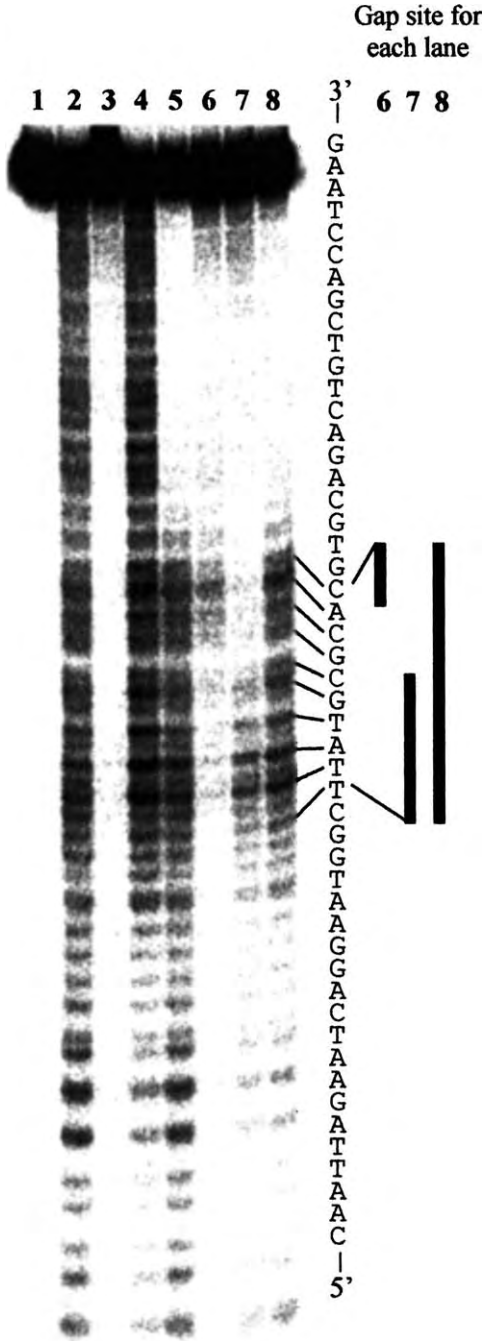


Fig. 18. Gap strategy for site-selective hydrolysis of DNA by the Ce(IV)/EDTA complex. Lane 1, control; lane 2, single-stranded DNA; lane 3, completely double-stranded DNA; lane 4, part of the DNA substrate (bottom region in the gel) is kept single-stranded; lane 5, another part of the DNA substrate (top region in the gel) is kept single-stranded; lane 6, 3-base gap; lane 7, 5-base gap; lane 8, 10-base gap. The bars on the right-hand side designate the gap sites. Reaction conditions: [Ce(IV)/EDTA complex] = 500 μ M, [NaCl]₀ = 100 mM, and [spermine] = 100 μ M at pH 7.0 and 37 °C.

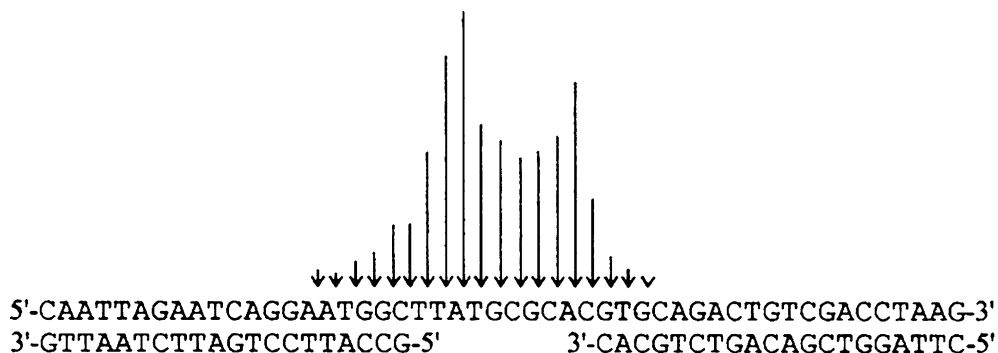


Fig. 19. Relative intensities of the DNA scission by Ce(IV)/EDTA complex with 10-base gap: lane 8 in fig. 18 is quantitatively analyzed.

any specific base-preference (lane 2). When gap structures are formed by using two oligonucleotide additives, however, the scission is strictly restricted to the corresponding gap-site. In lane 6, the nucleotides C28, A29, and C30 in the DNA substrate are unpaired, and the others are forming Watson–Crick base pairs (the position of the gap site is shown by the bar in the right-hand side of the gel). The scission by the Ce(IV) complex selectively occurs at these three unpaired nucleotides. With the 5-base gap (lane 7) and the 10-base gap (lane 8), the scission takes place also satisfactorily within the gap (see the quantitative analysis in fig. 19). The double-stranded region is not hydrolyzed to a measurable extent. Both the site-selectivity and the scission-efficiency are not much dependent on the sequence of substrate. As expected, the scission site concurrently moves when the gap site is shifted to the desired position by using appropriate oligonucleotide additives. The selective scission can be freely modulated.

12.2. *Bulge structures for site-selective DNA scission (Kitamura and Komiyama, 2002)*

Site-selective DNA scission by the Ce(IV)/EDTA complex is also successful when bulge-structures are formed at the target site by using appropriate oligonucleotide additives (fig. 20). These additives are complementary with most of substrate DNA, but shorter than the substrate. Thus, some nucleotides in the substrate could not find their partners and remain single-stranded (this kind of structure is referred to as a “bulge”). As depicted in lanes 4–7, the scission selectively occurs at the bulge-site. The scission efficiency is the largest around the center of the bulge. With increasing bulge length (5-, 6-, 8-, and 10-base bulge in lanes 4, 5, 6, and 7, respectively), the scission efficiency monotonously increases. Even with large bulges, as seen in lanes 6 and 7, the scission is sufficiently restricted to the bulge-site. The addition of 3-base gap at the joint of a bulge causes no effect.

Significantly, the bulge-induced site-selective DNA hydrolysis by the Ce(IV)/EDTA complex is notably accelerated when an oligoamine (e.g., spermine, spermidine, and ethylenediamine) is added to the reaction mixture. The acceleration by these oligoamines of the gap-induced site-selective DNA hydrolysis is also evident. In both cases, double-stranded DNA is hardly hydrolyzed by the Ce(IV)/EDTA complex even in presence of oligoamines. Only the

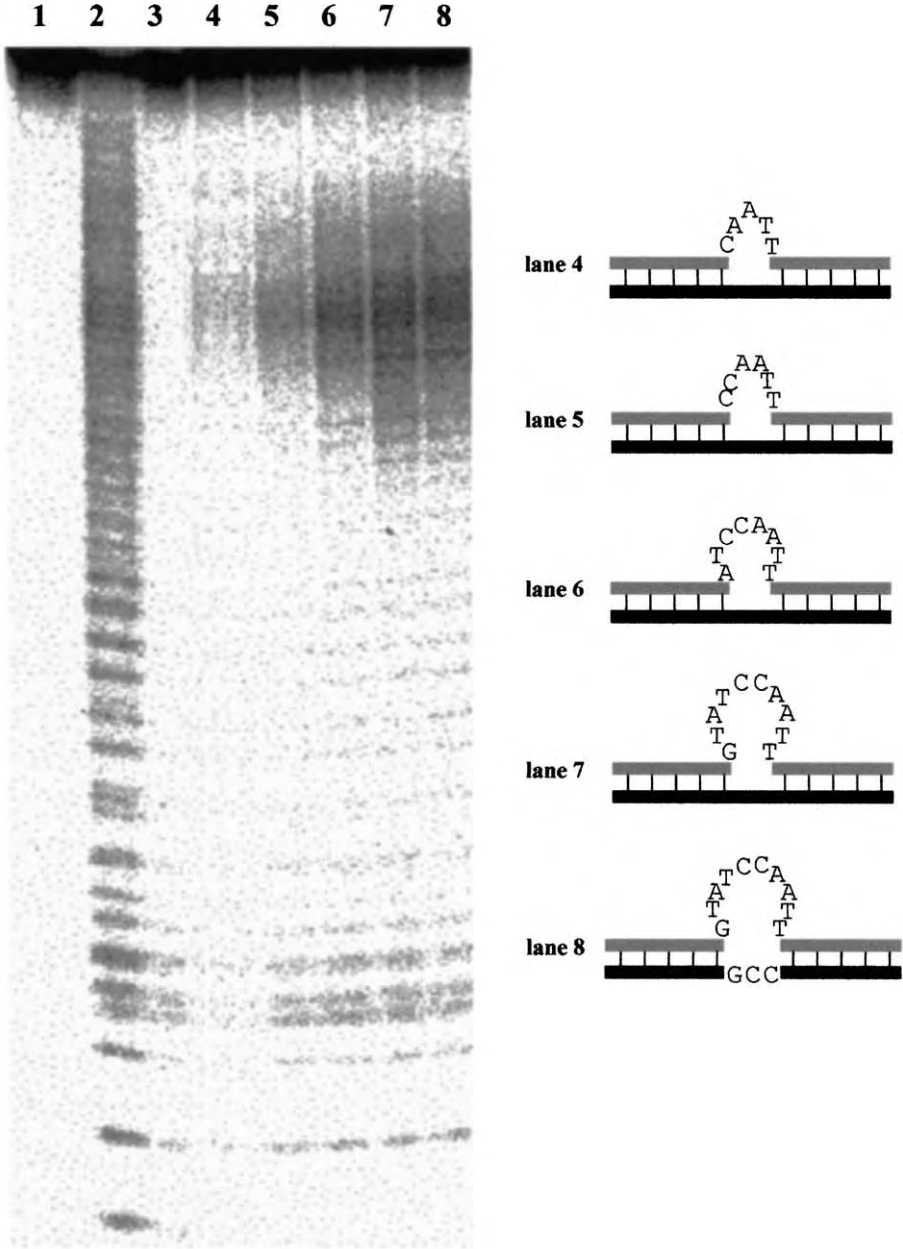


Fig. 20. Bulge strategy for the site-selective DNA hydrolysis by the Ce(IV)/EDTA complex. Lane 1, control; lane 2, single-stranded DNA; lane 3, completely double-stranded DNA; lane 4, 5-base bulge; lane 5, 6-base bulge; lane 6, 8-base bulge; lane 7, 10-base bulge; lane 8, 10-base bulge + 3-base gap.

hydrolysis of either the gap or bulge structures is selectively promoted. These findings present various possibilities for further improvement of this strategy, and one of them is described in sect. 12.4.

12.3. *Catalytic effect of a Ce(IV) hydroxide gel on the hydrolysis of gap and bulge sites*

In contrast with the remarkable substrate specificity in the DNA hydrolysis by Ce(IV)/EDTA complex, heterogeneous gels of Ce(IV) hydroxide, obtained by the addition of $\text{Ce}(\text{NH}_4)_2(\text{NO}_3)_6$ to buffer solutions in the absence of EDTA, hardly distinguished between single-stranded DNA and double-stranded one. With these gels, both of these two types of DNA were hydrolyzed at almost the same rates. Accordingly, no site-selective scission took place, even when gap- or bulge-structures were formed in the DNA substrate. Homogeneous Ce(IV)/EDTA complex is absolutely necessary for the present site-selective reactions based on either gap-strategy or bulge-strategy.

As shown in table 2 and described in sect. 3.2, the catalysis by the Ce(IV)/EDTA complex is specific to polynucleotides which are longer than tetranucleotides. Trinucleotides are not hydrolyzed, but are subject to the catalysis when a monophosphate is attached to their termini. Apparently, the catalysis of this complex requires three or more phosphoesters in the substrate. On the basis of this remarkable substrate-specificity, it was proposed that two (or more) phosphodiester linkages of the DNA substrate are simultaneously coordinated to the Ce(IV) ion (Sumaoka et al., 2001). As a result of this coordination, the phosphodiester linkages are sufficiently activated and hydrolyzed under physiological conditions. Undoubtedly, these catalytic processes must be accompanied by notable conformational changes of the DNA backbone, since the metal ions are bound by two or more phosphoesters in the substrate. These factors are responsible for the structure-reactivity relationship in the present gap- and bulge-induced site-selective DNA scission. The gap strategy is successful only when the size of gap (the number of unpaired nucleotides) is greater than three, since otherwise the conformational change of the DNA main chain for the coordination to the Ce(IV) induces unacceptably large strain. The double-stranded portion in DNA is too rigid for this conformational change and is hardly hydrolyzed. In the bulge strategy, the bulge length must be 5-base or longer to provide the required molecular flexibility.

12.4. *Covalent conjugates of oligoamine and acridine for the promotion of gap-selective DNA hydrolysis by Ce(IV)/EDTA complex (Yamamoto et al., 2003)*

As described in the previous sections, both gap sites and bulge sites in substrate DNA are preferentially hydrolyzed by homogeneous Ce(IV)/EDTA complex under physiological conditions. Notable site-specificity in DNA hydrolysis has been for the first time substantiated by non-covalent strategy which involves no fixation of molecular scissors to sequence-recognizing moieties. By using appropriate oligonucleotides as the additives, the sites of selective scission can be freely chosen according to our needs.

In order to further promote the scission rate and the site-selectivity, both (i) the accelerator of catalysis by the Ce(IV)/EDTA complex and (ii) a DNA-binding molecule were covalently conjugated. In typical examples, spermidine, dipropylentriamine, and propylenediamine (all

of them accelerate the catalysis of the DNA hydrolysis by the Ce(IV)/EDTA complex, see sect. 3.2) were bound to acridine, a well-known intercalator, via a hexamethylene linker. At pH 7.0, these conjugates have 4, 4, and 3 positive charges, respectively. The ring-nitrogen atoms of the acridine are mostly protonated there and all the aliphatic amino residues are also protonated. As shown on fig. 21, gap structures of desired length were formed in the DNA substrate by using appropriate oligonucleotides. In lanes 4 and 5, 10-base gap ranging from T40 to C49 is formed. In the presence of the spermidine-acridine conjugate, the gap site is preferentially hydrolyzed (lane 5). This gap-selective DNA scission assisted by the conjugate is far faster than the scission without the conjugate (lane 4). Similar synergetic cooperation between the Ce(IV)/EDTA complex and spermidine-acridine conjugate is also observed when 5-base gap or 15-base gap is formed in the DNA substrate (lanes 2–3 and lanes 6–7, respectively). The dipropylenetriamine-acridine conjugate and the propylenediamine-acridine conjugate also significantly enhance the selective DNA scission at the gap site. These conjugates themselves are entirely inactive for the DNA hydrolysis, so that the cooperation of the Ce(IV)/EDTA complex and these conjugates is evident.

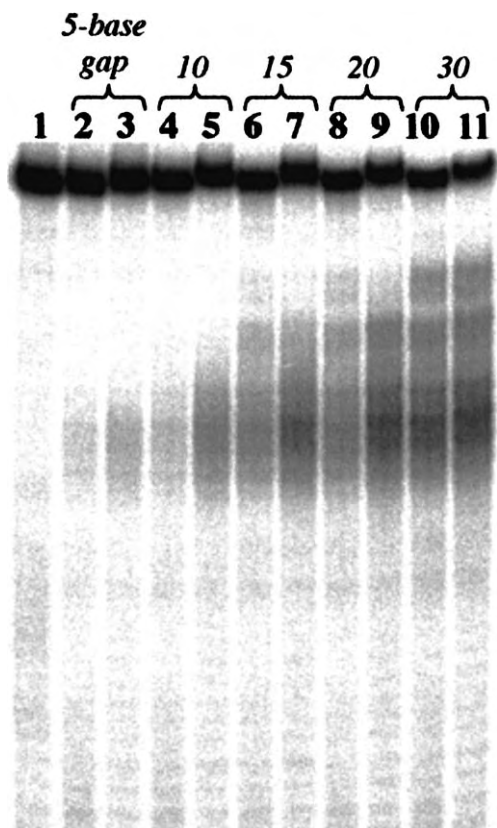


Fig. 21. Autoradiographs for the hydrolysis of gaps of different lengths by the combination of spermidine-acridine conjugate and Ce(IV)/EDTA complex. Lane 1, control; lane 2, 5-base gap without the conjugate; lane 3, 5-base gap with the conjugate; lane 4, 10-base gap without the conjugate; lane 5, 10-base gap with 1; lane 6, 15-base gap without the conjugate; lane 7, 15-base gap with the conjugate; lane 8, 20-base gap without the conjugate; lane 9, 20-base gap with the conjugate; lane 10, 30-base gap without the conjugate; lane 11, 30-base gap with the conjugate.

In contrast with the remarkable acceleration by these oligoamine-acridine conjugates, quinacrine (an acridine derivative having only an alkylated exocyclic amino group) shows no measurable effect on the hydrolysis at the gap site under the conditions employed. Without being bound to acridine, spermidine, dipropylentriamine, and propylenediamine yield only poor activity. The efficient promotion of the Ce(IV)/EDTA complex-induced hydrolysis of gap site absolutely requires the intramolecular cooperation of oligoamine and acridine. The rate of hydrolysis at the gap site monotonously increases with increasing concentration of these conjugates, whereas the hydrolysis of double-stranded portion is little affected. Accordingly, the gap-selective scission becomes much more clear-cut with increasing concentration of the conjugates.

12.5. *Hybridization of covalent and non-covalent strategies for improved site-selective DNA scission (Arishima et al., 2003)*

Still more efficient and clear-cut site-selective scission was achieved when Ce(IV)/EDTA complex was fixed near a gap in the DNA substrate. Oligonucleotides bearing ethylenediamine-*N,N,N'*-triacetate groups are remarkable cofactors for this purpose and enormously promote the selective hydrolysis at the gap site. At pH 7.0 and 37 °C, a DNA substrate (41-mer) was treated with the Ce(IV)/EDTA complex in presence of various modified oligonucleotide additives. Figure 22(A) shows the typical gel electrophoresis patterns while the corresponding structures formed from the substrate and the additives are schematically depicted in fig. 22(B). In lane 2, one of the oligonucleotide additives used is complementary with the 5'-side half of the DNA substrate, and bears an ethylenediamine-*N,N,N'*-triacetate group on the X residue at its 5'-terminus. The other additive is complementary with the 3'-side half of the DNA substrate, and bears an ethylenediaminetriacetate group at its 3'-terminus. As the result, in the duplex formed from the DNA substrate and these two additives, two ethylenediamine-*N,N,N'*-triacetate groups are placed near T21 which remains unpaired at the gap site. Significantly, the gap site is efficiently hydrolyzed with high selectivity. When unmodified oligonucleotides bearing no ethylenediaminetriacetate groups are used as additives under the same conditions, no DNA scission occurs. With these unmodified oligonucleotide additives, even 5-base gaps are hydrolyzed much less efficiently (lane 1). Note that the scission efficiency of the gap strategy (without ethylenediaminetriacetate groups) is evident only when the gap is 5-base or longer (see sect. 12.1). It is conclusive that the ethylenediaminetriacetate groups at the gap site enormously promote the selective DNA scission. The gap-selective scission, promoted by these modified oligonucleotides, is still more efficient when both of the additives bore two ethylenediaminetriacetate groups, and four ethylenediamine-*N,N,N'*-triacetate groups are placed near the gap site (lane 3). The system involving six ethylenediaminetriacetate groups at the gap site is also successful for site-selective scission (lane 4). Thus, highly selective DNA scission can be achieved at the gap site by attaching two or more ethylenediaminetriacetate groups to it. In a proposed mechanism, two (or more) Ce(IV)/EDTA complexes are bound by the ethylenediamine-*N,N,N'*-triacetate groups, and accumulated at the gap-site. These complexes show cooperative catalysis, resulting in unprecedentedly efficient site-selective DNA hydrolysis. Such a mechanism is reminiscent of the

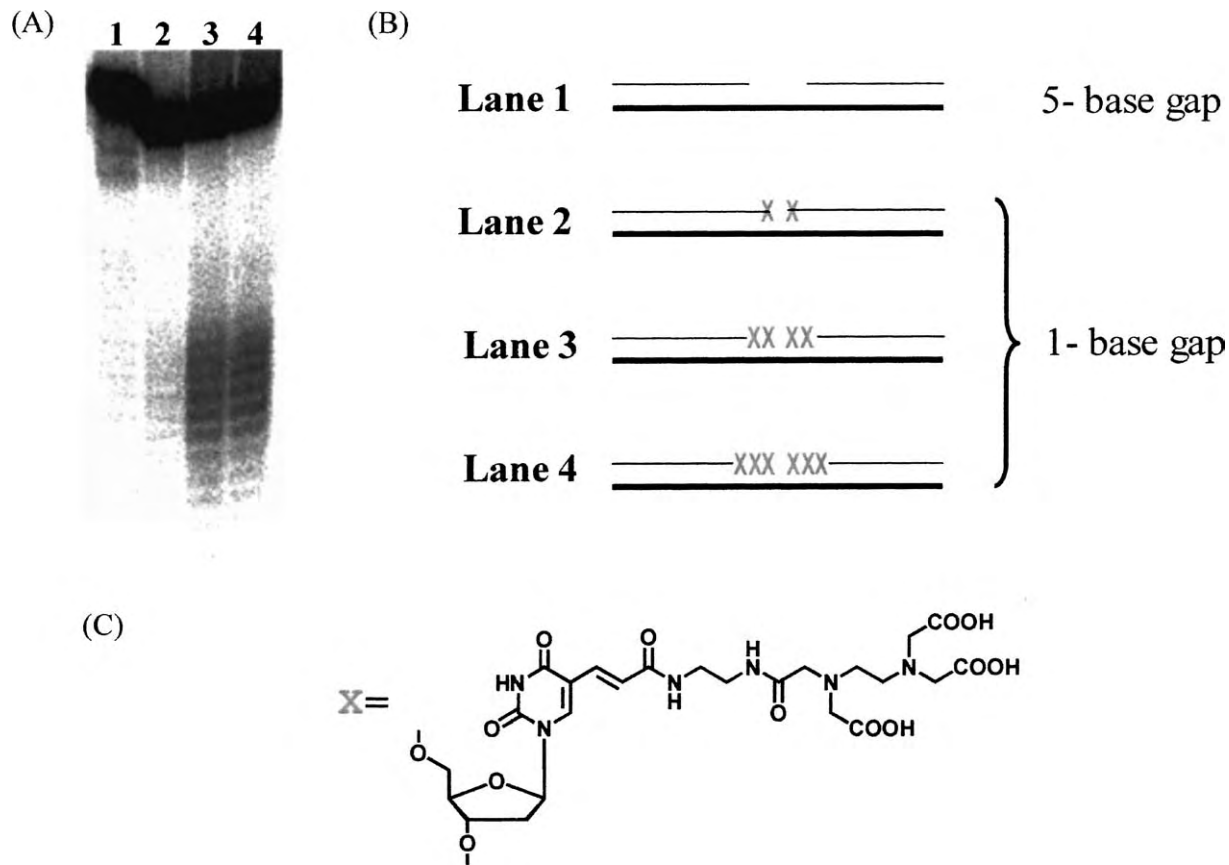


Fig. 22. Combination of non-covalent and covalent strategies for improved site-selective DNA scission. Lane 1, 5-base gap without ethylenediamine-*N,N,N'*-triacetate groups; lane 2, 1-base gap with two ethylenediaminetriacetate groups at the gap site; lane 3, 1-base gap with four ethylenediaminetriacetate groups at the gap site; lane 4, 1-base gap with six ethylenediaminetriacetate groups at the gap site. The systems are schematically depicted in (B). The residue X is a derivative of thymidine and bears an ethylenediamine-*N,N,N'*-triacetate group as presented in (C).

cooperation of two Ce(IV) ions in the $[\text{Ce}^{\text{IV}}_2(\text{OH})_4]^{4+}$ hydroxide cluster for DNA hydrolysis by Ce(IV) ions in absence of EDTA (see sect. 4). Consistently, the gap-selective DNA scission vanishes when all the carboxylate groups in the ethylenediaminetriacetate groups in these modified oligonucleotide additives are converted into their amides. Although ethylenediaminetriacetate is inferior to EDTA in metal-binding ability, the phosphodiester residues adjacent to the target linkage can assist the binding. The gap site is necessary for the scission, mainly because this catalytic process is accompanied by notable conformational change of the main chain of DNA, as is the case of reactions without ethylenediaminetriacetate groups.

13. Covalent strategy for site-selective RNA hydrolysis

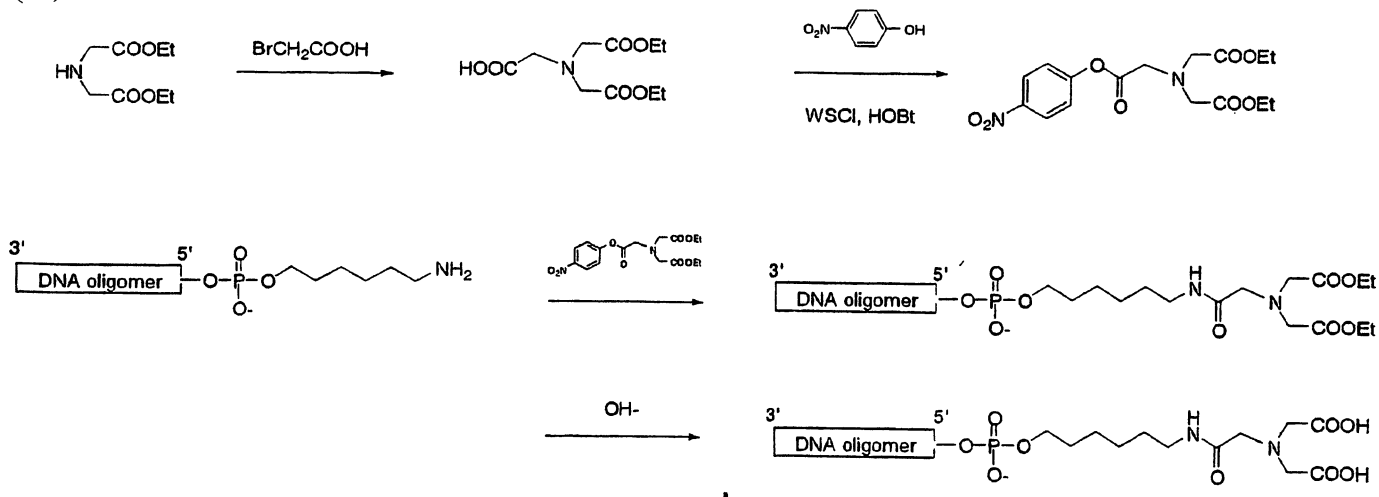
Conjugates of an iminodiacetate and DNA oligomers were synthesized as shown in fig. 23(A) (Matsumura et al., 1994). First, the DNA oligomer, which is complementary with the RNA substrate (near the targeted scission site), was prepared on an automated synthesizer. In the final stage of the DNA synthesis, an amino linker was attached to the 5'-end of DNA by using the commercially available phosphoramidite monomer. This modified DNA was reacted with the *p*-nitrophenyl ester of *N,N*-bis(ethoxycarbonylmethyl)glycine, and then the ethyl esters were hydrolyzed under alkaline conditions. By these procedures, an iminodiacetate group was bound to the DNA via an amide linkage. The artificial enzymes were prepared in situ by mixing these conjugates with lanthanide(III) chloride in water. According to the polyacrylamide gel electrophoresis, the RNA scission occurred selectively at the target site where the lanthanide complex was fixed (fig. 23(B)). When $[\text{DNA-iminodiacetate conjugate}]_0 = [\text{Lu(III)}]_0 = 10 \mu\text{M}$ at pH 8 and 37 °C, the conversion for the sequence-selective RNA scission was around 20 mol% after 8 h. In order to achieve selective scission, the $[\text{Lu(III)}]/[\text{iminodiacetate}]$ ratio must be 1.0 or smaller. Otherwise, the solution contains free Lu(III) ions and non-selective RNA scission by them concurrently occurs.

In place of the iminodiacetate group, so-called "texaphyrins" (fig. 12(C)) can also be used as molecular scissors (Magda et al., 1997, 1994). In a typical example, the Dy(III)/texaphyrin complex was attached to the 5'-end of the 20-mer DNA, and an RNA substrate was treated with the conjugate of the Dy(III)-texaphyrin complex with this DNA at pH 7.5 and 37 °C. The sequence-selectivity for the scission was satisfactorily high. The half-life of RNA cleavage depended on the length of the linker between the Dy(III)/texaphyrin complex and the DNA for sequence-recognition. In general, shorter linkers provided better results.²

In order to activate the target phosphodiester linkage and promote the site-selective scission, a bulge structure was intentionally formed in the RNA substrate (fig. 24) (Hall et al., 1996; Hüsken et al., 1996). The DNA oligomer, used as the sequence-recognizing moiety in these attempts, was complementary with the target RNA, but a few nucleotides in the middle were absent to form the bulge-structure. When the molecular scissors, the lanthanide complexes

² In the second-generation artificial ribonucleases, molecular scissors are incorporated into the inside of DNA strand in order to achieve efficient catalytic turnover. Upon scission, the RNA fragment used for the binding to DNA is divided into two small fragments. The stability of the RNA/DNA hetero-duplex decreases as the RNA becomes shorter, so that the small RNA fragments are spontaneously removed from the artificial enzymes.

(A)



CUTTING DNA AND RNA

(B)

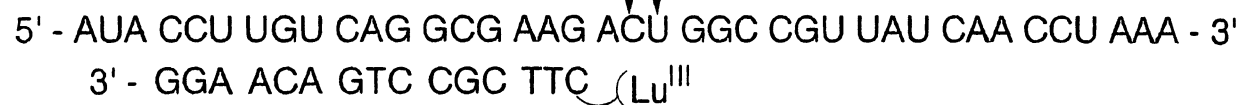


Fig. 23. Lu(III)/DNA hybrid as sequence-selective ribonuclease: (A) synthetic procedure for DNA-iminodiacetate hybrid and (B) the RNA scission pattern.

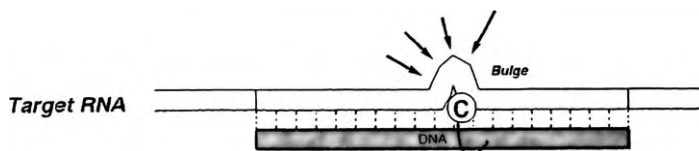


Fig. 24. Schematic view of sequence-selective RNA scission by artificial ribonucleases involving bulge-forming DNA. The black ribbons show the oligonucleotides used for the artificial enzymes to recognize the target sites.

of Schiff-base macrocycles (fig. 12(B)) were bound to this DNA oligomer, the phosphodiester linkages in the bulge were selectively hydrolyzed. The scission efficiency was increased by the bulge formation. In a proposed mechanism, the conformations of the ribose residues in the bulge-structures are more suitable for the intramolecular attack by the 2'-OH towards the phosphorus atom.

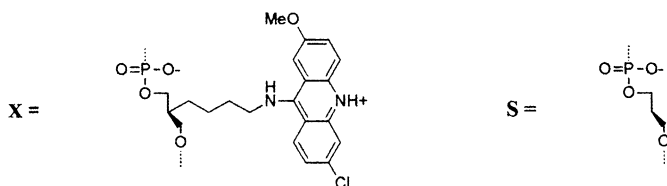
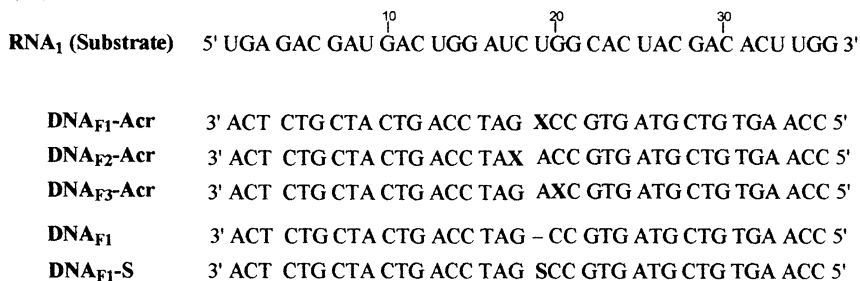
14. Non-covalent strategy for site-selective RNA scission

14.1. Novel RNA cutters

The second generation artificial ribonucleases employ “non-covalent strategy”. Their site-selective scission ability is based on two factors: (i) the target site in the RNA substrate is activated by non-covalent interactions with the “activator”, and (ii) the RNA in RNA/DNA hetero-duplex is strongly resistant against the digestion by lanthanide ions used as the molecular scissors. In contrast with “covalent strategy”, the lanthanide ions are never bound to any sequence-recognizing moiety, and thus can develop their intrinsic activity. As expected, the scission efficiency is satisfactorily high. Typical examples are presented in fig. 25. These “non-covalent” artificial ribonucleases are composed of an RNA-activator (chemically modified oligonucleotide(s)) and a catalyst for RNA scission (Kuzuya and Komiyama, 2000; Kuzuya et al., 2002b). The type-I RNA-activator is an oligonucleotide which bears an acridine in the middle (fig. 25(A)). On the other hand, the type-II activator is the combination of an oligonucleotide bearing an acridine and an unmodified oligonucleotide (fig. 25(B)). When the RNA substrate forms a hetero-duplex with the oligonucleotide(s) in these RNA-activators, most of the ribonucleotides in the RNA form Watson–Crick base pairs with the counterpart nucleotides. However, the ribonucleotide, which is located in front of the acridine, remains unpaired. As a result, the phosphodiester linkages adjacent to this unpaired ribonucleotide are selectively activated, and preferentially hydrolyzed by lanthanide ions over the other linkages.

As shown in fig. 25(A), DNA_{F1}-Acr has an acridine moiety in its internal position, and is complementary with most part of the substrate RNA₁. In the RNA₁/DNA_{F1}-Acr hetero-duplex, only ribonucleotide U19 (in front of the acridine) is kept free from Watson–Crick base-pairing. When this system was treated with LuCl₃, the substrate RNA was site-selectively and efficiently hydrolyzed (lane 9 in fig. 26). The selective scission sites are the 5'-side of U-19 (major scission-site) and its 3'-side (minor scission-site), as schematically depicted in fig. 27(A). At pH 7 and 37 °C, more than half of the substrate RNA was cleaved

(A)



(B)

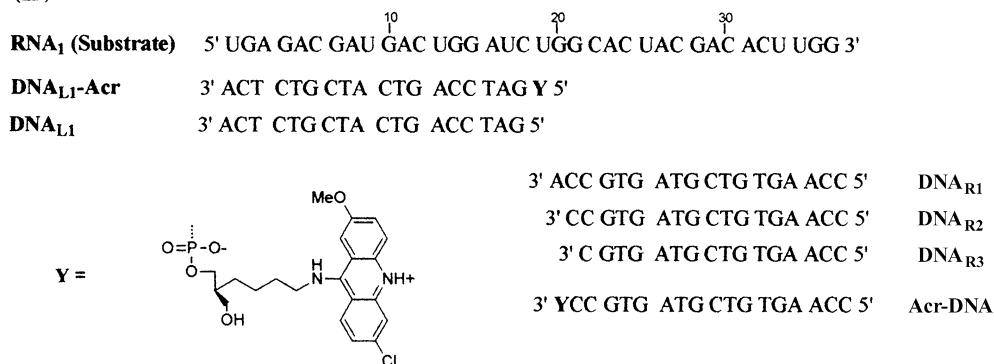


Fig. 25. Structures of the type-I RNA-activators (A) and the type-II RNA-activators (B) for “non-covalent strategy” for site-selective RNA hydrolysis.

within 6 h. The site-selectivity is satisfactorily high throughout the whole process. In contrast, the scission is marginal when a trimethylene spacer is inserted into DNA_{F1} in front of U19 (DNA_{F1}-S; lanes 2, 5, and 8). Thus the acridine residue is absolutely essential for the present site-selective scission. The activity of various lanthanide ions at pH 8 is as follows: Ho(III), Dy(III), Tb(III), Gd(III) > Lu(III), Yb(III), Tm(III), Er(III) > Sm(III), Eu(III) > La(III) > Ce(III) > Pr(III) > Nd(III).

Site-selective scission was also successful, when the type-I activator was divided into an oligonucleotide bearing an acridine and another unmodified oligonucleotide (type-II RNA-activator, fig. 27(B)). For example, DNA_{L1}-Acr is complementary with the 5'-side portion of the substrate RNA and bears an acridine at the 5'-end, while DNA_{R1} is complementary with

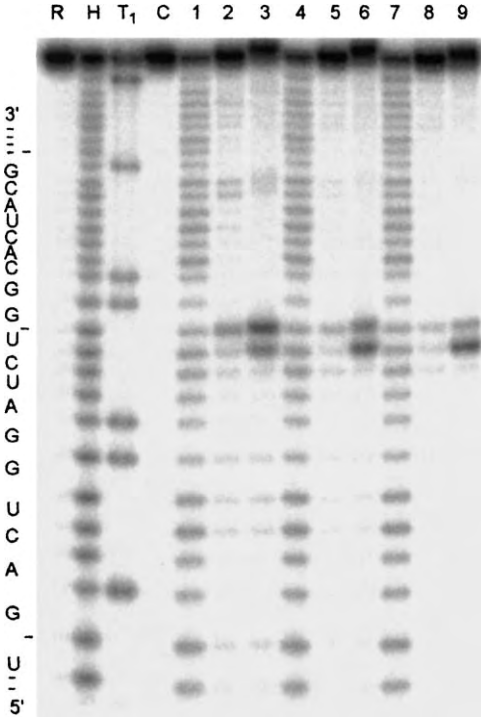


Fig. 26. Site-selective RNA scission by combinations of the type-I activator and lanthanide(III) ion. Lane 1, La(III) only; lane 2, DNA_{F1}-S/La(III); lane 3, DNA_{F1}-Acr/La(III); lane 4, Eu(III) only; lane 5, DNA_{F1}-S/Eu(III); lane 6, DNA_{F1}-Acr/Eu(III); lane 7, Lu(III) only; lane 8, DNA_{F1}-S/La(III); lane 9, DNA_{F1}-Acr/Lu(III). At pH 8.0 and 37 °C for 2 h; [RNA₁]₀ = 1, [DNA_{F1}-S]₀ = [DNA_{F1}-Acr]₀ = 10, and [LnCl₃]₀ = 100 μM; [NaCl]₀ = 200 mM. R, RNA₁ only; H, alkaline hydrolysis; T₁, RNase T₁ digestion; C, control reaction in buffer solution.

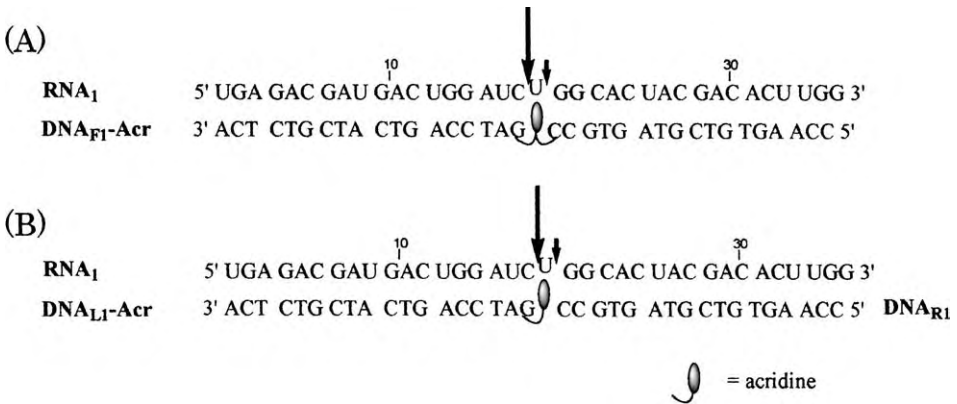


Fig. 27. Site-selective RNA scission by “non-covalent strategy”: (A) the system composed of the type-I activator (DNA_{F1}-Acr) and Lu(III) and (B) the system composed of the type II activator (DNA_{L1}-Acr + DNA_{R1}) and Lu(III).

the 3'-side portion of the RNA (see fig. 25(B)). Accordingly, only U-19 of the substrate RNA is unpaired. Upon addition of Lu(III), this RNA is selectively and efficiently hydrolyzed at the phosphodiester linkage in the 5'-side of U-19 (lane 3 in fig. 28). Another weak scission

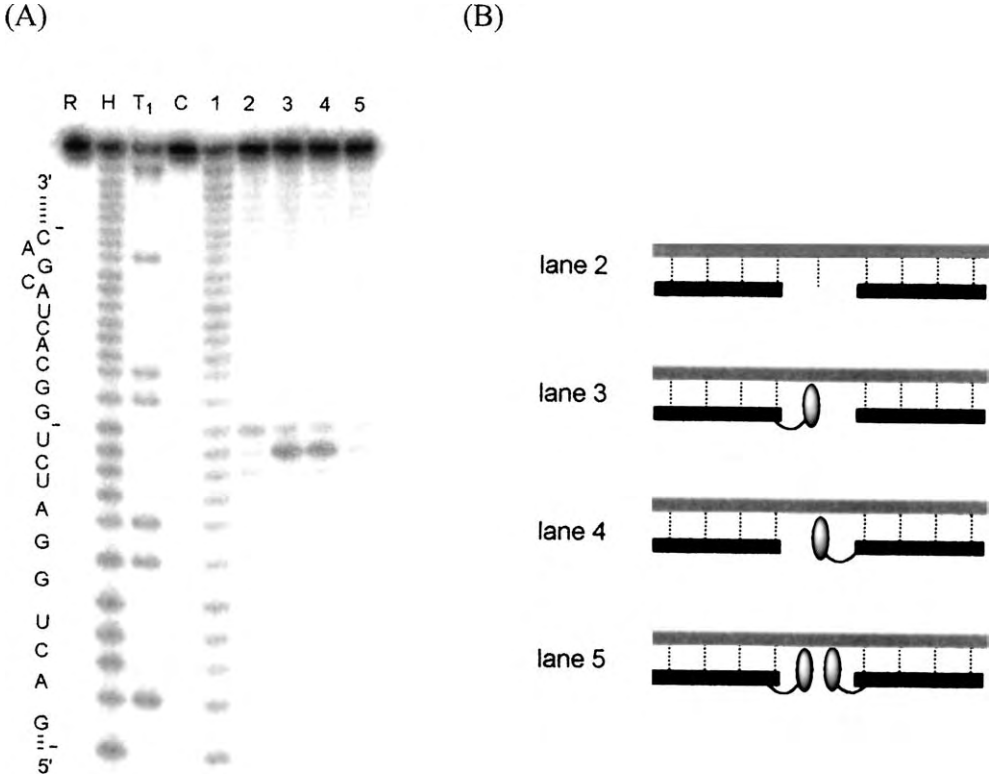


Fig. 28. Site-selective RNA scission by various combinations of type-II activator and Lu(III): (A). Lane 1, Lu(III) only; lane 2, $\text{DNA}_{L1}/\text{DNA}_{R1}/\text{Lu(III)}$; lane 3, $\text{DNA}_{L1}\text{-Acr}/\text{DNA}_{R1}/\text{Lu(III)}$; lane 4, $\text{DNA}_{L1}/\text{Acr-DNA}_{R1}/\text{Lu(III)}$; lane 5, $\text{DNA}_{L1}\text{-Acr}/\text{Acr-DNA}_{R1}/\text{Lu(III)}$. At pH 8.0 and 37 °C for 2 h; $[\text{RNA}]_0 = 1$, [each of modified or unmodified oligonucleotides] $_0 = 10$, and $[\text{LuCl}_3]_0 = 100 \mu\text{M}$; $[\text{NaCl}]_0 = 200 \text{ mM}$. (B) Schematic representations of the combinations used in (A).

occurs at its 3'-side. These scission sites are exactly identical with those using $\text{DNA}_{F1}\text{-Acr}$ as the type-I activator. The site-selective RNA scission is also successful, when an unmodified oligonucleotide DNA_{L1} is combined with a modified oligonucleotide Acr-DNA_{R1} which bears an acridine at the 3'-end (lane 4 in fig. 28). The scission efficiency is comparable with that of the $\text{DNA}_{L1}\text{-Acr}/\text{DNA}_{R1}/\text{Lu(III)}$ system. Thus, an acridine residue can be attached to either of the two oligonucleotides. When either one of $\text{DNA}_{L1}\text{-Acr}$ and DNA_{R1} was used, however, the RNA was cleaved randomly throughout the region which remained single-stranded without the coverage by the oligonucleotides. No activation by the acridine occurred at either U-19 or the other sites. In order to activate RNA satisfactorily and achieve site-selective scission, both these oligonucleotides are necessary and, in addition, one of them must have an acridine residue at the end.

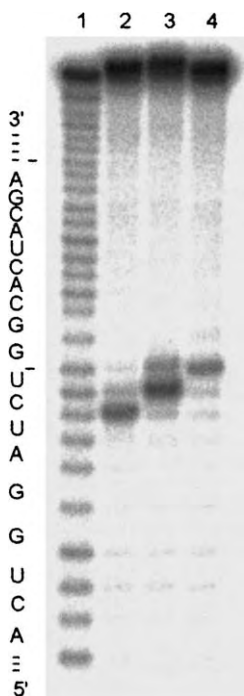


Fig. 29. Effect of the sequence of target site on the site-selective RNA scission by “non-covalent strategy”. Lane 1, Lu(III) only; lane 2, DNA_{F2}-Acr/Lu(III); lane 3, DNA_{F1}-Acr/Lu(III); lane 4, DNA_{F3}-Acr/Lu(III). At pH 8.0 and 37 °C for 2 h; [RNA₁]₀ = 1, [modified oligonucleotide]₀ = 10, and [LuCl₃]₀ = 100 μM; [NaCl]₀ = 200 mM.

One of the most significant advantages of these non-covalent systems is the fact that any phosphodiester linkage in the RNA substrate is effectively hydrolyzed. There is no noticeable sequence-specificity for the scission (fig. 29). The site can be selectively cut by simple placing of an acridine in front of the target site. This is significant from the viewpoints of various applications, since ribozymes strictly choose a specific sequence (usually triad) at the scission site. In the DNA/RNA hetero-duplexes, the acridine groups are sandwiched by the two Watson–Crick base pairs (see fig. 30). The acridine is so large in size that it cannot be simultaneously accommodated together with the unpaired RNA base. As a result, the unpaired RNA base is pushed out of the hetero-duplex, perturbing the conformation of the target site in the RNA. The 2'-OH at the scissile linkage is located near the corresponding phosphorus atom, and its intramolecular nucleophilic attack is greatly promoted. Furthermore, the acridine, which is protonated under the reaction conditions, acts as an acid catalyst and promotes the removal of leaving 5'-OH of oligoribonucleotide (Kuzuya et al., 2002a, 2002b). Because of these two factors, stable phosphodiester linkages in RNA are promptly hydrolyzed.

14.2. Two-site RNA cutters for SNPs genotyping (Kuzuya et al., 2003)

By extending the non-covalent strategy described in sect. 14.1, new RNA cutters which selectively cut RNA substrates at two designated sites were prepared. With these tools, any portion of fragment can be clipped out of RNA substrates (fig. 31). These RNA cutters were prepared

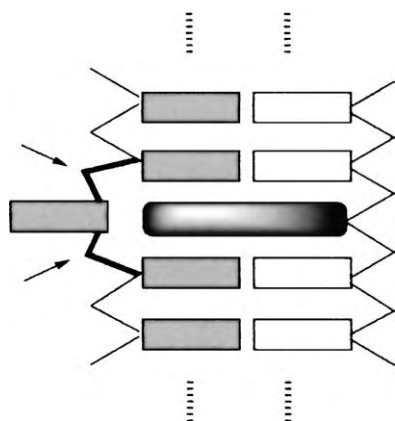


Fig. 30. Proposed mechanism of site-selective scission by the non-covalent RNA cutters. The acridine is shown by a rounded rectangle, and the activated phosphodiesters are shown by arrows.

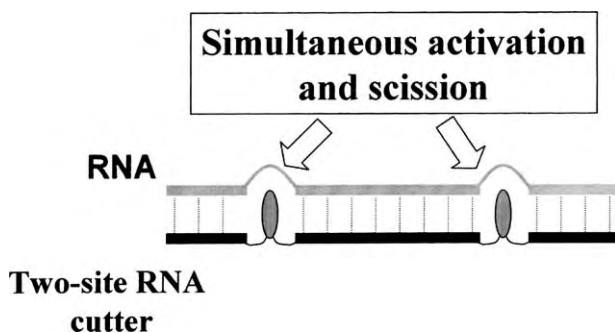
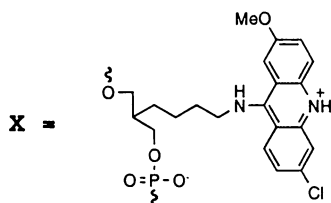
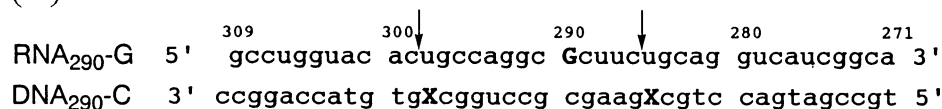


Fig. 31. Two-site RNA cutters based on “non-covalent strategy” for clipping selected fragment from the RNA substrate. The two phosphodiester linkages in front of the two acridines are simultaneously activated and selectively hydrolyzed by lanthanide ions.

by attaching two acridines to oligonucleotides (fig. 32(A)). When these modified oligonucleotides form duplexes with the sample RNA, the two phosphodiester linkages in front of the two acridines are selectively activated and cut by lanthanide ions (the scission sites are shown by arrows). The scission efficiency is hardly dependent on either the nature of the nucleobases in front of the acridines or the RNA sequence in their vicinity. Thus, any predetermined fragment of desired length can be clipped out from RNA substrates in high yields.

As an application of this method, designated RNA fragments are clipped out from human genomes and analyzed by mass spectrometry. This method is quite useful for genotyping of various kinds of single nucleotide polymorphisms (SNPs). SNPs are the alteration of one DNA base in genes of human beings. Since they are strongly related to hereditary diseases, the design of tailored drugs, and many other biomedical properties, precise and rapid detection of SNPs is one of the most attractive themes at present. In an example, RNA from the human genome was treated with the two-RNA cutter/Lu(III) system, and the products of the two-site RNA hydrolysis were analyzed by MALDI-TOF MS. As shown in fig. 32(B), three peaks were clearly observed. The signal at $m/z = 4168.8$ is assignable to the 13-mer fragment ranging from U298 to C286 (theoretical value = 4169.5). Two other peaks ($m/z = 3542.6$ and 4787.7) correspond to the 5'-side portion of the RNA substrate (G309-C299) and its 3'-side fragment

(A)



(B)

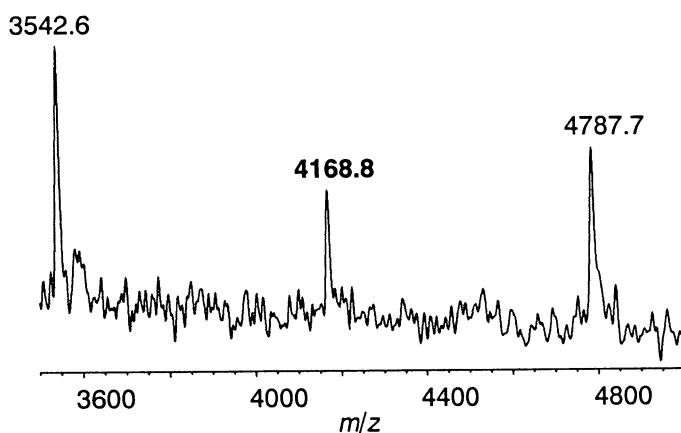


Fig. 32. Typical MALDI-TOF MS spectrum for the products of site-selective scission of RNA from human gene by Lu(III) in presence of oligonucleotides bearing two acridines (the sequences are presented in (A)). The signal at $m/z = 4168.8$ corresponds to the 13-mer fragment (U298-C286) which involves a potent SNP site (the nucleotide at position 290). The signals at $m/z = 3542.6$ and 4787.7 are for the 5'-side fragment (G309-C299) and the 3'-side fragment (U285-A271), respectively.

(U285-A271), respectively. Apparently, both target sites (5'-sides of U298 and U285) were efficiently activated and hydrolyzed by the Lu(III) ion. It was concluded that the nucleobases at the potent SNP site (number 290) in this sample is guanine (G). If this nucleobase is altered to adenine (A) in another patient, for example, this alternation should be directly detected by the difference (16.0) in the mass numbers of fragments. In the same way, various SNPs can be successfully analyzed. The present two-site RNA cutters have the following advantages:

- (1) the scission selectively takes place at two designated sites,
- (2) these scissions are prompt irrespective of the RNA sequence,
- (3) the distance between the two sites for the scission is easily controllable, and

(4) the RNA fragments, prepared by the two-site scission, are sufficiently protected from subsequent digestion.

These methods should be also valuable for further developments of RNA science. For example, RNA fragments, which have complicated tertiary structures or involve modified nucleobases, are easily obtainable from naturally occurring RNAs. Preparation of chimera of two modules from two sources should be also greatly facilitated.

15. Conclusions

For a long period of time, rare-earth science did not impact much on biotechnology, and vice versa. About 10 years ago, however, it was found that lanthanide ions efficiently hydrolyze DNA and RNA under physiological conditions. These findings were critical for the developments of biotechnology and molecular biology in that we could for the first time cut DNA and RNA without using naturally-occurring enzymes. At the same time, they greatly contributed to close the gap between rare-earth science and biotechnology. The most significant point for rare-earth science is the fact that efficient catalytic effects for the hydrolysis of DNA and RNA are entirely specific to the lanthanide ions. At present, only Ce(IV) ion can hydrolyze non-supercoiled DNA with reasonable efficiency, apart from naturally occurring enzymes. The catalytic activities of lanthanide(III) ions for RNA hydrolysis are far greater than those of other non-enzymatic catalysts. Furthermore, Ce(IV) is also effective for the hydrolysis of proteins which are important biopolymers; these reactions are beyond the scope of this article so that the readers who are interested in them should refer to the published literature (Takarada et al., 2000; Komiyama and Takarada, 2003). Thus, from now on, lanthanide ions will be inevitable tools for biotechnology and molecular biology.

The remarkable activity of lanthanide ions has been further taken advantage of for site-selective scission of DNA and RNA, which is essential for the manipulation of huge DNAs of higher animals and higher plants and the relevant RNAs. Two strategies were used for the sequence-selective scission: (i) "covalent strategy" in which lanthanide complexes are covalently bound to the oligonucleotides that are complementary with the substrate DNA and RNA, and (ii) "non-covalent strategy", in which the target phosphodiester linkage is differentiated from the others in the substrate in terms of intrinsic reactivity. In "non-covalent strategy", lanthanide ions are not linked to any sequence-recognizing moiety. For site-selective hydrolysis of DNA, Ce(IV) ion and Ce(IV) complexes are being exclusively used, since they are the sole catalysts available for the hydrolysis of non-supercoiled DNA at present. For RNA hydrolysis, various lanthanide(III) ions and their complexes are widely used because of their far greater activities than any other catalysts. Sufficiently selective artificial enzymes have been already obtained, and further improvements of their molecular design are still being made.

Recent detailed studies have shed light on the mechanism of these exciting catalytic activities of lanthanide ions. For DNA hydrolysis, the tetracationic bimetallic hydroxo cluster $[\text{Ce}^{\text{IV}}_2(\text{OH})_4]^{4+}$ is the active species. The Ce(IV) ion notably activates the phosphodiester linkages in DNA through electron-withdrawal from these linkages. The stability of the trivalent state of Ce is favorable for this electron-withdrawal. Furthermore, the orbitals of the

Ce(IV) being mixed with the orbitals of phosphate, the electrophilicity of the P atom is enhanced. As a result, the nucleophilic attack by Ce(IV)-bound hydroxide ion towards this P atom for the formation of pentacoordinated intermediate is remarkably promoted. The removal of the leaving group (5'-OH of oligonucleotide) from the intermediate is also facilitated by the acid catalysis by the bimetallic cluster. In RNA hydrolysis, $[\text{R}^{\text{III}}_2(\text{OH})_2]^{4+}$ is the active species. The breakdown of the pentacoordinated intermediate, which is rate-limiting, is accelerated by this bimetallic cluster. The activity at pH 7 increases with increasing atomic number of the lanthanide(III) ion, since the concentration of the active species increases in this order. The cooperation of two metal ions in DNA and RNA hydrolysis is reminiscent of the recent findings that binuclear and trinuclear metal complexes are far more active for the hydrolysis of phosphoesters than are the corresponding mononuclear metal complexes (Yashiro et al., 1995, 1997; Young and Chin, 1995; Molenveld et al., 1999). Lanthanide ions are suitable for the multi-metallic cooperation, since they automatically form aggregates of metal hydroxide in neutral solutions and in these aggregates two or more metal ions are placed nearby.

These mechanistic understandings on the catalysis of lanthanide ions should be valuable for the design of still more active catalysts for the hydrolysis of DNA and RNA, which should lead to the preparation of advanced artificial enzymes for site-selective scission of DNA and RNA. By accumulating more detailed knowledge on the mechanisms of the catalyses, the applications of lanthanide ions to biotechnology, molecular biology, gene therapy, and others should be further widened. Such attempts are currently being made in our laboratory and others.

Acknowledgements

This work was supported by Bio-oriented Technology Research Advancement Institution. The financial support by a Grant-in-Aid for Scientific Research from the Ministry of Education, Science, Sport, Culture, and Technology, Japan is also acknowledged.

References

- Arishima, H., Yokoyama, M., Komiyama, M., 2003. *Nucleic Acids Res. Suppl.* **3**, 137.
- Basile, L.A., Raphael, A.L., Barton, J.K., 1987. *J. Amer. Chem. Soc.* **109**, 7550.
- Branum, M.E., Tipton, A.K., Zhu, S., Que Jr., L., 2001. *J. Amer. Chem. Soc.* **123**, 1898.
- Breslow, R., Zhang, B.L., 1994. *J. Amer. Chem. Soc.* **116**, 7893.
- Cech, T., Zaug, A., Grabowski, P., 1981. *Cell* **27**, 487.
- Chin, J., Zou, X., 1987. *Canad. J. Chem.* **65**, 1882.
- Chin, K.O.A., Morrow, J.R., 1994. *Inorg. Chem.* **33**, 5036.
- Copeland, K.D., Fitzsimons, M.P., Houser, R.P., Barton, J.K., 2002. *Biochemistry* **41**, 343.
- Franklin, S.J., 2002. *Curr. Opin. Chem. Biol.* **5**, 201.
- Hall, J., Hüskén, D., Häner, R., 1996. *Nucleic Acids Res.* **24**, 3522.
- Hashimoto, S., Nakamura, Y., 1996. *J. Chem. Soc., Perkin Trans.* **1**, 2623.
- Hay, R.W., Govan, N., 1990. *J. Chem. Soc., Chem. Commun.* **714**.
- Hegg, E.L., Burstyn, J.N., 1998. *Coord. Chem. Rev.* **173**, 133.
- Hettich, R., Schneider, H.J., 1997. *J. Amer. Chem. Soc.* **119**, 5638.

- Hüsken, D., Goodall, G., Blommers, M.J.J., Jahnke, W., Hall, J., Häner, R., Moser, H.E., 1996. *Biochemistry* **35**, 16591.
- Igawa, T., Sumaoka, J., Komiyama, M., 2000. *Chem. Lett.* **356**.
- Kajimura, A., Sumaoka, J., Komiyama, M., 1998. *Carbohydr. Res.* **309**, 345.
- Kitamura, Y., Komiyama, M., 2002. *Nucleic Acids Res.* **30**, e102.
- Komiyama, M., 1995. *J. Biochem.* **118**, 665.
- Komiyama, M., Takarada, T., 2003. *Metal Ions in Biological Systems* **40**, 355.
- Komiyama, M., Sumaoka, J., 1998. *Curr. Opin. Chem. Biol.* **2**, 751.
- Komiyama, M., Matsumura, K., Yonezawa, K., Matsumoto, Y., 1993. *Chem. Express* **8**, 85.
- Komiyama, M., Shiiba, T., Kodama, T., Takeda, N., Sumaoka, J., Yashiro, M., 1994a. *Chem. Lett.* **23**, 1025.
- Komiyama, M., Shiiba, T., Takahashi, Y., Takeda, N., Matsumura, K., Kodama, T., 1994b. *Supramol. Chem.* **4**, 31.
- Komiyama, M., Takeda, N., Shiiba, T., Takahashi, Y., Matsumoto, Y., Yashiro, M., 1994c. *Nucleosides and Nucleotides* **13**, 1297.
- Komiyama, M., Takeda, N., Takahashi, Y., Uchida, H., Shiiba, T., Kodama, T., Yashiro, M., 1995. *J. Chem. Soc., Perkin Trans. 2*, 269.
- Komiyama, M., Kamitani, J., Sumaoka, J., Asanuma, H., 1996. *Chem. Lett.* **25**, 869.
- Komiyama, M., Takeda, N., Shigekawa, H., 1999. *Chem. Commun.* **1443**.
- Komiyama, M., Sumaoka, J., Kuzuya, A., Yamamoto, Y., 2001. *Methods Enzymol.* **341**, 455.
- Kuzuya, A., Komiyama, M., 2000. *Chem. Commun.* **2019**.
- Kuzuya, A., Machida, K., Komiyama, M., 2002a. *Tetrahedron Lett.* **43**, 8249.
- Kuzuya, A., Mizoguchi, R., Morisawa, F., Komiyama, M., 2002b. *J. Amer. Chem. Soc.* **124**, 6887.
- Kuzuya, A., Mizoguchi, R., Morisawa, F., Komiyama, M., 2003. *Chem. Commun.* **770**.
- Magda, D., Miller, R.A., Sessler, J.L., Iverson, B.L., 1994. *J. Amer. Chem. Soc.* **116**, 7439.
- Magda, D., Crofts, S., Lin, A., Miles, D., Wright, M., Sessler, J.L., 1997. *J. Amer. Chem. Soc.* **119**, 2293.
- Matsumoto, Y., Komiyama, M., 1992. *Nucleic Acids, Symp. Ser.* **27**, 33.
- Matsumura, K., Komiyama, M., 1992. *Chem. Commun.* **640**.
- Matsumura, K., Komiyama, M., 1997. *J. Biochem.* **122**, 387.
- Matsumura, K., Endo, M., Komiyama, M., 1994. *Chem. Commun.* **2019**.
- Miyama, S., Asanuma, H., Komiyama, M., 1997. *J. Chem. Soc., Perkin Trans. 2*, 1685.
- Molenveld, P., Engbersen, J.F.J., Reinhoudt, D.N., 1999. *Angew. Chem. Internat. Ed. Eng.* **38**, 3189.
- Morrow, J.R., Buttrey, L.A., Shelton, V.M., Berback, K.A., 1992. *J. Amer. Chem. Soc.* **114**, 1903.
- Morrow, J.R., Aures, K., Epstein, D., 1995. *Chem. Commun.* **2431**.
- Oivanen, M., Kuusela, S., Lönnberg, H., 1998. *Chem. Rev.* **98**, 961.
- Schnaith, L.M.T., Hanson, R.S., Que Jr., L., 1994. *Proc. Natl. Acad. Sci. USA.* **91**, 569.
- Shigekawa, H., Ikawa, H., Yoshizaki, R., Iijima, Y., Sumaoka, J., Komiyama, M., 1996. *Appl. Phys. Lett.* **68**, 1433.
- Shigekawa, H., Ishida, M., Miyake, K., Shioda, R., Iijima, Y., Imai, T., Takahashi, H., Sumaoka, J., Komiyama, M., 1999. *Appl. Phys. Lett.* **74**, 460.
- Shiiba, T., Yonezawa, K., Takeda, N., Matsumoto, Y., Yashiro, M., Komiyama, M., 1993. *J. Mol. Catal.* **84**, L21.
- Sreedhara, A., Cowan, J.A., 2001. *J. Biol. Inorg. Chem.* **6**, 337.
- Sumaoka, J., Yashiro, M., Komiyama, M., 1992. *Chem. Commun.* **1707**.
- Sumaoka, J., Miyama, S., Komiyama, M., 1994. *Chem. Commun.* **1755**.
- Sumaoka, J., Uchida, H., Komiyama, M., 1995. *Nucleic Acids, Symp. Ser.* **34**, 83.
- Sumaoka, J., Azuma, Y., Komiyama, M., 1998. *Chem. Eur. J.* **4**, 205.
- Sumaoka, J., Igawa, T., Yagi, T., Komiyama, M., 2001. *Chem. Lett.* **30**, 20.
- Takarada, T., Yashiro, M., Komiyama, M., 2000. *Chem. Eur. J.* **6**, 3906.
- Takasaki, B.K., Chin, J., 1993. *J. Amer. Chem. Soc.* **115**, 9337.
- Takasaki, B.K., Chin, J., 1994. *J. Amer. Chem. Soc.* **116**, 1121.
- Takasaki, B.K., Chin, J., 1995. *J. Amer. Chem. Soc.* **117**, 8582.
- Takeda, N., Imai, T., Irisawa, M., Sumaoka, J., Yashiro, M., Shigekawa, H., Komiyama, M., 1996. *Chem. Lett.* **25**, 599.
- Trawick, B.N., Daniher, A.T., Bashkin, J.K., 1998. *Chem. Rev.* **98**, 939.
- Williams, N.H., Takasaki, B., Wall, M., Chin, J., 1999. *Acc. Chem. Res.* **32**, 485.

- Yamamoto, Y., Tsuboi, W., Komiyama, M., 2003. *Nucleic Acids Res.* **15**, 4497.
- Yashiro, M., Ishikubo, A., Komiyama, M., 1995. *Chem. Commun.* **1793**.
- Yashiro, M., Ishikubo, A., Komiyama, M., 1997. *Chem. Commun.* **83**.
- Young, M.J., Chin, J., 1995. *J. Amer. Chem. Soc.* **117**, 10577.

AUTHOR INDEX

- Aarts, J., see Steglich, F. 183
Abdollahi, S. 349
Abe, H., see Suzuki, H. 117
Abrikosov, A.A. 150, 174
Adam, J.L. 368
Adam, M., see Galadzhun, Ya.V. 38, 57, 122
Adams, K.M., see Pan, L. 387, 391
Adenwalla, S. 205
Adrian, H., see Dressel, M. 146, 199, 216
Adrian, H., see Hessert, J. 217
Adrian, H., see Jourdan, M. 217, 225, 226
Adroja, D.T. 4, 28, 101
Adroja, D.T., see De Teresa, J.M. 115
Adroja, D.T., see Malik, S.K. 36, 101–103, 117, 118
Adroja, D.T., see Nyayate, M.N. 102
Aeppli, G. 156, 205, 206
Aeppli, G., see Mason, T.E. 217, 223, 224
Aeppli, G., see Wei, B. 113
Affleck, I., see Sikkema, A.E. 236
Agarwal, P., see Grosche, F.M. 183, 191
Agarwal, P., see Saxena, S.S. 199, 230
Agterberg, D., see Frigeri, P. 160
Agterberg, D., see Sigrist, M. 248
Ahlheim, U., see Geibel, C. 199, 216, 228
Ahlheim, U., see Schlabitz, W. 236
Ahllan, K., see Saxena, S.S. 199, 230
Ahuja, R., see Söderlind, P. 147
Aime, S. 338
Aime, S., see Bruce, J.I. 341
Akayama, M., see Fujii, H. 101
Aksel'rud, L.G., see Kalychak, Ya.M. 10, 14, 15, 42, 76, 81, 82, 86
Aksel'rud, L.G., see Skolozdra, R.V. 47
Aksel'rud, L.G., see Sysa, L.V. 33, 49, 124
Alam, M.A., see Dugdale, S.B. 251, 253
Alami-Yadri, K. 119
Albers, R. 162, 200, 204
Albers, R.A., see Runge, E. 185
Albers, R.C., see Norman, M.R. 199, 200
Albertsson, J. 313
Albertsson, J., see Hansson, E. 360
Albessard, A.K. 185, 186
Albessard, A.K., see Aoki, H. 145, 185
Alexander, M.G., see Gordon, R.A. 61, 95
Alfieri, G.T. 118
Allemand, J. 66
Allen, J.W. 143, 145, 200
Allen, J.W., see Denlinger, J.D. 146, 187
Allenspach, P., see Cavadini, N. 260
Allenspach, P., see Gasser, U. 260
Alleyne, B.D. 389
Alver, U. 111, 193
Alver, U., see Hall, D. 111, 113
Alwood, J., see Kim, J.S. 112
Amado, M.M., see Pinto, R.P. 107
Amato, A., see Feyerherm, R. 216–218
Amaya, K., see Kobayashi, T.C. 231, 234, 235
Amaya, K., see Tateiwa, N. 236
Amici, A. 258–261, 263, 264, 267
Amin, I., see Valiev, U.V. 351, 352
Amitsuka, H. 237–239
Amitsuka, H., see Yokoyama, M. 239, 241
Amoretti, G., see Santini, P. 236, 237, 240, 243
Anderson, P.W. 154
Andersson, S. 79
Andoh, Y., see Fujii, H. 4, 101
Andraka, B., see Kaczorowski, D. 36, 102, 105
Andraka, B., see Rotundu, C.R. 271
André, G. 33
Andres, K., see Schuberth, E.A. 205
Annett, J.F. 161
Ansai, T., see Morita, M. 323, 327, 345
Aoki, D. 230, 270
Aoki, D., see Fujimori, S. 193, 194
Aoki, D., see Haga, Y. 111
Aoki, D., see Ikeda, S. 114
Aoki, D., see Kawasaki, S. 113
Aoki, D., see Kimura, N. 199, 203
Aoki, D., see Mito, T. 113
Aoki, D., see Shishido, H. 193, 194
Aoki, D., see Takeuchi, T. 114, 194
Aoki, D., see Zheng, G.-Q. 113, 194
Aoki, H. 145, 185, 194
Aoki, H., see Albessard, A.K. 185, 186

- Aoki, H., see Kimura, N. 199, 203
 Aoki, Y. 270, 275
 Aoki, Y., see Bauer, E. 109
 Aoki, Y., see Ikeda, S. 114
 Aoki, Y., see Kohgi, M. 271
 Aoki, Y., see Kotegawa, H. 272
 Aoki, Y., see Rotundu, C.R. 271
 Aoki, Y., see Shishido, H. 193, 194
 Aoki, Y., see Sugawara, H. 269
 Aoki, Y., see Tayama, T. 270, 272
 Appel, J., see Fay, D. 229, 234
 Araki, S., see Kawasaki, S. 192
 Araki, S., see Kohgi, M. 271
 Araki, S., see Shishido, H. 111
 Aranson, I., see Metlushko, V. 252
 Arishima, H. 440
 Arko, A.J., see Cornelius, A.L. 111
 Armstrong, P.E., see Denlinger, J.D. 146, 187
 Arnold, Z., see De Teresa, J.M. 115
 Arons, R.R., see Siouris, I.M. 18, 70, 122, 123
 Aronsson, B. 74, 79
 Asano, H., see Kojima, K. 18, 114
 Asanuma, H., see Komiya, M. 427
 Asanuma, H., see Miyama, S. 410
 Asayama, K., see Kyogaku, M. 228
 Asayama, K., see Nakamura, H. 115
 Asayama, K., see Tou, H. 214, 217–219
 Aso, N., see Bernhoeft, N. 146, 217, 224
 Aso, N., see Sato, N. 217, 224
 Aso, N., see Sato, N.K. 146, 217, 225, 227
 Assmus, W., see Bruls, G. 189
 Assmus, W., see Gegenwart, P. 168, 190
 Assmus, W., see Hunt, M. 187
 Assmus, W., see Maetz, J. 29, 33, 74
 Assmus, W., see Steglich, F. 190, 191
 Aubry, A., see Dimos, A. 391
 Aubry, A., see Michaelides, A. 360
 Audebrand, N., see Daigubonne, C. 363
 Auffrédic, J.P., see Bataille, T. 360
 Aures, K., see Morrow, J.R. 411
 Azuma, Y., see Sumaoka, J. 411, 434

 Babateen, M. 120
 Bach, A., see Kromer, F. 244, 246
 Bäckman, M., see Aronsson, B. 79
 Baenziger, N.C., see Duwell, E.J. 69
 Baenziger, N.C., see Florio, J.V. 45
 Baer, Y., see Garnier, M. 144
 Baer, Y., see Malterre, D. 143
 Baerlocher, Ch., see Xue, B. 31
 Baggio, R., see Rizzi, A.C. 367

 Baines, C., see Heffner, R.H. 246
 Bak, P. 261
 Bakalbassis, E., see Guillou, O. 366
 Bakar, A.M. 18, 23
 Bakar, A.M., see Kalychak, Ya.M. 18, 24–26
 Bakar, A.M., see Sysa, L.V. 18, 40, 81, 82
 Bakker, K., see Brück, E. 102
 Balakrishnan, G., see Majumdar, S. 114
 Bałanda, M. 102–104
 Balatsky, A.V., see Monthoux, P. 154
 Balster, H. 120
 Baltensperger, W. 266
 Bandyopadhyay, B., see Ghoshray, K. 107
 Bandyopadhyay, B., see Sen, M. 107
 Banks, E., see Alfieri, G.T. 118
 Baranyak, V.M. 10, 14, 18–22, 39, 47, 48, 58, 70, 88
 Baranyak, V.M., see Kalychak, Ya.M. 10, 14, 18, 42, 48, 49, 54, 55, 61, 72, 80, 81, 85, 88, 89
 Baranyak, V.M., see Sysa, L.V. 10, 14, 18, 40, 68, 81, 82
 Baranyak, V.M., see Zarembo, V.I. 14, 52
 Barash, Y.S. 175
 Bardeen, J. 154
 Barnett, C.J. 311
 Bärnighausen, H. 78
 Barthelet, K. 363
 Barton, J.K., see Basile, L.A. 414
 Barton, J.K., see Copeland, K.D. 407
 Bashkin, J.K., see Trawick, B.N. 407
 Basile, L.A. 414
 Basletic, M. 179, 182
 Basletic, M., see Dóra, B. 182
 Basletic, M., see Korin-Hamzic, B. 179
 Basletic, M., see Maki, K. 179, 181, 182
 Batail, P., see Guillou, O. 366
 Batail, P., see Oushoorn, R.L. 366
 Bataille, T. 360
 Batlogg, B., see Cava, R.J. 248
 Batlogg, B., see Golding, B. 246
 Batten, S.R. 360
 Bauer, E. 109, 160
 Bauer, E., see Fischer, P. 108, 110
 Bauer, E., see Giovannini, M. 18, 26, 31, 38, 71, 108, 109
 Bauer, E., see Hauser, R. 110
 Bauer, E., see Kaczorowski, D. 31, 108–110
 Bauer, E., see Pillmayr, N. 116
 Bauer, E.D. 268, 269, 271
 Bauer, E.D., see Goll, G. 113, 194
 Bauer, E.D., see Kohori, Y. 113, 194

- Bauer, E.D., see Maple, M.B. 269, 270
 Bauer, E.D., see Oeschler, N. 271, 272
 Bauer, E.D., see Vollmer, R. 269–272
 Bauer, E.D., see Zapf, V.S. 111, 114
 Baumann, J., see Aeppli, G. 205, 206
 Baumann, J., see Schlabit, W. 236
 Baux, C., see Camara, M. 397, 398
 Baux, C., see Daiguebonne, C. 363
 Bazela, W., see André, G. 33
 Bazela, W., see Szytuła, A. 38, 102, 106
 Becher, H.J. 71, 89
 Bedard, T.C., see Wu, S. 323, 325
 Beeby, A. 334, 340, 341
 Behnia, K., see Jaccard, D. 183
 Behr, G., see Drechsler, S.-L. 251, 252
 Beille, J., see Nowik, I. 115
 Belair, S.D. 301, 315, 322
 Belan, B.D., see Zaremba, V.I. 36, 102, 106
 Belitz, D., see Kirkpatrick, T.R. 231
 Belsky, V.K., see Baranyak, V.M. 18, 20, 39
 Belsky, V.K., see Kalychak, Ya.M. 18, 48, 80, 85
 Belsky, V.K., see Zaremba, V.I. 14, 65
 Belyavina, N.N., see Markiv, V.Ya. 64
 Benelli, C. 367
 Benesovsky, F., see Rieger, W. 71, 72, 89
 Benfatto, L. 179
 Benton, C.L., see Sarrao, J.L. 116
 Berback, K.A., see Morrow, J.R. 409, 427
 Berger, St., see Bauer, E. 109
 Bergerat, P., see Guillou, O. 366
 Berk, N. 154, 155
 Berlinsky, A.J. 196
 Bernardinelli, G., see Cantuel, M. 312
 Bernhoeft, N. 146, 199, 217, 224, 227
 Bernhoeft, N., see Kohgi, M. 271
 Bernhoeft, N.R., see Brison, J.-P. 200
 Berry, M.T. 295, 298
 Besnus, M.J. 36, 38, 63, 118, 119
 Besnus, M.J., see Lahiouel, R. 120
 Besnus, M.J., see Najib, A. 120
 Beuers, J., see Felten, R. 245
 Bi, W., see Cao, R. 363
 Bianchi, A. 195, 196
 Bianchi, A.D. 121, 122
 Biasini, M. 146
 Bickers, N.E., see Pao, C.H. 155
 Bilbro, G. 163
 Binnemans, K., see Parac-Vogt, T.N. 315, 331
 Birkedal, H., see Muller, G. 342
 Birrer, P., see Heffner, R.H. 246
 Bishop, D.J., see Golding, B. 246
 Bishop, D.J., see Yaron, U. 267
 Bitterlich, H., see Drechsler, S.-L. 251, 252
 Blake, A.J., see Long, D.L. 389
 Blazina, N. 36
 Blöchl, P.E., see Dronskowski, R. 100
 Blok, P.M.L. 307, 308
 Blommers, M.J.J., see Hüskén, D. 442
 Blount, E. 161, 162, 212
 Boaknin, E. 250, 252
 Bobba, G. 341
 Bobet, J.-L., see Chevalier, B. 4, 107
 Bodak, O.I., see Kalychak, Ya.M. 14, 18, 39, 45, 61, 63, 81, 86–88
 Bodak, O.I., see Kurenbaeva, J.M. 27
 Bodak, O.I., see Zaremba, V.I. 14, 64, 97
 Boekman, C., see Heffner, R.H. 199
 Böhm, A. 201
 Böhm, A., see Geibel, C. 199, 216
 Böhm, A., see Grauel, A. 201, 216, 218
 Bolender, J.P. 323, 324
 Bolender, J.P., see Glover-Fischer, D.P. 323, 324, 328, 329
 Bolender, J.P., see Hopkins, T.A. 298
 Bolender, J.P., see Metcalf, D.H. 323, 324, 328, 329
 Bömmel, H.E., see Müller, V. 246
 Bonelli, T., see Fischer, P. 108, 110
 Bonville, P., see Bauer, E. 109
 Booth, C.H., see Cornelius, A.L. 116
 Booth, C.H., see Lawrence, J.M. 114
 Borges, H.A., see Nicklas, M. 112
 Boring, A.M., see Albers, R. 162, 200, 204
 Boring, A.M., see Norman, M.R. 199, 200
 Borth, R., see Trovarelli, O. 36, 105
 Botta, M., see Aime, S. 338
 Botta, M., see Bruce, J.I. 341
 Boubekeur, K., see Camara, M. 397, 398
 Boubekeur, K., see Daiguebonne, C. 363, 366, 368–370, 372, 389, 392, 397, 399
 Boubekeur, K., see Guillou, O. 366
 Boubekeur, K., see Oushoorn, R.L. 366
 Boulet, P., see Sarrao, J.L. 192
 Bouquet, F., see Thompson, J.D. 28, 34, 111, 183
 Bourdarot, F., see Detlefs, C. 261
 Bourdarot, F., see Santini, P. 243
 Bouree, F., see Gravereau, P. 71, 91
 Bourges, P., see Cavadini, N. 260
 Bourlet, P., see Detlefs, C. 261
 Bowen, P., see Jongen, N. 360
 Boysen, H., see Landrum, G.A. 98
 Braga, M.E., see Pinto, R.P. 107

- Braithwaite, D. 191
 Braithwaite, D., see Aoki, D. 230, 270
 Braithwaite, D., see Huxley, A. 230
 Braithwaite, D., see Measson, M.-A. 272
 Braithwaite, D., see Saxena, S.S. 199, 230
 Brandt, E.H. 196
 Branum, M.E. 415
 Brathwaite, D., see Demuer, A. 191
 Brauer, G. 4
 Braun, E., see Pleger, H.R. 102, 103, 119
 Braun, H.F., see Schmidt, H. 253, 263
 Bredl, C.D., see Geibel, C. 199, 216, 228
 Bredl, C.D., see Schlabit, W. 236
 Bredl, C.D., see Steglich, F. 183
 Breslow, R. 411
 Breuer, K., see Garnier, M. 144
 Bridges, F., see Cornelius, A.L. 116
 Brison, J.-P. 200
 Brison, J.-P., see Aoki, D. 230, 270
 Brison, J.-P., see Braithwaite, D. 191
 Brison, J.-P., see Keller, N. 175, 244
 Brison, J.-P., see Martinez-Samper, P. 251
 Brison, J.-P., see Measson, M.-A. 272
 Brison, J.P., see Suderow, H. 214
 Brittain, H.G. 292, 305, 311, 330, 332, 333, 346–348
 Brittain, H.G., see Calienni, J.J. 348
 Brittain, H.G., see Richardson, F.S. 351, 352
 Brittain, H.G., see Schwartz, R.W. 351, 352
 Brittain, H.G., see Spaulding, L. 347
 Brittain, H.G., see Yan, F. 332
 Broholm, C. 236, 237, 243
 Broholm, C., see Aeppli, G. 205, 206
 Broholm, C., see Gaulin, B.D. 228
 Browne, D.A., see Macaluso, R.T. 10, 28, 34
 Bruce, J.I. 299, 320, 338–341
 Bruce, J.I., see Dickins, R.S. 339
 Brück, E. 101, 102
 Brück, E., see Pleger, H.R. 102, 103, 119
 Bruls, G. 189, 204, 210
 Bruls, G., see Thalmeier, P. 209
 Bruskov, V.A., see Baranyak, V.M. 14, 58, 88
 Bruskov, V.A., see Kalychak, Ya.M. 10, 14, 18, 49, 54, 55, 72, 88, 89
 Bruskov, V.A., see Zarembo, V.I. 14, 71, 72, 89
 Bu, X.H. 395, 396
 Bu, X.H., see Li, J.R. 395, 396
 Bucher, E., see Aeppli, G. 156, 205, 206
 Bucher, E., see Müller, V. 246
 Buchgeister, M., see Gasser, U. 260
 Buchholtz, L.J. 170
 Bud'ko, S.L., see Canfield, P.C. 229, 259, 262, 267
 Bud'ko, S.L., see Detlefs, C. 261
 Bud'ko, S.L., see Petrovic, C. 111, 194, 195
 Bull, M.J., see Park, J.-G. 237, 257
 Bullock, M., see Dervenagas, P. 253
 Bulyk, I.I. 107
 Bulyk, I.I., see Yartys, V.A. 107
 Bünzli, J.-C.G. 341
 Bünzli, J.-C.G., see Muller, G. 342–344
 Burstyn, J.N., see Hegg, E.L. 407
 Buschinger, B., see Trovarelli, O. 36, 105
 Buschow, K.H.J. 14, 29, 31, 68, 102, 105, 118
 Buschow, K.H.J., see De Mooij, D.B. 62
 Buschow, K.H.J., see De Vries, J.W.C. 102, 104, 119, 120
 Buschow, K.H.J., see Moze, O. 14, 121
 Buschow, K.H.J., see Mulder, F.M. 14, 121
 Buschow, K.H.J., see Oppelt, A. 118
 Butch, N.P., see Frederick, N.A. 269
 Buttrey, L.A., see Morrow, J.R. 409, 427
 Buyers, W.J.L. 224
 Buyers, W.J.L., see Broholm, C. 236, 237, 243
 Buyers, W.J.L., see Sikkema, A.E. 236
 Buyers, W.J.L., see Walker, M.B. 236
 Buzdin, A., see Brison, J.-P. 200
 Buzdin, A., see Keller, N. 175, 244
 Cable, J.W. 33, 118
 Caciuffo, R., see Santini, P. 243
 Calemczuk, R., see Huxley, A. 230
 Calienni, J.J. 348
 Calvo, R., see Rizzi, A.C. 367
 Camara, M. 397, 398
 Camara, M., see Daignebonne, C. 363
 Campbell, A.J. 261
 Canepa, F. 4, 10, 78, 122, 123
 Canepa, F., see Cirafici, S. 31, 69, 102, 104
 Caneschi, A., see Mahé, N. 401
 Canfield, P.C. 6, 229, 259, 262, 267
 Canfield, P.C., see Boaknin, E. 250, 252
 Canfield, P.C., see Cavadini, N. 260
 Canfield, P.C., see Dervenagas, P. 253
 Canfield, P.C., see Detlefs, C. 261
 Canfield, P.C., see Dugdale, S.B. 251, 253
 Canfield, P.C., see Eskildsen, M.R. 196
 Canfield, P.C., see Fisher, I.R. 108, 110, 253
 Canfield, P.C., see Martinez-Samper, P. 251
 Canfield, P.C., see Metlushko, V. 252
 Canfield, P.C., see Petrovic, C. 111, 194, 195
 Canfield, P.C., see Yaron, U. 267
 Canters, G.W., see Meskers, S.C.J. 323, 326, 329

- Cantuel, M. 312
 Cao, R. 363, 369, 382, 385, 396
 Capan, C., see Bianchi, A. 195, 196
 Caprara, S., see Benfatto, L. 179
 Car, P.E., see Mahé, N. 401
 Cardoso, R., see Trovarelli, O. 36, 105
 Carducci, M.D., see Wang, R. 398, 400
 Carter, F.V., see Grosche, F.M. 183, 191
 Carter, R.C., see May, P.S. 298
 Carter, R.C., see Metcalf, D.H. 343
 Caspary, R. 217, 219
 Caspary, R., see Geibel, C. 199, 216
 Castro, C.D., see Benfatto, L. 179
 Cava, R.J. 248
 Cava, R.J., see Nohara, M. 250, 253, 255, 257
 Cavadini, N. 260
 Cech, T. 408
 Cenzual, K. 79
 Cenzual, K., see Parthé, E. 79
 Chabot, B., see Parthé, E. 79
 Chae, H.K., see Eddaoudi, M. 364
 Chainani, A., see Takahashi, T. 146
 Chakravarty, S. 179, 180, 183
 Champness, N.R., see Long, D.L. 389
 Chan, J.Y., see Macaluso, R.T. 10, 28, 34
 Chandra, P., see Ramirez, A.P. 245
 Chane-Ching, J.-Y. 401
 Chane-Ching, J.-Y., see Mahé, N. 401
 Chang, H.-C., see Tong, M.-L. 363, 366
 Chao, B.K., see Dervenagas, P. 253
 Charmant, J.P.H., see Chui, S.S.-Y. 362, 364
 Charvolin, T., see van Dijk, N.H. 191
 Chatterjee, N., see Ghoshray, K. 107
 Chatterjee, N., see Sen, M. 107
 Cheetham, A.K., see Serpaggi, F. 360
 Chen, B. 363, 365
 Chen, G., see Ohara, S. 112
 Chen, H.-Y., see Yuan, Q. 170, 255
 Chen, W., see Bu, X.H. 395, 396
 Chen, X.M., see Tong, M.-L. 363, 366
 Chen, X.M., see Zhao, Y. 364
 Cheng, D. 363
 Chernikov, M.A., see Bianchi, A.D. 121, 122
 Chevalier, B. 4, 107
 Chevalier, B., see Gravereau, P. 71, 91
 Chia, E.E. 275
 Child, H.R., see Cable, J.W. 33, 118
 Chin, J. 419
 Chin, J., see Takasaki, B.K. 408, 410, 427
 Chin, J., see Williams, N.H. 407
 Chin, J., see Young, M.J. 452
 Chin, K.O.A. 427
 Chisdes, S.J., see Glover-Fischer, D.P. 301, 322, 328
 Chitra, R. 198
 Cho, B., see Doh, H. 263
 Cho, B.K., see Canfield, P.C. 259
 Choi, C. 174, 205
 Choi, E.M., see Park, T. 177
 Chowdhury, M., see Sen, A.C. 299
 Christensen, N.E., see Albers, R. 162, 200, 204
 Christensen, N.E., see Norman, M.R. 199, 200
 Christensen, N.E., see Runge, E. 185
 Christensen, N.E., see Zwicknagl, G. 185, 186
 Christianson, A.D. 111
 Christianson, A.D., see Pagliuso, P.G. 111
 Chui, S.S.-Y. 362, 364, 369, 384, 388
 Cichorek, T., see Kaczorowski, D. 36, 105
 Cichorek, T., see Kromer, F. 244, 246, 247
 Cichorek, T., see Stockert, O. 168, 190
 Cirafici, S. 31, 69, 102, 104
 Cirafici, S., see Fornasini, M.L. 92
 Claessen, R., see Ehm, D. 191
 Coleman, P. 198
 Coleman, P., see Custers, J. 198
 Coleman, P., see Ramirez, A.P. 245
 Colineau, E., see Sarrao, J.L. 192
 Colinet, C. 83
 Collins, M.F., see Broholm, C. 237, 243
 Condon, E.U. 201
 Conner Jr., R.A., see Dwight, A.E. 3
 Contardi, V., see Rossi, D. 38, 68
 Continentino, M.A. 197
 Cooke, D.W., see Heffner, R.H. 199
 Cooper, J.R., see Fisher, I.R. 253
 Cooper, L.N., see Bardeen, J. 154
 Copeland, K.D. 407
 Copeland, R.A., see Yan, F. 332
 Corbett, J.D. 6
 Cordier, G., see Czech, E. 43
 Cornelius, A.L. 111, 112, 116
 Cornelius, A.L., see Pagliuso, P.G. 111
 Corruccini, L.R., see Tang, J. 4, 14, 122, 123
 Çoruh, N. 299, 314, 323, 325, 328, 330, 332, 349
 Çoruh, N., see Hilmes, G.L. 299, 314, 330, 331
 Çoruh, N., see Riehl, J.P. 349
 Costes, J.P. 367
 Cottrell, S.P., see Yaouanc, A. 146
 Cowan, J.A., see Liu, J. 367
 Cowan, J.A., see Sreedhara, A. 407
 Cox, D.L. 145, 245
 Crabtree, G.W., see Metlushko, V. 252

- Crangle, J., see Babateen, M. 120
 Crofts, S., see Magda, D. 427, 442
 Cromer, D.T. 80
 Cromer, D.T., see Larson, A.C. 69, 81
 Crosby, G.A., see Hipps, K.W. 350
 Crossland, C., see Parker, D. 338
 Curro, N.J. 113
 Curro, N.J., see Pagliuso, P.G. 111
 Curro, N.J., see Thompson, J.D. 28, 34, 111, 183
 Custers, J. 198
 Czech, E. 43
 Czopnik, A., see Tchoula Tchokonte, M.B. 121
- Dahm, T. 155, 167, 175, 253
 Dahm, T., see Steglich, F. 168, 189
 Daiguebonne, C. 363, 366, 368–370, 372, 389, 392, 397, 399
 Daiguebonne, C., see Camara, M. 397, 398
 Daiguebonne, C., see Deluzet, A. 369, 377, 380, 386, 390
 Daiguebonne, C., see Mahé, N. 401
 Daniher, A.T., see Trawick, B.N. 407
 Daniš, S. 31, 104
 Davis, C.E., see Li, H. 363, 369
 Davis, C.E., see Yaghi, O.M. 363
 Davydov, V., see Galadzhun, Ya.V. 36, 75
 Dawson, J.H., see Dooley, D.M. 351
 de Azevedo, M.M.P., see Pinto, R.P. 107
 de Boer, F.R., see Brück, E. 101, 102
 de Châtel, P.F., see Brück, E. 102
 De Mooij, D.B. 62
 de Réotier, P.D., see Kernavanois, N. 238, 240
 de Réotier, P.D., see Yaouanc, A. 146
 De Teresa, J.M. 115
 de V. Du Plessis, P., see Tchoula Tchokonte, M.B. 121
 de Visser, A. 236
 de Visser, A., see Bruls, G. 204, 210
 de Visser, A., see Mentink, S.A.M. 238
 de Visser, A., see van Dijk, N.H. 205, 209
 De Vries, J.W.C. 102, 104, 119, 120
 de Waard, H., see Felner, I. 114–116
 deBoer, F.R., see Frings, P.H. 199
 Decurtins, S. 360, 366, 367
 Degiorgi, L. 199
 Deguchi, H., see Mizuno, K. 250
 Dekkers, H.P.J.M. 310
 Dekkers, H.P.J.M., see Blok, P.M.L. 307, 308
 Dekkers, H.P.J.M., see Maupin, C.L. 323, 325, 328
 Dekkers, H.P.J.M., see Meskers, S.C.J. 295, 323, 325–327, 329
 Dekkers, H.P.J.M., see Rexwinkel, R.B. 307, 308, 323, 325, 328
 Dekkers, H.P.J.M., see Schippers, P.H. 305, 309
 del Moral, A., see De Teresa, J.M. 115
 Deluzet, A. 369, 377, 380, 382, 386, 390
 Deluzet, A., see Daiguebonne, C. 363
 Demas, J.N., see Metcalf, D.H. 301, 303, 307, 308, 313–315, 322–325, 328
 Demuer, A. 191
 Demuer, A., see Braithwaite, D. 191
 Denison, A.B., see Heffner, R.H. 199
 Denlinger, J.D. 146, 187
 Dennison, C., see Meskers, S.C.J. 323, 326
 Denys, R.V., see Bulyk, I.I. 107
 Denys, R.V., see Yartys, V.A. 107
 Dertinger, A. 266
 Dervenagas, P. 253
 Dervenagas, P., see Detlefs, C. 261
 Detlefs, C. 261
 Devare, H.G., see Nyayate, M.N. 102
 Devare, S.H., see Nyayate, M.N. 102
 Dewhurst, C.D., see Eskildsen, M.R. 196
 Dhar, S.K. 7, 26, 106
 Dhar, S.K., see Manfrinetti, P. 106
 Dhar, S.K., see Nagarajan, N. 248
 Dhar, S.K., see Sampathkumaran, E.V. 115
 Di Bari, L. 339
 Dickey, R.P., see Zapf, V.S. 114
 Dickins, R.S. 318, 319, 334–336, 339, 341
 Dickins, R.S., see Aime, S. 338
 Dickins, R.S., see Beeby, A. 334, 340, 341
 Dickins, R.S., see Bobba, G. 341
 Dickins, R.S., see Bruce, J.I. 341
 Dickins, R.S., see Di Bari, L. 339
 Dickins, R.S., see Maupin, C.L. 314, 330, 334, 336, 337, 340, 341
 Dickins, R.S., see Parker, D. 338
 Didierjean, C., see Dimos, A. 391
 Dimos, A. 391
 Dirkmaat, A.J., see Palstra, T.T.M. 199, 236
 DiSalvo, F.J., see Gordon, R.A. 31, 61, 95, 108
 DiSalvo, F.J., see Ijiri, Y. 31, 109, 121, 122
 DiSalvo, F.J., see Poduska, K.M. 123
 Dmytrakh, O.V. 18, 19
 Dmytrakh, O.V., see Baranyak, V.M. 14, 18, 58, 70, 88
 Dmytrakh, O.V., see Kalychak, Ya.M. 14, 18, 39, 45, 48, 54, 61, 63, 72, 80, 85, 87–89
 Dmytrakh, O.V., see Zaremba, V.I. 14, 53
 Do, T.D., see Frederick, N.A. 269
 Doh, H. 263

- Dolg, M., see Liu, W. 146
 Doniach, S. 145
 Donnevert, L., see Gegenwart, P. 168, 190
 Donnevert, L., see Steglich, F. 191
 Dönni, A., see Kita, H. 217, 218
 Donohue, J. 83, 97, 98
 Dooley, D.M. 351
 Dóra, B. 179, 182
 Dóra, B., see Maki, K. 179, 181, 182
 Dóra, B., see Virosztek, A. 242
 Dormann, E., see Buschow, K.H.J. 29, 118
 Dormann, E., see Oppelt, A. 118
 Dossing, A. 316
 Dossing, A., see Gawryszewska, P. 315–317
 Downey, J.W., see Dwight, A.E. 3
 Drake, A.F., see Barnett, C.J. 311
 Drechsler, S.-L. 251, 252
 Drechsler, S.-L., see Rosner, H. 253
 Drechsler, S.-L., see Shulga, S.V. 252
 Dressel, M. 146, 199, 216
 Driver, M.S., see Metcalf, D.H. 323, 324, 328, 329
 Dronskowski, R. 100
 Dronskowski, R., see Pöttgen, R. 14, 38, 97, 98,
 102, 104, 106, 107, 121–123
 Du, M., see Bu, X.H. 395, 396
 du Tremolet de Lacheisserie, E., see Nowik, I. 115
 Duan, C.Y., see Li, J.R. 395, 396
 Dubenskii, V.P. 10
 Dubenskii, V.P., see Zaremba, V.I. 14, 28, 31, 64,
 97, 102, 105
 Dubenskiy, V.P., see Zaremba, V.I. 6, 31, 36, 44, 51
 Dugdale, S.B. 251, 253
 Dumont, E. 248
 Dumschat, J., see Mallik, R. 110
 Dupuis, A., see Costes, J.P. 367
 Duwell, E.J. 69
 Dwight, A.E. 3, 14, 15, 18, 31, 33, 36, 38, 63
 Dyer, R.B. 345
 Dzero, M.O. 115
 Dzyaloshinski, I.E., see Abrikosov, A.A. 150

 Ebihara, T., see Albessard, A.K. 185, 186
 Ebihara, T., see Hall, D. 113
 Eckert, H., see Müllmann, R. 102, 105
 Eckert, H., see Pöttgen, R. 14, 122, 123
 Eddaoudi, M. 360, 364, 367
 Eddaoudi, M., see Chen, B. 363, 365
 Eddaoudi, M., see O’Keeffe, M. 360
 Eddaoudi, M., see Reneike, T.M. 369, 375, 377,
 378, 381
 Edelstein, A.S., see Malik, S.K. 36, 117, 118

 Efremov, D. 147, 149, 220
 Eguchi, K., see Morita, M. 352
 Eguchi, K., see Murata, K. 345, 346
 Ehm, D. 191
 Ehm, D., see Reinert, F. 144
 Einzel, D. 171
 Eisaki, H., see Cava, R.J. 248
 Eisenmann, B. 58
 Elding, L.I., see Albertsson, J. 313
 Ellman, B., see Lussier, B. 199, 205, 213
 Emeis, C.A. 291
 Emsley, J. 95, 98
 Endo, K., see Mizuno, K. 250
 Endo, M., see Matsumura, K. 442
 Endoh, Y., see Bernhoeft, N. 146, 217, 224
 Endoh, Y., see Kita, H. 217, 218
 Endoh, Y., see Nakao, H. 241
 Endoh, Y., see Sato, N. 217, 224
 Engbersen, J.F.J., see Molenveld, P. 452
 Epstein, D., see Morrow, J.R. 411
 Eriksson, O., see Lundin, U. 147
 Eriksson, O., see Söderlind, P. 147
 Erkelens, W.A.C., see Regnault, L.P. 185
 Ernet, U., see Müllmann, R. 105
 Erwin, R.W., see Wei, B. 113
 Eschrig, H., see Drechsler, S.-L. 251, 252
 Eschrig, H., see Rosner, H. 253
 Eskildsen, M.R. 196
 Eskildsen, M.R., see Yaron, U. 267
 Esmaeilzadeh, S. 27
 Esquinazi, P., see Ocana, R. 177
 Estermann, M., see Xue, B. 31
 Etourneau, J., see Chevalier, B. 4, 107
 Etourneau, J., see Gravereau, P. 71, 91
 Etourneau, J., see Pinto, R.P. 107
 Evers, J., see Landrum, G.A. 98
 Ewing, F.J., see Shoemaker, D.P. 39
 Eyert, V., see Ehm, D. 191

 Faisst, A., see Mock, S. 110
 Faisst, A., see Vollmer, R. 269–272
 Fak, B. 191
 Fak, B., see Brison, J.-P. 200
 Fak, B., see Demuer, A. 191
 Fak, B., see Santini, P. 243
 Fak, B., see van Dijk, N.H. 191
 Falko, C., see Kadanoff, L. 172
 Fally, M., see Valiev, U.V. 351, 352
 Farrell, D., see Canfield, P.C. 259
 Faulhaber, E., see Stockert, O. 168, 190
 Faulkner, L.R., see Morley, J.P. 352

- Fauth, F., see Babateen, M. 120
 Fauth, F., see Fischer, P. 108, 110
 Fauth, F., see Gasser, U. 260
 Fay, D. 229, 234
 Fay, D., see Layzer, A. 154
 Fayer, M.D., see Gochanour, C.R. 323
 Fazekas, P. 141, 219
 Fedorova, E.G., see Yatsenko, S.P. 83
 Fehr, M., see Reneike, T.M. 369, 375, 377
 Feil-Jenkins, J.F. 389
 Felder, E., see Bianchi, A.D. 121, 122
 Felder, R.J., see Cava, R.J. 248
 Felner, I. 15, 18, 114–116
 Felner, I., see Nowik, I. 115
 Felten, R. 245
 Feng, S. 396
 Feng, X., see Chui, S.S.-Y. 369, 384, 388
 Férey, G., see Barthelet, K. 363
 Férey, G., see Millange, F. 391, 395
 Férey, G., see Serpaggi, F. 360, 391, 394
 Férey, G., see Serre, C. 374–376, 379, 382
 Ferlay, S., see Decurtins, S. 360, 366, 367
 Ferro, R. 3, 10, 14, 28, 31, 34, 36, 63, 68
 Ferro, R., see Giovannini, M. 28, 29, 31, 108, 109
 Ferro, R., see Marazza, R. 36, 38, 63
 Ferro, R., see Mazzone, D. 26, 69
 Ferro, R., see Rossi, D. 28, 33, 34, 36, 38, 68, 69
 Fetter, A.L., see Berlinsky, A.J. 196
 Feyerherm, R. 216–218
 Field, J.E. 306
 Finsterbusch, D., see Bruls, G. 189
 Fischer, H., see Grauel, A. 201, 216, 218
 Fischer, O. 141, 250, 267
 Fischer, P. 108, 110
 Fischer, P., see Krimmel, A. 217
 Fisher, I.R. 108, 110, 253
 Fisher, I.R., see Dugdale, S.B. 251, 253
 Fisher, R.A. 200, 204, 206
 Fisher, R.A., see Brison, J.-P. 200
 Fisher, R.A., see Thompson, J.D. 28, 34, 111, 183
 Fisk, Z., see Alver, U. 111, 193
 Fisk, Z., see Canfield, P.C. 6
 Fisk, Z., see Cornelius, A.L. 111, 116
 Fisk, Z., see Curro, N.J. 113
 Fisk, Z., see Denlinger, J.D. 146, 187
 Fisk, Z., see Golding, B. 246
 Fisk, Z., see Hall, D. 111, 113
 Fisk, Z., see Hegger, H. 4, 28, 111, 191, 194
 Fisk, Z., see Hundley, M.F. 36, 121, 122
 Fisk, Z., see Immer, C.D. 115
 Fisk, Z., see Lawrence, J.M. 115
 Fisk, Z., see Moshopoulou, E.G. 4, 28, 34
 Fisk, Z., see Movshovich, R. 114, 183
 Fisk, Z., see Nicklas, M. 112
 Fisk, Z., see Ott, H.R. 141, 199, 244
 Fisk, Z., see Pagliuso, P.G. 28, 34, 111, 112, 114
 Fisk, Z., see Petrovic, C. 111, 183, 191, 192, 194
 Fisk, Z., see Ramirez, A.P. 245
 Fisk, Z., see Sarrao, J.L. 116
 Fisk, Z., see Stewart, G.R. 141, 199
 Fisk, Z., see Susaki, T. 116
 Fisk, Z., see Taillefer, L. 199
 Fisk, Z., see Thompson, J.D. 28, 34, 111, 183
 Fisk, Z., see Wei, B. 113
 FitzGerald, S., see Beeby, A. 334, 340, 341
 Fitzsimons, M.P., see Copeland, K.D. 407
 Fjellvåg, H., see Vajeeston, P. 100, 107
 Fjellvåg, H., see Yartys, V.A. 107
 Florio, J.V. 40, 45
 Flouquet, J., see Aoki, D. 230, 270
 Flouquet, J., see Braithwaite, D. 191
 Flouquet, J., see Brison, J.-P. 200
 Flouquet, J., see Demuer, A. 191
 Flouquet, J., see Fak, B. 191
 Flouquet, J., see Fisher, R.A. 200, 204, 206
 Flouquet, J., see Hasselbach, K. 170, 171, 243
 Flouquet, J., see Hayden, S.M. 199, 204, 206, 208
 Flouquet, J., see Huxley, A. 230
 Flouquet, J., see Keller, N. 175, 244
 Flouquet, J., see Kernavanois, N. 231
 Flouquet, J., see Measson, M.-A. 272
 Flouquet, J., see Morin, P. 192
 Flouquet, J., see Regnault, L.P. 185
 Flouquet, J., see Saxena, S.S. 199, 230
 Flouquet, J., see Suderow, H. 214
 Flouquet, J., see van Dijk, N.H. 205, 209
 Fomin, I.A. 235
 Fornasini, M.L. 92
 Fornasini, M.L., see Canepa, F. 4, 10, 78, 122, 123
 Foster, D.R. 352, 353
 Foster, D.R., see Stephens, E.M. 352
 Fournes, L., see Gravereau, P. 71, 91
 Frank, F.C. 95
 Franklin, S.J. 407
 Franse, J.J.M., see de Visser, A. 236
 Franse, J.J.M., see Frings, P.H. 199
 Franse, J.J.M., see Marabelli, F. 199
 Franse, J.J.M., see Mulder, F.M. 14, 121
 Franse, J.J.M., see van Dijk, N.H. 205, 209
 Franz, M., see Berlinsky, A.J. 196
 Franz, W., see Steglich, F. 183
 Frederick, N.A. 269

- Frederick, N.A., see Bauer, E.D. 268, 269, 271
 Frederick, N.A., see Maple, M.B. 269, 270
 Frederick, N.A., see Oeschler, N. 271, 272
 Frederick, N.A., see Zapf, V.S. 111, 114
 Freeman, E.J., see Zapf, V.S. 114
 Freimuth, A., see Pleger, H.R. 102, 103, 119
 Freudenberg, J., see Drechsler, S.-L. 251, 252
 Freye, D.M., see Mathur, N.D. 183
 Freye, D.M., see Walker, I.R. 183
 Frigeri, P. 160
 Frings, P.H. 199
 Fronczek, F.R., see Kahwa, I.A. 360
 Fronczek, F.R., see Macaluso, R.T. 10, 28, 34
 Fuchs, G., see Drechsler, S.-L. 251, 252
 Fuchs, G., see Shulga, S.V. 252
 Fudo, H., see Mizuno, K. 250
 Fujii, H. 4, 101
 Fujii, H., see Fujita, T. 101
 Fujii, H., see Kurisu, M. 4, 103
 Fujii, H., see Maeno, Y. 101, 102
 Fujii, H., see Satoh, K. 101
 Fujii, H., see Suzuki, T. 103
 Fujii, H., see Yagasaki, K. 29, 33, 118
 Fujii, H., see Yamaguchi, Y. 101
 Fujimori, A., see Fujimori, S. 193, 194
 Fujimori, A., see Ogawa, S. 116
 Fujimori, A., see Susaki, T. 116
 Fujimori, S. 193, 194
 Fujisawa, M., see Ogawa, S. 116
 Fujita, T. 101
 Fujita, T., see Fujii, H. 4, 101
 Fujita, T., see Kojima, K. 18, 114
 Fujita, T., see Maeno, Y. 101, 102
 Fujita, T., see Satoh, K. 101
 Fujita, T., see Suzuki, T. 103
 Fujiwara, H., see Yagasaki, K. 29
 Fukase, T., see Izawa, K. 175, 178
 Fukuhara, T., see Braithwaite, D. 191
 Fukuhara, T., see Fak, B. 191
 Fukuhara, T., see Ōnuki, Y. 231
 Fulde, P. 141, 154, 170, 195, 250
 Fulde, P., see Amici, A. 259, 261, 263, 267
 Fulde, P., see Efremov, D. 147, 149, 220
 Fulde, P., see Liu, W. 146
 Fulde, P., see McHale, P. 228
 Fulde, P., see Rauchschtalbe, U. 246
 Fulde, P., see Sato, N.K. 146, 217, 225, 227
 Fulde, P., see White, R. 146, 147, 202, 238
 Fulde, P., see Zwicknagl, G. 146, 148, 198, 201–203, 220, 221, 238, 265, 271
 Furrer, A., see Babateen, M. 120
 Furrer, A., see Gasser, U. 260
 Furukawa, N., see Kawano-Furukawa, H. 262, 267, 268
 Furuno, H., see Iananaga, J. 368
 Gabani, S., see Bauer, E. 109
 Gafni, A., see Schauerte, J.A. 308, 350
 Gafni, A., see Steinberg, I. 311
 Galadzhun, Ya.V. 31, 33, 36, 38, 57–59, 75, 122
 Galadzhun, Ya.V., see Kalychak, Ya.M. 3, 10, 14, 15, 40, 76, 82, 97, 99
 Galadzhun, Ya.V., see Rodewald, U.-Ch. 36, 51
 Galadzhun, Ya.V., see Sysa, L.V. 18, 33, 40, 49, 81, 82, 124
 Galadzhun, Ya.V., see Zarembo, V.I. 28, 36, 47, 57, 102, 106, 124
 Galatanu, A., see Giovannini, M. 18, 26, 31, 38, 71, 109
 Galera, R.M. 33, 119, 120
 Galera, R.M., see Lahiouel, R. 120
 Gammel, P.L., see Yaron, U. 267
 Gamou, K., see Morita, M. 334
 Gan, J., see Sikkema, A.E. 236
 Ganglberger, E. 59
 Gangopadhyay, A.K. 253
 Gao, S., see Ma, B.Q. 398
 Gao, S., see Wan, Y. 389
 Gardant, N., see Millange, F. 391, 395
 Gardant, N., see Serre, C. 375, 376
 Garland, M.T., see Rizzi, A.C. 367
 Garnier, M. 144
 Garrett, J.D., see Gaulin, B.D. 228
 Garrett, J.D., see Walker, M.B. 236
 Gasser, U. 260
 Gatteschi, D., see Benelli, C. 367
 Gaulin, B.D. 228
 Gaviko, V.S., see Mushnikov, N.V. 117
 Gawryszewska, P. 315–317
 Gawryszewska, P., see Huskowska, E. 302, 314, 315, 322, 323
 Ge-Cheng, W., see Zhi-Bang, D. 369
 Gegenwart, P. 168, 190, 191
 Gegenwart, P., see Bianchi, A. 195
 Gegenwart, P., see Custers, J. 198
 Gegenwart, P., see Oeschler, N. 271, 272
 Gegenwart, P., see Steglich, F. 168, 189–191
 Gegenwart, P., see Won, H. 196
 Geibel, C. 199, 216, 228
 Geibel, C., see Böhm, A. 201
 Geibel, C., see Caspary, R. 217, 219
 Geibel, C., see Custers, J. 198

- Geibel, C., see Ehm, D. 191
 Geibel, C., see Feyerherm, R. 216–218
 Geibel, C., see Gegenwart, P. 168, 190, 191
 Geibel, C., see Grauel, A. 201, 216, 218
 Geibel, C., see Ishida, K. 229
 Geibel, C., see Kawasaki, Y. 113
 Geibel, C., see Krimmel, A. 217
 Geibel, C., see Kyogaku, M. 228
 Geibel, C., see Reinert, F. 144
 Geibel, C., see Sato, N.K. 146, 217, 225, 227
 Geibel, C., see Steglich, F. 168, 189–191
 Geibel, C., see Stockert, O. 168, 190
 Geibel, C., see Tou, H. 217–219
 Geibel, C., see Trovarelli, O. 36, 105
 Gelato, L., see Parthé, E. 79
 Georges, A. 198
 Geraldès, C.F.G.C., see Bobba, G. 341
 Gérault, Y., see Camara, M. 397, 398
 Gérault, Y., see Daiguebonne, C. 363, 366, 369, 372
 Gérault, Y., see Mahé, N. 401
 Ghirardelli, R.G., see Dyer, R.B. 345
 Ghirardelli, R.G., see Metcalf, D.H. 343
 Ghoshray, A., see Ghoshray, K. 107
 Ghoshray, A., see Sen, M. 107
 Ghoshray, K. 107
 Ghoshray, K., see Sen, M. 107
 Giacovazzo, C. 363
 Giester, G. 397, 401
 Giester, G., see Zak, Z. 397, 401
 Ginzburg, V. 229, 267
 Giorgi, A.L., see Fisher, R.A. 200, 204, 206
 Giorgi, A.L., see Heffner, R.H. 199
 Giorgi, A.L., see Rauchschalbe, U. 246
 Giovannini, M. 18, 26, 28, 29, 31, 38, 71, 108, 109
 Giovannini, M., see Bauer, E. 109
 Giovannini, M., see Fischer, P. 108, 110
 Giovannini, M., see Kaczorowski, D. 31, 108–110
 Giri, S., see Sen, M. 107
 Gladun, A., see Drechsler, S.-L. 251, 252
 Gladyshevskii, E.I. 52
 Gladyshevskii, E.I., see Grin, Yu.N. 45, 49, 55, 88, 192
 Gladyshevskii, E.I., see Kalychak, Ya.M. 14, 18, 24, 25, 45, 81, 86, 87
 Gladyshevskii, E.I., see Zaremba, V.I. 14, 65
 Gladyshevskii, R.E. 76
 Gladyshevskii, R.E., see Grin, Yu.N. 80, 83, 86, 88
 Gladyshevskii, R.E., see Parthé, E. 79
 Gliemann, G., see Schultheiss, R. 350, 352
 Gloos, K., see Bruls, G. 189
 Glover, D.P. 323, 324
 Glover, D.P., see Richardson, F.S. 323, 324
 Glover-Fischer, D.P. 301, 322–324, 328, 329
 Gochanour, C.R. 323
 Godart, C., see Bauer, E. 109
 Godart, C., see Lynn, J.W. 258
 Godart, C., see Nagarajan, N. 248
 Golding, B. 246
 Goldman, A.I., see Aeppli, G. 156
 Goldman, A.I., see Dervenagas, P. 253
 Goldman, A.I., see Yaron, U. 267
 Golhen, S., see Dimos, A. 391
 Golhen, S., see Kiritsis, V. 390, 393
 Golhen, S., see Mörtl, K.P. 360
 Golhen, S., see Sutter, J.P. 367
 Goll, G. 113, 194
 Gompf, F., see Felten, R. 245
 Gondek, Ł. 103
 Gondek, Ł., see Szytuła, A. 38, 102, 106
 Goodall, G., see Hüskén, D. 442
 Goodrich, R.G., see Alver, U. 111, 193
 Goodrich, R.G., see Hall, D. 111, 113
 Goodrich, R.G., see Macaluso, R.T. 10, 28, 34
 Goodwin, T.J., see Tang, J. 4, 14, 122, 123
 Gopalakrishnan, K.V., see Nagarajan, N. 248
 Gordon, R.A. 31, 61, 95, 108
 Goremychkin, E.A. 187, 188
 Goremychkin, E.A., see Christianson, A.D. 111
 Goreschnik, E.A., see Dubenskii, V.P. 10
 Gorkov, L. 161
 Gorkov, L.P. 180
 Gorkov, L.P., see Abrikosov, A.A. 150
 Gorkov, L.P., see Dzero, M.O. 115
 Gorkov, L.P., see Volovik, G.E. 156, 161, 243, 274
 Görlich, E.A., see Pöttgen, R. 38, 97, 98, 102, 104, 106, 122, 123
 Görrler-Walrand, C., see Parac-Vogt, T.N. 315, 331
 Gorshunov, B., see Dressel, M. 146, 199, 216
 Goryo, J. 274
 Goryo, J., see Izawa, K. 268, 272–274
 Goto, T., see Mitsuda, A. 117
 Goto, T., see Mushnikov, N.V. 117
 Goto, T., see Nakamura, S. 271
 Goto, T., see Shimizu, T. 116
 Goto, T., see Yoshimura, K. 116
 Goto, T., see Zhang, W. 117
 Gottwick, U., see Steglich, F. 185
 Govan, N., see Hay, R.W. 411
 Govenlock, L.J. 341
 Govenlock, L.J., see Beeby, A. 334, 340, 341
 Govenlock, L.J., see Bruce, J.I. 341

- Govenlock, L.J., see Maupin, C.L. 314, 330, 334, 336, 337, 340, 341
- Grabowski, P., see Cech, T. 408
- Graf, M.J. 171–173, 205, 211, 214
- Graf, T., see Movshovich, R. 183
- Graser, S., see Dahm, T. 253
- Gratz, E., see Felner, I. 114–116
- Gratz, E., see Severing, A. 115
- Gratz, G., see Nowik, I. 115
- Grael, A. 201, 216, 218
- Grael, A., see Böhm, A. 201
- Grael, A., see Geibel, C. 199, 216, 228
- Grael, A., see Krimmel, A. 217
- Gravereau, P. 71, 91
- Grenier, B., see Kernavanois, N. 231
- Grewe, N. 141
- Grewe, N., see Steglich, F. 185
- Gribanov, A., see Bauer, E. 160
- Gribanov, A.V., see Kurenbaeva, J.M. 27
- Grin, Yu.N. 45, 49, 53, 55, 80, 83, 86, 88, 192
- Grin, Yu.N., see Gladyshevskii, R.E. 76
- Grin, Yu.N., see Pöttgen, R. 36, 38
- Grin, Yu.N., see Sichevich, O.M. 66, 86
- Grin, Yu.N., see Trovarelli, O. 36, 105
- Griioni, M., see Malterre, D. 143
- Grisham, C.M., see Metcalf, D.H. 323, 326
- Grisham, C.M., see Stockman, T.G. 323, 325
- Grosche, F.M. 183, 191
- Grosche, F.M., see Mathur, N.D. 183
- Grosche, F.M., see Saxena, S.S. 199, 230
- Grosche, F.M., see Trovarelli, O. 36, 105
- Grosche, F.M., see Walker, I.R. 183
- Gross, M., see Decurtins, S. 360, 366, 367
- Groy, T.L., see Li, H. 363, 369
- Groy, T.L., see Yaghi, O.M. 360, 363, 369, 380, 383
- Grüner, G. 179
- Grüner, G., see Dressel, M. 146, 199, 216
- Gschneidner Jr., K.A., see Tang, J. 4, 14, 122, 123
- Gubbens, P.C.M., see Yaouanc, A. 146
- Guillot, M., see Balanda, M. 102–104
- Guillot, M., see Guillou, O. 366
- Guillou, O. 366
- Guillou, O., see Camara, M. 397, 398
- Guillou, O., see Chane-Ching, J.-Y. 401
- Guillou, O., see Daiguebonne, C. 363, 366, 368–370, 372, 389, 392, 397, 399
- Guillou, O., see Deluzet, A. 369, 377, 380, 382, 386, 390
- Guillou, O., see Kahn, O. 366
- Guillou, O., see Mahé, N. 401
- Guillou, O., see Oushoorn, R.L. 366
- Guimarães, A.P., see Larica, C. 118
- Gukasov, A., see Kohgi, M. 271
- Gulacsi, M., see Gulacsi, Z. 157, 180, 241
- Gulacsi, Z. 157, 180, 241
- Gulden, T., see Pöttgen, R. 4
- Gunnarsson, O. 103, 143
- Gunnlaugsson, T., see Bruce, J.I. 341
- Gunnlaugsson, T., see Dickins, R.S. 336, 341
- Gupta, L.C., see Lynn, J.W. 258
- Gupta, L.C., see Nagarajan, N. 248
- Gutschke, S.O.H. 363
- Gweon, G.-H., see Denlinger, J.D. 146, 187
- Gygax, F.N., see Feyerherm, R. 216–218
- Gygax, F.N., see Heffner, R.H. 246
- Haas, S., see Won, H. 196
- Habuta, E., see Kawano-Furukawa, H. 267, 268
- Haemmerle, W.H., see Golding, B. 246
- Haen, P., see Najib, A. 120
- Haga, Y. 111
- Haga, Y., see Fujimori, S. 193, 194
- Haga, Y., see Hiroi, M. 217, 219
- Haga, Y., see Ikeda, S. 114
- Haga, Y., see Inada, Y. 219–221
- Haga, Y., see Kawasaki, S. 113
- Haga, Y., see Kimura, N. 199, 203
- Haga, Y., see Kitaoka, Y. 205, 214, 215, 218
- Haga, Y., see Kobayashi, T.C. 231, 234, 235
- Haga, Y., see Koike, Y. 205
- Haga, Y., see Metoki, N. 146
- Haga, Y., see Mito, T. 113
- Haga, Y., see Ohkuni, H. 238, 244
- Haga, Y., see Sakakibara, T. 114
- Haga, Y., see Shishido, H. 111, 193, 194
- Haga, Y., see Sugiyama, K. 243
- Haga, Y., see Takeuchi, T. 113, 114, 194
- Haga, Y., see Tateiwa, N. 236
- Haga, Y., see Tayama, T. 114
- Haga, Y., see Tou, H. 214
- Haga, Y., see Watanabe, T. 228
- Haga, Y., see Zheng, G.-Q. 113, 194
- Hall, D. 111, 113
- Hall, D., see Pagliuso, P.G. 112
- Hall, D.W., see Alver, U. 111, 193
- Hall, J. 442
- Hall, J., see Hüsken, D. 442
- Hall, L.A., see Alleyne, B.D. 389
- Hammel, P.C., see Curro, N.J. 113
- Hammel, P.C., see Thompson, J.D. 28, 34, 111, 183

- Han, S., see Pan, L. 369, 376, 378
 Hanazono, K., see Kobayashi, T.C. 231, 234, 235
 Häner, R., see Hall, J. 442
 Häner, R., see Hüskén, D. 442
 Hanson, R.S., see Schnaith, L.M.T. 414
 Hansson, E. 360, 361
 Hao, N., see Li, Y. 363
 Harima, H. 187
 Harima, H., see Fujimori, S. 193, 194
 Harima, H., see Haga, Y. 111
 Harima, H., see Ikeda, S. 114
 Harima, H., see Kimura, N. 199, 203
 Harima, H., see Miyake, K. 274
 Harima, H., see Shishido, H. 193, 194
 Harima, H., see Sugawara, H. 269
 Harima, H., see Takegahara, K. 269
 Harita, A., see Sakakibara, T. 114
 Harita, A., see Tayama, T. 114
 Harmon, B.N., see Dervenagas, P. 253
 Harmon, B.N., see Rhee, J.Y. 253, 258
 Harris, I.R., see Bulyk, I.I. 107
 Harris, W.R., see Abdollahi, S. 349
 Harrison, N. 243
 Harrison, N., see Alver, U. 111, 193
 Harsha, K.S., see Mason, J.T. 81
 Haselwimmer, R.K.W., see Grosche, F.M. 183, 191
 Haselwimmer, R.K.W., see Mathur, N.D. 183
 Haselwimmer, R.K.W., see Saxena, S.S. 199, 230
 Hashimoto, S. 414
 Hasselbach, K. 170, 171, 243, 244
 Hasselbach, K., see Fisher, R.A. 200, 204, 206
 Hasselmann, N., see Efremov, D. 147, 149, 220
 Hattori, Y., see Pan, L. 387, 391
 Hauback, B.C., see Yartys, V.A. 107
 Hauser, R. 110
 Hauser, R., see Kaczorowski, D. 31, 108–110
 Hay, R.W. 411
 Hayano, T., see Iananaga, J. 368
 Hayashi, H., see Kojima, K. 115, 116
 Hayden, S.M. 199, 204, 206, 208
 Hedo, M. 115
 Heffner, R.H. 157, 199, 246
 Hegg, E.L. 407
 Hegger, H. 4, 28, 111, 191, 194
 Hegger, H., see Thompson, J.D. 28, 34, 111, 183
 Heinecke, M., see Shulga, S.V. 252
 Held, K., see McMahan, A.K. 150
 Helfrich, C. 245, 246
 Helfrich, R., see Gegenwart, P. 168, 190
 Helfrich, R., see Geibel, C. 199, 216, 228
 Helfrich, R., see Kromer, F. 244, 246
 Helfrich, R., see Steglich, F. 191
 Hellmann, P., see Caspary, R. 217, 219
 Hellmann, P., see Steglich, F. 191
 Henggeler, W., see Gasser, U. 260
 Hengsberger, M., see Garnier, M. 144
 Hentschel, S., see Robl, C. 363, 369, 382
 Hernandez, H.E., see Pan, L. 387, 391
 Herren, M. 334
 Herren, M., see Morita, M. 323, 327, 345
 Herren, M., see Murata, K. 345, 346
 Herring, C. 264
 Herrmann, W.A., see Brauer, G. 4
 Herrmannsdorfer, T., see Fischer, P. 108, 110
 Hertz, J.A. 197
 Hess, D.W. 207, 210
 Hessert, J. 217
 Hettich, R. 414
 Heusler, O. 63
 Hewson, A.C. 141, 143
 Heying, B., see Schlüter, M. 64
 Hidaka, Y., see Yagasaki, K. 29, 118
 Hiebl, K., see Kaczorowski, D. 14, 18, 28, 36, 38, 108–110
 Hiebl, K., see Weitzer, F. 7, 66, 86
 Hiess, A., see Bernhoeft, N. 146, 217, 224
 Higemoto, W., see Amitsuka, H. 237–239
 Higemoto, W., see Aoki, Y. 270, 275
 Hihara, T., see Kojima, K. 18, 114–116
 Hihara, T., see Oomi, G. 115
 Hill, R.W., see Boaknin, E. 250, 252
 Hilmes, G.L. 299, 300, 312–315, 320, 330, 331, 347, 348
 Hilmes, G.L., see Çoruh, N. 299, 314, 323, 325, 328, 330, 332, 349
 Hilmes, G.L., see Metcalf, D.H. 307, 308, 323, 325
 Hilmes, G.L., see Wu, S. 314, 330, 333
 Hilscher, G. 141, 248, 250–252
 Hilscher, G., see Bauer, E. 109, 160
 Hilscher, G., see Felner, I. 114–116
 Hilscher, G., see Giovannini, M. 18, 26, 31, 38, 71, 108, 109
 Hilscher, G., see Hauser, R. 110
 Hilscher, G., see Kaczorowski, D. 31, 108–110
 Hinks, D.G., see Adenwalla, S. 205
 Hinks, D.G., see Shivaram, B.S. 205
 Hinze, P., see Kromer, F. 244, 246, 247
 Hinze, P., see Steglich, F. 168, 189, 190
 Hippius, K.W. 350
 Hirasawa, T., see Ito, T. 104

- Hiroi, M. 217, 219
 Hiromitsu, I., see Ito, T. 104, 105
 Hirooka, Y., see Nishigori, S. 102–104
 Hirota, K., see Nakao, H. 241
 Hirschfeld, P. 170
 Hirschfeld, P.J., see Kübert, C. 171, 175
 Hirschfeld, P.J., see Norman, M.R. 171, 172, 205, 213
 Hirschfeld, P.J., see Vekhter, I. 175, 176
 Hitti, B., see Heffner, R.H. 246
 Ho, P.-C., see Bauer, E.D. 268, 269, 271
 Ho, P.-C., see Frederick, N.A. 269
 Ho, P.-C., see Maple, M.B. 269, 270
 Ho, P.-C., see Vollmer, R. 269–272
 Ho, P.-C., see Zapf, V.S. 111
 Hof, K.D., see Zapf, V.S. 111
 Hoffmann, R., see Landrum, G.A. 98
 Hoffmann, R.-D. 3, 28, 31, 38, 54, 59, 93, 97, 122
 Hoffmann, R.-D., see Esmaeilzadeh, S. 27
 Hoffmann, R.-D., see Galadzhun, Ya.V. 31, 36, 38, 57, 59, 122
 Hoffmann, R.-D., see Kalychak, Ya.M. 3, 14, 40, 99
 Hoffmann, R.-D., see Kußmann, D. 6
 Hoffmann, R.-D., see Lukachuk, M. 14, 74
 Hoffmann, R.-D., see Müllmann, R. 105
 Hoffmann, R.-D., see Pöttgen, R. 4, 6, 14, 28, 96, 102, 105, 122, 123
 Hoffmann, R.-D., see Rodewald, U.-Ch. 36, 51
 Hoffmann, R.-D., see Zaremba, V.I. 6, 10, 14, 28, 31, 36, 44, 47, 51, 64, 102, 105
 Hofmann, H., see Jongen, N. 360
 Hofmann, M., see Javorský, P. 103
 Hofmann, W. 70
 Holden, T.M., see Buyers, W.J.L. 224
 Holt, E.M., see Dyer, R.B. 345
 Holtmeier, S., see van Dijk, N.H. 205, 209
 Hong, M., see Cao, R. 363, 369, 382, 385, 396
 Honma, T., see Inada, Y. 219–221
 Honma, T., see Ohkuni, H. 238, 244
 Honma, T., see Sugiyama, K. 243
 Hoogenboom, B.W., see Eskildsen, M.R. 196
 Hopfgartner, G., see Muller, G. 342, 343
 Hopkins, T.A. 295, 298
 Hopkins, T.A., see Glover-Fischer, D.P. 301, 322, 328
 Horn, R., see Gegenwart, P. 168, 190
 Horrocks, W.d.J. 346
 Hossain, Z., see Lynn, J.W. 258
 Hossain, Z., see Nagarajan, N. 248
 Hotta, T. 170
 Hotta, T., see Yanase, Y. 141
 Houser, R.P., see Cheng, D. 363
 Houser, R.P., see Copeland, K.D. 407
 Hovestreydt, E., see Jorda, J.L. 31
 Howard, J.A.K., see Dickins, R.S. 318, 319, 334–336
 Howard, J.A.K., see Parker, D. 338
 Howie, R.A., see Plater, M.J. 363
 Hu, C., see Li, Y. 363
 Huang, J.-S., see Wu, C.-D. 369, 381, 384
 Huang, Q., see Lynn, J.W. 258
 Huang, X., see Pan, L. 369, 376, 378, 389
 Hufnagl, J., see Aeppli, G. 205, 206
 Hüfner, S., see Ehm, D. 191
 Hüfner, S., see Reinert, F. 144
 Hughes, R.J., see Dugdale, S.B. 251, 253
 Hulliger, F. 18, 28, 31, 36, 38, 108, 109
 Hulliger, F., see Bianchi, A.D. 121, 122
 Hulliger, F., see Schoenes, J. 146
 Hulliger, F., see Xue, B. 31, 62
 Hundley, M.F. 36, 121, 122
 Hundley, M.F., see Christianson, A.D. 111
 Hundley, M.F., see Cornelius, A.L. 111, 112, 116
 Hundley, M.F., see Hegger, H. 4, 28, 111, 191, 194
 Hundley, M.F., see Macaluso, R.T. 28, 34
 Hundley, M.F., see Pagliuso, P.G. 28, 34, 111, 112, 114
 Hundley, M.F., see Petrovic, C. 111, 183, 191, 192, 194
 Hundley, M.F., see Thompson, J.D. 28, 34, 111, 183
 Hundley, M.F., see Wei, B. 113
 Hunt, M. 187
 Huse, D.A., see Yaron, U. 267
 Hüsken, D. 442
 Hüsken, D., see Hall, J. 442
 Huskowska, E. 302, 314–317, 319–323, 330, 332, 333
 Huth, M., see Dressel, M. 146, 199, 216
 Huth, M., see Hessert, J. 217
 Huth, M., see Jourdan, M. 217, 225, 226
 Hutson, R.L., see Heffner, R.H. 199
 Huxley, A. 230
 Huxley, A., see Aoki, D. 230, 270
 Huxley, A., see Brison, J.-P. 200
 Huxley, A., see Demuer, A. 191
 Huxley, A., see Keller, N. 175, 244
 Huxley, A., see Kernavainois, N. 231
 Huxley, A., see Saxena, S.S. 199, 230

- Huxley, A., see Suderow, H. 214
Huxley, A.D., see Pfeleiderer, C. 234, 236
Hyde, S.T., see Chen, B. 363, 365
- Iananaga, J. 368
Iandelli, A. 69, 97
Ibarra, M.R., see De Teresa, J.M. 115
Ichioka, M. 274
Ichioka, M., see Nakai, N. 253
Igawa, T. 415
Igawa, T., see Sumaoka, J. 416, 438
Ihrig, H. 29, 33, 73, 118
Ihrig, H., see Balster, H. 120
Iijima, Y., see Shigekawa, H. 419
Iizuka, T., see Shishido, H. 193, 194
Ijiri, Y. 31, 109, 121, 122
Ijiri, Y., see Gordon, R.A. 108
Ikawa, H., see Shigekawa, H. 419
Ikeda, H. 179, 236, 241, 242
Ikeda, H., see Yanase, Y. 141
Ikeda, S. 114
Ikeda, S., see Fujimori, S. 193, 194
Ikeda, S., see Haga, Y. 111
Ikeda, S., see Shishido, H. 193, 194
Ikeda, S., see Takeuchi, T. 113
Imai, M., see Suzuki, H. 117
Imai, T., see Shigekawa, H. 419
Imai, T., see Takeda, N. 414
Imamoto, T. 389
Imamura, Y., see Kotegawa, H. 272
Immer, C.D. 115
Immer, C.D., see Sarrao, J.L. 116
Inada, Y. 219–221
Inada, Y., see Haga, Y. 111
Inada, Y., see Ohkuni, H. 238, 244
Inada, Y., see Shishido, H. 111, 193, 194
Inada, Y., see Sugawara, H. 269
Ingersent, K., see Si, Q. 197
Iniotakis, C., see Dahm, T. 253
Ino, A., see Fujimori, S. 194
Inoue, T., see Fujii, H. 4, 101
Inoue, T., see Takeuchi, T. 114, 194
Irisawa, M., see Takeda, N. 414
Ishida, K. 229
Ishida, K., see Kawasaki, Y. 113
Ishida, K., see Kitaoka, Y. 205, 214, 215, 218
Ishida, K., see Mito, T. 113
Ishida, K., see Tou, H. 173, 214, 218
Ishida, M., see Shigekawa, H. 419
Ishiguro, A., see Inada, Y. 219
Ishikawa, F., see Mushnikov, N.V. 117
Ishikawa, M., see Jorda, J.L. 31
Ishikubo, A., see Yashiro, M. 452
Islam, Z., see Fisher, I.R. 108, 110
Isshiki, M., see Nohara, M. 250, 253, 255, 257
Ito, K., see Nakamura, H. 117
Ito, T. 104, 105
Ito, T., see Nishigori, S. 102–104
Iverson, B.L., see Magda, D. 427, 442
Iwamoto, Y., see Kohori, Y. 113, 194
Iwamura, M., see Morita, M. 374
Iwasa, K., see Kohgi, M. 221
Iye, Y., see Kagayama, T. 120
Izawa, K. 113, 175, 178, 194, 195, 250, 256, 257, 268, 272–274
Izawa, K., see Maki, K. 273, 274
Izawa, K., see Matsuda, Y. 194
Izawa, K., see Watanabe, T. 228
Izumi, F., see Kojima, K. 18, 114
Izyumov, Y.A. 141
- Jaccard, D. 183
Jaccard, D., see Alami-Yadri, K. 119
Jahnke, W., see Hüsken, D. 442
Jaime, M. 239, 242, 243
Jaime, M., see Harrison, N. 243
Jaime, M., see Hundley, M.F. 36, 121, 122
Jaime, M., see Movshovich, R. 114
Jaime, M., see Petrovic, C. 111, 183, 191, 194
Jaime, M., see Thompson, J.D. 28, 34, 111, 183
Jäniche, W., see Hofmann, W. 70
Japaridze, G.I., see Nersesyan, A.A. 180, 181
Jarlborg, T., see Dugdale, S.B. 251, 253
Javorský, P. 103
Javorský, P., see Daniš, S. 31, 104
Jaworska-Gołąb, T., see Szytuła, A. 38, 102, 106
Jayprakash, C. 145
Jeevan, H., see Stockert, O. 168, 190
Jeitschko, W., see Kanatzidis, M.G. 6
Jeitschko, W., see Niepmann, D. 5
Jellinek, F., see Rundqvist, S. 66
Jensen, J. 222, 258, 262
Jeong, Y.H., see Shivaram, B.S. 205
Jex, H., see Maetz, J. 29, 33, 74
Jeziński, A., see Gondek, Ł. 103
Jia-Zan, N., see Zhi-Bang, D. 369
Jin, L., see Wan, Y. 389
Jin, T., see Wang, R. 398, 400
Jin, T.Z., see Ma, B.Q. 398
Jiricek, J., see Muller, G. 343
Johansson, B., see Lundin, U. 147
Johansson, B., see Söderlind, P. 147

- Johnson, C.R., see Brittain, H.G. 347
 Johnston-Halperin, E., see Canfield, P.C. 259
 Johrendt, D., see Pöttgen, R. 6, 98
 Jones, B. 145
 Jones, C.D.W., see Gordon, R.A. 61, 95
 Jongen, N. 360
 Jorda, J.L. 31
 Jorge, G., see Jaime, M. 239, 242, 243
 Jourdan, M. 217, 225, 226
 Jourdan, M., see Hessert, J. 217
 Joynt, R. 141, 203–205, 207
 Joynt, R., see Wu, W.C. 171
 Ju, J., see Zhao, Y. 364
 Jujo, T., see Yanase, Y. 141
 Julian, S.R., see Grosche, F.M. 183, 191
 Julian, S.R., see Mathur, N.D. 183
 Julian, S.R., see Saxena, S.S. 199, 230
 Julian, S.R., see Tautz, F.S. 145, 185
- Kaczorowski, D. 14, 18, 28, 31, 36, 38, 102, 105, 108–110
 Kaczorowski, D., see Galadzhun, Ya.V. 36, 75
 Kaczorowski, D., see Geibel, C. 199, 228
 Kaczorowski, D., see Hauser, R. 110
 Kaczorowski, D., see Tchoula Tchokonte, M.B. 121
 Kaczorowski, D., see Zaremba, V.I. 14, 28, 31, 36, 47, 57, 102, 106
 Kadanoff, L. 172
 Kadena, Y., see Yagasaki, K. 118
 Kadono, R., see Aoki, Y. 270, 275
 Kadowaki, H., see Fak, B. 191
 Kadowaki, K., see Kawano, H. 262
 Kadowaki, K., see Kawano-Furukawa, H. 262, 267, 268
 Kaganov, M.I. 188
 Kagayama, T. 120, 121
 Kagayama, T., see Oomi, G. 115, 121
 Kahn, M.L., see Chevalier, B. 4, 107
 Kahn, M.L., see Daiguebonne, C. 366, 369, 389
 Kahn, M.L., see Sutter, J.P. 367
 Kahn, O. 366
 Kahn, O., see Daiguebonne, C. 366, 369, 389
 Kahn, O., see Guillou, O. 366
 Kahn, O., see Larionova, J. 360
 Kahn, O., see Mörtl, K.P. 360
 Kahn, O., see Oushoorn, R.L. 366
 Kahn, O., see Sutter, J.P. 367
 Kahwa, I.A. 360
 Kai, T., see Morita, M. 334
 Kaisaki, S., see Sanada, T. 367
- Kaiser, C.T., see Yaouanc, A. 146
 Kajimura, A. 415
 Kakurai, K., see Kita, H. 217, 218
 Kalatsky, V., see Canfield, P.C. 259
 Kallin, C., see Berlnsky, A.J. 196
 Kalvius, G.M., see Felner, I. 114–116
 Kalychak, Ya.M. 3, 7, 8, 10, 14, 15, 18, 20, 23–26, 39, 40, 42, 45, 48, 49, 54, 55, 61–63, 72, 76, 80–83, 85–89, 97, 99
 Kalychak, Ya.M., see Bakar, A.M. 18, 23
 Kalychak, Ya.M., see Baranyak, V.M. 10, 14, 18–22, 39, 47, 48, 58, 70, 88
 Kalychak, Ya.M., see Bulyk, I.I. 107
 Kalychak, Ya.M., see Dmytrakh, O.V. 18, 19
 Kalychak, Ya.M., see Dubenskii, V.P. 10
 Kalychak, Ya.M., see Esmaeilzadeh, S. 27
 Kalychak, Ya.M., see Galadzhun, Ya.V. 33, 36, 38, 59, 75
 Kalychak, Ya.M., see Hoffmann, R.-D. 3, 28, 31, 38, 54, 97
 Kalychak, Ya.M., see Koterlyn, M.D. 116
 Kalychak, Ya.M., see Lukachuk, M. 5, 14, 28, 74
 Kalychak, Ya.M., see Sysa, L.V. 10, 14, 18, 33, 40, 49, 68, 69, 81, 82, 124
 Kalychak, Ya.M., see Yartys, V.A. 107
 Kalychak, Ya.M., see Zaremba, V.I. 6, 10, 14, 28, 31, 36, 44, 47, 51–53, 57, 64, 65, 69, 71, 72, 78, 80, 89, 97, 102, 105, 124
 Kamarád, J., see De Teresa, J.M. 115
 Kamata, K. 257
 Kamata, K., see Izawa, K. 250, 256
 Kambe, S., see Braithwaite, D. 191
 Kamimura, H., see Fujii, H. 101
 Kamimura, T., see Li, D.X. 102, 104
 Kamitani, J., see Komiyama, M. 427
 Kan, H., see Zheng, G.-Q. 113
 Kanatzidis, M.G. 6
 Kanayama, T., see Aoki, Y. 270, 275
 Kaneko, K., see Pan, L. 387, 391
 Kanematsu, K., see Alfieri, G.T. 118
 Kang, Z., see Li, Y. 363
 Kankare, J., see Glover-Fischer, D.P. 301, 322, 328
 Kappler, J.P., see Besnus, M.J. 36, 38, 63, 118, 119
 Kappler, J.P., see Lahiouel, R. 120
 Karraker, D.G. 368
 Kartsovník, M., see Maki, K. 179, 181, 182
 Kartsovník, M.V., see Dóra, B. 182
 Kasahara, Y., see Watanabe, T. 228
 Kasamatsu, Y., see Kojima, K. 115, 116
 Kasaya, M. 20
 Kasper, J.S., see Frank, F.C. 95

- Kasper, N., see Dressel, M. 146, 199, 216
 Kasuya, T., see Takegahara, K. 116
 Kato, H., see Ōnuki, Y. 120
 Kato, M. 163, 166–168, 244, 248
 Kawanaka, H., see Fujii, H. 101
 Kawanaka, H., see Yamaguchi, Y. 101
 Kawano, H. 262
 Kawano-Furukawa, H. 262, 267, 268
 Kawarazaki, S., see Amitsuka, H. 237, 239
 Kawarazaki, S., see Yokoyama, M. 239, 241
 Kawasaki, S. 113, 192
 Kawasaki, S., see Mito, T. 113
 Kawasaki, S., see Zheng, G.-Q. 113, 194
 Kawasaki, Y. 113
 Kawasaki, Y., see Ishida, K. 229
 Kawasaki, Y., see Kawasaki, S. 113, 192
 Kawasaki, Y., see Kotegawa, H. 272
 Kawasaki, Y., see Mito, T. 113
 Kayzel, F.E., see de Visser, A. 236
 Kean, S.D., see Bobba, G. 341
 Kean, S.D., see Muller, G. 315, 319
 Kee, H.-Y. 172
 Kee, H.-Y., see Chakravarty, S. 179, 180, 183
 Keller, J., see Fulde, P. 141, 154, 170, 195, 250
 Keller, L., see Fischer, P. 108, 110
 Keller, M., see Caspary, R. 217, 219
 Keller, N. 175, 244
 Keller, N., see Brison, J.-P. 200
 Kelley, D., see Li, H. 363, 369
 Kelley, D., see Reneike, T.M. 369, 375, 377
 Keltz, S.P., see Brittain, H.G. 348
 Kemp, J.C. 308
 Kern, S., see Christianson, A.D. 111
 Kernavanois, N. 231, 238, 240
 Kernavanois, N., see Huxley, A. 230
 Ketterson, J.B., see Adenwalla, S. 205
 Khan, M.A., see Cheng, D. 363
 Kido, G., see Suzuki, H. 117
 Kido, G., see Tsujii, N. 18, 26, 109
 Kido, G., see Yoshimura, K. 116
 Kido, J. 368
 Kim, H.J., see Park, T. 177
 Kim, J.S. 112
 Kim, J.S., see Eddaoudi, M. 360, 364, 367
 Kim, J.S., see Kromer, F. 244, 246, 247
 Kim, K.H., see Jaime, M. 239, 242, 243
 Kim, S., see Fisher, R.A. 200, 204, 206
 Kim, Y.B., see Kee, H.-Y. 172
 Kimball, C.W., see Dwight, A.E. 14, 18, 31, 33, 36, 38
 Kimeridze, I.G., see Nersesyan, A.A. 180, 181
 Kimura, J., see Inada, Y. 219
 Kimura, N. 199, 203
 Kimura, N., see Kitaoka, Y. 205, 214, 215, 218
 Kimura, N., see Koike, Y. 205
 Kimura, N., see Tou, H. 214
 Kindo, K., see Shishido, H. 193, 194
 Kindo, K., see Sugiyama, K. 243
 Kindo, K., see Takeuchi, T. 114, 194
 King, C.A. 186
 Kiritsis, V. 390, 393
 Kirkpatrick, T.R. 291
 Kirtley, J.R., see Hasselbach, K. 170, 171, 243, 244
 Kirtley, J.R., see Tsuei, C.C. 141
 Kita, H. 217, 218
 Kitagawa, S., see Tong, M.-L. 363, 366
 Kitamura, Y. 434, 436
 Kitaoka, Y. 205, 214, 215, 218
 Kitaoka, Y., see Ishida, K. 229
 Kitaoka, Y., see Kawasaki, S. 113, 192
 Kitaoka, Y., see Kawasaki, Y. 113
 Kitaoka, Y., see Kotegawa, H. 272
 Kitaoka, Y., see Kuramoto, Y. 141
 Kitaoka, Y., see Kyogaku, M. 228
 Kitaoka, Y., see Mito, T. 113
 Kitaoka, Y., see Nakamura, H. 115
 Kitaoka, Y., see Tou, H. 173, 214, 217–219
 Kitaoka, Y., see Zheng, G.-Q. 113, 194
 Kitazawa, H., see Geibel, C. 199, 216
 Kitazawa, H., see Suzuki, H. 117
 Kitazawa, H., see Tsujii, N. 18, 26, 109
 Kitô, H., see Tsujii, N. 18, 26, 109
 Kjekshus, A., see Vajeeston, P. 100, 107
 Kjems, J.K., see Aeppli, G. 205, 206
 Kjems, J.K., see Broholm, C. 236, 237, 243
 Klaasse, J.C.P., see Brüch, E. 101, 102
 Klemm, R., see Scharnberg, K. 170
 Klevickis, C.A., see Stockman, T.G. 323, 325
 Knetsch, E.A., see Heffner, R.H. 246
 Knöpfle, K. 219
 Knott, H., see Dwight, A.E. 3
 Kobayashi, N., see Hiroi, M. 217, 219
 Kobayashi, T.C. 231, 234, 235
 Kobayashi, T.C., see Shishido, H. 111, 193, 194
 Kobayashi, T.C., see Tateiwa, N. 236
 Kobori, A., see Ōnuki, Y. 120
 Kockel, A., see Balster, H. 120
 Koda, A., see Aoki, Y. 270, 275
 Kodama, T., see Komiyama, M. 409, 410, 433
 Koehler, W.C., see Cable, J.W. 33, 118
 Koepernik, K., see Rosner, H. 253

- Koga, A., see Frigeri, P. 160
 Koga, N., see Sato, N. 229
 Kogan, V.G., see Petrovic, C. 111, 194, 195
 Kohara, T., see Amitsuka, H. 237–239
 Kohara, T., see Kohori, Y. 113, 194
 Kohara, T., see Matsuda, K. 217, 219, 243
 Kohgi, M. 271
 Köhler, R., see Caspary, R. 217, 219
 Köhler, R., see Grauel, A. 201, 216, 218
 Kohno, H., see Miyake, K. 274
 Kohori, Y. 113, 194
 Kohori, Y., see Amitsuka, H. 237–239
 Kohori, Y., see Matsuda, K. 217, 219, 243
 Koike, Y. 205
 Koike, Y., see Kuriki, K. 368
 Koike, Y., see Metoki, N. 146
 Kojima, K. 18, 114–116
 Kojima, K., see Oomi, G. 115
 Komarovskaya, L.P., see Skolozdra, R.V. 85
 Komatsubara, T., see Bernhoeft, N. 146, 217, 224
 Komatsubara, T., see Böhm, A. 201
 Komatsubara, T., see Feyerherm, R. 216–218
 Komatsubara, T., see Inada, Y. 219
 Komatsubara, T., see Kagayama, T. 120, 121
 Komatsubara, T., see Kimura, N. 199, 203
 Komatsubara, T., see Kita, H. 217, 218
 Komatsubara, T., see Onuki, Y. 120
 Komatsubara, T., see Oomi, G. 121
 Komatsubara, T., see Sato, N. 217, 224, 229
 Komatsubara, T., see Sato, N.K. 146, 217, 225, 227
 Komatsubara, T., see Takahashi, T. 146
 Komatsubara, T., see Tateiwa, N. 228
 Komiyama, M. 407–410, 427, 433, 451
 Komiyama, M., see Arishima, H. 440
 Komiyama, M., see Igawa, T. 415
 Komiyama, M., see Kajimura, A. 415
 Komiyama, M., see Kitamura, Y. 434, 436
 Komiyama, M., see Kuzuya, A. 444, 448
 Komiyama, M., see Matsumoto, Y. 409
 Komiyama, M., see Matsumura, K. 411, 426, 428, 442
 Komiyama, M., see Miyama, S. 410
 Komiyama, M., see Shigekawa, H. 419
 Komiyama, M., see Shiiba, T. 409
 Komiyama, M., see Sumaoka, J. 411, 416, 419, 427, 434, 438
 Komiyama, M., see Takarada, T. 451
 Komiyama, M., see Takeda, N. 414
 Komiyama, M., see Yamamoto, Y. 438
 Komiyama, M., see Yashiro, M. 452
 Konczykowski, M., see Morin, P. 192
 Konno, R. 166
 Korin-Hamzic, B. 179
 Korin-Hamzic, B., see Basletic, M. 179, 182
 Korin-Hamzic, B., see Dóra, B. 182
 Korin-Hamzic, B., see Maki, K. 179, 181, 182
 Koshelev, A., see Metlushko, V. 252
 Kosuge, K., see Mitsuda, A. 117
 Kosuge, K., see Yoshimura, K. 116
 Kosuge, K., see Zhang, W. 117
 Kotegawa, H. 272
 Koterlyn, M.D. 116
 Kotliar, G., see Chitra, R. 198
 Kotliar, G., see Georges, A. 198
 Kotur, B.Ya., see Kalychak, Ya.M. 14, 45, 87
 Kotzyba, G., see Galadzhun, Ya.V. 31, 38, 122
 Kotzyba, G., see Hoffmann, R.-D. 38, 59, 122
 Kotzyba, G., see Müllmann, R. 102, 105
 Kotzyba, G., see Pöttgen, R. 4, 6, 28, 38, 97, 98, 102, 104–106, 122, 123
 Kouroudis, I., see Bruls, G. 189
 Koyama, K., see Mizuno, K. 250
 Koyama, K., see Nakao, H. 241
 Krajewski Jr., J.J., see Cava, R.J. 248
 Krausz, E.R., see Schatz, P.N. 350
 Krauth, W., see Georges, A. 198
 Kremer, R.K., see Müllmann, R. 105
 Kremer, R.K., see Pöttgen, R. 14, 96, 122, 123
 Krimmel, A. 217
 Kripyakevich, P.I. 63, 66, 78, 79, 82–85, 88, 91
 Kripyakevich, P.I., see Gladyshevskii, E.I. 52
 Kripyakevich, P.I., see Yarmolyuk, Ya.P. 61
 Krishna-murthy, H.-R., see Jayprakash, C. 145
 Krogmann, K., see Becher, H.J. 71, 89
 Kroha, J., see Reinert, F. 144
 Kromer, F. 244, 246, 247
 Kromer, F., see Gegenwart, P. 191
 Krug, K., see Shulga, S.V. 252
 Krug, K., see Winzer, K. 258
 Kuang, J.P., see Brück, E. 102
 Kübert, C. 171, 175
 Kübler, J., see Ihrig, H. 29, 33, 73, 118
 Kübler, J., see Knöpfe, K. 219
 Kübler, J., see Sandratskii, L.M. 219
 Kuentzler, R., see Sampathkumaran, E.V. 115
 Kumar, P., see Yip, S.-K. 210
 Kundaliya, D., see Raj, P. 107
 Kunii, S., see Nakamura, S. 271
 Kunii, S., see Nakao, H. 241
 Künnen, B., see Galadzhun, Ya.V. 31, 38, 122
 Künnen, B., see Hoffmann, R.-D. 38, 59, 122

- Künnen, B., see Pöttgen, R. 4, 6, 28, 102, 105
 Kuramoto, Y. 141
 Kurenbaeva, J.M. 27
 Kuriki, K. 368
 Kurisu, M. 4, 103
 Kurisu, M., see Ito, T. 104, 105
 Kuroda-Sowa, T., see Wu, L.P. 369, 383, 387
 Kußmann, D. 6
 Kußmann, D., see Pöttgen, R. 6, 28, 44, 96, 98
 Kuusela, S., see Oivanen, M. 407
 Kuwahara, K., see Amitsuka, H. 237, 239
 Kuz'ma, Yu.B. 86, 88, 90
 Kuzuya, A. 444, 448
 Kuzuya, A., see Komiyama, M. 407, 408
 Kwei, G.H., see Cornelius, A.L. 116
 Kwei, G.H., see Lawrence, J.M. 115
 Kyogaku, M. 228
- Lacerda, A., see Bianchi, A. 195, 196
 Lacerda, A., see Canfield, P.C. 259
 Lacerda, A., see Immer, C.D. 115
 Lacerda, A.H., see Christianson, A.D. 111
 Lacerda, A.H., see Pagliuso, P.G. 111
 Lachowski, E.E., see Plater, M.J. 363
 Laffargue, D., see Gravereau, P. 71, 91
 Lahiouel, R. 120
 Lahiouel, R., see Besnus, M.J. 36, 38, 63, 118
 Lal, H.B. 29, 33, 73, 118, 119
 Landau, L.D. 150
 Lander, G.H., see Bernhoeft, N. 146, 217, 224
 Lander, G.H., see Sarrao, J.L. 192
 Lander, G.H., see Sato, N. 217, 224
 Landrum, G.A. 98
 Lang, A., see Pöttgen, R. 6
 Lang, M. 141
 Lang, M., see Bruls, G. 189
 Lang, M., see Gegenwart, P. 168, 190, 191
 Lang, M., see Kromer, F. 244, 246, 247
 Lang, M., see Steglich, F. 168, 189–191
 Langhammer, C., see Gegenwart, P. 168, 190
 Langhammer, C., see Kromer, F. 244, 246, 247
 Langhammer, C., see Steglich, F. 168, 189–191
 Lapertot, G., see Fak, B. 191
 Lapunova, R.V., see Sichevich, O.M. 66, 86
 Larica, C. 118
 Larionova, J. 360
 Larson, A.C. 69, 81
 Larson, A.C., see Cromer, D.T. 80
 Lasailly, Y., see Morin, P. 192
 Łątko, K., see Pöttgen, R. 38, 97, 98, 102, 104, 106, 122, 123
- Laughlin, R.B., see Chakravarty, S. 180
 Laurent, J.P., see Costes, J.P. 367
 Lawrence, J.M. 114, 115
 Lawrence, J.M., see Christianson, A.D. 111
 Lawrence, J.M., see Cornelius, A.L. 116
 Lawrence, J.M., see Sarrao, J.L. 116
 Layzer, A. 154
 Le Dret, F., see Camara, M. 397, 398
 Le Dret, F., see Daiguebonne, C. 369
 Lecerf, A., see Daiguebonne, C. 366, 369, 372
 Lee, J.O., see Cava, R.J. 248
 Lee, S., see Yuan, Q. 170, 255
 Lee, S.-H., see Gaulin, B.D. 228
 Lee, S.-I., see Doh, H. 263
 Lee, S.-I., see Park, T. 177
 Lees, M.R., see Majumdar, S. 114
 Legendziewicz, J., see Dossing, A. 316
 Legendziewicz, J., see Gawryszewska, P. 315–317
 Legendziewicz, J., see Huskowska, E. 302, 314–316, 322, 323
 Legendziewicz, J., see Sokolnicki, J. 301, 302, 314, 315, 322, 323
 Lehmann, C.W., see Dickins, R.S. 334–336
 Leifer, L., see Maupin, C.L. 321
 Leithe-Jasper, A., see Weitzer, F. 7, 66, 86
 Lejay, P., see Brison, J.-P. 200
 Lejay, P., see Hasselbach, K. 244
 Lejay, P., see Keller, N. 175, 244
 Lejay, P., see Kernavainois, N. 238, 240
 Lejay, P., see Martinez-Samper, P. 251
 Lejay, P., see Regnault, L.P. 185
 Lejay, P., see van Dijk, N.H. 191
 Lemaître, J., see Jongen, N. 360
 Letant, A., see Allemand, J. 66
 Levy, M., see Adenwalla, S. 205
 Lhotel, E., see Aoki, D. 230, 270
 Lhotel, E., see Measson, M.-A. 272
 Li, C.Q.H., see Hall, D. 111, 113
 Li, D.X. 102, 104
 Li, G., see Yaghi, O.M. 360, 363
 Li, H. 363, 369
 Li, H., see O'Keeffe, M. 360
 Li, H., see Yaghi, O.M. 360, 363, 369, 380, 383
 Li, J., see Pan, L. 369, 376, 378, 389
 Li, J.-Y., see Brück, E. 102
 Li, J.R. 395, 396
 Li, J.R., see Bu, X.H. 395, 396
 Li, T., see Yip, S.-K. 210
 Li, X., see Zhao, Y. 364
 Li, Y. 363
 Liang, Y., see Cao, R. 369, 382, 385, 396

- Licht, R.L., see Heffner, R.H. 199
 Lieke, W., see Steglich, F. 183
 Lifshits, I.M., see Kaganov, M.I. 188
 Light, B.E., see Pagliuso, P.G. 111
 Lin, A., see Magda, D. 427, 442
 Lin, H., see Broholm, C. 237, 243
 Lin, S.W., see Adenwalla, S. 205
 Link, A., see Gegenwart, P. 168, 190
 Lipp, D., see Drechsler, S.-L. 251, 252
 Lippelt, E., see Heffner, R.H. 246
 Liß, K.D., see Kernavanois, N. 238, 240
 Lister, S.J.S., see Grosche, F.M. 183, 191
 Liu, H., see Wang, R. 398, 400
 Liu, J. 367
 Liu, W. 146
 Lo, S.M.-F., see Chui, S.S.-Y. 362, 364
 Loewenhaupt, R., see Stockert, O. 168, 190
 Logue, M.W., see Belair, S.D. 301, 315, 322
 Löhle, J., see Schoenes, J. 146
 Loidl, A., see Krimmel, A. 217
 Long, D.L. 389
 Lönnberg, H., see Oivanen, M. 407
 Lonzarich, G.G. 145, 186
 Lonzarich, G.G., see Bernhoeft, N. 199
 Lonzarich, G.G., see Grosche, F.M. 183, 191
 Lonzarich, G.G., see King, C.A. 186
 Lonzarich, G.G., see Mathur, N.D. 183
 Lonzarich, G.G., see Monthoux, P. 157
 Lonzarich, G.G., see Saxena, S.S. 199, 230
 Lonzarich, G.G., see Taillefer, L. 199, 205
 Lonzarich, G.G., see Tautz, F.S. 145, 185
 Lonzarich, G.G., see Walker, I.R. 183
 Lopinski, S., see Bruce, J.I. 299, 320, 338–341
 Löser, W., see Drechsler, S.-L. 251, 252
 Louër, D., see Bataille, T. 360
 Lowe, M.P., see Bruce, J.I. 341
 Lu, C.-Z., see Wu, C.-D. 369, 381, 384
 Lu, S., see Wan, Y. 389
 Lu, S.-F., see Wu, C.-D. 369, 381, 384
 Lu, Y., see Li, Y. 363
 Luchier, N., see Martinez-Samper, P. 251
 Luck, R.L. 315, 319
 Lüders, K., see Müller, V. 246
 Lühmann, T., see Steglich, F. 190
 Luk, C.K. 291
 Lukachuk, M. 5, 14, 28, 74
 Lukachuk, M.O., see Dubenskii, V.P. 10
 Lundin, U. 147
 Lupien, C., see Boaknin, E. 250, 252
 Lussier, B. 199, 205, 213
 Lüthi, B., see Bruls, G. 189, 204, 210
 Lüthi, B., see Thalmeier, P. 141, 209, 240
 Lutziv, R.V., see Koterlyn, M.D. 116
 Lux-Steiner, M.-C., see Aeppli, G. 156
 Luxbacher, T., see Serpaggi, F. 360
 Lynn, J.W. 258
 Lynn, J.W., see Maple, M.B. 269, 270
 Lynn, J.W., see Wei, B. 113

 Ma, B.Q. 398
 Macaluso, R.T. 10, 28, 34
 Machida, K. 161, 163, 171, 172, 207, 210, 211, 231, 235
 Machida, K., see Aoki, H. 194
 Machida, K., see Ichioka, M. 274
 Machida, K., see Kato, M. 163, 166–168, 244, 248
 Machida, K., see Kuzuya, A. 448
 Machida, K., see Nakai, N. 253
 Machida, K., see Ohmi, T. 215
 Machida, K., see Ozaki, M. 161
 Mackenzie, A.P. 141
 Mackintosh, A.R., see Jensen, J. 222
 MacLaughlin, D.E., see Heffner, R.H. 199, 246
 Maekawa, M., see Wu, L.P. 369, 383, 387
 Maeno, Y. 101, 102
 Maeno, Y., see Fujii, H. 4, 101
 Maeno, Y., see Fujita, T. 101
 Maeno, Y., see Mackenzie, A.P. 141
 Maeno, Y., see Satoh, K. 101
 Maetz, J. 29, 33, 74
 Maezawa, K., see Braithwaite, D. 191
 Maezawa, K., see Kitaoka, Y. 205, 214, 215, 218
 Maezawa, K., see Koike, Y. 205
 Maezawa, K., see Tou, H. 214
 Magda, D. 427, 442
 Magishi, K., see Nakao, H. 241
 Mahé, N. 401
 Mahé, N., see Chane-Ching, J.-Y. 401
 Mai, Z., see Zhao, Y. 364
 Majumdar, S. 114
 Mak, T.C.W., see Chui, S.S.-Y. 369, 384, 388
 Maki, K. 141, 179, 181, 182, 215, 251, 254, 256, 273, 274
 Maki, K., see Basletic, M. 179, 182
 Maki, K., see Dahm, T. 175
 Maki, K., see Dóra, B. 182
 Maki, K., see Izawa, K. 250, 256, 268, 272–274
 Maki, K., see Kee, H.-Y. 172
 Maki, K., see Korin-Hamzic, B. 179
 Maki, K., see Rauchschalbe, U. 246
 Maki, K., see Sun, Y. 170
 Maki, K., see Thalmeier, P. 215, 228, 256, 257

- Maki, K., see Virosztek, A. 242
 Maki, K., see Watanabe, T. 228
 Maki, K., see Won, H. 175–177, 196, 256
 Maki, K., see Yang, G. 174, 212
 Maki, K., see Yuan, Q. 170, 255
 Maletta, H., see Krimmel, A. 217
 Malik, S.K. 36, 101–103, 117, 118
 Malik, S.K., see Adroja, D.T. 4, 28, 101
 Malik, S.K., see Nyayate, M.N. 102
 Malik, S.K., see Raj, P. 107
 Malinowski, A., see Macaluso, R.T. 28, 34
 Mallik, R. 110
 Mallik, R., see Sampathkumaran, E.V. 107
 Malterre, D. 143
 Mamiya, K., see Fujimori, S. 193, 194
 Mamula, O., see Muller, G. 343, 344
 Mandrus, D., see Lawrence, J.M. 115
 Mandrus, D., see Movshovich, R. 183
 Mandrus, D., see Sales, B.C. 268
 Mandrus, D., see Sarrao, J.L. 116
 Mandzyk, V.M., see Skolozdra, R.V. 47
 Manfrinetti, P. 106
 Manfrinetti, P., see Canepa, F. 10, 122
 Manfrinetti, P., see Dhar, S.K. 7, 26, 106
 Mao, M., see Gaulin, B.D. 228
 Maple, M.B. 269, 270
 Maple, M.B., see Bauer, E.D. 268, 269, 271
 Maple, M.B., see Denlinger, J.D. 146, 187
 Maple, M.B., see Fischer, O. 250
 Maple, M.B., see Frederick, N.A. 269
 Maple, M.B., see Goll, G. 113, 194
 Maple, M.B., see Kohori, Y. 113, 194
 Maple, M.B., see Oeschler, N. 271, 272
 Maple, M.B., see Vollmer, R. 269–272
 Maple, M.B., see Zapf, V.S. 111, 114
 Marabelli, F. 199
 Marazza, R. 36, 38, 63
 Marazza, R., see Ferro, R. 3, 10, 14, 28, 31, 34, 36, 63, 68
 Marazza, R., see Mazzone, D. 26, 69
 Marazza, R., see Rossi, D. 28, 33, 34, 36, 38, 68, 69
 Markiv, V.Ya. 64
 Markiv, V.Ya., see Kripyakevich, P.I. 66
 Marr, J., see Plater, M.J. 363
 Marrot, J., see Barthelet, K. 363
 Marrot, J., see Millange, F. 391, 395
 Marrot, J., see Serre, C. 379, 382
 Marsh, R.E., see Shoemaker, D.P. 39
 Martinez-Samper, P. 251
 Martins, G.B., see Curro, N.J. 113
 Marucha, Cz., see Kaczorowski, D. 102, 105
 Mason, J.T. 81
 Mason, S.F. 332
 Mason, S.F., see Barnett, C.J. 311
 Mason, T.E. 217, 223, 224
 Mason, T.E., see Broholm, C. 237, 243
 Mason, T.E., see Mentink, S.A.M. 238
 Mathieu, C.E., see Bobba, G. 341
 Mathieu, C.E., see Govenlock, L.J. 341
 Mathieu, C.E., see Maupin, C.L. 314, 330, 334, 336, 337, 340, 341
 Mathur, N.D. 183
 Mathur, N.D., see Grosche, F.M. 183, 191
 Matsubara, T., see Machida, K. 163
 Matsuda, K. 217, 219, 243
 Matsuda, K., see Amitsuka, H. 237–239
 Matsuda, Y. 194
 Matsuda, Y., see Izawa, K. 113, 175, 178, 194, 195, 250, 256, 257, 268, 272–274
 Matsuda, Y., see Maki, K. 273, 274
 Matsuda, Y., see Watanabe, T. 228
 Matsumara, T., see Nakamura, S. 271
 Matsumoto, T. 116
 Matsumoto, T., see Hedo, M. 115
 Matsumoto, Y. 409
 Matsumoto, Y., see Komiyama, M. 409, 433
 Matsumoto, Y., see Shiiba, T. 409
 Matsumura, K. 411, 426, 428, 442
 Matsumura, K., see Komiyama, M. 409, 433
 Mattenberger, K., see Schoenes, J. 146
 Mattheis, L.F. 253
 Matthews, P., see Broholm, C. 236
 Matthews, P.T., see Broholm, C. 237, 243
 Maudez, W., see Deluzet, A. 369, 377, 380, 386, 390
 Maupin, C.L. 292, 311, 314, 321, 323, 325, 328, 330, 334, 336, 337, 340, 341
 Maupin, C.L., see Aime, S. 338
 Maupin, C.L., see Beeby, A. 334, 340, 341
 Maupin, C.L., see Belair, S.D. 301, 315, 322
 Maupin, C.L., see Dickins, R.S. 318, 319, 334–336
 Maupin, C.L., see Govenlock, L.J. 341
 Maupin, C.L., see Huskowska, E. 302, 314, 315, 319–323
 Maupin, C.L., see Luck, R.L. 315, 319
 Maupin, C.L., see Muller, G. 342
 Maurer, D., see Müller, V. 246
 Mavromaras, A., see Knöpfler, K. 219
 May, P.S. 298
 Mayer, H.M., see Schlabit, W. 236
 Mayer, H.M., see Steglich, F. 185

- Mayer, P., see Galadzhun, Ya.V. 36
Mazumda, C., see Nagarajan, N. 248
Mazzone, D. 26, 69
Mazzone, D., see Rossi, D. 28, 33, 34, 36, 69
McCall, S., see Jaime, M. 239, 242, 243
McEwen, K.A., see Park, J.-G. 237, 257
McHale, P. 157, 228
McIntyre, G.J., see Campbell, A.J. 261
McK Paul, D., see Majumdar, S. 114
McMahan, A.K. 150
McMillan, W.L., see Bilbro, G. 163
McMullen, G.J. 199–201, 203
McMullen, G.J., see Tautz, F.S. 145, 185
Measson, M.-A. 272
Mederle, S., see Trovarelli, O. 36, 105
Meeson, P., see Hunt, M. 187
Mehner, A., see Geibel, C. 199, 228
Mekata, M., see Shimizu, T. 116
Mekata, M., see Yoshimura, K. 116
Mel'nyk, Ya.V., see Kripyakevich, P.I. 66
Menchetti, C., see Giacomazzo, C. 363
Menovsky, A.A., see Broholm, C. 236, 237, 243
Menovsky, A.A., see Bruls, G. 204, 210
Menovsky, A.A., see de Visser, A. 236
Menovsky, A.A., see Frings, P.H. 199
Menovsky, A.A., see Mentink, S.A.M. 238
Menovsky, A.A., see Palstra, T.T.M. 199, 236
Menovsky, A.A., see Thalmeier, P. 209
Menovsky, A.A., see Walker, M.B. 236
Menovsky, A.A., see Yaouanc, A. 146
Mentink, S.A.M. 238
Mentink, S.A.M., see Moze, O. 14, 121
Merlo, F., see Canepa, F. 4, 10, 78, 122, 123
Meschede, D., see Steglich, F. 183
Meskers, S.C.J. 295, 323, 325–327, 329
Meskers, S.C.J., see Maupin, C.L. 323, 325, 328
Meskers, S.C.J., see Mondry, A. 301, 315, 321, 322
Meskers, S.C.J., see Rexwinkel, R.B. 307, 308, 323, 325, 328
Mesot, J., see Gasser, U. 260
Metcalf, D.H. 301, 303, 307, 308, 313–315, 322–326, 328, 329, 343
Metcalf, D.H., see Bolender, J.P. 323, 324
Metcalf, D.H., see Dyer, R.B. 345
Metcalf, D.H., see Glover, D.P. 323, 324
Metcalf, D.H., see Glover-Fischer, D.P. 301, 322–324, 328, 329
Metcalf, D.H., see Hopkins, T.A. 295, 298
Metcalf, D.H., see May, P.S. 298
Metcalf, D.H., see Richardson, F.S. 323, 324
Methfessel, S., see Balster, H. 120
Methfessel, S., see Ihrig, H. 29, 33, 73, 118
Methfessel, S., see Lal, H.B. 29, 33, 73, 118, 119
Metlushko, V. 252
Metoki, N. 146, 206
Metoki, N., see Amitsuka, H. 237, 239
Metoki, N., see Kohgi, M. 271
Metoki, N., see Koike, Y. 205
Meyer, A., see Besnus, M.J. 36, 38, 63, 118, 119
Meyer, G., see Starynowicz, P. 389
Meyers, E.A., see Liu, J. 367
Michaelides, A. 360
Michaelides, A., see Dimos, A. 391
Michaelides, A., see Kiritsis, V. 390, 393
Michel, L. 161
Michels, T., see Kromer, F. 244, 246
Michor, H., see Bauer, E. 109, 160
Michor, H., see Giovannini, M. 18, 26, 31, 38, 71, 108, 109
Michor, H., see Hauser, R. 110
Michor, H., see Hilscher, G. 141, 248, 250–252
Michor, H., see Kaczorowski, D. 31, 108–110
Mielke, C., see Immer, C.D. 115
Mignot, J.-M., see Kohgi, M. 271
Mignot, J.-M., see Morin, P. 192
Mignot, J.-M., see van Dijk, N.H. 191
Mihalik, M., see Yaouanc, A. 146
Miles, D., see Magda, D. 427, 442
Miliyanchuk, K.Y., see Kalychak, Ya.M. 3, 14, 40, 99
Millange, F. 391, 395
Millange, F., see Serre, C. 375, 376, 379, 382
Miller, C.E., see May, P.S. 298
Miller, R.A., see Magda, D. 427, 442
Miller-Ricci, E., see Hall, D. 111, 113
Millis, A.J. 157, 197
Minami, A., see Kojima, K. 115
Mineev, V.P. 141, 161, 165, 214, 231
Mineev, V.P., see Barash, Y.S. 175
Mirambet, F., see Gravereau, P. 71, 91
Miranović, P., see Aoki, H. 194
Miranović, P., see Nakai, N. 253
Mita Sen, see Ghoshray, K. 107
Mitamura, H., see Zhang, W. 117
Mito, T. 113
Mito, T., see Kawasaki, S. 113, 192
Mito, T., see Kawasaki, Y. 113
Mito, T., see Zheng, G.-Q. 113, 194
Mitra, C., see Dhar, S.K. 7, 106
Mitra, C., see Manfrinetti, P. 106
Mitsuda, A. 117

- Mitsuda, A., see Zhang, W. 117
Miyake, K. 154, 156, 229, 274
Miyake, K., see Okuno, Y. 236
Miyake, K., see Sato, N.K. 146, 217, 225, 227
Miyake, K., see Schmitt-Rink, S. 170
Miyake, K., see Shigekawa, H. 419
Miyake, K., see Watanabe, S. 231, 236
Miyako, Y., see Amitsuka, H. 237, 239
Miyama, S. 410
Miyama, S., see Sumaoka, J. 419
Miyazaki, S., see Amitsuka, H. 237–239
Mizoguchi, R., see Kuzuya, A. 444, 448
Mizuhashi, K., see Cava, R.J. 248
Mizuno, K. 250
Mock, S. 110
Modler, R., see Bruls, G. 189
Modler, R., see Grauel, A. 201, 216, 218
Molenveld, P. 452
Molinier, M., see Gutschke, S.O.H. 363
Möller, M.H., see Pöttgen, R. 4, 28, 102, 105
Möller, M.H., see Zaremba, V.I. 6, 14
Moloney, J.M., see Dickins, R.S. 318, 319, 334–336
Mombelli, B., see Larionova, J. 360
Mondry, A. 301, 315, 321, 322
Mondry, A., see Maupin, C.L. 321
Monien, H., see Scharnberg, K. 170
Monthoux, P. 154, 157
Monthoux, P., see McHale, P. 157
Monthoux, P., see Petrovic, C. 111, 183, 192
Monthoux, P., see Saxena, S.S. 199, 230
Moraal, P.F., see Dekkers, H.P.J.M. 310
Morales, L.A., see Sarrao, J.L. 192
Moran, D.M. 298
Moreau, J.M., see Allemand, J. 66
Moreno, N.O., see Alver, U. 111, 193
Moreno, N.O., see Christianson, A.D. 111
Moreno, N.O., see Macaluso, R.T. 10, 28, 34
Moreno, N.O., see Nicklas, M. 112
Moreno, N.O., see Pagliuso, P.G. 111
Moreno, N.O., see Sarrao, J.L. 192
Morimoto, H., see Amitsuka, H. 237, 239
Morimoto, T., see Takahashi, T. 146
Morin, P. 192
Morisawa, F., see Kuzuya, A. 444, 448
Morita, M. 323, 327, 334, 345, 352, 353
Morita, M., see Herren, M. 334
Morita, M., see Murata, K. 345, 346
Morita, M., see Rau, D. 334
Morita, M., see Tsubomura, T. 345
Moriya, T. 141, 197
Morley, J.P. 299, 352
Morokhivsky, B.S., see Koterlyn, M.D. 116
Morosov, A.I. 265
Morr, D.K., see Chakravarty, S. 180
Morrow, J.R. 409, 411, 427
Morrow, J.R., see Chin, K.O.A. 427
Mortensen, K., see Yaron, U. 267
Mörtl, K.P. 360
Mosel, B.D., see Hoffmann, R.-D. 38, 59, 122
Mosel, B.D., see Müllmann, R. 102, 105
Mosel, B.D., see Pöttgen, R. 4, 6, 14, 28, 102, 105, 122, 123
Moser, H.E., see Hüsken, D. 442
Moser, J., see Felner, I. 114–116
Moshopoulou, E.G. 4, 28, 34
Moshopoulou, E.G., see Hegger, H. 4, 28, 111, 191, 194
Mosset, A., see Romero, S. 360
Mosset, A., see Trollet, D. 360
Mota, A.C. 248
Mota, A.C., see Dumont, E. 248
Movshovich, R. 114, 183
Movshovich, R., see Bianchi, A. 195, 196
Movshovich, R., see Hundley, M.F. 36, 121, 122
Movshovich, R., see Pagliuso, P.G. 112
Movshovich, R., see Petrovic, C. 111, 183, 191, 192, 194
Movshovich, R., see Thompson, J.D. 28, 34, 111, 183
Mowery, R.L., see Schatz, P.N. 350
Moze, O. 14, 121
Mueller, M.H., see Dwight, A.E. 3
Muellner, M., see Maetz, J. 29, 33, 74
Mulder, F.M. 14, 121
Muller, G. 314, 315, 319, 331, 333, 342–344
Muller, G., see Cantuel, M. 312
Muller, G., see Field, J.E. 306
Muller, G., see Gawryszewska, P. 315–317
Muller, G., see Sokolnicki, J. 302, 315
Müller, H., see Dóra, B. 182
Müller, J., see Lang, M. 141
Müller, K., see Drechsler, S.-L. 251, 252
Müller, K.-H. 141, 248, 250, 258
Müller, K.H., see Shulga, S.V. 252
Müller, U., see Bärnighausen, H. 78
Müller, V. 246
Müllmann, R. 102, 105
Müllmann, R., see Pöttgen, R. 6, 14, 122, 123
Munakata, M., see Wu, L.P. 369, 383, 387
Murakami, Y., see Nakao, H. 241
Murakawa, M., see Haga, Y. 111

- Muramatsu, T., see Shishido, H. 111
 Muramatsu, Y., see Fujimori, S. 193, 194
 Murani, A.P., see Galera, R.M. 33, 119, 120
 Murani, A.P., see Lahiouel, R. 120
 Murani, A.P., see Najib, A. 120
 Murata, K. 345, 346
 Mürner, H.-R., see Muller, G. 343, 344
 Murphy, T.P., see Alver, U. 111, 193
 Murphy, T.P., see Hall, D. 111, 113
 Mushnikov, N.V. 117
 Mydosch, J.A., see Amitsuka, H. 237, 239
 Mydosch, J.A., see Broholm, C. 236, 237, 243
 Mydosch, J.A., see Harrison, N. 243
 Mydosch, J.A., see Heffner, R.H. 246
 Mydosch, J.A., see Jaime, M. 239, 242, 243
 Mydosch, J.A., see Mentink, S.A.M. 238
 Mydosch, J.A., see Palstra, T.T.M. 199, 236
 Mydosch, J.A., see Yokoyama, M. 239, 241

 Nag, K. 360
 Nagamine, K., see Amitsuka, H. 237–239
 Nagao, M., see Kawano-Furukawa, H. 267, 268
 Nagarajan, N. 248
 Nagarajan, R., see Lynn, J.W. 258
 Nagasawa, M., see Fujii, H. 101
 Nagashima, K., see Watanabe, M. 360, 397
 Nagata, T., see Kawano-Furukawa, H. 262, 267, 268
 Najib, A. 120
 Najib, A., see Nowik, I. 115
 Naka, T., see Braithwaite, D. 191
 Nakai, N. 253
 Nakai, N., see Ichioka, M. 274
 Nakai, Y., see Kojima, K. 18, 114
 Nakajima, K., see Nakamura, H. 115
 Nakajima, M., see Kohgi, M. 271
 Nakajima, S. 155
 Nakajima, Y., see Izawa, K. 250, 256, 268, 272–274
 Nakamura, H. 115, 117
 Nakamura, N., see Shishido, H. 193, 194
 Nakamura, S. 271
 Nakamura, Y., see Hashimoto, S. 414
 Nakao, H. 241
 Nakashima, M., see Ikeda, S. 114
 Nakashima, M., see Sugiyama, K. 243
 Nakawaki, H., see Haga, Y. 111
 Nakawaki, H., see Shishido, H. 193, 194
 Nakotte, H., see Brück, E. 102
 Nambudripad, N., see Sampathkumaran, E.V. 115
 Namiki, T., see Aoki, Y. 270
 Namiki, T., see Ikeda, S. 114
 Namiki, T., see Shishido, H. 193, 194
 Napoletano, M., see Canepa, F. 4, 10, 78, 122, 123
 Narayanan, R., see Kirkpatrick, T.R. 231
 Narikiyo, O., see Okuno, Y. 236
 Narozhnyi, V.N., see Müller, K.-H. 141, 248, 250, 258
 Nash, K.L., see Feil-Jenkins, J.F. 389
 Nayak, C., see Chakravarty, S. 179, 180, 183
 Nayak, C., see Yang, X. 182
 Nekvasil, V., see Valiev, U.V. 351, 352
 Nenkov, K., see Drechsler, S.-L. 251, 252
 Nersesyan, A.A. 180–182
 Neumaier, K., see Custers, J. 198
 Neumann, K.-U., see Babateen, M. 120
 Newbury, R., see Taillefer, L. 199
 Ng, T.K. 267
 Nicklas, M. 112
 Nicol, E.J., see Vekhter, I. 175, 176
 Nicolay, G., see Ehm, D. 191
 Nicolay, G., see Reinert, F. 144
 Niepmann, D. 5
 Nieuwenhuys, G.H., see Moze, O. 14, 121
 Nieuwenhuys, G.J., see de Visser, A. 236
 Nieuwenhuys, G.J., see Mentink, S.A.M. 238
 Nieuwenhuys, G.J., see Palstra, T.T.M. 199, 236
 Nishigori, S. 102–104
 Nishigori, S., see Fujita, T. 101
 Nishigori, S., see Ito, T. 105
 Nishigori, S., see Javorský, P. 103
 Nishimura, E., see Morita, M. 352
 Nishira, T., see Machida, K. 161, 171, 172
 Nishiyama, K., see Aoki, Y. 270, 275
 Nitta, T., see Nakamura, H. 115
 Nitta, T., see Shimizu, T. 116
 Nitta, T., see Yoshimura, K. 116
 Noel, H., see Bauer, E. 160
 Noël, H., see Weitzer, F. 7, 66, 86
 Nohara, M. 250, 253, 255, 257
 Nohara, M., see Izawa, K. 250, 256
 Nohara, M., see Suzuki, T. 103
 Nomura, T., see Yanase, Y. 141
 Norman, M.R. 157, 171, 172, 199, 200, 205, 213
 Norman, M.R., see Heffner, R.H. 157
 Nowik, I. 115
 Nowik, I., see Felner, I. 15, 114–116
 Nowotny, H., see Rieger, W. 71, 72, 89
 Nozières, J.P., see Allemand, J. 66
 Nozières, P. 144
 Nozue, T., see Li, D.X. 102, 104
 Nyayate, M.N. 102

- Ocana, R. 177
 Ochiai, A., see Ōnuki, Y. 231
 Ochiai, A., see Steglich, F. 191
 Ochiai, M., see Kawano-Furukawa, H. 262
 O'Connor, L.H., see Spaulding, L. 347
 Oeschler, N. 271, 272
 Oeschler, N., see Bianchi, A. 195
 Oeschler, N., see Kromer, F. 244, 246, 247
 Oeschler, N., see Won, H. 196
 Oesterreicher, H. 102, 103, 115
 Ogawa, S. 116
 Ogryzlo, M.M., see Kalychak, Ya.M. 18, 39, 63
 Ohara, S. 112
 Ohashi, Y., see Ikeda, H. 179, 236, 241, 242
 Ohishi, K., see Aoki, Y. 270, 275
 Ohkubo, K., see Ito, T. 104
 Ohkuni, H. 238, 244
 Ohkuni, H., see Sugiyama, K. 243
 Ohmi, T. 215
 Ohmi, T., see Machida, K. 161, 171, 172, 207, 210, 211, 231, 235
 Ohsaki, S., see Aoki, Y. 270
 Ohsaki, S., see Kotegawa, H. 272
 Oikawa, K., see Haga, Y. 111
 Oikawa, K., see Sugawara, H. 269
 Oivanen, M. 407
 Okamoto, J., see Fujimori, S. 193, 194
 Okamoto, K., see Ishida, K. 229
 Okamoto, T., see Fujii, H. 101
 Okamoto, T., see Maeno, Y. 101, 102
 Okamoto, T., see Yagasaki, K. 29, 33, 118
 Okamoto, Y., see Kido, J. 368
 Okamoto, Y., see Kuriki, K. 368
 Okane, T., see Fujimori, S. 193, 194
 O'Keeffe, M. 360
 O'Keeffe, M., see Chen, B. 363, 365
 O'Keeffe, M., see Eddaoudi, M. 360, 364, 367
 O'Keeffe, M., see Reneike, T.M. 369, 378, 381
 Okuno, Y. 236
 Okusawa, M., see Susaki, T. 116
 Oleksiv, G.I., see Kripyakevich, P.I. 63
 Oleś, A., see André, G. 33
 Olson, C.G., see Denlinger, J.D. 146, 187
 Omi, T., see Ōnuki, Y. 120
 Ono, A., see Kasaya, M. 20
 Ōnuki, Y. 120, 231
 Ōnuki, Y., see Albessard, A.K. 185, 186
 Ōnuki, Y., see Aoki, H. 145, 185, 194
 Ōnuki, Y., see Fujimori, S. 193, 194
 Ōnuki, Y., see Haga, Y. 111
 Ōnuki, Y., see Hiroi, M. 217, 219
 Ōnuki, Y., see Ikeda, S. 114
 Ōnuki, Y., see Inada, Y. 219–221
 Ōnuki, Y., see Izawa, K. 113, 175, 178, 194, 195
 Ōnuki, Y., see Kagayama, T. 120, 121
 Ōnuki, Y., see Kawasaki, S. 113, 192
 Ōnuki, Y., see Kimura, N. 199, 203
 Ōnuki, Y., see Kitaoka, Y. 205, 214, 215, 218
 Ōnuki, Y., see Kobayashi, T.C. 231, 234, 235
 Ōnuki, Y., see Koike, Y. 205
 Ōnuki, Y., see Metoki, N. 146
 Ōnuki, Y., see Mito, T. 113
 Ōnuki, Y., see Ohkuni, H. 238, 244
 Ōnuki, Y., see Oomi, G. 121
 Ōnuki, Y., see Sakakibara, T. 114
 Ōnuki, Y., see Shishido, H. 111, 193, 194
 Ōnuki, Y., see Sugawara, H. 269
 Ōnuki, Y., see Sugiyama, K. 243
 Ōnuki, Y., see Takeuchi, T. 113, 114, 194
 Ōnuki, Y., see Tateiwa, N. 236
 Ōnuki, Y., see Tayama, T. 114
 Ōnuki, Y., see Tou, H. 214
 Ōnuki, Y., see Watanabe, T. 228
 Ōnuki, Y., see Zheng, G.-Q. 113, 194
 Oomi, G. 115, 121
 Oomi, G., see Kagayama, T. 120, 121
 Oostens, J., see Heffner, R.H. 199
 Oosterhof, L.J., see Emeis, C.A. 291
 Opahle, I., see Drechsler, S.-L. 251, 252
 Opahle, I., see Rosner, H. 253
 Oppelt, A. 118
 Oppelt, A., see Buschow, K.H.J. 29, 118
 Orpen, A.G., see Chui, S.S.-Y. 362, 364
 Osaki, S., see Izawa, K. 268, 272–274
 Osaki, S., see Sugawara, H. 269
 Osborn, R., see Goremychkin, E.A. 187, 188
 Osborn, R., see Lawrence, J.M. 114, 115
 Oster, F., see Pleger, H.R. 102, 103, 119
 Ott, H.R. 141, 199, 244
 Ott, H.R., see Bianchi, A.D. 121, 122
 Ott, H.R., see Golding, B. 246
 Ott, H.R., see Heffner, R.H. 246
 Ott, H.R., see Ramirez, A.P. 245
 Ouahab, L., see Dimos, A. 391
 Ouahab, L., see Kiritsis, V. 390, 393
 Ouahab, L., see Mörtl, K.P. 360
 Ouahab, L., see Sutter, J.P. 367
 Ouchi, A. 368
 Oushoorn, R.L. 366
 Oushoorn, R.L., see Daigebonne, C. 366, 389
 Oushoorn, R.L., see Guillou, O. 366
 Ozaki, M. 157, 161, 180, 241

- Ozaki, M., see Machida, K. 207, 210, 211
 Ozawa, T., see Morita, M. 352, 353
- Padalia, B.D., see Adroja, D.T. 4, 28, 101
 Padalia, B.D., see Malik, S.K. 36, 101–103, 117, 118
 Padalia, B.D., see Nagarajan, N. 248
 Pagliuso, P.G. 28, 34, 111, 112, 114
 Pagliuso, P.G., see Alver, U. 111, 193
 Pagliuso, P.G., see Bianchi, A. 195, 196
 Pagliuso, P.G., see Christianson, A.D. 111
 Pagliuso, P.G., see Cornelius, A.L. 112
 Pagliuso, P.G., see Curro, N.J. 113
 Pagliuso, P.G., see Hall, D. 111, 113
 Pagliuso, P.G., see Macaluso, R.T. 10, 28, 34
 Pagliuso, P.G., see Movshovich, R. 114
 Pagliuso, P.G., see Nicklas, M. 112
 Pagliuso, P.G., see Petrovic, C. 111, 183, 191, 192, 194
 Pagliuso, P.G., see Thompson, J.D. 28, 34, 111, 183
 Pagliuso, P.G., see Wei, B. 113
 Pal, D., see Manfrinetti, P. 106
 Palenzona, A. 81
 Palenzona, A., see Cirafici, S. 31, 69, 102, 104
 Palenzona, A., see Dhar, S.K. 7, 26, 106
 Palenzona, A., see Manfrinetti, P. 106
 Palenzona, R., see Dhar, S.K. 7, 106
 Palm, E.C., see Alver, U. 111, 193
 Palm, E.C., see Hall, D. 111, 113
 Palmer, R.A., see Dyer, R.B. 345
 Palmer, R.A., see May, P.S. 298
 Palmer, R.A., see Metcalf, D.H. 343
 Palstra, T.T.M. 199, 236
 Palstra, T.T.M., see Broholm, C. 236
 Pan, L. 369, 376, 378, 387, 389, 391, 393
 Pao, C.H. 155
 Parac-Vogt, T.N. 315, 331
 Park, J.-G. 237, 257
 Park, T. 177
 Parker, D. 338, 341
 Parker, D., see Aime, S. 338
 Parker, D., see Beeby, A. 334, 340, 341
 Parker, D., see Bobba, G. 341
 Parker, D., see Bruce, J.I. 299, 320, 338–341
 Parker, D., see Di Bari, L. 339
 Parker, D., see Dickins, R.S. 318, 319, 334–336, 339, 341
 Parker, D., see Govenlock, L.J. 341
 Parker, D., see Huskowska, E. 315, 319–321
 Parker, D., see Luck, R.L. 315, 319
 Parker, D., see Maupin, C.L. 314, 330, 334, 336, 337, 340, 341
 Parker, D., see Muller, G. 315, 319
 Parker, F.T., see Oesterreicher, H. 115
 Parthé, E. 79
 Parthé, E., see Cenzual, K. 79
 Pasturel, M., see Chevalier, B. 4, 107
 Paul, C., see Bauer, E. 109, 160
 Paul, D.M., see Campbell, A.J. 261
 Pauling, L., see Shoemaker, D.P. 39
 Paulose, P.L., see Manfrinetti, P. 106
 Paulsen, C., see Measson, M.-A. 272
 Peabody, L., see Hall, D. 111, 113
 Peacock, R.D., see Bobba, G. 341
 Peacock, R.D., see Bruce, J.I. 299, 320, 338–341
 Peacock, R.D., see Dickins, R.S. 318, 319, 334–336, 341
 Pearson, K.H., see Spaulding, L. 347
 Pecharsky, V.K., see Grin, Yu.N. 53
 Pecharsky, V.K., see Kalychak, Ya.M. 10, 62, 88
 Pecharsky, V.K., see Zaremba, V.I. 14, 53, 65
 Peck, W.F., see Cava, R.J. 248
 Peisker, E., see Becher, H.J. 71, 89
 Pelle, F., see Millange, F. 391, 395
 Pelle, F., see Serre, C. 375, 376
 Pena, O., see Rizzi, A.C. 367
 Penc, B., see Gondek, Ł. 103
 Penc, B., see Szytuła, A. 38, 102, 106
 Peng, Z., see Winzer, K. 258
 Penzo, M., see Parthé, E. 79
 Pepin, C., see Custers, J. 198
 Perek, M., see Rizzi, A.C. 367
 Perenboom, J.A.A.J., see Mentink, S.A.M. 238
 Perlitz, H. 63, 97
 Perrier de la Bathie, R., see Allemand, J. 66
 Perry, J.J.B., see Bruce, J.I. 341
 Peters, J.A., see Brittain, H.G. 348
 Petersen, K., see Geibel, C. 199, 228
 Petříček, V., see Poduska, K.M. 123
 Petricka, J., see Zapf, V.S. 114
 Petrovic, C. 111, 183, 191, 192, 194, 195
 Petrovic, C., see Eskildsen, M.R. 196
 Petrovic, C., see Hall, D. 111, 113
 Petrovic, C., see Hegger, H. 4, 28, 111, 191, 194
 Petrovic, C., see Hundley, M.F. 36, 121, 122
 Petrovic, C., see Movshovich, R. 114
 Petrovic, C., see Nicklas, M. 112
 Petrovic, C., see Pagliuso, P.G. 112
 Petrovic, C., see Thompson, J.D. 28, 34, 111, 183
 Petukhov, K., see Dressel, M. 146, 199, 216
 Pfeleiderer, C. 230, 234, 236

- Pfleiderer, C., see Vollmer, R. 269–272
 Phillips, N.E., see Brison, J.-P. 200
 Phillips, N.E., see Caspary, R. 217, 219
 Phillips, N.E., see Fisher, R.A. 200, 204, 206
 Phillips, N.E., see Thompson, J.D. 28, 34, 111, 183
 Pickett, W.E. 253
 Pickett, W.E., see Shick, A.B. 230–233
 Pierre, J., see Besnus, M.J. 36, 38, 63, 118
 Pierre, J., see Galera, R.M. 33, 119, 120
 Pierre, J., see Lahiouel, R. 120
 Pierre, J., see Najib, A. 120
 Pietraszko, A., see Galadzhun, Ya.V. 33, 38
 Pietri, R., see Kaczorowski, D. 36, 105
 Piguët, C., see Bünzli, J.-C.G. 341
 Piguët, C., see Cantuel, M. 312
 Piguët, C., see Muller, G. 342, 343
 Pikul, A., see Zaremba, V.I. 36, 102, 106
 Pikul, A.P., see Galadzhun, Ya.V. 36, 75
 Pillmayr, N. 116
 Pillmayr, N., see Felner, I. 114–116
 Pines, D., see Monthoux, P. 154
 Pintacuda, G., see Di Bari, L. 339
 Pinto, H., see Felner, I. 114–116
 Pinto, R.P. 107
 Piotrowski, H., see Galadzhun, Ya.V. 36
 Plater, M.J. 363
 Pleger, H.R. 102, 103, 119
 Poduska, K.M. 123
 Pokrovsky, V.L., see Canfield, P.C. 259
 Poliakova, V.P., see Savitskiy, E.M. 31
 Politt, B., see Pleger, H.R. 102, 103, 119
 Politt, B., see Schlabititz, W. 236
 Pollmann, F. 149
 Poppe, U., see Steglich, F. 185
 Pott, R., see Zell, W. 106
 Pöttgen, R. 4, 6, 14, 26, 28, 31, 36, 38, 44, 68, 69, 72, 96–98, 100, 102, 104–107, 121–123
 Pöttgen, R., see Esmaeilzadeh, S. 27
 Pöttgen, R., see Galadzhun, Ya.V. 31, 36, 38, 57–59, 122
 Pöttgen, R., see Hoffmann, R.-D. 3, 28, 31, 38, 54, 59, 93, 97, 122
 Pöttgen, R., see Kalychak, Ya.M. 3, 14, 40, 99
 Pöttgen, R., see Kanatzidis, M.G. 6
 Pöttgen, R., see Kußmann, D. 6
 Pöttgen, R., see Lukachuk, M. 5, 14, 28, 74
 Pöttgen, R., see Müllmann, R. 102, 105
 Pöttgen, R., see Niepmann, D. 5
 Pöttgen, R., see Rodewald, U.-Ch. 36, 51
 Pöttgen, R., see Schlüter, M. 64
 Pöttgen, R., see Zaremba, V.I. 6, 10, 14, 28, 31, 36, 44, 47, 51, 64, 97, 102, 105
 Pöttgen, R., see Zumdick, M.F. 80
 Potzel, U., see Felner, I. 114–116
 Powell, A.K., see Gutschke, S.O.H. 363
 Prasad, K.G., see Felner, I. 114–116
 Premo Chiotti, see Mason, J.T. 81
 Prior, T.J. 363
 Probst, P.A., see Hunt, M. 187
 Prots', Yu.M., see Niepmann, D. 5
 Proust, C., see Boaknin, E. 250, 252
 Pugh, E., see Saxena, S.S. 199, 230
 Pugh, V.J., see Glover-Fischer, D.P. 301, 322, 328
 Pulst, U. 187, 188
 Pulst, U., see Zwicknagl, G. 187–189
 Purdie, D., see Garnier, M. 144
 Puschmann, H., see Parker, D. 338
 Qiu, Y., see Gaulin, B.D. 228
 Que, W., see Walker, M.B. 236
 Que Jr., L., see Branum, M.E. 415
 Que Jr., L., see Schnaith, L.M.T. 414
 Rabello, S., see Si, Q. 197
 Rafaja, D., see Daniš, S. 31, 104
 Rainford, B.D., see De Teresa, J.M. 115
 Rainford, B.D., see Severing, A. 115
 Raj, P. 107
 Ramakrishnan, S., see Manfrinetti, P. 106
 Rambaldi, G., see Ferro, R. 3, 10, 14, 28, 31, 34, 36, 63, 68
 Ramirez, A.P. 245
 Ramirez, A.P., see Yaron, U. 267
 Ran, Q.Z., see Adenwalla, S. 205
 Rapenne, G., see Meskers, S.C.J. 323, 327
 Raphael, A.L., see Basile, L.A. 414
 Rau, D. 334
 Rau, D., see Morita, M. 323, 327, 334, 345
 Rau, M., see Geibel, C. 199, 216
 Rauchschalbe, U. 246
 Rauchschalbe, U., see Schlabititz, W. 236
 Rauchschalbe, U., see Steglich, F. 185
 Ravet, M.F., see Besnus, M.J. 36, 38, 118, 119
 Ravindran, P., see Vajeeston, P. 100, 107
 Rebizan, J., see Sarrao, J.L. 192
 Regnault, L.P. 185
 Reid, M.F. 350
 Reid, M.F., see May, P.S. 298
 Reinders, P., see Hunt, M. 187
 Reinert, F. 144
 Reinert, F., see Ehm, D. 191

- Reinhoudt, D.N., see Molenveld, P. 452
 Remp, H.D., see Heffner, R.H. 199
 Reneike, T.M. 369, 375, 377, 378, 381
 Reneike, T.M., see O'Keeffe, M. 360
 Renker, B., see Felten, R. 245
 Res, P.H., see Palstra, T.T.M. 199, 236
 Ressouche, E., see Aoki, D. 230, 270
 Ressouche, E., see Huxley, A. 230
 Ressouche, E., see Kernavanois, N. 231
 Rexwinkel, R.B. 307, 308, 323, 325, 328
 Rhee, J.Y. 253, 258
 Riabov, A.B., see Yartys, V.A. 107
 Rice, T.M., see Ott, H.R. 244
 Rice, T.M., see Sigrist, M. 244
 Rice, T.M., see Ueda, K. 156, 161
 Richardson, F.S. 292, 298, 323, 324, 350–352
 Richardson, F.S., see Berry, M.T. 295, 298
 Richardson, F.S., see Bolender, J.P. 323, 324
 Richardson, F.S., see Foster, D.R. 352, 353
 Richardson, F.S., see Glover, D.P. 323, 324
 Richardson, F.S., see Glover-Fischer, D.P. 301, 322–324, 328, 329
 Richardson, F.S., see Hopkins, T.A. 295, 298
 Richardson, F.S., see Luk, C.K. 291
 Richardson, F.S., see May, P.S. 298
 Richardson, F.S., see Metcalf, D.H. 301, 303, 307, 308, 313–315, 322–326, 328, 329
 Richardson, F.S., see Moran, D.M. 298
 Richardson, F.S., see Morley, J.P. 299, 352
 Richardson, F.S., see Riehl, J.P. 292, 294, 297, 305, 306, 310, 311, 347, 348, 350
 Richardson, F.S., see Schwartz, R.W. 351, 352
 Richardson, F.S., see Stephens, E.M. 352
 Richardson, F.S., see Stockman, T.G. 323, 325
 Rieck, C.T. 174
 Rieck, C.T., see Hessert, J. 217
 Rieger, W. 71, 72, 89
 Riehl, J.P. 292, 294, 297, 305, 306, 310, 311, 314, 347–350
 Riehl, J.P., see Abdollahi, S. 349
 Riehl, J.P., see Aime, S. 338
 Riehl, J.P., see Beeby, A. 334, 340, 341
 Riehl, J.P., see Belair, S.D. 301, 315, 322
 Riehl, J.P., see Cantuel, M. 312
 Riehl, J.P., see Çoruh, N. 299, 314, 323, 325, 328, 330, 332, 349
 Riehl, J.P., see Dekkers, H.P.J.M. 310
 Riehl, J.P., see Dickins, R.S. 318, 319, 334–336
 Riehl, J.P., see Dossing, A. 316
 Riehl, J.P., see Field, J.E. 306
 Riehl, J.P., see Gawryszewska, P. 315–317
 Riehl, J.P., see Govenlock, L.J. 341
 Riehl, J.P., see Hilmes, G.L. 299, 300, 312–315, 320, 330, 331, 347, 348
 Riehl, J.P., see Huskowska, E. 302, 314–317, 319–323, 330, 332, 333
 Riehl, J.P., see Luck, R.L. 315, 319
 Riehl, J.P., see Maupin, C.L. 292, 314, 321, 323, 325, 328, 330, 334, 336, 337, 340, 341
 Riehl, J.P., see Meskers, S.C.J. 295
 Riehl, J.P., see Metcalf, D.H. 307, 308, 323, 325
 Riehl, J.P., see Mondry, A. 301, 315, 321, 322
 Riehl, J.P., see Muller, G. 314, 315, 319, 331, 333, 342–344
 Riehl, J.P., see Rexwinkel, R.B. 323, 325, 328
 Riehl, J.P., see Richardson, F.S. 292, 350, 351
 Riehl, J.P., see Schwartz, R.W. 351, 352
 Riehl, J.P., see Sokolnicki, J. 301, 302, 314, 315, 322, 323
 Riehl, J.P., see Wu, S. 314, 323, 325, 330, 333
 Rietschel, H., see Felten, R. 245
 Riou, D., see Barthelet, K. 363
 Riseborough, P.S., see Christianson, A.D. 111
 Riseborough, P.S., see Lawrence, J.M. 114
 Rizzi, A.C. 367
 Roberts, A.J., see Plater, M.J. 363
 Robl, C. 363, 369, 382
 Robson, R., see Batten, S.R. 360
 Roden, B., see Pleger, H.R. 102, 103, 119
 Roden, B., see Zell, W. 106
 Rodewald, U.-Ch. 36, 51
 Rodewald, U.-Ch., see Zarembo, V.I. 6, 10, 14, 28, 31, 36, 47, 51, 64
 Roessli, B., see Bernhoeft, N. 146, 217, 224
 Roessli, B., see Krimmel, A. 217
 Roessli, B., see Sato, N. 217, 224
 Rogers, K.L., see Zapf, V.S. 111
 Rogers, R.D., see Feil-Jenkins, J.F. 389
 Rogl, P., see Bauer, E. 160
 Rogl, P., see Giovannini, M. 18, 26, 28, 29, 31, 38, 71, 108, 109
 Rogl, P., see Kaczorowski, D. 14, 18, 28, 36, 38, 108–110
 Rogl, P., see Weitzer, F. 7, 10, 66, 86
 Röhler, J., see Wohlleben, D. 103
 Roisnel, T., see Camara, M. 397, 398
 Roisnel, T., see Mahé, N. 401
 Romero, S. 360
 Romero, S., see Trollet, D. 360
 Roof, R.B., see Cromer, D.T. 80
 Rosch, A. 197
 Rosenbaum, T.F., see Shivaram, B.S. 205

- Rosenhahn, C., see Hoffmann, R.-D. 38, 59, 122
 Rosenhahn, C., see Pöttgen, R. 4, 6, 28, 102, 105
 Rosenkranz, S., see Gasser, U. 260
 Roser, M.R., see Tang, J. 4, 14, 122, 123
 Rosi, N., see Eddaoudi, M. 360, 364, 367
 Rosner, H. 253
 Rosner, H., see Drechsler, S.-L. 251, 252
 Rossat-Mignot, J., see Regnault, L.P. 185
 Rosseinsky, M.J., see Prior, T.J. 363
 Rossi, D. 28, 33, 34, 36, 38, 68, 69
 Rossi, D., see Marazza, R. 36, 38, 63
 Rossi, D., see Mazzone, D. 26, 69
 Roth, C., see Müller, V. 246
 Rotundu, C.R. 271
 Roy, A., see Nag, K. 360
 Rozenberg, M.J., see Georges, A. 198
 Ru, J., see Tong, M.-L. 363, 366
 Rudigier, H., see Ott, H.R. 199, 244
 Rundle, R.E., see Florio, J.V. 40, 45
 Rundqvist, S. 66
 Rundqvist, S., see Aronsson, B. 79
 Runge, E. 185
 Runge, E., see Efremov, D. 147, 149, 220
 Runge, E., see Zwicknagl, G. 185, 186
 Rupp, R.A., see Valiev, U.V. 351, 352
 Rustamov, U.R., see Valiev, U.V. 351, 352
 Rykhal, R.M. 54
- Saccone, A., see Bauer, E. 109
 Saccone, A., see Ferro, R. 63
 Saccone, A., see Giovannini, M. 18, 26, 28, 29, 31, 38, 71, 109
 Sachdev, S. 197
 Sachdev, S., see Millis, A.J. 157
 Sacramento, P., see Schlottmann, P. 245
 Saha, S.R., see Aoki, Y. 270, 275
 Saha, S.R., see Sugawara, H. 269
 Saint-James, D. 195
 Saito, T., see Mizuno, K. 250
 Sakakibara, T. 114
 Sakakibara, T., see Amitsuka, H. 237–239
 Sakakibara, T., see Aoki, H. 194
 Sakakibara, T., see Shimizu, T. 116
 Sakakibara, T., see Tayama, T. 114, 270, 272
 Sakakibara, T., see Yoshimura, K. 116
 Sakamoto, I., see Ohara, S. 112
 Sakatsume, S., see Nakamura, S. 271
 Sakurai, J., see Fujii, H. 4, 101
 Sakurai, J., see Fujita, T. 101
 Sakurai, J., see Yamaguchi, Y. 101
 Sakurai, K., see Inada, Y. 219–221
- Sakurai, K., see Ohkuni, H. 238, 244
 Salamon, M.B., see Chia, E.E. 275
 Salamon, M.B., see Park, T. 177
 Sales, B.C. 101, 268
 Salvadori, P., see Di Bari, L. 339
 Samoilov, B.N. 291
 Samokhin, K.V., see Mineev, V.P. 141, 161, 165, 214
 Sampathkumaran, E.V. 107, 115
 Sampathkumaran, E.V., see Mallik, R. 110
 Sanada, T. 367
 Sanchez, J.-P., see Kernavanois, N. 231, 238, 240
 Sanchiz, J., see Larionova, J. 360
 Sandalov, I., see Lundin, U. 147
 Sandratskii, L.M. 219
 Sandratskii, L.M., see Knöpfle, K. 219
 Sangregorio, C., see Mahé, N. 401
 Santi, G., see Dugdale, S.B. 251, 253
 Santini, P. 236, 237, 240, 241, 243
 Sarma, B.K., see Adenwalla, S. 205
 Sarma, G., see Saint-James, D. 195
 Sarrao, J.L. 115, 116, 192
 Sarrao, J.L., see Alver, U. 111, 193
 Sarrao, J.L., see Bianchi, A. 195, 196
 Sarrao, J.L., see Christianson, A.D. 111
 Sarrao, J.L., see Cornelius, A.L. 111, 112, 116
 Sarrao, J.L., see Curro, N.J. 113
 Sarrao, J.L., see Denlinger, J.D. 146, 187
 Sarrao, J.L., see Hall, D. 111, 113
 Sarrao, J.L., see Hedro, M. 115
 Sarrao, J.L., see Hegger, H. 4, 28, 111, 191, 194
 Sarrao, J.L., see Hundley, M.F. 36, 121, 122
 Sarrao, J.L., see Immer, C.D. 115
 Sarrao, J.L., see Kim, J.S. 112
 Sarrao, J.L., see Kohori, Y. 113, 194
 Sarrao, J.L., see Lawrence, J.M. 114, 115
 Sarrao, J.L., see Macaluso, R.T. 10, 28, 34
 Sarrao, J.L., see Moshopoulou, E.G. 4, 28, 34
 Sarrao, J.L., see Movshovich, R. 114
 Sarrao, J.L., see Nicklas, M. 112
 Sarrao, J.L., see Pagliuso, P.G. 28, 34, 111, 112, 114
 Sarrao, J.L., see Petrovic, C. 111, 183, 191, 192, 194
 Sarrao, J.L., see Susaki, T. 116
 Sarrao, J.L., see Thompson, J.D. 28, 34, 111, 183
 Sarrao, J.L., see Wei, B. 113
 Sasaki, T., see Izawa, K. 175, 178, 257
 Sathyamoorthy, A., see Raj, P. 107
 Sato, H., see Aoki, Y. 270, 275
 Sato, H., see Bauer, E. 109

- Sato, H., see Chia, E.E. 275
 Sato, H., see Ikeda, S. 114
 Sato, H., see Izawa, K. 268, 272–274
 Sato, H., see Kohgi, M. 271
 Sato, H., see Kotegawa, H. 272
 Sato, H., see Measson, M.-A. 272
 Sato, H., see Ōnuki, Y. 231
 Sato, H., see Rotundu, C.R. 271
 Sato, H., see Shishido, H. 193, 194
 Sato, H., see Sugawara, H. 269
 Sato, H., see Tayama, T. 270, 272
 Sato, M., see Amitsuka, H. 237, 239
 Sato, N. 217, 219, 224, 229
 Sato, N., see Bernhoeft, N. 146, 217, 224
 Sato, N., see Böhm, A. 201
 Sato, N., see Feyerherm, R. 216–218
 Sato, N., see Inada, Y. 219
 Sato, N., see Kita, H. 217, 218
 Sato, N., see Mitsuda, A. 117
 Sato, N., see Steglich, F. 168, 189, 190
 Sato, N., see Takahashi, T. 146
 Sato, N., see Tateiwa, N. 228
 Sato, N., see Zhang, W. 117
 Sato, N.K. 146, 217, 225, 227
 Sato, T., see Tsubomura, T. 345
 Satoh, K. 101
 Satoh, K., see Albessard, A.K. 185, 186
 Satoh, K., see Fujii, H. 4, 101
 Satoh, K., see Fujita, T. 101
 Satoh, K., see Ōnuki, Y. 231
 Satoh, N., see Kasaya, M. 20
 Sauls, J.A. 141, 174, 203, 205, 210
 Sauls, J.A., see Adenwalla, S. 205
 Sauls, J.A., see Choi, C. 174, 205
 Sauls, J.A., see Graf, M.J. 171–173, 205, 211, 214
 Sauls, J.A., see Hess, D.W. 207, 210
 Sauvage, J.-P., see Meskers, S.C.J. 323, 327
 Savitskiy, E.M. 31
 Sawabe, K., see Morita, M. 352
 Sawada, A., see Inada, Y. 219
 Saxe, J.D., see Morley, J.P. 299
 Saxena, S.S. 199, 230
 Saxena, S.S., see Grosche, F.M. 183, 191
 Saymon, S., see Demuer, A. 191
 Scalapino, D.J. 141
 Scalett, R.T., see McMahan, A.K. 150
 Schaefer, H., see Czech, E. 43
 Schäfer, H., see Eisenmann, B. 58
 Schäfer, H., see Steglich, F. 183
 Schäfer, W., see Semitelou, J.P. 33, 123
 Schäfer, W., see Siouris, I.M. 18, 70, 122, 123
 Schäfer, W., see Siouris, J. 123
 Schakel, P., see Blok, P.M.L. 307, 308
 Schakel, P., see Rexwinkel, R.B. 307, 308
 Schank, C., see Böhm, A. 201
 Schank, C., see Caspary, R. 217, 219
 Schank, C., see Geibel, C. 199, 216
 Schank, C., see Grauel, A. 201, 216, 218
 Schank, C., see Krimmel, A. 217
 Schank, C., see Kyogaku, M. 228
 Schank, C., see Tou, H. 217–219
 Scharnberg, K. 170
 Scharnberg, K., see Hessert, J. 217
 Scharnberg, K., see Rieck, C.T. 174
 Schatz, P.N. 350
 Schauerte, J.A. 308, 350
 Scheidt, E.W., see Bauer, E. 160
 Scheidt, E.W., see Müller, V. 246
 Schenck, A., see Feyerherm, R. 216–218
 Schenck, A., see Heffner, R.H. 246
 Schenk, K.J., see Muller, G. 342
 Scherba, I.D., see Koterlyn, M.D. 116
 Schillaci, M.E., see Heffner, R.H. 199
 Schilling, A., see Bianchi, A.D. 121, 122
 Schilling, J.S., see Gangopadhyay, A.K. 253
 Schipper, P.E. 330, 333
 Schippers, P.H. 305, 307, 309, 311
 Schlabitz, W. 236
 Schlottmann, P. 245
 Schlüter, M. 64
 Schlyer, B.D., see Schauerte, J.A. 308, 350
 Schmale, H.W., see Decurtins, S. 360, 366, 367
 Schmidt, B., see Muller, G. 343
 Schmidt, H. 253, 263
 Schmidt, L., see Brison, J.-P. 200
 Schmidt, L., see Keller, N. 175, 244
 Schmidt, S., see Ehm, D. 191
 Schmidt, S., see Reinert, F. 144
 Schmiester, G., see Felner, I. 114–116
 Schmitt, D., see Semitelou, J.P. 33, 123
 Schmitt-Rink, S. 170
 Schmitt-Rink, S., see Miyake, K. 154, 156, 229
 Schmitt-Rink, S., see Shivaram, B.S. 205
 Schmitzer, C., see Felner, I. 114–116
 Schnaith, L.M.T. 414
 Schneider, H.J., see Hettich, R. 414
 Schneider, M., see Cavadini, N. 260
 Schnelle, W., see Pöttgen, R. 14, 96, 122, 123
 Schoenes, J. 146
 Schönhammer, K., see Gunnarsson, O. 103, 143
 Schopohl, N., see Dahm, T. 253
 Schopohl, N., see Rieck, C.T. 174

- Schrieffer, J.R. 154
 Schrieffer, J.R., see Bardeen, J. 154
 Schrieffer, J.R., see Berk, N. 154, 155
 Schröder, M., see Long, D.L. 389
 Schuberth, E.A. 205
 Schultheiss, R. 350, 352
 Schulz, H. 157, 180, 241
 Schwartz, R.W. 351, 352
 Schwartz, R.W., see Morley, J.P. 352
 Schwartz, R.W., see Sen, A.C. 299
 Schwer, H., see Xue, B. 31, 62
 Schwieters, C., see Berry, M.T. 295, 298
 Scordari, F., see Giacomazzo, C. 363
 Seidel, B., see Geibel, C. 199, 228
 Sekizawa, K. 29, 118, 119
 Selbin, J., see Kahwa, I.A. 360
 Semitelou, J.P. 33, 123
 Semitelou, J.P., see Siouris, I.M. 18, 70, 122, 123
 Semitelou, J.P., see Siouris, J. 123
 Semyannikov, A.A., see Yatsenko, S.P. 83
 Sen, A.C. 299
 Sen, M. 107
 Senba, Y., see Morita, M. 334
 Sera, M., see Hiroi, M. 217, 219
 Sereni, J., see Besnus, M.J. 36, 38, 63, 118
 Seropegin, Y., see Bauer, E. 160
 Seropegin, Yu.D., see Kurenbaeva, J.M. 27
 Serpaggi, F. 360, 391, 394
 Serre, C. 374–376, 379, 382
 Serre, C., see Millange, F. 391, 395
 Sessler, J.L., see Magda, D. 427, 442
 Settai, R., see Aoki, H. 194
 Settai, R., see Ikeda, S. 114
 Settai, R., see Izawa, K. 113, 175, 178, 194, 195
 Settai, R., see Kawasaki, S. 192
 Settai, R., see Kobayashi, T.C. 231, 234, 235
 Settai, R., see Ohkuni, H. 238, 244
 Settai, R., see Sakakibara, T. 114
 Settai, R., see Shishido, H. 111, 193, 194
 Settai, R., see Sugawara, H. 269
 Settai, R., see Takeuchi, T. 113
 Settai, R., see Tateiwa, N. 236
 Settai, R., see Tayama, T. 114
 Severing, A. 115
 Seyfarth, G., see Measson, M.-A. 272
 Shah, N. 241
 Shakarov, H.O., see Yatsenko, S.P. 83
 Shapiro, S.M., see Gaulin, B.D. 228
 Shashikala, K., see Raj, P. 107
 Sheikin, I., see Braithwaite, D. 191
 Sheikin, I., see Demuer, A. 191
 Sheikin, I., see Huxley, A. 230
 Shelkin, I., see Saxena, S.S. 199, 230
 Shelton, V.M., see Morrow, J.R. 409, 427
 Shi, Q., see Cao, R. 363, 369, 382, 385, 396
 Shiba, H., see Shiina, R. 270
 Shibasaki, M. 389
 Shick, A.B. 230–233
 Shiga, M., see Nakamura, H. 117
 Shigekawa, H. 419
 Shigekawa, H., see Komiyama, M. 407, 408
 Shigekawa, H., see Takeda, N. 414
 Shiiba, T. 409
 Shiiba, T., see Komiyama, M. 409, 410, 433
 Shiina, R. 217, 270
 Shiina, R., see Sato, N.K. 146, 217, 225, 227
 Shikama, M., see Ōnuki, Y. 231
 Shillady, D., see Foster, D.R. 352, 353
 Shimizu, T. 116
 Shimizu, T., see Albessard, A.K. 185, 186
 Shimizu, T., see Matsumoto, T. 116
 Shimizu, T., see Ogawa, S. 116
 Shimizu, T., see Yoshimura, K. 116
 Shioda, R., see Shigekawa, H. 419
 Shiokawa, Y., see Li, D.X. 102, 104
 Shirane, G., see Aeppli, G. 156
 Shishido, H. 111, 193, 194
 Shishido, H., see Aoki, H. 194
 Shishido, H., see Fujimori, S. 193, 194
 Shishido, H., see Haga, Y. 111
 Shishido, H., see Ikeda, S. 114
 Shishido, H., see Izawa, K. 113, 175, 194, 195
 Shishido, H., see Kawasaki, S. 192
 Shishido, H., see Sakakibara, T. 114
 Shishido, H., see Sugawara, H. 269
 Shishido, H., see Takeuchi, T. 113
 Shishido, H., see Tayama, T. 114
 Shivaram, B.S. 205
 Shoemaker, C.B. 68
 Shoemaker, D.P. 39
 Shoemaker, D.P., see Shoemaker, C.B. 68
 Shomi, T., see Ohara, S. 112
 Shore, S.G., see Liu, J. 367
 Shortley, G.H., see Condon, E.U. 201
 Shulga, S.V. 252
 Shulga, S.V., see Drechsler, S.-L. 251, 252
 Si, Q. 197, 198
 Si, Q., see Smith, J.L. 198
 Siaud, E., see Besnus, M.J. 36, 38, 63, 118
 Siaud, E., see Galera, R.M. 33, 119, 120
 Siaud, E., see Lahiouel, R. 120
 Siaud, E., see Najib, A. 120

- Sichevich, O.M. 66, 86
 Sidorov, V.A., see Nicklas, M. 112
 Siegrist, T., see Cava, R.J. 248
 Sierro, J., see Jaccard, D. 183
 Sigrist, M. 141, 156, 161, 170, 173, 244, 246–248
 Sigrist, M., see Bauer, E. 160
 Sigrist, M., see Doh, H. 263
 Sigrist, M., see Frigeri, P. 160
 Sikkema, A.E. 236
 Sil, S., see Sen, M. 107
 Siligardi, G., see Beeby, A. 334, 340, 341
 Siligardi, G., see Bobba, G. 341
 Siligardi, G., see Dickins, R.S. 318, 319, 334–336
 Siligardi, G., see Govenlock, L.J. 341
 Simon, A. 100
 Simon, A., see Pöttgen, R. 4
 Simovic, B., see Curro, N.J. 113
 Singh, D.J., see Pickett, W.E. 253
 Sinha, S.K., see Lynn, J.W. 258
 Siouris, I.M. 18, 70, 122, 123
 Siouris, J. 123
 Siouris, J., see Semitelou, J.P. 33, 123
 Sirvent, C., see Zapf, V.S. 114
 Siu, A., see Chui, S.S.-Y. 369, 384, 388
 Skanthakumar, S., see Lynn, J.W. 258
 Skolozdra, R.V. 47, 85
 Skolozdra, R.V., see Sysa, L.V. 33, 49, 124
 Skoulika, S., see Dimos, A. 391
 Skoulika, S., see Kiritsis, V. 390, 393
 Skoulika, S., see Michaelides, A. 360
 Smith, J.L. 198
 Smith, J.L., see Fisher, R.A. 200, 204, 206
 Smith, J.L., see Golding, B. 246
 Smith, J.L., see Heffner, R.H. 199, 246
 Smith, J.L., see Movshovich, R. 183
 Smith, J.L., see Ott, H.R. 199, 244
 Smith, J.L., see Ramirez, A.P. 245
 Smith, J.L., see Si, Q. 197
 Smith, J.L., see Stewart, G.R. 141, 199
 Smith, J.L., see Taillefer, L. 199
 Smith, M.J., see Bobba, G. 341
 Snow, A.I., see Florio, J.V. 40
 Snyder, S.W., see Metcalf, D.H. 301, 303, 307, 308, 313–315, 322–326, 328
 Sobolev, A.N., see Sichevich, O.M. 66, 86
 Sobolev, A.N., see Zaremba, V.I. 10, 69, 80
 Söderlind, P. 147
 Soininen, P.I., see Berlinsky, A.J. 196
 Sokol, A., see Gorkov, L.P. 180
 Sokolnicki, J. 301, 302, 314, 315, 322, 323
 Sokolnicki, J., see Dossing, A. 316
 Sokolnicki, J., see Gawryszewska, P. 315–317
 Sokolov, B.Y., see Valiev, U.V. 351, 352
 Sokolov, B.Y., see Valiev, U.V. 351, 352
 Sorada, K., see Zhang, W. 117
 Sousa, J.B., see Pinto, R.P. 107
 Sparn, G., see Caspary, R. 217, 219
 Sparn, G., see Gegenwart, P. 168, 190, 191
 Sparn, G., see Steglich, F. 168, 185, 189–191
 Sparn, G., see Trovarelli, O. 36, 105
 Spaulding, L. 347
 Spencer, C.M., see Gordon, R.A. 108
 Springford, M., see Hunt, M. 187
 Sreedhara, A. 407
 Starynowicz, P. 389
 Stassis, C., see Dervenagas, P. 253
 Stassis, C., see Yaron, U. 267
 Steel, D.G., see Schauerte, J.A. 308, 350
 Steglich, F. 168, 183, 185, 189–191
 Steglich, F., see Bianchi, A. 195
 Steglich, F., see Böhm, A. 201
 Steglich, F., see Bruls, G. 189
 Steglich, F., see Caspary, R. 217, 219
 Steglich, F., see Custers, J. 198
 Steglich, F., see Felten, R. 245
 Steglich, F., see Feyerherm, R. 216–218
 Steglich, F., see Gegenwart, P. 168, 190, 191
 Steglich, F., see Geibel, C. 199, 216, 228
 Steglich, F., see Grauel, A. 201, 216, 218
 Steglich, F., see Grewe, N. 141
 Steglich, F., see Ishida, K. 229
 Steglich, F., see Kawasaki, Y. 113
 Steglich, F., see Krimmel, A. 217
 Steglich, F., see Kromer, F. 244, 246, 247
 Steglich, F., see Kyogaku, M. 228
 Steglich, F., see Oeschler, N. 271, 272
 Steglich, F., see Rauchschalbe, U. 246
 Steglich, F., see Sato, N.K. 146, 217, 225, 227
 Steglich, F., see Stockert, O. 168, 190
 Steglich, F., see Tou, H. 217–219
 Steglich, F., see Trovarelli, O. 36, 105
 Steinberg, I. 292, 311
 Steinbrenner, U., see Simon, A. 100
 Steiner, M.J., see Saxena, S.S. 199, 230
 Steiner, W., see Weitzer, F. 7, 66, 86
 Stepanov, A., see Brison, J.-P. 200
 Stephens, E.M. 352
 Stephens, P.J. 351
 Stępień-Damm, J., see Galadzhun, Ya.V. 33, 36, 38, 75
 Stępień-Damm, J., see Kalychak, Ya.M. 10, 14, 15, 76, 82, 97

- Stepień-Damm, J., see Zaremba, V.I. 36, 57, 102, 106
 Stets', I.N., see Sysa, L.V. 33, 40, 81, 82, 124
 Stewart, G.R. 141, 197, 199
 Stewart, G.R., see Kim, J.S. 112
 Stewart, G.R., see Kromer, F. 244, 246, 247
 Stewart, G.R., see Rauchschalbe, U. 246
 Stewart, G.R., see Steglich, F. 191
 Stewart, J.M.M., see Metcalf, D.H. 323, 326
 Stockert, O. 168, 190
 Stockman, T.G. 323, 325
 Strässler, S., see Baltensperger, W. 266
 Strickler, B., see Schubert, E.A. 205
 Strydom, A.M., see Tchoula Tchokonte, M.B. 121
 Stuesser, N., see Stockert, O. 168, 190
 Stüsser, N., see Javorský, P. 103
 Stüsser, N., see Szytuła, A. 38, 102, 106
 Suderow, H. 214
 Suderow, H., see Martinez-Samper, P. 251
 Sudnick, D.R., see Horrocks, W.d.J. 346
 Suenaga, K., see Kagayama, T. 121
 Suga, S., see Ogawa, S. 116
 Sugawara, H. 269
 Sugawara, H., see Aoki, Y. 270, 275
 Sugawara, H., see Chia, E.E. 275
 Sugawara, H., see Izawa, K. 268, 272–274
 Sugawara, H., see Kohgi, M. 271
 Sugawara, H., see Kotegawa, H. 272
 Sugawara, H., see Measson, M.-A. 272
 Sugawara, H., see Rotundu, C.R. 271
 Sugawara, H., see Tayama, T. 270, 272
 Sugiyama, K. 243
 Sugiyama, K., see Shishido, H. 193, 194
 Sugiyama, K., see Takeuchi, T. 114, 194
 Suhr, D., see Muller, G. 343
 Sumaoka, J. 411, 416, 419, 427, 434, 438
 Sumaoka, J., see Igawa, T. 415
 Sumaoka, J., see Kajimura, A. 415
 Sumaoka, J., see Komiyama, M. 407–410, 427
 Sumaoka, J., see Shigekawa, H. 419
 Sumaoka, J., see Takeda, N. 414
 Sumiyama, K., see Li, D.X. 102, 104
 Sun, D., see Cao, R. 363, 369, 382, 385, 396
 Sun, W., see Bruls, G. 189
 Sun, W., see Hunt, M. 187
 Sun, Y. 170
 Susaki, T. 116
 Suski, W., see Zaremba, V.I. 124
 Sutter, J.P. 367
 Sutter, J.P., see Mörtl, K.P. 360
 Suzuki, H. 117
 Suzuki, M., see Izawa, K. 175, 178
 Suzuki, O., see Nakamura, S. 271
 Suzuki, O., see Suzuki, H. 117
 Suzuki, T. 103
 Suzuki, T., see Fujita, T. 101
 Suzuki, T., see Kojima, K. 18, 114
 Suzuki, T., see Sanada, T. 367
 Svidzinskii, A.A., see Barash, Y.S. 175
 Svoboda, P., see Javorský, P. 103
 Sysa, L.V. 10, 14, 18, 33, 40, 49, 68, 69, 81, 82, 124
 Sysa, L.V., see Baranyak, V.M. 14, 47
 Sysa, L.V., see Kalychak, Ya.M. 14, 18, 72, 89
 Sysa, L.V., see Koterlyn, M.D. 116
 Szytuła, A. 38, 102, 106
 Szytuła, A., see André, G. 33
 Szytuła, A., see Bałanda, M. 102–104
 Szytuła, A., see Gondek, Ł. 103
 Tagaki, H., see Cava, R.J. 248
 Taillefer, L. 199, 205
 Taillefer, L., see Adenwalla, S. 205
 Taillefer, L., see Boaknin, E. 250, 252
 Taillefer, L., see Fisher, R.A. 200, 204, 206
 Taillefer, L., see Hayden, S.M. 199, 204, 206, 208
 Taillefer, L., see Joynt, R. 141, 203–205
 Taillefer, L., see Lussier, B. 199, 205, 213
 Taillefer, L., see Trappmann, T. 204, 206, 207
 Taillefer, L., see van Dijk, N.H. 205, 209
 Takabatake, T., see Fujii, H. 4, 101
 Takabatake, T., see Fujita, T. 101
 Takabatake, T., see Kurisu, M. 4, 103
 Takabatake, T., see Suzuki, T. 103
 Takabatake, T., see Yamaguchi, Y. 101
 Takada, K., see Morita, M. 334
 Takagi, H., see Izawa, K. 250, 256
 Takagi, H., see Nohara, M. 250, 253, 255, 257
 Takahashi, H., see Izawa, K. 175, 178
 Takahashi, H., see Shigekawa, H. 419
 Takahashi, M., see Maeno, Y. 101, 102
 Takahashi, S., see Ohkuni, H. 238, 244
 Takahashi, T. 146
 Takahashi, Y., see Komiyama, M. 409, 410, 433
 Takano, Y., see Rotundu, C.R. 271
 Takarada, T. 451
 Takarada, T., see Komiyama, M. 451
 Takasaki, B., see Williams, N.H. 407
 Takasaki, B.K. 408, 410, 427
 Takayanagi, S., see Onuki, Y. 120, 231
 Takeda, N. 414
 Takeda, N., see Komiyama, M. 407–410, 433

- Takeda, N., see Shiiba, T. 409
 Takegahara, K. 116, 269
 Takeshita, H., see Kawano-Furukawa, H. 262
 Takeuchi, J., see Ito, T. 104
 Takeuchi, T. 113, 114, 194
 Takeuchi, T., see Shishido, H. 193, 194
 Takeya, H., see Kawano, H. 262
 Takeya, H., see Kawano-Furukawa, H. 262, 267, 268
 Takimoto, T., see Moriya, T. 197
 Takke, R., see Maetz, J. 29, 33, 74
 Tanabe, K., see Zheng, G.-Q. 113, 194
 Tang, J. 4, 14, 122, 123
 Taniguchi, M., see Ogawa, S. 116
 Tateiwa, N. 228, 236
 Tateiwa, N., see Kobayashi, T.C. 231, 234, 235
 Tatsumi, K., see Cao, R. 369, 382, 385, 396
 Tautz, F.S. 145, 185
 Tayama, T. 114, 270, 272
 Tayama, T., see Kromer, F. 244, 246, 247
 Tayama, T., see Sakakibara, T. 114
 Tayama, T., see Steglich, F. 168, 189, 190
 Tchoula Tchokonte, M.B. 121
 Tenya, K., see Amitsuka, H. 237–239
 Tenya, K., see Kromer, F. 244, 246, 247
 Tenya, K., see Yokoyama, M. 241
 Tešanović, Z., see Valls, O.T. 154
 Teshima, F., see Yamaguchi, Y. 101
 Tesliuk, M.J., see Gladyshevskii, E.I. 52
 Tewordt, L., see Dahm, T. 155
 Tewordt, L., see Scharnberg, K. 170
 Thalmeier, P. 141, 163, 166, 179, 180, 209, 215, 223, 228, 240, 243, 256, 257
 Thalmeier, P., see Amici, A. 258–261, 263, 264, 267
 Thalmeier, P., see Bruls, G. 189, 204, 210
 Thalmeier, P., see Izawa, K. 250, 256, 268, 272–274
 Thalmeier, P., see Maki, K. 215, 251, 254, 256, 273, 274
 Thalmeier, P., see McHale, P. 228
 Thalmeier, P., see Oeschler, N. 271, 272
 Thalmeier, P., see Sato, N.K. 146, 217, 225, 227
 Thalmeier, P., see Shiina, R. 270
 Thalmeier, P., see Varelogiannis, G. 234, 236
 Thalmeier, P., see Watanabe, T. 228
 Thalmeier, P., see Won, H. 256
 Thalmeier, P., see Yaresko, A. 232, 233
 Thalmeier, P., see Yuan, Q. 170, 254, 255
 Thessieu, C., see Kawasaki, Y. 113
 Thiel, R.C., see De Vries, J.W.C. 102, 104, 119, 120
 Thiel, R.C., see Mulder, F.M. 14, 121
 Thies, S., see Geibel, C. 199, 216, 228
 Tholence, J.L., see Brison, J.-P. 200
 Tholence, J.L., see Keller, N. 175, 244
 Thomas, E.J., see Saint-James, D. 195
 Thompson, J.D. 28, 34, 111, 183
 Thompson, J.D., see Bianchi, A. 195
 Thompson, J.D., see Christianson, A.D. 111
 Thompson, J.D., see Cornelius, A.L. 116
 Thompson, J.D., see Curro, N.J. 113
 Thompson, J.D., see Hedo, M. 115
 Thompson, J.D., see Hegger, H. 4, 28, 111, 191, 194
 Thompson, J.D., see Hundley, M.F. 36, 121, 122
 Thompson, J.D., see Immer, C.D. 115
 Thompson, J.D., see Kim, J.S. 112
 Thompson, J.D., see Lawrence, J.M. 114, 115
 Thompson, J.D., see Macaluso, R.T. 28, 34
 Thompson, J.D., see Moshopoulou, E.G. 4, 28, 34
 Thompson, J.D., see Movshovich, R. 114, 183
 Thompson, J.D., see Nicklas, M. 112
 Thompson, J.D., see Pagliuso, P.G. 28, 34, 111, 112, 114
 Thompson, J.D., see Petrovic, C. 111, 183, 191, 192, 194
 Thompson, J.D., see Sarrao, J.L. 116, 192
 Thompson, J.D., see Wei, B. 113
 Thouvenot, C., see Serre, C. 375, 376
 Timper, J.M., see Dekkers, H.P.J.M. 310
 Timper, J.M., see Hilmes, G.L. 312, 314, 320
 Ting, C.S., see Yuan, Q. 170, 255
 Tipton, A.K., see Branum, M.E. 415
 Tokiwa, Y., see Custers, J. 198
 Tokiwa, Y., see Fujimori, S. 193, 194
 Tokiwa, Y., see Haga, Y. 111
 Tokiwa, Y., see Inada, Y. 219–221
 Tokiwa, Y., see Ohkuni, H. 238, 244
 Tokiwa, Y., see Takeuchi, T. 114, 194
 Tokuyasu, T.A., see Hess, D.W. 207, 210
 Tong, M.-L. 363, 366
 Tou, H. 173, 214, 217–219
 Tou, H., see Kitaoka, Y. 205, 214, 215, 218
 Tozer, D.J., see Bruce, J.I. 320, 339
 Tozer, D.J., see Dickins, R.S. 339
 Tozer, S.W., see Alver, U. 111, 193
 Tozer, S.W., see Hall, D. 111, 113
 Trappmann, T. 204, 206, 207
 Trawick, B.N. 407

- Troarelli, O., see Ishida, K. 229
 Trollet, D. 360
 Trombe, J.C., see Romero, S. 360
 Trombe, J.C., see Trollet, D. 360
 Trovarelli, A. 368
 Trovarelli, O. 36, 105
 Trovarelli, O., see Custers, J. 198
 Trovarelli, O., see Reinert, F. 144
 Trovarelli, O., see Steglich, F. 168, 189
 Tsaousis, D., see Dimos, A. 391
 Tsonis, S., see Varelogiannis, G. 234, 236
 Tsuboi, W., see Yamamoto, Y. 438
 Tsubomura, T. 345
 Tsubomura, T., see Morita, M. 352, 353
 Tsuchiya, A., see Aoki, Y. 270, 275
 Tsuei, C.C. 141
 Tsuji, H., see Rotundu, C.R. 271
 Tsujii, N. 18, 26, 109
 Tsujii, N., see Suzuki, H. 117
 Tsuneto, T. 172
 Tun, Z., see Walker, M.B. 236
 Tung, L.D., see Mulder, F.M. 14, 121
 Turowska-Tyrk, I., see Huskowska, E. 316
 Tursina, A.I., see Kurenbaeva, J.M. 27
 Tyvanchuk, Yu.B., see Kalychak, Ya.M. 14
 Tyvanchuk, Yu.B., see Zaremba, V.I. 6, 14
- Ubbink, M., see Meskers, S.C.J. 323, 326, 329
 Uchida, H., see Komiyama, M. 409, 410
 Uchida, H., see Sumaoka, J. 427
 Uchida, S., see Cava, R.J. 248
 Ueda, K. 156, 161
 Ueda, K., see Konno, R. 166
 Ueda, K., see Moriya, T. 141
 Ueda, K., see Ott, H.R. 244
 Ueda, K., see Sigrist, M. 141, 156, 161, 170, 173, 244, 246, 247
 Ueda, T., see Shishido, H. 111
 Uenishi, A., see Nakamura, H. 117
 Uji, S., see Albessard, A.K. 185, 186
 Uji, S., see Aoki, H. 145, 185
 Ukon, I., see Ōnuki, Y. 231
 Umehara, I., see Albessard, A.K. 185, 186
 Umeharhara, I., see Ōnuki, Y. 231
 Unfried, P., see Giester, G. 397, 401
 Unfried, P., see Zak, Z. 397, 401
 Urvachev, V.P., see Savitskiy, E.M. 31
 Uwatoko, Y., see Fujii, H. 101
 Uwatoko, Y., see Fujita, T. 101
 Uwatoko, Y., see Hedo, M. 115
 Uwatoko, Y., see Maeno, Y. 101, 102
- Uwatoko, Y., see Satoh, K. 101
 Uwatoko, Y., see Yagasaki, K. 33
- Vachnadze, G.E., see Nersesyan, A.A. 180–182
 Vajeeston, P. 100, 107
 Vaknin, D., see Felner, I. 114–116
 Valiev, U.V. 351, 352
 Vallarino, L.M., see Foster, D.R. 352, 353
 Valls, O.T. 154
 van den Beukel, A., see Schippers, P.H. 305
 van der Berg, J., see de Visser, A. 236
 van Dijk, N.H. 191, 205, 208–210
 van Dover, R.B., see Cava, R.J. 248
 van Harlingen, D.J. 141
 van Sprang, M., see Brück, E. 101, 102
 vandenBerg, J., see Palstra, T.T.M. 199, 236
 Varelogiannis, G. 234, 236
 Varelogiannis, G., see Sato, N.K. 146, 217, 225, 227
 Varelogiannis, G., see Steglich, F. 168, 189
 Varma, C.M., see Jones, B. 145
 Varma, C.M., see Millis, A.J. 157
 Varma, C.M., see Miyake, K. 154, 156, 229
 Varma, C.M., see Ng, T.K. 267
 Varma, C.M., see Schmitt-Rink, S. 170
 Vekhter, I. 175, 176
 Venkataraman, D., see Field, J.E. 306
 Venkateswara Rao, C.R., see Raj, P. 107
 Vettier, C., see Brison, J.-P. 200
 Vettier, C., see Hayden, S.M. 199, 204, 206, 208
 Vettier, C., see Morin, P. 192
 Vidya, R., see Vajeeston, P. 100, 107
 Vieira, S., see Martinez-Samper, P. 251
 Vigren, D.T., see Ihrig, H. 29, 33, 73, 118
 Vijayaraghavan, R., see Adroja, D.T. 4, 28, 101
 Vijayaraghavan, R., see Malik, S.K. 36, 101–103, 117, 118
 Vijayaraghavan, R., see Nagarajan, N. 248
 Vijayaraghavan, R., see Sampathkumaran, E.V. 115
 Virosztek, A. 242
 Virosztek, A., see Dóra, B. 179, 182
 Virosztek, A., see Maki, K. 179, 181, 182
 Vodak, D., see Eddaoudi, M. 360, 364, 367
 Vogt, O., see Schoenes, J. 146
 Voiron, J., see Nowik, I. 115
 Vojta, T., see Kirkpatrick, T.R. 231
 Vollhardt, D. 154
 Vollhardt, D., see Hirschfeld, P. 170
 Vollmer, R. 269–272
 Volovik, G.E. 156, 161, 175, 243, 252, 274

- von Boehm, J., see Bak, P. 261
 von Löhneysen, H. 205
 von Löhneysen, H., see Goll, G. 113, 194
 von Löhneysen, H., see Mock, S. 110
 von Löhneysen, H., see Trappmann, T. 204, 206, 207
 von Löhneysen, H., see Vollmer, R. 269–272
 von Zelewsky, A., see Muller, G. 343
 Vorderwisch, P., see Gasser, U. 260
- Wachter, J., see Eddaoudi, M. 360, 364, 367
 Wachter, P., see Marabelli, F. 199
 Wada, H., see Mitsuda, A. 117
 Wada, H., see Nakamura, H. 117
 Wada, N., see Önuki, Y. 120
 Wagnière, G. 350
 Wakabayashi, Y., see Nakao, H. 241
 Walker, D., see Scharnberg, K. 170
 Walker, I.R. 183
 Walker, I.R., see Mathur, N.D. 183
 Walker, I.R., see Saxena, S.S. 199, 230
 Walker, M.B. 236
 Wall, M., see Williams, N.H. 407
 Wan, Y. 389
 Wang, E., see Li, Y. 363
 Wang, R. 398, 400
 Wang, R., see Zhao, Y. 364
 Wang, R., see Zheng, Z. 398
 Wang, X., see Pan, L. 387, 391, 393
 Wang, X., see Rhee, J.Y. 253, 258
 Wassilew, C., see Caspary, R. 217, 219
 Wastin, F., see Sarrao, J.L. 192
 Watanabe, K., see Yokoyama, M. 239, 241
 Watanabe, M. 360, 397
 Watanabe, N., see Haga, Y. 111
 Watanabe, S. 231, 236
 Watanabe, T. 228, 251
 Watanabe, T., see Izawa, K. 250, 256
 Weber, D., see Bruls, G. 204, 210
 Weber, D., see Thalmeier, P. 209
 Weber, G., see Böhm, A. 201
 Weber, G., see Felten, R. 245
 Weber, G., see Geibel, C. 199, 216
 Weber, G., see Grauel, A. 201, 216, 218
 Wei, B. 113
 Weickert, F. 189
 Weickert, F., see Oeschler, N. 271, 272
 Weickert, F., see Won, H. 196
 Weill, F., see Gravereau, P. 71, 91
 Weitzer, F. 7, 10, 66, 86
 Welp, U., see Metlushko, V. 252
 Welp, U., see Morin, P. 192
 Weng, W., see Bu, X.H. 395, 396
 Westgren, A., see Perlitz, H. 63, 97
 White, A.J.P., see Alleyne, B.D. 389
 White, R. 146, 147, 202, 238
 White, S.J., see Tang, J. 4, 14, 122, 123
 Wiebe, C.R., see Gaulin, B.D. 228
 Wiesinger, G., see Weitzer, F. 7, 66, 86
 Wilhelm, H., see Alami-Yadri, K. 119
 Wilhelm, H., see Custers, J. 198
 Wilkins, J.W., see Jayprakash, C. 145
 Wilkinson, I., see Dugdale, S.B. 251, 253
 Williams, A.R., see Alleyne, B.D. 389
 Williams, D.J., see Alleyne, B.D. 389
 Williams, I.D., see Chui, S.S.-Y. 362, 364, 369, 384, 388
 Williams, J.A.G., see Aime, S. 338
 Williams, J.A.G., see Beeby, A. 334, 340, 341
 Williams, J.A.G., see Bobba, G. 341
 Williams, J.A.G., see Dickins, R.S. 334–336
 Williams, J.A.G., see Govenlock, L.J. 341
 Williams, J.A.G., see Huskowska, E. 315, 319–321
 Williams, J.A.G., see Luck, R.L. 315, 319
 Williams, J.A.G., see Maupin, C.L. 314, 330, 334, 336, 337, 340, 341
 Williams, N.H. 407
 Williams, R.K., see Sales, B.C. 268
 Willis, J.O., see Heffner, R.H. 199, 246
 Willis, J.O., see Stewart, G.R. 141, 199
 Wills, J.M., see Hall, D. 111, 113
 Wills, J.M., see Söderlind, P. 147
 Wilson, C., see Long, D.L. 389
 Wilson, K.G. 144
 Wilson, N.J., see Grosche, F.M. 183, 191
 Winpenny, R.E.P., see Gutschke, S.O.H. 363
 Winzer, K. 258
 Winzer, K.H., see Shulga, S.V. 252
 Wochowski, K., see Zaremba, V.I. 124
 Wohlleben, D. 103
 Wohlleben, D., see Pleger, H.R. 102, 103, 119
 Wohlleben, D., see Sales, B.C. 101
 Wohlleben, D., see Zell, W. 106
 Wolczyk, M., see Zaremba, V.I. 28
 Wolf, B., see Bruls, G. 189, 204, 210
 Wolf, B., see Thalmeier, P. 209
 Wölfle, P., see Hirschfeld, P. 170
 Wölfle, P., see Vollhardt, D. 154
 Won, H. 175–177, 196, 256
 Won, H., see Dahm, T. 175
 Won, H., see Maki, K. 141, 251, 254, 256, 273, 274

- Won, H., see Yuan, Q. 170, 255
 Wong, K.M.C., see Li, J.R. 395, 396
 Wood, P.T., see Gutschke, S.O.H. 363
 Woodfield, B.F., see Fisher, R.A. 200, 204, 206
 Woodlock, E.B., see Pan, L. 393
 Woodward, F.M., see Maple, M.B. 269, 270
 Wortmann, G., see Felner, I. 114–116
 Wortmann, G., see Mallik, R. 110
 Wright, M., see Magda, D. 427, 442
 Wu, C.-D. 369, 381, 384
 Wu, L.P. 369, 383, 387
 Wu, S. 314, 323, 325, 330, 333
 Wu, S., see Çoruh, N. 323, 325, 328
 Wu, S., see Metcalf, D.H. 307, 308, 323, 325
 Wu, W.C. 171
 Wu, Y. 389
 Wu, Y., see Pan, L. 389
 Wu, Y.-M., see Pan, L. 369, 376, 378
 Wu, Y.-M., see Tong, M.-L. 363, 366
 Wyder, U., see Mentink, S.A.M. 238
- Xu, G.X., see Ma, B.Q. 398
 Xu, H., see Wu, Y. 389
 Xu, R., see Feng, S. 396
 Xue, B. 31, 62
 Xue, B., see Hulliger, F. 31, 108
- Yabuta, H., see Kojima, K. 116
 Yagasaki, K. 29, 33, 118
 Yaghi, O.M. 360, 363, 369, 380, 383
 Yaghi, O.M., see Chen, B. 363, 365
 Yaghi, O.M., see Eddaoudi, M. 360, 364, 367
 Yaghi, O.M., see Li, H. 363, 369
 Yaghi, O.M., see O'Keeffe, M. 360
 Yaghi, O.M., see Reneike, T.M. 369, 375, 377, 378, 381
 Yagi, R., see Kagayama, T. 120
 Yagi, T., see Sumaoka, J. 416, 438
 Yakamoto, M., see Wu, L.P. 369, 383, 387
 Yakinthos, J.K., see Semitelou, J.P. 33, 123
 Yakinthos, J.K., see Siouris, I.M. 18, 70, 122, 123
 Yakinthos, J.K., see Siouris, J. 123
 Yam, V.W.W., see Li, J.R. 395, 396
 Yamada, K., see Yanase, Y. 141
 Yamada, K.I., see Shibasaki, M. 389
 Yamada, Y., see Matsumoto, T. 116
 Yamagami, H., see Denlinger, J.D. 146, 187
 Yamagami, H., see Inada, Y. 219–221
 Yamagami, H., see Ohkuni, H. 238, 244
 Yamaguchi, H., see Izawa, K. 113, 175, 178, 194, 195, 257
 Yamaguchi, Y. 101
 Yamaguchi, Y., see Fujii, H. 4, 101
 Yamamoto, E., see Hiroi, M. 217, 219
 Yamamoto, E., see Inada, Y. 219–221
 Yamamoto, E., see Kimura, N. 199, 203
 Yamamoto, E., see Kitaoka, Y. 205, 214, 215, 218
 Yamamoto, E., see Koike, Y. 205
 Yamamoto, E., see Ohkuni, H. 238, 244
 Yamamoto, E., see Sugiyama, K. 243
 Yamamoto, E., see Tou, H. 214
 Yamamoto, Y. 438
 Yamamoto, Y., see Komiyama, M. 407, 408
 Yamane, H., see Ijiri, Y. 31, 121, 122
 Yamato, Y., see Kohori, Y. 113, 194
 Yamazaki, T., see Ōnuki, Y. 120
 Yan, C.H., see Ma, B.Q. 398
 Yan, F. 332
 Yanagisawa, T., see Inada, Y. 219–221
 Yanagisawa, T., see Ohkuni, H. 238, 244
 Yanase, A., see Harima, H. 187
 Yanase, A., see Takegahara, K. 269
 Yanase, Y. 141
 Yang, F.-M., see Brück, E. 102
 Yang, G. 174, 212
 Yang, R., see Pan, L. 369, 376, 378
 Yang, R., see Wu, Y. 389
 Yang, W.-B., see Wu, C.-D. 369, 381, 384
 Yang, X. 182
 Yaouanc, A. 146
 Yaouanc, A., see Kernavainois, N. 238, 240
 Yaresko, A. 232, 233
 Yaresko, A., see Zwicknagl, G. 146, 148, 198, 201–203, 220, 221, 238, 271
 Yarmolyuk, Ya.P. 61
 Yarmolyuk, Ya.P., see Gladyshevskii, R.E. 76
 Yarmolyuk, Ya.P., see Grin, Yu.N. 45, 49, 53, 55, 88, 192
 Yarmolyuk, Ya.P., see Kalychak, Ya.M. 81, 86
 Yarmolyuk, Ya.P., see Rykhal, R.M. 54
 Yarmolyuk, Ya.P., see Sichevich, O.M. 66, 86
 Yaron, U. 267
 Yartys, V.A. 107
 Yartys, V.A., see Bulyk, I.I. 107
 Yartys, V.A., see Vajeeston, P. 100, 107
 Yasaku, K., see Tsubomura, T. 345
 Yashiro, M. 452
 Yashiro, M., see Komiyama, M. 409, 410, 433
 Yashiro, M., see Shiiba, T. 409
 Yashiro, M., see Sumaoka, J. 419
 Yashiro, M., see Takarada, T. 451
 Yashiro, M., see Takeda, N. 414

- Yasukōchi, K., see Sekizawa, K. 29, 118, 119
 Yasuoka, H., see Ogawa, S. 116
 Yasuoka, H., see Yoshimura, K. 116
 Yatsenko, S.P. 83
 Ye, E., see Wu, Y. 389
 Yeakel, W., see Schwartz, R.W. 351, 352
 Yip, S.-K. 210
 Yip, S.-K., see Graf, M.J. 171–173, 205, 211, 214
 Yogi, M., see Kotegawa, H. 272
 Yokohama, M., see Amitsuka, H. 237, 239
 Yokoya, T., see Takahashi, T. 146
 Yokoyama, M. 239, 241
 Yokoyama, M., see Amitsuka, H. 237–239
 Yokoyama, M., see Arishima, H. 440
 Yonezawa, K., see Komiyama, M. 409
 Yonezawa, K., see Shiiba, T. 409
 Yoshida, T., see Sanada, T. 367
 Yoshida, Y., see Izawa, K. 175, 178
 Yoshikawa, N., see Shibasaki, M. 389
 Yoshimura, K. 116
 Yoshimura, K., see Matsumoto, T. 116
 Yoshimura, K., see Mitsuda, A. 117
 Yoshimura, K., see Mushnikov, N.V. 117
 Yoshimura, K., see Nakamura, H. 115
 Yoshimura, K., see Ogawa, S. 116
 Yoshimura, K., see Pillmayr, N. 116
 Yoshimura, K., see Severing, A. 115
 Yoshimura, K., see Shimizu, T. 116
 Yoshimura, K., see Zhang, W. 117
 Yoshizaki, R., see Shigekawa, H. 419
 Yoshizawa, H., see Kawano, H. 262
 Yoshizawa, H., see Kawano-Furukawa, H. 262, 267, 268
 Yoshizawa, H., see Yokoyama, M. 239, 241
 Young, M.J. 452
 Yuan, Q. 170, 254, 255
 Yuan, Q., see Maki, K. 273, 274
 Yuan, Q., see Won, H. 256
 Yuhasz, W.M., see Maple, M.B. 269, 270
 Yun, S.W., see Ōnuki, Y. 231

 Zak, Z. 397, 401
 Zak, Z., see Giester, G. 397, 401
 Zakharko, O.Ya., see Zaremba, V.I. 14, 64, 97
 Zandbergen, H.W., see Cava, R.J. 248
 Zapf, V.S. 111, 114
 Zapf, V.S., see Bauer, E.D. 268, 269, 271
 Zapf, V.S., see Frederick, N.A. 269
 Zapf, V.S., see Goll, G. 113, 194
 Zapf, V.S., see Maple, M.B. 269, 270
 Zarechnyuk, O.S., see Rykhal, R.M. 54
 Zaremba, V.I. 6, 10, 14, 28, 31, 36, 42, 44, 47, 51–53, 57, 64, 65, 69, 71, 72, 78, 80, 89, 97, 102, 105, 106, 124
 Zaremba, V.I., see Dubenskii, V.P. 10
 Zaremba, V.I., see Esmaeilzadeh, S. 27
 Zaremba, V.I., see Galadzhun, Ya.V. 33, 36, 38, 59, 75
 Zaremba, V.I., see Hoffmann, R.-D. 3, 28, 31, 38, 54, 97
 Zaremba, V.I., see Kaczorowski, D. 36, 102, 105
 Zaremba, V.I., see Kalychak, Ya.M. 3, 10, 14, 15, 18, 40, 42, 49, 54, 55, 62, 72, 76, 81–83, 88, 89, 99
 Zaremba, V.I., see Rodewald, U.-Ch. 36, 51
 Zaremba, V.I., see Sysa, L.V. 10, 14, 18, 33, 49, 68, 124
 Zarestky, J., see Dervenagas, P. 253
 Zaug, A., see Cech, T. 408
 Zavaliĭ, P.Yu., see Zaremba, V.I. 10, 14, 52, 69, 71, 72, 78, 80, 89
 Zavaliĭ, P.Yu., see Baranyak, V.M. 10, 14, 18, 20, 39, 48, 58, 70, 88
 Zavaliĭ, P.Yu., see Kalychak, Ya.M. 10, 14, 18, 49, 54, 55, 61, 72, 76, 83, 88, 89
 Zavodnik, V.E., see Markiv, V.Ya. 64
 Zavodnik, V.E., see Zaremba, V.I. 10, 52
 Zawadowski, A., see Cox, D.L. 145
 Zell, W. 106
 Zhang, B.L., see Breslow, R. 411
 Zhang, D.S., see Ma, B.Q. 398
 Zhang, L., see Wan, Y. 389
 Zhang, R.H., see Bu, X.H. 395, 396
 Zhang, R.H., see Li, J.R. 395, 396
 Zhang, W. 117
 Zhang, W., see Mitsuda, A. 117
 Zhang, W., see Mushnikov, N.V. 117
 Zhang, Z.Y., see Chui, S.S.-Y. 369, 384, 388
 Zhao, L.J., see Bu, X.H. 395, 396
 Zhao, Y. 364
 Zhao, Y., see Cao, R. 363
 Zhao, Z., see Adenwalla, S. 205
 Zheng, C., see Pan, L. 387, 391
 Zheng, C., see Wang, R. 398, 400
 Zheng, G.-Q. 113, 194
 Zheng, G.-Q., see Kawasaki, S. 113, 192
 Zheng, G.-Q., see Kawasaki, Y. 113
 Zheng, G.-Q., see Kotegawa, H. 272
 Zheng, G.-Q., see Mito, T. 113
 Zheng, N., see Pan, L. 369, 376, 378, 389
 Zheng, N., see Wu, Y. 389
 Zheng, Z. 398

- Zheng, Z., see Wang, R. 398, 400
Zhi-Bang, D. 369
Zhong-Sheng, J., see Zhi-Bang, D. 369
Zhu, S., see Branum, M.E. 415
Zhuang, H.-H., see Wu, C.-D. 369, 381, 384
Ziebeck, K.R.A., see Babateen, M. 120
Zou, X., see Chin, J. 419
Zumdick, M.F. 80
Zvezdin, A.K., see Dzero, M.O. 115
Zvyagin, A.A. 245
Zwicknagl, G. 141, 144, 146, 148, 151, 154,
185–189, 198, 201–203, 220, 221, 238, 265, 271
Zwicknagl, G., see Buchholtz, L.J. 170
Zwicknagl, G., see Efremov, D. 147, 149, 220
Zwicknagl, G., see Fulde, P. 141, 154, 170, 195
Zwicknagl, G., see Runge, E. 185
Zwicknagl, G., see Stockert, O. 168, 190
Zygmunt, A., see Gondek, Ł. 103
Zygmunt, A., see Szytuła, A. 38, 102, 106

SUBJECT INDEX

- 1,2,4,5 benzene tetracarboxylate 363, 369, 380, 382
- Co₂(btc)(H₂O)₁₈ 363
- Cu₂(btc)(H₂O)₄·2H₂O 363
- [Eu₂(btc)(H₂btc)(H₂O)]·4H₂O 369, 381, 384
- Ni₂(2,2'-bipy)₂(OH)₂(H₂btc) 363
- Tb₂(btc)(H₂btc)(H₂O)₂·4H₂O 369, 382, 385
- Yb₄(btc)₃(H₂O)₈·6H₂O 369, 382, 385
- 1,3,5 benzene tricarboxylate 363, 368, 369, 375, 389
- Ca(Hbtc)·2H₂O 363
- Co(Hbtc)(C₅H₅N)₂·2/3C₅H₅N 363
- Cu₃(btc)₂(C₃H₃N₂CH₃)₆(H₂O)_x·xH₂O with $x = 7$ or 16 363
- [Cu₃(btc)₂(H₂O)₃]_n 362, 364
- Er(btc) 374
- Er(btc)·6H₂O 368, 370
- Er(btc)(H₂O)₃·1.5H₂O 370, 371, 373
- Er(btc)(H₂O)₅·3.5H₂O 369–373
- Er(btc)(H₂O)₅·H₂O 369, 370, 373
- Er(btc)(H₂O)₆ 373
- Eu₃(H₂O)(OH)₆(btc)·3H₂O 374
- Eu(H₂O)(OH)₆(btc)·3H₂O 374
- Gd(btc)(H₂O)₃·1.5H₂O 369
- Ln(btc)(H₂O)₅·3.5H₂O 397
- Lu(btc)(H₂O)₅·4H₂O 369
- M(Hbtc)(H₂O)₂·(H₂O)_{0.5} 363
- Mn₃(btc)₂ 363
- Ni₃(btc)₂(H₂O)₁₂ 363
- Ni₅(btc)₂(Hbtc)₂(C₅H₅N)₁₅(H₂O)₅·xH₂O·yC₄H₉OH·zC₅H₅N 363
- R(btc) 375, 376
- Y(btc)(H₂O)₆ 369
- Zn₂(btc)(NO₃)·(H₂O)(C₂H₅OH)₅ 363
- 1,3,5-benzene-tricarboxylic acid 368
- 1,3-adamantanedicarboxylate ligands 392
- 1,3-adamantanedicarboxylic acid 392
- 1,4-benzene dicarboxylate 363, 369, 373, 375, 377, 378
- Eu₂(H₂O)₂(OH)₄(bdc) 379, 382
- Eu₂(OH)₄(bdc) 379, 382
- Ln₂(bdc)₃·4H₂O 369
- Ln₂(bdc)₃(H₂O)₆ 369
- Tb₂(bdc)₃·4H₂O 377
- Tb₂(bdc)₃·(H₂O)₄ 375
- Tb(bdc)(NO₃)·2DMF 369, 378, 381
- V(OH)(bdc)·0.75(bdcH₂) 363
- Zn₃(bdc)₃·6(CH₃OH) 363
- 1,4-phenylenedicarboxylic acid 389
- 2,6-naphthalenedicarboxylate 386
- 2,6-naphthalenedicarboxylic acid 389
- 3,5-pyrazoledicarboxylic acid 393, 395
- 4,4',4''-benzene-1,3,5-triyl-benzoate
- Cu₃(BTB)₂(H₂O)₃·(DMF)₉(H₂O)₂ 363, 365
- 4f-3d interactions 366
- α -Fe 92
- (α -Fe) type 83
- activation energy 322
- adipate
- {La₂(adipate)₃(H₂O)₄·6H₂O}_n 390, 393
- R₂(adipate)₃(H₂O)₄·xH₂O 391
- adsorption 390
- agarose gel 371, 397
- AlB₂ 92
- AlB₂ type 10, 26, 70, 79, 80, 83, 86, 92
- amino acids 332
- antiferromagnetic order 165, 218
- PrOs₄Sb₁₂ 270
- UPT₃ 205, 208
- antiferroquadrupolar order 240, 269
- AuCu 92
- AuCu₃ 88, 92
- AuCu₃ type 83, 88
- B*–*T* phase diagram
- CeCu₂Si₂ 189
- HoNi₂B₂C 261
- PrOs₄Sb₁₂ 270, 274
- UPT₃ 209
- URu₂Si₂ 242
- BaAl₄ 92
- band structure 146, 150, 151, 185, 219, 231, 253, 269
- BaPtIn₂ 97

- BaRhIn₂ 97
 BCS ratio 171, 194
 benzene hexacarboxylate 363, 369, 382
 – Al₂(bhc)·16H₂O 363
 – Co₃(bhc)·18H₂O 363
 – La₂(bhc)(H₂O)₉·2H₂O 369, 383, 387
 – Ln₂(bhc)(H₂O)₁₀·4H₂O 369
 – Ln₂(bhc)(H₂O)₄·H₂O 369, 384, 388
 – Ln₂(bhc)(H₂O)₆ 369, 384, 388
 – R₂(bhc)(H₂O)₁₀·4H₂O 382
 – R₂(bhc)(H₂O)₄·(H₂O) 384
 – R₂(bhc)(H₂O)₆ 384
 – Tm₂(bhc)(μ-H₂O)₂(H₂O)₂ 369, 384, 386, 388
 benzene-1,4-dicarboxylic acid 375
 biexponential 304
 Blount's theorem 162, 212
 Boltzmann distribution 351
 borocarbides 165, 248

 CaCo₂Al₈ type 43
 CaCu₅ 54, 83, 85
 CaCu₅ type 82, 88, 89
 CaIn₂ 80, 92
 CaIn₂ type 26, 33, 69, 97, 123
 catalysis 360, 366, 368, 384, 389
 Ce–Co–In 7
 Ce–Cu–In 19
 Ce–Ni–In 8
 Ce–Pd–In 28
 Ce_{0.72}Cu_{8.80}In_{3.84} 15
 Ce_{1-x}La_xCu₅In 121
 Ce_{1-x}Y_xRhIn₅ 111
 Ce_{1.95}Pd_{2+2x}In_{1-x} 29
 Ce₁₂Pt₇In 35
 – structure 75
 Ce₁₂Pt₇In type 75
 Ce_{2+x}Pd_{1.85}In_{1-x} 29
 Ce₂AgIn 32
 Ce₂AgIn₃ 32
 Ce₂Au₂In 37, 108–110
 Ce₂Au₃In₅ 37, 94, 122
 – structure 57
 Ce₂Au₃In₅ type 57
 Ce₂CoIn₈ 7, 9, 55, 110
 – structure 56
 Ce₂Cu_{2+x}In_{1-x} 107
 Ce₂Cu₂In 15, 107, 108, 110
 Ce₂CuIn₃ 122
 Ce₂IrIn₈ 34, 112
 Ce₂Ni₂In 12, 72, 109
 – structure 73
 Ce₂Ni_{2x}Pd_{2-2x}In 109
 Ce₂Pd_{2+x}In_{1-x} 107, 109
 Ce₂Pd_{2+x}Sn_{1-x} 109
 Ce₂Pd_{2.05}In_{0.95} 107
 Ce₂Pd₂In 30, 107–110
 Ce₂Pt₂In 35, 108, 110
 Ce₂Rh₂In 27, 109, 110
 Ce₂RhIn₈ 27, 112, 193
 Ce₂T₂In 109, 110
 Ce₂TIn₈ 4, 113
 Ce₃NiIn₂ 8
 Ce₃Pt₄In₁₃ 35, 121, 122
 Ce₄Ni₇In₈ 8, 12, 61, 88
 – structure 59
 Ce₄Ni₇In₈ type 58, 79, 88
 Ce₄Pd₁₀In₂₁ 30, 45
 – structure 46
 Ce₅Ni₆In₁₁ 4, 12, 122, 123
 Ce₅NiIn₃ 8
 Ce₈Pd₂₄In 29, 30, 61, 95
 – structure 62
 Ce₈Pd₂₄Sb type 29, 61, 79
 Ce_xLa_{1-x}CoIn₅ 111
 Ce_xLa_{1-x}RhIn₅ 111
 CeAg 29
 CeAg₂In 32, 119
 CeAg_{5.4}In_{6.6} 32
 CeAg_{6.4}In_{5.6} 124
 CeAu₂In 37, 119
 CeAu_{3.5}In_{2.5} 37
 CeAuIn 37, 102, 103
 CeCdIn 34
 CeCl₃ 409
 CeCo₃B₂ 88
 CeCoIn₅ 7, 9, 110, 112, 113, 192–194
 Ce(Cu_{0.25}In_{0.75})₂ 70
 CeCu_{0.5}In_{1.5} 15
 CeCu_{0.8-0.4}In_{1.2-1.6} 15, 20
 CeCu₂ 92
 CeCu₂ type 26, 69
 CeCu_{2-x}In_{2-y} 15, 20
 CeCu₂Ge₂ 184
 CeCu₂In 15, 120, 121
 CeCu₂(Si_{1-x}Ge_x)₂ 168, 190
 CeCu₂Si₂ 144, 167
 CeCu_{4.2}In_{4.8} 19
 CeCu_{4.32}In_{1.68} structure 49
 CeCu_{4.32}In_{1.68} type 48
 CeCu_{4.38}In_{1.62} 15, 80
 CeCu_{4.38}In_{1.62} type 79, 81, 84, 85
 CeCu_{5.1-4.2}In_{0.9-1.8} 15, 20

- CeCu_{5.1}In_{6.9} 15
 CeCu₆ 80
 CeCu₆ type 80, 81
 CeCu_{6-x}In_x 20
 CeCu_{9.0-8.0}In_{2.0-3.0} 15, 20
 CeCuIn 15, 102, 103
 Ce(Hbtc)·H₂O 369, 380, 383
 CeIn 29
 CeIrIn₅ 34, 111–114, 193
 CeLaRh₂In 110
 CeM₂X₂ 184
 CeMg₂Si₂ 83, 84
 CeMg₂Si₂ type 86, 88
 CeMnIn₅ 191
 Ce(Mn_{0.45}Ni_{0.55})₁₁ 80, 81
 Ce(Mn_{0.55}Ni_{0.45})₁₁ 86
 Ce(NH₄)₂(NO₃)₆ 410
 CeNi_{0.3-0.2}In_{1.7-1.8} 12
 CeNi_{0.5}In_{1.5} 12
 CeNi₂Ge₂ 184, 190
 CeNi₃In₆ 12
 CeNi₄In 12
 – structure 53
 CeNi₅In 12, 48
 – structure 47
 CeNi₅Sn type 47, 79, 84, 85
 CeNi₉In₂ 12, 121
 CeNi_xIn_{2-x} 8
 CeNiAl_{4-x}In_x 123
 CeNiIn 4, 12, 100, 101, 103
 CeNiIn type 103
 CeNiIn_{1.8} 107
 CeNiIn₂ 6, 12
 CeNiIn₄ 12, 122, 123
 CeNiInH_{1.0} 107
 CeNiInH_{1.6} 107
 CeNiInH_{1.8} 4, 107
 CeNiInH_x 107
 CePd_{0.2}Rh_{0.8}In 103
 CePd_{0.6}Rh_{0.4}In 103
 CePd₂In 29, 30, 121, 122
 CePd₂Si₂ 184, 190
 CePd_xRh_{1-x}In 102
 CePdIn 28, 30, 101, 102
 CePdIn type 103
 CePdIn₂ 28, 30, 122
 CePt₂In₂ 35
 – structure 56
 CePt₂In₂ type 56
 CePt₄In 35, 117, 118
 CePtIn 35, 101
 CePtIn type 103
 CePtIn₃ 35
 CeRh_{1-x}Co_xIn₅ 114
 CeRh₂Si₂ 184
 CeRhIn 4, 27, 101, 102
 CeRhIn₂ 27
 CeRhIn₅ 27, 111, 113, 193
 CeRhInH_{0.55} 107
 CeRhInH_{1.55} 107
 cerium (IV)
 – [Ce^{IV}₂(OH)₄]⁴⁺ cluster 423
 – Ce(IV)/EDTA complex 415, 436, 438
 – Ce(IV)/iminodiacetate complex 433
 – Ce(IV)/saccharide complexes 415
 – cooperation of Ce(IV) and Pr(III) 414
 – homogeneous Ce(IV) complexes for DNA hydrolysis 414
 – hydrolysis of cyclic adenosine 3',5'-monophosphate (cAMP) by Ce(NH₄)₂(NO₃)₆ 419
 – mechanism of DNA hydrolysis by Ce(IV) 424
 – quantum chemical calculations on [Ce^{IV}₂(OH)₄]⁴⁺ 423
 CeRu₂Ge₂ 186
 CeRu₂Si₂ 187
 CeRuIn₂ 27
 CeTGe 101
 CeTIn 101
 CeTIn₅ 4, 113
 CeT₂Sn 101
 CeTX 101
 CeZnIn 26
 chain-like molecular motifs 396
 charge density wave 158, 162, 178
 chemical bonding 3, 94, 95
 chiral recognition 328, 329
 circular dichroism 292, 298–300, 305, 311, 313, 329, 331, 339, 345, 349–351
 circularly polarized excitation 295, 299–301, 305, 306, 312, 313, 316, 318, 321, 323, 330, 331
 cis,cis-1,3,5-cyclohexanetricarboxylate 389
 Co₂Si 92
 controlled hydrolysis 398
 conventional pairing 161, 163, 179
 coordination polymers 360, 361, 363, 368, 377
 – 1-dimensional 363, 369, 376, 387, 401, 402
 – 2-dimensional 363, 369
 – 3-dimensional 362–364, 368, 369, 374, 375, 377, 378, 381–384, 386, 390–392, 397, 398, 402
 – containing transition metal ions 362, 364

- lanthanide-containing 359, 365, 367, 368, 386, 389, 401, 402
- porous network 363, 364, 368, 374–376, 379, 386, 389, 391, 397, 401, 402
- Coulomb interaction 148, 155, 201
- covalent strategy 432
- for site-selective RNA hydrolysis 442
- Cr₃AlB₄ type 90
- Cr₅B₃ 86
- Cr₅B₃ type 86
- crystalline electric field excitations 188, 202, 221, 237, 260, 269
- crystallographic data of ternary compounds
 - R–Ag–In 32
 - R–Au–In 37
 - R–Cd–In 34
 - R–Co–In 9
 - R–Cu–In 15
 - R–Ir–In 34
 - R–Ni–In 11
 - R–Pd–In 30
 - R–Pt–In 35
 - R–Rh–In 27
 - R–Zn–In 26
- CsCl 88
- CsCl type 29, 73, 83, 86, 89, 118, 120
- structure 74
- CuAl₂ type 86

- d-wave gap 165, 167, 168, 175, 178, 180, 194, 196
- de Haas–van Alphen effect 186, 238
 - UPd₂Al₃ 220
 - UPt₃ 203
- depollution 368, 402
- differential photon counter 307
- diffusion through gels 396
- dipole strength 297
- DNA
 - cleavage of plasmid DNA 414
 - homogeneous Ce(IV) complexes for DNA hydrolysis 414
 - hydrolysis 409, 411
 - site-selective scission 431, 434, 440
- Doppler shift 175, 176, 256
- dual model 145, 200, 220
- Dy–Cu–In 25
- Dy₁₄Co₂In₃ 9
- Dy₂AgIn 33
- Dy₂AgIn₃ 33
- Dy₂Au₂In 38, 108
- Dy₂CoIn₈ 9
- Dy₂Cu₂In 17, 108, 110
- Dy₂CuIn₃ 122
- Dy₂Ni_{2–x}In 13
- Dy₂Ni₂In 13
- Dy₂Pd₂In 31, 108
- Dy₂Pt₂In 36
- Dy₂Pt₇In₁₆ 6, 36
- structure 42
- Dy₂Pt₇In₁₆ type 41
- Dy₃Co₂In₄ 9
- Dy₆Co_{2.14}In_{0.86} 9
- DyAg_{0.5}In_{0.5} 119
- DyAg₂In 32, 119
- DyAg_{3.5}In_{2.5} 32
- DyAu₂In 38, 119
- DyAuIn 38, 102, 106
- DyCdIn 34
- DyCo₂In 9
- DyCo₄In 9
- DyCoIn₅ 9
- DyCu_{0.65–0.32}In_{1.35–1.68} 17, 25
- DyCu₂In 17
- DyCu₄In 17
- DyCu_{5–4}In_{0–1} 17
- DyCu_{5.1}In_{6.9} 17
- DyCuIn 17
- DyMn₂ 106
- DyMnIn 7, 106
- DyNi_{1.0–0.6}In_{1.0–1.4} 13
- DyNi₂B₂C 263
- DyNi₄In 13
- DyNi₉In₂ 13
- DyNiIn 13
- DyNiIn₂ 13
- DyPd₂In 31
- DyPdIn 31, 102, 103
- DyPdIn₂ 31
- DyPt₂In 36
- DyPt₄In 36, 118
- DyPtIn 36
- DyRhIn 28
- DyRhIn₅ 28
- DyZnIn 26

- E*_{2*u*}-model 209, 211
- effective interaction 155, 157, 159, 226, 265
- electroluminescent materials 368
- electron–electron pairing 153, 179
- electron–hole pairing 153, 163
- electron–phonon superconductivity 251
- Eliashberg equations 226, 227
- enantiomeric excess 303–305, 323, 331, 332

- energy transfer 301, 302, 322, 323, 328, 335, 350
 enzymatic transformation 414
 Er-Cu-In 26
 Er₁₀Co₉In₂₀ 10
 Er₁₀Ni₉In₂₀ 14
 Er₁₄Co₂In₃ 10
 Er₂AgIn 33
 Er₂AgIn₃ 33
 Er₂Au₂In 38, 108
 Er₂(bdc)₃·4H₂O 377
 Er₂(bdc)₃(H₂O)₆ 377, 380, 387
 Er₂(bhc)(H₂O)₁₀·4H₂O 386
 Er₂(C₂O₄)₃·10H₂O 361
 Er₂CoIn₈ 10
 Er₂Cu₂In 17, 108
 Er₂(ndc)₃(H₂O)₆ 386, 390
 Er₂Ni_{2-x}In 14
 Er₂Ni₂In 14
 Er₂Pd₂In 31, 108
 Er₃(btc)₃(H₂O)₈·4H₂O 369–371, 373
 Er₃Co₂In₄ 10
 Er₄(bdc)₆ 377
 Er₄(bdc)₆·6H₂O 369, 376–379
 [Er₄(μ₃-OH)₄(C₅H₉NO₄)₃(H₂O)₈](ClO₄)₅·
 6H₂O 398, 400
 Er₅Ni₂In₄ 14
 Er₆Co_{17.92}In₁₄ 10
 [Er₆(μ₆-O)(μ₃-OH)₈(NO₃)₄(H₂O)₁₁(OH)
 (ONONO₂)]Cl₃·2H₂O 401
 Er₈(btc)₆(H₂O)₁₆·16H₂O 369, 382, 385
 ErAg_{0.5}In_{0.5} 119
 ErAg₂In 33, 119
 ErAg_{3.5}In_{2.5} 33
 ErAu₂In 38, 119
 ErAuIn 38
 [Er(C₉H₉O₆)(H₂O)₂]₂·5H₂O 392
 ErCdIn 34
 ErCo₄In 10
 ErCu_{0.44-0.35}In_{1.56-1.65} 17, 26
 ErCu_{1.0-0.64}In_{1.0-1.36} 17, 26
 ErCu₂In 17
 ErCu₄In 17
 ErCu₅ 26
 ErCu₅₋₄In₀₋₁ 17
 ErCu_{5.1}In_{6.9} 17, 40
 – structure 41
 [Er(μ₃-OH)₄]⁸⁺ 400
 ErMnIn 7
 ErNi_{1-0.6}In_{1-1.4} 14
 ErNi₂B₂C 262, 267
 ErNi₄In 14
 ErNi₉In₂ 14
 ErNiIn 14
 ErPd₂In 31
 ErPdIn 31, 102
 ErPdIn₂ 31
 ErPt₄In 36, 118
 ErPtIn 36
 ErRhIn 28
 ErRhIn₅ 28
 ErZnIn 26
 Eu-Cu-In 23
 Eu₂Au₃In₄ 37, 59, 122
 – structure 60
 Eu₂(O₂C-C₁₀H₁₄-CO₂)₃ 391, 395
 EuAg_{0.5}In_{0.5} 32
 EuAg₄In₈ 32, 80, 81
 – structure 41
 EuAg₄In₈ type 40, 79, 81, 82
 EuAg_{5.4}In_{6.6} 32
 EuAuIn 37, 102, 105
 EuAuIn₂ 37, 97
 EuCu_{0.5}In_{1.5} 16, 23
 EuCu_{6.5}In_{6.5} 16, 23, 124
 EuCu_{8.5}In_{2.5} 16, 23
 EuCuIn₄ 16, 23, 124
 EuIn₂ 97
 EuIn₄ 92
 Euler matrix 297
 EuNi_{0.5}In_{1.5} 13
 EuNi₃In₆ 13
 EuNi₅In 13
 EuNi₇In₆ 13
 EuNi₉In₂ 13
 EuNiIn₂ 13
 EuNiIn₄ 13, 122, 123
 EuPdIn 30, 102, 104, 105
 – structure 68
 EuPdIn₂ 30, 97, 122
 EuPdIn₄ 30
 EuPt₄In 35, 117, 118
 EuPtIn 35, 102, 105
 EuRh₂In₈ 28, 96
 – structure 43
 EuRhIn 4, 28, 102, 105
 EuRhIn₂ 28
 EuTIn 6, 105
 EuTIn₂ 97
 EuZnIn 26, 100, 102, 105
 – structure 69

- Fe_2P type 28, 66
 Fermi
 – Golden Rule 294
 – liquid 150, 152–154, 245
 – surface 165, 181, 186
 – CeCu₂Si₂ 188
 – CeRu₂Si₂ 186
 – UPd₂Al₃ 220
 – UPt₃ 201
 – velocity 151
 – wave vector 151
 ferromagnetic order 229–231, 262, 267
 form factor 167, 171
 Förster critical transfer distances 323
 free energy 207, 241, 260
 – of mixing 330

 gap
 – equations 163, 165
 – function 158, 163, 211, 254, 273, 274
 – nodes 165, 175, 254
 – strategy for site-selective DNA scission 434
 gas sorption 379
 gas storage 360, 386
 Gd–Cu–In 23
 Gd_{0.4}In_{0.6}Cu₂ 115
 Gd₁₂Ni₆In 13
 Gd₁₂Pt₇In 36
 Gd₁₄Co₂In₃ 9
 Gd₁₄Co₃In_{2.7} 9, 78, 122, 123
 Gd₂AgIn₃ 32
 Gd₂Au₂In 38, 108
 Gd₂CoIn₈ 9
 Gd₂Cu₂In 16, 108
 Gd₂IrIn₈ 34, 114
 Gd₂Ni_{1.88}In 72
 Gd₂Ni_{2–x}In 13
 Gd₂Ni₂In 13
 Gd₂Pd₂In 31, 108
 Gd₂Pt₂In 36
 Gd₂RhIn₈ 28, 114
 Gd₃Pt₄In₁₂ 35
 – structure 52
 Gd₃Pt₄In₁₂ type 51
 Gd₄Pd₁₀In₂₁ 30
 Gd₆Co_{2.14}In_{0.86} 9
 Gd₆Co_{2.2}In_{0.8} 9, 122, 123
 Gd_xTh_{1–x}PdIn 105
 GdAg_{0.1}In_{0.9} 119
 GdAg_{0.2}In_{0.8} 119
 GdAg_{0.3}In_{0.7} 119
 GdAg_{0.5}In_{0.5} 29, 119
 GdAg_{0.7}In_{0.3} 119
 GdAg_{0.8}In_{0.2} 119
 GdAg_{0.9}In_{0.1} 119
 GdAg_{1–x}In_x 32, 118
 GdAg₂In 32, 119, 120
 GdAg_{3.5}In_{2.5} 32
 GdAu_{0.44}In_{1.56} 38, 97, 122, 123
 GdAu₂In 37, 119
 GdAuIn 37, 102, 104, 106
 GdCdIn 34
 GdCo₂In 9
 GdCoIn₅ 9
 GdCu_{0.59–0.35}In_{1.41–1.65} 16
 GdCu_{0.6–0.4}In_{1.4–1.6} 24
 GdCu₂In 16
 GdCu_{4.7–4.0}In_{0.3–1.0} 16, 23
 GdCu₄In 16, 117
 GdCu_{5.1}In_{6.9} 16
 GdCu_{9.0–8.4}In_{2.0–2.6} 23
 GdCu_{9.00–8.36}In_{2.00–2.64} 16
 GdCuIn 16, 102, 104
 GdIrIn₅ 34, 114
 GdMn₂ 106
 GdMnIn 7, 106
 GdNi_{1–0.65}In_{1–1.35} 13
 GdNi₄In 13
 GdNi₉In₂ 13, 121
 GdNiIn 13, 102, 104
 GdNiIn₂ 13
 GdPd₂In 31
 GdPdIn 31, 102, 104, 105
 GdPdIn₂ 31
 GdPt₂In 36
 GdPt₂Sn type 29, 62, 79, 92
 GdPt₄In 36, 117, 118
 GdPtIn 36
 GdRhIn 28, 102
 GdRhIn₂ 28, 97
 GdRhIn₅ 28, 114
 GdZn_{1–x}In_x 118
 GdZnIn 26

 gel
 – diffusion method 371, 377, 378, 386, 397
 – medium 382, 397
 giant diamagnetism 181
 Ginzburg–Landau theory 161, 210, 235
 glutamate 400
 glutamic acid 398, 399
 glutarate 391
 Green's function 323

- Hamiltonian 294
 heavy fermions 143, 144, 146, 150, 188, 200, 201, 269
 Heusler phases 118
 HfNiGa₂ type 64
 hidden order 163, 179, 234, 236, 241
 high temperature superconducting ceramics 155, 360
 Ho–Cu–In 26
 Ho₁₀Ni₉In₂₀ 13, 80
 – structure 67
 Ho₁₀Ni₉In₂₀ type 65
 Ho₁₂Pt₇In 36
 Ho₁₄Co₂In₃ 10
 Ho₂AgIn 33
 Ho₂AgIn₃ 33
 Ho₂Au₂In 38, 108
 Ho₂CoGa₈ 88
 Ho₂CoGa₈ type 55, 79, 88, 92, 100, 110
 Ho₂CoIn₈ 9
 Ho₂Cu₂In 17, 108
 Ho₂CuIn₃ 122
 Ho₂Ni_{2–x}In 13
 Ho₂Ni₂In 13
 Ho₂Pd₂In 31, 108
 Ho₂Pt₂In 36, 109
 Ho₃Co₂In₄ 10
 Ho₄Ni₁₀Ga₂₁ type 45
 Ho₅Ni₂In₄ 13
 Ho₆Co_{2+x}In_{1–x} 76
 – Ho₆Co_{2.135}In_{0.865} structure 77
 Ho₆Co_{2.14}In_{0.86} 10
 Ho₆Co₂Ga 80
 Ho₆Co₂Ga type 76, 83, 122
 HoAg_{0.5}In_{0.5} 119
 HoAg₂In 33, 119
 HoAg_{3.5}In_{2.5} 33
 HoAu₂In 38, 119
 HoAuIn 38, 102, 106
 HoCdIn 34
 HoCo₂Ga 89
 HoCo₂Ga type 89
 HoCo₂In 9
 HoCo₄In 9
 HoCoGa₅ 56, 88
 HoCoGa₅ type 49, 79, 88, 92, 100, 110, 111
 HoCoIn₅ 9, 42, 49, 51
 – structure 50
 HoCu_{0.41–0.29}In_{1.59–1.71} 17, 26
 HoCu₂In 17
 HoCu₄In 17
 HoCu₅ 26
 HoCu_{5–4}In_{0–1} 17
 HoCu_{5.1}In_{6.9} 17
 HoCuIn 17
 honeycomb-like molecular motif 360
 HoNi_{1–0.5}In_{1–1.5} 13
 HoNi_{2.6}Ga_{2.4} type 53, 80, 88
 HoNi₂B₂C 259, 263
 HoNi₄In 13
 HoNi₉In₂ 13
 HoNiIn 13
 HoPd₂In 120
 HoPdIn 31, 102
 HoPdIn₂ 31
 HoPt₂In 36
 HoPt₄In 36, 118
 HoPtIn 36
 HoRhIn 28
 HoRhIn₅ 28
 HoZnIn 26
 Hubbard model 155
 Hund's rules 149
 hybridization 143, 148
 hydrogenation of RNiIn 106
 hydrolysis of monophosphates 410
 hydrostatic pressure 207, 208, 232, 266
 – UGe₂ 230
 – URu₂Si₂ 239
 hydrothermal synthesis 374–376, 378–384, 387, 391, 393, 396, 397

 impurity scattering 176, 255
 incommensurate order 168, 190, 259, 260
 induced moment magnetism 222
 inelastic neutron scattering
 – UPd₂Al₃ 225
 – URu₂Si₂ 243
 integrated rotatory (or rotational) strength 297
 isothermal section of the phase diagram
 – Ce–Co–In system 8
 – Ce–Cu–In system 19
 – Ce–Ni–In system 11
 – Ce–Pd–In system 29
 – Dy–Cu–In system 23
 – Er–Cu–In system 24
 – Eu–Cu–In system 21
 – Gd–Cu–In system 22
 – Ho–Cu–In system 23
 – La–Cu–In system 19
 – Lu–Cu–In system 25

- Nd-Cu-In system 20
- Pr-Cu-In system 20
- Pr-Fe-In system 8
- Sm-Cu-In system 21
- Tb-Cu-In system 22
- Tm-Cu-In system 24
- Y-Cu-In system 18
- Yb-Cu-In system 25

- jj*-coupling 162, 200

- KHg₂ type 26, 69
- Knight shift 172, 218
- UPt₃ 214
- Kondo
 - lattice 143, 198
 - resonance 143, 244
 - temperature 143

- La-Ag-In 29
- La-Cu-In 19
- La_{1-x}Ce_xInCu₂ 120
- La₁₂Co₆In 9
- La₁₂Ni₆In 11
- La₂AgIn 32
- La₂AgIn₃ 32
- La₂Au₂In 37, 110
- La₂Cu₂In 15, 110
- La₂IrIn₈ 34
- La₂Ni₂In 11, 110
- La₂Pd₂In 30, 110
- La₂Pt₂In 35, 110
- La₂Rh₂In 27, 110
- La₂RhIn₈ 27
- La₂T₂In 110
- La₃Au₄In₇ 37
 - structure 60
- La₃Au₄In₇ type 59
- La₃Pt₄In₁₃ 35, 122
- La₄Ag₃In 32
- La₄Ni₇In₈ 11
- La₄Pd₁₀In₂₁ 30
- La₅Ni₆In₁₁ 11
- La₆Co₁₁Ga₃ type 66, 86
- La₆Co₁₃In 9, 66, 86
 - structure 67
- La₈Pd₂₄In 30
- LaAg 29
- LaAg_{0.5}In_{0.5} 29
- LaAg₂In 32
- LaAg_{5.4}In_{6.6} 32
- LaAg_xIn_{1-x} 118, 120
 - structure 74
- LaAgIn 80
- LaAu₂In 37, 118
- LaAuIn 37
- laboratory coordinate frame 297
- LaCdIn 34
- LaCoAl₄ 94
- LaCoAl₄ type 54
- LaCoIn₅ 9
- LaCu_{0.5-0.2}In_{1.5-1.8} 15, 19
- LaCu_{0.5}In_{1.5} 15
- LaCu₂In 15, 120, 121
 - structure 63
- LaCu₂In₃ 19
- LaCu_{5.2-4.3}In_{0.8-1.7} 19
- LaCu_{5.23-4.25}In_{0.77-1.75} 15
- LaCu_{6.5}In_{6.5} 15
 - structure 39
- LaCu₉In₂ 15, 19
- LaCuIn 15
- LaIn 29
- LaIrIn₅ 34
- Landau
 - levels 181, 182
 - parameters 207
- LaNi_{0.5}In_{1.5} 11
- LaNi₂In 11
- LaNi₃In₂ 11, 53
 - structure 54
- LaNi₃In₆ 11, 87
 - structure 45
- LaNi₃In₆ type 45, 80, 87
- LaNi₅In 11
- LaNi₇In₆ 11, 99
 - structure 40
- LaNi₇In₆ type 39
- LaNi₉In₂ 11
- LaNiIn 11, 100
- LaNiIn₄ 11
- LaNiInH_{1.33} 100
- LaNiInH_{2.0} 107
- LaPd₂In 30, 62, 121
 - structure 63
- LaPdIn 30, 101
- LaPdIn₂ 30
- LaPorte (parity) forbidden 298
- LaPt₂In₂ 35
- LaPt₄In 35, 118
- LaPtIn 35

- LaPtIn₃ 35
 – structure 58
 LaPtIn₄ 35
 LaRhIn 27, 102
 LaRhIn₂ 27
 LaRhIn₅ 27, 111
 LaRu₂Si₂ 187
 LaRuSn₃ type 58
 laser amplifiers 368
 LaTIn 101
 LaZnIn 26
 LiCu₂Sn 63
 ligands 362
 ligase 407
 linear polarization 295, 296, 301, 305, 306, 310
 LT–LaAg_xIn_{1–x} type 74
 Lu–Cu–In 26
 Lu_{0.4}In_{0.6}Cu₂ 115
 Lu_{1.6}Ce_{0.4}Pd₂In 110
 Lu₁₀Co₉In₂₀ 10
 Lu₁₀Ni₉In₂₀ 14
 Lu₁₄Co₂In₃ 10, 80
 – structure 77
 Lu₁₄Co₂In₃ type 76
 Lu₂AgIn₃ 33
 Lu₂Au₂In 38
 Lu₂Cu₂In 18
 Lu₂Ni_{2–x}In 14
 Lu₂Ni₂In 14
 Lu₂Pd₂In 31
 Lu₃Co_{1.87}In₄ 10, 80
 – structure 70
 Lu₃Co_{1.87}In₄ type 69, 79
 Lu₃Co_{2–x}In₄ type 62
 Lu₃CoGa₅ 80
 Lu₅Ni₂In₄ 14, 80
 – structure 73
 Lu₅Ni₂In₄ type 72, 80, 89, 90
 Lu₆Co_{17.92}In₁₄ 10
 – structure 53
 Lu₆Co_{17.92}In₁₄ type 52
 Lu₆Co_{2.14}In_{0.86} 10
 Lu₆Co_{26–x}In₁₄ type 79
 Lu₆CuIn 26
 LuAg_{3.5}In_{2.5} 33
 LuAu₂In 38
 LuCo₄In 10
 LuCoIn₅ 10
 LuCu_{1.0–0.41}In_{1.0–1.59} 18, 26
 LuCu₂In 18
 LuCu₄In 18, 117
 LuCu₅ 26
 LuCu_{5–4}In_{0–1} 18
 LuCu_{5.1}In_{6.9} 18
 LuCuIn 18
 LuNi_{1.1–0.65}In_{0.9–1.35} 14
 LuNi₂B₂C 250
 LuNi₄In 14
 LuNiIn 14
 – structure 68
 LuPd₂In 31
 LuPdIn 31
 LuPdIn₂ 31
 LuPtIn 36
 LuRhIn 28
 macrocyclic ligands 316
 magnetic devices 360
 magnetic exciton 216, 222, 223, 243
 magnetic properties 366, 381, 395
 magnetic refrigeration 4
 magnetostriction
 – UPT₃ 209
 magnetotransport 175, 180–182, 215, 273
 magnets 360
 mass enhancement 146, 201, 221, 238
 mellitate 383, 384, 386
 metal-organic
 – frameworks 364, 398
 – infinite framework 360
 – open frameworks 360
 metalloproteins 323, 329
 metamagnetism 242, 259, 261
 MgCu₂ type 7, 106, 115
 MgCu₄Sn type 52, 79, 100, 114
 MgCuAl₂ 94
 MgCuAl₂ type 27, 29, 63, 79, 87, 92, 93, 97, 121
 MgZn₂ type 7, 106
 microporous materials 360, 364, 371, 374, 376,
 390, 397
 Mn₂AlB₂ type 71, 79, 89, 90
 MnCu₂Al type 36, 63, 79
 Mo₂FeB₂ type 72, 79, 89, 90, 109
 Mo_{5–x}Ni₂In_{1–x} 14
 Mo₅B₂Si type 74
 molecular networks 395
 molecular precursor 360
 molecular topologies 360
 multiphase superconductivity 199, 272
 N-(4-pyridinylmethyl)-4-pyridinecarboxamide
 – [Ag₂(ppa)₂(ox)]·9H₂O 364, 366
 nano-porous open frameworks 360

- NaZn₁₃ type 39, 79
 Nd–Cu–In 21
 Nd₁₂Co₆In 9
 Nd₁₂Ni₆In 12
 Nd₁₂Pt₇In 35
 Nd₂AgIn₃ 32
 Nd₂Au₂In 37, 108
 Nd₂Au₃In₅ 37
 Nd₂CoIn₈ 9
 Nd₂Cu₂In 16
 Nd₂CuIn₃ 122
 Nd₂IrIn₈ 34, 114
 Nd₂Ni₂In 12
 Nd₂Pd₂In 30, 108
 Nd₂Pt₂In 35, 109
 Nd₂Rh₂In 28, 109
 Nd₂RhIn₈ 28, 114
 Nd₄Ni₇In₈ 12
 Nd₄Pd₁₀In₂₁ 30
 Nd₅Ni₆In₁₁ 12, 96, 97, 122, 123
 Nd₆Fe₁₃In 7
 Nd₆Fe₁₃Si 66
 Nd₆Fe₁₃Si type 7, 79, 86
 NdAg₂In 32, 119
 NdAg_{5,4}In_{6,6} 32
 NdAg₆In₆ 124
 NdAu₂In 37, 119
 NdAuIn 37
 NdCdIn 34
 NdCo₂In 9
 NdCoIn₅ 9
 NdCu_{0,5}In_{1,5} 16
 NdCu_{0,7–0.3}In_{1,3–1.7} 16, 21
 NdCu₂In 16
 NdCu_{4,38}In_{1,62} 16
 NdCu_{4,9–4.0}In_{1,1–2.0} 16, 21
 NdCu₄In 16
 NdCu_{5,1}In_{6,9} 16
 NdCu_{9,0–8.4}In_{2,0–2.6} 16, 21
 NdCuIn 16
 NdFe₁₃Si type 84
 NdIrIn₅ 34, 114
 NdMnIn 7
 NdNi_{0,3–0.2}In_{1,7–1.8} 12
 NdNi_{0,5}In_{1,5} 12
 NdNi₂In 12
 NdNi₃In₆ 12
 NdNi₄In 12
 NdNi₅In 12
 NdNi₉In₂ 12
 NdNiIn 12, 100
 NdNiIn_{1,7} 107
 NdNiIn₂ 12
 NdNiIn₄ 12
 NdPdIn 30
 NdPdIn₂ 30
 NdPt₂In₂ 35
 NdPt₄In 35, 118
 NdPtIn 35
 NdPtIn₃ 35
 NdRhIn 28
 NdRhIn₂ 28
 NdRhIn₅ 28, 114
 NdZnIn 26
 near infrared 307, 340, 341
 nesting property 165, 167, 180, 190, 241, 253
 neutron diffraction 180
 – CeCu₂Si₂ 190
 Ni₂In 92
 non-covalent strategy 432
 – for site-selective RNA scission 444
 non-Fermi liquid state 244
 nuclear magnetic resonance 172, 214, 311, 329,
 335, 336, 338, 339, 343, 345
 optical properties 366, 368, 386, 402
 optical rotation 332
 opto-electronic 360
 order parameter 157
 oxalate
 – hydrated lanthanide(III) complexes 360
 – lanthanide compounds 397
 – Ln₂(C₂O₄)₃·18H₂O 398
 – R₂(C₂O₄)₃·18H₂O 397
 Pfeiffer effect 304, 330
 phase shifts 151
 photon counting 305, 307–309, 311
 pigments 360
 Pm–3*d*-metal–In 7
 Pm–5*d*-metal–In 33
 point nodes 212, 216, 256, 257
 polarizability 299, 338
 poly-hydroxo-lanthanide clusters 397, 401
 power laws 170, 173
 Pr–Cu–In 20
 Pr–Fe–In 7
 Pr₁₂Co₆In 9
 Pr₁₂Ni₆In 12
 Pr₁₂Pt₇In 35
 Pr₂AgIn₃ 32
 Pr₂Au₂In 37, 108
 Pr₂Au₃In₅ 37

- Pr_2CoIn_8 9
 $\text{Pr}_2\text{Cu}_2\text{In}$ 16
 Pr_2CuIn_3 122
 $\text{Pr}_2\text{Ni}_{16.0}\text{In}_{1.0}$ 45
 – structure 46
 $\text{Pr}_2\text{Ni}_{16.6}\text{In}_{0.4}$ 12
 $\text{Pr}_2\text{Ni}_2\text{In}$ 12
 $\text{Pr}_2\text{Pd}_2\text{In}$ 30, 108
 $\text{Pr}_2\text{Pt}_2\text{In}$ 35, 109
 $\text{Pr}_2\text{Rh}_2\text{In}$ 28, 109
 $\text{Pr}_4\text{Ni}_7\text{In}_8$ 12
 $\text{Pr}_4\text{Pd}_{10}\text{In}_{21}$ 30
 $\text{Pr}_5\text{Ni}_6\text{In}_{11}$ 12, 88
 – structure 61
 $\text{Pr}_5\text{Ni}_6\text{In}_{11}$ type 61, 79, 88
 $\text{Pr}_6\text{Fe}_{13}\text{In}$ 7
 $\text{Pr}_6\text{Fe}_{13}\text{Pb}$ 66
 $\text{PrAg}_{1-x}\text{In}_x$ 32
 PrAg_2In 32, 119
 $\text{PrAg}_{5.4}\text{In}_{6.6}$ 32
 PrAg_6In_6 124
 PrAu_2In 37, 119
 PrAuIn 37
 PrCdIn 34
 PrCo_2Ga type 61, 79, 88
 PrCo_2In 9
 PrCoIn_5 9
 $\text{PrCu}_{0.5-0.2}\text{In}_{1.5-1.8}$ 16, 20
 $\text{PrCu}_{0.5}\text{In}_{1.5}$ 16
 PrCu_2In 16
 $\text{PrCu}_{4.38}\text{In}_{1.62}$ 15
 $\text{PrCu}_{5.1-4.2}\text{In}_{0.9-1.8}$ 16, 20
 $\text{PrCu}_{5.1}\text{In}_{6.9}$ 15
 $\text{PrCu}_{9.0-8.1}\text{In}_{2.0-2.9}$ 15, 20
 PrCuIn 16
 pressure 321, 328
 $[\text{Pr}(\text{H}_2\text{O})_2]_2[\text{O}_2\text{C}(\text{CH}_2)_2\text{CO}_2]_3 \cdot \text{H}_2\text{O}$ 394
 $\text{PrNi}_{0.5}\text{In}_{1.5}$ 12
 PrNi_2In 12
 PrNi_3In_6 12
 PrNi_4In 12, 117
 PrNi_5In 12
 PrNi_9In_2 12
 PrNiIn 12
 PrNiIn_2 12
 – structure 65
 PrNiIn_2 type 64
 PrNiIn_4 12
 $\text{PrNiInH}_{1.29}$ 107
 $\text{PrOs}_4\text{Sb}_{12}$ 268
 proteins 329, 349
 PrPdIn 30
 PrPdIn_2 30, 64
 – structure 66
 PrPt_2In_2 35
 PrPt_4In 35, 118
 PrPtIn 35, 102, 106
 PrPtIn_3 35
 PrRhIn 28, 102, 105
 PrRhIn_2 27
 PrRhIn_5 27
 PrZnIn 26
 PtHg_2 type 88
 pyridine dicarboxylate
 – $\text{Ln}_2(\text{pda})_3$ 389
 – $\text{Ln}_2(\text{pda})_3(\text{H}_2\text{O}) \cdot 2\text{H}_2\text{O}$ 387, 389, 391
 quantum critical point 145, 191, 196, 234
 quasiparticle
 – density of states 165, 170, 175, 176, 182, 227, 252, 255
 – excitations 164, 167
 – tunneling 251
 – UPd_2Al_3 225, 226
 – $\text{YNi}_2\text{B}_2\text{C}$ 255
 quenching 302–304, 323, 328–330, 336, 350

 $R\text{-Ag-In}$ 29
 $R\text{-Cd-In}$ 33
 $R\text{-Cu-In}$ 7, 14
 $R\text{-Pd-In}$ 28
 $R\text{-Rh-In}$ 27
 $R\text{-Ru-In}$ 27
 $R\text{-Zn-In}$ 26
 $R_2\text{AgIn}_3$ 123
 $R_2\text{Au}_2\text{In}$ 109
 $R_2\text{CoIn}_8$ 88
 $R_2\text{Cu}_2\text{In}$ 89, 110
 $R_2\text{CuIn}_3$ 123
 $R_2\text{IrIn}_8$ 34, 112
 $R_2\text{Ni}_2\text{In}$ 89
 $R_2\text{Pd}_2\text{In}$ 109, 110
 $R_2\text{Rh}_2\text{In}$ 109
 $R_2\text{RhIn}_8$ 112
 $R_2T_2\text{In}$ 107
 $R_3\text{Ni}_3\text{In}_3\text{H}_4$ 100, 107
 $R_5\text{Ni}_2\text{In}_4$ 89
 racemization rate 301, 322
 $R\text{Ag}$ 29, 73
 $R(\text{Ag}_{0.25}\text{In}_{0.75})_2$ 69
 $R\text{Ag}_{0.5}\text{In}_{0.5}$ 118
 $R\text{Ag}_2\text{In}$ 120
 $R\text{Ag}_6\text{In}_6$ 124

- RAg_xIn_{1-x}* 73
RAu₂In 36, 118
RAuIn 106
RCdIn 69
RCO₂In 88
RCoIn₅ 88
RCu₂In 63
 reentrance behaviour 234, 263, 267
 restriction enzymes 407
RIn 29, 73
RIn₅ 34
 RKKY interaction 198, 223, 260, 261
RMnIn 106
 RNA hydrolysis 409, 427
 – by lanthanide ions 426, 430
 – sequence-selective scission 408
 – site-selective scission 431, 442, 445
RNi_{0.33}In_{1.67} 10
RNi₂B₂C 166, 248, 258
RNi₂In 88
RNi₃In₆ 87
RNiIn 3, 10
RNiIn₂ 87, 97
RNiIn₄ 87
RNiInH_{1.33} 100
 rotatory strength 298, 338
RPdIn 3, 103
RPt₂In 63
RPt₄In 117
RPtIn 3, 34
RRhIn 3
RRhIn₂ 97
RTIn 66
RZnIn 69

Sc–Cu–In 14
Sc_{1-x}PdIn_x 30
Sc₂Au₂In 37
Sc₂Cu₂In 15
Sc₂Ni₂In 11, 107, 121
Sc₂Pd₂In 30
ScAg₂In 32
ScAu₂In 37
ScCu₂In 15
ScNi₂In 11
ScNi₄In 11
ScPd₂In 30
ScPt₂In 35
ScPtIn 35
 silica gel 391, 397

 single nucleotide polymorphism
 – genotyping 448
 singlet pairing 153, 159, 162, 163, 174, 194, 204,
 211
 singlet state 146, 188
 site-selective scission 433
 size-selective separation 360
 skutterudites 165, 268
 slabs in
 – CeNi₅Sn and CeCu_{4.38}In_{1.62} 85
 – EuIn₄ 92
 – HoCoGa₅, Ho₂CoGa₈, MgCuAl₂, PrNiIn₂,
 YNiAl₄, LaCoIn₄, LaNi₃In₆, and Ce₂Au₃In₅
 94
 – HoCoIn₅ and Ho₂CoIn₈ 88
 – Mn₂AlB₂ and Cr₃AlB₄ 91
 – Nd₆Fe₁₃Si 86
 – Pr₅Ni₆In₁₁ and Ce₄Ni₇In₈ 89
 – TbCo₂In and Sm₂Co₉In₃ 90
 – ThMn₁₂ and in YNi₉In₂ 84
 slow diffusion 368, 377, 397
 – in gels 397
Sm–Cu–In 22
Sm₁₂Co₆In 9
Sm₁₂Ni₆In 13, 80
 – structure 76
Sm₁₂Ni₆In type 76, 82, 83
Sm₂AgIn₃ 32
Sm₂Au₂In 37
Sm₂Au₃In₅ 37
Sm₂Co₉In₃ 9, 89
 – structure 48
Sm₂Co₉In₃ type 48, 80, 88, 89
Sm₂CoIn₈ 9
Sm₂Cu₂In 16
Sm₂IrIn₈ 34, 114
Sm₂Ni_{2-x}In 13
Sm₂Ni₂In 13
Sm₂Pd₂In 30, 108
Sm₂Pt₂In 35
Sm₂Rh₂In 28
Sm₂RhIn₈ 28, 114
Sm₄Ni₇In₈ 12
Sm₄Pd₁₀In₂₁ 30
Sm₆Co₂In 9
Sm₆Fe₁₃In 7
SmAg₂In 32, 119, 120
SmAg_{3.5}In_{2.5} 32
SmAg_{5.4}In_{6.6} 32
SmAu₂In 37, 119

- SmAuIn 37
 SmCdIn 34
 SmCo₂In 9
 SmCoIn₅ 9
 SmCu_{0.5}In_{1.5} 16
 SmCu_{0.6-0.2}In_{1.4-1.8} 16, 22
 SmCu₂In 16
 SmCu_{4.38}In_{1.62} 16
 SmCu_{4.9-4.0}In_{0.1-1.0} 16
 SmCu_{4.9-4.0}In_{1.1-2.0} 22
 SmCu₄In 16
 SmCu_{5.1}In_{6.9} 16
 SmCu_{9.0-8.0}In_{2.0-3.0} 16, 22
 SmCuIn 16
 SmIrIn₅ 34, 114
 SmNi_{0.4-0.3}In_{1.6-1.7} 13
 SmNi_{0.5}In_{1.5} 13
 SmNi_{1.0-0.7}In_{1.0-1.3} 13
 SmNi₄In 12
 SmNi₅In 12
 SmNi₉In₂ 12
 SmNiIn 13
 SmNiIn₂ 12
 SmPdIn 30, 104
 SmPdIn₂ 30
 SmPt₄In 35, 118
 SmPtIn 35, 106
 SmPtIn₃ 35
 SmRhIn 28
 SmRhIn₂ 28
 SmRhIn₅ 28, 114
 SmZn₁₁ 80
 SmZn₁₁ type 81, 83
 SmZnIn 26
 sol-gels 293, 302, 322, 323
 specific area 390
 specific heat 169, 170, 252
 – CeCoIn₅ 195
 – PrOs₄Sb₁₂ 272
 – U_{1-x}Th_xBe₁₃ 247
 – UPt₃ 207
 – URu₂Si₂ 171, 239
 – YNi₂B₂C 177
 spin density wave 158, 162, 168, 179
 spin fluctuation 152, 197, 229
 spin orbit coupling 162, 203, 214
 succinate 391
 sugars 333
 superclean limit 176
 surface area 375
 susceptibility 224, 232, 233
 – UPd₂Al₃ 216
 symmetry group 160
 synthesis conditions of ternary indides 5, 6
 – annealing 6
 – arc-melting 4
 – high-frequency melting 6
 – indium flux 6
 T_c-splitting 207, 208, 271
 Tb–Cu–In 24
 Tb₁₄Co₂In₃ 9
 Tb₂AgIn 32
 Tb₂AgIn₃ 32, 123, 124
 Tb₂Au₂In 38, 108
 Tb₂CoIn₈ 9
 Tb₂Cu₂In 17, 108
 Tb₂CuIn₃ 17, 70, 122, 123
 Tb₂Ni_{2-x}In 13
 Tb₂Ni₂In 13
 Tb₂Pd₂In 31, 108
 Tb₂Pt₂In 36, 109
 Tb₃Pt₄In₁₂ 36
 Tb₆Co_{2.14}In_{0.86} 9
 Tb₆Pt₁₂In₂₃ 6, 36
 – structure 51
 Tb₆Pt₁₂In₂₃ type 49
 TbAg_{0.5}In_{0.5} 119
 TbAg_{1-x}In_x 32, 118
 TbAg₂In 32, 119
 TbAg_{3.5}In_{2.5} 32
 TbAu₂In 38, 119
 TbAuIn 38, 102, 106
 TbCo₂In 9, 61
 – structure 62
 TbCoIn₅ 9
 Tb(Cu_{0.25}In_{0.75})₂ 70
 TbCu_{0.56-0.32}In_{1.44-1.68} 17, 24
 TbCu₂In 17
 TbCu₅ 24
 TbCu₅₋₄In₀₋₁ 17
 TbCu_{5.1}In_{6.9} 17
 TbCuIn 17
 TbNi_{1.0-0.5}In_{1.0-1.5} 13
 TbNi₄In 13
 TbNi₉In₂ 13
 TbNiIn 13
 TbNiIn₂ 13, 63
 – structure 64
 TbPdIn 31, 102–104
 TbPdIn₂ 31

- TbPt₂In 36
 TbPt₄In 36, 118
 TbPtIn 36
 TbRhIn 28
 TbRhIn₅ 28
 terephthalate 379, 387
 – coordination polymer 378
 – organic groups 377
 tetracritical point 210
 Th_{1-x}U_xRu₂Si₂ 237
 Th₂Ni₁₇ type 45, 79, 82
 thermal conductivity 169, 171, 177, 252, 256, 272, 275
 – CeCoIn₅ 178
 – UPt₃ 213
 – YNi₂B₂C 257
 thermal expansion 240
 – PrOs₄Sb₁₂ 272
 – U_{1-x}Th_xBe₁₃ 246, 247
 – UPt₃ 209
 thermal stability 363, 364, 368, 376, 379, 381, 389, 391, 396
 ThMn₁₂ 88
 ThMn₁₂ type 40, 42, 79, 82, 84, 124
 ThMnIn 106
 ThTIn 3
 tight binding model 166, 180
 time reversal symmetry 160, 169, 180, 235, 241
 TiNiSi type 68, 79, 92, 105
 Tm–Cu–In 26
 Tm₁₀Co₉In₂₀ 10
 Tm₁₀Ni₉In₂₀ 14
 Tm_{14-x}Ni₃In_{3+x} 14
 Tm₁₄Co₂In₃ 10
 Tm₂AgIn 33
 Tm₂AgIn₃ 33
 Tm₂Au₂In 38, 71, 108
 – structure 72
 Tm₂CoIn₈ 10
 Tm₂Cu₂In 17, 108
 Tm₂CuIn₃ 122
 Tm₂Ni_{2-x}In 14
 Tm₂Ni₂In 14
 Tm₂Pd₂In 31, 108
 Tm₃Co₂In₄ 10
 Tm_{4,82}Ni₂In_{1,18} 74
 – structure 75
 Tm₅Ni₂In₄ 14
 Tm₆Co_{17,92}In₁₄ 10
 Tm₆Co_{2,14}Im_{0,86} 20
 Tm₆CuIn 26
 TmAg_{0,5}In_{0,5} 119
 TmAg₂In 33, 119
 TmAg_{3,5}In_{2,5} 33
 TmAu₂In 38, 119
 TmCo₄In 10
 TmCoIn₅ 10
 TmCu_{0,4-0,3}In_{1,6-1,7} 17, 26
 TmCu_{1,0-0,56}In_{1,0-1,44} 17, 26
 TmCu₂In 17
 TmCu₄In 17
 TmCu₅ 26
 TmCu₅₋₄In₀₋₁ 17
 TmCu_{5,1}In_{6,9} 17
 TmCuIn 17
 TmNi_{1+x}In_{1-x} 5
 TmNi_{1-0,6}In_{1-1,4} 14
 TmNi₄In 14
 TmNiIn 14
 TmPd₂In 31
 TmPdIn 31
 TmPdIn₂ 31
 TmPt₄In 36, 118
 TmPtIn 36
 TmRhIn₅ 28
 triplet pairing 153, 159, 162, 163, 174, 204, 211, 228, 235
 tunable physical properties 365
 U_{1-x}Th_xBe₁₃ 244
 U₂Pt₂Sn 80
 U₂Pt₂Sn type 71
 U₃Si₂ type 86, 100, 107
 UBe₁₃ 244
 UGe₂ 229
 ultrasonic attenuation 172
 – UPt₃ 173
 unconventional pairing 161, 163, 179, 241
 UNi₂Al₃ 228
 unitary state 207
 UPd₂Al₃ 146, 216
 UPdIn 101
 upper critical field 174, 210, 235, 252
 – CeCoIn₅ 195
 – HoNi₂B₂C 263, 267
 – UBe₁₃ 246
 – UGe₂ 234
 UPt₃ 146, 199
 URu₂Si₂ 179, 236
 UTIn 3
 V₂(OH)₄[C₆H₂(CO₂)₄].4H₂O 363
 Volovik effect 176

- volume of activation 328
 vortex phase 169, 175, 195, 215, 256, 267, 275
- W_2CoB_2 type 71, 109
 wave gap 254, 257
 Wiedemann–Franz law 183
- X-ray 299, 316, 321, 335, 336, 341
- $Y-Cu-In$ 18
 $Y_{1-x}Ce_xInCu_2$ 120
 $Y_{1.6}Ce_{0.4}Pd_2In$ 110
 $Y_{12}Ni_6In$ 11
 $Y_{14}Co_2In_3$ 9
 Y_2AgIn_3 32
 Y_2Au_2In 37
 Y_2CoIn_8 9
 Y_2Cu_2In 15
 $Y_2Ni_{2-x}In$ 11
 Y_2Ni_2In 11
 – structure 71
 Y_2Pd_2In 30
 Y_2Pt_2In 35
 $Y_6Co_{2.14}In_{0.86}$ 9
 YAg_2In 32
 $YAg_{3.5}In_{2.5}$ 32
 YAu_2In 37
 $YAuIn$ 37
 YCd_6 81
 YCd_6 type 81
 YCo_2In 9
 $YCoIn_5$ 9
 $YCu_{0.53-0.32}In_{1.47-1.68}$ 15, 18
 YCu_2In 15
 $YCu_{4.64-4.00}In_{0.36-1.00}$ 15, 18
 YCu_4In 15, 117
 $YCu_{5.1}In_{6.9}$ 15
 $YCuIn$ 15
 $YMnIn$ 7
 $YNi_{1-0.50}In_{1-1.50}$ 11
 $Y(Ni_{1-x}Pt_x)_2B_2C$ 255, 257
 YNi_2B_2C 250
 YNi_4In 11
 YNi_9In_2 11, 80, 81, 86, 88
 – structure 43
 YNi_9In_2 type 42, 79, 81, 84
 $YNiAl_4$ 87
 $YNiAl_4$ type 54, 79, 87, 92, 93
 $YNiIn$ 11
 $YNiIn_2$ 11
 YPd_2In 30
- $YPdIn$ 30, 105
 YPt_2In 35
 $YPIIn$ 35
 $YRhIn$ 27, 102
 $YRhIn_5$ 27
 $Yb-Cu-In$ 26
 $Yb_{0.4}Cu_2In_{0.6}$ 15
 $Yb_{0.5}In_{0.5}Ni_2$ 115
 $Yb_{0.8}Y_{0.2}InCu_4$ 117
 $Yb_{1-x}R_xInCu_4$ 117
 $Yb_{1-x}Y_xInCu_4$ 117
 Yb_2Au_2In 38, 109
 Yb_2Cu_2In 18, 26, 109
 – structure 71
 Yb_2Pd_2In 31, 108, 109
 $Yb_2Pd_6In_{13}$ 31
 – structure 44
 $Yb_2Pd_6In_{13}$ type 44
 Yb_2T_2In 109
 $Yb_xIn_{1-x}Cu_2$ 114–116
 $YbAg_{0.5}In_{0.5}$ 119
 $YbAg_2In_4$ 33, 80, 81, 124
 – structure 50
 $YbAg_2In_4$ type 49, 79
 $YbAg_{5.4}In_{6.6}$ 33
 $YbAgCu_4$ 116
 $YbAu_{1.27}In_{0.73}$ 38
 $YbAu_2In$ 38, 106, 119
 $YbAuIn$ 36, 38, 106
 $YbAuIn_2$ 38
 $YbCd_6$ 80, 82
 $YbCd_6$ type 81
 $YbCdIn$ 34
 $YbCoIn_5$ 10
 $YbCu_{4.8-4.0}In_{0.2-1.0}$ 17, 26
 $YbCu_4In$ 17, 114, 116
 $YbCu_{5.1}In_{6.9}$ 17, 26
 $YbIn_{0.9}Ag_{0.1}Cu_4$ 116
 $YbIn_{0.9}Au_{0.1}Cu_4$ 116
 $YbIn_{1-x}Ag_xCu_4$ 116
 $YbIn_2$ 97
 $YbInCu_4$ 116
 $YbNi_4In$ 14, 116
 $YbNiIn_4$ 14, 54
 – structure 55
 $YbPd_2In$ 120
 $YbPdIn$ 31, 104, 106
 $YbPdIn_2$ 31, 97, 122
 $YbPdIn_4$ 31
 $YbPtIn$ 36, 102, 105
 $YbPtIn_4$ 36

- YbRh₂Si₂ 198
YbRhIn 28
YbRhIn₄ 28, 54
– structure 55
YbRhIn₅ 28
YbTIn 6
YbTIn₂ 97
YbZnIn 26
- Zintl phase
– *AEIn*₂ 97
– *AETIn*₂ 97
Zr₃Al₂ type 80, 91, 100, 107
Zr₄Al₃ type 83, 84, 86
ZrNiAl type 26, 62, 66, 68, 79, 80, 100, 101, 104,
107
ZrPt₂Al 63
ZrPt₂Al type 63